SELCUK UNIVERSITY
FACULTY OF TECHNOLOGY

ICENTE'22

INTERNATIONAL CONFERENCE ON ENGINEERING TECHNOLOGIES

November 17-19, 2022

Konya/TURKEY

PROCEEDINGS BOOK

Editor
Prof. Dr Sakir TASDEMIR

E-ISBN: 978-605-72066-2-6

International Conference on Engineering Technologies

6th International Conference, ICENTE
Konya, Turkey, November 17-19, 2022

Proceedings Book

Editor
Sakir TASDEMIR

International Conference on Engineering Technologies, **ICENTE'22**
Konya, Turkey, November 17-19, 2022

6TH INTERNATIONAL CONFERENCE ON ENGINEERING TECHNOLOGIES

17-19 NOVEMBER 2022

Editör
Şakir TAŞDEMİR

EBOOK ISBN: 978-605-72066-2-6
KEYKUBAT YAYINLARI
Akademi Mah. Yeni İstanbul Cad. No:343 /Z01 Selçuklu / KONYA
MATBAA SERTİFİKASI: 46389

Konya Kasım 2022

KEYKUBAT YAYINLARI
Akademi Mah. Yeni İstanbul Cad. No:343 /Z01 Selçuklu / KONYA
T.C. KÜLTÜR BAKANLIĞI YAYINCI SERTİFİKASI: 46389

EDITOR :

Prof. Dr. Sakir TASDEMIR
Selcuk University, Turkey
Depertmant of Computer Engineering, Faculty of Technology
Alaeddin Keykubat Campus, 42031, Konya, TURKEY
stasdemir@selcuk.edu.tr

PREFACE

International Conference on Engineering Technologies (ICENTE'22) was organized in Konya, Turkey on 17-19 November 2022.

The main objective of ICENTE'22 is to present the latest research and results of scientists related to Biomedical, Computer, Electrics & Electronics, Mechanical, Mechatronics, Metallurgy & Materials and Civil Engineering fields. This conference provides opportunities for the delegates from different areas in order to exchange new ideas and application experiences, to establish business or research relations and to find global partners for future collaborations.

All paper submissions have been double blind and peer reviewed and evaluated based on originality, technical and/or research content/depth, correctness, relevance to conference, contributions, and readability. Selected papers presented in the conference that match with the topics of the journals will be published in the following journals:

- Artificial Intelligence Studies (AIS)
- Gazi Journal of Engineering Sciences (GJES)
- International Journal of Applied Mathematics, Electronics and Computers (IJAMEC)
- International Journal of Automotive Engineering and Technologies (IJAET)
- International Journal of Energy Applications and Technology (IJEAT)
- MANAS Journal of Engineering (MJEN)
- New Trends in Computer Sciences
- Open Journal of Nano (OJN)
- Selcuk University Journal of Engineering Sciences (SUJES)
- Intelligent Methods In Engineering Sciences (IMIENS)

At this conference, there are 260 paper submissions. Each paper proposal was evaluated by two reviewers. and finally, 215 papers were presented at the conference from 9 different countries (Turkey, Ukraine, Iraq, Macedonia, Algeria, Georgia, Tunisia, Romania, Albania) with 151 local and foreign universities and organizations participating,

In particular, we would like to thank Prof. Dr. Metin AKSOY, Rector of Selcuk University, conference scientific committee, session chairs, invited speakers, referees, technical team, participants, and all our colleagues who have contributed. They have made a crucial contribution to the success of this conference. Our thanks also go to our colleagues in our conference office.

Prof. Dr. Sakir TASDEMIR
Editor

PROGRAMME COMMITTEES

HONORARY CHAIR :

Metin Aksoy, Rector of Selcuk University, Turkey

GENERAL CHAIRS :

Sakir Tasdemir, Selcuk University, Turkey

SECTION EDITORS :

Adem Golcuk, Selcuk University, Turkey
Ali Yasar, Selcuk University, Turkey
Eyub Canli, Selcuk University – Turkey
Fatih Basciftci, Selcuk University, Turkey
Gokhan Arici, Selcuk University, Turkey
Ilkay Cinar, Selcuk University, Turkey
Ismail Saritas, Selcuk University, Turkey
Mehmet Cunkas, Selcuk University, Turkey
Murat Ciniviz, Selcuk University, Turkey
Mustafa Acarer, Selcuk University, Turkey
Mustafa Altin, Konya Technical University, Turkey
Yunus Emre Acar, Selcuk University, Turkey

INTERNATIONAL ADVISORY BOARD :

Abdullah Erdal Tumer, Kirgizistan Turkiye Manas University, Kyrgyzstan
Ahmet Yonetken, Afyon Kocatepe University, Turkey
Ahmet Fenercioglu, Gaziosmanpasa University, Turkey
Ahmet Afsin Kulaksiz, Konya Technical University, Turkey
Alexander Sudnitson, Tallinn University of Technology, Estonia
Alina Ivan Dramogir, Gheorghe Asachitechnical University Of Iasi, Romania
Almoataz Youssef Abdelaziz, Ain Shams University, Egypt
Amar Ramdane Cherif, University of Versailles, France
Anca Loana Andreescu, Academy of Economic Studies, Bulgaria
Anne Villems, University of Tartu, Estonia
Antonella Reitano, University of Calabria, Italy
Antonio Mendes, Universidade De Coimbra, Portugal
Arif Gok, Amasya Teknoloji Faculty, Turkey
Aristomenis Antoniadis, Technical University Of Crete, Greece
Artan Luma, South East European University, Macedonia
Bahattin Karakaya, Istanbul University, Turkey
Biagio Lenzitti, University of Palermo, Italy
Binod Kumar, Jspm Jayawant Institute Of Computer Applications Pune, India
Boris Akanaev, Kazak National University, Kazakhistan
Domenico Tegolo, Universita Degli Studi Di Palermo, Italy
Eisha Akanksha, Mvj College of Engineering, India
Elinda Kajo Mece, Polytechnic University of Tirana, Romania
Engin Ozdemir, Kocaeli University, Turkey
Erol Turkes, Kirklareli University, Turkey
Ertugrul Durak, Suleyman Demirel University, Turkey
Gabriel Luna Sandoval, Sonora State University, Mexico
Hamit Saruhan, Duzce University, Turkey
Hamza Bensouilah, Laboratoire de Mecanique et Structures, Algeria
Hasan Gokkaya, Karabuk University, Turkey

ORGANIZING COMMITTEE :

Abdullah Engin Ozcelik, Selcuk University, Turkey
Angel Smrikarov, Rousse University, Bulgaria
Ilker Ali Ozkan, Selcuk University, Turkey
Lilia Georgieva, Heriot Watt University, United Kingdom
Murat Koklu, Selcuk University, Turkey
Polyxeni Arapi, Technical University of Greece, Greece
Silyan Sibinov Arsov, Rousse University, Bulgaria

TECHNICAL COMMITTEE :

Abdulkadir Saday, Selcuk University, Turkey
Musa Dogan, Selcuk University, Turkey
Yusuf Eryesil, Selcuk University, Turkey

CONTENTS

THE EFFECT OF PULSE WIDTH AND FREQUENCY IN A MULTISCALE COMPUTATIONAL MODEL OF A SINGLE CELL **1**
MAHMUT EMIN CELIK
ECG ARTIFACTS REMOVING USING ZERO PHASE FILTERING **5**
SEMA YILDIRIM
ELELECTRONIC PERSONALITY AND THE LEGAL LIABILITY ARISING FROM ARTIFICIAL INTELLIGENCE AI **10**
ALPER UYUMAZ
INVESTIGATION OF THE EFFECT OF DATA AUGMENTATION ON TURKISH PARAPHRASE DETECTION **14**
ZEYNEP BANU OZGER,SERDAR ERTEM
ON THE USE OF TIME SERIES DATASETS THROUGH GOOGLE EARTH ENGINE TO MONITOR THE FOREST COVER LOSS IN TURKIYE BETWEEN 2001 AND 2021 **20**
CIGDEM SERIFOGLU YILMAZ
THE IMPACT OF RESEARCH AND CITATIONS ON WORLD RANKINGS OF COUNTRIES WITH THE BEST UNIVERSITIES **25**
LUAN GASHI,ARTAN LUMA,YLBER JANUZAJ
MOVING THE TEACHING FROM TRADITIONAL CLASS TO LEARNING MANAGEMENT SYSTEM HELPING STUDENTS LEARN FROM HOME **31**
BESNIK DURIQI,ARTAN LUMA,YLBER JANUZAJ,HALIL SNOPCE,AZIR ALIU
OPEN DATA IN EDUCATION A SYSTEMATIC REVIEW **35**
ARBNOR RUSHITI,ARTAN LUMA,YLBER JANUZAJ,AZIR ALIU,HALIL SNOPCE
A USE CASE FOR CUSTOMER SEGMENTATION IN THE SAVINGS FINANCE SECTOR USING DESCRIPTIVE ANALYTICS **42**
MURAT AYYILDIZ,ZEKERIYA KOSE,MUGE OLUCOGLU,CEVHERNUR SOYLEMEZ PEKTAS
HOW DO PANSHARPENING STRATEGIES AFFECT SPECTRAL INDICES ON WORLDVIEW 2 DATASETS **46**
VOLKAN YILMAZ
STATIC ANALYSIS OF MALWARE DETECTION USING MACHINE LEARNING ALGORITHMS **50**
NISA VURAN SARI,MEHMET ACI
A REVIEW ON DEEP LEARNING BASED METHODS DEVELOPED FOR LUNG CANCER DIAGNOSIS **54**
TURKAN BEYZA KARA,AHMET CEVAHIR CINAR
AGENT BASED MODELLING OF CELL CYCLE BEHAVIOR **59**
AYNUR SEN,KASSIM KINGALU,SEVCAN EMEK,SEBNEM BORA
DUPLICATION DETECTION IN VIDEOS USING DWT ALGORITHM **65**
ISILAY BOZKURT,GUZIN ULUTAS
A PERFORMANCE WAY COMPARISON OF DOCKER SWARM AND KUBERNETES **69**
ONUR YURTSEVER,EYUP EMRE ULKU

DUPLICATION FORGERY DETECTION BASED ON WEBER ALGORITHM **73**
ISILAY BOZKURT,GUZIN ULUTAS
DETECTION OF SUSPICIOUS ACTIVITIES ON WINDOWS SYSTEMS WITH LOG ANALYSIS **77**
ALI OZTURK,EYUP EMRE ULKU
AN EMPIRICAL ANALYSIS OF HOW USERS WITH DIFFERENT GENDERS ARE NOT EQUALLY AFFECTED BY THE RECOMMENDATIONS **81**
EMRE YALCIN
VOICE CONTROL OF VIRTUAL OBJECTS IN AUGMENTED REALITY APPLICATIONS **86**
TUBA EMEKLI COBAN,ALI OZTURK
ANALYSIS OF DRYING CHARACTERISTICS OF DRIED DAMSON PLUM BY MICROWAVE DRYING **92**
NECATI CETIN,BERFIN ALSAN,SANIYE IVECAN
THE EFFECT OF GRADUALLY INCREASING MICROWAVE POWER ON THE DRYING KINETICS COLOR PARAMETERS AND ENERGY ASPECTS OF CARROTS **97**
NECATI CETIN,SEDA GUNAYDIN
A CLASSIFICATION AND SHORT LITERATURE REVIEW ON 3D USER INTERFACE 3D UI SENSING TECHNOLOGIES **103**
COSKUN DENIZ
WORD CLOUD IMPROVEMENTS WITH NATURAL LANGUAGE PROCESSING TECHNIQUES FOR TURKISH LANGUAGE **108**
ANIL ATVAR,MUSTAFA ERSAHIN
USAGE AND PERFORMANCE COMPARISONS OF MACHINE LEARNING METHODS FOR TEXT CLASSIFICATION **113**
HASAN AKYOL,MUSTAFA ERSAHIN
DESIGN AND DEVELOPMENT OF SMART CONTRACT FOR PUBLIC ADMINISTRATION FOCUSED ON REAL ESTATE CERTIFICATES MANAGEMENT BY USING ETHEREUM AND IPFS **117**
ADMIRIM ALITI,MARIKA APOSTOLOVA,ARTAN LUMA
A REAL LIFE USE CASE FOR PREDICTING SALES OF BUS TICKETS **122**
HINCAL TOPCUOGLU,BEHCET MUTLU,CEVHERNUR SOYLEMEZ
THE NEXT GENERATION VIDEO PROCESSING TECHNOLOGY A GUIDE TO AWS DEEPLENS **125**
PINAR ERSOY,MUSTAFA ERSAHIN
THE INFLUENCE OF DONOR AND RECEIVER COMBINATIONS ON IMMUNE PLASMA PROGRAMMING IN SYMBOLIC REGRESSION PROBLEMS **131**
BEGUM YETISKIN,SIBEL ARSLAN
USING PERMISSIONED BLOCKCHAIN IN EDUCATION SYSTEM FOR INTERNSHIP **137**
OZGUR OKSUZ
A BORDA COUNT BASED INITIALIZATION METHOD FOR SELF ORGANIZING MAPS **143**
SUMEYRA SENOL,FIRAT ISMAILOGLU

EVALUATION OF TIME SERIES DECOMPOSITION ON STATISTICAL AND MACHINE LEARNING BASED FORECASTING MODELS **148**
ZEYNEP IDIL ERZURUM CICEK
A RECOMMENDATION SYSTEM STUDY ON USER PRODUCT DATA **152**
BEGUM UYANIK,GUNCE KEZIBAN ORMAN
ANALYSIS OF DATA SECURITY AND PRIVACY IN PUBLIC INSTITUTIONS ACCORDING TO GDPR IN THE REPUBLIC OF KOSOVO **159**
ELISSA MOLLAKUQE, ERSAN HAMDIU, NIDA SANTURI FISHEKQIU, SAMIR JAKUPI
COMPARISON OF FEATURE SELECTION METHODS IN THE ASPECT OF PHISHING ATTACKS **164**
ALI SENOL
DATA SECURITY ANALYSIS BASED ON DATA CLASSIFICATION ACCORDING TO DATA SENSITIVITY CASE STUDY DATA ON PUBLIC AND PRIVATE UNIVERSITIES IN THE REPUBLIC OF KOSOVO **168**
ELISSA MOLLAKUQE,VESNA DIMITROVA
ELECTROMAGNETIC COMPATIBILITY EMC SIMULATION AND APPLICATION IN AUTOMOTIVE ELECTRONICS **171**
ALPEREN YAZAR,METIN HUNER
IMPLEMENTATION OF MODIFIED KARNIK MENDEL ALGORITHM BASED INTERVAL TYPE 2 FUZZY INFERENCE SYSTEM FOR AIRCRAFT PITCH CONTROL **175**
MUHAMMET OZTURK,TARIK UNLER,GIZEM BEDENLI,SAKINE KURTAR,NUR YILDIRIM,TOLUNAY DAG
EFFECTS OF VOLTAGE SAGS ON VARIABLE FREQUENCY DRIVE IN INDUSTRIAL FACILITIES **181**
HALIL YASAR USTUNEL,OGUZHAN TIMUR
VIOLENCE DETECTION IN VIDEOS BASED ON DEEP LEARNING APPROACHES **184**
LEVENT CIVCIK,OSAMA ALKAYAL
ENSURING BUSH DEBURRING OPERATION PROCESS TRACEABILITY AND AUTOMATIC PROCESS CONTROL **190**
MUHAMMED ABDULLAH OZEL,SELIM SEFA BAYSAL,MUSTAFA ACARER
USING TEMPLATE MATCHING ALGORITHM IN WELDING ROBOTS **193**
LEVENT CIVCIK,MUHAMMED ALPEREN AKSIN
C BAND MICROSTRIP ANTENNA ARRAY ON PHOTOGRAPH PAPER SUBSTRATE **200**
DILEK UZER,AYSE OZGE CINAR,ZEYNEP IREM KOFUN,NEBI BERHAN TAS
ISM 2 4 GHZ BAND ANTENNA DESIGN FOR RF ENERGY HARVESTING SYSTEMS **204**
CEM GOCEN,ISMAIL AKDAG,MEHMET ALI BELEN,PEYMAN MAHOUTI,ADNAN KAYA,MERIH PALANDOKEN
THERMAL BEHAVIOR ASSESSMENT OF XLPE INSULATED MV POWER CABLES UNDER DIFFERENT CONDITIONS **207**
CIHAT CAGDAS UYDUR
DETERMINATION OF THE SAR VALUES OF THE ELECTROMAGNETIC FIELD EMITTED FROM THE PATCH ANTENNAS AT 900 MHZ AND 1800 MHZ FREQUENCIES **212**
UGUR SORGUCU

PULSE DENSITY MODULATION CONTROLLED HIGH FREQUENCY RESONANT CONVERTER FOR WIRELESS POWER TRANSFER SYSTEMS **215**
CEM KUTLU,HARUN OZBAY
DIGITAL CURRENCY TIME SERIES PREDICTION BASED ON FINANCIAL SIGNAL PROCESSING ANT COLONY OPTIMIZATION AND MACHINE LEARNING TECHNIQUES **220**
SECKIN KARASU,NEDIM AKTAN YALCIN
A METHOD TO IMPLEMENT TERNARY LOGIC GATES VIA MULTI THRESHOLD TRANSISTORS **225**
AHMET UNUTULMAZ
MATHEMATICAL MODELING AND SIMULATION OF SOLAR PHOTOVOLTAIC MODULE IN MATLAB SIMULINK **229**
MUSTAFA SACID ENDIZ
PRINCIPLES AND UTILIZATION OF A SINGLE PHASE Z SOURCE INVERTERS **234**
HUSSEIN AL BAYATY,FIDAN T SEDEEQ,MUNA SUDDEQ KIDER
STIFFNESS IN THE KNITTED FABRICS WITH VORTEX YARNS **238**
SEVAL UYANIK,PINAR DURU BAYKAL
THE EFFECTS OF HARD WASTE ON YARN QUALITY **242**
SEVAL UYANIK,FATMA DEMIRCI
LEVULINIC ACID PRODUCTION BY CATALYTIC DECOMPOSITION OF FRUCTOSE GLUCOSE AND CELLULOSE **245**
CHINGIZ NASIRLI,NIHAL CENGIZ,LEVENT BALLICE
FATIGUE PROPERTIES OF HOT DIP ALUMINIZED INCONEL 718 SUPERALLOY **249**
IBRAHIM GOKDEMIR,MERTCAN KABA,ERDEM BALCI,AHMET KAVUKCU,MURAT BAYDOGAN
INFLUENCE OF ALUMINUM OXIDE ON MAIN ELECTRICAL RESISTIVITY FEATURES OF BI 2212 CERAMIC COMPOUNDS **254**
MUHAMMED OZ,GURCAN YILDIRIM,CABIR TERZIOGLU
EFFECT OF ALUMINUM OXIDE ON MAIN SUPERCONDUCTING FEATURES OF BI2 1SR2 0CA1 1CU2 0OY CERAMICS **259**
MUHAMMED OZ, CABIR TERZIOGLU, GURCAN YILDIRIM
THE ATOMIC FORCE MICROSCOPY STUDY OF AMORPHOUS BISBTE THIN FILM WITH THE VARIOUS DEPOSITION PRESSURE **264**
MEHMET CETIN,GIZEM DURAK YUZUAK,ERCUMENT YUZUAK
FABRICATION AND CHARACTERIZATION OF ANODIC FILMS ON 304 STAINLESS STEEL **268**
NIHAN AGIRLAR,NIHAT CAN BAGCI,ECE ARKALI,CEVAT SARIOGLU,GORKEM YUMUSAK
SOUND PROBLEM OF SHIP ENGINES AND ITS EFFECT ON SEAFARERS **274**
OKAN BUYUKACAR,GULENAY ALEVAY KILIC,SEMIN KAYA
DYNAMICS ANALYSIS OF A HEAD NECK REHABILITATION ROBOT USING NEWTON EULER EQUATIONS **277**
ATILLA BAYRAM,AHMET SADIK DURU
TOWARDS AN EFFICIENT MAINTENANCE MANAGEMENT PLAN **282**
NOR EL HOUDA KHANFRI,NOUARA OUAZRAOUI,ANTAR SI MOHAMMED,HAFED TOUAHAR

RAPID LASER PROTOTYPED MICROFLUIDIC DEVICES FOR ON CHIP EMULSION GENERATION **287**
SINAN GUCLUER
INVESTIGATION OF THE EFFECT OF THE USE OF TOP DEFLECTORS ON AERODYNAMIC PERFORMANCE IN VEHICLES WITH CFD ANALYSIS **292**
HAYDAR KEPEKCI
NUMERICAL ANALYSIS OF LAMINAR HEAT TRANSFER FOR NANOFLUIDS IN A MICROCHANNEL **297**
ILKER GOKTEPELI,ULAS ATMACA
EASY TO CARRY AND MOBILE BIOGAS SYSTEM DESIGN **303**
RAHMI GUNDESLI,KUBRA BUYUKHAN
EVALUATION OF HEMP SEED IN THE FIELD OF ENERGY BIODIESEL PRODUCTION **307**
HIDAYET OGUZ,MERVE CELIK TOLU
LARGE DEFLECTIONS OF BI DIRECTIONAL FUNCTIONALLY GRADED CANTILEVER BEAMS **311**
AYHAN HACIOGLU,ADEM CANDAS,CEMAL BAYKARA
EXPERIMENTS AND SIMULATIONS OF A LIQUID CONTAMINANT PROPAGATION IN A VEGETATED BOTTOM CHANNEL **315**
ROMDHANE HELA,SOUALMIA AMEL
DETERMINATION OF GEOMETRICAL PROPERTIES OF FORMED SHEET METAL PARTS WITH 3D SCANNING METHOD **320**
MEVLUT AYDIN,OSMAN OZTURK,MEVLUT TURKOZ
A STUDY ON NANOBEAM WITH SPRING **324**
BURAK EMRE YAPANMIS
INVESTIGATION OF CLASSIC AND NON CLASSIC FUNCTIONALLY GRADED BEAMS MODEL **327**
BURAK EMRE YAPANMIS,SULEYMAN MURAT BAGDATLI
ANALYSIS OF POSITION LEVEL FORWARD KINEMATIC SINGULARITIES OF PLANAR RPRPR PARALLEL ROBOTS **331**
MUSTAFA OZDEMIR,LEVENT KARAKAYA
COMPARISON OF PLACEMENT HEURISTICS IN SIMULATED ANNEALING FOR THE ONE DIMENSIONAL CUTTING STOCK PROBLEM **335**
BANU ICMEN ERDEM,REFAIL KASIMBEYLI
EXPERIMENTAL STUDY AND GREY CORRELATION ANALYSIS OF UNCONSOLIDATED UNDRAINED TRIAXIAL COMPRESSION BEHAVIOR FOR GEOTEXTILE REINFORCED CLAY **339**
MUHAMMET NURI ODEMIS,MUGE ELIF ORAKOGLU FIRAT
MICROSTRUCTURE ANALYSIS OF RECYCLED FERROCHROME FILLED POLYMER CONCRETES CONTAINING SWCNT **345**
SERKAN SUBASI,FATIH DOGAN,HEYDAR DEHGHANPOUR,MUHAMMED MARASLI
REAL ESTATE VALUATION WITH REGRESSION ANALYSIS THE CASE OF MERAM DISTRICT OF KONYA PROVINCE **351**
TANSU ALKAN,OMER FARUK ATIZ,SULEYMAN SAVAS DURDURAN,MUHAMMED IKBAL BAYRAKDAR

DEVELOPING A NOVEL PHOTOGRAMMETRY METHODOLOGY IN CULTURAL HERITAGE DOCUMENTATION MARDIN MELIK MAHMUT MOSQUE **354**
IZZETTIN KUTLU,ASENA SOYLUK,ALI IHSAN UNAY
DETERMINATION OF G0 SHEAR MODULUS OF SANDY PUMICE SOIL **360**
IBRAHIM YIGIT,ABDURRAHMAN USAL,ELIFNUR SAKALAK
FUNDAMENTAL PERIODS OF ISOLATED BRIDGES WITH TALL COLUMN BENTS AND SOIL INTERACTION **363**
ALI IHSAN KARAKAS
ECONOMIC FEASIBILITY ASSESSMENT IN DESIGN OF SUSTAINABLE PREFABRICATED INDUSTRIAL BUILDINGS AND THE CASE STUDY OF DEMIR EKOSAN **369**
DENIZ CAGLA BAL,SELIN KOCA
MODAL ANALYSIS OF THE STEEL INDUSTRY STRUCTURE BY FINITE ELEMENT METHOD ACCORDING TO TBDY 2018 REGULATION **375**
HAKAN AYDIN
A CASE STUDY FOR VALIDATION OF KP505 PROPELLER OPEN-WATER CHARACTERISTICS VIA COMPUTATIONAL FLUID DYNAMICS **382**
MUHAMMED CINAR; HAKAN UCAR, FERHAT DIKMEN
ARCHITECTURAL RESEARCH OF THE INTERACTION BETWEEN THE STRUCTURAL SYSTEM OF BUILDINGS AND CURTAIN WALL: AN ANALYSIS ON SELECTED BUILDINGS IN ANKARA **388**
TUGCE ERARTSIN, ALI IHSAN UNAY
DESIGN OF A CMOS OPERATIONAL TRANSCONDUCTANCE AMPLIFIER FOR CURRENT CONTROLLED 2ND ORDER ACTIVE FILTER DESIGN **392**
SERHAN YAMACLI
BIOMASS ENERGY POTENTIAL, ITS CURRENT USAGE STATUS, AND DEVELOPMENTS IN BIOMASS ENERGY PRODUCTION SYSTEMS IN TURKEY **397**
FARUK KOSE, SULEYMAN KOSE
INVESTIGATION OF ENERGY SUPPLY OF A RESIDENTIAL AREA FROM RENEWABLE ENERGY SOURCES: THE CASE OF "OUR CITY-KONYA PROJECT" **402**
FARUK KOSE, ILHAN KOC
PULSATING PERFORMANCE TESTS OF HYDROFORMING PRESS **408**
OMER FARUK GOKCEPINAR, MEVLUT AYDIN, HARUN MERT ILBEYLI, MEVLUT TURKOZ, MURAT DILMEC, HUSEYIN SELCUK HALKACI
PCA-SVM-RANDOM SEARCH OPTIMIZATION BASED APPLICATION FOR CLASSIFICATION OF DATE FRUITS ACCORDING TO PHYSICAL PROPERTIES **413**
MUHAMMET FATIH ASLAN
A DESIGN STUDY FOR MEMS COMB-DRIVE RESONATOR **417**
SERDAR TEZ
LOW-COST ENERGY MANAGEMENT SYSTEM IN HOMES **421**
FURKAN ACUN, MEHMET CUNKAS

THE ROLE OF THICKNESS AND POSITION OF PARTIAL METAL FOAM IN JET IMPINGEMENT COOLING **428**
MELISA ALBAYRAK, KAYHAN DAGIDIR, BUGRA SARPER
THE IMPACT OF GEOMETRICAL PARAMETERS OF STENOSIS ON BLOOD FLOW MODELING **434**
ALI MUFTUOGULLARI, MELISA ALBAYRAK, MUNIR SUNER, BUGRA SARPER
INVESTIGATION AND OPTIMIZATION OF THE EFFECT OF ANHYDROUS BORAX MINERAL ON THE VICKERS HARDNESS AND INDENTATION MODULUS VALUES OF IRON MATERIAL **439**
SENOL SAHIN, AYSEGUL BODUR YILMAZ, TALHA TUNAHAN KESEMENLI
INVESTIGATION OF DIFFERENT AIR CURTAIN DESIGN IN INDUSTRIAL TYPE VERTICAL REFRIGERATOR CABINETS **444**
MEHMET HALUK ERDOGAN, SERCAN DOGAN, SERCAN YAGMUR, AZIZ HAKAN ALTUN
DEEP LEARNING RESEARCH IN DAMAGE DETECTION OF RC STRUCTURES **449**
BEYZA GULTEKIN, GAMZE DOGAN
AHP AND GIS BASED SITE SELECTION FOR MEDICAL WASTE DISPOSAL FACILITY KAHRAMANMARAS TURKOGLU DISTRICT **458**
OMER FARUK ATIZ, TANSU ALKAN, SULEYMAN SAVAS DURDURAN, SEVIM KAPUKAYA
PERFORMANCE OF AN UPSTREAM COFFERDAM AT DAM CONSTRUCTION SITE DURING A FLOOD EVENT BERDAN DAM CASE STUDY **462**
SERIFE PINAR GUVEL, MEHMET ALI AKGUL, SERIFE DUYGU BABACAN, SEDA SEVER, RECEP YURTAL
THERMAL BEHAVIOR OF RADIATOR IN PASSIVE LIQUID COOLING SYSTEMS FOR SPRING SEASON **467**
G ALEVAY KILIC
DEVELOPMENT OF A SURROGATE MODEL FOR DESIGN OF A PASSIVE VIBRATION ISOLATOR USED FOR AN INERTIAL MEASUREMENT UNIT **471**
COSKU VARDALLI, CEYHUN TOLA, OSMAN TAHA SEN
STRUCTURAL ANALYSIS FOR TOPOLOGY OPTIMIZATION OF A JET ENGINE BRACKET **478**
ALP TIMUCIN KOCAK, ISMAIL SARAC
AN INVESTIGATION OF HYPERSPECTRAL IMAGE FUSION STRATEGIES ON REAL DATASETS **483**
VOLKAN YILMAZ
EXAMINATION OF THE VERTICAL EARTHQUAKE FORCE ON A SAMPLE BUILDING WITH DIFFERENT OUTPUTS ACCORDING TO TEC 2018 **487**
FATMA BUSRA SELVI AKAY, ALPTUG UNAL, MUSTAFA KOCER
GEOMETRIC MEASUREMENT SYSTEM FOR ENGINE VALVE PARTS VIA MACHINE VISION **493**
MURAT AKDOGAN, ISRAFIL BAYRAM, AHMET DUZYOL, MEHMET ALI ARI

A REVIEW OF POWER LINE DISTURBANCES AND THEIR MITIGATION DEVICES **497**
HALIL YASAR USTUNEL, OGUZHAN TIMUR
INVESTIGATION OF EFFECTS OF COOLING CHANNELS ON FLOW PROPERTIES IN NASA C3X TURBINE BLADE **502**
MUHAMMED EMIN TOLU, OSMAN BABAYIGIT, DILEK NUR OZEN
THE ROLE OF THICKNESS AND POSITION OF PARTIAL METAL FOAM IN JET IMPINGEMENT COOLING **507**
MELISA ALBAYRAK, KAYHAN DAGIDIR, BUGRA SARPER
A NUMERICAL APPROACH FOR MODELING THE SHUNT DAMPING OF THIN PANELS WITH ARRAYS OF SEPARATELY PIEZOELECTRIC PATCHES **513**
PEYMAN LAHE MOTLAGH, MUSTAFA KEMAL ACAR

The Effect of Pulse Width and Frequency in a Multiscale Computational Model of a Single Cell

Mahmut Emin ÇELİK[1]

[1] Electrical Electronics Engineering, Faculty of Engineering, Gazi University, Ankara, Turkey,
mahmutemincelik@gazi.edu.tr

Abstract **- In the last decade, electrical stimulation has been frequently used clinically with significant progress to treat certain neurological and psychiatric disorders like Parkinson's disease, sensory restoration for patients suffering from loss of vision, hearing, and touch, resulting in improved quality of life. Most of the research covers neuron's responses to electrical stimulation. However, computational modeling with mathematical theory is a promising complementary approach to experimental studies. This work aims to show the effect of several electrical stimulation parameters such as pulse width and frequency on stimulation threshold. It includes a multi-scale approach that combines a 3-dimensional finite element head model for brain stimulation with a multi-compartmental pyramidal neuron with 3-dimensional morphology. An ideal point source was used for extracellular stimulation. NEURON v8.0 was used for building a computational neuron model. Electrical current threshold was analyzed while other parameters were constant. Frequency was 20 Hz and pulse width is 1 ms. Threshold was sought between 1-500 µA. Pulse width varied between 0.1 and 2.5 ms, while frequency ranges between 1 and 100. The increasing pulse width resulted in a significant decrease in the stimulation threshold to some extent. These results are consistent with the well-known experimental studies. Increasing frequency after a certain value decreased the threshold, which was related to the neuron's characteristics. It was concluded that realistic multi-scale computational models can be used to investigate parameter space in advance, providing valuable approximations before experimental works.**

Keywords **– computational, modeling, brain, electrical, stimulation.**

I. INTRODUCTION

THERE has been a growing interest in brain research toward improving the knowledge of the links between brain functions and neurological disorders for the last two decades. Implantable neural interface devices advance rapidly as an emerging technology for therapeutic purposes in clinical practice. Recording and stimulation functions bring considerable potential in medical applications. Continuous recording of neural activity can help us understand how local neurons function, process and retrieve information especially from different areas in the brain, which provides personalized, effective diagnosis and treatment [1-2]. Neural electrical stimulation is also used for therapeutic purposes like Parkinson's diseases and epilepsy [3-7] by applying small electrical pulses. Electric stimulation of viable neurons contributes greatly to the research on motor control, neural decoding, and neural therapy [8].

On the other hand, a neuroprosthetic device includes electrodes for recording or stimulation to restore lost sensory or motor functions. It can help people with neurological impairments such as visually impaired vision, spinal cord injury and stroke [9-13]. Microelectrode arrays (MEAs) are the most frequently used neural interfacing modality for research [14,15]. MEAs are implanted chronically or acutely to a targeted neural tissue so that they can either record electrical activity nearby or deliver electrical stimulation with high density to modulate neural activity precisely [16].

Computational modeling is used to examine technical and physiological factors affecting neural activity. Optimal stimulation settings and better understanding of the mechanisms can be provided. A neuron is divided into separate compartments that membrane voltage is approximated continuously based on cable theory. The number of compartments, the length of the neuron in addition to its experimentally validated biophysical properties mainly affects how accurate a multi-compartment model can mimic a real neuron.

The aim of this work is to investigate the effect of several electrical stimulation parameters, such as pulse width and stimulation frequency, on the neuron responses. This work includes a multi-scale computational model which couples two main parts, namely volume conductor head model and a neuron model. Electrical stimulation is performed by an ideal point source. First part outputs voltage gradient in each point, which is then applied to the neuron as an extracellular stimulation. Pyramidal neuron model has realistic 3-dimensional morphology. As two different stimulation pulse parameters, pulse width is varied between 0.1 and 2.5 ms while frequency ranges between 1 and 100. Stimulation current formation is observed and current threshold is determined considering membrane potential that crosses 0 V line after stimulation onset.

II. Materials and Methods

The computational model of intracortical stimulation is used to evaluate action potential generation and stimulation threshold. There are two main parts of the computational model (i) finite element model (FEM) of head with implanted electrode, and (ii) multi-compartmental cable model of neuron from sensory cortex. The action potential generation and stimulation threshold are examined depending on the electrode size and distance to the neuron. The extracellular voltages generated by the electrode near itself are calculated and taken from the FEM. Then, the extracellular voltages of different circumstances are applied to the neuron model to see its response. The flowchart is presented in Fig. 1. Electrical stimulation settings are used to prepare FEM model. This is then coupled to the neuron model consisting of different neural compartments, morphology, and biophysical properties.

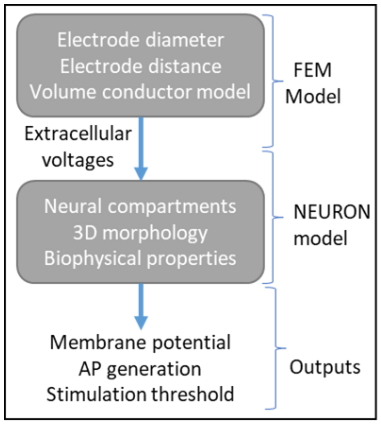

Figure 1: Flowchart of the work.

A. Volume Conductor Head Model

Three-dimensional head model is developed to calculate the extracellular voltages due to electrical stimulation. The head model has a layered structure with 4 concentric spheres representing scalp, skull, cerebrospinal fluid and brain. The electrode is placed to the brain region near the neuron to perform an intra-cortical electrical stimulation. Electrical conductivities of each layer are assigned according to the previous values in the literature [17]. Electrical stimulation is delivered via an ideal point source which is placed near the neuron in the brain. Resulting voltages at each coordinate in the finite element model of the head is determined under quasi-static conditions and resistive homogeneous tissue assumptions.

B. Multicompartmental Cable Model of Neocortical Pyramidal Neuron

A neocortical pyramidal neuron with 190 sections in total consisting of soma, dendrite and axon is used. It has a realistic three dimensional morphology complying with neocortex area. Biophysical properties of the neuron are determined based on Mainen's pyramidal neuron model [18]. Simulations are performed using NEURON v8.0 with dt=0.01. Stimulation pulse is a monophasic, anodic, pulse, with width of 1 ms and frequency of 20 Hz. Simulation time is 25 ms. When the frequency is varied, the pulse width is 0.5 ms to show any possible change better. Threshold current is defined as the lowest current amplitude that generates an action potential for a single stimulation pulse.

The Hodgkin–Huxley model explains how action potentials are formed and propagated in squid giant axon using voltage-dependent ion channels that refer nonlinear differential equations [19]. There were three types of ions, namely sodium, potassium, and a leak current with Cl− ions mostly. Between intracellular and extracellular region of the cell, the Hodgkin–Huxley model was shown in Fig. 2. In the model, C referred the capacitor of the cell membrane, each type of channels was presented by a resistor. Leak resistance was shown by R while ion channels' resistances were presented by varying resistors R_{Na} and R_K. Different Nernst potentials for each ion type and leak were given by E_{Na}, E_K and E_L. The current I acts as an input current injected to the cell.

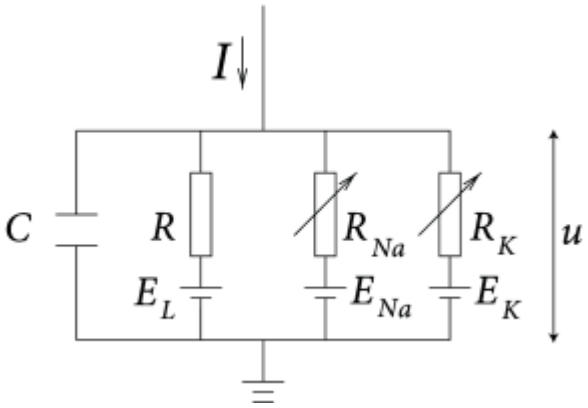

Figure 2: Hodgkin-Huxley model for the cell.

III. Results

The neuron model replicates experimental data of the corresponding neuron type, resulting to predict neuron's response to electrical stimulation. After checking the neuron is viable, the stimulation threshold is calculated for each case while either pulse width or frequency is varied. Electrode position was fixed, enough close to the cell to trigger an action potential. When a single stimulation pulse is applied, membrane voltages of different compartments are presented in Figure 3. It shows that action potential is generated and propagated through all compartments properly. This part validates that 3-d morphology is successfully connected to each other, enabling propagation of action potential from/to any section of the neuron.

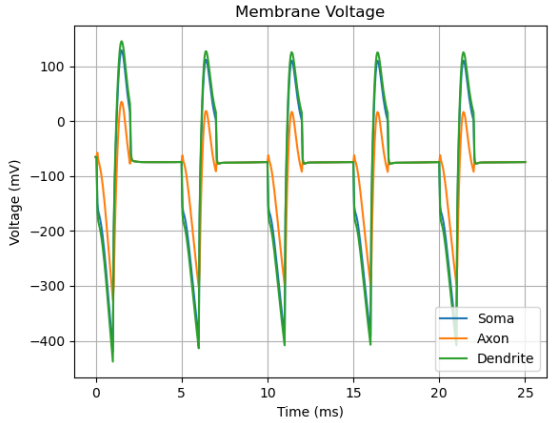

Figure 3: Membrane potential from different compartments.

The effect of varying pulse width and frequency on stimulation threshold are then examined. Threshold current is determined for each pulse width and frequency separately. Fig 4 shows how threshold changes depending on increasing pulse width and frequency. When the effect of pulse width on threshold is analyzed, it is seen that increasing pulse width results in a significant decrease in threshold. Additionally, pulse width that is greater than 1 ms has a limited effect on the threshold compared to the interval up to 1 ms.

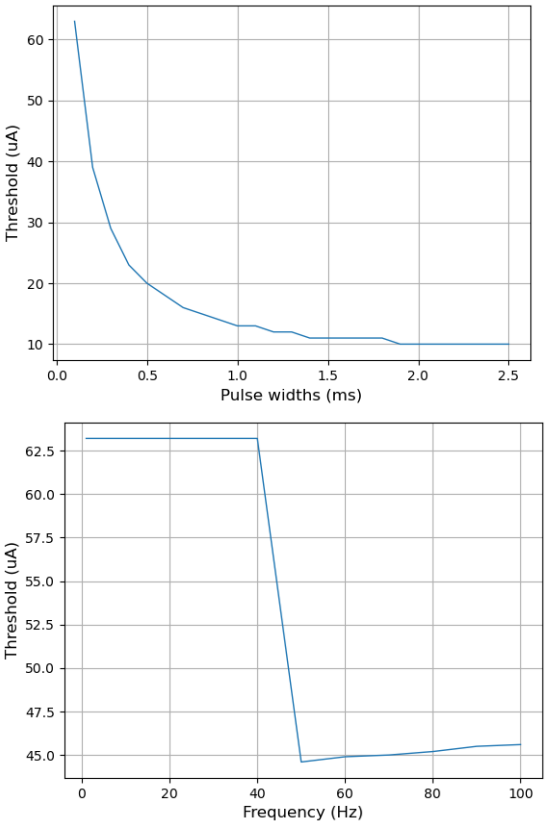

Figure 4: Stimulation threshold for varying pulse width and frequency.

Frequency affected the threshold significantly after 40 Hz which is primarily dependent to the neuron's characteristics. Denser frequency interval can show its effect better.

It is mostly desirable to stimulate each neuron with a single separate electrode, it does not seem possible because of biological and technical constraints for now. Previous works show that the change in stimulation electrode size, shape and stimulation pulse parameters affect neural responses to electrical stimulation [20-23].

The threshold difference is comparatively apparent at low pulse widths, it becomes lower and then negligible for higher pulse widths. Similarly, stimulation frequency can affect threshold depending on the neuron's dynamics. These findings are consistent with the previous literature and well-known [24-29].

IV. Conclusions

This work includes both a realistic volume conductor model and a neuron model with realistic 3D morphology and biophysical properties. Recent decades witnessed remarkable technical advancements on how to use electrical stimulation for therapeutic purposes for some of neurological disorders. Clinical research and experiments with animal and human subjects can be optimized by integrating multi-scale computational models. Realistic computational models are very useful tools to make a research plan and to calculate lower and upper limits of parameters for an animal experiment.

References

[1] Kandel, E. R., Schwartz, J. H., Jessell, T. M., Siegelbaum, S., Hudspeth, A. J., & Mack, S. (Eds.). (2000). Principles of neural science (Vol. 4, pp. 1227-1246). New York: McGraw-hill.

[2] Nicolelis, M. A., & Lebedev, M. A. (2009). Principles of neural ensemble physiology underlying the operation of brain–machine interfaces. Nature reviews neuroscience, 10(7), 530-540.

[3] Olchik, M. R., Ghisi, M., Ayres, A., Schuh, A. F. S., Oppitz, P. P., & Rieder, C. R. D. M. (2018). The impact of deep brain stimulation on the quality of life and swallowing in individuals with Parkinson's disease. International archives of otorhinolaryngology, 22, 125-129.

[4] Naesström, M., Blomstedt, P., & Bodlund, O. (2016). A systematic review of psychiatric indications for deep brain stimulation, with focus on major depressive and obsessive-compulsive disorder. Nordic journal of psychiatry, 70(7), 483-491.

[5] Sprengers, M., Vonck, K., Carrette, E., Marson, A. G., & Boon, P. (2017). Deep brain and cortical stimulation for epilepsy. Cochrane Database of Systematic Reviews, (7).

[6] Ryvlin, P., Rheims, S., Hirsch, L. J., Sokolov, A., & Jehi, L. (2021). Neuromodulation in epilepsy: state-of-the-art approved therapies. The Lancet Neurology, 20(12), 1038-1047.

[7] Seo H and Jun SC (2017) Multi-Scale Computational Models for Electrical Brain Stimulation. Front. Hum. Neurosci. 11:515. doi: 10.3389/fnhum.2017.00515

[8] Pan, T., & Zou, Y. (2022). Fully Implantable Neural Stimulator with Variable Parameters. Electronics, 11(7), 1104.

[9] Ethier C, Oby ER, Bauman MJ, Miller LE. Restoration of grasp following paralysis through brain-controlled stimulation of muscles. Nature. 2012 May 17;485(7398):368-71. doi: 10.1038/nature10987. PMID: 22522928; PMCID: PMC3358575.

[10] Velliste, M., Perel, S., Spalding, M. C., Whitford, A. S., & Schwartz, A. B. (2008). Cortical control of a prosthetic arm for self-feeding. Nature, 453(7198), 1098-1101.

[11] Barriga-Rivera, A., Bareket, L., Goding, J., Aregueta-Robles, U. A., & Suaning, G. J. (2017). Visual prosthesis: interfacing stimulating electrodes with retinal neurons to restore vision. Frontiers in neuroscience, 11, 620.

[12] Yue, L., Weiland, J. D., Roska, B., & Humayun, M. S. (2016). Retinal stimulation strategies to restore vision: Fundamentals and systems. Progress in retinal and eye research, 53, 21-47.

[13] Ayton, L. N., Barnes, N., Dagnelie, G., Fujikado, T., Goetz, G., Hornig, R., ... & Petoe, M. A. (2020). An update on retinal prostheses. Clinical Neurophysiology, 131(6), 1383-1398.
[14] Luan, L., Robinson, J. T., Aazhang, B., Chi, T., Yang, K., Li, X., ... & Xie, C. (2020). Recent advances in electrical neural interface engineering: minimal invasiveness, longevity, and scalability. Neuron, 108(2), 302-321.
[15] Luan, L., Robinson, J. T., Aazhang, B., Chi, T., Yang, K., Li, X., ... & Xie, C. (2020). Recent advances in electrical neural interface engineering: minimal invasiveness, longevity, and scalability. Neuron, 108(2), 302-321.
[16] Lee, H. S., Eom, K., Park, M., Ku, S. B., Lee, K., & Lee, H. M. (2022). High-density neural recording system design. Biomedical Engineering Letters, 1-11.
[17] Moffitt, M. A., & McIntyre, C. C. (2005). Model-based analysis of cortical recording with silicon microelectrodes. Clinical neurophysiology, 116(9), 2240-2250.
[18] Mainen, Z. F., Joerges, J., Huguenard, J. R., & Sejnowski, T. J. (1995). A model of spike initiation in neocortical pyramidal neurons. Neuron, 15(6), 1427-1439.
[19] Hodgkin, A. L., & Huxley, A. F. (1952). A quantitative description of membrane current and its application to conduction and excitation in nerve. The Journal of physiology, 117(4), 500.
[20] Paknahad, J., Loizos, K., Humayun, M., & Lazzi, G. (2020). Targeted stimulation of retinal ganglion cells in epiretinal prostheses: A multiscale computational study. IEEE Transactions on Neural Systems and Rehabilitation Engineering, 28(11), 2548-2556.
[21] Çelik, M. E. (2021). Multi-Compartmental Modeling for Extracellular Stimulation of Neocortex . Avrupa Bilim ve Teknoloji Dergisi , Ejosat Special Issue 2021 (ISMSIT) , 76-80 . DOI: 10.31590/ejosat.1013879
[22] Celik, M. E. (2021, October). Spiking Activity of L5 Pyramidal Neuron: A Computational Modeling. In 2021 5th International Symposium on Multidisciplinary Studies and Innovative Technologies (ISMSIT) (pp. 778-780). IEEE.
[23] Celik, M.E., Karagoz, I. Comparison of Monophasic and Biphasic Electrical Stimulation by Using Temporal Analysis for Different Inter-electrode Spacings in the Hexagonal Arrays. Arab J Sci Eng 43, 2889–2898 (2018). https://doi.org/10.1007/s13369-017-2918-z.
[24] Shannon, R. V. (1992). A model of safe levels for electrical stimulation. IEEE Transactions on biomedical engineering, 39(4), 424-426.
[25] Stuart F Cogan et al 2016 J. Neural Eng. 13 021001.
[26] McIntyre, C. C., & Grill, W. M. (2001). Finite element analysis of the current-density and electric field generated by metal microelectrodes. Annals of biomedical engineering, 29(3), 227-235.
[27] Fried, S. I., Lasker, A. C., Desai, N. J., Eddington, D. K., & Rizzo 3rd, J. F. (2009). Axonal sodium-channel bands shape the response to electric stimulation in retinal ganglion cells. Journal of neurophysiology, 101(4), 1972-1987.
[28] Jeng, J., Tang, S., Molnar, A., Desai, N. J., & Fried, S. I. (2011). The sodium channel band shapes the response to electric stimulation in retinal ganglion cells. Journal of neural engineering, 8(3), 036022.
[29] Paul Werginz et al 2020 J. Neural Eng. 17 045015.

ECG Artifacts Removing using Zero-Phase Filtering

Sema YILDIRIM

Selcuk University, Konya/Turkey, semayildirim@selcuk.edu.tr

Abstract **- In addition to cerebral activities in the brain, electrical activities originating from places outside the brain are also recorded with Electroencephalogram (EEG). Since the waveforms of these signals, called artifact, are measured like real brain waves, removing these artifacts from EEG signals is extremely important for diagnosis and treatment. Therefore, in this study, Zero Phase Filtering method is proposed to remove Electrocardiogram (ECG) artifact from EEG recordings. The performance of this method was tested using the Boston's Beth Israel Hospital Sleep Laboratory (MIT-BIH) Polysomnographic EEG dataset. The results obtained using various statistical performance measurement methods showed that the Zero Phase Filtering method is an effective method for removing ECG artifacts in the EEG signal. With this proposed method, almost all cerebral activity was preserved, while ECG artifacts were successfully removed.**

Keywords **- Artifact, brain, electroencephalogram, electrocardiogram, zero phase filtering.**

I. INTRODUCTION

Electroencephalography (EEG) is a method where the electrical circumstances on the brain are recorded. Furthermore, EEG records the electrical circumstances occurring from different areas other than brain, which are named as artifacts. Therefore, it is extremely considerable to eliminate artifacts from the analog EEG signals (EEGs) [1]. It is very difficult to analyze EEGs that are distorted by artifacts. These artifacts affecting EEGs are divided into two main categories: physiological (eye movement, muscle activity, Electrocardiogram (ECG)) and extra-physiological artifacts (50 Hz power grid noise, electrode artifact) [2].

EEG technicians can modify the recording protocol as needed to eliminate artifacts interfering with the brain waves. On the other hand, they must record the contaminated EEGs when modification is not possible [3]. Despite the advances in technology, the EEG recordings are mostly interpreted manually. Manual review/examination of EEG recordings of 20-30 minutes or even hours takes quite a long time [4], [5]. To make a faster and more accurate diagnosis, various signal processing algorithms and computer programs have been developed in recent years [6]. One of these studies, Yang and Ma (2015) have been used Discrete Wavelet Transform (DWT) algorithm to remove ECG features from original signals [7]. In a similar study, Park et al. (2015) have been present the method of the rejection of the same artifact from the sleep EEG. They have been used the Lagrange Polynomial Interpolation and Least Square Error AR Interpolation to recover the missing ECG R-wave segment [8]. In another study, Vázquez et al. (2012) have been proposed some techniques like blind source separation (SOBI-RO), noise removal and supervised classification methods to remove various artifacts [9]. In a different study, Routray et al. (2018) have been used an adaptive artifact removal method using the Functional Link Adaptive Neural Network-three layered Radial Basis Functional Network (FLANN-RBFN) algorithm for ECG artifact reduction in the MIT-BIH dataset [10]. On the other hand, Jafarifarmand and Badamchizadeh (2018) proposed a new approach using a hybrid of Independent Component Analysis (ICA) and Adaptive Noise Reduction (ANR) to remove real-time ECG artifacts from EEGs. In this compound method, BBA is used to obtain the reference signal of ANR. The method was applied to several EEG channels without simultaneous ECG channels. With this study, cardiac artifacts were removed efficiently while preserving cerebral information [11]. In a different artifact removing study, Dora and Biswal (2020) have been used the mVMD method to decompose the EEGs. ECG artifact components were defined by using the correlation between mode functions obtained in the study. Along with the predicted ECG reference, the QRS-complexes were suppressed, thus eliminating the ECG artifact [12].

There are many techniques in the literature for removing artifacts on the EEGs. In this study, a new method of removing ECG artifact is presented using Zero-Phase Filtering. The purpose of this method is to eliminate losses in the EEGs while removing ECG artifact.

This study for extracting ECG signals from EEGs is organized as follows. In Section II, the methods that form the basis of the whole study and the datasets used are mentioned. The experimental results obtained with the performed method are discussed in Section III. Finally, Section IV presents a brief summary of the study and the scope of future research.

II. METHODOLOGY

A. ECG Artifacts in EEG Signals

An international standard has been developed for the connection types of electrodes placed on the scalp so that the signals produced by the brain can be measured. According to this international standard, electrodes are usually placed taking

into account the 10-20 standard and its versions [13]. The frequency of a EEGs is between 0.01 Hz and 100 Hz. In addition to this, its voltage ranges from a few microvolts to 100µV. Since artifacts can easily interfere with such low frequency EEGs, the analysis and interpretation of the signal is very difficult [10]. By removing the artifacts in the EEGs, it will be possible to analyze the significant wave(s) in the signals in a shorter time [14].

ECG artifacts are caused by connecting EEG electrodes to any vein or artery [15]. ECG artifacts can be measured with the characteristic regular pattern and recorded with cerebral activity. Therefore, it is relatively easy to remove such artifacts using only one reference waveform [16]. ECG artifact can be seen in all channels as well as in a few channels as shown Figure 1 and 2.

Figure 1: Ipsilateral ear referential montage (Cardiac artifacts) [17].

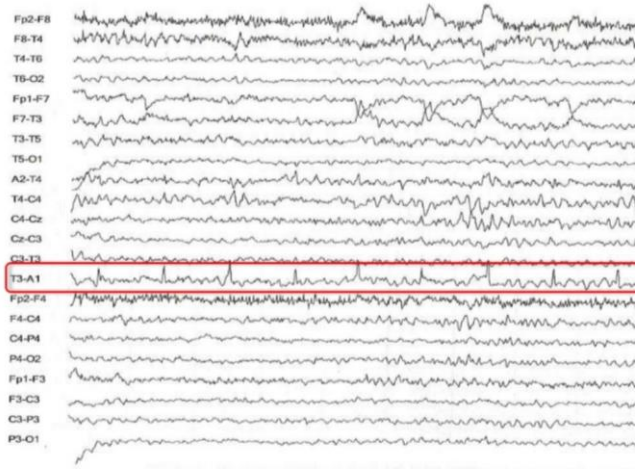

Figure 2: ECG artifact with constant period and morphology in channel T3-A1 in bipolar montage (Cardiac artifacts) [17].

B. Zero-Phase Filtering

Artifacts in the EEGs can be removed by filtering methods. While unwanted signals are prevented by filtering, signals suitable for the operation of the system are filtered. In this study, the Zero Phase Filtering (ZPF) method was used to eject the ECG artifact in the EEGs. The ZPF method preserves the original QRS-complexes while reducing artifact in EEGs, which are difficult and complex to interpret. While performing zero-phase digital filtering with the ZPF method, the input data is first filtered forward and then backward. After further filtering, the filtered string is retrieved and filtered again. The resulting new array will have zero phase distortion. Thus, the filter order is doubled. It also sets the initial conditions for the signal to match the DC component. Additionally, it tries to minimize first passes by using an inverted version of the input signal and several filter lengths of a mirrored copy [18].

C. Dataset

In this study, the publicly available Physionet database (MIT–BIH Polysomnography Data) was used to remove ECG artifacts in EEGs. This dataset consists of EEGs recordings recorded during sleep. Signals for subjects in the database were recorded at the Sleep Laboratory of Beth Israel Hospital in Boston to test the effects of constant positive airway pressure (CPAP). Over 80 hours, these recordings include an ECG signal, an invasive blood pressure signal (measured using a catheter in the radial artery), a EEGs, and a respiratory signal (in most cases from a nasal thermistor). The sampling rate of the obtained signals is 250 Hz. Ages of 16 subjects included in this database ranged from 32 to 56. In addition, the average age range of the records in the database is 43. Records slp01a and slp01b are segments of one subject's polysomnogram, separated by a gap of about one hour; records slp02a and slp02b are segments of another subject's polysomnogram, separated by a ten-minute gap. The remaining 14 records are all from different subjects [19]. Some features of the records in the MIT-BIH dataset are given in Table 1.

Table 1: Some information of the records in the MIT-BIH dataset.

Record	length	EEG
slp01a	2:00	2 (C4-A1)
slp01b	3:00	2 (C4-A1)
slp02a	3:00	2 (O2-A1)
slp02b	2:15	2 (O2-A1)
slp03	6:00	2 (C3-O1)
slp04	6:00	2 (C3-O1)
slp14	6:00	2 (C3-O1)
slp16	6:00	2 (C3-O1)
slp32	5:20 am	2 (C4-A1)
slp37	5:50	2 (C4-A1)
slp41	6:30 pm	2 (C4-A1)
slp45	6:20	2 (C3-O1)
slp48	6:20	2 (C3-O1)
slp59	4:00	2 (C3-O1)
slp60	5:55	2 (C3-O1)
slp61	6:10 am	2 (C3-O1)
slp66	3:40	2 (C3-O1)
slp67x	1:17	2 (C3-O1)

III. Experimental Results

Since the EEGs consists of signals coming from the brain and outside the brain, it has a very complex structure. Therefore, its interpretation and analysis is quite difficult compared to other signals. Despite these negative aspects, it still continues to be an important tool for diagnosis and treatment due to its low cost. However, long-term EEG recordings are needed to obtain accurate information for diagnosis and treatment from EEGs. However, examining such long EEG recordings is a time-consuming and costly process. In addition, wave/waves (spiked waves, sharp waves etc.) that are important for diagnosis are overlooked during the examination of long EEG recordings. Especially in a non-artifact EEGs, it is more difficult to reach meaningful information. Considering all these situations, it is necessary to eliminate the artifacts in the EEGs in the best way. The method used in this study to get out ECG artifact from EGGs is demonstrated in Figure 3 with a flowchart.

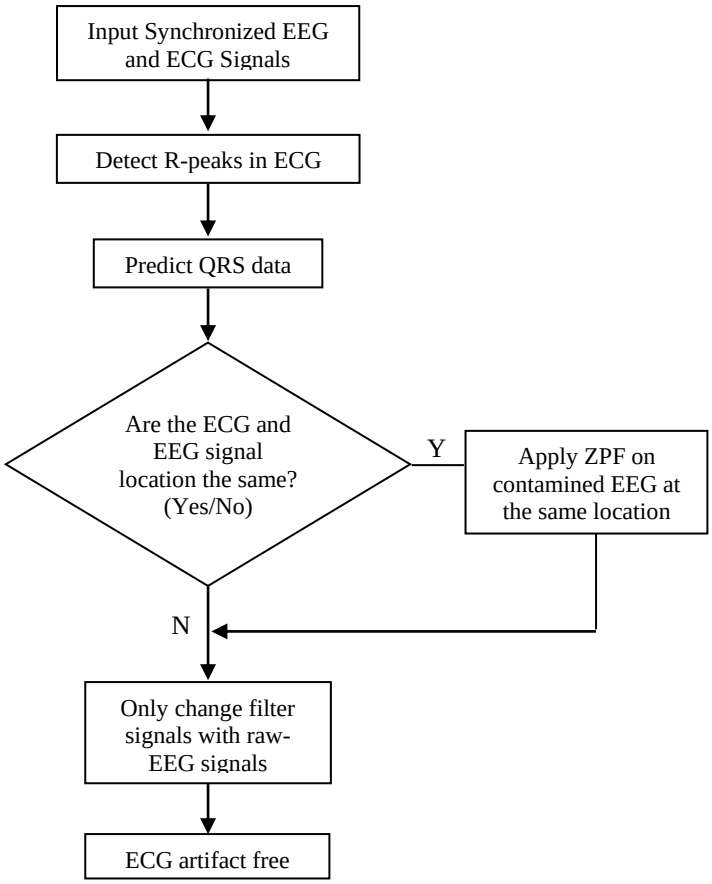

Figure 3: Flowchart of ECG artifact removing in EEGs.

Although the ECG signal has a regular pattern, its amplitude and frequency can be different, as seen in Figure 4. In such cases, ECG artifact will appear in different forms in the EEGs. Therefore, in this study, instead of ECG signal synchronization for ECG artifact reduction, artifact reduction was performed by using QRS-complexes and positions in the existing ECG signal.

Figure 4: An example of an ECG signal.

Elimination of artifact in the EEGs is a situation that requires attention. The purpose of artifact reduction is to both remove the artifact in the EEGs from the EEGs in the best way and not to lose the information in the EEGs during artifact reduction. Otherwise, potentially important information in the EEGs may be lost when the entire EEGs is filtered out. Therefore, the filtering process was applied only where QRS-complexes were present.

The first step in detecting the QRS-complex is the detection of the R wave. In the study, a ready-made function R-peak-detection.m is used for the detection of R waves. Then, QRS-complexes were determined by means of these R waves (Figure 5).

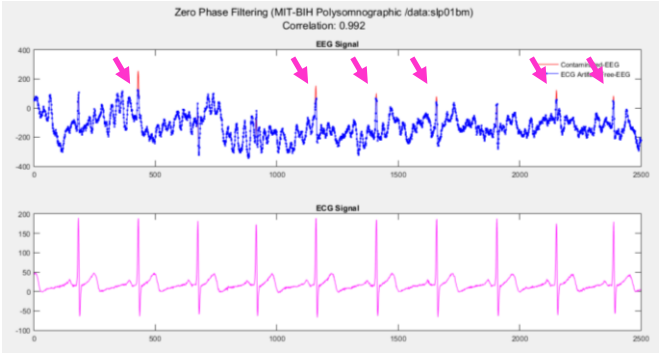

Figure 5: Removing ECG artifacts in EEGs.

Table 2: Results obtained for removing ECG artifact from EEGs by ZPF method.

Record	Correlation	R-peak number on ECG

	(R)	signal
slp01a	0.995	20253
slp01b	0.992	25009
slp02a	0.993	95454
slp02b	0.987	81383
slp03	0.995	61354
slp04	0.975	276855
slp14	0.992	93205
slp16	0.991	111741
slp32	0.994	30719
slp37	0.963	157507
slp41	0.994	35562
slp45	0.995	32715
slp48	0.994	21472
slp59	0.996	14875
slp60	0.997	7994
slp61	0.996	11906
slp66	0.995	63377
slp67x	0.994	39577

The correlation value was checked to determine the accuracy of this research as given Table 2. As is known, correlation determines the direction and strength of the linear relationship between two random variables. Correlation values in this study were found to be quite high as seen in Table 2. These values show that there is no major change in the filtered EEGs, and the pre- and post-filter EEGs is almost preserved while removing. This is because only the ECG signal that overlaps with the EEGs is filtered out. Thus, the EEGs is more accurately output while the EEGs is generally preserved. As a result, it can be said that the EEGs is not lost while the ECG signal is extracted with this study. Thus, since the important waves in the EEGs are not lost, the experts who will interpret the signal will be able to examine the noise-free EEGs more easily and quickly.

In Table 3, ECG artifact reduction studies in the literature are given chronologically. As can be clearly seen in Table 3, these studies were performed using the MIT-BIH dataset. Of these studies, Issa et al. (2019) and Jiang et al. (2007) tried to eliminate the ECG signal without using a reference. In other studies, artifact reduction has been performed using QRS-complexes. In this study, artifact removal was performed using QRS-complex waves of the ECG signal.

Table 3: Studies in the literature for ECG removing.

Author(s)	Dataset(s)	Materials and Methods
(Jiang et.al., 2007) [21]	MIT-BIH Polysomnography, NTUH (National Taiwan University Hospital, Department of Neurology)	Performance measurement by using Adaptive Thresholding (ADT) and Continuous Wavelet Transform (CWT) without using ECG reference signal.
(Thomas et.al., 2015)[23]	MIT-BIH Arrhythmia	Dual-Tree Complex Wavelet Transform (DTCWT) and Multilayer Artificial Neural Network (MNN) to extract QRS-complex features.
(Dora and Biswal, 2016) [24]	MIT/BIH Polysomnography, MIT/BIH Arrhythmia, CAP Sleep	Regression analysis to remove artifact. QRS estimation with R-peak.
(Dora and Biswal, 2019) [25]	MIT-BIH Polysomnography	Modified S-Transform for detection ECG signal. Continuous Wavelet Transform (CWT) and Empirical Ensembled Mode Decomposition (EEMD).
(Issa et. al., 2019) [27]	MIT-BIH Polysomnography, MIT-BIH Arrhythmia, CAP Sleep	Artifact removing by using Independent Component Analysis (ICA) without ECG reference signal.
(Yildirim, 2022)	MIT-BIH Polysomnography	Zero-Phase Filtering (ZPF) to eliminate artifacts and R-peak-detect to predict QRS-complex.

IV. Conclusion

In this study, a study was conducted on epileptic activities in retrospectively obtained EEGs. However, one of the shortcomings of this study is that sufficient amount of EEGs data could not be included in the study. Therefore, in a future study, the effects of more EEG data on neurological wave(s) can be examined.

The purpose of eliminating artifact in EEGs is to ensure that the artifacts in EEG recordings can be removed in the most accurate and fast way. In this context, new approaches in which different filtering techniques are used together can be suggested to increase the effect of filtering techniques used in artifact removal. The use of the DWT method, which is especially effective in non-stationary EEGs, as a hybrid with different methods may contribute to the literature. With an embedded interface program that will not allow any epileptiform waves to be overlooked and will perform automatic artifact reduction, the diagnostic decision-making process can be performed in a shorter time. Thus, an improvement will be achieved in terms of time for the specialist doctor to examine and examine the EEG.

References

[1] J. M. Stern, *Atlas of EEG patterns*. Lippincott Williams & Wilkins, 2005.

[2] C. K. Paulraj, M.P., Yaccob, S.B., Yogesh, "Fractal feature based detection of muscular and ocular artifacts in EEG signals," *IEEE Conf. Biomed. Eng. Sci.*, pp. 916–921, 2014.

[3] A. Duffy, F.H., Iyer, V.G., Surwillo, W.W. and Gevins, "Clinical Electroencephalography and Topographic Brain Mapping," *J. Clin. Neurophysiol.*, vol. 7, no. 2, pp. 296–299, 1990.

[4] A. J. Wilson, S.B., Scheuer, M.L., Emerson, R.G. and Gabor, "Seizure detection: Evaluation of the Reveal algorithm," *Clin. Neurophysiol.*, vol. 115, no. 10, pp. 2280–2291, 2004.

[5] M. L. Wilson, S.B., Turner, C.A., Emerson, R.G., Scheuer, "Spike detection II: Automatic, perception-based detection and clustering," *Clin. Neurophysiol.*, vol. 110, no. 3, pp. 404–411, 1999.

[6] Mathworks, "Find local maxima - MATLAB findpeaks - MathWorks Benelux," *International Journal of Neural Systems*, 2012. https://nl.mathworks.com/help/signal/ref/findpeaks.html.

[7] H. P. Yang, W.L. and Ma, "A configurable wavelet processor for biomedical applications," *2015 Int. Symp. VLSI Des. Autom. Test, VLSI-DAT 2015*, 2015, doi: 10.1109/VLSI-DAT.2015.7114539.

[8] K. S. Park, H.J., Han, J.M., Jeong, D.U. and Park, "A study on the

elimination of the ECG artifact in the polysomnographic EEG and EOG using AR model," vol. 20, no. 3, pp. 1632–1635, 2002, doi: 10.1109/iembs.1998.747219.

[9] L. Vázquez, R.R., Velez-Perez, H., Ranta, R., Dorr, V.L., Maquin, D. and Maillard, "Blind source separation, wavelet denoising and discriminant analysis for EEG artefacts and noise cancelling," *Biomed. Signal Process. Control*, vol. 7, no. 4, pp. 389–400, 2012, doi: 10.1016/j.bspc.2011.06.005.

[10] S. R. Routray, L., Biswal, P., Pattanaik, "ECG Artifact Removal of EEG signal using Adaptive Neural Network," *2018 13th Int. Conf. Ind. Inf. Syst. ICIIS 2018 - Proc.*, no. December, pp. 103–106, 2018, doi: 10.1109/ICIINFS.2018.8721423.

[11] M. A. Jafarifarmand, A., Badamchizadeh, "Real-time cardiac artifact removal from EEG using a hybrid approach," *Proc. Int. Conf. BIOMDLORE*, pp. 3–7, 2018, doi: 10.1109/BIOMDLORE.2018.8467207.

[12] P. K. Dora, C. and Biswal, "Correlation-based ECG artifact correction from single channel EEG using modified variational mode decomposition," *Comput. Methods Programs Biomed.*, vol. 183, p. 105092, 2020, doi: 10.1016/j.cmpb.2019.105092.

[13] S. Sanei and J. A. Chambers, *EEG Signal Processing*, vol. 1999, no. December. 2006.

[14] S. Bajpai, H. Kumar Moolchandani, M. Sahu, and S. Mohdiwale, "Artifacts Removal in EEG Data," p. 2018, 2018.

[15] J. R. Goncharova, I.I., McFarland, D.J., Vaughan, T.M., Wolpaw, "EMG contamination of EEG: spectral and topographical characteristics," *Clin. Neurophysiol.*, vol. 114, no. 9, pp. 1580–1593, 2003.

[16] L. B. Lee KJ, Park C, "Elimination of ECG Artifacts from a Single-Channel EEG Using Sparse Derivative Method," *Proc. - 2015 IEEE Int. Conf. Syst. Man, Cybern. SMC 2015*, pp. 2384–2389, 2015.

[17] M. Sudhakar, "EEG Artifacts," 2012.

[18] R. Wang, M. Perreau-Guimaraes, C. Carvalhaes, and P. Suppes, "Using phase to recognize English phonemes and their distinctive features in the brain," *Proc. Natl. Acad. Sci. U. S. A.*, vol. 109, no. 50, pp. 20685–20690, 2012, doi: 10.1073/pnas.1217500109.

[19] Y. Ichimaru and G.B. Moody, "Development of the polysomnographic database on Cd-ROM," *Psychiatry Clin. Neurosci.*, vol. 53, pp. 175–177, 1999.

[20] R. Jiang, J.A., Chao, C.F., Chiu, M.J., Lee, R.G., Tseng, C.L., Lin, "An automatic analysis method for detecting and eliminating ECG artifacts in EEG," *Comput. Biol. Med.*, vol. 37, no. 11, pp. 1660–1671, 2007, doi: 10.1016/j.compbiomed.2007.03.007.

[21] J. A. Jiang, C. F. Chao, M. J. Chiu, R. G. Lee, C. L. Tseng, and R. Lin, "An automatic analysis method for detecting and eliminating ECG artifacts in EEG," *Comput. Biol. Med.*, vol. 37, no. 11, pp. 1660–1671, 2007, doi: 10.1016/j.compbiomed.2007.03.007.

[22] S. Thomas, M., Das, M.K., Ari, "Automatic ECG arrhythmia classification using dual tree complex wavelet based features," *AEU - Int. J. Electron. Commun.*, vol. 69, no. 4, pp. 715–721, 2015, doi: 10.1016/j.aeue.2014.12.013.

[23] M. Thomas, M. K. Das, and S. Ari, "Automatic ECG arrhythmia classification using dual tree complex wavelet based features," *AEU - Int. J. Electron. Commun.*, vol. 69, no. 4, pp. 715–721, 2015, doi: 10.1016/j.aeue.2014.12.013.

[24] C. Dora and P. K. Biswal, "Robust ECG artifact removal from EEG using continuous wavelet transformation and linear regression," *2016 Int. Conf. Signal Process. Commun. SPCOM 2016*, pp. 2–6, 2016, doi: 10.1109/SPCOM.2016.7746620.

[25] P. K. Dora, C. and Biswal, "Efficient detection and correction of variable strength ECG artifact from single channel EEG," *Biomed. Signal Process. Control*, vol. 50, pp. 168–177, 2019, doi: 10.1016/j.bspc.2019.01.023.

[26] Z. Issa, M.F., Tuboly, G., Kozmann, G., Juhasz, "Automatic ECG Artefact Removal from EEG Signals," *Meas. Sci. Rev.*, vol. 19, no. 3, pp. 101–108, 2019, doi: 10.2478/msr-2019-0016.

[27] M. F. Issa, G. Tuboly, G. Kozmann, and Z. Juhasz, "Automatic ECG Artefact Removal from EEG Signals," *Meas. Sci. Rev.*, vol. 19, no. 3, pp. 101–108, 2019, doi: 10.2478/msr-2019-0016.

Electronic Personality and the Legal Liability Arising from Artificial Intelligence (AI)

ALPER UYUMAZ[1]

[1] Selçuk University, Faculty of Law, Konya/Turkey, alperuyumaz@gmail.com

Abstract – Artificial intelligence is a concept that has emerged due to the rapid development of computer technology in recent years. It was first mentioned by the cognitive scientist MIT professor John McCarthy in the USA in 1956. It has developed enormously and has a very important place in social life today. Artificial intelligence refers to the machine and the software that operates the machine, which is used instead of a human in some kind of work that requires a certain intelligence. Thanks to artificial intelligence, computers that can run this software perform tasks such as driving a car, collecting garbage, playing instruments, making smarter decisions, operating an automation system, medical diagnosis and treatment, and surgical intervention. In such cases, which require human intelligence and behavior, artificial intelligence can achieve near-perfect results with far fewer errors than humans. Artificial intelligence can learn like humans, thanks to its improvable feature. These computers, robots, and machines that are using artificial intelligence are constantly improving themselves thanks to their ability to learn. There is no doubt that this irresistible development and progress will make artificial intelligence dominate many fields very soon. It is an indisputable fact that this rapid development and change will result in new legal problems. The main question is: What kind of a solution should be offered to these new legal problems, which the classical legal doctrine is not accustomed to due to artificial intelligence? Should solutions be sought to these problems by developing the classical legal doctrine just like artificial intelligence and adapting the existing regulations? For example, if an artificial intelligence-controlled subway or a self-driving taxi collides with a pedestrian, will those responsible for pedestrians and passengers be liable under the revised tort provisions? Or will there be a need for new branches of law and liability regimes such as robot law, artificial intelligence law, and electronic law? In this study, an answer to this question will be sought and it will be discussed how to find a solution to such disputes in Turkish Law, where there is no regulation yet.

Keywords – Artificial intelligence, legal liability, electronic personality, strict liability, hazard liability.

I. INTRODUCTION

Legally, the types of personality in Tukish law are real (natural) and legal (artificial) personalies. There are two ways to acquire personality: Birth and legal conditions that the law requires. While birth is required for real persons, acquiring legal requirements is necessary for legal persons [1]. According to Turkish Civil Law, people gain personality with complete and live birth. The acquisition of personality by legal entities is achieved by completing the legally sought procedure [2].These conditions and procedures differ in terms of the gaining personality of each legal person. What is important here is that legal persons can be legal subjects of rights, just like real persons, if the legal conditions are met and the relevant procedure is completed. Because, legal persons are entitled to all rights and obligations except those that are dependent on human-specific qualities by nature such as gender, age, and kinship (Turkish Civil Code Article 48/1). It is necessary to acquire personality in order to be entitled and take responsibility [3]. Having a right also creates responsibility [4]. It is possible to say that everyone who is legally recognized as a person has rights. But it is not possible for everyone to use these rights [5]. In order to exercise a certain right, both the real person and the legal person must have the capacity to act [6]. In real persons, it is necessary to have the power to distinguish, to be interdicted and to be of legal age in order to be able to disposal. Legal entities, on the other hand, must have the legally necessary organs. Like the board of directors, the general assembly.

According to the traditional understanding and universally accepted principle, the personality belongs to either a human or a legal person person [7]. However, there are now new agents that fulfill the task that a human would take on, thanks to the developing technology. These agents are classified as electronic agents/products in terms of their rights and responsibilities [8]. This would be a new addition to existing and legally recognized personality types, although its acceptance and necessary integration is not yet universally valid. This study deals with the legal responsibility arising from the actions of electronic persons (artifial intelligence-AI) who do not have a specific legal personality in Turkish law yet. Therefore, the issue that this study seeks to solve who will be responsible for the damages caused by electronic persons (AI) in light of the Turkish Code of Obligations. For this reason, this article attempts to define electronic persons and electronic personalities. In addition, the article deals with the issue of responsibility and the determination of the responsible person in case of violation of the obligations of electronic persons.

II. PERSONALITY AND ELECTRONIC PERSONALITY

A. Real and Legal Person's Personality

Legal entity refers to the ability of an unreal entity that does not actually exist but is legally attributed as a person to be entitled and to assume responsibility [9]. Acceptance of legal entity ensures that public law and private law relations are made between legal persons and real persons and sometimes with other legal persons [10]. In order to determine the legal responsibility, it is necessary to determine to whom the personality is attributed. According to Turkish law of obligations, both legal persons and real persons are legally liable. This liability can be both contractual and tortious liability.

People acquire personality from the moment they are born (TCC. Art. 28). In this context, it is stated that the personality starts with full and live birth, ends with death [11]. According to the Art. 28, the child gains personality from the moment it is in the womb of mother, provided that it is born full and alive. Here, the law carried the acquisition of personality into the past under certain conditions [12]. However, even if the law did not make this regulation, it would have been necessary to accept the future rights of the child in the mother's womb should be protected. As stated in TCC.Art.28, a real person is entitled the personality with birth, except for the baby in the mother's womb. However, the legal capacity requires the existence of certain conditions. These conditions, in accordance with TCC.Art.10, are to have the capacity to distinguish, not to be interdicted and to be age of maturity. According to the Art. 13 of the code, if there are no factors that affect the ability to distinguish, such as pupilage, mental illness or substance abuse, the power of distinguish is considered to exist [13]. Those who do not have the legal capacity to act cannot exercise their rights if they do not have appropriate legal representation, and the legal transactions they have made on their own will not be legally valid. These people are called incompetent persons in Turkish legal doctrine [14]. As a rule, it is assumed that every person with the power of discernment is capable of legal action if he/she has reached the age of 18. However, being under the age of 18 and being legally restricted causes incompetence [15]. In this case, the real person may enter into a legal relationship with the permission or authorization of his legal representative. According to TCC.Art.16, persons in this category can make personal rights and free gains on their own [16].

Legal persons have rights and obligations based on legal regulations [17]. The beginning of personality in legal person is the end of their legal establishment procedure [18]. In Turkish law, foundations and associations established for the ideal purpose gain the legal capacity to act by having the legally necessary organs. Commercial companies gain personality according to the Turkish Commercial Code. After legal person acquires a personality, it will have all the rights and obligations in law, unless these rights are reserved for people only. Accordingly, the rules regarding age, gender, kinship, marriage, engagement, and heirship capacity do not apply to a legal persons.

B. The Electronic Personality

It is difficult to immediately translate the innovations brought by technological developments into law. But it is necessary to introduce new rules for the problems that arise due to technological developments. Recently, it has been mentioned that autonomous electronic agents should be brought into law as individuals. Particularly in European law, there are attempts to accept electronic personality [19]. However, it must be admitted that not every country has yet considered the advantages and disadvantages of giving legal personality to products which use artificial intelligence.

Electronic personality is difficult to define. However, at the point reached in technology, we must now define the electronic person and personality [20]. For this reason, an electronic entity/person can be defined as a human-made product that performs tasks autonomously with the support of artificial intelligence [21]. Thereafter, we may need to understand artificial intelligence and its benefits. In a recent study, European Union Legal Affairs defines artificial intelligence as computing machines and intelligence [22]. Today, it is predicted that computers can simulate human intelligence by evaluating natural language conversations between machines and humans. Although highly technical as it may seem, artificial intelligence is the consciousness of a machine/product that independently analyzes and performs a specific task set by human beings. Technically artificial intelligence is the consciousness of a human-made product that independently analyzes and performs a specific task. One of the most obvious examples of artificial intelligence-supported electronic existence is autonomous vehicles developed today and still in the trial phase, robots used in cleaning works or surgeries.

We need to answer three important issues regarding the electronic personality proposal. The first of these is the technical issue and concerns the technological capability of electronic products. The second is an ethical issue. How ethical is this? The final issue concerns whether recognition of the electronic personality is legally required.

1. The Technical Issue

This problem is related to the fact that technology, an artificial entity, or even a product can be the subject of the right. The fact that a product using artificial intelligence has complex legal responsibilities regarding personality is related to how much technology has developed. What is meant here is the consciousness of electronic assets. That is, responsibility relates to the capacity to understand the consequences of a particular action or legal transaction accordingly. In traditional legal personality theory, the power to distinguish or understand is effective in accepting them as legal persons. As stated above, as a principle, an action or a legal transaction by something incapable of distinguishing and understanding has no effect in terms of Turkish civil law and law of obligations. For example, it has been observed that a driverless vehicle using artificial intelligence belonging to a company makes simple mistakes that human beings would not make. In an unofficial video circulating on social media, it is seen that he cannot correctly perceive a horse-drawn carriage in front of the vehicle. In the video, the vehicle reacts accordingly by perceiving the horse-drawn carriage as a truck, a pedestrian on the vehicle, or another vehicle coming towards it. Undoubtedly, it is clear that this technology will be developed. Artificial intelligence is renewing itself every day, like a child growing and developing mentally. It also has the unique feature of learning and experiencing without human-specific barriers. However, according to today's technology, it is difficult to say that artificial intelligence can act fully conscious like a human. Therefore, today it is not possible for artificial intelligence to control its actions, for example, as a robot or machine, and to act with the awareness of acting by the law by foreseeing the consequences. However, it is possible to say that when this condition is fulfilled in the future, artificial intelligence will maybe have a personality.

2. Ethical Issue

The second issue is whether it is ethical for a human-made entity using artificial intelligence to be subject to the same legal

regime as a human. Our constitutionally protected rights are inalienable and indispensable rights that exist automatically granted to us simply because we are born as human beings. If someone thus rewarded has not kept his promise in a contract or has deliberately harmed someone by tort, he/she will be liable. Moreover, if he/she has hurt another person through an act considered a crime under criminal law, he/she will be punished with imprisonment.

Another question here is, will we limit artificial intelligence's rights if it is given personality? Or will they have the same rights as humans? Will they be able to establish family or a unity among themselves? Will they go to jail for their deliberate crime? Even if it has consciousness, does it make any sense to deprive a machine of freedom like a human? A human being can make a logical decision by evaluating the harm and benefits of his actions with emotions. The purpose of responsibility in law is to protect personality against violations of personality and to ensure that people live in a peaceful society. It is to bring order to human behavior and to ensure that people live in a stable and safe environment. Technology and technological products are produced to make people's lives better and easier. Products are objects of law, people are subjects of rights. Therefore, we are faced with an ethical problem. This problem is related to the ethical appropriateness of making the object of law the subject of the right.

3. Issue of Legal Necessity

While personality gives rights to the subject of the right, it also imposes obligations. Thus, we can maintain public order in the inevitable human interactions to avoid chaos and bring maximum benefit to the human community. Therefore, the essence of legal personality recognition is basically to maintain stable human interaction, whether contractual or non-contractual. The main question in this context is who will benefit from giving artificial intelligence personality. This benefit must undoubtedly belong to human beings. It is also not the right approach to avoid the legal difficulties of determining the responsible person by giving personality to artificial intelligence. In any case, it should be possible if giving an electronic personality to artificial intelligence is beneficial to humans.

III. LIABILITY REGIME IN TURKISH LAW

Having a personality confers both rights and liability. Legal liability has three sources. These are tort, contract, and unjust enrichment [23]. Pacta sunt servanda expresses the obligation to act by the agreement in a contractual relationship [24]. The party that does not fulfill its promise in the contract, in other words, the party that does not perform properly will have to pay compensation [25]. In non-contractual liability, a liability arises when all the elements of unlawful action, damage, fault, and causation occur [26]. However, the exception to liability based on fault in tort law is strict liability. In some cases, according to the principle of strict liability, a person may be held liable for damage caused by things in his possession, even if he is not at fault. Motor vehicles, and the responsibility of the operators of dangerous enterprises can be given as an example. The liability of the operator of a motor vehicle or the operator of a dangerous undertaking is characteristic cases of strict liability.

IV. DETERMINING LIABILITY ARISING FROM ARTIFICIAL INTELLIGENCE UNDER TURKISH LAW

Two questions await answers, whether in contractual or tortious liability of artificial intelligence. First, who should be responsible for the damages? Secondly, the scope of this responsibility will be determined according to which responsibility regime. If electronic personality had been accepted in Turkish law, an electronic person/product would have been responsible. However, this answer cannot be given since the electronic personality principle is not yet found in the Turkish legal system. Because, due to its technical capacity, it will not be possible to talk about such responsibility for a while. Moreover, even if we attribute responsibility to artificial intelligence, they will not have individual responsibilities because they do not have assets, and penalties such as prison sentences are ineffective for them. It would be the right choice to see this responsibility as a danger liability within the framework of today's legal rules and to accept it as the responsibility of the person who has or programs the thing that can create this danger. The practical solution for today would be to apply the existing tort provisions to determine the provisions governing liability and the person responsible (Turkish Code of Obligations Art. 49 ff. and 114/2). The real or legal persons involved in the production and financing of the use of artificial intelligence may be held individually or severally liable for the damages caused by the use of artificial intelligence. These include the owner, programmer, tenant, data trainer, manufacturer, operator, or designer of artificial intelligence. Among these persons, it can be discussed which tort clauses the liability will be subject to. In this regard, it seems more appropriate to prefer strict and joint responsibility. Thus, in cases where the injured party is the consumer, the universal principle of consumer protection is also preserved.

V. CONCLUSION

In this paper, the possibility of the adoption of electronic personality and the legal liability of artificial intelligence supported autonomous entities are tried to be discussed. In fact, this new personality hypothesis was introduced to address the complex nature of AI-powered products with autonomous functionality. Although controversial, thanks to its ever-advancing technology, AI-powered products will logically be able to perform all human-specific operations independently in the near future. However, those who argue that electronic personality should be adobted should offer solutions to the issue of ethical, technical and legal necessity. Although it is claimed that electronic personality is legally required, it would be a more appropriate solution to produce new types of liability by adapting current regulations to developments, instead of attributing personality to entities using artificial intelligence. Today, it is possible to apply the principles of strict and joint liability to products using artificial intelligence. Hazard liability may also be proposed if they pose a significant hazard to humans.

REFERENCES

[1] B. Smith, "Legal Personality", *Yale Law Journal*, vol. XXXVII, no.3, pp.283-299; 1928.

[2] M. K. Oğuzman and Ö. Seliçi, *Kişiler Hukuku*, Filiz Kitapevi: İstanbul, 2021.

[3] J. Dewey, "The historic background of corporate legal personality", *Yale Law Journal*, vol. XXXV, no. 6, pp. 655-673, 1926.

[4] P. De Schoutheete and S. Andoura, "The legal personality of the European Union", *Studia Diplomatica*, vol. LX, no.1, pp. 1-9, 2007.

[5] M. Dural and T. Öğüz, *Kişiler Hukuku,* Filiz Kitapevi: İstanbul, 2021.

[6] B. Öztan, *Kişiler Hukuku,* Yetkin: Ankara, 2022.

[7] L. Series, "Relationships, autonomy and legal capacity: Mental capacity and support paradigms". *International Journal of Law and Psychiatry*, vol. 40, pp. 80-91, 2015.

[8] C. Lachi, "Civil legal capacity-determining factor in establishing and making legal relations", *Contemporary Legal Institutions*, vol. 6, no.1, pp. 186-191, 2014.

[9] S. Chesterman, S., "Artificial intelligence and the limits of legal personality", *International & Comparative Law Quarterly*, vol. 6, no.4, pp. 819-844, 2020.

[10] M. Myrzakhanova and Y. Myrzakhanov, "Active Legal Capacity in Civil Law", *Administrative and Criminal Justice*, vol. 3, no. 76, pp. 70-75, 2016.

[11] F. K. Kalbaevich, "Legal Entities–As Subjects of Civil Law", *Periodical Journal of Modern Philosophy, Social Sciences and Humanities*, vol. 8, pp. 57-59, 2022.

[12] F. B. Uzun, "Gerçek kişilerin hak ehliyeti ve hak ehliyetine uygulanacak hukukun tespiti" *Hacettepe Hukuk Fakültesi Dergisi*, vol. 6, no. 2, pp. 11-48, 2016.

[13] L. M. Kurt, (2011). "Ceninin malvarlığı hakları", *İnönü Üniversitesi Hukuk Fakültesi Dergisi*, vol. 2, no. 1, pp. 177-209, 2011.

[14] H. Hatemi, Kişiler Hukuku, Filiz Kitapevi: İstanbul, 2021.

[15] V. U. Erkan and İ. Yücer, "Ayırt Etme Gücü", *Ankara Üniversitesi Hukuk Fakültesi Dergisi*, vol. 60, no. 3, pp. 485-522, 2011.

[16] M. Şahin, "İsviçre Medeni Kanunu'nda Yapılan Değişiklikler Çerçevesinde Türk Hukukunda Ayırt Etme Gücüne Sahip Küçük ve Kısıtlıların (Sınırlı Ehliyetsizlerin) Nişanlanma Ehliyeti (TMK m. 16/I, 118/II)", *Ankara Barosu Dergisi*, no. 4, pp. 81-104, 2014.

[17] H. İmamoğlu, "İsviçre Medeni Kanununun Yurtlarda veya Bakım Kurumlarında Kalan Ayırt Etme Gücü Bulunmayan Kişiler Hakkındaki Hükümleri ve Türk Hukuku Açısından Değerlendirilmesi", *Ankara Üniversitesi Hukuk Fakültesi Dergisi*, vol. 68, no.1, pp. 213-240, 2019.

[18] T. Ansay, "Legal Capacity of Corporations, Discharge of the Board of Directors, Liability Suit against the Board of Directors and a Decision of the Civil General Assembly of the Court of Cassation", *Banka Hukuk Dergisi*, no. 3, p. 407, 1965.

[19] D. Muhvic, "Legal personality as a theoretical approach to non-state entities in international law: the example of transnational corporations", *Pecs Journal of International and European Law*, no.1, p. 7, 2017.

[20] R. H. van Genderen, "Do we need new legal personhood in the age of robots and AI?" *In Robotics, AI and the Future of Law*, pp. 15-55, 2018.

[21] E. Doğan, "Dijital Çağda Yeni Bir Hukukî Kişilik Arayışı: Yapay Zekâ", Türkiye Barolar Birliği Dergisi, no. 158, pp.213-256, 2022.

[22] S. Beck, "Intelligent agents and criminal law—Negligence, diffusion of liability and electronic personhood", *Robotics and Autonomous Systems*, no. 86, pp.138-143, 2016.

[23] A. Bertolini, *Artificial intelligence and civil liability*, Brussels: European Parliament, 2020.

[24] H. Wehberg, "Pacta sunt servanda", *American Journal of International Law*, vol. 53, no. 4, pp. 775-786, 1959.

[25] F. Eren, *Borçlar Hukuku Genel Hükümler*, Yetkin Hukuk Yayınları: Ankara, 2021.

[26] M. M. Pillay, *The impact of pacta sunt servanda in the law of contract*, Dissertation, University of Pretoria, 2015.

[27] G. L. Priest, "The modern expansion of tort liability: its sources, its effects, and its reform", *Journal of Economic Perspectives*, vol. 5, no. 3, pp. 31-50, 1991.

Investigation of the Effect of Data Augmentation on Turkish Paraphrase Detection

Z. B. OZGER[1] and S. ERTEM[2]

[1] Kahramanmaras Sutcu Imam University, Kahramanmaras/Turkey, zeynepozger@ksu.edu.tr
[2] Fırat University, Elazig/Turkey, serdarertem@msn.com

***Abstract* - Natural languages are extremely complex structures and require high cognitive abilities. The general aim of natural language processing research is to enable the understanding and interpretation of this complex structure to be partially or completely done by computers. Paraphrase is a different syntax form of a text with the same semantic content in the same language. Determining whether a collection of texts contains synonyms for another text is an important research topic for natural language processing. Large datasets and human-labeled data are needed to develop a model that can detect paraphrase. Within the scope of the study, the effect of data augmentation for the detection of paraphrase in the dataset consisting of limited and short texts was examined. The dataset includes 41 different texts and 2 paraphrases of each text. There are 121 texts in total. Vector representations of texts were obtained with Word2Vec and FastText which are word embeddings, Bidirectional Encoder Representations from Transformers (BERT) which is a language model, and Term frequency-Inverted document frequency (Tf-Idf) which is the common traditional method. Experimental studies proved that data augmentation improves classification performance. Furthermore, it has been seen that the BERT representations of the texts achieved successful results with an accuracy of 0.878 in the original data using Naïve Bayes and with an accuracy of 0.976 in the augmented data using Support Vector Machine in the detection of paraphrases in short texts.**

***Keywords* – Paraphrase detection, Data augmentation, BERT.**

I. INTRODUCTION

NATURAL language processing (NLP) is a field of study that focuses on analyzing texts created by humans and machines, by converting them into formats that computers can process [1]. Paraphrase detection is one of the important fields of study for natural language processing. The purpose of paraphrase detection is to determine whether 2 texts are semantically equivalent. If two texts have the same meaning even with different words and/or syntax, these two texts are equivalent [2]. The texts investigated for paraphrase can be document collections, paragraph pairs, and phrase pairs [3]. Paraphrase is seen at 3 different levels: lexical, phrasal, and sentential. At the lexical level, some words in the text have been replaced with different words such as synonyms. At the phrasal level phrases have been replaced by other phrases with the same meaning. At the sentential level, the sentences are structurally different but have the same meaning [4].

Paraphrase detection is used in many NLP problems. Identifying sentences with the same meaning in the text summary systems and not including them in the summary prevents the repetition of information in summary texts [5]. Identifying questions that require the same answer in question-answer systems facilitates the selection of the appropriate answer [6]. It helps to improve the quality of translated text in machine translation systems [7]. Better results can be obtained in search engines based on text similarity [8]. In addition, there are many usage areas such as query expansion (Jones et. al. 2006), information extraction [9], language generation [10], and plagiarism detection [11].

Paraphrase detection is considered a binary classification problem if it is desired to determine whether 2 texts have the same meaning. In this case, the labels are defined as paraphrase or non-paraphrase. However, it is a multiple classification problem when it is desired to determine which of the existing texts is similar to a certain text. The number of labels is equal to the number of semantically different texts. In both cases, texts must be represented by fixed-size vectors to provide a classification solution. That is, texts should be converted to feature vectors in a way that preserves contextual content [7].

Machine learning algorithms use features that include syntactic and semantic information extracted from texts for paraphrase detection [12]. The success of the Paraphrase detection system is directly proportional to the extraction of well-representing features from the texts. Feature extraction can be done at word level or sentence level.

Many studies have been carried out on different feature extraction methods to increase the success of the systems. feature extraction was performed such as N-grams and weighted term frequencies [13], the number of matching POS tags, named entities, words and word roots [14], simple distributional semantic space [15], distributional memory tensor [16], word embeddings [17], similarity measurements based on the lexical database [18]. Sources such as Wordnet are widely used in paraphrase detection problems, by replacing the words in a text with their synonyms and hyponyms to obtain another text [1].

Studies at the sentence level are more semantic-oriented. Like topic modeling methods [19], methods based on similarity of syntactic trees [20], machine translation metrics [21], and sentence parsing trees [22] are the commonly used sentence level feature extraction methods. It is also a common approach to use lexical, syntactic and semantic features together to increase the success of the developed systems [23].

Deep learning algorithms are also applied for paraphrase

detection with word embeddings, part of speech tag embeddings instead of manually extracted features. Convolutional neural network (CNN) [24], stacked residual long-short term memory (LSTM) networks [25], deep reinforcement learning [26], siamese recurrent networks [27], CNN, LSTM and attention LSTM [7] are deep learning methods applied for this purpose.

Due to the morphological structure of Turkish, very small differences in words and sentences may affect the determination of paraphrase [2]. In addition, the lack of a comprehensive structure for Turkish as WordNet causes the studies to be limited. Karaoglan et. al. [2] proposed a Word2Vec-based method for paraphrase detection. They represented texts by combining word vectors with different methods such as splicing and averaging. In the studies conducted on Turkish and English corpus, the highest accuracy value was obtained as 0.778 for the Turkish Parder corpus. In another Word2Vec-based study [28], the Word2Vec model was used together with Fisher coding. Euclidean distance is used to measure text distances. The text with the least distance value was accepted as the paraphrase of the input text. The accuracy value of the proposed method was obtained as 0.69.In another study, Karaoglan et. al. [3] trained syntactic and semantic features with a bayes classifier. Common word ratio, sentence length ratio, common sequential word ratio and word sequence similarity were determined as syntactic features. Tense and polarity differences were used as semantic features. When both feature groups are used together, the f-measure value of the classifier is obtained as 0.74.

Yıldız and Fındık [29] performed paraphrase detection for questions to improve the performance of a question answering system. For this purpose, they created a question dataset for the banking sector. Lexical and semantic features were used together. The success of the proposed system was measured with the mean average precision (mAP) metric which is commonly used in question similarity studies and LSTM-based siamese iterative neural network and it was obtained as 0.67. Soleymanzadeh et. al. [12] used 18 metrics that were based on machine translation and text similarity and they represented texts with these feature vectors. The authors worked on the Turkish Parder corpus. When comparing the performances of text vectors classified with support vector machine (SVM), C 4.5, naive bayes (NB), logistic regression (LR), and random forest (RF), the model trained with SVM was the most successful method with an f-measure value of 0.844.

It is a difficult and costly process to obtain a large number of labeled texts with a similar meaning to a particular text. However, classification algorithms need extensive data to learn adequately. Within the scope of the study, the effect of data augmentation on paraphrase detection performance was investigated in a small dataset. The augmentation process was performed on the basis of both word embedding (Word2Vec and FastText) and language model (BERT). It has been seen that generating new texts from an existing text with a pre-trained language model provides a solution to the insufficient learning problem encountered in small datasets.

As there is more content information in large and long texts, it is easier to detect semantic similarity [30]. Although lexical matching is a widely used technique, it fails when different words giving the same meaning are used in short texts [1]. In the study, the success of Word2Vec, FastText, BERT and Tf-Idf methods for short texts consisting of a single sentence were compared and it was seen that short texts represented by BERT got better results.

II. PROPOSED METHOD

The block diagram of the proposed method is given in Figure 1. Both original data and augmented data are represented with different vectorization methods. Augmentation process is applied using Word2Vec, FastText and BERTurk pre-trained models separately. The effect of data augmentation on success and the performance of different vectorization methods were compared.

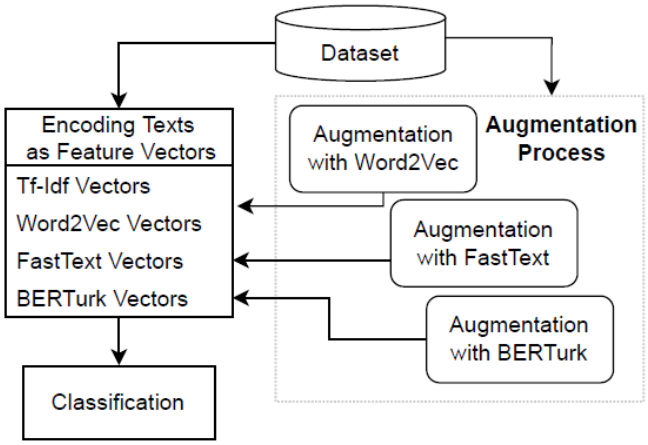

Figure 1: The block diagram of the proposed method

A. *Dataset Description*

The aim of the study is to investigate the effect of data augmentation by obtaining synthetic data on the problem of paraphrase detection. For this purpose, a dataset consisting of questions from ÖSYM (Öğrenci Seçme ve Yerleştirme Merkezi-Student selection and placement center) exams was created to be used in the experiments carried out in the study. One of the main methods used for measurement and selection in these exams is to determine reading, writing, and interpretation abilities in the native language [31]. The dataset consists of 41 questions asked for semantic similarity from YKS (Yükseköğretim Kurumları Sınavı-Higher education institutions exam), DGS (Dikey Geçiş Sınavı-Vertical transfer exam), KPSS (Kamu Personeli Seçme Sınavı-Public personnel selection exam) and ALES (Akademik personel ve Lisansüstü Eğitimi giriş Sınavı-Academic personnel and graduate entrance exam) as stated below, and the answers of these questions. The dataset is limited due to the limited access to the questions.

- .. which of the following is intended to be explained? (.. anlatılmak istenen aşağıdakilerden hangisidir?)
- .. which one is closest in meaning? (.. hangisi anlamca en

yakındır?)
- .. which one has the same meaning as the given sentence? (.. hangisi verilen cümle ile aynı anlamdadır?)

In these questions, a short text is given and asked to find the text with the closest meaning to it. With the text in the question and the correct answer, a pair of paraphrased texts were obtained from each question. In addition, one more paraphrase text is written manually for each question. Thus, there are 2 synonymous texts for each sentence in the dataset. The total number of texts is 123. An example of paraphrases in the data set is given in Table 1.

Each group of paraphrase texts is given a label in order to treat it as a classification problem. Since there are 41 groups of paraphrases in the dataset, there are 41 classes, and three paraphrases in each class. Of these three texts, one randomly selected one was included in the test set, and the remaining two were included in the training set. Thus, before the augmentation process, there are 82 samples in the training dataset and 41 samples in the test set.

Table 1: Examples for paraphrases in dataset.

Başımdan geçen kimi olayların öyküsünü yazarken, o olayları yeniden, hem de zamanında ayrımına varamadığım yönleriyle yaşamanın, küçümsenir bir mutluluk olmadığını söylemeliyim. *While writing the story of some of the events that happened to me, I must say that it is not a happiness to be underestimated to experience those events again, with aspects that I could not distinguish at the time.*
Öykü yazarken, geçmişteki olayların fark etmediğim yönlerini tekrar yaşamaktan mutluluk duyuyorum. *As I write stories, I am happy to relive aspects of past events that I had not noticed.*
Yaşadığım kimi olayları sonradan öyküye dönüştürürken onların fark etmediğim yanlarını tekrar yaşamak bana mutluluk veriyor. *While I turn some of the events I have experienced into stories, it gives me happiness to relive the sides of them that I did not notice.*

B. Data Augmentation

Because language is a complex structure, generating synthetic text data is a challenging process. Large data sets are required for paraphrase detection with classification-based methods [32]. Obtaining multiple synonymous copies of a text requires human cost. Data augmentation in NLP problems increases performance in problems where data is limited [33]. Shakeel et. al. [7] proposed a synthetic data generation technique based on set and graph theory and it was seen that data augmentation improves performance.

Within the scope of the study, synthetic data was produced using the nplaug[1] library in Python. The nplaug library produces synthetic text data by making changes to texts at the character, word, or context level. Within the scope of the study, the library's word and context level augmentation method was used. Word level augmenter generates data by changing the word and word vectors Wordnet, Word2Vec, FastText, Glove. Contextual augmenter, on the other hand, obtains synthetic data using BERT models. In word embedding-based methods such as Word2Vec and Fast text, it augments by replacing one or more words in the text with the word represented by the nearest vector in the embedding model. BERT augmenter uses the language model to predict a possible word. Within the scope of the study, augmentation was performed with Word2Vec [34], FastText [35] and BERT [36]. Pre-trained Word2Vec[2], Fasttext[3] and BERTurk[4] models were used. In the training set, the number of paraphrases in each group was 10, and data were produced separately for each model.

C. Encoding Texts as Feature Vectors

Classification algorithms generally require numerical data. Therefore, numerical representations of texts should be obtained in solving NLP problems. The success of representation methods has a direct impact on the performance of the method.

In the process of identifying paraphrases, feature vectors are usually obtained by extracting some linguistic features for each text. These features are generally extracted manually. Word embedding methods obtain vectorial representations of words according to their semantic proximity. The basic assumption in the study is that semantically similar texts will be vectorally closer to each other. Within the scope of the study, Word2Vec and FastText from word embedding methods, BERT from language model methods and Tf-Idf (Term Frequency-Inverse Document Frequency) method from traditional methods were used to represent texts.

Tf-Idf is a statistical value that shows how much a word represents the document it contains. Tf represents the frequency of the relevant word in the document. The Df value is calculated by dividing the number of documents by the number of documents in which the relevant word occurs. Idf is the logarithm of the Df value. Tf and Idf metrics are calculated as in Eq. (1), (2) and (3).

$$Tf - Idf = Tf * Idf \quad (1)$$

$$Tf = \frac{the\ frequency\ of\ word\ in\ the\ document}{\#\ words\ in\ the\ document} \quad (2)$$

$$Idf = log(\frac{\#\ documents}{\#\ documents\ that\ contain\ related\ word}) \quad (3)$$

III. Experimental Results

The main purpose of the study is to examine whether augmenting of the dataset with synthetic data contributes to the data collection problem for paraphrase detection. In addition, the success of word embedding and language model methods in detecting similar texts was also investigated. Feature vectors of texts for original data and augmented data were obtained with Word2Vec, FastText, BERT and Tf-idf.

[1] https://github.com/makcedward/nlpaug

[2] https://github.com/akoksal/Turkish-Word2Vec
[3] https://fasttext.cc/docs/en/crawl-vectors.html
[4] https://fasttext.cc/docs/en/crawl-vectors.html

Data augmentation was done in 2 ways. Word2Vec and FastText models were applied for word level augmentation and BERT model was applied for context level augmentation. The traditional and widely used Tf-Idf method in NLP was applied separately to both the original data and the augmented data produced with different models. By comparing the classification performances of the original data and augmented data, the effect of data augmentation on success was examined. In the classification phase, Naive Bayes, stochastic gradient descent (SGD), RF, SVM, and logistic regression algorithms were applied.

Naive Bayes is a method based on Bayes' theorem that shows the relationship between conditional probabilities and marginal probabilities within the probability distribution for a random variable. SGD is a classification method that allows to apply the stochastic gradient descent learning process with different loss functions and classification penalties. Decision trees are structures that allow to represent data in a hierarchical structure by dividing data sets into one or more nodes according to certain decision rules. The random forest classifies with more than one decision tree and ensures that the final decision is determined according to the majority of votes. Trees are trained with different data subsets of the dataset. SVM is a vector space-based method that aims to find the optimal decision boundary that can separate the classes in the training data. Logistic regression defines an equation that can express the relationship between dependent and independent variables with a straight line in classification problems.

The classification performances of the augmented data with different models and the original data were compared according to the vectorial representations obtained by different feature extraction methods. Data augmentation does not show much improvement in Tf-Idf vectors as seen in Figure 2, when the results are compared. Overall, the best performance was seen with the Word2Vec-based augmenter data, but the results were very close to each other. A similar situation exists for Word2Vec vectors. As can be seen from Figure 3, the accuracy values of the augmented data and the original data were very close to each other and remained around 0.7.

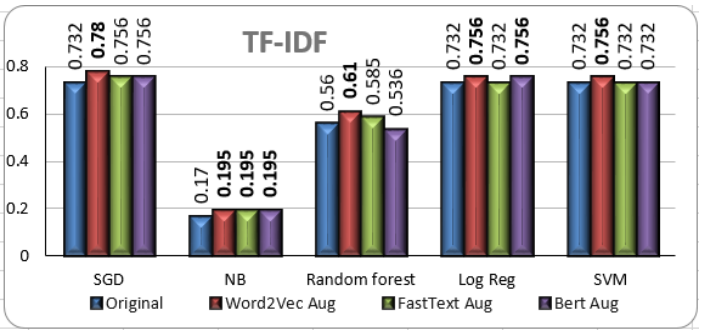

Figure 2: The results of Tf-Idf vectors for augmented and original data

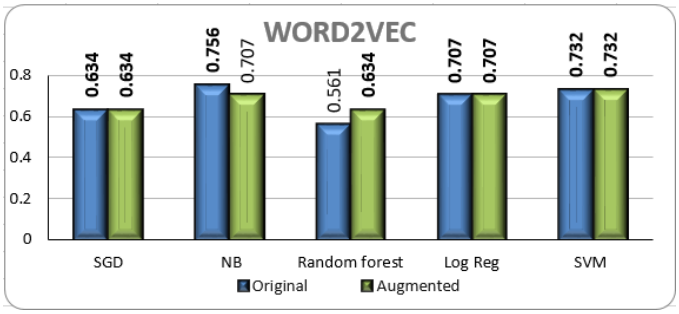

Figure 3: The results of Word2Vec vectors for augmented and original data

Accordingly, increasing data with syntetic data did not increase the success of Tf-Idf and Word2Vec vectors.

More promising results were obtained for FastText as seen in Figure 4. For Naive Bayes, augmented data did not improve the success of paraphrase detection, but performance increased in all other methods compared to the original data. The best performance was obtained with BERT based modeling. Figure 5 shows the result of the BERT model. BERT vectors, whose classification performance for the original data was better than other vector representations, showed superior performance for the paraphrase detection problem after augmentation. Considering all the results, although BERT is more successful than other methods in small data, synthetic data has improved the performance of the system.

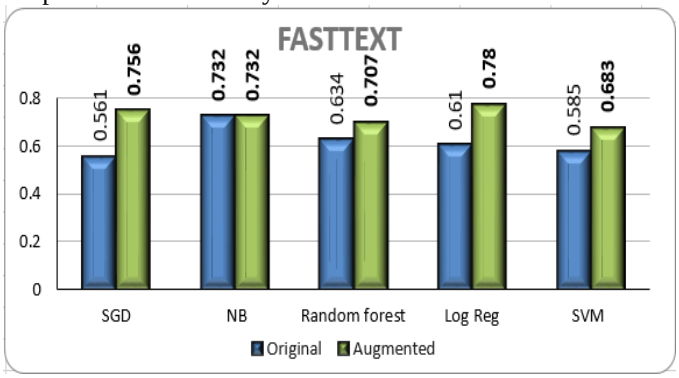

Figure 4: The results of FastText vectors for augmented and original data

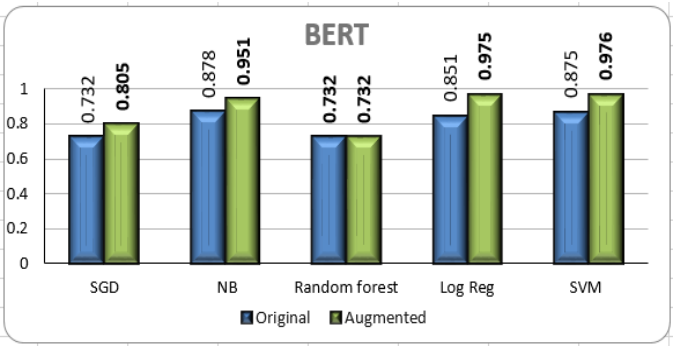

Figure 5: The results of BERT vectors for augmented and original data

IV. Conclusion and Future Works

If two sentences give the same message despite structural or lexical differences, they are considered as paraphrases of each other. Paraphrase detection is one of the basic steps that can be used to develop solutions to NLP problems. However, creating labeled datasets for training is a difficult and costly process. In order to provide a solution to the data acquisition problem, paraphrase detection was carried out by increasing a small labeled dataset by generating synthetic data within the scope of the study. Syntactic and semantic features are used in studies for paraphrase detection but these features are manually extracted from sentences. Within the scope of the study, the texts were represented by Word2Vec, FastText, and BERT vectors, and their performances in short texts were compared in order to model the meaning at the sentence level sensitively and accurately. The results show that the proposed method for data augmentation improves performance and BERT representations for short texts provide superior performance. Naive bayes, logistic regression and SVM methods showed promising results. In original data, Naive Bayes performed best with an accuracy of 0.878, while on augmented data the SVM outperformed the other methods with an accuracy of 0.976.

Within the scope of the study, the effect of the proposed method was evaluated on a small dataset and it was found to be successful. In addition, different text encoding methods were compared and the appropriate method was determined. In future studies, it is planned to apply the method for public datasets used for paraphrase detection.

References

[1] V. S. M. M. R. S. Vaishnavi, M. Saritha, and R. S. Milton. "Paraphrase identification in short texts using grammar patterns", in 2013 IEEE International Conference on Recent Trends in Information Technology (ICRTIT), pp. 472-477.

[2] B. Karaoğlan, H. E. Yorgancioğlu, T. Kişla, and S. K. Metın. "The Impact of Sentence Embeddings in Turkish Paraphrase Detection", in 2019 27th Signal Processing and Communications Applications Conference (SIU), pp. 1-4

[3] B. Karaoğlan, T. Kişla, and S. K. Metin. "Contribution of syntactic and semantic attributes in paraphrase identification", in 2018 26th Signal Processing and Communications Applications Conference (SIU), pp. 1-4.

[4] S. Demir, I. D. El-Kahlout, E. Unal, and H. Kaya. "Turkish paraphrase corpus", in Proceedings of the Eighth International Conference on Language Resources and Evaluation (LREC'12), pp. 4087-4091.

[5] R. Barzilay and K. R. McKeown. "Sentence fusion for multi document news summarization," Computational Linguistics, 31(3), 297-328, 2005.

[6] P. Nakov, D. Hoogeveen, L. Màrquez, A. Moschitti, H. Mubarak, T. Baldwin and J. Verspoor, K. "SemEval-2017 task 3: Community question answering", arXiv preprint arXiv:1912.00730, 2019.

[7] M. H. Shakeel, A. Karim andI. Khan. "A multi-cascaded model with data augmentation for enhanced paraphrase detection in short texts", Information Processing & Management, 57(3), 102204, 2020.

[8] K. Anyanwu, A. Maduko, and A. Sheth. "Semrank: ranking complex relationship search results on the semantic web", in Proceedings of the 14th international conference on World Wide Web, pp. 117-127.

[9] S. Sekine. "On-demand information extraction", in Proceedings of the COLING/ACL 2006 Main Conference Poster Sessions, pp. 731-738.

[10] R. Power and D. Scott. "Automatic generation of large-scale paraphrases", in: 3rd International Workshop on Paraphrasing (IWP2005), 14 Oct 2005, Jeju Island, South Korea.

[11] E. Hunt, R. Janamsetty, C. Kinares, C. Koh, A. Sanchez, F. Zhan, ... and P. Oh. "Machine learning models for paraphrase identification and its applications on plagiarism detection", in 2019 IEEE International Conference on Big Knowledge (ICBK), pp. 97-104.

[12] K. Soleymanzadeh, B. Karaoğlan, S. K. Metin and T. Kişla. "Combining machine translation and text similarity metrics to identify paraphrases in Turkish", in 2018 26th Signal Processing and Communications Applications Conference (SIU), pp. 1-4.

[13] Y. Ji, and J. Eisenstein. "Discriminative improvements to distributional sentence similarity", in Proceedings of the 2013 conference on empirical methods in natural language processing, pp. 891-896.

[14] D. Charlet, and G. Damnati. "Simbow at semeval-2017 task 3: Soft-cosine semantic similarity between questions for community question answering", in Proceedings of the 11th International Workshop on Semantic Evaluation (SemEval-2017), pp. 315-319.

[15] J. Mitchell and M. Lapata. "Composition in distributional models of semantics", Cognitive science, 34(8), 1388-1429, 2010.

[16] M. Baroni and A. Lenci. "Distributional memory: A general framework for corpus-based semantics", Computational Linguistics, 36(4), 673-721, 2010.

[17] R. Collobert and J. Weston. "A unified architecture for natural language processing: Deep neural networks with multitask learning", in Proceedings of the 25th international conference on Machine learning, pp. 160-167.

[18] J. Oliva, J. I. Serrano, M. D. Del Castillo and A. Iglesias. "SyMSS: A syntax-based measure for short-text semantic similarity", Data & Knowledge Engineering, 70(4), 390-405, 2011.

[19] A. S. Mohammad, Z. Jaradat, A. A. Mahmoud and Y. Jararweh. "Paraphrase identification and semantic text similarity analysis in Arabic news tweets using lexical, syntactic, and semantic features", Information Processing & Management, 53(3), 640-652, 2017.

[20] D. Das and N. A. Smith. "Paraphrase identification as probabilistic quasi-synchronous recognition", in Proceedings of the Joint Conference of the 47th Annual Meeting of the ACL and the 4th International Joint Conference on Natural Language Processing of the AFNLP, pp. 468-476.

[21] N. Madnani, J. Tetreault and M. Chodorow. "Re-examining machine translation metrics for paraphrase identification", in Proceedings of the 2012 conference of the north american chapter of the association for computational linguistics: Human language Technologies, pp. 182-190.

[22] R. Socher, E. Huang, J. Pennin, C. D. Manning and A. Ng. "Dynamic pooling and unfolding recursive autoencoders for paraphrase detection", Advances in neural information processing systems, 24, 2011.

[23] R. Ferreira, G. D. Cavalcanti, F. Freitas, R. D. Lins, S. J. Simske and M. Riss. "Combining sentence similarities measures to identify paraphrases". Computer Speech & Language, 47, 59-73, 2018.

[24] H. He, K. Gimpel and J. Lin. "Multi-perspective sentence similarity modeling with convolutional neural networks", in Proceedings of the 2015 conference on empirical methods in natural language processing, pp. 1576-1586.

[25] A. Prakash, S. A. Hasan, K. Lee, V. Datla, A. Qadir, J. Liu and O. Farri. "Neural paraphrase generation with stacked residual LSTM networks", arXiv preprint arXiv:1610.03098, 2016.

[26] Z. Li, X. Jiang, L. Shang and H. Li. "Paraphrase generation with deep reinforcement learning", arXiv preprint arXiv:1711.00279, 2017.

[27] J. Mueller and A. Thyagarajan. "Siamese recurrent architectures for learning sentence similarity", in Proceedings of the AAAI conference on artificial intelligence, Vol. 30, No. 1.

[28] M. A. Arabacı, E. Esen, M. S. Atar, E. Yılmaz and B. Kaltalıoğlu. "Detecting similar sentences using word embedding", in 2018 26th Signal Processing and Communications Applications Conference (SIU), pp. 1-4.

[29] E. Yıldız and Y. Fındık. "Question Similarity Detection in Turkish Using Semantic Textual Similarity Methods", in 2019 27th Signal Processing and Communications Applications Conference (SIU), pp. 1-4.

[30] J. Rashid, S. M. A. Shah and A. Irtaza. "Fuzzy topic modeling approach for text mining over short text", Information Processing & Management, 56(6), 102060, 2019.

[31] G. Ercan, O. Erkek, O. Açıkgöz, R. Özçelik, S. Parlar and O. T. Yıldız. "Data Set Generation for Analysing of Turkish Semantic and Sentence Similarity", in 2018 3rd International Conference on Computer Science and Engineering (UBMK), pp. 347-351.

[32] K. Dey, R. Shrivastava and S. Kaushik. "A paraphrase and semantic similarity detection system for user generated short-text content on microblogs", in Proceedings of COLING 2016, the 26th International

Conference on Computational Linguistics: Technical Papers, pp. 2880-2890.
[33] A. Bağcı and M. F. Amasyali. "Comparison of Turkish Paraphrase Generation Models", in 2021 International Conference on INnovations in Intelligent SysTems and Applications (INISTA), pp. 1-6.
[34] T. Mikolov, I. Sutskever, K. Chen, G. S. Corrado and J. Dean. "Distributed representations of words and phrases and their compositionality", Advances in neural information processing systems, 26, 2013.
[35] A. Joulin, E. Grave, P. Bojanowski, M. Douze, H. Jégou and T. Mikolov. "Fasttext. zip: Compressing text classification models", arXiv preprint arXiv:1612.03651, 2016.
[36] J. Devlin, M. W. Chang, K. Lee and K. Toutanova. "Bert: Pre-training of deep bidirectional transformers for language understanding", arXiv preprint arXiv:1810.04805, 2018.

On the Use of Time Series Datasets Through Google Earth Engine to Monitor the Forest Cover Loss in Türkiye Between 2001 and 2021

C. SERIFOGLU YILMAZ

Karadeniz Technical University, Trabzon/Turkey, cigdem_srf@hotmail.com

***Abstract* - As in the whole world, detailed information on global forest resources and their changes over the years is needed for forest management applications in Türkiye. Caused by various reasons, deforestation is one of the most important environmental problems of Türkiye. Determining deforestation in country-scale areas with traditional terrestrial techniques is very challenging, especially in cases where urgent actions need to be taken. Today, the ease of access to satellite images has enabled the observation of forests at different spatial and temporal resolutions. As a widely-used cloud computing platform, Google Earth Engine (GEE) makes it easy to observe the Earth and perform various analyses. The present study aims to monitor forest cover loss in Türkiye from 2001 to 2021 through the Hansen Global Forest Change (HGFC) data that is available on GEE platform. The pixels that had a tree cover density greater than 30% in the tree cover data for the year 2000 were used to specify the forest areas used for comparison. The results showed that, in Türkiye, the highest forest loss was observed in 2021, with an increase rate of 72.85%, compared to 2020. The analysis conducted on seven different geographical regions of Türkiye revealed that the greatest amount of forest loss was seen in the Mediterranean, Aegean, and Marmara regions.**

***Keywords* – Google Earth Engine, Hansen Global Forest Change Data, Forest Change Detection, Time Series Analysis.**

I. INTRODUCTION

COUNTRIES' forest cover can be considered as a very important indicator in terms of economic, political, technological and socio-cultural aspects. Deforestation, which is caused by natural or man-made effects, is one of the most important problems faced by developing countries [1-3]. Since the it is not possible to take quick actions with time-consuming ground measurements, the use of remotely sensed data in large scale areas seems to be quite necessary. With the high-resolution Global Forest Change data presented by Hansen et al. [4], temporal and spatial forest loss or gain information has become easily available. The Hansen Global Forest Change (HGFC) data has great potential to assist countries in periodically monitoring their national forest inventory. However, of course, there will be some benefits and drawbacks in using global data for studies to be carried out at the country level. According to Shimizu et al. [5], to ensure more stable and higher accuracy, using local forest disturbance data is more logical than the HGFC data. They also stated that the HGFC data can provide comparable accuracies with local forest disturbance data in areas larger than 3 ha. Examining the accuracy of the HGFC dataset of small forest areas to determine forest loss, Yamada et al. [6] indicated that studies conducted in small forest areas did not give high accuracy. Likewise, Galiatsatos et al. [7], stated that the HGFC dataset, when appropriately calibrated for percentage tree cover, provide a good first approximation of forest loss. On the other hand, generation of a highly accurate local map for forest distribution at country scale requires excessive time, extreme field work, experienced specialists and computational resources [8]. Taking all this into account, it seems that using HGFC dataset at country scale could be feasible for initial assessment.

In light of all these, this study aimed to reveal the forest loss in Turkey between 2001 and 2021 using the Hansen Global Forest Change (HGFC) data provided through the Google Earth Engine (GEE) (with JavaScript API code editor) platform.

II. MATERIAL AND METHODS

The study aims to examine the loss of forest area in Türkiye between the years 2001-2021. Covering an area of approximately 78,3000 km^2, Turkey is located in the South-eastern Europe and South-western Asia region (latitudes of 36–42°N and longitudes 26–45°E). With reference to the 2021 data of the General Directorate of Forestry of Turkey, 29.5% of Turkey's land is covered with forest areas [9]

The HGFC data version 1.9 [4] was used for mapping forest loss. Annually updated HGFC data, which was generated by the University of Maryland from Landsat time series images, have been used to analyze the global forest change since 2000. At a 30-m spatial resolution, HGFC data offers tree cover, forest loss, gain, and forest loss year. The following bands provided in the HGFC data were utilized for the current study: (1) "treecover2000" refers to the canopy closure in the year 2000 for all vegetation taller than 5m in height. It is stored as a percentage per grid cell ranging from 0 to 100. (2) "loss", the loss band is encoded in binary format, where a pixel value of '0' indicates no loss and '1' indicates loss. (3) "lossyear", in this band, pixels take a value between '1' and '21' to represent the year of the loss, or '0' if no loss happened [4,10].

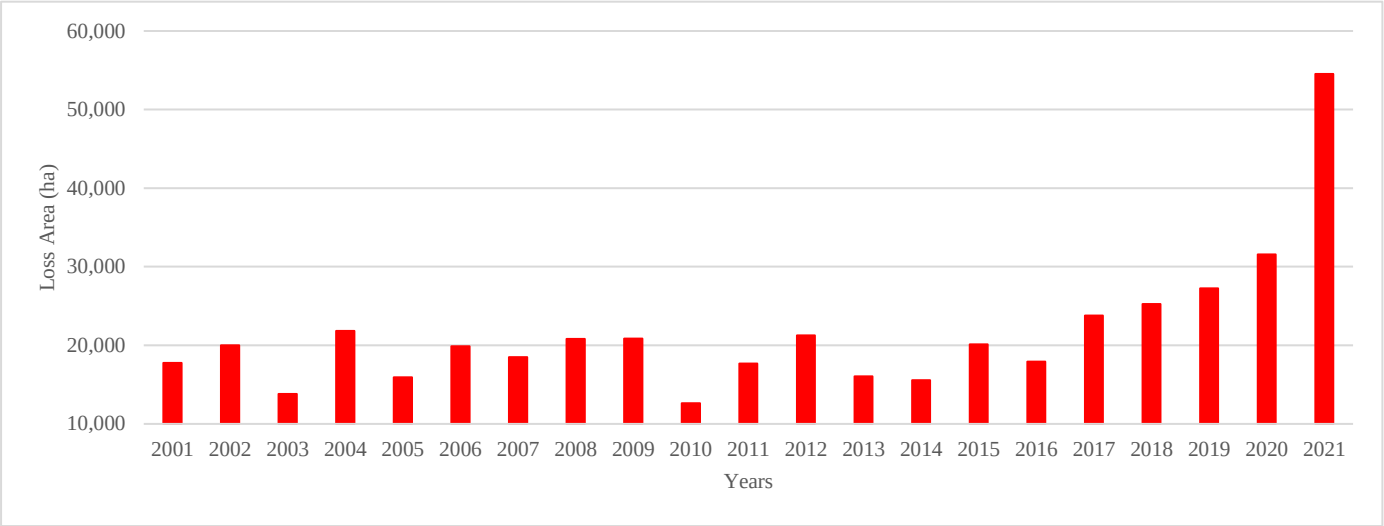

Figure 1: Forest loss between 2001 and 2021.

In the study, the HGFC data were initially imported with collection id: "UMD/hansen/global_forest_change_2021_v1_9 ". The "treecover2000" layer was then obtained and clipped according to Türkiye' s borders. As mentioned before, the "treecover2000" layer takes a value between 0-100 in percentage units indicating tree density. In order to increase the accuracy, "treecover2000" layer was filtered to eliminate the areas with a density less than 30%, as advised by many research in the literature [5, 7]. Then, the pixel values of this layer were multiplied by the grid cell area to obtain the forest cover area. The "loss" layer was also used to visualize the total forest loss since 2001. Then the "loss" band was correlated with the "lossyear" band to determine the amount of loss in each year. Finally, to investigate the forest area loss throughout Türkiye' s geographical regions, the shape file data for seven regions were imported into the GEE platform and linked with the HGFC data to determine the forest area loss between the years 2001-2021.

III. Results and Discussion

According to the tree cover data provided by the HGFC for the year 2000, taking the tree cover density above 30% led to a total of 452,922.23 hectares of forest area loss in Türkiye between the years 2001 and 2021. It can be seen that the forest loss has increased in the recent years rapidly, especially in 2021 with a rate of 72.85% compared to 2020 (see Figure 1). The increase in forest loss in 2021 is 173.8 % higher than the average of the other years.

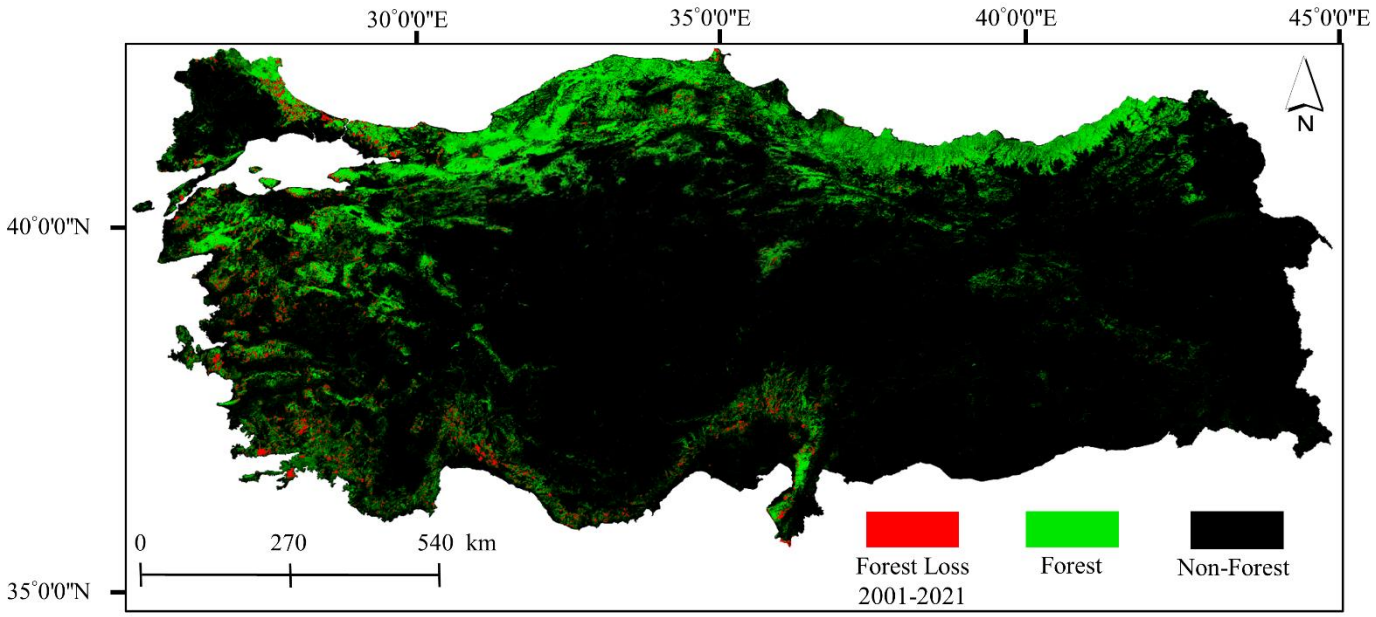

Figure 2: Forest loss between the years 2001 and 2021 (Forest areas with a high density of trees are shown in brighter green)

Figure 2 shows the total forest loss between the years 2001 and 2021. As can be seen in the figure, forest loss occurred mostly in specific regions. The forest loss observed in seven geographical regions of Türkiye between 2001 and 2021 was also analysed to understand the amount of forest loss by region. Table 1 shows the area of forest loss for each geographical region. According to Table 1, the majority of forest loss in Türkiye occurs in the Mediterranean, Aegean, and Marmara regions. The regions Marmara, Aegean and Mediterranean faced the greatest amount of forest loss between the years 2001 and 2021, with rates of 33.14%, 29.74% and 20.21% across the country, respectively. The forest loss was found to be quite low in the regions of Central Anatolia, Eastern Anatolia and South-eastern Anatolia, where the continental climate is dominant. The forest loss is relatively lower in the Black Sea region, which has a large proportion of forest areas in the country. Table 1 also reveals that a significant amount of forest loss in the Aegean and Mediterranean regions was observed in the last year. In 2021, forest loss in the Aegean region increased by 128.36% compared to the previous year. Looking at the average of the other years except 2021 in the Aegean region, it is observed that there is a 234.34% increase in forest loss in 2021. The forest loss in the Mediterranean region increased by 78.46% in 2021 when compared to the previous year. When 2021 forest loss is compared to the average of the previous years in the Aegean region, it is shown that there is a 252.13% increase in 2021. The extreme forest loss in the Aegean and Mediterranean regions in the last year was largely due to the forest fires occurred in these regions in 2021 [9]. Figure 3 depicts the forest loss in the regions Aegean, Mediterranean and Marmara, which have experienced the highest forest area loss.

Table 1: Forest loss in seven geographical regions of Türkiye between 2001-2021.

	Forest Loss (ha)						
	Geographic Regions of Türkiye						
Loss Years	**Mediterranean**	**Aegean**	**Marmara**	**Black Sea**	**Central Anatolia**	**Eastern Anatolia**	**South-eastern Anatolia**
2001	2,509.88	3,730.46	9,930.64	1,107.85	194.36	181.11	67.21
2002	1,610.41	4,293.71	10,591.98	2,474.27	911.57	105.11	27.65
2003	2,394.09	3,378.48	7,172.38	603.57	174.26	42.79	24.77
2004	2,836.97	3,579.26	9,146.72	5,399.31	648.21	187.33	53.90
2005	2,180.76	3,510.76	8,063.53	1,528.67	611.86	37.63	16.60
2006	3,434.46	7,044.62	7,103.06	1,819.64	375.34	91.15	24.58
2007	3,714.96	7,132.44	4,115.72	2,302.12	1,136.81	100.81	34.88
2008	6,894.12	6,795.15	4,368.11	2,448.42	204.10	98.84	32.69
2009	6,207.32	6,815.70	4,161.78	2,837.94	628.94	128.17	63.52
2010	2,490.98	4,626.13	3,297.22	1,972.43	142.55	94.11	59.46
2011	3,695.89	6,103.71	4,546.94	2,583.73	716.60	71.26	18.20
2012	5,121.92	6,223.28	6,980.06	2,532.56	179.34	89.18	33.76
2013	3,125.79	4,292.67	5,558.64	2,836.09	166.70	69.79	20.48
2014	2,797.65	4,023.94	6,342.49	2,175.50	166.61	44.75	19.65
2015	2,893.73	7,260.46	7,166.32	2,418.57	354.87	22.98	9.83
2016	3,184.61	5,502.42	5,932.43	2,861.42	492.72	53.37	4.00
2017	4,213.08	7,873.84	8,131.41	3,056.63	514.24	26.66	6.80
2018	5,486.86	6,815.31	7,666.84	4,234.56	1,022.61	51.17	11.73
2019	5,417.11	8,065.91	8,335.03	4,115.15	1,272.35	83.17	21.79
2020	7,684.93	8,456.97	9,411.05	4,250.60	1,575.91	175.09	16.90
2021	13,714.59	19,312.49	12,220.40	7,471.05	1,622.52	144.71	39.75

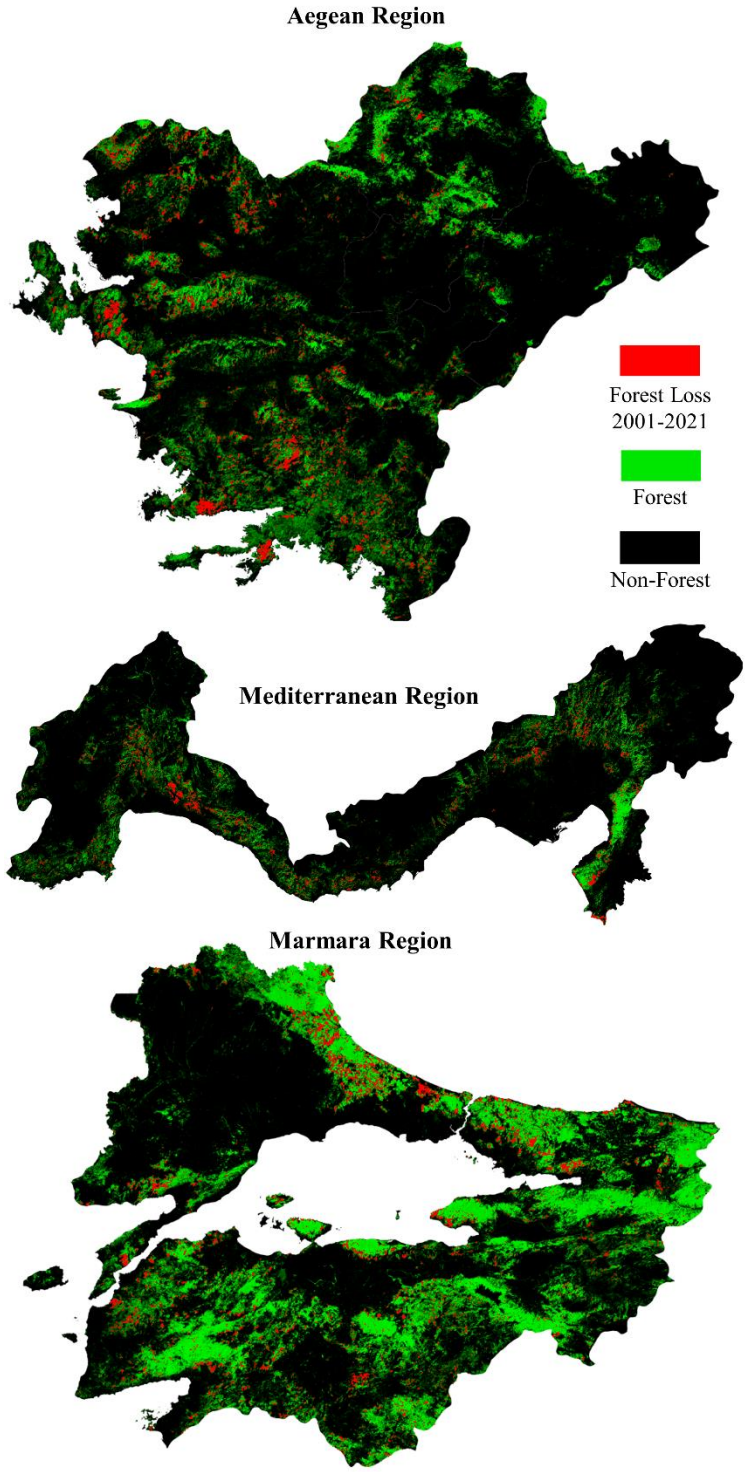

Figure 3. Forest loss in the regions Aegean, Mediterranean and Marmara

IV. CONCLUSION

The current study used the HGFC data provided in the GEE platform to reveal the forest loss occurred in Türkiye between the years 2001 and 2021. A tree cover density greater than 30% was considered for each pixel to increase the accuracy, as in many previous studies. Experiments revealed that the forest loss increased in Türkiye in the recent years. The greatest amount of forest loss was observed in the regions Mediterranean, Aegean, and Marmara. It can be concluded that the use of GEE provides prior knowledge to reveal the change in forest inventory in large-extent areas. Its rich data content, easy-to-use interface and fast analyses capability make it one of the very first platforms that can be resorted for forest management applications.

REFERENCES

[1] H. J. Geist and E. F. Lambin. What drives tropical deforestation. *LUCC Repor Series 4*, 2001.

[2] R. S. DeFries, T. Rudel, M. Uriarte, and M. Hansen. "Deforestation driven by urban population growth and agricultural trade in the twenty-first century," *Nature Geoscience*, vol. 3, no. 3, pp. 178-181, 2010.

[3] M. A. Brovelli, Y. Sun, and V. Yordanov. "Monitoring forest change in the amazon using multi-temporal remote sensing data and machine learning classification on Google Earth Engine,". *ISPRS International Journal of Geo-Information*, vol. 9, no. 10, pp. 580, 2020.

[4] M. C. Hansen, P. V. Potapov, R. Moore, M. Hancher, S. A. Turubanova, A. Tyukavina, D. Thau, S. V. Stehman, S. J. Goetz, T. R. Loveland, A. Kommareddy, A. Egorov, L. Chini, C. O. Justice, and J. R. G. Townshend. "High-Resolution Global Maps of 21st-Century Forest Cover Change," *Science*, vol. 342, pp. 850-853, 2013.

[5] K. Shimizu, T. Ota, and N Mizoue. "Accuracy assessments of local and global forest change data to estimate annual disturbances in temperate forests," *Remote Sensing*, vol. 12, no. 15, 2020.

[6] Y. Yamada, T. Ohkubo, and K. Shimizu. "Causal analysis of accuracy obtained using high-resolution global forest change data to identify forest loss in small forest plots," *Remote Sensing*, vol. 12, no. 15, 2020.

[7] N. Galiatsatos, D. N. Donoghue, P. Watt, P. Bholanath, J. Pickering, M. C. Hansen, and A. R. Mahmood. "An assessment of global forest change datasets for national forest monitoring and reporting," *Remote Sensing*, vol. 12, no. 11, 2020.

[8] W. Turner, C. Rondinini, N. Pettorelli, B. Mora, A. K. Leidner, Z. Szantoi, G. Buchanan, S. Dech, J. Dwyer, M. Herold, L. P. Koh, P. Leimgruber, H. Taubenboeck, M. Wegmann, M. Wikelski, and C. Woodcock. "Free and open-access satellite data are key to biodiversity conservation," *Biological Conservation*, vol. 182, pp. 173-176, 2015.

[9] General Directorate of Forestry, https://www.ogm.gov.tr/tr/e-kutuphane/resmi-istatistikler, access date: 10.10.2022.

[10] M. Mishra, C. A. G. Santos, T. V. M. do Nascimento, M. K. Dash, R. M. das Silva, D. Kar, and T. Acharyya. "Mining impacts on forest cover change in a tropical forest using remote sensing and spatial information from 2001–2019: A case study of Odisha (India)," *Journal of Environmental Management*, vol. 302, 2022.

The impact of research and citations on world rankings of countries with the best universities

L. GASHI[1], A. LUMA[1] and Y. JANUZAJ[2]

[1] South East European University, Tetovo/ Republic of North Macedonia, {lg29758 & a.luma}@seeu.edu.mk
[2] University "Haxhi Zeka", Peja/Kosovo, ylber.januzaj@unhz.eu

Abstract - **The ranking of world universities is based on several attributes that also consider research and citations, where their impact on the country's global positioning as having the best universities could change its current position. These attributes must be measured for this effect to look reasonable.**

The Times Higher Education World University Rankings (THE) provides a data set that ranks various universities around the world based on total common attributes, among others including research and citations. But this positioning can be discerned using a specific statistical approach, such as considering only research and citations, by giving such universities a different ranking position that is different from what is known.

This approach has also affected the ranking of countries with the best universities. The statistical relationship of research and citations, as well as the global ranking positions of the best universities and their respective countries are shown in this study by processing THE's dataset using SPSS program. Understanding the importance of research and citations to science and society, results of these contrasting positioning approaches can have a profound impact on how university rankings are conducted, and depending on how these occur, the study shows the changed global positioning of countries with the best universities.

Keywords **– Research, Citations, World Ranking Universities, Best Universities.**

I. INTRODUCTION

WORLD ranking of universities is taken as a significant factor when the assessment of universities is treated. Governments as well as many other institutions use world ranking to argue their statement about any worldwide university. On the other hand, ranking universities is not an easy task, since each of them has its own research area and offers different academic programs, and additionally, each country has its own history and higher education system, which can affect the structure of universities and how they compare to other countries [1].

Furthermore, there are several rankings conducted by magazines, websites, governments, or academics which provide their lists by using different methodologies to do the university ranking. The common approach is by gathering several attributes through which the ranking is done, but this approach might be doubtful due to fairness conductivity of ranking because overall scores of indicators for world's universities ranks that are taken are calculated internally on background [2].

One of the well-known world ranking magazines is the Times Higher Education World University Rankings (THE). According to THE, performance indicators are grouped into five areas which include education (learning environment), research (volumes, income, reputation), citations (research impact), internationality (staff, students, research) and industry income (knowledge transfer) [3].

Considering that research and citations are the qualitative aspects of university studies, specific world ranking based only on these indicators would define if these had the main impact at world ranking and if this ranking is different only with these indicators. This approach gives a distinct perspective of ranking systems, which is the aim of this study. To define this, the research is conducted, and its results are presented on this paper. For more, since the common ranking is based on universities, the paper presents the countries with top ranked universities. The impact of research and citations as the main keywords is analyzed, interpreted, and statistically presented by using the ratio of overseas staff to domestic staff and number of THE records. The results are based only on this source, so it is vowed that having at least another source would give us the possibility of comparing the outputs. The first part of the paper is the introduction, the second part shows different approaches about world ranking universities and continues with detailed THE ranking which is reviewed with current literature found at respective sources. The third part includes the method and statistical approach of this study. Results are presented in the fourth part, while the meaning, significance and the final impact is discussed in the fifth part of this paper.

The acceptance of limitations as well as the need for future studies are included in the sixth part, which precedes the final part of this paper where the conclusion is given. By using factor analyses, correlation and regression, a significant impact of research and citations is shown on world rankings of countries with the best universities.

II. LITERATURE REVIEW

Ranking of world universities is used as a reference point by students and agencies as a choice to study across the globe and helps make decisions about that choice since they provide positioning and measuring of institutions that offer higher education within countries or worldwide [4].

All ranking methods rely on data input from various external sources. This often includes the three examples below, but varies depending on the niche and focus of each ranking system [16]:

- University institutional and researcher data from bibliographic or citation index databases such as Scopus (based on research results) [16], [17];
- Relevant human resources, student administration and financial data [16], [17];
- Surveys and their reputations received from faculty, students, alumni, and employers [16], [17].

A. World ranking systems

The ranking university as a practice was started in 1925 by Professor Donald Hughes who ranked graduate programs based on peer reputations in the United States [5]. Since then, many initiatives on ranking the universities and institutions of graduate programs have been deployed by academic researchers and by research institutes in the past century like Cartter in 1966, Drew and Karpf 1981, Conrad and Blackburn in 1985 and Ehrenberg and Hurst in 1996 [6-9].

The common dimensions of university ranking were based on measuring teaching, research, and service quality. These dimensions are used even nowadays, only that the list of indicators is extended.

Among more than 20 different world ranking systems, the oldest and most influential are ARWU (produced by ShanghaiRanking Consultancy), Times Higher Education (THE) and Quacquarelli Symonds (QS) [10].

Characteristics of these three chosen ranking systems are:

1) The Academic Ranking of World Universities (ARWU), which was first published in June 2003 by the Center for World-Class Universities (CWCU), while the Academic Ranking of World Universities (ARWU) has been published since 2009 and copyrighted by ShanghaiRanking Consultancy [18]. ARWU counts the number of Nobel and Field Prize-winning alumni and staff, the number of top citation analysts selected by Clarivate Analytics, the number of articles published in Nature and Science journals, and the Science Citation Indexes - Expanded and Social Citations Index, and the per capita performance of the top 1000 publishing universities, ranking over 1800 universities each year [11].
2) The Times Higher Instruction makes rankings to evaluate the performance of universities according to a worldwide arrangement through which it is supplied a resource for readers to understand range differences of higher educational institutions based on activities such as research, teaching, and impact [12].
   Each university within the rankings incorporates a point by point profile, with a breakdown of its in general scores over the rankings and supplementary information outlined to assist understudies, but a few colleges have upgraded profiles to exhibit their understudy offer and their person qualities and qualities of the past rankings information, where THE's rich information have ended up an imperative asset for understudies, supporting them on how to make one of the most important choices of their lives on who to believe about their education, so the rankings are broadly utilized by staff to advise career choices, by college pioneers to assist set key needs and by governments to assist screen arrangement [12].
3) Quacquarelli Symonds (QS) has successfully developed and implemented comparative data collection and analysis methods to highlight institutional strengths through an annual publication of university rankings, including global overall and subject rankings, produced by the same groups like: Graduate Employability Rankings, Best Student Cities, University System Strength Rankings, by location ranking, a series of business school rankings including Global MBA, EMBA, Distance Online MBA, Business Masters [13].

Commonly, the three ranking systems (ARWU, QS, THE) distribute their comes about online utilizing ordinal positioning lists.

This research paper is based on THE's ranking list, so the further focus is oriented at its indicators.

B. The Times Higher Education ranking

THE system uses 13 measures for 5 dimensions. First, the education dimension is weighted by 30%, and second, the research dimension has a 30%, the third dimension is citation impact, given a weight of 30%, the fourth dimension is research funding from industry contributing 2.5% to the overall score [19-21] and finally, the international outlook dimension of an institution which has a weight of 7.5% [14], [20], [21].

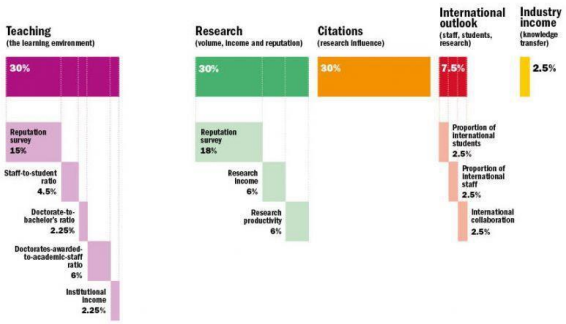

Figure 1. Five dimensions of The Times Higher Education ranking. [14]

These five dimensions are weighted according to THE's relative importance rating, once the final set of colleges and indicators is created, a score is created for each college by weighting the indicator to represent the total score or a percentage of it between 1 and 100 [15], [19].

C. Calculation of metrics for Research and Citations

Since the paper is focused on Research and Citations, only these indicators are presented showing the calculation metrics description based on the THE's method.

1) Research by THE is based on a metric derived from the indexing of Elsevier's Scopus database of the total number of articles published in scientific journals, considering research reputation, research income and research productivity [15], [19-23].
2) Citations according to THE's research impact indicator examines the role of universities in disseminating new knowledge and innovative ideas by examining the impact of research by measuring the average number of times university publications are cited by scholars worldwide like Elsevier's Scopus database [15], [19-23].

D. The research question and hypotheses

This study analyses the impact of research and citations on world ranking universities, emphasizing this impact at countries with top ranked universities accepted as the best universities. The question about this impact is answered by proving the hypotheses which are as follows:

H1: Research does impact on the world ranking of countries with top universities.

H2: Citations do impact on the world ranking of countries with top universities.

H3: Research has more impact than citations on the world ranking of countries with top universities.

H4: Countries with top universities have different world ranking positions considering only research or only citations.

By proving these hypotheses, the study provides a different approach for world ranking countries with top ranked universities compared to mentioned world ranking systems. There are only two indicators taken into consideration from the used dataset and their impact is shown separately. Also, this study shows if there is a difference in ranking countries with top ranked universities according to this approach by comparing outputted results with those of the THE's system.

III. METHOD

World ranking of universities are defined by The Times Higher Education World University Rankings annual publication. By using its dataset, countries with top universities are defined. The subjects of research are countries with top universities where a different world ranking approach is used to define their positions. By quantifying the attributes included within the dataset, through statistics extracted with the SPSS program, the world rank of countries with top universities is shown.

There are 31 countries represented by 200 top ranked universities worldwide. Variables which are used to define the world ranking are: world_rank, country, research, and citations. *Country* and *world_rank* are dependent variables (DV) while *research* and *citations* are independent variables (IV).

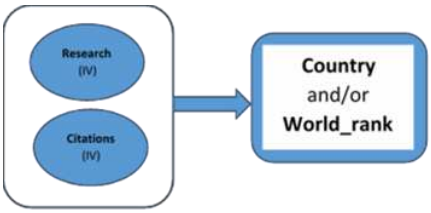

Fig. 2. Used variables and their dependence.

By using factor analyses, correlation and regression, the impact of research and citations is shown on world ranking of universities and their respective countries. The probability of obtaining data results is expressed with P- Value, where for P-Value < 0.001 the data are treated as reliable and are considered as a significant factor to run the hypothesis test.

IV. RESULTS

The results are extracted from the dataset by using the SPSS program and are presented through the following sections.

A. *Exploratory factor analysis*

Firstly, the KMO test is run where its critical value is 0,5. If the value < 0,5 then the factor analyses can be continued, in our case as it is shown in the table, it is 0,421 so it is close to 0,05 so the analyses can be continued.

Table 1. KMO and Bartlett's Test showing the factor analyses.

KMO and Bartlett's Test

Kaiser-Meyer-Olkin Measure of Sampling Adequacy.		,421
Bartlett's Test of Sphericity	Approx. Chi-Square	2326,823
	df	6
	Sig.	,000

Results from the section of exploratory factor analysis argue that data are significant and that there is a relation between variables. Within the same table is shown also the Bartlet's test which tells if data are significant or not as well as if there is a relation between variables. If value < 0,05 then it tells that there is a significance, and the factor analysis can be continued because the data are useful. In our case it is 0,000 which means it is significant and the factor analysis can be continued.

B. *Correlation*

According to the bellowed table where it is shown the Correlation between variables, there is a significance between variables since the value of Pearson Correlation is <0,01.

Table 2. Correlation between variables.

Correlations

		world_rank	research	citations	country
world_rank	Pearson Correlation	1	-,831**	-,515**	-,152**
	Sig. (2-tailed)		,000	,000	,000
	N	1201	1201	1201	1201
research	Pearson Correlation	-,831**	1	,190**	,079**
	Sig. (2-tailed)	,000		,000	,006
	N	1201	1201	1201	1201
citations	Pearson Correlation	-,515**	,190**	1	,380**
	Sig. (2-tailed)	,000	,000		,000
	N	1201	1201	1201	1201
country	Pearson Correlation	-,152**	,079**	,380**	1
	Sig. (2-tailed)	,000	,006	,000	
	N	1201	1201	1201	1201

**. Correlation is significant at the 0.01 level (2-tailed).

Table 2 shows the significance between variables. According to this table, the value of Pearson Correlation for all variables is significant, which means that the null hypothesis of non-existing impact of research and citation on the world ranking of countries with top ranked universities does not stand. The value for the variable world_rank in correlation with variable research is -0,831 which proves the first hypothesis and its impact. Also, the second hypothesis is proved with the value of variable citation which is -0,515 by telling the impact that citation has on the world ranking of countries with top ranked universities.

C. *Regression*

The regression is calculated with the formula $Y = \beta_1 + \beta_2 X_1 + \beta_3 X_2 + u_i$ where the Y represents the dependent variable (world_rank) while X_1 and X_2 the independent ones (research, citations) respectively. The test is conducted only for the variable *world_rank* considering that the other dependent variable (country) derives from this variable, so it is shown only through the table of model summary at the end of this section.

The model summary table shows dependence between variables, for instance R Square = 0,691 tells that the variable *research* explains 69,1% of variance for the variable *world_rank*, while the variable *citation* explains 82,3% of this variance.

Firstly, the ANOVA table shows tests of significance for the variance of variables, where the referenced value for comparison is 0,05.

Table 3. Tests of significance for the variance of variables

ANOVA[a]

Model		Sum of Squares	df	Mean Square	F	Sig.
1	Regression	2754078,673	1	2754078,673	2680,229	,000[b]
	Residual	1232036,581	1199	1027,553		
	Total	3986115,254	1200			
2	Regression	3282197,368	2	1641098,684	2792,991	,000[c]
	Residual	703917,886	1198	587,578		
	Total	3986115,254	1200			

a. Dependent Variable: world_rank

b. Predictors: (Constant), research

c. Predictors: (Constant), research, citations

Table 3 shows that significance's values at both models are 0,000 which is less than the reference value of 0,05 taken for comparison. This means that all variables of this research are good predictors.

Secondly, the table of Coefficients shows the impact of predictors. In this case there are two models expressed by the regression formula:

Model 1: *world_rank* = 227,550 – 2,437 * *research* + uí

Model 1: *world_rank* = (227,550 – 2,437 * *research*) + (227,550 – 2,437 * *citation*) + uí

Table 4. The impact of predictors.

Coefficients[a]

Model		Unstandardized Coefficients B	Unstandardized Coefficients Std. Error	Standardized Coefficients Beta		Sig.
1	(Constant)	227,550	2,627		86,606	,000
	research	-2,437	,047	-,831	-51,771	,000
2	(Constant)	322,563	3,740		86,236	,000
	research	-2,230	,036	-,761	-61,512	,000
	citations	-1,375	,046	-,371	-29,980	,000

Both models show that as higher the research and the citations are, the sum for the variable *world_rank* (Y) decreases which means that the representative number for ranking is lower. Regression is presented also through graphics with respective Figures 3 and 4.

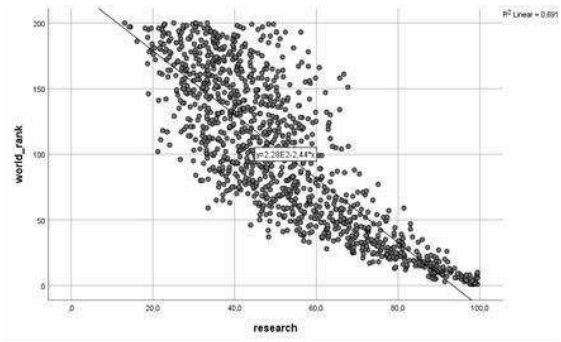

Figure 3. Regression graphic of research.

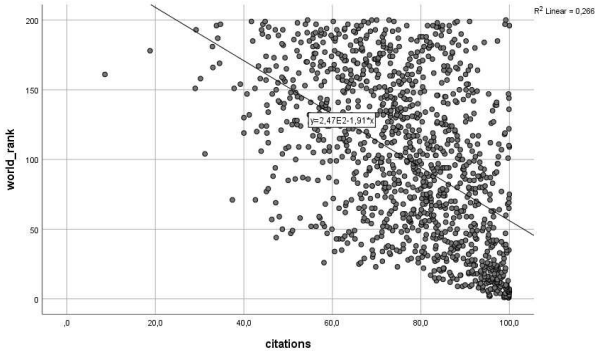

Figure 4. Regression graphic of citation.

The difference of values for the variable research and the variable citations at all tables also show the different level of impact that these variables have at the variable *world_rank*. These values shown above tell that research has a higher impact than citations on the world ranking of countries with top ranked universities, proving the third hypothesis of this study.

Lastly, model summary tables show dependence between variables, for instance R Square = 0,691 tells that the variable research explains 69,1% of variance for the variable *world_rank,* while the variable citation explains 82,3% of this variance.

Table 5. Dependence between variables.

Model Summary

Model	R	R Square	Adjusted R Square	Std. Error of the Estimate
1	,831[a]	,691	,691	32,055
2	,907[b]	,823	,823	24,240

a. Predictors: (Constant), research

b. Predictors: (Constant), research, citations

This means that both independent variables are good predictors for the dependent variable and that the world ranking of universities for top ranked countries is dependent from research and citations. This proves again the first and second hypotheses of the impact that research and citation have on the world ranking of countries with top ranked universities.

In order to present results which are related to the variable Country, the table of Model summary of regressions by Countries is extracted and shown below.

Table 6. Model summary of regressions by Countries.

Model Summary[c]

Country	Model	R	R Square	Adjusted R Square	Std. Error of the Estimate	Change Statistics: R Square Change	F Change	df1	df2	Sig. F Change
Australia	1	,877[a]	,769	,763	24,079	,769	143,014	1	43	,000
	2	,935[b]	,874	,868	17,979	,105	35,127	1	42	,000
Belgium	1	,911[a]	,830	,821	21,361	,830	97,578	1	20	,000
	2	,936[b]	,876	,863	18,725	,046	7,027	1	19	,016
Brazil	1	1,000[a]	1,000	.	.	1,000	.	1	0	.
Canada	1	,898[a]	,806	,802	27,433	,806	191,119	1	46	,000
	2	,916[b]	,839	,832	25,277	,033	9,182	1	45	,004
China	1	,860[a]	,740	,724	31,589	,740	45,612	1	16	,000
	2	,931[b]	,867	,849	23,363	,127	14,252	1	15	,002
Denmark	1	,596[d]	,356	,315	21,657	,356	8,828	1	16	,009
	2	,814[e]	,663	,618	16,181	,307	13,660	1	15	,002
France	1	,808[a]	,653	,642	30,138	,653	63,870	1	34	,000
	2	,868[b]	,753	,738	25,775	,101	13,486	1	33	,001
Germany	1	,819[a]	,670	,666	29,519	,670	156,397	1	77	,000
	2	,908[b]	,824	,819	21,711	,154	66,347	1	76	,000
Hong Kong	1	,837[a]	,700	,685	31,739	,700	46,681	1	20	,000
	2	,955[b]	,911	,902	17,730	,211	45,088	1	19	,000
Japan	1	,952[a]	,906	,902	15,248	,906	240,969	1	25	,000
	2	,963[b]	,926	,920	13,764	,020	6,680	1	24	,016
Netherlands	1	,681[a]	,463	,455	30,047	,463	57,806	1	67	,000
	2	,860[b]	,739	,731	21,095	,276	69,936	1	66	,000
Norway	1	,890[a]	,792	,750	12,302	,792	19,009	1	5	,007
Republic of Ireland	1	,794[d]	,630	,589	22,556	,630	15,322	1	9	,004
	2	,949[e]	,901	,876	12,387	,271	21,843	1	8	,002
Russian Federation	1	1,000[d]	1,000	.	.	1,000	.	1	0	.
Singapore	1	,817[a]	,668	,635	32,017	,668	20,107	1	10	,001
	2	,952[b]	,906	,886	17,906	,239	22,971	1	9	,001
South Africa	1	,830[d]	,690	,612	5,827	,690	8,885	1	4	,041
South Korea	1	,635[a]	,403	,375	40,236	,403	14,182	1	21	,001
	2	,896[b]	,803	,784	23,672	,400	40,671	1	20	,000
Sweden	1	,741[a]	,549	,534	31,948	,549	36,485	1	30	,000
	2	,891[b]	,793	,779	22,002	,244	34,251	1	29	,000
Switzerland	1	,817[a]	,667	,659	27,262	,667	78,155	1	39	,000
	2	,929[b]	,863	,856	17,689	,196	54,636	1	38	,000
Taiwan	1	,740[d]	,547	,482	17,513	,547	8,455	1	7	,023
United Kingdom	1	,871[a]	,758	,757	28,493	,758	576,988	1	184	,000
	2	,920[b]	,846	,845	22,774	,088	105,034	1	183	,000
United States of America	1	,878[a]	,770	,770	28,850	,770	1458,847	1	435	,000
	2	,925[b]	,856	,855	22,887	,085	257,192	1	434	,000

a. Predictors: (Constant), research

b. Predictors: (Constant), research, citations

c. Dependent Variable: world_rank

d. Predictors: (Constant), citations

e. Predictors: (Constant), citations, research

From the column of significance at Table 6 it is shown that for all countries variables are significant. Also, the R Square values tells that both models explain in high percentage the variance of dependent variable *world_rank* which means that research and citation have high impact at university ranking as well as respective countries arguing the raised hypotheses.

Table 7 presents the summary for each variable, shown through a customized table. The first column represents countries with top ranked universities, while other columns represent the sum of each variable taken from the dataset.

Table 7. Countries and the sum of variables.

		research Sum	citations Sum	world_rank Sum
Country	Australia	2581,2	3099,0	3982
	Austria	294,7	380,7	1177
	Belgium	1081,5	1498,8	2746
	Brazil	123,7	49,0	336
	Canada	2756,1	3441,6	4555
	China	1044,3	1119,9	1516
	Denmark	716,6	1286,9	2493
	Egypt	28,0	99,8	147
	Finland	313,6	467,1	581
	France	1236,2	2985,3	4209
	Germany	3447,4	5751,7	9709
	Hong Kong	1278,2	1492,9	2033
	Israel	460,7	435,3	1531
	Italy	149,7	335,8	553
	Japan	1773,0	1431,0	2549
	Luxembourg	26,7	84,8	193
	Netherlands	3607,7	4761,1	7638
	New Zealand	221,5	396,9	990
	Norway	250,0	484,5	1195
	Republic of Ireland	348,2	892,5	1507
	Russian Federation	108,8	42,4	357
	Singapore	817,1	784,1	801
	South Africa	233,7	494,6	693
	South Korea	1337,4	1432,2	2205
	Spain	243,6	691,1	1296
	Sweden	1757,2	2205,5	3449
	Switzerland	1980,8	3277,3	3689
	Taiwan	514,4	447,8	1318
	Turkey	226,9	607,3	1065
	United Kingdom	8942,8	14676,2	20025
	United States of America	24853,0	37238,3	35843

Providing the summary of results for all variables, Table 7 shows that each variable has different values related to countries with top ranked universities. This difference indicates that research, citations, and world ranking can provide distinct positions for countries if they are considered separately.

In the end, Table 8 shows the ranking of countries based on variables which are taken for study.

Table 8. Ranking of countries based on variables.

	world_rank	research	citation
No.	Country	No.	Country	No.	Country
1	United States of America	1	United States of America	1	United States of America
2	United Kingdom	2	United Kingdom	2	United Kingdom
3	Germany	3	Netherlands	3	Germany
4	Netherlands	4	Germany	4	Netherlands
5	Canada	5	Canada	5	Canada
6	France	6	Australia	6	Switzerland
7	Australia	7	Switzerland	7	Australia
8	Switzerland	8	Japan	8	France
9	Sweden	9	Sweden	9	Sweden
10	Belgium	10	South Korea	10	Belgium
11	Japan	11	Hong Kong	11	Hong Kong
12	Denmark	12	France	12	South Korea
13	South Korea	13	Belgium	13	Japan
14	Hong Kong	14	China	14	Denmark
15	Israel	15	Singapore	15	China
16	China	16	Denmark	16	Republic of Ireland
17	Republic of Ireland	17	Taiwan	17	Singapore
18	Taiwan	18	Israel	18	Spain
19	Spain	19	Republic of Ireland	19	Turkey
20	Norway	20	Finland	20	South Africa
21	Austria	21	Austria	21	Norway
22	Turkey	22	Norway	22	Finland
23	New Zealand	23	Spain	23	Taiwan
24	Singapore	24	South Africa	24	Israel
25	South Africa	25	Turkey	25	New Zealand
26	Finland	26	New Zealand	26	Austria
27	Italy	27	Italy	27	Italy
28	Russian Federation	28	Brazil	28	Egypt
29	Brazil	29	Russian Federation	29	Luxembourg
30	Luxembourg	30	Egypt	30	Brazil
31	Egypt	31	Luxembourg	31	Russian Federation

Table 8 shows these positioning whereas it seems, except the United States of America, United Kingdom, Canada, Sweden, and Italy, all other countries have different positions at top word ranking based only on research, citations or world ranks provided from annual reports of the Times Higher Education.

V. Discussion

The section of results proves that there is a significant impact of research and citations on the world ranking of countries with top ranked universities. Raised hypotheses are supported with results of data shown at respective tables and figures.

The first and second hypotheses are proved with values at Table 2 and Table 5 where is shown the impact that research and citation have on the world ranking of countries with top ranked universities. High values at respective tables mean that there is a strong impact of these attributes at world ranking universities. Negative values show the negative correlation, meaning that as greater as the research and the citations are, the world rank is higher, and so does the rank of countries.

The third hypothesis is argued with Figures 3 and 4 where graphics show the dispersion of research and citation. According to these graphs, research is more concentrated than citations. And finally, the summarized table argues the fourth hypothesis which says that world ranking of countries with top ranked universities have different ranking positions considering only research or only citations.

VI. Limitations and Future Studies

This research study is based on annual reports of the Times Higher Education world university rankings, where the dataset includes the period 2011-2016. Having the last annual reports would accurately reflect the current issue which is raised in this study. Another issue is that the results are based only on two of five dimensions and their indicators. Even though these dimensions provide the highest percentage of the total score which are used for ranking universities, according to results of this study, the impact of other dimensions should not be neglected. This research is conducted based on only one source of data, which is the Times Higher Education. Conducting research by having other sources like well-known global ranking systems such as the Academic Ranking of World Universities or Quacquarelli Symonds would give the possibility of comparing the outputs. Taking these into consideration, there are new opportunities for future studies which should be conducted.

VII. Conclusion

This research study is based on annual reports of the Times Higher Education world university rankings, where the dataset includes the period 2011-2016. Having the last annual reports would accurately reflect the current issue which is raised in this study. Another issue is that the results are based only on two of five dimensions and their indicators. Even though these dimensions provide the highest percentage of the total score which are used for ranking universities, according to results of this study, the impact of other dimensions should not be neglected. This research is conducted based on only one source of data, which is the Times Higher Education. Conducting research by having other sources like well-known global ranking systems such as the Academic Ranking of World Universities or Quacquarelli Symonds would give the possibility of comparing the outputs. Taking these into consideration, there are new opportunities for future studies which should be conducted.

References

[1] Shin, J. C., & Toutkoushian, R. K. (2011). The Past, Present, and Future of University Rankings. In J. C. Shin, R. K. Toutkoushian, & U. Teichler (Eds.), University Rankings: Theoretical Basis, Methodology and Impacts on Global Higher Education (pp. 1–16). Springer Netherlands. https://doi.org/10.1007/978-94-007-1116-7_1

[2] Mori, M. (2016). How Do the Scores of World University Rankings Distribute? 2016 5th IIAI International Congress on Advanced Applied Informatics (IIAI-AAI), 482–485. https://doi.org/10.1109/IIAI-AAI.2016.36

[3] World University Rankings 2022: Methodology. (2021, August 26). Times Higher Education (THE). https://www.timeshighereducation.com/world-university-rankings/world-university-rankings-2022-methodology

[4] Hou, Y.-W., & Jacob, W. J. (2017). What contributes more to the ranking of higher education institutions? A comparison of three world university rankings. International Education Journal: Comparative Perspectives, 16(4), 29–46. Google Scholar

[5] Hughes, R. (1925). A study of the graduate schools of America. Oxford, OH: Miami University Press, 3. Hughes, R. (1934). Report on the committee on graduate instruction. Educational Record, 15, 192–234. Google Scholar

[6] Cartter, A. (1966). An assessment of quality in graduate education.Washington, DC: American Council on Education. Google Scholar

[7] Drew, D., & Karpf, R. (1981). Ranking academic departments: Empirical findings and a theoretical perspective. Research in Higher Education, 14, 305–320. Google Scholar

[8] Conrad, C., & Blackburn, R. (1985). Correlates of departmental quality in regional colleges and universities. American Education Research Journal, 22, 279–295. Google Scholar

[9] Ehrenberg, R., & Hurst, P. (1996). The 1995 NRC ratings of doctoral programs: A hedonic model. Change, 28(3), 46–50. Google Scholar

[10] World university rankings: Explained. (n.d.). Retrieved February 9, 2021, from https://www.nature.com/nature-index/news-blog/world-university-rankings-explainer-times-higher-education-arwu-shanghai-qs-quacquarelli-symonds

[11] About Academic Ranking of World Universities | About ARWU. (n.d.). Retrieved February 9, 2021, from http://www.shanghairanking.com/aboutarwu.html

[12] About the Times Higher Education World University Rankings. (n.d.). Retrieved February 9, 2021, from https://www.timeshighereducation.com/world-university-rankings/about-the-times-higher-education-world-university-rankings

[13] QS | World University and MBA rankings. (n.d.). QS. Retrieved February 9, 2021, from https://www.qs.com/rankings/

[14] World University Rankings. (n.d.). Retrieved February 8, 2021, from https://www.timeshighereducation.com/search

[15] Ross, D. (2017). Times Higher Education World University Rankings. In F. J. Cantú-Ortiz (Ed.), Research Analytics (1st ed., pp. 137–146). Auerbach Publications. https://doi.org/10.1201/9781315155890-8

[16] Elsevier. (n.d.). University Rankings: A Closer Look for Research Leaders. Elsevier.Com. Retrieved March 5, 2021, from https://www.elsevier.com/research-intelligence/university-rankings-guide

[17] Understand Scopus and SciVal's role in university rankings | Elsevier Scopus Blog. (n.d.). Retrieved March 5, 2021, from https://blog.scopus.com/posts/understand-scopus-and-scival-s-role-in-university-rankings

[18] About Us. (n.d.). Retrieved October 18, 2021, from https://www.shanghairanking.com/about-arwu

[19] Impact Ranking. (2022, April 3). Times Higher Education (THE). https://www.timeshighereducation.com/impactrankings

[20] Hou, Y.-W., & Jacob, W. J. (n.d.). What contributes more to the ranking of higher education institutions? A comparison of three world university rankings. Retrieved September 8, 2021, from https://core.ac.uk/outputs/229430750

[21] Sydney Open Journals. (n.d.). Retrieved October 7, 2021, from https://openjournals.library.sydney.edu.au/

[22] Assessing the Big Three higher education ranking systems: Broad issues and THE WUR detail. (n.d.). Ebrary. Retrieved September 8, 2021, from https://ebrary.net/177272/education/assessing_three_higher_education_ranking_systems_broad_issues_detail

[23] Ross, D. (2017). Times Higher Education World University Rankings. In F. J. Cantú-Ortiz (Ed.), Research Analytics (1st ed., pp. 137–146). Auerbach Publications. https://doi.org/10.1201/9781315155890-8

Moving the teaching from traditional class to Learning Management System - helping students learn from home

B. Duriqi[1], A. LUMA[1], Y. JANUZAJ[2], H. SNOPCE[1], and A. ALIU[1]

[1] South East European University, Tetovo, {bd30521 & a.luma & h.snopce & azir.aliu}@seeu.edu.mk
[2] University "Haxhi Zeka", Peja/Kosovo, ylber.januzaj@unhz.eu

***Abstract* - Online and distance teaching and learning has progressively gained in popularity among teachers and students with the introduction of various Learning Management Systems (LMS). Moving teaching and course content from traditional classroom to LMS can assist teachers in creating a more dynamic learning environment, as well as students in focusing their learning and mastering learning objectives even if they are unable to attend their classes with physical presence. This paper will look at ways to transition teaching from a typical traditional classroom to LMS so that absent students can learn online from home.**

***Keywords* - Learning Management System (LMS), distance teaching, distance learning.**

I. INTRODUCTION

Learning Management System (LMS) is a software application used to manage, track, report on, and provide electronic educational technology (also known as e-learning) courses and programs. [1] Learning management systems encourage student' participation in order to create a learning environment that leads to the achievement of the desired learning goals. [2]

There are a variety of learning management systems nowadays; these platforms provide a diversified set of capabilities for a large range of users. [3] Edmondo, Moodle, Canvas, and Schoology are the most common LMS services used by teachers today. [4]

Online, hybrid and distance teaching and learning has progressively gained in popularity among teachers and students since the advent of various Learning Management Systems (LMS). [5] Moving teaching and course content from traditional classroom to the LMS can help teachers create a more dynamic learning environment, as well as assist students in focusing their learning and mastering learning objectives even if they are not able to attend their classes physically. [6]
This paper will explore moving the teaching from traditional classroom to Canvas LMS in order to bring the possibility for online teaching and learning. [7]

Canvas

Canvas is a web-based learning management system, or LMS. Learning institutions, educators, and students utilize it to access and administer online courses and learning resources as well as communicate about skill growth and achievement.

Canvas has a number of customizable course development and management capabilities, as well as course and user analytics and data, as well as internal communication features.

Canvas comes with a number of built-in course creation and administration capabilities that can be utilized to build unique and accessible teaching and learning environments.

Canvas is a learning management system that allows teachers to share e-learning courses, organize classrooms, keep gradebooks, and communicate with other teachers and students using a variety of collaborative features.

Canvas also allows building course media albums to organize the photos, videos, and audio files for various courses.

Teachers can use Canvas to create an interactive discussion for their students. The comments of students can be monitored, which means that a teacher must approve each post before it is published.

Canvas can be used to construct tests and quizzes, as well as elaborative reports and statistics on students' progress. Students can examine their grades in Gradebook, which includes tests, quizzes, and conversations. Furthermore, the progress of the students can be assessed based on specific instructor-defined targets.

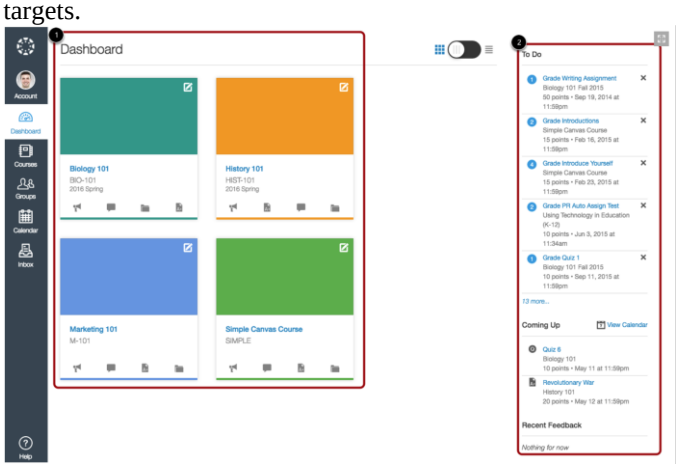

Fig.1. Canvas Dashboard

Moodle and Canvas are the most used LMS in IHE for learning, but Canvas seems to be widely used in IHE from developed countries like the United States, United Kingdom,
Australia and others, whereas Moodle is much more popular in IHE from developing
countries such as those in South Africa, Brazil, India and others. [8]

Table 1: Canvas: Advantages and Disadvantages.

Advantages	Disadvantages
User friendly interface Configuration for assessment and quizzes (multiple choice, open- ended questions, multiple attempts, time limitations etc.) Cloud based functionalities for assignment sharing Notifications by email, sms, push notifications in app Synchronized with Google Docs Roll Call feature for attendance tracking Web based gradebook Canvas Community guidelines Seamless Integration with Copy leaks	Canvas is not mobile friendly Automatic eraser of assignment when the due date is not set at midnight Technical problems faced by users in audio recording

Canvas as a LMS shares some advantages such as the easy to use, intuitive and cloud capabilities but it is yet to be improved for mobile platforms. Table 1 summarizes the advantages and disadvantages of Canvas LMS.

II. INVERTED TEACHING AND LEARNING

Implementing an inverted classroom is the best way to move teaching and course content from traditional classrooms to the learning management system.

While often defined simplistically as "schoolwork at home and homework at school," Inverted Learning is a methodology that allows teachers to implement various methodologies, in their classrooms.

In inverted teaching, which is also known as flipped classroom, reversing instruction, reversing the classroom, and reverse teaching, students are assigned readings, video lectures, or research assignments online before class. The class time is allocated to interactive activities, exercises, illustrating concepts, projects, and discussions.

The Flipped classroom can be summarized into four pillars:

F – Flexible Environment
L – Learning Culture
I – Intentional Content
P – Professional Educator

Students are first requested to conduct pre-lecture, online individual learning outside the classroom (typically, watching instructional videos posted on the learning management system [LMS]) and then take part in related in-lecture, face-to-face peer learning in the classroom. [9]

Instead of lecturing, students receive personalized guidance through learning materials and more interaction with course topics instead of lectures.

In general, from the practical perspective, the implementation of Flipped Classroom entails the combination of (1) pre-lecture, individual video-based learning in the form of "online homework," and (ii) in-lecture, group-based peer learning in the form of "face-to-face classwork". [10]

The primary goal of implementing an inverted classroom is to transition from a passive to an active learning model. The Table 2, 3 and 4 summarizes the key differences between traditional and inverted teaching.

To implement an inverted classroom successfully, teachers must first determine whether course content can be reversed. Courses in computer science, such as programming, dealing with databases and SQL, server operating systems, and producing web pages, can all benefit from the inverted classroom method. Transitions from traditional to inverted teaching may be easier because students have already participated in computer-based activities in class and have completed various tasks at home.

Different instructional methodologies, such as peer instruction, case-based learning, and process- oriented guided inquiry learning, can be used with reversed teaching to create an engaging school environment.

The basic goal of inverted teaching is to engage students in a variety of learning activities that allow them to independently explore course content and achieve course goals at their own speed. Teachers must devise suitable evaluation tasks to determine if students have mastered the learning objectives for a certain teaching unit. Canvas, Schoology, Edmodo etc. - are some online platforms that may be utilized to do reverse teaching. These systems provide a wide range of options for structuring course content and developing student comprehension exams. The material of the course should be divided into three sections based on what students need to learn before, during, and after class. Teachers and students can utilize Google Drive storage to organize developed course materials in addition to individual LMS systems. Using websites like TED-Ed, YouTube, Vimeo, School Tube, Khan Academy, and Open Culture can assist teachers in finding pre-made content that can be used in the classroom.

Table 2 provides the description of the roles of teacher and student in an Inverted Classroom before the Class starts. While in a traditional classroom, teachers before the class prepare and deliver lectures and home assignments, the students engage in exploring course materials and do the homework, on the other hand, in inverted classroom, teachers before the class prepare web based lectures, quizzes etc. - thus allowing students to complete the web based learning, enhances the skills, prepares class activities, explores new topics etc.

During the class (Table 3), teachers in traditional classroom

usually present lectures and students are passively engaged only by listening and taking notes, on the inverted classroom on the other hand, teachers usually guide the learning process by providing additional explanations and their availability to instant support to the students; students on the other hand focus more on practicing the skills and providing feedback for the course and teachers.

While in the traditional classroom, teachers after the class usually engaged on grading the work and the students on memorizing the material and doing the homework, in the inverted classroom, teacher are actively engaged after class also by providing additional resources to students, while on the other hand, students continue to apply their knowledge and skills and focus on learning more complex tasks (Table 4)

The fundamental benefit of reversed teaching is that teachers may dedicate more in-class time to assisting students and can quickly identify students who are struggling. Teachers can also extend ideas covered in class by providing additional problem-solving activities for students to work on after class. Students may learn and evaluate course material at their own pace by accessing learning resources from home. The biggest issue in attempting to adopt reversed teaching is that both teachers and students must have access to the appropriate equipment, including a computer with internet connection and essential software, both at home and at school.

The flipped classroom is considered an initial path to introduce blended learning. [11]

III. WORKING WITH ABSENT AND ONLINE STUDENTS

Teachers can begin to use LMS portals to practice reversed teaching, which allows online and non- attending students to explore course content and master required learning goals at their own pace.

Course materials

For absent students, all course resources, such as learning materials or video teaching, must be provided. To distribute course materials, teachers can utilize an LMS portal such as Canvas, Edmodo, Schoology, or Google Drive. In addition, absent students must be able to participate in all course activities. Absent students can use LMS portals to keep track of in-class activities as well as supplementary problem tasks and complete them from home. Students can easily contact their teacher via e-mail or the LMS portal if they are having difficulties with a task.

Table 2: Traditional versus Inverted Teaching: Before Class.

Traditional teaching		Inverted teaching	
Teacher	Student	Teacher	Student
Lectures Presentations Homework assignments	Explore course materials Mostly do no work	Prepares web based lectures such as audio/video recordings,	Complete interactive learning, prepare in class activities -
	Do homework assignments	content-rich websites, blogs, quizzes, projects, problem based learning, simulations etc. Establish spaces and time frames that permit students to interact and reflect on their learning	Work on gaining knowledge or skills - Explore new topics etc

Table 3: Traditional versus Inverted Teaching: During Class.

Traditional teaching		Inverted teaching	
Teacher	Student	Teacher	Student
Present learning materials usually with presentations Repeats what was in the lecture and assigns homework	Listens to the lectures Follows the instruction Takes notes	Guides the learning process and gives support Offers additional explanations for specific topics Availability to all students for individual, small group, and class feedback in real time as needed	Practice skills - via quizzes and polls students provide anonymous feedback for teachers about the course

Table 4: Traditional versus Inverted Teaching: After Class.

Traditional teaching		Inverted teaching	
Teacher	Student	Teacher	Student
Grades past work	Memorize Notes Do the homework	Posts additional resources and explanations	Continuing the application of their knowledge and skills Learning more complex tasks

IV. ASSIGNMENT SUBMISSION AND EVALUATION

Depending on the assigned activity, students can submit their work in a variety of methods. They can, for example, send their assignment via email or through Canvas platform. Additionally, students can create a Google Drive folder that is shared with the teacher. As a result, the instructor gets access to all of the students' work in one location for review. The created folder can be used as a student portfolio for that particular course. The instructor would be able to readily assess the progress of the students in this manner.

An online test using one of the LMS portals – such as Canvas, Schoology, Edmodo, and others – or an examination of the students' portfolio on Google Drive can be used to evaluate absent students' work. Using a video conferencing platform such as Skype or Zoom, the teacher can gain extra explanations on the work completed by the student.

Assisting the absent students

Absent students can name trustworthy classmates, and the teacher then asks and encourages them to

share class notes. Responsibility can be distributed among numerous students to avoid overburdening one student. Alternatively, each student may be assigned the task of sharing their notes for a set amount of time, such as a week. These peers can also help the absent student by informing them of what they missed out on socially and checking in via phone or social media. If a class has already established a Messenger, Viber or WhatsApp group, interaction between absent students and their classmates can be

done on a daily basis. A teacher can also plan one-on-one time with an absent student to contact them over the phone or through one of the online platforms.

Absent students can participate in in-class computer- based activities, allowing them to engage with them.

Peers during school hours.

V. CONCLUSION

It might be challenging to go from a traditional classroom to a specialized learning management system. Teachers must radically alter their teaching methods. Various platforms and software can assist, but teachers must possess technical literacy, as well as the time and motivation to become acquainted with the necessary tools and platforms. Both at school and at home, students and teachers require the necessary material conditions, such as computer and internet access, smartphones or tablets. Teachers will have a learning management platform with course information to assist students study even if they are absent from class once the adjustment period is through.

REFERENCES

[1] "What is Flipped Learning", flippedlearning.org

[2] Falcone, Kelly. "A Case Study of Faculty Experience and Preference of Using Blackboard and Canvas LMS", University of Phoenix ProQuest Dissertations Publishing, 2018.

[3] Caglar Sulun, "The Evolution and Diffusion of Learning Management Systems: The Case of Canvas LMS", The Ohio State University Pressbooks, 2018.

[4] " Fernandez, A.R., González, F.S., Merino, P.J., & Kloos, C.D. (2017). A Data Collection Experience with Canvas LMS as a Learning Platform. LASI-SPAIN.

[5] Judy Lever-Duffy and Jean McDonald, "Teaching and Learning with Technology, with Revel -- Access Card Package", 6th Edition, 2017.

[6] M. F. Tretinjak, "Moving teaching from blackboard to the learning management system — Helping absent students learn from home," 2018 41st International Convention on Information and Communication Technology, Electronics and Microelectronics (MIPRO), 2018, pp. 0500-0502, doi: 10.23919/MIPRO.2018.8400095.

[7] Aaron Rubio Fernandez, Fernando Santamaría González, Pedro J. Muñoz Merino, Carlos Delgado Kloos. A Data Collection Experience with Canvas LMS as a Learning Platform. In Manuel Caeiro Rodríguez, Ángel Hernández-García, Pedro J. Muñoz Merino, Salvador Ros, editors, Proceedings of the Learning Analytics Summer Institute Spain 2017: Advances in Learning Analytics, Madrid, Spain, July 4-5, 2017. Volume 1925 of CEUR Workshop Proceedings, pages 109-123, CEUR-WS.org, 2017.

[8] CedricBhekiMpungose, SimonBhekiKhoza, "Postgraduate Students' Experiences on the Use of Moodle and Canvas Learning Management System", Springer 2020

[9] Morris Siu-Yung Jong, "Flipped classroom: motivational affordances of spherical video-based immersive virtual reality in support of pre-lecture individual learning in pre-service teacher education", Journal of Computing in Higher Education, 2022

Lo, C. K., & Hew, K. F. (2021). Developing a flipped learning approach to support student engagement: A design-based research of secondary school mathematics teaching. Journal of Computer Assisted Learning, 37(1), 142–157

Camila Maria Bandeira Scheunemann, Paulo Tadeu Campos Lopes, "Academic Performance and Perceptions Regarding the Flipped Classroom Strategy in the Subject of Human Anatomy", Acta Sci. (Canoas), 24(5), 54-83, Sep./Oct. 2022

Open Data in Education – A Systematic Review

A. RUSHITI[1], A. LUMA[1], Y. JANUZAJ[2], A. ALIU[1] and H. SNOPCE[1]

[1] SEEU University, Tetovo/Republic of North Macedonia, {ar26730 & a.luma & azir.aliu & h.snopce}@seeu.edu.mk

[2] 2 University "Haxhi Zeka", Peja/Kosovo, ylber.januzaj@unhz.eu

Abstract **- A new trend has already appeared for open data, which now has a great importance in the digital transformation of education as a growing innovation through students, professors and researchers for the purpose of data collection and after enable them to understand the concept of data through different methods such as analysis and interpretation in the real world.**

The aim of this research is the application of open data in order to improve the universities in order to better rank and review the research papers. The systematic literature review aims to collect and process the data that we select and in which case we obtain information about current solutions. To have more detailed information about, I collected publications from the last six years from the most popular bookstores such as Springer, IEEE Xplore, Elsevier, and DL ACM. The information processed in the research papers shows that there is a possibility of having a model that can rank the publications of university professors on an open data platform. The process of research papers gives us the data from the research done by systematically reviewing where the specified findings are discussed and have a conclusion on it.

Keywords **- Open data, Open Education, Big Data, Machine Learning, Data Mining, Higher Education.**

I. INTRODUCTION

Nowadays, the use of technologies and data are already part of our daily lives and our daily activities. Technology plays a very important role in almost all areas; therefore, it is necessary to have knowledge about the data, which enables us to understand the data and the proper way how the new digital technology works.

Currently there is a very large amount of data in the field of education. But these data, if not converted into useful information, remain as unnecessary data. It is imperative that these data be converted and extracted from the information they can use. Data extraction itself is not sufficient; we also need to do data cleansing, integration, transformation, mining, and presentation.

Open data is a new trend that has already begun to emerge. It can be crucial in bringing new digital innovations to education through the activities of students, professors, and researchers through various activities that collect data and make it easier for them to comprehend the concept of data through analyses and interpretations that connect them with the present.

Effective use of large amount of data obtained by the progress of information technology is an important issue to improve management, student support, quality education etc. in the university [1].

Open data has the potential to be used as a resource for educational activities. Approaches of use this, though, are not well-known or widely used in education. [2]. Learning, teaching, and research resources known as open educational resources (OER) intend to utilize various materials that may be collected, processed, and used for particular goals. [3]. The majority of publishers of data sets on Open Data portals are public institutions, hence the majority of attention surrounding Open Data focuses on Open Government Data. However, Open Data is not just for use in education or government. This is also evident in academia, where there has been limited research done on private entities publishing Open Data is available. [4]. The public release of government data in the form of open data also has significant advantages. First, it is believed that open data is essential to enhancing the efficacy and efficiency of governmental programs and services. [5].

The purpose of this study is to define and design an automated model proposal for integrating accumulation, interpretation, and exploitation of open data in university education in order to rank the published scientific works by applying Data Mining techniques.

The goal of a systematic literature review is to gather and analyze data that sheds light on digitalization, open data, and educational data mining (EDM).

The research is carried out by collecting as many papers as possible and analyzing them in terms of obtaining data from some relevant papers that have been published in the last six years by well-known libraries such as Springer, IEEE Xplore, Elsevier and DL ACM. The works that are collected from the searches are filtered and categorized based on the necessary information and the conditions for saving or not those for later use. From the filters made, those that were irrelevant are excluded, while those that contain necessary information are included to be used in the further study.

This paper is constructed in three sections, the first part presents a description of the models that exist in the framework of Open Data in Education. Then the second part is the content part of the paper, where the methodology that we will use is described in that part and the main data for the research works that have been selected for analysis and

extraction of data for further work are shown there. The process of obtaining the necessary data in each article is carried out by searching for information in the systematic literature review (SLR) on the collected literature. The systematic review of the data that we have found in the following is processed to evaluate the quality and importance of these data that we have extracted. The conclusions and discussions based on the classified research papers are raised in the last section. The findings and upcoming projects based on the identified outcomes of the research are summarized in the section of the conclusions that comes last.

II. LITERATURE REVIEW

The literature search was conducted in the most well-known publishers, including Springer, Elsevier, IEEE Xplore, and DL ACM. These searches revealed usage and applications of open data in primary or secondary education, but not in higher education, particularly with regard to a model for ranking publications. The authors' work on their publications related to open data, open education, big data, machine learning, and data mining is carried out in this study. The study makes a systematic contribution to the identification of the incorporations of these technologies and demonstrates their shared correlations through a comprehensive review of the literature.

A. Methodology

This study is based on the systematic literature review (SLR) technique, which has been chosen for analysis in order to examine the use of open data in higher education. The new technologies and models being utilized in educational institutions were the subject of the research that needed to be found and examined. These new developments include a model for a novel approach of recognizing and endorsing the usage of open data in education as well as the supporting infrastructure. In order to have a more thorough overview and a following notion, the data collected on specific works are identified using various Internet research techniques, with a focus on research publications from the most well-known databases like Elsevier, Springer, IEEE Xplore, and DL ACM. The objective is to use open data to help institutions rank and evaluate research articles more effectively.

The state of research is based on research, and research is based on a review of the literature, with a systematic review of the literature being the primary methodology. Open data, open educational resources, machine learning, and data mining techniques are all used in research with the sole aim of addressing the research question. The purpose of the research question is to identify the ranking model and whether universities will be able to modify the suggestions in the context of the Ranking Research Platform that our model provides.

B. Relevant studies

The proper way to find studies of our personal interest is by searching the first strings ((“Open Data” AND “Open Educational Resources” AND “Higher Education”)). The search time frame comprises articles between the years 2016 and 2022 in order to find the required articles and the most recent technologies for our goals. The four most popular databases, Elsevier, Springer, IEEE Xplore, and DL ACM, which always adapt to the study disciplines, are searched for existing works or relevant to our research. The generated results are added to the filtering procedure in accordance with the required computer science and open data disciplines. The obtained results which have been found from the research in numerical form are presented in the table before:

TABLE I
COLLECTED PAPERS

Nr.	Name of database	Research articles	Conference papers	Total number
1.	Springer	54	16	70
2.	Elsevier	35	0	35
3.	IEEE Xplore	26	79	105
4.	DL ACM	29	0	29

Research papers that have been collected are put through a categorization process, and filters are applied depending on the content details and the standards that we choose to include or exclude from the pertinent research. Filtering is done in a similar manner, with some research papers being eliminated and others being included in our ongoing work if they include the data we need to conduct the research. The selection process was typically based on the chosen keywords we came across in the research papers and the solutions they provided in regard to the research we established.After filtering and selecting the papers on the principle that they fulfill those criteria or conditions from us, the number of works that we will need for future work was reduced and remained at only 38 papers.

C. Data extraction and checking

Based on the 35 works that were chosen for primary studies, the final filtering was used to gather the necessary data. The process of extracting the necessary information is done in such a way that each article looks at the material it includes to meet the systematic literature review (SLR) checklist in order to collect the information from the studies and assess their values. These questions can be answered by looking for relevant keywords, reading the abstract, examining the results, and carefully examining the articles, techniques, and data-description styles of the chosen papers. The list of selected works is shown below.

TABLE II
RELEVANT PAPERS

Number of relevant papers	Reference of relevant papers
35	[1] [2] [3] [4] [5] [6] [7] [8] [9] [10] [11] [12] [13] [14] [15] [16] [17] [18] [19] [20] [21] [22] [23] [24] [25] [26] [27] [28] [29] [30]

	[31] [32] [33] [34] [35]

The Systematic Review of the Data Found expands further to evaluate the accuracy and reliability of the information we receive, always referring to the checklist. We can see from the checklist's results that not all tasks, like data analysis, are of the same unique value. In light of this, the evaluation of the selected works is based on the choice of the works that have received the most favorable comments and are directly related to the research on the given topic. This way has reduced the number of works that have been chosen as the best. The authors of the qualitative works that were chosen are listed in a table below and these works will be used for future research with the primary goal of determining the findings of the study.

TABLE III
AUTHORS OF QUALITATIVE PAPERS

Order no.	Author	Year of publication	Reference no.
1.	Tim Coughlan	2020	1
2.	Keisuke Abe	2019	2
3.	Michael Yosep Ricky, Harco Leslie Hendric Spits Warnars, Wdodo BudihartoBahtiar Saleh Abbas	2017	3
4.	Yongxu Li	2020	4
5.	Mubashrah Saddiqa, Marite Kirikova, Rikke Magnussen, Birger Larsen, Jens Myrup Pedersen	2020	5
6.	Mubashrah Saddiqa, Rikke Magnussen, Birger Larsen, Jens Myrup Pedersen	2021	6
7.	Qingzheng Xu , Na Wang , Balin Tian , Lipeng Xing , Wenhua Bai	2020	7
8.	Tianchong Wang, Dave Towey	2017	8
9.	Mubashrah Saddiqa , Lise Rasmussen , Rikke Magnussen , Birger Larsen , Jens Myrup Pedersen	2019	9
10.	Annalisa Manca,Javiera Atenas, Chiara Ciociola, Fabio Nascimbeni	2017	10
11.	T Renuka; C. Chitra; T.S. Pranesha; Dhanya G.; Shivkumar M.	2017	11
12.	Lei Zheng , Wai-Min Kwok , Vincenzo Aquaro , Xinyu Qi , Wenzeng Lyu	2020	12
13.	Martin Beno; Kathrin Figl; Jürgen Umbrich; Axel Polleres	2017	13
14.	Mubashrah Saddiqa, Marite Kirikova & Jens Myrup Pedersen	2019	14
15.	Mubashrah Saddiqa, Birger Larsen, Rikke Magnussen	2019	15
16.	Lameck M. Amugongo; Shawulu H. Nggada; Jürgen Sieck	2016	16
17.	D. Gunawan and A. Amalia	2016	17
18.	KeiranHardya and AlanaMaurushat	2016	18
19.	Maxat Kassen	2017	19
20.	Marco Torchiano; Antonio Vetrò; Francesca Iuliano	2017	20
21.	Antonio Vetro, Lorenzo Canova, Marco Torchiano, Federico Morando	2016	21
22.	Matthew Love, Charles Boisvert, Elizabeth Uruchrutu, Ian Ibbotson	2016	22
23.	Mubashrah Saddiqa, Rikke Magnussen, Birger Larsen, Jens Myrup Pedersen	2021	23
24.	*Mubashrah Saddiqa, Marite Kirikova, Rikke Magnussen, Birger Larsen, Jens Myrup Pedersen*	2021	24
25.	T.D.B Weerasinghe	2019	25
26.	Kenneth Li-Minn Ang; Feng Lu Ge; Kah Phooi Seng	2020	26
27.	Adeboye, Nureni Olawalea, Popoola, Peter Osuolaleb, Ogunnusi, Oluwatobi Nurudeen	2020	27
28.	Georgios Mylonas, Dimitrios Amaxilatis, Ioannis Chatzigiannakis, Aris Anagnostopoulos, Federica Paganelli	2018	28
29.	Fabio Nascimbeni; Daniel Burgos; Ahmed Tlili	2017	29
30.	José Luis Martín Núñez; Edmundo Tovar Caro; José Ramón Hilera González	2017	30
31.	Yunus Santur; Mehmet Karaköse; Erhan Akin	2016	31
32.	Kate Farrell , Judy Robertson	2019	32
33.	Anastasios Tsolakidis;	2017	33

	Evangelia Triperina; Cleo Sgouropoulou; Nikos Christidis		
34.	Marcio Victorino; Halley Magalhães; Luan Cardoso; Maristela Holanda; Edison Ishikawa	2017	34
35.	Antônio J. Alves Neto , Danilo F. Neves , Lidiany C. Santos , Max C. Rodrigues Junior , Rogério P. C. do Nascimento	2018	35
36.	Manju Jose; Preethy Sinu Kurian; V. Biju	2016	36
37.	Diana Andone; Andrei Ternauciuc; Radu Vasiu	2017	37
38.	Shu-Yen Yao; Shein-Yung Cheng	2017	38

The findings and discussions will be provided in the following parts based on the study and data collected from the works that we considered to be chosen.

III. FINDINGS AND DISCUSSIONS

Today in modern times, there is a growing interest in publishing data that is public in an open format, on the web, giving the necessary space to all interested parties to use and reuse that data.

In the beginning, as an idea, it was supported only by governments and then also by companies so it got a big boost worldwide. Already those interested governments and companies have made their public data available on open platforms. During the literature review, it was discussed that data reuse is the key to Open Government Data, due to the fact that all services, statistical findings, and applications require free manipulation of data that is provided to the stakeholder. It is in such cases that data standardization and support are the main geneses that encourage re-users to generate value from the data provided to them. [7]. Now the big data age offers new ideas for education reform and development in general and higher education in particular [8] which offers opportunities but also presents a new challenge for the use and reuse of available data that we find in educational institutions. Secondary school educators also have certain difficulties while utilizing open data platforms since they frequently are unaware of the open data portal that is available in their city or struggle to incorporate some open data sets as a teaching resource. [9]. By using data open at the school level, we can also have a positive impact. The Open Data web interface will allow students and teachers to experiment with these datasets as part of their daily learning and take advantage of the potential of Open Data as educational material [10]. In conclusion, by aiming to encourage data education in schools, we may empower young children to become data specialists. Young people who are familiar with open data will be able to comprehend the different types of information they use to solve problems in their daily lives and will have the chance to use cutting-edge visual technology to search open data in a more sophisticated manner and display it in a clear and understandable manner. [11].

Related to what was previously said, it is important to give school students the opportunity to fully comprehend and work with open data visualizations, data format presentation, data preparation, and data cleaning concepts so that they can play a significant role in enhancing students' learning behaviors. This is because teachers and students can relate real problems from various perspectives in everyday teaching. [12].

The use of effective videos produced by worldwide specialists is one of the new objectives, along with striving to prevent the complete loss of the intermediary function. More contrasting studies are required to come to a consensus on the optimal method for creating and utilizing OER despite the fantastic prospects that Open Education provides for both online courses and traditional classroom settings. [13]. Pedagogically, the tremendous potential of ODs in education lies in the fact that their use can cause critical reflections on empathic care: in fact, the act of discovering, searching for and recognizing a reality through ODs is a care modality that refers precisely to pedagogical action [14].

The source of public data to carry out analysis and research seems to be the most suitable for students of the first cycle of study at the university.

Advanced research skills, in-depth knowledge, and problem-solving indicate a favorable feeling for the subject, motivation, and devotion that a student demonstrates at the conclusion of the project, which confirms the quality of the education provided. [15]. One of the ways that helps potential future students in terms of developing digital skills is the good and fair use of open data. For students or users to have this knowledge about how to use open data appropriately, the development of these skills should start from the early stages of education (eg starting from secondary school), with the aim of only increasing their potential. in the near future to make them competitive with the labor market and to help you in the future challenges and opportunities that will be faced [16]. Nowadays, it is usually aimed towards sophisticated educational systems for the use of open data for the purpose of creating a greater quality of the educational process. One of today's best known educational platforms, MOOCs, include course materials, related learning activities like video and text, quizzes, and projects, as well as statistics pertaining to the millions of participants they have reached since their launch in 2012. [17].

In addition to the fact that we must give knowledge to students for the use of platforms for the use of open data, importance must also be given to teachers for the use of such platforms. This indicates that implementing OEP and preparing teachers to use them in a particular pedagogical setting might be advantageous for student engagement, stimulate their interest in particular activities, yet ultimately fail to achieve the objectives of greater memorization and

higher grades. [18]. Based on the literature review, we came across the facilitation, adoption and application of Open Educational Practices (OEP) in universities. Some recommendations on how to encourage the flexibility of open education practices within universities are based on the strengths and problems of higher education and higher education teachers, i.e., university professors. These recommendations always refer to the findings for expert input. [19]. One of the new challenges that have started to be used in the most technologically developed countries is sensors. The next challenge for researchers is how to find the most appropriate ways to introduce sensors for use through school curricula so that students have an easier way to understand their implementation. The way sensors are used represents one of the newest contemporary technologies and gives a greater advantage if they really know how to use them [20].

Dealing with open data in the education system is a challenge even for less developed countries, as was a case study for African countries. Such opportunities can be achieved through the topics covered in data science courses can and should be included in a variety of statistics courses at the university level, while providing adequate facilities for its teaching and learning and being part of the statistics curriculum. university where the main goal is to increase the quality of teaching, advancing students' skills in machine learning, improving the understanding of the role of data in the global [21]. In some research it is found that even in Sri Lanka as one of the least developed countries in terms of IT technology, it is now growing rapidly with more advanced technology platforms as well as an intelligent and skilled workforce. Furthermore, according to a survey conducted by several researchers, the tendency to pursue a postgraduate course in IT and open data is on the "high" side for IT professionals in Sri Lanka [22]. A similar situation for open data is presented in the state of Brazil, they have a portal known as INEP where they provide a broad overview of Brazilian education and, as an important transparency tool, is a safe source for obtaining data, accessible to researchers, students, managers, and society in general [23]. A high-stakes effort to teach students ages 3–18 data literacy and data citizenship This is what the "Data Education in Schools" project of the Scottish Government seeks to accomplish. This project's objective is to empower young people to support data innovation and to develop into informed activists who are skeptical of the role of data in society (citizen data). The Data Education in Schools initiative offers a professional development program to help a variety of instructors from various industries and topic specialties to become more competent in using and instructing data capabilities. [30]

In most nations with untapped potential for promoting sustainable development, open government data are still in the early stages of development, as opposed to those of educational institutions. According to study, just 47% of the UN member states have launched national open government data portals, and the OGD development levels of roughly 61% of countries are low and below average. [24]. In a study for ODG on the advantages and disadvantages of open data, various measurements were done beginning with the XML files published by the PAs which were automated by open source software. Metrics from datasets made available by Italian universities were then used to confirm this. The research findings showed that any reuse undermines the primary goals of open government data: promoting transparency in public administration, enabling active citizenship, and stimulating economic expansion. It was evident that such a part of the data would result in inaccurate or incomplete results. [25]. The approaches that we currently have in the literature to the problem of the quality of OGD lack a comprehensive theoretical framework. Additionally, rather than datasets, the majority of evaluations concentrate on open data platforms. In this study, we address these two issues and offer a methodology for measuring the quality of OGD in terms of numbers.

The metrics showed both the advantages of centralized data discovery, which was used as an example of high-quality OGD, and the problems with decentralized data discovery samples that the researchers studied at.[26].

As we already stated, the less technologically advanced nations have begun to use open data in education, but they have also begun to use open data in state institutions in addition to education. The adoption of an open data portal that adheres to the open innovation approach in Namibia will level the playing field for innovation and encourage the commercialization of data, according to another case study collected from the literature review. [27]. The development of the open data movement, which recently passed specific legislation for free access to information and began executing its own projects in this area, presents Kazakhstan as a typical emerging and post-totalitarian nation in an atypical cultural setting. [28]. According to the open stage concept, the state of Indonesia is still in the first stage. Indonesia continues to gather and publish official statistics without connecting it to other data. Researchers advise policy modification, rule enforcement, open data socializing, and technical training to give open data to enhance the adoption of open data. [29].

The field of big data research is constantly evolving, and among other resources, readers can refer to the various learning forums to stay up-to-date on open data developments. Moreover the fact that open data serves to obtain direct knowledge about the educational process, it also, through various machine learning techniques, creates spaces in the classification of different approaches to analytics, which includes various predictive analytics, learning styles, recommender systems, graph analysis, visual manipulation, social media analysis, and learning and in short a comprehensive breakdown [31].

In summary, one of the intriguing systems I came across when conducting my literature search was the e-Research information system, which is focused on open data. This system's goal is to make it easier for higher education institutions to manage, advertise, and suggest research papers. The outcomes of academic research are gathered, shared, and presented in order to foster networking and open up new prospects for collaboration.

By offering academics suggestions for research papers relevant to their areas of interest and competence, e-Research can also improve the research process.

[33]. Data mining technology has recently grown in importance as a result of science and technology's ongoing development and advancement. The use of data mining technology has a highly noticeable impact on all aspects of life. Artificial intelligence, which makes use of a huge number of data samples to practice and then automatically determine operating parameters and patterns, is the technology behind machine learning algorithms. The use of machine learning algorithms is crucial for the process of extracting data. [34]. The ranking of activities is important, in addition to the collecting and utilization of available data. This difficulty can be overcome by using different techniques with relevant ranking algorithms. There are several types of sorting techniques Bipartite Sorting, k-partite Sorting and Sorting by pairwise comparison where each of the sorting has its own specifics and usefulness for a certain purpose [35].

IV. Conclusion

We must be aware of and keep in mind that the opportunities provided by open data for students do not come about easily: creating a task that offers a sufficient challenge for every student and limitless opportunities for the best requires data discovery and consideration in detail of their options ahead, leaving the students to investigate them. Some of the frequent challenges that database professionals have when collecting data from non-traditional sources include utilizing data warehousing and data mining tools on data gathered from non-traditional sources from the Internet rather than receiving adequately prepared data sets. [32]. In this paper, we indicate that while modern technologies provide some beneficial solutions, they are not without limitations when it comes to making proactive use of open data.These issues are addressed in several different ways, starting from primary education, then continuing to secondary education and finally to higher education. In addition to being used in education, open data is also being implemented in government through a process known asE-Government.

However, there are challenges in our way, and all of these new open data application technologies require for a suitable operating environment, which means that the necessary conditions must exist. In this regard, some proposed solutions have been offered since we saw cases in less developed countries where the implementation of OD was very limited due to the infrastructure and the stagnation of technology development compared to other developed countries where some of those governments had the way of using open data was also introduced in the primary education curricula and had the final goal of creating a data citizen. In order to lay the foundation for the use of open data in education, our future research will focus on creating a more efficient model for the country's use of open data in the process of our education.

Acknowledgment

I would state my appreciation to Professor Dr. Sc. Artan Luma, as my research supervisor, for his advice, enthusiastic support and helpful critiques of this research work.

References

[1] K. Abe, "Data Mining and Machine Learning Applications for Educational Big Data in the University," 2019 IEEE Intl Conf on Dependable, Autonomic and Secure Computing, Intl Conf on Pervasive Intelligence and Computing, Intl Conf on Cloud and Big Data Computing, Intl Conf on Cyber Science and Technology Congress (DASC/PiCom/CBDCom/CyberSciTech), 2019, pp. 350-355, doi: 10.1109/DASC/PiCom/CBDCom/CyberSciTech.2019.00071.

[2] Coughlan, T. The use of open data as a material for learning. Education Tech Research Dev 68, 383–411 (2020). https://doi.org/10.1007/s11423-019-09706-y

[3] T. Wang and D. Towey, "Open educational resource (OER) adoption in higher education: Challenges and strategies," 2017 IEEE 6th International Conference on Teaching, Assessment, and Learning for Engineering (TALE), 2017, pp. 317-319, doi: 10.1109/TALE.2017.8252355.

[4] M. Beno, K. Figl, J. Umbrich and A. Polleres, "Open Data Hopes and Fears: Determining the Barriers of Open Data," 2017 Conference for E-Democracy and Open Government (CeDEM), 2017, pp. 69-81, doi: 10.1109/CeDEM.2017.22.

[5] Keiran Hardy, Alana Maurushat, Opening up government data for Big Data analysis and public benefit, Computer Law & Security Review, Volume 33, Issue 1, 2017, Pages 30-37, ISSN 0267-3649, https://doi.org/10.1016/j.clsr.2016.11.003.

[6] F. a. S. R. Neiva, "Systematic Literature Review in Computer Science - A Practical Guide," Federal University of Juiz de Fora, 2016.

[7] Antônio J. Alves Neto, Danilo F. Neves, Lidiany C. Santos, Max C. Rodrigues Junior, and Rogério P. C. do Nascimento. 2018. Open Government Data Usage Overview: A Systematic Literature Mapping. In

[8] Qingzheng Xu, Na Wang, Balin Tian, Lipeng Xing, and Wenhua Bai. 2020. Challenges and Countermeasures of Education in the Era of Big Data. In Proceedings of the 2020 9th International Conference on Educational and Information Technology (ICEIT 2020). Association for Computing Machinery, New York, NY, USA, 215–218. https://doi.org/10.1145/3383923.3383964

[9] Mubashrah Saddiqa, Rikke Magnussen, Birger Larsen, Jens Myrup Pedersen, Open Data Interface (ODI) for secondary school education, Computers & Education, Volume 174, 2021, 104294, ISSN 0360-1315, https://doi.org/10.1016/j.compedu.2021.104294

[10] Saddiqa, Mubashrah & Kirikova, Marite & Magnussen, Rikke & Larsen, Birger & Pedersen, Jens. (2019). Enterprise Architecture Oriented Requirements Engineering for the Design of a School Friendly Open Data Web Interface. Complex Systems Informatics and Modeling Quarterly. 1-20. 10.7250/csimq.2019-21.01.

[11] Saddiqa, Mubashrah & Rasmussen, Lise & Magnussen, Rikke & Larsen, Birger & Pedersen, Jens. (2019). Bringing open data into danish schools and its potential impact on school pupils. 1-10. 10.1145/3306446.3340821.

[12] Saddiqa, Mubashrah & Larsen, Birger & Magnussen, Rikke. (2019). Open Data Visualization in Danish Schools: A case Study. 10.24132/CSRN.2019.2902.2.3.

[13] J. L. Martín Núñez, E. Tovar Caro and J. R. Hilera González, "From Higher Education to Open Education: Challenges in the Transformation of an Online Traditional Course," in IEEE Transactions on Education, vol. 60, no. 2, pp. 134-142, May 2017, doi: 10.1109/TE.2016.2607693.

[14] Manca, Annalisa & Atenas, Javiera & Ciociola, Chiara & Nascimbeni, Fabio. (2016). Critical Pedagogy and Open Data as Means for Educating to Social Cohesion.. Tecnologie Didattiche. 10.17471/2499-4324/917.

[15] T. Renuka, C. Chitra, T. S. Pranesha, D. G. and S. M., "Open Data Usage by Undergraduate Students," 2017 5th IEEE International Conference on MOOCs, Innovation and Technology in Education (MITE), 2017, pp. 46-51, doi: 10.1109/MITE.2017.00014.

[16] Saddiqa, M., Magnussen, R., Larsen, B., & Pedersen, J. M. (2021). Digital innovation in education: Perspectives, opportunities and challenges of educational open data and sensor data. In BIR 2021 Workshops and Doctoral Consortium: 12th Workshop on Information

Logistics and Digital Transformation (ILOG) (Vol. 2991, pp. 74-83). CEUR Workshop Proceedings. CEUR Workshop Proceedings http://ceur-ws.org/Vol-2991/paper07.pdf

[17] Y. Santur, M. Karaköse and E. Akin, "Improving of personal educational content using big data approach for mooc in higher education," 2016 15th International Conference on Information Technology Based Higher Education and Training (ITHET), 2016, pp. 1-4, doi: 10.1109/ITHET.2016.7760728.

[18] D. Andone, A. Ternauciuc and R. Vasiu, "Using Open Education Tools for a Higher Education Virtual Campus," 2017 IEEE 17th International Conference on Advanced Learning Technologies (ICALT), 2017, pp. 26-30, doi: 10.1109/ICALT.2017.149.

[19] F. Nascimbeni, D. Burgos and A. Tlili, "Fostering Teachers-Led Open Education in Universities: Recommendations Emerging from Research," 2019 7th International conference on ICT & Accessibility (ICTA), 2019, pp. 1-4, doi: 10.1109/ICTA49490.2019.9144977.

[20] Saddiqa, Mubashrah & Kirikova, Marite & Magnussen, Rikke & Larsen, Birger & Pedersen, Jens. (2021). Towards Using Sensors as Data Sources in Teaching: Requirements for School Curricula-Compatible Sensors. Complex Systems Informatics and Modeling Quarterly. 78-93. 10.7250/csimq.2021-26.05.

[21] Adeboye, Nureni Olawale, Popoola, Peter Osuolale, and Ogunnusi, Oluwatobi Nurudeen. 'Data Science Skills: Building Partnership for Efficient School Curriculum Delivery in Africa'. 1 Jan. 2020 : 49 – 62.

[22] T. D. B. Weerasinghe, "A survey study on higher education trends among Information Technology Professionals in Sri Lanka," 2019 IEEE International Conference on Engineering, Technology and Education (TALE), 2019, pp. 1-6, doi: 10.1109/TALE48000.2019.9226014.

[23] M. Victorino, H. Magalhães, L. Cardoso, M. Holanda and E. Ishikawa, "Open data analysis on teacning in Brazilian higher education: A case study of the Anísio Teixeira National Institute for study and research," 2017 12th Iberian Conference on Information Systems and Technologies (CISTI), 2017, pp. 1-7, doi: 10.23919/CISTI.2017.7975992.

[24] Lei Zheng, Wai-Min Kwok, Vincenzo Aquaro, Xinyu Qi, and Wenzeng Lyu. 2020. Evaluating global open government data: methods and status. In Proceedings of the 13th International Conference on Theory and Practice of Electronic Governance (ICEGOV 2020). Association for Computing Machinery, New York, NY, USA, 381–391. https://doi.org/10.1145/3428502.3428553

[25] M. Torchiano, A. Vetrò and F. Iuliano, "Preserving the Benefits of Open Government Data by Measuring and Improving Their Quality: An Empirical Study," 2017 IEEE 41st Annual Computer Software and Applications Conference (COMPSAC), 2017, pp. 144-153, doi: 10.1109/COMPSAC.2017.192.

[26] Vetro, Antonio & Canova, Lorenzo & Torchiano, Marco & Minotas, Camilo & Iemma, Raimondo & Morando, Federico. (2016). Open data quality measurement framework: Definition and application to Open Government Data. Government Information Quarterly. 33. 10.1016/j.giq.2016.02.001.

[27] L. M. Amugongo, S. H. Nggada and J. Sieck, "Open Data Portal - A Technical Enabler to Drive Innovation in Namibia," 2016 2nd International Conference on Open and Big Data (OBD), 2016, pp. 80-86, doi: 10.1109/OBD.2016.19.

[28] Kassen, Maxat. (2017). Open data in Kazakhstan: incentives, implementation and challenges. Information Technology & People. 30. 10.1108/ITP-10-2015-0243.

[29] D. Gunawan and A. Amalia, "The Implementation of open data in Indonesia," 2016 International Conference on Data and Software Engineering (ICoDSE), 2016, pp. 1-6, doi: 10.1109/ICODSE.2016.7936164.

[30] Kate Farrell and Judy Robertson. 2019. Interdisciplinary Data Education: Teaching Primary and Secondary learners how to be data citizens. In Proceedings of the 14th Workshop in Primary and Secondary Computing Education (WiPSCE'19). Association for Computing Machinery, New York, NY, USA, Article 17, 1–2. https://doi.org/10.1145/3361721.3362120

[31] K. L. -M. Ang, F. L. Ge and K. P. Seng, "Big Educational Data & Analytics: Survey, Architecture and Challenges," in IEEE Access, vol. 8, pp. 116392-116414, 2020, doi: 10.1109/ACCESS.2020.2994561.

[32] Love, Matthew & Boisvert, Charles & Uruchrutu, Elizabeth & Ibbotson, Ian. (2016). Nifty with Data: Can a Business Intelligence Analysis Sourced from Open Data form a Nifty Assignment?. 344-349.

[33] A. Tsolakidis, E. Triperina, C. Sgouropoulou and N. Christidis, "Measuring academic research impact based on open data: A case of engineering faculties," 2017 IEEE Global Engineering Education Conference (EDUCON), 2017, pp. 1611-1618, doi: 10.1109/EDUCON.2017.7943064.

[34] Y. Li, "Practice of Machine Learning Algorithm in Data Mining Field," 2020 International Conference on Advance in Ambient Computing and Intelligence (ICAACI), 2020, pp. 56-59, doi:

[35] M. Y. Ricky, S. W. H. L. Hendric, W. Budiharto and B. S. Abbas, "Machine Learning Approach to Task Ranking," 2017 14th International Symposium on Pervasive Systems, Algorithms and Networks & 2017 11th

A Use Case for Customer Segmentation in the Saving Finance Sector Using Descriptive Analytics

M. AYYILDIZ[1], Z. KÖSE [2], M. OLUÇOĞLU[3], C. SÖYLEMEZ PEKTAŞ[4]

[1]Eminevim, İstanbul/Turkey, murat.ayyildiz@emingrup.com.tr
[2]Eminevim, İstanbul/Turkey, zekeriya.kose@emingrup.com.tr
[3] İzmir Bakırçay University, İzmir/Turkey, muge.olucoglu@bakircay.edu.tr
[4] İzmir Bakırçay University, İzmir/Turkey, cevhernur.soylemez@bakircay.edu.tr

Abstract – **Eminevim is a company that has broken new ground in Turkey and in the world. The model of the system allows the people to buy the desired property from anywhere, according to their budget, without paying any interest. Since Eminevim has thousands of customers, it is inevitable to manage the customers according to their different characteristics and behaviors. At this point, customer segmentation is an important method to apply. Customer segmentation is the division of a company's customers into groups based on certain characteristics they have in common. Segmentation provides a simple way to organize and manage a company's relationships with its customers. There are many reasons why customer segmentation is critical, such as (i) profitability calculations based on clusters, (ii) campaigns, promotions, incentives, reward applications using customer segments, (iii) identifying customers on the verge of churn and taking preventive actions, (iv) regular segmentation assessments as part of membership and benchmarking. The most used method for segmentation in the literature is clustering algorithms. There are several types of clustering methods, such as partitioning methods (K–Means), hierarchical (Agglomerative), density-based (DBSCAN), and model-based (Gaussian) clustering. In the study, a pipeline was implemented with the steps of data selection, data preparation, and clustering, which are general steps in data science. First, a dataset was created by integrating information such as organization fee, organization amount, down payment, and term of customers from various data sources as a data selection process. Then, in the data preparation stage, the features in the dataset were normalized using standard scaling functions, and the size of the data was reduced by using PCA (Principal Component Analysis) dimensionality reduction algorithm. Finally, clustering of customers was performed using K-Means, one of the most commonly used clustering algorithms. To determine the number of clusters, both the opinions of experts were taken into account and the elbow method was used. Evaluating the results of experimental studies on datasets created using preprocessed and newly created features with feature engineering, it was found that customers can be successfully divided into different segments such as loyal, potential, and risky.**

Keywords **– Customer Segmentation, Finance Analytics, Data Science, Clustering, K-Means Algorithm.**

I. INTRODUCTION

Increasing amounts of data and scientific developments in parallel with technological developments are increasing interest in data science and machine learning applications: banking, e-commerce, real estate, mobile applications. Data science, which is used in many business areas, provides different solutions to the needs of companies in different fields. Areas where customer loyalty is gaining importance are also application areas. Customer grouping and recognition are very important, especially considering that the cost of acquiring a new customer is five times higher than the cost of retaining the customer.

The organizational structure of this document is as follows. In the section II, approaches and related studies are stated. Then, the suggested methods and approaches are explained in the section III. Also, section III is explained the architecture of the system. Section IV are presented the experimental evaluation of the approaches and the results of our study. Finally, future work is presented in section V.

Customer segmentation is the division the customer base into homogeneous groups, considering factors such as age, gender, interests, and buying habits. Since customers are different from each other in many respects, creating customer groups consisting of similar customers for each company operating in different fields primarily brings efficiency in resource consumption. In addition, customer segmentation provides recognition of customers' needs and behaviors, creating on-site cross-selling and up-selling opportunities for companies. Customer segmentation is a clustering problem in the unsupervised learning category. These kinds of problems do not have a target variable and differ from problems in the supervised learning [1].

In this paper, it is aimed to group the customers according to their general tendencies and characteristics. The main criteria to be used in determining the segmentation of customers; are spending/use behavior information, age, race, religion, preference, family size, ethnicity, income, education level, etc. information. Demographic information is psychographic

information that shows the geographic location information, social classes, lifestyles, and personality traits that people live/need.

Our work has helped to many companies' problems in segmenting their customer base into more manageable segments, easily identify target groups, identify potentially lost customers, and take action regarding those customers. Moreover, the customer segmentation solution also provides benefits such as segmentation-based profitability calculations, campaigns, promotions, incentives, reward applications according to the customer segments, regular segmentation evaluations in customer membership, and performance comparisons.

II. Literature Review / Related Works

Statistical studies require a large amount of data. However, the abundance of data leads to problems in applying many statistical techniques. This result in, the necessity of grouping the data arises to ensure the usability of the techniques.

In this study, segmentation was made for the customers of company Eminevim using clustering analysis. Customer segmentation, which is required in many fields and sectors, occupies a large space in the literature. In a similar study, a framework was presented for analyzing customer value and segmenting customers according to their values [2]. In addition, to create a conceptual narrative about segmentation; There is a study examining how an innovative multinational company (Migros Türk) developed an effective segmentation strategy [3]. This review also demonstrates how firms can create new and creative approaches that deliver great value. In another study, a modeling framework is presented, this time with a model-based clustering approach, to create predictive models at the segment level. As a result, a consumption-based customer segmentation model was created [4].

In another study, customer segmentation was analyzed by using the data, methods, and processes obtained from the customer segmentation study. In this study, while examining customer segmentation, it has been suggested that some variables such as the customer's time to look at the product in e-commerce applications should be used as variables in customer segmentation [5]. In another study, four segmentation schemes were created in the telecommunications industry: Customer Value Segmentation, Customer Behavior Segmentation, Customer Lifecycle Segmentation, and Customer Transition Segmentation. The article also provides information on customer retention and value factors [6].

Most customer segmentation approaches based on customer value do not consider the time factor and trend of value change in their analysis. In one study, customers were classified according to their value using the K-Means clustering method [7].

III. Material and Methods

Cluster analysis is the process of grouping information in a data set according to certain proximity criteria. Each of these groups is called a "cluster". Cluster analysis is a useful multivariate analysis technique for grouping data. The purpose of cluster analysis is to classify ungrouped data according to their similarities and assist the researcher in obtaining summative information.

Although it is assumed that the data are normally distributed to apply cluster analysis, this assumption remains in theory and is ignored in practice. Only the conformity of the distance values to the normal distribution is sufficient. If this assumption is met, a different assumption is not required for the covariance matrix in cluster analysis.

In the clustering process, the similarity of the elements within the cluster should be high and the similarity between the clusters should be low. Clustering goes from data mining techniques to descriptive models, that is, unattended classification. The purpose of unsupervised classification is to group the data in such a way that a given set and not yet classified data form meaningful subsets. Clustering is done completely according to the characteristics of the incoming data. An example of clustering analysis in the coordinate plane is shown in Figure 1.

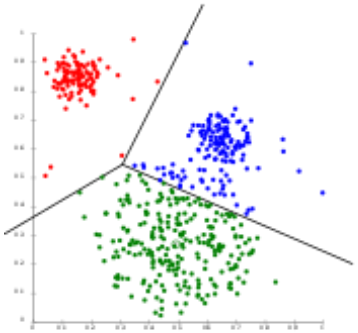

Figure 1: Clustering analysis.

A. *Types of Clustering*

While clustering methods are divided into two parts hierarchical and non-hierarchical (partitioned) clustering methods, research on this subject show that these algorithms can be further subdivided [8].

In the hierarchical clustering method, a tree graph is used specially to understand the operation more easily. The most frequently used hierarchical methods used based on the operations described in the hierarchical clustering method, Single link, Full link, Average link, Central and Ward methods. The clustering method of non-hierarchical K-Means and K-Medoids Clustering Algorithms is preferred if there is prior knowledge about the number of clusters or if the researcher has decided on the number of clusters that will be meaningful. The two most preferred methods in the non-hierarchical clustering method are the K-Means algorithm developed by Mac Queen [9].

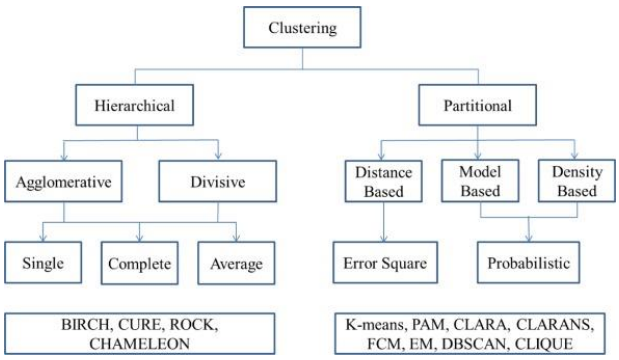

Figure 2: Types of clustering methods [10].

Clustering methods can be basically divided into partitioning or hierarchical (agglomerative). With the acceleration of studies in this field, various methods such as density-based, model-based, and connection methods have emerged. DBSCAN algorithm for density-based methods and Gaussian model methods for model-based methods can be given as examples.

B. K-Means Algorithm

It is one of the most widely used unsupervised learning methods. The assignment mechanism of K-means allows each data to belong to only one cluster (Evans, 2005). Therefore, it is a sharp clustering algorithm (partitioned clustering). The general logic of the k-means algorithm is to partition a dataset consisting of n data objects into k sets given as input parameters. The aim is to ensure that the clusters obtained at the end of the partitioning process have maximum similarities within clusters and minimum similarities between clusters. In this study method, clustering analysis was performed using the K-means clustering algorithm using the Euclidean distance formula shown in Figure 2 as the similarity criterion.

$$\sqrt{(p_1-q_1)^2+(p_2-q_2)^2+\cdots+(p_n-q_n)^2}=\sqrt{\sum_{i=1}^{n}(p_i-q_i)^2}.$$

Figure 3: Euclidean distance formula [11].

The distance between P and Q points in n-dimensional Euclidean space is calculated as in Figure 2.

The K-Means algorithm starts with randomly chosen K (number of clusters) center points. Each point in the dataset is assigned to the nearest set of centroids. The proximity is obtained by calculating the Euclidean distance formula. The value of the cluster center is calculated by averaging its points. This process continues until the values of the centers do not change. A flowchart seen in Figure 3 was created for the visual representation of the working steps of the algorithm.

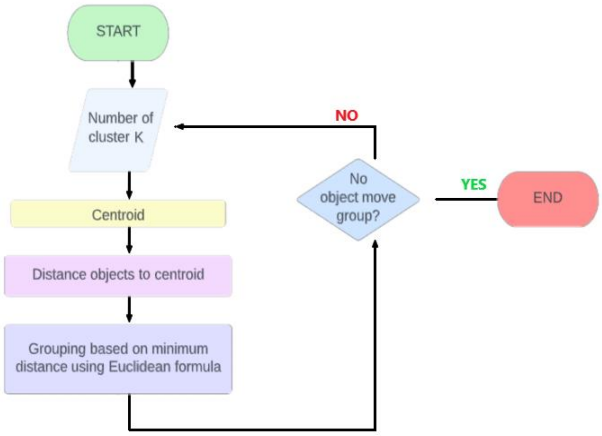

Figure 4: K-Means Algorithm.

C. Principle Component Analysis

PCA is a convenient statistical technique used in clustering and classification fields. This method's main goal is to keep the data set with the highest variance in high-dimensional data but to provide dimension reduction while doing this. By finding the general features in the over-dimensional data, reduces the number of dimensions and compresses the data. It is certain that some features will be lost with size reduction, but the intent is that these disappearing characteristics contain not much information about the population. This method combines highly correlated variables to create a smaller set of artificial variables, called "principal components", that make up the most variation in the data. The basic logic behind PCA, which is a very effective method in revealing the necessary information in the data, is to show multidimensional data with fewer variables by capturing the basic features in the data. This method was also used in this study.

IV. Experimental Results

Emin Group is a large-scale group of companies operating in many sectors such as insurance, automotive, energy and real estate. In such large organizations, customer segmentation for a large corporate group is a challenging task. To do this task, a sequential order was followed in this study. The first part of this pipeline is the identification of customer data.

The segmentation project was carried out for Eminevim sub-company of Emin Group. For the cluster analysis, the information listed in Table 1 belonging to Eminevim company customers was determined.

Table 1: Specified customer data.

Organization fee
Organization amount
Advance payment
Number of maturities
The duration of the relationship
The number of late maturities after delivery
The number of late maturities before delivery

In the pipeline, the data preparation process was carried out as the second step. In this step, normalization and finding outliers were performed. Different feature extractions were made using some customer information determined. The new attributes and the final version of the data to be used in segmentation are given in Table 2.

Table 2: Prepared customer data.

Organization fee/ Organization amount
Organization amount
Advance payment/ Organization amount
Number of maturities
The duration of the relationship
BD_DelayO : BD_Delay / AD Total Maturity
AD_DelayO : AD_Delay / AD Total Maturity
Delay: (BD_DelayO*n AD_DelayO*m)/(n+m)

The data grouping process, which was determined as the 3rd step in the pipeline, was carried out. Organization amount etc. expenditure information was collected under the heading 'Transaction Volume', the number of delayed maturities under the heading 'Payment Performance', and finally, time of relationship and the number of maturities under the heading 'Type of Relationship'.

Reducing the data to a single dimension by using the PCA reduction method in each data group constitutes the 5th stage of the pipeline.

- Transaction Volume Group Data
- Payment Performance Group Data
- Group Data

The determination of the segments and the selection of the clustering algorithm to be used were done in the 6th stage of the pipeline.

In the 6th stage of the pipeline, the segments were determined and the clustering algorithm to be used was selected.

Cluster analysis was performed after the K-means clustering algorithm was selected and the segments were determined. As the last step, clustering analysis and interpretation were performed. As a result of segmentation, customers; It is divided into 11 clusters: Champions, Loyal Customers, Potentially Loyal, End Customers, Promising Customers, Necessary Customers, About to Sleep, Risky, About to Lose, Hibernate, Lost. The segments are shown in Table 3.

Table 3: Prepared customer data.

Customer Segment	**Segment No**
Champions	Seg_1
Loyal Customers	Seg_2
Potentially Loyal	Seg_3
End Customers	Seg_4
Promising	Seg_5
Customers Needing Attention	Seg_6
About to Sleep	Seg_7
Risky	Seg_8
About to Lose	Seg_9
Hibernating	Seg_10
Lost	Seg_11

The results of clustering analysis including the formed segments are showed in Figure 5.

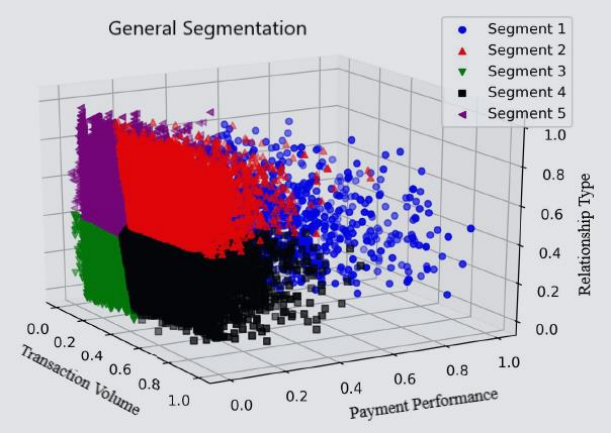

Figure 5: Customer segmentation what obtained as a result of clustering analysis.

V. CONCLUSION

The segmentation process grouped the customers and gave the company very comprehensive information about the operation of the company. Using this information, more advanced analytics applications related to customer satisfaction and loyalty can be made in future studies.

REFERENCES

[1] Han, J., Kamber, M. & Pei, J. (2012). Data mining concepts and techniques, third edition Morgan Kaufmann Publishers

[2] Su-Yeon K., Tae-Soo J., Eui-Ho S., Hyun-Seok H. *Customer segmentation and strategy development based on customer lifetime value: A case study, Expert Systems with Applications*, Volume 31, Issue 1, 2006, Pages 101-107.

[3] Cooil, B., Aksoy, L., & Keiningham, T. L. (2008). *Approaches to customer segmentation*. Journal of Relationship Marketing, *6*(3-4), 9-39.

[4] Wu, J., & Lin, Z. (2005, August). *Research on customer segmentation model by clustering*. In Proceedings of the 7th international conference on Electronic commerce (pp. 316-318).

[5] Sari, J. N., Nugroho, L. E., Ferdiana, R., & Santosa, P. I. (2016). *Review on customer segmentation technique on ecommerce*. Advanced Science Letters, *22*(10), 3018-3022.

[6] Bayer, J. (2010). *Customer segmentation in the telecommunications industry*. Journal of Database marketing & customer strategy management, *17*(3), 247-256.

[7] Hosseini, M., Shabani, M. *New approach to customer segmentation based on changes in customer value*. J Market Anal 3, 110–121 (2015).

[8] Berkhin, Pavel. 2004. *Survey of Clustering Data Mining Techniques*.

[9] MacQueen, J. (1967). Classification and analysis of multivariate observations. In *5th Berkeley Symp. Math. Statist. Probability* (pp. 281-297).

[10] Saxena A., Prasad M., Gupta A, Bharill N., Patel O. M., Tiwari A., Er M. J., Ding W., Lin C. *A review of clustering techniques and developments*, Neurocomputing, Volume 267, 2017, Pages 664-681

[11] *Euclidean Distance*, Wikipedia (Accessed on 22.09.2022).

How Do Pansharpening Strategies Affect Spectral Indices on WorldView-2 Datasets?

V. YILMAZ

Karadeniz Technical University, Trabzon/Turkey, volkanyilmaz.jdz@gmail.com

***Abstract* – Pansharpening, which aims to provide spatially enhanced multispectral (MS) images, produces images that can be used as base data for many applications. To date, the remote sensing community has come up with a large number of pansharpening strategies, some of which offer a better spatial fidelity whereas some provide a better spectral fidelity at the cost of spatial deterioration to some degree. The choice as to which pansharpening strategy should be used depends pretty much on the purpose of the application to be conducted. As known, spectral indices play a significant role in current remote sensing applications as they provide valuable information for land cover features. The aim of this study is to investigate the effects of some of the widely-used pansharpening strategies on the spectral indices normalized difference vegetation index (NDVI), normalized difference water index (NDWI) and optimized soil-adjusted vegetation index (OSAVI) calculated on a WorldView-2 dataset. The pansharpening strategies focused on included the Gram-Schmidt (GS), additive wavelet luminance proportional (AWLP), partial replacement adaptive component substitution (PRACS), haze-corrected Brovey transform (BT-H), band-dependent spatial detail with physical constraints (BDSD-PC), morphological half gradient (MF), full-scale regression-based generalized Laplacian pyramid with modulation transfer function matched filter (MTF-GLP-FS), principal component analysis/wavelet model-based fusion (PWMBF), sparse representation of injected details (SR-D), pansharpening neural network (PNN) and target-adaptive PNN (TA-PNN). The results showed that the pansharpened images produced with the PRACS, BT-H, PWMBF, PNN and TA-PNN strategies provided the optimum spectral indices.**

***Keywords* - pansharpening, image fusion, spectral indices, digital image processing.**

I. Introduction

MANY remote sensing applications resort spectral indices owing to their abilities to identify different land cover features. Spectral indices can be used for various purposes, such as discrimination of burned land [1], identification of plant diseases [2], estimation of leaf chlorophyll [3], monitoring water quality [4], assessment of fire severity [5], assessing nitrogen content in agricultural fields [6], biomass estimation [7], estimation of vegetation cover fraction [8], extraction of built-up area [9], classification of agricultural crops [10] etc. Hundreds of spectral indices have been introduced to date, all of which are calculated as linear combinations of spectral bands. Their usefulness has made them indispensable for a wide variety of remote sensing applications.

Spectral indices should be calculated from the best possible datasets to get the most out of them. Applications like object identification or classification of land cover objects may require spectral indices calculated from high-resolution imageries. However, it may not always be possible to obtain such imageries due to some technical or financial limitations. Pansharpening is the perfect fit for such cases. Pansharpening aims to spatially improve a coarse-resolution multispectral image with the spatial features of a higher-resolution panchromatic imagery. The remote sensing community has come up with a large number of pansharpening strategies to date. According to Serifoglu Yilmaz et al. [11], the pansharpening strategies can be caterorized into six classes as component substitution-based methods, multiresolution analysis-based methods, color-based methods, deep learning-based methods, variational optimization-based methods and hybrid methods. Each pansharpening method applies a different spatial detail improvement strategy. Some of the pansharpening strategies are more successful in preserving the color fidelity of the source multispectral images, whereas some of them offer sharper images at the cost of spectral deterioration to a certain degree [12]. This, of course, attaches importance on the selection of the pansharpening strategy that best suits the purpose of the application. If the pansharpened image is planned to be used for the calculation of spectral indices, then a pansharpening strategy offering the optimum compromise between the radiometric and spatial detail quality should be employed. However, selecting the pansharpening strategy that provides the best balance is not so easy, and mostly requires the comparison of the performances of many pansharpening methods. Hence, this study aims to assess the effects of some of the commonly-used pansharpening strategies on the spectral indices calculated from a WorldView-2 dataset. The following section presents further details on the methodology followed in this study.

II. Material and Methods

A. Data Used

The experiments were conducted in Surmene, Trabzon, Turkey. A 2-m multispectral and a 50-cm panchromatic image acquired by the WorldView-2 satellite in 2012 were used as the source images for pansharpening. The multispectral image contained four typical spectral bands (i.e., blue, green, red and near-infrared 1) and four spectral bands for advanced multispectral analysis (i.e., coastal blue, yellow, red edge and near-infrared 2). The WorldView-2 satellite is one of the commercial satellites offering the highest spatial resolution in the market. Both the multispectral and panchromatic images

used had a dynamic range of 11 bits.

B. Pansharpening

The spatial resolution of multispectral image was improved with the pansharpening methods Gram-Schmidt (GS) [13], additive wavelet luminance proportional (AWLP) [14], partial replacement-based component substitution (PRACS) [15], haze-corrected Brovey transform (BT-H) [16], physical constraints-based band-dependent spatial detail technique (BDSD-PC) [17], morphological half gradient (MF) [18], full-scale regression-based generalized Laplacian pyramid with modulation transfer function matched filter (MTF-GLP-FS) [19], principal component analysis/wavelet model-based fusion (PWMBF) [20], sparse representation-based (SR-D) [21], pansharpening neural network (PNN) [22] and target-adaptive PNN (TA-PNN) [23].

The GS injects the spatial features into the multispectral image by substituting the first component of the GS transform of the multispectral imagery by the panchromatic image [13]. The AWLP injects the spatial features obtained with wavelet transform into the multispectral image [14]. The PRACS algorithm computes the weighted sum of each multispectral band and pansharpened image to obtain each pansharpened band [15]. The BT-H strategy removes the haze effect to further enhance the performance of the classical Brovey transform-based pansharpening method [16]. The BDSD-PC takes into account physical constraints to optimize the coefficients used to calculate the pansharpened image [17]. The MF algorithm improves the spatial resolution through spatial details extracted with a morphological operator [18]. The MTF-GLP-FS strategy uses the injection coefficients computed at full-resolution to improve the spatial detail content [19]. The PWMBF algorithm adopts the principal component analysis transform of the observation model to compute the pansharpened data [20]. The SR-D technique uses low- and high-resolution dictionaries to calculate the pansharpened bands [21]. The PNN strategy uses a simple convolutional neural network to obtain the pansharpened image [22]. The TA-CNN employs some variations on the PNN [23]. Further information on the pansharpening methods used can be found in [11].

C. Calculation of Spectral Indices

Once the pansharpened images were produced using the aforementioned pansharpening methods, the widely-used spectral indices normalized difference vegetation index (NDVI), normalized difference water index (NDWI) and optimized soil-adjusted vegetation index (OSAVI) were calculated from the pansharpened images. The NDVI index, which is measures the greenness and the density of the vegetation, is calculated as [24];

$$NDVI = \frac{(NIR - RED)}{(NIR + RED)} \quad (1)$$

where, RED and NIR stand for the red and near-infrared bands, respectively. The NWDI is used to identify the water bodies and computed as [25];

$$NDWI = \frac{(GRN - NIR)}{(GRN + NIR)} \quad (2)$$

where, GRN represents the green band. The OSAVI, a soil-adjusted vegetation index [26], is calculated as [27];

$$OSAVI = \frac{(NIR - RED)}{(NIR + RED + 0.16)} \quad (3)$$

III. Results

A reference spectral index image was needed to see to what extent each pansharpening method affected the spectral indices computed. Since no reference spectral index images were available for the test site, the NDVI, NDWI and OSAVI indices calculated from the original WorldView-2 imagery were used as the reference spectral index images. The correlation coefficients between the reference spectral index images and the spectral index images calculated from the pansharpened images were calculated to see how each pansharpening method affected the spectral indices focused on. Table 1 presents the correlation coefficients calculated between the spectral index images obtained from the original multispectral image and pansharpened images. It should be noted that the optimum value for all spectral indices is 1.

Table 1: Calculated correlation coefficients (REF refers to the reference spectral index image).

Dataset	NDVI	NDWI	OSAVI
GS - REF	0.0086	0.9231	0.0160
AWLP - REF	0.1144	0.1831	0.2573
PRACS - REF	0.9990	0.9990	0.9980
BT-H - REF	0.9989	0.9993	0.9989
BDSD-PC - REF	0.1450	0.5781	0.2187
MF - REF	0.0872	0.4785	0.0546
MTF-GLP-FS - REF	0.0340	0.1891	0.0827
PWMBF - REF	0.9944	0.9973	0.9944
SR-D - REF	0.3762	0.9835	0.0327
PNN - REF	0.9903	0.9933	0.9903
TA-PNN - REF	0.9851	0.9944	0.9851

As seen in Table 1, the spectral index images derived from pansharpened images generated by the PRACS, BT-H, PWMBF, PNN and TA-PNN methods are strongly correlated with the reference spectral index images. The AWLP, BDSD-PC, MF and MTF-GLP-FS pansharpening strategies caused significant color deterioration on the pansharpened images, which is why they produced spectral index images that were less correlated to the reference spectral index images. Although the SR-D result provided a highly consistent NDWI image, the NDVI and OSAVI images calculated from this result were found to be incoherent with the reference NDVI and OSAVI index images. This was due to the fact that the SR-D technique causes more spectral distortion on some portions of the test area. The same can be said to be true for the spectral index image calculated from the result of the GS algorithm.

The spectral index images produced with the pansharpened images obtained with the PRACS, BT-H, PWMBF, PNN and TA-PNN are shown in Figure 1. As seen in the figure, there are slight color differences between the reference spectral index images and spectral index images produced by the pansharpening results, which justifies the statistical relationship revealed with correlation coefficients. The PRACS, BT-H, PWMBF, PNN and TA-PNN methods can be said to have kept the image features during pansharpening. It should be kept in mind that Figure 1 shows only the spectral index images that had the highest relationship with the reference spectral index images.

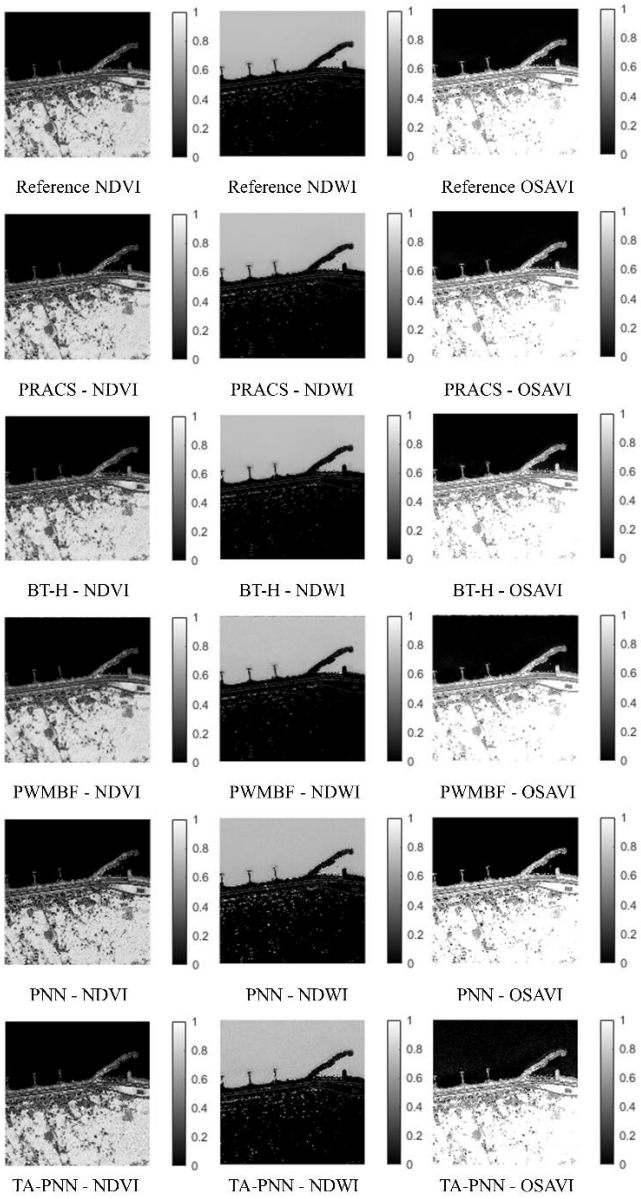

Figure 1: Spectral index images produced.

IV. Conclusion

The main goal of this study is to investigate the effects of different pansharpening approaches on some of the widely-used spectral indices (i.e., NDVI, NDWI and OSAVI) computed on WorldView-2 imageries. The evaluations revealed that the NDVI, NDWI and OSAVI images produced from the pansharpening methods PRACS, BT-H, PWMBF, PNN and TA-PNN had a high correlation with the reference spectral index images generated from the original WorldView-2 image.

References

[1] E. Chuvieco, M. P. Martin, and A. Palacios, "Assessment of different spectral indices in the red-near-infrared spectral domain for burned land discrimination," *Int. J. Remote Sens.*, vol. 23, no. 23, pp. 5103-5110, 2002

[2] A. K. Mahlein, T. Rumpf, P. Welke, H. W. Dehne, L. Plümer, U. Steiner, and E. C. Oerke, "Development of spectral indices for detecting and identifying plant diseases," *Remote Sens. Environ.*, vol. 128, pp. 21-30, 2013

[3] R. Main, M. A. Cho, R. Mathieu, M. M. O'Kennedy, A. Ramoelo, and S. Koch, "An investigation into robust spectral indices for leaf chlorophyll estimation," *ISPRS J. Photogramm. Remote Sens.*, vol. 66, no. 6, pp. 751-761, 2011.

[4] V. Sagan, K. T. Peterson, M. Maimaitijiang, P. Sidike, J. Sloan, B. A. Greeling, S. Maalouf, and C. Adams, "Monitoring inland water quality using remote sensing: Potential and limitations of spectral indices, bio-optical simulations, machine learning, and cloud computing," *Earth-Sci. Rev.*, vol. 205, 103187, 2020.

[5] B. N. Tran, M. A. Tanase, L. T. Bennett, and C. Aponte, "Evaluation of spectral indices for assessing fire severity in Australian temperate forests," *Remote Sens.*, vol. 10, no. 11, pp. 1680, 2018.

[6] I. Herrmann, A. Karnieli, D. J. Bonfil, Y. Cohen, and V. Alchanatis, "SWIR-based spectral indices for assessing nitrogen content in potato fields," *Int. J. Remote Sens*., vol. 31, no. 19, pp. 5127-5143, 2010.

[7] S. W. Todd, R. M. Hoffer, and D. G. Milchunas, "Biomass estimation on grazed and ungrazed rangelands using spectral indices," *Int. J. Remote Sens*., vol. 19, no. 3, pp. 427-438, 1998.

[8] S. Barati, B. Rayegani, M. Saati, A. Sharifi, and M. Nasri, "Comparison the accuracies of different spectral indices for estimation of vegetation cover fraction in sparse vegetated areas," *Egypt. J. Remote. Sens. Space Sci.*, vol. 14, no. 1, pp. 49-56, 2011.

[9] R. Kaur, and P. Pandey, "A review on spectral indices for built-up area extraction using remote sensing technology," *Arab. J. Geosci.*, vol. 15, no. 5, pp. 1-22, 2022.

[10] N. Kobayashi, H. Tani, X. Wang, and R. Sonobe, "Crop classification using spectral indices derived from Sentinel-2A imagery," *J. Telecommun. Inf. Technol.*, vol. 4, no. 1, pp. 67-90, 2020.

[11] C. Serifoglu Yilmaz, V. Yilmaz, and O. Gungor, "A theoretical and practical survey of image fusion methods for multispectral pansharpening," *Inf. Fusion*, vol. 79, pp. 1-43, 2022.

[12] C. Serifoglu Yilmaz, V. Yilmaz, O. Gungor, and J. Shan, "Metaheuristic pansharpening based on symbiotic organisms search optimization," *ISPRS J. Photogramm. Remote Sens.*, vol. 158, pp. 167-187, 2019.

[13] C. A. Laben, and B. V. Brower, U.S. Patent No. 6,011,875. Washington, DC: U.S. Patent and Trademark Office, 2000.

[14] X. Otazu, M. González-Audícana, O. Fors, and J. Núñez, "Introduction of sensor spectral response into image fusion methods, Application to wavelet-based methods," *IEEE Trans. Geosci. Remote Sens*., vol. 43, no. 10, pp. 2376-2385, 2005.

[15] J. Choi, K. Yu, and Y. Kim, "A new adaptive component-substitution-based satellite image fusion by using partial replacement," *IEEE Trans. Geosci. Remote Sens.*, vol. 49, no. 1, pp. 295-309, 2010.

[16] S. Lolli, L. Alparone, A. Garzelli, and G. Vivone, "Haze correction for contrast-based multispectral pansharpening," *IEEE Geosci. Remote. Sens. Lett.*, vol. 14, no. 12, pp. 2255-2259, 2017.

[17] G. Vivone, "Robust Band-Dependent Spatial-Detail Approaches for Panchromatic Sharpening," *IEEE Trans. Geosci. Remote Sens.*, vol. 57, no. 9, pp. 6421-6433, 2019.

[18] R. Restaino, G. Vivone, M. Dalla Mura, and J. Chanussot, "Fusion of multispectral and panchromatic images based on morphological operators," *IEEE Trans. Image Process.*, vol. 25, no. 6, pp. 2882-2895, 2016.

[19] G. Vivone, R. Restaino, and J. Chanussot, "Full scale regression-based injection coefficients for panchromatic sharpening," *IEEE Trans. Image Process.*, vol. 27, no. 7, pp. 3418-3431, 2018.

[20] F. Palsson, J. R. Sveinsson, M. O. Ulfarsson, and J. A. Benediktsson, "Model-based fusion of multi-and hyperspectral images using PCA and

wavelets," *IEEE Trans. Geosci. Remote Sens.*, vol. 53, no. 5, pp. 2652-2663, 2015.
[21] M. R. Vicinanza, R. Restaino, G. Vivone, M. Dalla Mura, and J. Chanussot, "A pansharpening method based on the sparse representation of injected details," *IEEE Geosci. Remote Sens. Lett.*, vol. 12, no. 1, pp. 180-184, 2015.
[22] G. Masi, D. Cozzolino, L. Verdoliva, and G. Scarpa, "Pansharpening by convolutional neural networks," *Remote Sens.*, vol. 8, no. 7, 594, 2016.
[23] G. Scarpa, S. Vitale, and D. Cozzolino, "Target-adaptive CNN-based pansharpening," *IEEE Trans. Geosci. Remote Sens.*, vol. 56, no. 9, pp. 5443-5457, 2018.
[24] S. Huang, L. Tang, J. P. Hupy, Y. Wang, and G. Shao, "A commentary review on the use of normalized difference vegetation index (NDVI) in the era of popular remote sensing," *J. For. Res.*, vol. 32, no. 1, pp. 1-6, 2021.
[25] S. K. McFeeters, "The use of the Normalized Difference Water Index (NDWI) in the delineation of open water features," *Int. J. Remote Sens.*, vol. 17, no. 7, pp. 1425-1432, 1996.
[26] M. D. Steven, "The sensitivity of the OSAVI vegetation index to observational parameters," *Remote Sens. Environ.*, vol. 63, no. 1, pp. 49-60, 1998.
[27] G. Rondeaux, M. Steven, and F. Baret, "Optimization of soil-adjusted vegetation indices," *Remote Sens. Environ.*, vol. 55, no. 2, pp. 95-107, 1996.

Static Analysis of Malware Detection Using Machine Learning Algorithms

N.VURAN SARI[1] and M. ACI[2]

[1]Mersin University, Mersin/Turkey, nvuran@mersin.edu.tr
[2]Mersin University, Mersin /Turkey, maci@mersin.edu.tr

Abstract **- Nowadays, the diversity of malware is rising rapidly and exponentially and, for accurate identification and detection new techniques must be investigated and utilized. Machine learning methods provide high performance in detecting malicious software. Analysis of a software without running it is known as static analysis. By looking at the features that the software uses, such as functions, libraries, digital signatures, and other features, the functioning structure of the software can be resolved. The proposed method presents a comparative study of 8 different well-known machine learning algorithms such as K-Nearest Neighbor, Random Forest, Decision Tree, Gaussian Naive Bayes, CatBoost, LightGBM, Gradient Boosting and eXtreme Gradient Boosting. The dataset used in the study contains 2000 (1000 malicious - 1000 benign) balanced cyber-attack software selected from the real world was used. The result shows that the use of eXtreme Gradient Boosting classification method gives the best classification accuracy by 99.25%.**

Keywords– **Malware Detection, Machine Learning, Static Analysis, Malware Analysis**

I. INTRODUCTION

In recent years, the age of technology has brought many innovations and made our lives easier in every sense, and it has also included cyber risks and threats in our lives. With the spread of information technologies, it is seen that the harmful software that threatens information systems diversifies and their effects increase. Malware are malicious programs that perform operations that are not authorized by the user. They can damage or gain unauthorized access to users' programmable devices, websites or networks.

Some viruses harm the computer in various ways, such as damaging applications, deleting files and reformatting the hard disk, while others are programmed to simply multiply inside the system, slowing down the system, rather than harming it. Viruses, worms, Trojan horses, root kits, back doors, botnets, spyware, and adware are examples of common malware [1]. Today, many methods are used for the analysis and detection of these malicious software. Malware analysis can be done in a variety of ways such as dynamic, static and hybrid.

Static analysis is used to extract information and features from patterns such as arrays, n-grams, functions, opcodes, byte arrays, libraries and call graphs to detect malware [1]. In general, static analysis is an automatic analysis that takes the source code of a program as input, examines this input without running the code, and also checks the code structure and expression sequences and outputs the result. Variable values are handled across different function calls [2]. The malicious code is executed in a controlled or virtual environment throughout dynamic analysis. A number of tools are used to evaluate the behavior of code during execution. Functions, parameters, information flows, instructions, etc. is also analyzed [1].

In addition to static and dynamic approaches, machine learning techniques can be utilized to automate and hasten the stages involved in malware analysis, detection, and classification. Data from static or dynamic analysis is examined in order to classify malware into families or to detect malware using machine learning techniques (i.e. clustering or classification).

The rest of the paper is organized as follows. Chapter 2 describes some of the relevant studies in the literature. Chapter 3 discusses methodology that includes machine learning-based algorithms used to detect malware and dataset pre-processing. Chapter 4 compares machine learning malware detection techniques and discusses the comparison of findings. Chapter 5 concludes this article by emphasizing the research aspects.

II. RELATED WORKS

Researchers have recently started to evaluate and categorize malware using a variety of ways. The current methods of operation might not be very efficient against new threats. Machine learning algorithms can enhance malware detections and outperform current methods.

Harshalatha and Mohanasundaram [3] presented the literature work of previously existing works of malware detection classification using machine learning algorithms. Classifier models used in this approach are Random Forest (RF), BayesNet, Multi-Layer Perceptron (MLP), and Support Vector Machine (SVM). First, all malware samples were tested under 10-fold cross-validation, and the classifier results showed that RF had the best performance (98% accuracy) and the same RF accuracy was down by 12% when the RF classifier was applied for different datasets.

Patil et al. [4] pointed out a framework that extracts numerous feature-sets from the malware files, including system calls, operational codes, sections, and byte codes. They used Microsoft's malware dataset available on the Kaggle website. It contained 10868 malware files from a variety of 9 malware families. The study compares the effectiveness of machine learning and deep learning-based methods on each of

these features, and the results show that feature vector for system calls achieved the best accuracy.

In order to find malicious executables in the wild, Kolter et al. [5] employed machine learning methods and used n-grams of byte codes as characteristics. As training examples, they encoded each of the 1651 malicious executables and the 1971 benign executables they collected. They tested several inductive techniques after choosing the most pertinent n-grams for prediction, including Naive Bayes (NB), Decision Tree (DT), SVM, and Boosting. The area under the Receiver Operating Characteristic (ROC) curve for boosted DT was 0.996, outperforming all other approaches in the end.

Algahtani et al. [6] focused on machine learning-based classifiers to identify malicious software on Android devices, this study covers the state of the art in Android malware detection strategies. Different machine learning algorithms, including SVM, NB, Perceptron, J48, OneRand Deep Network algorithms, provide the base for framework development. The dataset in use includes 2081 benign applications and 91 malicious ones. OneR and J48 algorithms achieved 100% accuracy with a 0.00% false positive rate.

In order to identify malware, Schultz et al. [7] applied three distinct approaches on Windows-based system portable executable files (PE). These techniques were employed to find known malware. They employed a method that utilized Dynamic Link Libraries (DLLs), function calls, and attributes for the frequency with which these functions were called. They used binary data that was extracted from PE files utilizing strings software for the second approach. Finally, they utilized the 2-byte strings provided by the program by utilizing the hex dump software. In this article, Schultz used RIPPER, NB, and several classifier techniques for detection. The system utilizing NB provided the highest detection rate per the data.

III. METHODOLOGY

It is being researched to see if machine learning techniques can detect novel malware. The dataset has been preprocessed and digitalized so that machine learning algorithms can use it. The effectiveness of eight well-known machine learning techniques for malware detection was evaluated.

A. Dataset

The dataset consists of 2000 samples of software labeled as malicious or benign, 1000 of which are malicious and 1000 are benign software, as shown in Table 1. File size, software digital signature status, libraries, and functions were all used as features.

Table 1: Number of collected data.

Class	Count
Malicious	1.000
Benign	1.000
Total	2.000

The dataset is split into a sub-dataset after being shuffled, with 80% (1600) of the data being used for training and 20% (400) for testing in the machine learning phase of the system.

The training datasets were imported into a Python module in order to create a model using machine learning methods (i.e., DT, RF, SVM, K-Nearest Neighbors (KNN), Boosting algorithms and so on) from the Scikit-learn library.

B. Preprocessing

Data preprocessing is the term used to describe any processing approach used on raw data to get it ready for next processing step. It transforms data into a format that classification algorithms can analyze more quickly and efficiently [8].

Some of the issues of signature-based malware detection can be overcome with the help of supervised machine learning classification. Building labeled training dataset is the initial step in using machine learning to categorize files as malicious or benign. Each file is classified as benign or malicious based on its properties, which are deduced from a few key aspects of the file [9].

Between the features in the dataset the function and library names in the functions and libraries (features) column were arranged as columns, so that each function and library name was also considered as a dataset feature. 195 unique libraries and 4,327 unique functions were obtained. Including size, digital signature, class and these unique functions and libraries are also used as features in the dataset. A total of 4,525 features were used.

Categorical input must be transformed into numerical terms for the model to work in machine learning. All features in the dataset were normalized to a binary value as "0" or "1".

Cross-validation technique, which divides the training set into numerous smaller training sets and a validation set, is used to prevent over-fitting [1]. The model is trained on smaller training sets and then tested on the test set.

C. Performance Measure

Precision, recall, accuracy and F1-score were computed to evaluate the effectiveness of machine learning methods. Below are the measures that used in the context of categorizing malware.

• F1-Score: Harmonic mean of recall and precision for a more accurate analysis of model effectiveness (1).

$$F1-Score = \frac{Precision \times Recall}{Precision + Recall} \quad (1)$$

• Accuracy: Percentage of how many malicious and benign files were properly classified (2).

$$Accuracy = \frac{TP+TN}{TP+TN+FP+FN} \quad (2)$$

• TP (True Positive): Defines the quantity of files that were correctly categorized as malicious.

• TN (True Negative): Defines the quantity of files that were correctly categorized as benign.

• FP (False Positive): Defines the quantity of files that were incorrectly categorized as malicious.

• FN (False Negative): Defines the quantity of files that

were incorrectly categorized as benign.

• Precision: Properly classified malicious and benign files' percentage. It is calculated by dividing the actual positives by any positive predictions (3).

$$Precision = \frac{TP}{TP+FP} \quad (3)$$

• Recall: Properly classified malicious and benign files' percentage. It is calculated by dividing the actual positives by any positive predictions that should have been made (4).

$$Recall = \frac{TP}{TP+FN} \quad (4)$$

D. Machine Learning Algorithms

Due to the shortcomings of the presently offered malware detection methods, machine learning techniques are integrated with existing detection methods to increase the detection process' efficiency [10]. Various researchers have demonstrated the effectiveness of machine learning in detecting malware. Therefore, many machine learning-based malware detection systems have been studied in this area.

It is obvious that employing machine learning to identify malware offers the benefit of superior detection accuracy. Due to their accuracy in identifying harmful samples, existing research demonstrates that employing decision trees to detect malware may be a suitable strategy[11].For this reason, algorithms with decision trees based were mainly studied.

GaussianNB, KNN,DT, RF, Catboost (CB), LightGBM (LGBM), eXtreme Gradient Boosting (XGB) and Gradient Boosting (GB) are the algorithms that were employed in this study to categorize the data as malware or benign.

The steps of the supervised machine learning process are as follows (Figure 1):

1. Data extraction and transformation into a format for machine learning models;
2. Using training data to train the models and determining the ideal hyper-parameters for a certain model;
3. Comparing and analyzing the models using test data.

These stages provide trained models that can classify samples in proposed malware detection system that were unknown samples.

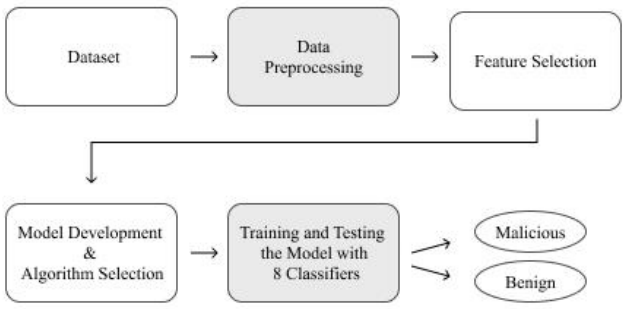

Figure 1: System Overview

IV. Experimental Results

2000 software have been labeled in dataset, 1000 of which are malicious and 1000 of which are benign. The common 10-fold cross-validation procedure was applied in experiments. In other words, the dataset is partitioned into ten smaller sub-datasets at random. Nine of these ten distinct sub-datasets were utilized to train the algorithms, while one was used to test the approaches.

For performance evaluation accuracy, f1-score, precision, and recall values were computed.

Table 2: Overall malware classification results

Algorithms	F1-Score	Accuracy	Precision	Recall
KNN	0.606357	0.5975	0.610837	0.60194
RF	0.978102	0.9775	0.980488	0.97572
DT	0.949640	0.9475	0.938389	0.96116
GaussianNB	0.673611	0.5300	0.524324	0.94174
CB	0.987893	0.9875	0.985507	0.99029
LGBM	0. 983133	0. 9875	0. 976077	0. 99029
GB	0.987893	0.9875	0.985507	0.99029
XGB	**0.992736**	**0.9925**	**0.990338**	**0.99514**

As shown in Table 2, according to the accuracy results, XGB outperformed seven algorithms with a very high detection rate of 99.25%. This was followed by CB, LGBM and GB other boosting algorithms with 98.25% accuracy, which showed the same accuracy although F1-score, precision and recall values were different. These three algorithms were followed by RF, DT, KNN and NB algorithms, respectively. It has been observed that the F1-score, precision and recall results give results proportional to the accuracy results. Boosting algorithms such as XGB, GB, and CB are more powerful than other algorithms for several reasons, as they are essentially decision tree-based algorithms. One of these reasons is that the tree structure they produce tends to reduce the error from the previous tree.

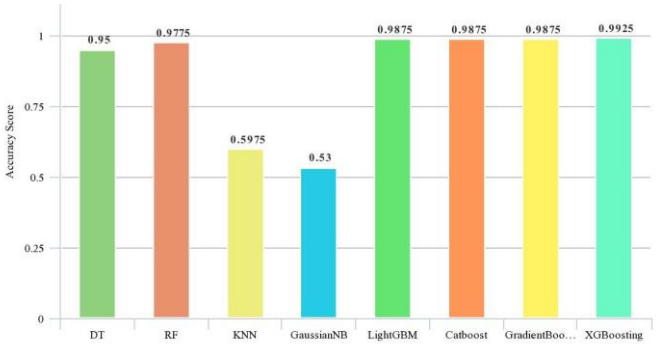

Figure 2: Accuracy of Algorithms

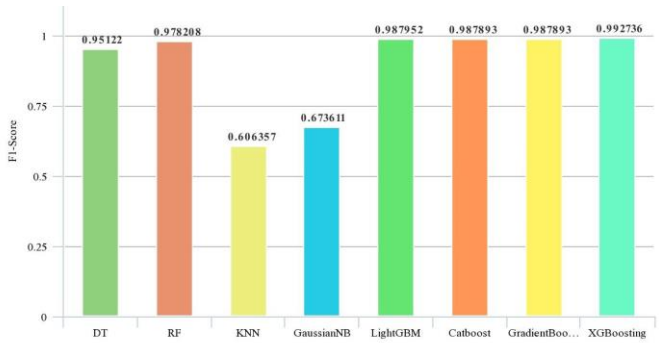

Figure 3: F1-Score of Algorithms

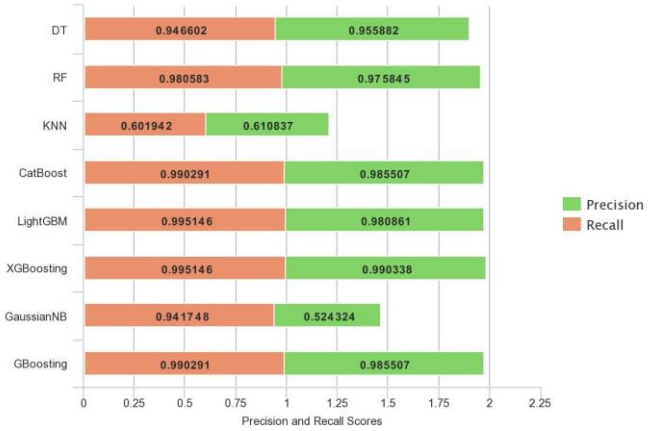

Figure 4: Precision and Recall Scores of Algorithms

V. Conclusion

In this work, eight different machine learning algorithms were applied the detect malware. Static code analysis-based studies that use signatures frequently fail to identify newly discovered malware. As a result, machine learning algorithms are utilized in this study to separate malicious software from software that isn't harmful by exploiting the structural elements of the software.

In our future work, the success rate of the model in detecting malware can be increased by using deep learning methods and algorithms. In addition, by weighting the features that are more important for malware detection in dataset, both the runtime and the accuracy performance can be improved.

Appendix

We would like to thank CHOMAR A.S. Company for sharing the dataset used in this study.

References

[1] Patil, R., & Deng, W. (2020, March). Malware Analysis using Machine Learning and Deep Learning techniques. In *2020 SoutheastCon* (Vol. 2, pp. 1-7). IEEE.

[2] Li, L., Bissyandé, T. F., Papadakis, M., Rasthofer, S., Bartel, A., Octeau, D., &Traon, L. (2017). Static analysis of android apps: A systematic literature review. *Information and Software Technology*, *88*, 67-95.

[3] Harshalatha, P., and R. Mohanasundaram. "Classification of Malware Detection Using Machine Learn-ing Algorithms: A Survey." *International Journal of Scientific & Technology Research* 9.02 (2020).

[4] Kolter, Jeremy Z., and Marcus A. Maloof. "Learning to detect malicious executables in the wild." *Proceedings of the tenth ACM SIGKDD international conference on Knowledge discovery and data mining*. 2004.

[5] Alqahtani, Ebtesam J., RachidZagrouba, and Abdullah Almuhaideb. "A Survey on Android Malware Detection Techniques Using Machine Learning Algorithms." *2019 Sixth International Conference on Software Defined Systems (SDS)*. IEEE, 2019.

[6] Schultz, M. G., Eskin, E., Zadok, F., &Stolfo, S. J. (2000, May). Data mining methods for detection of new malicious executables. In *Proceedings 2001 IEEE Symposium on Security and Privacy. S&P 2001* (pp. 38-49). IEEE.

[7] Iliou, T., Anagnostopoulos, C. N., Nerantzaki, M., &Anastassopoulos, G. (2015, September). A novel machine learning data preprocessing method for enhancing classification algorithms performance. In *Proceedings of the 16th International Conference on Engineering Applications of Neural Networks (INNS)* (pp. 1-5).

[8] Markel, Zane, and Michael Bilzor. "Building a machine learning classifier for malware detection." *2014 second workshop on anti-malware testing research (WATeR)*. IEEE, 2014.

[9] Chumachenko, Kateryna. "Machine learning methods for malware detection and classification." (2017).

[10] Palša, J., Ádám, N., Hurtuk, J., Chovancová, E., Madoš, B., Chovanec, M., &Kocan, S. (2022). MLMD—A Malware-Detecting Antivirus Tool Based on the XGBoost Machine Learning Algorithm. *Applied Sciences*, *12*(13), 6672.

A Review on Deep Learning-Based Methods Developed for Lung Cancer Diagnosis

T.B. KARA[1] and A.C. ÇINAR[2]

[1] Selcuk University, Konya/Turkey, 218273001009@lisansustu.selcuk.edu.tr
[1]Selcuk University, Konya/Turkey, accinar@selcuk.edu.tr

***Abstract* – Lung cancer is one of the leading causes of cancer death worldwide. Today, although the medical world has discovered the cure for many diseases, it is still insufficient in diseases such as cancer and continues to result in death in most patients. Early diagnosis is the most important factor in preventing cancer. Histopathological diagnosis is a very time-consuming and error-prone process for medical professionals. Today, many artificial intelligence-based studies are carried out on early diagnosis. Considering these studies, it is predicted that systems based on artificial intelligence will replace human effort in pathological studies in the future. In this study, deep learning-based methods developed using microscopic images of lung tissues were examined. The aim of the study is to guide future studies by referring to the successful results of deep learning-based methods.**

***Keywords* – Deep learning, Lung cancer detection, Classification, Histopathological image analysis.**

I. Introduction

LUNG cancer, one of the most common types of cancer in recent years, ranks second in the world, along with prostate cancer in men and breast cancer in women. The International Association of Cancer Society (IACS) estimates that in 2022, there will be 236,740 new cases of lung cancer in the United States and 130,180 related death [1].

Lung cancer is a disease caused by uncontrollable malignant tumors that form in the lung tissue [2]. Factors such as polluted air, gender, genes, and aging, especially cigarette consumption, cause lung cancer. Early diagnosis of lung cancer is very important for treatment to result in survival. Standard medical methods are available for early diagnoses, such as Computed Tomography (CT), Positron Emission Tomography (PET), and Magnetic Resonance Imaging (MRI). Lung tissues are analyzed by examining the images obtained with Computed tomography (CT) imaging, which is a medical screening test. However, CT images alone are not sufficient for an accurate diagnosis.

In lung cancer and other types of cancer, doctors use the Computer Aided Diagnosis (CAD) system as a helpful tool. As an effective diagnostic tool, the CAD system is a prerequisite for the practicality of imaging lung tissues. Lung segmentation is important for CAD systems.

In the literature, many image analysis methods have been proposed based on signal thresholding techniques and contrast information. While these methods are effective for normal lung segmentation, they fail in the case of abnormal tissues. In recent years, the success of CAD systems has increased with methods developed based on deep learning (DL). Using the power of Artificial Neural Networks (ANN), deep learning is a sub-branch of machine learning (ML). Deep learning, which consists of processing layers, has enabled machines to learn high-dimensional data representations such as video and multidimensional images.

In this article, deep learning-based studies for the diagnosis of lung cancer are reviewed. Information about the deep learning algorithms and databases used by researchers, especially in recent studies, and the accuracy and sensitivity rates obtained from them are presented. The rest of the article first explains the research criteria (Section 2). Then the main studies are mentioned (Section 3). Finally, the result obtained from the literature review is explained (Section 4).

II. Research Methodology

Studies based on deep learning in the diagnosis of lung cancer, which was at its lowest level in 2016, continued to increase until 2019. Thanks to the models developed based on deep learning, the success rate in the diagnosis of lung cancer continues to increase today. The studies conducted between 2019-2022 were examined and included in our article after passing through some criteria. The criteria that should be in the studies are as follows:

- English articles were reviewed.
- Studies published between 2019-2022 were taken into account.
- Evidence-oriented studies were given importance.
- In addition to popular databases, studies with current databases are also taken into consideration.

The abstracts and titles of the articles on lung cancer diagnosis based on deep learning were reviewed. Then, the articles that did not find enough relevance to our subject and did not meet the review criteria were eliminated and the main articles were determined.

III. Literature Review

Size, volume, and shape elements are important for the detection of the nodule in the diagnosis of lung cancer. CT imaging is insufficient to obtain this information. Based on this need, P.Sahu et al. [3]. They developed a Multi-Section CNN (Convolutional Neural Network) model. The model, which consists of main processes such as section nodule,

parameters, maximum pooling, and retraining of the last layer, is light enough to be carried on mobile devices. They conducted multiple experiments with the model they developed in 2019. The model, in which MobileNet is used as the basic CNN, was developed using the LIDC-IDRI (Lung image database consortium-Image database resource initiative) [4] dataset. It has a 93.18% success rate in detecting lung cancer.

Developing a CAD method for the detection of pulmonary nodules on CT images, J. Wang et al. [5] aimed to minimize false negatives (FNs) and false positives (FPs). The strategy proposed in 2019 was successful in detecting the most common small nodules in the clinic. The model, which provides coarse size information as well as location information in independent candidate detection, showed superior performance in reducing false positive values. With the method inspired by the object detection model Faster-RCNN [6], very fast candidate detection is performed. In the developed method, TIANCHI AI [7], LUNA-16(Lung Nodule Analysis-2016) [8] LIDC-IDRI, and INDEPENDENT datasets are used.

Y. Xie et al. [9] proposed a multi-view knowledge-based collaborative (MV-KBC) deep model. They aimed to distinguish malignant nodules from benign nodules by using limited chest CT data with the model they developed in 2019. In the model using the ResNet-50 [10] network, first, a 3D lung nodule is decomposed into 9 fixed views. Then, the overall appearance, voxel, and shape heterogeneity of each view are determined. A knowledge-based collaborative (KBC) submodel is created in which 3 types of image patches (overall view-OA, heterogeneity in voxel values-HVV, heterogeneity in shapes-HS) are designed for fine-tuning. In the method developed using the LIDC-IDRI dataset, lung nodules are segmented for patch removal. U-Net network [11], which is a fully convolutional network (FCN) model, is used for the segmentation process. The proposed model is successful at a rate of 91.60%.

In 2019, W. Wang et al. [12] developed a method for 3D pulmonary nodule sample segmentation. This method covers the Nodule-Plus R-CNN model and the Deep Self-Paced Active Learning (DSAL) framework. Using the idea of Mask R-CNN [13], the segmentation of very small pulmonary nodules was made easier. With the Deep Self-Paced Active Learning (DSAL) strategy, they aimed to train 3D neural networks and reduce unnecessary explanations. They used the LIDC-IDRI dataset in their work. The performance of the method, which increases the segmentation performance and reduces the effort of expert explanation, is determined as 0.66 Dice and 0.96 TP Dice.

Lakshmanaprabu S.K et al. [14] proposed the Optimal Deep Neural Network (ODNN) method with feature reduction functionality. This method, which was developed in 2019, is aimed to automatically classify lung cancer in order to reduce the time of manual labeling of CT images and to avoid human error. In the method in which Modified Gravity Search Algorithm (MGSA) is used in addition to the ODNN classifier, an accuracy of 94.56% and a sensitivity of 96.2% have been achieved by using the lung cancer dataset [15].

I.M. Nasser et al. [16] developed an Artificial Neural Network (ANN) in 2019. The proposed architecture consists of an input layer, a single hidden layer, two hidden layers, and an output layer. A questionnaire lung cancer dataset was used in the study. This dataset includes information from healthy people and people with lung cancer. The presented model achieved 96.67% accuracy with less than a 1% training error rate. They also concluded that the age factor is highly effective in lung cancer.

O. Özdemir et al. [17] developed the 3D Probabilistic Deep Learning System for the detection of lung cancer. With the low-dose CT scans they developed in 2020, they aimed to make it easier for experts to benefit from automated algorithmic solutions. Considering the connection between detection and diagnostic components, this study consists of Computer Aided Detection module (CADe) and Computer Aided Diagnosis module (CADx) systems. In the study, which used V-Net [18] architecture for 3D medical image segmentation, standard 3D U-Net [19] architecture was used to obtain comparable results from the full training and evaluation line. The diagnostic performance of the system, which was developed using LIDC-IDRI, LUNA-16, and Kaggle [20] datasets, reached 96.5%.

For the detection of lung cancer, A. Masood et al. [21] developed a Computer-Aided Diagnosis (CAD) system to provide radiologists with a reference opinion in 2020. The developed system is based on the 3D Deep Convolutional Neural Network (3DDCNN). The system, developed within the framework of Faster R-CNN, applied the Multi-Regional Proposal Network (mRPN) for candidate identification. False positive reduction is done with 3DDCNN. In the Cloud Based 3DDCNN system, Shanghai Hospital 's dataset and LIDC-IDR, LUNA16 and ANODE09 [22] datasets were used. The accuracy of the system reached 98.51%.

J. Zheng et al. [23] designed a pulmonary nodule risk classification network (STM-Net), emphasizing the importance of early detection of lung cancer. Since segmented pulmonary nodules are very small in size, they proposed a deep convolutional neural network (CNN) with multi-feature algorithms and a scale transfer module (STM). The data used in this study, conducted in 2020, were obtained from the Zhongshan Hospital Fudan University (ZSDB) dataset. STM-Net has a 95.455% accuracy rate in pulmonary nodule classification. With this success, it is very effective in diagnosing pulmonary nodule risk classification in adenocarcinoma at an early stage.

B. Hatuwal et al. [24] used Convolutional Neural Network (CNN) architecture to classify three different histopathological images (benign, Adenocarcinoma, and squamous cell carcinomas). The system, which consists of data collection, data shaping, model training, testing, and estimation, was developed using 15000 lung histopathological images in the LC25000 (Lung and Colon Cancer Histopathological Image Dataset) dataset [25]. In the study conducted in 2020, benign, adenocarcinoma, squamous cell carcinomas consisting of 5000 histopathology images were taken into account. The training and validation accuracy of the applied CNN model was 96.11% and 97.2%.

M.A. in 2020 Abbas et al. [26] conducted a study determining the effectiveness of convolutional neural networks in the histopathological diagnosis of lung cancer. In this study, 15000 histopathological images in the LC25000 dataset were used. VGG-19 [27], AlexNet [28], and ResNet architectures were used to classify data consisting of three classes (benign lung tissue, squamous cell carcinoma of the lungs, and lung adenocarcinoma). CNN architectures have generally achieved an accuracy of over 97% in the diagnosis of lung squamous cell carcinoma and adenocarcinoma.

F. Silva et al. [29] examined the suitability of physiological features obtained from CT images to evaluate the Epidermal growth factor receptor (EGFR) mutation status in 2021. In the examination performed with an MLP-based approach, different analysis regions were used. A 2D lung segmentation model was created within the framework of the U-Net architecture. The study using NSCLC-Radiogenomics [30] and LIDC-IDRI datasets shows that comprehensive approaches play an important role in providing superior performance.

P. Surendar et al. [31] aimed to identify malignant lung nodules and classify lung tumors with the method they developed in 2021. The LIDC-IDRI dataset was used in the system called DNN ASCCS (Deep neural network with adaptive sine cosine crow search). In the study, segmentation, feature selection, and classification methods were developed. 99.17% success was achieved in the diagnosis of lung cancer by using the adaptive optimization procedure and the hybrid deep neural network.

N. Joshua et al. [32] In 2021, they developed 3D CNN using 3D AlexNet with lightweight architecture. In the study, the LUNA16 dataset was used to classify benign and malignant lung tumors. The 3D AlexNet preferred in the study has less complexity than other deep learning models. Compared to the proposed model classification algorithms and low-dose CT scan images, it showed superior performance by 97.17%.

M.A. Heuvelmans et al. [33] proposed a system called Lung Cancer Prediction Convolutional Neural Network (LCP-CNN) to identify benign lung tumors in lung cancer detection. The system, which enables to identification and ruling out of benign nodules using deep learning methods, was developed using the NLST(National Lung Screening Trial) dataset [34]. Unnecessary examinations can be avoided thanks to the study with 99% sensitivity. This system, which was proposed in 2021, reached an accuracy rate of 94.5%. The study could enable about one-fifth of patients to avoid follow-up scans.

P. Aonpong et al. [35] In 2021, they presented a low-cost, high-performance genotype-guided radiomics method (GGR). The method, which was developed using the NSCLC radiographic dataset containing CT images and gene expression data, consists of two stages with two models. The first is the gene prediction model. The second model predicts recurrence using the first model. The method using ResNet50 in deep feature extraction achieved 83.28%, outperforming existing radiomics methods and ResNet50.

In 2022, S.Dodia et al. [36] proposed a receptive field-regularized V-net (RFR V-Net) architecture. They also proposed the lung nodule classification NCNet (nodule classification network). The work, which developed both a new segmentation algorithm (RFR V-Net) and a nodule classification network, led to successful developments in existing CAD systems. The system that detects lung cancer nodules with reduced false positives (FP) used the LUNA16 dataset. The proposed system showed 98.21% success in detecting lung nodules.

T. Vaiyapuri et al. [37] proposed a new CSO-CADLCC (cat swarm optimization-based computer-aided diagnosis model for lung cancer classification) for lung cancer diagnosis. The model proposed in 2022, is aimed to identify and classify lung cancer using CT images. In the developed system, firstly, the noise is eliminated. Then the properties of the images are determined. Finally, an advanced classification process is performed with the CSO algorithm. ELCAP (Public Lung Image Database) dataset was used in this study. Reaching a 98.89% success rate, the system outperformed the new approaches.

J. Feng et al. [38] analyzed the CT images of patients with lung cancer in their study in 2022. Mask-RCNN and DPN (Double Path Network) algorithms are combined for the segmentation of CT images. Work using the custom dataset has better segmentation than Mask-RCNN or DPN alone. The method correctly evaluated the diagnostic value of deep learning-optimized chest CT with a rate of 97.94%.

A.Shimazaki et al. [39] developed a deep learning (DL) based model for lung cancer detection. In the study conducted in 2022, CNN architecture using the segmentation method was adopted. A special dataset is used in this model. The pixel-level classification of lesions in the proposed CNN-based model, it resulted in an accuracy of 73% on the test dataset. Thanks to the segmentation method, the proposed model is more effective than other methods in the follow-up and treatment of lung cancer.

IV. Analysis of Literature Review

Studies based on deep learning in the detection and diagnosis of lung cancer were examined. Some inferences were made in the studies examined. These results are listed as follows:

- Python-PyTorch simulation is widely used in deep learning-based lung cancer diagnosis studies.
- In the studies, the LIDC-IDRI dataset, which includes CT images of approximately 1000 patients, was preferred more than other datasets.
- It is seen that Faster R-CNN, MobilNet, VGG-19, AlexNet, and ResNet architectures are widely used as frameworks in the developed models. In addition, it is seen that Mask-RCNN-DPN(Double Path Network), U-Net, V-Net, and Mask R-CNN architectures are used in the segmentation process.
- In the studies reviewed, CT images were commonly used. In addition to these, it is seen that 3D CT images and Low-Dose CT images are used.
- Candidate detection and feature extraction were generally used in the preprocessing of the data used in the studies.
- Hybrid methods and transfer learning are frequently used in studies with 2D and 3D architectures.

- In the studies reviewed, although the performance results were above 90%, there were rare underperformers.

V. CONCLUSION

Lung cancer is one of the leading causes of cancer death worldwide. Early diagnosis is very important to increase the survival rate. For early diagnosis, experts must be accurate and fast in detection. Experts make use of CAD (Computer Assisted Diagnosis) systems in the process of scanning CT images. Recently developed methods based on deep learning make CAD systems more efficient.

In this article, deep learning-based studies in the diagnosis and detection of lung cancer are examined. Twenty articles passed through various criteria were reviewed. Although the majority of the studies examined showed high performance, its performance in the clinical field should be given more importance and improved. As a result of the examination, it is seen that the diversity of the dataset is insufficient. This problem can be overcome if more institutions and organizations make their data public.

Methods developed based on deep learning in the detection and diagnosis of lung cancer are promising. However, more work needs to be done in this area, which is still in its infancy. Thus, time and effort can be saved for specialists in the clinical field. Thanks to early, rapid, and accurate diagnosis, deaths due to lung cancer can be reduced significantly.

REFERENCES

[1] (2022). *American Cancer Society*. Available: https://www.cancer.org/research/cancer-facts-statistics/all-cancer-facts-figures/cancer-facts-figures-2022.html

[2] B. A. Skourt, A. El Hassani, and A. J. P. C. S. Majda, "Lung CT image segmentation using deep neural networks," vol. 127, pp. 109-113, 2018.

[3] P. Sahu, D. Yu, M. Dasari, F. Hou, H. J. I. j. o. b. Qin, and h. informatics, "A lightweight multi-section CNN for lung nodule classification and malignancy estimation," vol. 23, no. 3, pp. 960-968, 2018.

[4] S. G. Armato III *et al.*, "The lung image database consortium (LIDC) and image database resource initiative (IDRI): a completed reference database of lung nodules on CT scans," vol. 38, no. 2, pp. 915-931, 2011.

[5] J. Wang *et al.*, "Pulmonary nodule detection in volumetric chest CT scans using CNNs-based nodule-size-adaptive detection and classification," vol. 7, pp. 46033-46044, 2019.

[6] S. Ren, K. He, R. Girshick, and J. J. A. i. n. i. p. s. Sun, "Faster r-cnn: Towards real-time object detection with region proposal networks," vol. 28, 2015.

[7] (2017). *TIANCHI challenge*. Available: https://tianchi.aliyun.com/competition/introduction.html

[8] C. Jacobs, A. A. A. Setio, A. Traverso, and B. v. Ginneken. (2017). *LUNA-16: Lung Nodule Analysis*. Available: https://luna16.grand-challenge.org

[9] Y. Xie *et al.*, "Knowledge-based collaborative deep learning for benign-malignant lung nodule classification on chest CT," vol. 38, no. 4, pp. 991-1004, 2018.

[10] K. He, X. Zhang, S. Ren, and J. Sun, "Deep residual learning for image recognition," in *Proceedings of the IEEE conference on computer vision and pattern recognition*, 2016, pp. 770-778.

[11] O. Ronneberger, P. Fischer, and T. Brox, "U-net: Convolutional networks for biomedical image segmentation," in *International Conference on Medical image computing and computer-assisted intervention*, 2015, pp. 234-241: Springer.

[12] W. Wang *et al.*, "Nodule-plus R-CNN and deep self-paced active learning for 3D instance segmentation of pulmonary nodules," vol. 7, pp. 128796-128805, 2019.

[13] K. He, G. Gkioxari, P. Dollár, and R. Girshick, "Mask r-cnn," in *Proceedings of the IEEE international conference on computer vision*, 2017, pp. 2961-2969.

[14] S. Lakshmanaprabu, S. N. Mohanty, K. Shankar, N. Arunkumar, and G. J. F. G. C. S. Ramirez, "Optimal deep learning model for classification of lung cancer on CT images," vol. 92, pp. 374-382, 2019.

[15] (2003). *ELCAP Public Lung Image Database*. Available: http://www.via.cornell.edu/lungdb.html

[16] I. M. Nasser, S. S. J. I. J. o. E. Abu-Naser, and I. Systems, "Lung cancer detection using artificial neural network," vol. 3, no. 3, pp. 17-23, 2019.

[17] O. Ozdemir, R. L. Russell, and A. A. J. I. t. o. m. i. Berlin, "A 3D probabilistic deep learning system for detection and diagnosis of lung cancer using low-dose CT scans," vol. 39, no. 5, pp. 1419-1429, 2019.

[18] F. Milletari, N. Navab, and S.-A. Ahmadi, "V-net: Fully convolutional neural networks for volumetric medical image segmentation," in *2016 fourth international conference on 3D vision (3DV)*, 2016, pp. 565-571: IEEE.

[19] Ö. Çiçek, A. Abdulkadir, S. S. Lienkamp, T. Brox, and O. Ronneberger, "3D U-Net: learning dense volumetric segmentation from sparse annotation," in *International conference on medical image computing and computer-assisted intervention*, 2016, pp. 424-432: Springer.

[20] (2017). *Data Science Bowl 2017*. Available: https://www.kaggle.com/c/data-science-bowl-2017

[21] A. Masood *et al.*, "Cloud-based automated clinical decision support system for detection and diagnosis of lung cancer in chest CT," vol. 8, pp. 1-13, 2019.

[22] B. Van Ginneken *et al.*, "Comparing and combining algorithms for computer-aided detection of pulmonary nodules in computed tomography scans: the ANODE09 study," vol. 14, no. 6, pp. 707-722, 2010.

[23] J. Zheng *et al.*, "Pulmonary nodule risk classification in adenocarcinoma from CT images using deep CNN with scale transfer module," vol. 14, no. 8, pp. 1481-1489, 2020.

[24] B. K. Hatuwal and H. C. J. I. J. C. T. T. Thapa, "Lung cancer detection using convolutional neural network on histopathological images," vol. 68, no. 10, pp. 21-24, 2020.

[25] A. A. Borkowski, M. M. Bui, L. B. Thomas, C. P. Wilson, L. A. DeLand, and S. M. J. a. p. a. Mastorides, "Lung and colon cancer histopathological image dataset (lc25000)," 2019.

[26] M. A. Abbas, S. U. K. Bukhari, A. Syed, and S. S. H. J. M. Shah, "The Histopathological Diagnosis of Adenocarcinoma & Squamous Cells Carcinoma of Lungs by Artificial intelligence: A comparative study of convolutional neural networks," 2020.

[27] K. Simonyan and A. J. a. p. a. Zisserman, "Very deep convolutional networks for large-scale image recognition," 2014.

[28] A. Krizhevsky, I. Sutskever, and G. E. J. C. o. t. A. Hinton, "Imagenet classification with deep convolutional neural networks," vol. 60, no. 6, pp. 84-90, 2017.

[29] F. Silva *et al.*, "EGFR assessment in lung cancer CT images: Analysis of local and holistic regions of interest using deep unsupervised transfer learning," vol. 9, pp. 58667-58676, 2021.

[30] S. Bakr *et al.*, "A radiogenomic dataset of non-small cell lung cancer," vol. 5, no. 1, pp. 1-9, 2018.

[31] P. J. J. o. C. S. Surendar, "Diagnosis of lung cancer using hybrid deep neural network with adaptive sine cosine crow search algorithm," vol. 53, p. 101374, 2021.

[32] E. S. Neal Joshua, D. Bhattacharyya, M. Chakkravarthy, and Y.-C. J. J. o. H. E. Byun, "3D CNN with visual insights for early detection of lung cancer using gradient-weighted class activation," vol. 2021, 2021.

[33] M. A. Heuvelmans *et al.*, "Lung cancer prediction by Deep Learning to identify benign lung nodules," vol. 154, pp. 1-4, 2021.

[34] J. Chin, L. Ashby, J. Hermansen, J. Hutter, and P. J. T. N. E. j. o. m. Conway, "Screening for lung cancer with low-dose CT--translating science into Medicare coverage policy," vol. 372, no. 22, pp. 2083-2085, 2015.

[35] P. Aonpong, Y. Iwamoto, X.-H. Han, L. Lin, and Y.-W. J. I. A. Chen, "Genotype-guided radiomics signatures for recurrence prediction of non-small cell lung cancer," vol. 9, pp. 90244-90254, 2021.

[36] S. Dodia, A. Basava, M. J. I. J. o. I. S. Padukudru Anand, and Technology, "A novel receptive field-regularized V-net and nodule classification network for lung nodule detection," vol. 32, no. 1, pp. 88-101, 2022.

[37] T. Vaiyapuri, H. Alaskar, R. Parvathi, V. Pattabiraman, and A. J. A. S. Hussain, "Cat Swarm Optimization-Based Computer-Aided Diagnosis Model for Lung Cancer Classification in Computed Tomography Images," vol. 12, no. 11, p. 5491, 2022.

[38] J. Feng, J. J. C. Jiang, and M. M. i. Medicine, "Deep Learning-Based Chest CT Image Features in Diagnosis of Lung Cancer," vol. 2022, 2022.

[39] A. Shimazaki *et al.*, "Deep learning-based algorithm for lung cancer detection on chest radiographs using the segmentation method," vol. 12, no. 1, pp. 1-10, 2022.

Agent Based Modelling of Cell Cycle Behavior

A.ŞEN[1], K. KINGALU[2], S. EMEK[3], Ş. BORA[4]

[1] Padova University, Padova/Italy, aynur.sen@studenti.unipd.it
[2]Intertech Ar-Ge, Istanbul/Turkey, kamiraki@gmail.com
Manisa Celal Bayar University, Manisa/Turkey, sevcan.emek@cbu.edu.tr
Ege University, Izmir/Turkey, sebnem.bora@ege.edu.tr

Abstract **- Cell cycle is a series of events that continue throughout the life of the cell. The cell cycle behavior is a vital process for cell growth and cell division. In this study, the biological life cycle of the stem cells is modelled by using Repast Simphony 2.7 agent-based simulation platform, making use of the agents, a new generation programming paradigm. The stem cell behavior is difficult to predict in the laboratory and costly for infrastructure. The simulation environment provides the opportunity to observe the behavior of the stem cell model at the micro level. In this study, the simulation environment includes 3 types of agents which are cell agent, growing cell agent, and blood vessel agents that feed the cells. Agents' attributes, their actions and relationship of agents are defined in the agent classes. This study presents an agent based model that includes in the processes about cell nutrition, cell growth, cell death, cell movements, cell division stages, and cell life cycle control mechanism. This study has the potential to be modelled on a large scale with studies such as tissue modeling, behavioral model of specialized cells by increasing agent classes and interactions.**

Keywords **– Cell, cell cycle, agent based modelling, interphase, Repast Simphony.**

I. INTRODUCTION

A STEM cell is a primitive cell that can regenerate itself or elicit more specific types of cells. In recent years, there has been increasing debate about how cells behave in the human body. There are several studies in the literature with traditional models and cellular automations to predict how and why these cells are formed [1-3]. According to the studies in the medical field, if a model is sufficiently detailed and accurate, as a reference, this model can be used as a guide to interpret experimental results and as a powerful tool to propose new hypotheses. It also enables researchers to experimentally test scenarios that are not feasible using simulation, potentially resulting in lower experimental costs [4-9].

The stem cells have the ability to self-renew and differentiate into specialized cells, and can transform into many different cell types when appropriate conditions are provided in the body or in the laboratory [10]. Stem cells have two basic features; division, proliferation and regeneration, differentiation [11, 12].

Today, the stem cell reaching a certain maturity and differentiation is observed in the laboratory. It is difficult to predict the stem cell behaviors in some substances. The infrastructure for the realization and conservation of the stem cell culture in the laboratory is very expensive. Thus, the stem cell model may have the potential to be used as a powerful tool to reduce the cost and accelerate the stem cell treatment.

A stem cell completes its vital activities within a cycle. This study describes how to perform cell cycle cell feeding, movements, number of divisions, division phases individually until necrosis and apoptosis and how to perform them in the computer based solution using the Repast Simphony that provides an agent-based simulation tool in order to better examine the cell cycle behavior. We have organized this paper as follows: the literature review, in which we describe several model approaches, is given in Section 2. The agent-based modelling approach of this study is presented in Section 3. Implementation and its results are illustrated in Section 4. Evaluated of the results of this study and suggestions are given in the conclusions section.

II. LITERATURE REVIEW

Computer based solutions to biological research provide a tool to observe, analyze, simulate, understand and make predictions of the behavior of the system [13]. Biological systems are complex systems that contain many micro and macro systems. Many experimental and theoretical studies are carried out on the behavior and functionality of the cell, which is a vital component of the system. Several computational modeling concepts on the cell cycle and cell progression are being carried out in various fields of biomedicine, bioengineering and biotechnology, such as continuous models (Ordinary Differential Equations, ODEs), rule based approaches, discrete models (e.g. Boolean), agent based models, control systems, etc [8, 14-17]. Borland et. al. have developed a Cell Cycle Browser (CCB), an interactive web interface that makes it easy to visualize, organize, simulate and predict the outcomes of perturbing cell-cycle parameters. Their modeling approach is based on a set of computational models that describe cell cycle progression for different cell types and molecular activities. [18]. Bernard et al. present a checkpoint-oriented cell cycle simulation model that uses agent-based simulation modeling to reproduce the dynamics of a cancer cell population in exponential growth. They have presented the experimental studies on cell cycle progression by the cell cycle checkpoint-oriented simulator they provided [19]. Sible and Tyson describe each step of the modeling process with an example for investigating cell cycle control networks. They construct a wiring diagram by using nonlinear

ordinary differential equations (ODEs) [20]. Gaglio et al. present a qualitative approach to cell growth modeling and simulation for cancer chemotherapy [21]. If we examine studies like these, several modeling approaches exist, such as mathematical modelling and computer simulation of cell synchrony, hybrid modeling and simulation of cell cycle progression [22], a multi-stage mathematical model of cell proliferation [23], modeling the cell cycle based on functional response curves [24], and etc. Simulation software that emerged in these studies or software tools that support the theoretical approach are also examined [8].

Mathematical model offers an advantage to biologists to describe the cell physiology and predict properties of the system parameters by observing the dynamical behavior of the system. In this study, unlike other studies, we present an abstract model of the cell cycle with an agent-based modeling approach. In the agent-based modeling method, we define each agent as a cell in this study. In this way, a large number of cells and dividing cells can be represented in the simulation environment until the computational capacity of the machine is sufficient. In this study, the number of parameters can be increased or the simulation environment boundary can be narrowed.

III. Methods and Technology

A. Agent Based Modelling

Agent-based modelling offers some advantages in solving problems compared to other modelling techniques. The agent-based modeling method abstracts the problem and initiates a process from the micro level to the macro level. Thus, the solution steps of complex problems become easier. If the insufficiency of the parts of the system is high, the solution methods in the central structure are more affected by the errors in the subsystems. If any part of the system is found to be faulty, the entire system will be damaged by the connections. However, if there is a problem in a part of the system in agent-based systems, an error usually occurs in that part due to its distributed structure and the general process continue to work. Agents do not act synchronously, and they do not have to wait for the decisions of other agents. Agent-based modeling is also a suitable approach for solving distributed system problems. Agent-based systems adapt the changes, adding and removing new agents to the system is easy [15-17, 25, 26].

Agent-based modeling and simulation executes the system behavior created by the autonomous agents. The most distinctive features of agent-based modelling approaches to solving problems are that they offer "cooperation and communication" mechanisms. The control of the agent-based model is distributed and the agents in the system interact with each other and their environment [26].

B. Agent-based Cell Model

The cell cycle is a vital process in the growth and regeneration of the organism. The cell cycle includes in the process of cell growth and cell division. The stages of the cell cycle are Gap 1 (G1), synthesis (S), Gap 2 (G2) and mitosis (M).

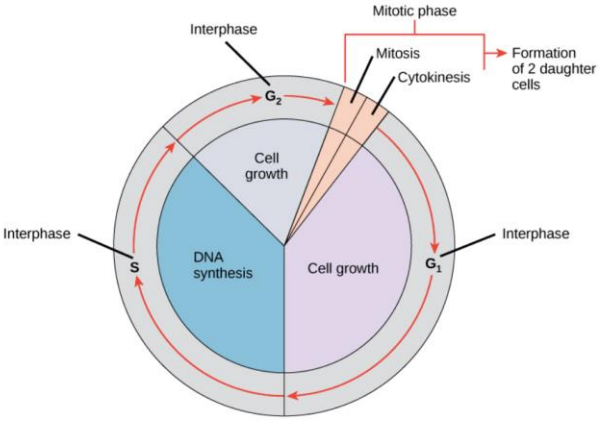

Figure 1: The cell cycle [27].

In Figure 1, interphase and the mitotic phase are two major phases which refers to the cell growth and the cell division [27]. Interphase includes three phases: G1, S and G2. G1 phase (gap 1) corresponds to the interval (gap) between mitosis and initiation of DNA replication [12]. During G1 phase, the cell is active and continuously grows. In S phase (synthesis), DNA replication takes place. During the second gap phase (G2), the cell, which genetic material has multiplied, grows not as fast as G1 to reach the size that can survive when divided. Proteins are synthesized in preparation for mitosis. M phase stands for the mitotic in which involves mitosis (karyokinesis) and cytokinesis. In mitosis, the spatial segregation of the duplicated contents occurs [28]. In cytokinesis, the cell partitions the two copies of the genetic material into the two daughter cells [11, 12].

As long as the cells do not receive a division signal, the active (G1, G2, S and M) phases of the cell cycle are not triggered and they wait in the G0 phase, called the resting phase. The resting (G0) cell is stimulated by growth factors and enters the G1 phase of the cell cycle. Cells that do not continue to divide and leave the G1 phase shift in a different direction, being differentiated. The cell grows in the G1 phase, resumes its normal functions and prepares for DNA synthesis. There is a checkpoint towards the end of this phase. DNA synthesis begins in the cell entering the S phase, then the cell enters G2, continues to grow and prepares for division, and finally, cell division is completed by entering the Mitotic phase.

There is a mechanism called checkpoint that monitors the cell throughout its life cycle. For each stage, there are control mechanisms that follow the G0, G1, Synthesis, G2 and similar stages, control the start/end of some events and thus prevent the undesired state of the cell. The cells in most grown tissues are in a quiescent state. This phase is called the Go phase of the cell cycle. The phases of the cell cycle, events, and checkpoints are described in Table 1[29, 30].

Table 1: Cell cycle and checkpoint

Phases	Events	Checkpoint
G0	The life cycle of the	Reversible, if appropriately

	cell starts.	stimulated.
G1	Protein synthesis for DNA replication	The restriction point, DNA damage.
S	DNA replication	Incomplete replication, DNA damage
G2	Preparation for mitosis	Detection damaged and unreplicated DNA
M	Cellular division	The spindle checkpoint, unattached to the spindle microtubules, incorrect number of chromosomes.

Considering the life cycle of the cell, it needs to receive the signal to initiate the cell cycle. If it does not receive any signal, it can stay in G0 phase. This signal can be a protein or any substance. At the end of the mitosis, two new cells are found in the G0 phase. It is possible to change this route depending on the signals received by the cell. Basically, during the G1 phase, the cell receives a signal to begin dividing, to develop if it is a stem cell, or to differentiate if it is an advanced cell. If it does not receive the signal, any cell can undergo apoptosis. If any internal process is going bad for the cell or the number of cells is too large, the cell will apoptosis itself. The cell death occurs in two ways: necrosis and apoptosis. Necrosis occurs as a result of damage to the cell in which starved of the oxygen or nutrients. Apoptosis is defined as programmed cell death, controlled death of the cell at a time when it is expected to die.

In this study, modelling and simulation of the cell agents are performed by using the Repast Simphony tool [31, 32]. In this framework, the cell model and the simulated environment are composed of the agents' classes and context builder. The context builder is created with the Repast Simphony tool, which represents the growth and division environment of cells.

The agent based stem cell model consists of three type of agent class; cell agent, growing cell agent and blood vessel agent. The properties of the cell and the actions (methods) that carry out the cell cycle are defined in agent classes. In Figure 2, the agent classes of the model are defined, including the agent properties and actions in the simulation environment.

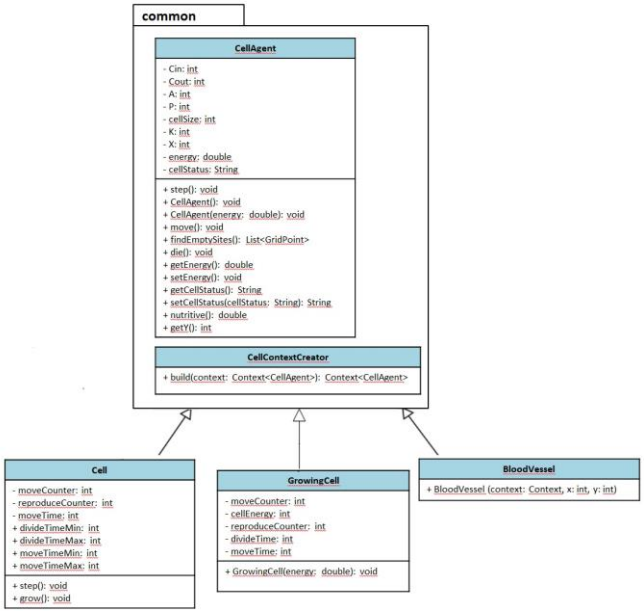

Figure 2: UML class diagram of agent based cell model.

IV. IMPLEMENTATION

A. Simulation Environment

The agents carry out their actions in a simulation environment. In this study, Repast Simphony based on the object-oriented programming using Java language provides an environment that enables the users/researchers with a graphical interface such as displaying the agents in the simulation environment, monitoring their behavior, managing the parameters, and interpreting the results graphically. Figure 3 shows the simulation environment of the initial agents.

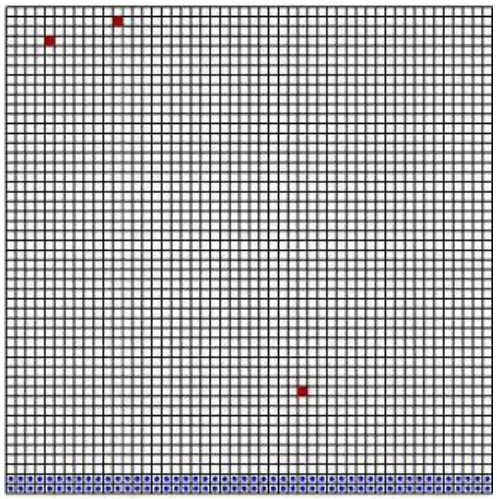

Figure 3: Initial agents in the context.

A context class is defined to involve the agents in the simulation environment. The CellContextCreator class, which implements context builder, creates the main content and provides a runtime environment that enables each step to run. The user-designed creator creates a root context for the modelers and adds the agents and some simulation parameters.

The simulation environment, which represents the cell agents' environment and shows the process of the cell cycle, is represented on the grid cells and continuous space. The cell agents and blood vessel agents defined as food sources of agents are shown in grid and continuous space. In Figure 3, the cell agents are represented in red color, the blood vessel agents are represented in blue color.

Simulation parameters, which can be adjusted in the graphical user interface (GUI) in the runtime, are added to set the initial number of the cell agent.

B. Parameters

Parameter tuning is very important in observing the behavior of the model. The model parameters that the user can set in the graphical user interface during the running of the model are described below.

Table 2: Model parameters.

Parameter	Function
divideTimeMin divideTimeMax	Minimum and maximum division time
height width	Boundary of the simulation environment
cellSize	Cell size
divideMinEnergy	Minimum energy for division
initialNumberOfBloodVessel	Initial number of blood vessel agent
initialNumberOfCell	Initial number of cell agent
reproduceMinEnergy	Minimum energy for reproduce
widthOfCellMembrane	Membrane width of the cell agent

The attributes of the agents and the system states are displayed in GUI. The model parameters are shown in Figure 4. The interaction of the agents and the system behavior can be observed by adjusting the parameter values.

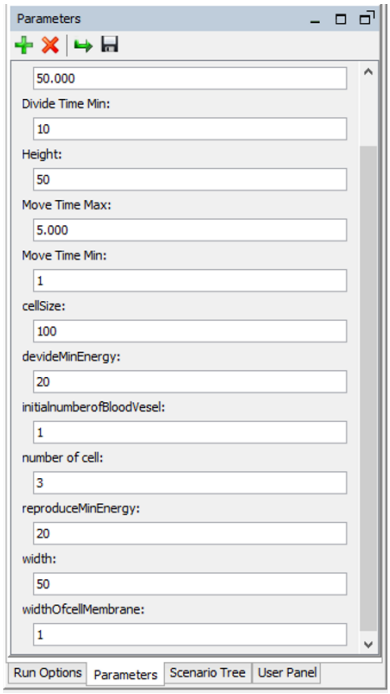

Figure 4: The model parameters

C. Algorithms

In this study, the agents perform their actions depending on the rules which define in the methods. In each phase transition of the cell cycle, the vital function algorithm of the agents runs. As indicated in the UML class diagram in Figure 2, the actions of the agents such as movement, growth, feeding, death, etc. functions are implemented with defined rules.

The model starts running with the initial number of cell. Movement on the grid is provided by the grid object and the coordinates of the agents are determined on the grid. Agents move by randomly choosing one of the eight nearest neighboring grid locations. The cell agents obtain their energy by feeding through blood vessels by diffusion. When the energies of the cell agents reach the threshold level of 0, the cell agents die and are removed from the simulation environment.

It is important for the survival of cell agents and the corresponding nutritional action to take place. It is also necessary to show the cell status during the growth and division phases of the cells.

move() method

```
1.  context, grid ∈ class CellAgent
2.  emptySites ← findEmptySites()
3.   if (emptySites.size())
4.      grid.moveTo(getX(), getY())
5.  end if
6.  findEmptySites()
7.    context ← getContext()
8.    grid ← getProjection()
9.  end method
```

die() method

```
1.  context.remove()
```

setEnergy() method

```
1.  energy ∈ class CellAgent
2.  if (energy > threshold value)
3.     energy ← threshold value
4.  else
5.     energy ← energy + nutritive()
6.  end if
```

nutritive() method

```
1.  X, P, A ∈ class CellAgent
2.  X ← getValue("widthOfcellMembrane")
3.  P ← random(1, 10)
4.  A ← X * X
5.  calculateNutritive(P, A, getValue(bloodVessel(getY()), getY())
```

step() method

```
1.  reproduceCounter, divideTime ∈ class CellAgent
2.   reproduceMinEnergy  ← getValue("reproduceMinEnergy")
3.  reproduceCounter ←  divideTime
4.  if (reproduceCounter ← 0){
5.      if(getEnergy() >= reproduceMinEnergy)
6.          grow()
7.       else
8.            die()
9.       reproduceCounter ← divideTime
10.         }
11.         end if
12.     else {
13.        reproduceCounter ← reproduceCounter - 1
14.        setEnergy()
```

```
15.    }
16.    end if
```

grow() method

```
1.    energy ∈ class CellAgent
2.    GrowingCell extends CellAgent
3.    GrowingCell(getEnergy())
```

Some of the algorithms belonging to the cell agent class are presented with its pseudocodes. The cell agents interact with other agents; for example, the diffusion event occurs with the blood vessel agents. The blood vessel agents act as a necessary nutrient source for the reproduction of the cell agents. The following variables shown in Table 3 are defined for the diffusion through a cell membrane [33, 34].

Table 3: Diffusion variables

n	number of molecules inside cell (mol)
t	time (seconds)
P	permeability constant for a particular molecule (cm/sec)
A	surface area of the cell membrane (cm2)
C	concentration of diffusing molecule (mol/cm3)
X	width of cell membrane (cm)
$\frac{dc}{dx}$	concentration gradient
dx	membrane thickness
dc	$C_{out} - C_{in}$
$\frac{dn}{dt}$	the rate of diffusion

The rate of diffusion is described as a function of the concentration gradient. The equation is shown in below [34].

$$\frac{dn}{dt} = P\ x\ A\ x\ \frac{dc}{dx}$$

The nutritive() method in CellAgent class is responsible for the diffusion process for cell energy. Each run step of the simulation is defined as a tick count, and the step method runs at each tick count. The Cell class is overridden to reuse the CellAgent() method. It has a single constructor that randomizes the division time for new cell generation. The step() method checks if the counter of the newly generated cell agent is equal to zero. If the cell agent is zero or less than zero, it checks whether the cell agent is dead. In Table 4, the number of cell agents in the CellAgent class is defines after each step.

Table 4: The number of the cell agents after each step (tick count)

Model variables	n. tick count	(n+1). tick count
The number of cells	n_t	$2n_{t+1}$
The remaining number of cell divisions	n_t	$n_{t+1} - 1$

In the simulation, the cell agents are fed by diffusion close to the blood vessel agents. As the cell agents move away from the blood vessel agents, starvation begins. After a while, when the cell agents become starved, the cell agents' death can occur. When the cell agents reach a certain growth rate, the cell division occurs. The growing cell agents represented as yellow color are shown in Figure 5.

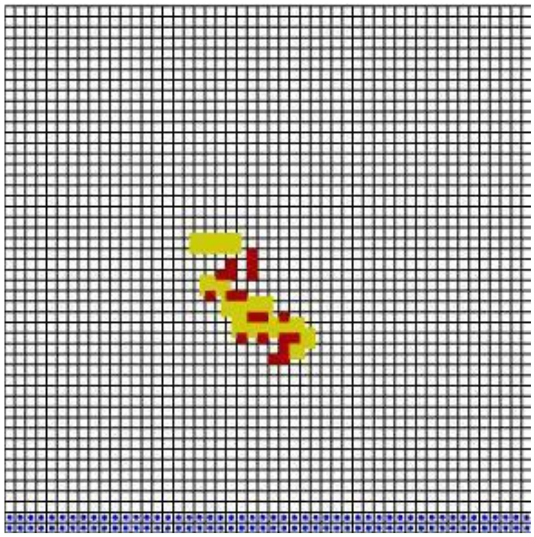

Figure 5: The growing cell agents

The cell agents that complete the cell cycle and the growing cell agents for reproduction are shown in Figure 6.

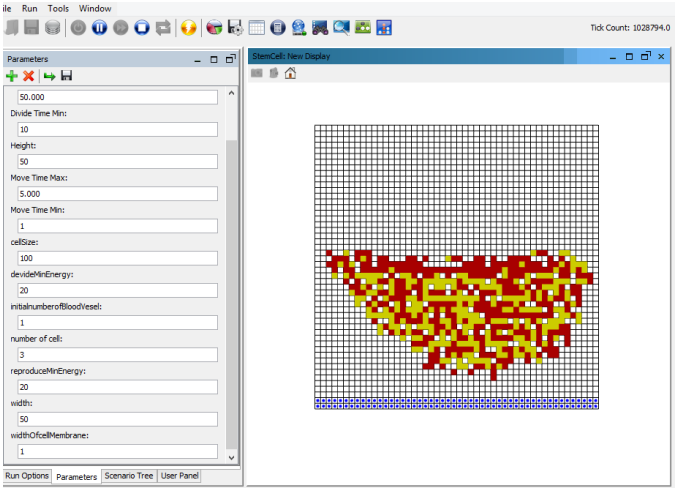

Figure 6: The cell agents

During the simulation, the normal state of the cell, overnutrition, starvation (low energy), and death of the cell agents can be observed by changing the inputs in the phases of the cell cycle. In the model, the effect of the cell cycle on the system behavior can be examined by adjusting the parameter values such as cell number, energy rate, division time, growth rate, etc.

V. Conclusion

In this study, we have proposed an abstract model of the cell cycle with an agent-based modeling approach. The cells

are represented by the agents, and the interaction of the agents with the environment and the other agents is rule-based to assign tasks to the agents. By further detailing the stage and intracellular complex interactions between the cells, the cancer cells, the specialized cells, more nutrients and more interactions can be added to the model. It is possible to model the genetic damage of the cell with genetic algorithms. By combining the intracellular model and intercellular interactions, a multi-scale model can be achieved. A more detailed model can be derived by taking into account the periodic changes in the cell's feeding rate and intermediates. Considering the performance of this model, it has the infrastructure to be used in modeling macro systems such as tissue modeling.

REFERENCES

[1] B. Alberts, A. Johnson, J. Lewis, M. Ra, K. Roberts, and P. Walter, "Molecular Biology of the Cell," Garland, 2002.

[2] H. Kitano, "Systems biology: a brief overview," *Science (New York, N.Y.)*, vol. 295, pp. 1662-1664, 2002.

[3] M.W. Kirschner, "The meaning of systems biology," *Cell*, vol. 121, pp. 503-504, 2005.

[4] A. del Sol, and S. Jung, "The Importance of Computational Modeling in Stem Cell Research," *Trends in Biotechnology*, 39(2). pp. 126-136, 2021.

[5] M. d'Inverno, and J. Prophet, "Modelling, Simulation and Visualization of Stem Cell Behaviour," *Fourth International Workshop on Network Tools and Applications, NETTAB*, pp. 105-111, 2004.

[6] E. Merelli, G. Armano, N. Cannata, F. Corradini, M. d'Inverno, A. Doms, P. Lord, A. Martin, L. Milanesi, S. Möller, M. Schroeder, and M. Luck, "Agents in bioinformatics, computational and systems biology," *Briefings in Bioinformatics*, 8(1), pp. 45-59. January 2007. https://doi.org/10.1093/bib/bbl014

[7] Z. Agur, Y. Daniel, and Y. Ginosar, "The universal properties of stem cells as pinpointed by a simple discrete model," *Mathematical Biology*, vol. 44, pp. 79–86, 2002.

[8] J. Zámborszky, "Compositional modeling of biological systems," *PhD Thesis*, University of Trento, 2010.

[9] H. Kitano, "Computational systems biology," *Nature*, vol. 420, 2002.

[10] L. Priori, and P. Ubezio, "Mathematical modelling and computer simulation of cell synchrony," *Methods Cell Sci.*, vol. 18, pp. 83–91, 1996. https://doi.org/10.1007/BF00122158

[11] G. M. Cooper, "The Eukaryotic Cell Cycle," *The Cell: A Molecular Approach, 2nd edition*, 2000.

[12] Bio-Rad Laboratories, Inc., "Understanding the Eukaryotic Cell Cycle — a Biological and Experimental Overview," Available: https://www.bio-rad-antibodies.com/

[13] D. Noble, "The rise of computational biology," *Nature reviews. Molecular cell biology*, vol. 3, pp. 459-63, 2002.

[14] M. Pisu, A. Concas, G. Cao, and A. Pantaleo, "Mathematical Modelling and Computational Simulation of Mammalian Cell Cycle Progression in Batch Systems," *European Journal of Biology and Biotechnology*, 3(1), pp. 1–10, 2022. https://doi.org/10.24018/ejbio.2022.3.1.315

[15] M. d'Inverno, and R. Saunders, "Agent-based modelling of stem cell self-organisation in a niche," *Engineering Self-Organising Systems*, Springer, Berlin, pp. 52–68, 2004.

[16] M. d'Inverno, P. Howells, S. Montagna, I. Roeder, and R. Saunders, "Agent-Based Modeling of Stem Cells," *Multi-Agent Systems: Simulation and Applications*, 2009 by Taylor and Francis Group, LLC.

[17] M. A. de c. Gatti, G. M. Faustino, D. Bispo, J. E. Vasconcellos, and C. J.P. de Lucena, "Agent-Oriented Stem Cell Computational Modeling," *SBC 2008*, pp. 31-45.

[18] D. Borland, H. Yi, G. D. Grant, K. M. Kedzior, H. X. Chao, R. A. Haggerty, J. Kumar, S. C. Wolff, J. G. Cook, and J. E. Purvis, "The Cell Cycle Browser: An Interactive Tool for Visualizing, Simulating, and Perturbing Cell-Cycle Progression," *Cell Syst.*, 7(2):180-184.e4, 2018. doi: 10.1016/j.cels.2018.06.004.

[19] D. Bernard, O. Mondésert, A. Gomes, Y. Duthen, V. Lobjois, S. Cussat-Blanc, and B. Ducommun, "A Checkpoint-oriented cell cycle simulation model," *Cell Cycle*, Taylor & Francis, 18(8), pp.795-808, 2019.

[20] J. C. Sible, and J. J. Tayson, "Mathematical modeling as a tool for investigating cell cycle control networks," *Methods*, 41(2), pp. 238-247, 2007.

[21] S. Gaglio, M. Giacomini, C. Nicolini, and C. Ruggiero, "A qualitative approach to cell growth modeling and simulation for cancer chemotherapy," *IEEE Transactions on Biomedical Engineering*, 38(4), pp. 386-389, April 1991, doi: 10.1109/10.133236.

[22] Z. Liu, Y. Pu, F. Li, C. A. Shaffer, S. Hoops, J. J. Tyson, and Y. Cao, "Hybrid modeling and simulation of stochastic effects on progression through the eukaryotic cell cycle", *The Journal of Chemical Physics*, 136(3). 10.1063/1.3677190, 2012.

[23] S. T. Vittadello, S. W. McCue, G. Gunasingh, N. K. Haass, and J. M. Simpson, "Mathematical models incorporating a multi-stage cell cycle replicate normally-hidden inherent synchronization in cell proliferation" *J. R. Soc. Interface*, 2019. https://doi.org/10.1098/rsif.2019.0382

[24] J. De Boeck, J. Rombouts, and L. Gelens, "A modular approach for modeling the cell cycle based on functional response curves," *PLOS Computational Biology*, 17(8): e1009008. https://doi.org/10.1371/journal.pcbi.1009008

[25] C. M. Macal, and M. J. North, "Agent-based modeling and simulation," *WSC'09 Winter Simulation Conference,* pp. 86–98, 2009.

[26] S. Emek, "Modeling and Simulation of Global Behaviors of the Self-Adaptive Systems by Using Agent Based System," *PhD Thesis*, Ege University, 2018.

[27] Image credit: "The cell cycle" (Opens in a new window) by OpenStax College, Biology (CC BY 3.0). Available: https://cnx.org/contents/GFy_h8cu@9.87:1tJ55Ot6@7/The-Cell-Cycle

[28] D.J. Lew, "Cell Cycle," *Brenner's Encyclopedia of Genetics (Second Edition)*, 2013.

[29] A. W. Murray, "The genetics of cell cycle checkpoints," *Current Opinion in Genetics and Development*, 5:5-11, 1995.

[30] M. Kastan, and J. Bartek, "Cell-cycle checkpoints and cancer," *Nature* vol. 432, pp. 316–323, 2004. https://doi.org/10.1038/nature03097

[31] C. Nikolai, and G. Madey, "Tools of the trade: a survey of various agent based modeling platforms," *J Artif Societies Social Simul.*,12(2): 2, 2009.

[32] Repast Simphony, available: https://repast.github.io/

[33] J. D. Enderle, and J. D. Bronzino, "Fick's Law of Diffusion," *Introduction to Biomedical Engineering (Third Edition)*, 2012

[34] M. Beals, L. Gross, and S. Harrell, "Diffusion through a cell membrane," 1999. Available: http://www.nimbios.org/~gross/bioed/webmodules/diffusion.htm

Duplication Detection in Videos Based on Dwt

I. BOZKURT[1] and G. ULUTAŞ[2]

[1] Karadeniz Technical University, Trabzon/Turkey, isilaybozkurt@ktu.edu.tr
[2] Karadeniz Technical University, Trabzon/Turkey, gulutas@ktu.edu.tr

Abstract **- Videos are the best evidential data that can be used to narrate events in today's technology. However, to be used as evidence, their accuracy needs to be determined. In this study, we propose a solution to duplication forgery in video forgery detection extracting DWT features. The proposed method consists of three stages: feature extraction from frames and visualization of these features in binary form, finding the correct positions on the image, eliminating the incorrect positions. The method solves the problem of frame duplication forgery using the slope of line by increasing and decreasing the number of consecutive frames at the same rate. The method was tested on three different databases. It was tested against compression and blurring attacks. While the average accuracy rate obtained from uncompressed videos from the SULFA database was 0.9973, the average accuracy rate was 0.9878 for blurred videos, 0.9510 for MPEG4 compressed videos, and 0.9683 for H264 compressed videos. In terms of time, the study gave effective results compared to the compared studies with an average of 0.0271sec per frame.**

Keywords **- Forensic, passive detection techniques, intra forensic, video forgery, duplication detection, blurring attack**

I. INTRODUCTION

Videos are multimedia data that contains flows of events and is formed by ordering the images. Thanks to the improving storage technology, hours of recording can be taken. These recordings are the best living evidence used to describe events. As the popularity of video editing applications has increased, the changes made on videos have become easily used by everyone. The ease of using these applications prevents videos from becoming evidence. In particular, videos captured by security cameras need to be tested for accuracy and integrity.

Studies in forgery detection area aim to validate the reliability of videos with important use fields. It tests integrity against video tampering attacks. In the literature, studies are divided into two groups as active and passive verification techniques [1]. Active techniques require additional application knowledge or hardware before or during the creation of the videos, so they cannot be used for every video recorded [2]. Therefore, when analyzing videos to be used as evidence, verification with passive methods that utilize statistical features is more widely used. Passive verification techniques can be categorized into two different classes: inter frame and intra temporal forgery detection techniques [3]. Forgery detection techniques are also named according to the application of the methods used. When these studies are examined, they are classified as studies based on camera noise, studies based on codec structure, studies based on learning, studies based on motion effect and statistical studies [4-13].

In this paper, we propose a novel high accuracy solution to inter-frame duplication forgery using statistical methods that has been tested against compression and blurring attacks. The method provides a solution to duplication forgery over 3 different databases mentioned in the literature. Comparisons are made on two different databases. With the Sulfa database, videos are tested in two different compression formats using two different quality metrics and subjected to blurring. In this study, existing videos were evaluated in the frequency domain using DWT. Since the difference between sequentially matched frames in duplication increases and decreases at the same rate, the slope of the line, which is a linear equation, is presented as a solution to the problem by making the slope of the line an angle of 135 degrees. The method in [14] was improved and a more effective solution to duplication forgery was presented. On the tested databases we obtain high accuracy using the method and according to the results, it is seen that the use of the DWT feature can improve the detection performance.

II. PROPOSED METHODS

In this section, we describe the stages of the study that offers a solution to duplication forgery that is done by copying a portion of the existing frames from the same video and pasting them into a different part of the video. The original video frames taken from YouTube is shown in Figure 1. The altered video frames after the duplication forgery is shown in Figure 2 and Figure 3. In Figure 1, it is seen that the red highlighted vehicle has parked incorrectly and has hitted the two vehicles in front of it.

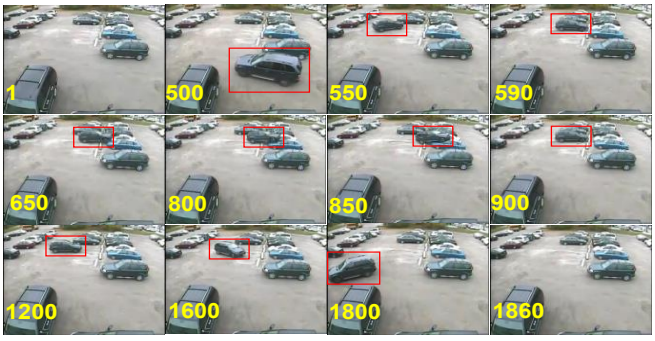

Figure 1: Original frames, it is boxed in red for vehicle tracking.

Then has stopped for a while in shock. After then left the camera view. The scenes with the crashed vehicle in the video can be covered with scenes without the crashed vehicle or with properly parked scenes. In Figure 2, the scene was closed by pasting the scenes where the vehicle was parked properly (155 frames between 940-1095 were pasted twice) on the frames where the collision occurred (310 frames between 592 and 902). The perpetrator may defend herself and deny the incident by saying that the vehicles were run over before she parked the vehicle.

Figure 2: The blue written frames fake frames were pasted over the frames in Figure 1 to cover the moment of the accident with duplication forgery

In Figure 3, the moment of impact is covered with frames where the vehicle is not in the scene at all. After the vehicle leaves the parking lot, that is, after the 1857th frame, it is pasted on the 218th frame and after, when the vehicle enters the scene. In this case, the person can defend herself by claiming that she was never in the parking lot and had nothing to do with the incident. In both scenarios, the suspect may try to prove his innocence with fake videos. Therefore, before a video can be used as evidence in court, it must first be determined that the accuracy and integrity of the videos are protected. Since the repeated frames are copied sequentially, the difference between them and their pasted positions is constant. This constant rate of increase allows the problem to be expressed by the slope of line equation. In this study, we first extract the DWT features of the frames using all channels. When DWT is applied to an image, 4 sub band components (low frequency sub band LL, horizontal features LH, HL vertical horizontal component and diagonal features HH) are obtained. In our study, these four components are zigzag scanned. Then, extracted features are converted to binary images and it is examined whether they are formed line on each image. The line segment is determined using the Hough transform algorithm. In the last stage, frames that are not forged but perceived as forged are eliminated.

Figure 3: Yellow frames are original frames; blue frames are fake frames.

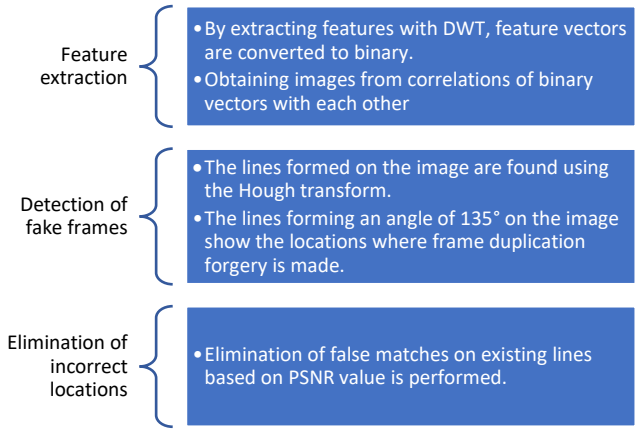

A. FEATURE EXTRACTION

Videos consist of sequences of images. Since the dimensions of the features to be extracted separately from all consecutive images will be large, it is aimed to obtain a smaller sized matrix that can represent each frame in the first stage of the algorithm. Frames extracted from videos are first converted to gray. Frames converted to gray are divided into 12x12 blocks. A single value representing the block is obtained by averaging each block vertically and horizontally. These averages are then converted into a matrix. Two-dimensional wavelet transform was applied to these matrices using the Haar filter. All channels obtained from the wavelet transform are assigned to a vector. At the end of this step, vectors with 144 elements are obtained for each frame.

B. DETECTION OF FAKE FRAMES

In this section, the type of forgery present is decided, and forged frame locations are found. First, the vectors obtained in feature extraction are binarized. Then the correlation of these vectors representing the frames is calculated as in Eq. 1.

$$r = \frac{\sum_{i=1}^{n}(x_i - \bar{x})(y_i - \bar{y})}{\sqrt{\sum_{i=1}^{n}(x_i - \bar{x})^2}\sqrt{\sum_{i=1}^{n}(y_i - \bar{y})^2}} \quad (1)$$

Figure 4 is derived from correlation values. Correlation values of forged locations are 1 for frames that are copies of each other. It looks bright. All frames are correlated with each other. Therefore, the upper triangular part of the matrix is symmetric to the lower triangular part. Therefore, only the upper triangular matrix of the acquired image is taken as a reference. Since a sequential copying process is performed, fake frames are linearly observed. The index values at locations where the correlation values of the features are one indicate the location of the fake frames.

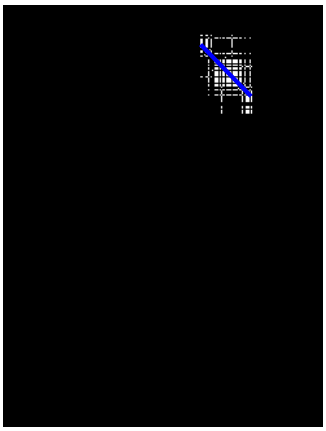

Fig 4.a. Video9 binary correlation image

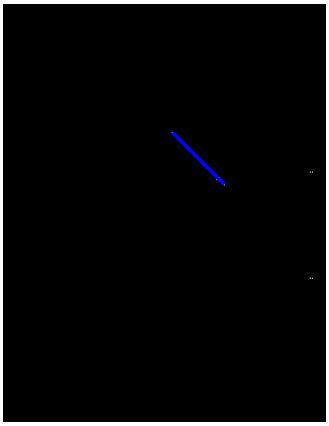

Fig 4.b. Video 16 binary correlation image

C. ELIMINATION OF INCORRECT LOCATIONS

The type of forgery made up to this stage and which positions are identical have been found. In order to increase the success, the places found to be faulty should be eliminated. Especially in fixed-scene videos, since the features of successive frames are very similar to each other, there may be incorrect matches. In this section, in order to eliminate them, the PSNRs of the existing frames are calculated based on the formula below, and the frames that are above the determined threshold are added to the candidate line. If they fall below the threshold, these frames are eliminated from the candidate line. PSNR and MSE equations are shown in Eq. 2 and Eq. 3, respectively.

$$PSNR = 10\log_{10}({}^{255^2}/_{MSE}) \quad (2)$$

$$MSE = \frac{1}{mn}\sum_{i=0}^{m-1}\sum_{j=0}^{n-1}[I(i,j) - R(i,j)]^2 \quad (3)$$

III. EXPERIMENTAL RESULTS AND DISCUSSION

In this section, the results obtained from multiple databases and comparisons with other studies in the literature are presented to demonstrate the effectiveness of the study. The method was run in Matlab2021b version on a computer with Intel Core i5 CPU (1.60 GHz) and 16GB RAM memory. Accuracy rate, precision, sensitivity and F1 score were used as evaluation criteria. During the evaluation, genuine frames were evaluated as negative and forged frames as positive. TP refers to frames that are forged but found to be correct; FP refers to frames that are genuine but found to be false, TN refers to frames that are genuine but found to be correct; FN refers to frames that are forged but not detected by the code. Table 1 shows the result values obtained from different databases.

Table 2 shows the results obtained from blurred videos using the SULFA database. [14] the success rates of the intended study are higher, as can be seen in the comparison with the study in this study. The duration of the study is almost the same.

Table 1: Duplication forgery detection

Database	DA	PR	RR	F1Score	Average Time (sec/frame)
1.Fadl et al. (2020) [16]	0.9947	0.9846	0.9953	0.9897	0.0283
2.Hongre et al. (2021) [19]	0.9995	0.9927	1	0.9962	0.0166
3.SULFA (2012) [15]	0.9974	0.9975	0.9814	0.9894	0.0195

Table 2: Duplication forgery detection with blurring attack

	DA	PR	RR	F1Score	Average Time (sec/frame)
Proposed	0.9877	0.9672	0.9579	0.9602	0.0246
Bozkurt et. al. [14]	0.9837	0.9360	0.9191	0.9269	0.0204

Comparison of success in videos with MPEG4 and H264 codec structure is shown in Table 3. The average frame count of the videos used is 372 and each frame takes approximately 0.023 seconds to process. Considering a video that shoots throughout the day, it can be concluded that the method will produce fast results.

Table 3:Duplication forgery detection with blurring attack

Database		DA	PR	RR	F1Score	Average Time (sec/frm)
MPEG4	QS1	0.9528	0.8524	0.8111	0.8301	0.0203
	QS16	0.9493	0.8443	0.7600	0.7955	0.0234
H264	CRF6	0.9740	0.9815	0.9375	0.9538	0.0236
	CRF24	0.9626	0.8800	0.8045	0.8348	0.0247

The performance of the method decreases as the compression quality increases; however, since the extracted features are obtained from the frequency plane, it does not affect the success too much.

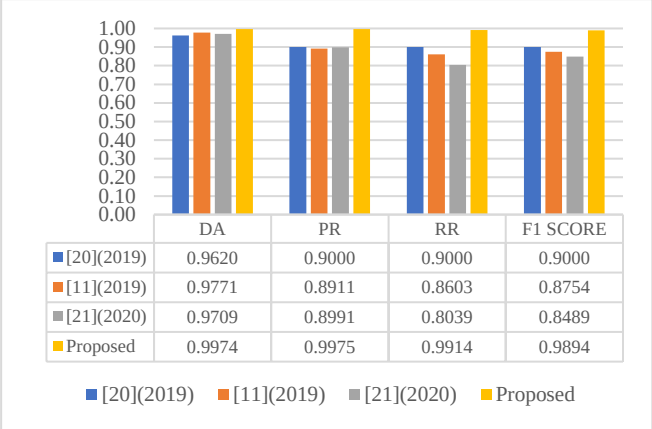

Fig. 5 Comparision of other studies

Figure 5 shows the comparison with other studies in the literature. The codes of the benchmarked studies were written by us. The threshold values specified in the studies were chosen to be the most appropriate according to the database used.

IV. CONCLUSION

In this study, we propose a new approach for the detection of duplication forgery in video. The method aims to find the forgery with the help of a pattern of features extracted from the frequency plane. It is observed that using DWT features helps to improve the performance. The proposed method provides a solution for detection of frame duplication forgery. This method is advantageous in terms of accuracy as well as its processing time. On the other hand, the proposed method can detect forgery not only in uncompressed videos but also in compressed videos. Moreover, it is seen that the method is resistant against the blurring attack. The method performs better in regard to accuracy, precision and f1 score values than compared works. Experimental results from different databases show that the method works more successfully and faster than similar studies against both compression and blurring attacks. However, it is seen that the performance of the method decreases as the compression quality factor increases. In future work, the method will be improved to address other inter-frame forgery types.

REFERENCES

[1] N. A. Shelke, and S.S. Kasana, (2021). A comprehensive survey on passive techniques for digital video forgery detection. *Multimedia Tools and Applications*, *80*(4), 6247-6310.

[2] N. Akhtar, M. Saddique, K. Asghar, I.U. Bajwa, M. Hussain, and Z. Habib, (2022). Digital Video Tampering Detection and Localization: Review, Representations, Challenges and Algorithm. *Mathematics*, *10*(2), 168.

[3] S. Kingra, N. Aggarwal, and N. Kaur, (2022). Emergence of deepfakes and video tampering detection approaches: A survey. *Multimedia Tools and Applications*, 1-45.

[4] S. Vatansever, A. E. Dirik, and N. Memon (2019). Analysis of rolling shutter effect on ENF-based video forensics. *IEEE Transactions on Information Forensics and Security*, *14*(9), 2262-2275.

[5] H. Han, Y. Jeon, B. K. Song, and J. W. Yoon (2022). A Phase-Based Approach for ENF Signal Extraction From Rolling Shutter Videos. *IEEE Signal Processing Letters*, *29*, 1724-1728.

[6] S. Verde, E. Cannas, P. Bestagini, S. Milani, G. Calvagno, and S. Tubaro, (2021). Focal: A forgery localization framework based on video coding self-consistency. *IEEE Open Journal of Signal Processing*, *2*, 217-229.

[7] Q. Li, S. Chen, S. Tan, B. Li, and J. Huang, (2021). One-class double compression detection of advanced videos based on simple Gaussian distribution model. *IEEE Transactions on Circuits and Systems for Video Technology*, *32*(4), 2496-2500.

[8] P. S. Raskar, and S. K. Shah (2021). Real time object-based video forgery detection using YOLO (V2). *Forensic Science International*, *327*, 110979.

[9] L. Koshy, S. Ajay, A. Paul, V. Hariharan, and A. Basheer (2021, October). Video Forgery Detection using CNN. In *2021 Smart Technologies, Communication and Robotics (STCR)* (pp. 1-6). IEEE.

[10] X. Ding, Y. Huang, Y. Li, and J. He (2020). Forgery detection of motion compensation interpolated frames based on discontinuity of optical flow. *Multimedia Tools and Applications*, *79*(39), 28729-28754.

[11] J. Bakas, R. Naskar, and S. Bakshi (2021). Detection and localization of inter-frame forgeries in videos based on macroblock variation and motion vector analysis. *Computers and Electrical Engineering*, *89*, 106929.

[12] N. A. Shelke, and S. S. Kasana (2022). Multiple forgery detection and localization technique for digital video using PCT and NBAP. *Multimedia Tools and Applications*, *81*(16), 22731-22759.

[13] V. Kumar and M. Gaur (2022). Multiple forgery detection in video using inter-frame correlation distance with dual threshold. *Multimedia Tools and Applications*, 1-20.

[14] I. Bozkurt, M. H. Bozkurt, and G. ULUTAŞ (2017). A new video forgery detection approach based on forgery line. *Turkish Journal of Electrical Engineering and Computer Sciences*, *25*(6), 4558-4574.

[15] G. Qadir, S. Yahaya, and A. T. Ho, Surrey university library for forensic analysis (SULFA) of video content, 2012, *IET Conference on Image Processing*.

[16] S. Fadl, Q. Han, and L. Qiong (2020). Exposing video inter-frame forgery via histogram of oriented gradients and motion energy image. *Multidimensional Systems and Signal Processing*, *31*(4), 1365-1384.

[17] W. Wang, and H. Farid, Exposing digital forgeries in video by detecting duplication. 2007, *Proceedings of the 9th workshop on Multimedia & security* (pp. 35-42).

[18] F. Li, and T. Huang, Video copy-move forgery detection and localization based on structural similarity. 2014 3*rd International Conference on Multimedia Technology (ICMT 2013)* (pp. 63-76). Springer, Berlin, Heidelberg.

[19] H. Ren, W. Atwa, H. Zhang, S. Muhammad, and M. Emam, "Frame duplication forgery detection and localization algorithm based on the improved levenshtein distance," *Scientific Programming*, vol. 2021, 2021, doi: 10.1155/2021/5595850.

[20] G. Singh, and K. Singh, (2019). Video frame and region duplication forgery detection based on correlation coefficient and coefficient of variation. *Multimedia Tools and Applications*, *78*(9), 11527-11562.

[21] J. Kharat, and S. Chougule, (2020). A passive blind forgery detection technique to identify frame duplication attack. *Multimedia Tools and Applications*, *79*(11), 8107-8123.

A Performance Way Comparison of Docker Swarm and Kubernetes

Onur Yurtsever[1] and Eyup Emre Ulku[2]

[1] Marmara University Institute of Pure and Applied Sciences, Istanbul/Turkey, yurtseveronr@gmail.com
[2] Marmara University Faculty of Technology, Istanbul/Turkey, emre.ulku@marmara.edu.tr

***Abstract* - People always try to find the best way to deploy their applications. Thus, the first solution was bare metal servers. In the bare metal server solution, each server was responsible for one application but that required as many servers as the number of applications, and in addition that this solution also required so much space in the server room. Subsequently, virtualization technology emerges. This technology is based on the abstraction of computer hardware. Virtualization technology enables us to host multiple operating systems in one host. Virtualization brings along with many advantages. One of the significant benefits is to reduce the quantity of physical equipment needed in the data center and helps to scale our applications.**

One of the remarkable developments in information technologies is container technology which emerged in the middle of 2010. Containers allow to package an application with all the parts it needs, such as libraries and other dependencies, and deliver it as a single package. Docker, developed by Google, is the essential tool to use in container technologies. Docker resembles a virtual machine, but as opposed to a virtual machine, instead of creating a whole virtual operating system, Docker allows applications to use the same Linux kernel as the system they use. This provides a performance boost and reduces the size of the application. Also, the development of microservice-based applications in recent years has made container technologies widely used. Now, we can run each of our applications, perhaps thousands of containers. However, this solution brings with it another problem, how do we manage these containers? In recent years, there have been a few breaks in the server side, which underlies the rapidly developing information technologies. The last of these is container technology. Before virtualization, companies were running all their applications on physical servers, and these systems were getting complex over time, making even simple problems inextricable. Accordingly, in this study we compare Docker Swarm and Kubernetes in terms of their performances under heavy load, two of the most used tools for container management. Thus, we aim to inform readers about container management.

Keywords: virtualization, containers, docker, docker swarm, kubernetes.

I. INTRODUCTION

In recent years, we have been encountering many different technologies in many different areas of our lives. In this direction, the software and applications used are increasing and becoming widespread day by day. Most of the developed software is put forward to serve a large number of users. When we look from the software window, users are in an area that we can describe as the outside world. The purpose of the development of the developed software is to provide services to the users in this outside world. For this reason, web-based software needs special devices called servers. From past to present, the way software is presented to the outside world has also changed. With the spread of web applications came problems such as accessibility and scaling. Concepts such as virtualization and containerization have emerged to solve this type of problem and many more. When it comes to the distribution of the application, there are 3 different ways: bare metal, virtualization and containerization.

A bare-metal server is a physical computer server dedicated to one user only. The user can be a consumer or a tenant. In this structure, each server allocated for lease is a separate piece of physical hardware. This separate build is a functional server in its own right. Therefore, we cannot refer to them as virtual servers running on multiple shared hardware [1].

Virtualization is a technique that involves creating computer-generated (virtualized) resources and mapping those resources to physical resources. This can be accomplished using hardware or software [2]. It abstracts the physical hardware that servers create into a large set of logical resources [3]. In virtualization, the host and virtual machine are completely independent and isolated. If something goes wrong with the virtual machine, the virtual machine can be rolled back [4].

Communities have embraced virtualization very quickly as it has many advantages. The most striking of these advantages is the reduction of costs. Enabling the consolidation of servers, providing centralized infrastructure management and providing the possibility of recovery in case of failure are the main benefits of virtualization apart from cost reduction [5].

Container is an operating system scale virtualization technology that contains operation system, our application, and its dependencies. As opposed to Virtual Machines, a container does not contain full functionalities of operation systems. A container is not platform specific [6].

Compared to virtualization and containerization, creating virtual machines takes minutes, while creating a container takes a very short time, taking about a second. In addition, when we consider in terms of storage, a virtual machine covers a larger area [7]. With this information, containerization can be considered a superior technology than virtualization. We can say that it is superior to virtualization in many ways, not only regarding boot time, but also containers as stated below [8]. We can list these advantages as follows:

- Virtual machines are generally OS-specific where Containers are application-specific
- Virtual machines require guest OS but containers can share the host OS.
- Since containers use less memory, they take a smaller number of servers required.

- File sharing among virtual machines is not possible, files can be shared between containers.

Docker is the container technology that is widely used today. Docker is a technique that helps users build and manage applications in the same environment, whether it's development or production. An application running in Docker is completely isolated from the host [9].

The Docker image represents a snapshot of our application and contains all parameters and system dependencies. A container is a running application built based on an image. The Docker registry is where docker images are stored. Using the repository, we can group our images and tags are useful when we use multiple versions of images [10]. To manage the application, the docker engine is not enough as it can only manage the application on a host. Therefore, an orchestration tool is required. Docker Swarm, Kubernetes, and Apache Mesos are exemplary container orchestration tools [11].

In studies comparing these container tools, it is stated that Docker Swarm is easier and more flexible to install and manage. However, it has been observed that Kubernetes is more preferred than Docker Swarm for orchestrating large clusters. In addition, it can be said that Kubernetes has received great support from the communities [12].

Apart from these container orchestration tools, a cluster manager called Apache Mesos was created by the University of Berkeley with the goal of facilitating resource sharing amongst distributed applications on a huge scale. Mesos is widely used by top companies in the industry, including Apple, Airbnb, Cisco, Twitter, Verizon Labs, and others [13, 14].

Also, public cloud providers like Amazon Web Services have container orchestration tools. AWS offers Elastic Container Service and Elastic Kubernetes Service. Amazon Elastic Container Service (ECS) is purpose-built to help you run your architecture effectively, automatically, and scalably. There are no additional charges for Amazon ECS except for underlying resources. A Kubernetes service called Amazon EKS enables Kubernetes workloads to collect data both locally and in the AWS Cloud. In order to manage containers in the cloud, their applicability in the cloud, and other essential duties with automatic scheduling, Amazon EKS oversees the simplicity and scalability of the Kubernetes control plane blocks [15, 16].

In this article, we compared Docker Swarm and Kubernetes in terms of performance, and observed their behavior under heavy workloads.

II. RELATED WORKS

Lubos Mercl et al., in their study, compared five different container orchestration tools (Docker Compose, Docker Swarm, Fleet, Apache Mesos, Kubernetes) in terms of their functions (Scalability, Failover, High Availability, Network plugins) [17]. For testing, Nginx, Memcached, MYSQL and OwnCloud are deployed using these tools. Different tools are suggested depending on the environment and your intended use. Kubernetes and Apache are recommended for production environment.

Isam Mashhour Al Jawarneh et al. compared four container orchestration tools (Docker Swarm, Kubernetes, Apache Mesos, and Cattle) in terms of provisioning time and failover time [18]. According to the study, Kubernetes stands out as the best solution for failover time. Kubernetes has the most provisioning time. In the study, it was stated that this situation was caused by its complex architecture.

In the study presented by Arsh Modak et al. [19], Cloud technologies are first introduced and Kubernetes and Docker Swarm technologies are compared. According to the study, Kubernetes is superior to Docker technology in many ways. However, it has been stated that the highly complex nature of Kubernetes technology poses a significant disadvantage.

Nikhil Marathe et.al. compared Docker Swarm and Kubernetes in terms of performance, flexibility, fault tolerance, libraries, and self-healing [20]. In terms of all these features, it is stated in the study that Kubernetes offers a more advanced structure than Docker Swarm.

Anshita Malviya et.al. have compared prominent container orchestration tools Kubernetes, Docker Swarm, and Redhat Openshift in numerous ways such as security, deployment, stability, scalability, cluster installation, and learning curve [12]. In the terms of simplicity, Docker Swarm is leading whereas Kubernetes has the best features and is mostly used in the industry. Also, Apache Mesos is decent at stability and Openshift is highly secure.

Marek Moravcik et.al. have compared Docker Swarm, Openshift, and Kubernetes, and listed their both advantages and disadvantages [21]. According to this article, Kubernetes is the most widely used, Openshift and Docker Swarm are following Kubernetes.

Yao Pan et.al have compared Docker Swarm and Kubernetes using five benchmarking tools [22]. In this study, they executed two types of benchmarking. One of them is to understanding processing times, the other of them is understanding the impact on the throughput achieved for memory access and disk I/O by the containerized applications. Both tools can manage container in a efficiently with different side.

In line with the studies reviewed, Docker Swarm and Kubernetes container orchestration tools were found to be the most frequently used tools. In this direction, these tools are discussed comparatively in the study.

III. CONTAINER ORCHESTRATION WITH DOCKER SWARM

As an open source tool, Docker offers Docker Swarm as a tool for creating and editing clusters. A cluster consists of clusters that can be manager nodes, worker nodes. A node can be both a manager and a worker node at the same time. [23].

Docker Service refers to a process running on the administrator or worker nodes of the cluster. Tasks refer to a containerized process that Swarm will schedule and run [24]. There are two types of services, global or replica. For replicated mode, the administrator distributes the task among existing worker nodes with a set of replicas; For global mode, the manager distributes the task to every node in the cluster [25].

One of the major advantages of Docker Swarm is that any configuration changes do not require a reboot [26]. Other advantages can be listed as being free, platform independent, built on the same Docker daemon, and sharing the same syntax [27].

Docker, determined from the configuration, always tries to maintain the desired state when any node becomes inaccessible [28].

Docker provides an overlay network for nodes to communicate. An overlay mesh sits on top of the physical layer and connects the other component [24]. In this type of network, only the registered node can communicate with each other [25].

IV. CONTAINER ORCHESTRATION WITH KUBERNETES

Kubernetes is an open source tool for container orchestration. Kubernetes is a container orchestration tool with important features like automatic deployment, scaling, load balancing, and more. We can say that Kubernetes is the most widely used orchestration tool today [29].

Kubernetes ensures service availability is at least 99.999%. This means almost zero downtime. In addition to these situations, Kubernetes offers the ability to self-heal in case of node failure [30].

Kubernetes consists of a Control Plane, also called master node, and worker nodes. The control plane has many different components. Kube-apiserver plays a role in communicating with the kubernates cluster while listening for requests made. Etcd is a database for Kubernates where the states and various configurations of clusters are stored. Another component, the Kube-scheduler, is the mechanism that decides which nodes the newly created pods will be assigned to. The component named Kube-controller manager is responsible for controlling the life cycles of the nodes. Each node has an agent, called a kubelet. This agent checks whether any Pods are scheduled to the node by listening to the API server. The component named kube-proxy is responsible for setting the network rules on the node [31].

Pod is the smallest component in the cluster, which harbors containers. Services have IP addresses and belong to pods [32]. In this article, we use NodePort service to expose our services to the internet. With the NodePort structure, Kubernetes can allocate a port on all nodes so that the same port number can be used on all nodes. It can also be made to route incoming connections to pods that are part of the service. [33].

V. RESULTS

In this paper, we compared Docker Swarm and Kubernetes in terms of their response in the heavy workload.

For this purpose, we created one manager node and three worker node in the cloud environment. All nodes is created t2.large type AWS EC2 instance. Table 1 shows these instance technical informations.

Table 1:Technical information of T2.large.

Machine type	T2.Large
CPU	Intel Xeon processors, vCPU=2
RAM	8 GB
Memory	8 GB SSD

Both tools have 9 replica of Nginx containers. For testing, JMeter was used, and different amount thread is conducted on master node of each tools. The minimum, maximum and average response times given by Docker Swarm for different user threads are presented in Table 2.

Table 2. Performance metrics for Docker Swarm.

User	Average Response Time (ms)	Minumum Response Time (ms)	Maximum Response Time (ms)
100	182	103	264
200	110	101	164
400	1207	393	2375
800	1162	117	3673

The minimum, maximum and average response times given by Kubernates for different user threads are also presented in Table 3.

Table 3: Performance metrics for Kubernetes.

User	Average Response Time (ms)	Minumum Response Time (ms)	Maximum Response Time (ms)
100	112	104	168
200	137	105	271
400	571	283	748
800	301	106	1241

When we examine the tables, we can say that Kubernates has better performance than Docker Swarm in heavy workload situations. It can be stated that Kubernates provides a significant advantage in terms of average response time in heavy workloads.

VI. CONCLUSION

In this study, we examine Docker Swarm and Kubernetes, compared their performance under heavy workload, created cluster with both tool in the same qualifications. Heavy workload is created by using JMeter tool.

As forementioned, Kubernetes surpassed Docker Swarm's performance. However Kubernetes is such a complicated environment in terms of learning and impelmenting. Docker Swarm is easier to learn and implement.

We recommend Docker Swarm to be used development and testing environment, Kubernetes is used in production environment.

VII. REFERENCES

[1] https://en.wikipedia.org/, "Bare-metal server", Access Time: 12 May 2022

[2] Vedran Dakic, Humble Devassy Chirammal, Prasad Mukhedkar, Anil Vettathu,Mastering KVM Virtualization - Second Edition,October 2020,s:4

[3] Charalampos Gavriil Kominos, Nicolas Seyvet, Konstantinos Vandikas, "Bare-metal, virtual machines and containers in OpenStack", 2017 20th Conference on Innovations in Clouds, Internet and Networks (ICIN)

[4] Cao Jiqing, "I/O Performance Optimization Analysis of Container on Cloud Platform",2020 IEEE International Conference on Power, Intelligent Computing and Systems (ICPICS)

[5] Artur Rot, Pawel Chrobak, "Benefits, Limitations and Costs of IT Infrastructure Virtualization in the Academic Environment. Case Study using VDI Technology", 13th International Conference on Software Technologies, ICSOFT 2018

[6] Jae-Geun Cha,Sun Wook Kim, "Design and Evaluation of Container-based Networking for Low-latency Edge Services",2021 International Conference on Information and Communication Technology Convergence (ICTC))

[7] Rajdeep Dua, A Reddy Raja, Dharmesh Kakadia, "Virtualization vs Containerization to support PaaS" 2014 IEEE International Conference on Cloud Engineering

[8] Anuj Kumar Yadav,M. L. Garg and Ritika, "Docker Containers Versus Virtual Machine-Based Virtualization", Emerging Technologies in Data Mining and Information Security (ss:141-150)

[9] Mochamad Rexa Mei Bella,Mahendra Data,Widhi Yahya,"Web Server Load Balancing Based On Memory Utilization Using Docker Swarm",2018 International Conference on Sustainable Information Engineering and Technology (SIET)

[10] Vivek Sharma, Harsh Kumar Saxena, Akhilesh Kumar Singh, "Docker for Multi-containers Web Application",Proceedings of the Second International Conference on Innovative Mechanisms for Industry Applications (ICIMIA 2020)

[11] Rajendar Kandan,Mohammad Fairus Khalid,Bukhary Ikhwan Ismail,Ong Hong Hoe,"Advanced resource allocation and Service level monitoring for container orchestration platform",2019 IEEE International Conference on Sensors and Nanotechnology

[12] Anshita Malviya, Rajendra Kumar Dwivedi "A Comparative Analysis of Container Orchestration Tools in Cloud Computing", 2022 9th International Conference on Computing for Sustainable Global Development (INDIACom)

[13] Gourav Rattihalli,Exploring Potential for Resource Request Right-Sizing via Estimation and Container Migration in Apache Mesos,2018 IEEE/ACM International Conference on Utility and Cloud Computing Companion (UCC Companion)

[14] Hamed Hamzeh,Sofia Meacham,Kashaf Khan,A New Approach to Calculate Resource Limits with Fairness in Kubernetes,2019 First International Conference on Digital Data Processing (DDP)

[15] https://aws.amazon.com/tr/ecs/pricing/ Access Time 04.11.2022 18.57

[16] https://aws.amazon.com/tr/eks/ Access Time 04.11.2022 19.41

[17] Lubos Mercl, Jakub Pavlik, "The Comparison of Container Orchestrators", International Congress on Information and Communication Technology (ICICT2018)

[18] Isam Mashhour Al Jawarneh,Paolo Bellavista,Filippo BosiLuca Foschini,Giuseppe Martuscelli,Rebecca Montanari,Amedeo Palopoli,"Container Orchestration Engines: A Thorough Functional and Performance Comparison",ICC 2019 - 2019 IEEE International Conference on Communications (ICC)

[19] Arsh Modak,S. D. Chaudhary,P. S. Paygude,S. R. Ldate,"Techniques to Secure Data on Cloud: Docker Swarm or Kubernetes?",2018 Second International Conference on Inventive Communication and Computational Technologies (ICICCT)

[20] Nikhil Marathe,Ankita Gandhi,Jaimeel M Shah,"Docker Swarm and Kubernetes in Cloud Computing Environment",2019 3rd International Conference on Trends in Electronics and Informatics (ICOEI)

[21] Marek Moravcik, Martin Kontsek, "Overview of Docker container orchestration tools", 2020 18th International Conference on Emerging eLearning Technologies and Applications (ICETA)

[22] Yao Pan, Ian Chen, Francisco Brasileiro, Glenn Jayaputera, Richard O Sinnnott, A Performance Based Comparison of Cloud-based Container Orchestration Tools,2019 IEEE International Conference on Big Knowledge (ICBK)

[23] Gaurav Bhatia,Arjun Choudhary,Krati Dadheech, "Behavioral Analysis of Docker Swarm Under DoS/ DDoS Attack", 2018 Second International Conference on Inventive Communication and Computational Technologies (ICICCT)

[24] Jeff Nickoloff, Stephen Kuenzli, Docker in Action, Manning Publication, October 2019,ss:662,663

[25] Russ McKendrick,Mastering Docker,Packt Publishing,October 2020,ss:ss:735-736

[26] Karar Haider Anun;Mahdi S. Almhanna, Web Server Load Balancing Based on Number of Client Connections on Docker Swarm, 2021 2nd Information Technology To Enhance e-learning and Other Application (IT-ELA)

[27] Nikyle Nguyen, Doina Bein, Distributed MPI Cluster with Docker Swarm Mode, 2017 IEEE 7th Annual Computing and Communication Workshop and Conference (CCWC)

[28] Ulug'bek Amirsaidov,Nargiza Usmanova, Bunyod Samandarov, Overlay Networking Issues: Implementation The Functional Components,2020 International Conference on Information Science and Communications Technologies (ICISCT)

[29] Jinyong Yin;Boming Liu, Hongwei Liu, A user-space virtual device driver framework for Kubernetes, 2022 IEEE 2nd International Conference on Power, Electronics and Computer Applications (ICPECA)

[30] Leila Abdollahi Vayghan, Mohamed Aymen Saied, Maria Toeroe;Ferhat Khendek, Microservice Based Architecture: Towards High-Availability for Stateful Applications with Kubernetes,2019 IEEE 19th International Conference on Software Quality, Reliability and Security (QRS)

[31] Sergii Telenyk, Oleksii Sopov, Eduard Zharikov, Grzegorz Nowakowski, A Comparison of Kubernetes and Kubernetes-Compatible Platforms, 2021 11th IEEE International Conference on Intelligent Data Acquisition and Advanced Computing Systems: Technology and Applications (IDAACS)

[32] M. Mohamed Khalel, M. Arul Pugazhendhi, G. Rohith Raj, Enhanced Load Balancing in Kubernetes Cluster By Minikube, 2022 International Conference on Smart Technologies and Systems for Next Generation Computing (ICSTSN)

[33] Marko Lukša, Kubernetes in Action, Manning Publication, December 2017, s:135

Duplication Forgery Detection Based On Multi-Scale Weber Local Descriptor and Local Binary Pattern

I.BOZKURT[1] and G. ULUTAŞ[2]

[1] Karadeniz Technical University, Trabzon/Turkey, isilaybozkurt@ktu.edu.tr
[2]Karadeniz Technical University, Trabzon/Turkey, gulutas@ktu.edu.tr

Abstract **- The use of videos is increasing day by day. This increases the usability of videos as evidence. In order to use videos as evidence and to increase their reliability, their accuracy and integrity must be determined. Changes to videos can be easily made by anyone who can use a mobile application. Especially inter-frame forgeries are used to cover up or hide an event without the need for time and expertise. In this paper, we propose a new texture-based solution to the frame duplication forgery that cover frauds in videos. In the proposed work, we first extract the features of video frames converted from RGB color space to gray level color space using Weber's algorithm. The structural similarity ratios of the extracted frame features with the reference frame are analyzed to determine whether the matching frames are duplicated. When the results obtained are viewed, it is shown that the study proposed high accuracy performance to detect frame duplications in videos.**

Keywords **- Video forensic, passive forgery detection, inter forgery, frame duplication, fraud analysis**

I. INTRODUCTION

Detection of multimedia forgeries offers solutions to the problems of alteration and tampering on video, image, and audio. Detecting the concealment of the changes made after the data has been changed and producing solutions that are resistant to attacks are within the field of study of forensic informatics and cyber security. When the studies in this field are examined, it is seen that the number of studies on image medias is higher than the number of studies on video and audio. The increase in storage areas in our daily lives, the use of videos for security purposes and the use of videos as social media content have increased the usage areas of videos. In order to prove an incident, especially in places require surveillance for security purposes, it is necessary to verify the accuracy of these videos that guide societies or serve as evidence in order to avoid damaging the reputations of countries and important people. This will increase too as videos become more and more prevalent in our lives. Therefore, the accuracy of this data needs to be determined for the reliability of the data. In Figure 1, three different forgery operations were performed for the theft of the chicken in the video taken from Youtube. In the first scenario, it is thought that the two women in the scene feed the chickens and leave. In the first scenario, it can be easily thought that the two women in the scene feed the chickens and leave. However, in reality they put the chicken in the saddlebag and this part is covered by the part where they feed the chickens. 105 frames between 1050 and 1155 are pasted over 105 frames between 1250-1355. In the second scenario, the parts where women are not present in the scene can be copied to give the impression that there are no women in the scene. In the last scenario, the owner of the chicken in court can claim that more than one chicken was stolen and duplicate the scene where the theft took place.

Figure 1: a original images, b and c duplication forgery images

Video forgery detection is analyzed in two ways: active and passive verification techniques [1]. Digital signature and watermarking are active techniques [2]. Unlike active techniques, passive techniques use the statistical properties of videos. In this way, they are more preferred for cost reduction [3]. Passive forgery detection techniques have been gaining popularity in recent years, especially in the field of face fake detection with learning-based approaches [4-10]. However, the databases that have been forged with deep learning techniques are made of fixed and small number of frames. Whereas videos contain hours of recordings in daily life.

Algorithms and hardware requirements that cannot work fast and effectively enough to make changes on such videos lead fraudsters to using forensic techniques between frames. Databases in this field should be created from videos shot in daily life, such as security cameras, and algorithms should be developed accordingly. In this study, the success rates of texture-based Multi scale Weber Local Descriptor (mWLD) and Local Binary Pattern (LBP) algorithms [18] were tested on a database of theft and accident videos from YouTube. Tests were also performed on the videos in the texture-based method used by Shelke et al. [11]. In their study, they provided solutions to four types of forgery over the same video. Considering the suitability of the videos they used for daily life, tests were performed from the database they used in this study and a comparison was made. In addition to the study in [11], the method was also tested on four other databases. These databases were chosen because they have different video lengths, video scales and forgery locations. Hongre et al. presented their study using YUV videos based on the improved Levenshtein distance Algorithm [12]. Wei et al. proposed a three-stage forgery location detection approach based on the normalized mutual information detection algorithm [13]. Both studies in [12] and [13] used a 352 × 288 video trace library data set. Fadl et al. presented a solution for multiple forgeries besides duplication forgery [14]. They tested duplication forgery on 10 videos they created as a database. In the following sections, the details of the algorithms used will be mentioned and the results and evaluation will be mentioned.

II. PROPOSED METHODS

In this section, the algorithms used in the proposed method and the details of the method will be explained. The algorithm aims to provide a solution to duplication forgery in three steps using two different texture-based algorithms. In the first stage, each frame obtained from the video frames was converted from RGB space to gray color space. A feature vector is then created for each frame. Texture-based LBP and WEBER algorithms are used for feature extraction. Texture-based methods are divided into two classes: sparse and dense descriptors. Both algorithms that we used belong to the class defined as dense local descriptors [15]. Feature extraction techniques in this class extract features from the image pixel by pixel. For each examined frame, its relationship with neighboring pixels is considered. In the algorithms used, a 3x3 square neighborhood around the center pixel is used for both texture-based methods. In the last stage, the feature vector of the first frame is used as a reference and the SSIM comparison with the rest of the frames is checked.

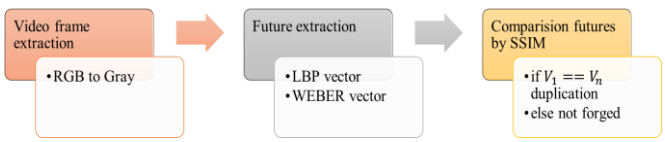

Figure 2: Algorithm steps

Figure 2 shows the steps of the algorithm. Since the method checks the one-to-one equality, the success rate will decrease for videos that have undergone any post-processing attack. For such cases, an experimental threshold can be set according to the databases used in the algorithm to overcome the problem. Feature vectors with a matching value equal to 1 are duplicates of each other, i.e. they represent repeatedly matched frames. The SSIM algorithm is calculated as in equation 1 [16]. μ_x and μ_y are the means of the compared traits, σ_x^2 and σ_y^2 are the variations of the traits. $\alpha = \beta = \gamma = 1$ has been selected. The SSIM value is used to detect the quality value of video frames. Here, it is used to measure the similarity value of frame features.

$$
\begin{aligned}
SSIM(x,y) &= \left[I(x,y)^{\alpha}.c(x,y)^{\beta}.s(x,y)^{\gamma}\right] \\
I(x,y) &= \frac{2\mu_x\mu_y + c_1}{\mu_x^2 + \mu_y^2 + c_1} \\
c(x,y) &= \frac{2\sigma_x\sigma_y + c_2}{\sigma_x^2 + \sigma_y^2 + c_2} \\
s(x,y) &= \frac{\sigma_{xy} + c_3}{\sigma_x\sigma_y + c_3} \\
c_3 &= \frac{c_2}{2}
\end{aligned}
\tag{1}
$$

In Sections 2.1 and 2.2, the details of the LBP and mWLD algorithms are explained.

A. *LBP algorithm*

The Local Binary Pattern (LBP) algorithm is a brightness robust algorithm that is frequently used in image processing applications [17]. LBP is a local variation coding method with four steps: linear filtering, quantization using the unit step function, encoding the binary codeword, and binary to decimal conversion. LBP has also been developed to employ varied neighborhood sizes and consistent LBP codewords, which contain no more than two transitions from 1 to 0 or 0 to 1. If a codeword includes more than two transitions, it is considered non-uniform. This concept was motivated by the fact that uniform codewords appear more frequently in photographs than non-uniform codewords [18].

The link between the core pixel and its neighbors is encoded by LBP. High-order local information is extracted by some local descriptors. More comprehensive discriminative information can be captured via a high-order descriptor. Other local descriptors represent various spatial interactions in a local region as well [18].

B. *WLD algorithm*

The WLD algorithm, which is computed using two components, Differential Excitation (DE) and Gradient Orientation (GO), has robust local texture features that are robust to changes such as edge detection, noise and illumination [19]. The WLD is derived from Weber's Law [20], which claims that a change may be identified only if the ratio of the change from a stimulus to the original stimulus is large enough. To acquire its two components, Weber's Law introduces two ratios to explain the textural properties of images: differential excitation and orientation [18]. The WLD

initially computes the salient micro-patterns by differential excitation and then accumulates statistics on these salient patterns as well as the gradient direction of the current pixel. As a result, the proposed WLD descriptor takes use of SIFT's benefits in computing the histogram utilizing the gradient and its direction, as well as LBP's advantages in processing efficiency and smaller support areas.

III. Experimental Results and Discussion

The experimental results of the proposed method and its comparison with other studies will be discussed in this section. The method was compared with other methods by calculating the detection accuracy (DA), precision rate (PR), recall rate (RR) and F1 score. In the evaluations, original videos were considered negative and fake videos were positive. Accordingly, the forged frames that our algorithm found to be correct were calculated as TP; when forged frame is detected as a forgery is increased true negative (TN) and the extra frames that our algorithm found to be not forged were calculated as FP. DA, PR, RR are defined as follows:

$$DA = \frac{TP + TN}{TP + TN + FP + FN} \quad (2)$$

$$PR = \frac{TP}{TP + FP} \quad (3)$$

$$RR = \frac{TP}{TP + FN} \quad (4)$$

$$F1_{score} = \frac{2 \times PR \times RR}{PR + RR} \quad (5)$$

The program was executed in Matlab 2021b environment on windows operating system. The computer on which the program is executed has a 10th generation intel i5 processor. The frequency of the processor is 1.60GHz.

Table 1 shows the result values obtained using the LBP algorithm from different databases and the average seconds per frame. Videos with an average of 2140 frames were used in the YouTube database. This shows the efficiency of the algorithm in terms of the average running time of real-life videos. For each video, it shows with 99% accuracy whether the duplication forgery is performed in an average of 0,155. Figure 3 shows frame samples of videos taken from YouTube.

Figure 3: YouTube video examples

Table 1: Duplication forgery detection using LBP

Database	DA	PR	RR	F1Score	Average Time
[11] Shelke et al.	0.9986	1	0.9631	0.9808	0.1705
[12] Ren et al.	1	1	1	1	0.0208
[13] Wei et al.	0.9924	0.8636	0.9073	0.8779	0.0614
[14] Fadl et al.	0.9674	0.8684	0.9941	0.9172	0.0564
YouTube	0.9993	0.9964	1	0.9982	0.1534

Table 2 shows the result values obtained using the mWLD algorithm from different databases and the average seconds per frame.

Table 2: Duplication forgery detection using mWLD

Database	DA	PR	RR	F1Score	Average Time
[11] Shelke et al.	0.9986	1	0.9643	0.9815	0.1553
[12] Ren et al.	1	1	1	1	0.0214
[13] Wei et al.	0.9967	1	0.98	0.9899	0.0241
[14] Fadl et al.	0.9674	0.8684	0.9942	0.9172	0.0635
YouTube	0.9993	0.9964	1	0.9982	0.1361

Figure 4 shows the comparison of the two algorithms. For both texture-based algorithms, the mWLD algorithm performed better than the LBP algorithm.

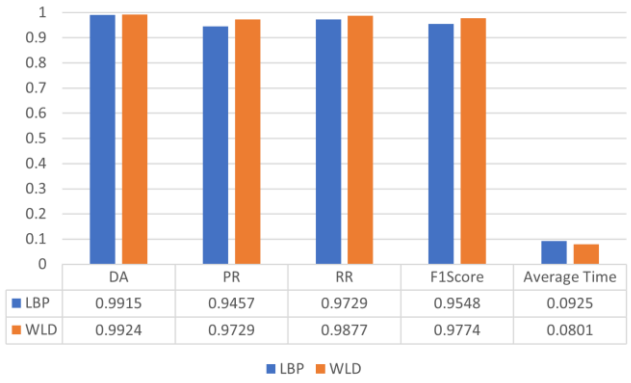

Figure 4: Comparision of LBP and mWLD

The comparison of the average success values of the methods used for the two algorithms and the other algorithms is as shown in Figure 5. The results obtained show the average results obtained by using the database run by Shelke et al. and the average results of our proposed method for the two algorithms. The method surpassed the work proposed by Shelke et al. in terms of accuracy and precision.

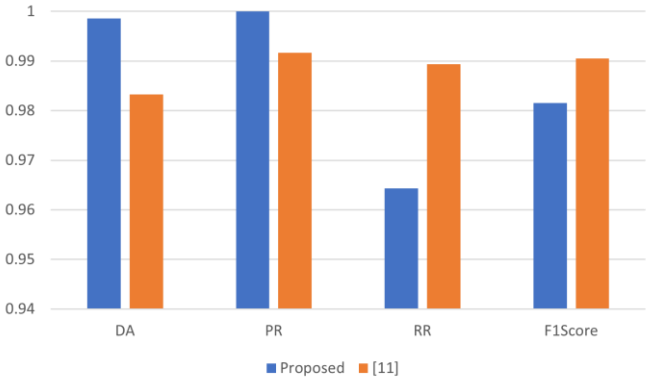

Figure 5: Comparison of the proposed method with the study in [11]

IV. CONCLUSİON

Video forgery detection is an increasingly popular and important field. Detection of the most preferred inter-frame forgery techniques used by fraudsters on videos will increase the reliability of the videos and make them evidence. In this study on the detection of duplication forgery, which is one of the inter-frame forgeries, a method that can work effectively and detects duplication forgery by researching the equality of pairs without using any threshold value is proposed. The method works by comparing the features extracted from videos using two different texture-based approaches with the SSIM value. In this study, we compare the texture-based LBP and mWLD algorithms using the databases of studies that are commonly used in the literature. The method has been tested with four different databases and YouTube videos that have been used in recent years, with successful results. When the databases used are compared, the videos used by Shelke et al. are the closest to the videos retrieved from YouTube. However, the development of a new database in future studies to test the success of the methods in this field will contribute to the literature.

REFERENCES

[1] A. R Javed, Z. Jalil, W. Zehra, T. R. Gadekallu, D. Y. Suh, and M. J. Piran, (2021). A comprehensive survey on digital video forensics: Taxonomy, challenges, and future directions. *Engineering Applications of Artificial Intelligence*, 106, 104456.

[2] S Tyagi, and D. Yadav, (2022). A detailed analysis of image and video forgery detection techniques. *The Visual Computer*, 1-21.

[3] S. T. Nabi, M. Kumar, P. Singh, N. Aggarwal, and K. Kumar, (2022). A comprehensive survey of image and video forgery techniques: variants, challenges, and future directions. *Multimedia Systems*, 1-54.

[4] Z. Lai, Y. Wang, R. Feng, X. Hu, and H. Xu, (2022). Multi-Feature Fusion Based Deepfake Face Forgery Video Detection. *Systems*, 10(2), 31.

[5] W. Pu, J. Hu, X. Wang, Y. Li, S. Hu, B. Zhu, ... and S. Lyu, (2022). Learning a deep dual-level network for robust DeepFake detection. *Pattern Recognition*, 130, 108832.

[6] F. Chamot, Z. Geradts, and E. Haasdijk, (2022). Deepfake forensics: Cross-manipulation robustness of feedforward-and recurrent convolutional forgery detection methods. *Forensic Science International: Digital Investigation*, 40, 301374.

[7] K. Y. Prashanth, R. Ujjini Matad, and S. M. Sarala, (2022). Securing Camera Based Active Driver Monitoring System from Video Forgery Attacks Using Deep Learning. *SAE Technical Paper*, 01-0115.

[8] X. Jin, Z. He, J. Xu, Y. Wang, and Y. Su, (2022). Video splicing detection and localization based on multi-level deep feature fusion and reinforcement learning. *Multimedia Tools and Applications*, 1-19.

[9] N. Singla, S. Nagpal, and J. Singh, (2022). Frame Duplication Detection Using CNN-Based Features with PCA and Agglomerative Clustering. In *Communication and Intelligent Systems* (pp. 383-391). Springer, Singapore.

[10] M. R. Oraibi and A. M. Radhi, (2022). Enhancement Digital Forensic Approach for Inter-Frame Video Forgery Detection Using a Deep Learning Technique. *Iraqi Journal of Science*, 2686-2701.

[11] N. A. Shelke and S. S. Kasana, (2022). Multiple forgeries identification in digital video based on correlation consistency between entropy coded frames. *Multimedia Systems*, 28(1), 267-280.

[12] H. Ren, W. Atwa, H. Zhang, S. Muhammad, and M. Emam, (2021). Frame duplication forgery detection and localization algorithm based on the improved levenshtein distance. *Scientific Programming*.

[13] W. Wei, X. Fan, H. Song, and H. Wang, (2019). Video tamper detection based on multi-scale mutual information. *Multimedia Tools and Applications*, 78(19), 27109-27126.

[14] S. Fadl, Q. Han, and L. Qiong, (2020). Exposing video inter-frame forgery via histogram of oriented gradients and motion energy image. *Multidimensional Systems and Signal Processing*, 31(4), 1365-1384.

[15] H. Dawood, H. Dawood, and P. Guo "Texture image classification with improved weber local descriptor". 2014, *International Conference on Artificial Intelligence and Soft Computing* (pp. 684-692). Springer, Cham.

[16] Z. Wang, A. C. Bovik, H. R. Sheikh, and E. P. Simoncelli (2004). Image quality assessment: from error visibility to structural similarity. *IEEE transactions on image processing*, 13(4), 600-612.

[17] L. Nanni, A. Lumini, and S. Brahnam, (2012). Survey on LBP based texture descriptors for image classification. *Expert Systems with Applications*, 39(3), 3634-3641.

[18] C. Turan, and K. M. Lam, (2018). Histogram-based local descriptors for facial expression recognition (FER): A comprehensive study. *Journal of visual communication and image representation*, 55, 331-341.

[19] M. Hussain, S. Q. Saleh, H. Aboalsamh, G. Muhammad, and G. Bebis, Comparison between WLD and LBP descriptors for non-intrusive image forgery detection. *2014 IEEE International Symposium on Innovations in Intelligent Systems and Applications (INISTA) Proceedings* (pp. 197-204). IEEE.

[20] R. Walecki, V. Pavlovic, B. Schuller, and M. Pantic, (2017). Deep structured learning for facial action unit intensity estimation. *2017 IEEE Conference on Computer Vision and Pattern Recognition* (pp. 3405-3414).

[21] S. Liu, Y. Zhang, and K. Liu, Facial expression recognition under partial occlusion based on Weber Local Descriptor histogram and decision fusion. 2014 *33rd Chinese Control Conference* (pp. 4664-4668). IEEE.

Detection of Suspicious Activities on Windows Systems with Log Analysis

A. OZTURK[1] and E.E. ULKU[2]

[1] Marmara University Institute of Pure and Applied Sciences, Istanbul/Turkey, ali.ozturk@marun.edu.tr
[2]Marmara University Faculty of Technology, Istanbul/Turkey, emre.ulku@marmara.edu.tr

***Abstract* - In recent years, rapid technological developments in many different fields have brought along various problems along with many innovations. One of these problems is cyber-attacks. Storing many records and data in digital media has made it very important to protect these records and data. Continuous log records play an important role in taking necessary precautions against cyber-attacks by system administrators.**

With the logging mechanism found in Windows systems, every transaction made on the system is recorded. These log records are analyzed with various algorithms and tools. As a result of these analyzes, suspicious or attacker behaviors on the system are detected. In this study, various cyber-attacks were tested in an environment where these Windows systems are located. As a result of these tests, the logs formed in the systems were collected and analyzed with the ELK Stack toolkit. As a result of these analyzes, the attacks were determined and associated with the tactics and techniques on Mitre ATT & CK.

***Keywords* - Log analysis, Mitre Att&CK, ELK Stack, Windows Systems**

I. INTRODUCTION

ONE of the most difficult parts of cyber security is detecting cyber-attacks. To stop an attack, it must first be detected. Cyber security engineers work hard to detect and stop these attacks. The most important source that cyber security engineers use to detect these attacks is the logs produced by the systems. Many complex attacks can be detected thanks to the detailed analysis made on the logs.

In order to adapt to the internet world and respond the emerging needs in this direction, companies are constantly expanding their information technology environments and moving many of their works to the virtual environment. The continuous growth of information technology environments and the increase in the number of transactions in the virtual environment cause the logs produced in the systems to reach gigantic sizes. Analyzing and making sense of these huge logs is becoming increasingly difficult due to the increasing size.

Various tools and algorithms are being developed to overcome this difficulty. Analyzes made with this program and algorithms are used in various fields. Cyber security, sales-marketing and performance management are at the forefront of these areas. Especially in the field of cyber security, tools developed to analyze log records are frequently used [1-4]. Many programs have been developed to analyze logs in cyber security. Splunk, Arcsight, IBM Qradar, ELK Stack are the main programs used for log analysis.

In this study, we used the ELK Stack program to collect and analyze the log records in the environment we installed. Another critical point in cyber security is to determine the type of attack and at what stage the attack is at that moment. Certain tactics and techniques are used in each cyber-attack. There is a knowledge base called Miter ATT & CK Matrix, which is accepted in the cyber security world about what these tactics and techniques are [5].

In this study, log analysis was carried out in Windows systems, which is one of the most used systems today. Some cyber-attacks were tested in the laboratory we created with Windows systems. The logs created on the systems as a result of these attacks were collected and analyzed with open source log analysis programs. The attacks were tried to be detected with the queries we wrote on the Elk stack. The attacks we detected were associated with the techniques and tactics on the miter att&ck matrix.

II. RELATED WORK

Log analysis is used in many areas. For this reason, many studies are carried out on log analysis. As a result of these studies, many new different techniques and products are emerging. In this section, some of the studies in the literature related to log analysis are examined and presented.

Threat hunting is one of the sub-areas of cyber security. The purpose of threat hunting is to detect existing or potential threats in IT environments. Log analysis is often used in threat hunting. In the study developed by R. Yamagishi et al. a visualization system proposal has been made for use in threat hunting [6]. This proposed system is made with visualization created by performing log analysis.

In the study of A. K. Meena et al. on log analysis, IPS, IDS, Firewall and DNS logs were analyzed with an open source log analysis tool [7]. With these analyzes, trends were tried to be determined and insight was gained.

One of the critical issues in cyber security is to detect malicious activities as soon as possible. The sooner a malicious

activity is detected, the faster defense can be made. H. L. Ngoc et al. proposed an early warning system design by examining the logs of passive scans on the systems [8].

III. Logging on Windows Systems

The logging mechanism in Windows systems categorizes and records the transactions according to the type of transactions. These categories are System, Application, and Security. In terms of cyber security, the most used logs are found under the security category [9, 10]. The operating system saves logs in a specific format. This format contains parameters that describe the event. Date, Username, Computer Name, Event ID, etc. are one of these parameters.

The system assigns an event id according to the type of each log it produces. These ids are specific to that event type. These event ids are mostly used in the rules we create in log analysis programs and in the analyzes we make. By associating these event ids with each other, event patterns on the system are extracted. Then, by looking at the other parameters in the logs, user and device associations related to the event are made.

Some critical events in Windows systems and their identities are presented in this section as subheadings.

A. Logon and Logoff

4624 and 4625 are identities used in log on and log off situations.

4624: An account was successfully logged on.

The system generates this log when successfully logged into the system.

4625: A failed logon attempt

The system generates this log whenever it tries to log into the system with the incorrect username or password or locked account.

B. Account Management

4720: A user account was created.

The system generates this log when new user was created in the system.

4726: A user account was deleted.

The system generates this log when a user was deleted from the system.

4740: A user account was locked out.

This log is created when any user account is locked in Windows systems. It usually occurs after wrong login attempts, most of the time.

4728: A member was added to a security-enabled global group

4732: A member was added to a security-enabled local group

4756: A member was added to a security-enabled universal group

There are various security groups on Active Directory. These logs are created when any user is added to these security groups.

C. Event Log

1102: The Audit Log Was Cleared

This log is created when the logs kept on Windows systems are deleted.

These event IDs are often encountered when investigating Windows systems that have been subjected to cyberattacks. This is why these event ids are often used in cyber-attack analysis and alert definitions. With these event ids, we can detect many cyber-attacks and suspicious behavior.

IV. Mitre ATT&CK Enterprise Matrix

Mitre ATT&CK Matrix is a frequently used knowledge base in cyber security. This knowledge base contains the tactics and techniques used in cyber-attacks.

The matrix includes 14 tactics and 222 techniques used under these tactics. And some techniques contain sub-techniques in themselves.

Reconnaissance
Resource Development
Initial Access
Execution
Persistence
Privilege Escalation
Defence Evasion
Credential Access
Discovery
Lateral Movement
Collection
Command And Control
Exfiltration
Impact

This matrix gives us information about what the attacker's next move might be during the cyber-attack. These tactics and techniques are also frequently used in cyber defense. Cyber security engineers test the IT environments they are responsible for in terms of the applicability of these tactics and techniques. According to the results of these tests, they increase the safety of their environment.

V. ELK Stack

The increase in the number of logs produced by the systems and applications makes it difficult to analyze the logs. Various log analysis tools have been developed to overcome this challenge. One of these tools is the ELK

Stack product developed by elastic company. In fact, the product was formed by combining 3 different products:

Elasticsearch: The system used to store data.

Logstash: A tool used to parse and enrich logs collected from systems and applications.

Kibana: Interface tool where operations such as searchand visualization are performed on the data stored on Elasticsearch. Elk stack architecture is presented in Figure 1.

Figure 1 - ELK Stack Architecture

Logs collected on Applications and Systems are processed through logstash. Processed logs are stored through elasticsearch. With Kibana, these logs are read and analyzed with the help of various queries over elasticsearch.

VI. Experiment

We tested some real-life cyber-attacks in our laboratory environment. We analyzed the logs created on Windows machines as a result of these attacks with the ELK tool stack. We showed the corresponding tactics and techniques of the attacks we detected on the mitre att&ck matrix with the help of ELK charts and tables.

A. Laboratory Environment

In the laboratory environment, there is 1 Windows 10 virtual machine, 1 Windows Server 2016 virtual machine, 1 Kali Linux virtual machine, 1 Ubuntu 18.04 virtual machine which include ELK stack [11]. We used the VMware virtualization tool to create the laboratory environment [12]. The architecture of the test environment used is presented in Figure 2.

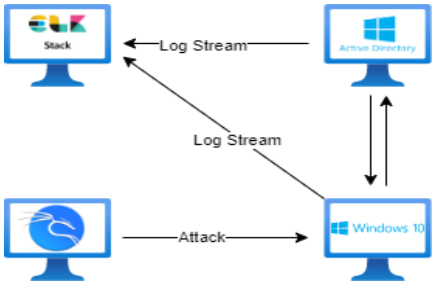

Figure 2 - Laboratory environment

B. Attack Scenario

We used some tools within the Kali Linux operating system to infiltrate the victim machine. After the infiltration step, we performed the privilege escalation process. Persistence was ensured by creating a new user account on the system. Then a critical file in the System was moved out of the system with using powershell scripts. Finally, the logs in the system were deleted and the logoff the system.

C. Log Collection

Winlogbeat tool has been developed by elastic company to collect logs on Windows systems. The Winlogbeat tool was installed on both windows systems, and the logs were collected and forwarded to the elk stack.

D. Log Analysis

After the cyber-attack tests, the logs of the systems were transmitted to the ELK stack with the winlogbeat tool. The logs stored by Elasticsearch were analyzed through kibana [13]. We developed some queries to perform these analyzes. Then we developed some visualization and dashboards with using the queries.

We have added new fields to the logs using painless scripts to assist in analysis. We have assigned mitre codes to the fields we have added, related to which tactic and technique in the mitre att&ck matrix. We used these fields to develop queries and dashboards. Thanks to all these queries and dashboards, we have clearly detected the attack tests we have carried out.

VII. Conclusion

In this study, we presented a method to collect and analyze logs on windows systems. Fast and correct log analysis is required to detect cyber-attacks. In this direction, we tested some cyber-attacks on Windows systems in our study. We created collected event logs as a result of these tests. Thanks to the queries and dahsboards we developed on ELK Stack, we made instant analyzes. Thanks to these analyzes, we detected the attacks. We have classified the events taking place according to the tactics and techniques in the Miter ATT&Ck matrix.

With this study, we have seen that we can detect some cyber-attacks in the real world with log analysis.

References

[1] M. Cersosimo and A. Lara, "Detecting Malicious Domains using the Splunk Machine Learning Toolkit," NOMS 2022-2022 IEEE/IFIP Network Operations and Management Symposium, 2022, pp. 1-6, doi: 10.1109/NOMS54207.2022.9789899

[2] I. Anastasov and D. Davcev, "SIEM implementation for global and distributed environments," 2014 World Congress on Computer Applications and Information Systems (WCCAIS), 2014, pp. 1-6, doi: 10.1109/WCCAIS.2014.6916651.

[3] S. S. Sekharan and K. Kandasamy, "Profiling SIEM tools and correlation engines for security analytics," 2017 International Conference on Wireless Communications, Signal Processing and Networking (WiSPNET), 2017, pp. 717-721, doi: 10.1109/WiSPNET.2017.8299855.

[4] R. Stoleriu, A. Puncioiu and I. Bica, "Cyber Attacks Detection Using Open Source ELK Stack," 2021 13th International Conference on Electronics, Computers and Artificial Intelligence (ECAI), 2021, pp. 1-6, doi: 10.1109/ECAI52376.2021.9515120.
[5] R. Kwon, T. Ashley, J. Castleberry, P. Mckenzie and S. N. Gupta Gourisetti, "Cyber Threat Dictionary Using MITRE ATT&CK Matrix and NIST Cybersecurity Framework Mapping," 2020 Resilience Week (RWS), 2020, pp. 106-112, doi: 10.1109/RWS50334.2020.9241271.
[6] R. Yamagishi, T. Katayama, N. Kawaguchi and T. Shigemoto, "HOUND: Log Analysis Support for Threat Hunting by Log Visualization," 2022 12th International Congress on Advanced Applied Informatics (IIAI-AAI), 2022, pp. 653-656, doi: 10.1109/IIAIAAI55812.2022.00130.
[7] A. K. Meena, N. Hubballi, Y. Singh, V. Bhatia and K. Franke, "Network Security Systems Log Analysis for Trends and Insights: A Case Study," 2020 IEEE International Conference on Advanced Networks and Telecommunications Systems (ANTS), 2020, pp. 1-6, doi: 10.1109/ANTS50601.2020.9342776.
[8] H. L. Ngoc, T. Cong Hung, N. D. Huy and N. Thi Thanh Hang, "Early Phase Warning Solution About System Security Based on Log Analysis," 2019 6th NAFOSTED Conference on Information and Computer Science (NICS), 2019, pp. 398-403, doi: 10.1109/NICS48868.2019.9023899.
[9] A. D. Moskvichev and M. V. Dolgachev, "System of Collection and Analysis Event Log from Sources under Control of Windows Operating System," 2020 International Multi-Conference on Industrial Engineering and Modern Technologies (FarEastCon), 2020, pp. 1-5, doi: 10.1109/FarEastCon50210.2020.9271520.
[10] Anthony, Russ. "Detecting security incidents using windows workstation event logs." SANS Institute, InfoSec Reading Room Paper (2013).
[11] Hertzog, Raphael, Jim O'Gorman, and Mati Aharoni. "Kali Linux Revealed." Mastering the Penetration Testing Distribution (2017).
[12] Nieh, Jason, and Ozgur Can Leonard. "Examining vmware." Dr. Dobb's Journal 25.8 (2000): 70.
[13] Al Shibani, M. O. Z. A., and E. Anupriya. "Automated Threat Hunting Using ELK Stack-A Case Study." Indian J. Comput. Sci. Eng 10 (2019): 118-127.

An empirical analysis of how users with different genders are not equally affected by the recommendations

Emre Yalcin[1]

[1] Computer Engineering Department, Sivas Cumhuriyet University, Sivas/Turkey, eyalcin@cumhuriyet.edu.tr

Abstract **- One of the main concerns related to personalized recommendations in recent years is how fair the provided referrals are for individuals differentiating in terms of particular features. In this study, we consider a critical protected attribute related to individuals, i.e., *gender*, and aim to analyze how the most prominent recommenders show varying performance for users of different genders. The experimental studies conducted on a real-world benchmark dataset and selecting eight state-of-the-art algorithms from different families demonstrate that males considerably receive more accurate recommendations than females. However, the obtained results also show that the recommendations produced for women are usually more qualified in diversity and novelty aspects when compared to those generated for men. These findings denote the unfair nature of the recommenders across users of different genders, and such disparities can occur differently for a specific aspect of the recommendations.**

Keywords **– Recommender systems, unfairness, gender discrimination, accuracy, beyond-accuracy.**

I. INTRODUCTION

As a prominent Artificial Intelligence technology, Recommender systems (RSs) provide personalized recommendations to individuals to ease their decision-making on many digital platforms. RSs mainly focus on featuring relevant products/services for users by filtering out inappropriate ones [1]. Due to the rapid increase in the amount of information on the Internet in recent years, the usage of RSs has significantly increased in many digital platforms serving different product/service categories such as hotel booking, social media, movies, music, and e-commerce websites.

Many approaches exist to provide individual recommendations, such as collaborative filtering (CF), content/knowledge-based filtering, and hybrid methods [2]. By working on a user-item rating matrix, these approaches typically perform the recommendation generation process for users by (*i*) predicting a numerical rating score for the unexperienced items or (*ii*) creating recommendation lists, including a set of items that would be desired. Although recommendation algorithms can provide recommendations with reasonable accuracy performance with the recent advances, it is known that they face many traditional issues such as sparsity, scalability, and cold-start [3]. In addition to such challenges, the literature has recently realized that these algorithms fail to provide unbiased recommendations [4].

Such unfairness issues of the algorithms are commonly evaluated for either user or item side. For example, due to imbalances in the distributions of the original ratings where they are trained, these algorithms recommend popular items too frequently compared to others even if they would be undesirable, also known as the popularity-bias problem [5]. Such unfair representation of the items results in a notable diminish in the quality of the recommendations regarding beyond-accuracy perspectives, such as catalog coverage, diversity, or novelty [6]. This problem might also result in a system that a few providers dominate, which unfortunately endangers competition in the market.

From the user side, on the other hand, recommendation algorithms might show different performances for particular groups of users. For instance, suppose that *X* and *Y* denote two different user groups; the utilized recommender system can be evaluated as unfair if it provides notably/consistently better recommendations for the *X* group than the *Y* group or vice versa; thus, it might significantly harm the satisfaction of the users; worse, lead to unfavorable social dynamics. Also, we can demonstrate that rather than unprotected groups (e.g., users with similar rating behavior), it might be much more problematic if such unfairness results in inadvertent discrimination against members of protected classifications like gender, ethnicity, or age [7].

In this study, therefore, we consider one crucial protected class, *gender*, and evaluate how the recommendation algorithms perform differently in the movie domain for male and female users. In doing so, we scrutinize eight state-of-the-art CF algorithms relying on different approaches, such as matrix factorization-based, probabilistic, clustering- and neural network-based, and measure their discrimination levels against individuals with different genders by considering accuracy and beyond-accuracy (diversity and novelty) recommendation quality. Note that the selected algorithms are the most prominent according to their followed recommendation strategy and are widely utilized in many recent related studies [8, 9].

The rest of the paper is organized as follows. The following section gives a brief literature summary on unfairness issues in RSs. Section III presents our analysis of the effects of recommendations on users of different genders, including the utilized datasets, considered recommendation algorithms, and

used assessment protocols. The following section, finally, concludes the obtained findings and explains our future directions.

II. Related work

In recent years, the concept of fairness has been one of the most studied topics in RSs, and it has been commonly evaluated from the perspective of one of three essential stakeholders of the system; *users*, *contents/items*, and *service providers*. In this study, we evaluate this issue from the view of the point of users.

A recent study has scrutinized the fairness concept for the popularity bias problem in movie recommendations [10]; the authors have concluded that recommendation algorithms are significantly biased towards popular items and explored that such bias propagation impacts users differently. More specifically, users less interested in popular items are more affected by this issue than those highly interested in popular items. This finding was also verified for music recommendations in another similar study [11]. In [12], the authors have introduced the calibration concept, meaning that the recommendations should be in the pattern same as users' original profiles. In other words, if a user has given 20% of her ratings to romance and 80% to horror movies, the recommendations should be generated with the same trend. In [11, 12], the calibration concept has also been evaluated for popularity; RSs should generate recommendation lists that include popular items with the same ratio as users' original profiles. Such a user-centric approach to popularity has also been adopted to combat the popularity bias problem more effectively [13].

Even if many studies have evaluated the fairness of the recommendations for the protected user groups so far [14, 15], to the best of our knowledge, only two studies consider gender-based user groups and evaluate the discriminatory performance of the recommendation algorithms across men and women [7, 16]. In the very related study to ours [7], the authors have considered three features of user profiles (i.e., profile anomaly, profile size, and profile entropy) and analyzed their possible associations with disparate behavior of the system towards different genders. Their experiments with four CF algorithms show that females usually receive less accurate recommendations than males based on all three stated features. However, the main shortcoming of this study is that they have compared such gender-based groups in terms of only predictive accuracy. The main superiority of our paper is that we investigate how the recommendations are differentiated for males and females by considering not only accuracy but also beyond-accuracy recommendation quality, such as diversity and novelty, which have become quite crucial in assessing the success of the RSs in the last few years. Also, our analysis includes more CF algorithms, which are relatively more modern when compared to those utilized in the mentioned study.

III. Analyzing the effects of recommendations on users of different genders

This section thoroughly examines how the most prominent recommendation algorithms perform differently in the movie domain for male and female users. To this aim, we first introduce the utilized dataset, recommendation algorithms, and the evaluation criteria (including both accuracy and beyond-accuracy metrics), and then present the obtained results and discuss them.

A. Dataset and experimentation methodology

In our analysis, we employ the Movielens-1M dataset collected and made publicly available by the Grouplens Research Team [17]. It consists of the preferences of users on different movies. The collected ratings are discrete and on a [1, 5] rating scale. We also present detailed information about MovieLens-1M in Table 1. In this dataset, the side information about users, such as age, gender, and occupation, is also available.

Table 1: Statistics of the Movielens-1M dataset

Domain	Movie
Rating Scale	[1, 5]
Number of users (Male/Female)	6,040 (4,331/1,709)
Number of Items (Movies)	3,952
Number of Ratings	1,000,209
Sparsity Ratio (%)	95.75

In the experiments, we follow the well-known leave-one-out experimentation methodology. Accordingly, we first select a user as the test user and the remaining ones as the train set, and then predict a rating score for all items of the test user by operating an algorithm explained in the following section on the train set. After that, we rank the predicted scores in descending order and select the top-*10* items as the recommendation list for the test user. This process is repeated for each user in the dataset.

B. Recommendation algorithms

We consider eight efficient recommendation methods from different CF families in the experiments, as in recent related studies [8, 9].

More specifically, we make use of *Maximum Margin Matrix Factorization (MMMF)* [18], *Weighted Matrix Factorization (WMF)* [19], and *Hierarchical Poisson Factorization (HPF)* [20] as matrix factorization-based methods. These algorithms are commonly aimed at representing both users and items in factor vectors formed from the patterns of the shared preferences and creating recommendation lists by considering the correspondence levels of such formed factors.

We also utilize the *Weighted Bayesian Personalized Ranking (WBPR)* [21] and *Indexable Bayesian Personalized Ranking (IBPR)* [22] as probabilistic approaches. These methods are introduced by following the probability theory to model the preference data of the users and then produce predictions. By following this theory, they model past events of the individuals, such as users' past choices for the items expressed explicitly, and predict the likelihood regarding prediction scores for untasted items.

Furthermore, we employ the *Spherical K-means (SKM)* [23] as a clustering-wise approach based on a weighted version of the online spherical *k*-means approach. It can overcome in a

short time the frequent updates in the original data, such as providing new ratings, updating existing ones, and the occurrence of new items/users. In the experiments, we also utilize *Neural Matrix Factorization (NEUMF)* [24] and *Variational Autoencoder for Collaborative Filtering (VAECF)* [25] as neural network-inspired techniques. Such methods model user-item interactions with a neural architecture and learn them using the multi-layer perceptron or variational auto-encoder. These non-linear probabilistic models help cope with the limited modeling capacity of linear factor models of traditional matrix-factorization-based approaches, thus achieving high-accurate recommendations.

We implement all mentioned algorithms via Cornac [26], a recently-introduced Python framework for RSs. Note that, when applying these algorithms, we consider default parameter-tuning suggested in their original papers for reproducibility purposes.

C. Evaluation criteria

When evaluating the potential disparity issues across genders propagated by the recommenders, we use several metrics measuring different aspects of the provided recommendations, as in [8]; *(i) normalized Discounted Cumulative Gain (nDCG)*, *Precision*, *Recall*, and *F1* metrics for accuracy performance, and *(ii) Average Percentage of Long-tail Items (APLT)* and *Novelty* for different aspects of the recommendations such as diversity and novelty.

The *nDCG* metric is highly-effective, as it measures the accuracy of recommended items by considering the actual ratings of the users and their positions in the produced list. More specifically, suppose that $r_{u,i}$ is the actual rating of user *u* on item *i*, and $\{i_1, i_2, \ldots, i_N\}$ is the Top-*N* list recommended to *u* with a particular algorithm. For that case, the *Discounted Cumulative Gain (DCG)* and *nDCG* for *u* can be calculated as in Eqs. 1 and 2, respectively.

$$DCG_N^u = r_{u,i_1} + \sum_{n=2}^{N} \frac{r_{u,i_n}}{log2(n)} \quad (1)$$

$$nDCG_N^u = \frac{DCG_N^u}{IDCG_N^u} \quad (2)$$

where $IDCG_N^u$ is the maximum possible gain for *u*, calculated by optimum re-ordering of *N* items suggested for the corresponding user.

We also utilized the F1 metric, which is a good option for measuring the accuracy level of the recommendations. It can be obtained by calculating the harmonic mean of *Precision (P)* and *Recall (R)* value of the generated top-*N* list, as formulated in Eq. 3. The former can be obtained by calculating the ratio of the number of recommended preferable items to the number of all suggested items (i.e., *N*). At the same time, the latter is defined as the ratio of the recommended preferable items to the number of all rated items in the user's profile. Here, to assign whether a recommended item is appropriate or not, we set the threshold value to 3.5, as positive ratings in a [1, 5] rating scale are usually considered as 4 and 5.

$$F1@N = \frac{2 \times P@N \times R@N}{P@N + R@N} \quad (3)$$

The *APLT* measures what percentage of items in the top-*N* list produced for *u* belong to the long-tail portion of the entire item catalog, as formulated in Eq. 4.

$$APLT_N = \frac{|\{i, i \in (N_u \cap T)\}|}{|N_u|} \quad (4)$$

where *T* denotes the set of tail items in the catalog, which is constructed by following the Pareto principle [27], i.e., Items excluding popular items receiving 20% of all ratings.

The last utilized metric is the *Novelty*, which measures the capacity of the utilized algorithm to suggest novel (i.e., unknown/unrated) items to *u*, as formulated in Eq. 5. Here, the set of items that user *u* has already rated is represented with I_u.

$$Novelty_N = \frac{|\{i, i \notin I_u\}|}{|N_u|} \quad (5)$$

D. The obtained experiment results

This section presents the results of the experiments to observe how the recommendation algorithms perform differently for users of different genders. To this end, we produce top-*10* recommendation lists and evaluate the quality of such generated lists for men and women separately from accuracy, diversity, and novelty aspects. Under these settings, we present in Table 2 the achieved average *nDCG*, *Precision*, *Recall*, *F1*, *APLT*, and *Novelty* scores of the suggested top-10 lists for the gender-based user groups in the Movielens-1M dataset. Here, we also compare the performances of eight CF algorithms, i.e., *MMMF*, *WMF*, *HPF*, *WBPR*, *IBPR*, *SKM*, *NEUMF*, and *VAECF*, in terms of the considered evaluation criteria to analyze the potential gender discrimination in recommendations more comprehensively. In the experiments, we also perform significance tests (i.e., *t*-test) to determine whether the observed differences for a particular metric across gender-based groups (i.e., males and females) are statistically significant or not, as can be followed in Table 2.

Although there are no significant divergences in achieved *Recall* and *F1* scores across gender-based user groups, we can conclude from the obtained *nDCG* and *Precision* results that males usually receive more accurate recommendations when compared to females. Also, we observe that the differences in the *nDCG* and *Precision* outcomes obtained for males and females seem to be statistically significant at a 95% confidence level for almost all utilized algorithms. This finding is also parallel with the previous literature since, in [7], the authors have verified that women are exposed to more poor recommendations than men in general and discussed that such an unfairness of the recommendations might stem from some features of users' profiles, such as profile anomaly or entropy.

Even if women are subject to suggestions that are relatively less accurate than men, their recommendations are more qualified in terms of beyond-accuracy aspects, as can be

followed from the *APLT* and *Novelty* results presented in Table 2. We also observe that the differences in the *APLT* and *Novelty* results achieved for males and females seem statistically significant at a 95% confidence level regardless of the utilized recommendation algorithm. Such a finding is as we expected because of the trade-off in such two different aspects of the recommendations (i.e., accuracy and beyond-accuracy aspects).

The main reason for unfair results of the recommendations across gender-based groups would be that females are usually more curious and open to new experiences by their nature compared to males, which ends up consuming and then voting for items of different kinds. This inevitably makes their provided ratings more diverse and informative; thus, the algorithms trained on their rating profiles can recommend more diverse and novel items for them. On the other hand, males usually avoid taking risks and aim to experience items on which a considerable consensus is provided (e.g., popular items), which ends up with profiles with the same characteristics. This way, the CF algorithms become more talented in constructing neighborhoods better for males and providing recommendations with a satisfactory accuracy level.

We also observe from the achieved *nDCG*, *Precision*, *Recall*, and *F1* results that the most accurate recommendations for both protected user groups are usually obtained by the *WBPR* algorithm, followed by *VAECF* and *NEUMF*, respectively. However, they seem to be the worst algorithms for providing recommendations qualified regarding diversity and novelty aspects, as shown in Table 2; This is not an unsurprising finding as such two aspects of the referrals are usually conflicting goals. On the other hand, we conclude that the *IBPR* is the superior algorithm for achieving the best recommendations when considering beyond-accuracy recommendation quality.

Table 2: The obtained *nDCG*, *Precision*, *Recall*, *F1*, *APLT*, and *Novelty* results for gender-based groups in the MovieLens-1M dataset

Recommendation Algorithm	*Gender*	*nDCG*	*Precision*	*Recall*	*F1*	*APLT*	*Novelty*
MMMF	Male	0.48*	0.42*	0.07	0.10	0.49	0.44
	Female	0.43	0.38	0.07	0.10	0.54*	0.50*
WMF	Male	0.42*	0.40*	0.06	0.10	0.01	0.56
	Female	0.35	0.31	0.06	0.09	0.02	0.63*
HPF	Male	0.56*	0.52*	0.08	0.13	0.05	0.39
	Female	0.47	0.42	0.08	0.12	0.08*	0.48*
IBPR	Male	0.22*	0.19	0.02	0.04	0.71	0.72
	Female	0.18	0.16	0.02	0.03	0.73	0.77*
WBPR	Male	0.64*	0.58*	0.11	0.16	0.26	0.28
	Female	0.58	0.52	0.11	0.16	0.37*	0.34*
SKM	Male	0.50*	0.48*	0.08	0.12	0.00	0.45
	Female	0.41	0.37	0.07	0.10	0.00	0.55*
NEUMF	Male	0.55*	0.50*	0.08	0.13	0.05	0.38
	Female	0.46	0.42	0.07	0.11	0.06	0.48*
VAECF	Male	0.58*	0.52*	0.09	0.14	0.21	0.34
	Female	0.52	0.46	0.09	0.14	0.25*	0.41*

* : For significance at 95% confidence level; the obtained differences across gender-based groups

IV. Conclusion and Future Work

In recent years, fairness of the algorithms has been one of the most studied issues in recommender systems and, more extensively, Artificial Intelligence. Therefore, in this study, we consider eight state-of-the-art collaborative filtering algorithms categorized into different types and analyze how they perform differently for users of different genders (i.e., males and females). To provide better analysis, we also consider several aspects of the provided recommendations: their accuracy and their beyond-accuracy quality.

The experiments realized on a well-known dataset demonstrate that the recommendation algorithms usually perform unfairly for users grouped based on their genders. More specifically, we observe that males receive more accurate recommendations in general when compared to females. However, our empirical results suggest that the recommendations generated for men are usually more qualified than those produced for women regarding beyond-accuracy aspects, such as diversity and novelty. We also conclude from the experiments that, with minor exceptions, especially neural-network-based recommendation approaches such as *NEUMF* and *VAECF*, are the most effective algorithms in achieving the most accurate recommendations. On the other hand, we observe that probabilistic approaches such as *IBPR* can be utilized to produce more diverse and novel recommendations.

The main limitation of our analysis is that it requires gender information of the users in addition to their provided ratings. However, even if some data collections utilized in the recommender system include detailed information about users such as gender, age, and social relationships, side information about such stakeholders is usually not released by the service

providers due to the privacy concerns of the individuals.

In future work, we plan to investigate the potential factors on why users of different genders are subject to unfair recommendations. In doing so, we will consider some discriminative features regarding their rating profiles, such as the level of their interaction with the system, or their personality traits, such as how stable their emotions are or how much they are extroverted.

REFERENCES

[1] J. Bobadilla, F. Ortega, A. Hernando & A. Gutiérrez, "Recommender systems survey", *Knowledge-based systems*, vol 46, pp. 109-132, 2013.

[2] K. Shah, A. Salunke, S. Dongare & K. Antala, "Recommender systems: An overview of different approaches to recommendations", in *2017 International Conference on Innovations in Information, Embedded and Communication Systems*, pp. 1-4.

[3] F. Ricci, L. Rokach & B. Shapira, "Recommender systems: introduction and challenges", in *Recommender systems handbook*, pp. 1-34, 2015.

[4] J. Chen, H. Dong, X. Wang, F. Feng, M. Wang & X. He, "Bias and debias in recommender system: A survey and future directions", arXiv preprint arXiv:2010.03240, 2020.

[5] E. Yalcin & A. Bilge, "Investigating and counteracting popularity bias in group recommendations", *Information Processing & Management*, 58(5), pp. 102608, 2021.

[6] L. Boratto, G. Fenu & M. Marras, "Connecting user and item perspectives in popularity debiasing for collaborative recommendation", *Information Processing & Management*, 58(1), pp. 102387, 2021.

[7] M. Mansoury, H. Abdollahpouri, J. Smith, A. Dehpanah, M. Pechenizkiy & B. Mobasher, "Investigating potential factors associated with gender discrimination in collaborative recommender systems", in *The Thirty-Third International Flairs Conference*, 2021.

[8] E. Yalcin & A. Bilge, "Evaluating unfairness of popularity bias in recommender systems: A comprehensive user-centric analysis", *Information Processing & Management*, 59(6), pp. 103100, 2022.

[9] M. Naghiaei, H. A. Rahmani & M. Dehghan, "The Unfairness of Popularity Bias in Book Recommendation", arXiv preprint arXiv:2202.13446, 2022.

[10] H. Abdollahpouri, M. Mansoury, R. Burke & B. Mobasher, "The unfairness of popularity bias in recommendation", arXiv preprint arXiv:1907.13286, 2019.

[11] D. Kowald, M. Schedl & E. Lex, "The unfairness of popularity bias in music recommendation: A reproducibility study", in *European conference on information retrieval*, pp. 35-42, 2020.

[12] H. Steck, "Calibrated recommendations", in *Proceedings of the 12th ACM conference on recommender systems*, pp. 154-162, 2018.

[13] H. Abdollahpouri, M. Mansoury, R. Burke, B. Mobasher & E. Malthouse, "User-centered evaluation of popularity bias in recommender systems", in *Proceedings of the 29th ACM Conference on User Modeling, Adaptation and Personalization*, pp. 119-129, 2021.

[14] S. Yao & B. Huang, "Beyond parity: Fairness objectives for collaborative filtering", *Advances in neural information processing systems*, vol 30, 2017.

[15] Z. Zhu, X. Hu & J. Caverlee, "Fairness-aware tensor-based recommendation", in *Proceedings of the 27th ACM international conference on information and knowledge management*, pp. 1153-1162, 2018.

[16] A. B. Melchiorre, N. Rekabsaz, E. Parada-Cabaleiro, S. Brandl, O. Lesota & M. Schedl, "Investigating gender fairness of recommendation algorithms in the music domain", *Information Processing & Management*, vol 58(5), pp. 102666, 2021.

[17] F. M. Harper & J. A. Konstan, "The movielens datasets: History and context", *Acm transactions on interactive intelligent systems (tiis)*, vol 5(4), pp. 1-19, 2015.

[18] M. Weimer, A. Karatzoglou & A. Smola, "Improving maximum margin matrix factorization", *Machine Learning*, vol 72(3), pp. 263-276, 2008.

[19] Y. Hu, Y. Koren & C. Volinsky, "Collaborative filtering for implicit feedback datasets", in *2008 Eighth IEEE international conference on data mining*, pp. 263-272.

[20] P. Gopalan, J. M. Hofman & D. M. Blei, "Scalable Recommendation with Hierarchical Poisson Factorization", in *UAI*, pp. 326-335, 2015.

[21] Z. Gantner, L. Drumond, C. Freudenthaler & L. Schmidt-Thieme, "Personalized ranking for non-uniformly sampled items", in *Proceedings of KDD Cup 2011*, pp. 231-247, 2012.

[22] D. D. Le & H. W. Lauw, "Indexable Bayesian personalized ranking for efficient top-k recommendation", in *Proceedings of the 2017 ACM on Conference on Information and Knowledge Management*, pp. 1389-1398, 2017.

[23] A. Salah, N. Rogovschi & M. Nadif, "A dynamic collaborative filtering system via a weighted clustering approach", *Neurocomputing*, vol 175, pp. 206-215, 2016.

[24] X. He, L. Liao, H. Zhang, L. Nie, X. Hu & T.S. Chua, "Neural collaborative filtering", in *Proceedings of the 26th international conference on world wide web*, pp. 173-182, 2017.

[25] D. Liang, R.G. Krishnan, M.D Hoffman & T. Jebara, "Variational autoencoders for collaborative filtering", in *Proceedings of the 2018 world wide web conference*, pp. 689-698, 2018.

[26] A. Salah, Q. T. Truong & H. W. Lauw, "Cornac: A Comparative Framework for Multimodal Recommender Systems", *J. Mach. Learn. Res.*, vol 21(95), pp. 1-5, 2020.

[27] R. Sanders, "The Pareto principle: its use and abuse", *Journal of Services Marketing*, vol 1(2), pp. 37-40, 1987.

Voice Control of Virtual Objects in Augmented Reality Applications

T.EMEKLI COBAN[1] and A. OZTURK[1,2]

[1] KTO Karatay University, Konya/Turkey, tubaemekli70@gmail.com
[1] KTO Karatay University, Konya/Turkey, ali.ozturk@karatay.edu.tr
[2] Havelsan A.S, Ankara/Turkey, aliozturk@havelsan.com.tr

Abstract **- Augmented reality (AR) is a technology that combines 3 Dimensional (3D) virtual objects created in a computer environment with real world images. In the scene created in this way, it is possible to interact with virtual objects in real time. AR technology applications are used in education, defense, medicine, e-commerce, manufacturing, tourism and many more. Interaction with sound in AR environment provides ease of use in applications. In this study, voice control of virtual objects in the AR environment created by using the Vuforia package in Unity software is provided. For this purpose, a data set was created with the voice recordings of five different commands taken from two people of different genders. Mel-frequency Cepstral Coefficients (MFCC), Linear Predictive Coding (LPC) and Mel-spectrogram features obtained from voice data were applied to Decision Tree, Random Forest and Support Vector Machines (SVM) algorithms and the results were compared. The best accuracy rates were found to be 87% for RF on male voice data set and 89% for SVM on female voice data set. The accuracy rate for the data set formed by the combination of the two data sets was found to be 85% for both RF and SVM. On the other hand, the accuracy rate of the k-Nearest Neighbor (kNN) algorithm, which used the Dynamic Time Warping (DTW) method with MFCC features, was found to be 89% and 88% for male and female voice datasets, respectively. The accuracy rate of kNN for the dataset formed by the combination of two data sets was found to be 83%. The results for all machine learning algorithms were obtained by cross validation.**

Keywords **- Augmented Reality, Voice Recognition, Machine Learning.**

I. INTRODUCTION

IN the augmented reality environment; real world objects and virtual objects and data are perceived together in the same environment by the user. An integrated image is obtained by adding virtual objects on top of real world objects. A camera is needed for the realization of AR applications. Mobile devices such as mobile phones and tablets contain hardware and sensors such as accelerometer, GPS, WiFi, gyroscope, compass, as well as cameras required for AR applications. In addition, they can meet the performance requirements of AR applications with their features such as high main memory capacity, high processor speed and graphics processor usage. It is predicted that the market share of augmented reality (AR) and virtual reality applications will increase gradually in the coming years. The importance of studies on AR, which has widespread application areas and is expected to increase, is of great importance [1].

When AR studies in the academic field are examined, areas such as education [2], survival in natural disasters and disasters [3], music and art [4-5], science [6], engineering [7], people with disabilities [8] and traffic [9] are encountered.

In the literature, the studies in the field of AR are basically divided into two different types as location-based and image-based [10]. In location-based AR applications, the appearance of virtual objects on the screen alongside real objects depends on GPS, Wireless Local Area Network (Wi-Fi), Radio Frequency Identification (RFID) or sensor data [11]. On the other hand, in image-based systems, objects such as pictures, graphics, QR codes, photographs, hand gestures or sound that are predefined in the AR environment are predefined and virtual objects are added by detecting them by the device. Most of the applications and studies developed in the field of AR are image-based [12]. In most of the studies conducted in the academic field, the marker-based AR method, which is one of the image-based methods, has been preferred. In marker-based AR applications, a marker associated with the virtual object to be displayed must be preloaded into the system [13, 14]. This marker may be, for example, an image of a book cover where the camera is pointed. Marker-based applications are easier to develop than other types. In markerless AR applications, the place where virtual objects will be displayed is not fixed. Interaction with virtual objects is provided by input such as hand gestures or sound.

Studies in which interaction with sound is made in markerless AR applications are found in the literature. Bartie and Mackaness [15] developed an AR application that detects certain voice commands to assist tourists visiting the city of Edinburgh. Mirzae et al. [16] is an example of a markerless AR application that uses sound as input. Kanno et al. [17] also used voice commands as an aid in the mobile AR application they developed to help Alzheimer's patients. Sheldon et al. [18] proposed an approach using voice recognition and hand gesture recognition to implement architectural design models in the AR environment. Siyaev and Jo [19] proposed a voice recognition system for the AR application they designed for

the maintenance and training of Boeing 737 aircraft.

In this study, voice control of virtual objects in the AR application is provided. The AR application was developed using the Vuforia AR package in the Unity environment. For the implementation of the voice recognition module, the feature extraction methods of the Librosa Python library were used. The sound properties obtained with the Librosa functions were applied to the k-Nearest Neighbor algorithm, in which the Dynamic Time Warping method was used as the distance criterion. In addition, comparative results were obtained by applying the sound properties to Random Forest, Decision Tree and Support Vector Machines algorithms. The voice recognition module developed with Python was integrated into the AR application with the help of Unity Python Scripting Package.

The remaining part of the paper is organized as follows: Section II describes the hardware and software tools used in the study as well as the dataset, feature extraction methods and machine learning algorithms. The experimental results are given in Section III and Section IV concludes the study.

II. MATERIAL AND METHODS

A. Software Packages

In this study, Unity 2020.3.3f1 was used with Vuforia 10.3.2 AR Engine for building the AR application. The Unity Python Scripting 6.0.0 package was used for the integration of our voice recognition Python module into Unity. This package provides the means to import the Python Runtime Environment as a namespace and execute Python scripts within the Unity Editor. For voice feature extraction, Librosa 0.9.2 Python library was used. Spyder IDE with Python 3.7 was used for the implementation of voice recognition module. The Operating System was Windows 11 Home Edition.

B. Hardware

During this study, Realtek(R) Audio Microphone Array with 6.0.8921.1 driver was used for voice recordings. The input format was 2 channels, 16 bit and 48000 Hz. The computer system was Lenovo Legion Y540-15IRH Laptop with 16 GB RAM and Intel Core i7-9750H CPU of 2.60 GHz. The graphics card was NVIDIA GForce RTX 2060.

C. Data Set

The data set was created with the voice recordings of five different Turkish commands taken from two people of different genders. The recorded voice commands were "Stop", "Forward", "Turn Left", "Turn Right" and "Back". The sound recording was carried out in both noisy and noiseless environments. First, each of the 5 commands was recorded 10 times giving 50 recordings for each of the people. Therefore, the data set contained 100 voice recordings in total. After recording was carried out the silence parts of the voices were removed. As an example, Figure 1 shows the plot of the voice recordings of "Turn Left" command received from both genders (female and male, respectively). To evaluate the performance of the machine learning algorithms, MFCC, Melspectogram and LPC features were extracted from the voice recordings. After evaluating the performances of the machine learning algorithms with the initial dataset of 100 voice recordings, we extended the dataset with additional 100 more voices to make further analysis. Therefore, the total size of the extended dataset included 200 voice recordings.

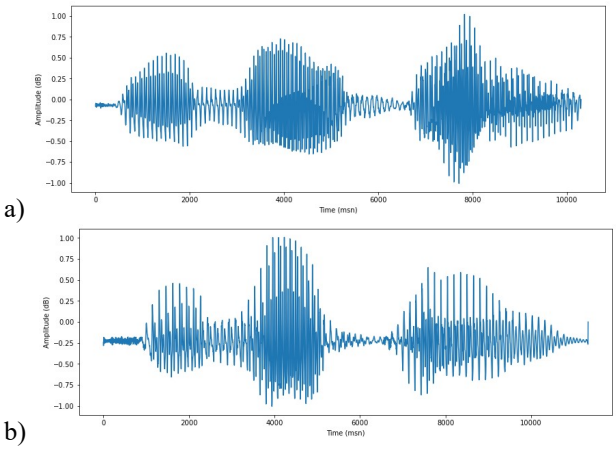

Figure 1: Voice recording plot of "turn left" command received from a) female and b) male

D. Feature Extraction from Voice Recordings

The following features were extracted from voice recordings and applied to the machine learning algorithms.

1) Mel Frequency Cepstral Coefficients (MFCC)

MFCC were first described by Davis and Mermelstein [20]. There are many successful applications of the MFCC to speech recognition. The mel-scale filter bank mimics the frequency selectivity of the human ear, achieving good speaker discriminating. In addition, MFCC coefficients are much less affected by the changes in sound wave structure. The details of MFCC feature extraction method is defined below.

The signal is first split into short-frames to ensure that the FFT calculation is not affected by the frequency changes in the entire signal. With the Hamming windowing method, the spectral changes that will occur at the end of the frames are avoided. For each frame n,

$$w_n = 0.54 - 0.46\cos\left(\frac{2\pi n}{N-1}\right) \quad (1)$$

Where, 0≤n≤N-1 and N is the window length.

Then the power spectrum is computed as following, after calculating FFT for each frame.

$$P = \frac{|FFT(x_i)|^2}{N} \quad (2)$$

Where, xi is the ith frame of the signal.

At the next step, the filter banks are computed by applying triangular filters on mel-scale. The mel is calculated for frequency *f* as in the following.

$$mel(f) = 2595 \times log_{10}\left(1 + \frac{f}{700}\right) \quad (3)$$

Since the filter bank coefficients are highly correlated, the compression is achieved by applying Discrete Cosine Transform (DCT). The voice recognition applications typically use 2-13 MFCC features.

2) Linear Predictive Coding (LPC)

The basic idea in LPC is to predict a sound sample using a linear combination of previous sound samples [21].

The first two steps of LPC method are framing and windowing as in the MFCC method. The next step is to auto correlate each frame of the windowed signal. The highest autocorrelation value is the order of the LPC coder. In the next step, LPC cepstral coefficients are obtained from the frames of auto correlations.

The prediction error is the difference between the predicted and actual value. If the current sample x_i will be predicted by the previous p samples and x_i^p is the predicted value, then

$$x_i^p = -a_2 x_{i-1} - a_3 x_{i-2} - \cdots - a_{p+1} x_{i-p} \quad (4)$$

Where, $\{1, a_2, \cdots, a_{p+1}\}$ are the (p+1) filter coefficients. The signal passes through an LPC filter resulting in a feature vector.

3) Mel-spectrogram

To obtain the mel-spectrogram features, first the spectrogram is calculated. For this, FFT is computed on over-lapping windows on signal. Then, the frequency is converted to log scale which results in spectrogram. Finally, the frequency is mapped onto mel scale as indicated in (3) to obtain the mel-spectrogram.

E. Machine Learning Algorithms

The features extracted from voice recordings were applied to the following machine learning algorithms.

1) Decision Tree

The algorithm which builds a decision tree from a dataset was firstly introduced by Quinlan [22] as ID3 (Iterative Dichotomiser 3). The C4.5 algorithm was an extension to the ID3 algorithm for handling both discrete and continuous values. C4.5 was also handling missing values and attributes with different costs. C4.5 builds the tree structure using entropy concept (5) from information theory.

$$Entropy(S) = -\sum_{i=1}^{c} p_i \log_2(p_i) \quad (5)$$

The algorithm chooses the next attribute having the highest information gain (6) while building the tree.

$$Gain(S, A) = Entropy(S) \sum_{v \in Values(A)} \frac{|S_v|}{|S|} Entropy(S_v) \quad (6)$$

The C4.5 algorithm also applies pruning to simplify the decision tree after creation.

2) Random Forest (RF)

The RF algorithm creates small decision trees and combines theirs outputs using the ensemble logic based on bagging [23]. Each small decision tree is a weak classifier. The forest is formed by a large number of small trees, varying with the size of the dataset and the number of features. During the creation of small trees, the Gini Index criterion (7) is usually used to select the next feature in the nodes.

$$Gini = 1 - \sum_{i=1}^{C} (p_i)^2 \quad (7)$$

First, using bootstrapping, small training sets are created by randomly selecting the rows in the dataset with replacement. Also, instead of all features, a few randomly selected features are used without replacement when the nodes in the trees are splitting. Due to bootstrapping, some rows of the original dataset may not be selected at all. These rows are used to measure the out-of-bag error of the RF.

3) Support Vector Machines (SVM)

The general idea of SVM is to separate training samples of different classes by using a hyperplane which has a margin in the area from which the samples are taken. The DVM algorithm has to minimize the classification error while maximizing this margin [24].

SVMs map input dataset to a higher dimensional feature space using a nonlinear mapping function. The estimation function used by SVM is

$$f(x) = \big(w \times \emptyset(x)\big) + b \quad (8)$$

Where, w and b are the coefficients estimated from the data set and $\emptyset(x)$ is the non-linear function in feature space.

The risk function to be minimized is

$$R(w, \xi^*) = \frac{1}{2}\|w\|^2 + C \sum_{i=1}^{N} (\xi_i + \xi_i^*) \quad (9)$$

$$d_i - w\emptyset(x_i) - b \leq \in + \xi_i \quad (10)$$

$$\big(w\emptyset(x_i)\big) + b - d_i \leq \in + \xi_i^* \quad (11)$$

Where, C is the penalty strength and $\xi_i, \xi_i^* > 0$.

The Support Vector estimation function can beis

$$f(x) = \sum_{i=1}^{NSV} (\alpha_i - \alpha_i^*) K(X, X_i) + b \quad (12)$$

Where α_i and α_i^* are Lagrange coefficients and NSV is the number of support vectors.

The kernel function $K(X, X_i) = \emptyset(X_i)\emptyset\big(X_j\big)$ can be selected as polynominal, radial basis function (rbf) or sigmoid.

The parameters C, $\in$ and the kernel function are specified by the user. In this study, rbf was used as the kernel function. For C and $\in$, 1.0 and 0.001 were used respectively.

4) K-Nearest Neighbors (kNN)

The kNN algorithm is a sample-based learning method. All of the data samples are stored in the training phase of the algorithm. Then, the kNN uses a specific distance measure to classify a new sample using the k nearest data samples as in (13).

$$f(y) \leftarrow argmax_{v \in V} \sum_{i=1}^{k} \delta(v, f(x_i)) \quad (13)$$

Where δ is the distance function, v is the data vector, V is the data set and k is the number of neighbors [25].

In this study, the Dynamic Time Warping (DTW) method is used for the distance measure to determine the class of the new voice recordings.

Dynamic Time Warping (DTW)

The DTW method is used to measure the similarity of two signals that differ in time or velocity [26].

If the similarity of the signals $P = p_1, p_2, \ldots, p_n$ and $R = r_1, r_2, \ldots, r_m$ is to be found, first a matrix of nxm is

created. The i^{th} and j^{th} elements of this matrix return $d(p_i, r_j)$, which is the distance in amplitude between the points r_i and p_j. The typical distance measure is the Euclidean distance.

$$d(p_i, r_j) = \sqrt{|p_i^2 - r_j^2|} \quad (14)$$

III. EXPERIMENTAL RESULTS

This study constitutes two different parts. First, an augmented reality environment was created using Vuforia AR Engine within Unity Editor. Figure 2 shows the augmented reality environment on the mobile phone screen. The application is markerless that the virtual objects are displayed on the surface.

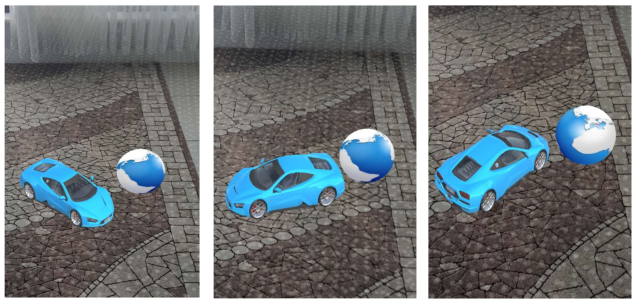

Figure 2: The augmented reality application implemented for this study

Then, voice recognition functionality was implemented using Python within *Spyder IDE*. The Python code included sound feature extraction methods of *Librosa* [27] package along with *scikit-learn* library package for implementing the machine learning algorithms.

As the first step, the voice dataset was created. Five different voice commands were recorded in both noisy and noiseless environments by two people of different genders. Each of the recordings was made for duration of 2 seconds with 8000 frame size (fs). Therefore, the number of frames per buffer was 16000. The *pyaudio* Python library was used to make the voice recordings. After making each recording, the silence was removed from the sound using the *split_on_silence* function of *pydub* Python library. The split_on_silence function splits the sound into chunks using the *min_silence_length* as 100 ms and *silence_threshold* as *dBFS-1* to detect and remove the silence part. The chunks without silence were combined with the *export* function of *AudioSegment* class. The noise removal from the voice recording was made using *filtfilt* function of *scipy.signal* Python library which applies *Finite Impulse Response (FIR)* filter twice. Figure 3 shows, a) the original plot of "Turn Left" voice signal, b) plot after silence removal and c) plot after noise filtering.

After applying silence removal and noise filtering, MFCC features are extracted from the signals using *mfcc* function of *Librosa* Python library. The number of extracted MFCC features was 12 and the hop length was 512. In Figure 3, the effects of silence removal and noise filtering applied to the original voice signal can be observed. Figure 4 shows the MFCC values, Melspec values and LPC values extracted from "Turn Left" voice signal after silence removal and noise filtering.

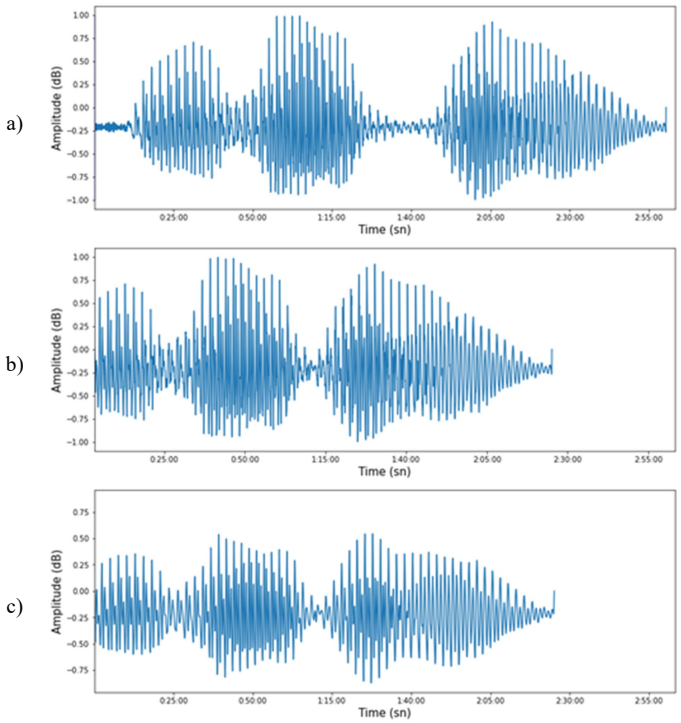

Figure 3. a) The "Turn Left" command voice signal b) Silence removal c) Noise filtering

The signals were classified with kNN algorithm using DTW as the distance measure between the MFCC features. To calculate the DTW values the the *fastdtw* Python function was used. The number of neighbours *k* in kNN was determined as 6 giving the best accuracy rate.

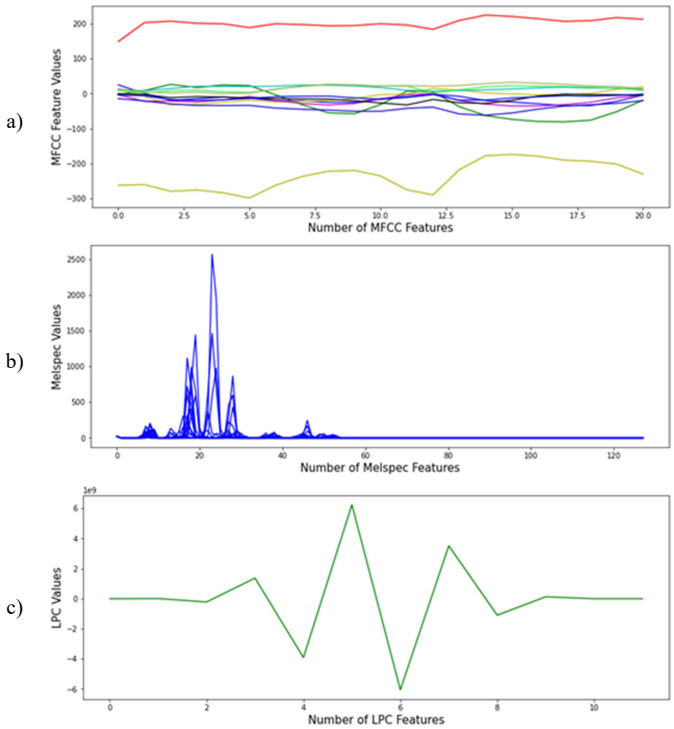

Figure 4. a) The MFCC values b) Melspec values c) LPC values

The accuracy rates were found as 88% and 92% for male and female voice data sets, respectively. The accuracy rate of

the data set formed by the combination of two data sets was found as 84%. The confusion matrix of the kNN for male dataset is given in Table 1.

Table 1: The confusion matrix of kNN for male dataset.

Real \ Predicted	Stop	Forward	Turn Left	Turn Right	Back
Stop	10	4			
Forward		6			
Turn Left			8		
Turn Right			2	10	
Back					10

According to Table 1, 5 of the *Forward* voice commands were incorrectly classified as *Stop* and 2 of the *Turn Left* voice commands were incorrectly classified as *Turn Right*.

The confusion matrix of the kNN classification result for female dataset is given in Table 2.

Table 2: The confusion matrix of kNN for female dataset.

Real \ Predicted	Stop	Forward	Turn Left	Turn Right	Back
Stop	10	1	1		
Forward		7			
Turn Left		2	9		
Turn Right				10	
Back					10

According to Table 2, 1 of the *Forward* voice commands was incorrectly classified as *Stop* and 2 of them as *Turn Left*. One of the Turn Left voice commands was misclassified as *Stop* and the other as *Forward*. Only one *Turn Right* command was incorrectly classified as *Back*.

The confusion matrix of the kNN for the combined dataset is given in Table 3.

Table 3: The confusion matrix of kNN for the combined dataset.

Real \ Predicted	Stop	Forward	Turn Left	Turn Right	Back
Stop	20	3	1	2	
Forward		12	4		
Turn Left		4	13		
Turn Right		1	2	18	
Back					20

According to Table 3, *Stop* and *Back* commands had no misclassifications while *Turn Right* command had only 2 misclassifications. *Forward* and *Turn Left* commands had more misclassifications as is the case for the male and female only datasets.

For comparison purposes, MFCC, LPC and Mel Spectrogram features were extracted from the voice signals after applying silence removal and filtering. Then, using the averages and standard deviations of these features, new datasets of 6 features, namely *mfcc_avg*, *mfcc_std*, *lpc_avg*, *lpc_std*, *mel_std* and *mel_avg*, were obtained. The new data sets were applied to RF, DT and SVM machine learning (ML) algorithms after scaling the features into 0-1 range with *MinMaxScaler* function of *sklearn.preprocessing* library. The RF, DT and SVM algorithms were evaluated with 3-fold cross validation to obtain accuracy scores.

The average accuracy scores are given in Figure 5.

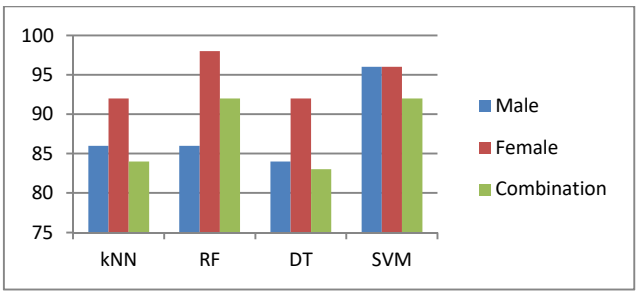

Figure 5: The average accuracies of the algorithms on the initial dataset

According to Figure 5, SVM algorithm has the highest accuracy of %96 for the male dataset, while RF gave the highest accuracy of %98 for the female dataset. The RF and SVM have the highest score of %92 for the combined data set.

The confusion matrix of the SVM classification result for the whole dataset is given in Table 5.

Table 5: The confusion matrix of SVM for the combined dataset.

Real \ Predicted	Stop	Forward	Turn Left	Turn Right	Back
Stop	18	1			
Forward	2	19	2		
Turn Left			18	3	
Turn Right				17	
Back					20

According to Table 5, 3 of the *Turn Right* commands were misclassified as *Turn Left*, 2 of the *Turn Left* commands were incorrectly classified as *Forward*. *Stop* commands had 2 misclassifications as *Forward* and 1 of the *Forward* commands was misclassified as *Stop*.

To make further analysis, the dataset was extended with 50 more voice recordings from each gender making 200 in total. All of the methods were evaluated with this extended dataset. The results are given in Figure 6.

As can be seen from Figure 6, the accuracies of all algorithms decreased for the extended female dataset. The accuracies of kNN and RF increased for the extended male dataset, while the accuracies of DT and SVM decreased significantly. The accuracy of kNN for the combined extended dataset did not differ too much. However, the performance of the other algorithms decreased significantly.

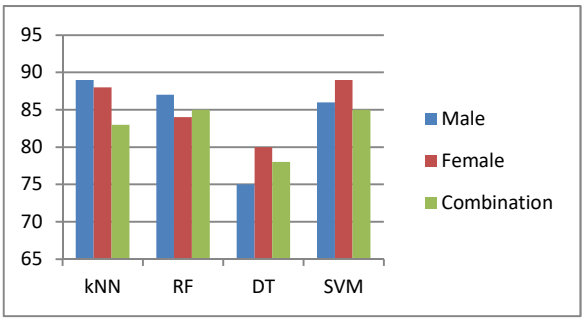

Figure 6: The average accuracies of the algorithms on the extended dataset

According to Figure 6, kNN has the highest performance of %89 accuracy on the male dataset, while SVM has the highest

accuracy of %89 on the female dataset. RF and SVM have the same most accurate results of %85 for the combined set.

The overall degradations in the performance of the algorithms can be due to the content of the extended dataset. Because, the new voice recordings were made in a different time and in different environmental conditions. The pitch and tone of the voices might be affected due to diseases or environmental noises.

The studies in the literature either did not discuss their voice recognition performances quantitatively [15, 18] or used a ready-to-use automated speech recognition engine [16, 17]. Only study [19] gives quantitative evaluation on the performance results. They used the Google Cloud Text-To-Speech API to generate artificial human sounds for obtaining the training dataset. The training data set included 45,244 audio files from 46 various artificial speakers. Their proposed model had %94.7 accuracy on real voice recordings. In our study, we created our dataset with real voice recordings of two speakers in different genders. The accuracy of %92 was obtained by SVM and RF algorithms on the initial data set of 100 recordings, while the accuracy was %85 on the extended data set of 200 recordings.

IV. CONCLUSION

In Unity, there are different commercial libraries which can be used for voice recognition. To name, Microsoft's Windows Speech, Google's Cloud Speech Recognition and IBM's Watson SDK are the most known products. However, using these products for a voice command recognition task is not considered to be cost effective. Furthermore, they may also be unsuccessful in voice recognition occasionally, due to environmental conditions or pronunciation differences. In this study, we implemented our own voice command recognition utility in Python and integrated into Unity for the control of virtual objects in augmented reality applications. As a future study, the performance of the voice recognition module will be improved by extending the dataset with more voice recordings of different people. Furthermore, different sound features may be extracted and used in the machine learning algorithms to improve their performances. Additional commands can be easily added to the voice recognition utility according to the requirements of new AR applications.

REFERENCES

[1] İçten, T., Bal, G. (2017). "Artırılmış Gerçeklik Üzerine Son Gelişmelerin ve Uygulamaların İncelenmesi", Gazi Üniversitesi Fen Bilimleri Dergisi PART C: TASARIM VE TEKNOLOJİ, 5(2): 111-136.

[2] Motejlek, J., Alpay, E. (2021). "Taxonomy of Virtual and Augmented Reality Applications in Education", IEEE Transactions on Learning Technologies, 14(3): 415-429.

[3] Tsai, M.K., Liu, P.H.E., Yau, N.J. (2013). "Using electronic maps and augmented reality-based training materials as escape guide lines for nuclear accidents: An explorative case study in Taiwan", British Journal of Educational Technology, 44(1): 18–21.

[4] Trujano, F., Khan, Mina, Maes, P. (2018). "ARPiano Efficient Music Learning Using Augmented Reality", International Conference on Innovative Technologies and Learning, pp. 3-17.

[5] Petrović, N. (2020). "Augmented and Virtual Reality Web Applications for Music Stage Performance", 55th International Scientific Conference on Information, Communication and Energy Systems and Technologies (ICEST), pp. 33-36.

[6] Enyedy, N., Danish, J.A., Delacruz, G. and Kumar, M.. (2012). "Learning physics through play in an augmented reality environment". International journal of computer-supported collaborative learning, 7(3):347-378.

[7] Su, S., Perry, V., Luis, B., Kase, S., Heather, R. Katherine, C., Dasari, V.R. (2020)."Virtual and Augmented Reality Applications to Support Data Analysis and Assessment of Science and Engineering,", Computing in Science & Engineering, 22(3): 27-39.

[8] Yoon, C., Louie, R., Ryan, J., Vu, M., Bang, H., Derksen, W., Ruvolo, P. (2019). "Leveraging augmented reality to create apps for people with visual disabilities: A case study in indoor navigation", The 21st International ACM SIGACCESS Conference on Computers and Accessibility, pp. 210-221.

[9] M. Zhang, Real-time traffic flow prediction using augmented reality, Yüksek Lisans Tezi, the University of Windsor, School of Computer Science, 2016.

[10] K. H. Cheng ve C. C. Tsai, (2013). "Affordances of augmented reality in Science learning: Suggestions for future search." Journal of Science Education and Technology 22.4, 449-462,.

[11] M. Sırakaya ve S. S. Seferoğlu, (2016). "Öğrenme Ortamlarında Yeni Bir Araç: Bir Eğitlence Uygulaması Olarak Artırılmış Gerçeklik", Eğitim Teknolojileri okumaları TOJET Sakarya Üniversitesi, 417-438.

[12] Abdüsselam, M.S. , Karal, H. (2012). "Fizik öğretiminde artırılmış gerçeklik ortamlarının öğrenci akademik başarısı üzerine etkisi: 11. Sınıf manyetizma konusu", Eğitim ve Öğretim Araştırmaları Dergisi, 1(4): 170-182.

[13] Wojciechowski, R., Wojciech, C. (2013). "Evaluation of learners' attitude to ward learning in ARIES augmented reality environments", Computers & Education, 68, 570-585.

[14] İbili, E., Şahin, S. (2013). "Artırılmış Gerçeklik ile İnteraktif 3D Geometri Kitabı Yazılımın Tasarımı ve Geliştirilmesi: ARGE3D", Afyon Kocatepe University Journal of Science and Engineering, 13:1-8.

[15] Bartie, P.J, Mackaness, W.A., (2006). "Development of a Speech-Based Augmented Reality System to Support Exploration of Cityscape", Transactions in GIS, 10(1): 63– 86.

[16] Mirzaei, M.R., Ghorshi, S., Mortazavi, M. (2012). "Combining Augmented Reality and Speech Technologies to Help Deaf and Hard of Hearing People", 14th Symposium on Virtual and Augmented Reality, pp.174-181.

[17] Kanno, K.M., Lamounier, E.A., Cardoso, A., Lopes, E.J., and Mendes de Lima, G.F., (2018). "Augmented Reality System for Aiding Mild Alzheimer Patients and Caregivers," 2018 IEEE Conference on Virtual Reality and 3D User Interfaces (VR), pp. 593-594.

[18] Sheldon, A., Dobbs, T., Fabbri, A., Gardner, N., Haeusler, M.H., Ramos, C. and Zavoleas, Y. (2019). "Putting the AR in (AR)chitecture - Integrating voice recognition and gesture control for Augmented Reality interaction to enhance design practice", Proceedings of the 24th CAADRIA Conference Vol. 1, Victoria University of Wellington, Wellington, New Zealand, 15-18 April 2019, pp. 475-484.

[19] Siyaev, A. Jo, G. (2021). "Neuro-Symbolic Speech Understanding in Aircraft Maintenance Metaverse", IEEE Access, vol.9, pp.154484-154499.

[20] Davis, S. and Mermelstein, P. (1980). "Comparison of parametric representations for monosyllabic word recognition in continuously spoken sentences", IEEE Transactions on Acoustics, Speech and Signal Processing, 28, 357-366.

[21] Kurzekar, P. K., Deshmukh, R. R., Waghmare, V. B., & Shrishrimal, P. P. (2014). A comparative study of feature extraction techniques for speech recognition system. International Journal of Innovative Research in Science, Engineering and Technology, 3(12), 18006-18016.

[22] Quinlan, J. R. (1993). C4.5: *Programs for Machine Learning*. Morgan Kaufmann Publishers.

[23] Breiman, L. ((2001). "Random Forests", Machine Learning, 45:5–32.

[24] Cortes, C., & Vapnik, V. (1995). Support-vector networks. Machine learning, 20(3), 273-297.

[25] Mitchell, T. (1997). "Machine Learning", New York, NY:McGraw-Hill.

[26] Salvador, S., Chan, P., (2004). "FastDTW: Toward Accurate Dynamic Time Warping in Linear Time and Space", KDD Workshop on Mining Temporal and Sequential Data, pp. 70–80, 2004.

[27] McFee, Brian, Colin Raffel, Dawen Liang, Daniel PW Ellis, Matt McVicar, Eric Battenberg, and Oriol Nieto. "librosa: Audio and music signal analysis in python." In Proceedings of the 14th python in science conference, pp. 18-25. 2015.

Analysis of drying characteristics of dried damson plum by microwave drying

N. ÇETİN[1], B. ALSAN[1] and S. İVECAN[2]

[1] Erciyes University, Kayseri/Turkey, necaticetin1990@gmail.com; berfinalsan98@gmail.com
[2] Necmettin Erbakan University, Konya/Turkey, saniyeivecan69@gmail.com

Abstract **- Due to the high moisture content, respiration rate and rapid ripening process, most of the fruits turn into waste product. For this reason, products must be dried and stored to maintain their availability and allow consumption even out of season. Plum is one of the most important fruits preferred by consumers due to its high vitamin, mineral and antioxidant content. In this study, the effects of different microwave drying conditions on the kinetics, rehydration, energy, and thermal properties of damson plum were determined. In addition, the color properties of the dried products were determined by the image processing analysis and the classification of the products according to the drying conditions was performed using machine learning. In addition, the moisture ratio was modeled by using a multilayer perceptron-artificial neural network (MLP) algorithm. The studied parameters were subjected to comparative statistical analysis. According to the findings, successful results were obtained for classification (accuracy>0.80) and prediction (R>0.85).**

Keywords **- Plum, kinetic, energy, color, image processing.**

I. INTRODUCTION

Plum is one of the edibles and commonly grown stone fruit species of the Rosaceae family belonging to the Prunus species. Plum contains potassium, phosphorus, sodium, iron, fiber, and vitamins A, B1, B2, B3, B6, C, and E. It also contributes significantly to human nutrition because it is rich in fiber and antioxidants. Damson plum (*Prunus domestica* subsp. Insititia), which is among the European-Asian species [1]. Plum can be used in various forms such as dried, fruit juice, condensed jam, marmalade, and ice cream. Dried plums are sweetener, color and aroma enhancer, moisture retainer, and healthy diet snack, as well as in the mixture of muesli, cereal and in dessert, pudding, and chocolate, as biscuits and cakes [2].

Drying is a food preservation method, which is the removal of water from the material. It plays an important role in processes such as the chemical, biochemical, and food industries. With the drying process, undesirable changes in water activity are brought into appropriate conditions to prevent microbiological activities in food products [3]. Microwave drying is successfully applied today and has a bright future. Because microwave provides an equal distribution of energy and heat towards the inner surface of the materials, prevents thermal deterioration, promises very high-end product quality, and provides energy savings with short drying times [4]. In microwave drying, the drying function is high, the product does not show any structural deterioration, the melted substances contained in the product are not transported, and the drying time is shorter than other drying methods [5]. Microwave drying reaches the depths of the product and allows the water in the product to boil. Thus, the vapor pressure difference between the inside of the product and its surface increases, and the moisture is rapidly evacuated [6]. Visible shrinkage and color changes occur in the dried products. The shrinkage starts at the beginning of the drying process and the change in its size and internal structure depends on the operating conditions (microwave power, temperature, and air velocity) of the drying method applied [7].

Drying is a complex process due to simultaneous heat and mass transfer. For this reason, effective models are developed to determine the effect of process parameters, optimize the drying process, and provide energy control [8]. Machine learning techniques can provide more rapid and successful results than conventional techniques [9]. In addition, the texture-based color characteristic is considered the most important parameter in dried products. Consumers also consider color and appearance when choosing a product [10].

The aim of this study is to determine the effect of drying on the kinetic, rehydration, energy, and thermal properties of damson plum under different microwave drying conditions. In addition, the color properties of the dried products were determined by the image processing method, and the discrimination of the products according to the drying conditions was performed using machine learning. In addition, the moisture ratio was modeled by a multilayer perceptron-artificial neural network (MLP) algorithm.

II. MATERIAL AND METHOD

Plum (*Prunus domestica* L.) was used as a sample in the study. Before drying, the plums were divided into 8 equal parts, and then drying processes were carried out. 150±2 g of plum was used in each application. The average slice thickness was measured as 12.23 mm. Microwave drying processes were carried out with a hybrid dryer (Arçelik KMF 833 I, Turkey) at 100, 200, and 300W power. Plums before and after drying are given in Figure 1. In the study, nine different thin layer drying models were applied as Page [11], Henderson & Pabis [12], Newton [13], Two-term [14], Wang & Singh [15], Verma [16], Logistic [17], Jena & Das [18], and Alibaş [19]. The moisture ratio (MR) of plums during drying

was determined using equation (1) [11], the drying rate (DR), which indicates moisture removal per unit time, was calculated using equation (2) [20], and moisture content (M_c) values on a wet basis (wet basis, w.b.) were determined using equation (3) [5]:

$$MR = \frac{M_t - M_e}{M_o - M_e} \quad (1)$$

$$DR = \frac{M_{t+dt} - M_t}{dt} \quad (2)$$

$$M_c = \frac{W_i - W_f}{W_i} \times 100 \quad (3)$$

Where, M_t, moisture content (g water g dry matter^{-1}) at a particular time, M_e, equilibrium moisture, and M_o, initial moisture, W_i, initial weight (g) W_f, final weight (g), Mt+dt, moisture content at time t dt (g water. g dry matter^{-1}), dt, drying time (min).

The color properties of fresh and dried plums were measured in the CIELab color space with the aid of a colorimeter (PCE-CSM 5 PCE Instruments, Germany). Chroma and total color change values were calculated by equations (4, 5) [11].

$$C = \sqrt{(a^*)^2 + (b^*)^2} \quad (4)$$

$$\Delta E = \sqrt{(L^* - L^*_0)^2 + (a^* - a^*_0)^2 + (b^* - b^*_0)^2} \quad (5)$$

A digital wattmeter (Tt Technic PM-001, Turkey) was used to determine the energy consumption of the microwave dryer. Specific energy consumption (SEC), specific moisture absorption rate (SMER), energy efficiency (η_{en}), and thermal efficiency (η_{th}) were calculated with the equations (6-10) [13, 20].

$$SEC = \frac{E_c}{m_w} \quad (6)$$

$$SMER = \frac{m_w}{E_c} \quad (7)$$

$$\eta_{en} = \frac{m_w \lambda_{wp}}{E_c} \quad (8)$$

$$\frac{\lambda_{wp}}{\lambda_w} = 1 + 23\exp(-0.4X) \quad (9)$$

$$\eta_{th} = \frac{P A \lambda_w (M_o - M_e)}{F t (100 - M_e)} \quad (10)$$

Where m_w is the evaporated water mass (kg), X is the sample moisture content (kg water kg dry matter^{-1}), λ_w is the water latent heat (J kg^{-1}) and λ_{wp} is the latent heat of the product (J kg^{-1}), P is the amount of product in the system (kg m^{-2}), A is the area of the tray (m^2), λ_w is the latent heat of evaporation of water (kJ kg^{-1}), M_e is the amount of water evaporated from the product (kg), F is the heating capacity utilization (kW), and t is drying time.

In the study, a multilayer perceptron (MLP) artificial neural network algorithm was used for the estimation of moisture content, moisture content, and drying rate. In these estimations, the ANN parameters were kept constant and the number of neurons in the hidden layer was changed to 4, 8, 12. The k-nearest neighbor (k-NN), random forest (RF), and decision trees (DT) algorithms were used for the classification of dried products based on image processing and color properties. In all models, 70% of the data was used for training and 30% for testing [9, 21]. In the study, 4-8-1 MLP-ANN structure applied for moisture content, moisture ratio and drying rate are given in Figure 2. Model performance was assessed through the following statistical indices: root mean square error (RMSE), mean absolute error (MAE), mean absolute percentage error (MAPE) were calculated by equations (11-13) [22].

$$MAE = \sum_{i=1}^{n} \frac{| E_i - M_i |}{n} \quad (11)$$

$$RMSE = \sqrt{\frac{\sum_{i=1}^{n} (E_i - M_i)^2}{n}} \quad (12)$$

$$MAPE = \frac{1}{n} \sum_{i=1}^{n} \left| \frac{E_i - M_i}{E_i} \right| \times 100 \quad (13)$$

Where; n: Number of data, M_i: Measured target value, E_i: Estimated target value, $\dot{M}$: Average of measured target values, $\dot{E}$: Average of estimated target values, S_E: Sum of estimated target values, S_M: Sum of measured target values. Correlation coefficients (R) were analyzed to assess the success of estimations in accordance with the principles specified in Colton [23]. Experimental data were subjected to analysis of variance (ANOVA) in accordance with full-factorial design. Significant means were compared with the use of Tukey's multiple comparison test at 95% significance level. Statistical analyses were performed with the use of SPSS v20.0 software [24].

III. RESULTS AND DISCUSSION

Experimental data for the drying of plums were converted to moisture content and handled with nine different mathematical models. In the current study, the model that defined drying with the highest success was Logistic (Table 1). In the study, statistically, the change in L*, a*, b*, and C (outer) color properties were found to be significant at the level of 99%, while the change in only C (inner) color properties was found to be significant at the 95% level. Color change and rehydration properties were not statistically significant. The highest L*, a*, b*, and C values and rehydration values were obtained at 100W drying. The most color change was seen at 200W drying (Table 2).

Figure 1: Plums before and after drying.

Table 1: Statistical results of different thin layer drying models.

Method	Models	Page	Henderson & Pabis	Newton	Two-term	Wang& Singh	Verma	Logistic	Jena& Das	Alibaş
100W	R^2	0.9979	0.9859	0.9800	0.9859	0.9990	0.9979	0.9992	0.9967	0.9945
	SEE	0.0140	0.0365	0.0429	0.0374	0.0099	0.0143	0.0085	0.0180	0.0238
200W	R^2	0.9990	0.9875	0.9821	0.9875	0.9964	0.9939	0.9979	0.9980	0.9956
	SEE	0.0150	0.0374	0.0431	0.0407	0.0199	0.0272	0.0160	0.0164	0.0252
300W	R^2	0.9977	0.9795	0.9715	0.9795	0.9988	0.9972	0.9990	0.9988	0.9975
	SEE	0.0154	0.0466	0.0534	0.0494	0.0113	0.0176	0.0108	0.0120	0.0179

Table 2: Color characteristics of plum samples.

Method	L* (outer)	L* (inner)	a* (outer)	a* (inner)	b* (outer)	b* (inner)	C (outer)	C (inner)	ΔE (outer)	ΔE (inner)	Rehydration
Fresh	27.39±4.99^{a}	48.59±5.17^{a}	5.38±1.61^{b}	3.26±0.63^{b}	-5.01±1.54^{b}	20.41±2.98^{a}	7.61±0.77^{b}	20.41±2.98^{ab}	-	-	-
100W	26.20±3.17^{a}	28.72±3.36^{a}	11.99±1.75^{a}	17.45±1.32^{a}	-0.86±1.54^{a}	9.20±2.93^{b}	12.13±1.64^{a}	19.89±1.78^{b}	10.00±2.74	27.44±4.59	2.27±0.22
200W	18.35±4.00^{b}	22.86±3.14^{d}	10.44±2.42^{a}	16.40±1.88^{a}	-0.99±2.64^{a}	12.19±5.60^{b}	10.82±2.23^{a}	20.73±4.65^{ab}	12.17±4.22	31.03±4.99	2.00±0.20
300W	23.21±3.63^{a}	24.91±3.00^{bc}	10.86±3.46^{a}	16.91±2.17^{a}	-1.23±1.50^{a}	16.66±3.58^{a}	11.08±3.27^{a}	23.85±3.42^{a}	9.66±3.16	28.34±5.61	1.83±0.18
Mean	23.78±5.24	31.27±10.95	9.67±3.48	13.50±6.19	-2.02±2.51	14.62±5.75	10.41±2.71	21.22±3.62	10.61±3.51	28.93±5.17	2.03±0.26
F values	12.15**	117.39**	17.62**	216.28**	13.67**	18.91**	9.60**	3.38*	1.88	1.63	3.54

* Means shown with different letters in the same column represent statistical difference ($p<0.05$), **: $p<0.01$.

Table 3: Performance metrics of dried plums according to *R, G, B, L, a, b, H, S* and *B* color channels of machine learning algorithms.

Algorithm	Accuracy (%)	TPR	FPR	Precision	Recall	F-measure	MCC	ROC Area	PRC Area
k-NN	96.10	0.961	0.019	0.961	0.961	0.961	0.943	0.971	0.937
RF	92.18	0.922	0.037	0.922	0.922	0.922	0.885	0.985	0.969
DT	89.92	0.899	0.051	0.921	0.899	0.897	0.860	0.971	0.922

TPR – True positive rate, FPR – False positive rate, MCC - Matthews correlation coefficient, ROC Area - Receiver operating characteristic, PRC Area - Precision-recall curve.

E-ISBN: 978-605-72066-2-6

Table 4: Energy aspects of the drying conditions.

Method	Drying time (min)	E_c (kWh)	Total E_c (kW)	SEC (kWh kg^{-1})	SMER (kg kWh^{-1})	η_{en} (%)	η_{th} (%)
100W	492	0.20	100.37	0.58	1.73	7.07	1.44
200W	84	0.54	45.36	1.57	0.64	15.31	8.27
300W	57	0.86	49.25	2.27	0.44	15.55	13.44

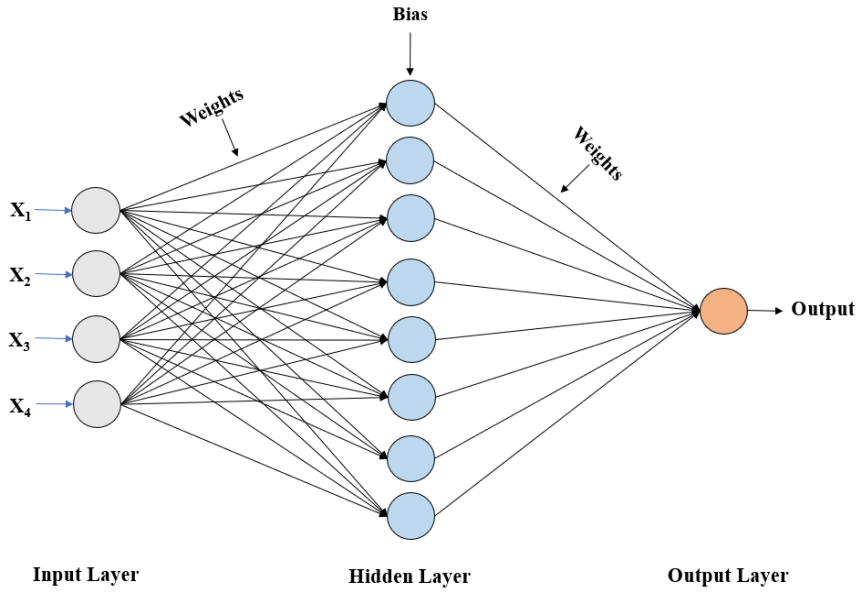

Figure 2: 4-8-1 MLP-ANN structure applied in the study for moisture content, moisture ratio and drying rate.

Table 5: Performance results of models in estimating drying characteristics.

Moisture content (w.b.)				
Model	R^2	MAE	RMSE	MAPE
MLP-ANN (4-4-1)	0.996	0.017	0.020	0.048
MLP-ANN (4-8-1)	0.997	0.012	0.016	0.024
MLP-ANN (4-12-1)	0.997	0.011	0.016	0.027
Moisture ratio				
Model	R^2	MAE	RMSE	MAPE
MLP-ANN (4-4-1)	0.993	0.013	0.024	0.079
MLP-ANN (4-8-1)	0.998	0.008	0.013	0.105
MLP-ANN (4-12-1)	0.995	0.013	0.020	0.149
Drying rate				
Model	R^2	MAE	RMSE	MAPE
MLP-ANN (4-4-1)	0.868	0.051	0.089	0.225
MLP-ANN (4-8-1)	0.855	0.055	0.093	0.213
MLP-ANN (4-12-1)	0.840	0.056	0.098	0.208

*MLP-ANN parameters; η: learning rate: 0.3; α: momentum coefficient:0.2; NoE: number of epocs:500; activation function: sigmoid, train - test ratio (%70, %30).

In the study, the algorithm that classified the dried products with the highest success was k-NN with 96.10%, while this algorithm was followed by RF with 92.18%. In ROC area values, which is another performance metric that supports the accuracy of classification, the highest value of 0.985 was obtained in the RF algorithm. The k-NN and DT algorithms had the same values as 0.971 (Table 3).

Total energy consumption values are measured as 100.37, 45.36, and 49.25 kWh for 100, 200, and 300W, respectively. The highest SEC value was calculated with 2.27 kWh kg^{-1} in 300W drying, and the highest SMER value was calculated in 100W drying with 1.73 kg kWh^{-1}. In the study, it was determined that the energy and thermal efficiency increased as the microwave power increased (Table 4).

In the study, similar R^2 results were obtained for all MLP structures for moisture content estimation. The highest R^2 value for the estimation of moisture ratio was determined in the 4-8-1 model with 0.998. RMSE and MAPE results also support this model. In the estimation of drying rate, the highest R^2 value was found in the 4-4-1 model with 0.968, and the lowest MAE and RMSE values were found in the same model (Table 5).

IV. Conclusion

It has been determined that all developed ANN structures are proper for the estimation of drying properties. In addition, dried plums have been successfully classified by machine learning. In addition, when all criteria were evaluated, it was determined that the condition that gave the most successful results for drying plums was 100W.

References

[1] S. Özvardar, and K. Önal, *Erik Yetiştiriciliği*. İstanbul, Türkiye: Kocaoluk Yayınevi, 1990.

[2] Anonim. Mürdüm Eriği, Erişim adresi: http://www.ahufrenk.com/2012/10/murdum-erigidamson.html. (Erişim Tarihi: 03.10.2021)

[3] A. S. Kartal, Mikrodalga ve Kuru Hava Yardımıyla Kurutma Yöntemlerinin Meyve Pestillerinin Kuruma Sürelerine Etkilerinin İncelenmesi. İstanbul Teknik Üniversitesi, Fen Bilimleri Enstitüsü, Gıda Mühendisliği Anabilim Dalı, Yüskek Lisans Tezi, İstanbul, 91 s, 2011.

[4] A. Sarimeseli, "Microwave drying characteristics of coriander (*Coriandrum sativum* L.) leaves," *Energy Conversion and Management*, vol. 52, pp. 1449-1453, 2011.

[5] A. Yagcıoglu, *Drying Techniques of Agricultural Products*. Ege University, Faculty of Agriculture, Publication No: 536, Bornova,Izmir, Turkey (in Turkish), 1999.

[6] P. W. Y. Sham, C. H. Scaman, and T. D. Durance, "Texture of vacuum microwave dehydrated apple chips as affected by calcium pretreatment, vacuum level, and apple variety," *Journal of Food Science*, vol. 66, pp. 1341-1347, 2001.

[7] P. P. Lewicki, and E. Jakubczyk, "Effect of hot air temperature on mechanical properties of dried apples", *Journal of Food Engineering*, vol. 64: pp. 307-314. 2004.

[8] D. Kumar, S. Prasad, and G. S. Murthy, "Optimization of microwave-assisted hot air drying conditions of okra using response surface methodology", *Journal of Food Science and Technology*, vol. 51, pp. 221-232. 2014.

[9] N. Çetin, "Prediction of moisture ratio and drying rate of orange slices using machine learning approaches", *Journal Food Processing and Preservation*, e17011, 2022.

[10] N. Cetin, M. Yaman, K. Karaman, and B. Demir, "Determination of some physicomechanical and biochemical parameters of hazelnut (*Corylus avellana* L.) cultivars", *Turkish Journal of Agriculture and Forestry*, vol. 44, pp. 439-450, 2020.

[11] H. Pinar, N. Çetin, B. Ciftci, K. Karaman, and M. Kaplan, "Biochemical composition, drying kinetics and chromatic parameters of red pepper as affected by cultivars and drying methods", *Journal of Food Composition and Analysis*, vol. 102:103976, 2021.

[12] I. Doymaz, "Convective air drying characteristics of thin layer carrots", *Journal of Food Engineering*, vol. 61, pp. 359-364, 2004.

[13] O. Taskin, "Evaluation of freeze drying for whole, half cut and puree black chokeberry (*Aronia melanocarpa* L.)", *Heat Mass Transfer*, vol. 56, pp. 2503-2513, 2020.

[14] İ. T. Toğrul, D. and Pehlivan, "Modelling of thin layer drying kinetics of some fruits under open-air sun drying process". *Journal of Food Engineering*, vol. 65, pp. 413-425, 2004.

[15] D. Arslan, and M. M. Özcan, "Study the effect of sun, oven and microwave drying on quality of onion slices", *LWT-Food Science and Technology*, vol. 43, pp. 1121-1127, 2010.

[16] Y. Soysal, S. Öztekin, and Ö. Eren, "Microwave drying of parsley: modelling, kinetics, and energy aspects", *Biosystem Engineering*, vol. 93, pp. 403-413, 2006.

[17] S. Jena, and H. Das, "Modelling for vacuum drying characteristics of coconut presscake, *Journal of Food Engineering*, vol. 79, pp. 92-99, 2007.

[18] İ. Alibaş, "Microwave drying of grapevine (Vitis vinifera L.) leaves and determination of some quality parameters", *Journal of Agricultural Science*, vol. 18, pp. 43-53, 2012.

[19] N. Therdthai, and W. Zhou, "Characterization of microwave vacuum drying and hot air drying of mint leaves (*Mentha cordifolia* Opiz ex Fresen)", *Journal of Food Engineering*, vol. 91, pp. 482-489, 2009.

[20] M. Beigi, "Energy efficiency and moisture diffusivity of apple slices during convective drying", *Food Science and Technology*, vol. 36, pp. 145-150, 2016.

[21] C. Sağlam, and N. Çetin, "Machine learning algorithms to estimate drying characteristics of apples slices dried with different methods", *Journal Food Processing and Preservation*, e16496, 2022.

[22] J. R. Parker, "Rank and response combination from confusion matrix data", *Information Fusion*, vol. 2, pp. 113-120, 2001.

[23] T. Colton, *Statistics in Medicine*. Little Brown and Co, New York, pp. 179, 1974.

[24] IBM SPSS® *Statistical Software*. SSS Inc., IBM Company©, Version 20.0, 2010.

The effect of gradually increasing microwave power on the drying kinetics, color parameters and energy aspects of carrots

N. ÇETİN[1] and S. GÜNAYDIN[1]

[1] Erciyes University, Kayseri/Turkey, necaticetin1990@gmail.com; sedagunaydın07@gmail.com

Abstract **- Carrot is an important food source rich in vitamins, carotene, and dietary fibers. Due to its perishable nature, it is critical to choose a proper preservation method to preserve its nutritive properties. By drying the carrots, the products are evaluated economically in the post-harvest processes and the shelf life of the products is extended. In the present study, the effects of gradually increasing microwave power levels on the drying kinetics, color and rehydration properties were determined. In addition, the specific energy consumption, specific moisture extraction rate, energy efficiency, thermal efficiency, effective moisture diffusivity and activation energy values of different microwave power levels were determined. In the study, the color characteristics *(R, G, B, L, a, b, H, S,* and *V)* of the dried products were obtained by image processing method and the discrimination of the products according to the drying conditions was performed by machine learning approach. As a result, accuracy values above 0.85 were obtained in the discrimination. Additionally, color characteristics were found to be statistically significant in the study ($p<0.05$).**

Keywords **- Microwave, carrot, rehydration, energy, machine learning.**

I. INTRODUCTION

The carrot is a member of the family Apiaceae [1], and it is a two-year herbaceous cultivated plant grown for its cone-shaped fleshy root. It is an herbaceous cultivar cultivated for its cone-shaped fleshy root [2]. Carrot is very rich in minerals, vitamins A and E, antioxidants, total phenolics, beta carotene, and anthocyanins [3], and there is purple, orange, black, white, red, and yellow varieties [4]. Carrots with many health benefits, strengthen the immune system [5], prevents heart diseases [4], provides high blood pressure [6], protects the skin from harmful sun rays thanks to the β-carotene it contains, has a healing effect on skin diseases [7], with its abundant vitamin A effect and it is also preventing fatty liver [8]. Carrots are also important to increase the shelf life of products with high moisture content by drying them. Drying is the reduction of high moisture of agricultural products to a level where microorganism activities cease [9]. The main purpose of drying; is the optimization of nutritional quality properties of foods by reducing drying time and energy consumption [10]. The microwave drying method is based on the principle that the energy of motion, which occurs because of the vibration of the water molecules in the structure of the products by the magnetron in the oven, is converted into heat energy. This method, from the innermost part of the products to the outermost part, dries with its own internal energy [11]. The microwave drying method saves drying time and energy consumption [12]. At the same time, microwave-dried products give very good results in terms of color and nutrient content [13]. The high risk of burning in the microwave drying of sugary products, the fact that the products do not dry homogeneously, and the high initial investment are among the disadvantages [14].

The aim of this study is to determine the effects of microwave levels on drying time, energy consumption, color parameters, and rehydration capacity by drying carrot slices with microwave at 100 W, 200 W and 300 W. In addition, the color properties of the dried products were determined by the image processing method, and the discrimination of the products according to the drying conditions was performed using machine learning.

II. MATERIAL AND METHOD

The carrots used in the study were obtained from a local market in Kayseri. In order not to lose moisture, the fresh products were brought to the drying laboratory in refrigerator and stored at +4 °C during the drying period. Carrot slices to be dried were weighed 30.00 ± 0.05 g for each trial. The average slice thickness was measured as 15.00 mm. Microwave drying processes were carried out with a hybrid dryer (Arçelik KMF 833 I, Turkey) at 100, 200, and 300W power. The study was carried out with 3 replications. To determine the initial moisture content of the carrot, the products were kept in an oven at 70 °C for 48 hours (Memmert UN55, Germany). Dried carrots with different color channels are given in Figure 1. In the study, six different thin layer drying models were applied as Page [15], Henderson & Pabis [16], Newton [17], Verma [18], Logistic [19], and Alibaş [20]. The moisture ratio (MR) of carrots during drying was determined using equation (1) [15], the drying rate (DR), which indicates moisture removal per unit time, was calculated using equation (2) [21], and moisture content (M_c) values on a wet basis (wet basis, w.b.) were determined using equation (3) [22]:

$$MR = \frac{M_t - M_e}{M_o - M_e} \quad (1)$$

$$DR = \frac{M_{t+dt} - M_t}{dt} \quad (2)$$

$$M_c = \frac{W_i - W_f}{W_i} \times 100 \quad (3)$$

Where, M_t, moisture content (g water g dry matter^{-1}) at a particular time, M_e, equilibrium moisture, and M_o, initial moisture, W_i, initial weight (g) W_f, final weight (g), Mt+dt, moisture content at time t dt (g water. g dry matter^{-1}), dt, drying time (min).

The color properties of fresh and dried carrots were measured in the CIELab color space with the aid of a colorimeter (PCE-CSM 5 PCE Instruments, Germany). Chroma and total color change values were calculated by equations (4, 5) [15].

$$C = \sqrt{(a^*)^2 + (b^*)^2} \quad (4)$$

$$\Delta E = \sqrt{(L^* - L^*_0)^2 + (a^* - a^*_0)^2 + (b^* - b^*_0)^2} \quad (5)$$

A digital wattmeter (Tt Technic PM-001, Turkey) was used to determine the energy consumption of the microwave dryer. Specific energy consumption (SEC), specific moisture absorption rate (SMER), energy efficiency (η_{en}), and thermal efficiency (η_{th}) were calculated with the equations (6-10) [17, 23].

$$SEC = \frac{E_c}{m_w} \quad (6)$$

$$SMER = \frac{m_w}{E_c} \quad (7)$$

$$\eta_{en} = \frac{m_w \lambda_{wp}}{E_c} \quad (8)$$

$$\frac{\lambda_{wp}}{\lambda_w} = 1 + 23\exp(-0.4X) \quad (9)$$

$$\eta_{th} = \frac{P A \lambda_w (M_o - M_e)}{F t (100 - M_e)} \quad (10)$$

Where m_w is the evaporated water mass (kg), X is the sample moisture content (kg water kg dry matter^{-1}), λ_w is the water latent heat (J kg^{-1}) and λ_{wp} is the latent heat of the product (J kg^{-1}), P is the amount of product in the system (kg m^{-2}), A is the area of the tray (m^2), λ_w is the latent heat of evaporation of water (kJ kg^{-1}), M_e is the amount of water evaporated from the product (kg), F is the heating capacity utilization (kW), and t is drying time.

The rehydration capacity of carrot slices was calculated according to the method proposed by Lewicki and Witrowa-Rajchert [24]. In this context, dried carrot slices, weighing approximately 3 g, were kept in 100 mL of distilled water for 8 hours. At the end of this period, the samples were on the filter paper for 30 minutes to remove the unabsorbed water accumulated on the outer surface of the samples taken from the pure water. The rehydration capacity of the products was determined using the equation (11):

$$RR = \frac{m_2}{m_1} \quad (11)$$

Where, m_1 and m_2 are the weights before and after drying, respectively.

The resulting single slice carrot images were taken with a black background. Then, the background was performed white by removing by Photoshop and processed by Image J software and converted to *R, G, B, L, a, b, H, S* and *B* color channels. The minimum, maximum, mean and median values of the color channels were used for classification. The 60 single images were taken for each drying method. The k-nearest neighbor (k-NN), random forest (RF) and decision trees (DT) algorithms were used for the classification of dried products based on image processing and color properties. In all models, 70% of the data was used for training and 30% for testing. Model performances of machine learning algorithms for classification were determined by the following metrics (12-19) [25].

Accuracy=(TP+TN)/(TP+FP+TN+FN) x 100 (12)
TPR (Recall)=TP/(TP+FN) (13)
FPR=FP/(FP+TN) (14)
Precision=(TP/TP+FP) (15)
F-Measure=2TP/(2TP+FP+FN) (16)
MCC=((TP∗TN)-(FN∗FP))/
√((TP+FN)∗(TN+FP)∗(TP+FP)∗(TN+FN)) (17)
ROC Area= Area Under TPR vs. FPR Curve (18)
PRC Area= Area Under Precision vs. Recall Curve (19)

Where, TP: true positive, TN: true negative, FP: false positive, FN: false negative.

Experimental data were subjected to analysis of variance (ANOVA) in accordance with full-factorial design. Significant means were compared with the use of Tukey's multiple comparison test at 95% significance level. Statistical analyses were performed with the use of SPSS v20.0 software [26].

III. RESULTS AND DISCUSSION

Carrot slices with an initial moisture content of 7.00 ± 0.33 kgwater kg dm^{-1} were dried at 100, W, 200 W and 300 W microwave powers until the final moisture content was 0.1363 ± 0.001 kgwater kgdm^{-1} (12% w.b.). These drying processes were completed 100, 54 and 45 minutes, respectively. In the study, drying at 100 W compared to 200 W and 300 W, respectively; it has been found that it takes 1.85 and 2.22 times longer. When evaluated in terms of dryer performance, it was reported that the lowest energy consumption was measured at 300 W microwave power, which has the shortest drying time. The statistical parameters (R^2, *SEE*) related to the experimental data and the estimation data obtained from six different thin layer drying model used in this study are presented in Table 1 for drying at 100 W, 200 W and 300 W. According to the Figure 2, it has been determined that the estimation model that gives the closest results to the experimental data is the Logistic model for 100 and 200 W, and the Verma model for 300 W.

Experimental moisture contents of carrot slices dried by

microwave drying method and estimated moisture contents calculated by estimation model and curves of drying rate-moisture content are presented in Figure 2. According to Figure 1, it was determined that 17% of the separable moisture in the first 20 minutes was removed from the product in the drying method at 100 W. Following this, the separable humidity rate in the first 20 minutes at 200 W and 300 W, and was reported that 62% and 84% evaporated, respectively. According to the data obtained, it was seen that the method with the slowest moisture remove was 100 W, which is the lowest microwave power. According to John and Solomon [27] microwave drying of carrot slices at 180 W and 360 W, the separable moisture content in the first 20 minutes was authors determined that 20% and 86%. These values comply with present study. Albayrak and Külcü [28] dried the carrot slices, which authores determined to have an initial moisture content of 88%, by microwave drying method until the final moisture content was 10%. In the study, it was found that at a power density of 2.16 Wg^{-1}, approximately 65% of the separable moisture content in the first 20 minutes was removed from the product. The time-dependent drying rate curves of carrot slices in the present study are given in Figure 2. According to Figure 2, while the drying rate tended to increase at the beginning of drying for all three methods, after a while, the products entered the drying phase at a constant speed. The drying phase with decreasing speed was recorded in the final stages of drying when the products started to approach the equilibrium moisture. It was determined that the drying rate increased with the increase in microwave level. In the first phase of drying, the products have a high moisture content. Çelen and Moralar [29] stated that in the microwave drying of carrot slices at 1050 W, 1500 W, and 2100 W, drying occurs rapidly since the products have high moisture content in the first stage of drying, but the drying rate decreases as the products begin to lose most of moisture content. According to Table 1, the regression values is the main criterion by taking into account the determination of the best estimation model, and this value should be close to 1.00. Similarly, the numerical readers of the standard error of the estimation are required to be close to 0.00. In this study, the Logistic model was the best model for microwave drying at 100 and 200 W, and the Verma model for drying at 300 W. The R^2 values were determined for 100 W and 200 W in the logistic model as 0.9859 and 0.9882, respectively. However, the R^2 value was found to be 0.9992 in the Verma model, which was the best model for 300 W. In the Logistics model, the *SEE* values were determined for 100 W and 200 Was 0.0384 and 0.0423, respectively. In addition, it was determined that the *SEE* was 0.0101 in the Verma model for 300 W.

The color properties of the carrot slices are shown in Table 2. The lowest value of the *L* which expresses the brightness and darkness of the samples was measured at 100 W microwave power. It was noted that the darkness increased by 2.05 times at 100 W compared to the fresh product. This is thought to be related to the fact that products are exposed to microwave energy for a long time at the lowest microwave power of 100 W. It was observed that *a*, which represents the greenness and redness of the color, is almost the same with the fresh product at 100 W and 300 W microwave power. It was determined that there was no significant difference between the groups in terms of the greenness/redness (*a*) value. The closest value of *b* value, which is the yellowness/blueness indicator of the products, to the fresh product was measured at 200 W. It was determined that the highest value of chroma which is the indicator of light and pastel tones of the color, is in the fresh product in carrots dominated by orange color. The chroma value closest to the fresh product was obtained in the microwave drying method at 200 W. Since the fresh product was taken as the basis for the determination of the total color change, the total color change in the fresh product was accepted as zero. It was determined that the method with the highest total color change, which is an important criterion in determining how the products are affected by the drying process. The lowest color change was measured at 200 W. Yildiz [30] reported that the highest *b* value was measured at 200 W in the drying of carrot slices at 55, 65, and 75 °C by convective, freeze, and microwave powers of 100 W and 200 W. In the present study, the highest *b* value was also measured in the microwave drying method at 200 W.

According to Altikat et al. [31] microwave-dried oyster mushrooms at 90 W, 180 W, 360 W, and 600 W. Comply to present study, it was reported that the greatest total color change was recorded at 90 W in about longer drying time. Darici et al. [32] was reported that the maximum total color change occurred at 90 W in the microwave drying of a bell pepper at 90 W, 180 W, and 90 + 180 W applications. Fathabadi et al. [33] indicated that the maximum total color change was measured at 180 W microwave power in microwave drying of red beet at 180, 360, and 600 W. Rehydration capacity values are also presented in Table 2. The highest rehydration capacity value was measured at 200 W microwave power. On the other hand, the lowest rehydration capacity was found at 100 W microwave power. The rehydration capacity measured at 200 W was found to be 39% higher than at 100W. Total energy consumption values are measured as 28.56, 29.16 and 38.88 kWh for 100, 200 and 300W, respectively. The highest SEC value was calculated with 11.85 kWh kg^{-1} in 300W drying, and the highest SMER value was calculated with 0.36 kg kWh^{-1} in 100W drying. In the study, as the microwave power increased, the energy efficiency decreased, and the thermal efficiency increased (Table 3).

In the present study, the most successful algorithm for all color parameters was RF (92.59%), followed by DT (87.16%). The most successful color space was the *Lab* color space. The highest accuracy result in the *Lab* color space was also obtained in the RF (90.37%) algorithm. Among all color channels, the most successful color channel was *b*, and the accuracy rates were 93.33%, 93.33% and 95.56% for k-NN, RF and DT, respectively (Table 4). The confusion matrix created for classification according to all color channels is presented in Table 5. It was given that the algorithm with the highest true positive value is RF. However, the success of the RF algorithm is also supported by the results of the performance metrics (Table 6). Performance metrics of dried carrots according to L, a, b color space of machine learning algorithms is given in Table 7. It was determined that the performance metrics here also support the classification results.

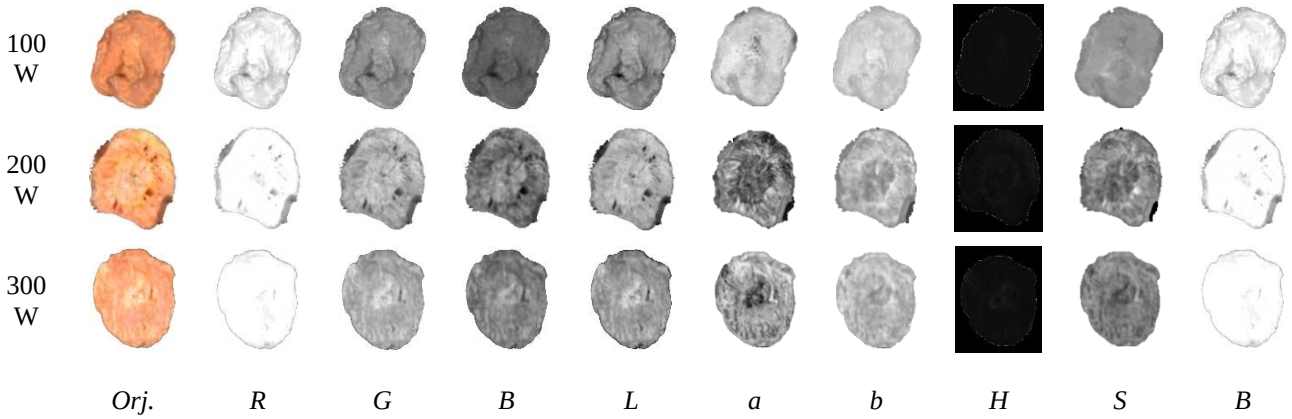

Figure 1: Images of carrot slices subjected to microwave drying converted to different color channels.

Table 1: Statistical results of different thin layer drying models according to methods.

Method	Models	Page	Hend.&Pabis	Newton	Verma	Logistic	Alibaş
100W	R^2	0.9722	0.9599	0.9596	0.9601	0.9859	0.9812
	SEE	0.0525	0.0631	0.0617	0.0648	0.0384	0.0473
200W	R^2	0.9810	0.9566	0.9536	0.9624	0.9882	0.9862
	SEE	0.0502	0.0759	0.0740	0.0756	0.0423	0.0542
300W	R^2	0.9983	0.9860	0.9843	0.9992	0.9860	0.9908
	SEE	0.0134	0.0384	0.0343	0.0101	0.0410	0.0384

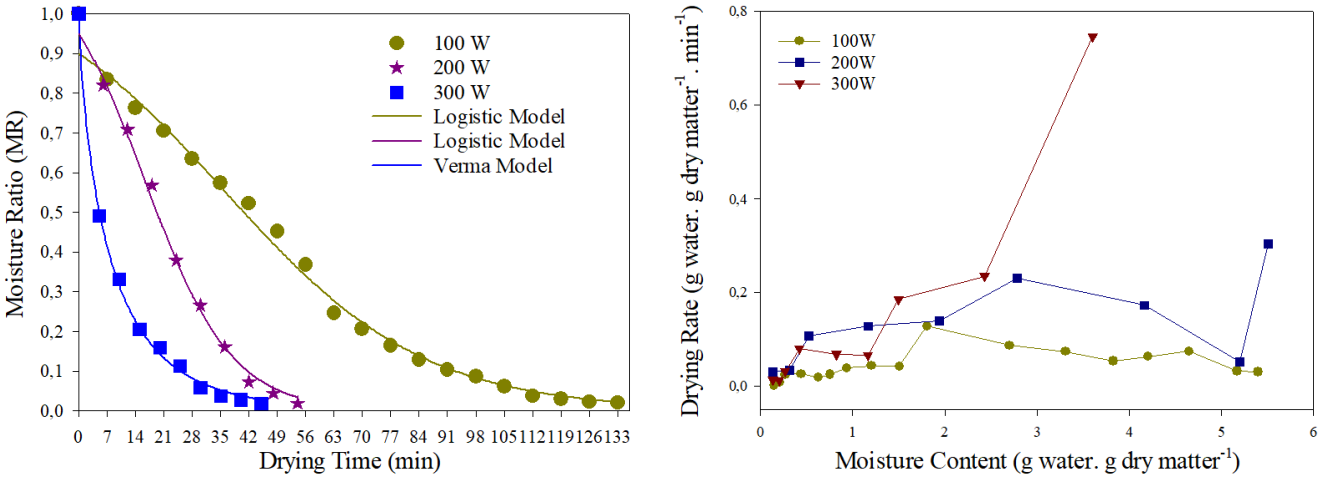

Figure 2: Time dependent moisture ratio curves (left) and curves of drying rate-moisture content

Table 2: Color and rehydration characteristics of carrot samples.

Method	*L**	*a**	*b**	*C**	*ΔE**	Rehydration
Fresh	47.04±0.79^{a}	24.75±0.35^{a}	42.61±0.57^{a}	49.29±0.63	0.00±0.00^{c}	
100W	22.95±2.11^{c}	24.96±0.69^{b}	30,92±0.23^{b}	40.46±1.54	27.65±3.00^{a}	4.40±0.68
200W	43.07±0.75^{ab}	25.50±0.49^{b}	32.63±0.95^{b}	41.48±0.95	12.34±1.11^{b}	6.14±1.22
300W	40.26±1.26^{b}	24.31±0.77^{b}	30.05±1.12^{b}	38.72±1.27	16.25±1.25^{b}	4.73±0.20
Mean	38.39±1.21	24.89±0.29	34.03±0.87	42.47±0.72	14.01±1.39	5.10±4.48
F values	62.65**	0.67*	18.01**	16.34**	44.05**	1.27*

* Means shown with different letters in the same column represent statistical difference ($p<0.05$), **: $p<0.01$.

Table 3: Energy aspects of the drying conditions.

Method	Drying time (min)	E_c (kWh)	Total E_c (kW)	SEC (kWh kg^{-1})	SMER (kg kWh^{-1})	η_{en} (%)	η_{th} (%)
100W	140	0.20	28.56	2.77	0.36	5.18	1.06
200W	54	0.54	29.16	8.18	0.12	4.56	2.46
300W	45	0.86	38.88	11.85	0.08	3.78	3.26

Table 4. Classification accuracy results of different machine learning algorithms for all color channels and color spaces.

Algorithm	*All*	*RGB*	*Lab*	*HSB*	*R*	*G*	*B*	*L*	*a*	*b*	*H*	*S*	*B*
k-NN	85.43	89.63	88.15	79.26	97.78	91.11	88.89	91.11	93.33	93.33	75.56	77.78	95.56
RF	92.59	87.40	90.37	85.19	93.33	91.11	95.56	91.11	91.11	93.33	73.33	88.89	91.11
DT	87.16	82.96	84.44	79.26	86.67	88.89	88.89	86.67	82.22	95.56	75.56	73.33	84.44

Table 5: Confusion matrix for classification by all color channels.

k-NN			
100W	200W	300W	
117	5	5	100W
5	111	21	200W
8	15	118	300W
RF			
100W	200W	300W	
122	3	2	100W
0	125	12	200W
4	9	128	300W
DT			
100W	200W	300W	
113	6	8	100W
2	120	15	200W
6	15	120	300W

Table 6: Performance metrics of dried carrots according to *R, G, B, L, a, b, H, S* and *B* color channels of algorithms.

Algorithm	TPR	FPR	Precision	Recall	F-measure	MCC	ROC Area	PRC Area
k-NN	0.854	0.074	0.854	0.854	0.854	0.780	0.891	0.783
RF	0.926	0.038	0.926	0.926	0.926	0.888	0.988	0.977
DT	0.872	0.066	0.873	0.872	0.872	0.807	0.927	0.858

TPR – True positive rate, FPR – False positive rate, MCC - Matthews correlation coefficient, ROC Area - Receiver operating characteristic, PRC Area - Precision-recall curve.

Table 7. Performance metrics of dried carrots according to L, a, b color space of machine learning algorithms.

Algorithm	TPR	FPR	Precision	Recall	F-measure	MCC	ROC Area	PRC Area
k-NN	0.881	0.060	0.884	0.881	0.881	0.823	0.911	0.819
RF	0.904	0.048	0.913	0.904	0.903	0.860	0.982	0.968
DT	0.844	0.089	0.858	0.844	0.846	0.772	0.879	0.773

TPR – True positive rate, FPR – False positive rate, MCC - Matthews correlation coefficient, ROC Area - Receiver operating characteristic, PRC Area - Precision-recall curve.

IV. CONCLUSION

In this study, carrot slices were dried at 100 W, 200 W and 300 W by microwave drying method. The drying time for the specified drying methods, respectively; It was completed in 100, 54 and 45 minutes. It has been determined that the drying time is shortened with the increase of the microwave power level, and accordingly the energy consumption is reduced. At the same time, since the products contain intense moisture in the first stages of drying, drying took place very quickly. However, when the products started to lose a large part of their moisture, their drying speed decreased. The best results in terms of color parameters and rehydration capacity were obtained in the microwave drying method at 200 W. In our study, it was determined that the highest darkening was measured in products dried at 100 W, which has the longest drying time. It was found appropriate to use 200 W microwave power for drying carrot slices. In addition, all developed models offered classification accuracy over 0.85. In this sense, the most successful algorithm was RF, and the most successful color space was *Lab*. In addition, it was determined that the condition that gave the most successful results for the drying of carrots was 100W.

REFERENCES

[1] N. Rajora, V. Thakral, S. Vats, G. Padalkar, S. Sudhakaran, S. Kumawat, and Deshmukh, R. "Understanding aquaporins regulation and silicon uptake in carrot (Daucus carota)", Journal of Plant Biochemistry and Biotechnology, vol. 213, pp. 1-12, 2022.

[2] S. Surbhi, R. C. Verma, R. Deepak, H. K. Jain, and K. K. Yadav, "A review: Food, chemical composition and utilization of carrot (Daucus carota L.) pomace", International Journal of Chemical Studies, vol. 6, pp. 2921-2926, 2018

[3] A. Al-Achi, A Concise Treatise on Natural Remedies. Cambridge Scholars Publishing, 2020.

[4] M. N. Singh, R. Srivastava, and I. Yadav, "Study of different varietis of carrot and its benefits for human health: a review", Journal of Pharmacognosy and Phytochemistry, vol. 10, pp. 1293-1299, 2021.

[5] B. K. Baidya, and P. Sethy, "Importance of fruits and vegetables in boosting our immune system amid COVID19", Food and Scientific Reports, vol. 1, pp. 50-55, 2020.

[6] H. Rasheed, M. Shehzad, R. Rabail, P. Ł. Kowalczewski, M. Kidoń, P. Jeżowski, and Aadil, R. M. "Delving into the nutraceutical benefits of purple carrot against metabolic syndrome and cancer: A review", Applied Sciences, vol. 12, 3170, 2022.

[7] U. R. Chaudhari, C. Jaydeep, V. Jigar, and G. Janhvi, "Herbal radish and carrot topical gel", Research Journal of Topical and Cosmetic Sciences, vol. 11, pp. 65-69, 2020.

[8] M. Romero-Gómez, R. Aller, and F. Martín-Bermudo, "Dietary Recommendations for the Management of Non-alcoholic Fatty Liver Disease (NAFLD): A Nutritional Geometry Perspective", In Seminars in Liver Disease. Thieme Medical Publishers, Inc, 2022.

[9] D. Alp, and Ö. Bulantekin, "The microbiological quality of various foods dried by applying different drying methods: a review", European Food Research and Technology, vol. 247, pp. 1333-1343, 2021

[10] S. Günaydın, C. Sağlam, and N. Çetin, "Drying methods used in drying of agricultural products", ETHAB, vol. 5, pp. 30-45, 2022.

[11] S. L. Talebzadeh, H. Fatemi, M. Azizi, M. Kaveh, A. Salavati Nik, M. Szymanek, and R. Kulig, "Interaction of Different Drying Methods and Storage on Appearance, Surface Structure, Energy, and Quality of Berberis vulgaris var. asperma", Foods, vol. 11(19), 3003, 2022.

[12] K. K. Hnin, M. Zhang, A. S. Mujumdar, and Y. Zhu, "Emerging food drying technologies with energy-saving characteristics: A review", Drying Technology, vol. 37, pp. 1465-1480, 2018.

[13] G. Behera, M. Madhumita, J. Aishwarya, and V. Gayathri, "Comparative evaluation of drying kinetics of carrot slices in hot air and microwave drying", The Journal of Phytopharmacology, vol. 10, pp. 242-248, 2021.

[14] J. Li, J. Tao, B. Yan, L. Jiao, G. Chen, and J. Hu, "Review of microwave-based treatments of biomass gasification tar", Renewable and Sustainable Energy Reviews, vol. 150, 111510, 2021.

[15] H. Pinar, N. Çetin, B. Ciftci, K. Karaman, and M. Kaplan, "Biochemical composition, drying kinetics and chromatic parameters of red pepper as affected by cultivars and drying methods", Journal of Food Composition and Analysis, vol. 102:103976, 2021.

[16] I. Doymaz, "Convective air drying characteristics of thin layer carrots", Journal of Food Engineering, vol. 61, pp. 359-364, 2004.

[17] O. Taskin, "Evaluation of freeze drying for whole, half cut and puree black chokeberry (Aronia melanocarpa L.)", Heat Mass Transfer, vol. 56, pp. 2503-2513, 2020.

[18] Y. Soysal, S. Öztekin, and Ö. Eren, "Microwave drying of parsley: modelling, kinetics, and energy aspects", Biosystem Engineering, vol. 93, pp. 403-413, 2006.

[19] S. Jena, and H. Das, "Modelling for vacuum drying characteristics of coconut presscake, Journal of Food Engineering, vol. 79, pp. 92-99, 2007.

[20] İ. Alibaş, "Microwave drying of grapevine (Vitis vinifera L.) leaves and determination of some quality parameters", Journal of Agricultural Science, vol. 18, pp. 43-53, 2012.

[21] N. Therdthai, and W. Zhou, "Characterization of microwave vacuum drying and hot air drying of mint leaves (Mentha cordifolia Opiz ex Fresen)", Journal of Food Engineering, vol. 91, pp. 482-489, 2009.

[22] A. Yagcıoglu, Drying Techniques of Agricultural Products. Ege University, Faculty of Agriculture, Publication No: 536, Bornova,Izmir, Turkey (in Turkish), 1999.

[23] M. Beigi, "Energy efficiency and moisture diffusivity of apple slices during convective drying", Food Science and Technology, vol. 36, pp. 145-150, 2016.

[24] P.P. Lewicki, and D. Witrowa-Rajchert, "Rehydration Properties of Dried Onion", International Journal of Food Properties, vol. 1, pp. 275-290, 1998.

[25] Çetin, N. "Machine learning for varietal binary classification of soybean (Glycine max (L.) Merrill) seeds based on shape and size attributes", Food Analytical Methods, vol. 15, pp. 2260-2273. (2022).

[26] IBM SPSS® Statistical Software. SSS Inc., IBM Company©, Version 20.0, 2010.

[27] I. John, and O. A. Solomon, "Modelling of the Drying of Milled Carrot Using Microwave and Laboratory Oven", Annals Food Science and Technology, vol. 20, pp. 268-280, 2019.

[28] Albayrak, A., Külcü, R. "Havuç dilimlerinin farklı mikrodalga güç yoğunluklarında kurutulması", Proceedings on 2nd International Conference on Technology and Science, November 14-16, 2019.

[29] S. Çelen, and A. Moralar, "Determination of Some Drying Parameters of Carrot Dried Using Microwave Method", El-Cezeri, vol. 7, pp. 31-42, 2020.

[30] Yildiz, G. "Color, microstructure, physicochemical, textural and sensory properties with the retention of secondary metabolites in convective-, microwave- and freeze-dried carrot (Daucus carota) slices", British Food Journal, vol. 124, pp. 3922-3935, 2022.

[31] S. Altikat, M. H. Alma, A. Gulbe, K. Kucukerdem, and E. Kus, "Effects of Different Power Levels Used in Microwave Drying Method on Color Changes of Oyster Mushroom (Pleurotus Ostreatus)", Journal of the Institute of Science and Technology, vol. 12, pp. 2045-2053, 2022.

[32] M. Darıcı, Ö. Süfer, and M. Simsek, "Determination of microwave drying and rehydration kinetics of green peppers with the bioactive and textural properties", Journal of Food Process Engineering, vol. 44, e13755, 2021.

[33] M. Fathabadi, R. Tabatabaee koloor, and A. Motevali, Investigation of different drying methods on color and shrinkage parameters in drying of red beetroot. Journal of food science and technology (Iran), vol. 16, pp. 127-142, 2019.

A Classification and Short Literature Review on 3D-User Interface (3D-UI) Sensing Technologies

C. DENIZ

Aydın Adan Menderes University, Aydın/Turkey, cdeniz@adu.edu.tr

***Abstract* - Since the 3D-UI sensing technologies involve precise electrical measurement of physical parameters like light intensity, pressure, temperature, etc. in a user dependent dynamic environment where human-computer interaction occurs, a multidisciplinary work from sensor design to signal processing and even further to the artificial intelligence techniques are involved. In the 3D-UI applications, physical quantities under measurement are first sensed and turned into an electrical quantity (or quantities) like voltage, current or impedance and then an instantaneous user-action is required to be simultaneously implemented with an appropriately developed signal processing technique as fast and precisely as possible. Here, a classification discussion of 3D-UI sensing technologies regarding the application fields (i.e., proximity, tactile, brain wave, etc.), physical principles and methods (i.e., laser based, camera based, etc.), instrumentation methods (i.e., direct sensing, indirect sensing, analog/digital signal processing, etc.), and application style (i.e., wearable, mobile, etc.) are discussed and the related literature is classified accordingly. Our dimensional analysis of the essential literature according to these classifications is intended to be helpful as a quick guide especially for the scholars and researchers in the field.**

***Keywords* - 3D-UI, 3DUI, 3D User interface, 3D-UI sensing technologies, Human-Computer interaction.**

I. INTRODUCTION

Sensors are conventionally known as electrical devices or equipment improved for sensing mostly non-electrical physical quantities such as temperature, velocity, force, fluid-flow rate, etc. by converting them to the electrical quantities like voltage, current, resistance, etc. Sensing technologies involve instrumentation techniques where sensors and other devices with the related equipment such as electrical signal conditioning via some circuit design are involved. When it comes to the 3D UI sensing technologies, these acquired electrical signals as a measure of the related physical quantity under question should be converted to the appropriate digital signals that the computer can understand and process it. Moreover, since there is a continuous bi-directional human-computer interaction in a 3D UI process, these sensed physical quantities exhibit a dynamic nature which brings the task to even much more complicated situations. Since the human action is processed, many parameters like hysteresis regarding repeatability and life-span of the sensor, response time, sensitivity, efficiency, etc. then becomes essential due to the motor demands of cognitive human actions in the 3D UI systems. This complexity in human-computer interaction brings about that sensor technologies in 3D UI involve multidisciplinary work in a collaboration with the other disciplines such as: physics, mathematics, chemistry, electrical and/or electronics, computer, robotics, artificial intelligence (AI), psychology, etc. [1-3]. One of the pioneering work in 1999, namely, [3], has a huge citation record (*now in 595 citations*) and it shows the multidisciplinary nature of the field along with the crucial point in year 1999 with an accumulated multidisciplinary knowledge to explode 3D UI sensing technologies with increasing papers pioneered by it. We also see from the literature hat 3D UI sensing technologies are being improved very fast in parallel to the advances in such other related fields with various design that study of 3D UI sensing technologies involve the following main topics [1,3]:

i) Study of sensor design for 3D UI applications: Everybody today knows that our modern life is connected to the sensor technology such as in sensing darkness for street lights, sensing proximity for the entrance gates in our modern buildings, sensing locations and/or directions in our smartphones, etc. Sensors have various classifications and among which the one for the "purpose of use" such as *temperature sensor* for the purpose of *sensing temperature*, *light sensor* for the purpose of *sensing light intensity*, etc., obviously emphasizes the first prerequisite functionality of the sensing technologies, namely, *"it should sense the related physical quantity"*. In a more complicated human-computer interaction regarding the 3D UI systems, sensors where the purpose is to *"sense the related physical quantities"* becomes very complicated, namely, *"it should sense the related physical quantity associated with a complicated human-computer interaction"*, and it makes designing a special type sensor to sense the related physical quantity for 3D UI applications a major task.

ii) Study of sense and control methods for 3DUI applications: We can suppose that the previous study for *"sensing"* mentioned above has been successfully achieved and a perfect sensor in a special purpose of use for sensing as a specific 3D UI application has been manufactured but the methods of sensing and controlling in these applications still become a major task to be faced since the applications in this field is not as simple as an ordinary light sensor to detect the darkness to decide whether turning the street lights on or off.

First of all, a 3D UI sensing system is a very dynamic system since it senses the changes in physical quantities by the action of the users such as an exerted force in some space domain by the user's hands, displacement or position and velocity of the user beside the other natural physical quantities such as temperature, light intensity, displacement, etc. in the environment when needed. Some of the physical quantities can be derived from the initially measured physical quantities just as deriving the velocity of the user from derivative of the user's measured displacement. We see that 3D UI sensing systems involve more than a simple sensing systems we are used to and they require an advanced instrumentation with the following mechanisms*: i-well achieved sensing, ii-well achieved measurement, iii-well achieved derivation and controlling mechanisms.*

These instrumentation mechanisms can also be subdivided further, for example; proximity sensing for the user's displacement might involve a laser sensing mechanism, or a GPS (Global Positioning System) mechanism, or a 3D accelerometer mechanism, or a magnetic induction mechanism involving hall sensors, or any other appropriate mechanisms. Some specific applications may also involve multi sensor usage. Consequently, literature in the field could be classified according to the interests of the scholars or researchers in this multidisciplinary field and it is obvious that such classifications could be helpful for the scholars or researchers to acquire the necessary information from the literature in the field. In this work we analyze the related literature since 1999 (since being a crucial year for the 3D UI technologies) up till now by the dimensional analyses by using such classifications as described in the next section in the field.

II. CLASSIFICATIONS

Some pictures of modern 3D UI sensing technologies are given in Figure 1. Considering various aspects of them, i.e., application fields, physical working principles, etc., fundamental classifications we discuss here are as follows:

A. Classification according to the application fields (Appl. field)

- *Proximity sensing (PS):* It involves sensing and measurement of user's location or displacement with respect to an object such as a camera or a real physical object.
- *Tactile sensing (TS):* It involves sensing and measurement of physical quantities caused by the user's gimmicks or pinching to control a virtual physical object or a controller in design, i.e., game control buttons, by the whole body or parts of the body like hands via a joy-stick-like physical objects haptically.
- *Brain wave sensing (BWS):* It involves sensing and measurement of the physical quantities produced by the user's brain directly without requiring any physical object like a joystick to control a virtual physical object or a controller in design, i.e., game control buttons.
- *Speech sensing (SpS):* It involves sensing and measurement of the physical quantities produced by the user's speech to control a virtual physical object or a controller in design, i.e., game control buttons.
- *Sound sensing (SoS):* It involves sound sensing like music, or any specific sound type.
- *Force or pressure sensing (FOPS):* It involves sensing and measurement of the physical quantities produced by the force exerted by the user's fingers, hands, or body to control a virtual physical object or a controller in design, i.e., game control buttons.
- *Touch-screen sensing (TSS):* It involves keystrokes, stylus, or fingerprints on a touchscreen.

B. Classification according to the physical principles and methods (Phys. Princ. and Meth.)

Our classification of 3D UI sensing system according to the physical principles and application methods in this work are simply any of the followings or any combinations of them:

- *Electromagnetic induction based (EmIB):* It involves Faraday's law of induction where a changing electromagnetic field induces an emf on a closed conducting loop.
- *Laser based (LB):* It involves a laser beam, which is physically in the form of a coherent, directed, and polarized electromagnetic wave, incident on a sensing element like an LDR (Light Dependent Resistor), photo-detector or such a sensor with a specific conventional technique like triangularization.
- *Camera based (CB):* It involves objects' vision as a measure of the reflected ordinary light, which is physically in the form of an incoherent and not necessarily both directed and polarized electromagnetic wave, incident on a camera, or such a visualization equipment. Note that, any design may fall in both LB and CB classes where both are involved.
- *Generic sensor(s) based (GSB):* It involves any generic sensor or some combinations of such generic sensors as a sensing element (or sensing elements) like LDRs (Light Dependent Resistors), thermocouples, strain gauges, etc.
- *Semiconductor based (ScB):* It involves semiconductor based sensing elements like hall sensors where a very small magnetic field even in a steady state, i.e., static or non-periodic signal, can be measured by the principles of semiconducting devices (note: dynamic magnetic fields can also be measured by the electromagnetic induction based class but the mechanisms are completely different and very small magnetic fields can be measured by the hall sensors which is made up of semiconducting materials to be referred to as semiconducting devices).
- *Geometric-Optical based (G-OpB):* It involves geometric-optical sensor technologies involving mirrors and lenses which is known as a subject class of geometric optics in physical sciences where wavelength of the light used is much smaller than the physical dimensions of the sensing mechanism.
- *Wave-Optical based (W-OpB):* It involves wave-optical sensor technologies involving interferometers and spectrometers which is known as a subject class of wave optics in physical sciences where wavelength of the light used is comparable with the physical dimensions of the sensing mechanism.

a) a handheld wireless trackball device used in AR, mobile, and immersive 3D environments.

b) Examples of modern 3D mice that make use of optical and inertial sensing to produce 3D position, orientation, and motion data by mappings.

c) A marker-based outside-in optical tracking system. Multiple camera sensors are placed strategically in the environment, and the user wears several retroreflective markers to track the body and face.

d) A user wearing Interaction Slippers

e) A camera-based finger tracking using a depth camera (passive sensing).

f) An optical-marker based finger tracking (active sensing).

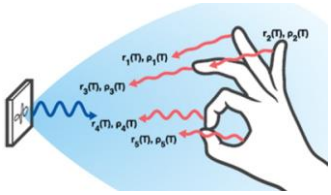

g) EMW (milimeter-wave radar) based 3D hand gesture recognition (passive sensing).

h) A conductive cloth-based Pinch Glove (conductive cloth at each of the fingertips, active sensing).

i) A multisensor data glove that uses accelerometers, gyroscopes, and magnetometers to capture information about each finger (active sensing).

j) An example of a device tht tracks finger movements and gestures by using EMG sensors to detect muscle activity in the forearm (active sensing).

Figure 1: Various types of modern 3D UI sensing mechanisms [1].

▪ *Touch-Screen based (TSB):* It involves sensing touch-screen inputs of the user by means of some specific methods such as, capacitive, resistive, inductive, etc.

It should be noted here that, by considering light as an electromagnetic wave, EmIB, LB, G-OpB, and W-OpB given above might be thought as the same class, however, mechanisms are completely different. Though, any combination of a series of sensing mechanisms given above in a work may fall in more than one of these classes.

C. Classification according to the instrumentation methods (Instr. Meth.)

▪ *Direct sensing method (DSM):* Direct sensing method senses the physical quantity under question such as position directly by an appropriate sensor or sensors such as accelerometer(s).

▪ *Indirect sensing method (IDSM):* Indirect sensing method senses the physical quantity under question indirectly by using an appropriate instrumentation technique to derive it from other sensed physical quantities, such as deriving the velocity of the user's hand from sensing its displacement first by using an appropriate circuit technique such as a differentiator circuitry (because velocity, which is a vector, is defined as the derivative of the displacement vector in physics).

▪ *Digital Signal Processing method (DSPM):* It involves direct or indirect sensing and controlling mechanisms in the design under question where Digital Signal Processing methods are used.

▪ *Analog Signal Processing method (ASPM*): It involves direct or indirect sensing and controlling mechanisms in the design under question where Analog Signal Processing methods are used.

▪ *Digital Image Processing method (DIP):* It involves digital image processing in its instrumentation design.

▪ *Artificial Intelligence method (AIM):* It involves artificial intelligence in its instrumentation design.

D. Classification according to the application style (Appl. Style)

▪ *Wearable technology (WT):* It involves wearable sensor instrumentation styles.

▪ *Multisensor technology (MsT):* It involves multisensor instrumentation styles of the same kind or any combination of them.

▪ *Mobile application technology (MobAT):* It involves mobile application technologies.

Note that, sensing with wearable sensors are called *active sensing* whereas sensing with stationary or unworn sensors are called *passive sensing* (see Figure 1 for illustrations).

E. Classification according to the literature property (Lit. Property)}:

3D UI sensing system in the literature studied here since 1999 up till now can fall in any property of the literature such as being a *tutorial work (TW)*, an *industrial work (IW)*, *an application work (AW)*, *a research work (RW)*, *a state of art (SART) work*, etc., or any combination of them. Here, it is intended to guide the readers with a quick review of the recent work in the literature in a tabular form in this dimension.

Consequently, our classification according to the literature property (Lit. Property) can be listed as follows:

- *Tutorial work (TW):*
- *Industrial work (IW):*
- *Application work (AW):*
- *research work (RW):*
- *State of art (SART) work:*

III. Results and Discussion

In this work, a classification of the acquired literature since 1999 up till now is given with the necessary discussions to give the readers an idea about the recent developments in the field with the future trends in the scope of the studied classifications given above. Here we aimed to provide a material with a quick review to the readers especially for the scholars via Table 1.

Table 1: Our dimensional analyses via the studied classifications of the recent acquired work since 1999 up till now in the literature

Work	Appl. field	Phys. Princ. &Meth.	Instr. Meth.	App. Style	Lit. Prop.
[1]	All types	All types	All types	All types	SART, TW
[2]	All types	All types	All types	All types	SART,RW,TW
[3]	TS	All types	All types	All types	TW, SART
[4]	TSS	GS, EmIB	IDSM	WT, MobAT	AW,RW
[5]	All types	All types	All types	All types	SART,TW
[6]	All types	All types	All types	All types	SART(bib.list)
[7]	TS,FOPS	All types	DSM,ISM, DSPM,ASPM	MS	SART,TW
[8]	TS,FOPS, TSS	CB,GS, GOpB	ISM,DSP	MS	TW,AW,RW
[9]	TS,PS, TSS	CB,GS	ISM,DSPM, DIPM	WT, MsT	AW,RW
[10]	TS,FOPS, TSS	GS	DSM,ISM, ASPM	WT,MsT	TW,AW, RW
[11]	BWS	EmIB,W-OpB	ASPM,DSPM	MoAT,WT	AW,RW
[12]	All types	All types	All types	All types	TW,AW,RW
[13]	TS,PS, EnS	GS,CB	DIP,AIP,DSP	WT,MsT	AW,RW
[14]	FOPS, SOS, TSS	CB, TSB	DIP, IDSM	WT,MsT, MobAT	TW,AW, SART
[15]	PS,EnS	LB,CB, GoB	DSPM,DIP, ASP,IDSM	MsT	RW, TW
[16]	TS	CB (type IR)	DSPM	WT, MsT	RW
[17]	PS,TS, FOP	CB	DIP,DSP, ISM	WT	AW,TW, RW
[18]	TSS,FOPS	CB,GS	DSM,IDSM, ASPM,DSPM	WT	TW,AW, RW
[19]	TSS,PS	G-OpB, CB,EmIB	ASP,DSP	WT	TW,SART, AW,RW
[20]	TSS,PS	G-OpB, CB,EmIB	ASP,DSP	WT	ASP,DSP
[21]	BWS	EmIB,W-OpB	ASPM, DSPM, ISM	WT	AW,RW
[22]	BWS	EmIB,W-OpB	ASPM, DSPM, ISM	WT	AW,RW
[23]	PS,EnS,TSS	LB,CBH, G-OpB, W-OpB	DSM, ASPM, DIPM	MST	IW, AW, RW
[24]	PS,TS,FOPS	GS	ISM, DSP	MS,WT	TW,RP
[25]	FOPS	GSB(type: force)	DSM, ASPM	MST	RW

We see that sensing technologies in 3DUI applications improve parallel to the developments in the other related fields such as in physics, electrical and electronics engineering, robotics, etc. and our classification in this study is preferred accordingly to give a highlight in this respect. Reader can focus any of the classifications given here, such as, tactile sensing regarding the application field and may wish to search recent literature on what methods this application can be achieved, such as by camera based, generic sensor based, etc., and may continue similarly with what instrumentation methods, what application methods, and what literature types (i.e., a tutorial work, industrial work, etc.) are available.

References

[1] J. J. LaViola, E. Kruijff, R.P. McMahan, D. A. Bowman, and I. Poupyrev, 3D User Interfaces Theory and Practice, 2nd ed., Addison-Wesley, 2017.

[2] D. A. Bowman, S. Coquillart, B. Froehlich, M. Hirose, Y. Kitamura, K. Kiyokawa, and W. Stuerzlinger, "3D User Interfaces: New Directions and Perspectives", *IEEE computer graphics and applications*, Vol. 28, pp.20-36, Dec. 2008.

[3] M. H. Lee and H.R. Nicholls, "Review Article Tactile sensing for mechatronics—a state of the art survey", *Mechatronics*, vol. 9, issue 1, pp.1-31, 1999.

[4] A. Basu, C. Saupe, E. Refour, A. Raij, and K. Johnsen, "Immersive 3DUI on one dollar a day," 2012 *IEEE Symposium on 3D User Interfaces (3DUI)*, pp. 97-100, doi: 10.1109/3DUI.2012.6184191. https://ieeexplore.ieee.org/document/6184191.

[5] L. Besançon, A. Ynnerman, D. F. Keefe, L. Yu, and T. Isenberg, "The State of the Art of Spatial Interfaces for 3D Visualization", *Computer Graphics Forum*, vol.: 40, pp. 293-326, 2021.

[6] D. Bowman, M. Billinghurst, J. Cugini, R. Dachselt, K. Hinckley, J. LaViola, R. Lindeman, J. Pierce, A. Steed, W. Stuerzlinger, *"20th Century 3DUI Bib: Annotated Bibliography of 3D User Interfaces of the 20th Century*", Compiled by Ivan Poupyrev and Ernst Kruijff, 1999, 2000, 3rd revision". *https://people.cs.vt.edu/~bowman/3dui.org/bibs/3duibib.pdf*

[7] R. Dsouza, R., "The Art of Tactile Sensing: A State of Art Survey", *International Journal of Sciences: Basic and Applied Research (IJSBAR)*, vol. 26. pp. 252-266, May 2016.

[8] P. De Barros, and R. Lindeman., "Multi-sensory urban search-and-rescue robotics: improving the operator's omni-directional perception", *Frontiers in Robotics and AI*, vol. 1, 2014.

[9] S. Dijkstra-Soudarissanane, K.M. El-Assal, S. Gunkel, F. Haar, R. Hindriks, J.W. Kleinrouweler, O. Niamut, "Multi-sensor capture and network processing for virtual reality conferencing" in *Proceedings of the 10th ACM Multimedia Systems Conference, 2019.*

[10] M. Do, T. Asfour, R. Dillmann, "Towards a unifying grasp representation for imitation learning on humanoid robots" in *IEEE International Conference on Robotics and Automation, 2011*, pp. 482-488.

[11] K. Dobosz and P. Wittchen, "Brain-Computer interface for mobile devices", *Journal of Medical Informatics & Technologies* vol. 24, pp. 215-222, Sep. 2015.

[12] C. Domingues, S. Otmane, and M. Mallem, "3DUI-EF: Towards a Framework for Easy Empirical Evaluation of 3D User Interfaces and Interaction Techniques", *International Journal of Virtual Reality*, vol.9, issue: 1, pp.73–80, 2010.

[13] A. Erol, G. Bebis, M. Nicolescu, R.D. Boyle, and X. Twombly, "A Review on Vision-Based Full DOF Hand Motion Estimation," in *IEEE Computer Society Conference on Computer Vision and Pattern Recognition (CVPR'05)-Workshops* 2005, pp. 75-75.

[14] M. Hachet, 3D User Interfaces, from Mobile Devices to Immersive Virtual Environments, Human-Computer Interaction, *Université Sciences et Technologies - Bordeaux I*, pp. 1-94, Dec. 2010.

[15] H. Higuchi, H. Fujii, A. Taniguchi, M. Watanabe, A. Yamashita, and H. Asama, "3D Measurement of Large Structure by Multiple Cameras and a Ring Laser," *J. Robot. Mechatron.*, vol.31, no.2, pp. 251-262, 2019.

[16] D. Kim, O. Hilliges, S. Izadi, A.D. Butler, J. Chen, I. Oikonomidis, and P. Olivier, "Digits: freehand 3D interactions anywhere using a wrist-worn gloveless sensor" in *Proceedings of the 25th annual ACM symposium on User interface software and technology. Association for Computing Machinery, 2012 NY, USA*, pp. 167–176.

[17] I. Infantino, A. Chella, A., H. Dzindo, and I. Macalsuo, "Human Hand Posture Reconstruction for a Visual Control of an Anthropomorphic

Robotic Hand" in *Conf. Intelligent Robots and Systems, 2003. (IROS 2003). Proceedings. 2003 IEEE/RSJ International Conference on Vol.: 2*, pp. 1266-1271.

[18] M. Meier, P. Streli, A. Fender, and C. Holz, "TapID: Rapid Touch Interaction in Virtual Reality using Wearable Sensing," *IEEE Virtual Reality and 3D User Interfaces (VR)*, 2021, pp. 519-528, 2021.

[19] A. Nguyen, "3DTouch: A wearable 3D input device for 3D applications", MSc Thesis in Computer Science, University of Wyoming, 2014.

[20] A. Nguyen and A. Banic "3DTouch: A wearable 3D input device for 3D applications," *IEEE Virtual Reality (VR)*, pp. 55-61, 2015.

[21] Z. Patel and P. Patel, "Brain Computer Interface for detecting brain activity and controlling an external object", in *Proc. of NCRAES'15, 2015*, pp. 1-4.

[22] L. Paya, A. Gil, O. Reinoso, "A State-of-the-Art Review on Mapping and Localization of Mobile Robots Using Omnidirectional Vision Sensors", *Journal of Sensors*, vol. 2017, p. 3497650 (article ID.), Apr. 2017.

[23] G. Sansoni, M. Trebeschi, and F. Docchio, "State-of-The-Art and Applications of 3D Imaging Sensors in Industry, Cultural Heritage, Medicine, and Criminal Investigation", *Sensors (Basel, Switzerland)*, vol. 9, iss. 1, pp. 568–601, 2009.

[24] L. Seminara, P. Gastaldo, S. J. Watt, K. F. Valyear, F. Zuher, and F. Mastrogiovanni, "Active Haptic Perception in Robots: A Review", *Frontiers in Neurorobotics*, vol. 13, July 2019.

[25] Y. Visell, S. Smith, A. Law, R. Rajalingham, and J. R. Cooperstock, "Contact sensing and interaction techniques for a distributed, multimodal floor display," *in on 3D User Interfaces (3DUI2010 IEEE Symposium)*, 2010, pp. 75-78.

Word Cloud Improvements with Natural Language Processing Techniques for Turkish Language

A.ATVAR[1] and M.ERSAHİN[1]

[1] Commencis, Turkey, anil.atvar@commencis.com
[1] Commencis, Turkey, mustafa.ersahin@commencis.com

***Abstract* – In this study, Natural Language Processing (NLP) based methods are recommended to make more descriptive and straightforward regarding the word cloud, which is produced by calculating the frequency of the words in the documents. The proposed method aims to find the syntactic similarity of words or bigrams after the preprocessing operations and then group belonging to the same root. Within the scope of this study, the Turkish dataset was studied, and rule-based algorithms were proposed. Since Turkish is an agglutinative language, it aims at the group by using root information of words or bigrams. As a result of the study, it was observed that the use of bigrams rather than the use of single words summarizes the documents better while creating the word cloud.**

***Keywords* – Word Cloud, Turkish, Bigram, Lemmatization, NLP, Preprocessing**

I. INTRODUCTION

Today, users actively share their opinions about the products and services used or bought by them through many platforms. Shared comments can be a guide for future users about products or services. On the other hand, these comments are also feedback for the developers or owners of the products. A good analysis of the comments makes it possible to identify the product's deficiencies and solve the errors. However, extracting meaningful and summary analysis from these comments, which users make, brings with it some difficulties. Day by day, increasing the number of comments is one of these difficulties. It is not practical in today's conditions to read and analyze all of the comments, which are too many in number, by a real person. On the other hand, the fact that the comments are not written in a specific format or rule increases the algorithms' complexity.

It is possible to analyze documents with Natural Language Processing (NLP) techniques. These algorithms can produce solutions to the problems with many methods, starting from preprocessing and moving words and bigrams into vector space. Word cloud is one of these algorithms. It is a method that visualizes the words in the document for the users by using the frequency of occurrence in the document. In this method, terms used more frequently in the documents, are shown in a larger font than the others. Using word clouds makes it possible to analyze documents' content easily [1]. For instance, it is possible to have information about the most used words or bigrams and summarize of content in the document at a glance. Word clouds are more visually interesting for the users than a graphic or table representation. However, simply being visually attractive is not enough. At the same time, it is expected to present accurate and summary information about the documents.

Within the scope of this study, some rule-based approaches have been proposed by using NLP techniques to provide more accurate and summary information from the word cloud created from the comments of mobile bank applications. Because the dataset studied is in Turkish, NLP libraries and frameworks such as the Zemberek library, which were developed specifically for Turkish, were used [2]. The fact that Turkish is an agglutinative language has also been a challenging point in simplifying the words in the word cloud.

In the proposed methods in the study, the similarities between the root of the word and the suffixes used in the phrase were emphasized rather than the semantic similarities of the words or bigrams in the word cloud. In the continuation of the study, the dataset is explained in Section 2 and the methods are explained in Section 3. Section 4 details the conclusion and future work.

II. PREPARING OF DATASET

The dataset used within the scope of this study was obtained by collecting and picking the user comments, which are written for bank applications, from the mobile application stores. Only Turkish comments are included in the dataset. In the mobile application stores, users can also give stars as an indicator of appreciation for the application in addition to comments. However, no correlation was established between the scores and comments given by the users within the scope of this study. The comments made by the users during the data collection phase were used directly as input to the algorithms that will be explained in Section 3 without any preprocessing.

When the user comments, located in the prepared dataset, are examined, the misuse of punctuation marks in sentences and the abundance of spelling errors are observed. Therefore, word-specific normalization should be applied to give more

accurate results with the frequency of the comments in the document.

Within the scope of this study, 1000 user comments belonging to a certain time period were studied, and the results were detailed.

III. Method

Preprocessing steps are essential for the methods which are included in this study. In addition, finding syntactic similarities between words or phrases has been accepted as the primary approach for this study. Also, simplification has a massive impact on results.

It is possible to examine the recommended methods under two subheadings. The first method is creating a word cloud by considering the words as singular. The second method is about creating a word cloud by considering the phrase, both singular and in pairs.

Common areas used in the preprocessing stages are used in the proposed methods for this study. These fields are shown in Table 1. However, apart from the basic steps, there are differences in approach between these two methods in terms of other NLP techniques. The primary purpose of this study is that a word cloud created from documents is composed of words or bigrams that summarize the document as much as possible and do not repeat each other. Some libraries and frameworks were used for the preprocessing stages in this context. For instance, the NLTK library was used for tokenization and cleaning non-alpha characters [3]. Zemberek library was also used for the normalization operation [2].

Table 1: Preprocessing Stages

Tokenization
Convert to Lowercase
Remove Non Alpha Characters
Normalization
Remove Stop Words

One of the common points used in both methods is the preparation of stop words. Stop words are a list of words that are frequently used in sentences in documents and have less representative power. Primarily, word structures such as prepositions and conjunctions are included in these lists. Some study results prepared in Turkish were combined to prepare this stop words list. In this context, the stop words list, which is located in NLTK library [3], and the stop word list of Can et al. [4] have been combined. In addition, after the first results were obtained within the scope of this study, it was observed that some of the stop words which are created for the word cloud of bigrams should be removed from the list. This is related to the method described in Section B. Because even if one or two of the words in the bigrams are in the stop words list, they can create a meaningful structure when they come together. Examining the bigrams which are belonging to the domain of the data set is essential for determining the words to be removed from the stop words list. For example, It has been observed that in comments on bank applications, the phrase 'güncellemeden sonra' is often used. Because after the application update, good or bad experiences are reported by users or written as comments. However, the word 'sonra' is found in most stop word lists prepared for Turkish. Even if there are stand-alone stop words, when it is considered a word group, a use like 'güncellemeden sonra' will be an excellent summarizing usage for the word cloud. On the other hand, if the word 'sonra' had continued to be on the stop words list, the word 'güncellemeden' would not have made any sense either.

A. Word Cloud For Singular Words

In this method of study, the main target is handling and processing the words in the document singularly and creating a word cloud from these words.

In this context, the documents were combined, and preprocessing stages were applied for all the words. In this way, before the algorithms process the words, they are cleared of typos, punctuation marks, and letter deficiencies as much as possible, and they are arranged in lowercase letters.

In Turkish, the meaning of a word can be changed with the addition of a suffix. The words should be separated from their suffixes but should not change semantically. Overcoming this situation is the most challenging part of this method.

The essential thing that is aimed within the scope of this study is to make the word cloud simple and meaningful. In order to achieve this, the syntactically close words must be grouped for the same root. Also, to be able to group, both the root of the word should be known, and the suffixes which were added to the word should be found separately, and the types of these suffixes should be determined. Extracting the morphology of the words is the basis of this study method.

In the study, the Zemberek library was used to extract the morphology of words [2]. In this way, it has been possible to identify both the word's root and the suffixes and their types added to the root.

The next step is to decide which suffixes added to the root of the word will remain and which suffixes should be removed. In this point, the algorithm's approach removes the affixes, such as possessive affixes, that do not change the meaning of the word but keep the affixes, such as derivational affixes and negation affixes, that change the meaning of the word. The lists of allowed and disallowed suffix types are as below..

Ignore Suffix List = ['P1sg', 'P2sg', 'P3sg', 'P2pl', 'P3pl', 'A1sg', 'A2sg', 'A3sg', 'A1pl', 'A2pl', 'A3pl', 'Opt', 'Acc', 'Ins', 'Cop', 'Gen', 'Past', 'Dat', 'Det', 'Conj', 'Det', 'Abl', 'Loc', 'Dat', 'Aor', 'Postp', 'NarrPart', 'Caus', 'PastPart', 'WithoutHavingDoneSo', 'FutPart', 'AfterDoingSo', 'PresPart', 'Fut', 'NarrPart', 'Desr']

Allow Suffix List = ['Neg', 'Ness', 'With', 'Adj', 'Noun', 'Postp', 'Verb', 'Inf2', 'Inf3', 'Without', 'Unable', 'Prog1', 'Agt', 'Pass']

Using these lists, words have been simplified by separating from their suffixes without losing their meaning. In this way, the words that are not considered as the same word syntactically due to their suffixes are grouped and their representation power has increased. Another rule applied at this stage is that if all the affixes of the word are removed, the root of the word is added to the word cloud with the infinitives suffix. This is done automatically by the Zemberek library when extracting the word's morphology [2]. The word cloud obtained only after the preprocessing operations is shown in Figure 1. The word cloud obtained after the operations performed as a result of root finding and suffix extraction is shown in Figure 2. Wordcloud library, which was developed for python language, was used to visualize these word clouds [5].

Figure 1: Word cloud of after preprocessing for singular word

Figure 2: Word cloud of after suffix extraction for singular word

When Figure 2 is examined, it can be seen that words with different suffixes belonging to the same root are grouped. In Figure 1, it can be observed that words belonging to the same basis but with different suffixes appear in the word cloud as if they were separate words. For example, the words 'uygulaması', 'uygulamaya', 'uygulamayı' and 'uygulama' are grouped into the word 'uygulama' after possessive suffix separation, as shown in Figure 2.

On the other hand, when looking at the word cloud, which is shown in Figure 2, it can be easily seen that the document is related to a mobile bank application. However, the representation of the comments in the document and the summary information about the document is not yet at a sufficient level. The method located in Section B has been proposed to solve this problem.

B. Word Cloud For Bigrams

Even if words, which have the same syntactic, are grouped within the scope of the study detailed in Section A, the word cloud should be more summarizer and descriptive about the documents.

In this section, the frequency of the words in the document as both singular and bigrams was found, and a word cloud was created. With the inclusion of bigrams, the representativeness of user actions in comments has increased.

Within the scope of this study, as explained in title A, first of all, preprocessing processes were applied to the documents. However, since bigrams are at the forefront, not all of the comments were combined, and each comment was processed separately. In this way, the situation where the last word of a sentence and the first word of the next sentence are accepted as bigrams is prevented.

In this method, the root information of words or bigrams was extracted without additional control. Words or bigrams belonging to the same root were inserted into a hash-based dictionary data structure in the order of high-frequency occurrence to reach faster when needed. The cumulative sum of frequencies was calculated for words and bigrams that belonged to the same root. Then the responsibility of representing roots was assigned to the word or bigram, which is the highest frequency for the root. For example, when the root 'uygulamak' is taken into the process, 'uygulama' will represent the root because it is the word with the highest frequency for this root. Frequencies of other words which are also belonging to the same root, such as 'uygulamaya', 'uygulamayı', 'uygulaması' have been added to the frequency of the word 'uygulama'. In this way, the most used word, which belongs to the root group in the document, was added directly to the word cloud without any suffix extraction.

Another applied method is grouping bigrams which are belonging to the same roots. For this reason, even if the roots of the elements of bigrams change places, they are included in the same group of words and their frequency is added to this group. To give an example, after frequencies of 'kötü uygulama' and 'uygulama kötü' were sorted, bigrams that have low frequency were transferred to other bigrams which have a high frequency. The word cloud, which is obtained as a result of these studies, is shown in Figure 3.

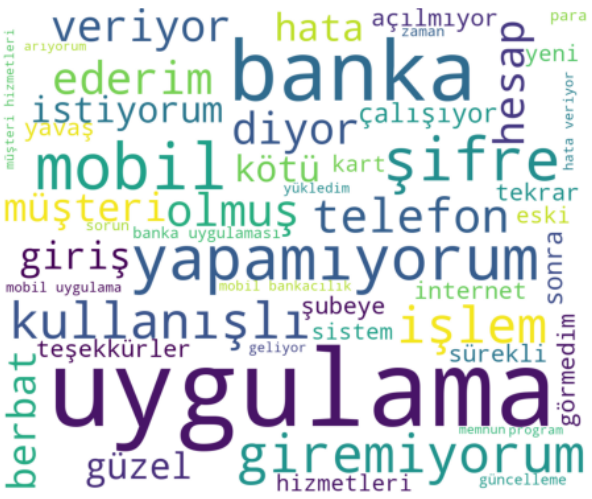

Figure 3: Word cloud of combined words and bigrams

As seen in Figure 3, although words and bigrams are syntactically grouped within themselves, bigrams and terms with similar syntax can be located separately in the word cloud. For instance, while the bigram 'mobil uygulama' is situated in the word cloud, the words 'mobil' and 'uygulama' are also located in the word cloud separately. To avoid this problem, a concatenation process was also applied between bigram and words with similar syntax. In this way, the frequencies of bigrams also increased, and bigrams that contained more descriptive information started to appear more prominent in the word cloud.

The word cloud was processed starting from the highest frequency in the merging process. In this context, if the words of bigrams are located in the word cloud separately, the frequencies of these words were reduced to half each time and added to the frequency of bigram. In this way, the representation power of bigrams has been increased for the word cloud. On the other hand, since a word can be used in different bigrams, the frequency of the word was distributed to all bigrams which included this word. For example, the frequency of 'uygulama' was added orderly for both 'banka uygulaması' and 'mobil uygulama' bigrams. The results obtained from this method are also shown in Figure 4.

As observed in Figure 4, words and bigrams with similar syntax are combined. The word cloud obtained by this method provides more descriptive information about the documents. Now, when the word cloud is examined, it is possible to get information about the content of the documents, not only the subject.

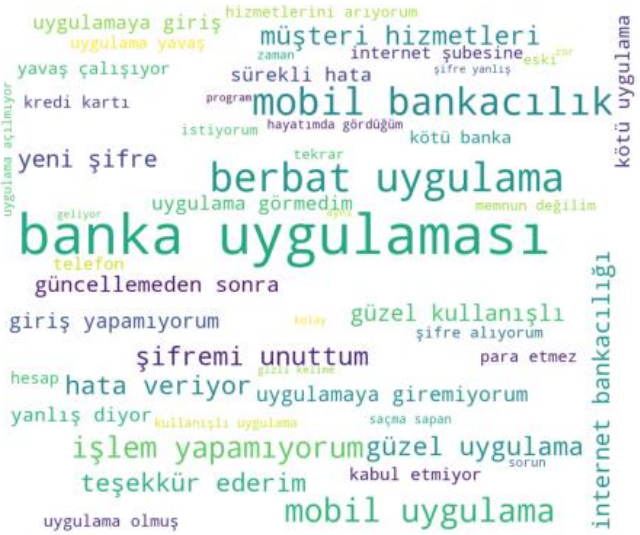

Figure 4: Word cloud of merged words and bigrams

IV. Conclusion and Future Work

When the results obtained within the scope of the study are examined, it can be observed that the word cloud created from bigrams represents the documents better than the word cloud, which was created from singular words. Thus, users can easily see summary information at a glance using the word cloud, which is created from bigrams.

One of the difficulties encountered during the study is that the Turkish language is agglutinative, and the affixes that come to the root of the word can change the meaning of the word. On the other hand, the fact that the noun and adjective phrases may have the same meaning when the words' location is switched is another difficulty.

In this study, the primary focus of the methods is finding the syntactic similarities of the words and the bigrams. For future works, it is planned to find the semantic similarities between the words and the bigrams in addition to the syntactic similarities. In this way, it is aimed to create a more brief and summarizer word cloud by removing the words that will be synonymous. In this context, tf-idf [6] and Word2Vec [7,8] methods will be used to represent the words, and the bigrams in vector space and clusters for close-meaning words will be created. Afterward, the word cloud will be recreated by selecting representative words or the bigrams for each cluster.

REFERENCES

[1] Heimerl, Florian, et al. "Word cloud explorer: Text analytics based on word clouds." 2014 47th Hawaii international conference on system sciences. IEEE, 2014.

[2] Akın, Ahmet Afsin, and Mehmet Dündar Akın. "Zemberek, an open source NLP framework for Turkic languages." Structure 10.2007 (2007): 1-5.

[3] Bird, Steven. "NLTK: the natural language toolkit." Proceedings of the COLING/ACL 2006 Interactive Presentation Sessions. 2006.

[4] Can, Fazli, et al. "Information retrieval on Turkish texts." Journal of the American Society for Information Science and Technology 59.3 (2008): 407-421.

[5] wordcloud, https://amueller.github.io/word_cloud/index.html

[6] Ramos, Juan. "Using tf-idf to determine word relevance in document queries." Proceedings of the first instructional conference on machine learning. Vol. 242. No. 1. 2003.

[7] Mikolov, Tomas, et al. "Efficient estimation of word representations in vector space." arXiv preprint arXiv:1301.3781 (2013).

[8] Mikolov, Tomas, et al. "Distributed representations of words and phrases and their compositionality." Advances in neural information processing systems 26 (2013).

Usage and Performance Comparisons of Machine Learning Methods for Text Classification

Hasan AKYOL[1] and Mustafa ERŞAHİN[2]

[1] Commencis A.Ş., İzmir/Turkey, hasan.akyol@commencis.com
[2] Commencis A.Ş, İzmir/Turkey, mustafa.ersahin@commencis.com

***Abstract* - Natural language processing describes the method by the machines which understand human language. Thanks to NLP, inferences can be made using artificial intelligence's power in areas such as e-commerce, banking, and social media. The text classification method is mostly used for these operations. With machine learning, the text classification process takes place much faster than the classification with the human eye. In this way, analyzes are made on big data. Rule-based classification or machine learning-based classification methods can be used for text classification. The methods we discuss in this article are the deep learning method with Bert under the heading of machine learning and the Term Frequency Inverse Document Frequency (TF-IDF) method. The deep learning method is developed with inspiration from the human brain. In this technique, artificial neural networks are created between the input and output data in the training data. With this approach, high-performance results can be achieved with little effort. The TF-IDF method is to vectorize documents over calculated values using the frequency of each term in the data set and the frequency in the document. The document vectors created are also classified by processing with classifiers such as Naive Bayes and Support Vector Machines (SVM). In this method, preprocessing texts gains more importance compared to deep learning. For this reason, more work is required to obtain successful results. It is of great importance to compare these two methods, which are frequently used in the industry, in terms of accuracy, performance, and ease of development.**

***Keywords* - artificial intelligence, machine learning, text classification, bert, deep learning, TF-IDF**

I. INTRODUCTION

Natural language processing is one of today's popular artificial intelligence topics. Artificial intelligence supported software, which is used effectively in almost every area of our daily life, uses audiovisual and textual data as input, just like us. It also makes our lives easier with the inferences it makes based on these data. At this point NLP helps machines understand human language. Thanks to NLP, software can be developed in many areas such as smart assistants, social media analysis and foreign language translation.

To achieve successful results, it is necessary to understand the language being studied correctly and to create the artificial intelligence model accordingly. Natural languages differ in word and sentence structure [1]. Especially agglutinative languages such as Turkish change the structure of the word according to its meaning in the sentence. This makes it difficult for artificial intelligence to recognize and make sense of the word. At this point, the stage called preprocessing gains importance. At this stage, sentences are divided into words and words, if necessary, into their roots. In this way, the sentence is divided into semantic parts. In addition to these, word cleaning is done, which is called "stop word", which contributes relatively little to the meaning of the text in terms of artificial intelligence and can cause noise in the data. The data obtained through these processes is more meaningful for artificial intelligence algorithms.[2]

One of the primary methods used to make sense of texts is classification. With text classification, large volumes of text are classified much faster than humans can. In this way, inferences can be made from large data sets or real-time labeling can be performed. There are different methods for text classification. Rule-based classification is the most basic method. In this method, large word dictionaries with pre-defined categories are used. These dictionaries define which category each word predominantly belongs to and how close it is numerically to that category.

An example of this is the mood state. In an emotion dictionary, there is information about whether the word is positive or negative and how much weight this emotion has. The average category of the text is obtained by adding the category and value of each word in the input text. This method takes its success from the power of the dictionary [3]. The other method is machine learning. In machine learning, training datasets and classification algorithms are used instead of a dictionary. The training dataset is a manually labeled dataset with a wide variety of examples in each category. Classify algorithms work on mathematical formulas. For this reason, texts cannot be processed directly. In order for the algorithms to process this data, the texts are first converted to vectors of equal length. This is done using the words in the text. Then, each vector is processed in the classification algorithm with its corresponding category, and the classifier artificial intelligence model emerges. This structure, also known as the trained model, predicts the next categories of inputs [4].

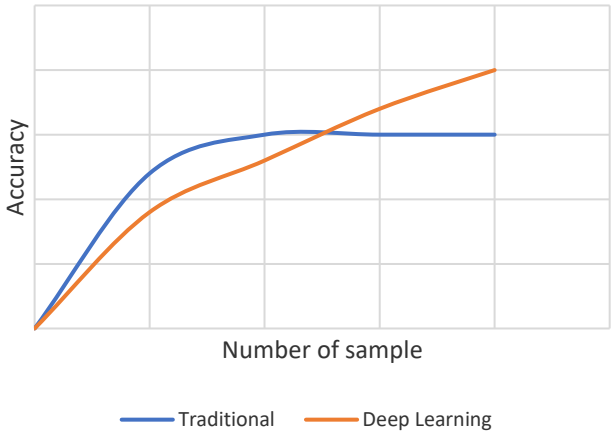

Figure 1: Accuracy curve according to the number of samples.

There are various machine learning algorithms used for different conditions and data. Popular examples of these include Naive Bayes, and Support Vector Machines. These algorithms classify data using statistical formulas and vector spaces. In addition to these algorithms, which are also defined as traditional classification algorithms, there is also a deep learning technique. Deep learning works by imitating the working principles of neural networks in the human brain. In this technique, artificial neural networks are created by associating words and phrases in texts with each other and with their categories [5]. With this method, it can produce more successful results than traditional algorithms. However, deep learning requires much more training data and resources than traditional algorithms. In addition, the training periods are longer [6].

II. METHOD

A comprehensive data set is needed to compare machine learning methods in our study. For this purpose, the "Multi-Class Classification data for Turkish (TC32) [7]" data set in Kaggle was used. The selected data set contains 431335 Turkish classified texts in 32 categories, with an average of 13 thousand from each. The data set consists of customer comments and complaints on the internet.

As the number of categories increases, classification success is expected to decrease. In this respect, this 32-category dataset is a good benchmark. On the other hand, the large number of samples also increases the success in the training phase. Especially in deep learning methods, the size of the data set positively affects the success.

In order to compare the classification methods with different types of data sets, the TTC-3600[8] dataset, which has fewer examples and categories but consists of longer texts, was used compared to TC32. This data set consists of 3600 news texts in total, 600 of which were taken from Turkish news sites in 6 categories.

Thanks to the software library ecosystem developed in Python, machine learning processes have gained speed. In particular, the sklearn-learn library contains almost all the tools that may be needed in the field of machine learning. In this way, developers can focus on understanding the data and increasing performance. There are frequently used classifiers such as naive bayes and SVM in sklearn-learn [9]. On the deep learning side, pre-trained BERT models provide a strong infrastructure. These models, which are available on Huggingface, are obtained by scanning very large amounts of text and creating artificial neural networks between all words. This process requires a lot of time and processing power. To give an example, the Turkish Bert model "dbmdz/bert-base-turkish-cased" is trained with a dataset of 44 million tokens, with a total size of 35 GB [10]. A classifier deep learning model is created by training this powerful model with a properly classified data set. When the model trained with Bert is fed with enough data, it does not need preprocessing as in traditional machine learning algorithms. Because almost every word is a trained model, and millions of words used in the training phase of the basic model have created neural networks with their original form. Therefore, the deep learning method shortens the preprocessing stage in the natural language processing process. And yet it provides a high performance. However, the training costs of deep learning are much higher than traditional methods. It requires more processing power and time. The training of the data set we use takes 132 seconds with SVM, while the creation of a deep learning model with bert takes 2 hours and 42 minutes with the Nvidia 2080TI graphics card. Even though deep learning processes are accelerated thanks to the CUDA cores in Nvidia's graphics cards, they remain slow due to the cost of neural networks compared to the speed of traditional algorithms.

In general, there are some common metrics used to measure the performance of all forecasting models. The first of these metrics is accuracy. Accuracy is simply defined as the ratio of the number of correctly predicted samples to the total number of samples. Although this metric provides general information about model performance, there are more detailed metrics. The Confusion Matrix is at the core of detailed performance measurement [11]. This matrix is the ratio of correctly and incorrectly predicted samples to actually correct and incorrect ones. It is more clearly understood as follows (Figure 2).

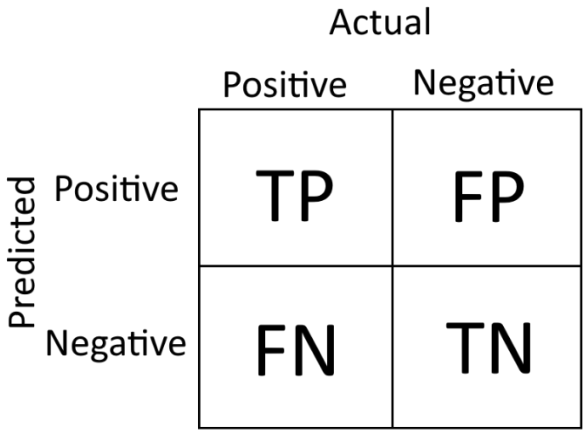

Figure 2: Confusion matrix.

Using the data obtained with this matrix, the precision value, which defines how many of the correctly predicted samples are actually positive, can be found (1). The information of how many of the actually positive samples can be found in total is called recall (2). The ratio of these two metrics to each other gives us the F1 value (3). These metrics are calculated individually for each category and the average success of the model is found. For this reason, they are metrics that provide more information than accuracy. All of these seemingly complex success measurement metrics can be easily calculated using the ready-made methods in the sklearn-learn library.

$$Precision = \frac{True\ Positive}{True\ Positive + False\ Positive} \quad (1)$$

$$Recall = \frac{True\ Positive}{True\ Positive + False\ Negative} \quad (2)$$

$$F1 = 2 \times \frac{Precision \times Recall}{Precision + Recall} \quad (3)$$

III. Conclusion

Bert and deep learning versus machine learning method SVM were compared in terms of performance. In comparison, the most significant difference was seen in training times. Bert training was completed in 2 hours and 42 minutes, while this time was measured as only 132 seconds on the SVM side. This difference may be preferred for making systems that are constantly learning, or when the model is frequently updated. On the other hand, when we compare the accuracy values, an accuracy of 98% was achieved with Bert, while this rate remained at 92% in SVM. Moreover, no pre-treatment was applied during the training with Bert. Thanks to the trained language model used, classification training can be done using the dataset directly. Thus, a costly research and development process is skipped. On the SVM side, stop word deletion and root separation processes are applied. The quality of these preprocesses directly affects performance and takes time to develop. Accuracy drops drastically if this operation is not done at all or is done unsuccessfully. In the study conducted in this data set, a decrease of 5 points was observed. Considering these results, the fact that the deep learning method is more effortless and stable success comes to the fore.

Table 1: TC32 Dataset Results.

	Precision	Recall	F1
SVM	92	92	92
BERT	98	98	98

In these two different types of data sets, the deep learning method with BERT was superior. Moreover, the fact that no pre-processing has been carried out highlights this success.

Table 2: TTC 3600 Dataset Results without preprocessing.

	Precision	Recall	F1
SVM	94	94	94
BERT	96	96	96

Pre-processing on the TTC 3600 data set slightly increased the performance in the classification made with SVM. This shows the sensitivity of traditional machine learning methods to the structure of the text and the importance of preprocessing. On the other hand, preprocessing did not make a significant difference in the deep learning method. This is due to the way the deep learning method handles the text.

Table 3: TTC 3600 Dataset Results with preprocessing.

	Precision	Recall	F1
SVM	95	95	95
BERT	96	96	96

References

[1] Ateş, Emre. (2021). Doğal Dil İşleme (Natural Language Processing). September 02, 2021, Siber Ansiklopedi: Siber Ortama Çok Disiplinli Bir Yaklaşım (pp.169-174)

[2] Amasyalı M. F., Balcı S., Mete E., Varlı E. N., "Türkçe metinlerin sınıflandırılmasında metin temsil yöntemlerinin performans karşılaştırılması" EMO Bilimsel Dergi, vol. 2, no. 4, 2012

[3] Tan, Li & Phang, Wai & On, Chin & Anthony, Patricia. (2015). Rule-Based Sentiment Analysis for Financial News. 1601-1606. 10.1109/SMC.2015.283.

[4] Dan, MUNTEANU. (2007). Vector space model for document representation in information retrieval. Annals of Dunarea de Jos. 2007.

[5] Minaee, Shervin & Kalchbrenner, Nal & Cambria, Erik & Nikzad Khasmakhi, Narjes & Asgari-Chenaghlu, Meysam & Gao, Jianfeng. (2020). Deep Learning Based Text Classification: A Comprehensive Review.

[6] Hotho, Andreas & Nürnberger, Andreas & Paass, Gerhard. (2005). A Brief Survey of Text Mining. LDV Forum - GLDV Journal for Computational Linguistics and Language Technology. 20. 19-62.

[7] Yıldırım Savaş, Multi-Class Classification data for Turkish (TC32), October 25, 2022 [Online].Available: https://www.kaggle.com/datasets/savasy/multiclass-classification-data-for-turkish-tc32

[8] Kılınç, D., Özçift, A., Bozyigit, F., Yıldırım, P., Yücalar, F., & Borandag, E. (2017). TTC-3600: A new benchmark dataset for Turkish text categorization. Journal of Information Science, 43(2), 174–185.

[9] scikit-learn, Machine Learning in Python, October 25, 2022 [Online].Available: https://scikit-learn.org/

[10] MDZ Digital Library team (dbmdz), dbmdz Turkish BERT model, May 19, 2021, [Online] Available: https://huggingface.co/dbmdz/bert-base-turkish-cased
[11] monkeylearn, Text Classification: What it is And Why it Matters , [Online].Available: https://monkeylearn.com/text-classification/

Design and Development of Smart Contract for Public Administration focused on Real Estate Certificates' Management by using Ethereum and IPFS

A. ALITI[1], M. APOSTOLOVA[2], A. LUMA[3]

[1] South East European University, Tetovo/North Macedonia, aa03511@seeu.edu.mk
[2]South East European University, Tetovo/North Macedonia, m.apostolova@seeu.edu.mk
[3]South East European University, Tetovo/North Macedonia, a.luma@seeu.edu.mk

***Abstract* – In this work, we provide a smart contract design technique for the implementation of a project that allows users to safely access real property certificates. The majority of current implementations concentrate on centralized, single-point-of-failure solutions. This implies that assaults like DDoS can make the service unavailable. Furthermore, if required backups have been made, such attacks may even completely wipe out the data. The fact that the data is kept in one location without encryption is another significant drawback because it makes server data theft easier. Our blockchain technology employs several nodes as entry points/gateways to guard against any kind of DoS. Such attacks would be very unfeasible in the event of a public blockchain like Ethereum. Additionally, saved data is encrypted. Additionally, the encryption key used to decrypt the data is kept off-site, making it impossible for an attacker to access the data unless he also has access to all of the encryption keys. Because more nodes than a single server can be used to provide data, this system shows to be more responsive under severe demand. Due to its immutability and ability to prevent tampering, it may also simplify administrative recordkeeping requirements.**

***Keywords* – smart contracts, blockchain, IPFS, e-government, real estate's certificate**

I. INTRODUCTION

In recent years, blockchain has received a lot of attention and is now employed in many different fields. Blockchain enhances security and efficiency. Blockchain has quickly evolved from a technology with limited uses connected to digital currencies to one with significant applications in many fields, grabbing the interest of authorities at all levels [1,2]. It could be used in a variety of industries, such as financial services, reputation management, Internet of Things, and public services like healthcare, education, and land administration systems [3-5]. Despite the evidence that blockchain technology has the potential to address some of the most important issues in business and society right now, there are still challenges in making many use cases a reality, especially from a strategic perspective.

The purpose of this article is to provide a blockchain-based smart contract implementation for use in public administration that will provide reliable transactions, improve service accessibility, and promote transparency. We used the handling of real estate certificates as our case study. We suggest implementing a prototype to manage those certificates using Ethereum [6] and IPFS [7].

Despite the complexity of the system, distinct services and outputs will be produced. A detailed output will include: (1) *Blockchain network*, a blockchain network with many nodes connected together and configured to use the blockchain's Ethereum Virtual Machine (EVM) to distribute and store certificates will be produced; (2) the *IPFS network*, which is exclusively used to store files and images; (3) *Smart Contracts*, which are blocks of code deployed on the blockchain, and are responsible to assign network roles and store encrypted data; (4) *Gateways*, because common devices (phones, PCs, tablets) cannot connect directly to a decentralized network, they act as an intermediary between the interface and the blockchain/IPFS network. (5) The JavaScript-based *Cadaster interface*, which will be used to deploy a certificate to the IPFS network and blockchain, respectively. Before a certificate is sent to a network, this will handle certificate encryption; (6) *User interface* - a JavaScript framework-built interface that will allow users to examine certificates from the IPFS network and blockchain, respectively. Before a certificate is retrieved from the networks, this will conduct certificate decryption.

The structure of the paper is as follows. The background is presented in Section II. Section III describes the technology required for system development, while Section IV discusses the creation of smart contracts. The study is concluded with Section VI after Section V describes the interfaces we have developed.

II. BACKGROUND

Blockchain is a distributed ledger that keeps track of transactions in unchangeable blocks of data that are sent to all network participants [8]. Additionally, the blockchain makes use of a cryptographic hash function to guarantee the accuracy

of the data contained in each block. We must design a data structure within the smart contract itself in accordance with the type of data we will be storing because, despite the fact that blockchain functions as a shared database, we are not given the option of employing a predefined data structure [9]. Additionally, this smart contract will determine how certifications are issued and confirmed. EVM is built on a low-level foundation, making it possible to develop and use high-level programming languages. The programming language used to generate smart contracts, Solidity [10], is exactly that. It is translated into bytecode, which is then executed inside the EVM [11]. A smart contract enables the execution of programmed instructions without the need for additional input. These smart contracts will be used to implement certificate issuance and verification.

Contrarily, the consensus procedures are essential for enabling participating nodes to concur on the blockchain information. The following characteristics of a consensus mechanism need to be true: (1) If an honest party validates a transaction (accept or reject), all other honest nodes will eventually do the same operation (2) *Liveness:* Any transaction should be finally performed; (3) *Persistence:* If an honest party validates a transaction (accept or reject). Numerous variables, including [12]: blockchain type, transaction pace, scalability, participation fees, and trust condition, have been used to differentiate between various consensus models. Because we have chosen Ethereum to execute our suggested solution, we will compare Proof of Work (PoW), the algorithm that Ethereum actually employs, with Proof Authority, which we intend to use because of the advantages it could provide for our system.

By having nodes compete to determine the hash value of the upcoming block and then waiting for confirmation from other nodes, the PoW mechanism was developed by Satoshi to ensure consistency and security in the Bitcoin network [12]. The winning nodes are rewarded when the block is added to the existing blockchain. The greatest consensus for securing a public blockchain is PoW, which has been the foundation for many protocols and services. In the case of PoW, the system is completely independent, and the cost of adding data to the blockchain and verifying it is paid to the blockchain network and depends on a lot of external factors. This indicates that there will be a time, size, and price limit on the total number of certificates that are issued in our case. We would be able to produce a certificate every three to four minutes in its simplest form. This is an unacceptable option given the number of certifications that may feasibly be provided.

In our solution, we advocate the use of Proof of Authority (PoA). This sort of consensus, known as a "sealer," only permits one number to confirm a new block. The network's integrity is increased by the remaining members. This agreement is significantly faster because we don't need to find a solution to a cryptographic challenge, but it has a cap on the number of individuals who can confirm fresh blocks. If a new sealer with the address 0x... is required, then 50% of the current sealers must take the same step by adding this address to the sealers list [13]. Every x seconds, as indicated in the genesis block, a block is confirmed. This is often set to 15 seconds by default, however it can be altered such that it is confirmed each time a transaction occurs. As a result, each transaction consists only a single block. The PoA system is dependent on a single entity or set of related entities. Disabling a private network is not straightforward, but it is not impossible either. A case in point would be the network's keeper becoming bankrupt. The cost of sustaining a node would be the primary consideration in this situation. By allowing others to contribute to the blockchain, the cost can be reduced. This agreement is ideal in our situation because just one institution will be able to provide certifications.

III. Used Technologies For System Development (Supplementary Technologies)

Blockchain is a tremendous technology, but it needs outside assistance to function. To integrate the user with this technology and enable the secure, straightforward, and secure transfer of data from the user to the network, further tools will be needed. Other tools will be required to integrate the user with this technology and enable secure, simple, and safe information transfer from the user to the network.

A. Web Apps & PWA

We will use technologies that are generally available to bring blockchain to modern devices. PWA (Progressive Web Apps) is one such technology that makes it simpler to create user interfaces and issue and verify certificates. These apps will interact with the blockchain in an indirect manner, retrieving information from the network and carrying out smart contract-specific tasks. The project will be accessible through these apps. Verification, scanning, or the issue of a certificate are examples of processes.

Typically, only certain systems may execute native programs, but this requires a lot of work for little gain because we must build separate apps for each platform (Linux, Windows, Android, iOS), but in exchange, we get superior performance. In our situation, this is ineffective. On the other hand, we have websites that are simple to create, consistent across platforms, but lack the features we require and cannot be put on the hardware.

This is where PWA comes into the equation, a brand-new technology that offers specialized platform operations, is reliable, and can be deployed (in 2021 PWA was supported by iOS, making it officially acknowledged by all major platforms). Actually, PWA is a mindset for creating web apps rather than a single technology [14]. It is a blend of several technologies.

B. InterPlanetary File System (IPFS)

A certificate can now contain considerably more information thanks to IPFS. It is built on a peer-to-peer protocol for distributed system data storage and retrieval. The content addressing method is used by IPFS to locate files. Data is shared among peers (network users) and can be retrieved via DHT (distributed hash table) similar to BitTorrent [15,16]. IPFS is based on:

- Content Addressing

- Directed Acyclic Graphs (DAG)
- Distributed Hash Tables (DHT)

Data is identified based on content, not location, using a technique called content addressing. In modern systems, content is typically found via locations.

We require this information's location in order to access it. In a distinct process, IPFS gives this item a title. Based on the file contents, this title was produced using a hash. This is known as CID in IPFS (Content Identifier). Directed Acyclic Graphs are then used to connect the information. The main use of this is to link files to directories. Finally, we use Distributed Hash Tables to identify the peer that holds the data or file we require.

C. *Docker Containers*

An environment-controlled platform called Docker allows for the development, distribution, and low-maintenance operation of applications. Additional factors like operating system versioning, packet versioning, the operating system itself, etc. are all things that Docker wants to minimize. Each Dockerized program is expected to operate consistently across all possible server configurations [17]. By simplifying initial configuration and processes, this technology will enable the deployment of new nodes quickly and simply. Docker operates on a software level as opposed to a virtual machine (VM), which emulates a whole operating system, docker works on a software level. As a result, a server's or a node's environment uses fewer resources. On top of that, we can build a complete environment that includes a node, database, web server, and gateway using other technologies like docker-compose.

IV. Deployment of Ethereum Smart Contract

We will outline the smart contract deployments used in our proposed project in this section. The certificates' validity and secrecy will be upheld by us. It is essential to build each of the following components in order to implement the system we suggest:

1. ***A Blockchain network*** will be implemented, with numerous nodes spread across various host providers and regions.
2. ***IPFS Network*** – The deployment environment will be the same as the blockchain network.
3. ***Smart contracts*** – The blockchain EVM will be used to deploy and operate smart contracts.
4. ***Gateways,*** which will consist of a few additional servers set up for NGINX reverse proxying Every n-th server should ideally have a gateway acting as a reverse proxy.
5. ***Interfaces*** – CloudFlare and/or Netlify are used to host them on the edge network. Alternately, numerous additional servers might be set up with NGINX and Apache to provide the interfaces.

A. *The Architecture of the System*

The entry-point of our data would be on the front end. his data will be altered before being transmitted to the appropriate gateways. The system's fundamental overall architecture is shown in Figure 1 below.

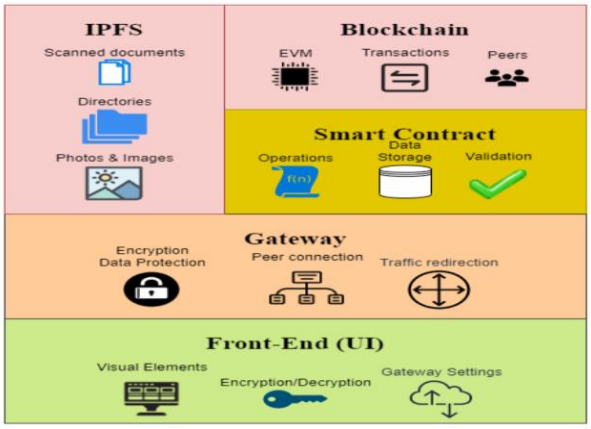

Figure 1: The overall architecture of the system.

The appropriate networks, IPFS or Blockchain, will get the information according to how it was categorized before to its inception. Along "its journey" on the internet, the data is encrypted using both a private key and the HTTPS protocol. The statement "No encryption key is sent to the network!" is crucial. This significantly improves security but makes these data unavailable if the encryption key is misplaced.

This information is separated after being transmitted to its corresponding gateways, and each gateway then sends the information to the network peers or nodes. In IPFS, it is directly stored on the network, whereas in blockchain, it is changed via a series of procedures laid forth in the smart contract. It should be obvious that data supplied to a smart contract is accessible to the general public. Because of this, data is "scrambled" before being transmitted over the network using encryption or short-term addresses. These addresses are not required in our situation.

B. *Smart Contract*

There will be two distinct pieces to the smart contract. The certificates will be stored in the first section, and the roles and address management will be handled in the second. The certificate's data structure will be as follows:

- string rawData
- string encData
- uint256 created
- State state
- string photoHash

'State' is an enumerator that accepts the values "pending," "approved," and "declined." The certificate's initial value is "pending." The addition of the certificate is the subsequent function. Being an entirely transparent system, we must take care to avoid disclosing any personally identifiable information about users while still upholding the integrity and transparency we require. This presents a problem on its own. Data encryption would be the only option, but since data was previously made accessible during the transaction, this encryption should be handled by the smart contract.

The ideal course of action would be to encrypt data before deployment, which entails having the program issue certificates before releasing the owner's key. This indicates that without this

key, the certificate can no longer be obtained.

Below is presented the pseudocode of adding a certificate to the blockchain network.

Algorithm 1: Pseudocode of adding a certificate

```
1  function getCert (PropertyID[], publicData[], encryptedData[], State[], photoHash[]) {
2      if(isIssuer)
3          return;
4      for (i = 0, i < totalCerts, i++) {
5          if(certificateExists)
6              return;
7          certificates [PropertyID[i] = {
8              PropertyID[i],
9              publicData[i],
10             encryptedData[i],
11             State[i],
12             photoHash[i]
13     }
14     TotalCerts+1;
15   }
16 }
```

Figure 2: The pseudocode of adding a certificate to blockchain network.

Figure 2 illustrates how we first determine whether the address has the necessary permissions. Then, we obtain an array of deployed certificates and push it to the array containing all currently issued certificates. The process is parallelized using the array. The total number of certificates that can be deployed at once will eventually have a limit added. We halt the procedure if a certificate with an identical ID is discovered.

The address roles are responsible for the remaining tasks. The most fundamental and crucial rule is to verify the certificate's issuer. We must confirm that adding certificates is permitted for the address. Every address on the blockchain has the ability to send transactions to the network and our smart contract, and we can use an address's private key to confirm that the transaction was sent from that address. This enables us to be absolutely certain that the address is legitimate for this transaction. Additionally known as transaction signing, this is.

Additionally, we have the issuing institution, which is like the certificate:

- address issuerAddress
- string issuerName
- bool issuerState

In this instance, the constructor specified the contract's master address as well as the sender's identity as root.

Algorithm 2: Pseudocode of adding issuer

```
1  function addIssuer(issuerAddress, name) {
2      if(issuer OR master) {
3          updateIssuersList(issuerAddress, name, valid);
4      totalIssuers++;
5      }
6  }
```

Figure 3: The pseudocode of adding issuers.

Adding new issuer addresses is possible with the aforementioned function. A different cadastral blockchain address, for instance, is needed before this user can be added to the list of issuers.

Algorithm 3: Pseudocode of toggling an issuer

```
1  function switchIssuer(address) {
2      if (isMaster(txSender)) {
3          forEach(Issuer)
4              if (issuerFound) {
5                  if (issuerValid) {
6                      disableIssuer;
7                  } else {
8                      enableIssuer;
9                  }
10             }
11         }
12     }
13: }
```

Figure 4: The pseudocode of toggling an issuer.

When necessary, this part disables or enables users. The only address that can perform this function is the master address.

V. INTERFACES

The solution we suggest intends to enable significantly more complex systems for issuing and verifying real estate property certificates solely on blockchain. This entails the creation of various certificates in accordance with state regulations and validation by other third parties utilizing decryption keys. Only the property ID and decryption key fields must be filled out by the user. Every device that has an internet connection is able to access these services. We can deploy the product to a private or public blockchain in each scenario. We have thought about how the actual implementation shouldn't be overly complicated in comparison to other implementations and how to match maintenance expenses as closely as possible.

We have designed two interfaces for our system: the "User Interface" and the "Cadaster Interface." The blockchain gateway network address, issuer address, and contract's address are all specified during configuration. These will be used to sign transactions and connect to the blockchain network.

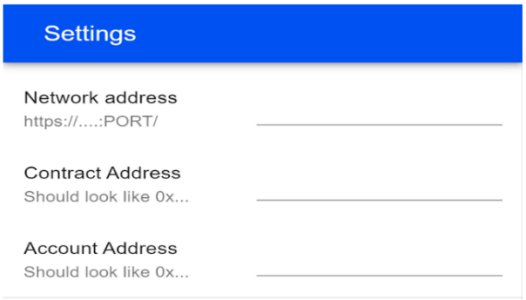

Figure 4: Configuring the application.

The app can now be used to issue certificates after being configured. The user must wait until a transaction receipt is accessible once the issuer fills out the necessary information and clicks "Issue," which sends the certificate to the blockchain network. This stage marks the end of the process.

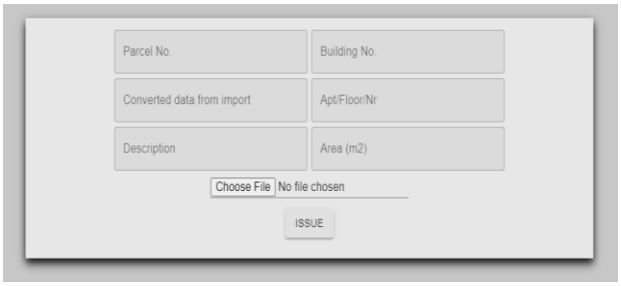

Figure 5: The Issuer interface.

The user interface can be seen in Figure 5. Users can enter the property certificate serial number and then a decryption key, as can be shown. The user will see the certificate and the location on the map after selecting "OK.".

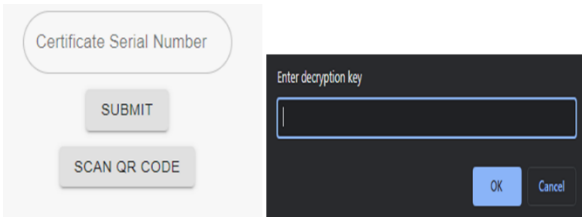

Figure 6: User Interface.

The serial number of the property certificate can be entered by users, followed by the decryption key. The certificate and the position on the map will be displayed to the user after they click "OK".

VI. Conclusion

We discussed the implementation of smart contracts for the system we provide in this study. Following a description of the primary purposes of smart contracts, the development of the required environment, and the required tools, we showed the two interfaces we have so far created for the system we suggest.

We intend to expand the system's functionality in the future, as well as conduct testing and assessments to assess how effectively the CPU, RAM, and network can handle the demands of the deployed smart contracts.

References

[1] N. Radzwill, "Blockchain Revolution: How the Technology Behind Bitcoin is Changing Money, Business, and the World" *Quality Management Journal*, pp. 64-65, Vol. 25, No. 1, 1st 2018, DOI: 10.1080/10686967.2018.1404373.

[2] P.R.P. Chelliah, K. Saini, C. Surianarayanan, "Blockchain Technology and Applications", ISBN: 9781003081487, July 2020, DOI: 10.1201/9781003081487.

[3] M. Krichen, M. Ammi, A. Mihoub, M. Almutiq, "Blockchain for Modern Applications: A Survey" *Sensors* 2022, vol. 22, pp. 5274 - 5301, DOI: 10.2290/s22145274, Published by MDPI

[4] M. Shabbir, "Blockchain in Real Estate Sector: Benefits and Challenges", January 2021.

[5] I. Racetin, J. K. Pamukovic, M. Zrinjsk, M. Peko, "Blockchain-Based Land Management for Sustainable Development", *Sustainability 2022*, Published by MDPI, 14, 10649, DOI: 10.3390/su141710649.

[6] F. Shamsi, A. Ahmed, "Compiling Smart Contracts into Machine Code using Ethereum Virtual Machine (EVM)", 2022. DOI: 10.13140/RG.2.2.10993.35682.

[7] J. Benet, "IPFS-Content Addressed, Versioned, P2P File System", *arXiv:1407.3661*, 2014, Available: https://arxiv.org/abs/1407.3561.

[8] P. Purwono, A. Ma'arif, W. Rahmaniar, Q. M. U. Haq, "Blockchain Technology", Journal Ilmah Teknik Elektro Komputer dan Informatika (JITEKI), Vol. 8, No. 2, June 2022, pp. 199-205, ISSN: 2338-3070, DOI: 10.26555/jiteki.v812.24327.

[9] C. Wu, J. Xiong, H. Xioing, Y. Zhao, W. Yi, "A Review on Recent Progress of Smart Contract in Blockchain", *IEEE Access*, Volume 10, 2022, pp. 50839-50863, DOI: 10.1109/ACCESS.2022.3174052.

[10] C. Zhu, Y. Liu, X. Wu, Y. Li, "Identifying Solidity Smart Contract API Documentation Errors," *Conference on Automated Software Engineering (ASE '22)*, October 10-14, 2022, Rochester, MI, USA, Published by Association for Computing Machinery (ACM), ISBN: 978-1-4503-9475-8/22/10 New York, NY, USA, 13 pages, DOI: https://doi.org/10.1145/3551349.3556963.

[11] N. Thakur, V. Shinde, "Ethereum Blockchain Based Smart Contract for Secured Transactions between Founders/Entrepreneurs and Contributors under Start-up Projects", *International Journal of Scientific Research in Computer Science, Engineering and Information Technology*, ISSN: 2456-3307, Vol. 7, Issue 5, pp. 01-08, ISSN: 2456-33007, DOI: 10.32628/CSEIT2174140.

[12] A. Meneghetti, M. Sala and D. Taufer, "A Survey on PoW-based Conesnus", *Annals of Emerging Technologies in Computing (AETiC)*, Print ISSN: 2516-0281, Online ISSN: 2516-029X, pp. 8-18, Vol. 4, No.1, 1st January 2022, Published by International Association of Educators and Researchers (IAER), DOI: 10.33166/AETiC.2020.01.002.

[13] C. Lepore, M. Ceria, A. Visconti, A, U. P. R. Rao, K. A. Shah and L. Zanolini,, "A Survey on Blockchain Consensus with a Performance Comparison of PoW, PoS and Pure PoS". *Mathematics 2020*, Vol. 8, pp. 1782, DOI: 10.3390/math8101782.

[14] A. Biorn-Hansen, T. A. Majchrazak, T. Gronli, "Progressive Web Apps: The Possible Web-native Unifier for Mobile Development", 2017.

[15] R. C. Roychaudhary, M. Gill, A. Chahande, C. Panjabi, U. Kakde, "Integrating Blockchain and the Interplanetary File System, a resilience for Storing Student's File", *Journal of Interdisciplinary Cycle Research*, Vol. 13, Issue 6, June 2021, pp. 1089-1097, ISSN: 0022-1945.

[16] Juan Benet, "IPFS-Content Addressed, Versioned, P2P File System", 2014

[17] J. Cito, V. Ferme, H. C. Gall, "Using Docker Containers to Improve Reproducibility in Software and Web Engineering Research," *In Proceedings of International Conference on Web Engineering ICWE 2016: Web Engineering. Lecture Notes in Computer Science ()*, pp 609-612, Vol 9671. Published by Springer, Cham. Print ISBN: 978-3-319-38790-1, Onilne ISBN: 978-3-319-38791-8, DOI: 10.1007/978-3-319-38791-8_58.

A Real Life Use Case for Predicting Sales of Bus Tickets

Hıncal TOPÇUOĞLU[1], Behçet MUTLU, Cevhernur SÖYLEMEZ [3]
[1] Enuygun TURKEY, hincal.topcuoglu@enuygun.com
[2] Enuygun TURKEY, behcet.mutlu@enuygun.com
[3] Computer Engineering, İzmir Bakırçay University, TURKEY, cevhernur.soylemez@bakircay.edu.tr

Abstract **- Enuygun.com lets users search, list, and evaluate domestic and international flights, bus tickets, and tens of thousands of hotels within seconds. In the bus ticket sales business, Enuygun works with different providers to get trip information between cities. So, many bus trips are coming from different providers that must be sorted smartly with regard to user preferences. This paper develops and proposes a machine learning-based ranking system using sales predictions of each bus company, route, and hour of departure. Different regression algorithms are utilized when predicting each company's route's sales prediction using collected historical data. Successful regression model results were obtained and the process was concluded by integrating the output scores into an intelligent ranking system.**

Keywords **- Machine learning, intelligence sorting, sales prediction, regression**

I. INTRODUCTION

ENUYGUN.COM is an online platform that allows users to search quickly, list, and compare thousands of domestic and international flights, bus tickets, and hotels. To make bus sales, the organization collaborates with various bus transportation companies via vendors [1]. It is critical to improve the user experience of bus travel firms' excursions and to promote trips that are more relevant to users. We developed a machine learning-based intelligent ranking (sorting) software depending on bus trip sales predictions. We grouped each company, route, and departure hour, and then with some features generated, set up a regression model and got a result score for each company, way, and hour. Then we used these scores to sort bus trips intelligently.

When the literature is considered, it is seen that there are different articles on the bus sales business. Yu et al. [2] proposed forecasting bus passenger trip flow for transit route design and optimization. They estimated bus passenger journey flow using an Artificial Neural Network (ANN) and tested it with a dataset from China. Kinene [3] used the Random Forest machine learning technique to forecast hourly bus demand for all lines in Orebro, Sweden. They used data such as the day of the week, the weather season, the time of day, customer types, and so on to forecast the hourly demand for buses. Janine [4] proposed creating an Automated Bus Origin-Destination Matrix (ABODM) using farebox and Automatic Vehicle Location (AVL) data.

One of the ways to involve customers in their marketing strategy is known as the referral strategy. This strategy has been applied in various marketing areas, one of which is in the field of transportation. Another study aimed to reveal the solution of the mathematical model of bus ticket sales by using a routing strategy [5]. Based on the solution obtained, the routing strategy in bus ticket sales can increase bus passengers by up to 39.92%.

In addition, in a study that considers intelligent suggestion sorting of where to go as a prediction problem based on supervised machine learning algorithms, namely Random Forests, a 56-dimensional feature set from tourist historical travel data is proposed. Five machine learning algorithms were compared in this feature set, and the results show that Random Forests outperform other algorithms [6]. Talia et al. [7] developed a machine learning model using 3.23 million user-generated logs to predict whether a user will buy a bus ticket or not. They achieved a score of 95% accuracy in their model. On the other hand, Laksono et al. [8] developed a bus ticket booking information system during the pandemic to avoid users going to bus offices to buy tickets. Rajagopalan et al. [9] developed a demand forecasting model for ticket sales using bus transportation data, and this study helps understand the spatiotemporal bus ridership demand in Bangalore.

In this paper, the standard machine learning pipeline was applied. After the data collection and pre-processing stages, the conversion amounts of the relevant time and route of the bus companies to sales were obtained and the sales amounts were predicted on a weekly basis with the trained regression models. The results showed that the prediction performance of ensemble models was more successful and promising. The results showed that the predictive performance of ensemble models was more successful and promising. We also observed that click-through rates increased significantly in the performance results of A/B tests, which is the user experience research methodology.

The rest of the paper is organized as follows: Section 2 introduces the dataset used, materials, and methods. Section 3 presents the experimental results that are obtained. At last, the conclusion and future works are part of Section 4.

II. Material and Methods

This section explains the dataset used and the applied regression-based machine learning algorithms SVM, Lasso, and Random Forest.

A. Dataset

The data were obtained from different providers between 16 August and 19 September 2021, and the total number of samples was 226,459. The data set includes information (features) such as the company information of the providers, the date and time of the trip, the remaining time to the travel date, the departure-arrival terminal, the number of stops on the route, the length of the way, the order of the show, and the ticket price. Table 1 shows most of the critical features and their descriptions.

Table 1: Features of datasets.

Feature Name	Description
timestamp	timestamp
ctxt_P1_provider_count	Provider1's ticket count
ctxt_P2_provider_count	Provider2's ticket count
ctxt_P3_provider_count	Provider3's ticket count
ctxt_P4_provider_count	Provider4's ticket count
ctxt_P5_provider_count	Provider5's ticket count
ctxt_P6_provider_count	Provider6's ticket count
ctxt_P7_provider_count	Provider7's ticket count
ctxt_request_id	request_id
ctxt_company	Identifier of the company
ctxt_departure_date	Departure date
ctxt_departure_hour	Departure hour
days_to_travel	Number of days left to travel
ctxt_destination	Location of destination
ctxt_destination_terminal	Arrival terminal
ctxt_origin	Place of departure
ctxt_origin_terminal	Departure terminal
Route	Route
ctxt_route_stops	Number of stops on the route
ctxt_seats_available	Number of seats available
ctxt_ticket_price	Ticket price
isThankYou	Was it been purchased?
Provider	Identifier of the provider

B. Regression-based Machine Learning Algorithms

Regression which is one of the main areas of interest in statistical science, estimates the value of the dependent variable (y) based on the value of at least one independent variable (X) and explains the effects of changes in the independent variable on the dependent variable [10]. In this study, three different regression algorithms are trained and evaluated. The first algorithm, named SVR (Support Vector Regression), is similar to the SVM (Support Vector Machine) classifier and is characterized using kernels, sparse solution, and VC (Vapnik-Chervonenkis) control of the margin and the number of support vectors [11]. Lasso Regression is a method of linear regression that conducts both feature selection and regularization to improve the accuracy of estimation and generalizability of the mathematical model it generates [12]. Random Forest is an ensemble (collaborative) method that can execute regression and classification tasks using multiple decision trees, and a technique called Bootstrap Aggregation, widely known as bagging [13].

C. Evaluation Metric

Many different metrics can be used to evaluate regression models. R2 score is one of the most important metrics for assessing a continuous target regression model. In this article, we used the R2 score metric, one of the metrics used in the regression problem. Of the many existing metrics, the R2 Score remains the most popular. The formula required to obtain the R2 score is shown in Figure 1.

$$R2 = 1 - \frac{\sum_{i=1}^{N}(y_i - \hat{y}_i)^2}{\sum_{i=1}^{N}(y_i - \bar{y})}, \qquad \bar{y} = \frac{1}{N}\sum_{i=1}^{N} y_i$$

Figure 1: R2 Formula.

Where R2 Score is between 0 and 1, the closer to 1, the better the regression fit.

III. Experimental Results

In this work, we separate the dataset into two parts training and test set. We realize the training process on the training set and trained models evaluated on test samples. Although SVM and Lasso Regression are successful regression algorithms commonly used in the literature, the best result in this study was obtained with Random Forest.

We use the Grid-Search hyperparameter search approach to find the best hyperparameter values to obtain the best performances of each algorithm [14]. Obtained best hyperparameter values are shown in Table 2. For example, Random Forest performs best when the n_estimator and n_depth parameters take values of 100 and 3, respectively.

Table 2: Best hyperparameter values as a result of hyperparameter tuning process.

Algorithms	Parameters
SVR Regressor	C = 1, epsilon = 0.2
Lasso Regressor	alpha = 0.01
Random Forest	n_estimator = 100, n_depth = 3

We used the best hyperparameter values for each model training. The evaluation results of each model are shown in Table 3. As we can see, the best performance was achieved by the Random Forest algorithm [14]. The score of the R2 metric obtained as the evaluation results of algorithms SVM, Lasso, and Random Forest are 0.75, 0.84, and 0.86, respectively.

Table 3: Evaluation results.

Algorithms and Parameters	R2 Score
SVR Regressor	0.75
Lasso Regressor	0.84
Random Forest	0.86

When the results are considered, it is seen that Random Forest has a better performance. Random Forest, a state-of-the-art algorithm, doesn't require normalization or scaling of features in data preprocessing and can work with missing values. For these reasons, it may have produced better results in this data and feature set.

IV. Conclusion and Future Works

This paper explains how a real life bus sales prediction system is developed using machine learning-based predictive models. Grouping data by product or as in our work bus company, route, departure hour and making feature engineering regard to this groups is the data preparation step before machine learning algorithm works. The best prediction results obtained after running 3 different machine learning algorithms with the best parameters are used as sorting values for the grouping variables. As a future work, a version of K-Means clustering algorithm can be run to measure similar routes that can change the order of the sorting.

References

[1] www.enuygun.com. Accessed on 19 Jan 2022.

[2] Yu, S., Shang, C., Yu, Y., Zhang, S., & Yu, W. (2016). Prediction of bus passenger trip flow base

on artificial neural network. *Advances in Mechanical Engineering* 8(10).

[3] A. Kinene (2016). Modelling the Passenger Demand for Buses in Orebro City. Orebro University School of Business, Sweden.

[4] Farzin J.M. (2008). Constructing an Automated Bus Origin-Destination Matrix Using Farecard and Global Positioning System Data in São Paulo, Brazil. Transportation Research Record: Journal of the Transportation Research Board, 2072:30-37.

[5] Putra, D. P., & Ruditho, M. (2022). The Solution of Mathematical Model of Otobus Ticket Sales with referral marketing strategy. *BAREKENG: Jurnal Ilmu Matematika Dan Terapan*, *16*(1):229-234.

[6] Zheng, S., Liu, Y., & Ouyang, Z. (2016). A machine learning-based tourist path prediction. In *2016 4th International Conference on Cloud Computing and Intelligence Systems (CCIS)*, 38-42. IEEE.

[7] Branda, F., Marozzo, F., & Talia, D. (2020). Ticket sales prediction and dynamic pricing strategies in public transport. *Big Data and Cognitive Computing*, *4*(4):36.

[8] Wibawaa, S. C., Fatahb, D. A., Firmansyahb, M. M. H., Mustafitb, N. H., Putrib, E. R., & Laksonob, C. S. (2021). BUS TICKET BOOKING INFORMATION SYSTEM. *Journal homepage: https://journal. trunojoyo. ac. id/ijseit*, *6*(01).

[9] Jayabal, Y., & Rajagopalan, S. (2020). An Analysis of Bus Ticket Sales in East Bangalore.

[10] Uyanık, G. K., & Güler, N. (2013). A study on multiple linear regression analysis. *Procedia-Social and Behavioral Sciences*, *106*, 234-240.

[11] Awad, M., & Khanna, R. (2015). Support vector regression In Efficient Learning Machines (67–80). *Apress, Berkeley, CA*.

[12] Ranstam, J., & Cook, J. A. (2018). LASSO regression. *Journal of British Surgery*, *105*(10):1348-1348.

[13] Liaw, A., & Wiener, M. (2002). Classification and regression by Forest. *R news*, *2*(3):18-22.

[14] Özçift, A., Kılınç, D., & Bozyiğit, F. (2019). Application of grid search parameter optimized Bayesian logistic regression algorithm to detect cyberbullying in turkish microblog data. *Academic Platform-Journal of Engineering and Science*, *7*(3):355-361.

The Next Generation Video Processing Technology: A Guide to AWS DeepLens

P. ERSOY[1] and M. ERSAHIN[2]

[1] Department of Technology, Dataroid, İstanbul/Turkey, pinar.ersoy@dataroid.com
[2] Department of Software Development, Commencis, İstanbul, Turkey, mustafa.ersahin@commencis.com

Abstract* - Internet of things applications can handle more information operations owing to computational frameworks and improvements in hardware. In addition to improving latency and bandwidth, the proximity of resources also enables developers to handle security issues with sensitive data by lowering the risks involved with transferring information to distant servers. As a result, this is especially helpful for enhancing home and business security systems, whose present setups put their targets in danger by sending all their recordings straight to a virtualized platform for assessment. Using the product of AWS DeepLens, which is a customizable camera that offers consumers the chance to practice real-time streaming techniques for video and image processing, this study intends to investigate how to recognize things in real time from a perspective. In addition, its advantages are listed in a sequenced manner as the client computers can experience fewer delays while transmitting live video to the data center by using AWS DeepLens. Also, a remote process utilizes fewer resources than a server does. Once data is exchanged at the periphery, fewer resources are used in the data transmission process. Additionally, there are other opportunities that AWS DeepLens provides as the content to be captured by attackers is lessened due to the lack of transfer of sensitive information over the network.

***Keywords* – AWS DeepLens, object detection, real-time processing, video processing, computer vision.**

I. INTRODUCTION

COMPUTER vision innovations are being used in numerous domains, such as retail, industrial, and medical, to enable cellular devices to provide recommendations similar to those made by humans without the requirement for human interaction.

The challenge of identifying and finding a figure in tracking photographs or videos has been the most demanding, difficult, and dynamic study field in computer vision over the past few generations. The study field has attracted significant interest and focus, particularly since the advent of machine learning (ML) and object tracking.

II. RELATED WORKS

The advancement of all-purpose algorithms with real-world applications is the main objective of machine learning and deep learning. Neural networks, computer models of biological neurons, are one type of artificial intelligence system often utilized. A neural network is composed of tiers of synapses that analyze inputs from lower-level neurons and pass them on to the higher-level cell types. Each cell can block or transmit signals, each of which is symbolized by a transfer function [1]. By evaluating a linear combination of inputs and scaling the total using an encoder to a value of binary numbers.

For a structured learning dataset, the parameters employed in every tuple and they are progressively updated by the perceptron since it trains to execute a job. As the image recognition, it reduces the gradient descent. A neural system may detect diverse sequences in a way that is analogous to the brain, even though a single neuron can do mere computations. Due to their capability for complicated comprehension, generative models with numerous levels are a prevalent information extraction paradigm [2]. A typical algorithm processing path of convolution-based models [3] is presented in the Figure 1.

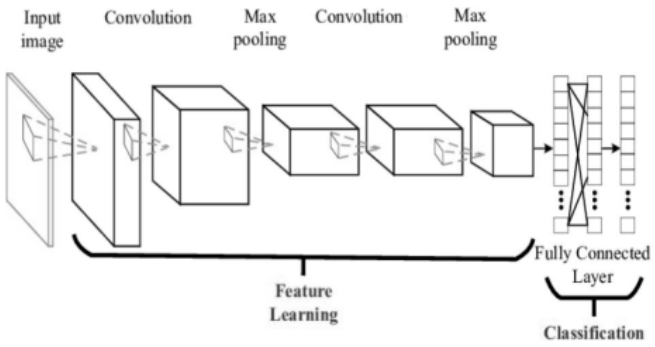

Figure 1: The processing path of convolution model..

A basic pattern of CNN architecture for computer vision is convolutional neural networks. Convolutions and method pooling are two characteristics of the network. These two characteristics are designed to identify spatial connections between pixels that a conventional neural network cannot [4].

Data gathering, tagging, building, and monitoring are all steps in developing a predictive image model. Data is collected, either from internal information sources or open data sources. The information is preprocessed and put into the appropriate format for the modeling. For learning, the input is categorized and classified into several groups.

The quantity of the data set and the variability of the hypotheses are two variables that affect how well a machine learning algorithm performs. They are implemented using testing data to clarify the model's generalizability. They are also required to adjust parameters to maximize efficiency based on the experimental outcomes.

Growth areas of cloud-based object detection include population monitoring, driverless cars, business work cycle, individual capturing, attitudinal interpretation, movement identification, and position classification [5, 6].

A significant portion of sophisticated monitoring systems is built to use cloud services since large data-relevant jobs require a lot of processing capacity. As a result, they have a significant amount of processing power and extensibility. However, cloud-based systems encounter significant difficulties. Large-scale unprocessed video material would need to be sent to the cloud to achieve real-time object recognition and identification. This not only creates temporal inconsistency but also heavily utilizes the communications infrastructure. In particular, when considering the processing of video feeds from a broad range of devices.

There may be several benefits to being able to identify items on hardware at the edge nodes [7]. Some of the positive aspects can be listed as by processing information in real-time. With this advantage, each edge device can eliminate the lag caused by exporting raw video to the data center. Also, a peripheral system utilizes a limited number of resources compared to a server. Data transfer consumes less energy when information is transmitted at the edge. In addition, since there is no transmission of confidential material over the internet, there are fewer risks for information to be intercepted by cybercriminals.

A. AWS DeepLens

Throughout this article, as an object detection solution, AWS DeepLens is used to generate outputs. AWS DeepLens is an AWS cloud-integrated portable video recording device created primarily for machine learning tasks. Developers may capture, archive, and analyze photos using the AWS DeepLens and use them explicitly in neural network models. A model was developed in Amazon SageMaker for this platform, and it was distributed to AWS DeepLens. Amazon SageMaker enables hosting providers to model, serve and consolidate computer vision models into software programs [8]. The hardware of AWS DeepLens [9] is represented in the Figure 2.

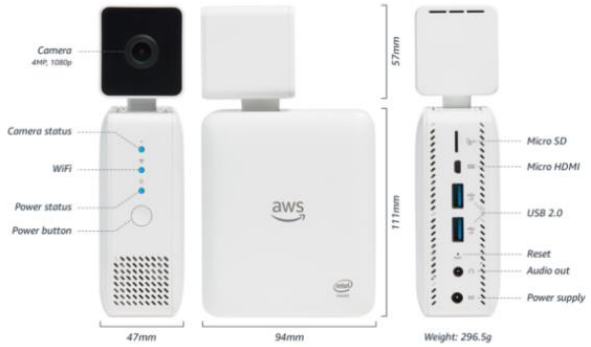

Figure 2: The AWS DeepLens.

Lambda operations manage the hosts required to run the script, streamlining the implementation stage. They act to enable the video processor to provide simultaneous inferences. Lambda manages storage, processing capability, and connectivity. The user-specified controller, which refers to a method inside that script that AWS Lambda might call whenever the script is launched, it is used by Lambda methods. A message containing data from the event that was given as an argument by the controller is returned [10] The internal processing path of AWS DeepLens is depicted in the Figure 3.

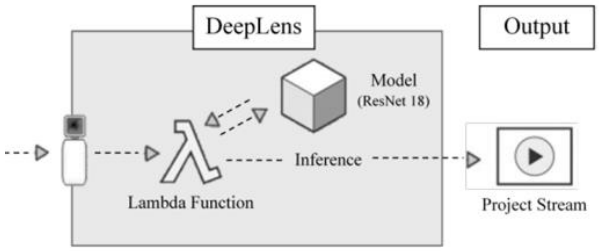

Figure 3: The processing of AWS DeepLens.

The output content is generated by the DeepLens and sent to the processed model. After drawing a conclusion using an AWS Lambda function, the program publishes the prediction to the project stream [11].

III. MATERIALS AND METHODS

The significant aspect of AWS DeepLens can be accepted as a reconfigurable sensor that gives customers an opportunity to examine simultaneous streaming processing methods more quickly. Three distinct modeling types are available that may be used with AWS DeepLens. For this article, we focused on the Pre-Trained Object Detection framework in this article [12].

A. Project Type

To decide on the project type, from the AWS DeepLens interface, viewers of this task can deliver a newly trained method on their peripherals. In the Figure 4, the project type selection interface of AWS DeepLens is presented.

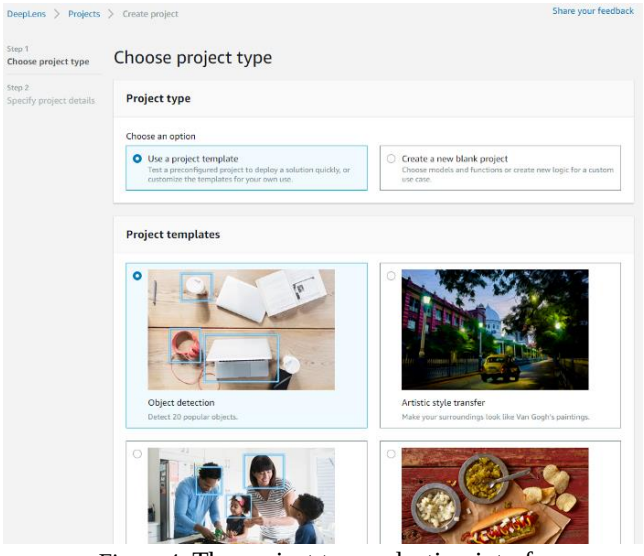

Figure 4: The project type selection interface.

B. *Model Type*

AWS Sagemaker is a solution that is necessary to utilize a SageMaker Notebook entity as a coding platform so that you may distribute your configurations onto your camera utilizing the model type. The AWS SageMaker-based pretrained and externally trained model type can be selected from the interface of the importing model step. The model import of project type selection interface of AWS DeepLens is represented in the Figure 5.

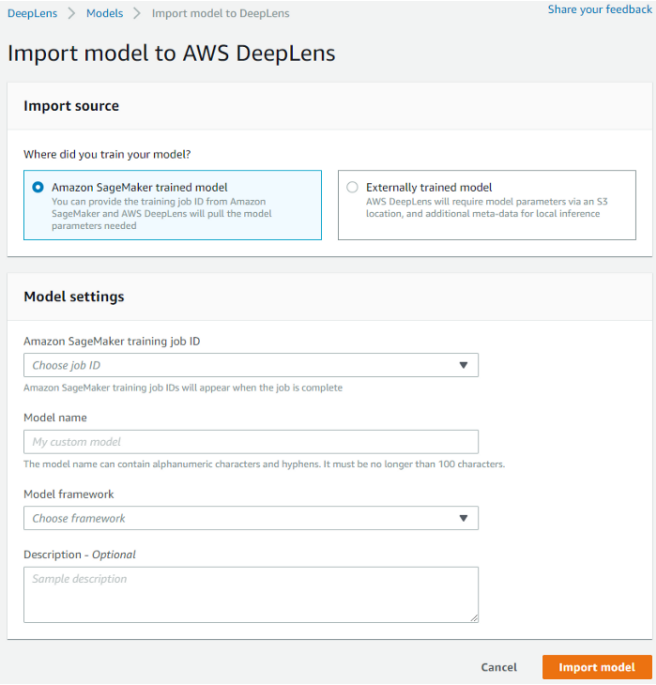

Figure 5: The project type selection interface of AWS DeepLens.

C. *Region Type*

To successfully utilize any application, the required authorization must be configured as in the linked page before you begin using it. AWS DeepLens is utilized as the initial service. The region must be chosen from the list of areas in order to access this provider.

In the AWS Management Console's services section, solutions may be chosen by putting their names into the text box after configuring framework regulations and locations as presented in the Figure 6.

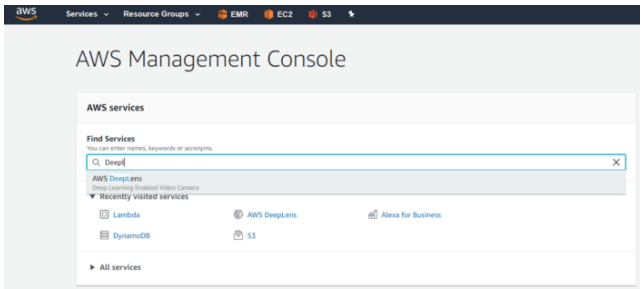

Figure 6: The services selection interface of AWS Management Console.

Basic facts regarding the service are provided on this site. Under the "More Resources" menu, there exists a section for documentation for more comprehensive relevant information.

D. *Device Registration*

The first action to take when the item is available is to correctly identify the gadget with the AWS DeepLens platform. The hardware model can be chosen after the equipment is linked to the PC. The gadget may be really registered after it is integrated into the computer.

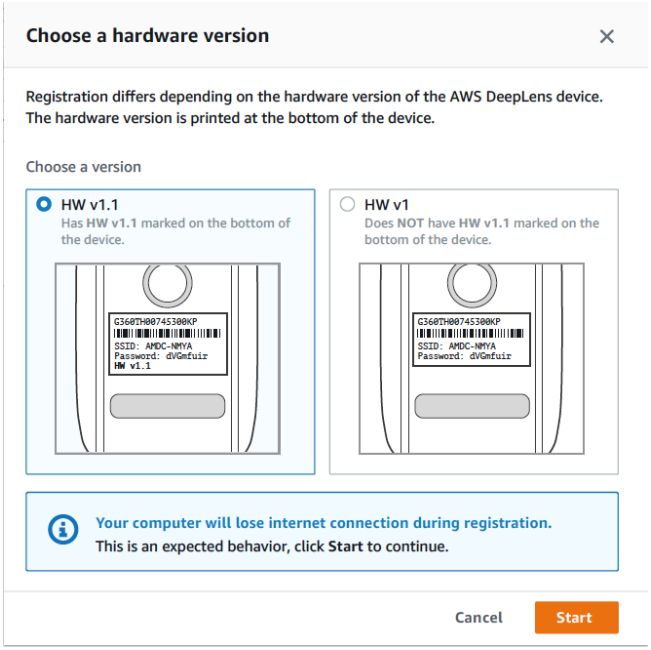

Figure 7: The hardware selection interface of AWS DeepLens.

The initial step is to switch on the power button and attach the gadget to the power supply using its adapter. The battery led will turn into blue color when the gadget is turned on. By connecting the USB connection to the product's registration connector, the gadget may be wired to the computer. The device interface of the AWS DeepLens is represented in the Figure 8.

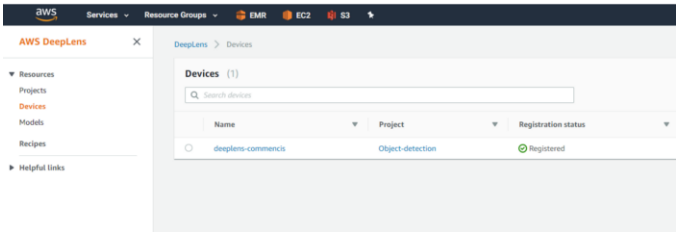

Figure 8: The device interface of the AWS DeepLens.

E. *Pretrained Model Deployment*

By choosing the appropriate button located at the upper right corner of the "Projects" area, one may create a new project and view the available project kinds. A template from the pre-populated program layouts shall be selected at this phase. The project type and object detection sections can both be selected from the related interface. The project type template interface of the AWS DeepLens is presented in Figure 9.

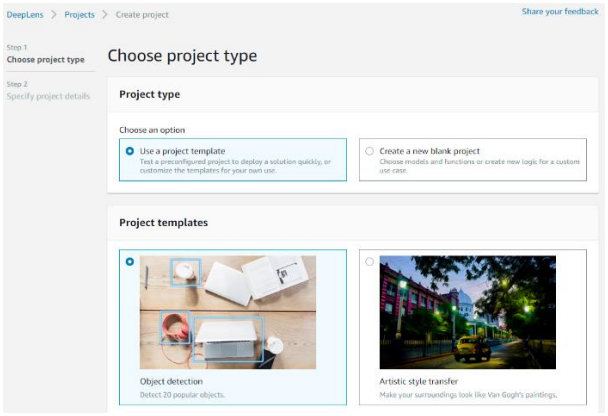

Figure 9: The project type interface of the AWS DeepLens.

The project title and summary input standard settings can be set on the *"Specify project information"* screen. The parameters for choosing the project content can be observed at the bottom of the page. The default settings can be validated and kept in place for both model and function. The interface of project content details is shown in the Figure 10.

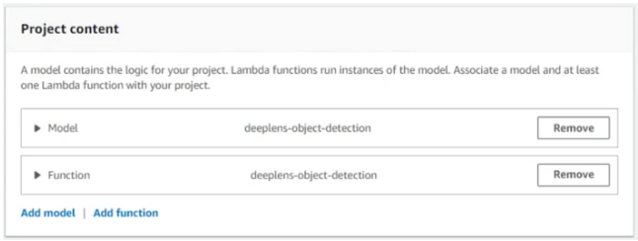

Figure 10: The interface of project content.

The object detection solution may be configured correctly at this phase. Proper listing of the newly formed project in the "*Projects*" section is required. The button may be chosen after seeing the related project, and then the "*Deploy to device*" option on the right top can be used to proceed. The interface of the created projects list is represented in the Figure 11.

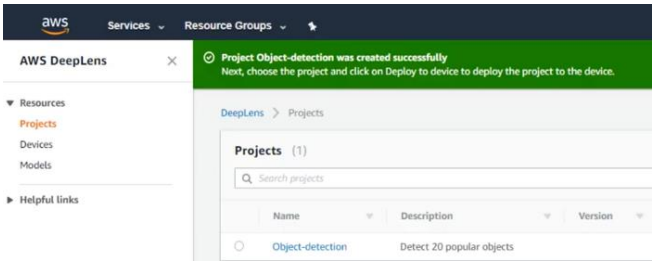

Figure 11: The interface of the projects list.

The gadget must be selected, and the "*Review*" option must be selected on the "*Target device*" screen. The target device interface of the AWS DeepLens project is shown in the Figure 12.

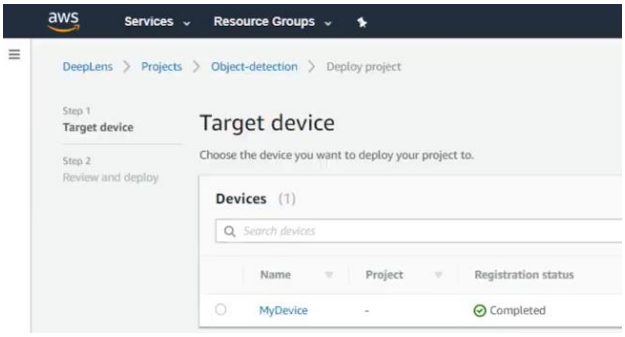

Figure 12: The target device interface.

The deployment material, containing specifics on "*Type*" "*Function*," and "*Model*" will be on a separate page. The "*Deploy*" option can be chosen to proceed after a review. The interface of review and deploy screen is presented in the Figure 13.

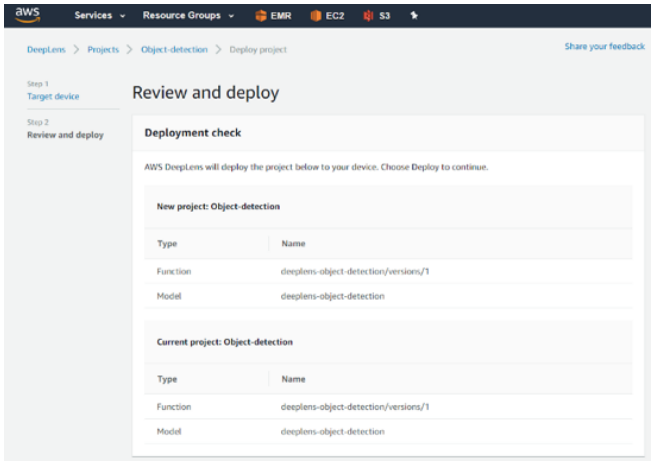

Figure 13: The review and deploy screen.

When "*Deploy*" is selected, AWS DeepLens will display the model's download progress before uploading it to the device. The deployment processing interface is shown in the Figure 14.

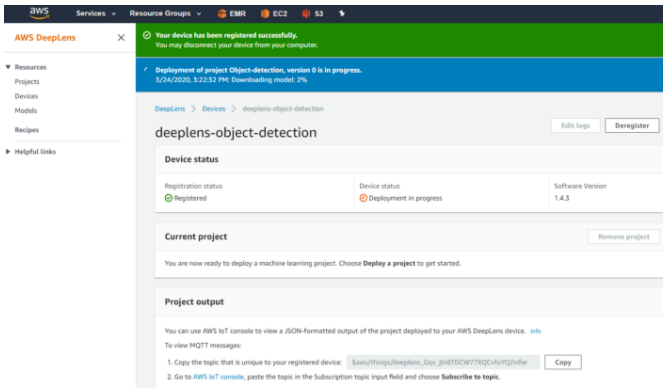

Figure 14: The deployment processing interface.

Following the project serving step, the "*View Output*" option for the website of the appropriate certification transfer may be chosen in the "*Devices*" section. The browser preference and certification integration phase interface is presented in the Figure 15.

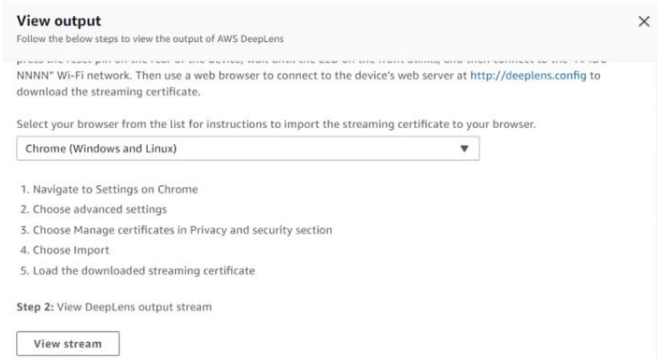

Figure 15: The integration phase screen.

IV. RESULTS

There exist two ways to investigate the results of the model. These two specific output generation approaches can be observed in the upcoming sections.

A. *MQTT Topic Value in AWS IoT Core*

The browser can be prompted to determine the correct edition of the certificate. The "Copy" option has the ability to create a subject that is specific to needs whenever a JSON-formatted outcome has to be created. The "AWS IoT console" may then be launched. The output generated by using the MQTT technique interface is shown in the Figure 16.

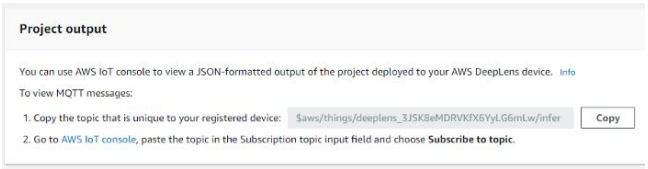

Figure 16: The MQTT technique.

The subject can be replicated and inserted under the "*Subscribe to topic*" before choosing the "*Publish to topic*" once it has been formatted as *"$aws/things/deeplens uuid>/infer*." Afterward, JSON-formatted results began to be released after the *"Publish to the topic"* button was hit. The "*Pause*" option is available on the upper right if the publication needs to be stopped. The AWS IoT Core interface to publish topic is represented in the Figure 17.

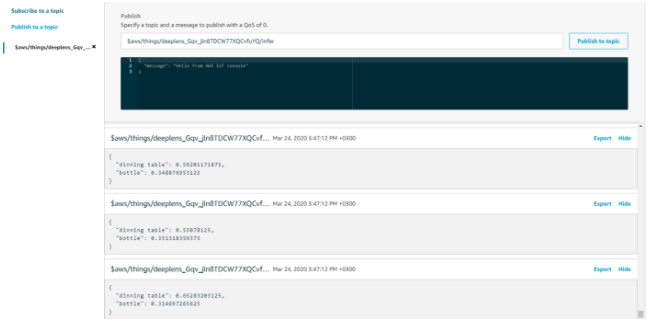

Figure 17: The publish topic interface.

B. *The Project Stream*

When the browser's license has been transferred, selecting "*View video stream*" in the *"Video streaming"* area will launch a new tab with the IP address *"192.168.1.47:4000"* inside it. The interface of video stream is presented in the Figure 18.

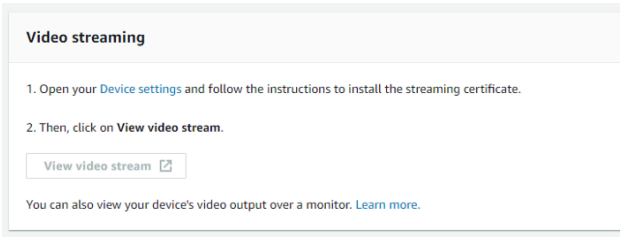

Figure 18: The interface of video stream

The two separate modules may be accessed when the stream is enabled on the provided IP address. The *"Project Stream"* page is the initial tab, and it represents the flow on which the object detection method was implemented. The blue outlines around the items on this stream can be seen, and the recognized names of the items with associated probability proportions can be seen on the upper edge of the windows. Due to the model's restricted training series of items, not all of the things on the screen can be identified. A customized model extract is necessary if additional items than those that can be recognized by the pre-trained object detection template are required. The final output of the AWS DeepLens object detection model is shown in the Figure 19.

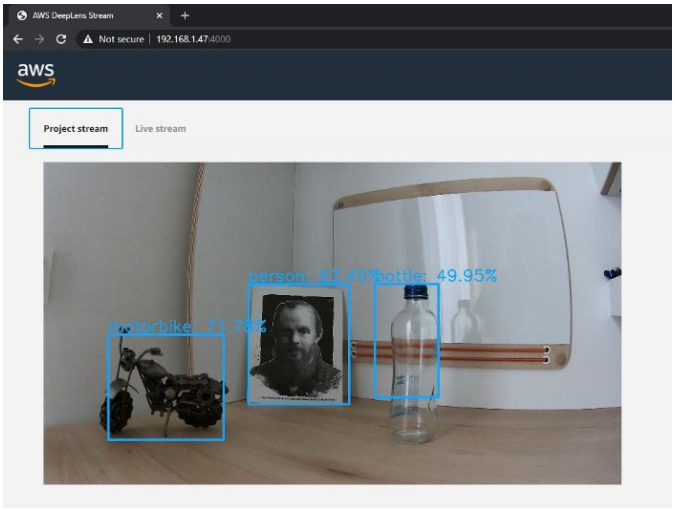

Figure 19: The final output object detection model.

V. DISCUSSION

"*Live Stream*" version is the name of the second stream. The regular camera's live feed displays frames more rapidly than "*Project Stream*". The reason is that it does not fit any model of the objects. Also, it may be inspected once this option is enabled.

As an additional future improvement field, an external model might be imported from the project type step. By using the externally imported, manually-trained model, the "*Live Stream*"

module can experiment.

In addition, the outputs of the "*Project Stream*" and "*Live Stream*" streams' the detected objects, and their accuracy ratios can be compared from the same angle by using the same object sets.

What's more, the object-detecting versions of AWS DeepLens can be analyzed in an extra metric. The versions may be measured by their time lengths while detecting the objects. This time-based parameter might be impactful in expressing a different dimension by stream versions.

REFERENCES

[1] R. Schapire, *COS 511: Theoretical Machine Learning*, Princeton University, 2008.

[2] A. Ng and K. Katanforoosh, *Deep Learning-CS229 Lecture Notes*, Stanford University.

[3] P. Kamencay, M. Benco, T. Mizdos and R. Radil, *A New Method for Face Recognition Using Convolutional Neural Network*, Advances in Electrical and Electronic Engineering, vol. 15, no. 4, 2017.

[4] Deeplearning.stanford.edu, *Unsupervised Feature Learning and Deep Learning Tutorial*, 2019.

[5] M. Ahmad, I. Ahmed, K. Ullah, I. Khan, A.Khattak, A. Adnan. *Person detection from overhead view: A survey*. International Journal of Advanced Computer Science and Applications, 10, 01 2019.

[6] M. Ahmad, I. Ahmed, K. Ullah, I. Khan, A.Khattak, A. Adnan. *Person detector for different overhead views using machine learning. International Journal of Machine Learning and Cybernetics*, 10(10):2657–2668, 2019.

[7] R. Xu, S. Y. Nikouei, Y. Chen, A. Polunchenko, S. Song, C. Deng, T. R. Faughnan. *Real-time human objects tracking for smart surveillance at the edge.* IEEE International Conference on Communications (ICC), pages 1–6, 2018.

[8] *Deploy a Model on Amazon SageMaker Hosting Services - Amazon SageMaker*, Docs.aws.amazon.com.

[9] T. Soper, *Amazon Web Services unveils a $249 wireless deep learning video camera for developers*, *GeekWire*, 2017.

[10] *Best practices for working with AWS Lambda functions*, AWS Lambda Official Developer Guide Documentation, https://docs.aws.amazon.com/lambda/latest/dg/best-practices.html

[11] *AWS DeepLens Project Workflow - AWS DeepLens*, AWS DeepLens Official Developer Guide Documentation, https://docs.aws.amazon.com/deeplens/latest/dg/how-it-works.html

[12] E. Pınar, *New Generation Computer Vision: AWS DeepLens*, Towards Data Science, 2020. https://medium.com/towards-data-science/new-generation-computer-vision-aws-deeplens-45052e39b4bc

The Influence of Donor and Receiver Combinations on Immune Plasma Programming in Symbolic Regression Problems

B.YETİŞKİN[1] and S. ARSLAN[1]

[1] Sivas Cumhuriyet University, Sivas/Turkey, 20209257002@cumhuriyet.edu.tr
[1] Sivas Cumhuriyet University, Sivas/Turkey, sibelarslan@cumhuriyet.edu.tr

Abstract **- Evolutionary computation is a computer intelligence system inspired by natural evolution. Automatic programming methods based on evolutionary computation, such as genetic programming (GP), ant programming (AP), artificial bee colony programming (ABCP), and immune plasma programming (IPP), successfully find effective solutions to various types of problems in many fields. This paper sets out to investigate the results of different configurations of IPP with the number of recipients (NoR) and the number of donors (NoD). To distinguish between these results, we used 10 different donor and receiver combinations and applied them to 15 symbolic regression problems. These results shows that IPP can successfully solve symbolic regression problems and the best combination of NoR and NoD is 2-1.**

Keywords **– evolutionary computation, automatic programming, immune plasma programming, donor receiver configurations, symbolic regression problem.**

I. INTRODUCTION

Nowadays, there are many methods that provide effective solutions to complex problems. Automatic programming, one of these methods, is a machine learning approach. It allows predicting the outputs with the least error by evolutionary computation of the inputs in a system [1]. Many automatic programming methods, such as Genetic Programming (GP) [5], Ant Programming (AP) [6], and Immune Plasma Programming (IPP) [7], are used to solve variety problems including classification [2], flow friction [3], and feature selection [4].

Symbolic regression is a sample of regression analysis that aims to find the most appropriate nonlinear model for a given data set [8]. It aims to identify the inputs that affect the outputs and model them mathematically [9]. Symbolic regression problems have already been successfully solved using evolutionary computation-based automatic programming methods [10]. In this paper, we solved these problems by trying different combinations to select the optimal initial number of donors number of receivers of IPP.

Other contributions of the work are listed as follows:

- According to the literature review, IPP was used for the first time to solve the symbolic regression problem.
- Performance analysis was performed with different donor and receiver configurations of IPP.
- The parameters of IPP were tuned to rise the predictive accuracy of the model.

We organize the rest of this work as follows: Detailed information about the IPA and IPP is explained in Section 2. The problem definition, parameters, and experimental studies are given in Section 3. The results and future work are summarized in Section 4.

II. MATERIAL AND METHOD

This section explains the immune plasma algorithm (IPA) and the IPA-inspired IPP.

A. Immune Plasma Algorithm (IPA)

Experts have tried many methods to solve the global health crisis caused by Coranavirus disease. One of these methods is immune plasma treatment. This involves taking blood plasma from people who have previously been diagnosed with coranavirus disease and have recovered after completing the treatment. The goal is to transfer the antibodies in the recovered people's blood to the patients and ensure their recovery. Aslan and Demirci introduced IPA, a population-based meta-heuristic method inspired by immune plasma treatment [1]. They match the stage of spreading infection among individuals to the research of the algorithm and the stage of plasma transfer to the development of solutions. The individuals represent possible solutions, and the quantity of individuals represents the abundance of antibodies. The better the quality of the solution, the more antibodies an individual generates. IPA consists of 3 phases. The basic structure of the algorithm is given below:

Produce initial solutions
REPEAT
Phase 1 → Spread phase of infection
Phase 2 → Plasma transfer phase
Phase 3 → Control phase of donor immune memory
UNTİL (until the stopping criteria are)

Produce initial solutions: First, the initial solutions in the population are produced. The assignment for the j dimension of the solution x_k is done by Eq. (1).

$$x_{kj} = x_j^{min} + rand(0,1)\left(x_j^{max} - x_j^{min}\right) \quad (1)$$

The largest value that the jth dimension can assume is represented by x_j^{max} and the smallest value by x_j^{min}, while $rand(0,1)$ is the random number between 0 and 1.

Spreading phase of infection: Individuals are infected to expand the research area of the algorithm. The spread of infection among individuals in the population is shown in Eq. (2).

$$x_{kj}^{inf} = x_{kj} + rand(-1,1)\left(x_{kj} - x_{mj}\right) \quad (2)$$

x_{kj}^{inf} is the value of the randomly determined jth dimension of the infected solution. x_{mj} represents the jth dimension of a randomly selected solution and is different from the solution x_{kj}. $k = \{1, 2, 3, \dots, PS\}$, $j = \{1, 2, 3, \dots, D\} - \{k\}$ and the value $rand(-1,1)$ is a randomly determined value in the range -1 to 1.

IPA determines the immune response of individuals according to the predetermined objective function for the problem. The dimension of individual j is denoted by $f(x_{kj})$ before infection and $f(x_{kj}^{inf})$ after infection. For minimization problems, when the value of $f(x_{kj}^{inf})$ is smaller than the value of f $f(x_{kj})$, the value of individual x_{kj} is updated with x_{kj}^{inf} as in Eq. (3); for maximization problems, if the $f(x_{kj}^{inf})$ is greater than the of $f(x_{kj})$, the value of individual x_{kj} is updated with x_{kj}^{inf} as in Eq. (4). So, there is a greedy selection between x_{kj} and x_{kj}^{inf}.

$$x_{kj} = \begin{cases} x_{kj}^{inf}, & if \quad f(x_{kj}^{inf}) < f(x_{kj}) \\ x_{kj}, & else \end{cases} \quad (3)$$

$$x_{kj} = \begin{cases} x_{kj}^{inf}, & if \quad f(x_{kj}^{inf}) \geq f(x_{kj}) \\ x_{kj}, & else \end{cases} \quad (4)$$

Plasma transfer phase: After the infection process has occurred in all individuals of the population in the spreading phase of infection, donor and receiver individuals are defined as fixed depending on the immune response in this phase. The number of donor solutions with the best immune response is represented as Number of Donors (NoD) and the number of receiver solutions with the worst response is represented as Number of Receivers (NoR). The plasma transfer to the receiver solution with a randomly selected donor from the donor solutions is given in Eq. (5).

$$x_{kj}^{rcv-p} = x_{kj}^{rcv} + rand(-1,1)\left(x_{kj}^{rcv} - x_{mj}^{dnr}\right) \quad (5)$$

Where $k = \{1, 2, 3, \dots, NoR\}$ and $j = \{1, 2, 3, \dots, D\}$, the value $rand(-1,1)$ corresponds to a randomly determined number in the range -1 to 1. x_{kj}^{rcv} is the variable of the jth dimension of the x_k^{rcv} receiver before plasma transfer; x_{kj}^{rcv-p} represents the immune response after plasma transfer to the x_k^{rcv} receiver. x_{mj}^{dnr} is the variable of the jth dimension of the x_m^{dnr} donor.

If the $f(x_k^{rcv-p})$ is better than the $f(x_m^{dnr})$, the x_k^{rcv} is updated with the transferred x_k^{rcv-p}solution and a second plasma dose It is applied again as given in Eq. (5). In the other case, the x_k^{rcv} is updated with the x_{mj}^{dnr} and the plasma transfer process is completed. To observe the effect of the second and subsequent doses when the plasma transfer process continues, you need to compare the $f(x_k^{rcv-p})$ and $f(x_k^{rcv})$. If the $f(x_k^{rcv-p})$ is better than the $f(x_k^{rcv})$, the x_k^{rcv} is updated by the x_k^{rcv-p} and the plasma transfer process continues. If the $f(x_k^{rcv-p})$ is worse than the $f(x_k^{rcv})$, the transfer phase is terminated.

Control phase of donor immune memory: The response of antibodies generated against infections from donors thought to have recovered in the population may differ over time. IPA assesses the time-dependent diversity in donor immune response by calculating the rate of the number of evaluations $((t_c)$ to the total number of evaluations $((t_{max})$. If the result $((t_c/t_{max})$ for the x_{mj}^{dnr} is less than the randomly produced value between 0 and 1, the donor x_m^{dnr} is completely replaced using Eq. (5), otherwise using Eq. (6), each jth parameter of the donor x_m^{dnr} is changed.

$$x_{mj}^{dnr} = x_{mj}^{dnr} + rand(-1,1)(x_{mj}^{dnr}) \quad (6)$$

B. Immune Plasma Programming (IPP)

Arslan proposed IPP by adapting the phases of IPA to high-level automatic programming [2]. One of the main differences that distinguishes IPP from IPA is the representation of solutions. While solutions in IPA are expressed as fixed-size arrays, in IPP they are represented as variable-size trees. The smallest unit of trees, nodes, consists of functions and terminals. While the function set contains mathematical and logical functions and arithmetic operators, the terminal set contains constants and variables. The shallowest node of the tree is named the root. An example of a representation of a solution in IPP can be found in Fig. (1). To represent the independent variables x_1 and x_2, the dependent variable $f(x_1, x_2)$, the mathematical equation of the solution in Fig. (1) is found by calculating the deepest node to root in Eq. (7).

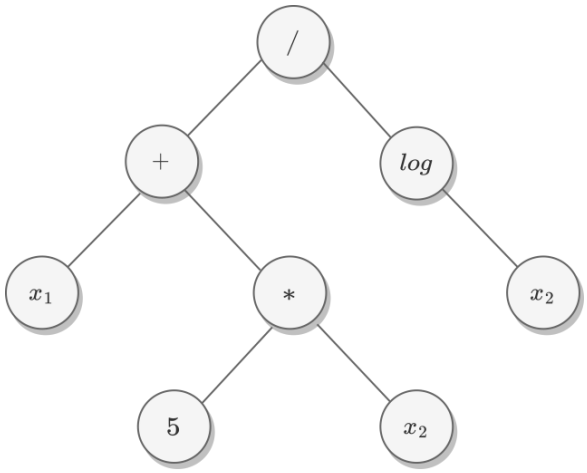

$$f(x_1, x_2) = \frac{x_1 + 5x_2}{\log(x_2)} \quad (7)$$

Figure 1: Representation of solutions in IPP.

Another difference between IPP and IPA is the improvement. This mechanism is adapted from the information sharing mechanism used by Karaboğa et al. in ABCP [11]. Fig. (2) shows the improvement mechanism. Fig. 2(a) and 2(b) show the individual to be cured and the individual to be used for treatment, respectively. Fig. 2(c) shows the information received from the individual to be used for the treatment, and 2(d) shows the individual to whom this information was transferred. In the mechanism, random pruning points of individuals are selected. The nodes below the pruning point are considered. The subtree below the pruning point of the individual to be cured is discarded and replaced by the subtree below the pruning point of the individual to be used for the treatment. In this way, an attempt is made to improve the individual development mechanism. Fig. (3) shows the flowchart of the IPP.

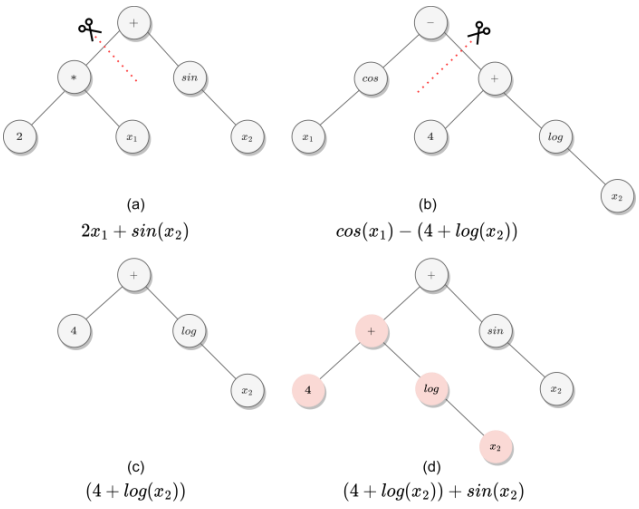

Figure 2: IPP improvement mechanism

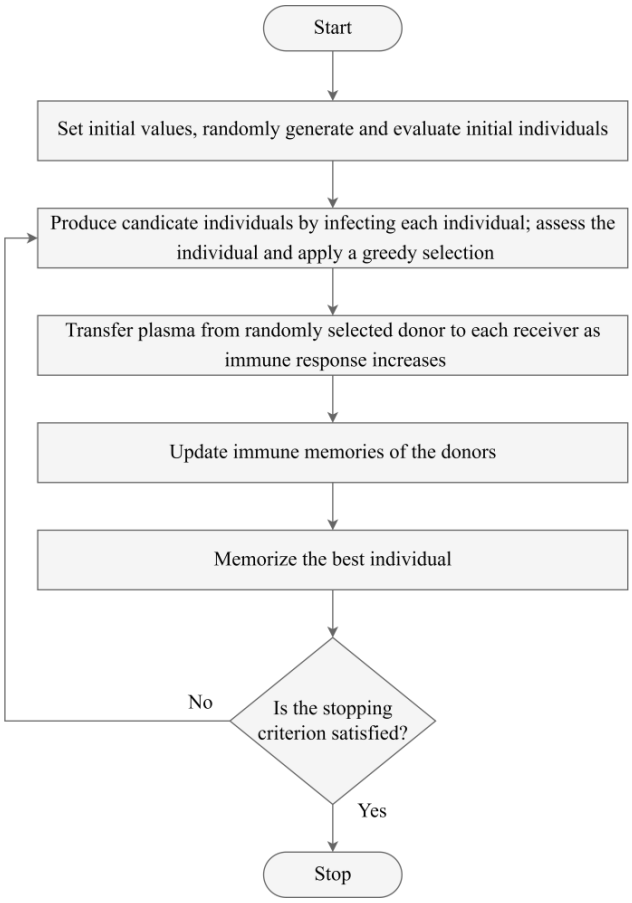

Figure 3: IPP flowchart.

III. EXPERIMENTAL DESIGN

In this section, the configurations of IPP with different numbers of donors and receivers were tested and their success in symbolic regression problems was observed. Thus, an attempt was made to determine the optimal number of donors and receivers.

A. *Problem Description and Parameters*

In this work, 15 benchmark functions were used to compare the success of IPP on symbolic regression problems. These functions, which have been used in various studies [11-14], are presented in Table 1. The initial parameters of IPP, which are the same in all experiments except the donor and receiver numbers, are listed in Table 2. This work also attempted to determine the optimal donor and receiver numbers by fitting the 10 different donor and receiver configurations. In the experiments, IPP was run 30 times independently for each combination. Thus, $30 \times 10 = 300$ runs were performed for each test function. The cost function used in the execution is explained in Eq. (8).

$$(x_i) = \sum_{j=1}^{N} |g_j - t_j| \quad (8)$$

Table 1: Benchmark functions [11].

Name	Function	Range
F_1	$f(x) = x^4 + x^3 + x^2 + x$	[-1,1]
F_2	$f(x) = x^5 + x^4 + x^3 + x^2 + x$	[-1,1]
F_3	$f(x) = \sin(x) + \sin(x + x^2)$	[0,1]
F_4	$f(x) = \sin(x^2)\cos(x) - 1$	[0,π/2]
F_5	$f(x) = \log(x + 1) + \log(x^2 + 1)$	[0,2]
F_6	$f(x) = \sqrt{x}$	[0,4]
F_7	$f(x, y) = \sin(x) + \sin(y^2)$	[0,1] x [0,1]
F_8	$f(x, y) = 2\sin(x)\cos(x)$	[0,1] x [0,1]
F_9	$f(x) = x^3 + x^2 + x$	[-1,1]
F_{10}	$f(x) = x^6 + x^5 + x^4 + x^3 + x^2 + x$	[-1,1]
F_{11}	$f(x) = \sin(x) + x^2 + 1$	[-1,1]
F_{12}	$f(x) = \sin(x^3 + x)$	[-1,1]
F_{13}	$f(x, y, z) = (30xz)/((x - 10)y^2)$	x,z ⊂ [-1,1]; y ⊂ [1,2]
F_{14}	$f(x, y) = x^4 + x^3 + x^2/2 - y$	[-3,3] x [-3,3]
F_{15}	$f(x, y) = x^y$	[0,1] x [0,1]

Table 2: Parameters.

Parameter	Value
Population size	500
Evaluation number	25.000
Function set	+, -, *, /, sin, cos, exp, log
Maximum tree size	15

N is the sum of fitness samples to assess a tree. g_j is the output of the tree for a sample j, while t_j is the target for the same sample.

B. Simulation Result and Discussion

This subsection analyses the simulation results of the runs and focuses on the following comments:

- For the F_1 function, the best mean for the combination is 6-6. The standard deviations are close for all combinations. However, the most successful model was obtained with the combination 6-3.
- Although the F_2 function is best mean in combination 7-7, its standard deviation is quite high compared to the other combinations. All combinations except combination 1-1 were able to achieve good models. Among them, the most successful model is in combination 5-5.
- In function F_3, combination 4-2 has about 2 times better mean than combinations 4-4, 5-5, 6-6 and 7-7, but in the best models, all except combination 6-6 have achieved the optimal value.
- For function F_4, all combinations except combination 2-1 have a lower mean success, but the best model was observed for combination 1-1. The best model of combination 1-2 has about 0.01 higher error than 1-1.
- Combination 6-3 with the most successful mean at function F_5 gave about 0.2 lower error values than combinations 5-5 and 7-7, and the best model was obtained with combination 1-2.
- For function F_6, the best mean and lowest standard deviation are with combination 4-2, but combination 2-1 with the best model for this function has a very low error value compared to the other combinations.
- For functions F_7 and F_8, it can be noted that all combinations give optimal results with an error value close to 0 and all combinations are successful for this function.
- Looking at the mean error values in the F_9 function, the error value of the combination with 6 donors of two combinations with 6 receiver is about 3 times lower than the error value of the combination with 3 donors. 6-3 has the worst mean value of all combinations and 6-6 has the best mean value. Thus, we conclude that NoD is critical to the success of IPP.
- The combination 4-2 has the best mean in the F_{10} function. However, three different combinations (5-5, 6-6 and 7-7) were able to produce the best models with the same error values.
- Similiar to the F_{11}, F_{12}, F_{13} and F_{14} functions, the best average values were obtained with the 2-1 combination. However, optimality was achieved for many combinations of functions F_{11} and F_{12}. The best model of F_{14} in combination 2-1 has a very low error value compared to all other combinations. The error value of this model is almost half of the error value of the best models of combinations 2-2, 3-3, 4-4 and 5-5.
- It has the best mean value and the model of combination 4-2 in function F_{15}.

Table 3: Results of different NoR and NoD configurations for 15 different benchmark functions.

Function		$NoR=1$ $NoD=1$	$NoR=2$ $NoD=1$	$NoR=2$ $NoD=2$	$NoR=3$ $NoD=3$	$NoR=4$ $NoD=2$	$NoR=4$ $NoD=4$	$NoR=5$ $NoD=5$	$NoR=6$ $NoD=3$	$NoR=6$ $NoD=6$	$NoR=7$ $NoD=7$
F_1	Mean	7.34E-01	5.87E-01	7.44E-01	7.99E-01	7.80E-01	6.28E-01	5.00E-01	4.64E-01	**3.80E-01**	4.83E-01
	Std.	4.14E-01	4.05E-01	4.75E-01	4.91E-01	**3.33E-01**	4.95E-01	5.32E-01	3.88E-01	4.67E-01	4.62E-01
	Best	1.48E-15	7.91E-16	1.20E-15	1.42E-15	1.70E-15	1.05E-15	1.20E-15	**4.86E-16**	9.99E-16	1.05E-15
F_2	Mean	9.99E-01	8.37E-01	8.77E-01	9.36E-01	8.11E-01	9.63E-01	8.53E-01	6.96E-01	8.74E-01	**6.78E-01**
	Std.	**1.92E-01**	2.29E-01	2.82E-01	3.49E-01	2.68E-01	1.97E-01	4.11E-01	3.47E-01	3.80E-01	4.98E-01
	Best	5.25E-01	4.02E-16	3.12E-16	4.23E-16	4.86E-16	6.57E-01	**2.64E-16**	3.19E-16	2.91E-16	2.91E-16
F_3	Mean	3.33E-01	2.51E-01	3.81E-01	4.69E-01	**2.21E-01**	4.48E-01	4.80E-01	3.14E-01	5.96E-01	6.48E-01
	Std.	2.05E-01	**1.86E-01**	2.18E-01	2.76E-01	1.88E-01	2.46E-01	2.51E-01	2.39E-01	2.57E-01	2.43E-01
	Best	**0.00E+00**	**0.00E+00**	**0.00E+00**	**0.00E+00**	**0.00E+00**	**0.00E+00**	**0.00E+00**	**0.00E+00**	1.30E-01	**0.00E+00**
F_4	Mean	1.02E+00	**8.58E-01**	1.19E+00	1.52E+00	8.74E-01	1.65E+00	1.72E+00	1.02E+00	1.86E+00	1.80E+00
	Std.	3.58E-01	4.15E-01	4.57E-01	5.63E-01	4.51E-01	6.07E-01	4.92E-01	4.34E-01	**3.29E-01**	4.81E-01
	Best	**0.00E+00**	9.76E-02	3.93E-01	3.95E-01	2.92E-01	4.33E-01	8.74E-01	4.92E-01	9.71E-01	6.93E-01
F_5	Mean	5.71E-01	4.99E-01	5.21E-01	5.63E-01	4.89E-01	5.58E-01	6.15E-01	**4.20E-01**	5.31E-01	6.14E-01
	Std.	**8.72E-02**	1.39E-01	1.66E-01	1.23E-01	1.47E-01	1.85E-01	2.15E-01	1.27E-01	1.87E-01	3.18E-01
	Best	3.93E-01	**1.62E-01**	2.12E-01	2.15E-01	1.83E-01	3.02E-01	2.05E-01	1.62E-01	2.14E-01	2.06E-01
F_6	Mean	1.56E+00	9.24E-01	1.55E+00	1.75E+00	**7.20E-01**	1.79E+00	1.83E+00	9.82E-01	2.10E+00	1.98E+00
	Std.	8.11E-01	7.13E-01	8.49E-01	7.79E-01	**5.01E-01**	9.84E-01	9.67E-01	6.81E-01	8.41E-01	9.18E-01
	Best	3.43E-01	**1.05E-15**	2.11E-01	2.18E-01	8.81E-02	3.41E-01	5.19E-01	4.62E-02	7.56E-01	6.53E-01
F_7	Mean	2.59E-17	**0.00E+00**	**0.00E+00**	**0.00E+00**	**0.00E+00**	**0.00E+00**	1.90E-02	**0.00E+00**	**0.00E+00**	9.49E-03
	Std.	1.42E-16	**0.00E+00**	**0.00E+00**	**0.00E+00**	**0.00E+00**	**0.00E+00**	7.22E-02	**0.00E+00**	**0.00E+00**	5.20E-02
	Best	**0.00E+00**	**0.00E+00**	**0.00E+00**	**0.00E+00**	**0.00E+00**	**0.00E+00**	**0.00E+00**	**0.00E+00**	**0.00E+00**	**0.00E+00**
F_8	Mean	2.95E-15	3.08E-15	3.26E-15	**2.78E-15**	3.48E-15	2.82E-15	3.33E-15	3.85E-15	2.98E-15	3.33E-15
	Std.	1.66E-15	1.57E-15	1.36E-15	1.72E-15	1.12E-15	1.73E-15	1.33E-15	**0.00E+00**	1.61E-15	1.33E-15
	Best	**0.00E+00**	**0.00E+00**	**0.00E+00**	**0.00E+00**	**0.00E+00**	**0.00E+00**	**0.00E+00**	3.85E-15	**0.00E+00**	**0.00E+00**
F_9	Mean	8.49E-02	1.34E-01	1.13E-01	1.27E-01	1.12E-01	1.96E-01	1.30E-01	1.83E-01	**4.87E-02**	1.72E-01
	Std.	**2.38E-01**	2.83E-01	2.88E-01	3.33E-01	3.49E-01	4.59E-01	3.98E-01	2.72E-01	2.67E-01	5.09E-01
	Best	**0.00E+00**	**0.00E+00**	**0.00E+00**	6.18E-16	**0.00E+00**	**0.00E+00**	4.51E-16	**0.00E+00**	**0.00E+00**	**0.00E+00**
F_{10}	Mean	1.15E+00	8.68E-01	1.19E+00	1.14E+00	**7.87E-01**	1.28E+00	1.11E+00	8.00E-01	9.87E-01	9.86E-01
	Std.	4.16E-01	2.62E-01	3.01E-01	3.23E-01	2.37E-01	3.69E-01	3.57E-01	**2.05E-01**	2.90E-01	3.93E-01
	Best	3.50E-01	1.45E-01	6.54E-01	6.04E-01	4.46E-01	6.32E-01	**1.17E-15**	3.05E-01	**1.17E-15**	**1.17E-15**
F_{11}	Mean	4.45E-01	**3.09E-01**	9.20E-01	8.19E-01	3.48E-01	1.14E+00	1.06E+00	3.84E-01	1.07E+00	1.32E+00
	Std.	3.38E-01	**2.83E-01**	4.49E-01	5.38E-01	3.32E-01	5.00E-01	6.24E-01	3.11E-01	4.64E-01	7.43E-01
	Best	**0.00E+00**	**0.00E+00**	2.44E-15	**0.00E+00**	**0.00E+00**	**0.00E+00**	**0.00E+00**	**0.00E+00**	6.66E-16	6.66E-16
F_{12}	Mean	4.72E-01	**2.47E-01**	5.71E-01	8.24E-01	3.28E-01	6.70E-01	8.48E-01	4.09E-01	8.42E-01	9.03E-01
	Std.	3.74E-01	**2.94E-01**	3.70E-01	3.23E-01	3.50E-01	3.32E-01	3.29E-01	3.57E-01	3.16E-01	3.05E-01
	Best	**0.00E+00**	**0.00E+00**	**0.00E+00**	3.16E-02	**0.00E+00**	**0.00E+00**	**0.00E+00**	**0.00E+00**	1.99E-01	2.14E-01
F_{13}	Mean	4.61E+00	**3.50E+00**	5.77E+00	5.90E+00	3.51E+00	6.53E+00	6.01E+00	3.66E+00	6.33E+00	6.66E+00
	Std.	2.68E+00	2.07E+00	2.11E+00	2.39E+00	**1.43E+00**	2.64E+00	2.65E+00	1.76E+00	2.63E+00	2.43E+00
	Best	7.55E-01	**3.42E-01**	2.46E+00	2.42E+00	1.46E+00	2.30E+00	1.92E+00	8.27E-01	1.79E+00	1.67E+00
F_{14}	Mean	1.60E+02	**1.46E+02**	1.95E+02	1.89E+02	1.55E+02	1.88E+02	1.82E+02	1.52E+02	1.84E+02	1.86E+02
	Std.	3.38E+01	4.35E+01	3.98E+01	3.76E+01	3.93E+01	4.36E+01	4.27E+01	4.05E+01	**3.15E+01**	4.38E+01
	Best	7.32E+01	**5.71E+01**	1.18E+02	1.04E+02	8.25E+01	1.12E+02	1.13E+02	6.45E+01	9.77E+01	8.74E+01
F_{15}	Mean	2.04E+00	1.70E+00	2.02E+00	1.97E+00	**1.64E+00**	2.16E+00	2.17E+00	1.83E+00	2.14E+00	2.29E+00
	Std.	**3.09E-01**	3.34E-01	3.41E-01	3.48E-01	3.59E-01	4.54E-01	4.92E-01	4.32E-01	5.16E-01	5.42E-01
	Best	1.44E+00	9.56E-01	1.39E+00	1.24E+00	**5.53E-01**	1.50E+00	1.49E+00	9.52E-01	1.30E+00	1.35E+00

Table 4: Number of models most succesfull in combinations of IPP

Combination	Mean	Best
$NoR=1, NoD=1$	-	7
$NoR=2, NoD=1$	6	10
$NoR=2, NoD=2$	1	5
$NoR=3, NoD=3$	2	4
$NoR=4, NoD=2$	5	7
$NoR=4, NoD=4$	1	6
$NoR=5, NoD=5$	-	7
$NoR=6, NoD=3$	2	6
$NoR=6, NoD=6$	3	3
$NoR=7, NoD=7$	1	4

According to the simulation results in Table 3, Table 4 provides information on how many of each combination is most successful in the mean and best models. The results show that all combinations, except for the 1-1 and 5-5, are most successful in the mean in at least 1 model. The combination that is most successful in both the mean and the best model overall is the 2-1. It can be noted from the table that the 4-2 combination is also second. Of all the combinations, the 2-2, 3-3 and 7-7 combinations has the least success compared to the others.

IV. CONCLUSIONS

Symbolic regression is a methodology that attempts to create a nonlinear model of the relationship between the dependent and independent parameters of a system. In symbolic regression, to develop a mathematical model with high predictive accuracy, the initial parameters must be set optimally. In this study, experiments on symbolic regression problems were conducted to optimally set NoR and NoD in the IPP. The results of the experiments show that $NoR = 2$ and $NoD = 1$ is the combination with the highest success and $NoR = 2$ and $NoD = 2$, $NoR = 3$ and $NoD = 3$ and $NoR = 7$ and $NoD = 7$ are the lowest combinations. Moreover, the results of this paper support the idea that IPP is a useful method for dealing with symbolic regression problems. Future work is planned to compare IPP with other automatic programming methods in solving various real-world problems and to improve new versions.

REFERENCES

[1] S. Aslan, and S. Demirci, "Immune Plasma Algorithm: A Novel MetaHeuristic for Optimization Problems", *IEEE Access*, vol. 8, pp. 220227- 220245, 2020.

[2] S. Arslan, and C. Ozturk, "Feature Selected Data Cancer Classification with Genetic Programming", *2017 21st National Biomedical Engineering Meeting (BIYOMUT)*, November - December 2017.

[3] B. Yetişkin, and S. Arslan, "Approximation of the Colebrook Equation for Flow Friction with Immune Plasma Programming", *2022 30th Signal Processing and Communications Applications Conference (SIU),* pp. 1-4, May 2022.

[4] E. Scalco, G. Rizzo W. and Gómez-Flores, "Automatic Feature Construction Based on Genetic Programming for Survival Prediction in Lung Cancer Using CT Images", *2022 44th Annual International Conference of the IEEE Engineering in Medicine & Biology Society (EMBC),* pp. 3797-3800, July 2022.

[5] J. R. Koza, *"Genetic programming on the programming of computers by means of natural selection*", MIT Press, Cambridge, 2022.

[6] O. Roux, C. Fonlupt, *Ant programming: or how to use ants for automatic programming*, 2nd International Workshop on Ant Algorithms, 2000.

[7] S. Arslan, *Zaman Serisi Tahmin Probleminin İmmün Plazma Programlama Kullanılarak Çözülmesi*, Avrupa Bilim ve Teknoloji Dergisi, 2021.

[8] M. D. Schmidt, H. Lipson, *Co-evolving fitness predictors for accelerating and reducing evaluations*, Genetic Programming Theory and Practice IV, Genetic and Evolutionary Computation, vol. 5, Springer, 2006.

[9] J. Kleijnen, R. Sargent, *A methodology for fitting and validating metamodels in simulation,* European Journal of Operational Research vol. 120, pp. 14–29, 2000.

[10] A. E. Eiben, J. E. Smith, *Introduction to Evolutionary Computing*, Springer, 2003.

[11] D. Karaboğa, C. Öztürk, N. Karaboğa, and B. Görkemli, *Artificial Bee Colony Programming for Symbolic Regression,* Information Sciences, vol. 209, pp. 1-15, 2012.

[12] N. X. Hoai, R. I. McKay, D. Essam, R. Chau, "Solving the symbolic regression problem with tree-adjunct grammar guided genetic programming: the comparative results", *Proceedings of the IEEE Congress on Evolutionary Computation*, CEC'02, pp. 1326–1331, 2002.

[13] C. Johnson, *Genetic programming crossover: does it cross over*. Springer, pp 97–108, 2009.

[14] M. Keijzer, *Improving symbolic regression with interval arithmetic and linear scaling*, Springer, 2003.

Using Permissioned Blockchain In Education System for Internship

Ozgur OKSUZ[1]

[1] Konya Technical University, Department of Software Engineering, Konya/Turkey, ooksuz@ktun.edu.tr

***Abstract* – Blockchain technology has been used in many sectors such as healthcare, supply-chain management, and energy. In this paper, we use blockchain technology in the education system for internship. We provide a system that allows the recruiter to choose an appropriate candidate (student) that satisfies the requirements of the internship position. Moreover, the student's data privacy (grade, identity, course information) is preserved in the blockchain. Furthermore, storing the students' data in the blockchain and the centralized database does not allow students to lie about their academic history. In addition, the recruiters can only be able to view/retrieve students' records once they are authorized to.**

***Keywords* – Blockchain, Education, Internship, Privacy, Authorization.**

I. INTRODUCTION

Blockchain technology was firstly introduced in using a crypto-currency known as Bitcoin [1]. Then, it has been widely used in many sectors such as healthcare [2], supply-chain management [3], Internet of things (IoT) [4], energy [5] and education [6]. Current education system lacks of transparency of data and privacy issues. Students can easily lie about their academic achievements to get a job or an internship since there is no integrity mechanism to check if the student indeed has committed achievements. Moreover, carrying transcripts and certificates all the time with them results inefficiency when they apply for internships or jobs since the documents can easily be lost or damaged. Furthermore, storing these documents in institutions is also problematic. The documents can be lost, stolen or damaged by human mistakes or natural disasters such as flooding.

In this paper, we address these problems by introducing a system that uses blockchain in education system. In this system, the students' academic achievements (grades, certificates) are stored in a blockchain and a centralized database by authorized entities (academic personnel). The students' information cannot be altered or deleted since the blockchain has immutability property. Since each entity (node) has a copy of the blockchain, it is infeasible to lose blockchain data. Once a student applies for an internship, the recruiter asks the corresponding academic personnel if the given information about the student is correct by using blockchain. In current education system, students can provide fake information about their academic histories. In the blockchain, the students' data (grades) cannot be altered and integrity of this information is preserved. Moreover, the students' data privacy is also preserved that any unauthorized entity cannot learn any student's private information such as the student's grade, real identity of the student (name, date-of-birth, address, phone number, social security number, etc.). Moreover, the proposed system is academic personnel oriented. In other words, academic personnel are the authorized entities issue transactions. Since internship position requirements differ from company to company, a company can require a student to take a specific course from specific academic personnel. In this case, the applicant (student) needs to prove that the student indeed has taken the course from that specific academic personnel.

II. RELATED WORK

There have been some studies that applying blockchain to education system. The work in [6] proposes a system that uses blockchain in the education system for applying for internships and jobs. However, in [6], students' information (grades, real identities) is stored in blockchain (on-chain). Using blockchain as on-chain storage results in scalability problems since each node in the system has limited-source capabilities such as storage. If the data in the blockchain grows faster, the nodes cannot handle that much data to process. The first university [7] uses blockchain technology to issue academic certificates. All completed courses of the students are in the blockchain and they are disclosed. It results that students' data privacy is not preserved. The work [8] uses two blockchains (private and public). [9-10] put students' certificates into the blockchain. However, they do not examine putting students' grades to blockchain. The work in [11] uses a permissioned blockchain but it does not provide privacy protection for the data. The same disadvantage is also seen in [12] that it does not have privacy protection mechanism. The studies in [13-17] use permissionless blockchain in education system. In study [18], the protocol uses Hyperledger that uses anonymous credentials ([19-20]) that introduce heavy cryptographic algorithms. Moreover, in [18] it is difficult to manage different credentials since each student needs to have multiple credentials to describe its private information.

In this work, students' original data is not stored in the blockchain (on-chain) to have scalability problems. Students' original data are stored in an off-chain database to prevent scalability problems. The corresponding address of the original file in the off-chain database is stored in the blockchain. This proposed scheme does not leak any private information about students before they apply for internships.

Our scheme leaks only the required information about the students that the internships require. Moreover, our scheme has only one blockchain and students' grades, courses and programs are stored in the blockchain and the centralized database. Furthermore, our system uses permissioned blockchain that more secure than permissionless blockchain. In addition, our scheme does not use heavy cryptographic tools.

III. PRELIMINARIES

In this section, we provide some building blocks that are used in our system.

A. Hash Function

A hash function, H, is a mathematical algorithm that maps an input a of any size to an output of fixed size b. This is represented as $H(a) = b$. A hash function is deterministic algorithm. If the algorithm retakes a as input, the output is always b. Another property of a hash function is efficiently computable. If an output b is given, it is infeasible to compute a from b. This property is called as "One Way". It is infeasible to find another c that satisfies $H(a) = H(c) = b$. This is called as "Collision Resistant".

B. Symmetric/Private Key Encryption

A symmetric encryption key scheme consists of Key Generation (KG), Encryption (Enc), and Decryption (Dec) algorithms. KG is the key generation algorithm takes a security parameter and outputs a key for user s, sk_s which is also the decryption key. Encryption algorithm takes a message m and the secret key sk_s, outputs ciphertext $C = Enc(m, sk_s)$. Decryption algorithm takes the secret key sk_s and C, outputs message $m = Dec(C, sk_s)$.

C. Asymmetric/Public Key Encryption

An asymmetric encryption scheme consists of Key Generation (KG), Encryption (Enc'), and Decryption (Dec') algorithms. KG is the key generation algorithm takes a security parameter and outputs a secret and public key for user s, $sk_s{}'$ and $pk_s{}'$. Encryption algorithm takes a message m and public encryption key $pk_s{}'$, outputs a ciphertext $C = Enc'(m, pk_s{}')$. Decryption algorithm takes the secret key $sk_s{}'$ and C, outputs message $m = Dec'(sk_s', C)$.

D. Signature

A digital signature scheme consists of Key Generation (KG), $Sign$, and $Verify$ algorithms. KG is the key generation algorithm takes a security parameter and outputs a signature secret key and public key (verification) for user s, $sigsk_s$ and $sigpk_s$. $Sign$ algorithm takes a message m and signature secret key $sigsk_s$, outputs a signature $Signature = Sign(sigsk_s, \mathrm{m})$. $Verify$ algorithm takes signature public key $sigpk_s$, signature $Signature$, and message m, outputs 1 ($Verify(sigpk_s, m, Signature) == 1$) if the signature is generated by user s using message m. Otherwise, the algorithm outputs 0.

E. Blockchain

Blockchain is a peer-to-peer decentralized system that nobody owns the system. It has the ledger technology that it keeps the information (transaction) up to date and it is immutable. Each node (computer) keeps a copy of this ledger. Since it is decentralized, other nodes check each transaction's validity. If the transaction is valid, then it is added to the ledger and transactions are kept as blocks. Security in Blockchain comes from two mathematical structures: hash functions and signatures. The use of the hash functions is to make transaction immutable. The use of signatures in the blockchain allows receivers to know the origin of the data. The first block is a special block known as genesis block.

There are two kinds of blockchain network: Permissionless and Permissioned. In a permissionless blockchain, anyone can join and leave the network without any permission from anyone. When a participant joins the network, it has the copy of entire blockchain. Anyone can validate the transactions publicly. In other words, all data in the blockchain is available to everyone. There is no trust between the participants. Permissionless blockchain network is used in Bitcoin [1] and Ethereum [21]. On the other hand, in a permissioned blockchain, not anyone can join the network. Permission is provided to certain identifiable participants to join the network. This requirement adds an additional level of security. Participants are known to each other. The trusted parties only write to the ledger. Permissioned blockchain is also used in many protocols since permissioned blockchain has an additional level of security. Moreover, permissioned blockchain is more efficient and more scalable.

IV. PROPOSED SYSTEM

In this section, we give the details of our system. Our focus is to provide secure, efficient, and transparent solutions for students to apply for internships. Our system has four entities: a central authority ***CA***, academic personnel (***AP***), students (***St***) and recruiters (***R***). ***CA*** is responsible for setting the algorithms used in the protocol. Moreover, ***CA*** also registers the entities public keys to the system. This results that in the system everyone knows each other. ***CA*** is a trustable entity that everyone relies on. ***CA*** can be government (ministry of education). ***AP*** is an entity that offers courses, prepares exams and grades the students' exams and stores the students' information in the blockchain. ***AP*** is also a trusted entity and can be a full professor, an associate professor, an assistant professor or a lecturer in a university**.** ***R*** is an entity that hires qualified students for a specific work task. ***R*** is not trusted that it can try to learn students' private information if it is not authorized. ***St*** is a student who takes courses and exams. Moreover, it wants to work in a company as an intern. ***St*** is also not trustable. It can lie about its academic information to get an internship.

In the system each entity is defined as a node. Only the trusted nodes issue transactions to the ledger. Since entities are known in advance, our protocol uses permissioned blockchain. In the proposed system, there is also a centralized database

controlled by ***CA*** that stores students' original data. Using a centralized database is for authorized access control management to students' private documents. Moreover, storing all the students' documents in the blockchain results scalability problem since each entity has limited resource capabilities. Once the data in the blockchain is getting more and more, the entities need more power sources and storage space to process the data. The workflow of the proposed scheme as follows:

1. ***CA*** registers each entities' (***AP,R***) public keys (signature public key and asymmetric encryption key).
2. ***St*** takes the exam from ***AP***. ***AP*** then put the encrypted grade and student's original identity to the central database.
3. The centralized database returns a hash pointer that locates the files in the storage to ***AP***. ***AP*** generates a transaction for the student that contains the hash pointer. Then, ***AP*** sends the transaction to all trusted nodes (entities). If at least 51% of the nodes agree with this transaction, ***AP*** puts the transaction to the blockchain.
4. ***St*** applies to an internship job by sending a message to corresponding ***R***. ***St*** also sends this message to ***AP*** to inform them of its intention and their possible future message exchanges.
5. ***R*** asks ***AP*** for getting corresponding information (based on requirements of the internship position) about the student on the blockchain. Once ***R*** gets the corresponding information in the blockchain, it gets the actual data of the student from the centralized database. Our system has the following phases:

Setup*:* In this phase, ***CA*** decides which signature (Sign), asymmetric/symmetric key encryption and hash function algorithms to use for the system. ***CA*** then announces these algorithms with appropriate security parameters to all nodes. Each node (***AP, R,*** and ***CA***) chooses their secret and public keys for these algorithms. A node's (entity w) public and secret key for asymmetric key encryption algorithm is shown as $pk_w{}'$ and $sk_w{}'$, a node's public/secret key for signature algorithm is shown as $sigpk_w$ and $sigsk_w$ and a node's encryption (decryption) key for symmetric encryption algorithm is shown as sk_w, where $w \in \{CA, AP, R\}$. ***CA*** also acts as certificate authority that registers entities public keys to the system and announces these keys to public. This results that in the system everyone knows each other. Moreover, each student (***St***) also chooses its signature public and secret keys as $sigpk_{St}/sigsk_{St}$. The student gives $sigpk_{st}$ to the faculties when the student enrolls each course. The student's pseudonym identity is set to $sigpk_{St}$.

Transactions: This phase happens when a student takes the exam, then the corresponding academic personnel generates a transaction. Firstly, ***AP*** sends the following tuple to the centralized database:

$$\left\langle \begin{matrix} sigpk_{AP}, Enc(G_{St}, k_1), Enc(SOI_{St}, k_2), \\ Enc(CID, k_3), \\ Enc(PID, k_4), TS', H(data'), \\ Sign(sigsk_{\boldsymbol{AP}}, H(data')) \end{matrix} \right\rangle,$$

where $sigpk_{\boldsymbol{AP}}$ is the identity of academic personnel, $Enc(G_{St}, k_1)$, is the encryption of the student's grade (G_{St}), $Enc(SOI_{St}, k_2)$ is the encryption of the student's original identity, CID is the course identity that student has taken, PID is the program identity that the student has enrolled, TS' is the time stamp, and $H(data')$ is the hash of data. The academic personnel chooses four secret keys, k_1, k_2, k_3, k_4 randomly. The student's real/original identity (SOI_{St}) consists of its real name, social security number, age, home address, phone number, email address, etc. Moreover, $data' = (sigpk_{AP}||Enc(G_{St}, k_1)||Enc(SOI_{St}, k_2) ||Enc(CID, k_3)||Enc(PID, k_4)||TS')$, where || is the concatenation operation. The centralized database sends a hash pointer, ptr, to ***AP***. The hash pointer is the hashing all data sent to the centralized database. This pointer is the address of location that the original data is stored in the centralized database. At last, ***AP*** generates the following tuple as a storage transaction (T):

$$T = \left\langle \begin{matrix} sigpk_{AP}, sigpk_{St}, ptr, H(data''), \\ Sign(sigsk_{AP}, H(data'')) \end{matrix} \right\rangle,$$

where $data'' = sigpk_{AP}||sigpk_{St}||ptr$. Then ***AP*** broadcasts T to other academic personnel. Once ***AP*** gets more than 50% of the votes that the transaction is valid, ***AP*** generates the following block (B) that consists of the following information:

$$B = \left\langle \begin{matrix} BI, T, HPB, TS, H(data), \\ Sign(sigsk_{AP}, H(data)) \end{matrix} \right\rangle,$$

where BI is the block index, HPB is the hash of the previous block. Moreover, there are other transactions that provide information about PID and CID ([6]). To get any information about PID, there is program policy transaction is defined. Program policy transaction gives information about the program that the student has enrolled for. These information consists of program requirements that a student needs to complete such as number of credits that the students must take, program description, program identity number, courses that the student must take, description of each course, etc. There is also course policy transaction ([6]). This transaction gives information about the requirements of the course that the student needs to complete. These requirements can be number of exams that the student needs to take, course description, course identity number, academic personnel information, course credit information, number of hours a week that the course takes, etc. These transactions (program policy and course policy) are issued by ***CA***. In Figure 1, we give an illustration for each transaction in a different block.

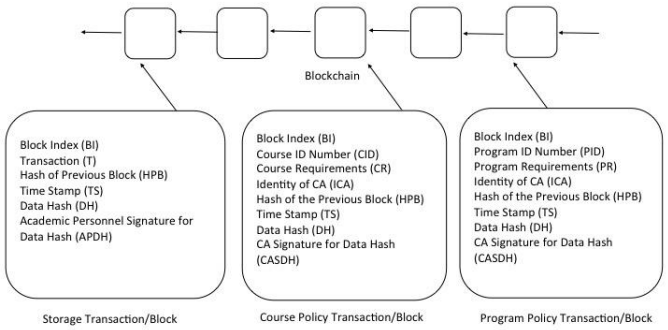

Figure 1. Blocks with Different Transaction Types

***Internship**:* In this phase, the student applies for an internship by sending a message to the corresponding recruiter, $\boldsymbol{R}$**.** Moreover, the student also sends the same message to all academic personnel $\boldsymbol{AP}$ so that $\boldsymbol{AP}$ provides the corresponding required internship conditions to $\boldsymbol{R}$. For example, if an open internship position requires taking programming courses. The student contacts to all academic people taught programming courses such as PYTHON, C++, and MATLAB. Moreover, the student can contact other academic people offered projects that the student used programming abilities during the projects. Moreover, $\boldsymbol{R}$ also contacts with each $\boldsymbol{AP}$ to get the student's original results. If the student indeed applies for internship, each $\boldsymbol{AP}$ sends the corresponding block indexes and the decryption keys to $\boldsymbol{R}$**.** $\boldsymbol{R}$ then searches block indexes from the blockchain and retrieves the pointers so that it gets the original encrypted records from the centralized database. Once the encrypted records are received form the centralized database, $\boldsymbol{R}$ decrypts them using decryption keys. The message flow of this process is shown in Figure 2.

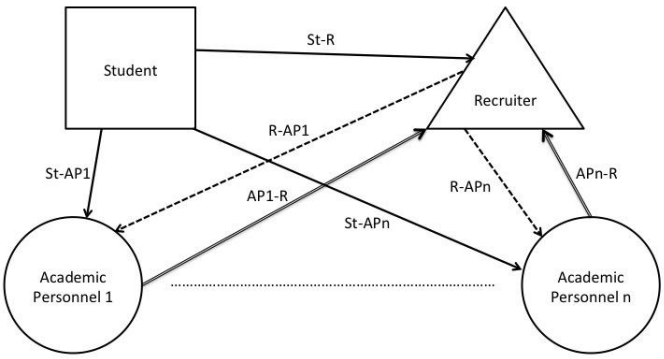

Figure 2. Message Flow Between Entities

In the figure, S-AP1 means that a message is sent from student to academic personnel 1, R-AP1 means that a message is sent from recruiter to academic personnel 1, APn-R means that a message is sent from academic personnel n to recruiter. We assume that internship position requires the student to contact n academic personnel. In other words, there are n different conditions that a candidate student needs to provide to get the internship. The messages are formed by the entities as follows:

St-R: The student sends
$Enc'(m, pk'_R)$ and $Sign(sigsk_{St}, Enc'(m, pk'_R))$ to $\boldsymbol{R}$.

St-AP1: The student sends
$Enc'(m, pk'_{AP1})$ and $Sign(sigsk_{St}, Enc'(m, pk'_{AP1}))$ to $\boldsymbol{AP1}$.

St-APn: The student sends
$Enc'(m, pk'_{APn})$ and $Sign\big(sigsk_{St}, Enc'(m, pk'_{APn})\big)$ to $\boldsymbol{APn}$**,** where $m = (InReq||sigpk_{St}||sigpk_R||sigpk_{AP1}||$ ... $||sigpk_{APn})$ and $InReq$ is the requirements of the internship position.

R-AP1: Once $\boldsymbol{R}$ receives $Enc'(m, pk'_R)$ and $Sign(sigsk_{St}, Enc'(m, pk'_R))$, it recovers m via decrypting the ciphertext. Then, it checks the integrity of the message sent from the student. If $Verify(sigpk_{St}, Enc'(m, pk'_R), Sign(sigsk_{St}, Enc'(m, pk'_R))) == 1$, $\boldsymbol{R}$ sends $Enc'(m, pk'_{AP1})$ and $Sign(sigsk_R, Enc'(m, pk'_{AP1}))$ to $\boldsymbol{AP1}$**.**

R-APn: $\boldsymbol{R}$ does follow the similar steps as that in **R-AP1.** At last, $\boldsymbol{R}$ sends $Enc'(m, pk'_{APn})$ and $Sign(sigsk_R, Enc'(m, pk'_{APn}))$ to $\boldsymbol{APn}$**.**

AP1-R: Once $\boldsymbol{AP1}$ receives messages from $\boldsymbol{R}$ and $\boldsymbol{St}$**,** it decrypts the ciphertexts received from $\boldsymbol{R}$ and $\boldsymbol{St}$**.** $\boldsymbol{AP1}$ then obtains $m = Dec'\big(sk'_{AP1}, Enc'(m, pk'_{AP1})\big)$ (from $\boldsymbol{St}$**)** and $m = Dec'\big(sk'_{AP1}, Enc'(m, pk'_{AP1})\big)$ (from $\boldsymbol{R}$). Moreover, it checks the integrity of the messages using signature verification algorithm. If all the signature-message information is valid and two messages (after decryption) are the same, $\boldsymbol{AP1}$ finds the student's required information from the blockchain and sends the corresponding block indexes and secret keys to $\boldsymbol{R}$**.** The information sent from $\boldsymbol{AP1}$ to $\boldsymbol{R}$ is $Enc'(M_1, pk'_R)$ and $Sign(sigsk_{AP1}, Enc'(M_1, pk'_R))$, where $M_1 = BI_1 \big|\big|k_{1,1}\big|\big| k_{1,2}||k_{1,3}||k_{1,4}$. These keys $k_{1,1}, k_{1,2}, k_{1,3}, k_{1,4}$ are used to decrypt the student's grade, course identity, program identity and original identity stored in the centralized database.

APn-R: $\boldsymbol{APn}$ does follow the similar steps as that in **AP1-R.** At last, $\boldsymbol{APn}$ sends $Enc'(M_n, pk'_R)$ and $Sign(sigsk_{APn}, Enc'(M_n, pk'_R))$, where $M_n = BI_n \big|\big|k_{n,1}\big|\big| k_{n,2}||k_{n,3}||k_{n,4}$.

As a result, $\boldsymbol{R}$ gets the messages from all n academic personnel. Then, it decrypts each message, retrieves the each block index from M_i ($i \in \{1, .., n\}$), searches each block index in the blockchain, retrieves corresponding pointer and gets the student's actual records from the centralized database. Since the student's actual records are encrypted, $\boldsymbol{R}$ decrypts each record using the decryption keys in M_i, where $i \in \{1, \dots, n\}$. Once $\boldsymbol{R}$ obtains the student's PID and CID values, it can search these values in the blockchain. It simply checks course policy transaction for getting information about CID and checks program policy transaction for getting information about PID. As a result, $\boldsymbol{R}$ gets more information to check if the student satisfies the internship requirements.

Note that the proposed system is not institution oriented ([6]) but it is academic personnel oriented. An academic personnel-oriented system provides better applications than an institution-oriented system. This is because each internship requirements is different. If an internship requirement is to

take a specific course from specific academic personnel, this scenario is the best for our system since our system is academic personnel oriented. An academic personnel generates transactions for students. In an institution-oriented system, an institution generates transactions. Different academic personnel can give a specific course. This situation is difficult to track in an institution-oriented system.

V. Security Analysis

In this section we examine the security analysis of our scheme. Our scheme preserves the student's data privacy, data integrity, data correctness and controlled disclosure of data.

Data Privacy: The data privacy of each student is obtained via encryption. Using encryption does not allow any intruder to learn private (sensitive) information about the student.

Data Integrity: Data integrity is obtained via signature. Each entity sends message-signature pair. This results that the receiver being convinced that the message comes from the expected sender.

Data Correctness: This property allows a recruiter to hire qualified students. The students cannot lie about their academic transcripts/history. In other words, the students cannot provide fake grades or achievements to get internships.

Controlled Disclosure of Data: the students' original identities are not leaked in the blockchain and the centralized database. Only the authorized entities (recruiters) can read/view them by getting corresponding secret keys form the academic personnel. Moreover, the recruiter cannot get the student's all academic records. The recruiter gets what it has to get based on the job/internship requirements. Furthermore, ***CA*** has access control mechanism that controls the centralized database. ***CA*** provides limited time access to the database for the recruiters.

VI. Conclusion

In this paper, a system uses blockchain technology in education system for internship. Each student based on its program and courses takes corresponding exam, the academic personnel of the course grades the exam and puts the actual grade of the student to a centralized database and address of the record to a permissioned blockchain. Based on the requirements, the students apply for internships and the academic personnel sends required academic information to the recruiter. The proposed system provides data privacy, data integrity, data correctness and controlled disclosure of data. Moreover, the proposed system is academic personnel oriented so that it has better applications than the institution-oriented system.

VII. References

[1] Nakamoto, S. (2008). *Bitcoin: A peer-to-peer electronic cash system*. Retrieved October 22, 2022, from http://bitcoin.org/bitcoin.pdf

[2] M. Hanley and H. Tewari, "Managing lifetime healthcare data on the blockchain," in *EEE SmartWorld, Ubiquitous In- tell. Comput., Adv. Trusted Comput., Scalable Comput. Com- mun., Cloud Big Data Comput., Internet People Smart City Innov.(SmartWorld/SCALCOM/UIC/ATC/CBDCom/IOP/SCI)*, Guangzhou, China, 8-12 October 2018, pp. 246–251.

[3] D. Salah, M. H. Ahmed, and K. ElDahshan, "Blockchain applications in human resources management: Opportunities and challenges," in *Proceedings of the Evaluation and Assessment in Software Engineering*. Trondheim, Norway: Association for Computing Machinery, New York NY, United States, 15-17 April 2020, pp. 383–389.

[4] K. Christidis and M. Devetsikiotis, "Blockchains and smart contracts for the internet of things," *IEEE Access*, vol. 4, pp. 2292–2303, 2016.

[5] Juszczyk, O. S. (2022). Blockchain Technology for Renewable Energy: Principles, Applications and Prospects. *Energies , 15* (13).

[6] Oksuz, O. (2022). Preserving Identity Leakage, Data Integrity and Data Privacy Using Blockchain in Education System. *International Journal of Information Security Science , 11*.

[7] University of Nicosia. Blockchain certificates (academic and others). https://www.unic.ac.cy/iff/blockchain-certificates. Accessed October 22, 2022. [Online]. Available: https: //www.unic.ac.cy/iff/blockchain-certificates

[8] K. Kuvshinov, I. Nikiforov, J. Mostovoy, D. Mukhutdinov, K. Andreev, and V. Podtelkin, "Disciplina: Blockchain for education," Yellow Paper, Tech. Rep., 2018.

[9] R. Arenas and P. Fernandez, "Credenceledger: A permissioned blockchain for verifiable academic credentials," in *2018 IEEE International Conference on Engineering, Technology and In- novation (ICE/ITMC)*, Stuttgart, Germany, 17-20 June 2018, pp. 1-6.

[10] Blockcerts, the open standard for blockchain certificates. http://www.blockcerts.org/. Accessed October 22, 2022. [Online]. Available: http://www.blockcerts.org/

[11] E. E. Bessa and J. S. Martins, "A blockchain-based educational record repository," 2019, arXiv preprint arXiv:1904.00315.

[12] M. Sharples and J. Domingue, "The blockchain and kudos: A distributed system for educational record, reputation and reward," in *Adaptive and Adaptable Learning*, Cham: Springer International Publishing, 2016, pp. 490–496.

[13] M. Han, Z. Li, J. S. He, D. Wu, Y. Xie, and A. Baba, "A novel blockchain-based education records verification solution," in *Proceedings of the 19th Annual SIG Conference on Information Technology Education*, ser. SIGITE '18. New York, NY, USA: Association for Computing Machinery, 2018, pp. 178–183. [Online]. Available: https://doi.org/10.1145/3241815.3241870

[14] M. Turkanović, M. Hölbl, K. Košič, M. Heričko and A. Kamišalić, "Eductx: A blockchain-based higher education credit platform," *IEEE Access*, vol. 6, pp. 5112–5127, 2018.

[15] W. Gra¨ther, S. Kolvenbach, R. Ruland, J. Schu¨tte, C. Torres, and F. Wendland, "Blockchain for education: lifelong learning passport," in *Proceedings of 1st ERCIM Blockchain workshop 2018, 2018: European Society for*

Socially Embedded Technolo- gies (EUSSET). Amsterdam, Netherlands: European Society for Socially Embedded Technologies (EUSSET), 2-8 May 2018, pp. 1–8.

[16] P. Ocheja, B. Flanagan, H. Ueda, and H. Ogata, "Managing lifelong learning records through blockchain," *Research and Practice in Technology Enhanced Learning*, vol. 14, no. 1, p. 4, 2019. [Online]. Available: https://doi.org/10.1186/ s41039-019-0097-0

[17] R. A. Mishra, A. Kalla, A. Braeken, and M. Liyanage, "Privacy protected blockchain based architecture and implementation for sharing of students' credentials," *Information Processing and Management*, vol. 58, no. 3, p. 102512, 2021

[18] M. Lodder and B. Zundel. Hyperledger indy hipe. Accessed October 22, 2022. [Online]. Available: https://hyperledger-indy.readthedocs.io/projects/hipe/en/latest/text/0109-anoncreds-protocol/README.html

[19] J. Camenisch and A. Lysyanskaya, "An efficient system for non- transferable anonymous credentials with optional anonymity revocation," in *Advances in Cryptology — EUROCRYPT 2001*, B. Pfitzmann, Ed. Berlin, Heidelberg: Springer Berlin Heidel- berg, 2001, pp. 93–118.

[20] J. Camenisch and A. Lysyanskaya, "A signature scheme with efficient protocols," in *Security in Communication Networks*, S. Cimato, G. Persiano, and C. Galdi, Eds. Berlin, Heidelberg: Springer Berlin Heidelberg, 2003, pp. 268–289.

[21] Ethereum. https://www.ethereum.org. Accessed October 22, 2022. [Online]. Available: https://www.ethereum.org

A Borda Count Based Initialization Method for Self-Organizing Maps

S. ŞENOL[1] and F. İSMAİLOĞLU[1]

[1] Sivas Cumhuriyet University, Sivas/Turkey, sumeyrasenol43@gmail.com
[1] Sivas Cumhuriyet University, Sivas/Turkey, fismailoglu@cumhuriyet.edu.tr

Abstract **- In data science, data visualization has long been of interest since it is necessary to explore the patterns and underlying structure of data. Over the years, various data visualization methods have been developed. Among them, Self-Organizing Maps (SOM) is one of the most widely used methods due to its simplicity. However, the robustness of a SOM largely depends on the initial choice of prototype vectors in it. On the other hand, this problem has not been extensively studied in the literature. In this study, we introduce a novel method for initializing the prototype vectors of SOM, which we call BCI and which has its roots in Borda Count (BC), a ranked voting system. A large set of experiments confirmed the effectiveness of BCI and showed that it outperforms both the random initialization and PCI, the state-of-the-art initialization method, in terms of quantization error, which indicates how well the SOM reflects the original feature space.**

Keywords **– Data Mining, Data Visualization, Self-Organizing Maps, Borda Count.**

I. INTRODUCTION

Regardless of the type of data we are interested in, e.g., images, audio, sensors, etc., the data often has a high dimension. On the other hand, we humans cannot see more than three dimensions. This makes it difficult to understand the underlying structure of the data. For this reason, more and more data visualization methods have been developed not only in data science but also in various other fields [1,2].

Among all data visualization methods developed so far, Self-Organizing Maps occupy a special place [2]. Since its introduction by Kohonen in 1990, SOM has found various and numerous applications [3]. The main reason for the success of SOM is the fact that SOM is a simple yet powerful visualization method and can preserve the topology of data. Although it is inherently a heuristic method, the theoretical aspects of SOM have also been addressed so that SOM comes with theoretical guarantees [4].

The working principle of SOM can be summarized as follows. A SOM consists of a series of adjacent cells, generally arranged in a 2D map, with each cell associated with a prototype (weight) vector of the same dimension as the original data. Training a SOM involves learning these vectors. Once the training process is complete, each instance is mapped to one of the cells in the map based on its distances from the prototype vectors. Here, the prototype vectors are learned using an iterative algorithm where the initial values for the vectors are randomly selected [2]. Such a random process not only increases the learning time, but also leads to different visualization results.

To illustrate the above random problem, we provide a small dataset in Table 1. This dataset represents seven G7 countries based on five features: population (millions), life expectancy (years),Co2 emissions (MTCo2e), rule of law and GDP per capita (Dollars). With this data, we construct two SOMs of dimensions 3 by 3 and initialize the prototype vectors differently. Even after one thousand iterations in both applications, the underlying algorithm does not converge, resulting in two different SOMs: SOM1 and SOM2. See Figure 1. Here, a natural question to ask is which is the correct one?

Table 1: G7 Countries (Population (millions), life expectancy (years), Co2 emissions (MTCo2e), rule of law and GDP per capita (Dollars)) (Source: World Economics 2021)

Country	Pop.	Life Exp.	Co2	Law	GDP
Canada	38.1	82	576.7	89.5	53509
France	65.4	83	323.6	81.4	52721
Germany	83.9	81	702	87.1	58283
Italy	60.4	84	337.1	54.6	50764
Japan	126.1	85	1106.7	86.3	44744
UK	68.2	81	369.9	85.6	49858
USA	332.9	79	5284.7	82.4	67651

USA		
Germany Japan	France	
Italy	Canada UK	

a) SOM1

Germany Italy	France	
UK	Japan	
	Canada USA	

b) SOM2

Figure 1: Two SOMs using the G7 data in Table 1 with different initializations

Although random selection of the prototype vectors is a serious problem and leads to quite different SOM results, there are few studies addressing this issue. One notable study is [5], which is based on using PCA to reduce the original dimensionality to two, and then finding the nearest cell for each datum based on the (2D) coordinates of the cells. However, this method requires an eigendecomposition, which

is costly, especially for high dimensions.

In this paper, we introduce a novel initialization method for SOM. In particular, our method addresses initialization of the prototype vectors in SOM so that the SOM algorithm can converge faster and end up with the same map for each run. The proposed method has its roots in the Borda count, a voting method that has been used for centuries to determine the ranking of candidates that best fits voters' preferences [6]. In short, we rank the cells of a SOM using Borda count from the most central to the least central; and we rank the data instances from the most central to the most distant. We then match these two rankings and assign the instances to the cells. Finally, the mean of the instances that are assigned to a particular cell becomes the initial prototype vector of that cell. This method offers several advantages, including *i)* ease of implementation *ii)* faster convergence *iii)* robustness.

In the remainder of the paper, we first review the literature on data visualization methods and SOM in particular, and then provide background information on SOM. We then proceed to the proposed method and conduct experiments to test its effectiveness. Finally, we summarize the study and point out possible future developments.

II. RELATED WORK

Data visualization refers to the visual representation of data, and this representation can consist of charts, plots, graphs, or even animations. With these tools, one can effortlessly gain useful insights from the data at hand. Common data analysis tasks such as outlier detection, correlation analysis, and highlighting trends can all be performed with ease by visualizing the data. Because of these advantages, data visualization has gained an increasing popularity and is being studied by researchers with diverse backgrounds, from statisticians to psychologists [7].

Millions of data are obtained during the day from the internet searches we make every day, the records kept when we go to the hospital, the receipts of the products we buy while shopping, the transactions we make at the bank and many other areas of our daily life. Various data visualization methods are used to understand what these data mean.

As emphasized above, visualizing data is of crucial importance to get to know the data. Nevertheless, data often has a high dimension, which makes it nontrivial to visualize. In this sense, it is common to reduce the dimension of the data to two or three so that we can easily plot it. One of the most common methods for this purpose is PCA, which is based on projecting the data into the space spanned by the eigenvectors of the covariance matrix of the data. Although it offers the advantage of projecting the data into an uncorrelated space, it involves an eigendecomposition problem and is therefore computationally expensive.

Another popular method for data visualization is t-SNE, which, unlike PCA, provides nonlinear dimensionality reduction [8]. In fact, t-SNE is commonly used as the de facto standard for visualizing data in 2D spaces. Generally speaking, t-SNE creates two probability distributions, one for the original high-dimensional data and one for the reduced 2D data. It then tries to minimize the KL divergence between these two probability distributions, where the minimization imposes a non-convex optimization problem. The resulting problem is usually solved using a gradient descent with random initialization. Therefore, t-SNE may get stuck at local minima and not guarantee a global solution [8].

Self-Organizing Maps (SOM) have long served as the primary data visualization method. The reason for its popularity lies in its simplicity and the fact that it allows for clustering of data, in addition to being a visualization method [2, 3].

At a high level, SOM maps instances in a 2D map consisting of a series of adjacent cells of square shape. See Figure 1. The rule that governs the mapping is to assign each instance to the cell whose associated prototype vector is nearest to the vector. Learning the prototype vectors is equivalent to building a SOM. We will detail this process in the next section.

Considering the fact that SOM has been widely used for a long time, it is not surprising that there are several variants of it. One of the best known variants is the growing SOM (GSOM), which (usually) starts with a SOM of size 2x2 and then grows it from all cells based on a heuristic criterion [9]. In contrast to the conventional case, here, there is no fixed shape for the map, in fact it is tailored to the data at hand. Another important variant is the hexagonal SOM, in which the cells have a hexagonal shape. The distinguishing element of this variant is that each cell has six neighbors, not four as is the case with square cells. Finally, Kohonen, the inventor of SOM, proposed a batch version of SOM [10], which proposes to update the prototype vectors only at the end of each iteration of the training, whereas in the conventional case they are updated after the presentation of each instance. The main advantage of this version is that the learning of the prototype vectors is independent of the order of the instances.

As mentioned earlier, Kohonen proposed to randomize the initial values for the prototype vectors. In practice, however, this results in different final values for the vectors, which in turn results in different maps each run of the SOM. Therefore, it is necessary to initialize the vectors deterministically. For this purpose, the most commonly used initialization method is principal component initialization (PCI) [5]. The working principle of PCI is as follows. Let e_1 and e_2 be the first two eigen vectors of the data; and a and b are two real numbers such that $a<b$. Suppose that we have a SOM with m cells in the vertical axis and n cells in the horizontal axis and that $u=(a, a+\frac{b-a}{m},...,b)$ and $v=(a, a+\frac{b-a}{n},...,b)$ are two sequences. PCI determines the initial prototype vector of the cell with coordinates (i, j) as $u(i)e_1+v(j)e_2$, where $u(i)$ denotes the i th element of the sequence u.

III. SELF-ORGANIZING MAPS

Let X be a given data matrix consisting of k instances with dimension d, thus $X \in \Re^{k \times d}$. Also let $X[a:b]$ be a submatrix formed by the rows of X from the a th row to b th row. Our task is to map such instances to a SOM, a grid of cells (units) organized as a 2D map. Here, each cell is associated with a prototype vector (weight vector) of the dimension d, i.e. that of the original input space. Training a SOM means learning these vectors, and after the training is complete, each instance is matched to a cell with the prototype vector closest to it. In the literature, these cells are called as Best Matching Units (BMU).

Conventionally, the prototype vectors are randomly initialized and then iteratively updated. In each iteration, an instance is picked randomly and its BMU is calculated. Based on the BMU, all prototype vectors are updated. For the update of the j th prototype vector at iteration $(t+1)$ is as follows:

$$w_j(t+1) = w_j(t) + \alpha(t) h_{jc(x)}(x - w_j(t)), \quad (1)$$

where $\alpha(t)$ denotes the learning rate and $h_{jc(x)}$ the magnitude of the closeness between the j th prototype vector and $c(x)$, the BMU of the randomly picked instance x. In particular, α is chosen as a decreasing function of time, and typically specified as:

$$\alpha(t) = \alpha_0 \exp(-t \times \eta) \quad (2)$$

where α_0 is the initial learning rate and $\eta > 0$ is the decay rate specified by the user. For $h_{jc(x)}$, it is typically to consider the Gaussian neighborhood function:

$$h_{jc(x)} = \exp\left(\frac{-\left\| r_j - r_{c(x)} \right\|}{2\sigma(t)^2} \right) \quad (3)$$

where r_j and $r_{c(x)}$ are the coordinates of the j -th prototype vector and the BMU respectively. Here $\sigma(t)$ corresponds to the width of the neighborhood and decreases over time, and the decrease can be calculated using (2) ensuring that α_0 is replaced by σ_0, the initial value for width. The rationale behind decreasing α and σ over time is to is to reduce the effect of updating of prototype vectors over time so that the learning process converges. We also note that the underlying idea of the update rule given (1) is to draw the prototype vectors in proportion to their closeness to the instance of interest.

IV. PROPOSED METHOD

As mentioned earlier, the initial prototype vectors, i.e. $w_j(0), \left(j \in \{1,..., m \times n\}\right)$, are determined randomly, which leads to instability and slow convergence when learning the prototype vectors. To address this problem, we propose the following method based on Borda Count (BC). We thus name this method as BCI.

Our method consists of three phases. In the first phase, we rank the cells of SOM using BC. Specifically, for a SOM with $m \times n$ cells, we construct a ranking vector for each cell which is a permutation of integers from 1 to $m \times n$. For the i -th cell, this vector is denoted as p_i^{cell} whose l -th element is the rank of l -th cell for i -th cell, where the ranking is based on the closeness to the i -th cell. In the case of a tie, that is, when more than one cell is equidistant from the cell of interest, each cell is assigned the average rank. For example, for a SOM of size 3×3, as shown in Figure 2, the ranking vector for the first cell is $p_1^{cell} = (1, 2.5, 5.5, 2.5, 4, 7.5, 5.5, 7.5, 9)$.

1	2	3
4	5	6
7	8	9

Figure 2: A 3x3 SOM with indices

BC receives these ranking vectors from all cells as input and then outputs the final ranking by summing all vectors and sorting the cells based on this sum. For the example above, the final ranking of the SOM cells is $cell\_rank = (5,2,4,6,8,1,3,7,9)$. This result reflects the original layout of the SOM, in fact the fifth cell is the most central cell and therefore comes first in the final ranking. Also, the cells with indices 1, 3, 7, and 9 are located in the corners of the SOM hence they share the last places in the ranking.

In the second phase of the proposed method, we instead rank the instances, following much the same procedure used for the cells. We thus omit the details of ranking instances with BC. As an example, if we rank the G7 countries with BC based on the data matrix in Table 1, then the final ranking is France, Canada, Italy, UK, Germany, Japan and USA. We shall denote the rank associated with the instances as $inst\_rank$.

In the final step, we assign the instances to the cells based on the (final) ranking of the cells and the instances obtained in the previous two phases. For the G7 data, this assignment is done as follows:

Ranking of the instances		Ranking of the SOM cells
France	→	5
Canada	→	2
Italy	→	4
UK	→	6
Germany	→	8
Japan	→	1
USA	→	3
		7
		9

Finally, the initial prototype vector of a cell is considered to be the instance assigned to that cell. For example, the initial prototype vector of the fifth cell is [65.4, 83,323.6, 81.4,

52721] data vector corresponding to France. If the number of instances is less than the number of cells, as in the above example, some cells are not matched with any instances. If this is the case, we can initialize the prototype vectors corresponding to these cells randomly. Normally, however, the number of instances is almost always greater than the number of cells. Below we explain how to use the proposed initialization method if this is the case.

Suppose we have k instances and $m \times n$ cells, where $k > m \times n$. In this case we rank the instances and the cells using BC, as described above, and then split the instances into $k/(m \times n)$ chunks, starting with the first instance in the ranked list. Each chunk of the instance is then assigned to a cell, starting with the first cell in the ranked list of cells. Finally, the mean of the instances in the same chunk is considered the initial prototype vector for the cell to which the chunk is assigned.

Here, we provide a pseudocode for our proposed initialization method for SOM. We also note that the notation $\lceil \ \rceil$ acts like a ceil operator, returning the smallest integer greater than its parameter.

Algorithm 1: BCI: A Borda Count Based Initialization Method for Self-Organizing Maps

Input: Data matrix: $X \in \Re^{k \times d}$, SOM with size $m \times n$

Output: Initial values for the prototype vectors of the SOM: $w_i(0) \in \Re^d \ (i \in \{1,..., m \times n\})$

Phase -1: Rank the cells

1: **for** i =1: $m \times n$ **do**

2: calculate p_i^{cell}

3: **end for**

4: Using p_i^{cell}, rank the cells using BC, get $cell\_rank$

Phase -2: Rank the instances

5: **for** i =1: k **do**

6: calculate p_i^{inst}

7: **end for**

8: Using p_i^{inst} rank the instances using BC, get $inst\_rank$

9: Based on $inst\_rank$ replace (shuffle) the rows of X

Phase -3: The initialization

11: $c = \lceil k / m \times n \rceil$ (chunk size)

10: $t = 1$

11: **for** i in $cell\_rank$:

12: $w_i(0) = mean(X[(t-1) \times c + 1 : t \times c])$

13 $t += 1$

V. EXPERIMENTS

In this section we present the results of a range of experiments to verify the efficiency of the proposed method. In this sense, we first give the statistics for the datasets used, then explain the evaluation criterion, and finally provide the results and the related discussion.

A. The Datasets Used

We conducted experiments using different types of UCI datasets. The statistics for these datasets can be found in Table 2.

Table 2: Statistics of the Used UCI Datasets

Dataset	Number of instances	Number of features
Abalone	4177	8
Breast Cancer	569	32
Ecoli	336	7
Glass	214	9
Iris	150	4
Yeast	1484	8
Zoo	101	17

B. EVALUATION CRITERION

Conceptually, Self-Organizing Maps are examples of unsupervised learning, where there is no actual truth, i.e., classes. Therefore, we cannot simply compare the predictions and the actual truths to evaluate the performance of the proposed method. Instead, to assess the quality of a SOM, the quantization error (QE) is often used. QE measures how well the SOM reflects the original feature space, which is basically the average of the distances between instances and the prototype vectors of the cells to which they are assigned. This is calculated as:

$$QE = \frac{1}{k} \sum_{i=1}^{k} \left\| X_i - m(X_i) \right\|_2 \quad (4)$$

where X_i denotes the i-th instance of , i.e., the i-th row and $m(X_i)$ is the prototype vector of its BMU in the SOM.

C. RESULTS

We compare the results of QE, obtained with the proposed BCI, with those obtained with random initialization and PCI. When it comes to determine size of the SOM for each dataset of interest, we set it to 10×10, resulting in a SOM with 100 cells, which is less than the number of instances in all the datasets used. Table 3 shows the QE results. The best results are highlighted for each dataset. We also note that the QE values obtained with the random initialization are the average of 100 runs for each dataset.

Table 3: The QE Results Obtained with the Random Initialization, PCI and BCI

Dataset	Random Init.	PCI [4]	BCI (Ours)
Abalone	0.47	**0.24**	0.27
Breast Cancer	1.79	0.52	**0.47**

Ecoli	0.47	0.36	**0.17**
Glass	0.62	0.36	0.**25**
Iris	0.24	0.31	**0.04**
Yeast	0.56	0.26	**0.21**
Zoo	1.61	1.17	**0.19**

D. DISCUSSIONS

The immediate conclusion that can be drawn from Table 3 is that one should not randomly initialize the prototype vectors in a SOM. The difference between the QE values from the random initialization and from PCI and BCI is significant. In fact, for Zoo dataset the QE value is about 8 times higher than the value obtained with the proposed method BCI. This means that random initialization of prototype vectors in SOM is risky and can lead to slow convergence, since it does not yield ideal initial values.

Comparing the state-of-the-art initialization method, PCI, and the proposed BCI, it is evident that BCI outperforms PCI all datasets except Abalone. The difference between the QE scores ranges from 0.05 to 0.98 in favor of BCI. Relying on these results, we conclude that the proposed method BCI is a powerful initialization method for prototype vectors of SOM and can be used for datasets with different number of instances and different number of features.

VI. CONCLUSION

Data visualization has long been of interest not only to data scientists, but also to researchers in other fields, because it allows for obtaining useful insights from the data at hand. In this sense, a range of data visualization methods have been developed. Of them, Self-Organizing Maps (SOM) is one of the most commonly used methods due to its simplicity and efficiency. However, the conventional use of SOM suggests initializing the prototype vectors randomly, which may ultimately lead to instability and low convergence.

In this study, we propose a novel method for initializing prototype vectors based on Borda Count (BC). Thus, we call the proposed method BCI. Basically, BCI first ranks cells of SOM and instances separately with BC and then assigns the instances to the cells based on these two rankings. Finally, BCI calculates the mean of the instances assigned to the same cell and then considers this mean value as the initial value for the prototype vector of the cell. The experiments conducted on seven different UCI datasets confirm the efficiency of BCI and show that BCI outperforms both the random initialization and PCI, the state-of-the-art initialization method based on PCA. Future research will focus on the application of PCI to different types of SOM, such as growing SOM (GSOM).

REFERENCES

[1] M. Sadiku, A. Shadare, S. M. Musa, C.M. Akujuobi and R. Perry, R. "Data visualization". International Journal of Engineering Research And Advanced Technology (IJERAT), vol: 2(12) pp. 11-16, 2016.

[2] T. Kohonen. "The self-organizing map". *Proceedings of the IEEE*, vol: 78(9), pp: 1464-1480, 1990.

[3] T. Kohonen. "Essentials of the self-organizing map." *Neural networks*, vol: 37, pp: 52-65, 2013.

[4] M. Cottrell, M. Olteanu, F. Rossi and N. Vialaneix. "Theoretical and applied aspects of the self-organizing maps". WSOM 2016.

[5] A. Akinduko, A. E. Mirkes. and A. N. Gorban. "SOM: Stochastic initialization versus principal components". *Information Sciences*, vol: 364, pp: 213-221, 2016.

[6] P. Emerson. "The original Borda count and partial voting". *Social Choice and Welfare*, vol:40(2), pp:353-358.2013.

[7] K. Healy. "Data visualization: a practical introduction" *Princeton University Press*. 2018.

[8] S. Arora, W. Hu and P.K. Kothari. "An analysis of the t-sne algorithm for data visualization". *In Conference On Learning Theory*, pp. 1455-1462, PMLR, 2018.

[9] D. Alahakoon, S. K. Halgamuge, and B. Srinivasan. "Dynamic self-organizing maps with controlled growth for knowledge discovery". *IEEE Transactions on neural networks*, vol: 11(3), pp: 601-614, 2000.

[10] T. Kohonen. "Things you haven't heard about the Self-Organizing Map" *In IEEE international conference on neural networks*. pp:1147- 1156. 1993.

Evaluation of time series decomposition on statistical and machine learning-based forecasting models

Zeynep Idil ERZURUM CICEK[1]

[1] Eskisehir Technical University, Eskisehir/Turkey, zierzurum@eskisehir.edu.tr

Abstract **- Decomposition separates the time series into components as trend, seasonality, and random effect. The aim of the decomposition of the time series is to increase forecast accuracy. In this study, a comparison of two decomposition methods Seasonal and Trend decomposition using Loess and Moving Averages on statistical and machine learning forecasting models is presented. These forecasting models are Naïve and Autoregressive Integrated Moving Averages (ARIMA) methods from statistical methods, and Support Vector Regression (SVR), K-Nearest Neighborhood, and Random Forests algorithms from machine learning methods. The forecasting results showed that decomposition mostly increased forecasting accuracy on considered datasets.**

Keywords **- Time series forecasting, decomposition, statistical forecasting, machine learning**

I. Introduction

A time series is a set of observations y_t, each one being recorded at a specific time t [1]. Trend, seasonality, and cyclical patterns are the components of the time series. A time series may contain one or more of these components. In addition to these components, random effects are also included in the time series. Often, cyclicality is handled along with the trend. If a time series is expressed as the sum of these components, it is defined as "additive", if it is expressed as a product, it is defined as "multiplicative" and is formulated as in equations (1) and (2), respectively:

$$y_t = T_t + S_t + \varepsilon_t \quad (1)$$

$$y_t = T_t \times S_t \times \varepsilon_t \quad (2)$$

where T_t, S_t and ε_t depicts trend, seasonal and random components respectively.

The process applied to separate the time series into its components and reveal the remaining random effect is called time series decomposition. If the trend and seasonality components in the time series can be detected correctly, the remaining challenge is to make accurate forecasts for only random effect. For this purpose, many decomposition methods have been presented in the literature to model time series. Methods such as Empirical Mode Decomposition (EMD), Moving Averages (MA), X11, Seasonal Extraction in ARIMA Time Series (SEATS), Seasonal and Trend Decomposition using Loess (STL) are used for decomposition.

In this study, it is aimed to observe the effect of the use of decomposition on time series forecasting. For this purpose, forecasting models were generated with Naïve and Autoregressive Integrated Moving Averages (ARIMA) methods from statistical methods, and Support Vector Regression (SVR), K-Nearest Neighborhood, and Random Forests algorithms from machine learning methods. Thus, the effect of MA and STL decomposition methods can be revealed through the model performances generated.

The remaining of the study is as follows. In Section 2, related works about time series decomposition are summarized. The background of the study is explained in Section 3. The computational experiments and the results are reported in Section 4. The discussion of the obtained results and future works are given in Section 5.

II. Related Works

One of the areas studied in time series analysis is decomposition methods. Some of the studies in recent years have aimed to increase the accuracy of forecasts by applying decomposition.

Buyuksahin and Ertekin [2] improved the performance of a novel hybrid ARIMA and Artificial Neural Networks (ANN) forecasting model using EMD. Similarly, Abdollahi [3] proposed an artificial intelligence hybrid model for a time series decomposed with EMD. In order to predict dam displacement, Li et al. [4] decomposed the considered dataset with STL, then an extremely randomized tree model was used to forecast seasonal components, while the stacked Long-Short Term Memory (LSTM) model was used to forecast trend and random components. Nava et al. [5] proposed a combination of EMD and SVR for financial time series forecasting.

There are also comparative studies about time series decomposition methods. Abbes et al. [6] compared STL, breaks for the additive season and trend (BFAST) and multi-resolution analysis-wavelet transform (MRA-WT) decomposition methods, and found that BFAST gave the most accurate for multiple time series data. Qian et al. [7] adopted EMD-based decomposition methods as EMD, Empirical Mode Decomposition (EEMD), Wavelet Decomposition (WD),

Wavelet Packet Decomposition (WPD). Ouyang et al. [8] showed that STL decomposition can benefit forecasting with statistical methods.

As seen from the literature review, various decomposition methods are used in time series forecasting studies. Starting from this point, it is aimed to compare two decomposition methods for statistical and machine learning-based time series forecasting models in this study.

III. BACKGROUND

A. Decomposition methods

Time series data can display many different patterns; hence it is frequently useful to divide a time series into numerous components, each of which represents a different type of underlying pattern to obtain better forecasts. A time series is divided into its components using a process called time series decomposition. Each component represents a type of underlying pattern, a trend, a seasonality, and any remaining randomness. As mentioned before, there are numerous time series decomposition methods. In this study, STL and MA decomposition methods are considered.

Originating in the 1920s, moving averages were a popular time series decomposition technique until the 1950s. Many time series decomposition techniques still use it as their foundation.

STL decomposition was first introduced by Cleveland et al. [9]. Hyndman and Athanaspoulos [10] defined STL decomposition as a versatile and robust method for decomposing time series and claimed STL has advantages over the classical, SEATS, and X11 decomposition methods. Barely, STL can be adopted for only additive decompositions.

B. Statistical forecasting methods

In this study, Naïve method and ARIMA method are used as statistical forecasting methods.

In Naïve method, all forecasts are set to be the value of the last observation.

Autoregressive Integrated Moving Average Method (ARIMA) was first proposed by Box and Jenkins [11]. ARIMA processes are a type of stochastic process used to analyze time series. Moving averages (MA), autoregressive moving averages (ARMA), and autoregressive integrated moving averages (ARIMA) techniques can all be used to address the aforementioned stochastic processes.

A non-stationary time series is rendered stationary in ARIMA models by using finite differences between the data points. The future value of a variable is expressed in an ARIMA model as a linear function of the historical observations and random errors.

C. Machine learning methods

Since it is similar to a regression model in its structure, machine learning and deep learning models used to solve the regression problem can be used to forecast time series and generally successful forecasts can be obtained. As mentioned before, SVR, KNN and RF models are generated in this study.

Support Vector Machines (SVM), one of the machine learning methods for classification, is a precursor to Support Vector Regression (SVR). Schlköpf et al. [12] extended Vapnik's presentation of SVM for classification to include regression modeling. Pai et al. [13] defined SVR as a technique based on the structured risk minimization principle and emphasized that it aims to minimize an upper bound of the generalization error.

K-Nearest Neighborhood (KNN) regression is a non-parametric technique that, by averaging the data in the same neighborhood, intuitively approximates the relationship between independent variables and the continuous result.

Random Forests (RF) were first introduced by Breiman [14] for classification and regression problems. Because it is based on ensemble learning, it is known as a powerful machine learning method that often provides successful predictions. RF Regression combines several random decision trees, each of which has been trained on a subset of data. The algorithm is more stable as many trees are used. Each tree is produced by the algorithm using a unique sample of input data. A different sample of characteristics is chosen for splitting at each node, and the trees proceed independently of one another. A single outcome, the forecast of the RF, is produced by averaging the forecasts from each of the trees.

IV. COMPUTATIONAL EXPERIMENTS

A. Datasets

The two most known time series datasets AirPassengers and Lynx are considered in this study. AirPassengers contains monthly totals of international airline passengers between 1949 and 1960. There are 144 observations in this dataset. The Lynx time series dataset contains the count of annual lynx trappings in Canada from 1821-1934. There are 114 observations in the Lynx dataset.

When the coefficient of variation, which measures the variability of a set of data as a statistical measure, is calculated, the AirPassengers dataset varies approximately 43% within itself; the Lynx dataset is almost 100% variable. These high variation values are also an indication that datasets are difficult to forecast.

Before the generation of forecasting models, both datasets are decomposed. The decomposed forms of AirPassengers and Lynx datasets are visualized in Figure 1 and 2 respectively.

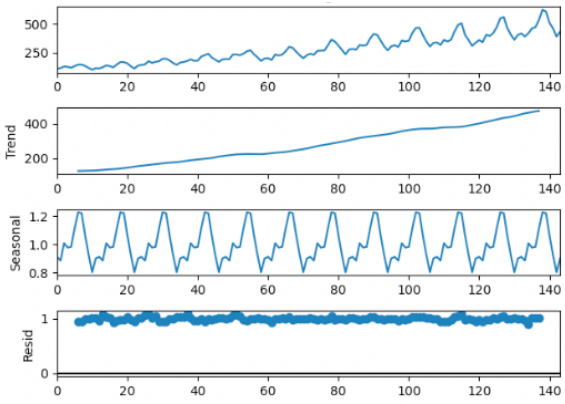

Figure 1: The decomposed form of AirPassengers dataset.

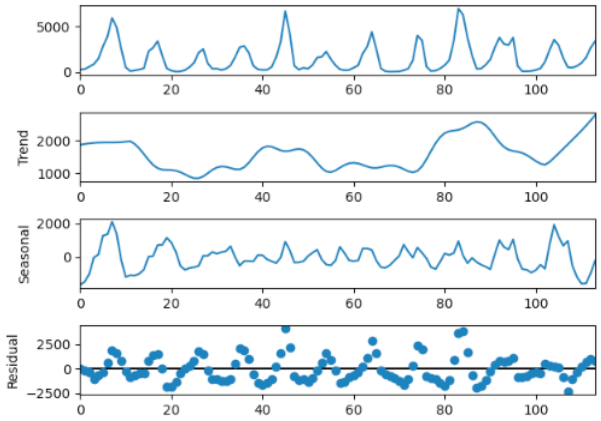

Figure 2: The decomposed form of Lynx dataset.

As seen from the Figure 1 and 2, while AirPassengers dataset contains clearly trend and seasonality; Lynx dataset contains only slight seasonality. There is also no trend in Lynx dataset.

B. Computational results

Before conducting test, STL and MA decomposition are applied for both of the dataset. The generated forecasting models are trained for each component and tested. Then the forecasts obtained for each component are combined via summing or multiplication whether the decomposition is additive or multiplicative. Besides, tests are performed for the original datasets without decomposition. The applied model generation approach is visualized in Figure 3.

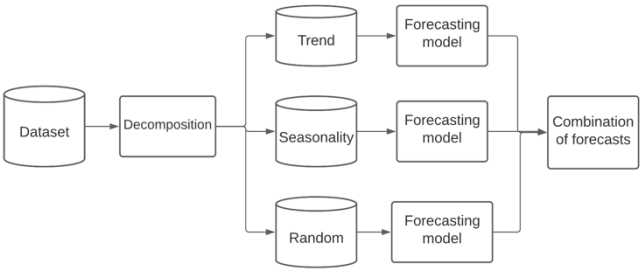

Figure 3: The model generation approach.

80 % of each dataset is divided into training dataset, while 20% as test. Model parameters are obtained through experience were used. Root-mean-square error (RMSE) is used for performance evaluation. RMSE is formulated as in (3).

$$RMSE = \sqrt{\frac{\sum_{i=1}^{n}(x_i - \hat{x}_i)^2}{n}} \quad (3)$$

The test results for AirPassengers and Lynx datasets are reported in Table 1 and 2; visualized in Figure 4 and 5 respectively.

Table 1: The forecasting results of AirPassengers Dataset.

	No decomposition	STL	MA
Naïve	93.134	93.134	93.134
ARIMA	66.688	26.199	24.768
SVR	434.509	255.259	250.649
KNN	410.114	272.211	258.945
RF	402.048	269.236	258.624

Table 2: The forecasting results of Lynx Dataset.

	No decomposition	STL	MA
Naïve	1366.460	1366.460	1366.460
ARIMA	1024.346	725.697	797.744
SVR	1094.185	945.945	989.340
KNN	2277.044	1549.1634	1663.631
RF	2029.335	1550.319	1685.087

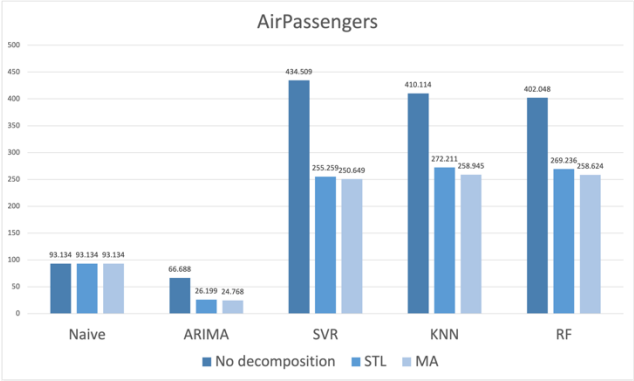

Figure 4: The forecasting results of AirPassengers Dataset.

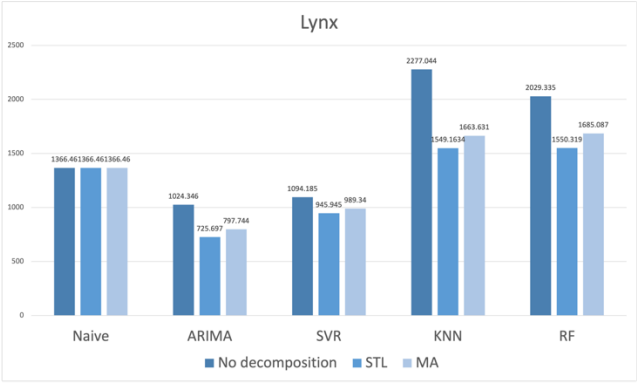

Figure 5: The forecasting results of Lynx Dataset.

When Table 1 and Figure 4, which include the test results for the AirPassengers dataset, are examined, better forecasts can be obtained regardless of whether the separation is made with statistical forecasting methods. It has been seen that the decomposition of the results of the tests applied for all models except the Naïve model has a positive effect on the forecasting success. When the parsing methods for the AirPassengers

dataset were compared within themselves, STL and MA showed almost similar performance.

When Table 2 and Figure 5, which include the test results for the Lynx dataset, are examined, it is seen that similar forecasts are obtained with SVR and ARIMA and are better than other models. Besides, it can be said that STL gives better results for the Lynx dataset.

V. CONCLUSIONS

A statistical procedure called time series decomposition breaks down a time series into its components, each of which represents one of the underlying types of patterns. Mostly, decomposition before forecast is a useful method to obtain more successful forecasting results.

In this study, statistical and machine learning-based models have been developed to see the effect of decomposition in time series forecasting. As a result, it was seen that decomposition utilized forecasts for the two datasets with high variability, except for the Naïve method.

Based on these results, it is planned to develop original decomposition-based deep learning models. In addition, since it is thought that more successful forecasts can be obtained by using different forecast models for each component obtained when the time series is decomposed, future studies will proceed in this direction. Moreover, a parameter optimization process will be also applied for both statistical and machine learning models.

REFERENCES

[1] P. J. Brockwell, *Introduction to Time Series and Forecasting*, Springer, 2016.

[2] U. C. Buyuksahin ve S. Ertekin, Improving forecasting accuracy of time series data using a new ARIMA-ANN hybrid method and empirical mode decomposition, *Neurocomputing,* cilt 361, pp. 151-163, 2019.

[3] H. Abdollahi, A novel hybrid model for forecasting crude oil price based on time series decomposition, *Applied Energy,* cilt 267, no. 115035, 2020.

[4] Y. Li, T. Bao, J. Gong, X. Shu ve K. Zhang, The Prediction of Dam Displacement Time Series Using STL, Extra-Trees, and Stacked LSTM Neural Network, *IEEE Access ,* cilt 8, pp. 94440-94452 , 2020.

[5] Nava, N. Nava, T. D. Matteo ve T. Aste, Financial Time Series Forecasting Using Empirical Mode Decomposition and Support Vector Regression, *Risks,* cilt 6, no. 7, 2018.

[6] A. B. Abbes, O. Bounouh, R. I. Farah, R. d. Jong ve B. Martínez, Comparative study of three satellite image timeseries decomposition methods for vegetation change detection, *European Journal of Remote Sensing,* cilt 51, no. 1, pp. 607-615, 2018.

[7] Z. Qian, Y. Pei, H. Zareipour ve N. Chen, A review and discussion of decomposition-based hybrid models for wind energy forecasting applications, *Applied Energy,* cilt 235, pp. 939-953, 2019.

[8] Z. Ouyang, P. Ravier ve M. Jabloun, STL Decomposition of Time Series Can Benefit Forecasting Done by Statistical Methods but Not by Machine Learning Ones, *Engineering Proceedings*, cilt 5, no. 42, 2021.

[9] R. B. Cleveland, W. S. Cleveland, J. E. McRae ve I. Terpenning , STL: A Seasonal - Trend Decomposition Procedure Based on Loess, *Journal of Official Statistics ,* cilt 6, no. 1, pp. 3-73, 1990.

[10] R. J. Hyndman ve G. Athanasopoulos, *Forecasting: Principles and Practice,* Otexts, 2021.

[11] G. Box ve G. Jenkins, Time Series Analysis: Forecasting and Control, San Francisco: Holden-Day: 1970.

[12] B. Schölkopf, J. C. Platt, J. Shawe-Taylor ve A. J. Smola, Estimating the support of a high-dimensional distribution, *Neural Computation,* cilt 13, pp. 1443-1471, 2011.

[13] P.-F. Pai, K.-P. Lin, C.-S. Lin ve P.-T. Chang, Time series forecasting by a seasonal support vector regression model, *Expert Systems with Applications,* cilt 37, no. 6, pp. 4261-4265, 2010.

[14] L. Breiman, Random Forests, *Machine Learning ,* cilt 45, pp. 5-32, 2001.

A Recommendation System Study on User-Product Data

B.UYANIK[1] and G.K. ORMAN[2]

[1] Galatasaray University, İstanbul/Turkey, begum.uyanik@ogr.gsu.edu.tr
[2]Galatasaray University, İstanbul /Turkey, korman@gsu.edu.tr

Abstract **- This study presents a new recommendation system for the online reservation of tourism customers for hotels with the features they need, saving customers time. This new system combined collaborative and content-based filtering approaches and created a new hybrid recommendation system. Two datasets containing customer information and hotel features were analyzed by Recency, Frequency, Monetary (RFM) method in order to identify customers according to their purchasing nature. The main idea of the recommendation system is establishing correlations between users and products and make the decision to choose the most suitable product or information for a particular user. For example, there is an issue of data overload, which is a potential problem for many internet users, due to the many options available on the internet. Filtering, prioritizing and beneficially presenting relevant information reduces this overload. There are following three main ways that recommendation systems can generate a recommendation list for a user; content-based, collaborative-based and hybrid approaches1. This paper describes each category and their techniques in detail. RFM Analysis is used to identify customer segments by measuring customers' purchasing habits. It is the process of labeling customers by determining the Recency, Frequency and Monetary values of their purchases and ranking them on a scoring model. Scoring is based on how recently they bought (Recency), how often they bought (Frequency) and purchase size (Monetary).**

Keywords **- Recommender system, hybrid approach, RFM Analysis, collaborative filtering, content based filtering.**

I. INTRODUCTION

NOWADAYS, people widely use online reservation systems to plan their holidays. The large number of options makes it difficult for hotel customers to decide when and where to go. In addition, due to the wealth of information available in online reservation systems, customers may miss out on a more suitable option for them. In this sense, recommendation systems play a major role in customers' choice.

The "Recommender System" first appeared as a concept in 1997 in the journal "Communications of the ACM" [2]. Web 2 age has brought the internet to grow and develop at a tremendous speed [1].

In the last 15 years, the Internet has evolved from a group work tool to support the work of scientists at CERN, but rather a global knowledge space with more than a billion users. With the spread of the internet, many opportunities have emerged, such as sharing information and ideas with other users [3].

Nevertheless, this time, users encountered with a new problem with the internet. The amount of data and units has increased greatly, leads to data overload. Finding out what the user is actually looking for has become a big problem. With the need to filter and sort items and information, developers found recommendation systems as a solution.

Recommender systems have following different types of filtering to create an effective recommendation engine; content-based, collaborative-based and hybrid [4].

Recommendation systems are useful for service providers and users [5]. They decrease transaction costs for finding and choosing products in an online shopping environment [6].

They reduce transaction costs for finding and selecting products in an online shopping environment.

Recommender systems also have some benefits for businesses. Firstly, Revenue- Algorithm studies using recommendation systems to increase revenue by increasing the number of sales for companies with online customers such as Amazon sites. Secondly, Personalization - Data collected indirectly can be used to ensure that the services of the website are suitable for the user's preference. Thirdly, Discovery - giving recommendations to people like shopping, movies, songs, etc. increases the chances of revisiting a web page when they find it [4].

In this study, a hybrid recommendation system was developed by combining two recommendation systems based on content-based and collaborative filtering to increase the real-life performance of the hotel recommendation system. While determining customer profiles, RFM method is used. Unlike similar studies in the literature, a rich hotel attribute list was used in the content-based method in this study. In addition, in the collaborative filtering method, the interaction matrix is created with the preference amounts of the guests and resembles the user-product score matrix.

To present the details of the work done, the rest of this paper is structured as follows. In section II, the developed hotel recommendation system and the three types of recommendation system filtering methods are introduced. In section III, RFM analysis of the hotel data is reviewed. In section IV, results of tests are given. Finally, we conclude in Section V.

II. RECOMMENDATION SYSTEM CREATION

The recommender system is the biggest subfield of the data mining and there are two main approaches:

1) Non-customized
2) Customized.

Each approach has different techniques in machine learning. The non-customized recommender system gives the same item recommendation to all system users, rather than individual user data. Users' individual interests are not considered. In contrast, the personalized recommendation system considers the preference or interest of each user, thus recommending certain items to the user more effectively.

There are three basic approaches in the customized recommender system:

1) Content based filtering approach: Characteristics are derived from information items.
2) Collaborative filtering approach: Characteristics derived from the user's environment.
3) Hybrid filtering approach: Each of all of content based filtering approach and collaborative filtering approaches has its own pros and cons. To cope with these disadvantages, the hybrid approach, a combination of both approaches, is used [1].

A. Content Based Filtering

Content based filtering method, in other words "cognitive filtering", works according to user profiles that were created in the beginning. The creation of such profiles is provided by the user creating an account for himself and logging into the system.

A profile contains information about a user and their tastes. During profile creation, it is necessary to provide initial information about the user, and for this reason, the recommendation systems prepare a survey.

The recommendation engine compares the items that users have rated positively with each other and determines their similarities [3]. The more a user interacts with the system, the stronger the user profile is created. In this content based filter, only the recorded information of the user is sufficient instead of other similar users [1].

Content-based recommendation systems are formed of three basic parts in terms of high-level architecture. Firstly, system preprocesses units with a content analyser. After that, a professional profile learner gets information with regard to the users.

Eventually, the filtering component reveals a number of suitable suggestions [12].

Creating a model for the user's preference from user history is a classification learning style. It is divided into binary categories such as "user likes" and "user dislikes". For example, if a user buys a product, it is a sign that the user likes that product.

However, if the user buys the product and returns it, this is a sign that the user does not like the product. Generally, implicit methods can collect large amounts of data with some uncertainty as to whether the user really likes the item [10].

In this study, the features of the hotels customers visited before is taken as basis in order to create the profiles of the users.

For example, in Table I, user 1 has gone to hotels A and B. The capacities of the hotels that User 1 visits are 300 and 400 people, respectively, their distance to the sea is 200 and 100 meters, and breakfast is served in these two hotels. Therefore, when calculating User 1's profile, this content information is used and the average values of the relevant rows in Table I are taken. In this case, the capacity of the hotels where User 1 goes is 350 people on average, and their distance from the sea is 150 meters. It also seeks breakfast service at the hotels that User 1 visits. On the other hand, User 2 displayed a different profile by choosing hotels with less capacity and hotels farther from the sea. As a result, the profiles of these users will be as in Table II.

Table 1: User-Hotel Features Example

User	Hotel	Capacity	Distance to the Sea	Breakfast
1	A	300	200	1
1	B	400	100	1
2	C	100	600	0
2	D	150	1250	0
2	E	125	1500	1

Table 2: User Profiles with CB

User	Capacity	Distance to the Sea	Breakfast
1	350	150	1
2	125	1100	0.33

Using Microsoft Excel, the hotels selected by the customer and the features of the hotels are combined in a single table.

Hotel list data has been cleaned by preprocessing steps. Some hotels selected by customers are not in the hotel feature list, they were detected using excel and removed from the list.

These pre-processing steps consist of correcting missing data (Ex: Hotel names), removing inconsistent data (Ex: Number of rooms). Currency code and foreign currency sales amounts columns, which will not be used in the setup of the recommendation system, are deleted and a comparison was made in Turkish Lira.

The names of districts and towns were removed, and the cities remained.

Branch name, code, and type; sales, entry and exit dates, and how many people stayed overnight are removed. Then, the most important 8 features (pool, beach, breakfast etc.) of the hotels is determined by subtracting the features with less than 600 selections of customers. Thus, by reducing the size of the data, it is ensured that the working time was shortened while calculating the similarity between the profiles and the hotels.

The average of the features in the hotels selected by the customers is calculated using the pivot table in excel. Customers with a binary value of 0 for the features of all selected hotels are removed from the study and the data set

was simplified by removing them from the data set.

B. Collaborative Filtering

Collaborative filtering is a popular user recommendation approach. The collaborative filtering approach was first described and explained in 1997 by Paul Resnick and Hal Varian [7].

If two users have common items with similar ratings, it is assumed that they have similar tastes. Such users form a group or a so-called neighborhood.

A user receives recommendations for items that they have not previously rated but are already rated positively by users in their neighborhood [15].

In CF systems, a recommendation is made to a user collectively based on past ratings of all users. The Grundy system is the first recommendation system to propose the use of stereotypes as a mechanism to create user models based on limited information about each user.

The system creates the model of the individual user and relevant books are recommended for each user [1]. Video Recommender [13] and amazon.com [14] are some examples of collaborative filtering.

Collaborative filtering suggestions improve their accuracy as the amount of data on items increases [11].

In this study while using CF method, the number of times a customer went to each hotel is accepted as the score the customer gave to the hotel. In order to simplify the number of hotels, hotels with less than a total of 10 selected by the customers are removed from the dataset.

C. Hybrid Approach

For better results, some recommendation systems use a combination of the collaborative and content-based approaches to take advantage of each of them. By using the hybrid approach, the limitations of the content-based and collaborative approaches such as cold-started problem can be avoided. The combination of these two approaches can be achieved in different ways:

• Applying both methods separately and combining the results.

• Combining some content-based features with a collaborative approach.

• To include some collaborative features in the content-based approach.

Babodilla, et al has classified the collaborative filtering and content based filtering combined into four different groups as in figure 1 to make a hybrid method [9].

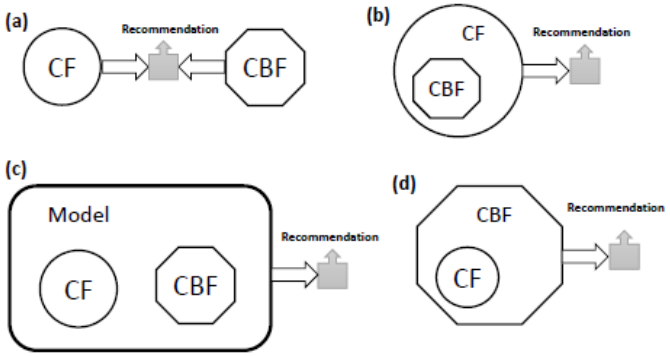

Figure 1: Different methods of combining CF and CBF [9]

Figure 1.a shows the hybrid method combining CF and CBF with a weighting method.

Figure 1.b shows the methods using CBF methods to extract the features and send the recommendation to CF.

Figure 1.c shows a combined model using CF and CBF to obtain the outputs of another classifier such as the probability model.

Figure 1.d shows a model for CBF using output from CF. For example, user ratings can help CBF better identify users [9].

Probability methods are used in hybrid filtering. Examples such as genetic algorithms, neural networks, Bayesian networks can be given [8].

III. RFM ANALYSIS OF CUSTOMER FEATURES

For RFM analysis, each customer's Invoice number, Sales Date and Sales Amount information is used in this study. A customer may have made more than one purchase. Since RFM is about customers, sales amounts are aggregated by customer ID.

The data is grouped with the pivot table feature in the Excel program. With the pivot table, operations such as sorting, summing, and averaging can be performed.

In the pivot table, customers are added to the "rows" column. Thus, each customer appears only once.

For "Recency" calculation; customers need to know when the last time they visited the site.

The "maximum" of the data in the "Sales Date" column is selected from the pivot table, and the last time they visited is shown in the column.

For "Frequency", due to the need for information about how often he visits the website, it is calculated how many invoice belong to the same customer to find out how many times the customer has visited the website.

"Monetary" requires information on how much the customer has made a total purchase. The total amount spent by the same customer is calculated with the pivot table.

To calculate RFM scores, from 1 to 5 points are distributed (eg frequency value of frequent customer should be 5). Recency, frequency and monetary matrices is created with formulas in Excel. For recency, for example, the customer who visited the website the longest time takes the value 1.

The time elapsed since the last visit is divided into groups

according to percentiles. The last visitor was given after the 80% slice and took the value of 5.

The customer who spends the least money should get 1 as its monetary value. According to these calculations, the RFM scores of all customers are determined.

IV. RESULTS

In this section, the outputs obtained after performing the above-mentioned analyzes are shared.

A. Data Analysis Results by Using Content Based Filtering Method

Two different data sets are used in this study.

One of them is the "Hotel Features" data set which includes which of the 30 features (rows of the first data set) such as bed & breakfast, spa-thermal hotel, casino hotel, all inclusive, half board, pool, sandy beach of 2562 different hotels meet.

Table 3: A Brief Example from the Hotel Features Data Set

HotelID	Child-Baby Friendly	Pool	Pool-Summer	Beach	Spa-Termal Otel
370	1	1	1	1	1
371	1	1	1	1	1
374	1	1	1	1	0
377	1	1	1	1	1
378	1	1	1	1	1
379	1	1	1	0	1
380	1	1	1	0	1
381	1	1	1	1	0
383	1	1	1	1	1
384	0	1	1	1	1
385	1	1	0	0	1
386	1	1	1	1	1
388	1	1	1	1	1
389	1	1	1	0	1

Another is a "Sales Data" data set containing 40599 sales data (rows of data set) of a company and 32 sales information (columns of data set) such as Hotel ID, the code of the customer from whom the sale was made, the gender of the customer, the date of sale, the name of the branch where the sale was made.

Table 4: A Brief Example from the Sales Data Set

Customer ID	Hotel ID	City Name	Tkl Master ID	Number of Rooms	AdultCount
13	466	Antalya	267826	1	3
13	466	Antalya	267826	1	2
31	3235	Amasya	34737	1	2
31	418	Antalya	34737	1	3
31	2019	Konya	34737	1	3
141	9831	İzmir	34805	1	2
166	492	Girne	34820	1	2
166	492	Girne	34820	1	2
171	512	Antalya	34823	1	2
171	475	Antalya	34823	1	2
171	786	Antalya	34823	1	2
179	1291	Muğla	60499	1	2
179	1291	Muğla	60499	1	2
179	1291	Muğla	60499	1	2
191	373	Muğla	34834	1	2
217	396	Bursa	77242	1	2
254	1539	Ankara	34878	1	2
294	1023	İzmir	326046	1	2
296	1909	Girne	34893	1	1
300	454	Bolu	166854	1	2
318	786	Antalya	140287	1	2

It is mentioned in section 2.B that hotel features and sales data features that are not needed for this study are cleared from these two data sets.

The following features, which will not affect the

results of the analyzes in the sales dataset, are not considered in this study:

1) Currency code and foreign currency sales amount columns were deleted, and a comparison was made in TL.
2) The names of districts and towns were removed, and the cities remained.
3) Branch name, code and type are removed.
4) Sales, entry and exit dates, and how many people stay overnight are excluded because they will not be used in classification and RFM methods.

The 19 features, which contain relatively little data in the hotel features dataset, are not considered in this study and the following 8 features are used:

1) Child-Baby Friendly
2) Pool

3) Pool-Summer
4) Other Beach
5) Spa-Thermal Hotel
6) Sauna-Turkish Bath
7) fitness
8) Room breakfast

In these two data sets, only the data to be used in this study is obtained, the sales data are sorted on the basis of the customers' code, and the hotel features data are kept to be integrated with the customers' choices.

After determining the hotels selected by the customer with that code in return for the code assigned to each customer, the value of 1 or 0 assigned to the hotel selected by the customer from the data set with the characteristics of the hotels is positioned with "=VLOOKUP()" in Microsoft Excel Program.

It is determined by the IFERROR formula that some of the hotels selected by the customers are not in the hotel feature list and are deleted from the list.

In order to obtain content-based filtering, the average value of the features selected by the customers in the hotels is taken with the pivot table, and the values given by the customers to each hotel feature are assigned as this average value. The brief section of result matrix is given in Table 5.

Table 5: A Brief Example of Result Matrix of Content Based Filtering

Customer ID	Average-Child-Baby Friendly	Average-Pool	Average-Spa-Thermal Hotel	Average-Sauna-Hamam	Average Fitness
13	1	1	1	1	1
31	1	1	1	1	1
141	0	0	0	0	0
166	1	1	1	1	1
300	1	1	1	1	1
318	1	1	1	1	1
329	1	1	1	1	1
430	0,6667	1	1	1	1
446	1	1	1	1	0
458	1	1	1	1	0
644	1	1	0,5	0,5	0
732	1	1	1	1	1
825	1	1	1	1	0
982	1	1	1	1	1
1032	1	1	1	1	0,667
1080	0,75	0,75	0,75	0,75	0,5
1090	1	0	0	0	0

B. Data Analysis Results by Using Collaborative Filtering Method

For collaborative filtering, due to the need to calculate the points given by each customer to each hotel, the number of visits by the customer to the hotels is calculated as the score given by that customer to the relevant hotel, and the result matrix is obtained. At the same time, customers whose customer code is included in the data set and none of the hotels that are selected are included in the hotel properties (whole row is 0) are excluded from the data set and it is aimed to increase reliability.

While applying this collaborative filtering method, the total number of selections of the hotels is calculated with the pivot table and hotels with less than 10 visits by customers are excluded from the matrix in order to obtain clearer and more reliable results.

At the end, a matrix is obtained with customers in the rows and hotels in the columns, and the scores given by the customers to each hotel as seen in Table 6.

Table 6: A Brief Example of Result Matrix of Collaborative Filtering

	HOTEL ID SCORES							
CUSTOMER ID	370	383	384	385	386	419	445	466
430	2							
732					1			
821								1
825						1		
1080		1						
1134							1	
16230								1
16234							1	
16247								1
16278					1			
16378								3
16379								1
16381								
16383								2
16385					1			
16440	1							
16465								5
16467								1
16468								
16469								1
16516			1					
16546								1
16559								1
16583								1
16584								10

C. Data Analysis Results by Using RFM Method

Since the values we will calculate with RFM analysis are recency, frequency, and monetary, the values we will use in our 2 separate data sets are as follows:

1) Customer code
2) Billing information
3) Sales date
4) Sales Price

While analyzing these values, the pivot table is used and the customer code is selected as the line, the date of the last sale, how many invoices are issued, and the total sales price are determined.

Recency Scores:

A recency matrix is created to find customers' recency scores. The recency matrix is divided into percentiles with the PERCENTILE.INC formula. The customer who visited us the longest time is determined and scored 1, then the matrix is divided into following percentages, in order: 20, 40, 60 and 80. The recency scores are assigned as in Table VII.

Table 7: Recency Matrix

RECENCY MATRIX	
Recency	Recency Score
1.01.2019	1
12.04.2019	2
18.07.2019	3
18.12.2019	4
30.07.2020	5

According to the created recency matrix (Table 7), R-Scores are assigned to customers by VLOOKUP formula.

Examples of the result of the R-Score processed into the RFM matrix are shown in table 10.

Frequency Scores:

While assigning frequency values to customers, the PERCENTILE.INC formula is used. The customer who visits the company at least should get 1 as the frequency value. After calculating the customer with the least visits to the company with the pivot table, the most recent visit dates are divided into the following percentages, in order: 20, 40, 60, 80, 90, and 95. The frequency matrix is given in table 8.

Table 8: Frequency Matrix

FREQUENCY MATRIX	
Frequency	Frequency Score
1	
1	
1	1
1	2
1	3
2	4
3	5

As seen in Table 8, the frequency value of the customer is 1 up to the 80% slice. This value means that at least 80% of customers shopped from the company only once.

According to the created frequency matrix (Table 8), F-Scores are assigned to customers by VLOOKUP formula.

Examples of the result of the F-Score processed into the RFM matrix are shown in table 10.

Monetary Scores:

According to the total sales price amount created with the pivot table in the RFM table, the monetary matrix is created with the PERCENTILE.INC formula and monetary scores are assigned. The results are given in Table 9.

Table 9: Monetary Matrix

MONETARY MATRIX	
Monetary	Monetary Score
0	1
5572800	2
11696000	3
18920000	4
30100000	5

According to the created frequency matrix (Table V), M-Scores are assigned to customers by VLOOKUP formula.

Examples of the result of the M-Score processed into the RFM matrix are shown in table 10.

Table 10: Recency, Frequency, and Monetary Scores of the Customers

Customer ID	The Last Sale Date	Number of Master ID	Total Selling Price	**R Score**	**F Score**	**M Score**
13	15.07.2020	2	84753000	4	4	5
31	17.07.2020	3	19541300	4	5	4
141	16.07.2020	1	13557900	4	3	3
166	19.12.2019	2	31471700	4	4	5
171	29.09.2020	3	38562100	5	5	5
179	5.08.2020	3	10294200	5	5	2
191	29.08.2020	1	64396800	5	3	5
217	8.10.2019	1	1654400	3	3	1
254	10.02.2020	1	2285900	4	3	1
300	28.12.2019	1	9967400	4	3	2
318	5.08.2019	1	17028000	3	3	3

V. CONCLUSION

The recommendation system is an area in the industrial system that has multiple content-based, collaborative and hybrid approaches to increase companies' growth and productivity.

Recommendation systems provide access to personalized information on the web and have progressed in the last 10 years.

Recommendation systems created new options for information search and filtering. For instance, online shopping stores have increased their profits and music lovers discovered new songs.

Besides the positive effect of the recommendation system on customers, there are some limitations and deficiencies. This paper has reviewed three different recommendation approaches in detail. Additionally, this paper has reviewed Recency, Freqency, and Monetary analysis in detail.

ACKNOWLEDGEMENT

This article is partially supported by Galatasaray University Research Fund (BAP) within the scope of project number fba-2021-1063, and titled "Niteliklendirilmiş çift yönlü ağlarda bağlantı tahmini ile öneri sistemleri geliştirilmesi".

REFERENCES

[1] H. Poor, *An Introduction to Signal Detection and Estimation*. New York: Springer-Verlag, 1985.

[2] S. Chen, B. Mulgrew, and P. M. Grant, "A clustering technique for digital communications channel equalization using radial basis function networks," *IEEE Trans. Neural Networks*, vol. 4, pp. 570–578, July 1993.

[3] G. R. Faulhaber, "Design of service systems with priority reservation," in *Conf. Rec. 1995 IEEE Int. Conf. Communications*, pp. 3–8.

[4] J. Williams, "Narrow-band analyzer (Thesis or Dissertation style)," Ph.D. dissertation, Dept. Elect. Eng., Harvard Univ., Cambridge, MA, 1993.

[5] *Motorola Semiconductor Data Manual*, Motorola Semiconductor Products Inc., Phoenix, AZ, 1989.

[6] R. J. Vidmar. (1992, August). On the use of atmospheric plasmas as electromagnetic reflectors. *IEEE Trans. Plasma Sci.* [Online]. *21(3).* pp. 876—880. Available: http://www.halcyon.com/pub/journals/21ps03-vidmar

[7] Isinkaye, F. O., Folajimi, Y. O., & Ojokoh, B. A. (2015). Recommendation systems: Principles, methods and evaluation. Egyptian Informatics Journal, 16(3), 261-273.

[8] Bobadilla, J., Ortega, F., Hernando, A., & Gutiérrez, A. (2013). Recommender systems survey. Knowledge-based systems, 46, 109-132.

[9] Seyednezhad, S. M., Cozart, K. N., Bowllan, J. A., & Smith, A. O. (2018). A review on recommendation systems: Context-aware to social-based. arXiv preprint arXiv:1811.11866.

[10] Pazzani, M. J., & Billsus, D. (2007). Content-based recommendation systems. In The adaptive web (pp. 325-341). Springer, Berlin, Heidelberg.

[11] Shani, G., & Gunawardana, A. (2011). Evaluating recommendation systems. In Recommender systems handbook (pp. 257-297). Springer, Boston, MA.

[12] Seyednezhad, S. M., Cozart, K. N., Bowllan, J. A., & Smith, A. O. (2018). A review on recommendation systems: Context-aware to social-based. arXiv preprint arXiv:1811.11866.

[13] Hill, W., Stead, L., Rosenstein, M., & Furnas, G. (1995, May). Recommending and evaluating choices in a virtual community of use. In Proceedings of the SIGCHI conference on Human factors in computing systems (pp. 194-201).

[14] Chien, Y. H., & George, E. I. (1999, January). A bayesian model for collaborative filtering. In AISTATS.

[15] Sun, Z., & Luo, N. (2010, August). A new user-based collaborative filtering algorithm combining data-distribution. In 2010 International Conference of Information Science and Management Engineering (Vol. 2, pp. 19-23). IEEE.

Analysis of data security and privacy in public institutions according to GDPR in the Republic of Kosovo

Elissa Mollakuqe[1], Ersan Hamdiu[1], Nida Santuri Fishekqiu[1] and Samir Jakupi[1]
[1] Faculty of Computer Science- AAB College/ Pristina 10000, Republic of Kosovo
elissa.mollakuqe@universitetiaab.com, ersan.hamdiu@universitetiaab.com,
nida.santuri@universitetiaab.com, samir.jakupi@universitetiaab.com,

Abstract - **Data security is a major issue for every institution. The data for each individual who interacts with an institution, whether an employee or a seeker of services from the institution, must be stored and protected. The process of securing data and implementing privacy requires a high degree of investigation and certain professionalism. In order to provide such a service, many institutions use high standards to prevent data attacks and privacy violations. GDPR - 2016/679 - General Data Protection Regulation) comes in two versions OJ L 119, 04.05.2016; cor. OJ L 127, 23.5.2018. In this paper, we present the harmonization between the regulation which contains the privacy laws and the current state of data security in public institutions and the preservation of privacy. The paper used the method of analysis of current documents and comparison with GDPR - 2016/679 - General Data Protection Regulation.**

Keywords **–attack, security, privacy, GDPR, data, and institution**

I. INTRODUCTION

The General Data Protection Regulation 2016/679 is applicable to the following types of processing of personal data: processing that is entirely or partially automated; processing that is not automated but incorporates or is intended to incorporate personal data into a filing system. (ico. Information Commisioner's Office, 02.Aug.2018)

According to the General Data Protection Regulation 2016/679 - "personal data" refers to any information pertaining to a named, recognizable, or locatable individual (a "data subject"). An identifiable natural person is one who can be located, directly or indirectly, especially by reference to an identifier like a name, identification number, location information, online identifier, or one or more characteristics unique to that natural person's physical, physiological, genetic, mental, economic, cultural, or social identity [4].

To be able to implement suitable security measures, it is crucial to distinguish between processed personal data and sensitive personal data. Personal Information is any information a person may possess about another is deemed personal information as long as it may be used to identify a natural person. illustrative personal. Name, address, phone number, social security number, email, photographs, as well as license number, IP address, and cookies, are all examples of data [11].

Additionally covered by the General Data Protection Regulation 2016/679 are "special category" and "sensitive" personal data. Such information might relate to the data subject's race, ethnicity, politics, religion, union membership, genetics, biometrics (if used for identification reasons), health, sexual orientation, or sex life [4].

The most significant ones to which we make reference in this article are listed below. Personal data represent all information relating to an individual who can be directly or indirectly identified is considered personal data. Email addresses and names are obviously personal information. Political viewpoints, browser cookies, ethnicity, gender, biometric data, and location details can all be considered personal data. The term can also apply to pseudonymous data if it's pretty simple to identify a person using it. Data processing are any data-related action, whether automatic or human. Examples given in the text include gathering, recording, structuring, using, deleting, and arranging. therefore, anything. Data controller present person will be in charge of deciding how personal data will be processed. If you have access to data in your organization, this is you. Data Processor are the third party that processes personal data on behalf of a data controller. The General Data Protection Regulation 2016/679 has specific rules for these individuals and organizations. They could include cloud-based services such as Tresorit or email providers such as Proton Mail.

In this paper, are present data security in public enterprises according to General Data Protection Regulation 2016/679 in the Republic of Kosovo. In section 2, are provided details for the management and administration of enterprises according to General Data Protection Regulation 2016/679.

In section 3, is a complete guide about the process of resolving issues related to data security, the staff responsible for the prevention and investigation of security breaches, encryption standards and the recovery of access in case of any incident.

At the end are presented some conclusions and recommendations are given.

II. DATA SECURITY AND PRIVACY

As long as users are entirely anonymous and cannot be identified from the data you retain; you are permitted to store and collect certain information under the GDPR. The information must be retained for as short a time as possible.

Organizations must only gather personal data on a legal basis, according to the GDPR. The following 6 legal bases are provided under Article 6 of the GDPR: (Privacy research team, 2022)

- Consent
- Contact performance
- Observing a legal requirement
- Important interest
- Social interest
- Authentic interest

A. Data retention

The GDPR data retention regulations typically provide that any personal data gathered or processed must only be maintained for as long as it is required to achieve the purpose for which it was collected, with a few exceptions, such as for scientific or historical study. The GDPR also provides the "right to be forgotten" or the right to erasure.

In the following situations, data subjects have the right to request that their personal data be deleted (and to stop that personal data from being processed):

a) When the personal data is no longer needed for the original reason, it was collected or processed [8].

b) When the data subject withdraws their consent[8].

c) When the data subject objects to the processing of their personal data and the Organization does not have an overriding legitimate interest [8].

d) When the personal data is processed unlawfully (i.e., in violation of the GDPR)[8].

A local data protection authority (DPA) must be notified of a data breach that potentially endangers data subjects within 72 hours. In accordance with GDPR, affected subjects must be informed: "without undue delay." Test breach management processes and answers to data subject requests on a regular basis to make sure staff members can achieve these dates [2].

B. Data verification

To fulfill a data access request, you must confirm the identity of the consumer making the request and the consumer to whom you are disclosing the personal information.

Identity verification guarantees that the consumer and the individual requesting their data are the same person in order to comply with GDPR. It accomplishes this by conducting an identification check on the requester using both previously collected consumer identity data and extra information [5].

The right to request that their personal data be deleted or otherwise disposed of (notwithstanding the retention periods otherwise set forth in this Data Retention Policy), the right to limit the use of their personal data by the Organization, and additional rights relating to automated decision-making and profiling are all provided to data subjects with regard to the personal data held by the Organization[4].

C. What exactly is the right to information

The right to information protects several of the most significant GDPR transparency principles. It requires telling people in clear, explicit terms what you do with their personal information.

When information is acquired directly, the individual must be told as soon as possible, or at the time the information is acquired. (ico. Information Commisioner's Office, 02.Aug.2018)

Additionally, the right to be informed covers details such as how long personal data will be kept, the data subject's rights, the capacity to revoke consent, the right to file a complaint with the appropriate authorities, and whether or not providing personal data is required by law or contract. In addition, all automated decision-making processes, including profiling, must be disclosed to the data subject [7].

The right to information in a clear, visible, understandable, and freely available format belongs to the data subject. It is possible to fulfill the obligation to inform in writing or electronically.[7]

D. Data Principels Protection

If you process data, you have to do so according to seven protection and accountability principles

- Processing must be lawful, fair, and transparent to the data subject in order to protect their privacy.
- Purpose Limitation - They must process the data for the legitimate purposes expressly indicated to the data subject at the time of collection.
- Data minimization - You should only collect and process as much data as is strictly necessary for the stated purposes.
- Accuracy You must keep Personal Data accurate and up to date.
- Storage limitation You may only store personal data for as long as is necessary for the stated purpose.
- Integrity and confidentiality - Processing must be carried out in a way that ensures appropriate security, integrity and confidentiality (e.g. by using encryption).
- Accountability - The data controller is responsible for being able to demonstrate compliance with all of these principles by the GDPR [5]

Data protection by design and by default - Art. 25 GDPR

- Taking into account the state of the art, the implementation costs and the nature, scope, context and purposes of the processing, as well as the risks of different likelihood and severity associated with the processing for the rights and freedoms of natural persons, the person responsible both at the time of determining the Means of processing as well as at the time of the processing itself appropriate technical and organizational measures, such as way and to integrate into the processing the necessary guarantees to meet the requirements of this Regulation and to protect the rights of the data subjects [5].

- The person responsible takes appropriate technical and organizational measures to ensure that by default only the personal data required for the respective processing purpose are processed. This obligation applies to the amount of personal data collected, the scope of their processing, the duration of their storage and their accessibility. In particular, such measures ensure that, by default, personal data is not made available to an indefinite number of natural persons without individual intervention [5].

E. Appropriate technical and organisational measures

The protection of the rights and freedoms of natural persons with regard to the processing of personal data requires that appropriate technical and organizational measures are taken to ensure that the requirements of this regulation are met. In order to be able to demonstrate compliance with this regulation, the controller should issue internal guidelines and implement measures that correspond in particular to the principles of data protection by design and data protection by default [5]. Such measures could include, inter alia, reducing the processing of personal data to a minimum, pseudonym mising personal data as soon as possible, enabling transparency in relation to the functions and the processing of personal data, enabling the data subject to monitor data processing and enable the person responsible to create and improve security functions. When developing, designing, selecting and using applications, services and products that rely on the processing of personal data or process personal data to fulfill their task, manufacturers of the products, services and applications should be encouraged to take the right to data into account To protect data protection in the development and design of such products, services and applications and to ensure, taking into account the state of the art, that controllers and processors can fulfill their data protection obligations [5]. The principles of data protection by design and by default should also be taken into account in the context of public tenders.

F. Role of the Right of access

The right of access plays a central role in the General Data Protection Regulation (GDPR). On the one hand, because only the right of access allows the data subject to exercise further rights (such as rectification and erasure) [5]. On the other hand, because an omitted or incomplete disclosure is subject to fines. In the GDPR, the right of access plays an important role, because the right of the access allows data subject exercise further rights (such as rectification and erasure) also an incomplete or omitted disclosure is subject to fines.

There are two stages to request right of access. First the controller must check whether any personal data of the person seeking information is being processed at all and must report a result based on search. If the answer is positive, the second stage involves a whole range of information[5].

The right of access includes information about the processing purposes, the categories of personal data processed, the recipients or categories of recipients, the planned duration of storage or criteria for their definition, information about the rights of the data subject such as rectification, erasure or restriction of processing, the right to object, instructions on the right to lodge a complaint with the authorities, information about the origin of the data, as long as these were not collected from the data subject himself, and any existence of an automated decision-taking process, including profiling, with meaningful information about the logic involved as well as the implications and intended effects of such procedures[5].

Depending on the circumstances, information can be disclosed to the data subject in writing, electronically, or verbally under Art. 12(1) sentences 2 and 3 of the GDPR[5]. According to GDPR Article 12(3), information must be shared as soon as possible, but no later than one month. Only in extraordinary circumstances may this one-month limit be exceeded. In most cases, the information must be provided free of charge. If more copies are required, a reasonable fee reflecting administrative costs can be requested. The controller may also refuse a data subject's right of access request if it is unjustified or excessive. If the controller is processing a large volume of information on the data subject, he or she has the additional right to specify their request within the right of access for specific data processing or kind of information [5].

"The Right of Access." *Data Protection Commission*, https://www.dataprotection.ie/en/individuals/know-your-rights/right-access-information. Accessed 13 November 2022.

"Right of Access - General Data Protection Regulation." *GDPR*, https://gdpr-info.eu/issues/right-of-access/. Accessed 13 November 2022

G. Data Processing based on Contract

The General Data Protection Regulation (GDPR) provides a standard, Europe-wide option for so-called "commissioned data processing," which is the collection, processing, or use of personal data by a processor in accordance with the controller's contractual instructions.

In most circumstances, commissioned data processing follows a contract. GDPR Article 28(3) specifies the minimal standards. The contract must specify the sort of personal data that will be processed, as well as the object and purpose of the processing [5]. In addition, the processor has other responsibilities. For example, he must keep a record of the processing activities, which contains the names and contact information of each controller for whom he works, as well as the processing categories carried out for them [5].

The controller must ensure, in selecting the processor, that it has implemented sufficient technical and organisational measures to ensure that processing meets the requirements of the Regulation.

Basically, the controller is the first contact for the data subject and responsible that the data processing complies with the legal requirements [5].

"Processing - General Data Protection Regulation." *GDPR*, https://gdpr-info.eu/issues/processing/. Accessed 13 November 2022.

H. Data Security Regulations

A crucial component of regulatory compliance is data security. Data security is a crucial part of compliance in the majority of regulatory frameworks in our case GDPR. As a result, you must take data security seriously and collaborate with a knowledgeable compliance partner to make sure you're taking all the necessary precautions [5]. The right data security technologies can help your organization in preventing breaches, lowering risk, and sustaining protective security measures. To prevent data breach you may use Data Auditing, Data Real-Time Alerts, Data Risk Assessment, Data Minimization, Purge Stale Data To minimize the chances of a data breach, loss, and exposure we have to Quarantine Sensitive Files, Behavior-

Based Permissions, Prepare for Cyber Threats, Delete Unused Data.

The analysis of the current state of data security in public institutions was done by analyzing the appropriate technical and organizational security measures according to Article 32 of the General Data Protection Regulation (GDPR). A total of 18 institutions were analyzed, which belong to different categories: government institutions, municipal institutions, public service institutions, public schools and public universities.

Table 1. Number of public institutions

institution	government institutions	municipal institutions	public service institutions	public schools	public universities
in total	2	5	2	3	6

Government institutions, municipal institutions, public service institutions, public schools and public universities have been analyzed by dealing with the assessment of risks during data processing, the documentation of the security program during the processing of personal data which specifies technical, administrative and physical protections, the process of solving the problem in the event of filing a complaint, determining an individual who is responsible for the prevention and investigation of security breaches, the use of encryption standards, personal information is systematically destroyed, deleted or anonymized when it is no longer legally required to be stored , the return of personal data in time in case of a physical or technical incident.

III. Analysis of data security and privacy in public institutions according to GDPR in the Republic of Kosovo

The strictest privacy and security law in the world is the General Data Protection Regulation (GDPR). Although it was created and approved by the European Union (EU), it imposes requirements on any organizations that target or gather information about individuals residing in the EU. An exhaustive list of legal terminology is defined in the General Data Protection Regulation 2016/679. Based on the General Data Protection Regulation (GDPR), 18 public institutions were analyzed. Table 2 presents the results generated after the analysis done for: the assessment of risks during data processing, the documentation of the security program during the processing of personal data which specifies the technical, administrative and physical protections, the process of solving the problem in in case of filing a complaint, determining an individual who is responsible for the prevention and investigation of security breaches, the use of encryption standards, personal information is systematically destroyed, deleted or anonymized when it is no longer legally required to be stored, the recovery of data personal in time in case of a physical or technical incident.

Table 2. Analysis of public institution based on the General Data Protection Regulation (GDPR)

	GI	**MI**	**PSI**	**PS**	**PU**
Have you assessed the risks involved in processing personal data and put measures in place to mitigate them	yes	no	no	no	yes
Is there a documented security program that specifies the technical, administrative, and physical safeguards for personal data?	yes	yes	no	no	no
Is there a documented process for resolving security-related complaints and issues?	no	no	no	no	no
Is there a designated individual who is responsible for preventing and investigating security breaches?	yes	yes	no	no	no
Are industry-standard encryption technologies employed for transferring, storing, and receiving individuals' sensitive personal information?	yes	no	no	no	no
Is personal information systematically destroyed, erased, or anonymized when it is no longer legally required to be retained?	yes	yes	no	no	no
Can access to personal data be restored in a timely manner in the event of a physical or technical incident?	no	no	no	no	no

The obtained results presented in table 2: government institutions (GI), municipal institutions (MI), public service institutions (PSI), public schools (PS) and public universities (PU) for each of these, the current conditions are initialized, where "YES" means that the institution is equipped with that request and "NO" means that the institution is not equipped with that request. The requests are according to the General Data Protection Regulation (GDPR) Article 32.

IV. Conclusion

Strategies for combating cybercrime, current policies and regulations of public institutions are outdated and do not meet the requirements of the General Data Protection Regulation (GDPR). And as such it results that:

- municipal institutions, public service institutions, public schools do not have risk assessors involved in the processing of personal data measures to mitigate the risks
- public service institutions, public schools and public universities do not have a security program documented that specifies the technical, administrative and physical safeguards for personal data
- government institutions, municipal institutions, public service institutions, public schools and public universities not have a documented process for resolving complaints and issues related to security?
- public service institutions, public schools and public universities do not have a designated individual responsible for the prevention and investigation of security breaches
- municipal institutions, public service institutions, public schools and public universities do not have an industry standard encryption technology for transfer, storing and receiving sensitive personal information of individuals
- public service institutions, public schools and public universities do not have any mechanism that systematically destroys, deletes or anonymizes personal information when it is no longer legally required to be stored
- government institutions, municipal institutions, public service institutions, public schools and public universities do not have techniques that can restore access to personal data at the right time in case of a physical or technical incident.

Public institutions must review the management documents of cybercrimes and adapt them according to the Regulation General Data Protection Regulation (GDPR).

REFERENCES

[1] Gerardus Blokdyk, *Sensitive Data A Complete Guide - 2019 Edition*, 5STARCooks (July 12, 2021), ISBN-10 : 0655817905, ISBN-13 : 978-0655817901

[2] Cobb, M. (2021, November). TechTarget Search Security. Retrieved from 7 best practices to ensure GDPR compliance: https://www.techtarget.com/searchsecurity/tip/7-best-practices-to-ensure-GDPR compliance?utm_source=google&int=off&pre=off&utm_medium=cpc&utm_term=GAW&utm_content=sy_lp09222022GOOGOTHR_GsidsSecurity_OneTrust_Essential_IO163813_LI2595380&utm_campaign=OneTr

[3] Elissa Mollakuqe, V. D.-M. (2022). Data Classification Based on Sensitivity in Public and Private Enterprises in the Republic of Kosovo. ICT Innovations 2022 (pp. 192-200). Skopje: Association for Information and Communication Technologies www.ict-act.org.

[4] Every one . (2021, 07). every one making wellbeing personal. Retrieved from GDPR Data Retention Policy: https://every-one.org.uk/wp-content/uploads/2021/07/EveryOne-GDPR-Data-Retention-Policy.pdf

[5] GDPR, G. D. (2022, 9 19). IT GOVERNANCE EUROPE. Retrieved from General Data Protection Regulation GDPR: https://www.itgovernance.eu/blog/en/the-gdpr-what-is-sensitive-personal-data ico. Information Commisioner's Office. (02.Aug.2018).

[6] Guide to the General Data Protection Regulation (GDPR). United Kingdom.

[7] Intersoft consulting. (n.d.). Intersoft consulting.eu. Retrieved from GDPRRight to be Informed: https://gdpr-info.eu/issues/right-to-be-informed/#:~:text=The%20data%20subject%20has%20a,in%20writing%20or%20electronic%20form.

[8] NetSec.news. (2018). NetSec.news. Retrieved from GDPR Data Retention: https://www.netsec.news/gdpr-data-retention/#:~:text=Generally%20speaking%2C%20GDPR%20data%20retention,or%20historical%20research%20for%20example.

[9] Organization, S. (2022, 09 10). SINA Organization. Retrieved from SINA Organization: https://www.snia.org/education/what-is-data-protection Privacy research team. (2022, September 2).

[10] Securiti.ai. Retrieved from GDPR Data Collection Requirements: https://securiti.ai/blog/gdpr-data-collection/#:~:text=Data%20Collection%20Requirements%20under%20GDPR,-You%20can%20store&text=The%20GDPR%20requires%20organizations%20to,one%20or%20more%20specific%20purposes.

[11] Serenhov, M. (2018). Forensic Breach Response in Compliance with GDPR. Sweden : Tryckeriet i E-huset, Lund. veratad. (2021, March 2). veratad.com. Retrieved from How to Verify Identity for GDPR Data Access Requests: https://veratad.com/verify-identity-gdpr-data-access-requests/#:~:text=For%20GDPR%20compliance%2C%20identity%20verification,check%20of%20the%20requester's%20identity.

[12] G. Ateniese, K. Fu, M. Green, and S. Hohenberger, "Improved proxy re-encryption schemes with applications to secure distributed storage". In Proceedingsof the 13th Annual Network and Distributed SystemSecurity

[13] Symposium, San Diego, CA, Feb. 2006.

[14] D. Akhawe, P. Saxena, and D. Song, "Privilege separation in HTML5 applications". In Proceedings ofthe 21st Usenix Security Symposium, Bellevue, WA, Aug. 2012.

[15] J. Li, M. Krohn, D. Mazieres, and D. Shasha, "Secure untrusted data repository (SUNDR)". In Proceedings of the 6th Symposium on Operating Systems Design and Implementation (OSDI), pages 91–106, San Francisco, CA, Dec. 2004.

[16] A. J. Feldman, W. P. Zeller, M. S. Bajaj and R. Sion."TrustedDB: a trusted hardware based database with privacy and data confidentiality", In Proceedings of the 2011 ACM SIGMOD International Conference on Management of Data, pages 205– 216, Athens, Greece, June 2011.

[17] G. Ateniese, K. Fu, M. Green, and S. Hohenberger, "Improved proxy re-encryption schemes with applications to secure distributed storage". In Proceedingsof the 13th Annual Network and Distributed System Security Symposium, San Diego, CA, Feb. 2006.

Comparison of Feature Selection Methods in the Aspect of Phishing Attacks

Ali ŞENOL

Department of Computer Engineering, Engineering Faculty, Tarsus University, Mersin, alisenol@tarsus.edu.tr

***Abstract* - Feature selection methods are commonly used to reduce the number of features that are believed to be more relevant to the classes. These methods aim to decrease the run-time complexity of the models without reducing their accuracy. In some cases, they also may increase the accuracy. On the other hand, phishing attacks are internet fraud attacks that target stealing the valuable information of users by using fake web pages. Therefore, feature selection methods can be used on phishing datasets to increase the performance of models without reducing the accuracy. In this study, we compared the efficiency of feature selection methods on phishing datasets by using Multilayered Perceptron (MLP) algorithms. According to obtained results the Information Gain (IG), Fisher's Score (FS) was the best ones although the number of the selected features is low.**

***Keywords* - feature selection, phishing, classification.**

I. INTRODUCTION

FEATURE selection methods are used to reduce the number of features that the dataset has. These methods are commonly used in many areas like bioinformatics, data mining, image processing, scientific applications, etc. Correlation Correlation-based feature selection (CC), MI (Mutual Information), Information Gain, Chi-square test (CS), and Variance Threshold-based (VT) feature selection methods are some examples of these kinds of methods [1].

Phishing attacks are kinds of attacks that aim to steal the valuable information of users like credit card information and account information by using various methods like using fake e-mails and fake messages. In general, these attacks try to enforce users to enter their information on fake web pages that are thought to be real ones by the users. These attackers send e-mails or messages to the users to update their account information. When the user clicks on the sent link, the link redirects the user to the fake web page, which at first glance is thought to be the same as the original. The final step of the attack is for the user to enter his/her information on the web page [2].

On the other hand, classification is a branch of machine learning that try to classify any new arrival data according to past data [3]. These approaches divide the datasets as training and test datasets for both purposes of training and testing [4, 5]. Support Vector Machine (SVM), Naïve Bayes (NB), k-Nearest Neighbors (kNN), Decision Trees (DT), and Artificial Neural Networks (ANN) are some examples of classification algorithms that are used in many areas like engineering applications, scientific applications, financial applications, health systems, and education areas, etc. [6].

In past decades, some studies which use various classification algorithms with feature selection methods on phishing attacks have been proposed. One of these studies is proposed by Pan and Ding [7]. They used Chi-square (x^2) test on a phishing dataset to select the best features and SVM as the classifier. The aim is to extract textual features. The lacks of their method are high computational complexity and dependent feature selection outputs on training datasets. In another research which was carried out by Ma et al. [8], they performed two classification algorithms with IG feature weighting on seven phishing datasets and compared the classifiers' accuracies. The main problem related to their study was to have low dimensional feature space. A similar study was implemented by Toolan and Carthy. They used IG as the feature selection method with machine learning classifiers on three phishing datasets and compared the results. According to obtained results, the accuracies of classifiers are different among all the datasets and the main problem of their study was to have high computational complexity and high dimensional hybrid feature space. Hassan [9] proposed a hybrid embedded feature selection method with four classifiers on phishing datasets to omit redundant and irrelevant features. The main disadvantage of his model was to be dependent to feature selection outputs on training datasets and classifiers. Similarly, Joshi and Pattanshetti [10] proposed an embedded method which consists of a classifier and a feature selection method, to find the best combination of them among various methods. According to their approach, the combination of Random Forest classifier and ReliefF was the best combination on the phishing dataset. Additionally, Moedjahedy et al. [11] proposed a correlation-based feature selection methods with machine learning algorithms to detect phishing websites. Their aim also was to find the best combination of a method and an algorithm. According to their study, the obtained results were satisfying.

In this study, we compared major feature selection methods by using MLP algorithm on the Phishing Legitimate dataset. This study aims to reveal the efficiency of feature selection techniques on phishing datasets.

The rest of the paper is organized as follows. In the next section details about phishing attacks, feature methods, and classification algorithms are given, while the used model is explained in the 3th section. Then, the experimental study and

its results are given in 4th section. Finally, the study is concluded in the 5th section.

II. BACKGROUND

A. Phishing Attacks

Phishing attacks are a kind of internet fraud that is similar to fishing. These kinds of attacks send users e-mails or messages in which various links to the fake web pages of organizations like banks, government agencies, or any account on social media are contained. To hide from the user that the link is fake, they use various techniques. One of these techniques is using @ symbol in the links. When @ symbol is used inside any link, the left characters on the left side of @ symbol are ignored by the internet browsers. For example, if the link given below is clicked, it will redirect the user to the domain given on the right side, while the majority of internet users think that it will redirect to the web address given on the left side [2].

http://www.gazi.edu.tr@www.google.com

In this example, it is clear that the link has two web addresses. To hide the fake web address, attackers mask the address with URL-encode values instead of using ASCII characters. The masked version of the above link is given below. This technique is known as link manipulation. In addition to this technique, there are many phishing methods such as SMiShing (Short Message Service Phishing) [12], Phishing by telephone call [13], social media phishing [13], ClickJacking [14], etc.

http://www.gazi.edu.tr@%77%77%77%2E%67%6F%6F%67%6C%65%2E%63%6F%6D

B. Feature Selection Methods

Feature selection techniques are preprocessing stage of data mining and machine learning that are used to reduce the number of features without reducing the accuracy of the model. The aim is to select features that have more effect on class as much as possible. In general, feature selection methods are classified as follows [15]:

- Filter methods: These techniques use statistical approaches to evaluate the features. The most important advantage of filter methods is speed. Some of these methods can be said as the Chi-square test, Correlation Coefficient (CC), Information Gain, Fisher's Score, Variance Threshold (VT), and Mean Absolute Difference (MAD).
- Wrapper methods: In these methods, all possible subsets of features are candidates for the best-selected features. Each subset is assessed and the subset which produces the best results is determined as selected features. In the assessment stage, machine learning techniques are used. The most important risk for these methods is overfitting. SVM-Recursive Feature Elimination (RFE) and Greedy Forward Selection (GFS) can be given as examples of these methods.
- Embedded methods: Embedded methods try to combine the benefit of both filter and wrapper methods. These methods use a training stage to find the best features. The most important advantage of these methods is computational complexity compared with wrapper methods. LASSO Regularization (L1) and Random Forest Importance are two examples of these methods.

C. Classification Algorithms

Classification algorithms are the most known approaches of machine learning techniques. These algorithms use existing datasets to learn and then could decide any new arrival data to which class will be assigned [3]. These techniques divide the datasets as train and test datasets. The main flow chart of these kinds of algorithms is given in Figure 1. The test dataset is used to assess the classification performance of the model. Some examples of classification algorithms are Support Vector Machine, Naïve Bayes, k-Nearest Neighbors, Decision Trees, Random Forest, and Artificial Neural Networks.

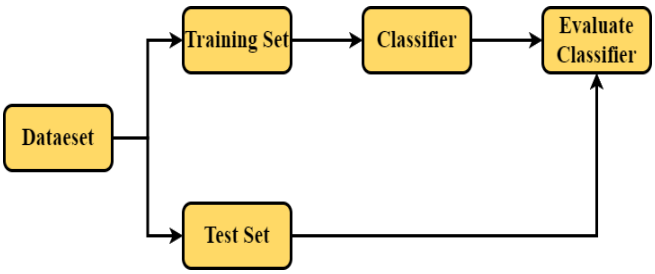

Figure 1: Flowchart of classification algorithms

III. METHODOLOGY

A. Experimental Environment

In this study, we used Python programming language in Anaconda Spyder environment using libraries like scikit-learn. We carried out all experiments on a computer that has i7 processor, 16 GB of RAM, and Windows 11 operating system installed.

B. Used Feature Selection Methods

In this study, we used state-of-the-art feature selection methods on Phishing Legitimate dataset by using MLP algorithm. The purpose is to find which feature selection method is the most efficient for phishing datasets. For this purpose, we used Fisher's score, Information Gain, Correlation Coefficient, Variance Threshold, and Mean Absolute Difference on the dataset

C. Phishing Legitimate Dataset

Phishing Legitimate dataset has 10 thousands of records and each record has 49 attributes one of which is the class label indicating whether the record is the attack or not. The first 10 records of the dataset are given in Figure 2.

Figure 2: First 10 records of Phishing Legitimate dataset

	A	B	C	D	E	F	G	H	I	J	K	L	M	N	O	P	Q	R	S	T	U	V	W	X	Y	Z	AA	AB	AC	AD	AE	AF	AG	AH	AI	AJ	AK	AL	AM	AN	AO	AP	AQ	AR	AS	AT	AU	AV	AW	AX
1		0	3	1	5	72	0	0	0	0	0	0	0	0	0	1	0	0	0	0	0	21	44		0	0	0	0	0	0	1	1	0	0	0	0	0	0	0	0	0	0	1	1	0	1	1	-1	1	1
2		2	3	1	2	58	0	0	0	0	0	0	0	0	0	1	0	0	0	0	0	27	24		0	0	0	0	1	1	1	0	0	0	0	0	0	0	0	0	0	0	1	0	-1	1	-1	0	1
3		3	3	1	6	79	1	0	0	0	0	0	0	0	0	1	0	0	0	1	0	22	50		0	0	0	1	1	0	1	1	0	0	0	1	0	0	0	1	0	0	0	1	-1	1	1	1	-1	1
4		4	3	0	4	46	0	0	0	0	0	0	0	0	0	2	1	1	0	0	1	0	10	29		0	0	0	0	1	1	0	0	0	1	0	0	1	0	0	0	0	1	0	0	1	1	-1	0	-1	-1	1
5		5	3	1	1	42	1	0	0	0	0	0	0	0	0	1	0	0	0	1	0	23	12		0	0	0	0	0	1	1	1	0	0	0	0	0	0	0	0	0	0	1	1	0	1	1	1	-1	1	1
6		6	2	0	5	60	0	0	0	0	0	0	0	0	0	1	1	0	0	0	1	0	17	36		0	0	0	1	1	1	0	1	0	0	0	0	1	0	0	0	0	0	0	1	0	1	1	-1	-1	1
7		7	1	0	3	30	0	0	0	0	0	0	0	0	0	3	1	1	0	0	1	0	12	11		0	0	0	0	0	0	1	0	0	0	0	0	0	0	0	0	0	0	0	1	1	1	1	1	1	1
8		8	8	7	2	76	1	1	0	0	0	0	0	0	0	2	1	1	0	1	1	0	65	4		0	0	0	0	0	0	1	0	0	0	1	0	0	0	0	0	0	0	0	-1	-1	1	1	1	-1	1
9		9	2	0	2	46	0	0	0	0	0	0	0	0	0	1	0	0	0	1	0	14	25		0	0	0	1	1	1	1	1	0	0	0	1	0	0	0	0	0	0	0	1	1	1	1	-1	-1	1
10		10	5	4	2	64	1	1	0	0	0	0	0	0	0	3	1	1	0	1	1	0	53	4		0	0	0	0	0	0	1	0	0	0	1	0	0	0	1	0	0	0	0	0	-1	0	1	1	-1	1

D. *Used Classification Algorithm*

There are many classification algorithms have been proposed. In this study, we used MLP as the classification algorithm for our model. MLP is a multilayered neural network algorithm that models the neural system of humans. As an example is given in Figure 3, it has more than one hidden layer. It has two types as feed forward and back forward.

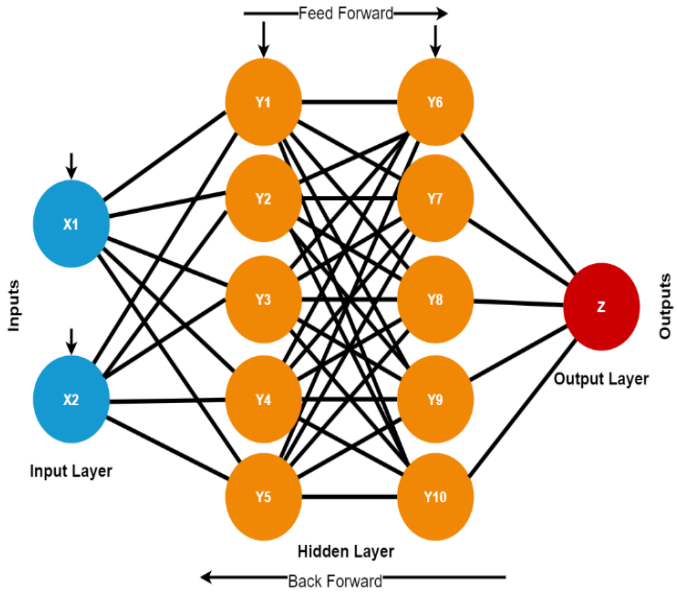

Figure 3: An example of MLP layers

E. *Test Procedure*

To compare the success of each feature selection method, we used the model that is given in Figure 4. In the experimental study, we used a variable as a threshold value for feature selection. This threshold is a percentage that limits the number of selected features according to the algorithm given in Figure 5.

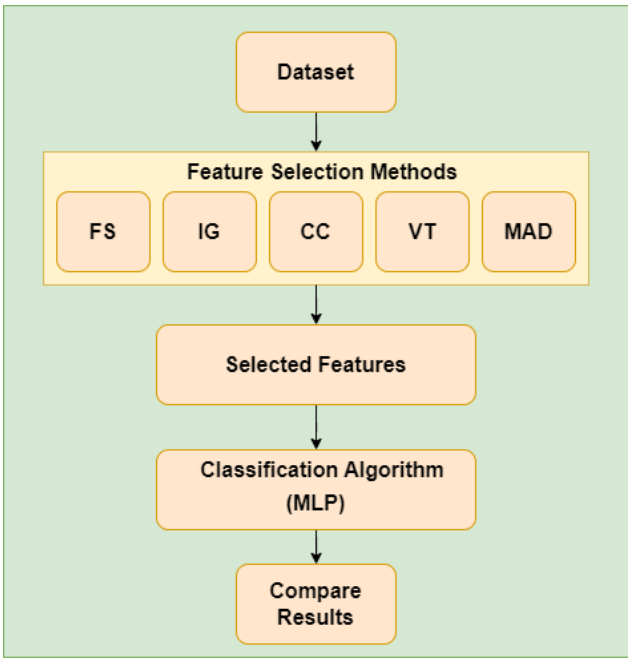

Figure 4: Used model

Algorithm 1: Feature Selection Operation

```
Input: Values;                    ▷Feature values calculated by FS method for each feature
ratio;                            ▷threshold percentage
Output: SF;                       ▷the List of Selected Features
Features ← DesOrder(Values);      ▷sort in descending order
sum=0;
foreach f ∈ Features do
    if sum ≤ ratio then
        sum=sum+f;
        SF← f;
    end
end
return SF;
```

Figure 5: Used algorithm to select features according to predefined variable ratio

F. *Parameter Setting*

To compare the feature selection methods, Accuracy is the selected classification result evaluation method. We used 10 as the k-fold value, the maximum iteration value for MLP as 300, and solver='lbfgs'. For ratio value, we used {0.75, 0.80, 0.85, 0.90, 0.95, 0.99, 0.99} in the experiments to find the best ratio value.

IV. RESULTS AND DISCUSSION

All obtained results for each feature selection method according to ratio values are given in Table 1. Classification accuracy without using any feature selection method is 0.9302 and given in the last row of the table. As can be seen in the table, Fisher's Score and Information Gain-based feature selection methods are the most successful. The top accuracy value is achieved by Fisher's Score method which is 0.9379 and it is achieved when ratio=0.85 that is cause to 30 features be selected. Similarly, the highest accuracy of the Information Gain method was 0.9318 and it is achieved when ratio=0.75 that is cause to 10 features be selected. Although the accuracy of Information Gain is very near to Fisher's Score's, it is expected to the computational complexity of the model that

uses Information Gain to be lower than the model that uses Fisher's Score because of using very less features. On the other hand, the Variance-Threshold-based method is the less successful method in which the accuracy is below 0.90s.

Table 1: Comparison of feature selection methods.

Method	ratio	# of selected features	Accuracy
IG	0.75	10	0.9318
IG	0.8	13	0.9121
IG	0.85	16	0.9047
IG	0.9	18	0.9193
IG	0.95	27	0.9241
IG	0.99	34	0.9249
FS	0.75	24	0.9318
FS	0.8	27	0.9376
FS	**0.85**	**30**	**0.9379**
FS	0.9	33	0.9289
FS	0.95	37	0.9352
FS	0.99	43	0.9222
MAD	0.75	4	0.6982
MAD	0.8	5	0.7237
MAD	0.85	7	0.7716
MAD	0.9	12	0.8315
MAD	0.95	19	0.8689
MAD	0.99	31	0.9304
CC	0.75	12	0.8181
CC	0.8	13	0.8174
CC	0.85	15	0.8731
CC	0.9	17	0.8726
CC	0.95	19	0.8917
CC	0.99	23	0.9026
VT	0.75	5	0.7237
VT	0.8	5	0.7237
VT	0.85	7	0.7716
VT	0.9	13	0.8335
VT	0.95	18	0.8704
VT	0.99	29	0.8909
Without Feature Selection	1	48	0.9302

V. CONCLUSION

In this study, we compared feature selection methods on a phishing dataset to show their efficiency. According to the results, it can be said that feature selection methods are very effective on phishing datasets. Even, it can be said that these methods could also exceed the accuracy of methods in which feature selection methods are not used. To come to the comparison among them, Fisher's Score was the most successful one among the others.

REFERENCES

[1] Dhal, P. and C. Azad, *A comprehensive survey on feature selection in the various fields of machine learning.* Applied Intelligence, 2022. **52**(4): p. 4543-4581.

[2] Şenol, A. and H. Karacan. *Sazan avlama (phishing): Kullanılan teknikler ve bunlardan korunma yöntemleri*. in *5th International Conference on Information Security and Cryptolog (ISCTurkey 2012)*. 2012. ODTÜ, Ankara.

[3] Cunningham, P., M. Cord, and S.J. Delany, *Supervised Learning*, in *Machine Learning Techniques for Multimedia: Case Studies on Organization and Retrieval*, M. Cord and P. Cunningham, Editors. 2008, Springer Berlin Heidelberg: Berlin, Heidelberg. p. 21-49.

[4] YaĞLi, T.U., K.U. Kübra, and Emre, *Gözetimli Makine Öğrenmesiyle Noktalama ve Etkisiz Kelime Sıklıkları Kullanarak Yazar Tanıma.* 14, 2022.

[5] Erdem, A.Ö. and Hamit, *Saldırı Tespit Sistemlerinde Kullanılan Kolay Erişilen Makine Öğrenme Algoritmalarının Karşılaştırılması.* 5, 2022.

[6] Şenol, A., Y. Canbay, and K. Mahmut, *Trends in Outbreak Detection in Early Stage by Using Machine Learning Approaches.* 14, 2022.

[7] Pan, Y. and X. Ding. *Anomaly Based Web Phishing Page Detection*. in *2006 22nd Annual Computer Security Applications Conference (ACSAC'06)*. 2006.

[8] Ma, L., et al. *Detecting Phishing Emails Using Hybrid Features*. in *2009 Symposia and Workshops on Ubiquitous, Autonomic and Trusted Computing*. 2009.

[9] Hassan, D.J.I.J.o.C.A., *On Determining the Most Effective Subset of Features for Detecting Phishing Websites.* 2015. **122**: p. 1-7.

[10] Joshi, A. and P. Pattanshetti, *Phishing Attack Detection using Feature Selection Techniques.* SSRN Electronic Journal, 2019.

[11] Moedjahedy, J., et al., *CCrFS: Combine Correlation Features Selection for Detecting Phishing Websites Using Machine Learning.* 2022. **14**(8): p. 229.

[12] Mambina, I.S., J.D. Ndibwile, and K.F.J.I.A. Michael, *Classifying Swahili Smishing Attacks for Mobile Money Users: A Machine-Learning Approach.* 2022. **10**: p. 83061-83074.

[13] Chanti, S. and T. Chithralekha, *A literature review on classification of phishing attacks.* 2022.

[14] Dong, G., et al. *Security analysis and reinforcement of an in-use system*. in *Second International Conference on Cloud Computing and Mechatronic Engineering (I3CME 2022)*. 2022. SPIE.

[15] Khaire, U.M., R.J.J.o.K.S.U.-C. Dhanalakshmi, and I. Sciences, *Stability of feature selection algorithm: A review*. 2019.

Data security analysis based on data classification according to data sensitivity. Study case: data on Public and Private Universities in the Republic of Kosovo

E.MOLLAKUQE[1] and V.DIMITROVA[1]

[1] Faculty of Information Sciences and Computer Engineering/Skopje, Republic of North Macedonia,
elissamollakuqe@gmail.com, vesna.dimitrova@finki.ukim.mk

Abstract - **Sensitive data represents information that has a level of confidentiality. These data have a wide range of comprehensiveness and are not only personal data. The large volume of data that is constantly transmitted through different computer systems made many of us start to think about data threats. In recent times, the threat to privacy is quite worrying because we have a lot of personal data that circulates in computer networks and that it is very easy to fall into the hands of criminals. Preservation of privacy can be done by providing integrity in the software where these data are processed, integrity in the computer networks where these data circulate and, in any case, the prohibition of unauthorized access to information. A solution to prevent unauthorized access is by setting the level of sensitivity of the data. In our research, the collected data are classified into two categories (student data and employee data) and into three subcategories according to their sensitivity: the nature of the data, the amount of data and the inclusion of these data in computer systems. The purpose of our research is to provide a classification of the sensitivity of data against access to sensitive information.**

Keywords **– data, sensitivity, confidentiality, privacy and unauthorized access.**

I. INTRODUCTION

Data security and protection in universities is one of the priority points of the administration and management of the information systems of the educational institution. In May 2018, the General Data Protection Regulation (GDPR) was approved in the EU, which protects the personal data of each individual or legal entity.

Sensitive data in universities represents the group of data where the university is legally required to protect that information. Based on the classification models of this data we refer to it as confidential and restricted data. Referring to the General Data Protection Regulation (GDPR), doubt often arises between personal data and sensitive data because only 20% of institutions think that personal data and sensitive data are in compliance with GDPR [2].

According to the General Data Protection Regulation (GDPR), organizations can process data in two classes:

- Personal data (names, identification numbers, location data, as well as other examples of structured and unstructured data).
- Sensitive personal data (Racial or ethnic origin, Political opinions, Religious or philosophical beliefs, Trade union membership, Genetic data, Biometric data and Gender identity or sexual orientation) [2]

In universities, sensitive data is categorized based on role and the relationship that the individual has with the institution, example: teachers store sensitive data about students' grades, IDs, classroom activities, etc., the office for academic affairs stores data for: registrations, scholarship information and student achievements, etc. All these data are sensitive and require constant protection. According to SNIA Organization data protection is defined as: Data protection is the process of safeguarding important data from corruption, compromise or loss and providing the capability to restore the data to a functional state should something happen to render the data inaccessible or unusable. Data protection assures that data is not corrupted, is accessible for authorized purposes only, and is in compliance with applicable legal or regulatory requirements. Protected data should be available when needed and usable for its intended purpose [4]. The attack at this data is called a cyber attack.

In this paper, are present the characteristics of data security in 13 universities in the Republic of Kosovo by classifying data according to the level of their sensitivity and exposure to cyber threats.

In section 2, the criteria used for data classification in universities are defined. Using these criteria, the search results were obtained. In section 3, a complete classification is given where the collected data are classified into two categories (student and employee data) and into three subcategories according to their sensitivity based on criteria: nature of data,

amount of data and the inclusion of these data in computer systems. At the end are presented some conclusions and recommendations are given.

II. DATA SECURITY, DATA SENSITIVITY AND UNAUTHORIZED ACCESS

Based on the General Data Protection Regulation (GDPR), data security must be handled in a technically secure manner (*users of that data are required to use two-factor authentication of all employees in accounts where they store personal data*) sensitive) and organizational (*including staff training, increased security policies, new strategic adaptations to preserve privacy, etc.).*

Sensitive personal data require specific conditions for storage, administration, management and processing. This data contains information about racial origin, ethics, religious beliefs, health data, sexual orientation, biometric and genetic data.

Unauthorized access is achieved when an attacker manages to enter a computer system, application, database without prior permission. This process violates the rules, policies and security statements of the system owner and operator. In the University, unauthorized access is considered the use of each resource inside and outside the university without a permission to use.

Classification of data based on sensitivity, universities should do it based on General Data Protection Regulation (GDPR), which lists the data as: restricted, confidential/private and public.

Table 1. Data Classification According to General Data Protection Regulation GDPR

Classification	
Restricted	the most sensitive data that could cause great risk if compromised, and the access must be on a need-to-know basis only [2]
Confidencial/Private	moderately sensitive data that would cause a moderate risk to the company if compromised, and the access is internal to the company or department that owns the data [2]
Public	this is non-sensitive data that would cause little or no risk to the company if compromised and access is loosely, or not, controlled [2]

In the current research, the same model was used as used by the authors: Elissa Mollakuqe, Vesna Dimitrova and Aleksandra Popovska Mitrovikj. This classification model sorted university data into categories according to sensitivity. For data classification, the data keeper - the employee of the institution - is used. The collected data are classified as: restricted data, private data and public data, these collected data contained information: first name, last name, staff_id, student_id, email address, phone number, gender, grades, homework logs, health status, etc.

The classification model was used, first an overview of the current classification of the data was created, this type of classification was used with the purpose of matching the data collected through the classification process according to sensitivity according to sensitivity, the data were processed in the nature of the data, the amount of data and the inclusion of these data in computer systems.

III. STUDY CASE: DATA SECURITY ON UNIVERSITY BASED ON DATA CLASSIFICATION ACCORDING TO DATA SENSITIVITY

In this part, we analyze the data collected for 13 different universities (6 public university and 7 private university) in the Republic of Kosovo. This data belongs to one of three levels of sensitivity: restricted, private or public. After the sensitivity classification, the data are processed based on the processing according to the nature of the data, the amount of the data and the inclusion of the data in computer systems. The collected data are: data protection regulations, data security regulations, scientific research information (name, surname, university, faculty, scientific publication, journal link), financial data (name, surname, address, budget, salary) personal data (account number, access codes to computer systems).

The table below (table 2) provides details on the classification of this data based on sensitivity:

Table 2. Classification on data collected at university

Classification	Types of data collected
Restricted data	Employee_account number, Employee _access codes to computer systems Student_account number, Student_access codes to computer systems
Private data	Employee_financial data Employee_address, Employee_ budget, Employee_salary Student_financial data Student_address, Student_ scholarship
Public data	data protection regulations, data security regulations Employee_name, Employee_surname, Employee_university, Employee_faculty, Employee_scientific Employee_publication, Employee_journal Employee_link, Student_name, Student_surname, Student_university, Student__scientific Student_publication, Student_journal Student_link,

A. *Nature and amount of the data for employees and students*

According to the nature of the data for employees and students in public and private universities, 55% of the data are sensitive personal data, 30% of the data are personal data and only 15% are public data.

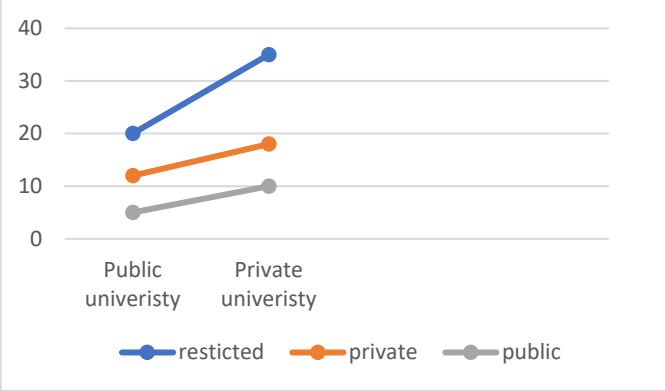

Figure 1. Nature of data in public and private university

In public universities, 20% of the data are restricted, 12% of the data are private and only 5% of the data are public. While in private universities, 35% of the data are restricted, 18% of the data are private and 10% of the data are public.

B. *The inclusion of the data in computer systems for employee and students*

Each of the universities use at least two systems at the same time, for example: for the distribution of literature and materials per student, for the management of grades, tasks and activities, for the management of teaching hours (check-in-out systems). These systems are designed from two components: the staff component and the student component. Data in these systems circulate continuously using networks and collaborative configurations. According to the researches in both public and private universities, it results that the data is fully integrated with other systems and is fully included in more than one computer system. The designed systems are not very secure and often encounter problems and there are opportunities for attacks on them because their architecture and construction are not fully compatible with General Data Protection Regulation (GDPR) requirements.

IV. CONCLUSION

Data classification is missing and as such gives the possibility that many sensitive data are directly exposed to attacks. In universities, there is no filter for classifying data according to sensitivity, and as such it allows each attacker to have direct access to each piece of information. The recommendations resulting from the research propose that each university first classify data according to the General Data Protection Regulation (GDPR)model, then adapt the current systems based on General Data Protection Regulation (GDPR) requirements.

Also, according to the analysis, we come to the conclusion that public and private universities should invest more in data security, especially in unauthorized access to systems.

REFERENCES

[1] Gerardus Blokdyk, *Sensitive Data A Complete Guide - 2019 Edition*, 5STARCooks (July 12, 2021), ISBN-10 : 0655817905, ISBN-13 : 978-0655817901

[2] Elissa Mollakuqe, V. D.-M. (2022). *Data Classification Based on Sensitivity in Public and Private Enterprises in the Republic of Kosovo.* ICT Innovations 2022 (pp. 192-200). Skopje: Association for Information and Communication Technologies www.ict-act.org.

[3] GDPR, G. D. (2022, 9 19). IT GOVERNANCE EUROPE. Retrieved from General Data Protection Regulation GDPR: https://www.itgovernance.eu/blog/en/the-gdpr-what-is-sensitive-personal-data

[4] Organization, S. (2022, 09 10). SINA Organization. Retrieved from SINA Organization: https://www.snia.org/education/what-is-data-protection

[5] Rauthan, Jitendra & Vaisla, Dr. Kunwar. (2017). Privacy and Security of User's Sensitive Data: A Viable Analysis. 67-71. 10.15439/2017R45.

[6] Xu, Lei & Jiang, Chunxiao & Wang, Jian & Yuan, Jian & Ren, Yong. (2014). Information Security in Big Data: Privacy and Data Mining. IEEE Access. 2. 1-28. 10.1109/ACCESS.2014.2362522.

[7] Fung, Benjamin & Wang, Ke & Fu, Ada & Yu, Philip. (2010). Introduction to Privacy-Preserving Data Publishing: Concepts and Techniques. 10.1201/9781420091502.

[8] Salini . S, Sreetha . V. Kumar, Neevan .R, https://www.researchgate.net/publication/281398949_Survey_on_Data_Privacy_in_Big_Data_with_K-_Anonymity

[9] Deepa, N & Jeevan, Sounder. (2022). CYBER SECURITY AND PRIVACY OF BIG DATA. XIV. 702-714.

[10] Bhatia, Reenu & Sood, Manu. (2022). Big Data Security Trends. 10.1007/978-981-19-3679-1_15.

Electromagnetic Compatibility (EMC) Simulation and Application in Automotive Electronics

Alperen YAZAR[1] and Metin HÜNER[2]

[1] Istanbul Technical University, Istanbul/Turkey, yazar20@itu.edu.tr
[2] Istanbul Technical University, Istanbul/Turkey, metinhuner@itu.edu.tr

Abstract **- To ensure electromagnetic compatibility in automotive electronics, some standards and design methods should be considered during design. One of these standards is UNECE R10 which defines conducted and radiated emissions. In this study, a power supply was designed and simulated that meets the conducted emission standards by UNECE R10 with CISPR 25.**

Keywords **– EMC, EMI, LTspice, Automotive electronics, Artificial network (AN), Conducted emissions, Noise, CISPR 25.**

I. INTRODUCTION

EMC is the ability of an electronic component to operate successfully in the electromagnetic field and not affect other systems or components. A system can be affected from environment via radiated or conducted emissions. UNECE R10 is the international standard which defines the maximum emission limits for conducted and radiated emissions. Radiated emissions are measured by high frequency range antennas and spectrum analyzer in shielded rooms. So, radiated emissions cannot be simulated by LTspice. Unlike that, conducted emissions are measured by AN (Artificial Network) and spectrum analyzer. Therefore, using AN model, conducted emissions can be estimated by LTspice. AN model for UNECE R10 is shown in Figure 1 according to the UN Regulation No. 10 [1].

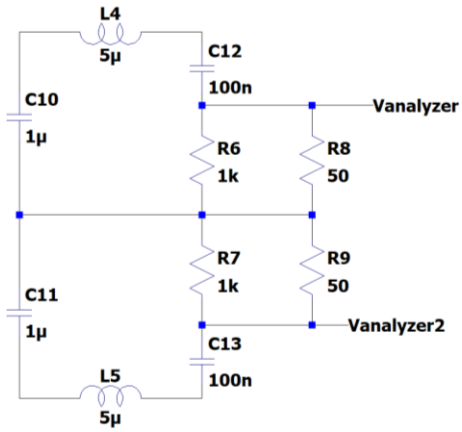

Figure 1: AN model

In a system, there may number of components such as electronic control unit (ECU), advanced driver assistance systems (ADAS), human media interface (HMI), battery management systems (BMS). All these components are supplied by low voltage battery which is 12V or 24V in automotive. So, whole components are connected via power supply line. Every single component should work properly.

Conducted emissions are the noise which is generated by a component to power supply line. Conducted emissions can be defined as differential-mode noise and common-mode noise. In differential-mode noise, noise current and current from main power supply line have same path. Differential-mode noise current path is shown in Figure 2.

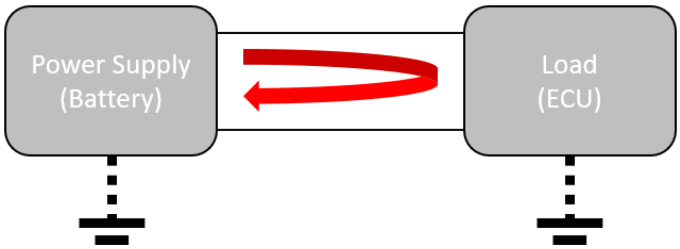

Figure 2: Differential-mode noise current path

Common-mode noise is generated by leakage current on stray capacitances or isolated grounded systems. Such ash, low voltage is used in automotive generally. With low voltage battery, hybrid vehicle or electric vehicle (EV) has high voltage batteries. So, high voltage batteries have different grounding. These high voltage and low voltage grounds are connected via stray capacitors. Common-mode noise current path is shown in Figure 3.

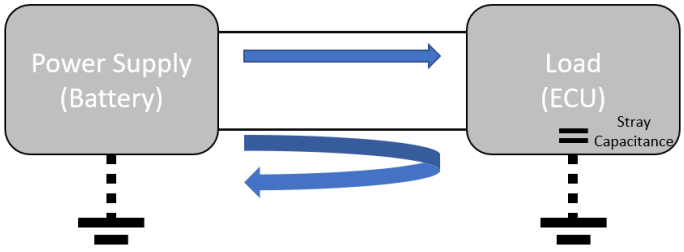

Figure 3: Common-mode noise current path

Conducted emissions are measured by AN and spectrum analyzer. Test environment is shown in Figure 4.

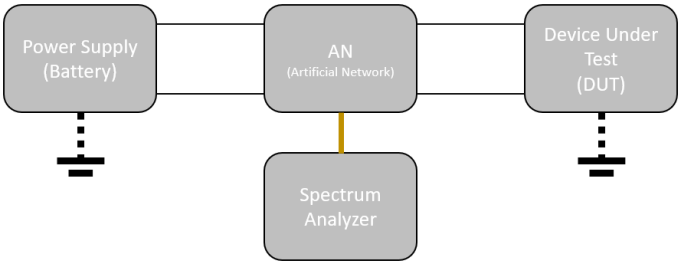

Figure 4: Conducted emissions test environment

In this work, a power supply of an electronic control unit (ECU) was designed and simulated to observe conducted emissions (differential-mode and common-mode noises) via LTspice.

II. Literature

EMI specifications are defined for different fields. According to the UNECE R10, CISPR 25 can be defined main EMI standards for automotive. Main electronic components which are existed in an automotive must comply with the CISPR 25 standards [2]. To test CISPR 25, shielded room is needed but there are some ways to estimate the results such as LTspice and MW Studio. [3]. Unlike CISPR 25, CISPR 22 covers the multimedia equipment which are used as external systems in the automotive [2].

To estimate common-mode and differential-mode noises, AN model can be considered as a resistor. So, equivalent circuit can be built with resistors [4]. Despite this approach, real AN model can be built with low-pass filters [5].

Common-mode and differential-mode noises can be reduced by using some filters. These filters have inductor and capacitors basically to block noises from DC-DC converter to main power supply line. To analyze attenuation level, current and voltage methods can be used. Current method is more efficient way because it has not source impedance. So, noise can be simulated as current source [6].

III. Design and Simulation Method

In automotive electronics, every single component should be AEC-Q (Automotive Electronics Council) qualified. AEC-Q qualified component ensure the work properly in stressed environments such as high temperature range and vibration. So, designed power supply has AEC-Q qualified active and passive components. Electronic control units have different modules such as power supply module, communication module, microcontroller module, input-output module etc. Generally, input voltage of all sub-modules is 5V. So, power supply module has a switch-mode power supply which generates 5V from battery voltage. For this work, LT8640A from Analog Devices is used [7]. It is a step-down converter with high-efficiency and ultra-low EMI (Electromagnetic Interference) emissions, and it can provide 5A from 5V output to microcontroller and others. Switching frequency also is adjustable. To use similar inductance, switching frequency is set to 1MHz via R_T resistance. Also, all passive components have not basic spice-models due to get realistic results. Capacitors and inductors are modelled with parasitic. To get 250mA from output, 20Ω load resistance is used. Also, electromagnetic compatibility tests are observed in continuous mode due to avoid start-up noises.

To observe differential-mode and common-mode emissions, "Vanalyzer" and "Vanalyzer2" nets are transformed from time domain to frequency domain via FFT analysis. LTspice FFT analysis has range with dBV scale but CISPR 25 defines the limits with dBµV. So, this conversation is actualized as in (1).

$$1dBV = 120dB\mu V \tag{1}$$

Differential-mode calculations are simulated with formula which shown as in (2).

$$Vdm = \frac{V(Vanalyzer) - V(Vanalyzer2)}{2} \tag{2}$$

Common-mode calculations are simulated with formula which shown as in (3).

$$Vcm = \frac{V(Vanalyzer) + V(Vanalyzer2)}{2} \tag{3}$$

IV. Simulations and Filter Design

Typical application schematic of LT8640A with AN model is designed in LTspice as shown in Figure 5.

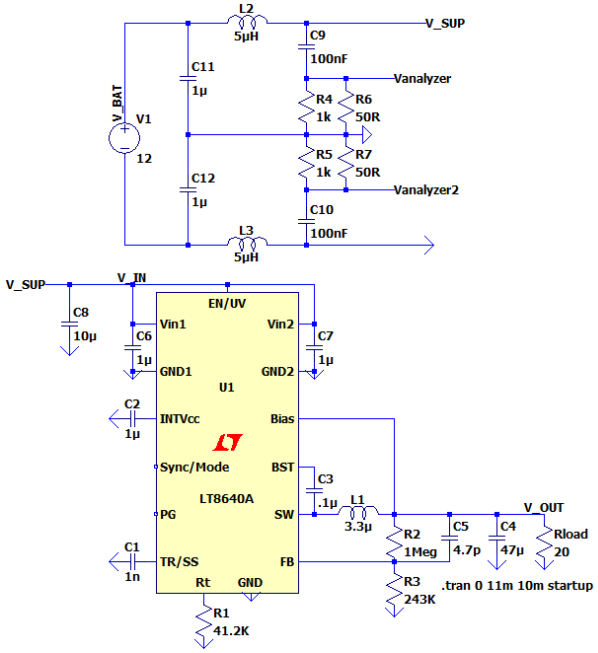

Figure 5: Typical application schematic with AN model

Differential-mode (red trace) and common-mode noises (blue trace) are simulated in frequency domain which shown in Figure 6. CISPR 25 limits are also shown as grey trace.

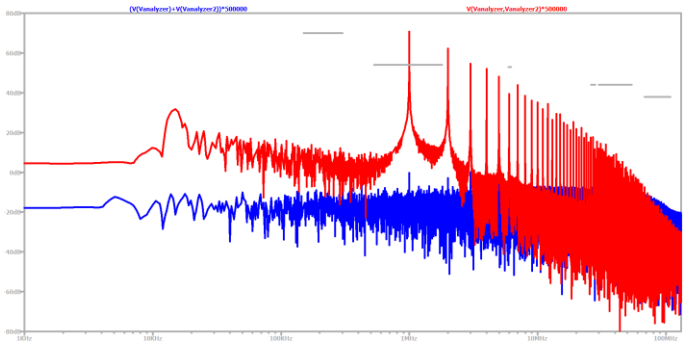

Figure 6: Differential-mode and common-mode noises of typical application schematic

As shown, differential-mode and common-mode noises exceed the limits around 1MHz which is switching frequency. In power supply systems, to prevent exceeding of the limits, common-mode chokes and LC low-pass filters are used. Common-mode choke is based on two coupled inductors [8]. In this system, common-mode noise is not detected. So, LC low-pass filter must be designed to block differential-mode noise.

To find attenuation rate, input of power supply can be simulated as current source and AN can be simulated as 100Ω basically [6]. Simulation schematic is shown in Figure 7.

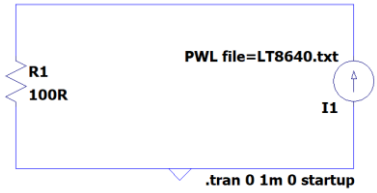

Figure 7: Simulation schematic for FFT analysis

Noise levels can be estimated on frequency domain via FFT analysis. FFT analysis (red trace) shows the frequency levels which exceed the limits (grey trace). Simulation results are shown in Figure 8.

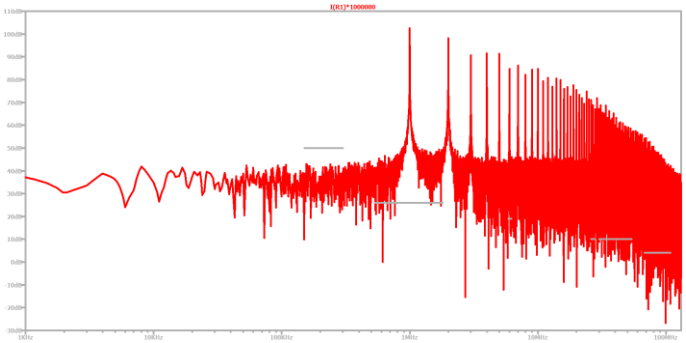

Figure 8: FFT analysis for differential-mode noise

To decrease differential-mode noise, second order LC filter can be used. According to the CISPR 25 current probe method Class 5 section, limit is 26dBµA. Unfortunately, power supply has 100dBµA noise level at 1MHz. So, the attenuation rate should be around 80dBµA.

Second order low-pass filters have -40dB/dec attenuation rate [9]. Second order low-pass filter should be designed to get -80dB/dec attenuation rate at 1MHz according to the Figure 9.

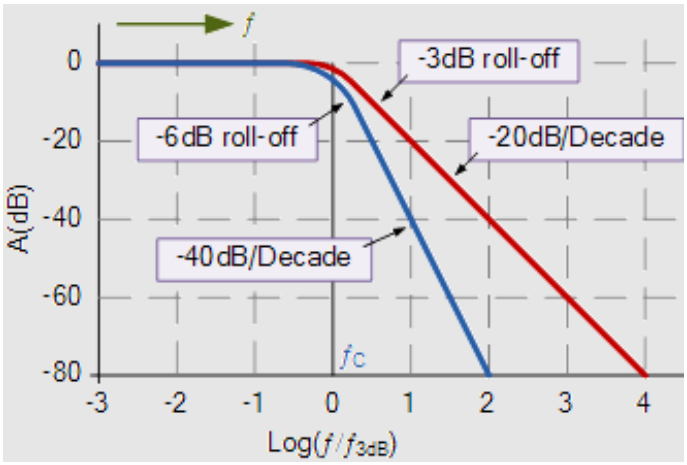

Figure 9: Attenuation graph for low-pass filters [9]

The formula shown in (4) can be used to find the cut-off frequency of the low-pass filter.

$$\log\left(\frac{f}{f3dB}\right) = 2 \quad (4)$$

During selecting inductor, current limits, power loss and impedance should be considered. LC filter values can be calculated following formula (5). So, cut-off frequency should be around 10kHz.

$$f3dB = \frac{1}{2\pi\sqrt{(LC)}} \quad (5)$$

In general applications, inductance may be selected as 10µH. So, capacitor value can be calculated via formula which is shown in (6) [6].

$$f3dB = \frac{1}{2\pi\sqrt{(LC)}} = \frac{1}{2\pi\sqrt{(10\mu H * 22\mu F)}} = 10.73kHz \quad (6)$$

Same typical application schematic is re-simulated with LC low-pass filter. Typical application schematic with LC low-pass filter is shown in Figure 10.

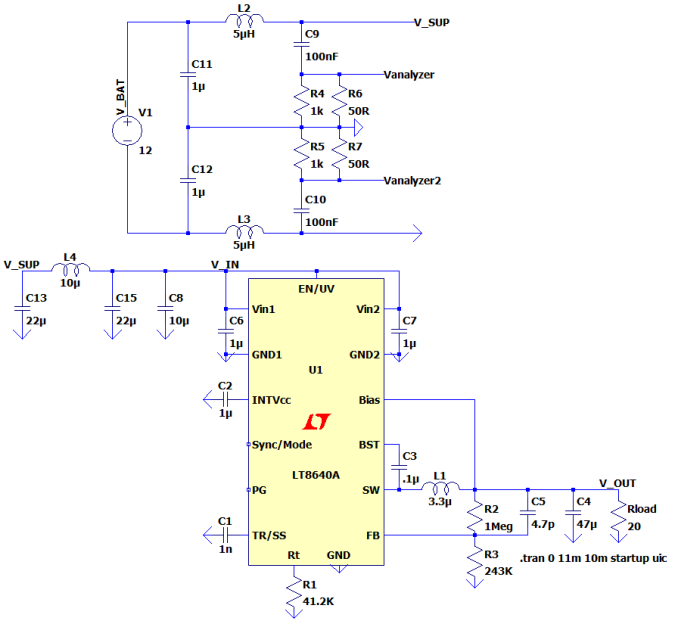

Figure 10: Typical application schematic with AN model and LC low-pass filter

LC low-pass filter should be placed to power supply line. Because, for all components connected to the main power supply line to continue to operate properly, differential mode noise from the step-down converter must be filtered.

Differential-mode (red trace) and common-mode noises (blue trace) are re-simulated with LC low-pass filter in frequency domain which shown in Figure 11. CISPR 25 limits also shown as grey trace.

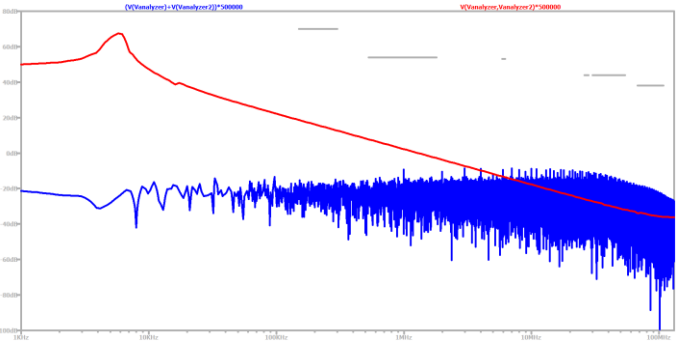

Figure 11: Differential-mode and common-mode noises of typical application schematic with LC low-pass filter

V. Conclusion

During the DC-DC converter design, EMC standards and design methods should be considered. In this work, a step-down convertor for automotive grade technology equipment was simulated and designed. Common-mode and differential-mode noises are estimated via LTspice using AN model.

Exceeding the conducted emission limits is suppressed by the second-order LC low-pass filter design.

References

[1] *United Nations Regulation No. 10*, pp. 42, November 2019
[2] *Texas Instruments Application Note SLYY136*, Texas Instruments, February 2018
[3] *Automotive Component EMC Testing*, Vicente Rodriguez, March 2022
[4] *Design of EMI Filters for DC-DC converter*, J. L. Kotny, T. Duquesne, N. Idir, France, 2010
[5] *Anticipate EMC with LTSPICE*, Wurth Electronics, May 2020
[6] T*exas Instruments Application Note AN2162*, Texas Instruments, November 2021
[7] *Analog Devices Data Sheet LT8640/8640-1*, Analog Devices, March 2022
[8] *ST Microelectronics Application Note AN4511*, ST Microelectronics, June 2016
[9] www.electronics-tutorials.ws/filter/second-order-filters

Implementation of Modified Karnik-Mendel Algorithm based Interval Type-2 Fuzzy Inference System for Aircraft Pitch Control

M.OZTURK[1], T. UNLER[2], G. BEDENLI[3], S. KURTAR[4], N. YILDIRIM[5] and T. DAG[6]

[1] Necmettin Erbakan University, Konya/Turkey, mozturk@erbakan.edu.tr
[2] Necmettin Erbakan University, Konya/Turkey, tunler@erbakan.edu.tr
[3] Necmettin Erbakan University, Konya/Turkey, gizembedenli50@gmail.com
[4] Necmettin Erbakan University, Konya/Turkey, sakinekurtar95@gmail.com
[5] Necmettin Erbakan University, Konya/Turkey, nur19996838@gmail.com
[6] Necmettin Erbakan University, Konya/Turkey, tolunaydag@gmail.com

Abstract – **In this paper, Modified Karnik-Mendel Algorithm is implemented for a control problem. This is the first control study of the Modified Karnik-Mendel Algorithm (M-KMA) in the open literature. Type-2 fuzzy inference systems need a type-reduction method to be reduced to interval type-2 fuzzy inference systems. Karnik-Mendel Algorithms is one of the type-reduction methods. The proposed type-reduction methods in the open literature do not allow Adaptive Neuro-fuzzy Inference System (ANFIS) training. So, the M-KMA is proposed in 2021 to train antecedent and consequent parameters of interval type-2 fuzzy logic systems by using ANFIS. In this study, the recently proposed M-KMA is tested on aircraft pitch control. PID controller is used as a conventional controller. The M-KMA based Interval Type-2 FIS is used to tune PID parameters with respect to error and error derivative. The performances of controllers are compared for settling time, overshoot, root mean square errors and steady-state errors. It is seen that the M-KMA gives superior results than conventional PID controllers.**

Keywords - **Karnik Mendel Algorithm, Modified Karnik Mendel Algorithm, Type-2 Fuzzy Inference System, Fuzzy PID, Aircraft Pitch Control.**

I. INTRODUCTION

The fuzzy inference system (FIS) is proposed in 1965 that is very useful to represent mathematically non-solvable problems and nonlinear systems [1]. In FIS, membership values are determined by using MFs. The determined membership values are used by rules to obtain output values. The mentioned type-1 FIS is used in many industrial applications [2].

Fuzzy parameters are determined by expert opinion in many studies in the open literature, but it is hard way to use expert opinion for complicated systems. Therefore, many training algorithms are proposed, of which Adaptive Neuro-Fuzzy Inference System (ANFIS) is the most used. The ANFIS is consist of two stages as consequent parameters training and antecedent parameters training [3]. Least Square Estimation (LSE) is used for consequent parameters training and Backpropagation (BP) method is used for both antecedent and consequent parameters training [4]. This training algorithm is used for control problems as online ANFIS controller [5].

The type-1 FIS is very effective for non-mathematical systems, but it is not effective for uncertainties. Because the type-1 MFs are precise and cannot handle undetermined effects. The type-1 FIS antecedent and consequent membership functions (MF) are precise [6]. A new inference system named type-2 FIS is proposed by Zadeh [7] to include the uncertainties in type-1 FISs. The type-2 FIS membership functions include uncertainties and so the computation is not possible without some assumptions. So, type-reduction methods are proposed those change the type-2 MFs to interval type-2 MFs [8]. Firstly, Karnik-Mendel algorithm (KMA) is proposed as a type-reduction method [9]. The Karnik-Mendel algorithm is an iterative approach that has a high computational load. To decrease the computational load following type-reduction methods are proposed as; Enhanced Karnik-Mendel Algorithms (EKMA) [10], Iterative Algorithm with Stop Condition (IASC) [11], Enhanced Iterative Algorithm with Stop Condition (IASC) [12], Direct Approach (DA) [13]. The type-reduction methods except DA are iterative methods, so they have computational loads that must be considered.

It is seen in the open literature that training of interval type-2 FIS parameters is still a research area [14]. The ANFIS structure for interval type-2 FIS (IT2FIS) is not convenient because of uncertainties [15]. The ANFIS needs to exact membership values. However, the interval type-2 membership values are uncertain. So, to implement ANFIS to IT2 FIS, the KMA structure is changed for ANFIS application and named as Modified Karnik-Mendel Algorithm (M-KMA) [16]. In this paper, the M-KMA which is the newest type-reduction method is tested for aircraft pitch control by tuning PID coefficients.

There is various fuzzy logic controller implementation to tune PID coefficients to overcome nonlinear systems. Various Fuzzy logic tuned PI and PD controllers are tested in literature to overcome nonlinearities. The fuzzy PD controllers are effective controllers but cannot remove the steady-state errors. The fuzzy PI controllers are effective at steady-state error but it does not have the fuzzy PD performance. So, type-1 fuzzy PID

controllers that is a combination of PI and PD, are used mostly in literature. The fuzzy tuned PID controllers have better performance at settling time, overshoot and steady-state error than others [17]. The type-1 fuzzy PID controller is tested for experimental applications like PLC controller [18, 19]. Results indicate that the fuzzy logic parameters must be determined by expert opinion under some assumptions as input scales [20]. The type-1 fuzzy PID controllers are tested with other control technics like observer design [21] model reference adaptive control [22] etc. for brushless DC motors. The type-1 fuzzy tuned PID controller has superior results compared to conventional PID controllers on pitch attitude control system that is an aircraft longitudinal motion [23]. The results show that the fuzzy tuned PID has less rise time with the same settling time and overshoot at subsonic and supersonic speeds. The studies in the literature show that fuzzy PID performance is superior compared to conventional PID controllers.

In this paper, general aviation aircraft longitudinal motion data is taken and used for implementation of interval type-2 fuzzy tuned PID controller [24]. The M-KMA based type-2 FIS tuned PID controller results are compared to conventional PID controllers. A sinusoidal signal with white noise is given to system to see reaction of controllers to disturbances.

II. AIRCRAFT DYNAMICS

General aviation airplane: NAVION is chosen for control applications. The aircraft longitudinal derivatives are given in Table 1 where "u" is velocity at x direction, "w" is velocity at z direction, "q" is angular rates at body y axis, "θ" is Euler angle at z axis, "δ_e" is elevator deflection and "δ_T" is throttle deflection. In aircraft pitch control, "q" angular rate is controlled.

Table 1: Longitudinal stability derivatives.

$X_u = -0.0457$	$X_w = 0.0361$
$Z_u = -0.3749$	$Z_w = -2.0272$
$M_u = 0$	$M_w = -0.1033$
$X_{\delta_e} = 0$	$X_{\delta_T} = 0$
$Z_{\delta_e} = -28.2738$	$Z_{\delta_T} = 0$
$M_{\delta_e} = -11.9382$	$M_{\delta_T} = 0$
$M_q = -2.0813$	$M_{\dot{w}} = -0.005165$

The simplified longitudinal set of equations are:

$$\dot{u} = X_u u + X_w w - g\theta + X_{\delta_e}\delta_e$$

$$\dot{w} = Z_u u + Z_w w + u_0 q + Z_{\delta_e}\delta_e \quad (1)$$

$$\dot{q} = (M_u + M_{\dot{w}}Z_u)u + (M_w + M_{\dot{w}}Z_w)w + (M_q + M_{\dot{w}}u_0)q + (M_{\delta_e} + M_{\dot{w}}Z_{\delta_e})\delta_e$$

III. METHODOLOGHY

In this chapter, the M-KMA structure is given and tested for an aircraft dynamic model.

A. M-KMA tuned PID Controller

The Interval type-2 FIS membership function is composed of two type-1 MFs as given in Figure 1. For every input, there are infinite MF values between upper (UMF) and lower (LMF) MFs. This area represents the uncertainty of IT2FIS named as Footprint of Uncertainty (FOU). This uncertainty makes the output of interval type-2 FIS impossible to calculate. So, type reduction methods are used.

The type-reduction methods calculate two switch points between upper and lower MFs. One of the switch points is calculated for the biggest value named "r" and the other is calculated for the lowest value named "l".

The M-KMA equations are given below:

Computing y_l:

1- Sort $\underline{f_i}$ in increasing order. Match the weights with $\underline{f_i}$.

2- Initialize w_i by calculating $w_i = \frac{\underline{w_i}+\overline{w_i}}{2}$ and compute

$$y = \frac{\sum_{n=1}^{N} \underline{f_i} w_i}{\sum_{n=1}^{N} w_i} \quad (2)$$

3- Find switch point "l" for $\underline{f_l} < y \leq \underline{f_{l+1}}$

4- Compute $y' = X_l W$ by setting

$$X_l = \frac{[\overline{w}_1 x_1 \quad \overline{w}_1 x_2 \quad \overline{w}_1 \quad \dots \quad \overline{w}_l x_1 \quad \overline{w}_l x_2 \quad \overline{w}_l \dots \quad \underline{w}_{l+1} x_1 \quad \underline{w}_{l+1} x_2 \quad \underline{w}_{l+1} \dots \quad \underline{w}_N x_1 \quad \underline{w}_N x_2 \quad \underline{w}_N]}{\sum_{n=1}^{l} \overline{w}_i + \sum_{n=l+1}^{N} \underline{w}_i} \quad (3)$$

5- If $y' = y$, set $y_l = y$; if not, set $y = y'$ and go to Step 3.

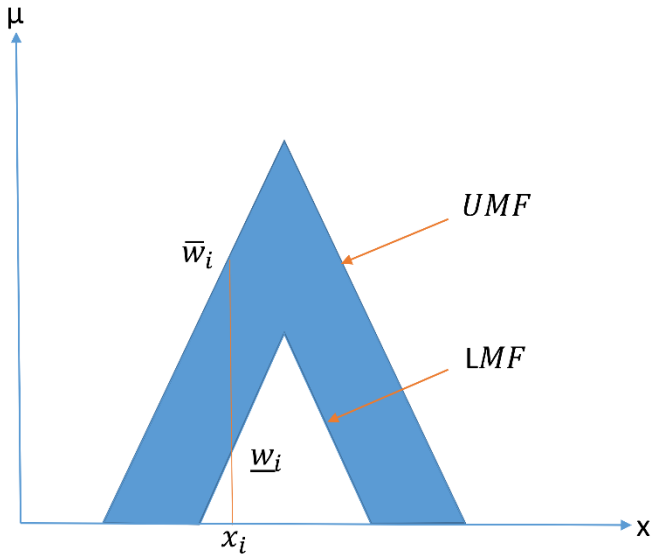

Figure 1: Interval type-2 membership functions.

Computing y_r:

1- Sort $\bar{f}_i$ in increasing order. Match the weights with $\bar{f}_i$.
2- Initialize w_n by setting $w_i = \frac{\underline{w}_i + \overline{w}_i}{2}$ and compute

$$y = \frac{\sum_{n=1}^{N} \bar{f}_i w_i}{\sum_{n=1}^{N} w_n} \tag{4}$$

3- Find switch point "r" for $\bar{f}_r < y \leq \bar{f}_{r+1}$
4- Compute $y' = X_r W$ by setting

$$X_r = \frac{[\underline{w}_1 x_1 \quad \underline{w}_1 x_2 \quad \underline{w}_1 \quad \dots \quad \underline{w}_r x_1 \quad \underline{w}_r x_2 \quad \underline{w}_r \dots \quad \overline{w}_{r+1} x_1 \; \overline{w}_{r+1} x_2 \; \overline{w}_{r+1} \dots \; \overline{w}_N x_1 \; \overline{w}_N x_2 \; \overline{w}_N]}{\sum_{n=1}^{r} \underline{w}_i + \sum_{n=r+1}^{N} \overline{w}_i} \tag{5}$$

5- If $y' = y$, set $y_r = y$; if not, set $y = y'$ and go to Step 3.

The result y can be calculated as

$$y = \frac{y_r + y_l}{2} = \frac{X_l W + X_r W}{2} = \frac{X_l + X_r}{2} W = XW \tag{6}$$

It is easily noticed that M-KMA can be implemented successfully since it gives X matrix explicitly.

B. *FIS tuned PID Controller*

The Proportional-Integral-Derivative (PID) control is a commonly used conventional control structure. In this study, the PID control coefficients are chosen by adjusting the coefficients and the controller parameters are set to $K_p = 41.5$, $K_i = 4$, $K_d = 9$.

In Fuzzy tuned PID controller structure, the FIS is used to tune PID coefficients as depicted in Figure 2. The FIS has two inputs as error and error derivative (e, de), three outputs as proportional, integral and derivative $(F_{K_p}, F_{K_i}, F_{K_d})$. The FIS outputs are summed with constant PID coefficients.

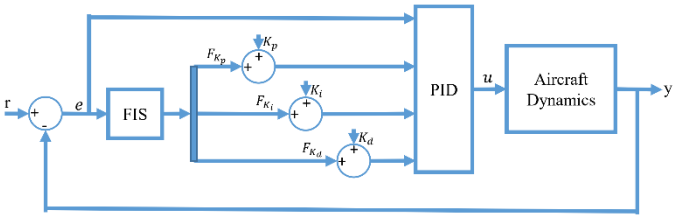

Figure 2: FIS tuned PID control structure

The FIS antecedent parameters are depicted in Figure 3 for both of error and error derivative. There are three MFs for every input.

The FIS is chosen as Sugeno FIS. Constant consequent MFs are used, and the parameters are assigned as depicted in Table 2. The rule tables are shown in Table 3.

Determining the rule table is very important for fuzzy logic studies. The rule table is especially based on error. The proportional, integral and derivative controller coefficient values are changed by considering the effects of every controller parameter (P, I, D).

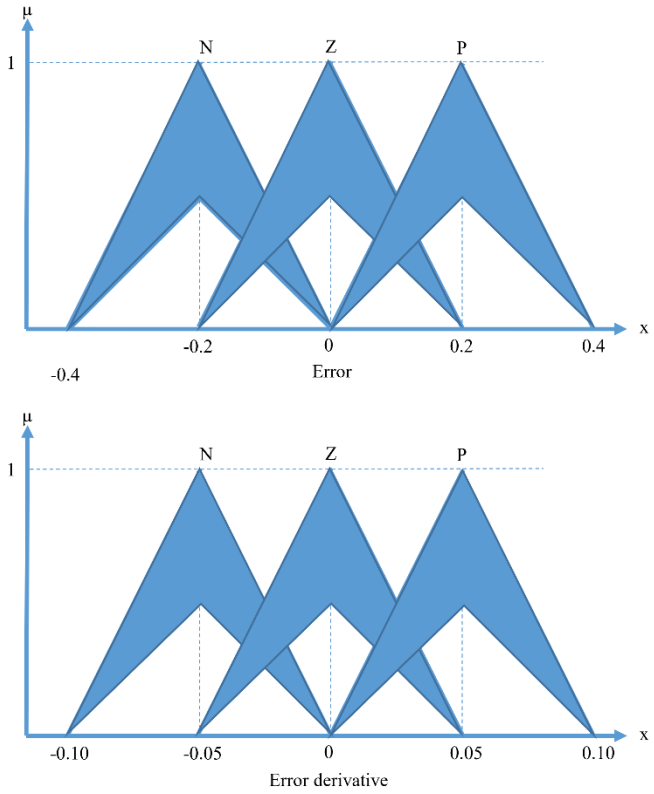

Figure 3: The input MFs (e, de)

Table 2: Membership functions of K_p, K_i and K_d.

	L	S	U
K_p	0	20	100
K_i	0.01	1	10
K_d	-5	-1	1

Table 3: Rule tables for two inputs and three outputs.

	e			
de	K_p K_i K_d	N	Z	P
N		U U U	S S S	U U U
Z		U U U	L L L	U U U
P		U U U	S S S	U U U

IV. RESULTS

The simulation results for PID and M-KMA tuned PID controllers are compared in Figure 4. The results show that the M-KMA has faster reaction than PID controller and has less overshoot. A sinusoidal wind and white noise implemented to

the system to see system results. The disturbance signal is depicted in Figure 5. The responses of the controllers are shown in Figure 6.

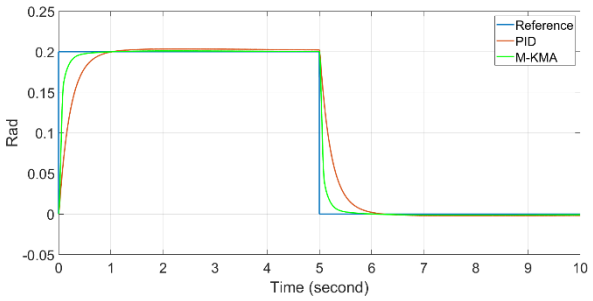

Figure 4: Comparison of PID and IT2 FIS tuned PID controllers

It is seen from the figures that the M-KMA tuned PID controllers has less settling time and overshoot for both situations with and without disturbances. The performances characteristics for both controllers are given in Table 4 quantitively.

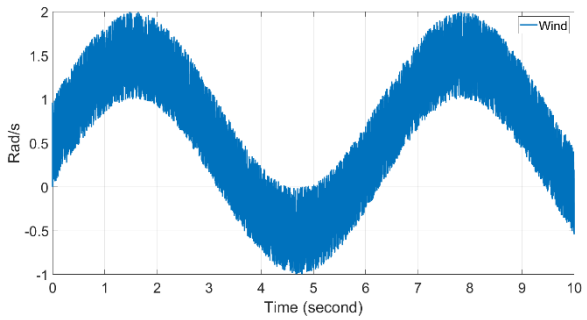

Figure 5: Wind speed with sinusoidal white noise

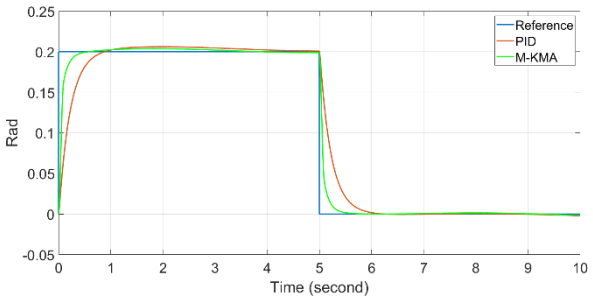

Figure 6: Comparison of PID and IT2 FIS tuned PID controllers under disturbances

Table 4: Performance characteristics of aircraft pitch control.

Parameters	No disturbance		Disturbance	
	PID	M-KMA tuned PID	PID	M-KMA tuned PID
RMSE	0.0307	0.0186	0.0305	0.0185
Settling Time (T_s) (second)	0.802	0.395	0.736	0.345
Percent Overshoot	%1.7	%0.47	%3.07	%1.19
Steady-state error (e_{ss})	$1.65x10^{-3}$	$0.89x10^{-3}$	$2x10^{-3}$	$1.4x10^{-3}$

The results show that M-KMA affects the system positively. The RMSE, settling time, percent overshoot and steady state error values becomes less compared to PID controller. Besides, the fuzzy logic controller is more robust to disturbances.

V. CONCLUSION

An aircraft pitch control structure is modelled and controlled by PID and M-KMA based IT2 FIS tuned PID controllers. This is the first control study for M-KMA in open literature. The results obtained that M-KMA based FIS is superior compared to PID. The fuzzy inference system tunes the PID coefficients with respect to error and error derivative. This tuning mechanism increase the performance of the controllers. The results indicate that both controllers handle on disturbances. However, the fuzzy inference system is better at handling disturbances. In future studies, the M-KMA based controller will be tested with ANFIS for real systems.

REFERENCES

[1] L. A. Zadeh, "Fuzzy sets," *Information control*, vol. 8, no. 3, pp. 338-353, 1965.

[2] R. E. Precup and H. Hellendoorn, "A survey on industrial applications of fuzzy control," *Computers in industry*, vol. 62, no. 3, pp. 213-226, 2011.

[3] J. S. Jang, "ANFIS: adaptive-network-based fuzzy inference system," *IEEE transactions on systems, man, cybernetics*, vol. 23, no. 3, pp. 665-685, 1993.

[4] J. W. Hines, *Fuzzy and neural approaches in engineering: Matlab Supplement*. New York, NY: John Wiley and Sons, 1997.

[5] M. Öztürk and İ. Özkol, "Comparison of self-tuned Neuro-Fuzzy controllers on 2 DOF helicopter: an application," *SN Applied Sciences*, vol. 3, no. 1, pp. 1-14, 2021.

[6] H. A. Hagras, "A hierarchical type-2 fuzzy logic control architecture for autonomous mobile robots," *IEEE Transactions on Fuzzy systems*, vol. 12, no. 4, pp. 524-539, 2004.

[7] L. A. Zadeh, "The concept of a linguistic variable and its application to approximate reasoning—I," *Information sciences*, vol. 8, no. 3, pp. 199-249, 1975.

[8] M. Öztürk, "A modified anfis system for aerial vehicles control," Graduate School, 2021.

[9] N. N. Karnik and J. M. Mendel, "Centroid of a type-2 fuzzy set," *Information Sciences*, vol. 132, no. 1-4, pp. 195-220, 2001.

[10] D. Wu and J. M. Mendel, "Enhanced karnik--mendel algorithms," *IEEE transactions on fuzzy systems*, vol. 17, no. 4, pp. 923-934, 2008.

[11] K. Duran, H. Bernal, and M. Melgarejo, "Improved iterative algorithm for computing the generalized centroid of an interval type-2 fuzzy set," in *NAFIPS 2008-2008 Annual Meeting of the North American Fuzzy Information Processing Society*, 2008, pp. 1-5: IEEE.

[12] D. Wu and M. Nie, "Comparison and practical implementation of type-reduction algorithms for type-2 fuzzy sets and systems," in *2011 IEEE International Conference on Fuzzy Systems (FUZZ-IEEE 2011)*, 2011, pp. 2131-2138: IEEE.

[13] C. Chen, R. John, J. Twycross, and J. M. Garibaldi, "A direct approach for determining the switch points in the Karnik–Mendel algorithm," *IEEE Transactions on Fuzzy Systems*, vol. 26, no. 2, pp. 1079-1085, 2017.

[14] C. Chen, R. John, J. Twycross, and J. M. Garibaldi, "An extended ANFIS architecture and its learning properties for type-1 and interval type-2 models," in *2016 IEEE International Conference on Fuzzy Systems (FUZZ-IEEE)*, 2016, pp. 602-609: IEEE.

[15] C. Chen, R. John, J. Twycross, and J. M. Garibaldi, "Type-1 and interval type-2 ANFIS: a comparison," in *2017 IEEE International Conference on Fuzzy Systems (FUZZ-IEEE)*, 2017, pp. 1-6: IEEE.

[16] M. Öztürk and İ. Özkol, "Comparison of modified Karnik-Mendel algorithm-based interval type-2 ANFIS and type-1 ANFIS," *Aircraft Engineering Aerospace Technology*, 2021.
[17] W. Z. Qiao and M. Mizumoto, "PID type fuzzy controller and parameters adaptive method," *Fuzzy sets systems*, vol. 78, no. 1, pp. 23-35, 1996.
[18] O. Karasakal, E. Yeşil, M. Güzelkaya, and İ. Eksin, "Implementation of a new self-tuning fuzzy PID controller on PLC," *Turkish Journal of Electrical Engineering Computer Sciences*, vol. 13, no. 2, pp. 277-286, 2005.
[19] M. Arrofiq and N. Saad, "Control of induction motor drives using modified-fuzzy logic methods," in *2010 IEEE International Conference on Systems, Man and Cybernetics*, 2010, pp. 612-619: IEEE.
[20] T. Wang, H. Wang, H. Hu, X. Lu, and S. J. S. A. S. Zhao, "An adaptive fuzzy PID controller for speed control of brushless direct current motor," vol. 4, no. 3, pp. 1-16, 2022.
[21] M. Güzelkaya, I. Eksin, and E. J. E. a. o. a. i. Yeşil, "Self-tuning of PID-type fuzzy logic controller coefficients via relative rate observer," vol. 16, no. 3, pp. 227-236, 2003.
[22] A. Adel and M. A. S. J. A. S. E. J. x. El-samahy, xxx–xxx, "Brushless DC motor tracking control using self-tuning fuzzy PID control and model reference adaptative control," 2016.
[23] A. Vick and K. Cohen, "Longitudinal stability augmentation using a fuzzy logic based PID controller," in *NAFIPS 2009-2009 Annual Meeting of the North American Fuzzy Information Processing Society*, 2009, pp. 1-6: IEEE.
[24] R. C. Nelson, *Flight stability and automatic control*. New York: WCB/McGraw Hill, 1998.

Effects of Voltage Sags on Variable Frequency Drive in Industrial Facilities

H.Y. USTUNEL[1] and O. TIMUR[2]

[1] Cukurova University, Adana/Turkey, halilyasarustunel@gmail.com
[2]Cukurova University, Adana/Turkey, otımur@cu.edu.tr

Abstract **- Thanks to the rapid development in technology, there is a remarkable increment in the amount of energy consumed all over the world. Especially in industrial facilities, the demand for energy has been developing day by day. With the increasing of energy consumption in the industry, some concepts such as efficient use of existing energy, energy saving and power quality gain importance. Power quality, which can be defined as the ability of power systems to transmit and distribute electricity to end users within predetermined reasonable limits, is of great importance in industrial facilities with continuous production. The fact that electrical energy goes beyond the determined limits will cause great problems for energy consumers. Today, many industrial establishments such as pharmaceutical, chemistry, paper, textile and semiconductor industries work 24 hours nonstop. Production stages of these systems form of extremely important and interrelated process stages. The corruption in power quality will affect the whole production. Devices, like variable frequency drives (VFDs), advanced microprocessors, programmable logic controllers (PLCs), relays, contactors and etc., used in all industrial sectors are easily affected by the variations in electrical power. In this study, the effect of "voltage sags" on the variable frequency drives are evaluated by measurements carried out. The obtained results have been evaluated by means of the MATLAB/SIMULINK program. When the simulation results were examined, it was determined that the DC bus voltage was kept within acceptable limits thanks to the battery-based solution that is installed and also, system connected to the variable frequency drive was not affected by voltage sag events.**

Keywords **- Power Quality (PQ), Voltage Sag, Variable Frequency Drive (VFD)**

I. INTRODUCTION

Variable frequency drives have a wide usage area in industrial facilities with their features such as high energy efficiency, energy saving capability and advanced process control. Despite these positive features, variable frequency drives are extremely vulnerable to events such as voltage sags, swells and other power quality problems where occur in the electrical power grid. Since variable frequency drives are used in very important and various processes in the industry, the effect of power quality problems on these devices is one of the most important reasons for downtime. The downtimes will occur in the facilities produce continuously could cause serious economic losses. In addition, since there is an extremely close relationship between the production stages, the downtime in one of these stages can affect the whole process. According to a report published in the USA, the annual total cost of these events is between 20-100 million $. [1]

II. EFFECTS OF PQ PROBLEMS TO THE INDUSTRIAL FACILITIES

Impacts of power quality problems are able to indicate their negative ways in many ways of industrial operations. These are loss of production, production interruption, loss of income, wasted energy, decreased equipment life, reduction in competitiveness and increased cost of labor. In the following, brief explanations are given that define these effects.

- **Loss of Production:** These are the losses that is caused by power quality problems that are not produced and naturally can not be sold when production is interrupted.
- **Production Interruption:** There are many closely related processes in continuous production systems. If any of these is affected by power quality problems, it will adversely affect the next process stage.
- **Loss of Income:** Power quality problem will directly affect the sales and cause disruptions in production plans.Naturally, income of the industrial facilities will decrease.
- **Wasted Energy:** Power quality problem where occur in the production process will cause serious energy wastage in the time that will pass until the entire process is restarted and the final product meets certain quality parameters. In fact, the energy in the time until the desired quality product is produced will be wasted.
- **Decreased Equipment Life:** Voltage sags-swells and short-term transients with high energy may cause high currents in electrical circuits. This situation can have serious adverse effects especially on electronic cards, controller unit and cause malfunctions.
- **Reduction in Competitiveness:** Encountered power quality problems may cause the poor quality specifications and this final products decrease the customer satisfaction.

- **Increased Cost of Labor:** Since it will take a certain time to eliminate the quality changes in the process conditions and to reproduce the desired quality product, extra personnel may be needed. This will result an increase in labor costs as it will result in overtime work. [2]-[3]

III. STRUCTURE OF VARIABLE FREQUENCY DRIVE

According to the latest researches, 70% of the electricity consumption of the industrial sector in the world is due to the consumption of electric motors.[4] Electric motors are served in a various implementation in the industrial facilities with different application and load characteristic such as fan, pumps, winders etc.

Different speed needs arise in different applications where electric motors are used. The speed of electric motors is proportional to the supply voltage frequency and also there is inverse relation to the number of poles. There are only two ways to change the speed of motors. These are; amendment the frequency of the voltage applied to the motor or changing the number of poles of the stator windings, respectively. Because it is practically not possible to change the number of poles of windings of motor, the speed of a motor is changed by using the relationship between the frequency of the supplied voltage and the supply voltage. Devices that is designed to meet the different speed need of motors are named as variable frequency drives. VFD's basically consist of four main units. These are AC/DC rectifier unit, DC bus and filter unit, DC/AC inverter unit, respectively. The following basic circuit diagram of the variable frequency drives and brief information about the components are given in the below.

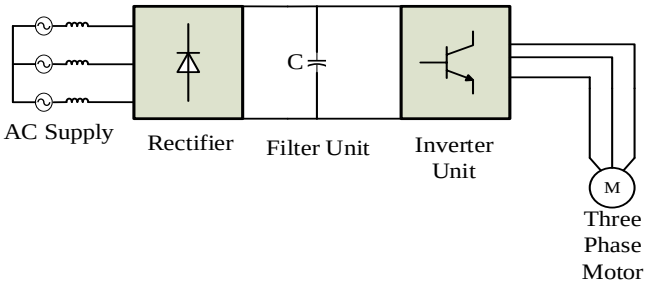

Figure 1: Basic Structure of VSD

Rectifier Unit: AC voltage is converted to the DC voltage and comprises of diodes or IGBT's.

DC Bus and Filter Unit: It eliminates ripples in DC voltage that occur as a result of AC-DC conversion in the rectifier unit and provides the energy to the inverter by means of capacitor it contains.

Inverter Unit: It is the part where the speed control of the motor is provided by converting the filtered DC voltage to AC voltage of adjustable magnitude and frequency. [5]- [6]

IV. POWER LINE DISTURBANCES

The main power quality problems that may cause disruption in the operation of adjustable speed drives used in continuous processes are given below.

Surges or Transients: can be defined as a short-term but high-energy electrical pulse that is induced on an electrical circuit or equipment. Short circuits, Lightning, bad weather conditions and loose connections are the primary reasons of this event.

Interruptions: It can be defined as an event that occurs when the supply voltage or load current drops below 0.1 pu for a period not exceeding one minute. Power system faults, equipment failures and control malfunctions are the main reasons of the interruptions.

Voltage Sags: A sag can be defined as a decrease in rms voltage between 0.1 pu and 0.9 pu for periods from 0.5 cycles to 1 minute. Some reasons of the voltage sags can be listed as weather conditions, switching of large loads and, commissioning of large asynchronous motors and power line failures, respectively. [7]

Although there are some other reasons why variable frequency drives are disabled, the most important thing to consider is undoubtedly the voltage sag events that occur in the electrical power grid. In the IEEE 1346 standard, the operations limits of the adjustable speed drives against the changes in the supply voltage are specified. According to the IEEE 1346 standards, variable frequency drives can operate up to a voltage sag of 15%. Means that, in 400 VAC system variable frequency drive can operate until 340 VAC.

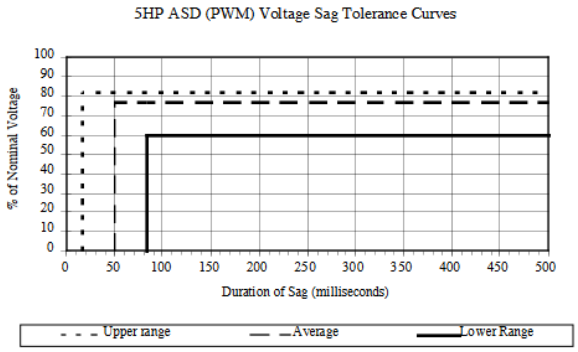

Figure 2: Voltage tolerance of VFD (IEEE 1346 standard)

As can be seen the above figure, out of the operation limits, variable frequency drive will fail. Voltage sag events occur in the AC mains supply of the drive will cause the voltage reduction in the DC bus of the VFD. If the DC bus voltage goes out of the predefined limits, inverter is not feeded and the speed of motor which the drive is connected will gradually decrease and related process may experience downtime. [8]

In 400 VAC, the DC bus voltage and the its lowest value at which the device can operate can be calculated using the formulas below.

$V_{DC} = 1.35 * V_{LL} = 540V$ (1) Where V_{LL}=400V

Adjustable speed drives trips when the value of DC bus is equal to 0.9 of its nominal value. In this case, the trip value of the DC bus voltage will be $V_{DC,trip}$ = 486 V.

The voltage of DC bus must remain within the specified operation limits, in order to maintain the proper variable

frequency drive operation that is used in extremely important process. To do this, there are various methods developed. Namely, these methods are divided into three subcategories, drive, hardware and energy storage based solutions. In this study, battery-based DC bus supply method, which is one of the energy storage-based solutions, will be evaluated with simulation results. [6]- [10-13]

V.BATTERY BASED SOLUTION

Besides acting as a filter, the DC bus section is the main energy source of the inverter unit thanks to the capacitors it contains. Voltage sag events where occur in the electrical power grid affects the DC bus voltage and causes a decrement on power supplied to the inverter unit, and as a result, the process in which the drive contains is affected by this situation.

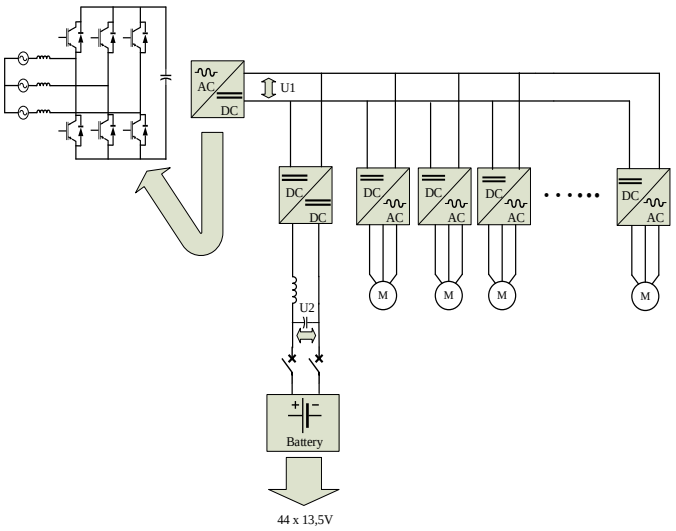

Figure 3: Modified Circuit of ASD by Adding a Battery Unit

To overcome this problem, battery-based solution is evaluated. The basic philosophy of the system is that when there is a voltage sag in the system supply voltage, this event also affects the DC bus voltage. When there is a voltage sag in the system, missing voltage of the DC bus will be provided by the battery units, and the effect of the event on the system will be reduced.

To obtain the required DC bus voltage, the batteries must be connected in series with each other. The current to be drawn from the batteries is directly proportional to the amount of the load. The modified drive circuit is shown in figure 3. Thanks to the active rectifier unit used in this study, DC bus voltage can be adjusted between 610-615 VDC and it feeds the inverter unit. The battery unit consists of 44 batteries with a voltage of 13.5 volts connected in series. DC bus voltage is continuously measured by voltage sensors. To prevent the DC bus voltage from falling below a certain value (554) when there is a voltage sag, the battery unit is activated as a discharge and feeds the DC bus unit its value reaches the 615V. Thus, the system is not affected by this voltage sag and remains within the operating limits. When the power grid returns to normal, the battery group is deactivated and charges itself with the system voltage.

In the below figures simulation results are shown. Figure 4 and figure 5 show the system supply voltage and DC bus voltage, respectively.

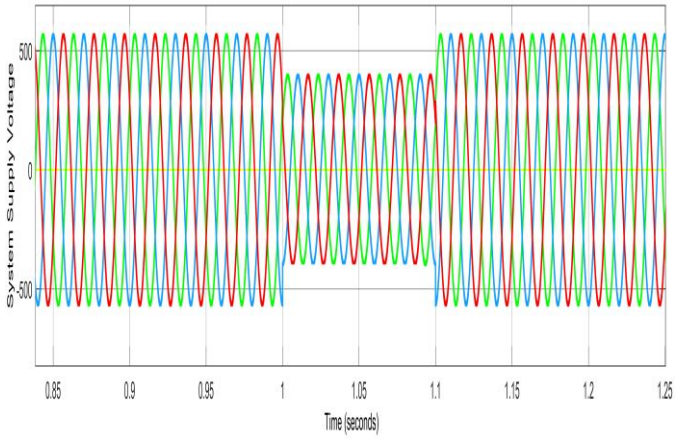

Figure 4: System Supply Voltage

In figure 4, a voltage sag between 1 and 1.1 seconds has occurred. During this period, the system supply voltage has decreased by 33%.

According to the obtained results, although the voltage sag caused the voltage drop on the DC bus for a very short time, value of DC bus voltage is within the acceptable limits. Simultaneously, battery unit sensed the voltage drop on the DC bus unit and activated to recover the DC bus voltage to the required value again.

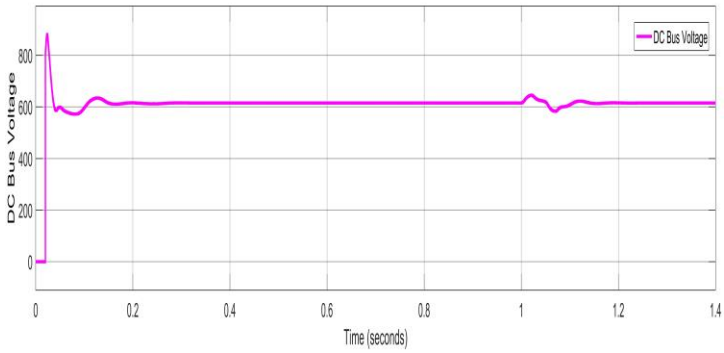

Figure 5: DC Bus Voltage

V. CONCLUSION

The concept of power quality is becoming an even more important issue in these last days, where the need for energy and its continuity are increasing. Since the majority of industrial facilities have the continues production feature, the concept of power quality has a special importance in these facilities. These facilities have production stages that are formed by the combination of production steps that are nested with each other. Variable frequency drives are the one of the most important components of these production steps and vulnerable to the power quality problems. A power quality problem in these critical processes can cause serious economic and technical problems. In this study, battery-based solutions carried out to increase the endurance of variable speed drives against the voltage sags, which have extremely important tasks

in critical processes, has been examined. According to the simulation results, thanks to the battery-based solution, the DC bus voltages of the adjustable speed drives remain within the acceptable limits during the voltage sag event and are not affected by the voltage sags.

REFERENCES

[1] A. von Jouanne and P. Enjeti, "ASD ride-through technology alternatives and development," Electric Power Research Institute, Palo Alto, CA, EPRI Final Rep. TR-109903, Dec. 1997.

[2] S.C.Vegunta, J.V. Milanovic '' Estimation of Cost of Downtime of Industrial Process Due to Voltage Sags '' *IEEE Trans.Power Delivery*,vol.26,no.2,April.

[3] M.I.Muhammed, N.Mariun and M.A Mohd Radzi '' The Effects of Power Quality to the Industries'' The 5th Student Conference on Research and Development –SCOReD 2007 11-12 December 2007, Malaysia

[4] D.F de Souza, F. A. M. Salotti, I.L. Sauer, H. Tatizawa, A. T. de Almeida and A. G. Kanashiro'' A Performance Evaluation of Three-Phase Induction Electric Motors between 1945 and 2020'' Energies 2022, 15, 2002. https:// doi.org/10.3390/en15062002

[5] A.Sudria, M.Teixido, S.Galceran, O. Gomis, D. Montesinos, F. Blaabjerg '' Grid Voltage Sags Effects on Frequency Converter Drives and Controlled Rectifiers''

[6] R. A. Epperly, F. L. Hoadley and R. W. Piefer'' Considerations When Applying ASD's in Continuous Processes '' *IEEE Trans on Indsutry applications* vol.33,no.2,March/April 1997

[7] IEEE Std 1159-2019''Recommended Practice for Monitoring Electric Power Quality''

[8] IEEE Std.1346-1198'' Recommended Practices for Evaluating Electric Power System Compatibility with Electronic Process Equipment''

[9] A.V. Jouanne, P. N. Enjeti and B. Banerjee'' Assessment of Ride-Through Alternatives for Adjustable-Speed Drives''*IEEE Trans on Indsutry applications* vol.35, no.4, July/August 1999

[10] F. Hoadley et al., "Motor drive/power systems interactions," in IEEE-IAS Tutorial Course. New York: IEEE Press, 1997, pp. 3-1–3-15.

[11] KR.Ramela and V.Sureshkumar '' Simulation of Ride Through Capability of Adjustable Speed Drive for Type A and Type B Voltage Sags and Well Using Buck–Boost Converter '' 2011 International Conference on Recent Advancements in Electrical, Electronics and Control Engineering.

[12] C.J. Melhorn, A.Braz ,P.Hoffman and J.Mauro '' An Evaluation of Energy Storage Techniques for Improving Ride-Through Capability for Sensitive Customers on Underground Networks '' *IEEE Trans on Industry applications* vol.33, no.4, July/August 1997

[13] M. H. J. Bollen and L D. Zhang'' Analysis of Voltage Tolerance of AC Adjustable-Speed Drives for Three-Phase Balanced and Unbalanced Sags'' *IEEE Trans on Industry applications* vol.36, no.3, May/June 2000

Violence Detection in Videos Based on Deep Learning Approaches

L.CİVCİK[1] and O. ALKAYAL[2]

[1] Konya Technical University, Konya/Turkey, lcivcik@ktun.edu.tr
[2] Konya Technical University, Konya/Turkey, ualkayyal@gmail.com

Abstract **- Violence detection in videos and live broadcasts using machine vision and artificial intelligence approaches has become a hot research area attracting the attention of many researchers worldwide. Detecting violence in videos is a challenge because videos have Spatio-temporal features that are difficult to analyze when compared to other types of data that only have spatial or temporal parts. Deep learning is a subclass of artificial intelligence that uses deep structures and hierarchical learning approaches that offer many solutions to such a challenging task. Due to their construction that contains many layers or networks between the input and output layers, deep learning approaches are very successful in pattern classification and extraction of Spatio-temporal features. This study aims to build a neural network using deep learning approaches to perform real-time violence detection in videos. Under this scope, this work suggests using MobileNets alongside ConvLSTM for violence detection in videos, making this work a pioneer in applying this combination to solve this problem. MobileNets is used to extract the spatial features from successive video frames. On the other hand, the ConvLSTM part analyzes the relations between these frames in time manners while maintaining the local spatial features. Around 2000 video clips were used to train and test the developed neural network. The proposed model achieves a test accuracy of 93.33%, exceeding the performance of the previous works.**

Keywords **- Artificial Intelligence, Deep Learning, Convolutional Neural Networks, Spatio-temporal Features, Violence**

I. INTRODUCTION

Violence is best defined by Kristine M. Jacquin where she stated that "**Violence**, an act of physical force that causes or is intended to cause harm. The damage inflicted by violence may be physical, psychological, or both." [1]. According to the National Coalition Against Domestic Violence, 1 in 4 women and 1 in 9 men will experience some form of domestic or interpersonal violence in their lifetime [2]. However, in a 2018 survey by the Bureau of Justice Statistics, only 47% of cases of domestic violence or interpersonal violence are reported to the police [3]. Empty places such as streets, subway stations, and markets where there are no people who can report violence are among the places where unreported violence is experienced. Reporting incidents of violence promptly to the relevant authorities ensures that the situation is better handled, both by aiding victims of violence and by arresting perpetrators.

Violence detection in videos is a unique scenario of the well-known human action recognition task that has become a hot research area attracting the attention of many researchers worldwide. While recognizing human actions aims to identify the actions taken by a person or a group of people, violence detection is aimed at determining whether the actions taken are of a violent nature.

Human actions are often series of events that must be analyzed collectively to form a general understanding of these actions. In other words, analyzing a human action by considering a single image (frame) rather than considering the entire sequence of images (video) that best represents the action can lead to inaccurate results. While images contain only spatial features, videos contain Spatial-temporal features that require both time-domain and space-domain analysis, making action recognition a challenging task.

Since the 1950s, a subset of Artificial Intelligence often referred to as Machine Learning, has been playing a revolutionary role in many application areas. Artificial Neural Networks (ANN) is a brain-inspired sub-field of Machine Learning that spawned Deep Learning. Supervised deep learning is one of the artificial intelligence technologies which uses deep neural networks and labeled data for classification processes [4]. The term "deep" refers to the number of processing layers between the input and the output layers. Deep neural networks have hierarchical architectures consisting of many stages of nonlinear computing units used for feature learning and pattern classification. Having deeper hidden layers has recently begun to surpass the performance of classical methods in different fields, especially in pattern recognition and classification tasks [5]. The general focus of deep neural networks is pattern learning from input data and generalizing learned patterns for use in future unseen data. In other words, learning is a process that consists of estimating model parameters so that the learned model can perform a specific task.

To include the temporal features in the process of violence detection, Mohtavipour et al. used handcrafted features extracted from the videos along with the raw frames of the videos. The researchers built a deep neural network that consists of three parallel 2-dimensional Convolutional Neural Network. The first CNN is trained using spatial stream (raw frames), the second CNN is trained using temporal stream and the third CNN is trained using spatiotemporal stream. The spatial stream is used to analyze the general environment of the video. The temporal stream is used to consider the speed

of movement for moving targets by using the optical flow image generated from multiple successive frames. In the spatiotemporal stream, the shape of actions that helps to understand the violence behavior is formed by building a differential motion energy image from multiple successive frames. The output of the 3 CNN mentioned above is then fed to a classifier to detect violent behaviors. The researchers obtained accuracies of 100% and 99,35% on Hockey and ViF dataset respectively [6].

Peixoto et al. stated that detecting violence from videos with no human supervision is not only technical, but also a conceptual problem. Accordingly, they built a deep neural network that consisted of 7 CNNs and each one of them is used to understand a different concept of violence, such as blood, bunching, fights, gunshots, etc. The outputs of these CNNs are then fed to a fusion network to generate a decision about the video. To include both the spatial and temporal features the researchers fed the CNNs with four different inputs which are the frame streams and three other streams manually extracted from the videos that describe the movements in the videos. The accuracy obtained by the researchers on MediaEval 2013 dataset was 78% [7].

Due to the importance of the temporal features in classifying the behavior of humans in videos, most researchers are using different varieties of CNNSs for the task of pattern recognition in videos. While the 2D CNNs themselves are used only to analyze spatial features, Abdali and Al-Tuma combined 2D CNN with a network called Long Short-Term Memory (LSTM) which are generally used to reconsider a part of previously trained features (successive frames in this case), which allowed the entire network to process both the spatial and temporal features. According to the researchers, this method is very beneficial when the amount of memory resources is limited. The test result of this model on the Hockey dataset was 98% with speed of 131 frames/sec [8].

Similarly, Halder and Chatterjee used Bidirectional LSTM that processes a feature map of certain frame coming from the 2D CNN with the feature maps of both the next and previous frames. This method analyzes the temporal features of the video that contain most of the information about the violence behaviors more deeply. The test results obtained by the researchers on Hockey Fights, Movies and ViolentFlow datasets were 99.27%, 100% and 98.64% respectively [9].

Sumon et al. applied transfer learning strategies and built a model that consists of a pretrained CNN model called ResNet50 and a LSTM network. The ResNet50 is a 2D CNN that consists of 50 layers pretrained with thousands of data and is used as spatial features extractor. The spatial features from 30 successive frames are then fed to the LSTM network for temporal analysis. The researchers retrained this model using a dataset they built consisting of 220 real-life videos and achieved test accuracy of 97% [10].

The LSTM-CNN models mentioned above have fully connected structure in LSTM part of the network. According to Sudhakaran and Lanz, this makes the network capable of extracting global spatiotemporal features but not local ones which reduce the performance of the model since the violence behaviors are more understandable using the local features. To overcome this, they used a model called Convolutional LSTM that consists of convolutional connections between the layers of the LSTM network. A ConvLSTM is a single network that can capture localized spatiotemporal features which enables analyzing the local motion taking place in the video. Besides that, rather than using the frames themselves as the input of the videos they used the difference between two adjacent frames. The accuracy achieved by the researchers on the Hockey dataset was 97,1 % [11].

Rather than focusing on the structure of the model itself, the work of Soliman et al. showed the importance of the datasets used to train the model and how models trained with famous datasets such as Hockey Fights, Movies and ViolentFlow have low accuracy when applied to real life situations. These datasets have similar videos that have similar environments with similar violence behavior. The researchers trained an CNN-LSTM model on these datasets and tested these models on real-life dataset that they built and the best accuracy they obtained was 71,5%. To build a more reliable model, they trained a model with a dataset they created in 2019 called Real-Life Violence Situations that consists of 2000 videos. The researchers used the VGG-16 CNN model as feature extractor and applied transfer learning by retraining the model on the dataset mentioned above. The best accuracy obtained by this model when tested on real-life videos was 88,2% [12].

The method proposed by Accattoli et al. suggested the use of 3D CNN as a spatiotemporal futures extractor and support vector machine as a binary classifier to detect violence in videos. The 3D CNNs that use 3D kernels can analyze both spatial and temporal features by processing multiple frames as a single input, where in this case the researchers suggested that 16 consecutive frames are enough for the network to detect violent behaviors. The neural network was trained and tested using Hockey Fight and Crowd Violence datasets and accuracies of 98.51% and 99.29% respectively were achieved [13].

The Real-life violence dataset were also used in [14] by Lima and Figueiredo the researchers combined an LSTM network with a CNN model and archived an accuracy of 91%.

The purpose of this work is to build a model that uses deep learning approaches for violence detection in videos. We aim to train and test our model on the dataset called Real-Life Violence Situations to make our model more reliable for real life situations.

The rest of this paper is organized as follows: In section II we discuss the dataset and how we are going to prepare it. While in section III we discuss the architecture and the component of the proposed model alongside transfer learning. Furthermore, in section IV we discuss the results obtained by the proposed model and the experimental setup of the model. Finally, In Section V we conclude this paper.

II. DATASET

In [12] the researchers stated that the networks trained with famous datasets such as Hockey Fights, Movies and ViolentFlow have low accuracy when applied to real life situations. Because of this, in 2019 they created an opensource dataset called Real-Life Violence Situations that contains 1000

videos labeled as NonViolence and 1000 videos labeled as Violence. The videos differ in length *L*, height *H* and width *W*. All videos are RGB colored which makes the general form of any video in the dataset to be *LxHxWx3*. Let's suppose having a scanning window called n and is defined as the following equation:

$$n = \frac{L}{20} \quad (1)$$

Using equation (1), all videos in the dataset are resized to a common size of 20x64x64x3 by taking a frame after every *n* frames while reading the videos, making every video in the dataset contains 20 frames and each frame has a size of 64x64 with three color channels (RGB). Figure 1 shows the pre-processing applied to the videos. 1500 videos will be used for training and 500 videos will be used for testing.

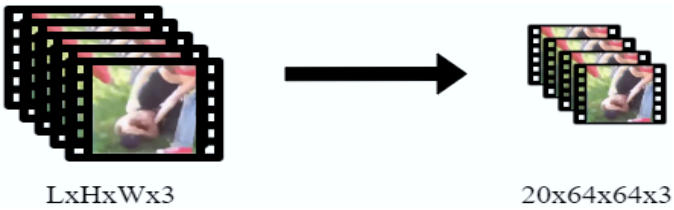

Figure 1: Data pre-processing.

III. The Proposed Model

This section explains the deep learning model suggested for violence detection in this work. The overall model is built by combining MobileNets, ConvLSTM, and the fully connected layer. Combining MobileNets with ConvLSTM is what distinguishes our proposed model for detecting violence in videos. We use MobileNets for spatial features extraction from the frames by applying transfer learning. On the other hand, we use ConvLSTM to extract Temporal features while maintaining the local spatial features. The fully connected layer receives the spatio-temporal features from the previous parts and gives a prediction regarding the input video. In the following sub sections, we explain these parts in detail.

A. MobileNets

MobileNets is CNN model developed by Howard et al. at Google company for mobile vision applications [15]. MobileNets uses depth-wise separable convolution within its structure which is very advantageous in reducing the processing power required by the network and thus making the model lighter and faster. This makes this network a good candidate to be spatial feature extractor in our model. The Idea of depth-wise separable convolution is that instead of convolving an input image with a dimension of *HxWx3* with a *KxKx3* filter, we convolve each input channel of size *HxW* with a *KxK* filter. After that a pointwise convolution is applied to the results of the depth wise separable convolution by convolving it with a filter of size *1x1x3*. These two operations lead to an output equivalent to the one obtained by the ordinary convolution but require much less processing power. MobileNets has a depth of 55 and its total number of parameters is 4.3 million. This network has achieved a Top-5 accuracy of 89.5% on the ImageNet dataset.

B. ConvLSTM

LSTM is a special type of Recurrent Neural Networks developed by Sepp Hochreiter and Jürgen Schmidhuber in 1997 [16]. Recurrent Neural Networks are powerful in learning temporal features such as the ones in texts, voice recordings, and videos. The main issues faced in standard Recurrent Neural Networks were the vanished and exploded gradients when applying backpropagation through time (BPTT) making the network unable to learn the parameters in the first layers of the network. This causes the network to only remember new inputs but not the old ones. By other words the network becomes a short-term memory. To solve this, Hochreiter and Schmidhuber introduced LSTM cells that contain a cell state and various types of gates. The cell state acts as a bridge that carries the information from previous time steps (LSTM cells) all through the last time step. The current input vector X_t and the previous hidden state vector h_{t-1} are used at the Forget Gate to decide whether the previous cell state C_{t-1} should be kept or not. Adding the output of the forget gate to the output of the input gate will result in a new cell state C_t. In the output gate, the new cell state C_t, the current input X_t, and the previous hidden h_{t-1} state are used to generate the new hidden state h_t. Both the new cell state C_t and the new hidden state will be passed to the next LSTM cell. The LSTM cells mentioned above are only capable of extracting temporal features. To include both temporal and spatial features in a single model, Shi et al. [17] used convolutional connections to connect the current input X_t, the previous cell state C_{t-1} and the previous hidden state h_{t-1} to the cell. Figure 2 shows an LSTM cell and Figure 3 shows a ConvLSTM cell [18].

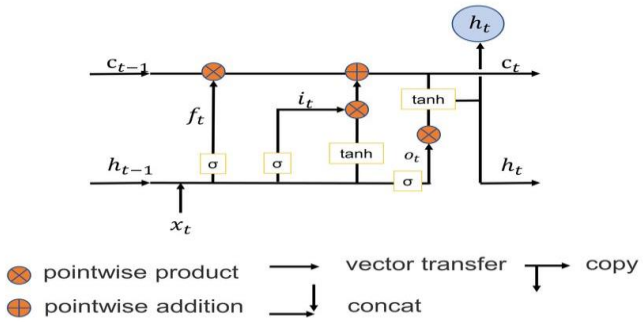

Figure 2: LSTM cell.

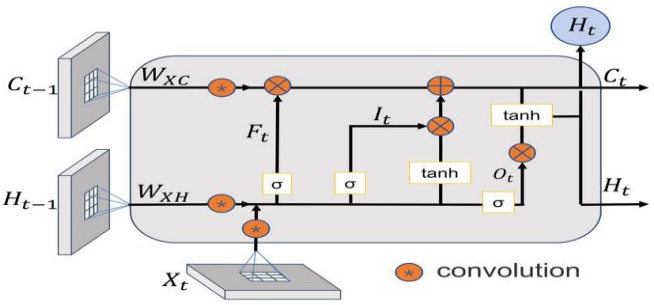

Figure 3: ConvLSTM cell.

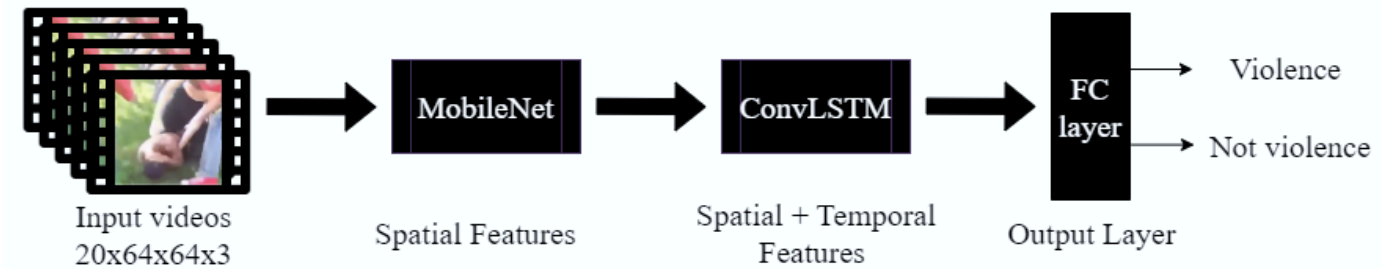

Figure 4: The overall architecture of the proposed model

C. Fully Connected Layer

This part receives the spatio-temporal features from the previous parts of the network after being flattened by a flattening layer. In this part, all neurons between the input and output layers are interconnected. In the output layer of this part, an activation function called Softmax is used. The Softmax activation function maps an n-dimensional vector *X* to an n-dimensional vector *Y* that has the property *sum* $(Y_i) = 1$ for all *i*'s. The Softmax activation function is defined as in equation (2) [19].

$$Y_i = \frac{e^{X_i}}{\sum_{n=1}^{n} e^{X_j}} \quad (2)$$

The sum of the outputs of the Softmax layer will be 1. Each of these outputs represents the probability of each class. After that, the value of the output with the greatest probability will be 1, and the value of the other classes will be 0. This process is called "Hot Coding". In our case we have two outputs regarding the violent nature of the video. If the video contains violence the class violence output will be 1 and the class NonViolence output will be 0 and vice versa.

D. Transfer Learning

A good example to understand transfer learning is to consider learning how to drive a motorcycle given that a person already knows how to drive a bike. In this case the person does not need to learn motorcycle from scratch. Instead, the person learns how to drive a motorcycle based on his knowledge about how to drive a bike while learning some new features or tasks that are specifically related to driving a motorcycle. Similarly in deep learning, instead of building a model from scratch and training it with initial random parameters, we can make use of some models that are trained with a huge amount of data and obtained an outstanding performance. The parameters of these trained models can be transferred to other networks for testing or retraining a similar new model. There are many reasons for using transfer learning. For instance, training big models on big data requires huge computation power. Additionally, it can take several weeks to train big models. Also, transfer learning can speed up model convergence as well as it improves the model's generalization [20].

The way we apply transfer learning in this work is by importing the MobileNets model and removing its top-level layers i.e., the fully connected part and retaining the spatial features extraction part. After that it will be connected to the next part of the network which is ConvLSTM part. The weights of the MobileNets will be frozen. Which means that the training process will only include the parameters within the ConvLSTM and the fully connected parts. In this case the MobileNets is used as a feature extractor. Figure 4 shows the overall architecture of the proposed model.

IV. Experimental Setup and Results

In this section we will discuss the experimental setup of the proposed model alongside the obtained results. We built the model with the help of the famous TensorFlow library [21]. We started by loading the MobileNets model, then we wrapped this model using a time distributed layer. This is necessary since the MobileNets model only receives single images and we want it to receive multi frames at a time. Figure 5 shows the setup of the proposed model built using TensorFlow library.

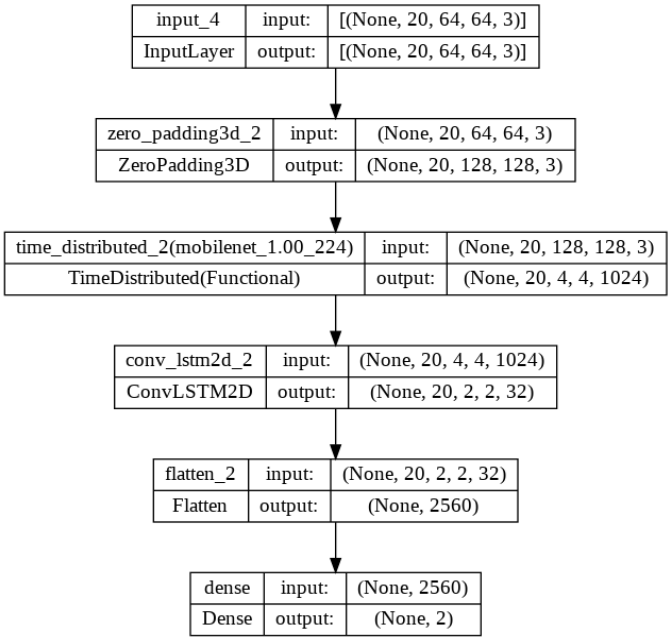

Figure 5: The proposed model built using TensorFlow library.

Hardware limitations are among the limitations faced during this work. The PC used to train the proposed model has 16 GB of RAM which makes it difficult to read the entire dataset at once and keep it in the RAM for the training. To overcome this, all videos were resized to a smaller size of *20x64x64x3* as mentioned earlier in section II. Doing this resizing caused the

outputs of MobileNets to shrink and thus the overall accuracy of the model to decrease. To overcome this, we applied zero padding to the input frames and resized them to the size of *128x128x3*.

As mentioned earlier the model is trained using 1500 videos and during the training process, we used categorical cross entropy as loss function and Adam as optimizer. We used a batch size equal to 20. To automatically stop the training when the optimum values are reached, we defined an early stopping criterion in a way such that the training stops if no noticeable change in the accuracy for 10 epochs. Although the total number of epochs were defined as 20, the training stopped after 17 epochs. The proposed model achieved a test accuracy of 93,33% and of course a training accuracy of 100%. Figure 6 shows the accuracy curves of the proposed model.

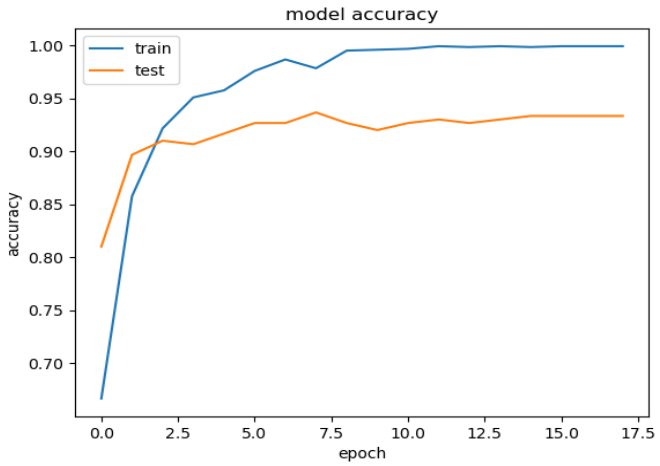

Figure 6: The accuracy of the model

As seen in Figure 6, the training process was stable in general. The stability of the training process depends on the batch size. Small batch size causes the training process to fluctuate and for the model to be unstable. Figure 7 shows the loss curves of the model.

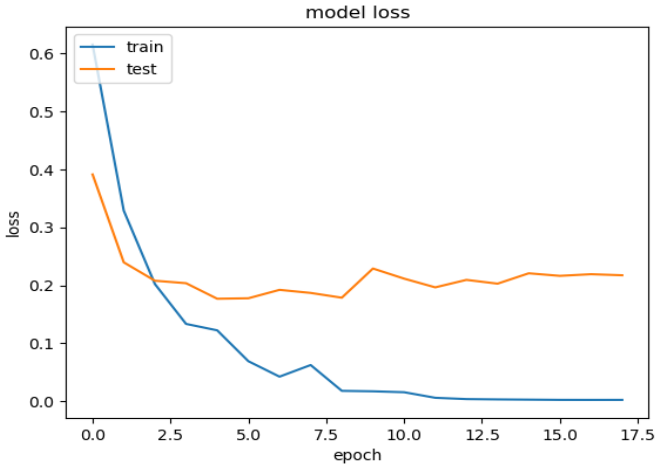

Figure 7: The loss of the model

As seen in Figure 7, the loss curves show stability like the accuracy curves. The training loss after 17 epochs is very close to zero and the test loss is approximately 0.25.

The speed of the proposed model is 400 frame/sec which makes it excellent for real-time applications that have a frame rate of 30 frame/sec. Table 1 shows the performance of the model proposed in this work compared to the previous models' performances on the Real-life Violence Situation dataset.

Table 1: Performance comparison between this work and previous works.

Model	Obtained Accuracy
Vgg16+LSTM [12]	88.2%
MobileNets+LSTM [14]	91%
This work	93.3%

As seen in Table 1, the performance of the model proposed in this work exceeds the performance of the previous state-of-the-art model on the Real-life Violence Situations dataset.

V. Conclusion

In conclusion, the outstanding results obtained in this work show the reliability and the stability of the use of deep learning for the task of violence detection in videos.

In this work, a pioneer model for violence detection in videos using MobileNets and ConvLSTM has been introduced. The proposed model archives an accuracy of 93.33% on the Real-life Violence Situations dataset exceeding the performance of the previous works.

For the future work, we plan to improve the performance of the model by increasing the RAM size to overcome the hardware limitation mentioned in section IV.

References

[1] J. M. Kristine. (2017, January). [Online]. Available: https://www.britannica.com/topic/violence.

[2] Anonymous. (2020). National Coalition Against Domestic Violence. *NATIONAL STATISTICS*. [Online]. Available: https://ncadv.org/STATISTICS

[3] M. Rennison and S. Welchans, "Intimate Partner Violence," *Bureau of Justice Statistics*, 2005.

[4] M. Najafabadi, F. Villanustre, T. Khoshgoftaar, R. Wald, and E. Muharemagic, "Deep learning applications and challenges in big data analytics," *Journal of Big Data*, vol. 2, no. 1, 2015.

[5] M. Dixit, A. Tiwari, H. Pathak, and R. Astya, "An overview of deep learning architectures, libraries and its applications areas," in *ICACCCN-2018*, Greater Noida, 2018.

[6] S. Mohtavipour, M. Saeidi, and A. Arabsorkhi , "A multi-stream CNN for deep violence detection in video sequences using handcrafted features," *The Visual Computer*, 2021.

[7] B. Peixoto, S. Avila, P. Bestagini, and Z. R. Dias, "Breaking down violence: A deep-learning strategy to model and classify violence in videos," in *ARES-2018*, 2018.

[8] A. Abdali and R. Al-Tuma, "Robust Real-Time Violence Detection in Video Using CNN And LSTM," in *2nd Scientific Conference of Computer Sciences*, Iraq, 2019.

[9] R. Halder and R. Chatterjee, "CNN-BiLSTM Model for Violence Detection in Smart Surveillance," *SN Computer Science*, vol. 1, no. 4, 2020.

[10] S. Sumon, R. Goni, N. Hashem, T. Shahria, and R. R, "Violence Detection by Pretrained Modules with Different Deep Learning Approaches," *Vietnam Journal of Computer Science*, vol. 7, no. 1, pp. 19-40, 2020.

[11] S. Sudhakaran and O. Lanz, "Learning to detect violent videos using convolutional long short-term memory," in *14th IEEE International Conference on Advanced Video and Signal Based Surveillance*, 2017.

[12] M. Soliman, M. Kamal, M. El-Massih, Y. Mostafa, and B. K. Chawky, "Violence Recognition from Videos using Deep Learning Techniques," in *9th International Conference on Intelligent Computing and Information Systems*, 2019.
[13] S. Accattoli, P. Sernani, N. Falcionelli, and D. Mekuria, "Violence Detection in Videos by Combining 3D Convolutional Neural Networks and Support Vector Machines," *Applied Artificial Intelligence*, vol. 34, no. 4, pp. 239-344, 2020.
[14] J. Lima and C. Figueiredo, "A Temporal Fusion Approach for Video Classification with Convolutional and LSTM Neural NetworksApplied to Violence Detection," *INTELIGENCIA ARTIFICIAL*, vol. 24, no. 67, pp. 40-50, 2021
[15] A. G. Howard, M. Zhu, B. Chen, D. Kalenichenko, W. Wang, T. Weyand, M. Andreetto, and H. Adam, "MobileNets: Efficient Convolutional Neural Networks for Mobile Vision," *arXiv:1704.04861*, 2017.
[16] S. Hochreiter and J. Schmidhuber, "LONG SHORT-TERM MEMORY," *Neural Computation*, vol. 9, no. 8, 1997.
[17] X. Shi, Z. Chen, H. Wang, D. Yeu, W. Wong, and W. Woo, "Convolutional LSTM Network: A Machine Learning Approach for Precipitation Nowcasting," *arXiv:1506.04214*, 2015
[18] C. Shi, Z. Zhang, W. Zhang, and Q. Xu, "Learning Multiscale Temporal–Spatial–Spectral Features via a Multipath Convolutional LSTM Neural Network for Change Detection With Hyperspectral Images," *IEEE Transactions on Geoscience and Remote Sensing*, vol. 60, pp. 1-16, 2022.
[19] F. Emmert-Streib, Z. Yang, H. Feng, S. Tripathi, and M. Dehmer, "An Introductory Review of Deep Learning for Prediction Models With Big Data," *Frontiers in Artificial Intelligence*, vol. 3, no. 4, 2020.
[20] Alom M. Z., Taha T. M., Yakop C., Westberg S., Sidike P., Nasrin M. S., Hasan M., Van Essen B. C., Awwal A. A. S., and Asari V. K., "A State-of-the-Art Survey on Deep Learning Theory and Architectures," *Electronics*, vol. 8, no. 3, 2019.
[21] M. Abadi et al. (2015). TensorFlow: Large-Scale Machine Learning on Heterogeneous Systems. [Online]. Available: https://www.tensorflow.org/

Ensuring Bush Deburring Operation Process Traceability and Automatic Process Control

M.OZEL[1], S. BAYSAL[2], M.ACARER[3]

[1] AYD Automotive Industry, Konya/Turkey, ozel.muhammed@aydtr.com
[2] AYD Automotive Industry, Konya/Turkey, baysal.selimsefa@aydtr.com
[3] Selcuk University, Konya/Turkey, macarer@selcuk.edu.tr

Abstract **- Bushings are used at the connection points of the suspension parts to transfer the movement, to prevent sudden movements and vibrations. The runner channels in the bushings ensure that the rubber material coming from the injection machine is transferred to the mold core surface. In the current system, the bushing cleaning process and the accuracy of the cleaned product are recorded with the operator's declaration. In this system, which is at the operator's discretion, the operator can keep his or her performance higher than it should be and can count the uncleaned bush as cleaned. This results in incorrect operator productivity or uncleaned product in the logs. In this study, which was carried out in order to eliminate similar errors; The operator places the products on the conveyor belt after cleaning. The bushing, which moves on the band, is first met by the areal laser sensor. The piece, which continues to move on the band, provides the inspection of the cleaning process of the runner points by using the image processing technique with the camera placed in the last process. If faulty cleaning is detected, the counted product is canceled and sent to the rejection conveyor. With this study, it is aimed to monitor personnel tracking and cleaning control more efficiently.**

Keywords **– Bushing, Image Processing, Runner channels, Cleaning**

I. INTRODUCTION

Traceability in production is the process of accessing and recording all information during the packaging, storage, transportation and final sale of a product starting from production, so that it can be tracked retrospectively. In the production line, on the other hand, it is necessary to provide a quality production by eliminating the problems that may be encountered after the production by controlling the instant product cleaning errors, and also to obtain accurate results by taking the margin of error from the operator and offering a more precise solution. The control of the workmanship in the deburring line of the Rubber-Bushing section is recorded with the personnel statement. This situation brings along major errors in the workmanship factor. Since there is no signal system to follow this operation, which is carried out entirely by hand, the Andon system cannot be installed. In this system, which is at the operator's discretion, the operator can keep his or her performance higher than it should be and can consider the uncleaned bush to be cleaned. This causes both the prolongation of the process by detecting the uncleaned bushings at the operator's initiative at the last control, and the wrong operator efficiency in the records. Cleaning line output will be controlled by using bush cleaning control image processing technique, operation information and all information required for traceability will be recorded. With this study, it is aimed to monitor and control personnel tracking and cleaning control more efficiently. The cleaned and uncleaned images of the bushes are given in Figure 1.

Figure 1: Uncleaned and cleaned sample bushing.

This project aims to follow the packaging, storage and production processes of a product step by step from production, to access and record all information during all operations, so that retrospective follow-up can be made, as well as automatic control of burr cleaning control after the operation with image processing technique and it is about developing an operation process for it.

II. MATERIAL AND METHOD

In this study, the accuracy of the cleaning control of the bushes after the bushing deburring operation was investigated. The study generally consists of 5 work packages. 1st work package is divided into literature review, 2nd work package is Mechanical design, 3rd work package is assembly, 4th work package is Programming and 5th work package is data pool creation. Mechanical design was carried out through Solidworks program.

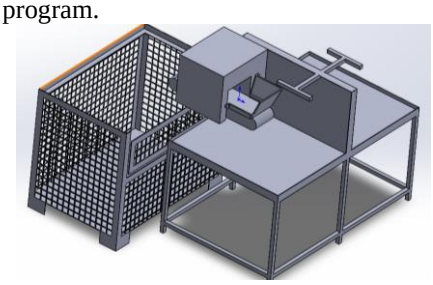

Figure 2: Mechanic design.

There are 2 most important points to consider for design. The design is basically seen in Figure 2. The first of these is to create a conveyor belt suitable for the work efficiency and

working conditions of the operator's work area, and the second is camera positioning and sensor positioning mechanisms that will detect appropriate cleaning for each product that will enter the deburring process.

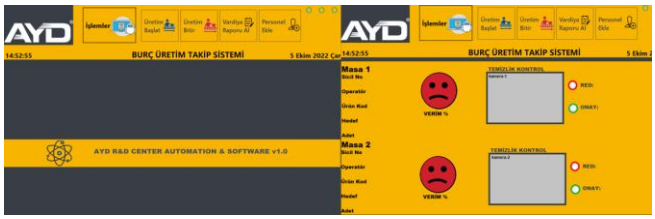

Figure 3: Interface design.

The programming is programmed with the Python programming language and the user interface is created with C#. The interface made with C# is given in Figure 3. In the study, operator cleanliness and data in the existing system were examined. Deburring end-of-process data of different operators were examined and compared. Images of each examined data will be collected from different angles before and after the process. Incorrect cleaning and correct cleaning data are stored in the collected images. In the evaluation made according to the stored data, the edge detection operator, which gives the most accurate and fast results from the image processing algorithms and edge detection operators, and an industrial type programmable camera were adapted to the program to perform the deburring process control. A spatial laser sensor was used for counting processes. Programmable logical controller is preferred for conveyor belt control and automation control.

Edge detection techniques are divided into 2 main parts as Gradient and Laplacian-based. It is a gradient finding approach. This method usually works well for step edges. Directional derivatives within the gradient are sensitive to noise due to the nature of the derivative. Operators based on the second derivative, such as Laplacian, may have trouble finding edges, even though they define object boundaries well. This is because the zero crossings of the second derivative correspond to the largest or smallest of the first derivative. In other words, the zero crossings in the second derivative may not correspond to the edges in the image.

Canny edge detection algorithm; It is a stepwise algorithm developed by John F. Canny to find sharply defined edges in an image. It is an algorithm that is used very effectively in finding edges. In order to reduce the noise of the image, it is reduced by convolution with the Gaussian kernel. Apart from the Gaussian filter, Mean or Median filters can also be used. The gradient operator is applied. In this way, the Gradient size and direction of the image are calculated.

Table 1: Different edge detection algorithms.

Edge detection algorithms	Accuracy Percentage
Canny	14 false / 86 true
Roberts	19 false / 81 true
Prewitt	32 false / 68 true
Sobel	28 false / 72 true

Experiments were carried out with different edge detection algorithms. The test results performed are shown in Table 1 and Figure 4.

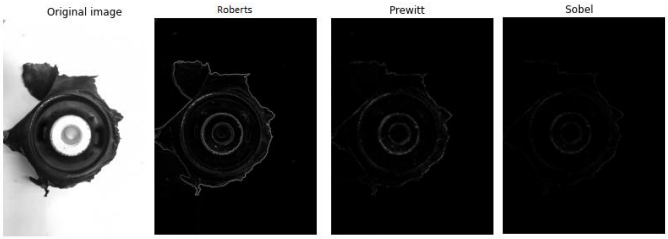

Figure 4: Compare different application.

Image processing algorithms were programmed with the Programmable Industrial Camera and Canny algorithms were used for surface circularity matching. Although there are many algorithms on this subject, the most widely used and most effective are the Canny algorithms. The Canny operator reveals areal high-frequency regions corresponding to the edges of an image. Canny algorithm is applied on the main picture and verified with the horoscope match map. An example Canny horoscope application is shown in Figure 6. The image taken from the camera should be read first. The reason for returning True or 1 in the while loop is to run the process in an infinite loop. The loop will then be exited with an if check.

It returns two parameters. The reason why I used HSV in the code I wrote earlier is that I want to convert the BGR Blue, Green and Red color tones to Hsv (Hue, Saturation, Value) in the name of saturation, brightness and color essence. If we itemize the stages; In order to reduce the noise of the image, it is reduced by convolution with the Gaussian kernel. Apart from the Gaussian filter, it can be used in Mean or Median filters. . The gradient operator is applied. In this way, the Gradient size and direction of the image are calculated. Sobel filter is the most used method for this process. Apart from this, Prewitt and Robert edge detection methods are also available. Edges are examined using Non Maxima printing. Binary thresholding is applied, thus eliminating unwanted details. After the strong-weak distinction is made, suppression is applied and the image is finalized with the original edges. Canny application is seen in Figure 5.

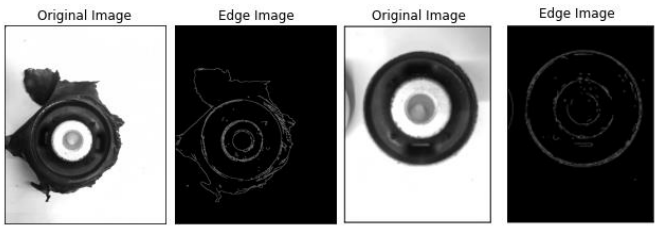

Figure 5: Canny Application.

In this study, the counting of the bushes, which are met by

the areal laser sensor, is carried out. After the counting process, the cleaning control is carried out with the image processing algorithm with an industrial camera positioned from a bird's eye view. Thanks to the created program interface, information such as product code, operator registration number, active working time, productivity, shift supervisor, applied operation, operation desk number and storage location can be recorded.

III. Conclusion

As a result, with the machine made in this study, the deburring operation process traceability of the bushings was ensured. In addition, the accuracy of the deburring operation was taken from the operator's initiative and controlled by the image processing algorithm. Thanks to PLC, faster and easier control is provided. Visual Studio program communication with SIEMENS S7-1200 series is provided with s7.net library. This facilitates communication.

The least erroneous algorithm is the Canny algorithm. The results are shown in Figure 6.

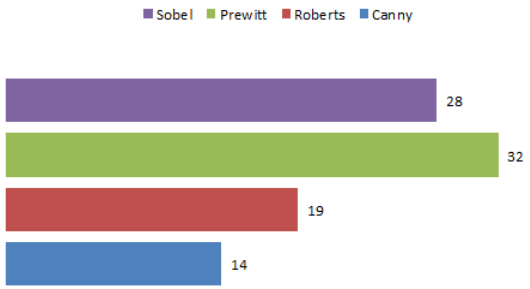

Figure 6: Canny Application.

Thanks to the created interface, it offers ease of use and provides fast results. The widespread use of image processing algorithms in production provides a higher quality production and can prevent time and financial losses that may occur in the final control. This system, which was developed as a prototype, can be developed to form a fully automatic production line by integrating with robotic systems together with more comprehensive inspection and artificial intelligence algorithms in future studies. The final designed and ready-to-use machine is shown in Figure 7.

Figure 7: Machine final.

Acknowledgment

This work was supported by the Project numbered AYD0122-05. We would like to thank AYD Automotive Industry, the R&D team and Mr. Ahmet CAKAL for their support in the study.

References

[1] Karaçalı, H. (2012). *Beş eklemli çapak alma robotu tasarımı* (Master's thesis, ESOGÜ, Fen Bilimleri Enstitüsü).

[2] El Naser, Y. H., Karayel, D., Ozkan, S. S., & Atali, G. (2017, September). Talaşlı İmalatta Otomatik Çapak Alma İşlemi için Endüstriyel Robot Kol Tasarımı. In *5th International Symposium on Innovative Technologies in Engineering and Science 29-30 September 2017 (ISITES2017 Baku-Azerbaijan)*.

[3] Yaman, O., Karaköse, M., Akın, E., & Aydın, İ. (2015, May). Image processing based fault detection approach for rail surface. In *2015 23nd Signal Processing and Communications Applications Conference (SIU)* (pp. 1118-1121). IEEE.

[4] Çil, M. M. (2015). *Temel Görüntü İşleme Algoritmalarının FPGA Üzerinde Gerçeklenmesi* (Doctoral dissertation, Fen Bilimleri Enstitüsü).

Using Template Matching Algorithm In Welding Robots

L.CİVCİK[1] and M. A. AKSİN[2]

[1] Konya Technical University, Konya/Turkey, lcivcik@ktun.edu.tr
[2] Konya Technical University, Konya/Turkey, alperenaksin@gmail.com

Abstract - **Intelligent robotic welding is an indispensable part of modern welding manufacturing, and vision-based seam tracking is one of the key technologies for performing intelligent welding. The biggest challenge in robotic applications is interaction with humans and a dynamic environment, typically constrained by the capacity of visual sensors and the computational cost of signal processing algorithms. The aim is to speed up the welding process and reduce the cost. Since the welding process is very fast, the process is accelerated by using image sensors and various image processing algorithms instead of operators. However, the adaptability and robustness of most image processing algorithms are insufficient during weld implementation. Addressing this issue, the study presents an event-driven embodied system for feature extraction and object recognition as a new and efficient sensory approach in robotic applications. By applying the event property "mapping", it is enhanced with additional information that can be used for object recognition. After the welding process of the robot is performed, it is aimed to decide which welding type is closer to the welding process. Thus, it can be checked that the weld is performed in a quality manner by making parameter selections and processing of the results easier according to the weld type. The test results prove that the algorithm has good adaptability for multiple typical weld seams and.**

Keywords: Image processing, Image Preprocessing, Feature Extraction from Image, Template Matching, Welding Robots

I. INTRODUCTION

With the rapid development of the modern manufacturing industry, more and more welding robots are applied in automated manufacturing processes. Welding robots are used in many areas thanks to their high efficiency, sustainability of quality and continuous operation even in adverse working conditions. Welding robots, which are widely preferred in areas such as the automotive sector and ship manufacturing processes, play an important role in equating operator-induced errors. In addition, more autonomous and flexible working conditions can be provided. In order to provide this flexibility and autonomous operation, more computer applications have started to be used. At the point reached today, computer vision systems are taking the place of operators. However, most welding robots are teach-and-play robots. By using the test results obtained before, the parameters can be taught to the computer and the welding made as a result of this learning can be evaluated. In addition, during the welding process, distortion, heat dissipation paths, gap variability, stepped edge, etc. cause the seam position to be often disturbed. If this seam position change is not corrected, it reduces the weld forming quality. Therefore, vision sensors should be used to fix this problem.

It is important to mimic the actions of a human welder for the development of intelligent robotic welding. Three basic technical steps are required to perform automatic welding similar to a welding machine. The first is to acquire and perceive information about the dynamic process of welding, like the way it is acquired by the human sensing organs, to detect internal and external welding conditions [1]. These detection processes are provided by cameras and software. At this point, the images taken from the cameras need to be processed quickly and accurately. In intelligent robotic welding, seam tracking is a major challenge, and visual sensing technology is an efficient way to deal with it. With the help of image-based seam tracking technology, traditional "teach-and-play" robots can overcome inconveniences during welding practice and meet high-quality welding requirements.

By tracing the laser line, the center and edges of the weld line can be found by extracting the feature points and taking the centers of these points. Thus, image processing algorithms can be used more easily. For example, the welding type can be easily determined by comparing the found points with certain templates. Again, the welding type can be determined by comparison directly after a simple pre-processing process of the image without processing.

The parameters to be used may vary according to the type of welding made. Welds are made in certain types, mainly I type, U type and V type and spot. It is envisaged to teach these welding types to the computer with the shape matching algorithm and to decide on the accuracy of the welding traces in the instantaneous camera data. In this study, it is aimed to use the shape matching algorithm to determine how accurately the spot-shaped welds are made. Thus, it is foreseen that the success percentage of the welding process will be increased by obtaining high rates of correctly processed data in a short time.

Image Processing techniques are the methods that convert the image into digital format and make the image into the desired form by performing some operations on the digitalized image or obtaining the required information from the image. They are signal processing applications that convert input recorded images into processed output images or image-related characteristics [2]. While applying the necessary signal processing methods to images in image processing, the image is considered as a two-dimensional matrix. A digital image with M rows and N columns is displayed in f(x, y) format. This is how values in (x, y) coordinates become discrete values. This notation makes it easy to specify image pixels. Thus, the values of the coordinates on the origin are shown as

(x, y) = (0,0). In Equation 1, an image with M rows and N columns is shown in coordinates. f(x, y) to represent a pixel for each element; An image with M rows and N columns has MxN pixels.

$$f(x,y) = \begin{bmatrix} f(0,0), & f(0,1), \ldots . f(0,N-1) \\ f(1,0), & f(1,1), \ldots \ldots f(1,N-1) \\ . & . \quad . \quad . \\ . & . \quad . \quad . \\ . & . \quad . \quad . \\ . & . \quad . \quad . \\ f(M-1,0), & f(M-1,1), \ldots . f(M-1,N-1) \end{bmatrix} \quad (1)$$

Many algorithms are used in Image Processing. If we examine these algorithms in basic groups, these are: Image Enhancement: Basically, the aim is to make some improvements on the image, to better detect the features of interest and thus to create a better input for the image processing algorithm to be applied [3]. The main purpose of image enhancement is to create a more suitable image for the observer by highlighting the features of the image. Image Renewal: It is possible to restore the image after it has lost some important features for various reasons or after it has deteriorated. The image may be distorted during digitization or transmission. During the image acquisition process, there may be some noise from the environment where the image was taken. By using image restoring methods, the noise on the image is removed so that the closest image to the original image can be obtained. Image Segmentation: It is the process that divides the image into meaningful parts or separates the parts from each other by taking similar features in the image into a field. Edge information and texture information in the image are also important features for segmentation [4]. Object Recognition: It is the process of finding the object to be searched for in an image. For any object in the image, there is a large number of points that can be extracted from the object to define the properties of the object. These points, which are extracted from the object and give quality information about the object, are used in the image where the object to be detected is in the same frame with more than one object, helping to recognize and detect the object [5]. Algorithms such as template matching can also perform object recognition by comparing pixels sequentially.

There are various methods used to eliminate the noise, which is the unwanted data in the obtained images and to keep the data of interest intact. In this way, it is aimed that the algorithm to be used will give healthy results. For example, thanks to various filters to be applied to the image containing noise, the noise is equalized so that the algorithm can give more accurate results. After performing these operations, the objects of interest on the image are made more specific and easier to process. In the filter application step, the salt and pepper noise on the image is removed and the unnecessary details in the image are reduced. In addition, these filters increase the data quality by making the contrast changes more evident and by making the edge information in the image clear.

In image processing, there are multiple approaches and methods to evaluate a part independently from the whole image from which that part is extracted and to determine the object included in its content. One of the basic methods of detecting the object is Template Matching. With the Template Matching method, the welding is detected on the weld image by scanning a template over it with the sliding window method. The template is placed on the source image at (0,0) coordinates, all pixels are shifted and matched one by one, a similarity ratio is created according to the similarity method used, and if the template and the current portion of the image are similar, it returns those pixels to you as a result. Accordingly, the objects in the photograph can be determined according to the similarity ratios of the pixels to each other and by choosing a threshold value for these ratios. The threshold value helps to ignore pixel similarities that hold unnecessary information and to find the results correctly.

II. METHODOLOGY

There are many types of welding seams in real industrial production. The seam removal method based on morphological image processing is always designed for a specific welding seam. To perform the seam removal of different types of seams, the feature removal operator must be considered according to the shape characteristics of different welding seams. Therefore, algorithm flexibility is relatively poor. Meanwhile, when faced with many images morphological processing steps, the real-time performance of stitch tracking will be affected [6].

The type of welding in the images in this study also distinguished the template matching algorithm from other image processing algorithms. Because the similarity of the welds, which are thrown in the shape of a spot, can be easily detected by the template matching algorithm. The template must contain the properties in the images. The similarity of such welds played an important role in determining the algorithm selection as Template Matching.

In the study, the welding robot KUKA brand robot arm was used. Welded materials are aluminum-nickel mixture cake molds. These molds are produced for use in production. In summary, the process is the process of welding the mold in which the welding cake dough will enter, to the tray-shaped material. These molds are made by attaching them to the tray from four corners. The images taken as an example were processed with the Template Matching algorithm using the OpenCV v4.5.3 library in the Python 3.9 version environment.

Figure 1: Wield Robot Process

Weld points can be determined by using the sample template for the detection of weld points. Since all welds are similar to each other, detection is not difficult thanks to the template taught. However, since the coordinates of the welding points are different, it can be an obstacle for the detection process. At this point, it is aimed to detect the welding points more accurately by applying the template matching algorithm, after subjecting both the template image and the welding image to the preprocessing process that consists of noise elimination and edge detection with the Canny edge detection algorithm.

Again, in order to more easily detect the welding points scattered in various parts of the image, the ROI region is selected from the image and the part where the welding point is being detected will be narrowed. Thus, easier detection can be performed by ignoring the parts where other welding points are located.

In this article, it is aimed to focus on the discontinuity points of the welding thanks to ROI, and to perform welding detection by subjecting the image to various pre-processing processes. If the butt weld seam is taken as an example, the detection of the discontinuous weld seam is described in detail as follows:

1)ROI Selection: Two ROI regions need to be selected, including laser strips and weld seams, respectively, before feature extraction. It can be very helpful in ROI selection if the image selected as the template contains only the welding type. Thus, only the welded area in the image can be focused more quickly.

$$\begin{cases} x = \frac{x_0}{2} \\ y = y_0 + \frac{n}{2} + w \\ w = n_0 + 2 \\ H = 2 * w \end{cases} \quad (2)$$

(X, Y) Image coordinates of the upper left corner of the weld seam ROI; (x0, y0) Image coordinates (W, H) of the upper left corner of the laser strip ROI width and height of the weld seam ROI; h is the height of the laser strip ROI; w is the width of the weld seam.

2) Removal of welding seam edges: Before edge removal, if the average gray value of the image is less than a threshold, logarithmic transformation and normalization are used to enhance the original image. Edges can be found by detecting high frequency transitions in the image using the Canny edge detection algorithm. Points that meet the edge criteria can be preserved as absolute edge points. Similarly, the previous model is provided to filter out false edge points.

3) Fitting edge equations: The gradients of the points on the two edges are opposite. Therefore, they can be easily distinguished [7].

Figure 2: Welded Cake Pan and ROI Area

A. Image Preprocessing

The purpose of applying the image filtering process is to reduce the noise as well as to protect the important information in the image. There are various types of noise because different factors cause noise formation. A good image filtering algorithm is expected to yield successful results when applied to different types of noise. The noisy image is defined as:

$$f(i,\ j)\ =\ g(i,\ j) + n(i,\ j) \quad (3)$$

Here, f(i, j) shows the intensity value of the image, n(i, j) shows the gray level value of the noise, and g(i, j) shows the intensity value of the pixel in the noise-free image. There are many filter methods to reduce noise in images. Spatial plane image filters are divided into linear and non-linear. Generally, in nonlinear method, the filtered image is determined by the intensity values of the pixels in the filter mask with the help of rank statistics methods. In linear methods, filtering is done by applying the filter mask to all pixels separately.

Due to the noise in the welding environment, median filtering, one of the nonlinear method filters, has been proposed to improve the input. The purpose of using the median filter is to remove unwanted data and highlight the data of interest. The median filter can also retain detailed information such as edge segments and sharp seam angles. In median filtering, the input intensity is replaced by the median of the intensities found in its neighboring pixels. The size of the filter used depends on the welding application and welding system configuration [8].

The use of the mean or gaussian filter, which is one of the linear filter types in the salt and pepper noise type, reduces the effect of the noise on the processed pixel, but it causes the information in the noiseless pixels to be corrupted. For this reason, linear filters are not preferred to remove salt and pepper noise, but non-linear filters are used. Because outliers can be easily removed in non-linear filters. The minimum filter, that is, the filter that assigns the smallest intensity value of the pixels in the region within the filter window to the processed pixel, gives good results only for images with salt noise. The maximum filter, on the other hand, gives successful results in eliminating pepper noise as it assigns the highest value from the density values in the filter mask to the processed pixel. However, the maximum filter does not give

good results in salt noise, and the minimum filter does not give good results in pepper noise. On the other hand, the median filter is one of the non-linear filters frequently used to reduce salt and pepper noise. Median filter is expressed using the following equation:

$$y(i,\ j) = median\{x(m,n),(m,n) \in w\} \quad (4)$$

Here, w indicates neighborhood pixels depending on the mask size, and the mask size can be determined by the user. Since the intensity values of the pixels in the neighborhood of the processed pixel in the median filter are ordered from smallest to largest, and the median value constitutes the intensity value of the processed pixel, values close to the maximum and minimum values are successfully eliminated. Intensity values with extreme values are eliminated, since values close to the maximum and minimum, that is, noisy pixels, will be found at the beginning or end of the order and will create the median value filtering result. Thus, the median filter is quite effective at eliminating salt and pepper noise or impulse noise. Another benefit of the median filter is that it reduces the distortion that happens as a result of filtering and allows the details of the image to be preserved [9].

Figure 3: Image filtered using the median filter

$$K = \begin{vmatrix} 1 & 1 & 1 & 1 & 1 \\ 1 & 1 & 1 & 1 & 1 \\ 1 & 1 & 1 & 1 & 1 \\ 1 & 1 & 1 & 1 & 1 \\ 1 & 1 & 1 & 1 & 1 \end{vmatrix} \quad (5)$$

The noise is removed by hovering the kernel image above. K refers to the core matrix used for filtering in NxN dimensions, I_R refers to the matrix of the color image taken from the camera, I_R^I refers to the new image matrix formed at the end of the filtering. In Equation 6, the formula showing the calculation of new values for each pixel is presented.

$$temp = \frac{N}{2}$$

$$I_R^I(x,y) = \frac{1}{NxN}\sum_{i=1}^{N}\sum_{j=1}^{N} K(i,j) * I_R(x + i - temp, y + i - temp) \quad (6)$$

During the filtering process, it is desired to use negative values in the I_R matrix. In this case, the value at the index closest to the relevant indices is used. For example, K(0, 0)* for I_R^I(0, 0) during calculation is multiplied by I_R(-1, -1), which is the closest value in the matrix, I_R(0, 0).) are used. Since the image has three channels and is taken in the RGB (Red, Grain, Blue) color space, the values for the three colors in the IR image matrix are updated using equation 6. After the filtering process, the graying step of the color image is performed. For example, during the calculation, I_R(0, 0), which is the closest value in the matrix, is used when multiplying K(0, 0)* I_R(-1, -1) for I_R^I(0, 0). Since the image has three channels and is taken in the RGB (Red, Grain, Blue) color space, the values for the three colors in the IR image matrix are updated using equation 2. After the filtering process, the graying step of the color image is performed. The median filter provided a simpler image after the image was reduced to gray level. Thus, it becomes easier to extract edge points with the Canny edge detection algorithm. As a result of these pre-processing processes, it is aimed to obtain the similarities between the template and the image more easily, to shorten the CPU operations and to prevent the decrease in the similarity rate due to unnecessary data. The results of the applied median filter are shown in Figure 3 and Figure 4. The differences created by this filtering process applied to eliminate the noise are clearly shown. The median filter was applied using a 5x5 kernel as a feature. This kernel size can be changed according to the nature of the picture and the amount of noise.

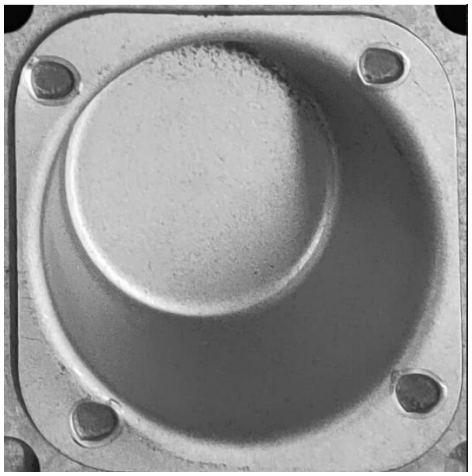

Figure 4: Image Reduced to Gray Level

B. Template Matching

It is a technique in digital image processing to find small parts of an image that match the stencil image. It can be used as part of quality control in production, as a way to navigate a mobile robot, or as a way to detect edges in images. Although the accuracy rate is high in this method, the processing load is very high. So much so that it is very difficult to implement with today's hardware without using acceleration techniques. When it comes to tracking an object, transactions need to be done in real time. This requires the

hardware and algorithms used to be very fast. In computer vision applications, it is very difficult to track an object in nature in real time [9]. Object tracking involves estimating the trajectory of a moving object in successive frames. Dynamic variables such as features expressing objects, motions and temporary changes of objects, or exact attachment of the tracked object need to be considered in tracking [10]. This monograph describes the development, methods and systems of object tracking systems, as well as object tracking system structure and new trends in proposed systems. According to Yılmaz et al., although the images in nature are 3-dimensional, the obtained images are 2-dimensional, noise on the image, the movements of the objects can be complex, the presence of irregular or fragmented objects [11], partial and full object overlaps, the presence of complex object shapes. Changes in image brightness, real-time application needs, and shadows from moving objects cause object tracking to be complex [12].

The main challenges in the template matching task are: occlusion, detection of non-strict transformations, lighting and background changes, background clutter, and scale changes. In this study, it is aimed to extract various weld seam features with shape matching algorithm. In the algorithm, firstly, the edges were found directly and then the source points were tried to be determined in the images that were converted to gray level. By comparing these points with the features in the target image with Shape Matching, it was tried to determine the types of welds or to determine to what extent the spot-shaped welds were made correctly. With template matching, it is aimed to make the decision mechanism faster and more accurate while the robot is working.

Although it is difficult to recognize the welding environment, it is only the initial position of the weld seam that we are interested in. It is a practical method to only look for the position we are interested in. Template matching is placing the template at a location in an image and detecting its presence at that point by comparing the intensity values in the template with the corresponding values in the image. This policy satisfies the requirements for initial weld location recognition, which avoids complex recognition of the entire weld environment. In fact, it's rare for density values to match exactly. A measure of difference is needed between the intensity values of the template and the corresponding values of the image. By specifying a threshold value, we can look for a similarity higher than a certain value. Thus, there is no need for an exact analogy.

$$\boldsymbol{R(i,j) = \sum_{m=1}^{M}\sum_{n=1}^{M}[s^{i,j}(m,n) * T(m,n)] \,/\, \sum_{m=1}^{M}\sum_{n=1}^{M}[s^{i,j}(m,n)]^2} \quad (7)$$

Here the full pattern, s is the searched image, $s^{i,j}$ is the image contained by the T pattern, i and j are the column and row values in an image [8].

In the images above, the results of the template matching algorithm applied to the weld images are given. Along with the values of the match rate, there are the positions of the matches found by the algorithm.

Some parameters of the algorithm used in this table are given. The threshold value giving the most positive result was determined as 0.7. The average algorithm time was determined as 189.9. This result was achieved with the AMD Ryzen 7 5600 processor. The most positive median filter kernel was chosen as 5x5 according to the type of images.

III. Experimental Setup and Results

The proposed feature extraction algorithm aims to improve between time consumption and performance. According to the data obtained as a result of the image processing processes, the images are processed in an average of 180 ms and the result is obtained. This time can be considered good depending on the applications. It has also been seen that as the size of the processed image decreases, the time taken for the response given by the algorithm also decreases. When we process all the cake pans used in the application, the elapsed time is around 500 ms, while focusing on the small pieces, the elapsed time decreases to around 180 ms. The use of ROI can be considered useful at this point.

Table 1: The parameters for which the algorithm is most efficient.

Model	Template Matching
Threshold	0.71
Average Algorithm Time (ms)	189.90
Median Filter Kernel	5x5

Figure 5: Result of Template Matching Algorithm

In the shadow of the results obtained, preprocessing gives very useful results when the results of the images with the median filter applied are compared with the results of the unfiltered images. The increase in the values of the similarity ratios obtained shows how accurate the pre-processing part is, rather than the threshold value determined by the increase of these similarity ratios. It is recommended to reduce the images to gray level for automatic threshold determination. Thus, it can be easier to process the cake pans produced in different colors. Pattern matching cannot be performed correctly until dark colored pans are reduced to gray level. It is aimed to determine the automatic threshold for the images by giving the images reduced to gray level as input to the Otsu function. Thus, it is not necessary to set the threshold again for each image. At the same time, it is aimed to prevent data loss by determining a single threshold.

The image preprocessing procedure gave high detection results even when the threshold value was set to 0.7. Because the threshold value decreased to 0.45 with the Otsu function in trials without image preprocessing. This has led to the processing of undesirable features. The application period has been prolonged and the success rate has decreased. In images without image preprocessing, it remained between 25% and 50% when each image was set to four source points and the threshold value was manually held at 0.7. But with image preprocessing this detection rate is 50% at 0.75 threshold and 75% at 0.7.

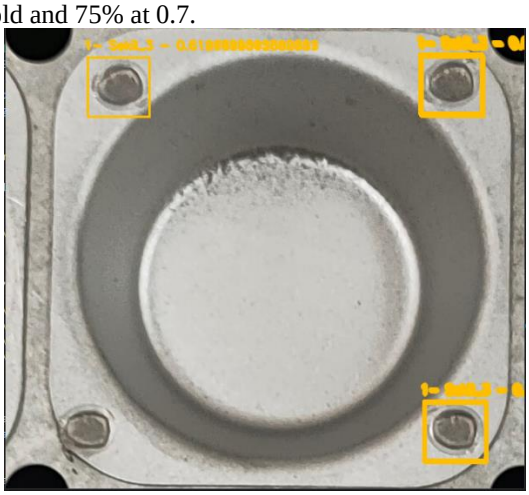

Figure 7: Result of Image Preprocessing

It is aimed to measure how similar the created weld areas are to the determined templates. According to the results obtained, deterioration occurs in the welding process due to the overheating of the torch tip at certain intervals and irritation over time. Again, it was observed that some welds shifted due to the misplacement of the initial position of the torch tips. The weld coordinates determined by the algorithm can be used to eliminate this slipperiness. It is aimed to determine the midpoints of the obtained coordinates and send them to the CPU and give feedback to the robot.

The Whole Frame Scan method was used in the template matching algorithm. All pixels on the template are processed for the matching process. In order to reduce the processing load, firstly, the method of using subpatterns has been proposed [14]. In this method, only one of every two pixels, horizontally and vertically, is processed to predict the degradation and find the match. Thus, the processing load is reduced four times in proportion to the square of the row and column. In this method, distortions are avoided by using Low Pass filters.

In this study, the median filter was used as a low-pass filter. In order to avoid distortions, it is proposed to apply four submodels to different search regions [15]. Thanks to this method used in this study, simultaneous matching instead of separate matching provided both more points of similarity than various templates and less computational overhead. Next, an adaptive pixel dilution scheme was proposed [16]. In this method, all templates are used for matching, and unnecessary operations are synchronized and distinctive features are used on the template that will provide the matching. According to the results of the algorithm, the ROI can be reduced to the order of 180 ms. Because the algorithm performed the matching process for the same pixels only once instead of four times.

It is also intended to be used for predicted maintenance algorithms by using the results of the algorithm for the detection of the torch tip that wears out over time.

In addition, it is aimed to prevent data loss by using 4 different templates in the algorithm. Weld points found with different templates are shown in different colors. As can be seen in the results, the weld points were found with various templates, so that the goal of reducing data loss was achieved. The number of templates can be increased or decreased. If the number of templates is increased, data loss will decrease, however, the algorithm will take longer. This situation should be decided by evaluating according to the application.

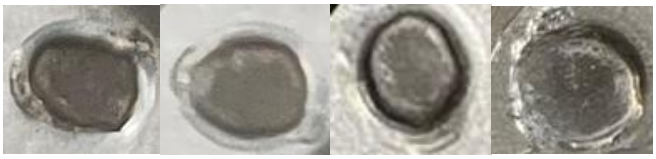

Figure 8: Used Templates

IV. Conclusion

The coordinates of the detected weld points can be compared with the region where the weld is made, and the amount of slip of the weld point can be obtained as input to the predictive maintenance algorithms. Faster or more accurate results can be obtained by increasing or decreasing the number of templates used in the algorithm according to the type of application. By using the obtained labeled results as inputs for deep learning algorithms, convolutional neural networks, faster and more reliable results can be obtained.

REFERENCES

[1] Runquan Xiao, Yanling Xu, Zhen Hou, Chao Chen, Shanben Chen, An adaptive feature extraction algorithm for multiple typical seam tracking based on vision sensor in robotic arc welding, Sensors and Actuators A: Physical 297 (2019) 111533.

[2] GONZALEZ, R.C., and RICHARD, E.W. 2008. Digital Image Processing. Prentice Hall.

[3] MAINI, R. and AGGARWAL, H. 2010. journal of computıng, volume 2, ıssue 3, march 2010, ıssn 2151-9617.

[4] PRATT, W.K. 2007. DIGITAL IMAGE PROCESSING, PIKS Scientific Inside, Fourth Edition, PixelSoft, Inc.Los Altos, California 2007.

[5] FERRARI, V., TUYTELAARS, T. and GOOL, L. V. 2004. "Simultaneous Object Recognition and Segmentation by Image Exploration". Computer Vision - ECCV 2004, Tomás Pajdla ve Jiří Matas, 40–54. Lecture Notes in Computer Science 3021. Springer Berlin Heidelberg. http://link.springer.com/chapter/10.1007/978-3-540-24670-1_4.

[6] Lei Yang, Yanhong Liu & Jinzhu Peng, Advances techniques of the structured light sensing in intelligent welding robots: a review, The International Journal of Advanced Manufacturing Technology (2020) 110:1027–1046.

[7] Runquan Xiao, Yanling Xu, Zhen Hou, Chao Chen, Shanben Chen, An adaptive feature extraction algorithm for multiple typical seam tracking based on vision sensor in robotic arc welding, Sensors and Actuators A: Physical 297 (2019) 111533.

[8] Jawad Muhammad & Halis Altun & Essam Abo-Serie, Welding seam profiling techniques based on active vision sensing for intelligent robotic welding, Int J Adv Manuf Technol (2017) 88:127–145.

[9] Gauss,2018

[10] KETTNAKER, V. and ZABIH, R. 1999. "Bayesian multi-camera surveillance". Computer Vision and Pattern Recognition, 1999. IEEE Computer Society Conference on., 2:-259 Vol. 2. doi:10.1109/CVPR.1999.784638.

[11] HANNA, G., 2011. Object Tracking. Hard Cover, Publisher: In Tech, Subject: Artificial Intelligence, pp: 284, ISBN: 978-953-307-360-6.

[12] XU, R.Y.D., ALLEN, J.G. and JIN, J.S. 2004. "Robust Real-time Tracking of Non-rigid Objects". Proceedings of the Pan-Sydney Area Workshop on Visual Information Processing, 95–98. VIP '05. Darlinghurst, Australia, Australia: Australian Computer Society, Inc. http://dl.acm.org/citation.cfm?id=1082121.1082138S. Sudhakaran and O. Lanz, "Learning to detect violent videos using convolutional long short-term memory," in *14th IEEE International Conference on Advanced Video and Signal Based Surveillance*, 2017.

[13] YILMAZ, A., JAVED, O. and SHAH, M. 2006. "Object Tracking: A Survey". ACM Comput. Surv. 38 (4). doi:10.1145/1177352.1177355.

[14] BIERLING, M. 1988. "Displacement estimation by hierarchical block matching", 942– 51. doi:10.1117/12.969046.

[15] LIU, B. and ZACCARİN, A. 1993. "New fast algorithms for the estimation of block motion vectors". IEEE Transactions on Circuits and Systems for Video Technology 3 (2): 148–57. doi:10.1109/76.212720.

[16] WANG, Y., WANG Y.and KURODA, H. 2000. "A globally adaptive pixel-decimation algorithm for block-motion estimation". IEEE Transactions on Circuits and Systems for Video Technology 10 (6): 1006–11. doi:10.1109/76.867940.

C-Band Microstrip Antenna Array on Photograph Paper Substrate

D.UZER, A.Ö. ÇINAR, Z.İ. KÖFÜN and N.B. TAŞ

Konya Technical University, Konya/Turkey, duzer@ktun.edu.tr
Konya Technical University, Konya/Turkey, aocinar@ktun.edu.tr
Konya Technical University, Konya/Turkey, zeynepiremkfn@gmail.com
Konya Technical University, Konya/Turkey, nebiberhantas@gmail.com

Abstract **– In this study, a 2x1 microstrip antenna array is designed for C band applications. Glossy photograph paper is used as dielectric substrate in four layers. The conductive surfaces of the antenna are manufactured using by self-adhesive copper tape and graphite based conductive spray paint then their performances are compared. Simulations of the antennas are realized in ANSYS HFSS. From measurements, it is seen that this antenna array is suitable for flexible C-band communication applications. In addition, the antenna manufactured with copper tape has a better performance than the conductive spray method.**

Keywords **– C-band, ANSYS HFSS, microstrip array, photograph paper**

I. INTRODUCTION

IN recent years, researchers from all over the world have been working on the C band, especially in the field of antenna design. The C band, which covers the 4 GHz to 8 GHz range according to IEEE, has started to attract great attention over time and to be used in many areas, with the effect of technological developments. Generally, Wi-Fi and ISM bands are used in areas such as satellite communication and radar systems [1-7]. Reasons such as increasing mobility, decreasing the size of mobile devices and increasing communication standards have increased the need for small, light, but also useful antenna systems that provide frequency ranges such as multi-band and broadband.

Nowadays, we come across antennas made of flexible materials more frequently to be used in smaller and portable devices. Many studies using photographic paper as substrate material are available in the literature [8-15]. Advantages of paper substrate are flexibility, lightness, being cheap and easily available, ease of production and termal resistance [13,16]. Silver or copper-based ink-jet printing, screen printing, self-adhesive copper tape and carbon-based conductive paint can be used in the fabrication of conductive surfaces [8-16]. In this study, an antenna array consisting of two rectangular patches that work at different two resonant frequencies so have different dimensions covering the C band was designed and simulated on Canon Glossy GP-501 photographic paper. In fabrication, conductive surfaces were obtained by using self-adhesive copper tape and graphite based conductive spray paint.

II. MATERIAL AND METHOD

A. Rectangular Patch Antenna Design on Photograph Paper

Rectangular patch antenna design is one of the most common designs, since its design simplicity and electrical modeling have been done before [3,4]. This common design is achieved by placing a rectangular patch over a rectangular dielectric layer, and a ground plane that generally has the same dimensions with its substrate is placed under the dielectric layer. Figure 1 shows the traditional inset-fed rectangular microstrip antenna.

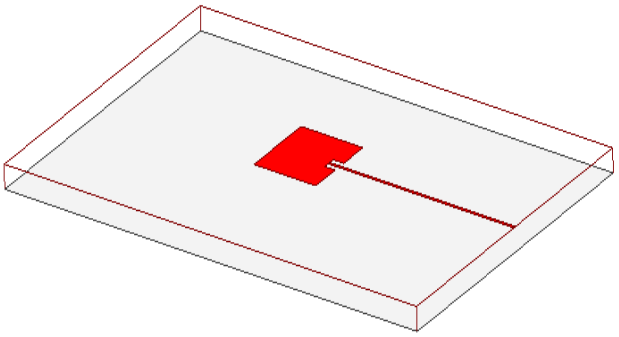

Figure 1: Traditional Rectangular Microstrip Patch Antenna with Inset-Fed Line

The patch sizes of the antenna can be calculated using the formulas given below:

$$W = \left(\frac{c}{f_c}\right) \times \left(\varepsilon_r + \frac{1}{2}\right)^{-1/2} \quad (1)$$

$$L = \left(\frac{c}{2f_c\sqrt{\varepsilon_e}}\right) - 2\Delta l \quad (2)$$

$$\varepsilon_e = \frac{(\varepsilon_r+1)}{2} + \frac{(\varepsilon_r-1)}{2} \times \left[1 + \left(\frac{12h}{W}\right)\right] \quad (3)$$

$$\Delta L = 0.412h \times \frac{\left[(\varepsilon_e+0.3)\left(\frac{W}{h}+0.264\right)\right]}{\left[(\varepsilon_e-0.258)\left(\frac{W}{h}+0.8\right)\right]} \quad (4)$$

Where,

W: Width of the patch
L: Length of the patch
ΔL: Effective length
f_c: Resonant frequency
c: Velocity of light in free space
ε_r: Relative dielectric constant of dielectric substrate
ε_e: Effective dielectric constant
h: Thickness of dielectric layer

In microstrip antennas, impedance matching must be made between the antenna and the feedline to keep the reflection at the minimum level and the power transfer at the maximum level. In the study, inset fed, one of the commonly used methods in the literature, was preferred aiming a good impedance matching. In this method, the point where the required impedance value is obtained is tried to be found by inserting a certain amount of the supply line into the patch. Optimum values were obtained after simulations [17-19].

In the study, first, rectangular inset fed antennas that will radiate at 4 GHz and 6 GHz frequencies are designed and produced separately. Afterwards, using the determined patch sizes, it is switched to a 2x1-elements antenna array. The array configuration is shown in Figure 2.

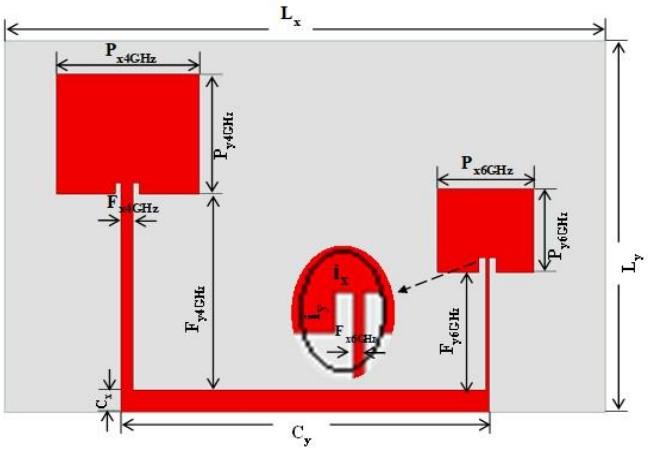

Figure 2: 2x1 Array Configuration

The thickness of the photograph paper is 0.254 mm, and it is used in four layers for a higher efficiency antenna. The ε_r value of the paper is 3.5 and the tanδ value is 0.0015 from the literature [20].

B. Double Patch Array for C-Band

The optimum parameters of the microstrip antenna array are given in Table 1. The ground plane and substrate dimensions were chosen as 100 x 150 mm, which is one of the standard sizes for the Canon GP-501 Glossy photopaper. Patch sizes have been used as calculated from expressions in the literature, and common line sizes combining inset fed lines have been optimized in the simulation.

TABLE 1: OPTIMUM 2X1 ARRAY PARAMETERS

L_x	100.00
L_y	150.00
h	1.016
P_{x4GHz}	32.30
P_{y4GHz}	35.60
P_{x6GHz}	22.50
P_{y6GHz}	24.00
i_{x4GHz}	1.50
i_{y4GHz}	3.00
i_{x6GHz}	1.75
i_{y6GHz}	3.85
F_{x4GHz}	3.00
F_{y4GHz}	59.85
F_{x6GHz}	0.84
F_{y6GHz}	38.75
C_x	7.00
C_y	91.92

* All parameters are in mm.

Where,

L_x: Length of the ground plane and dielectric substrate
L_y: Width of the ground plane and dielectric substrate
h: Total thickness of dielectric substrate
P_{x4GHz}: Length of the patch for 4GHz
P_{y4GHz}: Width of the patch for 4GHz
P_{x6GHz}: Length of the patch for 6GHz
P_{y6GHz}: Width of the patch for 6GHz
i_{x4GHz}: Length of the inset part for 4GHz
i_{y4GHz}: Width of the inset part 4GHz
i_{x6GHz}: Length of the inset part for 6GHz
i_{y6GHz}: Width of the inset part 6GHz
F_{x4GHz}: Length of the feed line for 4GHz
F_{y4GHz}: Width of the feed line for 4GHz
F_{x6GHz}: Length of the feed line for 6GHz
F_{y6GHz}: Width of the feed line for 6GHz
C_x: Length of the common feed line
C_y: Width of the common feed line

III. SIMULATION, FABRICATION AND MEASUREMENT

After theoretical calculations of the antennas, their simulations were carried out using ANSYS HFSS. HFSS is a 3D electromagnetic (EM) simulation software for designing and simulating high-frequency electronic products such as antennas, antenna arrays, RF or microwave components, high-speed interconnects, filters, connectors, IC packages and printed circuit boards. Engineers worldwide use HFSS software to design high-frequency, high-speed electronics found in communications systems, advanced driver assistance systems (ADAS), satellites, and internet-of-things (IoT) products [19]. In the simulation, the substrate material was defined using dielectric values in the literature. The substrate, which was used in four layers, reached a total height of 1.016 mm. The papers were united with the glossy side facing each other using double-

sided adhesive tape. The patch and ground planes of the antennas were fabricated using two different materials. First, 3M self-adhesive copper tape was cut into suitable sizes and attached to the substrate. Secondly, Graphite 33 graphene-based conductive spray paint was applied in two coats and conductive surfaces were created. In the painting process, a masking was made using adhesive foil. Precise cutting of both the copper tape and the foil mask was done automatically with the Silhouette Cameo 4 device. SMA type connector from the middle point of the common conductive part connecting the inset fed lines is adhered using copper tape. This method has been preferred instead of conventional soldering because the spray paint is damaged by high heat.

In order to determine the antenna performance, S parameters measurements are realized by using Rohde Schwarz ZVL-13 VNA in normal room conditions after calibrated by VNA calibration kit. Both fabricated antennas were connected to the analyzer using N-to-SMA type adapter.

IV. Results and Discussion

The measurement setups are given in Figure 3, and the simulation and measurement results are given in Figure 4 comparatively.

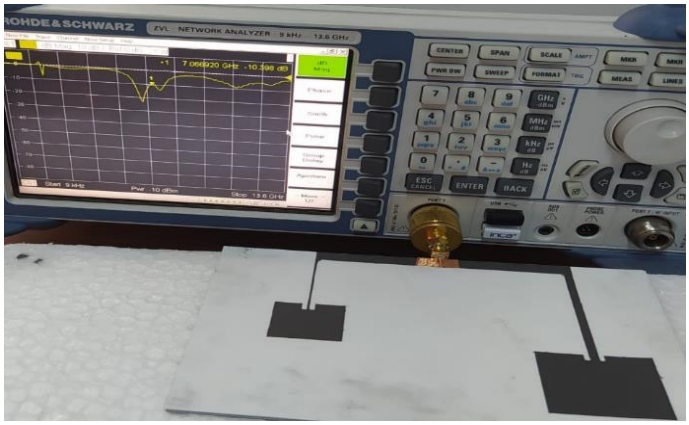

(a)

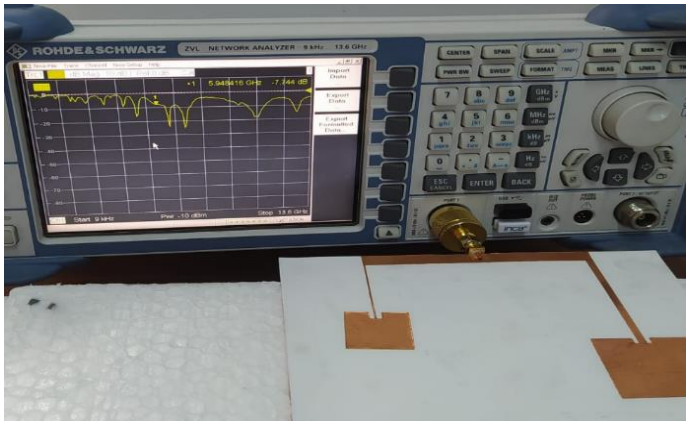

(b)

Figure 3: S_{11} Measurement of Arrays a) Fabricated with Spray paint b) Fabricated with Self-adhesive Copper Tape

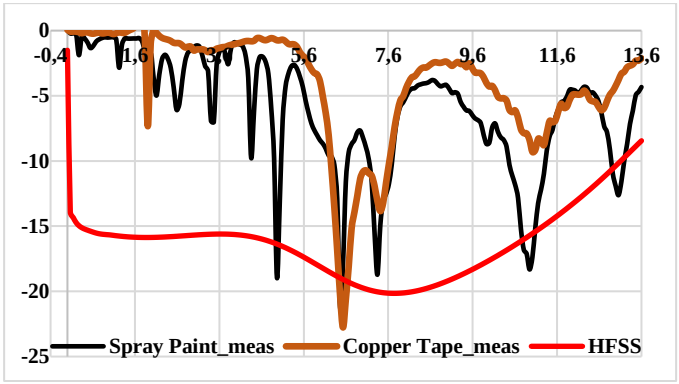

(a)

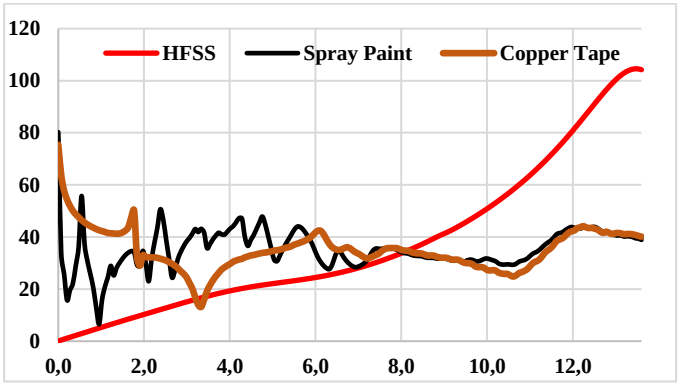

(b)

Figure 4: Comparison of Results a) S_{11} graphics b) Z_{11} graphics

The measurement results were compared with the simulation results and some differences between self-adhesive copper tape and graphite based conductive spray paint were evaluated. As a result of the evaluation, it was seen that the C band microstrip antennas produced with copper tape in this study gave values closer to the simulation results. It has been observed that antennas fabricated with graphite based conductive spray paint have lower efficiency and are far from simulation values. In the experiments with graphite based conductive spray paint, it was thought that more meticulous attention should be paid to the experiments with self-adhesive copper tape and more layers of spray paint should be applied. It is thought that the easier fabrication and better results with self-adhesive copper tape will highlight the use of copper tape in other studies. Again, as widely preferred in the literature, ink-jet printing, screen printing with copper or silver paints can be used for the fabrication of conductive parts.

As can be seen in Figure 4a, while the measurement results of both antennas are obtained close to each other, there is a difference between the measurements and the simulation. The reason is the effect of the double-sided adhesive tape used in production on the base dielectric. However, both the simulation and measurement results cover the frequency range around -20 dB, which can be used in C band applications.

From the impedance graph (Figure 4b), it is seen that the characteristic impedance matching with of the connector, by near 50 Ohm value, is obtained again in the C band frequency region, and so the antenna performance is improved.

V. CONCLUSION

In this study, a microstrip array antenna consisting of two rectangular patches operating at C-band frequencies is designed and manufactured. The antenna is designed on photograph paper and its conductive surfaces are produced with two different techniques. Both techniques have been found in the literature and are low cost, but also easy and fast. After the antenna parameters are calculated theoretically, the parameters are optimized in the simulation and antenna fabrication is started. When the measurement and simulation results of the antennas are compared, it is observed that the antenna fabricated with self-adhesive copper tape iave better results. Based on the measurements, it can be said that this array antenna has the performance to be used in C band applications.

REFERENCES

[1] J. Bruder, J. Carlo, J Gurney, J. Gorman, "IEEE standard for letter designations for radar-frequency bands," *IEEE Aerospace & Electronic Systems Society*, pp. 1-3, 2003.

[2] https://www.rfwirelessworld.com/Terminology/C-Band-Frequency.html

[3] C. A. Balanis, *Antenna Theory: Analysis and Design*. Wiley Press, 2016.

[4] R. Garg, P. Bhartia, I. J. Bahl and A. Ittipiboon, *Microstrip Antenna Design Handbook*, Artech House, 2001.

[5] Z.İ. Köfün and N. B. Taş, "Microstrip antenna design in C band," Final Thesis, Dept. of Elect. and Electro. Eng., Konya Technical University, Konya, 2022.

[6] G. Srilekha, P. Pardhasaradhi, B.T.P. Madhav, R.K.N.R. Manepalli, and M.C. Rao, "Design and analysis of 6CB nematic liquid crystal–based rectangular patch antenna for S-band and C-band applications," *Zeitschrift für Naturforschung*, pp. 863-875, 2020.

[7] S. Lakrit, H. Ammor, J. Terhzaz, and A. Tribak, "Design of a new high-gain multiband and wideband rectangular patch antenna for C, X, and Ku band applications," *Walailak Journal of Science and Technology (WJST)*, vol. 14, no. 4, pp. 339-351, 2017.

[8] M.A. Ullah, M.T. Islam, T. Alam, and F.B. Ashraf, "Paper-based flexible antenna for wearable telemedicine applications at 2.4 GHz ISM band," *Sensors*, vol. 18, no. 12, 4214, 2018.

[9] M.T. Islam, T. Alam, I. Yahya, and M. Cho, "Flexible radio-frequency identification (RFID) tag antenna for sensor applications," *Sensors*, vol. 18, no. 12, 4212, 2018.

[10] T.K. Saha, T.N. Knaus, A. Khosla, and P.K. Sekhar, "A CPW-fed flexible UWB antenna for IoT applications," *Microsystem Technologies*, pp. 1-7, 2018.

[11] S. Kim, Y.J. Ren, H. Lee, A. Rida, S. Nikolaou, and M.M. Tentzeris, "Monopole antenna with inkjet-printed EBG array on paper substrate for wearable applications," *IEEE Antennas and wireless propagation letters* 11, pp. 663-666, 2012.

[12] A.M. Mansour, N. Shehata, B.M. Hamza, and M.R.M Rizk, "Efficient design of flexible and low-cost paper-based inkjet-printed antenna" *International Journal of Antennas and Propagation*, 2015.

[13] X.Li, J. Siden, H. Andersson, and T. Schön, "A paper-based screen-printed HF RFID reader antenna system," *IEEE Journal of Radio Frequency Identification*, vol. 2, no. 3, pp. 118-126, 2013.

[14] F. Mutlu, B. Karaosmanoğlu and Ö. Ergül, "Radyo frekanslarında tanımlama uygulamaları için inkjet baskılı antenlerin tasarımları ve ölçümleri," *VIII. URSI-Turkey Congress*, Middle East Technical University, Ankara, 2016.

[15] O. Dundar, "Determination of Desing Parameters of Patch Antenna Array Using Neural Networks" PhD. Thesis, The Graduate School of Natural and Applied Science of Selçuk University, Konya, 2017.

[16] D. Tobjörk and R. Österbacka, "Paper electronics," *Advanced Materials*, vol. 23, no. 17, pp. 1935–1961, 2011.

[17] M.A. Matin, and A. I. Sayeed. "A design rule for inset-fed rectangular microstrip patch antenna," *WSEAS Transactions on Communications*, vol. 9, no. 1, pp. 63-72, 2010.

[18] Y. Hu, D.R. Jackson, J.T. Williams, S.A. Long, and V.R. Komanduri, "Characterization of the input impedance of the inset-fed rectangular microstrip antenna," *IEEE Transactions on Antennas and Propagation*, vol. 56, no. 10, pp. 3314-3318, 2008.

[19] ANSYS, HFSS. "High Frequency Electromagnetic Field Simulation http://www. ansys. Com," *ANSY S-HFSS*.

[20] F. Mutlu, "Design, Simulation, and Fabrication of Low-Cost Inkjet Antennas", Master Thesis, The Graduate School of Natural and Applied Sciences, Middle East Technical University, Ankara, 2016.

ISM 2.4 GHz Band Antenna Design for RF Energy Harvesting Systems

C. GOCEN[1,2], I. AKDAG[1,2], M.A. BELEN[3], P. MAHOUTI[4], A.KAYA[1,2] and M. PALANDOKEN[1,2]

[1] Department of Electrical and Electronics Eng. Izmir Katip Çelebi University, Izmir/Turkey,

cem.gocen@ikcu.edu.tr, ismail.akdag@ikcu.edu.tr, adnan.kaya@ikcu.edu.tr, merih.palandoken@ikcu.edu.tr

[2] Izmir Katip Celebi University Smart Factory Systems Application and Research Center, Izmir, Turkey

[3] Department of Electrical and Electronics Eng.Iskenderun Technical University Hatay,Turkey,
mali.belen@iste.edu.tr

[4] Department of Avionics Electronic, Yıldız Technical University, Istanbul, Turkey,

pmahouti@yildiz.edu.tr

***Abstract* - In this study, the design and optimization of a low profile, compact antenna that is easy to manufacture have been conducted for 2.4 GHz RF energy harvesting applications. The proposed antenna with the directivity of 2.33 dBi and radiation efficiency of 92.5% at 2.4 GHz resonance frequency is designed and numerically computed. The proposed antenna can be used in a wireless recharging element system for various on-body sensor applicances.**

***Keywords* – RF Energy Harvesting, ISM Band, Microstrip Antenna, 2.4 GHz, Rectifying Antenna**

I. INTRODUCTION

WITH today's technology era the power necessity of appliances has been greatly reduced because of low-power chips, as a result, some applicances need power in the order of mW and µW, such applicances could maintain their function of operation with energy harvested from RF sources. RF Energy harvesting is the collection and storage of ambient radio frequency energy for off-grid use if necessary [1]. There are numerous outdoor RF energy sources that emit RF power in all orientations, including TV and radio cell sites, cell phone towers, cell phones, and WLAN transceivers [2]. In RF energy harvesting, RF signals with frequencies ranging from 3 kHz to 300 GHz are used as the radio frequency input source signal to rectify the appropriate DC voltage rating [3].

According to a thorough literature analysis, there are numerous types, designs, and structures for RF energy harvesting system antennas. As a regenerable energy technique, RF energy harvesting has been studied in various applications such as wireless body sensor networks (WBSN), health IoT applicances, energizing applicances, recharging batteries, and so on [4-7]. The antenna in [8] operates at 2.45 GHz, has a 3 dBi gain, and measures 118 mm x 88 mm. [9-10] propose antennas for 2.4 and 2.45 GHz RF energy harvesting applications, respectively. In [11], a dielectric resonator antenna has been proposed and analysed with an RF to DC rectifying circuit.

The antenna design for RF energy harvesting applications in the ISM 2.4 GHz MHz band has been proposed in this paper. The antenna is modelled on a 1.6 mm thick FR-4 substrate for numerical calculations. Section 2 presents the proposed antenna's design parameters and leading factors. The proposed antenna's numerical calculation results have been presented in Section 3. Section 4 presents conclusion and recommendations.

II. RF ENERGY HARVESTING ANTENNA DESIGN

Figure 1 depicts the radiating and ground sections of the antenna structure with design specifications. The physical dimensions of the antenna are 44.4 x 29 mm, and the material thickness of the substrate is taken as 1.6 mm. The dielectric constant of the substrate is 3.38 and the loss tangent value is 0.0027. The proposed antenna design consists of a long feeding line in the top layer and three vertical ladder-shaped structures with different widths and lengths at the end of the feeding line. In addition, this ladder-shaped structure is placed at t1 on a structure feeding line in mirror symmetry. In the ground layer of the proposed design, the structure starting from the feeding direction and a longer structure that affects the resonance frequency and the return loss in the fully symmetrical position of the feeding line are placed.

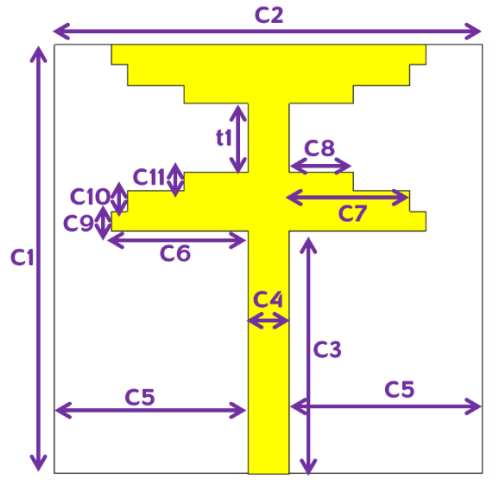

a

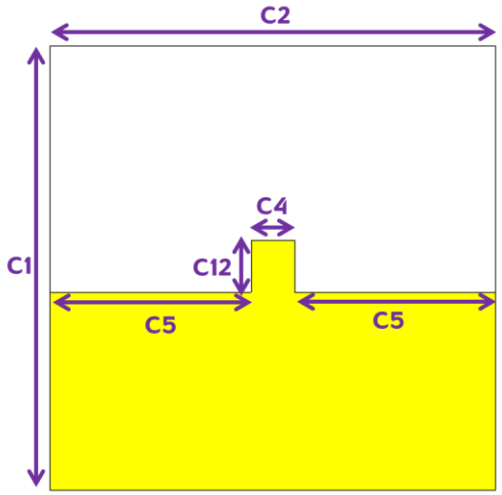

b

Figure 1: The proposed RF energy harvesting antenna structure design spesifications: (a) top and (b) bottom layers. (Dimensions (in mm); C1= C2=35, C3=19.8, C4=3.4, C5=15.8, C6=11.15, C7=9.85, C8=5.2, C9=1.5, C10=1.6, C11=1.7, C12=4.1, t1=5.6).

III. Numerical Analysis

The proposed antenna RF performance parameters are numerically calculated with transmission line matrix (TLM) and finite integration technique (FIT) based commercial 3D numerical computation program. The proposed antenna operating performance has been investigated in the 1 - 4 GHz range according to the numerical calculation results. The return loss value has been determined to be 30.3 dB at the 2.4 GHz center operating frequency, and the 10 dB bandwidth has been determined to be 330 MHz in the 2.23-2.56 GHz range. Figure 2 depicts the antenna return loss.

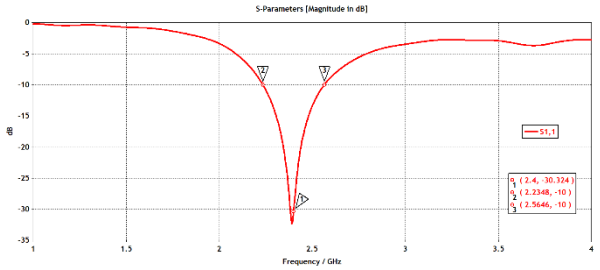

Figure 2: The antenna return loss.

In the radiating section of the antenna design, the t1 length, which separates the symmetrical ladder-shaped structures, has been changed parametrically in the numerical calculation and investigated through the antenna return loss. The numerical calculation results obtained are presented in Figure 3.

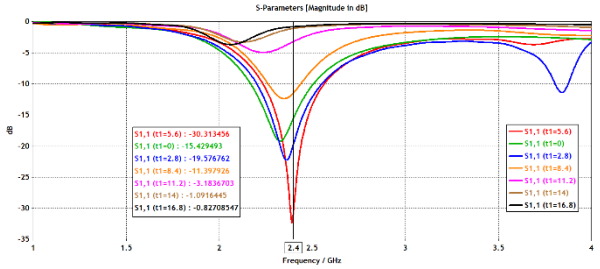

Figure 3: The antenna return loss at different t1 values.

Increasing or decreasing the t1 parameter has no clear effect on the return loss, this distance is optimally adjusted according to the ideal value range maximum operating bandwidth and resonant frequency of 2.4 GHz. Figure 4 illustrates the proposed antenna 3D radiation pattern. With a realized peak gain of 1.98 dBi at 2.4 GHz, the half-power beamwidth (HPBW) of the radiated field is 93 degrees in the az. plane. The proposed antenna directivity is 2.33 dBi, and its radiation efficiency is 92.5%.

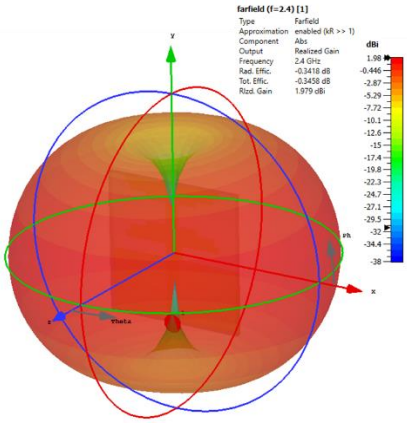

Figure 4: The 3D radiation pattern of antenna.

To examine the RF signal collecting performance of the proposed antenna design, a 50-ohm load has been placed between the antenna feeding points and energized by different magnitudes of plane waves from the opposite side. The collected RF power on the load in the proposed antenna from

sources of different magnitudes is calculated at the far field distance (500 mm) of resonance frequency and is shown in Figure 5.

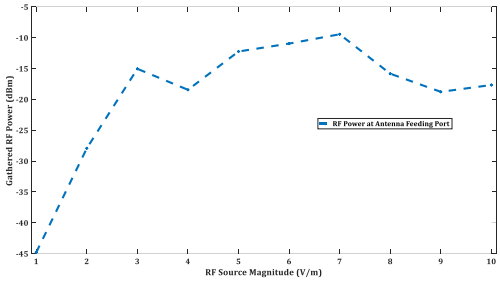

Figure 5: Collected RF power using with proposed antenna depending on 500 mm distance at different RF source magnitudes.

At the 1 V/m, 7 V/m, and 10 V/m RF signal magnitudes of the 2.4 GHz center operating frequency, -44.8, -9.4, and -17.6 dBm power have been obtained at the 500 mm distance, respectively.

IV. Conclusion

The proposed antenna has a total gain of 2.25 dBi at 2.4 GHz resonance frequency and indicates wide 10 dB bandwidth in the frequency range from 2.23 GHz to 2.56 GHz. According to the simulation results, the proposed antenna design has good operation performance parameters for 2.4 GHz RF energy harvesting applications with sufficient RF signal gathering capacity in a far-field distance from the freely available ambient RF electromagnetic field sources.

Acknowledgment

This work has been supported by Project 121N412 of TUBITAK (Scientific and Technological Research Council of Turkey).

References

[1] [1] Jeremy Bickerstaffe, Energy Harvesting, SAGENTIA, Steve Beeby, in "Energy Harvesting Systems", published by Springer, © Sagentia 2011.

[2] [2] M. Palandoken, C. Gocen, A. Kaya, F. Gunes, C. Baytore, F.C. Can, A Novel Split-Ring Resonator and Voltage Multiplier Based Rectenna Design for 900 MHz Energy Harvesting Applications, Radioengineering, 27 (3) (2018), pp. 711-717.

[3] [3] X. Lu, P. Wang, D. Niyato, D. I. Kim and Z. Han, "Wireless Networks with RF Energy Harvesting: A Contemporary Survey," in IEEE Communications Surveys & Tutorials, vol. 17, no. 2, pp. 757-789, Second quarter 2015.

[4] [4] Ouda, M.H., Arsalan, M., Marnat, L., Shamim, A., and Salama, K . N., "5.2-GHz RF Power Harvester in 0.18-µm CMOS for Implantable Intraocular Pressure Monitoring," IEEE Trans. Microw. Theory Tech., vo1.61, no.5, pp.2177-2184, May 2013.

[5] [5] S. Kim, R. Vyas, J. Bito, K. Niotaki, A. Collado, A. Georgiadis, and M. M. Tentzeris, "Ambient rf energy-harvesting technologies for self-sustainable standalone wireless sensor platforms," Proc. IEEE, vol. 102, no. 11 , pp. 1649- 1666, Nov. 2014.

[6] [6] Z. Zeya and R. K. Badhai, "RF Energy Harvesting: Design of Printed Hexagon Antenna for ISM Band 2.4 GHz," 2021 10th International Conference on Internet of Everything, Microwave Engineering, Communication and Networks (IEMECON), 2021, pp. 01-05.

[7] [7] A. A. Skuridin, A. A. Yelizarov, I. V. Nazarov, E. A. Zakirova and D. M. Ikonnikova, "A Dual-Band Wi-Fi Rectifying Antenna for RF Energy Harvesting in Cyber Physical Systems," 2021 Systems of Signal Synchronization, Generating and Processing in Telecommunications (SYNCHROINFO, 2021, pp. 1-4.

[8] [8] A. Eid, J. Costantine, Y. Tawk, A. H. Ramadan, M. Abdallah, R. ElHajj, R. Awad, I. B. Kasbah, "An Efficient RF Energy Harvesting System" In Proc. 11th Eur. Conf. Antennas and Propag (EuCAP) (2017) 896-899.

[9] [9] Palandöken, M. (2016), Microstrip antenna with compact anti-spiral slot resonator for 2.4 GHz energy harvesting applications. Microw. Opt. Technol. Lett., 58: 1404-1408.

[10] [10] Q. Awais, Y. Jin, H. T. Chattha, M. Jamil, H. Qiang, B. A. Khawaja."A compact rectenna system with high conversion efficiency for wireless energy harvesting" IEEE Access, Vol. 6, pp. 35857-35866, June 2018.

[11] Agrawal, S., Gupta, R.D., Parihar, M.S. and Kondekar, P.N., "A wideband high gain dielectric resonator antenna for RF energy harvesting application." AEU-International Journal of Electronics and Communications 78, pp. 24-31, 2017.

Thermal Behavior Assessment of XLPE Insulated MV Power Cables under Different Conditions

C.C. UYDUR

Trakya University, Edirne/Turkey, ccagdasuydur@trakya.edu.tr

***Abstract* - Population growth in central settlements necessitates the transmission and distribution of electrical energy from underground. Changes that may happen in ambient conditions during the use of cables cause the cables to breakdown, with a negative effect on the temperature change of the cable and therefore on the current carrying capacity. In this study, the effects of external factors and possible defects in cable insulation on the temperature change in the cable during the installation of XLPE cables were investigated. Thermal analysis was carried out using the Finite Element Method based COMSOL Multiphysics program, considering the presence of air gaps and water droplets in the cable insulation, the change in soil surface temperature and the change of cable burial depth in an XLPE insulated cable with a 20.3/35 kV, 240 mm^2 conductor cross section. It has been observed that the soil surface temperature affects the cable directly and linearly. It has been determined that the cable burial depth leads to different results and the qualification of the defects in the cable insulaton is important.**

***Keywords* – Cable, Electric Distribution, Finite Element Method, Thermal Assessment, XLPE.**

I. INTRODUCTION

THERMAL monitoring of underground cables is important for determining the current carrying capacity (ampacity). The ampacity of the power cables should be determined according to operating temperature that the insulation material can withstand [1]. Accurate calculation of current carrying capacity allows a power cable to be used with maximum efficiency. Since underground cables are much more expensive than overhead lines in terms of production and installation costs, they should be operated at the highest current they can transmit [2].

The ampacity of the cable depends not only on the cable structure and the materials used in the cable, but also on the way it is laid and the ambient conditions [3]. This situation reveals the necessity of examining many thermal parameters in the analysis. Some of those; thermal conductivity of the soil and bedding material, the surface temperature of the soil, the laying depth of the cables, the way of laying the cables inside the pipe or directly burying them in the ground.

There are many studies in the literature on the thermal analysis of cables. For example, Leon studied the change in cable ampacity by changing the amount, size and placement of bearing material with different thermal resistance values [4]. Olsen has developed an algorithm for dynamically calculating temperature of power cables depending on the changes in soil moisture content and thermal capacity [5]. Desmet made an experimental and simulative thermal analysis of underground cables placed in parallel for different loading conditions and various laying styles [6]. Wang investigated the effect of external heat source, spacing between wires and number of wires on ampacity [7].

Oclon et al. investigated the effect of bedding materials to be used in the laying of underground cables on the increase in ampacity [8]. Numerous studies have been carried out with the creation of multi-layered bedding materials. Vallaro et al. studied the effect of inhomogeneous bedding materials on the temperature of the underground cable [9-11].

In this study, thermal analysis of 20.3/35 kV, single core, XLPE insulated medium voltage (MV) underground cables with 240 mm^2 conductor cross section, which is widely used in the electricity distribution network in Turkey, was carried out. Considering the situations that may happen during the operation of MV power cables, three different scenarios were created for thermal analysis. In this context, thermal analysis simulation was carried out for the presence of water-air in the cable insulator, the change of burial depth and the change of soil surface temperature. COMSOL Multiphysics software was used during the simulation study.

II. METHODOLOGY

In this section, information is given about the theoretical background of the study and the parameters of the cable used in the simulation study are shared.

A. Theory

The temperature distribution of the system examined in this study can be obtained using a two-dimensional heat transfer model. The heat conduction equation is shared in Equation 1 [12].

$$k \cdot \left(\frac{\partial^2 T}{\partial x^2} + \frac{\partial^2 T}{\partial y^2}\right) + q = C_p \cdot \frac{\partial T}{\partial t} \quad (1)$$

Here, "T" is the temperature (K), "k" is the thermal conductivity of the materials (W/K.m), "q" is the heat produced (W/m^3), "C_p" is the specific heat capacity of the materials for a constant temperature (J/m^3.K), "x" and "y" represent system coordinates. Boundary conditions for the soil surface were

determined with the help of the Equation 2 and 3 [13].

$$T = T_{soil} \tag{2}$$

$$k \cdot \frac{\partial T}{\partial n} = h \cdot (T - T_{\infty}) \tag{3}$$

Here, "T" is the surface temperature (K), "h" is the convective heat transfer coefficient (W/m^{2}K), and "T_∞" is the ambient temperature (K). The convective heat transfer coefficient (h) is calculated as in Equation 4 depending on the wind speed [14].

$$h = 7.371 + 6.43 \cdot v^{0.75} \tag{4}$$

It has been determined as 20.155 W/m^{2}K with the assumption of 2.5 m/s wind speed on the soil surface.

B. Material

In this section, information is given about the parameters of the power cable samples used in the simulation study and the thermal conductivity values of the materials.

In this study, analyzes were carried out on 20.3/35 kV, single core, XLPE insulated MV power cables with 240 mm^2 conductor cross section. In Table 1, the parameters of the cables and in Table 2, the thermal conductivity values of the materials are shared.

Table 1: Specifications of Cable Sample [15,16]

Parameter	Cable Sample
Rated voltage (kV)	35
Conductor cross section (mm^2)	240
Diameter of conductor (mm)	18.8
Semiconductor diameter (mm)	20
Outer diameter of insulation (mm)	38
Outer diameter of sheath (mm)	46
Shield cross section (mm^2)	25
Ampacity (A)	576

Table 2: Thermal conductivity values of materials [15,16]

Material	Thermal Conductivity (W/m.K)
Copper	400
XLPE	0.2857
PVC	0.48
Bedding Material	1
Soil	1

The scheme showing the process of laying the cables underground is presented in Figure 1. Under ideal conditions, the burial depth is 0.7 m.

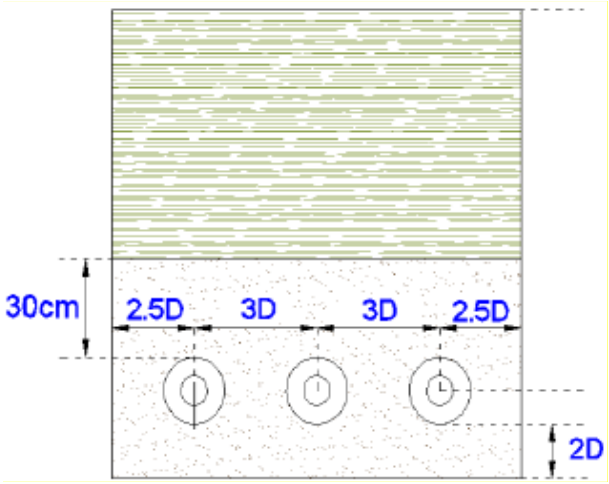

Figure 1: Scheme of underground burial application

III. SIMULATION ANALYSIS

In this section, the results obtained from the simulation study are shared under sub-headings based on the scenarios created.

First of all, thermal analysis study was carried out for XLPE insulated cable underground under ideal conditions under rated current. Reference values; The burial depth of the cables was determined as 0.7 m, surface temperature of soil was 20°C, the thermal conductivity was determined as 1 W/K.m for soil and 1 W/K.m for bedding material. Under these conditions, if the middle cable reaches the maximum operating temperature of 90 °C (363.15 K), the ampacity value is calculated as 576 A, depending on the heat produced.

The result of the simulation study for the ideal condition is shared in Figure 2.

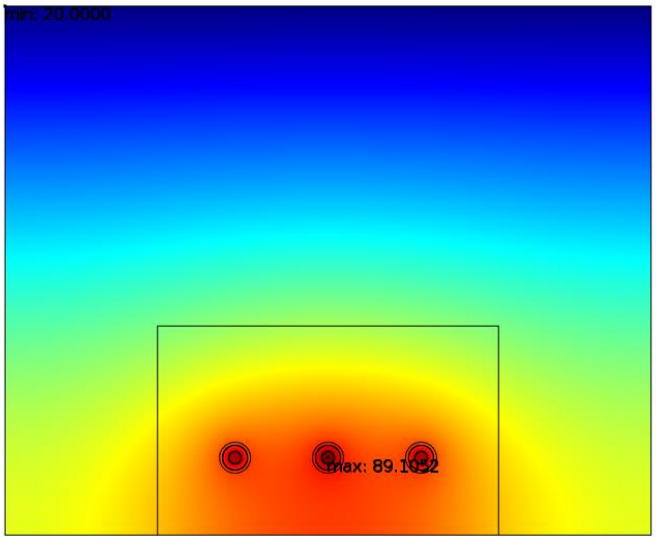

Figure 2: Results of thermal analysis in ideal condition

Figure 2 shows that the cable conductor temperature is 89.105 °C under ideal conditions. This situation coincides with the catalog values published by cable manufacturers.

A. *Scenario 1: Effect of Outdoor Temperature*

In this scenario, thermal analysis was performed for different soil surface temperatures in order to examine the effect of the variation of soil surface temperature on the thermal behavior of the cable. The scenario consists of two situations. In the first case, the soil surface temperature was accepted as 0 ℃, while in the second case it was accepted as 40 ℃. Results of thermal analysis are presented in Figure 3 and Figure 4, respectively.

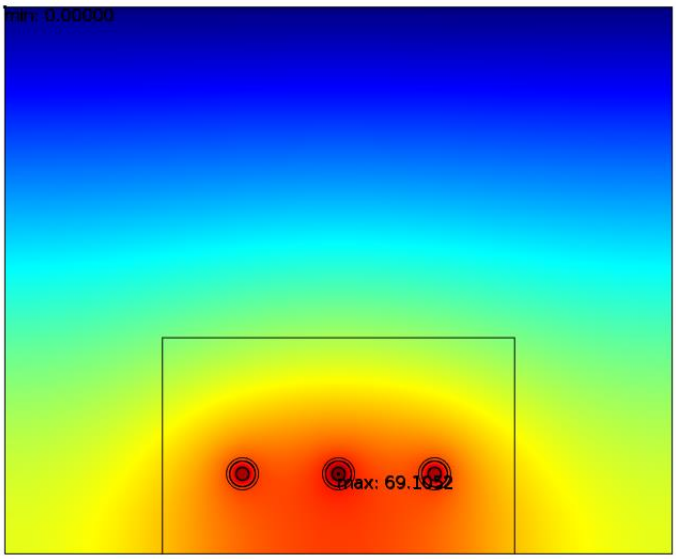

Figure 3: Results of thermal analysis when surface temperature of soil is 0 ℃

According to the analysis results in Figure 3, it is seen that the conductor temperature, which was 89.105 ℃ in the ideal situation, decreased to 69.105 ℃. A similar situation was also obtained from the analysis results in Figure 4. It was determined that with the increase of soil surface temperature, the conductor temperature increased linearly and reached 109.105 ℃.

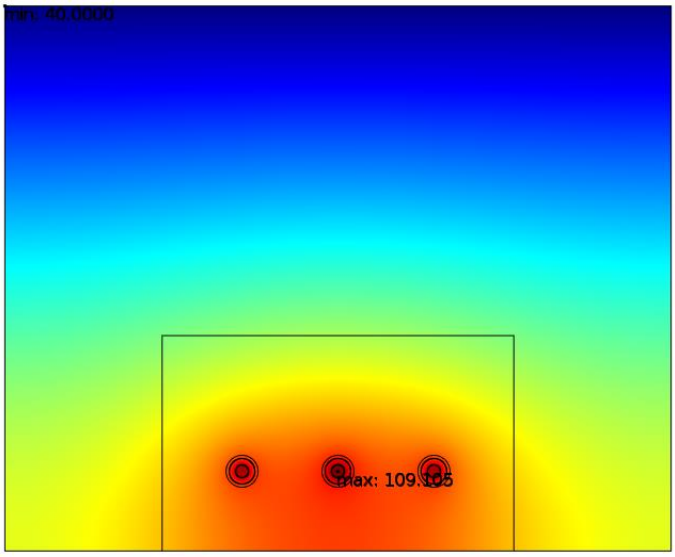

Figure 4: Results of thermal analysis when surface temperature of soil is 40 ℃

The surface temperature of the soil is a thermal parameter accepted as the boundary condition in the model created. As the soil surface temperature decreases, it creates a cooling effect on the cable conductor. The relationship between them is directly proportional. The cooler the soil, the more it cools the conductor.

B. *Scenario 2: Effect of Burial Depth*

One of the important parameters affecting the ampacity value that MV power cables can be transmitted at maximum operating temperature is the burial depth of the cables.

While the burial depth is 0.7 m in the ideal case, thermal analysis was performed using 0.5 m and 1 m values in this scenario. Thus, the effect of burial depth on the thermal behavior of the cables will be revealed. Thermal analysis results are presented in Figure 5 and Figure 6, respectively.

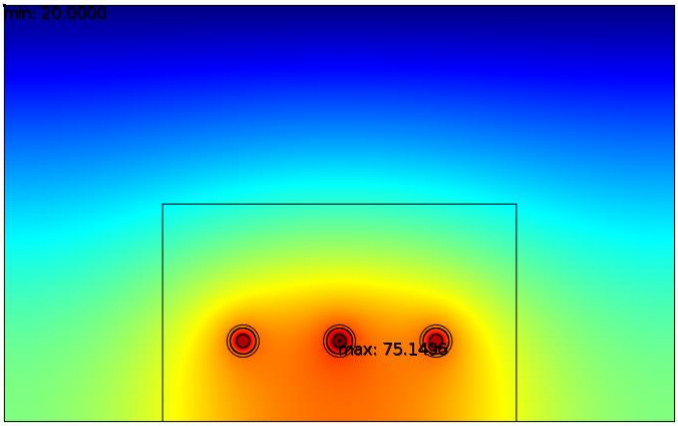

Figure 5: Results of thermal analysis when burial depth is 0.5 m

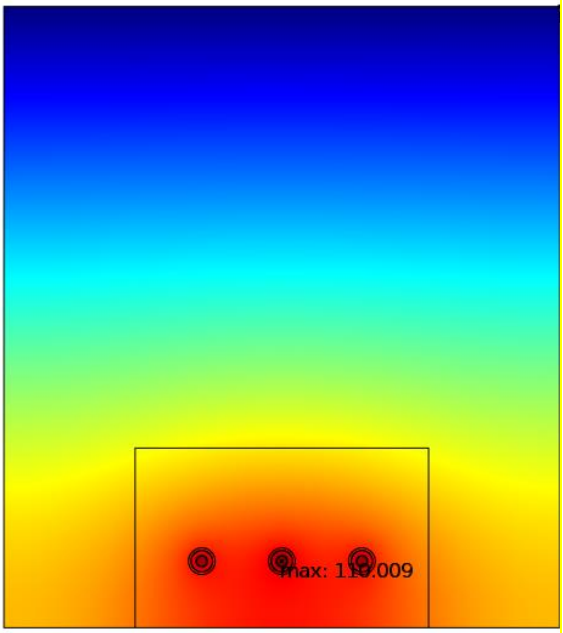

Figure 6: Results of thermal analysis when burial depth is 1 m

When the thermal analysis results in Figure 5 are examined, it is seen that the cable conductor reaches a temperature of 75.15 ℃ when the MV power cables are buried close to the ground surface. In the analysis results in Figure 6, it was determined

that when the burial depth is increased, the cable conductor heats up more and becomes 110 ℃.

As a result of the thermal analyzes carried out in this scenario, the effect of burial depth on the thermal behavior of cable conductor was clearly revealed. It has been clearly determined that the relationship between the burial depth and the thermal behavior of cable is not linear.

C. Scenario 3: Effect of Contaminants in Cable Insulation

Finally, scenario 3 was created to examine the thermal behavior of the cable in case of contaminant with a diameter of 0.5 mm in cable insulation material.

In this scenario, two different situations are examined. The thermal analysis was carried out by taking into account the presence of 0.5 mm diameter air gap in the cable insulation material in the first variation and the 0.5 mm diameter water droplet in the second variation. Thermal analysis results are presented in Figure 7 and Figure 8.

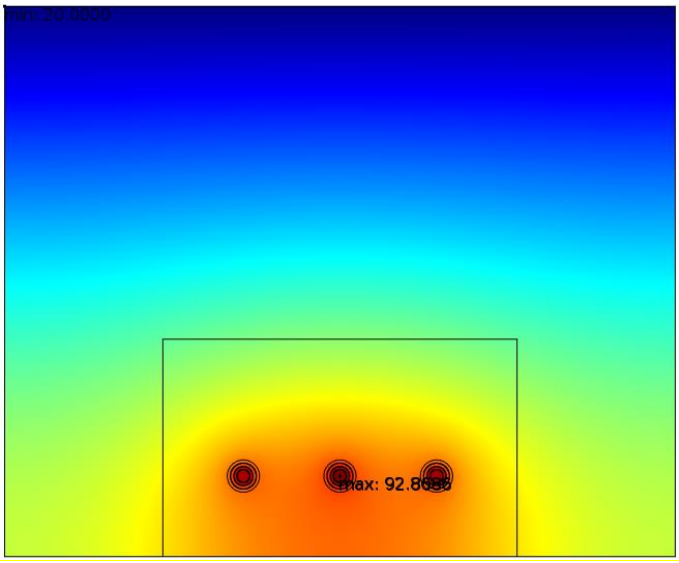

Figure 7: Results of thermal analysis when there is 0.5 mm air gap in the cable insulation

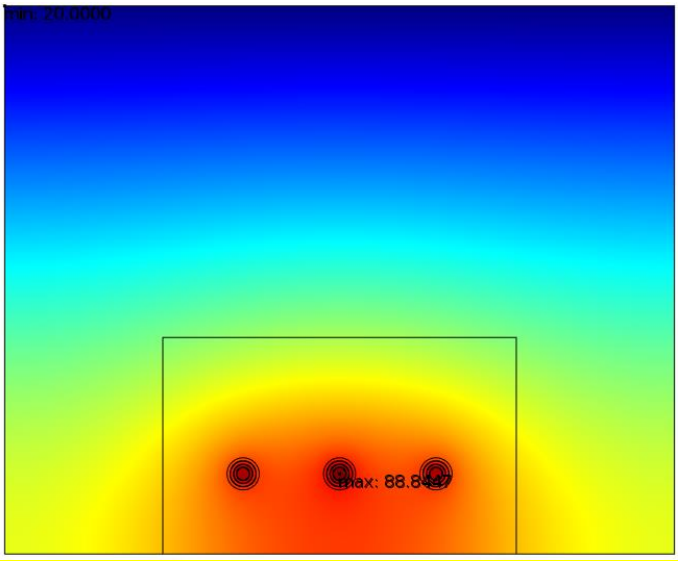

Figure 8: Results of thermal analysis when there is 0.5 mm water droplet in the cable insulation

If there is an air gap in the cable insulation, it is seen that the cable conductor temperature increases by 3.77 ℃ to 92.87 ℃. In the case of a water droplet of the contaminant in the cable insulation, it was determined that the cable conductor temperature decreased by 0.25 ℃ and was 88.85 ℃.

It is seen that the presence of contaminant in the cable insulation definitely affects the thermal behavior of the cable, but this situation depends on the material type. In this scenario, as a result of the analyzes made for contaminants such as air and water, it was determined that the thermal behavior of cable changed, but at a negligible level.

D. Evaluation of Thermal Analysis Results

In this section, thermal analysis results obtained from three different scenarios are evaluated comparatively. The results of the thermal analyzes carried out in three different scenarios in the study are presented in Table 3.

Table 3: Results of simulation analysis

Scenario	Condition	Temperature (℃)
-	Ideal	89.105
1	Soil Temperature: 0 ℃	69.105
1	Soil Temperature: 40 ℃	109.105
2	Burial Depth: 0.5 m	75.15
2	Burial Depth: 1 m	110
3	Contaminant: Air	92.87
3	Contaminant: Water	88.85

Considering the data presented in Table 3, it has been determined that the thermal analyzes made in ideal conditions match the catalog values published for MV power cables. In the thermal analyzes examining the soil surface temperature change, it has been determined that the relationship between soil surface temperature and cable conductor temperature is directly proportional. It has been revealed that careful attention should be paid to the determination of the burial depth in order not to adversely affect the ampacity of MV power cables. In addition, it has been observed that the presence of contaminant in the cable insulation directly affects the temperature of the cable. But its dependence on material type has been proven.

IV. CONCLUSION

In this study, thermal analysis of MV cables which is widely used in the electricity distribution network in Turkey, was carried out.

With the conducted study, it has been determined that as the burial depth of MV power cables increases, the conductor temperature increases and therefore ampacity decreases. For this reason, the importance of determining the ideal burial depth, taking into account other thermal factors, has emerged in order for the cables to be operated effectively and correctly.

In the study carried out to determine the effect of surface temperature, it was seen that the effect of the change in surface temperature on the temperature of cable conductor was The

relation between them is directly proportional. The simulation results revealed that the conductor temperature also showed a constant increase when the surface temperature was increased at equal intervals.

It is a surprising result that 0.5 mm diameter air gap in the cable insulaton has an effect on increasing the conductor temperature, while a water droplet with 0.5 mm diameter has a slight effect on decreasing its temperature.

In future studies, it is planned to examine the effect of the geometry of contaminants in the cable insulaton material on the thermal behavior of the cable.

REFERENCES

[1] L. Yanmu, S. Wenrong, "Coupled Electromagnetic-Thermal Modeling the Temperature Distribution of XLPE Cable", *Power and Energy Engineering Conference,* 2009, pp. 1-4.

[2] M. Al-Saud, "Improved Assessment of Power Cable Thermal Capability in Presence of Uncertainties", *Power and Energy Engineering Conference (APPEEC),* 2012, pp. 31-34.

[3] Y. Shen, H. Niu, "Promoting Cable Ampacity by Filling Low Thermal Resistivity Medium in Ducts", *Power and Energy Engineering Conference (APPEEC),* 2013, pp. 41-44.

[4] F. Leon, G. Anders, "Effects of Backfilling on Cable Ampacity Analyzed With the Finite Element Method", *IEEE Transactions on Power Delivery*, vol. 23, pp. 537-543, 2008.

[5] R. Olsen, G. Anders, "Modelling of Dynamic Transmission Cable Temperature Considering Soil-Specific Heat, Thermal Resisitivity, and Precipitation", *IEEE Transactions on Power Delivery*, vol. 28, pp. 1909-1917, 2013.

[6] J. Desmet, D. Putman, "Thermal Analysis of Parallel Underground Energy Cables", *18th International Conference on Electricity Distribution (CIRED)*, 2005.

[7] Y. Wang, S. Grzybowski, "Analysis of Influential Factors on the Underground Cable Ampacity", *Electrical Insulation Conference (EIC)*, 2011, pp. 430-433.

[8] P. Oclon, P. Cisek, M. Pilarczyk, D. Taler: "Numerical simulation of heat dissipation processes in underground power cable system situated in thermal backfill and buried in a multilayered soil", *Elsevier Energy Conversion and Management*, vol. 95, pp. 352-370, 2015.

[9] R.L. Vollaro, L. Fontana, A. Vallati: "Thermal analysis of underground electrical power cables buried in non-homogeneous soils", *Applied Thermal Engineering*, vol. 31, pp. 772-778, 2011.

[10] R.L. Vollaro, L. Fontana, A. Vallati: "Experimental study of thermal field deriving from an underground electrical power cable buried in non-homogeneous soils", *Applied Thermal Engineering*, Vol. 62, No. 2, 2014.

[11] F. Salata, F. Nardecchia, A.L. Vollaro, F. Gugliermetti: "Underground electric cables a correct evaluation of the soil thermal resistance", *Applied Thermal Engineering*, vol. 78, pp. 268-277, 2015.

[12] H.C. Huang, A.S. Usmani, *Finite element analysis for heat transfer: theory and software*, Springer Science & Business Media, 2012.

[13] C.C. Hwang, J.J. Chang, H.Y. Chen, "Calculation of ampacities for cables in trays using finite elements", *Electric Power Systems Research*, Vol. 54, pp. 75–81, 2000.

[14] M. A. Hanna, A. Y. Chikhani and M. M. A. Salama, "Thermal analysis of power cables in multi-layered soil. I. Theoretical model," in *IEEE Transactions on Power Delivery*, vol. 8, no. 3, pp. 761-771, July 1993, doi: 10.1109/61.252604.

[15] C.C. Uydur, O. Arikan and O. Kalenderli, "The Effect of Insulation Defects on Electric Field Distribution of Power Cables," *2018 IEEE International Conference on High Voltage Engineering and Application (ICHVE)*, 2018, pp. 1-4, doi: 10.1109/ICHVE.2018.8641936.

[16] C.C. Uydur, O. Arikan and O. Kalenderli, "The Effect of Insulation Defects on Electric and Magnetic Field Distributions in Power Cables", Tehnički vjesnik, vol.28, no. 4, pp. 1152-1160, 2021. [Online]. https://doi.org/10.17559/TV-2020020508423

DETERMINATION OF THE SAR VALUES OF THE ELECTROMAGNETIC FIELD EMITTED FROM THE PATCH ANTENNAS AT 900 MHZ AND 1800 MHZ FREQUENCIES

U.SORGUCU

Nevsehir Haci Bektas Veli University, Nevsehir/Turkey, sorgucu@nevsehir.edu.tr

***Abstract* - The effects of electromagnetic radiation emitted from mobile phones on human health continue to be an important topic of public debate. Due to the fact that the temperature increase in the tissues is felt by mobile phone users, the concern that GSM frequencies may be dangerous is considered in terms of public health day by day. In this study, a numerical analysis of the specific absorption rate (SAR) was presented and the temperature variation in the head region was demonstrated. While doing this, two separate antennas are designed to mimic cell phone radiation at frequencies of 900 MHz and 1800 MHz. Two separate antennas were applied to the head models, which imitate the electrical properties of the human head, from a distance of 3 cm. Then, the highest SAR values for both frequencies were observed as 0.0125 W/kg and 0.0390 W/kg. Antenna models designed to have these values below international standards have shown that they are successful.**

***Keywords* – GSM, SAR, 900MHz, 1800MHz, Thermal Effect.**

I. INTRODUCTION

ELECTROMAGNETIC fields have become one of the most important problems of today. The fact that electromagnetic field are introduced as an important problem that remains on the agenda is due to the increasing number of studies in this field. As a matter of fact, with every study carried out, another effect of electromagnetic fields comes to light. Although electromagnetic fields are a subject that is studied in a very wide spectrum, most of the studies are concentrated in the 900 MHz and 1800 MHz bands used by mobile phones. [1-3]. The concentration of the studies in this band is due to the high increase in the use of mobile phones in the last 2 decades. Because of the widespread use of mobile phones, a considerable amount of research has focused on analyzing the relationship between mobile phone antennas and the human head. [4,5]. Although some definite results were obtained as a result of these studies, many studies whose results could not be confirmed were also reported. For this reason, it cannot be argued that electromagnetic fields are harmful with certainty. However, it has been recommended by international organizations that it is necessary to take precautionary (preventive) measures. Recommendations of organizations such as IEEE, FCC, ICNIRP and CENELEC, which can be considered as influential organizations in this sense, can be examined in [6-9]. Taking into account the relevant reports of international organizations, Europen Coincil also published a recommendation and emphasized the importance of the issue [10].

In this study, a simulation was made to observe the thermal change caused by GSM frequencies in the head region. In this context, two different models were established for the most frequently used GSM frequencies, 900 MHz and 1800 MHz, and the SAR values created by the antenna outputs of the same power were determined.

II. METHODOLOGY

In order to explain the thermal relationship between electromagnetic fields and biological mass, two clear pieces of information are needed. The first of these relates to the radiation source, such as antenna type, applied power, and applied distance. The second is to determine which tissue this radiation will affect. An accurate research cannot be carried out without determining these variables.

In this study, patch antenna was chosen as the antenna type. 3 cm was chosen as the application distance. The head region was chosen as the tissue exposed to the Electromagnetic Field. In order to present the relationship between all these variables, the SAR variable was determined as a standard. As a matter of fact, the SAR value is an international variable and shows the electromagnetic energy absorbed in the tissue. SAR is used not only for mobile phones, but also to describe the electromagnetic energy emitted by many electronic devices such as laptops and modems. SAR can be defined as absorption per unit weight (W/kg).

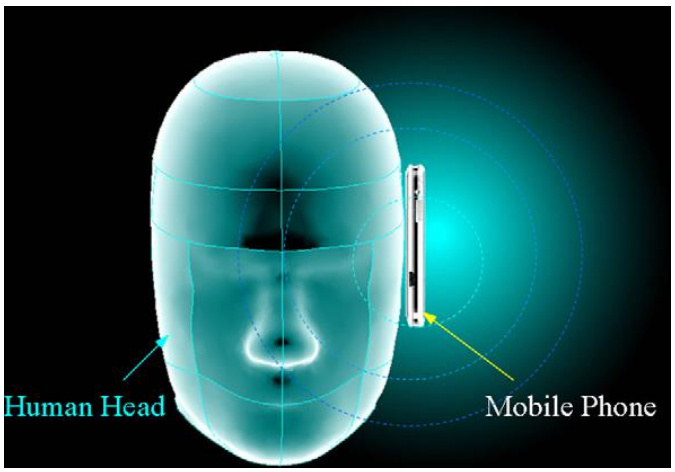

Figure 1. Human head model subjected to mobile phone radiation.

In order to determine the SAR value in the head, the model structure shown in Figure 1 was established. In this structure, a head model imitating the electrical properties of the human head and a patch antenna imitating a mobile phone were evaluated together.

III. ANTENNA DESIGN AND SAR ANALYSIS

Patch antennas are preferred gradually every day. It is becoming more and more common due to the fact that it is produced simply by printing on a circuit board. Microstrip antennas are also frequently used in applications in the microwave band. Patch antennas are preferred both in the scientific world and in the commercial side due to their advantages such as low cost and easy production.

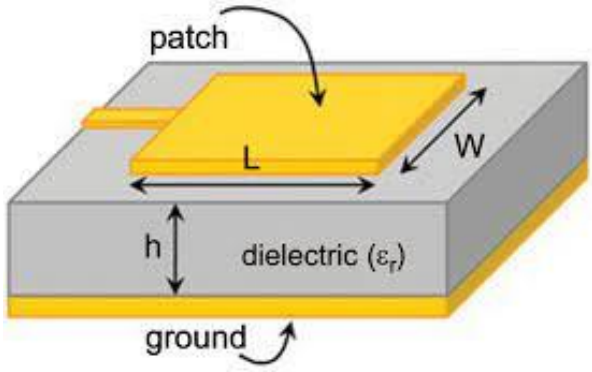

Figure 2 Patch Antenna Design [11]

Patch antennas are usually made of highly conductive metal (generally copper). The patch is L long, W wide and sits on a substrate of thickness h with dielectric constant. In antenna design, the plane structure of the substrate or the thickness of the microstrip are not the most important parameters. In general, the substrate height will be much smaller than the desired wavelength. However, much smaller than twenty-five thousandths of a wavelength should not be preferred, otherwise antenna efficiency will decrease.

In order to briefly explain the theory behind patch antennas, the width of the rectangular patch can be started from W.

$$w = \frac{1}{2f_c\sqrt{\mu_0\varepsilon_0}}\sqrt{\frac{2}{\varepsilon_r+1}} = \frac{c}{2f_c}\sqrt{\frac{2}{\varepsilon_r+1}} \quad (1)$$

Here "c" is the speed of light, "f_r" is the resonance frequency, "ε_r" is the dielectric constant of the cavity, "μ_0" is the magnetic permeability of the cavity. The actual length "L" of the rectangular patch is shown in equation 2.

$$L = \frac{c}{2f_r\sqrt{\varepsilon_{eff}}} - 2\Delta L \quad (2)$$

Here ε_{eff} is the effective dielectric constant. ε_{eff} and ΔL is given in equation (3) and (4) respectively.

$$\varepsilon_{ff} = \frac{\varepsilon_r+1}{2} + \frac{\varepsilon_r-1}{2}\left[1+12\frac{h}{W}\right]^{-1/2} \quad (3)$$

$$\Delta L = 0.412h\frac{(\varepsilon_{eff}+0.3)(\frac{W}{h}+0.264)}{(\varepsilon_{eff}-0.258)(\frac{W}{h}+0.8)} \quad (4)$$

In the light of this information, the dimensions of the dielectric material are presented in Equation (5) and Equation (6).

$$W_m = 6h + W \quad (5)$$

$$L_m = 6h + L \quad (6)$$

In this study, Patch antennas were designed in two different geometries. The first of these designs broadcasts at 900 MHz frequency. The second one broadcasts at 1800 MHz frequency. S Parameters of patch antennas broadcasting at 900 MHz and 1800 MHz frequencies are presented in Figure 3. The dimensions of the antennas designed for 900 MHz and 1800 MHz are also presented below the figure.

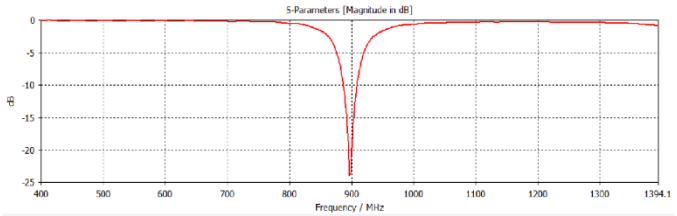

a) S parameter of the designed 900 MHz antenna
(W=95mm-L=77.5mm) (Drive Power=0.5w) (Dielectric material Wm=110mm – Lm=110mm)

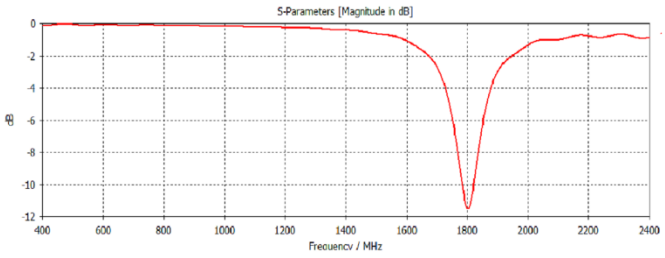

b) S parameter of the designed 1800 MHz antenna
(W=49.3mm-L=38.4mm) (Drive Power=0.5w) (Dielectric material Wm=80mm – Lm=80mm)

Figure 3. S parameter responses and antenna dimensions for the designed patch antennas

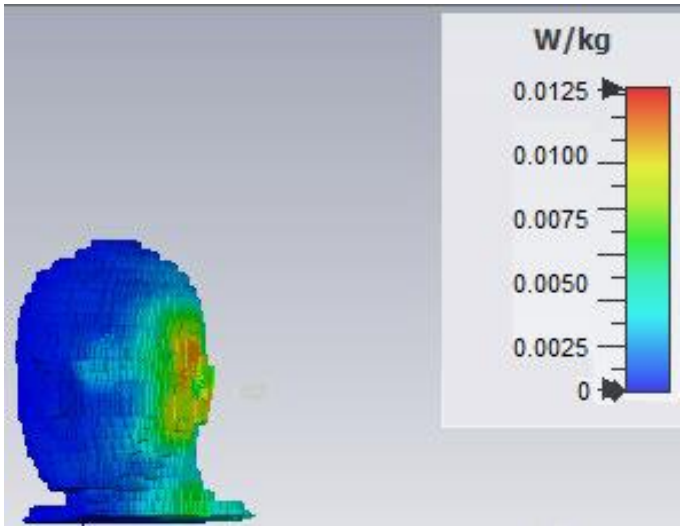

SAR graph for 900 MHz

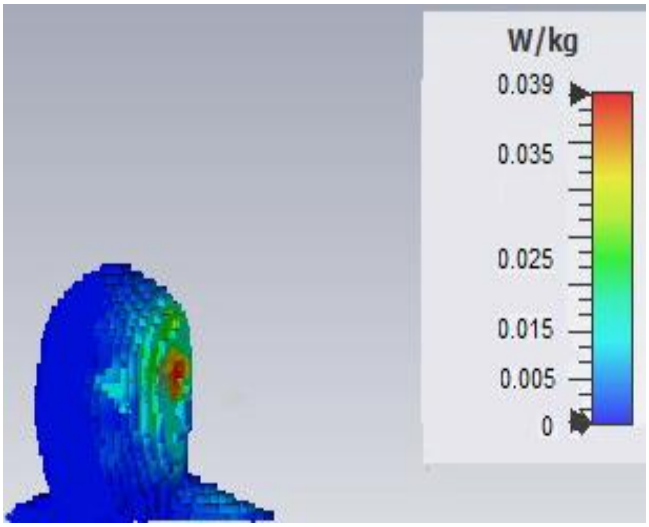

SAR graph for 1800 MHz

Figure 4. Application of a 0.5W patch antenna at 900MHz and 1800 MHz frequencies from a distance of 3cm

SAR exposure simulation for an adult exposed to a 900 MHz patch antenna from a distance of 3 cm was performed with the CST Studio program. The model used in this study represents a 40-year-old woman with the Donna voxel in CST Studio. The SAR value obtained when the phone is positioned 3 cm from the head-ear part of a 40-year-old female model is presented in Figure 4. It was observed that the maximum SAR value occurred in the ear region. The maximum SAR value acquired is set at 0.0125W/kg.

SAR exposure simulation for an adult exposed to a 1800 MHz patch antenna from a distance of 3 cm was performed with the CST Studio program. The resulting SAR value is presented in Figure 4. It was observed that the maximum SAR value arise in the ear region. The maximum SAR value obtained is 0.039 W/kg. As can be seen, higher SAR value was obtained at 1800 MHz.

As can be seen in Figure 4, the obtained SAR values are well below the international standard value of 1.6W/kg. This means that it is very important to protect a small distance like 3 cm in calls made with a mobile phone

IV. CONCLUSION

In this study, the thermal effect of electromagnetic fields emitted at two different frequencies on a realistic human head model is shown. It is shown by the figures that the highest thermal increase is observed in the region where the head model is closest to the mobile phone. Simulation results have shown that a distance of 3 cm has a very protective effect. At the same time, the observation of a higher SAR value at 1800MHz also shows that the temperature increase in the skin area due to the increased frequency is correlated. The study has shown that public concern can be minimized by increasing the diversity of studies in this direction. Due to the widespread use of 3G, 4G and 5G technologies, the effect of different frequencies will be examined more comprehensively as future works.

REFERENCES

[1] A., Kumar, S., Kaur, S., Chandel, H. P., Singh, D. R. Batish,, and R. K. Kohli, "Comparative cyto-and genotoxicity of 900 MHz and 1800 MHz electromagnetic field radiations in root meristems of Allium cepa," *Ecotoxicology and environmental safety*, vol 188, pp.109786, 2020

[2] M., Gunes, K., Ates, B., Yalcin, S., Akkurt, S., Ozen, and B. Kaya, "An Evaluation of the Genotoxic Effects of Electromagnetic Radiation at 900 MHz, 1800 MHz, and 2100 MHz Frequencies with a SMART Assay in Drosophila melanogaster," *Electromagnetic Biology and Medicine*, vol. 40(2), pp. 254-263, 2021.

[3] M., Akdag, S., Dasdag, F., Canturk, and M. Z. Akdag. "Exposure to non-ionizing electromagnetic fields emitted from mobile phones induced DNA damage in human ear canal hair follicle cells," *Electromagnetic biology and Medicine*,vol. 37(2), pp. 66-75, 2018.

[4] M., Benova, J., Mydlova, Z., Psenakova and M. Smondrk, "SAR Evaluation in Human Head Models with Cochlear Implant Near PIFA Antenna Inside a Railway Vehicle," *In Information Technology in Biomedicine* (pp. 289-300). Springer, ChamG. R. Faulhaber, "Design of service systems with priority reservation," in *Conf. Rec. 1995 IEEE Int. Conf. Communications*, pp. 3–8. 2021

[5] D., Bhargava, P., Rattanadecho, and T. Wessapan,. "The effect of metal objects on the SAR and temperature increase in the human head exposed to dipole antenna (numerical analysis)". Case Studies in Thermal Engineering, vol. 22, pp. 1-12, 2020

[6] Questions and Answers about Biological Effects and Potential Hazards of Radiofrequency Electromagnetic Fields", Federal Communications Commission Office of Engineering & Technology, OET Bulletin 56, Fourth Edition, August 1999.

[7] ICNIRP Guidelines, "Guidelines for limiting exposure to time-varying electric, magnetic and electromagnetic fields (up to 300 GHz)," Health Phys., vol. 74, no. 4, pp. 494–522–, 1998.

[8] CENELEC, "Exposition humaine aux champs electromagnetiques Hautes-Frequences (10 KHz à 300GHz),", Rep. ENV 50 166-2, Jan. 1995.

[9] IEEE Standart for Safety Levels with Respect to Human Exposure to Radio Frequency Electromagnetic Fields, 3 kHz to 300 GHz, IEEE C95.1, 1999.

[10] European Council, COUNCIL RECOMMENDATION of 12 July 1999 on the limitation of exposure of the general public to electromagnetic fields (0 Hz to 300 GHz), Official Journal of the European Communities, L 199/59, 1999/519/CE, July 1999.

[11] http://www.eurekaselect.com/article/91521 (Avaible at 26/10/2022)

Pulse Density Modulation Controlled High Frequency Resonant Converter for Wireless Power Transfer Systems

C. KUTLU[1] and H. ÖZBAY[1]

[1] Bandirma Onyedi Eylul University, Balikesir/Türkiye, cem.kutlu@ogr.bandirma.edu.tr
[1] Bandirma Onyedi Eylul University, Balikesir/Türkiye, hozbay@bandirma.edu.tr

Abstract - In this study, a wireless power transmission (WPT) system which has 4.1kW maximum power is simulated by controlling the output power of the high frequency resonant converter with pulse density modulation (PDM). In order to provide high-frequency wireless power transfer with maximum efficiency, the series resonant converter is controlled by PDM under zero current switching (ZCS) and zero voltage switching (ZVS) conditions. Implemented 8 irregular PDM control algorithm is provided with C block in PSIM software. ZCS and ZVS are achieved for each of 4 different reference power levels, 250W, 1kW, 2.2kW and 4.1kW. Considering the simulation results, the system efficiency is approximately %96 at all power levels.

Keywords **- Resonant converters, Soft switching, PDM. WPT**

I. INTRODUCTION

The basics of the studies on wireless power transfer (WPT) are laid by Hertz's demonstration of the existence of electromagnetic waves [1] and then by Nikola Tesla's idea of inductive power transfer [2].

WPT systems are the process of transferring electrical energy without any physical contact between the transmitter and the receiver. Compared to wired systems, WPT systems have been attracting more attention in recent years because they are more secure and practical. For this reason, it is used and studied in many areas such as portable devices, rail systems, electric vehicles, etc. [3][4].

In WPT systems, many control methods have been studied in order to ensure that the high-frequency inverter (HFI) works with high efficiency and to transfer power to the receiver part with the least energy loss. The most frequently used control methods in the literature are variable frequency control (VF), pulse width modulation (PWM), phase shift modulation (PSM) and pulse density modulation (PDM) [5][3].

Compared to other control methods, PDM is more suitable for WPT systems as it can provide soft switching conditions at any power level [6]. Likewise, compared to other resonant converters, WPT systems are also the most suitable applications for PDM because the quality factor of WPT systems is much higher than other resonant converters [7].

II. PULSE DENSITY MODULATION

PDM can be expressed in the simplest terms as adjusting the output power by changing the time the energy is transmitted to the load in a control period. Power control is obtained by erasing some control pulses without any change in switching frequency. As the number of deleted control pulses increases, the output power of the converter decreases. Therefore, the number of pulses deleted is inversely proportional to the output power. PDM is generally preferred in HFI applications because of providing increment in efficiency [5][8].

Two types of PDM are defined as regular and irregular named according to the distribution of pulses within the period. In the regular PDM control method, the pulses are lined up in a regular form. In the irregular PDM control technique, the pulses are distributed to keep the current distribution balanced throughout the period [9].

During a PDM period T_{PDM}, there are $4, 8, 16, 32, \dots, 2^n$ switching cycles [10]. For $N = 8$, where N is the total number of resonant or switching cycles, PDM pulses and current waveforms are shown in Figure 1.

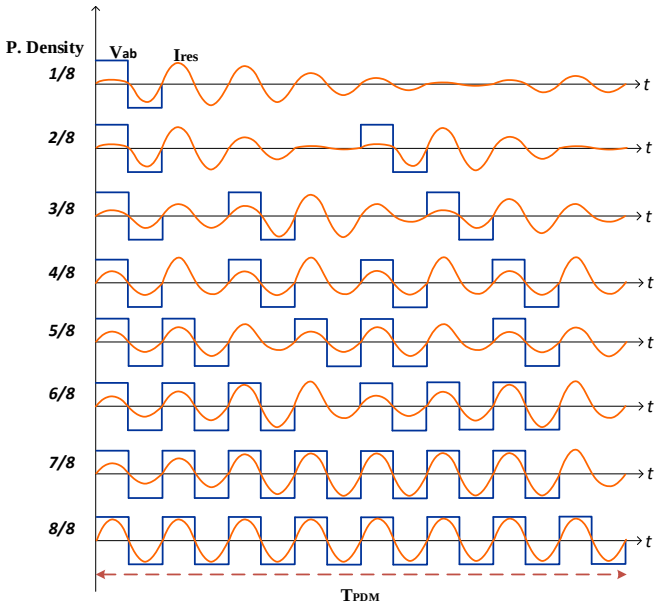

Figure 1: N=8 irregular PDM patterns and current waveforms

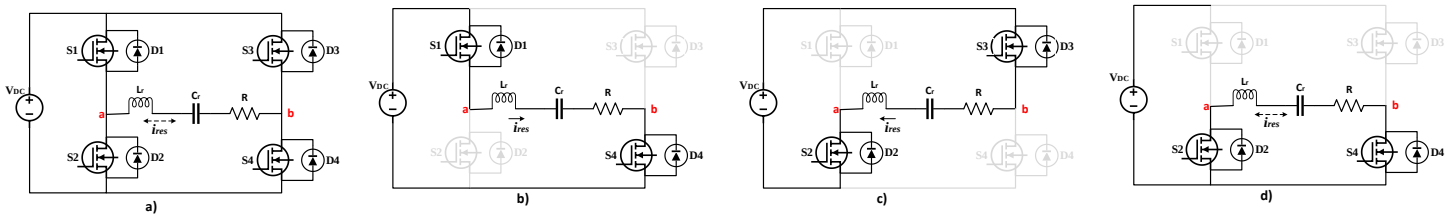

Figure 2: Full bridge series resonant inverter and switching modes a) equivalent circuit b) Mod I c) Mod II d) Mod III

One of the important features of irregular PDM control technique is that it prevents the occurrence of high current-voltage stresses. Thus, the dimensions and cost of the resonant circuit elements are reduced. At the same time, the amplitude of low frequency harmonics is also reduced [9][10].

Due to these advantages, irregular PDM control technique is preferred and the 8 irregular PDM patterns that are used in this study are given in Table 1.

Table 1: N=8 irregular PDM pulses

Pulse Density	PDM Pattern
1/8	1 0 0 0 0 0 0 0
2/8	1 0 0 0 1 0 0 0
3/8	1 0 1 0 0 1 0 0
4/8	1 0 1 0 1 0 1 0
5/8	1 1 0 1 1 0 1 0
6/8	1 1 1 0 1 1 1 0
7/8	1 1 1 1 1 1 1 0
8/8	1 1 1 1 1 1 1 1

III. SERIES RESONANT INVERTER

A full-bridge series resonant inverter, one of the most preferred topologies in WPT systems, is shown in Figure 2-a. The circuit consists of a DC voltage source, 4 switches and a resonant tank.

As presented in Figure 2-b, 2-c and 2-d, the inverter has 3 operating modes. In the first mode, when the switches S_1 and S_4 are turn-on, $+V_{DC}$ voltage is obtained at the output. In the second mode, when the switches S_2 and S_3 are turn-on, $-V_{DC}$ voltage is obtained at the output. In the third and last mode, the switches S_2 and S_4 are turn-on and the output is zero because there is no connection between the input and output.

In this mode, the current is damped through the D_2 and D_4 antiparallel diodes connected to the S_2 and S_4 switches.

$$f_r = \frac{1}{2\pi\sqrt{L_r C_r}} \quad (1)$$

$$R = a^2 R_{eq} \quad (2)$$

$$Q = \frac{1}{\mathrm{R}}\sqrt{\frac{L_r}{C_r}} \quad (3)$$

$$\alpha = \frac{\mathrm{R}}{2L} \quad (4)$$

The basic equations of the circuit are given in (1), (2), (3) and (4). They express the resonant frequency, effective resistance, quality factor and damping coefficient respectively [6], [8], [9]

$$i(t)=i_E(t)\sin w_r t \quad (5)$$

$$P = \frac{1}{T}\int_0^T v_{ab} i(t) dt \quad (6)$$

The current occurs in sinusoidal form when the quality factor Q is much larger than 1. While $i(t)$ is the resonant current and $i_E(t)$ is the envelope of it, the resonant current and average power are obtained by equations (5) and (6) [8]

IV. SIMULATION OF PDM CONTROLLED RESONANT INVERTER

A. System Design

The proposed system design is shown in Figure 3. With this system, high frequency power control is aimed with PDM for different power levels. The circuit consists of a fixed input voltage, full-bridge series resonant inverter, resonant tank, that is, the transmitter part, full-bridge rectifier, filter and load, that is, the receiver part.

Constant 400V DC voltage source is applied to the circuit input, and the PDM control algorithm is implemented using the C block in the PSIM software to provide soft switching conditions at 100kHZ resonant frequency and to transfer power with maximum efficiency.

The maximum power of the implemented circuit is approximately 4.1kW, and 4 different reference power values, 250W, 1kW, 2.2kW and 4.1kW, are defined to the PDM algorithm in order to transfer it to the output. At constant input voltage and constant resonant frequency, the PDM algorithm automatically determines the pulse density for each power level.

Switching operations were performed with the PWM signals produced depending on the pulse density determined by the control algorithm in the C block according to the reference power values.

Table 2: Circuit Parameters

Circuit Parameters	Values
V_{DC}	$400V$
L_r	$1{,}317mH$
C_r	$2nF$
R_L	150Ω
C_f	$4\mu F$
f_{res}	$100kHz$

.

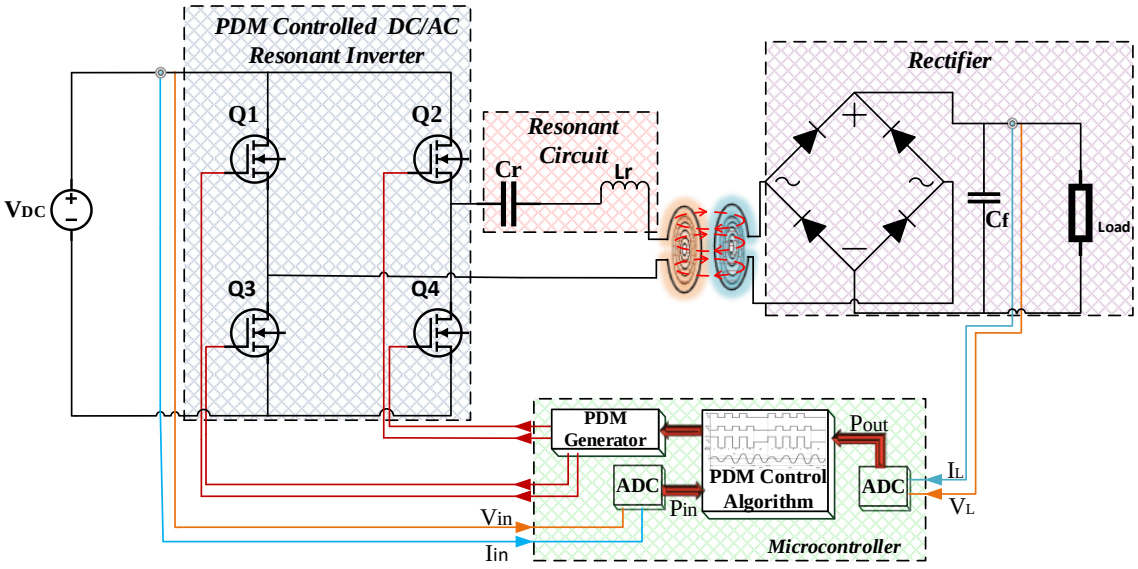

Figure 3: Design of PDM controlled WPT system

B. *Simulation and Outputs*

The proposed system design is implemented in PSIM software with the circuit presented in Figure 7. The circuit consists of a constant voltage source, resonant inverter, resonant inductor, resonant capacitor, full-bridge rectifier, filter capacitor and an ohmic load. The parameters of the parts mentioned above are given in Table 2.

In order to provide wireless power transfer in the circuit, a magnetically coupled inductor is used. A magnetic coupling occurs between two inductors positioned opposite each other at a certain distance. By this coupling, power transfer can be made between the inductors and this effect is defined as mutual inductance when modeling the equivalent circuit. The coupling coefficient K is directly proportional to the mutual inductance and inversely proportional to the distance between the inductors [11]

The coefficient K takes a value between 0 and 1. $K = 0$ means no coupling and no power transfer. $K = 1$ means perfect coupling, that is, almost lossless power transmission.

Since the coupling coefficient K could not be set to 1 in the PSIM software, $K = 0{,}99$ was chosen to provide a near-ideal power transfer in the inductors.

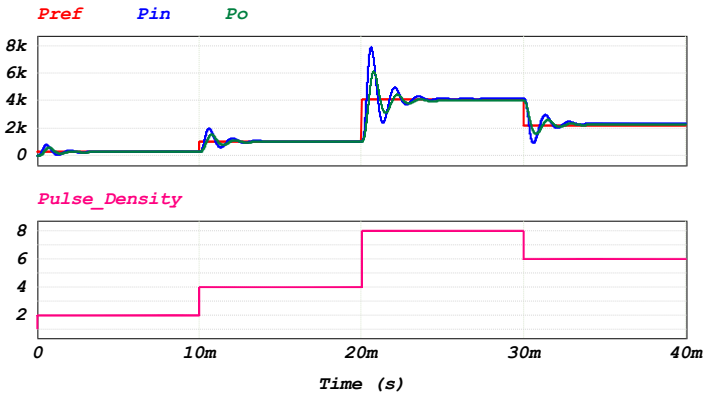

Figure 4. Reference, input, output power and determined pulse density

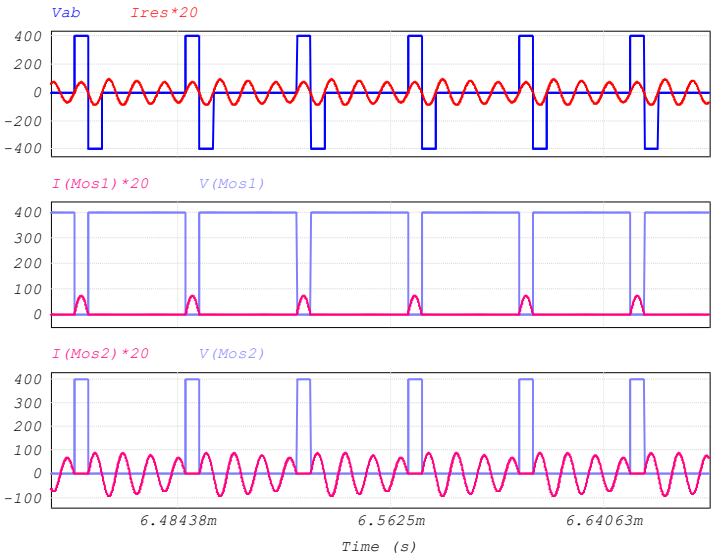

Figure 5: Current-Voltage waveforms for 250W reference power

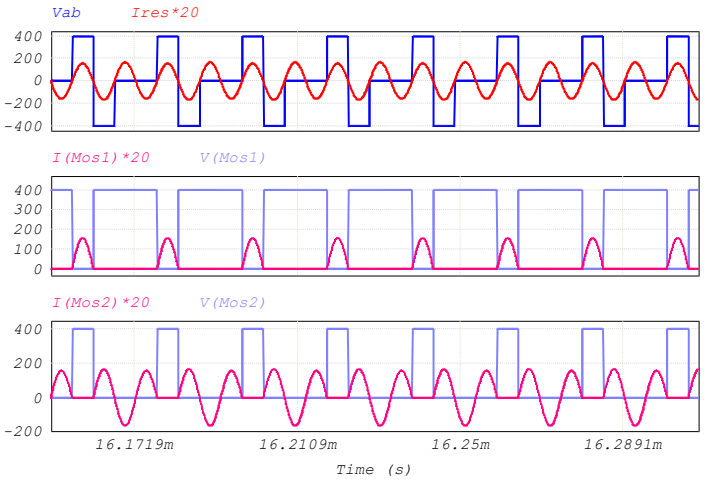

Figure 6: Current-Voltage waveforms for 1kW reference power

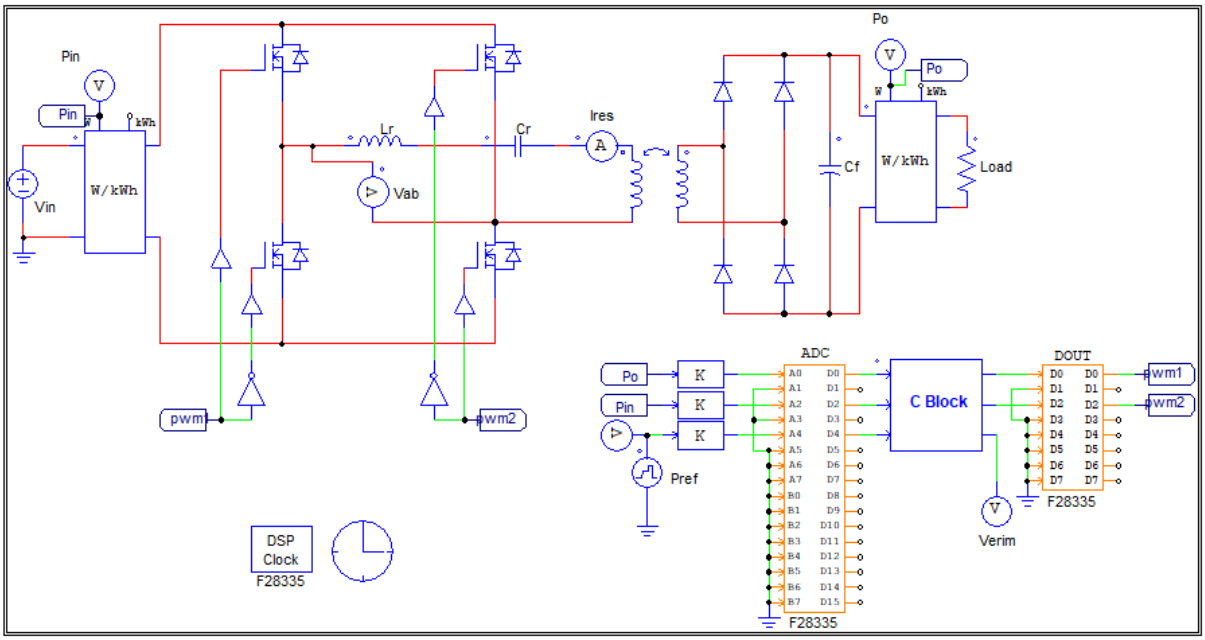

Figure 7: Circuit of PDM controlled WPT system in PSIM

In the simulation with a total duration of 40ms, the reference power values of 250W at 0-10ms, 1kW at 10-20ms, 4.1kW at 20-30ms and 2.2kW at 30-40ms is defined to the control algorithm.

According to these variable reference power values, the algorithm determines the pulse density value each time and the corresponding PDM signal is generated. With the obtained PDM signal, switching is performed and the power transferred to the output is controlled.

As can be seen in Figure 4, the input power is transferred to the output as much as the reference power. This shows that the control algorithm correctly determines the pulse density value according to the reference power.

Resonant inverter output voltage (v_{ab}) and resonant current (i_{res}) waveforms are shown together with current-voltage waveforms of switches S_1 and S_2 in Figure 5, Figure 6, Figure 8 and Figure 9 respectively for 250W, 1kW, 4.1kW and 2.2kW reference power values. Some parameters of the simulation results are given in Table 3.

Table 3: Simulation Results

Time	0-10ms	10-20ms	20-30ms	30-40ms
P_ref	250W	1kW	4.1kW	2.2kW
P_in	255,76W	1030,23W	4141,33W	2328,52W
P_out	248,22W	998,83	3997,87	2251,98W
Efficiency	%97	%96,95	%96,53	%96,71
Pulse Density	2/8	4/8	8/8	6/8
Soft Switching	achieved	achieved	achieved	achieved

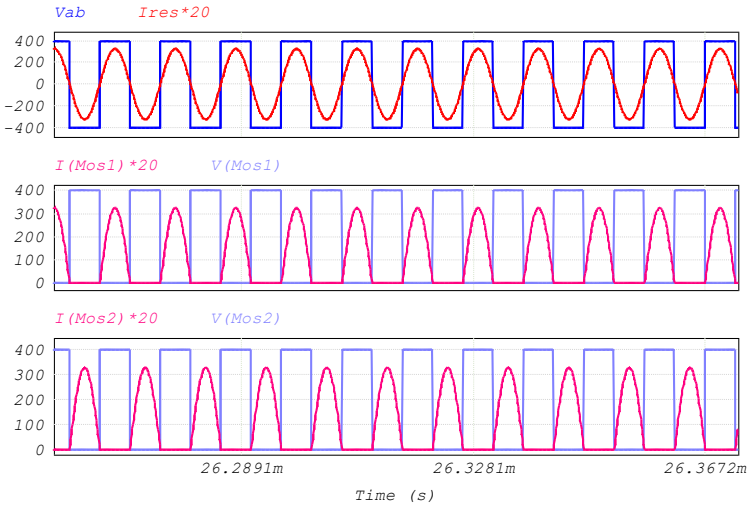

Figure 8: Current-Voltage waveforms for 4.1kW reference power

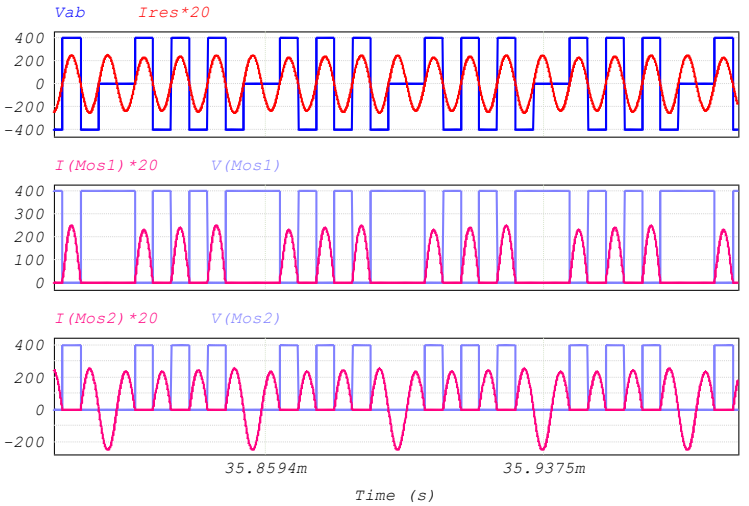

Figure 9: Current-Voltage waveforms for 2.2kW reference power

V. CONCLUSION

In this study, the main goal is to control the full bridge series resonant inverter output with PDM for different power levels in WPT systems. The reason of preferring PDM among many control methods is that soft switching can be successfully provided for different power levels in high frequency inverters.

As can be seen from the simulation results, while the switch currents and therefore the resonant current change in direct proportion to the PDM, ZCS and ZVS are provided at every power level. At each of the 4 different reference power levels, power transmission was achieved with an efficiency of approximately %96.

REFERENCES

[1] S. Niu, H. Xu, Z. Sun, Z. Y. Shao, and L. Jian, "The state-of-the-arts of wireless electric vehicle charging via magnetic resonance: principles, standards and core technologies," *Renew. Sustain. Energy Rev.*, vol. 114, no. July, p. 109302, 2019, doi: 10.1016/j.rser.2019.109302.

[2] F. Issi and O. Kaplan, "Design and application of wireless power transfer using Class-E inverter based on Adaptive Impedance-Matching Network," *ISA Trans.*, no. xxxx, 2021, doi: 10.1016/j.isatra.2021.07.050.

[3] V. Yenil and S. Cetin, "An Improved Pulse Density Modulation Control for Secondary Side Controlled Wireless Power Transfer System Using LCC-S Compensation," *IEEE Trans. Ind. Electron.*, vol. 69, no. 12, pp. 12762–12772, 2022, doi: 10.1109/TIE.2021.3134059.

[4] G. Bal, S. Oncu, N. Ozturk, and K. Unal, "An Application of PDM Technique for MPPT in Solar Powered Wireless Power Transfer Systems," *10th IEEE Int. Conf. Renew. Energy Res. Appl. ICRERA 2021*, pp. 305–309, 2021, doi: 10.1109/ICRERA52334.2021.9598582.

[5] X. Sheng, L. Shi, and M. Fan, "An Improved Pulse Density Modulation of High-Frequency Inverter in ICPT System," *IEEE Trans. Ind. Electron.*, vol. 68, no. 9, pp. 8017–8027, 2021, doi: 10.1109/TIE.2020.3013782.

[6] H. Özbay, "PDM-MPPT based solar powered induction heating system," *Eng. Sci. Technol. an Int. J.*, vol. 23, no. 6, pp. 1397–1414, 2020, doi: 10.1016/j.jestch.2020.06.005.

[7] H. Li, J. Fang, S. Chen, K. Wang, and Y. Tang, "Pulse Density Modulation for Maximum Efficiency Point Tracking of Wireless Power Transfer Systems," *IEEE Trans. Power Electron.*, vol. 33, no. 6, pp. 5492–5501, 2018, doi: 10.1109/TPEL.2017.2737883.

[8] A. Karafil, H. Ozbay, and S. Oncu, "Design and Analysis of Single-Phase Grid-Tied Inverter With PDM Mppt-controlled Converter," *IEEE Trans. Power Electron.*, vol. 35, no. 5, pp. 4756–4766, 2020.

[9] A. Karafil, "Comparison of the various irregular pulse density modulation (PDM) control pattern lengths for resonant converter with photovoltaic (PV) integration," *J. Fac. Eng. Archit. Gazi Univ.*, vol. 36, no. 3, pp. 1595–1611, 2021, doi: 10.17341/gazimmfd.685751.

[10] A. Karafil, H. Ozbay, and S. Oncu, "Comparison of regular and irregular 32 pulse density modulation patterns for induction heating," *IET Power Electron.*, no. August, pp. 1–12, 2020, doi: 10.1049/pel2.12012.

[11] A. A. Oraz, "Elektrikli araçlar için endüktif kuplaj yöntemi yle kablosuz güç aktariminin gerçeklenmesi yüksek lisans tezi," Mersin University, 2018.

Digital Currency Time Series Prediction Based on Financial Signal Processing, Ant Colony Optimization and Machine Learning Techniques

S. KARASU[1] and N. A. YALÇIN[2]

[1] Zonguldak Bülent Ecevit University, Zonguldak/Turkey, seckin.karasu@beun.edu.tr
[2]Bursa Uludağ University, Bursa/Turkey, aktanyalcin@uludag.edu.tr

***Abstract* - Nowadays, digital currencies are very popular among individual and institutional investors and their usage is becoming more and more common. It has started to be important for people in the whole sectors what the value of digital currencies, which emerged as an alternative to existing currencies at the beginning, will be compared to existing currencies for the next day. In this study, external time series are derived by using trend indicators and oscillators from financial signal processing approaches on BTCUSD, ETHUSD and BNBUSD time series data. Trend indicators such as Moving Average (MA), Average Directional Moving Index (ADX) and Parabolic Stop and Reverse (SAR) and oscillators such as Moving Average Convergence Divergence (MACD), Rate of change (ROC) and Commodity Channel Index (CCI) are used. A total of 155 features are extracted by using close, high and low price time series data. Using time series and derived data, Support Vector Machines (SVM) with Gaussian kernel from machine learning approaches are trained to predict accurately the next step close price. A wrapper-based approach is used to select relevant features by using Ant Colony Optimization (ACO) and SVM. The 10-fold cross validation approach is used for model validation. Model performances are compared using statistical error criteria such as Root Mean Square Error (RMSE) and Mean Absolute Error (MAE).**

***Keywords* – Digital Currency, Financial Signal Processing, Ant Colony Optimization, Bitcoin, Ethereum, Binance Coin.**

I. INTRODUCTION

CRYPTOCURRENCY has remarkable structure which has network-based form to provide security of records based on cryptographic algorithms. It is based on blockchain technology which gives it strength and robustness in terms of security, transparency and tractability [2]. Therefore, many financial systems are oriented to cryptocurrency. Uncontrollable nature of financial systems and cryptocurrency affect industry and many people in the world. Therefore, many researches are realized in order to predict its price based on its past values [1-5].

In order to estimation of cryptocurrency, two different machine learning methods which are linear regression (LR) and Support Vector Machines (SVM) are used in [1]. Methods are implemented after applying filters which are different window lengths and coefficient sizes on daily Ethereum cryptocurrency value closing prices. Cross validation procedure is also applied due to obtain strong performance model. The study shown that SVM method has more accuracy than LR method [1]. In another work, new prediction method which is hybrid approach which is constructed with Long Short-Term Memory (LSTM) and Gated Recurrent Unit (GRU) for cryptocurrency estimation is proposed. It is shown that proposed method gives high accuracy in cryptocurrency estimation [2]. The study which used bitcoin day-end close prices realized Bitcoin price estimation with LR and SVM. The study shown that SVM model gives high accuracy rate than LR according to Mean Absolute Error (MAE), Mean Squared Error etc. [3]. In [4], Bitcoin price is estimated with taking into account various parameters. In first phase, various features are obtained from past five years of Bitcoin price. In second phase of the study, daily price change is tried to estimated [4]. In [5], it is expressed that digital currencies depends on wide variety parameters and the prediction process cannot be realized based on a single model. Therefore, new hybrid forecasting technique which is based on LSTM, neural network and empirical wavelet transform (EWT) is proposed. It is shown that proposed method can capture nonlinear properties of digital currency time series with high accuracy [5]. In [6], LSTM method is applied for more accurate result of bitcoin price prediction. It is also shown that many LSTM models have advantages compared to many different machine learning methods [6]. In [7], decentralized nature of bitcoin and its influence on international trades and relations are emphasized. Forecasting studies which are realized between 2010-2020 are summarized and statistical approach and machine learning techniques for prediction of cryptocurrency are compared historically [7]. In [8], three types of recurrent neural network (RNN) are compared with three types of cryptocurrencies which are Bitcoin, Litecoin and Ethereum. It is reported that all model performs good performance based on mean absolute percentage error (MAPE). The other important result of study is GRU network gives superior performance with prediction of cryptocurrencies (compared to LSTM and bi-LSTM) [8]. In [9], it is stated that performance of LSTM and ARIMA models is applicable with historical data for cryptocurrency prediction. But in real world, cryptocurrency is affected other parameters more than its past price. Therefore, Fbprophet model is proposed for estimation for cryptocurrency. In the study it is also shown that proposed

method is successful when analyzing new cryptocurrency and has also superior performance than LSTM and ARIMA, if historical data are also considered [9]. In [10], it proposed an ensemble-enabled LSTM model with new model connections to examine both short-term effects and long-term effects to predict Bitcoin price. It is compared the proposed method with the ARIMA model for different time periods and it is shown that proposed method is higher than other prediction methods.

In this study, a model has been developed that includes SVM methods with Gaussian kernel and predicts the next close price for three different time series such as BTCUSD, ETHUSD and BNBUSD. By using 7 types of trend and oscillator-based indicators from financial time series, features that can affect prediction performance are determined under various parameters. A total of 155 features are extracted, and in the next step, the wrapper approach is established with Ant Colony Optimization (ACO) and SVM methods, and the model with the highest prediction performance is determined. Statistical errors such as MAE and RMSE are used to determine the error between the actual and predicted time series data. The rest of this paper is organized as follows. In section 2, it is described a prediction model procedure, containing indicators derived from Financial Signal Processing (FSP) techniques, SVM and ACO. In section 3, all parameters of models used in simulation study and obtained results are given. Finally, the conclusion and the future studies of the proposed model is given in section 4.

II. Digital Currency Time Series Prediction Model

The application sequence of the approaches that make up the proposed estimation model in the study is given with the flowchart in Figure 1. The digital currency time series prediction study begins with the data collection stage. When it is examined the data table, it is appeared that columns consist of close, open, high, low and volume labels. 4033 rows x 5 columns BTCUSD data, 2393 rows x 5 columns ETHUSD data and 1784 rows x 5 columns BNBUSD data are taken from the data center in [11-13]. Date range, data dimensions, statistical values such as mean, maximum, minimum and standard deviation for these time series are given in Table 1.

Table 1: Data dimensions and statistical properties.

Data	First-Last Date	Data Points	Mean	Max	Min	Std
BTCUSD	13.09.2011-27.09.2022	4033x5	927,69	67527,90	2,00	15053,86
ETHUSD	10.03.2016-27.09.2022	2393x5	857,99	480,84	6,70	1144,74
BNBUSD	9.11.2017-27.09.2022	1784x5	139,63	676,56	1,49	184,87

In the second stage, the whole data set is subjected to the normalization process by applying the equation in (1).

$$X_{normalized} = \frac{X - X_{minimum}}{X_{maximum} - X_{minimum}} \quad (1)$$

In the following parts, the next stages of proposed method such as Financial Signal Processing (FSP) techniques, Support Vector Machines (SVM), Ant Colony Optimization (ACO) explained in detail.

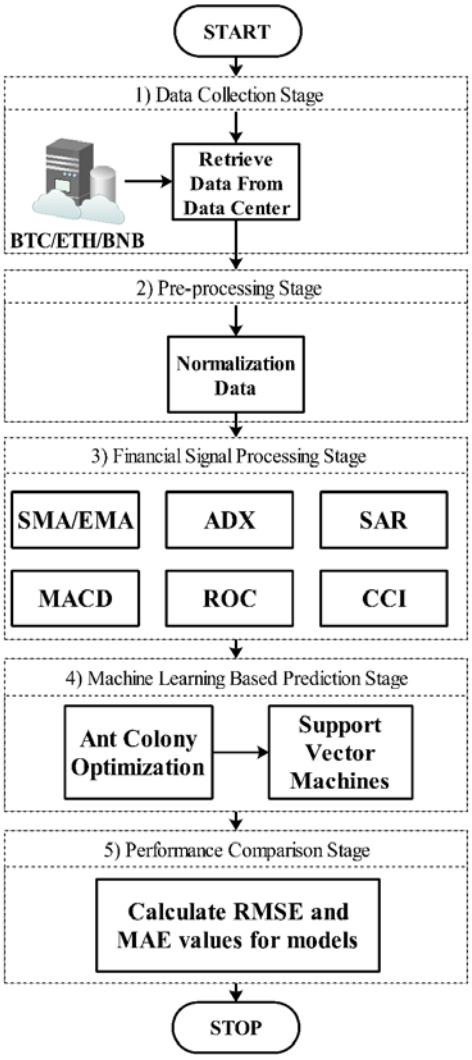

Figure 1: The flowchart of proposed digital currency prediction model.

A. Financial Signal Processing Techniques

In this section, an explanation is given about the trend indicators and oscillator types, which are among FSP methods used in the study. Trend indicators such as Simple and Exponential Moving Average (SMA, EMA), Average Directional Moving Index (ADX) and Parabolic Stop and Reverse (SAR) are explained in order. Besides, oscillator types such as Moving Average Convergence Divergence (MACD), Rate of change (ROC) and Commodity Channel Index (CCI) are also explained.

Simple Moving Average (SMA)

This trend indicator is created by taking the average of the price movements (such as close price time series data) within the specified period (N). The Simple Moving Average (SMA) equation is given in (2).

$$SMA[i] = \frac{1}{N}\sum_{n=1}^{N} C[i+n] \quad (2)$$

Exponential Moving Average (EMA)

The Exponential Moving Average (EMA) equation is given as in (3).

$$EMA[i] = \left(\frac{2}{1+N}\right)(C[i] - EMA[i-1]) + EMA[i-1] \quad (3)$$

In this equation, 2/(1+N) is weighting factor for Exponential Moving Average (EMA) where N is selected time period. For first calculation, initial value of EMA, EMA$[i-1]$ is an average of all close prices over N number of periods. In the next steps, the values obtained here are used in (3) to calculate the EMA value for the whole time series.

Average Directional Moving Index (ADX)

Average Directional Movement Index (ADX) indicator is developed by John Welles Wilder, JR. in 1978 [14]. ADX, called the Average Directional Index, is an indicator that takes values between 0-100. The ADX line does not say whether the value will be high or low for next value, but it gives information about the strength of the data's movement in one direction [15]. It is calculated as in (4). N value represents the period value of the ADX indicator.

$$ADX[i] = \left(\frac{ADX[i-1](N-1) + DX[i]}{N}\right) \quad (4)$$

Directional Index $DX[i]$ in (4) is calculated as in (5) by multiplying the ratio of the difference between Positive Directional Indicator (PDI) and Negative Directional Indicator (NDI) to the sum of PDI and NDI by 100.

$$DX[i] = \frac{100(PDI[i] - NDI[i])}{(PDI[i] + NDI[i])} \quad (5)$$

PDI and NDI are expressed as the ratio of Positive Directional Movement (+DM) to True Range (TR) and Negative Directional Movement (-DM) to TR respectively in (6,7).

$$PDI[i] = \frac{\sum_{n=1}^{N} +DM\,[i]}{\sum_{n=1}^{N} TR[i]} \quad (6)$$

$$NDI[i] = \frac{\sum_{n=1}^{N} -DM\,[i]}{\sum_{n=1}^{N} TR[i]} \quad (7)$$

where TR, +DM and -DM are calculated as in (8,9,10). C, H and L represent close, high and low prices time series data respectively.

$$TR[i] = max\begin{cases} H[i] - L[i] \\ |H[i] - C[i-1]| \\ |L[i] - C[i-1]| \end{cases} \quad (8)$$

$$+DM[i] = \begin{matrix} H[i] - H[i-1] & (H[i] - H[i-1]) > (L[i-1] - L[i]) \\ 0 & otherwise \end{matrix} \quad (9)$$

$$-DM[i] = \begin{matrix} L[i-1] - L[i] & (L[i-1] - L[i]) > (H[i] - H[i-1]) \\ 0 & otherwise \end{matrix} \quad (10)$$

Parabolic Stop and Reverse (SAR)

This indicator is developed by John Welles Wilder, JR. to find potential reversals price direction in volatile markets [15]. The SAR value is calculated as in (11).

$$SAR[i] = SAR[i-1] + \alpha(EP - SAR[i-1]) \quad (11)$$

In (11), EP is constantly updated as the highest of highs in the uptrend and the lowest of the lows in the downtrend. The α value represents the acceleration factor. α is 0.02 by default and can be increased by 0.02 step size to a maximum value of 0.2. This is where the expression 'parabolic' comes from as prices tend to stay in a parabolic curve in a strong trend.

Moving Average Convergence Divergence (MACD)

The MACD (Moving Average Convergence Divergence) indicator is developed by Gerard Appel in the 1970s [16]. MACD indicator is calculated as in (12), depending on the difference between the short-time and long-time exponential moving average (EMA) values.

$$MACD[i] = EMA_{short}[i] - EMA_{long}[i] \quad (12)$$

This is defined as the MACD line. A third time series called signal is obtained by averaging this value over a certain period. In addition, the histogram time series is obtained by visualizing the difference between MACD line and signal. MACD values 12, 26 and 9 are typically used [17].

Rate of change (ROC)

The Rate of Change (ROC), also known as Momentum, is another financial signal processing technique that measures the momentum of price movements. It compares the current price of any security with the previous price of the N period. The ROC value is calculated using the equation in (13).

$$ROC[i] = 100\frac{C[i] - C[i-1]}{C[i-1]} \quad (13)$$

Commodity Channel Index (CCI)

The Commodity Channel Index is an oscillator introduced by Donald Lambert in 1980 [18]. It measures the current price level relative to the average price level in a given time period. The CCI value is calculated as the ratio of the difference between the Typical Price (TP) and the SMA value of close to the Mean Deviation (MD) value as in (14) [19].

$$CCI[i] = \frac{1}{0.015}\frac{TP[i] - SMA[i]}{MD[i]} \quad (14)$$

In this equation, the TP value is calculated as the average of the H, L and C time series data, as in (15).

$$TP[i] = \frac{H[i] + L[i] + C[i]}{3} \quad (15)$$

The MD value is calculated as in (16) as the mean value of the difference between TP and SMA value for a given N period.

$$MD[i] = \frac{1}{N}\sum_{n=1}^{N} |TP[i+N] - SMA[i+N]| \quad (16)$$

B. Support Vector Machines (SVM)

Support Vector Machines, one of the machine learning approaches, are implemented by using a linear and non-linear function in classification and prediction studies. It is basically based on estimating the most appropriate function to separate the data from each other. Data separation is made with different function types, namely linear, polynomial and Gaussian kernels [20]. The Gaussian kernel formula used in this study is given as in (17). In this equation, σ is defined as the hyper parameter and is expressed as variance. $\|x - x'\|$ is expressed as the Euclidean distance between two points.

$$K(x_i, x_j) = \exp\left(-\frac{\|x - x'\|^2}{2\sigma^2}\right) \quad (17)$$

C. Ant Colony Optimization

The use of food-seeking behavior of ants to solve heuristic optimization problems was developed by Marco Dorigo [21]. Like genetic algorithms, this is a heuristic algorithm [21]. It is an optimization algorithm developed based on the food collection logic of ants. It has been noticed that an ant carries food to its colony, often over the shortest distance to the food, and it has been found that they achieve this thanks to the pheromone they leave while walking on the ground. An ant looking for food chooses the place with more pheromone by looking at the pheromone level of the road it will go. Since the ant that reaches the food first will be the first to return to the ant colony, there will be more pheromones on its path due to the fact that it passes over it twice. Meanwhile, another ant leaving the colony will be more likely to choose the path with more pheromones. As a result of repeating this process, the pheromone level of the shortest path will constantly increase, and after a while, all ants will converge to this path [21].

The ACO metaheuristic algorithm is given in Table 2. This algorithm consists of three stages. These are Construct Ant Solutions, Apply Local Search and Update Pheromones respectively. During the iteration, these steps are run sequentially. At each iteration, a set of possible solutions is created by the ants. Optionally, solutions are improved with a local search approach. Finally, the purpose of the pheromone is to produce the best result by replacing the bad one. After this update, the new iteration is started, if the stopping criterion is not met [21].

Table 2: The ACO Metaheuristic Algorithm [21].

Algorithm 1 The Ant Colony Optimization Metaheuristic
Set parameters, initialize pheromone trails
while termination condition not met **do**
ConstructAntSolutions
ApplyLocalSearch(optional)
UpdatePheromones
endwhile

III. Experimental Study and Results

In the simulation study, the close price of Bitcoin, Ethereum and Binance Coin in the next step is predicted separately with the SVM model with Gaussian kernel from machine learning methods. A data set consisting of daily data points from 13.09.2011 to 27.09.2022 for Bitcoin prediction, 2393 daily data points from 10.06.2016 to 27.09.2022 for Ethereum prediction and 1784 daily data points from 09.11.2017 to 27.09.2022 for Binance Coin prediction is used. The data set consists of daily open, close, highest price, lowest price and trading volume variables. For FSP techniques, 155 feature groups were created from 7 types of features, namely SMA, EMA, ADX, SAR, MACD, ROC and CCI, using the period and other parameters as in Table 3. The model with the lowest RMSE error is obtained by selecting the features with the ACO+SVM wrapper approach. The 10-fold cross validation method is used in the model training phase. The variation of the error in the stage of finding the features during the model training phase of 3 different financial time series versus iteration is given in Figure 2. The plot of the actual and estimated time series for the lowest RMSE value for the specified features is given in Figure 3-5. The features selected for each data set are given in Table 4.

Table 3: Features gathered from FSP techniques.

Techniques	Parameters (Initial: step: last)
SMA/ EMA	$N_{SMA/EMA}$=2:1:10
ADX	N_{ADX}=2:1:10
SAR	$SAR(\alpha)$ =0.02:0.02:0.10
MACD	$N_{short} = 10:1:14$ $N_{long} = 24:1:28$ $N_{MACD} = 7:1:11$
ROC	N_{ROC}=2:1:10
CCI	N_{CCI}=15:1:25

Table 4: MAE and RMSE values of models for selected features.

Data	Selected Features	MAE	RMSE
BTCUSD	SMA(6), SAR(0.02), MACD(10,27,8), MACD(11,28,9), MACD(11,26,10), MACD(11,26,11)	0.0105	0.01913
ETHUSD	SMA(9), EMA(2), ADX(10), +DX(7), MACD(11,28,7),MACD(13,24,9), MACD(13,28,7), MACD(14,25,10), MACD(14,25,11)	0.0141	0.02280
BNBUSD	EMA(8), MACD(11,24,7), MACD(12,25,8), MACD(14,27,8), MACD(14,28,11), CCI(20)	0.0172	0.02630

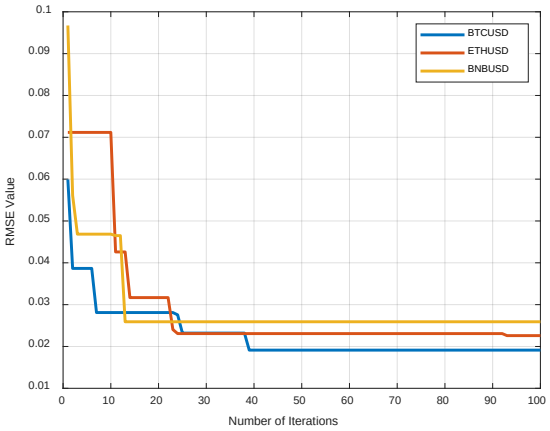

Figure 2: ACO results for time series data.

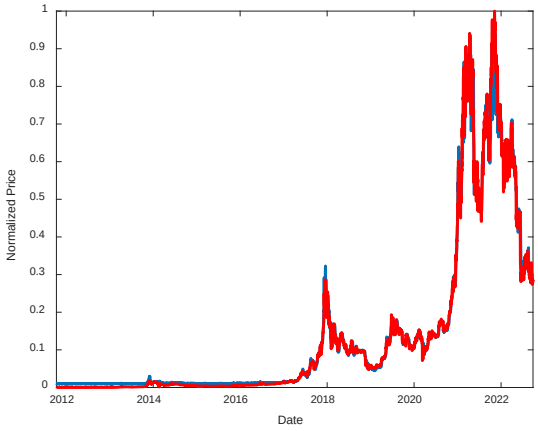

Figure 3: Prediction result of the ACO+SVM method for BTCUSD.

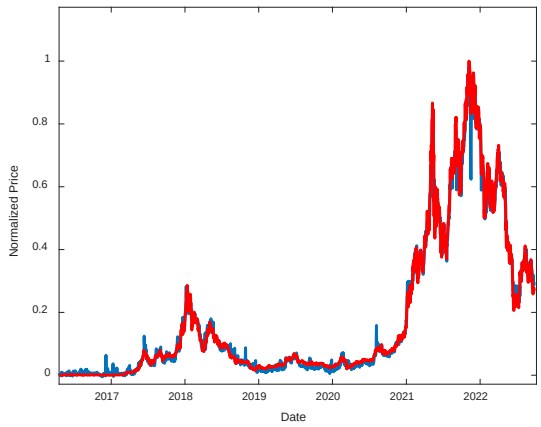

Figure 4: Prediction result of the ACO+SVM method for ETHUSD.

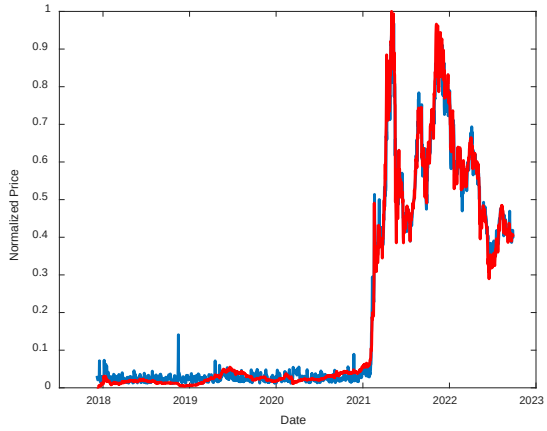

Figure 5: Prediction result of the ACO+SVM method for BNBUSD.

IV. Conclusion

In this study, 155 features produced by FSP techniques are used in the ACO+SVM wrapper model, and the prediction of the BTCUSD, ETHUSD and BNBUSD time series separately is made. In the study, the features produced under different parameters were applied as input to the SVM model with Gaussian kernel in different combinations. The most suitable ones of these features are selected with the ACO algorithm, and the model with the minimum model error is revealed. For BTCUSD, ETHUSD and BNBUSD time series, 4033, 2393 and 1784 time series are used. The training process of the models was completed with 10-fold cross validation. It has been seen that the model performances obtained for certain number of features are high for each time series prediction study. It is thought that the use of machine learning approaches based on different financial signal processing approaches and multi-objective optimization methods will be examined in future studies and will bring new perspectives for studies in this field.

References

[1] Poongodi, M., Sharma, A., Vijayakumar, V., Bhardwaj, V., Sharma, A. P., Iqbal, R., & Kumar, R. (2020). Prediction of the price of Ethereum blockchain cryptocurrency in an industrial finance system. Computers & Electrical Engineering, 81, 106527.

[2] Patel, M. M., Tanwar, S., Gupta, R., & Kumar, N. (2020). A deep learning-based cryptocurrency price prediction scheme for financial institutions. Journal of information security and applications, 55, 102583.

[3] Karasu, S., Altan, A., Saraç, Z., & Hacioğlu, R. (2018, May). Prediction of Bitcoin prices with machine learning methods using time series data. In 2018 26th signal processing and communications applications conference (SIU) (pp. 1-4). IEEE.

[4] Velankar, S., Valecha, S., & Maji, S. (2018, February). Bitcoin price prediction using machine learning. In 2018 20th International Conference on Advanced Communication Technology (ICACT) (pp. 144-147). IEEE.

[5] Altan, A., Karasu, S., & Bekiros, S. (2019). Digital currency ing with chaotic meta-heuristic bio-inspired signal processing techniques. Chaos, Solitons & Fractals, 126, 325-336.

[6] Andi, H. K. (2021). An accurate bitcoin price prediction using logistic regression with LSTM machine learning model. Journal of Soft Cmputing Paradigm, 3(3), 205-217.

[7] Khedr, A. M., Arif, I., El-Bannany, M., Alhashmi, S. M., & Sreedharan, M. (2021). Cryptocurrency price prediction using traditional statistical and machine-learning techniques: A survey. Intelligent Systems in Accounting, Finance and Management, 28(1), 3-34.

[8] Hamayel, M. J., & Owda, A. Y. (2021). A Novel Cryptocurrency Price Prediction Model Using GRU, LSTM and bi-LSTM Machine Learning Algorithms. AI, 2(4), 477-496.

[9] Rathore, R. K., Mishra, D., Mehra, P. S., Pal, O., HASHIM, A. S., Shapi'i, A., ... & Shutaywi, M. (2022). Real-world model for bitcoin price prediction. Information Processing & Management, 59(4), 102968.

[10] Shin, M., Mohaisen, D., & Kim, J. (2021, January). Bitcoin price forecasting via ensemble-based LSTM deep learning networks. In 2021 International Conference on Information Networking (ICOIN) (pp. 603-608). IEEE.

[11] Bitcoin Cryptocurrency Time Series Data (2022, Oct 27). Available: *https://www.investing.com/crypto/bitcoin/btc-usd*

[12] Ethereum Cryptocurrency Time Series Data (2022, Oct 27). Available: *https://www.investing.com/crypto/ethereum/eth-usd*

[13] Binance Coin Cryptocurrency Time Series Data (2022, Oct 27). Available: URL: *https://www.investing.com/crypto/bnb/bnb-usd*

[14] Wilder Jr., J. (1978). New Concepts in Technical Trading Systems. Greensboro, NC: Hunter Publishing Company. Trend Research.

[15] Szetela, B., Mentel, G., Mentel, U., & Bilan, Y. (2020). Directional movement distribution in the bitcoin markets. Engineering Economics, 31(2), 188-196.

[16] Appel, Gerald (2005) Technical Analysis: Power Tools For Active Investors, Financial Times/ Prentice Hall

[17] Kang, B. K. (2021). Improving MACD technical analysis by optimizing parameters and modifying trading rules: evidence from the Japanese Nikkei 225 futures market. Journal of Risk and Financial Management, 14(1), 37.

[18] Naved, M., & Srivastava, P. (2015). Profitability of Oscillators used in Technical analysis for Financial Market. Advances in Economics and Business Management (AEBM) Print ISSN, 2394-1545.

[19] Karasu, S., & Altan, A. (2022). Crude oil time series prediction model based on LSTM network with chaotic Henry gas solubility optimization. Energy, 242, 122964.

[20] Widodo, A., & Yang, B. S. (2007). Support vector machine in machine condition monitoring and fault diagnosis. Mechanical systems and signal processing, 21(6), 2560-2574.

[21] Dorigo, M., Birattari, M., & Stutzle, T. (2006). Ant colony optimization. IEEE computational intelligence magazine, 1(4), 28-39.

A Method to Implement Ternary Logic Gates via Multi Threshold Transistors

A. UNUTULMAZ [1]

[1] Marmara University, İstanbul/Türkiye, ahmet.unutulmaz@marmara.edu.tr

***Abstract* – Multi threshold transistors are available in advanced technology nodes. In this work, the author presents a methodology to implement ternary logic gates via multi-Vt transistors. The presented method is used to implement ternary AND and OR gates as well as a ternary half adder circuit. Functionality of the implemented circuits are verified via SPICE simulations.**

***Keywords* – Ternary Logic, Multi Threshold Design**

I. INTRODUCTION

IN chip design wire congestion is a significant problem and a solution may be the utilization of ternary logic. Ternary logic offers three logic level on a single wire. Let's assume three wires carrying binary information, these wires may carry 2^3 different information. However, using just two wires which carry ternary data 3^2 different data may be sent.

Research on ternary logic gained speed with the discovery of Carbon Nano-Tube FETs (CNTFETs) [1-4]. Threshold voltage of CNTFETs may be adjusted by changing their geometry. Recently, Hills, et al. [5] implemented a binary processor which contains about 15.000 CNTFETs. The implementation was the largest CNTFET circuit fabricated. Compared to standard CMOS which may be used for circuits with billions of transistors, CNTFET technology is immature and to the authors knowledge there are no fabrication methods to build multi-Vt VLSI circuits using CNTFETs.

For several decades, standard CMOS is being used to build binary circuits. Although, there were some initial trials [6] to implement ternary circuits via MOSFET technology, they were not successful. Author believes that this was mainly due to the limited implantation technology of those days. Recently, to improve the performance and to reduce power consumption, fabs, such as TSMC [7], started to offer multi-Vt devices in a single chip. These multi-Vt processes may be used implement ternary logic circuits, as done with CNTFETs.

In this work, a methodology to design ternary logic gates is presented and it is given in Section II. The methodology is applied to implement ternary AND, OR and half adder circuits in Section III. Implementation are verified via LTSPICE [8] simulations in Section IV. Conclusion are given in Section V.

II. METHODOLOGY

To minimize static power dissipation of binary digital gates, transistors in of a gate are utilized as on/off switches. To be able to extend the idea to ternary logic, one should convert a ternary signal to a binary signal which will turn on/off the transistors. In this work, two special inverters, Negative Ternary Inverter (NTI) and Positive Ternary Inverter (PTI), are used to convert a ternary signal into binary. Truth tables of these are listed in Table 1. The values 0,1 and 2 are the ternary logic values, which correspond to the ground, intermediate potential (Vd1) and the high potential (Vd2), respectively.

Table 1: Truth tables of NTI and PTI.

X	NTI (X)	PTI (X)
0	2	2
1	0	2
2	0	0

Implementing these inverters, the author utilized the open source PTM 32nm [9] technology. The model is extended via adding low threshold transistors with $|V_t|$=0.25V. Implementations are show in Figure 1.

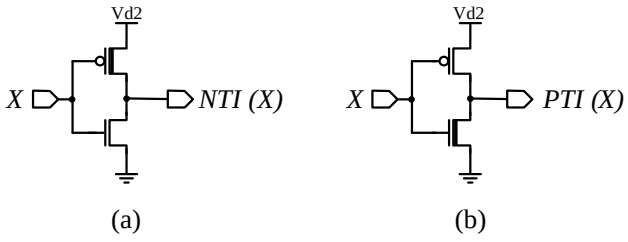

Figure 1: Implementations of NTI and PTI. (a) NTI is built using high threshold PMOS and low threshold NMOS. (b) PTI is built using low threshold PMOS and high threshold NMOS.

Using only NTI and PTI all output configurations cannot be obtained. Table 2 is generated based on Table 1 and extended via utilizing binary NOT, AND and OR gates. The table shows the expressions to obtain the remaining non-constant and binary output configurations. The tables are used to implement any ternary function.

Table 2: Truth tables of NTI and PTI.

X	NOT(NTI(X))	NOT(NTI(X)) AND PTI(X)	NOT(PTI(X))	NOT(PTI(X)) OR NTI(X)
0	0	0	0	2
1	2	2	0	0
2	2	0	2	2

The NTI, PTI and the extensions in Table 2 are used to turn on/off the networks in Figure 2. At any time only one network connects its supply to the output Y. This way, without any short circuit current, the output Y is pulled up to logic 1 or 2.

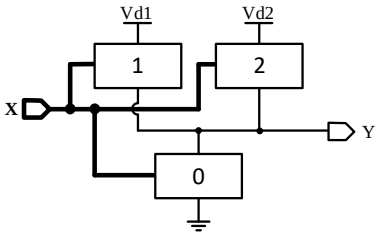

Figure 2: A general network for Ternary gates.

In Figure 2, Vd1 and Vd2 correspond to the potential level for logic 1 and 2, respectively. Summing up, depending on the function Y, one of the networks (Network 0, 1 or 2) is activated and it short circuits corresponding supply to the output node Y.

To clarify the methodology, it is used to design the standard ternary inverter (STI) for which the truth table is given in Table 3. States of the networks for all input configurations are also listed in the table.

Table 3: Truth tables for the STI.

X	STI(X)	Network 2	Network 1	Network 0
0	2	2	Off	Off
1	1	Off	1	Off
2	0	Off	Off	0

Network 2 is on and short circuits supply Vd2 to output Y only when the input X=0, this pull up network may be implemented with a switch which is controlled by NTI(X). Network 1 connects Vd1 to the output when X=1. As listed in Table 2, the corresponding network may be implemented with two serial switches which are controlled by the logic NOT(NTI(X)) and PTI(X). Note that the AND operation is implemented by serially connecting two switches. Similarly, an OR operation may be achieved via a parallel connection. Lastly Network 0, which pulls the output down to 0, is active when X=2. As seen from Table 2, the logic NOT(PTI(X)) may be used to control a switch to short circuit the output to ground. Circuit implementations with switches are given in Figure 3.

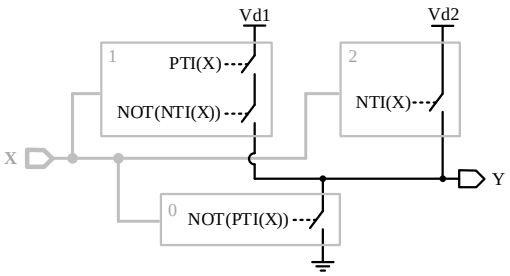

Figure 3: Implementation of the STI with switches.

Transistor level implementation of the STI is shown in Figure 4, where pull-down and pull-up switches are replaced with NMOS and PMOS transistors, respectively. A PMOS transistor inherently inverts the signal, thus the inputs to PMOS transistors are inverted. Low Vt PMOS transistor are used in network 1.

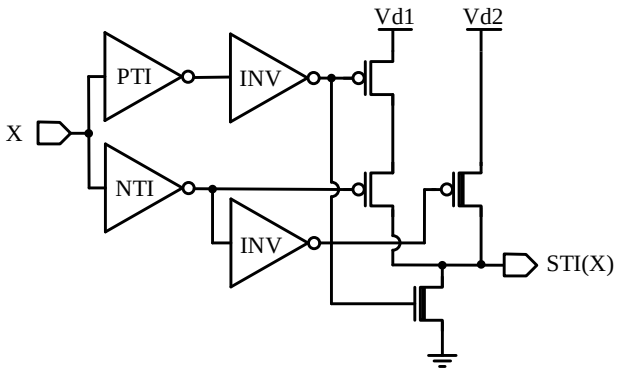

Figure 4: Transistor level implementation of STI.

III. APPLICATIONS

In this section, the methodology in Section II, is applied to design ternary AND, OR and half adder circuits.

A. Ternary AND Gate

There are different definitions of ternary AND gate. In this work, the definition in Table 4 is going to be implemented, which corresponds to the MIN function.

Table 4: Truth table for the ternary AND gate.

X	Y	AND(X, Y)	Network 2	Network 1	Network 0
0	0	0	Off	Off	0
0	1	0	Off	Off	0
0	2	0	Off	Off	0
1	0	0	Off	Off	0
1	1	1	Off	1	Off
1	2	1	Off	1	Off
2	0	0	Off	Off	0
2	1	1	Off	1	Off
2	2	2	2	Off	Off

Network 2 is active and pulls the output to Vd1 potential if both X and Y are 2. This functionality may be implemented by serially connecting two switches, which are controlled by the logics NOT(PTI(X)) and NOT(PTI(Y)), respectively. Network 0 is active if X=0 or Y=0. This function may be implementing by connecting two switches in parallel. The switches will be controlled with NTI(X) and NTI(Y) signals, respectively. Similarly, the network 1 is obtained. Transistor level implementation of the ternary AND gate is given in Figure 5. The circuit is tested in LTSPICE and the simulation results are given in Section IV.

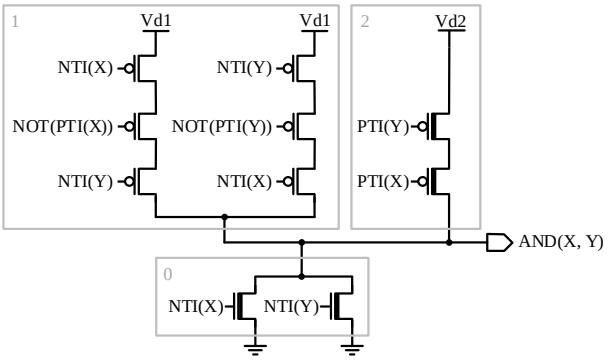

Figure 5: Transistor level implementation of the ternary AND.

B. *Ternary OR Gate*

In this work, the OR gate definition in Table 5 is used to implement the gate, which corresponds to the MAX function.

Table 5: Truth table for the ternary OR gate.

X	Y	OR(X, Y)	Network 2	Network 1	Network 0
0	0	0	Off	Off	0
0	1	1	Off	1	Off
0	2	2	2	Off	Off
1	0	1	Off	1	Off
1	1	1	Off	1	Off
1	2	2	2	Off	Off
2	0	2	2	Off	Off
2	1	2	2	Off	Off
2	2	2	2	Off	Off

The transistor level implementation is shown in Figure 6. The networks are also highlighted in the figure. The circuit is simulated in LTSPICE and the corresponding results are presented in Section IV.

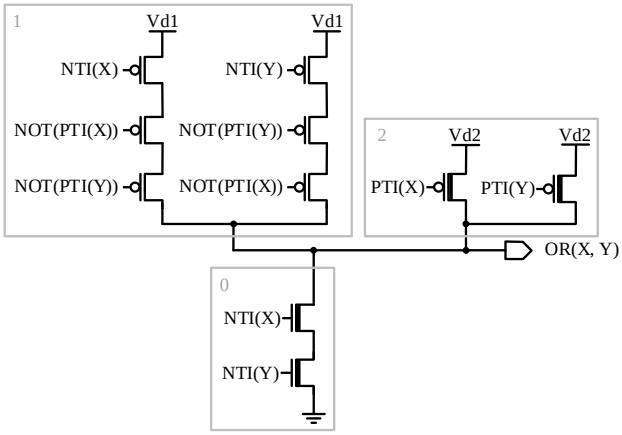

Figure 6: Transistor level implementation of the ternary OR gate.

C. *Ternary Half Adder Circuit*

A ternary half adders circuit has two outputs: carry and the sum. If the sum of two ternary inputs X and Y are bigger than 2, then the carry output is set to 1. Truth tables for the carry and sum outputs of the ternary half adder are given in Table 6 and Table 7, respectively.

Table 6: Truth table for the carry output of the ternary half adder.

X	Y	CRY(X, Y)	Network 2	Network 1	Network 0
0	0	0	Off	Off	0
0	1	0	Off	Off	0
0	2	0	Off	Off	0
1	0	0	Off	Off	0
1	1	0	Off	Off	0
1	2	1	Off	1	Off
2	0	0	Off	Off	0
2	1	1	Off	1	Off
2	2	1	Off	1	Off

Table 7: Truth table for the sum output of the ternary half adder.

X	Y	SUM(X, Y)	Network 2	Network 1	Network 0
0	0	0	Off	Off	0
0	1	1	Off	1	Off
0	2	2	2	Off	Off
1	0	1	Off	1	Off
1	1	2	2	Off	Off
1	2	0	Off	Off	0
2	0	2	2	Off	Off
2	1	0	Off	Off	0
2	2	1	Off	1	Off

The transistor level implementations of the carry and sum generator circuits are shown in Figure 7 and Figure 8. The networks are also highlighted in the figure. Simulation results are given in Section IV.

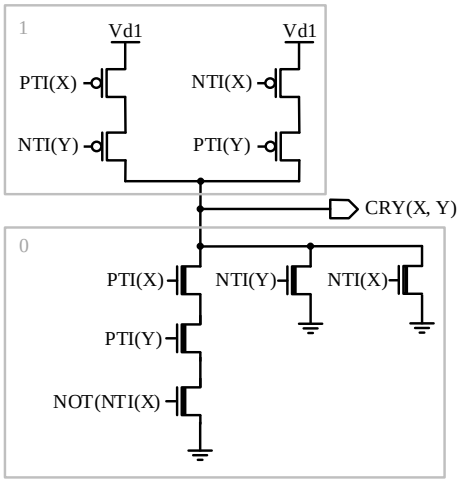

Figure 7: The ternary carry generator circuit.

IV. SIMULATION RESULTS

In this section, the methodology is verified by conducting LTSPICE simulations of the circuits in Section IV. For the simulations PTM 32nm technology models are used. In addition to the standard NMOS and PMOS models, low threshold devices are defined which has $|V_t|$=0.25V.

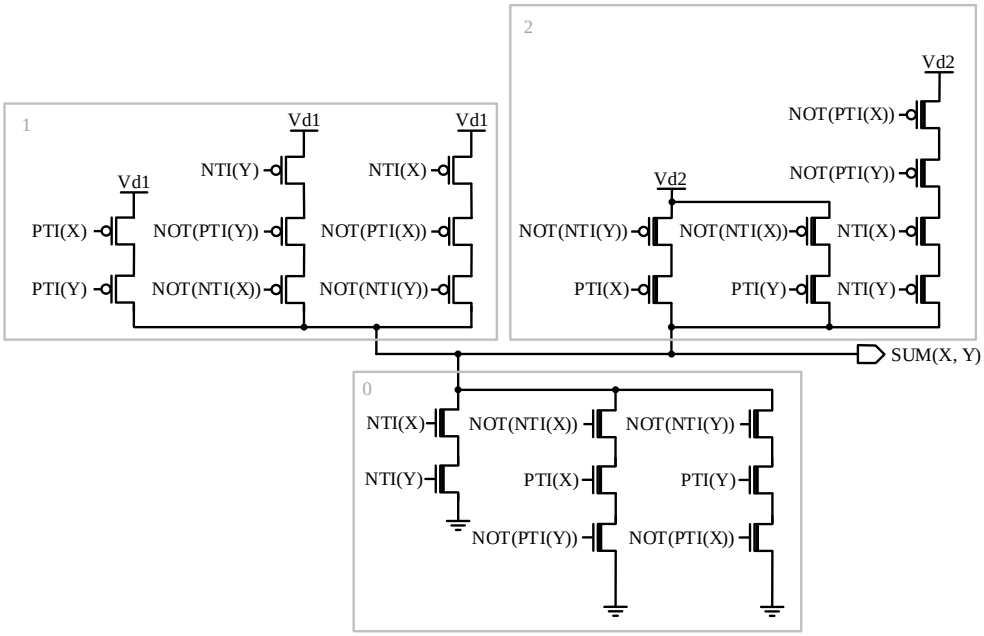

Figure 8: The ternary sum generator circuit.

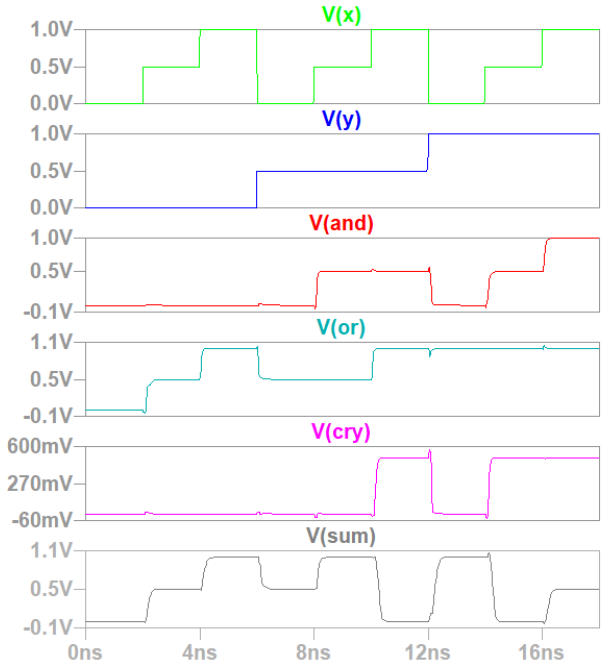

Figure 9: Simulation results.

Simulation results for the ternary AND, OR and half adder circuits are given in Figure 9. The simulation results are consistent with the truth tables given in Section IV which verifies the methodology. The aim of this work is to present a systematic way to synthesize ternary gates with MOSFETs. The author does not give any method to size the transistors, thus the performance of the resulting gates is not analyzed.

I. Conclusion

Recently, several research on CNTFET based ternary logic was done. However, scale of CNTFET circuits is limited to a few thousands and no fabrication techniques are available to build large scale ternary CNTFET circuits. Recent CMOS technologies offers multi-Vt devices in the same process. In this work, we designed ternary logic gates using a multi-Vt CMOS process and presented a methodology to build ternary CMOS logic gates. Correct functionality of the designed gates are verified via LTSPICE simulations.

References

[1] S. Lin, Y.-B. Kim and F. Lombardi, "CNTFET-based design of ternary logic gates and arithmetic circuits," *IEEE Transactions on nano technology*, vol. 10, no. 2, pp. 217–225, 2009.

[2] N. H. Bastani, M. H. Moaiyeri, and K. Navi, "Carbon nanotube field effect transistor switching logic for designing efficient ternary arithmetic circuits," *Journal of Nanoelectronics and Optoelectronics*, vol. 12, no. 2, pp. 118–129, 2017.

[3] B. Srinivasu and K. Sridharan, "Low-complexity multiternary digit multiplier design in CNTFET technology," *IEEE Transactions on Circuits and Systems II: Express Briefs*, vol. 63, no. 8, pp. 753–757, 2016.

[4] S. K. Sahoo, G. Akhilesh, R. Sahoo and M. Muglikar, "High-performance ternary adder using CNTFET," *IEEE Transactions on Nanotechnology*, vol. 16, no. 3, pp. 368–374, 2017.

[5] G. Hills, et al., "Modern microprocessor built from complementary carbon nanotube transistors," *Nature*, vol. 572 no. 7771, pp. 595–602, 2019.

[6] P. C. Balla, and A. Antoniou, "Low power dissipation MOS ternary logic family," *IEEE Journal of Solid-State Circuits*, vol. 19, no. 5, pp. 739–749, 1984.

[7] Taiwan semiconductor manufacturing company limited. URL: Logic Technology - Taiwan Semiconductor Manufacturing Company Limited (tsmc.com). Last Access: October 2022.

[8] Analog Devices LTSPICE. URL: https://www.analog.com/en/design-center/design-tools-and-calculators/ltspice-simulator.html. Last Access: October 2022.

[9] W. Zhao, Y. Cao, "New generation of Predictive Technology Model for sub-45nm early design exploration," *IEEE Transactions on Electron Devices*, vol. 53, no. 11, pp. 2816-2823, 2006.

Mathematical Modeling and Simulation of Solar Photovoltaic Module in Matlab/Simulink

M.S. ENDİZ[1]

[1] Necmettin Erbakan University, Konya/Turkey, msendiz@erbakan.edu.tr

Abstract **- In this paper, the mathematical modeling and simulation of a solar photovoltaic module are presented using the equivalent circuit of a solar photovoltaic cell with its parameters in Matlab/Simulink environment. The analysis is based on the equations of the single-diode equivalent circuit model. For the mathematical modeling and simulation, a 320W photovoltaic module is chosen. The main characteristics of the module required for the analysis are obtained from the datasheet supplied by the manufacturer. Under different environmental parameters such as temperature and solar radiation, the Current-Voltage and Power-Voltage characteristic curves are provided. The effects related to the changes in temperature and solar radiation on simulation results are observed.**

Keywords **– Solar energy, Photovoltaic cell, Modeling, Temperature, Solar radiation.**

I. INTRODUCTION

Due to the tremendous consumption and depletion of fossil fuels, renewable energy sources are becoming more and more important in recent years. Renewable energy is generated from natural processes and has the potential to provide an endless supply of clean energy [1].

As sunlight is the most abundant resource, solar photovoltaic energy is regarded as the most promising renewable source and is believed to form the basis of a sustainable energy economy. The solar photovoltaic system may be superior to other types of renewable energy sources because it generates electricity without making any noise, requires very little operation and maintenance, does not contribute to the direct pollution of the environment or the depletion of natural resources, and is entirely reliant on the unlimited supply of radiation from the sun. As a result, the use of solar power is expanding at a rate that is higher than that of any other type of renewable technology [2].

The physical configuration of a photovoltaic system is shown in Figure 1. The photovoltaic cell is the fundamental component of a solar power system. P-type and N-type semiconductor materials compose photovoltaic cells. Exposing the junction point of these semiconductors to photon radiation results in an electron flow across the external circuit. This phenomenon is known as the photovoltaic effect. An electric current is generated as a result of this process [3].

A module is composed of many photovoltaic cells connected in series. To increase the system voltage and current, the modules are connected in series or parallel to form a photovoltaic array. Typically, a solar power plant consists of a single or many photovoltaic arrays [4, 5].

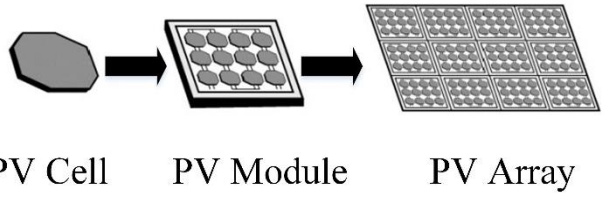

Figure 1: Physical configuration of a photovoltaic system.

Many factors influence module efficiency, including solar radiation intensity, temperature, tilt angle, shade, and surface dust-induced pollution. Most notable among these are the intensity of solar radiation and the ambient temperature. The amount of solar radiation has a direct impact on the amount of power produced by the module. As a consequence of this, the power output of the module will increase if the amount of solar radiation rises. However, an increase in temperature level has the opposite effect on the efficiency of the module. The amount of energy produced by the module decreases as the temperature rises since the increase in the level of resistance of the solar cell [6-8].

The main contribution of this paper is to perform the mathematical modeling and simulation of a solar photovoltaic module using the equivalent circuit of a solar photovoltaic cell with its parameters in Matlab/Simulink environment. Current-Voltage (I-V) and Power-Voltage (P-V) characteristic curves of a photovoltaic module are presented under different conditions. The effects of the environmental parameters such as changes in temperature and solar radiation on the behaviour of the photovoltaic characteristics are observed.

II. MODELING OF SOLAR PHOTOVOLTAIC MODULE

When the photovoltaic module is exposed to sunlight, the solar cells within the module absorb the photon energy from the sun and create electrical charges that move in the cell. If the photon energy is the same as or higher than the material's band gap, a photocurrent proportional to the solar radiation is generated. As a result of the photocurrent, the generation of electric current in the solar cell occurs [9].

The single-diode circuit model, which represents the electrical behavior, is the most often used model to determine the energy generation in solar cells [9, 10]. As can be seen in Figure 2, the ideal model of a solar cell's equivalent circuit is made up of a current source connected in parallel with a single diode and resistances that are connected in series and parallel. In the corresponding circuit configuration; G is the solar radiation, D is the diode that protects the source from potential reverse leakage currents, R_P is the shunt loss resistance, and R_S is the series loss resistance.

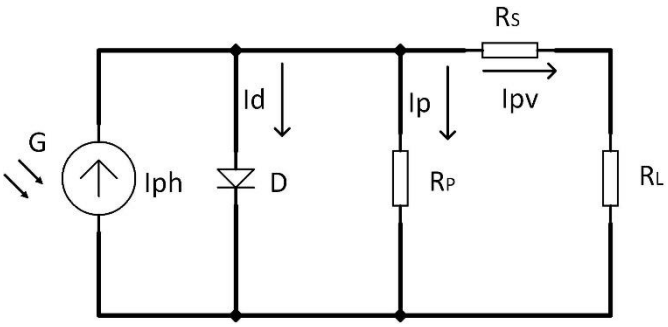

Figure 2: The ideal equivalent circuit model of a solar cell.

Since the generation of electricity is closely related to solar radiation and cell temperature, the following equations can be given to present the modeling of the solar photovoltaic module. The photocurrent can be calculated as the Equation (1):

$$I_{ph} = [I_{sc} + K_i * (T - 298)]\frac{G}{1000} \quad (1)$$

The saturation current and reverse saturation current are expressed in Eq. (2) and Eq. (3) respectively:

$$I_s = I_{rs} * \left\{\frac{T}{T_n}\right\}^3 * e^{\left\{\frac{q*E_g*(1/T_n - 1/T)}{n*K}\right\}} \quad (2)$$

$$I_{rs} = \frac{I_{sc}}{e^{\left\{\frac{q*V_{oc}}{n*N_s*K*T}\right\}} - 1} \quad (3)$$

The shunt loss current is calculated in Eq. (4):

$$I_p = \frac{V + I * R_S}{R_P} \quad (4)$$

Using Eqs. (1-4), the output current of the solar cell equivalent circuit can be found below:

$$I_{pv} = I_{ph} - \left(I_s * \left[e^{\left\{\frac{q*(V+I*R_S)}{n*N_s*K*T}\right\}} - 1\right]\right) - I_p \quad (5)$$

where I_{ph} is the photocurrent, I_d is the current flowing through the diode, I_{sc} is the short circuit current, V_{oc} is the open circuit voltage, K_i is the temperature coefficient of short circuit current, T is the operating temperature, T_n is the nominal temperature, I_s is the saturation current, I_{rs} is the reverse saturation current, q is the electron charge, E_g is the band gap energy of the semiconductor, n is the ideality factor of the diode, K is the Boltzmann constant, N_s is the number of cells connected in series, N_p is the number of cells connected in parallel, I_p is the shunt loss current, and I_{pv} is the output current.

III. Simulation Results

Using the constants and the variables that are given in the mathematical expressions based on the ideal equivalent circuit model of the solar cell, modeling and simulation of the solar photovoltaic module are carried out in Matlab/Simulink environment. Simulink has many blocks that can be used to build any desired models. Simulink provides access to the block libraries where these blocks are arranged. By adding blocks, specifying their behavior, and using signal lines to connect the blocks, different models can be generated.

The electrical parameters and the model parameters of the solar photovoltaic module are listed in Table 1 and Table 2 respectively. Using the corresponding blocks, the photocurrent model, the saturation current model, the reverse saturation current model, the shunt loss current model, and the output current model of the solar photovoltaic module are built in Simulink and presented in Figures 3-7 respectively.

Table 1: The electrical parameters of the solar photovoltaic module.

Parameters	**Values**
Maximum power (W)	320
Open circuit voltage V_{oc} (V)	49.5
Short-circuit current I_{sc} (A)	8.6
Voltage at maximum power point V_{mp} (V)	40.1
Current at maximum power point I_{mp} (A)	7.99
Number of cells in series	80
Number of cells in parallel	1
Temperature coefficient of V_{oc} (%/deg.C)	-0.37
Temperature coefficient of I_{sc} (%/deg.C)	0.041

Table 2: The model parameters of the solar photovoltaic module.

Parameters	**Values**
Light-generated current (A)	8.6148
Diode saturation current (A)	3.9672e-10
Diode ideality factor	1.0129
Series resistance (ohms)	0.40954
Shunt resistance (ohms)	238.5428

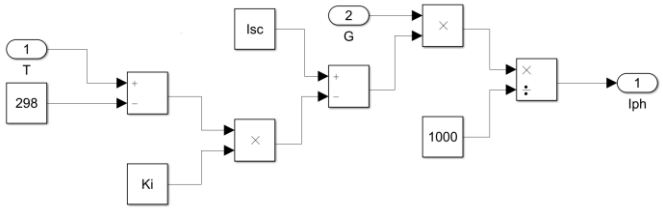

Figure 3: The photocurrent model of the solar cell.

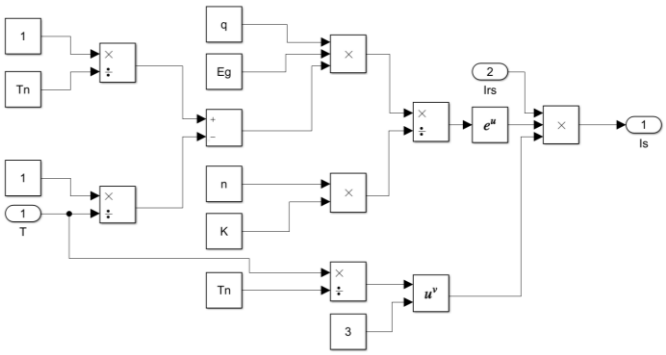

Figure 4: The saturation current model of the solar cell.

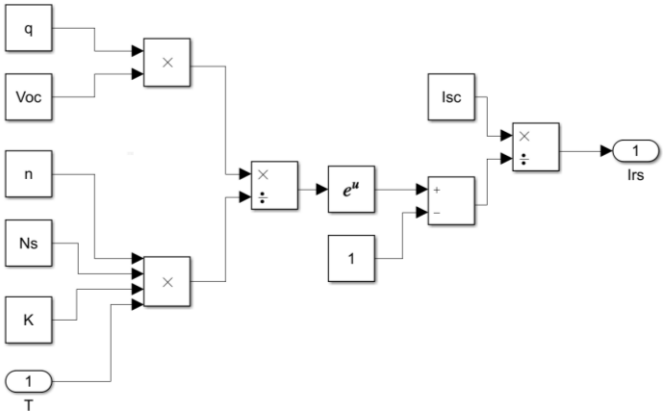

Figure 5: The reverse saturation current model of the solar cell.

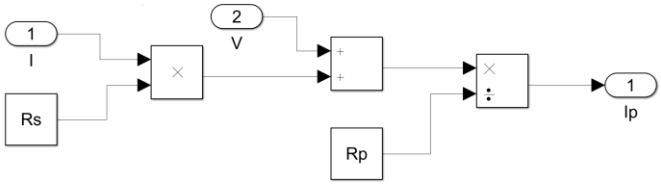

Figure 6: The shunt loss current model of the solar cell.

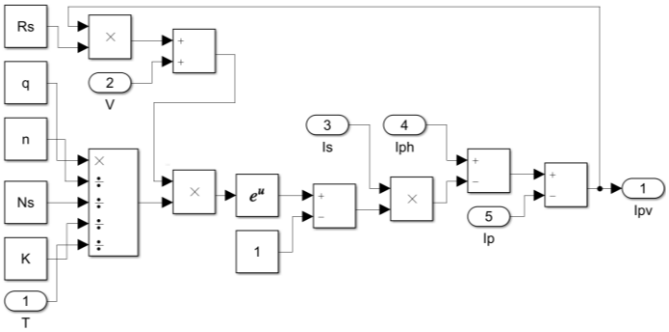

Figure 7: The output current model of the solar cell.

Under standard test conditions (STC) which are a radiation of 1kW/m^2 and a cell temperature of 25°C as given in Figure 8, the characteristic curves of the used photovoltaic module are depicted in Figure 9 and Figure 10 respectively.

Figure 11 and Figure 14 show the different solar radiation levels (400W/m^2, 600W/m^2, 800W/m^2, 1000W/m^2) with constant temperature (25°C), and the different temperature levels (25°C, 30°C, 35°C, 40°C) with constant irradiance (1000 W/m^2). In Figure 12, Figure 13, Figure 15, and Figure 16 are shown the corresponding I-V and P-V characteristic curves for various solar radiation and temperature conditions of the solar photovoltaic module.

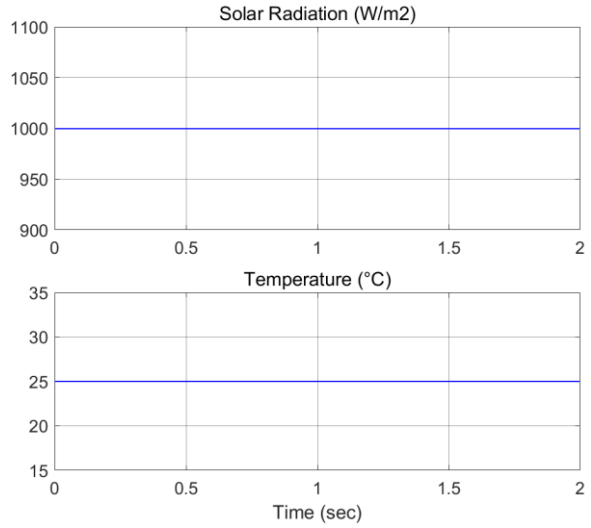

Figure 8: Solar radiation and temperature levels under STC.

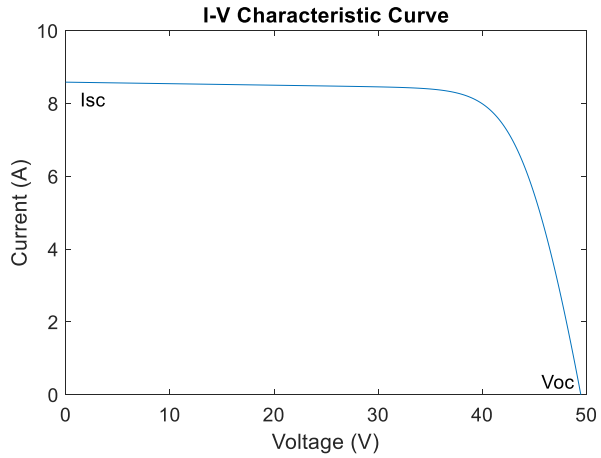

Figure 9: I-V characteristic curve under STC.

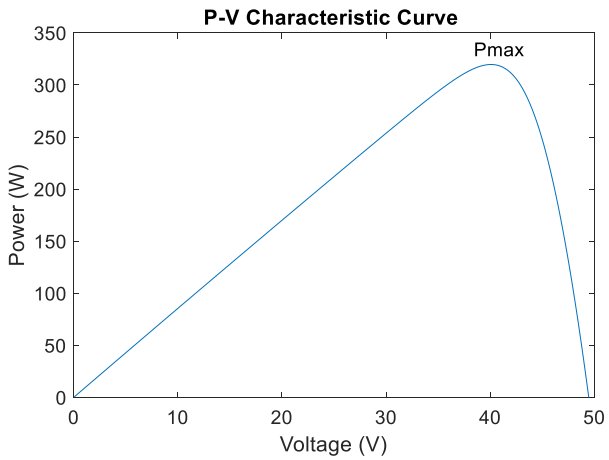

Figure 10: P-V characteristic curve under STC.

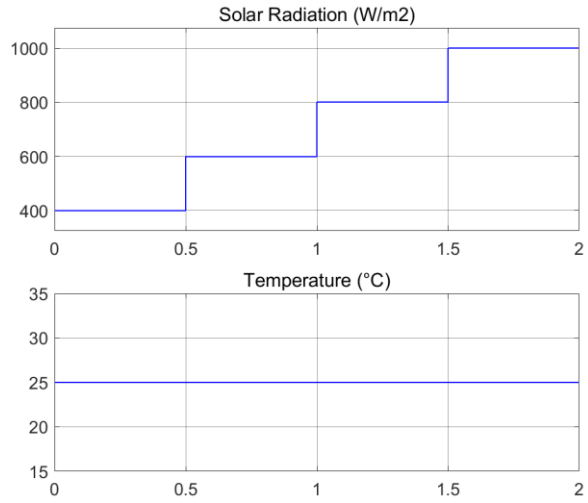

Figure 11: Different solar radiation levels at constant temperature.

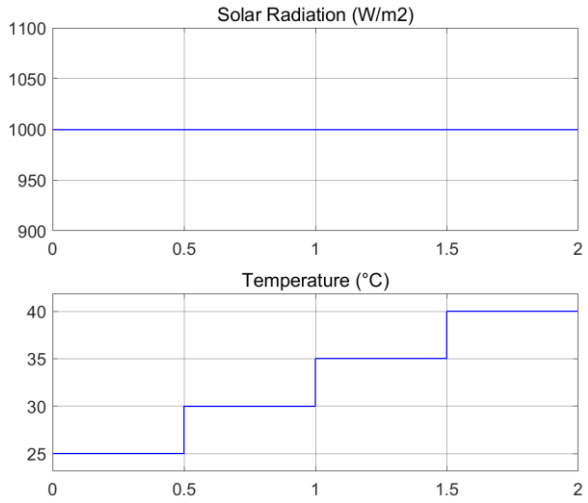

Figure 14: Different temperature levels at constant solar radiation.

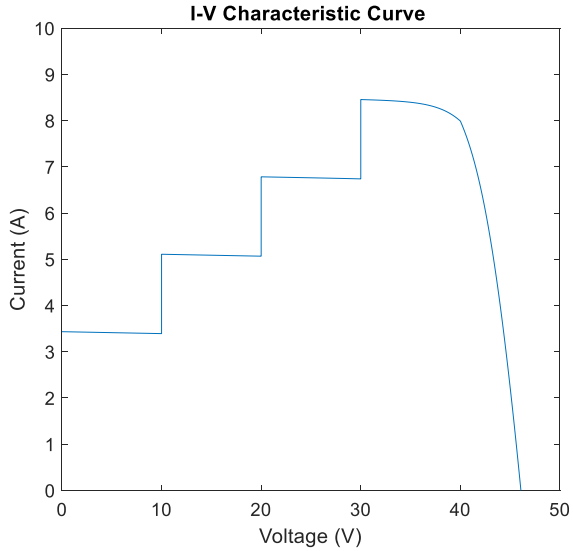

Figure 12: I-V characteristic curve for various G and constant T.

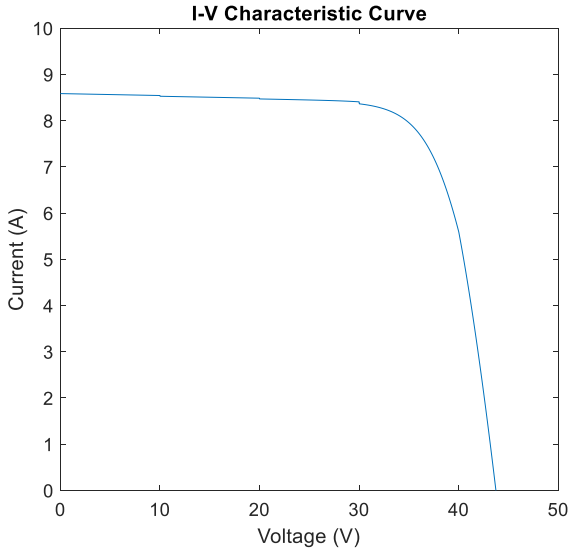

Figure 15: I-V characteristic curve for various T and constant G.

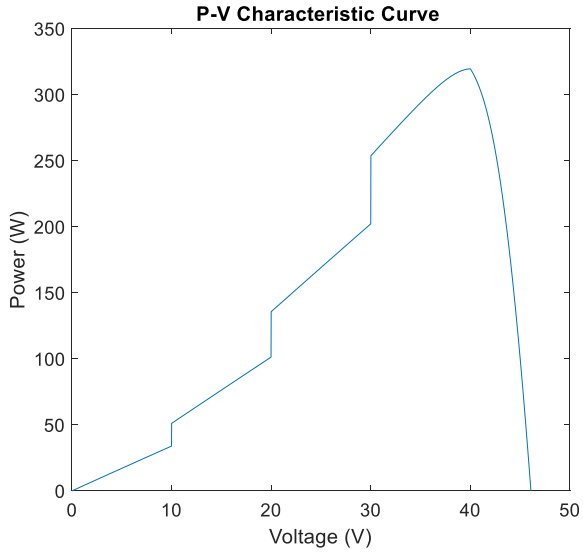

Figure 13: P-V characteristic curve for various G and constant T.

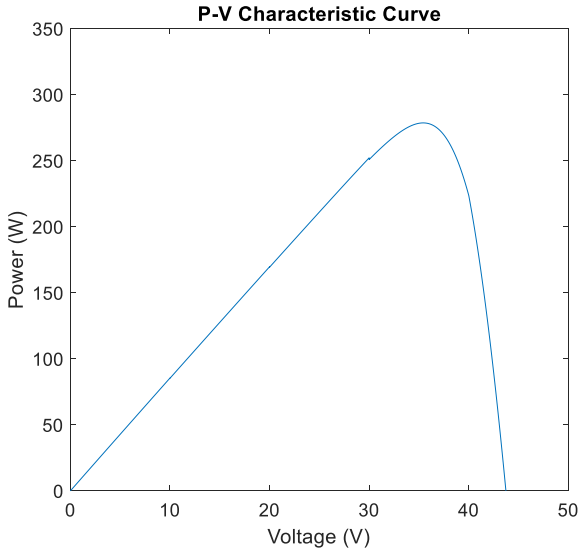

Figure 16: P-V characteristic curve for various T and constant G.

IV. CONCLUSION

Using the blocks for the mathematical expressions based on the ideal equivalent circuit model of the solar cell, the solar photovoltaic module is modeled and simulated in this study. The analysis is based on the equations of the single-diode equivalent circuit model. The behavior of the solar photovoltaic module for different solar radiation and temperature conditions is studied and the corresponding I-V and P-V characteristic curves are obtained.

The presented simulation results confirm that the solar photovoltaic module has a non-linear characteristic and it is clear that the efficiency of the module is affected by solar radiation intensity and ambient temperature. The effect of solar radiation on the photovoltaic module output power is greater than the temperature change. With the increase in solar radiation level, the electrons in the solar cell are given a greater amount of excitation energy. Thus more power is generated. On the other hand, temperature increases have a negative impact on the efficiency of the photovoltaic module, since the higher temperatures decrease the open circuit voltage of the solar cell and the generated output power. Solar photovoltaic systems represent a viable alternative to the rising need for energy and will eventually replace fossil fuel energy sources, which are expected to become rare in the long term. With effective modeling and simulating of the solar photovoltaic module, new approaches for optimizing system operation can be developed.

REFERENCES

[1] A. G. Olabi and M. A. Abdelkareem, "Renewable energy and climate change," *Renewable and Sustainable Energy Reviews,* vol. 158, pp. 112111, April 2022.

[2] O. A. Al-Shahri, F. B. Ismail, M. A. Hannan, M. H. Lipu, A. Q. Al-Shetwi, R. A. Begum, ... & E. Soujeri, "Solar photovoltaic energy optimization methods, challenges and issues: A comprehensive review," *Journal of Cleaner Production,* vol. 284, pp. 125465, February 2021.

[3] N. Rathore, N. L. Panwar, F. Yettou, and A. Gama, "A comprehensive review of different types of solar photovoltaic cells and their applications," *International Journal of Ambient Energy,* vol. 42(10), pp. 1200-1217, 2021.

[4] M. Alzahrani, K. Shanks, and T. K. Mallick, "Advances and limitations of increasing solar irradiance for concentrating photovoltaics thermal system," *Renewable and Sustainable Energy Reviews,* vol. 138, pp. 110517, March 2021.

[5] P. Pathipooranam, "An Enhancement of the Solar Panel Efficiency–A Comprehensive Review," *Frontiers in Energy Research,* vol. 10, July 2022.

[6] M. Gürtürk, H. Benli, and N. K. Ertürk, "Effects of different parameters on energy–Exergy and power conversion efficiency of PV modules," *Renewable and Sustainable Energy Reviews,* vol. 92, pp. 426-439, September 2018.

[7] C. Schill, S. Brachmann, and M. Koehl, "Impact of soiling on IV-curves and efficiency of PV-modules," *Solar Energy,* vol. 112, pp. 259-262, February 2015.

[8] T. Salmi, M. Bouzguenda, A. Gastli, and A. Masmoudi, "Matlab/simulink based modeling of photovoltaic cell," *International journal of renewable energy research,* vol. 2(2), pp. 213-218, 2012.

[9] A. Al-Subhi, "Parameters estimation of photovoltaic cells using simple and efficient mathematical models," *Solar Energy,* vol. 209, pp. 245-257, October 2020.

[10] B. K. Dey, I. Khan, N. Mandal, and A. Bhattacharjee, "Mathematical modelling and characteristic analysis of Solar PV Cell," *In 2016 IEEE 7th Annual Information Technology, Electronics and Mobile Communication Conference (IEMCON),* pp. 1-5.

Principles and Utilization of a Single-Phase Z-Source Inverters

H. AL-BAYATY [1], F.T. SEDEEQ[2] and M.S. KIDER[3]

[1] Engineering College, University of Kirkuk, Kirkuk, Iraq, dr.hussein@uokirkuk.edu.iq
[2] Engineering College, University of Kirkuk, Kirkuk, Iraq, fidansd@uokirkuk.edu.iq
[3] College of Computer Science, University of Kirkuk, Kirkuk, Iraq, muna@uokirkuk.edu.iq

***Abstract* – In this paper, the single-phase Z-source inverter simulation and modeling along with their methods of control for application of conversion dc-to-ac power is presented. The Z-network design and inverter as full bridge of a single-phase is performed in environment of MATLAB-Simulink. An input voltage as fixed DC is given to the inverter and an output voltage as controlled AC is gained through variable cycle of duty or adjusting the on and off periods of the inverter components. The duty variation of cycle might be attained through utilizing controlling methods of pulse width modulation (PWM). Two control PWM strategies are presented, like Simple Boost Control and Sinusoidal carrier-based PWM. In detail, such methods are defined and comparison was done on the simulation basis in MATLAB/ Simulink. The Z-source element ripple, voltage as output, current and the profile as harmonics, are controlled with modulation index variation and frequency of switching. Likewise, the shoot effect by state on the inverter as traditional is eliminated in the z- source inverter. Similarly, two diverse applications are offered for modeling and simulated system verification along with 2 strategies of controlling 1st is based on performance and simulation analysis of photo voltaic (PV) system based on Z-Source inverter. Second application is based on M&S of inverter of Z- source for controlling the Induction Motor speed.**

***Keywords* - Network topology, power system modeling, power system simulation.**

I. INTRODUCTION

EVERY power electronics system contains an input source, different converter topologies, and output loads. Every topology of converter has its particular limitations in respect to diverse aspects i.e., the utilized components number, various semi-conductor switches, and converter effectiveness [1-4].

Electronics of power have widely been utilized in several uses as long it was born. The inverter of single-phase (SP) that changes dc voltage/current into SP ac voltage/current is considered as mostly popular and important converters [5]. The newly presented Z-source inverter [6-9], is of some distinctive features and it able to overcome some of the traditional voltage source limitations and current inverters source. The aim of the current work is "for investigating the inverter of Z -source Modeling and the strategy of controlling for the application dc-to-ac power change.

Brief reviews of research which till now has been performed in the literature regarding the design and control the Z-source Inverter strategies is offered in this part. The modes of operating and the Z-Source inverter characteristics of minor inductance are conversed in [10]. In [11] Z-source network modeling with loading as inductive is set. A Pulse Width Modulation- a survey is announced in '90s [12]. Lastly, controllers intended for definite requests that is to say voltage sag and fuel cell compensation are set in [13].

In this paper, the single-phase Z-source inverter simulation and modeling along with their methods of control for application of conversion dc-to-ac power is presented. The Z-network design and inverter as full bridge of a single-phase is performed in environment of MATLAB-Simulink. An input voltage as fixed DC is given to the inverter and an output voltage as controlled AC is gained through variable cycle of duty or adjusting the on and off periods of the inverter components. Two control PWM strategies are presented, like Simple Boost Control and Sinusoidal carrier-based PWM. The method and obtained results are presented in subsequent titles.

II. METHODOLOGY

A. State Space Model of the Z-Source Inverter (ZSI)

The ZSI equivalent circuit is illustrated in Figure 1. In which shoot through operation is presented by switch S1. *IL* is the overall inverter input current during the non-shoot-through period.

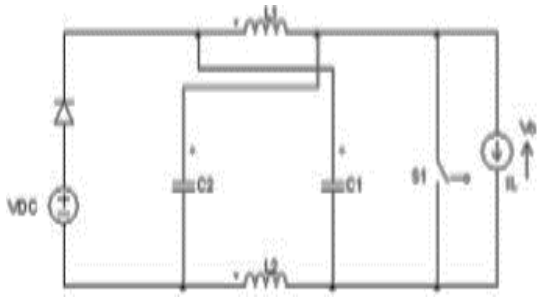

Figure 1: Z-Source Equivalent circuit inverter.

For S1= ON i.e. during shoot-through state from the equivalent circuit, Figure 1.

B. State Matrix

The state matrix is given in equation (1).

$$\begin{bmatrix} \dot{IL_1} \\ \dot{IL_2} \\ \dot{Vc_1} \\ \dot{Vc_2} \end{bmatrix} = \begin{bmatrix} 0 & 0 & 1/L1 & 0 \\ 0 & 0 & 0 & 1/L2 \\ -1/C1 & 0 & 0 & 0 \\ 0 & -1/C2 & 0 & 0 \end{bmatrix} \begin{bmatrix} IL_1 \\ IL_2 \\ Vc_1 \\ Vc_2 \end{bmatrix} \quad (1)$$

Figure 2 presents ZSI Equivalent circuit (a) Shoot via mode (b) non shoot-via mode For S1 = OFF equivalent circuit.

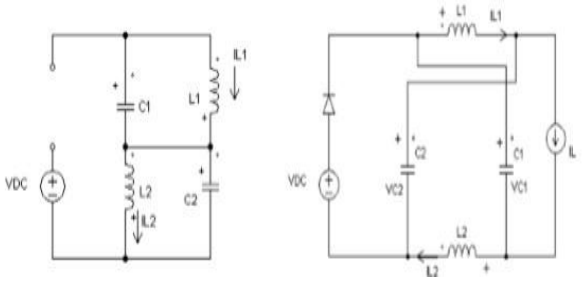

Figure 2: ZSI Equivalent circuit.

Another state matrix is given in equation (2).

$$\begin{bmatrix} \dot{IL_1} \\ \dot{IL_2} \\ \dot{Vc_1} \\ \dot{Vc_2} \end{bmatrix} = \begin{bmatrix} 0 & 0 & 0 & -1/L1 \\ 0 & 0 & -1/L2 & 0 \\ 0 & 1/C1 & 0 & 0 \\ 1/C2 & 0 & 0 & 0 \end{bmatrix} \begin{bmatrix} IL_1 \\ IL_2 \\ Vc_1 \\ Vc_2 \end{bmatrix} + \begin{bmatrix} V_{DC}/L1 \\ V_{DC}/L2 \\ -I_{DC}/C1 \\ -I_{DC}/C2 \end{bmatrix} \quad (2)$$

The state equations are averaged considering shoot-through duty ratio *D* (i.e. when S1 is on).

Averaging Two Matrices as;

$$(t) = D\,(A1x + B1\,u\,) + (1 - D)\,(\,A2x + B2\,u) \quad (3)$$

The state space model becomes;

$$\begin{bmatrix} \dot{IL_1} \\ \dot{IL_2} \\ \dot{Vc_1} \\ \dot{Vc_2} \end{bmatrix} = \begin{bmatrix} 0 & 0 & D/L & -(1-D)/L \\ 0 & 0 & -(1-D)/L & D/L \\ -D/C & (1-D)/C & 0 & 0 \\ (1-D)/C & -D/C & 0 & 0 \end{bmatrix} \begin{bmatrix} IL_1 \\ IL_2 \\ Vc_1 \\ Vc_2 \end{bmatrix} + \begin{bmatrix} (1-D)V_{DC}/L \\ (1-D)V_{DC}/L \\ -(1-D)I_{DC}/C \\ -(1-D)I_{DC}/C \end{bmatrix} \quad (4)$$

Taking Laplace transform, transfer functions can be derived as

$$\frac{\hat{\imath}_L(s)}{\hat{d}(s)} = \frac{(2V_c + V_{DC})sC - (2D-1)(2I_L - I_{DC})}{S^2LC + (2D-1)^2}$$

$$\frac{\hat{V}_c(s)}{\hat{d}(s)} = \frac{(2V_c + V_{DC})(1-2D) - sL(2I_L - I_{DC})}{S^2LC + (2D-1)^2} \quad (5)$$

III. Result and Discussion

Output current load of inverter and voltage is displayed in Figure 3, in which the current output is sinusoidal (13.98 A) and output voltage is square wave as fundamental (96.06V). It has several harmonics components because of that the average output voltage as fundamental is low. Figure 4 shows the capacitor voltage in Z-impedance network; at minor capacitor and inductor the ripple is related along the resonance between the capacitors and the inductors. By achieving the larger capacitor and inductor the ripple can be reduced.

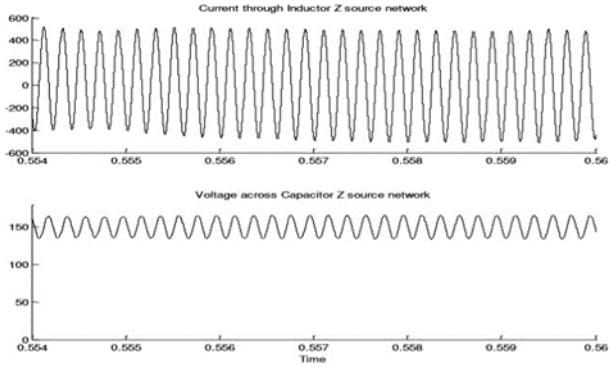

Figure 3: Inverter output load current and voltage.

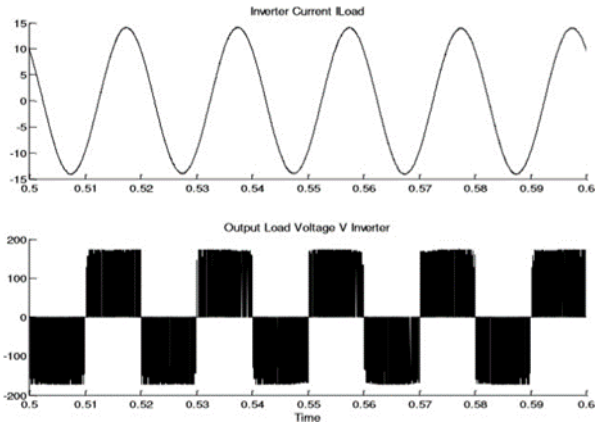

Figure 4: inductor current (IL1) and voltage across capacitor (VC1).

To illustrate the proposed inverter effectiveness, simulation was done on diverse modulation values index (*m*) with continuous switching frequency (10 kHz). The findings are stated in Table 1. For the same index of modulation and the Z-source inverter boost factor offers great output voltage as peak. To elevate the fundamental voltage and current the only method is to upsurge *m*. If index of modulation elevates the fundamental current and voltage improves and the influence of the total harmonics components (%THD) as well elevates. Such leads to non-linear component introduction in the output. Though, via preserving higher frequency of switching the influence of such non-linear components existing in the fundamental current and voltage is controlled.

Distortion of harmonics voltage on power system 69KV and under is restricted to 5% total distortion of harmonics with each singular harmonics restricted to 3%. The current harmonics restrictions might differ based on the system short circuit strength they are injected into. The current harmonics limit identifies the maximum harmonics current amount in which the customer able to inject into the system of utility.

Table 1: Variation of Modulation index with THD Based on standard of IEEE 519.

Input		Output		Method	Year and ref
m	Vdc	Vac	% THD		
0.8	100	95.75	3.46	Multilevel PWM	2006 [9]
0.8	300	241.19	68.02	Sine PWM	2007 [8]
0.8	300	287.52	57.67	ISCPWM	2007 [8]
0.7	150	190	--	MSVPWM	2009 [10]
0.88	200	199.6	4.14	Triangular CPWM	2010 [7]
0.88	200	300.1	2.53	Sine PWM	2010 [7]
0.8	150	211	0.05	Sine PWM	A.1
0.85	150	237.7	0.05	Sine PWM	A.1

The utility is of responsibility in supplying a clean voltage (low distortion) to the customer. However, the utility can be legitimately judged only, if the customer runs into the harmonics current limit. Because of such reason the diverse techniques displayed by researchers are compared with the suggested technique, the findings are presented in Table 2, We have used simple technique as sine wave PWM to control strategy of switching.

Table 2: Comparison of Modulation Index (m) and %THD with different techniques.

Type / Parameter	Traditional inverter		Z-source inverter	
	No Load	Full Load	No Load	Full Load
Fundamental V_L (V)	*150*	*95.27*	*172*	*96.5*
%THD of V_L	*12.46*	*12.46*	*12.01*	*12.01*
Fundamental I_L (A)	*18.72*	*11.56*	*19*	*14.01*
%THD of I_L	*22.59*	*27.41*	*0.18*	*0.11*

Because of parameter of design and worthy impedance matching between Z-source network, IGBT we can keep harmonic distortion as total as low as conceivable at high frequency of switching. Finally, the comparison of simulation traditional inverter responses, Z source inverter. The findings are presented in Table 3. The fundamental traditional inverter output voltage response is displayed in Figure 4 and the Z-source inverter of no filter is exposed in Figure 2. It is clear that they have square wave fundamental output voltage that differ with load as 150-95.27V, 172-96.5V with 12.46%, 12.01% of total harmonics distortion. Likewise, current traditional inverter response and the Z-source inverter are exposed in Figure 4. It is obvious that it has sine wave fundamental output current that differs with load as 18.72-11.56A, 19-14.01A with 22.59%, 0.18% of total harmonics distortion as illustrated in Figure 5 and 6.

Table 3: Inverter response comparison without and with filter Vdc =150v, m = 0.642 and freq. of switching 10 KHz.

Sr No	M	Fundamental IL	% THD in IL	Fundamental VL	% THD in VL
1	0.642	37.41	0.06	169.1	0.07
2	0.7	40.76	0.03	184.2	0.04
3	0.75	43.74	0.03	197.7	0.04
4	0.8	46.68	0.04	211	0.05
5	0.85	49.63	0.04	224.3	0.05
6	0.9	52.59	0.04	237.7	0.05

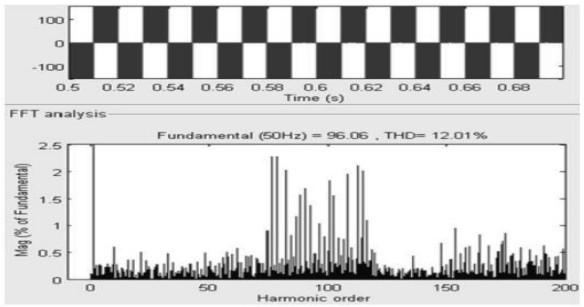

Figure 5: inductor current (IL1) and voltage across capacitor (VC1).

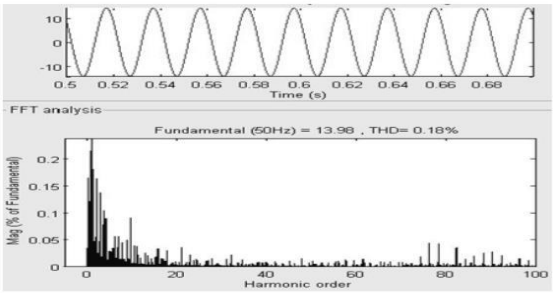

Figure 6: inductor current (IL1) and voltage across capacitor (VC1).

IV. CONCLUSION

The current work of many contributions as follow: The M&S of Z-network with full bridge as inverter of single phase is existing in the environment of MATLAB-Simulink for the design parameters confirmation.

Control strategies of 2 PWM circuits are suggested i.e., Simple Boost Control and Sinusoidal carrier-based PWM. Such methods are defined in detail and comparison is made on according to the simulation in MATLAB/ Simulink.

The ripple of Z-source element, voltage of output, current and their harmonics profile are differed with index of modulation and switching frequency of. Likewise, it emphases the shoot via state influence on the Z-source and inverter as traditional.

Likewise, 2 diverse uses effectively exist, 1st is based on photo voltaic (PV) system simulation and performance analysis according to z-Source inverter". 2nd application is

according to Z-source inverter M&S for controlling the Induction Motor speed.

Lastly, the simulated system verification is compared with the experimental single phase Z-source inverter prototype.

REFERENCES

[1] B. K. Bose, "*Modem Power Electronics and AC Drives*". Upper Saddle River, NJ: Prentice-Hall PTR, 2002.

[2] B. Kuo, "*Automatic Control Systems*", Prentice Hall, IL, 1994.

[3] N. Mohan, U. Riobbins, "Power Electronics", Media Enhanced Third Edition Converter Applications and Design, Wiley India Edition, ISBN 978-81-265- 1090-0, Year - 2009.

[4] H., Al-bayaty, M. Ambroze, and M. Zaki Ahmed. "*Utilization of harmonics current in single phase system*" 2016 17th International Conference on Harmonics and Quality of Power (ICHQP). IEEE, 2016.

[5] N. Hamrouni and A. Chérif, "*Modelling and control of a grid connected photovoltaic system*", Revue des Energies Renouvelables Vol. 10 No 3 (2007) 335 - 344.

[6] F. Z. Peng. "*Z-source inverter*", IEEE transactions on industry application, Vol.39, No.2, March/April 2003.

[7] F. Z. Peng and Y. Huang, "*Z-Source Inverter for Power Conditioning and Utility Interface of Renewable Energy Sources*", IEEE explorer 2008.

[8] H. Al-bayaty, M. Ambroze and M. Z. Ahmed, "*The benefit of harmonics current using a new topology of hybrid active power filter*," 2015 IEEE 5th International Conference on Power Engineering, Energy and Electrical Drives (POWERENG), 2015, pp. 330-336, doi: 10.1109/PowerEng.2015.7266339.

[9] M. Shen, F. Z. Peng, "*Control of the Z-Source Inverter for Fuel Cell-Battery Hybrid Vehicles to Eliminate Undesirable Operation Modes*", IEEE Industry Applications Conference, vol. 4, Oct. 2006, pp. 1667-1673.

[10] M. Shen, F. Z. Peng, "*Operating modes and characteristics of the z-source inverter with small inductance*", In proc. IEEE IAS, 2005.

[11] H. Al-bayaty, et al. "*Electrical distribution grid of Kirkuk City: A case study of load flow and short circuit valuation using ETAP*" Periodicals of Engineering and Natural Sciences (PEN) 10.3 (2022): 311-322.

[12] J. Jung and A. Keyhani, "*Control of a Fuel Cell Based Z-Source Inverter*", IE Transactions on Energy Conversion, vol. 22, no. 2, June 2007, pp. 467-476.

[13] M. Shen, F. Z. Peng, "*Operating modes and characteristics of the z-source inverter with small inductance*", In proc. IEEE IAS, 2005.

Stiffness in the Knitted Fabrics with Vortex Yarns

S. UYANIK[1] and P. DURU BAYKAL[2]

[1] Adıyaman University, Adıyaman/Turkey, suyanik@adiyaman.edu.tr
[2]Çukurova University, Adana/Turkey, pduru@cukurova.edu.tr

***Abstract* - Fabric stiffness is the resistance to bending and determines the touch of the fabric. Vortex knitted fabrics have less dimensional changes and stiffness values after washing compared to knitted fabrics with ring yarns. In the study, it is aimed to reveal the effects of fiber type, yarn, and fabric properties on the stiffness of single jersey fabrics knitted from pure and blended vortex yarns with different raw materials. The study results show that only effective factor on stiffness of knitted fabrics is yarn loop length (lfa), and fabric stiffness decreases with increasing loop length.**

***Keywords* – Fabric stiffness, vortex yarn, loop length, fiber type, yarn-fabric properties.**

I. INTRODUCTION

Although Vortex Spinning System with air jet, which emerged towards the end of the 1990s, cannot replace the ring spinning system, which is the most used conventional spinning system, it is increasingly used, especially in the finer count range than the open-end rotor spinning system.

Vortex spun yarns and fabrics have low hairiness, high pilling and abrasion resistance, high moisture absorption and diffusion properties, quick-drying characteristics, and better durability [1].

Fabric stiffness (bending resistance) and drape are the leading concepts that determine the touch of the fabric.

The stiffness of some fabrics constitutes the basic feature determining their suitability for a specific use. The bending stiffness of textiles has become a fundamental property in determining the complex parameter of fiber or fabric drapability and handle [2].

A lot of research were made on fabric stiffness, which is the resistance to bending and twisting. Özdil [3] stated that fiber type and structure, yarn properties, fabric properties (weight etc.) and finishing processes are the main factors affecting the bending strength of fabrics, and Grabowska et al. [2] expressed that fabric drape is the result of the interaction between stiffness and fabric weight, Örtlek and Ülkü [4] found that vortex knitted fabrics had less dimensional changes and hardness values after washing compared to knitted fabrics with ring yarns, Özdemir and Oğulata [5] signed that the effects of spinning systems and yarn count on fabric stiffness were statistically significant.

Özçelik Kayseri et al. [6] and Behery [7] stated in their studies that the most important factor affecting fabric stiffness is the fiber type, and each fiber has a unique stiffness. The details of the studies revealed that cotton, viscose, cotton-linen, and viscose-linen blend fabrics showed lower surface friction, surface roughness and bending stiffness than 100% linen fabrics. In addition, it has been stated that fine fibers create a flatter and more flexible yarn structure and give better fabric drape, while long fibers and less length variation create a flatter yarn and fabric surface. It was stated that another important factor is fiber-fiber friction that when the fiber friction coefficient increases, the fabric deformation, or in other words, the movement decreases due to the decrease in the slip ability of the fibers, and the bending resistance of the fibers with higher crystallinity is higher. Behery also pointed out in his study that yarn density (fiber linearity and fiber packing density in the yarn) affects the tactile fabric properties if it is not suppressed by the twist.

In this study, it is aimed to reveal the effects of fiber type, yarn, and fabric properties on the stiffness of single jersey fabrics knitted from pure and blended vortex yarns with different raw materials.

II. MATERIAL AND METHOD

For this study, 17 different yarn samples by using the fibers of cotton (CO), viscose (CV), modal (CMD), Flexsil-D2™ (FD2), polyester (PES), and nylon 6.6 (PA) fiber were obtained on vortex spinning system. Flexsil-D2™ incorporates 99.9% pure silver into polyester fibers using advance specialized extrusion technology with sustain ion release system, and it is used to provide the antibacterial effect, odor protection and UV protection [1].

The produced yarns were knitted as plain knit (single jersey) in a circular knitting machine, and then the knitted fabrics were dyed according to fiber types. The production parameters for the yarns and fabrics were shown in Table 1.

Table 1: Production parameters

Yarn production		**Fabric production**	
Machine type	Murata Vortex 861	Machine type	Mayer-Relanit
Delivery speed	350 m/min	Diameter	30 inch
Air pressure	5.5 bar	Gauge-E	28 needle/inch
Spindle diameter	1.1 mm	Loop length	2.7 mm - 3.0 mm
FR-SP distance*	19-20 mm	Dying process	According to fiber types
Yarn count	Ne 30		

*The distance between front roller and spindle for the yarns containing 90–100% cotton fiber is 19 mm, and for the yarns containing 0–60% cotton fiber is 20 mm

The properties of the yarns and fabrics tested according to the relevant standards were given in the following tables, respectively [1].

The stiffness values of samples were determined according to ASTM D4032 standard in SDL Atlas Digital Pnömatik Stiffness Tester, and the results were shown in Table 3 with other properties together.

ANOVA tests were carried out with SPSS 25 package program to statistically analyze the effects of factors on fabric stiffness.

Table 2: Yarn properties

Fiber ratios	Fiber types	Diameter mm	Shape	Density g/cm³	Unevenness CV%	Thin places -50%/km	Thick places +50%/km	Neps places +200%/km	Hairiness			Tenacity cN/tex	Elongation %
									H	S1+2	S3		
100%	CO	0.236	0.73	0.42	17.41	200.5	192	576	4.3	2511	23	10.39	4.98
	CV	0.221	0.78	0.51	12.65	4.5	20	17	4.04	1340	20	13.41	7.99
	CMD	0.207	0.78	0.58	12.11	0.5	4	15.5	3.55	723	5	19.25	8.18
95-5%	CO/FD2	0.226	0.73	0.43	18.08	264.5	244.5	485.5	4.09	3287	19	9.94	4.81
	CV/FD2	0.209	0.79	0.58	12.20	1.0	5	6.5	3.45	1537	5	14.66	8.63
	CMD/FD2	0.212	0.80	0.58	11.21	0.5	0	3.5	3.72	1697	5	18.35	7.13
90-10 %	CO/FD2	0.230	0.72	0.43	17.90	270.5	229	499	4.2	3367	26	10.89	4.80
	CV/FD2	0.206	0.81	0.60	11.99	1.0	1	5	3.32	1094	5	15.15	9.27
	CMD/FD2	0.211	0.79	0.58	11.46	0	0.5	3.5	3.52	893	2	18.47	6.91
50-45-5%	CO/CV/FD2	0.217	0.79	0.54	14.57	17.5	33	115.5	3.34	785	6	10.85	5.04
	CO/CMD/FD2	0.219	0.78	0.53	14.18	10.6	23.1	105.6	3.43	892	4	13.14	5.46
	CO/PES/FD2	0.219	0.78	0.51	15.40	56	81	194.5	3.46	1156	4	16.14	7.22
	CO/PA/FD2	0.230	0.76	0.46	16.71	123	109.5	102	3.56	685	7	15.78	12.59
60-30-10%	CO/CV/FD2	0.218	0.78	0.52	15.39	38	75	179.5	3.43	1166	10	10.83	5.29
	CO/CMD/FD2	0.219	0.78	0.52	15.75	45.5	71	201	3.42	915	5	12.84	5.71
	CO/PES/FD2	0.224	0.77	0.48	15.38	52.5	74.5	166	3.63	1097	10	14.42	6.82
	CO/PA/FD2	0.223	0.78	0.49	16.49	105	115	164	3.36	1136	12	12.92	9.61

Table 3: Fabric properties

Fabric samples		Courses/cm cpc		Wales/cm wpc		Stitch density/cm²		Mass per unit area g/m²		Thickness mm		Stiffness kg.f	
		2.7*	3.0*	2.7*	3.0*	2.7*	3.0*	2.7*	3.0*	2.7*	3.0*	2.7*	3.0*
100%	CO	18.83	15.50	14.08	14.00	265.1	217.0	129.8	114.2	0.477	0.460	0,055	0,030
	CV	20.50	15.92	14.08	14.00	288.6	222.9	148.3	128.2	0.410	0.410	0,047	0,024
	CMD	19.25	15.92	14.42	13.42	277.6	213.7	139.8	119.5	0.403	0.377	0,045	0,029
95-5%	CO/FD2	20.00	16.50	14.67	13.83	293.4	228.2	132.3	117.3	0.470	0.477	0,049	0,042
	CV/FD2	21.75	17.92	14.42	13.75	313.6	246.4	164.7	141.7	0.427	0.417	0,053	0,035
	CMD/FD2	20.58	17.00	14.67	13.83	301.9	235.1	162.3	136.3	0.420	0.403	0,058	0,037
90-10 %	CO/FD2	20.67	17.00	14.33	14.00	296.2	238.0	137.6	124.2	0.487	0.483	0,057	0,041
	CV/FD2	22.75	17.50	14.17	14.67	322.4	256.7	169.2	147.3	0.433	0.417	0,055	0,048
	CMD/FD2	21.67	16.75	14.00	13.92	303.4	233.2	160.7	139.5	0.427	0.410	0,056	0,028
50-45-5%	CO/CV/FD2	23.33	19.08	14.00	13.58	326.6	259.1	175.2	156.5	0.510	0.503	0,062	0,052
	CO/CMD/FD2	21.50	17.50	14.17	13.75	304.7	240.6	163.3	144.5	0.483	0.477	0,058	0,039
	CO/PES/FD2	22.00	17.92	14.33	13.83	315.3	247.8	163.3	143.2	0.503	0.490	0,058	0,039
	CO/PA/FD2	22.00	18.17	14.83	14.00	326.3	254.4	174.0	146.5	0.513	0.503	0,057	0,038
60-30-10%	CO/CV/FD2	22.58	18.50	14.17	13.83	320.0	255.9	169.2	149.2	0.500	0.503	0,055	0,033
	CO/CMD/FD2	21.75	17.83	14.50	14.00	315.4	249.6	161.7	143.5	0.487	0.493	0,058	0,033
	CO/PES/FD2	22.00	18.00	15.00	14.42	330.0	259.6	169.2	146.8	0.503	0.497	0,059	0,041
	CO/PA/FD2	22.33	18.00	14.08	14.00	314.4	252.0	161.3	142.5	0.503	0.503	0,055	0,031

III. RESULTS AND DISCUSSION

Loop length (stitch density) is the main factor influencing tightness, and so that cpc (courses per cm), wpc (wales per cm), stitch density, and mass per unit area expressing fabric tightness in a knitted fabric and increasing loop length reduces fabric tightness and parallel the other tightness parameters except thickness.

In Figure 1, the graphic created with stiffness values of 100% and blend fabrics with two fibers is given. When the graphic is examined, it is seen that the fabric stiffness values are affected by fabric tightness which is loop length (lfa). In other words, 3.0 lfa fabrics which are loose have lower stiffness than 2.7 lfa fabrics which are tigth. This finding is also supported by the study conducted by Özçelik Kayseri et al. (2012) in which it was stated that tightness factor of knitted fabrics is an important factor affecting the fabric touch, and that the stiffness and the associated bending stiffness increase with increasing tightness.

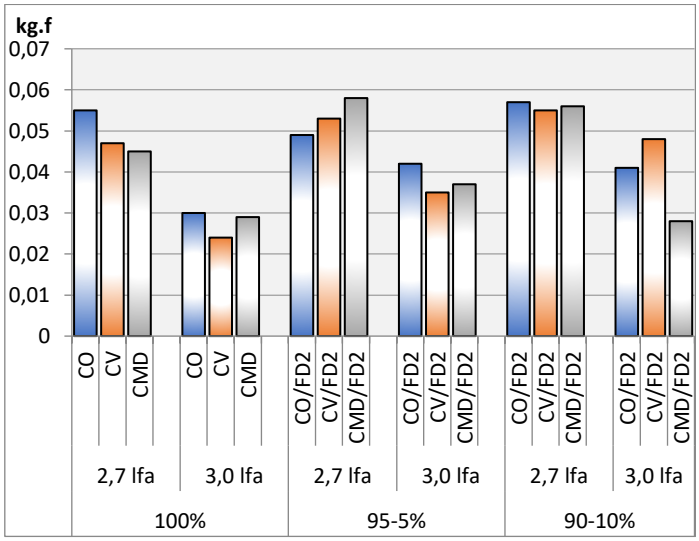

Figure 1: Stiffness values in pure and blend fabrics with two fibers

In 100% pure fabrics, cotton fabric appears to be harder than viscose and modal fabrics. However, the difference in stiffness decreased in 3.0 lfa fabrics. Here, it is expected that stiffness of cotton fabrics that are lower in terms of fabric weight will be lower, while the opposite situation has been observed, and it has been concluded that fiber type is more effective on stiffness in 100% fabrics.

In samples containing 5% Flexsil, fabric with modal fiber showed the highest stiffness at 2.7 lfa although it has the advantage of low weight, thickness, and soft fiber type, while the fabric containing cotton fiber due to its hard structure at 3.0 lfa value.

In samples containing 10% Flexsil, stiffness values of the fabrics containing cotton, viscose and modal were determined to be almost the same, with the decrease in the ratio of harder cotton at 2.7 lfa. Stiffness values at 3.0 lfa are as expected that fabric containing viscose with a higher weight, fabric containing cotton with a harder fiber structure, fabric containing modal with its lightness and soft fiber structure followed each other in stiffness values.

As can be seen from the graphic in which stiffness values of blend fabrics with three fibers are shown in Figure 2, the most effective factor on fabric stiffness is fabric tightness, as is the case with 100% and blend fabrics with two fibers. Loose fabrics (3.0 lfa) have lower stiffness values than tight (2.7 lfa) fabrics.

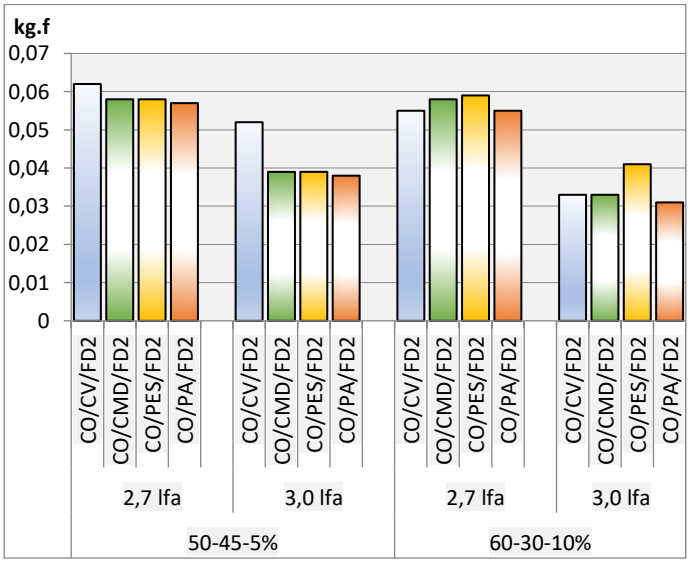

Figure 2: Stiffness values blend fabrics with three fibers

ANOVA results given in Table 4 show that fiber types and yarn properties don't have any statistically effect on stiffness as only fabric properties which are cpc, wpc, lfa, and mass have effect on stiffness since p values of these factors are higher than 0.05 of value. Especially lfa (loop length) expressing fabric tightness is very much effective on stiffness according to F values.

Table 4: ANOVA results

Factors		F	Sig.
Fiber types	CO	,456	,805
	CV	,851	,525
	CMD	,311	,902
	PES	,216	,807
	PA	,082	,922
	FD2	1,818	,179
Yarn properties	Diameter	,398	,954
	Shape	,256	,965
	Density	,363	,951
	Friction	,281	,993
	CV	,281	,993
	Thin	,275	,991
	Thick	,281	,993
	Neps	,303	,988
	H	,308	,987
	S12	,281	,993
	S3	,390	,938
	Elongation	,281	,993
	Tenacity	,281	,993
	cpc	**9,535**	**,001**

Fabric properties	wpc	**2,785**	**,019**
	lfa	**81,815**	**,000**
	Porosity	2,132	,097
	Mass	**38,446**	**,006**
	Thickness	1,310	,301

IV. CONCLUSION

The statistically significant factor on stiffness of knitted fabrics is yarn loop length (lfa), and fabric stiffness decreases with increasing loop length. The reduction rates in fabric stiffness vary between 13-50% and the average change is around 34%. As a result, it can be said that loose knitted fabrics with less loop density are softer.

ACKNOWLEDGMENT

The authors thank to Kara Holding for producing of yarns and fabrics.

REFERENCES

[1] S. Uyanık, "Vortex eğirme sisteminde pamuk ve yeni nesil lif karışımlarının eğrilmesi ve örme kumaştaki performanslarının belirlenmesi," Ph.D. dissertation, Dept. Text. Eng., Çukurova Univ., Adana, 2017.

[2] B. Grabowska-Goetzendorf, A. Karaszewska, V.I. Vlasenko, and A.T. Arabuli, "Bending stiffness of knitted fabrics-comparison of test methods," *Fibres&Textiles in Eastern Europe*, vol. 22, pp. 43-50, 2014.

[3] N. Özdil, *Kumaşlarda Fiziksel Kalite Kontrol Yöntemleri*. E.Ü. Tekstil ve Konfeksiyon Araştırma-Uygulama Merkezi Yayını, Bornova/İzmir, 2003.

[4] H.G. Örtlek, S. Ülkü, "The Comparison of The Properties of Murata Vortex Ring-and Rotor Spun Cotton Yarns," in *Conf. Rec. 2005 5th Int. Istanbul Textile Conf.*

[5] H. Özdemir, R.T. Oğulata, "Farklı eğirme sistemleri ile üretilmiş ipliklerin örme kumaşlarin eğilme dayanımı (sertlik) değerlerine etkisi," *Tekstil ve Konfeksiyon*, vol. 4, pp. 313-319, 2010.

[6] G. Özçelik Kayseri, N. Özdil, G. Süpüren Mengüç, *Sensorial Comfort of Textile Materials*, Intech Woven Fabrics Chapter 9, pp. 235-266, 2012.

[7] H.M. Behery, *Effect of Yarn Properties on Fabric Hand. Effects Of Mechanical and Physical Properties on Fabric Hand, Chapter 7*, Woodhead Publishing Ltd. Cambridge, England, 2005.

[8] TS EN 12127: 1999. Tekstil-Kumaşlar-Küçük Numuneler Kullanarak Birim Alan Başına Kütlenin Tayini.

[9] TS EN 14971: 2013. Tekstil-Örülmüş Kumaşlar-Birim Uzunluk ve Birim Alan Başına Örgü İlmeği Sayısının Tayini.

[10] TS 7128 EN ISO 5084: 1998. Tekstil-Tekstil ve Tekstil Mamullerinin Kalınlık Tayini.

[11] ASTM D4032-94: 1994. Standard Test Method for Stiffness of Fabric by The Circular Bend Procedure.

The Effects of Hard Waste on Yarn Quality

S. UYANIK[1] and F. DEMİRCİ[2]

[1] Adıyaman University, Adıyaman/Turkey, suyanik@adiyaman.edu.tr
[2]Memtextile, Kahramanmaraş/Turkey, fatmademirci@memtextile.com

***Abstract* - Recovery of textile solid waste materials by recycling methods provides economic, environmental and social advantages such as energy saving, protection of natural resources, and reduction of environmental pollution. During cotton yarn production, wastes such as licker-in waste, flat waste, sliver waste, sliver pneumafil waste, combed noil, roving pneumafil waste, roving waste, ring pneumafil waste, and hard waste arise in the yarn preparation and spinning part. -In this study aims to reveal the effects of hard waste on yarn quality and performance in compact yarns obtained by blending cotton waste. The study results show that waste content in blended yarns with hard waste negatively affects yarn quality of which evenness, imperfection, hairiness etc., and reduce yarn performance in terms of tensile properties.**

***Keywords* – Hard waste, combed compact yarn, cotton, yarn properties, blend yarn.**

I. Introduction

Sustainability is defined as an environmentalist world view that aims to ensure economic development with the principle of using environmental values and natural resources with rational methods [1].

In terms of sustainability, the textile and ready-made clothing industry has started to show a rapid acceleration in environmental damage, minimizing waste, re-use, upcycle, down-cycle and recycling studies in recent years [1].

The textile industry includes different production methods such as yarn, knitting, weaving and nonwoven surfaces, and wastes are generated in each of these productions. The wastes generated during the production processes and after the consumption of textile products should be evaluated and they should be used as an input to another production process, that is, recycling should be ensured [2].

Recycling process, as a term, is the recycling of recyclable waste materials that are out of use into the manufacturing processes as raw materials with various methods [3].

Recycling in textile is explained by various classifications in the literature. In these classifications, concepts such as the method used for recycling, the final state and value of the recycled product, and the possible usage areas of the obtained recycled product are determinative [4]. The recycling possibilities of textile wastes are given in Figure 1 [2].

,

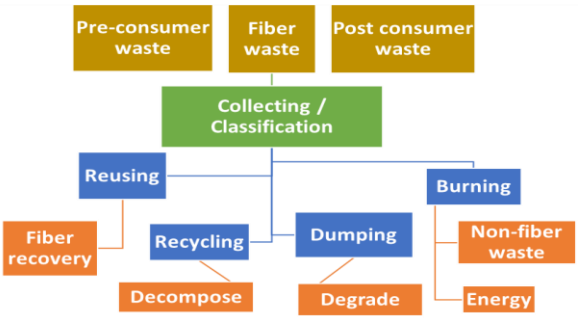

Figure 1: Recycling opportunities of textile waste [3].

Recovery of textile solid waste materials by recycling methods provides economic, environmental and social advantages such as energy saving, protection of natural resources, and reduction of environmental pollution.

Cotton fiber is the most used fiber among natural fibers. During cotton yarn production, wastes such as licker-in waste, flat waste, sliver waste, sliver pneumafil waste, combed noil, roving pneumafil waste, roving waste, ring pneumafil waste, and hard waste arise in the yarn preparation and spinning part. All of the wastes formed in the yarn winding process are hard waste [5]. Apart from these wastes, wastes called air conditioner dust are formed in the filters of the suction units during yarn production.

In terms of sustainability and recycling in the textile sector, in this study, it is aimed to reveal the effects of hard waste on yarn quality and performance in yarns obtained by blending cotton waste, in comparison with yarns that do not contain waste.

II. Material and Method

Within the scope of this study, 100% pure cotton (CO) yarns in 3 different yarn counts as Ne 20, Ne 24 and Ne 28 and blended yarns containing 20% hard waste were produced with a compact ring spinning system. The physical properties of the yarns produced were determined by Uster Tester 5 and their tensile performance properties were determined by Uster Tensorapid 4 test devices. The physical and performance properties of the yarns produced are given in Table 1.

.

Table 2: Yarn properties

Yarn Type	Ne	Unevenness CV%	Thin places -40%/km	Thin places -50%/km	Thick places +35%/km	Thick places +50%/km	Neps +200%/km	Neps +280%/km	Hairiness H	Tenacity cN/tex	Elongation %
100% CO	20	10,48	3.5	0	75,5	3,5	2,5	1	5,78	18,58	8,18
80-20% CO-Waste	20	14,42	150,6	1,9	899,4	140,6	120	13,8	7,28	15,41	5,66
100% CO	24	10,45	3	0	87	5	2,5	1	5,48	19,99	7,40
80-20% CO-Waste	24	14,57	137,5	5,8	1001	160,8	168,3	10	7,74	15,08	4,68
100% CO	28	11,42	16	0	145	9,5	10	4	5,24	19,18	5,72
80-20% CO-Waste	28	14,52	146,9	3,1	961,3	168,1	168,8	20,6	7,34	16,34	4,39

III. RESULTS AND DISCUSSION

The graphs created with the data obtained from the test results of the produced yarns are given in the following figures.

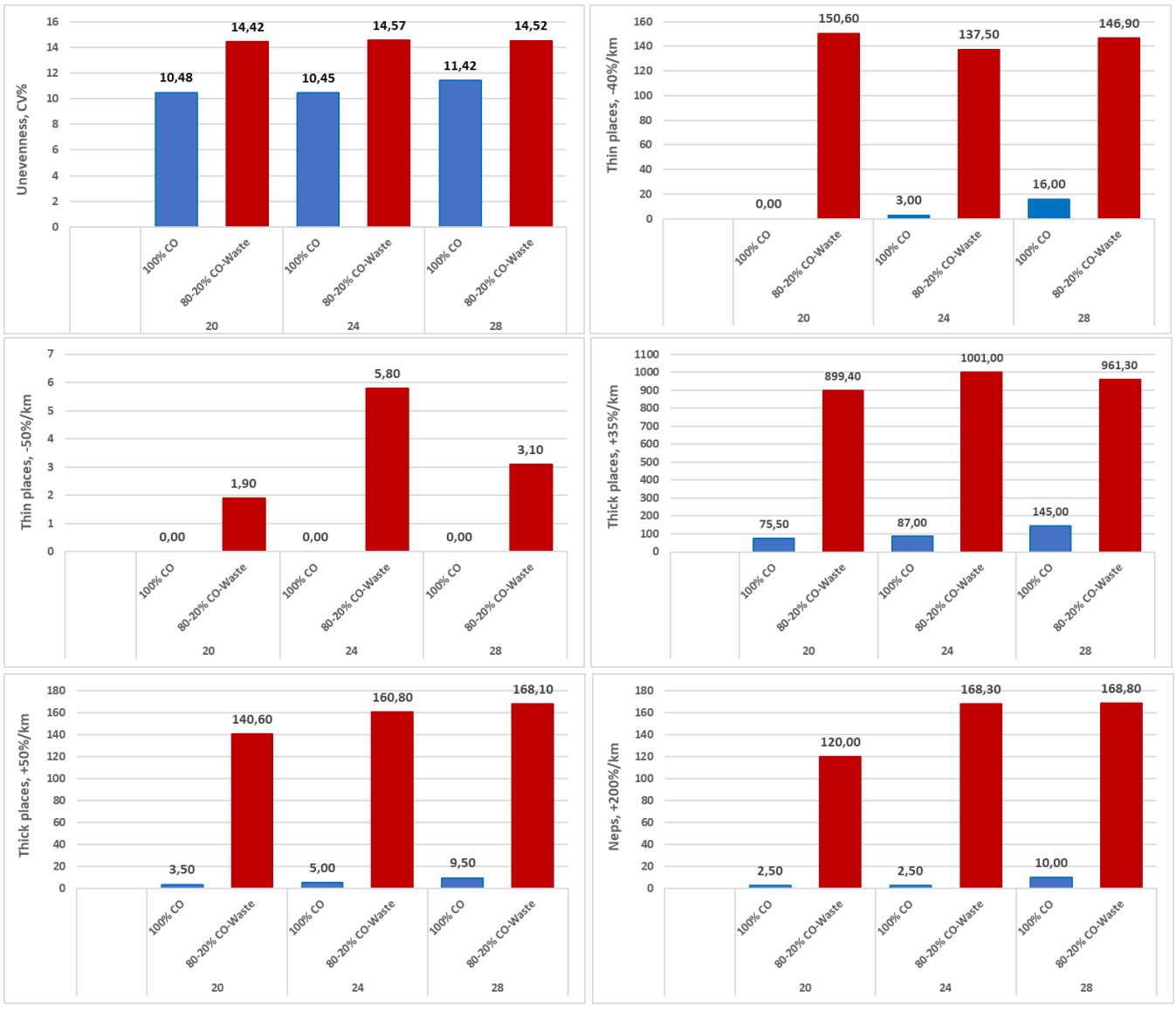

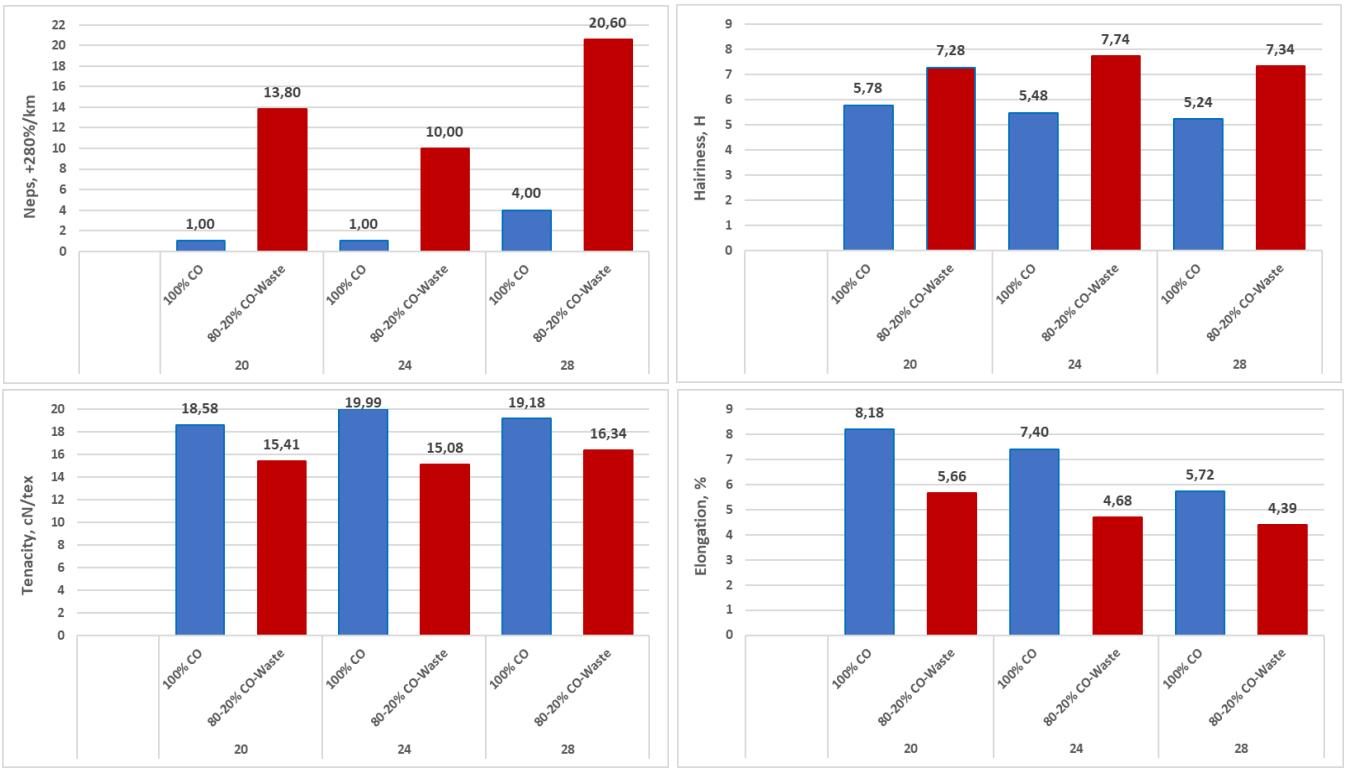

Figure 2: Yarn physical and tensile properties

Uster test results showed that when 20% waste is added to pure cotton yarn, there is a significant increase in yarn unevenness, imperfections, and hairiness, in other words, the physical properties of the yarn deteriorate. Likewise, significant decreases were observed in yarn strength and elongation values.

IV. CONCLUSION

The study results show that waste content in blended yarns with hard waste negatively affects yarn quality of which evenness, imperfection, hairiness etc., and reduces yarn performance in terms of tensile properties.

REFERENCES

[1] Kadem, D.F., Özdemir, Ş., Tüketici Sonrası Geri Dönüştürülen Denim Kumaşların Seçilmiş Konfor Özellikleri Üzerine Bir Çalışma, Çukurova Üniversitesi Mühendislik Mimarlık Fakültesi Dergisi, Sayı 35(2), Sayfa 379-388, 2020, Adana

[2] Özdinç, Ö., Tekstil Sektöründe Geri Dönüşüm, Gaziantep Üniversitesi.

[3] https://tr.wikipedia.org/wiki/Geri_d%C3%B6n%C3%BC%C5%9F%C3%BCm.

[4] Macit, H., Tayyar, A.E., Macit, Ş.A., Tekstil Sektöründe Geri Dönüşüm Olanakları ve Uşak İli'nde Güncel Durum, Uşak Üniversitesi Fen ve Doğa Bilimleri Dergisi, Sayfa 91-102, 2019.

[5] https://www.textilesphere.com/2019/09/waste-management-in-spinning.html

Levulinic acid production by catalytic decomposition of fructose, glucose, and cellulose

Chingiz NASIRLI[1], Nihal CENGİZ[1*], Levent BALLİCE[1]

[1] Ege University, İZMİR/Turkey nasirli93@hotmail.com
[1] Ege University, İZMİR/Turkey nihal.cengiz@ege.edu.tr
[1] Ege University, İZMİR/Turkey levent.ballice@ege.edu.tr

***Abstract* -** Levulinic acid (LA) is a platform chemical and may be used as a raw material in various types of chemical industrial processes with end products such as biofuels, resins, solvents, pharmaceuticals, etc. LA was first manufactured by heating fructose with hydrochloric acid. hydroxyl methyl furfural (HMF) is the most important intermediate product in biomass hydrolysis and the formation of levulinic acid[1, 2].

In the context of the study, representative monosaccharide molecules of fructose and glucose with the same chemical formula ($C_6H_{12}O_6$) were selected to identify the difference in the mechanism of decomposition of biomass in a hydrothermal medium based on the structural features. Fructose differs from glucose in the functional groups they have and its position in the molecular structure. This variation was investigated with the product yields and amounts obtained with fructose and glucose decomposition into LA. From this point of view, the decomposition characteristics of cellulose and cellulosic biomass will be enlightened [3, 4].

Experiments are done in batch autoclave reactor systems with PID temperature controllers. The objective of the study is to obtain maximum LA yields and to investigate the effect of temperature (120, 140, 160, and 180° C), reaction time (20, 30, 40, 60 min), pH levels of an aqueous hydrochloric acid catalyst (0.5, 1.0, 1.5). The analysis of the aqueous product is done by an HPLC instrument.

Remarkably fructose gives a higher yield (47%) than glucose (22%) and cellulose (20%). The most appropriate conditions are obtained as 30 min of reaction time, 140°C of reaction temperature, and the pH of the catalyst as 0.5, with 47 % of LA yield. For comparison, an additional experiment is done with a microwave reactor under these reaction conditions. Due to the more easily controllable heating and cooling feature, the short reaction time of the microwave reactor minimized the formation of the side products and gives a higher yield of LA, that is % 53**.**

Keywords: Hydrothermal decomposition, Biomass, Levulinic acid, fructose

I. INTRODUCTION

The increase in the consumption of non-renewable energy sources such as coal, natural gas, oil, etc., and the scarcity of its reserves make scientists and country policies direct to renewable sources. It is crucial to enlarge the share of energy renewable resources in the total energy supply for the countries. Turkey is suitable for agriculture and has geographical advantages in terms of wind, hydroelectric and geothermal resources. Biomass resources are also emphasized in Turkey and started to take their place as an alternative source [5].

While the damage caused by fossil-based energy types to the environment is undeniable, renewable energy sources are environmentally friendly. Therefore, the expansion of these resources will have positive effects on the environment.

The main components of lignocellulosic biomass are cellulose, hemicellulose, and lignin, although in varying proportions depending on the type of biomass. Cellulose consists of repeating units containing glucose monomers and is important in the production of valuable chemicals. Unlike hemicellulose, it has an amorphous structure. In addition, lignin is a substance that gives strength to plant tissue and fibers, and also provides resistance and structural strength against insects and pathogens. To obtain high product yields, biomass is pretreated in some processes [6–8]. The aim here is to isolate the lignin and hemicellulose components of lignocellulosic biomass and to increase the porosity of lignocellulosic materials. In these processes, it is aimed to improve sugar formation, eliminate carbohydrate loss, prevent the formation of unwanted by-products and increase economic efficiency.

Biomass is transformed by various technologies to produce biofuel and polymer production [9–12], and recovery of valuable chemicals. The most widely used biomass conversion techniques are direct combustion, pyrolysis, chemical hydrolysis, gasification, and biochemical conversion.

II. RESULTS AND DISCUSSION

In this study, glucose, fructose, and cellulose have been used as the model compound to represent the cellulosic part of the biomass, and the behavior of these model compounds in hydrothermal decomposition has been investigated in the production of valuable chemicals. The effect of reaction temperature, duration of the reaction, type of feed, and the effect of the reactor system have been evaluated on the yields of the organic acids and total organic carbon in the aqueous product.

Most of the studies were carried out in a batch reactor system and the effect of the parameters was evaluated in this setup. The reaction was carried out within 40 minutes to determine the most appropriate reaction time and the highest yield was obtained at the duration of 20 min with the feedstock of fructose at 180 °C of reaction temperature and was added H_2SO_4 as a catalyst. As found in the literature in the literature, decomposition was almost completed within the first 30 min. The yield of LA reached at the end of the 30 min was 41.4 % mole, after it started to decrease. This shows that the produced LA was decomposed into other by-

products. So, this reaction period is selected as the most appropriate time to get the highest yields of the products. The results were given in Table 1 for the mentioned reaction conditions. It can be seen clearly, there was no acetic acid and hydroxyl methyl furfural in the aqueous product, while a little amount of formic acid is detected. HMF was formed as an intermediate product and rehydrated rapidly to levulinic acid as expected, so it was not determined in the final product. The rehydration reaction of HMF results in formic acid formation in the same molar yield:

$$Fructose \xrightarrow[(-3H_2O)]{Dehydration} HMF \xrightarrow[(+2H_2O)]{Hydration} FA + LA \qquad \text{Eq.1}$$

Even so, the yield of FA is not high as LA, the reason for this inconsistency may be the conversion of FA by hydrogenation reaction with hydroxyl methyl furfural with the effect of the catalyst [13]. The optimum reaction times vary a lot depending on the type of catalyst, type of feedstock, and also operating temperature, and process specifications [2].

Table 1. Effect of reaction time on product concentration with 1.54 g of fructose and 20 mL of water at the reaction temperature of 180°C with H_2SO_4 at pH of 0.5 in the batch reactor system.

Feed	Fructose			
Reaction time (min)	10	20	30	40
LA yield (%mol)	42.9	43.0	41.4	38.7
LA (g/kg fructose)	276	277	267	249
Formic acid (g/kg fructose)	83	81	74	81
Acetic acid (g/kg fructose)	-	-	-	-
5-HMF (g/kg fructose)	-	-	-	-
TOC (mg/L)	4710	4687	4635	4652

The variation in the aqueous product yields with the effect of the reaction temperature is significant as seen in Table 2. The highest yield for LA was 47 % mole at 140 °C and the amount of FA was also the highest at this temperature. HMF was determined as very low at lower temperatures and above 140 °C, it was not detected. Similarly, the type of catalyst, type of feedstock, and process specifications change the optimum temperature to reach maximum yields [1, 14, 15]. In a study, fructose was represented as feedstock, H_2SO_4 was used as a catalyst and the optimum temperature was given as 140 °C [16]. In another study, catalytic production of 5-HMF and LA from monosaccharides was investigated in $InCl_3$–H_2O medium. 45% LA yield (60 min) was obtained at 180 °C [17]. These results suggest that a higher temperature favors LA formation. The reaction temperature may be milder relative to the required temperature with acidic catalysts.

Aqueous catalyst concentration is another important effect on the product yields and the amounts. In Table 3, the variation in the yields and the amounts of the products obtained were given with the various sulphuric acid concentrations adjusted to get pH levels of 0.5, 1.0, and 1.5. The yields of LA varied within 41.4-47.0 % in the operating temperature range, which is not a prominent ratio compared to the yields obtained in the different acidity levels of the catalyst. The increment in the yield of LA is dramatic between pH 1.5 and pH 1.0, which is almost 28 %. HMF amount is 183 g/kg fructose, while LA is only 62 g/kg fructose. This shows the crucial effect of acid concentration and corresponding pH on the product distribution and the reaction mechanism even in the same operating temperature and feedstock concentration. Elevated pH levels favor HMF formation stability and HMF does not convert to LA. In this study, the most effective parameter was found as acid catalyst concentration in fructose decomposition. In a study, an inference is done on the formation of the HMF and LA at pH levels and it indicates that no HMF was formed when pH is> 3.9 and no LA was formed when pH is> 2.7 at 175 °C [18]. The results support this inference since the yield of LA decreased to 10 % with a pH level of 1.5. Catalysts have a very important effect on the formation of HMF and LA from glucose/fructose. The catalysts employed in this process were categorized as organic acids (oxalic acid, p-Toluenesulfonic acid), inorganic acids (H_2SO_4, HCl, etc.), salts (e.g., $(NH_4)_2SO_4/SO_3$), lewis acids ($AlCl_3$, $ZnCl_2$, $CrCl_3$, etc.) and ion-exchange resins [15].

Table 2. Effect of reaction temperature on product concentration with 1.54 g of fructose and 20 mL of water at a reaction time of 30 min with H_2SO_4 at pH of 0.5 in the batch reactor system.

Feed	Fructose			
Temperature (°C)	120	140	160	180
LA yield (%mol)	42.2	47.0	42.8	41.4
LA (g/kg fructose)	272	303	276	267
Formic acid (g/kg fructose)	104	121	99	74
Acetic acid (g/kg fructose)	-	-	-	-
5-HMF (g/kg fructose)	1.95	0.65	-	-
TOC (mg/L)	4640	4772	4640	4635

In this study, the effect of type of the substrate is examined by using cellulose, glucose, and fructose to state the variations in the yields and amounts of the products. Cellulose, which is one of the basic constituents of biomass, cannot be dissolved in water directly without appropriate catalysts and conditions. The most effective and common catalysts are homogeneous mineral acid catalysts in the hydrolysis of cellulose and they dissolve cellulose and convert it into glucose monomers at moderate conditions. In the next step, glucose can be converted to HMF without the formation of fructose as an intermediate or isomerize to fructose and then yielded to HMF. In the second pathway, fructose is converted to HMF through a dehydration reaction as given in Eq. 1 results in a higher yield of HMF. The rehydration reaction of HMF in the presence of an acid catalyst produces equimolar LA and FA. As it is displayed in Table 4, the yield of LA from fructose is significantly higher than the yields with glucose and cellulose as the starting material. Garcés et al. found higher selectivity to LA from fructose similarly [19]. The amount of the produced FA is

also lower from glucose and cellulose as LA while HMF amounts are very low for all substrates. HMF degradation is very fast compared to LA decomposition to other byproducts.

Table 3. Effect of pH on product concentration with 1.54 g of fructose and 20 mL of water at a reaction time of 30 min and temperature of 140 °C with H_2SO_4 at different acidity levels of the reaction medium.

Feed	Fructose		
pH	0.5	1	1.5
LA (g/kg fructose)	303	242	62
LA yield (%mol)	47	38	10
Formic Acid (g/kg fructose)	121	106	41
Acetic Acid (g/kg fructose)	-	-	7
5-HMF (g/kg fructose)	0.65	9.22	183
TOC (mg/L)	4772	4635	4737

Table 4 and 5 represents the yields of the products obtained in two different reactor system, batch and microwave (MW) reactors. The main differences between them are fast heating and cooling, homogeneous heat distribution, and efficient control of heating/cooling. Due to the low volume of tubes, less amount of raw material is used during the experiments. Although the amount of raw material is less than in the case of a batch reactor, the reaction efficiency and the product yield are higher. LA yield obtained with fructose as the substrate is 47 % mole in a batch reactor system while 53 % in a microwave reactor. Efficient heating provides energy savings and reduces costs. In a study, using post-harvest tomato plants with 10 wt % as feedstock 63 % of yield is obtained at 225 °C and within 0.03 h reaction time in a microwave-assisted system [20]. MW reactors have the advantage of fast cooling while in batch autoclaves it takes a long time to cool down to room temperature which is necessary for the discharging and cleaning steps of the experiment.

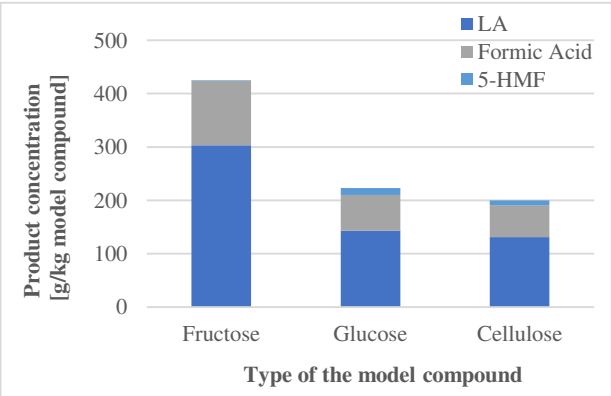

Figure 1. Effect of model compound type on product concentration with 1.54 g of fructose and 20 mL of water at reaction time of 30 min and temperature of 140 °C with H_2SO_4 at pH of 0.5 in batch reactor system.

Table 4. Effect of model compound type on LA yield and TOC of aqueous product with 1.54 g of fructose and 20 mL of water, H_2SO_4 at pH of 0.5 at a reaction time of 30 min and temperature of 140 °C in the batch reactor system.

Feed	Fructose	Glucose	Cellulose
LA yield (%mol)	47	22	20
LA (g/kg model compound)	303	143	131
Formic Acid (g/kg model compound)	121	67	60
Acetic Acid (g/kg model compound)	-	-	-
5-HMF (g/kg model compound)	1	13	9
TOC (mg/L)	4772	4885	4930

The variation and the sum of the aqueous product can be seen in Figures 1 and 2 clearly by the type of model compound as feedstock and the type of the system. The amount of the total product is approximately 20 % higher in the MW reactor than the product obtained in the autoclave reactor. There is a more pronounced difference in the amounts of LA and HMF in the batch reactor and MW using fructose as feedstock while the product distribution is similar using cellulose and glucose as feedstock in between the two reactor type.

Table 5. Effect of model compound type on LA yield and TOC of aqueous product with 0.6 g of the model compound and 3 mL of water at a reaction time of 30 min and temperature of 140 °C with H_2SO_4 at pH of 0.5 in the microwave reactor system.

Feed	Fructose	Glucose	Cellulose
LA (g/kg model compound)	341	108	91
LA yield (%mol)	53	17	14
Formic Acid (g/kg model compound)	161	64	54
Acetic Acid (g/kg model compound)	-	-	-
5-HMF (g/kg model compound)	2	10	9
TOC (mg/L)	16335	17262	17658

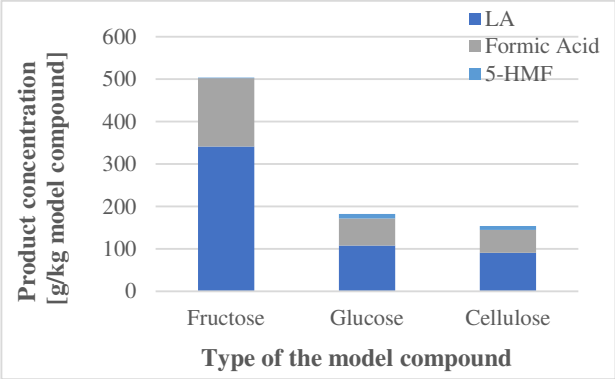

Figure 2. Effect of model compound type on product concentration with 1.54 g of fructose and 20 mL of water at a reaction time of 30 min and temperature of 140 °C with H_2SO_4 at pH of 0.5 in the microwave reactor system.

III. Material and Method

In this study model compounds (fructose, glucose, and cellulose) have been used as raw materials from MERCK company. Experiments were carried out in a batch autoclave reactor system consisting of a reactor, heater, and PID controller. Items are shown in Figure 3. This system can be operated at pressure and temperature up to 400-450 atm. and 600 °C respectively. At first water-catalyst solution and desired amount of raw material are prepared, then placed in the reactor. The reactor's cap is sealed using a seal with no intrusion and N_2 gas is passed through the system to remove the air in the system. Later, the reactor is heated to the desired temperature using the heater. After it is reached the desired temperature value, the autoclave is turned on and the reaction is continued up to desired reaction time, chosen before.

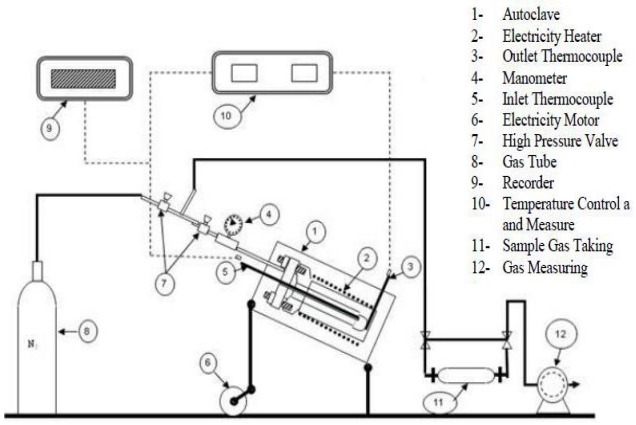

Figure 3. Batch reactor set-up

Characteristics of the HPLC device used to analyze the products of experiments using model compounds are shown in Table 6, below.

Table 6. Characteristics of HPLC-RI (Agilent 1200A) instrument equipped with HPX-87H column

Mobile Phase	Flow rate	Column temperature	Analysis time
0.5 mM H_2SO_4	0.6 mL/min	60°C	35 min

IV. Conclusion

- The highest yields of LA and HMF were reached with fructose as substrate, while yields are significantly lower when cellulose and glucose are used as substrate. The main reason for this is the hydrolysis of cellulose and isomerization reaction of glucose to fructose requires additional effort and the conditions should be appropriate. The hydrolysis step includes the cleavage of the β-1,4-glycosidic bonds of cellulose and isomerization of fructose/ glucose is needed for higher HMF production.
- The most appropriate reaction conditions are determined as 30 min, 140 °C, pH = 0.5, with H_2SO_4 as catalyst and fructose as substrate. The highest LA yield is obtained as 53 % mole in the MW reactor at these conditions.
- Higher temperature and lower pH levels enhance LA formation while the longer reaction time does not promote LA yields. As the reaction proceeds fructose was polymerized into soluble byproducts and therefore the yield of desired products has decreased.
- In the case of 5-HMF production being desired to maximize, higher pH should be preferred at mild reaction conditions.
- The microwave reactor is more effective than the autoclave reactor due to higher yields of LA, easy control of the heating and cooling system, short reaction time, minimized side products, etc.

Appendix

$$LA\ yield\ (\%) = \frac{LA\ conentration\ *\ MW_{substrate}}{Feed\ concentration\ *\ MW_{LA}}$$

$M_{W:}$ molecular weight

Acknowledgment

This study was supported by Ege University Research Foundation (Project Number: 17 MÜH 038). We are grateful to Ege University Research Foundation for the financial support.

References

1. D.W., R., W.O., D.: The conversion of lignocellulosic to levulinic acid. Biofuels, Bioprod. Biorefining. 5, 198–214 (2011). https://doi.org/10.1002/bbb.267
2. Morone, A., Apte, M., Pandey, R.A.: Levulinic acid production from renewable waste resources: Bottlenecks, potential remedies, advancements and applications. Renew. Sustain. Energy Rev. 51, 548–565 (2015). https://doi.org/10.1016Zj/rser.2015.06.032
3. Li, H., Yang, S.: Catalytic Transformation of Fructose and Sucrose to HMF with Proline-Derived Ionic Liquids under Mild Conditions. Int. J. Chem. Eng. 2014, 978708 (2014). https://doi.org/10.1155/2014/978708
4. Amarasekara, A.S., Williams, L.T.D., Ebede, C.C.: Mechanism of the dehydration of d-fructose to 5-hydroxymethylfurfural in

dimethyl sulfoxide at 150 °C: an NMR study. Carbohydr. Res. 343, 3021–3024 (2008). https://doi.org/10.1016/j.carres.2008.09.008
5. Yüksel Özşen, A.: Conversion of Biomass to Organic Acids by Liquefaction Reactions Under Subcritical Conditions. Front. Chem. (2020). https://doi.org/10.3389/fchem.2020.00024
6. Elumalai, S., Agarwal, B., Sangwan, R.S.: Thermo-chemical pretreatment of rice straw for further processing for levulinic acid production. Bioresour. Technol. 218, 232–246 (2016). https://doi.org/https://doi.org/10.1016/j.biortech.2016.06.037
7. Dziekońska-Kubczak, U., Berłowska, J., Dziugan, P., Patelski, P., Pielech-Przybylska, K., Balcerek, M.: Nitric acid pretreatment of Jerusalem artichoke stalks for enzymatic saccharification and bioethanol production. Energies. 11, (2018). https://doi.org/10.3390/en11082153
8. Muranaka, Y., Suzuki, T., Sawanishi, H., Hasegawa, I., Mae, K.: Effective production of levulinic acid from biomass through pretreatment using phosphoric acid, hydrochloric acid, or ionic liquid. Ind. Eng. Chem. Res. 53, 11611–11621 (2014). https://doi.org/10.1021/ie501811x
9. Guo, S., Guo, L., Cao, C., Yin, J., Lu, Y., Zhang, X.: Hydrogen production from glycerol by supercritical water gasification in a continuous flow tubular reactor. Int. J. Hydrogen Energy. 37, 5559–5568 (2012). https://doi.org/10.1016/j.ijhydene.2011.12.135
10. Werpy, T., Petersen, G.: Top Value Added Chemicals from Biomass Volume I. Us Nrel. Medium: ED; Size: 76 pp. pages (2004). https://doi.org/10.2172/15008859
11. Sabio, E., Álvarez-Murillo, A., Román, S., Ledesma, B.: Conversion of tomato-peel waste into solid fuel by hydrothermal carbonization: Influence of the processing variables. Waste Manag. 47, 122–132 (2016). https://doi.org/10.1016/j.wasman.2015.04.016
12. Yu, I.K.M., Tsang, D.C.W.: Conversion of biomass to hydroxymethylfurfural: A review of catalytic systems and underlying mechanisms. Bioresour. Technol. 238, 716–732 (2017). https://doi.org/10.1016/j.biortech.2017.04.026
13. Thananatthanachon, T., Rauchfuss, T.B.: Efficient production of the liquid fuel 2,5-dimethylfuran from fructose using formic acid as a reagent. Angew. Chemie - Int. Ed. 49, 6616–6618 (2010). https://doi.org/10.1002/anie.201002267
14. Signoretto, M., Taghavi, S., Ghedini, E., Menegazzo, F.: Catalytic Production of Levulinic Acid (LA) from Actual Biomass. Molecules. 24, 1–20 (2019). https://doi.org/10.3390/molecules24152760
15. Kang, S., Fu, J., Zhang, G.: From lignocellulosic biomass to levulinic acid: A review on acid-catalyzed hydrolysis, (2018)
16. Fachri, B.A., Rasrendra, C.B., Heeres, H.J.: Experimental and modeling studies on the conversion of inulin to 5-hydroxymethylfurfural using metal salts in water. Catalysts. 5, 2287–2308 (2015). https://doi.org/10.3390/catal5042287
17. Shen, Y., Xu, Y., Sun, J., Wang, B., Xu, F., Sun, R.: Efficient conversion of monosaccharides into 5-hydroxymethylfurfural and levulinic acid in InCl3-H2O medium. Catal. Commun. 50, 17–20 (2014). https://doi.org/10.1016/j.catcom.2014.02.019
18. Kuster, B.F.M., Temmink, H.M.G.: The influence of pH and weak-acid anions on the dehydration of d-fructose. Carbohydr. Res. (1977). https://doi.org/10.1016/S0008-6215(00)84808-9
19. Garcés, D., Díaz, E., Ordóñez, S.: Aqueous Phase Conversion of Hexoses into 5-Hydroxymethylfurfural and Levulinic Acid in the Presence of Hydrochloric Acid: Mechanism and Kinetics. Ind. Eng. Chem. Res. 56, 5221–5230 (2017). https://doi.org/10.1021/acs.iecr.7b00952
20. Tabasso, S., Montoneri, E., Carnaroglio, D., Caporaso, M., Cravotto, G.: Microwave-assisted flash conversion of non-edible polysaccharides and post-harvest tomato plant waste to levulinic acid. Green Chem. (2014). https://doi.org/10.1039/c3gc41103f

Fatigue Properties of Hot Dip Aluminized Inconel 718 Superalloy

İ.Gökdemir[1], M.Kaba, E.Balcı, A.Kavukcu, M.Baydoğan[2]

[1] Istanbul Technical University, Istanbul/Turkey, gokdemir20@itu.edu.tr
[2] Istanbul Technical University, Istanbul/Turkey, baydogan@itu.edu.tr

Abstract - **Hot dip aluminizing (HDA) is a diffusion based surface treatment applied to various metals to improve their oxidation and corrosion resistance due to the formation of aluminide layers at the surface. The purpose of diffusion annealing (DA) after HDA is to modify the aluminide layers for more homogeneous structure by interdiffusion of the elements in these layers to obtain improved properties. Even though there are several works concerning surface characteristics, wear and oxidation resistance of the surface after HDA and subsequent DA processes, their effects on fatigue properties of Inconel 718 superalloy have not been investigated much. Therefore, the effect of these processes on the fatigue behavior of a solution treated Inconel 718 superalloy was investigated in this study. Experimental results showed that application of these coating methods significantly reduced fatigue strength of Inconel 718. Considering the fact that fatigue cracks mostly start from the surface, it was concluded that the reduced fatigue properties were arisen from the brittle nature of the phases at the surface, and of the superalloy itself after the application of HDA and DA processes.**

Keywords **– Aluminizing, Diffusion Annealing, Fatigue, Inconel 718.**

I. Introduction

Nickel-based superalloys are widely used in high temperature applications where mechanical strength and oxidation resistance are required. For this reason, Inconel 718 has a wide range of applications in jet engines, rocket motors, nuclear fuel element spacers and hot extrusion tooling.

Inconel 718 superalloy has superior mechanical properties up to 649°C. This high temperature resistance is obtained thanks to the γ″-Ni_3Nb phase in the structure of the alloy. Above 649°C, the strength of the alloy decreases rapidly due to the conversion of the γ″ phase to the δ phase [1]. Furthermore, the oxidation resistance of Inconel 718 decreases due to the conversion of the Cr_2O_3 phase formed on the material surface into the volatile CrO_3 phase above 1000°C. Therefore, in applications above a certain temperature, Inconel 718 superalloy is used by applying a coating to its surface. Nickel aluminide coatings have become one of the most preferred coatings for nickel-based superalloys due to their high oxidation resistance and stable structure [2].

Among several aluminizing process, hot-dip aluminizing (HDA) is an easy and cost effective process. In HDA process, the sample is immersed in a molten aluminum bath of pure aluminum or Al-Si alloys. The addition of silicon to aluminum increases the solubility of the metal in the aluminum and thus reduces the thickness of the intermetallic layer formed. The coating thickness is also determined by the process temperature and cooling rate [3].

In the early stages of coating, the bath temperature drops locally when the substrate comes into contact with the liquid aluminum. At this time, heat transfer from the liquid aluminum to the substrate and a reaction between the two layers begins. In the next step, two-way diffusion, known as reaction diffusion, takes place and phases nucleate in a relatively short time. The growth of the nucleated phase occurs by mutual diffusion and simultaneous dissolution of the phase in contact with the aluminum bath [4].

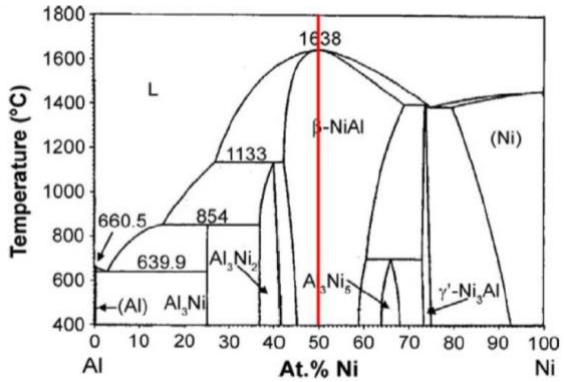

Figure 1: Al-Ni phase diagram [5].

Beside equilibrium phases, which are seen in Figure 1, non-equilibrium phases can also be formed during HDA process. The composition shown by the red line in the Al-Ni phase diagram in Figure 1 belongs to the stoichiometric β-NiAl phase. Higher Ni compositions are defined as sub-stoichiometric compositions, and compositions containing higher Al are defined as superstoichiometric compositions. Diffusion annealing (DA) after HDA leads to diffusion of atoms in a solid material, so that the material moves towards equilibrium. Aluminum-rich phases formed within the coating are known to be inherently brittle and undesirable [6].

Fatigue is one of the important design considerations in moving parts during service. For the parts working under elastic

stresses, number of cycles to failure due to fatigue is relatively high, leading to high cycle fatigue condition. Although fatigue failures can be resulted from several surface and bulk properties of the material such as surface roughness, coating layer and strength of the material, effect of surface quality is more marked. Therefore, in this study, it was the main objective to investigate the effect of HDA and subsequent DA processes on high cycle fatigue behavior of a solution treated Inconel 718 superalloy.

II. Experimental Procedure

Hourglass high cycle fatigue test samples shown in Figure 2 were machined from 25 mm diameter solution treated Inconel 718 superalloy according to BS 3518 Part 2 standard for rotational bending fatigue test condition.

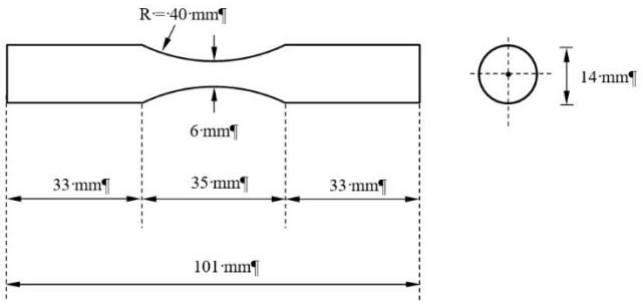

Figure 2: Fatigue test samples.

The bare samples were then ground in a direction to the long axis of the samples with emery papers up to 1200 mesh to remove the machining marks on the surface. For HDA process, the samples were ultrasonically cleaned with dilute HCl to remove oil and dirt for 3 minutes, washed with ethanol and dried with a hot air fan. The samples were tied with a thin steel wire prior to the immersion.

The aluminum ingots of Al-Si alloy were placed in the crucible and heated up to 700°C to melt the alloy. When the molten bath was reached to the desired temperature, a mixture of 40% KCl and 60% NaCl flux was added to the molten metal, and the slags formed on the surface were removed. Due to the heat loss in the molten metal during slag removal, an additional 10 minutes were allowed to maintain the uniform molten metal temperature. The prepared fatigue test samples were immersed into the molten bath and hold in the bath for 2 minutes. Following 2 minutes of immersion, the samples were removed from the molten bath and allowed to cool to the room temperature in air.

For diffusion annealing, the samples were placed in an electrical furnace, and heated with the furnace to 700°C with a heating rate of 12°C/min. After reaching the desired temperature, the samples were hold at 700°C for 10 hours, and they were furnace cooled to the room temperature.

Rotating bending fatigue tests were conducted on a Walter & Bai fatigue tester operating in four bending loading configurations. The test frequency was 30 Hz, and the stress ratio was R = -1. The desired stress amplitude was calculated by Eqs. (1) and (2), and the loads were applied by the dead weights.

$$\sigma = \frac{32M}{\pi D^3} \quad (1)$$

$$M = F.500 \quad (2)$$

where
σ is the stress amplitude (MPa),
M is the bending moment (N.mm),
D is the sample diameter (mm),
F is the bending load (N), and
The moment arm length is 500 mm.

In rotating bending fatigue tests, failure criteria were complete fracture of the samples. When the samples did not fail at 10^7 cycles, the tests were stopped, and these run-out samples were indicated in S-N curves by an arrow. Fracture surfaces of the samples were examined by a Leica stereo microscope with a magnification of 10x. Hardness of the substrate before and after HDA+DA processes were measured on a Wilson Tukon 1102 microhardness tester in HV0.025 scale.

III. Results and Discussion

Hot dip aluminizing and diffusion annealing parameters were selected based on our previous studies [7]. Figure 3 shows XRD patterns of the bare and the coated samples. It is seen that various nickel aluminide phases including NiAl, $NiAl_3$, Ni_2Al_3 phases were formed due to inward diffusion of Al and outward diffusion of Ni after HDA and DA processes [8]. Additional peaks belonging to SiO_2, Cr_2O_3, Cr_3Si, $AlCr_2$ and Al_2O_3 phases show that Si and Cr were also incorporated into the coating layer.

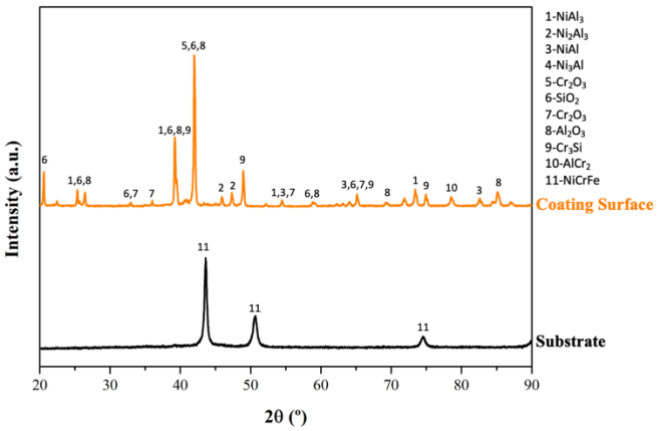

Figure 3: XRD patterns of the samples [7].

The S-N curve of the samples is given in Figure 4. Fatigue life of the samples varied with stress amplitude, the higher the stress amplitude, the lower is the fatigue life, as expected. After the coating processes (HDA+DA), fatigue life of the samples was significantly reduced. At a stress amplitude of 600 MPa, fatigue life of the coated samples was 2 to 20 times lower than those of the bare samples. At a lower stress amplitude, i.e. 500

MPa, the decrement in the fatigue life due to the coating process was much more marked. It is also seen that fatigue life of the bare samples varied from approximately 10^4 cycles to 10^7 cycles by reducing the stress amplitude by 200 MPa (from 700 to 500 MPa). However, the decline of the S-N curve was more marked for the coated samples. In this group, when the stress amplitude was reduced by 200 MPa (from 600 MPa to 400 MPa), less increment was observed in the corresponding fatigue life (approximately 6 times). This suggest that brittle nature of the coating and the substrate itself achieved by the coating process is responsible for such a sharp decrement in the S-N curve of the coated samples.

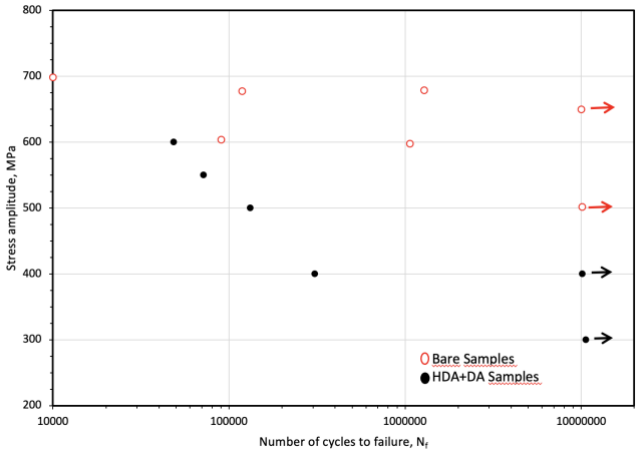

Figure 4: S-N curve of the samples.
(Arrow indicates that the sample did not fail at 10^7 cycles).

Figure 5 shows representative examples of the fracture surfaces after the rotating bending fatigue tests. The crack was initiated from the surface in both the bare and the coated samples. For the bare samples, crack propagation and final fracture regions are clearly identified.

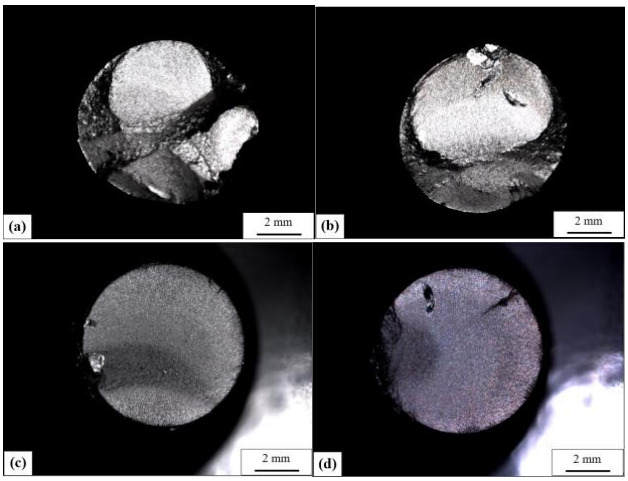

Figure 5: Representative stereo microscope images of the fatigue fracture surfaces. (a) The bare sample tested at 700 MPa, (b) The bare sample tested at 600 MPa, (c) The coated sample tested at 600 MPa, (d) The coated sample tested at 400 MPa.

Final fracture region was larger for the sample tested at a higher stress amplitude of 700 MPa (Figure 5a) with respect to the sample tested at a lower stress amplitude of 600 MPa (Figure 5b). This is an expected result of more rapid crack propagation at a higher stress amplitude. On the other hand, when compared to the fracture surfaces of the bare samples, the fracture surfaces of the coated samples (Figure 5c and 5d) are more flat regardless of the applied stress amplitude, without exhibiting an apparent final fracture region. Considering lower number of cycles to failure of these samples, as seen in Figure 6 that cracks were easily initiated from the surface and rapidly propagated in the coated samples.

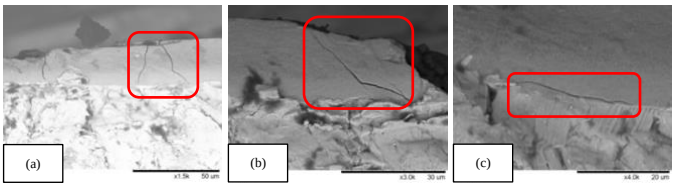

Figure 6: Representative scanning electron microscope images of the fatigue fracture surfaces. (a) 1500X magnification of the ruptured coated sample, (b) 3000X magnification of the ruptured coated sample, (c) 4000X magnification of the ruptured coated sample.

In order to explore the effect of coating processes on hardness, which is likely to effect the observed fatigue behavior, hardness was measured from the bare and the substrate of the coated samples. It is seen that average hardness of the bare sample was 310 HV0.025 while the substrate hardness of the coated samples was 478 HV0.025 and coating hardness was 1413 HV0.025. This indicates that HDA+DA processes result in a significant increment in hardness due to aging of materials beside it forms a brittle aluminide, silicide and oxide phases at the surface. When the fatigue test results, fracture surface examinations and hardness test results are considered, it was concluded that observed decrement in the fatigue life of the coated samples are likely arisen from the brittle nature of the coating.

IV. CONCLUSION

The effect of HDA and subsequent DA process on fatigue behavior of a solution treated Inconel 718 was investigated in the present study, and the following conclusions were drawn:

1. Fatigue life of the solution treated Inconel 718 is significantly reduced by HDA+DA processes.
2. Cracks are easily initiated and rapidly propagated in the coated samples when compared to the bare samples.
3. HDA and DA processes lead to a significant hardness increment in coating layer, which likely contributes to observed decrement in the fatigue life due to the notch effect.

ACKNOWLEDGEMENTS

The authors greatly acknowledge the financial support provided by Istanbul Technical University as a part of the ITU Scientific Research Projects with grant no. MYL-2021-43000.

REFERENCES

[1] L. Dul, "Application and processing of nickel alloys in the aviation industry," *Welding International*, vol. 27, pp. 48-56, 2013.

[2] M. J. Donachie, S. J. Donachie, *Superalloys: a technical guide*. ASM International, 2002.

[3] S. Han, H. Li, S. Wang, L. Jiang, X. Liu, (2010, April). Influence of silicon on hot-dip aluminizing process and subsequent oxidation for preparing hydrogen/tritium permeation barrier. International Journal of Hydrogen Energy. 35(7), pp. 2689-2693.

[4] P. Huilgol, K. U. Bhat, K. R. Udupa, "Hot-dip Aluminizing of Low Carbon Steel in Al & Al-5wt % Cr Baths," *Materials Today: Proceedings*, vol.5 (11). pp. 24702-24709, 2018.

[5] D. Das, (2013, March). Microstructure and high temperature oxidation behavior of Pt-modified aluminide bond coats on Ni-base superalloys. Progress In Materials Science. 58(2), pp. 151-182.

[6] S. Bose, *High temperature coatings*. Elsevier Butterworth-Heinemann, 2007.

[7] A. Kavukçu, "Investigating the Wear Behavior of Hot-Dip Aluminized and diffusion annealed Inconel 718 Superalloy at Elevated Temperature", MSc. Thesis, Graduate School of Science Engineering and Technology, Istanbul Technical Unıversity, 2021.

[8] B. Güleç, "Effect of Diffusion Annealing on the Surface Properties of Hot Dip Alumınized Inconel 718 Superalloy", MSc. Thesis, Graduate School of Science Engineering and Technology, Istanbul Technical Unıversity, 2019.

Influence of aluminum oxide on main electrical resistivity features of Bi-2212 ceramic compounds

M. ÖZ[1], C. TERZİOĞLU[2] and G. YILDIRIM[3]

[1] Bolu Abant İzzet Baysal University, Bolu/Turkey, oz_m@ibu.edu.tr
[2]Bolu Abant İzzet Baysal University, Bolu/Turkey, terzioglu_c@ibu.edu.tr
[3] Bolu Abant İzzet Baysal University, Bolu/Turkey, yildirim_g@ibu.edu.tr

Abstract **- In the present study, the variation of the basic dc electrical resistivity behaviors including conductivity property, resistivity at the room temperature state of 300 K, residual resistivity ratios (*RRR*), residual resistivity (ρ_{res}), resistivity at 90 K temperature, and the deduction parameters of ρ_{norm} and $\Delta\rho$ were determined as a function of the different aluminum oxide (Al_2O_3) mole-to-mole ratios between 0.0 and 0.10 of ceramic cuprate layered $Bi_{2.1}Sr_{2.0}Ca_{1.1}Cu_{2.0}O_yAl_x$ (Bi-2212) perovskite materials. The Al_2O_3 added ceramic materials searched were prepared at 840 °C annealing temperature for 24 h duration considering the standard solid-state reaction technique. The changes of dc electrical resistivity parameter against the environmental temperatures were performed in the temperature range of 30 K to 105 K. Besides, the differentiation of ρres quantity with the additional mechanism was semi-empirically examined by Matthiessen's rule $\rho(T) = \rho_i(T) + \rho_{res}$. The experimental and theoretical approach results indicated that the fundamental dc electrical behaviors depend sensitively on the addition level of aluminum oxide impurity. In this context, the increment in the aluminum oxide impurity atoms in the bulk ceramic system caused a dramatical decrement in the fundamental electrical resistivity proprieties. This was because the presence of Al_2O_3 materials in the main matrix triggers the formation of permanent basic crystal structure problems such as internal omnipresent flaws, stress raisers, microscopic structural faults, partial melting, grain misorientations, structural inhomogeneity, porosity, distortions, defects, crystallinity quality problems, lattice strains, impurity residues, main grain boundary coupling problems and weak-connectivity problems between grains. All in all, the addition idea of Al_2O_3 materials in the Bi-2212 crystal system was ploughed for the improvement of general electrical resistivity nature. Correspondingly, the un-added bulk Bi-2212 ceramic compound presented the highest electrical conductivity quantities while the maximum Al_2O_3 impurity added Bi-2212 sample obtains the minimum electrical conductivity features due to the serious increase in the fundamental problems in the crystal structure.**

Keywords **- Bi-2212 ceramics; Al_2O_3 impurity; Electrical resistivities; Basic crystal structure problems.**

I. INTRODUCTION

The growth in the world population, ever-increasing needs of human beings for their daily activities, desire for a comfortable life, and availability of advanced technological tools with the development of technology are the main reasons for the dramatic increment in gradual energy consumption. Consequently, the world faces serious global energy problems including energy production and consumption, energy protection and storage, energy distribution and meeting instant supply-demand balance of energy. The appearance of main problems triggers the issue of primary factors listed to be energy efficiency, resource conservation, cost savings and related climate protection systems founded on environmental awareness. The energy management discipline is directly interested in these factors. Amongst, the former factor takes the first place, and is about that the daily activities are conducted without any compromise but with low consumption of energy. With the dramatic development of technology, the desire of people to keep up with technology, and the increase in population growth significantly, energy consumption requirements worldwide are increasing much more, and therefore many more natural resources are being destroyed. Accordingly, the researchers and scientists have extensively studied and in fact discover new materials that consume less energy as compared to excess energy usage (overuse). In this regard, the superconductors discovered by Onnes in the year of 1911[1] are one of the most superior materials for the potential application fields, viz. the power transmission, electro-optic, motors, spintronics, network systems, metallurgy and materials engineering, particle accelerators, sensitive process control, medical diagnosis, hydrogen society, levitated trains, application-oriented material science, refrigeration, transformers, levitated trains, nuclear fusion, future hydrogen society, power transmission cable, heavy-industrial technology, energy-related sectors [2–7] as a consequence of less energy loss, energy dissipation and consumption characteristic behaviors as well as larger critical transition temperatures, current density and magnetic field carrying capability [8–10]. Namely, it can be summarized that the superconducting compounds are a strong motivation source for the energy efficient use. On the other hand, the problematic features sorted as relatively higher penetration depth size, brittleness, and layered structure nature (meaning grain boundary coupling problems and weak-connectivity problems between grains), and lower charge carrier density and coherence length size are thought to improve as much as possible to increase the application fields of Bi-2212 ceramic compounds [11, 12]. Thus, the scientists have widely struggled to improve the problematic quantities mentioned above as much as possible for

the increase in the potential usage fields of Bi-2212 ceramic solid materials by changing the content of main matrix with material addition mechanism for years. In the current work, the change of basic dc electrical resistivity behaviors as well as conductivity property, resistivity at the room temperature electrical resistivity state of 300 K, residual resistivity ratios (*RRR*), residual resistivity (ρ_{res}), resistivity at 90 K temperature, the deduction parameters of ρ_{norm} and $\Delta\rho$ with the different aluminum oxide (Al_2O_3) molar ratios of $0.0 \leq x \leq 0.10$ of cuprate layered $Bi_{2.1}Sr_{2.0}Ca_{1.1}Cu_{2.0}O_y$ perovskite superconducting solid compounds is sensitively examined by considering dc electrical resistivity parameters (ρ-T) against environmental temperature curves. The experimental and theoretical approach outcomes indicate that the increase in the aluminum oxide in the Bi-2212 crystal system decreases all the private conductivity features.

II. Experimental Procedure

The aluminum oxide added Bi-2212 superconducting ceramic solid compounds are produced by the typical ceramic production route in the atmospheric air conditions. In the sample fabrications, the chemical powders (Al_2O_3, Bi_2O_3, $CaCO_3$, CuO, and $SrCO_3$) with high purity greater than about %99.99 are used. Every material including oxide, ceramic and carbonate powder chemicals is accurately weighed by using the electronic balance to prepare the pure and aluminum oxide added $Bi_{2.1}Sr_{2.0}Ca_{1.1}Cu_{2.0}O_y$ ceramic solid compounds within the desired stoichiometric ratios. Hence, all the chemical powders are exposed to milling process for the time of 6 hours in the atmospheric conditions to develop the homogeneity of mixture of powders, and especially to minimize the desired size of chemical powders. After, the mixture of powders produced homogenously is manually ground in the agate mortar for the time of 30 minutes to produce the desired powder sizes of $Bi_{2.1}Sr_{2.0}Ca_{1.1}Cu_{2.0}O_y$ ceramic compound and to bring all the particles closer together for the increase in the possibility of covalent bonds between atoms. Then, the homogenously distributed particles are exposed to the calcination process at 800 °C constant temperature for the duration of 36 h in the furnace in the atmospheric air conditions. During the process of calcination, the heating and preservation to room temperature rates are adjusted to be 5 °C/minute. The preheated homogenous chemicals are manually ground in the agate mortar for 30-minute duration. The homogenously distributed particles are pelletized hydraulically in the rectangular bars of 10x10x2 mm^3 sizes at the manual load of 300 MPa in the atmospheric air conditions. All the solidified bars are thoroughly sintered at 840 °C annealing temperature for 24 hours. The ceramic cuprate layered pure and aluminum oxide added $Bi_{2.1}Sr_{2.0}Ca_{1.1}Cu_{2.0}O_y$ ceramic compounds fabricated at different Al_2O_3 concentration amount of x=0, 0.01, 0.03, 0.05, 0.07 and 0.10 are thereafter presented as un-added, Bi/Al-1, Bi/Al-2, Bi/Al-3, Bi/Al-4, and Bi/Al-5 in the paper.

Variation in the dc electrical resistivity parameters as a role of environmental temperatures between 30 K and 105 K is measured experimentally with the conventional four-probe route in the He closed-cycle cryostat. The electrical resistivity curves are recorded by using the dc current of 5 mA applying on the specimen surface. The signals deduced from experimental curves are measured by 2700 nano-voltmeter and 220 Keithley programmable current sources. The monitoring of the experimental results is recorded by using Labview software program. The dc electrical resistivity curves allow us to discuss the change of fundamental resistivity properties such as general conductivity parameters, resistivity at the room temperature electrical resistivity state of 300 K, residual resistivity ratios (*RRR*), residual resistivity (ρ_{res}), resistivity at 90 K temperature, and the deduction parameters of ρ_{norm} and $\Delta\rho$ quantities of $Bi_{2.1}Sr_{2.0}Ca_{1.1}Cu_{2.0}O_y$ ceramic compounds with the changed aluminum oxide impurity additional level.

III. Result and Discussion

A. Change of dc electrical resistivity quantities of bulk $Bi_{2.1}Sr_{2.0}Ca_{1.1}Cu_{2.0}O_y$ with Al_2O_3 impurity addition

In this study, the differentiation of basic dc electrical resistivity features (ρ_{90K}, ρ_{300K}, ρ_{res}, ρ_{norm}, $\Delta\rho$, and *RRR* parameters) belonging to the solidified $Bi_{2.1}Sr_{2.0}Ca_{1.1}Cu_{2.0}O_y$ superconducting ceramic compounds with the different aluminum oxide impurity addition amounts intervals of $0.0 \leq x \leq 0.10$ is experimentally determined by using the standard temperature-dependent dc electrical resistivity experiments. The measurements are done in the temperature ranges between 30 K and 105 K, and the related results for the pure and aluminum oxide added $Bi_{2.1}Sr_{2.0}Ca_{1.1}Cu_{2.0}O_y$ ceramic compounds are graphically represented in Fig. 1. It is obvious from the figure that the addition of Al_2O_3 impurity in the Bi-2212 ceramic matrix destroys considerably the basic dc electrical resistivity features. This is because the introduction of aluminum oxide impurity in the $Bi_{2.1}Sr_{2.0}Ca_{1.1}Cu_{2.0}O_y$ crystal system is performed thoroughly. At the same time, the ceramic cuprate layered pure and aluminum oxide added $Bi_{2.1}Sr_{2.0}Ca_{1.1}Cu_{2.0}O_y$ ceramic compounds all present the conventional metallic-like property after a higher environmental temperature than the critical transition temperature values. It is another important result deduced from the dc electrical resistivity findings embedded in Fig. 1 that there appears a positive linear change in the electrical resistivity with the increase in the environment temperature due to the presence of overlapping of Cu-3d and O-2p wave functions, creation of super-electrons, effective electronic state densities at Fermi energy level, and cooper-pair coupling probabilities in the strongly covalently bonded Cu-O_2 layers [13, 14]. However, Fig. 1 shows that the rise in the aluminum oxide impurity addition level results in the induction of new permanent basic crystal structure problems such as internal omnipresent flaws, stress raisers, microscopic structural faults, partial melting, grain misorientations, structural inhomogeneity, porosity, distortions, defects, crystallinity quality problems, lattice strains, impurity residues, main grain boundary coupling problems and weak-connectivity problems between grains [15]. In other words, the aluminum oxide impurity damages seriously the fundamental dc electrical resistivity quantities.

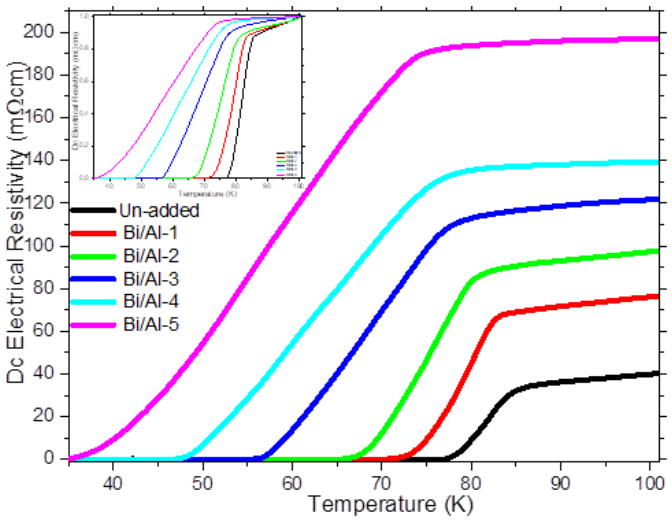

Fig. 1. Change in dc electrical curves of bulk $Bi_{2.1}Sr_{2.0}Ca_{1.1}Cu_{2.0}O_yAl_x$ materials

Additionally, it is obvious from the figure that the important characteristic natures including overlapping of Cu-3d and O-2p wave functions, construction of super-electrons, effective electronic state densities at Fermi energy level, and cooper-pair coupling probabilities in the strongly covalently bonded Cu-O_2 layers are damaged gradually depending on the increase in the aluminum oxide impurity addition level [16, 17]

Table 1. Basic dc electrical resistivity parameters for ceramic cuprate layered pure and aluminum oxide added $Bi_{2.1}Sr_{2.0}Ca_{1.1}Cu_{2.0}O_y$ ceramic compounds

Samples	ρ_{300K} *(mΩcm)*	ρ_{res} *(mΩcm)*	*RRR* (ρ_{300K}/ρ_{90K})	$\Delta\rho$ (ρ_{300K} - ρ_{90K}) *(mΩcm)*	ρ_{norm} ($\rho_{90}/\Delta\rho$)	ρ_{90K} *(mΩcm)*
Pure	117.802	5.221	3.129	80.152	0.470	37.650
Bi/Al-1	156.267	37.165	2.106	82.052	0.904	74.215
Bi/Al-2	176.345	58.218	1.844	80.698	1.185	95.647
Bi/Al-3	182.323	89.279	1.508	61.456	1.967	120.867
Bi/Al-4	184.104	120.548	1.323	44.955	3.095	139.149
Bi/Al-5	208.982	183.569	1.071	13.892	14.043	195.090

The change of all the basic dc electrical resistivity features such as resistivity at the room temperature electrical resistivity state of 300 K, residual resistivity ratios (*RRR*), residual resistivity (ρ_{res}), resistivity at 90 K temperature, and the deduction parameters of ρ_{norm} and $\Delta\rho$ over the environment temperatures is numerically given in Table 1. The detailed information related to these data is discussed in the following sections in the paper.

B. Differentiation of room temperature electrical resistivities at 300 K for $Bi_{2.1}Sr_{2.0}Ca_{1.1}Cu_{2.0}O_yAl_x$ superconducting ceramic system

According to the dc electrical results inserted in Table 1, the aluminum oxide impurity leads to the remarkable increase in the room temperature electrical resistivities at 300 K (ρ_{300K}) due to the induction of new permanent basic crystal structure problems; namely, the internal omnipresent flaws, stress raisers, microscopic structural faults, partial melting, grain misorientations, structural inhomogeneity, porosity, distortions, defects, crystallinity quality problems, lattice strains, impurity residues, main grain boundary coupling problems and weak-connectivity problems between grains in the solid bulk $Bi_{2.1}Sr_{2.0}Ca_{1.1}Cu_{2.0}O_yAl_x$ ceramic system. In this respect, the bulk Bi/Al-5 sample (the most Al_2O_3 distributed ceramic compound) has the maximum ρ_{300K} parameter of 117.802 mΩ.cm whereas the minimum ρ_{300K} parameter of 208.982 mΩ.cm is attributed to the un-added Bi-2212 superconducting ceramic compound. The other materials are noted to exhibit the moderate room temperature electrical resistivities.

C. Dc electrical resistivity at 90 K temperature

The change of the lattice strain and impurity scattering in the bulk $Bi_{2.1}Sr_{2.0}Ca_{1.1}Cu_{2.0}O_yAl_x$ ceramic system is easily determined from the variation of dc electrical resistivity at 90 K temperature (ρ_{90K}) parameter belonging to the materials. In this regard, the ρ_{90K} value is numerically deduced from transition between the isolated superconducting grains and the grains in the normal state. We find all the dc electrical resistivity at 90 K temperature values for the ceramic cuprate layered pure and aluminum oxide added $Bi_{2.1}Sr_{2.0}Ca_{1.1}Cu_{2.0}O_y$ superconducting materials from Fig. 1 and provide the numerical ρ_{90K} values in the third column of Table 1. Based on the table, it is apparent that the increment in the aluminum oxide impurity level triggers the regular enhancement in the dc electrical resistivity at 90 K temperature parameters depending on the systematic increase in the formation of impurity scattering and lattice strain in the bulk $Bi_{2.1}Sr_{2.0}Ca_{1.1}Cu_{2.0}O_yAl_x$ crystal system. As for the numerical values, the un-added bulk $Bi_{2.1}Sr_{2.0}Ca_{1.1}Cu_{2.0}O_y$ superconducting compound indicates global smallest ρ_{90K} value of 37.650 mΩ.cm. On the other hand, the other materials possess the ρ90K values of 74.215 m.Ωcm, 95.647 m.Ωcm, 120.867 m.Ωcm, 139.149 m.Ωcm, and 195.090 mΩcm for the bulk Bi/Al-1, Bi/Al-2, Bi/Al-3, Bi/Al-4, and Bi/Al-5 superconducting ceramic compounds.

D. Residual resistivity parameters of ceramic cuprate layered pure and aluminum oxide added $Bi_{2.1}Sr_{2.0}Ca_{1.1}Cu_{2.0}O_y$ ceramic compounds

In the part of paper, we deal sensitively with the change of residual resistivity (inferred from the temperature-dependent dc electrical resistivity curves) of $Bi_{2.1}Sr_{2.0}Ca_{1.1}Cu_{2.0}O_y$ superconducting ceramic compounds with aluminum oxide impurity addition using Matthiessen's rule approach provided in Ref. [18]. One can see the scientific relation below.

$$\rho(T) = \rho_i(T) + \rho_{res} \quad (1)$$

where in the relation given above, the $\rho(T)$ parameter exhibits the total dc electrical resistivity for the superconducting ceramic compound at any temperature values. Besides, the $\rho_i(T)$ electrical resistivity parameter varies from the temperature values when the abbreviation of ρ_{res} value ascribes to the residual resistivity. In this respect, the latter

parameter is not affected by the environmental temperature values. This is because the basic crystalline structure problems the bulk Bi-2212 ceramic system affect directly the ρ_{res} parameter [19]. Correspondingly, the numerical value of ρ_{res} property is evaluated from the temperature-dependent dc electrical resistivity graphs by a method of the data extrapolation approach. One can see all the ρ_{res} values belonging to the pure and aluminum oxide added $Bi_{2.1}Sr_{2.0}Ca_{1.1}Cu_{2.0}O_y$ superconducting compounds in Table 1. As seen from the table that the enhancement of aluminum oxide addition amount results in the considerable increase in the ρ_{res} parameters because of the monotonous increment in the crystallinity problems of bulk Bi-2212 superconducting ceramic compounds. In this respect, the lowest ρ_{res} value of 5.221 m.Ωcm ascribes to the un-added Bi-2212 ceramic material whereas the maximum ρ_{res} value of 183.569 m.Ωcm is observed for the bulk Bi/Al-5 ceramic material. The bulk Bi/Al-1, Bi/Al-2, Bi/Al-3, and Bi/Al-4 superconducting ceramic compounds possess the moderate ρ_{res} values of 37.165 m.Ωcm, 58.218 m.Ωcm, 89.279 m.Ωcm, and 120.548 m.Ωcm, respectively.

E. Variation of Δρ parameters

The $\Delta\rho$ parameter is calculated from the linear proportion of room temperature electrical resistivities at 300 K and dc electrical resistivity at 90 K temperature. Namely, the relation is equal to ρ_{300K}/ρ_{90K}. The parameter is directly on the existence of internal omnipresent flaws, stress raisers, microscopic structural faults, porosity, distortions, and defects in the crystal system. In other words, the $\Delta\rho$ parameter is sensitively changed by the dopant mechanism and preparation conditions. Here, the role of aluminum oxide impurity addition amount on the ρ_{300K}/ρ_{90K} is extensively examined by means of the temperature-dependent dc electrical resistivity measurement results. One can see the $\Delta\rho$ parameters of pure and aluminum oxide added $Bi_{2.1}Sr_{2.0}Ca_{1.1}Cu_{2.0}O_y$ superconducting compounds in Table 1. As it is observable from the table, the increase in the aluminum oxide impurity addition amount causes the decrement in the $\Delta\rho$ value up to the maximum addition level of x=0.1. Thus, the smallest $\Delta\rho$ value of 13.892 m.Ωcm is noted for the Bi/Al-5 superconducting ceramic material. Conversely, the other samples obtain generally larger $\Delta\rho$ value. Accordingly, it is obvious that the increase in the aluminum oxide impurity in the bulk Bi-2212 ceramic compound leads to the considerable enhancement in the internal omnipresent flaws, stress raisers, microscopic structural faults, porosity, distortions, and defects in the main matrix.

F. RRR parameter findings

We also study strongly on the change of another deduction ratio such as RRR parameter deduced from ratio between ρ_{300K} and ρ_{90K} to discuss the effect of aluminum oxide impurity addition level on the quality of prepared material for the potential application fields [20]. One can see every computed RRR parameter in Table 1. It is apparent that the RRR parameter is noted to decrease regularly depending on the impurity addition amount. Thus, it can be normal to mention that the presence (in fact the increment) of aluminum oxide impurity in the $Bi_{2.1}Sr_{2.0}Ca_{1.1}Cu_{2.0}O_y$ superconducting ceramic matrix damages dramatically the material quality. Numerically, the un-added Bi-2212 superconducting ceramic compound owns the global maximum RRR value of 3.129. On the other hand, the other ceramic compounds prepared show the RRR values in a range of 2.106-1.071. In this context, the bulk Bi/Al-5 ceramic compound obtains the smallest RRR value of 1.071.

G. Differentiation of ρ_{norm} parameter of $Bi_{2.1}Sr_{2.0}Ca_{1.1}Cu_{2.0}O_y$ superconducting ceramic structure with aluminum oxide impurity

Lastly, we experimentally investigate the effect of aluminum oxide impurity on the ratio between ρ_{90} and $\Delta\rho$ values to point out the variation of crystallinity mechanism of the bulk $Bi_{2.1}Sr_{2.0}Ca_{1.1}Cu_{2.0}O_y$ superconducting ceramic structure [21, 22]. The observed values are numerically given in Table 1. It is apparent form the table that the values of ρ_{norm} parameter are noted to increase systematically with increase in the aluminum oxide impurity addition amount. In this regard, the minimum value is found to be about 0.470 for un-added Bi-2212 superconducting ceramic compound while the maximum value of 14.043 is attributed to the bulk Bi/Al-5 ceramic material. The other Bi-2212 superconducting samples added Al_2O_3 structure exhibit the moderate ρ_{norm} parameters in a range of 0.904-3.095. The former value belongs to the bulk Bi/Al-1 ceramic material while the latter value ascribes to the Bi/Al-4 ceramic compound. We also depict a graphic related the change between the ρ_{norm} parameters and aluminum oxide impurity addition amount (Fig. 2). According to the figure, it is clear that the sharp increase begins with the addition level of x=0.50. Namely, after the critical point for the addition level, the basic structural problems such as internal omnipresent flaws, stress raisers, microscopic structural faults, porosity, distortions, and defects increase more rapidly in the crystal system. However, when the addition level is equal to x=0.1, the considerable increase in the basic structural problems appears as seen in Fig. 2.

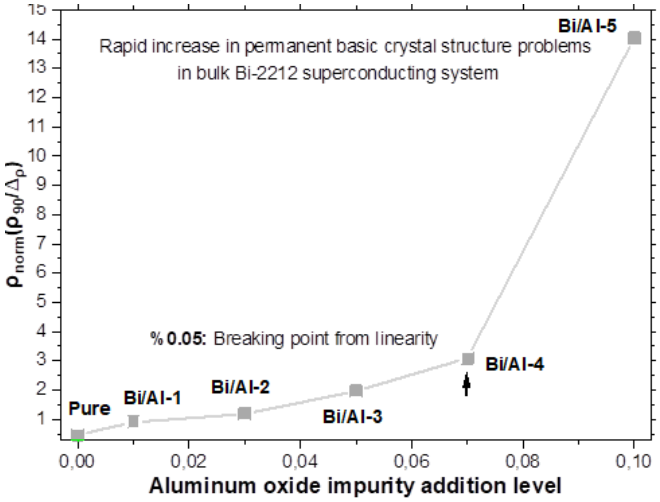

Fig. 2. Rapid increase point of basic structural problems in $Bi_{2.1}Sr_{2.0}Ca_{1.1}Cu_{2.0}O_y$ superconducting ceramic system

IV. CONCLUSION

In this study, we focus on the determination of the variation in the basic dc electrical resistivity features (conductivity, resistivity at the room temperature electrical resistivity state of 300 K, residual resistivity ratios, residual resistivity, resistivity at 90 K temperature, and the deduction parameters of ρ_{norm} and $\Delta\rho$ of ceramic cuprate layered $Bi_{2.1}Sr_{2.0}Ca_{1.1}Cu_{2.0}O_y$ perovskite materials depending on the different aluminum oxide impurity addition amount changing from $0.0 \leq x \leq 0.10$. The experimental results show that the presence of the aluminum oxide impurity causes the crucial change of basic dc electrical resistivity features. This means that the aluminum oxide impurity atoms introduce in the bulk Bi-2212 ceramic crystal structure. Moreover, it is found that the increment in the aluminum oxide impurity atoms in the bulk ceramic system leads to the considerable decrement in the fundamental electrical resistivity proprieties due to the formation of new permanent basic crystal structure problems in the $Bi_{2.1}Sr_{2.0}Ca_{1.1}Cu_{2.0}O_y$ crystal system. Correspondingly, the un-added Bi-2212 superconducting ceramic sample possesses the highest dc electrical conductivity for the future application fields.

REFERENCES

[1] H.K. Onnes, Further experiments with Liquid Helium. D. On the change of Electrical Resistance of Pure Metals at very low Temperatures, etc. V. The Disappearance of the resistance of mercury, Koninklijke Nederlandsche Akademie van Wetenschappen Proceedings, 14 (1911) 113–115.

[2] A. Kuczkowski, B. Kusz, High-T_c superconductor-polymer composites: $YB_2Cu_3O_{7-x}$-polyester polymer and $YBa_2Cu_3O_{7-x}$-Teflon, Synth. Met. 94 (1998) 145–148.

[3] M. Runde, Application of high-T_c superconductors in aluminum electrolysis plants, IEEE T. Appl. Supercond. 5 (1995) 813–816.

[4] S. Nagaya, N. Hirano, M. Naruse, T. Watanabe, T. Tamada, Development of a high-efficiency conduction cooling technology for SMES coils, IEEE T. Appl. Supercond. 23 (2013) 5602804–5602807.

[5] H.H. Xu, L. Cheng, S.B. Yan, D.J. Yu, L.S. Guo, X. Yao, Recycling failed bulk YBCO superconductors using the NdBCO/YBCO/MgO film-seeded top-seeded melt growth method, J. Appl. Phys. 111 (2012) 103910.

[6] B. Batlogg, Cuprate superconductors: Science beyond high T(c), Solid State Commun. 107 (1998) 639–647.

[7] W. Buckel, R. Kleiner, Superconductivity: Fundamentals and applications, 2nd ed., Wiley-VCH Verlag, Weinheim, 2004.

[8] A.T. Ulgen, T. Turgay, C. Terzioglu, G. Yildirim, M. Oz, Role of Bi/Tm substitution in Bi-2212 system on crystal structure quality, pair wave function and polaronic states, J. Alloy. Compd. 764 (2018) 755–766.

[9] S.Y. Oh, H.R. Kim, Y.H. Jeong, O.B. Hyun, C.J. Kim, Joining of Bi-2212 high-T_c superconductors and metals using indium solders, Physica C 463–465 (2007) 464–467.

[10] U. Erdem, Y. Zalaoglu, A.T. Ulgen, T. Turgay, G. Yildirim, Role of trivalent Bi /Tm partial substitution on active operable slip systems in Bi 2212 crystal structure, Cryogenics, 113

[11] H. Miao, M. Meinesz, B. Czabai, J. Parrell, S. Hong, Microstructure and Jc improvements in multifilamentary Bi-2212/Ag wires for high field magnet applications, AIP Conference Proceedings 986 (2008) 423–430.

[12] K. Koyama, S. Kanno, S. Noguchi, Electrical, Magnetic and superconducting properties of the quenched Bi2Sr2Ca1-XNdXCu2O8+y system, Jpn. J. Appl. Phys. 29 (1990) L53–L56.

[13] P.B. Allen, W.E. Pickett, H. Krakauer, Anisotropic normal-state transport-properties predicted and analyzed for high-Tc oxide superconductors, Phy. Rev. B 37 (1988) 7482–7490.

[14] A. Ianculescu, M. Gartner, B. Despax, V. Bley, Th Lebey, R. Gavrila, M. Modreanu, Optical characterization and microstructure of $BaTiO_{(3)}$ thin films obtained by RF-magnetron sputtering, Appl. Surf. Sci. 253 (2006) 344–348.

[15] D.M. Newns, P.C. Pattnaik, C.C. Tsuei, Role of van hove singularity in high-temperature superconductors: Mean field, Phys. Rev. B 43 (1991) 3075–3084.

[16] M.B. Turkoz, S. Nezir, C. Terzioglu, A. Varilci, G. Yildirim, Investigation of Lu effect on $YBa_2Cu_3O_{7-\gamma}$ superconducting compounds, J. Mater. Sci: Mater. El. 24 (2013) 896–905.

[17] Y. Zalaoglu, G. Yildirim, H. Buyukuslu, N.K. Saritekin, A. Varilci, C. Terzioglu, O. Gorur, Important defeats on pinning of 2D pancake vortices in highly anisotropic Bi-2212 superconducting matrix with homovalent Bi/La substitution, J. Alloy. Compd. 631 (2015) 111–119.

[18] J. Ekin, Experimental techniques for low-temperature measurements: cryostat design, material properties and superconductor critical-current testing, Oxford University Press, New York, (2006).

[19] M. Li, Y. Zhang, Y. Li, Y. Qi, Granular superconductivity in polycrystalline $Bi_2Sr_2CaCu_2O_{8+\gamma}$ by homovalent La substitution on Bi sites, J. Non-Cryst. Solids 356 (2010) 2831–2835.

[20] X. Xu, J.H. Kim, S. X. Dou, S. Choi, J.H. Lee, H. W. Park, M. Rindfleish, M. Tomsic, A correlation between transport current density and grain connectivity in MgB2/Fe wire made from ball-milled boron, J. Appl. Phys. 105 (2009) 103913.

[21] S.B. Guner, Y. Zalaoglu, T. Turgay, O. Ozyurt, A.T. Ulgen, M. Dogruer, G. Yildirim, A detailed research for determination of Bi/Ga partial substitution effect in Bi-2212 superconducting matrix on crucial characteristic features, J. Alloy. Compd. 772, (2019) 388–398.

[22] A.T. Ulgen, T. Turgay, C. Terzioglu, G. Yildirim, M. Oz, Role of Bi/Tm substitution in Bi-2212 system on crystal structure quality, pair wave function and polaronic states, J. Alloy. Compd. 764 (2018) 755–766.

Effect of aluminum oxide on main superconducting features of $Bi_{2.1}Sr_{2.0}Ca_{1.1}Cu_{2.0}O_y$ ceramics

M. ÖZ[1], C. TERZİOĞLU[2] and G. YILDIRIM[3]

[1] Bolu Abant İzzet Baysal University, Bolu/Turkey, oz_m@ibu.edu.tr
[2]Bolu Abant İzzet Baysal University, Bolu/Turkey, terzioglu_c@ibu.edu.tr
[3] Bolu Abant İzzet Baysal University, Bolu/Turkey, yildirim_g@ibu.edu.tr

Abstract **- This study was sensitively interested in the determination of the influence of aluminum oxide (Al_2O_3) impurity within the different molar addition amounts ($0.0 \leq x \leq 0.10$) on the fundamental superconducting topographies of bulk $Bi_{2.1}Sr_{2.0}Ca_{1.1}Cu_{2.0}O_yAl_x$ (Bi-2212-Al) superconducting ceramic compounds by means of the variations of dc electrical resistivity parameters over the environmental temperatures between 20 K and 105 K. The pure and Al_2O_3 added Bi-2212 superconducting chemical samples were produced using a standard solid phase reaction technique at the constant sintering temperature of 840 °C for the period of 24 h. The experimental curves measured enable us to find the change in the offset and offset critical transition temperatures (T_c^{offset} and T_c^{onset}) and degree of broadening ($\Delta T_c = T_c^{onset} - T_c^{offset}$) properties of Bi-2212 superconductors with the Al_2O_3 impurity addition. It was evaluated that all the main superconducting features mentioned above were obtained to depend dramatically on the impurity addition. It was determined that, the presence of Al_2O_3 impurity damages seriously the T_c^{offset}, T_c^{onset}, and ΔT_c quantities as a result of degradation in the hole mover concentrations (*P*) per Cu ions in the Cu-O_2 layer $x^2 - y^2$ bands in Bi-2212 crystal nature. Similarly, the increase in impurity level was noted to trigger destruction in the overlying of Cu-3d and O-2p wave functions, formation of super-electrons, cooper-pair coupling probabilities in the strongly covalently bonded Cu-O_2 layers, amplitude of pair wave function, equalities in the oxidation states, and hole trap energy values in the superconducting paths. Besides, the presence of impurity atoms in the Bi-2212 crystal system was found to worsen harshly the effective electronic state densities at Fermi energy level. Moreover, the decrease in the T_c^{offset}, T_c^{onset}, and ΔT_c parameters was determined to stem from the reduction of metallic connections depending on the increase of basic crystal structure problems including stress raisers, microscopic structural faults, internal omnipresent flaws/defects/distortions/porosity, weak-interaction problems between the superconducting grain, and grain borderline coupling difficulties in the Bi-2212 crystal system. We also determined the numerical values of T_c^{offset}, T_c^{onset}, ΔT_c, and *P* constraints for the pure and Al_2O_3 mixed Bi-2212 superconducting solid compounds in the paper.**

Keywords **- $Bi_{2.1}Sr_{2.0}Ca_{1.1}Cu_{2.0}O_y$ system; Al_2O_3 impurity; *P*, T_c^{offset}, T_c^{onset} and ΔT_c**

I. INTRODUCTION

With the first discovery of superconductivity in a material in 1911 [1], many scholars have widely studied on the enhancement of the vital characteristics such as electrical, superconducting, flux pinning, mechanical, physical, and opto-electronical features in different types of materials as regards metals, rare-earth borocarbide, alloys, semi-metals, carbonaceous sulfur hydride samples, dielectric compounds, pyrochlore oxides, chevrel phase, organic-materials, chalcogens, carbon-containing samples, nickelates, heavy fermion-based compounds, inorganic-including samples, magnesium-diboride, lanthanum decahydride, silicon-based compounds, iron-including samples, rutheno-cuprates, A-15 types of materials and perovskite ceramic structures [3, 4]. Thus, the superconducting materials have extensively found lots of application fields including application-oriented material science, levitated trains, cooling technology, medical diagnosis, cooling technology, hydrogen societies, levitated trains, refrigeration, particle accelerators, transformers, heavy-industrial technology, and sensitive process control areas [5–8]. Especially, the last group members of the teams possess largely transition temperature, current carrying capability, magnetic field carrying ability, and thermodynamic stability characteristic features [9, 10]. Besides, the ceramic materials exhibit lower energy consumption as compared to the other superconducting parents [11–18].

In the up-to-date study, we inspect the impact of aluminum oxide (Al_2O_3) impurity dopants varying molar ratios of $0.0 \leq x \leq 0.10$ on the main superconducting property values, viz. the offset and offset critical transition temperatures (T_c^{offset} and T_c^{onset}), the degree of broadening widths ($\Delta T_c = T_c^{onset} - T_c^{offset}$) and hole transporter concentrations (*P*) per Cu ions in the Cu-O_2 layer $x^2 - y^2$ bands in the bulk $Bi_{2.1}Sr_{2.0}Ca_{1.1}Cu_{2.0}O_y$ superconducting solid structures with the associate of the environmental temperature-dependent resistivity measurements executed at the environmental temperatures of 30 K-105 K. The experimental findings show that with the increase in the aluminum oxide (Al_2O_3) impurity dopants the

fundamental superconducting topographies of the solid $Bi_{2.1}Sr_{2.0}Ca_{1.1}Cu_{2.0}O_y$ superconducting ceramic structures are noted to degrade seriously.

II. Experimental Procedure

This study indicates the global differentiation in the main superconducting property values in the $Bi_{2.1}Sr_{2.0}Ca_{1.1}Cu_{2.0}O_y$ compounds with the aluminum oxide impurity dopants. In the study, the aluminum oxide added Bi-2212 ceramic samples are prepared by considering the conventional ceramic production method in the atmospheric air conditions. In the procedure of specimen production, the chemical powders including Al_2O_3, Bi_2O_3, $CaCO_3$, CuO, and $SrCO_3$ are obtained from an exclusive firm in Ankara. The oxide, ceramic, and carbonate chemicals of powders are in the high purity (%99.99). Firstly, with the aid of the electronic balance the high purity oxide, ceramic, and carbonate powders are weighed in the required stoichiometric ratios with respect to the $Bi_{2.1}Sr_{2.0}Ca_{1.1}Cu_{2.0}O_y$ so that we can produce the pure and aluminum oxide assorted $Bi_{2.1}Sr_{2.0}Ca_{1.1}Cu_{2.0}O_y$ ceramics within accurate proportions. Secondly, the homogeneity of every chemical of powders is wholly performed by grinding the chemicals during 6 h in the atmospheric air condition. Besides, the grinding process has been carried out perfectly to obtain chemical powders of the desired size. Thirdly, in order to bring all the oxide, ceramic, and carbonate atoms in the chemical powders together we manually grind all the powders in an agate mortar for 30 min. Moreover, this technique is used for enhancing the bonding between atoms. Fourthly, the end form of chemicals of residues are calcined in the furnace for 36 h at 800 °C ambient temperature by using 5 °C/min. rise and decrease rates. After the calcination process, new (calcined) formation of chemicals of powders is removed from the furnace, and right after is exposed to the grinding process for 30 min. in the agate mortar. Then, every chemical of powders is hydraulically pressed by utilizing 300 MPa applied loads in the rectangular bars with the sizes of 10x10x2 mm^3 in the medium of atmosphere. Finally, the chemicals of powders are prepared for the last procedure that is sintering process for 24 h at 840 °C temperature. Thenceforth, throughout the paper, the pure and aluminum oxide doped Bi-2212 samples, which are prepared at various addition levels such as x=0.00, 0.01, 0.03, 0.05, 0.07 and 0.10 are observed to be un-added, Bi/Al-1, Bi/Al-2, Bi/Al-3, Bi/Al-4, and Bi/Al-5, respectively.

Changes of resistivity measurement results depending on the temperature intervals 30 K-105 K are experimentally investigated by using four-probe contact techniques. The measurements ae taken in an He closed-cycle cryostat. The experimental signals gathered on the sample surfaces are conducted in the case of 5 mA dc current. The experimental findings are used to study the variation in the global differentiation in the main superconducting property parameters containing offset and offset critical transition temperatures (T_c^{offset} and T_c^{onset}) and degree of broadening ($\Delta T_c = T_c^{onset} - T_c^{offset}$) properties of Bi-2212 superconductors with the Al_2O_3 ceramic impurity addition level. All the experimental results are extensively discussed.

III. Result and Discussion

A. Variation of superconducting properties of $Bi_{2.1}Sr_{2.0}Ca_{1.1}Cu_{2.0}O_y$ ceramic structures

This following study clearly indicates the crucial effects of aluminum oxide (Al_2O_3) impurity dopants within the dissimilar molar ratios between x= 0.00 and 0.10 on the main superconducting property values as regards the offset and offset critical transition temperatures (T_c^{offset} and T_c^{onset}) and the degree of broadening ($\Delta T_c = T_c^{onset} - T_c^{offset}$) scientific parameters of the solidified $Bi_{2.1}Sr_{2.0}Ca_{1.1}Cu_{2.0}O_y$ bulk superconductors using the temperature-relied resistivity quantities. The experimental tests are wielded in the temperature ranges of 30 K-105 K. The value of T_c^{onset} parameter deduced from the experimental curves are directly related to the hole carrier concentrations (*P*) per Cu ions in the Cu-O_2 layer $x^2 - y^2$ bands, overlapping of Cu-3d and O-2p wave functions, gap coefficient, formation of super-electrons, cooper-pair coupling probabilities in the strongly covalently bonded Cu-O_2 layers, dirty or clean limit nature, amplitude of pair wave function, formation of bipolarons in the polarizable lattices, electronic state densities at Fermi energy level, hybridization mechanism, phase coherence, consistencies in oxidation states, and hole trap energy values in the superconducting paths [19–21]. In this respect, in the case of a lower ambient temperature value than the value of T_c^{onset} parameter, the ceramic compound displays the superconducting phenomenon.

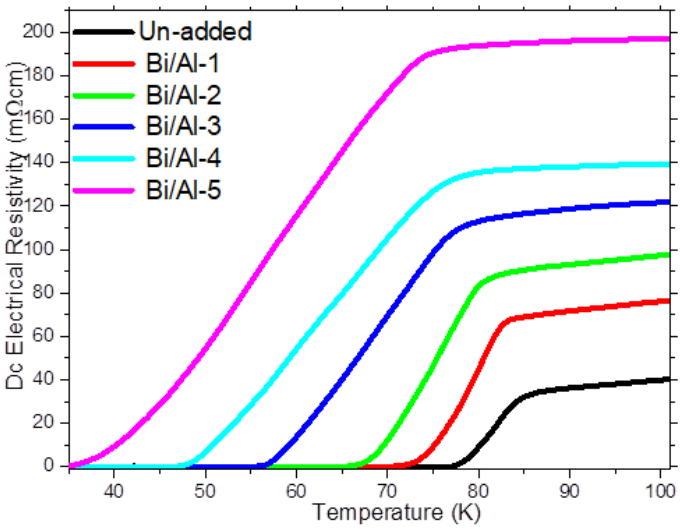

Fig. 1. Differentiation of main superconducting property values against the ambient temperatures of the pure and Al_2O_3 added Bi-2212 superconducting ceramic samples

As for the other critical transition temperature parameter of

the offset critical transition temperature value, T_c^{offset}, the critical temperature is associated to the phase change of inter-granular component between the superconducting state and normal state. On this origin, the phase volume fraction acts an important role in considering the value of T_c^{offset} parameter of the solidified $Bi_{2.1}Sr_{2.0}Ca_{1.1}Cu_{2.0}O_y$ superconducting solid ceramic specimens [22]. Correspondingly, the solidified $Bi_{2.1}Sr_{2.0}Ca_{1.1}Cu_{2.0}O_y$ compound presents the superconducting phenomenon at only smaller temperature values in comparison with the critical T_c^{offset} values. This is because the T_c^{offset} parameter is required to form cooper-pair coupling probabilities in the strongly covalently bonded Cu-O_2 layers, hole carrier concentrations per Cu ions in the Cu-O_2 layer $x^2 - y^2$ bands and bipolarons in the polarizable lattices [23]. One can see all the T_c^{onset} and T_c^{offset} temperature values belonging to the pure and aluminum oxide doped bulk $Bi_{2.1}Sr_{2.0}Ca_{1.1}Cu_{2.0}O_y$ superconducting ceramic samples in Table 1. As it has been clearly understood from the table that both T_c^{onset} and especially T_c^{offset} temperature values are measured to decrease regularly with increasing the aluminum oxide impurity additional level up to the maximum amount of x=0.10. Also, the changes in the onset/offset critical transition temperature values are inserted in Fig. 2. The decrement trend stems from the successful introduction of Al_2O_3 impurities in the $Bi_{2.1}Sr_{2.0}Ca_{1.1}Cu_{2.0}O_y$ superconducting ceramic matrix. The un-added bulk Bi-2212 superconducting arrangement obtains the global highest T_c^{offset} critical transition temperature value of 76.88 K and T_c^{onset} critical transition temperature value of 83.79 K. On the other hand, the bulk Bi/Al-5 superconductor has the smallest T_c^{offset} critical transition temperature value of 35.04 K and T_c^{onset} critical transition temperature value of 73.34 K, respectively. The other aluminum oxide doped bulk $Bi_{2.1}Sr_{2.0}Ca_{1.1}Cu_{2.0}O_y$ superconducting solid compounds show moderate T_c^{offset} and T_c^{onset} parameters.

Based on the offset and offset critical transition temperature values in Table 1, it is seen that the T_c^{offset} transition temperatures are noted to much more decrease seriously as matched against to the T_c^{onset} critical transition temperature values with the aluminum oxide impurity addition. In other words, the presence of the Al_2O_3 impurity materials in the bulk $Bi_{2.1}Sr_{2.0}Ca_{1.1}Cu_{2.0}O_y$ superconducting matrix damages significantly the formation of cooper-pair coupling probabilities in the strongly covalently bonded Cu-O_2 layers, hole carrier concentrations per Cu cations in the Cu-O_2 layer $x^2 - y^2$ bands and bipolarons in the polarizable lattices [24, 25]. At the same time, the crucial changes in both the T_c^{offset} and T_c^{onset} transition parameter values based on the aluminum oxide impurity addition amount result from the reduction of metallic connections depending on the increase of basic crystal structure problems including stress raisers, microscopic structural faults, internal omnipresent flaws/defects/distortions/porosity, weak-interaction difficulties between the superconducting grain, and grain frontier coupling complications in the Bi-2212 crystal system.

Table 1. Offset and offset critical transition temperatures and degree of broadening parameters for pure and aluminum oxide doped bulk $Bi_{2.1}Sr_{2.0}Ca_{1.1}Cu_{2.0}O_y$ superconducting ceramic compounds.

Samples	T_c^{offset} ***(K)***	T_c^{onset} ***(K)***	ΔT_c ***(K)***	P_{hole}
Pure	76.88	83.92	7.04	0.125992
Bi/Al-1	70.82	82.60	11.78	0.115059
Bi/Al-2	65.60	80.30	14.70	0.107434
Bi/Al-3	56.18	77.44	21.26	0.095931
Bi/Al-4	47.36	75.52	28.16	0.086781
Bi/Al-5	35.04	73.34	38.30	0.075645

Moreover, the difference between the fundamental offset and offset critical transition temperature values taken from the resistivity measurement results enables one to determine the effect of aluminum oxide contamination level on the degree of broadening width (ΔT_c) parameters in detail. It is well known that the ΔT_c parameter of a superconducting ceramic compound is related to the suitability of superconducting ceramic structures to potential application fields such as application-oriented material science, levitated trains, medical diagnosis, cooling technology, hydrogen societies, levitated trains, refrigeration, particle accelerators, transformers, and sensitive process control areas. One can see the variations of degree of broadening widths of bulk $Bi_{2.1}Sr_{2.0}Ca_{1.1}Cu_{2.0}O_y$ superconducting ceramic matrix with aluminum oxide impurity additional level in Table 1 clearly. It has been encountered that the increase in the aluminum oxide impurity addition amount leads to the considerable enhancement in the ΔT_c parameter values for the bulk $Bi_{2.1}Sr_{2.0}Ca_{1.1}Cu_{2.0}O_yAl_x$ superconducting ceramics. Numerically, the un-added $Bi_{2.1}Sr_{2.0}Ca_{1.1}Cu_{2.0}O_y$ compound is brought out to have the ΔT_c parameter of about 7.04 K whereas the other aluminum oxide added $Bi_{2.1}Sr_{2.0}Ca_{1.1}Cu_{2.0}O_y$ superconducting samples exhibit the ΔT_c values of 11.78 K, 14.70 K, 21.26 K, 28.16 K, and 38.30 K, respectively. In this regard, the largest ΔT_c value of 38.30 K is noted to ascribe to the Bi/Al-5 superconductor. The

decrement trend shows that the increase of aluminum oxide impurity addition amount triggers not only the degradation in the material quality but also the formation of the coexistence phases in the crystal natture. Thus, it is normally to approve that the penetration of aluminum oxide impurity is not ideal material to rise in the potential application fields of conventional Bi-2212 superconducting system.

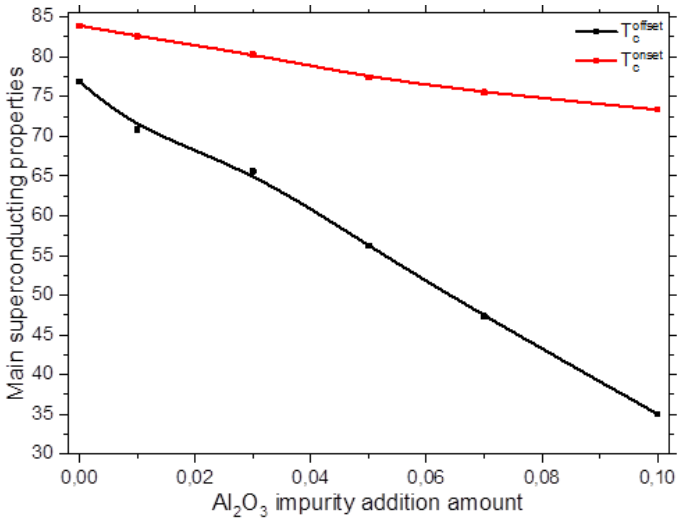

Fig. 2. Differentiation of T_c^{offset} and T_c^{onset} parameters belonging to $Bi_{2.1}Sr_{2.0}Ca_{1.1}Cu_{2.0}O_yAl_x$ materials with different Al addition concentration level

Furthermore, we define the change in the hole carrier concentration value abbreviated as P per Cu ions in the Cu-O_2 layer $x^2 - y^2$ bands of bulk $Bi_{2.1}Sr_{2.0}Ca_{1.1}Cu_{2.0}O_yAl_x$ superconducting ceramic structure with aluminum oxide impurity amount with the assistant of dc resistivity measurement results by using the following equation between the *P* and T_c^{offset} critical transition temperature parameter values [26]:

$$P = 0.16 - \left[\left(1 - \frac{T_c^{offset}}{T_c^{\max}}\right)/82.6\right]^{1/2} \quad (1)$$

in the equation, the $T_c^{\max}$ transition temperature parameter value for the bulk Bi-2212 ceramic structure phase is 85 K. We gather the experimental T_c^{offset} transition temperature parameter values from Table 1 so that we can easily find the variation of P values. One can observe numerical P parameters in Table 1. The differentiation of hole carrier concentration parameter values per Cu ions in the Cu-O_2 layer $x^2 - y^2$ bands of bulk $Bi_{2.1}Sr_{2.0}Ca_{1.1}Cu_{2.0}O_yAl_x$ superconducting ceramic structure with aluminum oxide impurity addition amount indicates that there is a reverse ratio between Al_2O_3 impurity addition amount and P parameter values. In more detail, as the aluminum oxide impurity addition amount increases in the bulk $Bi_{2.1}Sr_{2.0}Ca_{1.1}Cu_{2.0}O_yAl_x$ superconducting solid structure, the values of P parameters are obtained to enhance seriously due to the suppression of fundamental superconducting features. Accordingly, the un-added $Bi_{2.1}Sr_{2.0}Ca_{1.1}Cu_{2.0}O_y$ superconducting structure obtains the global largest P parameter value of about 0.125992. Furthermore, the bulk Bi/Al-5 superconducting ceramic material possesses the global lowest P parameter value of about 0.075645. The other bulk $Bi_{2.1}Sr_{2.0}Ca_{1.1}Cu_{2.0}O_yAl_x$ superconducting solid ceramic structures have moderate P values changing from 0.115059 (Bi/Al-1) to 0.086781 (for Bi/Al-4). All the experimental findings and semi-empirical outcomes clearly reveal that addition of aluminum oxide impurity in the bulk $Bi_{2.1}Sr_{2.0}Ca_{1.1}Cu_{2.0}O_yAl_x$ superconducting ceramic structure is not a good idea for the development of fundamental superconducting features.

IV. Conclusion

In this work, we examine the potency of aluminum oxide uncleanness addition on the fundamental superconducting features of bulk $Bi_{2.1}Sr_{2.0}Ca_{1.1}Cu_{2.0}O_yAl_x$ (when $0.0 \leq x \leq 0.10$) superconducting ceramic compounds by using the differentiation of dc electrical resistivity parameters as a function of the environmental temperatures between 20 K and 105 K. With the assistance of the experimental dc electrical resistivity survey results we determine the variation of the offset and offset critical transition temperatures and degree of broadening parameters and hole carrier concentration parameter values per Cu cations in the Cu-O_2 layer $x^2 - y^2$ bands of bulk $Bi_{2.1}Sr_{2.0}Ca_{1.1}Cu_{2.0}O_y$ superconducting ceramic structures with the Al_2O_3 impurity ratios The experimental discoveries and semi-empirical fallouts indicate that all the superconducting features are observed to degrade with increasing the Al_2O_3 impurity addition amount because of the reduction of the overlying of Cu-3d and O-2p wave functions, formation of super-electrons, cooper-pair coupling probabilities in the strongly covalently bonded Cu-O_2 layers, amplitude of pair wave function, homogeneities in the oxidation states, hole trap energy values in the superconducting paths, and the hole carrier concentrations per Cu cations in the Cu-O_2 layer $x^2 - y^2$ bands in the bulk Bi-2212 crystal nature system. Likewise, the analysis test results illustrate that the presence of the Al_2O_3 impurity triggers significantly the increase in the basic crystal nature problems; namely, the stress raisers, microscopic structural faults, internal omnipresent flaws/defects/distortions/porosity, weak-interaction hitches between the superconducting grain, and grain boundary coupling problems in the Bi-2212 crystal system. According to the investigational findings and semi-empirical results, it is obvious that the addition of aluminum oxide impurity in the bulk $Bi_{2.1}Sr_{2.0}Ca_{1.1}Cu_{2.0}O_yAl_x$ superconducting solid ceramics is not a good idea for the development of fundamental superconducting features enhancing the suitability to the potential application fields.

References

[1] H.K. Onnes, Further experiments with Liquid Helium. D. On the change of Electrical Resistance of Pure Metals at very low Temperatures, etc. V.

The Disappearance of the resistance of mercury, Koninklijke Nederlandsche Akademie van Wetenschappen Proceedings, 14 (1911) 113–115.
[2] G. Yildirim, Determination of optimum diffusion annealing temperature for Au surface-layered Bi-2212 ceramics and dependence of transition temperatures on disorders, J. Alloy. Compd. 699 (2017) 247–255.
[3] Keimer, B., Kivelson, S. A., Norman, M. R., Uchida, S., & Zaanen, J. (2015). From quantum matter to high-temperature superconductivity in copper oxides. Nature, 518(7538), 179-186.
[4] Saxena, A. K. (2012). High-temperature superconductors (Vol. 125). Springer Science & Business Media.
[5] P. Bordet, C. Chaillout, J. Chenavas, J.L. Hodeau, M. Marezio, J. Karpinski, E. Kaldis, Structure Determination of the New High-Temperature Superconductor $Y_2Ba_4Cu_7O_{14+X}$, Nature 336 (1988) 596–599.
[6] P. Marsh, R.M. Fleming, M.L. Mandich, A.M. Desantolo, J. Kwo, M. Hong, L.J. Martinez-Miranda, Crystal-Structure of the 80K Superconductor $YBa_2Cu_4O_8$, Nature 334 (1988) 141–143.
[7] Raveau, Bernard (2013). "Impact of Crystal Chemistry upon the Physics of Strongly Correlated Electrons in Oxides". Angewandte Chemie International Edition. 52 (1): 167–175.
[8] A.T. Ulgen, T. Turgay, C. Terzioglu, G. Yildirim, M. Oz, Role of Bi/Tm substitution in Bi-2212 system on crystal structure quality, pair wave function and polaronic states, J. Alloy. Compd. 764 (2018) 755–766.
[9] S.Y. Oh, H.R. Kim, Y.H. Jeong, O.B. Hyun, C.J. Kim, Joining of Bi-2212 high-T_c superconductors and metals using indium solders, Physica C 463–465 (2007) 464–467.
[10] Orhan, E., Kara, E., Kaya, Ş., Doğan, M. U., Terzioğlu, R., Yildirim, G., & Terzioğlu, C. (2022). Refinement of some basic features of Zr surface-layered Bi-2223 superconductor with diffusion annealing temperature. Journal of Materials Science: Materials in Electronics, 1-17.
[11] Fallah-Arani, H., Sedghi, A., Baghshahi, S., Moakhar, R. S., Riahi-Noori, N., & Nodoushan, N. J. (2022). Bi-2223 superconductor ceramics added with cubic-shaped TiO2 nanoparticles: Structural, microstructural, magnetic, and vortex pinning studies. Journal of Alloys and Compounds, 900, 163201.
[12] Wang, Y., & Zheng, Y. (2014). Review of research and measurement for application properties of HTS tapes. Science China Technological Sciences, 57(8), 1568-1577.
[13] Zalaoglu, Y., Terzioglu, C., Turgay, T., & Yildirim, G. (2018). Detailed survey on minimum activation energy for penetration of Ni nanoparticles into Bi-2223 crystal structure and temperature-dependent Ni diffusivity. Journal of Materials Science: Materials in Electronics, 29(4), 3239-3249.
[14] Slimani, Y., Almessiere, M. A., Hannachi, E., Baykal, A., Manikandan, A., Mumtaz, M., & Azzouz, F. B. (2019). Influence of WO3 nanowires on structural, morphological and flux pinning ability of YBa2Cu3Oy superconductor. Ceramics International, 45(2), 2621-2628.
[15] Y. Slimani, M.A. Almessiere, E. Hannachi, M. Mumtaz, A. Manikandan, A. Baykal, F. Ben Azzouz, Improvement of flux pinning ability by tungsten oxide nanoparticles added in YBa2Cu3Oy superconductor, Ceramics International, Volume 45, Issue 6, 2019, Pages 6828-6835,
[16] Ondřej Jankovský, Filip Antončík, Tomáš Hlásek, Vladimír Plecháček, David Sedmidubský, Štěpán Huber, Michal Lojka, Vilém Bartůněk, Synthesis and properties of YBa2Cu3O7-δ – Y2Ba4CuWO10.8 superconducting composites, Journal of the European Ceramic Society, Volume 38, Issue 6, 2018,.
[17] Ozturk, O., et al., Physical Properties and Diffusion-Coefficient Calculation of Iron Diffused Bi-2223 System. Journal of Superconductivity and Novel Magnetism, 2012. 25(7): p. 2481-2487
[18] H. Hilgenkamp, J. Mannhart, Grain boundaries in high T_c superconductors, J. Rev. Mod. Phys. 74 (2002) 485–549.
[19] C. Autret-Lambert, B. Pignon, M. Gervais, I. Monot-Laffez, A. Ruyter, L. Ammor, F. Gervais, J.M. Bassat, R. Decourt, Microstructural and transport properties in substituted $Bi_2Sr_2CaCu_2O_{8+delta}$ modulated compounds, J. Solid State Chem. 179 (2006) 1698–1706.
[20] S. Safran, H. Ozturk, F. Bulut, O. Ozturk, Experimental and theoretical approaches for electrical, magnetic, micromechanical, and structural characterization of BSCCO ceramic superconductors, Ceramics International, 44 (2018) 11674–11681.
[21] G. Burns, High-temperature Superconductivity: an Introduction, Academic Press, New York, (1991).
[22] R. Awad, A.I. Abou-Aly, M.M.H. Abdel Gawad, I. G-Eldeen, The influence of SnO_2 nano-particles addition on the vickers microhardness of (Bi, Pb)-2223 superconducting phase, J. Supercond. Nov. Magn. 25 (2012) 739–745.
[23] S.B. Guner, Y. Zalaoglu, T. Turgay, O. Ozyurt, A.T. Ulgen, M. Dogruer, G. Yildirim, A detailed research for determination of Bi/Ga partial substitution effect in Bi-2212 superconducting matrix on crucial characteristic features, J. Alloy. Compd. 772, (2019) 388–398.
[24] D. M. Rao, T. Somaiah, V. Haribabu, Y.C. Venudhar, Growth-kinetics of high-T_c and low-T_c phases in $Bi_{2-x}Pb_xCa_2Sr_2Cu_3O_y$ superconducting compounds, Cryst. Res. Technol. 28 (1993) 285–298.
[25] X.L. Lin, S.S. Ma, H.Y. Wang, H. Xu, Characteristics of hopping conductivity in one-dimensional binary disordered system with off-diagonal correlations, Acta Phys. Sin. 56 (2007) 2852–2857.
[26] M. Dogruer, G. Yildirim, E. Yucel, C. Terzioglu, Role of diffusion-annealing temperature on the microstructural and superconducting properties of Cu-doped MgB_2 superconductors, J. Mater. Sci: Mater. El. 23 (2012) 1965–1970.

Atomic Force Microscopy Study of Amorphous BiSbTe Thin-Film with the Various Deposition Pressure

Mehmet ÇETİN[1], Gizem DURAK YÜZÜAK[2], Ercüment YÜZÜAK[1,*]

[1] *Recep Tayyip Erdoğan University, Faculty of Engineering and Architecture, Rize, Turkey, mehmet_cetin21@erdogan.edu.tr, ercument.yuzuak@erdogan.edu.tr*
[2] *Munzur University, Rare Earth Elements Application and Research Center, Tunceli, Turkey, *ercüment.yuzuak@erdogan.edu.tr*

Abstract **- Designing and engineering superior features thin films with unique morphologies tailored to essential criteria for a number of particular applications has long been crucial. The implication from this is the surface microstructure of the materials is anticipated to be particularly significant for electron scattering in the electrical and thermal components and, consequently, for thermoelectric applications. The thermoelectric BiSbTe thin film is deposited on Si(100) substrates by the magnetron sputtering method with various deposition pressure circumstances to ensure the different atomic composition of thin films. X-ray diffraction XRD), scanning electron microscopy (SEM), and atomic force microscopy (AFM) measurements were used to characterize the film's structural properties in order to control its growth performance. Moreover, another specific goal of the study is to demonstrate the measurements made from amorphous crystals using AFM, which enables the calculation of the RMS roughness, the most common parameter used to characterize the morphology of surfaces.**

Keywords **– BiSbTe, AFM, Energy Harvesting, Thin Film, Amorphous**

I. INTRODUCTION

THERMOELECTRIC (TE) materials are currently the only devices that can generate power from waste heat, suggesting they may play a significant part in a global sustainable energy solution [1]. To keep up with the ever-growing demand for energy caused by innovations like the IoT (Internet of Things), scientists are exploring ways to harness the heat produced by our bodies at virtually every stage of the energy conversion process, from the heat generated by our footsteps to the heat produced by our fingertips when we touch a smartphone. As a result of its capacity to immediately transform thermal energy into electrical energy, the thermoelectric effect provides a novel, eco-friendly alternative for sustainable energy generation from waste heat sources. The way TE materials are made affects how well and efficiently TE effect devices work as a whole in terms of the power they produce.

The market's current mass production of TE materials has stymied their practical application, restricting the design, functionality, and form of cutting-edge TE gadgets. The use of nanotechnology to boost the performance of TE materials (300-500 K) whose Debye temperature is close to room temperature and thus approaching the efficiency threshold in bulk form has become increasingly relevant in recent years [2]. According to the fundamental sciences driving nanostructures, the evolution of thermoelectric materials has speed up as the structures themselves have shrunk from three to one dimension. Thanks to advancements in technology, today's TE materials can be nano-structured to have a thin film-like surface volume ratio while still being remarkably lightweight, efficient, and affordable. New generations of TE devices can be created since these materials are adaptable and small enough.

The designing and engineering of thin films with unique morphologies tailored to essential criteria for a number of particular applications has long been crucial. The implication from this is the surface microstructure of the materials is anticipated to be particularly significant for electron scattering in the electrical and thermal components and, consequently, for thermoelectric applications. Numerous surface effects found on textured structures in thin films were investigated using atomic force microscopy (AFM). Scanning electron microscopy (SEM), optical microscopy, and stylus profilometer methods of assessing surface morphology are contrasted, and it is clear that AFM is presented visually in a 3D manner that was not before available [3]. Also, AFM may be effectively utilized to obtain surface micro-roughness data with high vertical and spatial resolution [4].

II. EXPERIMENTAL

To determine the atomic composition of thin films, a conventional RF magnetron was used under various deposition pressure conditions. Argon gas (purity 6N) is employed, and three samples were developed at 5 mTorr, 10 mTorr, and 15 mTorr, and their characteristics were studied. Energy

dispersive X-ray (SEM-EDX) measurements are used to precisely define the stoichiometric ratio of the thin films, with an accuracy of greater than 0.5 at.%. X-ray Reflectometry (XRR) measurements are used to quantify and verify the film thickness of 100 nm. The study with regard to coverage of amorphous was maintained by selecting 50 W power, a 100 nm film thickness, a sample rotation of 10 rpm, and a 100 mm target-sample distance. When investing in an amorphous BiSbTe film, no heat treatment is applied. In order to characterize their structure and morphology, X-ray diffraction (XRD), scanning electron microscopy (SEM) with energy dispersive X-rays (EDX), and atomic force microscopy (AFM) were used in order to control their growth. Moreover, other specific goals of the study are to demonstrate the measurements made from amorphous crystals using AFM, which enables the calculation of the root mean square (RMS) roughness, the most common parameter used to characterize the morphology of surfaces.

III. Results and Discussion

Even as a sputtering target, the atomic concentration and working pressure of the Bi-Sb-Te alloy were realized. The surface stability at room temperature is closely related to the amorphous-to-electronic concentration ratio of the Bi-Sb-Te alloy target. The amorphous structures seen in the XRD patterns of Fig. 1a, b, and c are a result of this scenario. As a result of this higher operating pressure, the amorphous property has barely changed.

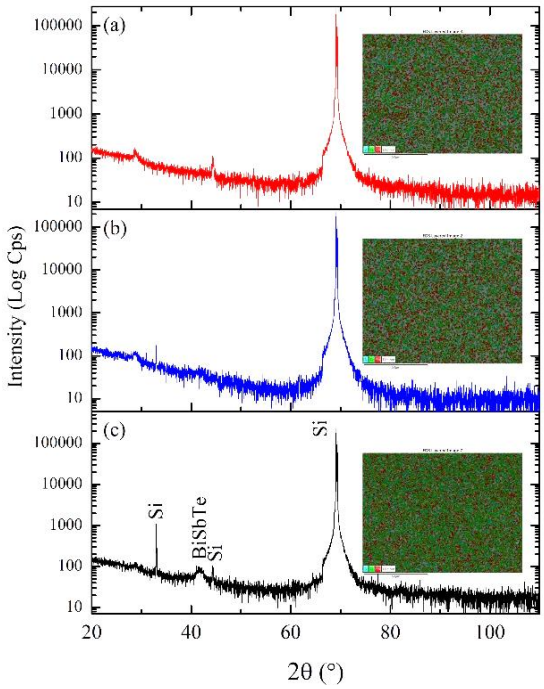

Figure 1: XRD patterns of thin films with the deposition pressure of 15 mTorr (a), 10mTorr (b), 5 mTorr (c)

Close inspection of the plots revealed that while only the BiSbTe crystal structure was visible in the 3mTorr sample. The rhombohedral crystals only presented a single, wide peak at $2\theta = 41°$, which is the location of the (110) Bragg reflection, and the BiSbTe(110) of the full width half maximum (I_{FWHM}) was relatively high. This further supports the idea that the particles are extremely tiny or amorphous. Particle sizes could not be deduced from XRD patterns using any approach due to the inaccuracy of the Bragg locations. The inset of Fig. 1a, b, and c also shows the images of elemental mapping captured by EDX in SEM. Regardless of the homogenous element distribution, the same image was obtained in all three samples. This finding indicates that the materials were manufactured without buildup or unintended consequences.

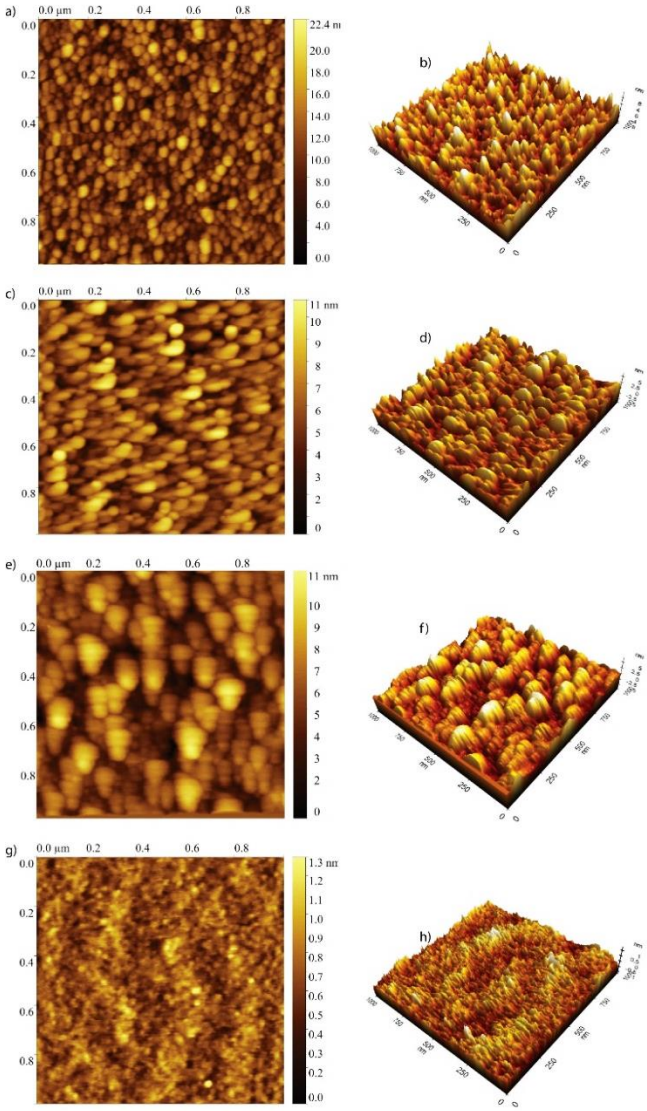

Figure 2: 2D and 3D AFM micrographs of the deposition pressure of 5 mTorr (a, b), 10mTorr (c, d), 15 mTorr (e, f) and substrate (g, h), respectively

Fig.2 reveals that AFM micrographs of the deposition

pressure of 5 mTorr (a, b), 10 mTorr (c, d), 15 mTorr (e, f) and substrate in 2D and 3D views. For comparison purposes before proceeding to the measurement evaluation, 2D and 3D AFM micrographs of the Si(100) single crystal used as substrate in 2.g and h are given. Basically, a very smooth surface was found and the average surface roughness value was concentrated at 0.5 nm. Whole measurements were performed for a 1 µm x 1 µm area. Both 2D and 3D AFM pictures of BiSbTe showed that the film morphology is drastically altered by increasing the deposition pressure. Images acquired at 10 mTorr and 15 mTorr indicate increased agglomeration, despite the fact that 3 mTorr contains spherical, non-agglomerated crystallites (spherical blocks) of identical size. The radical shift in composition may account for the observed morphological changes in thin films. Because of this, EDX tests reveal the following shifts in atomic percentages within the samples [5]. One such explanation could be that increased pressure causes the surface adhesion to weaken. Our findings indicated a strong correlation between Bi deficiency and grain enlargement.

Fig. 3. a, c, and e reveal the particle size distribution of thin films with a deposition pressure of 5 mTorr, 10 mTorr, and 15 mTorr, respectively. The data reveals that particle sizes grow with higher working pressure without affecting the interpretation of those results. This agrees with what has been found in another research [6].

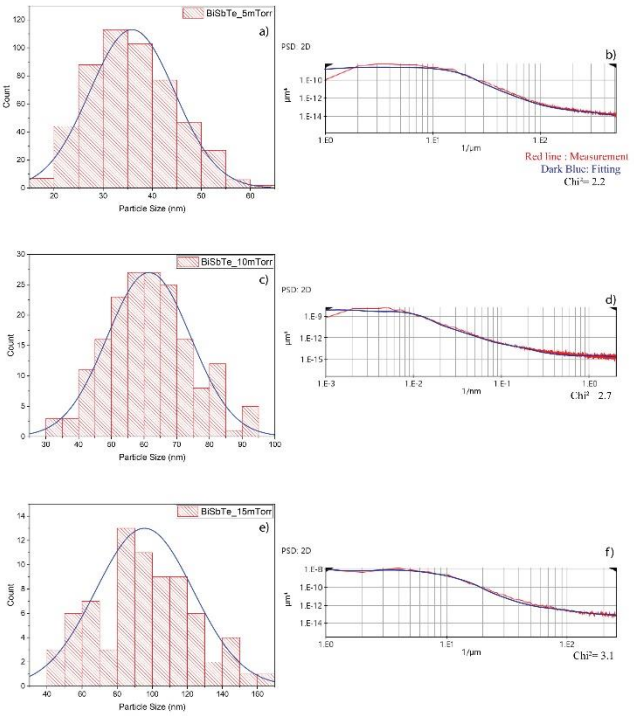

Figure 3: Particle size of thin films with the deposition pressure of 5 mTorr (a), 10mTorr (c), 15 mTorr (e) and PSD value of 5 mTorr (b), 10mTorr (d), 15 mTorr (f)

The so-called ABC of k-correlation model was used to provide a concise description of the thin film and substrate morphology, and it was found to be applicable to a wide variety of sample morphologies and to permit comparison study between samples [6]. This ABC model is equal;

$$S(f) = \frac{A}{[1+(B.f)^2]^{\frac{C}{2}}} \quad [1]$$

parameters (A, B, and C) of the model being examined [7]. The value of the spectrum in the low-frequency limit is denoted by A, the correlation length between the low- and high-frequency regimes is denoted by B, and the exponent of the power-law decline of frequency at high frequencies is denoted by C [7]. After fitting Eq.1 (the reliability parameters are given in Fig.3) to the present PSD values, Table I is created. According to Eq. 1, A, B and C are correlated with surface roughness, grain size, and power exponent, respectively. The numbers determined here with PSD are in agreement with the data on particle sizes and surface roughness acquired from the AFM results. This supports the interpretation of the mathematically predicted outcomes as literary knowledge.

Table I. A, B, and C values of thin films with different working pressure

	5mTorr	10mTorr	15mTorr
A	7450	5500	4100
B	72	145	187
C	4.2	4.7	4.9

IV. CONCLUSION

To summarize, the growth of Bi-Sb-Te thin films on Si(100) substrates with various deposition Ar^+ pressures was successfully achieved to deposit by using RF magnetron sputtering. It was found that all thin films evaluated had amorphous characteristics. Working pressure increases in AFM results led to bigger particles, which in turn led to the formation of surface-affecting zones. After making PSD plots to get a general idea of how rough the surface of a material is when it is made, it was found that the PSD data changed directly as the working pressure went up.

ACKNOWLEDGMENT

This work was supported by the Scientific and Technological Research Council of Turkey (TUBITAK) with project number 221M470.

REFERENCES

[1] D. Zhang, Yuanhao Wang, Ya Yang, Small 15(32) (2019), 1805241.
[2] X.L. Shi, J. Zou, and Z.-G. Chen, Chem. Rev. 120, 15, (2020) 7399-7515
[3] R. W. Phillips, Surface and Coatings Technology, 68-69, (1994) 770-775.

[4] G. Binnig, C.F. Quate, C. Gerber, Phys. Rev. Lett. 56 (1986) 930.
[5] F. Golgovici, A. Cojocaru, L. Anicai, T. Visan, Materials Chemistry and Physics, 126 (2011) 700-706.
[6] E.L. Church and R Z. Takacs, "7. Surface Scattering", In Handbook of Optics (2nd ed). Vol. I. "Fundamentals, Techniques and Design". McGraw Hill, New York, 1995.
[7] R. Gavrila, A. Dinescu and D. Mardare, International Semiconductor Conference, 2006, 167-170.

FABRICATION AND CHARACTERIZATION OF ANODIC FILMS ON 304 STAINLESS STEEL

N. AĞIRLAR[1], N. C. BAĞCI[1], E. ARKALI[1], C. SARIOĞLU[1] and G. YUMUŞAK[1]

[1] Marmara University, İstanbul/Turkey, agirlarnihan@gmail.com
[1]Marmara University, İstanbul/Turkey, nhtcnbgc@gmail.com
[1]Marmara University, İstanbul/Turkey, ecearkali@outlook.com
[1]Marmara University, İstanbul/Turkey, cevat.sarioglu@marmara.edu.tr
[1]Marmara University, İstanbul/Turkey, gorkem.yumusak@marmara.edu.tr

***Abstract* - On the 304 stainless steel, the anodization technique produces a layer (with a porous structure) formed by various oxide phases. Direct current anodization on 304 stainless steel creates anodic films. At different temperatures, ethylene glycol solution with different NH_4F and H_2O compositions is used as an electrolyte. The formed films can also be yellow, green, or grayish depending on the electrolyte composition. The calcination was carried out in a tube furnace at 500 °C for 2 hours. Current time graphs were investigated. The oxide layer created as a result of ion movement resulted in the formation of a porous structure. In accordance with the XRD and morphology observations, the Fe2O3 and FeCrO3 phases were more intensely identified in the anodic film at lower temperatures. Compared to the structure with no Fe_2O_3 and $FeCrO_3$ phases, more crack formation was observed in the structure formed at low temperatures. Anodic layers are also characterized electrochemically to get information about the corrosion characteristics of anodized 304-type stainless steel. Anodized samples show less corrosion resistance than non-anodized samples.**

***Keywords* - Anodization, stainless steel, glycerol, NH_4F**

I. INTRODUCTION

During the anodizing process, an electric current passes through the electrolyte. Thus, the surface of a metal is transformed into a form of its oxide. This oxide layer provides the material with decorative, safeguarding, and other preferable properties.

In this study, an anodization process was applied by using organic solutions containing NH_4F and H_2O. An evaluation of anodization was made on the 304-type stainless steel by changing the parameters such as temperature and quantity of NH_4F and H_2O. After the anodization, a heat treatment process was applied to the samples by using a tube furnace at 500 °C for 2 hours. An optical microscope and an X-ray diffractometer were used to examine the anodized products.

The anodization process also aims to change the corrosion properties of the materials. The Tafel Exploration Method was used to determine the corrosion behavior of the material. In the experiments, after the anodization and heat treatment were completed, the Tafel curve was formed from the corrosion potential and current identified. By looking at corrosion potential and current values, it can be understood that the corrosion resistance of the substrate is higher than the anodized samples. From the experiments, it can be realized that when anodizing time and temperature are increased to their optimum values, the thickness of anodic films also increases. This gives the material better anodic films, which can be better for longer use.

II. EXPERIMENTAL SECTION

A. Chemical and Materials

304 stainless steel was used. Specimens were cut to a size of 10 x 10 mm^2. Ethylene glycol, NH_4F, and distilled water were used for the anodization solution. Specimens were rinsed ultrasonically in ethanol for 15 min.

B. Anodization

The anodization process was applied to the ethylene glycol solutions, which contained different molarities of water and NH_4F (see Table 1). A total of 25 cm^3 of ethylene glycol was used for anodization. Solutions were stirred with a magnetic stirrer. After samples were prepared in the metallography laboratory, they were cleaned with an ultrasonic cleaner, and then they were masked with a special (corrosion-resistant) mask. Anodization was applied to a 1 cm^2 area of the samples. A type 304 stainless steel was used as an anode, and a graphite electrode was used as a cathode. The distance between the anode and cathode was kept at 3 cm. All anodization was applied at the same potential difference, which is 50 V. Anodization was applied at different temperatures, such as 10, 25, and 50 °C. An ice bath system was also prepared for the experiment, which was conducted at 10 °C. Anodization times are the same for all the samples, which is 1 hour.

Table 1: Experimental sets for all samples.

	Molarity of H_2O	Molarity of NH_4F	Temperature (°C)
Sample 1	0.25	0.1	25
Sample 2	0.25	0.1	50
Sample 3	0.1	0.1	25
Sample 4	0.1	0.1	50
Sample 5	0.1	0.25	25
Sample 6	0.1	0.25	50
Sample 7	0.1	0.1	10

After anodization was completed, anodized samples were cleaned with an ultrasonic cleaner for 15 minutes in ethanol. Finally, all samples were calcined in the tube furnace at 500 °C. The thermal treatment may be an option for improving the electrochemical response of oxide layers since it allows for the formation of more stable oxides and the removal of fluoride from anodic layers, as they have documented for titanium, iron, and their alloys [1]. At the end of the anodization experiments, different compositions led to different color changes.

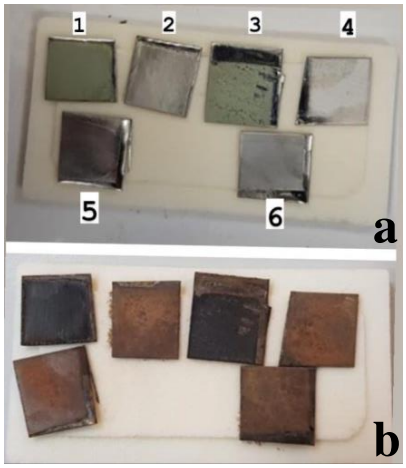

Figure 1: Samples before (a) and after (b) heat treatment.

C. Corrosion Behavior

A 0.6 M NaCl electrolyte was prepared to determine the corrosion behavior of anodized type 304 stainless steel. The corrosion behaviors were evaluated using potentiodynamic polarization. The scan rate was adjusted to 5 mV/s. To stabilize open circuit potential (OCP), samples remained in the solution for 30 minutes. After reaching the OCP, the Tafel experiment was started for samples 1, 3, and 5, and substrate [2-3].

D. Characterization

An automatic X-ray diffractometer (Bruker AXS, D2 Phaser) was used to investigate the phase composition of anodized and heat-treated samples in the 2θ range of 20°–80°. An optical microscope (Nikon EPIPHOT 300) and a scanning electron microscope (JEOL JSM-591OLV) were used to examine the samples.

III. RESULTS AND DISCUSSION

A. Current – Time Responses

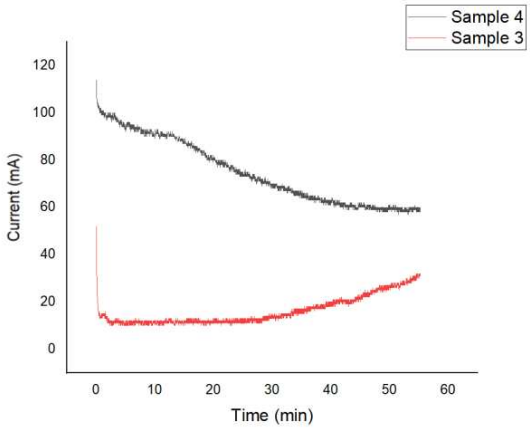

Figure 2: Current - Time plot for samples 3 and 4.

The current–time graph for samples 3 and 4 can be seen in Figure 2. By looking at this graph, it can be understood that temperature affects current. When initial potential jumps were compared, sample 3 indicates a higher potential jump than sample 4. This can be explained by increasing the bath temperature. When the bath temperature is increased, the current density decreases and is on the verge of disappearing, as shown in the results [4]. The quantity of ions diffusing to the anode is greatly reduced by the compact metal-oxide layer. As a result, the anodic current drops dramatically. Following that, the current progressively rose until it reached a stable amount [5].

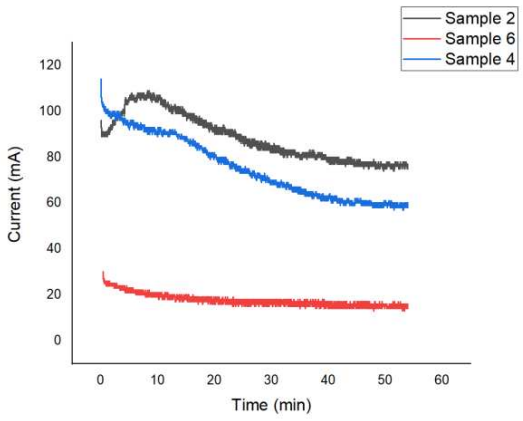

Figure 3: Current–time graphs for samples 2, 4, and 6.

Figure 3 shows the current–time graph for samples 2, 4, and 6. It can be observed that the effects of different compositions of H_2O and NH_4F on current can be different. When different amounts of H_2O and NH_4F are used in anodization reactions, the compounds that can be formed on the anodic layers can be different from each other [5]. Sample 4 contains 0.1 M H_2O and 0.1 M NH_4F. When sample 2 is examined, it can be observed that the current is increased initially, then decreased gradually up to a steady state because the molarity of H_2O increased to 0.25. When sample 6 is examined, the current is much lower than the others depending on the molarity of NH_4F, which is Figure 3 shows the current–time graph for samples 2, 4, and 6. It can be observed that the effects of different compositions of H_2O and NH_4F on current can be different. When different amounts of H_2O and NH_4F are used in anodization reactions, the compounds that can be formed on the anodic layers can be different from each other [5]. Sample 4 contains 0.1 M H_2O and 0.1 M NH_4F. When sample 2 is examined, it can be observed that the current is increased initially, then decreased gradually up to a steady state because the molarity of H_2O increased to 0.25. When sample 6 is examined, the current is much lower than the others depending on the molarity of NH_4F, which is 0.25.

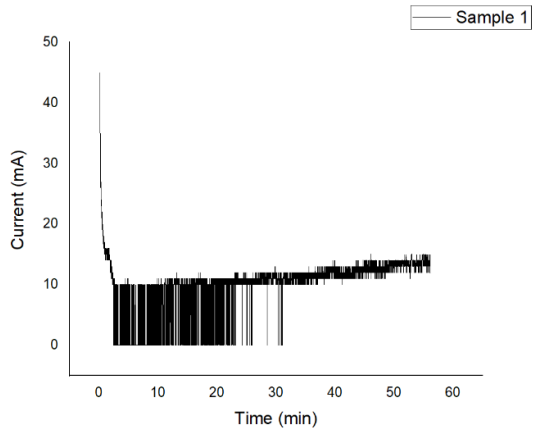

Figure 4: Current-time plot for sample 1.

The power supply cannot measure all the data properly because the power supply has low sensitivity, between 0 and 10 mA. As a result of this, some current data is measured as 0 mA (for Sample 1), as shown in Figure 4. In sample 5, most of the current data was measured between 0 and 10 continuously depending on the NH_4F content. For this reason, the current-time graph for sample 5 could not be created.

The current time graphs of the anodization samples can be explained in three stages. In the first stage, when the anodization process starts, the current decreases rapidly. This is due to the formation of oxide layers. Ions must pass through this layer to maintain the existence of the oxide layer. At this time, porosity is induced by the fluorine ion present. In the second stage, the current increases to the maximum level with the increase of the pores because the resistance of the anodic films decreases due to the increase in the movement of the ions. In the third stage, when the oxide layer reaches a constant value, the current also reaches a constant value [6].

B. Surface Morphology

Figure 5 shows the surface morphologies of anodized 304 stainless steels in different experiment sets. From Figure 5, the morphologies of samples 1 and 3 are similar. Cracks can be observed more clearly in these samples. This is explained by the fact that their anodization temperatures are the same (25 °C). Although sample 5's anodization temperature is 25 °C, its morphology differs from that of samples 1 and 3. This difference is a result of the quantity of NH_4F in sample 5, which is higher than the others. because its high NH_4F content may increase its acidic properties This may lead to etching occurring faster [4].

The surface morphologies of samples 2, 4, and 6 are highly similar. This similarity is a result of the anodization temperatures of these three samples being the same (50 °C).

In the anodization process, the colors of anodic films may be indicated by a difference. Anodic films can be observed as more intense, reddish, greenish, and, finally, grayish with increasing anodization time or voltage. However, since all the anodization times and voltage values of all samples are the same in this experiment, color differences are examined in terms of the amount of chemicals used in the anodization solution and temperature. When the amount of H_2O in the solution was 0.1 M or 0.25 M, yellow anodic films were observed, and the color of the solution after anodization also turned yellowish. However, when the quantity of NH_4F was increased to 0.25 M, anodic films were observed as greyish, and the color of the anodization solution turned greenish. This greenish color may occur as the fluoride ions that come from NH_4F and oxides of Ni and Cr that come from the substrate [4].

In addition to this, to observe the effect of a higher anodization voltage value, 75 V was applied to sample 3, whose solution contained 0.1 M H_2O and 0.1 M NH_4F, but after approximately 20 minutes, the surface of the steel started to burn out and deform. This can be explained by high voltage, and anodic film breakdowns may be observed. At high temperatures and constant voltages, NH_4F and 0.1 M H_2O solutions can form anodic films in the range of 30-60 V [4].

When anodic films are placed in water, the films can be dissolved partially. To prevent this, after anodization process, the films were cleaned with ethanol instead of water. However, this was not enough to protect the samples from cracks formation which can be seen in Figure 5.

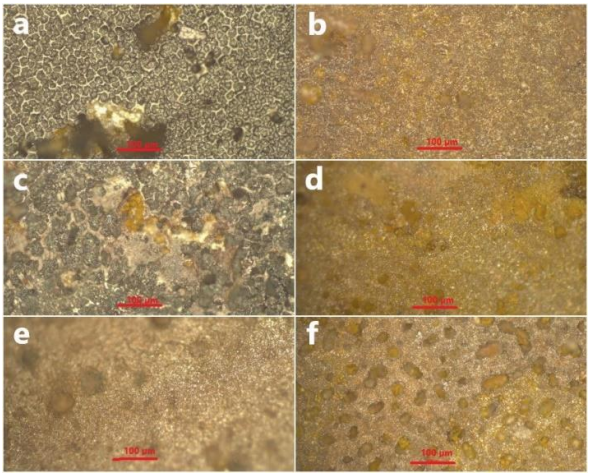

Figure 5: Optical microscope view (20x) of anodized samples after calcination: Sample 1 (a), Sample 2 (b), Sample 3 (c), Sample 4 (d), Sample 5 (e) and Sample 6 (f).

Figure 6 shows the SEM images of samples 3 and 4 after heat treatment. The crack formation was observed for sample 3. Depending on the temperature difference, crack formation was not observed for sample 4. As a result of this, it can be said that when temperature increases, the probability of crack formation decreases.

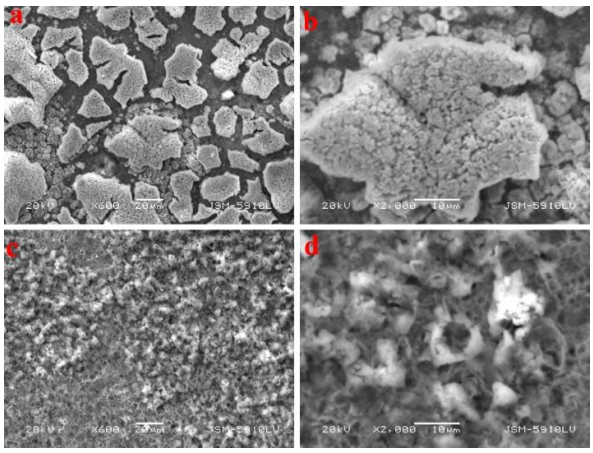

Figure 6: SEM images of samples. Sample 3 600x (a), sample 3 2000x (b), sample 4 600x (c) and sample 4 2000x (d).

A cross-section was obtained by precision cutting to estimate the anodic layer thickness of sample 3. A thick anodic coating with an average thickness of 8.23 µm was generated after long-time anodization at 50 V for 1 h. [5] Anodic layer thickness, shown in Figure 7, for sample 3, was determined to be around 4 µm when different places of the layer were examined.

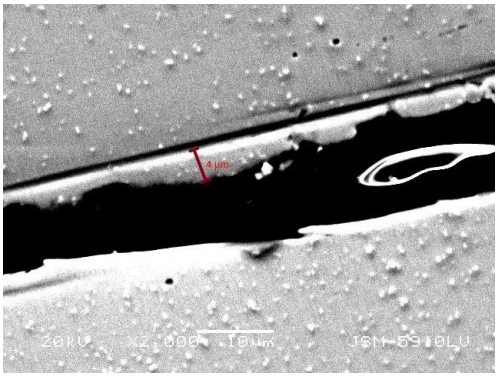

Figure 7: SEM image (2000x) of the cross-section of sample 3.

C. XRD Examinations

First, anodic films created with existing NH_4F and H_2O at room temperatures can be seen in Figure 8. Peaks are observed at 2θ = 21.15°, 30.08°, and 37.07°, which signify magnetite (Fe_3O_4) by looking at the XRD pattern. In addition, peaks are indicated as hematite (Fe_2O_3) can be seen at 2θ = 24.15°, 33.16°, 40.87°, and 54.07°. The substrate is attached at the 2θ = 43.58°, 50.79°, and 74.69°.

With the difference of the others, at 2θ = 24.36°, iron trifluoride (FeF_3) is observed for sample 1, which includes 0.25 M H_2O and 0.1 M NH_4F. This difference can be derived from the remaining fluoride ions in the electrolyte. It may compound with iron after the anodization reaction, although it is generally volatile since it is an organic compound. On the other hand, the chromium iron oxide ($CrFeO_3$) compound is observed at 2 = 63.02° and 64.57°.

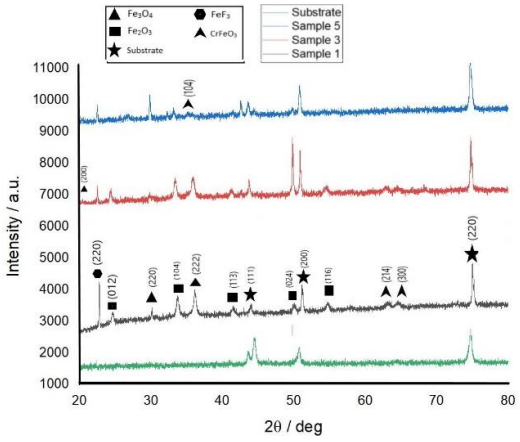

Figure 8: XRD Patterns of anodic films fabricated by type-304 stainless steel for samples 1, 3, and 5.

In Figure 9, XRD patterns for samples 2, 4, and 6 are shown. Anodization occurred at 50°C for these samples. Peaks are observed at 2θ = 21.15°, 30.08° for magnetite; 40.87°, 49.47° for hematite. Substrate peaks are specified at 2θ = 43.58°, 50.79°, and 74.69°. Iron trifluoride is

observed for sample 2 at 2θ = 24.36° and for sample 4 at 2θ = 34.72°.

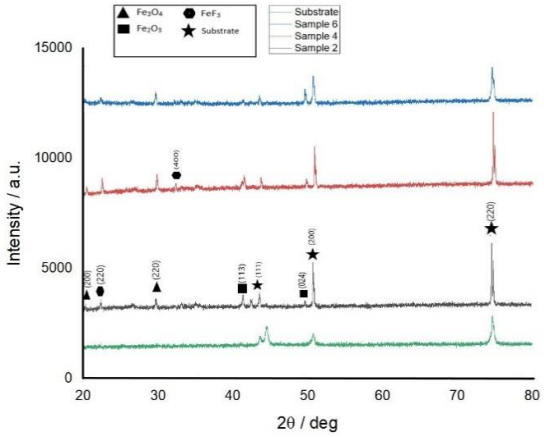

Figure 9: XRD Patterns of anodic films fabricated by type-304 stainless steel for samples 2, 4, and 6.

With respect to Figure 10, the effect of temperature on the anodization process can be seen. The molarities of H_2O and NH_4F are the same, which is 0.1 M for all samples. However, they have different temperatures. Sample 3 was done at room temperature, Sample 4 was done at 50°C, and Sample 7 was done at 10°C.

According to the XRD patterns, at elevated temperatures, many fewer peaks are observed compared to room temperature. Also, it can be said that at low temperatures, almost no peak is observed different from the substrate. There may be two reasons for this situation; since the reaction has occurred at a low temperature, no anodic film has occurred; or anodic film has occurred but since it is very thin, it could not be observed on the X-ray diffractometer that is used in the experiment. Since this is the case, lowering the temperature is not a good way to make anodic films on 304-type stainless steel.

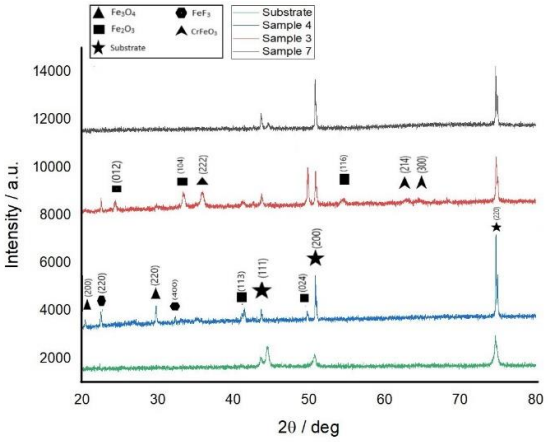

Figure 10: XRD Patterns of anodic films fabricated by type-304 stainless steel for samples 3, 4, and 7.

D. Corrosion Behavior

To determine the corrosion properties of samples after Tafel experiments were done, *E we/v vs. log(|<I>| / mA)* graphs were drawn for samples 1, 3, 5, and substrate as shown in Figure 11. Then, to calculate the corrosion values, which are E_{corr} and i_{corr}, slopes were added to graphs by the Tafel fit properties of the EC Lab program.

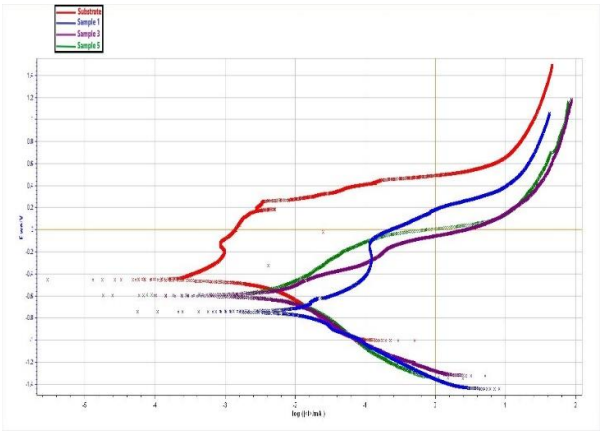

Figure 11: Potentiodynamic polarization curves of anodized samples (1, 3, 5) after calcination and substrate.

When the E_{corr} values of samples were compared, the substrate had the highest E_{corr} value, followed by samples 5, 3, and 1, respectively. As a result of this arrangement, it can be said that when E_{corr} values increase, the corrosion resistance of samples also increases. Layers formed by anodization indicated less passive and similar behaviors. From the values, the substrate has higher corrosion resistance than the anodized samples. This can be explained by the fluoride compounds on the anodized sample's layers, since fluoride leads to a decrease in corrosion resistance [1].

Since in this article, there was no heat treatment after anodization, the corrosion resistance of anodized samples was much lower than the substrate [1]. When heat treatment was applied, samples 1, 3, and 5 again had lower corrosion than the substrate. However, when results were compared to the samples that were not heat treated, better corrosion resistance properties were obtained, because heat treatment provides volatile fluoride, which is an organic compound.

IV. CONCLUSION

Considering the morphological structure of the anodized samples, different color changes were observed. The main reason for these changes is the different phases that occur depending on the temperatures. Since the Fe_2O_3 and $FeCrO_3$ phases are more intense with lower temperatures, more crack formation has been observed. The oxide layer that was created as a result of ion mobility led to the development of a porous structure. In addition to these, the

anodization process can be done in different environments. During the experiment, it can be done in an inert environment to avoid any undesirable reactions while the reactions are taking place. For instance, experiments can be done in a tube furnace by using argon gas.

REFERENCES

[1] L. P. Dominguez-Jaimes, M. A. A. Vara, E. I. Cedillo Gonzalez, J. J. R. Valdes, J. J. De Damorenea, A. c. D. Campo, F. J. Rodriguez-Varela, I. L. Alonso-lemus and J. M. Hernanez-Lopez, "Corrosion Resistance of Anodic Layers Grown on 304L Stainless Steel at Different Anodizing Times and Stirring Speeds," Coatings, 9 *(11)*, p. 706, 2019.

[2] D. A. Jones, "Principles and Prevention of Corrosion, Second Edition," 1996.

[3] P. Khadke, T. Tichter, T. Boettcher, F. Muench, W. Ensinger, and C. Roth, "A simple and effective method for the accurate extraction of kinetic parameters using differential Tafel plots," Sci Rep, 11 *(1)*, p. 8974, 2021.

[4] V. Klimas, V. Pakštas, I. Vrublevsky, K. Chernyakova, and A. Jagminas, "Fabrication and characterization of anodic films onto the type-304 stainless steel in glycerol electrolyte," Journal of Physical Chemistry C, 117 *(40)*, pp. 20730–20737, 2013

[5] Y. Wang, G. Li, K. Wang, and X. Chen, "Fabrication and formation mechanisms of ultra-thick porous anodic oxides film with controllable morphology on type-304 stainless steel," Applied Surface Science, 505, 144497, 2020.

[6] Y. Zhang, H. Fan, X. Ding, Q. Yan, L. Wang, and W. Ma, "Simulation of anodizing current-time curves and morphology evolution of TiO_2 nanotubes anodized in electrolytes with different NH_4F concentrations," Electrochimica Acta, 176, pp. 1083–1091, 2015.

Sound Problem of Ship Engines and Its Effect on Seafarers

O.BÜYÜKACAR [1] G.A.KILIÇ[1] S KAYA[2]

[1] Yalova University, Yalova/Turkey, okan.buyukacar@yalova.edu.tr
[1]Yalova University, Yalova/Turkey, gulenay.kilic@yalova.edu.tr
[2] Balikesir University, Balikesir/Turkey, skaya@balikesir.edu.tr

***Abstract*- The capacity of fishing, passenger, yacht and recreational vessels, especially dry cargo ships and tankers, is increasing day by day due to the geographical location of our country. Therefore, it is necessary to optimize the acoustics and vibration, which are dominant in the occupational health of seafarers, whose number reaches almost 2 million all around the world today . The most accurate method to be taken for the improvement of mechanical systems that cause noise, vibration and reverberation is to eliminate the problem at the source as much as possible. For this purpose, since the machine designs cannot be interfered with, it should be solved at the source of the vibro-acoustic with the use of sound absorbing materials in the machine spaces before it spreads to the space. In this study, the negative and positive effects of the materials used so far for the solution proposals for the sound and vibration problem are compared and the optimum solution proposals are listed. The nickel foam panel layer thickness is 5mm and the sound absorption coefficient in the frequency range of 1000–2000 Hz reaches approximately 0.4. The average sound absorption coefficient of the copper foam panel is 12.6% at the same thickness [1]. Therefore, sound absorption performance in the audible low frequency range for a nickel foam panel requires an appropriate structural design [2]. In addition, the occupational health and safety of seafarers were evaluated. The effect of exposure to noise and vibration, which consists of work routines on ships, high risk frequency and high-intensity operations, on work stress has been analyzed. The data were collected through a questionnaire and analyzed statistically through multiple and simple regression analyses.**

***Keywords* – seafarer, vibration, sound, acoustic, reverberation**

I. INTRODUCTION

Shipping by sea covers 85% of what is transported in the world. At the beginning of 2021, the global commercial shipping fleet reached a capacity of 2,134,639,907 dwt. It was estimated that approximately 1.9 million seafarers are actively working in early 2021 due to this increase in the number of ships. This expansion in the supply of seafarers also causes issues related to the health of seafarers to come to discuss [1].

Diseases such as alcohol, tobacco and drug use, blood pressure, various types of cancer, cholesterol, depression, diabetes, influenza and pneumonia, nutritional disorders, work-related musculoskeletal disorders and ergonomics are considered the most common occupational diseases among seafarers. It is suggested that the probability of contracting occupational diseases may be higher than the general population [2]. In some studies, it has been revealed that noise is perceived as harmful among marine workers as well. [3-4].

In the guide of Maritime Labor Convention 2006, the ILO has evaluated noise and vibration under the title of risks on ships. Accordingly, noise is defined as all sounds that can cause hearing impairment or be harmful to health or otherwise dangerous, while vibration is expressed as oscillatory movements transmitted from the movement of the ship or through vibrating machines, which can affect the whole body through the hands and arms. In the same guide, the effects of noise on human health such as increased adrenaline, poor sleep quality, rapid heartbeat, constriction of blood vessels, hearing loss, tinnitus, physical and mental discomfort, stress, heart disease and cognitive effects are mentioned. Furthermore, vibration-related effects include motion sickness, body instability, fatigue, vascular, neurological and/or musculoskeletal injury, poor circulation and circulatory pain, tingling, numbness or dexterity, carpal tunnel syndrome, whole body vibration: low back pain, sciatica pain or degenerative changes in the spine [5].

Reducing the negative impact of continuous noise on ships on human health, International Maritime Organization (IMO) accepted regulations in accordance with the "Code of Noise Levels on board Ships" in the "International Convention for the Safety of Life at Sea" in 2012,This code sets requirements to be built on ships in order to reduce the noise levels of ships and to protect seafarers from noise. This code determines maximum noise level limits for machinery spaces, control rooms, workshops, accommodation on ships. However, the development of materials that will help minimize structural material-induced vibro-acoustics and reverberation at the source may be very important to change the current situation.

Hommel et al. (2020) stated that there is a need for sandwich panel design support with the help of the practitioners and manufacturers of aluminum foam material in their work. In addition, with an overview of reference applications and processing possibilities, as well as bonding techniques, the use of aluminum foam can minimize barriers and increase its use [6]. Qingxian et al. (2015), aluminum foam materials; They mentioned that it has low density, efficient energy dissipation capacity, strength, stiffness, acoustic and sound damping, heat insulation, good energy dissipation capacity under impacts. In their work, the development of the method of preparation of aluminum foam

panels was reviewed and the benefits and shortcomings of the different processes were discussed. The manufacturers of these machines, which develop advanced technology around the world, are in search of solutions to reduce costs. In some studies, it is seen that the use of machines with low noise dose also contributes positively to fuel consumption. In an application made in 2017, the effects of variable speed generators on fuel consumption were compared to improve the power-propulsion system on ships. As a result of the study, it is mentioned that the reduction of the noise level by 5 dB(A) reduces the average fuel consumption by 30%.

II. MATERIAL and METHOD

Sound power level can be defined as the power of sound energy emitted by a sound source. The level of this power is called the sound power level L_w. Here, the sound power level L_w of a source with a sound power W is represented by equation 1.

$$L_w = 10log\frac{W}{10^{-12}} \quad (1)$$

The sound power of a machine is the sound radiated portion of the total power of that machine and is usually a very small fraction of the total power. The sound power of a source with a known sound power level is obtained using equation 2. The sound pressure level L_p is calculated by equation 3. In Equation 3, p0 is 20 micropascals (20 x 10^{-6} Pa or N/m^2), which is accepted as the international reference pressure, and p is the rms value of the sound pressure.

$$W = 10^{-12}x10^{(L_w/10)} \quad (2)$$

$$L_p = 10log\frac{p^2}{{p_0}^2} \quad (3)$$

Since sound intensity and sound intensity level are a sound characteristic that changes depending on the acoustic and geometric properties of the environment where the source is located and the distance from the source, if the sound waves coming out of a sound source with W sound power pass through the A field, the power in the unit area is the values that give the sound intensity. It is calculated by equation 4. The sound intensity for a spherical field is shown in Figure 3.

$$I = \frac{W}{A} \quad (4)$$

Stationary noise is known as fluctuating noise since it is not a pulsed noise and the equivalent continuous sound level is calculated by equation 5, where L_{eq} is a conceptual average sound level over a period T equal to the A-weighted sound energy at that time. The magnitude determined by the frequency of the sound and the sound pressure it creates is called loudness. According to the test results, the changes in sound pressure levels with frequency are evaluated according to Figure 2.

$$L_{eq} = 10log\left[\frac{1}{T}\int_0^T\left\{\frac{P_1(t)^2}{{P_0}^2}\right\}dt\right] \quad (5)$$

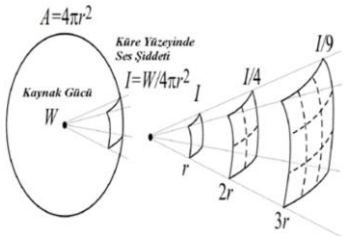

Figure 1. Sound intensity diagram for a spherical field.

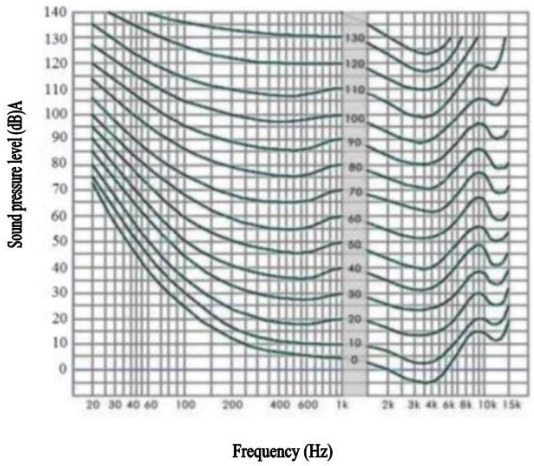

Figure 2. Contour distribution of sound pressure levels with frequency.

III. RESULTS and DISCUSSIONS

Noise and vibration occur from the movement of the ship or from the main and auxiliary machinery on the ship. A survey was conducted on how this situation was perceived by the seafarers. The survey participants were made with 146 participants working on the ships that came to the shipyard's region of Yalova province for docking and periodic maintenance. Survey responses were monitored using descriptive statistics and Likert scale valuation. Consistency in responses was tested with indirect indicators using linear regression and correlation testing.

More than 80% of the participants see ships as areas where they are exposed to noise and vibration. 40% of the participants stated that they had complaints related to noise and 50% due to vibration.

Equivalent continuous sound level is not sufficient in the evaluation of sounds that last very short and decrease after ascension. Therefore, when comparing various short-term noises, the sound exposure level is considered in the calculations. If L_{eq} is measured in such a case, there are different values depending on the time interval taken. In this study, the most appropriate method to determine the levels of such sounds is the sound exposure level (*SEL*). *SEL* is the sound level of a 1 second constant level sound with the energy of a sound that shows a significant level change in a short time and is measured in dBA. The relation in equation 6 is used

between the SEL value and the Leq value of the sound caused by an event lasting *T* second.

$$L_{eq} = SEL - 10logT \quad (6)$$

To read a reduced frequency nomogram:

i. Start by selecting the frequency (Hz) on the right-hand vertical axis.
ii. Follow this value horizontally to the left to where the diagonal temperature isotherm intersects.
iii. Draw a vertical line through the frequency and isotherm intersection, find the point where this line intersects the modulus and loss factor curves.
iv. Draw horizontal lines from these points to the lefthand vertical axis to read the values [8].

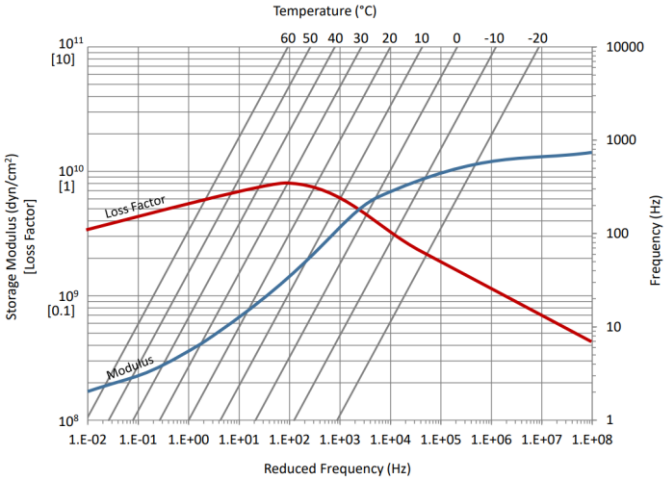

Figure 3. Diagram of acoustic performance [9].

In studies conducted for new generation metal foams, it has been understood that materials with 89% porosity, 5 mm thickness and an average transition diameter of 0.652 mm [10] can be applied as in-situ noise canceling on ships.

IV. CONCLUSION

In the results of the survey conducted with the seafarers in the shipyards region of Yalova province, more than 80% of the seafarers stated that they were exposed to noise and vibration on the ships. This shows that it is not enough to produce ships according to foreign standards. It has been understood that the sudden climatic changes caused by the navigation routes significantly affect the material dynamics. In addition, it is understood from the survey results that seafarers cause adverse health conditions due to noise and vibration.

The use of metal foam, high impact energy absorption, electromagnetic shielding performance, thermal insulation, temperature resistance, fire resistance and non-flammability properties have been demonstrated in studies conducted in the last 10 years. However, due to the high damping capacity of the material, it undergoes permanent deformation. The damping, corrosion, thermal insulation and thermal performance of the metal foam should be preserved, and the deformation and mechanical properties should be strengthened. In addition, the use of these panels reduces the load on the ships and increases the fuel savings on the ships.

V.REFERENCES

[1] UNCTAD, Review of Maritime Transport 2021
[2] Li Xue; Zhou Y,; Yuen K. F.; A systematic review on seafarer health: Conditions, antecedents and interventions, Transport Policy 122, 2022
[3] Vuki´c, L.; Mihanovi´c, V.; Fredianelli, L.; Plazibat, V. Seafarers' Perception and Attitudes towards Noise Emission on Board Ships. Int. J. Environ. Res. Public Health 2021
[4] Picu L.; Picu M.; Rusu E., An Investigation Into The Health Risks Associated with The Noise and Vibrations on Board af A Boat-A Case Study on The Danube River, J. Mar. Sci. Eng. 7 , 2019
[5] ILO, Guidelines for implementing the occupational safety and health provisions of the Maritime Labour Convention, 2006
[6] P. Hommel, D. Roth and H. Binz, Deficits in The Application of Aluminum Foam Sandwich: An Industrial Perspective, International Design Conference – Design 2020. https://doi.org/10.1017/Dsd.2020.13
[7] H. Qingxian, Q. Sawei, H. Yuebo. Development on Preparation Technology of Aluminum Foam Sandwich Panels, Rare Metal Materials and Engineering, Volume 44, Issue 3, March 2015, Pages 548-552. https://doi.org/10.1016/S1875-5372(15)30036-9.
[8] https://www.pyroteknc.com/dmsdocument/93/DECIDAMP-SP80-TDS-113IP.pdf
[9] Cheng, W., Duan, C. Y., Liu, P. S., & Miao, L. U. (2017). Sound absorption performance of various nickel foam-base multi-layer structures in range of low frequency. *Transactions of Nonferrous Metals Society of China*, *27*(9), 1989-1995.
[10] https://new.abb.com/marine/generations/generations-2017/businessarticles/onboard-dc-grid-a-system-platform-at-the-heart-of-shipping.

Dynamics Analysis of a Head-Neck Rehabilitation Robot using Newton-Euler Equations

A. BAYRAM[1] and A.S. DURU[2]

[1] Van Yüzüncü Yil University, Van/Turkey, atillabayram@yyu.edu.tr
[2]Ankara Yildirm Beyazit University, Ankara/Turkey, asduru@aybu.edu.tr

Abstract **- This study addressed the motion and dynamic analysis of a dual-arm rehabilitation robot proposed for the treatment of various head-neck orthopedic disorders. In this robotic system, each arm has six degrees of freedom (DOF) and only the first four joints of the arms are actuated. The whole system is designed kinematically to form as a closed loop and to move without locking during operations. A dynamic model was created using Newton-Euler equations to calculate the driving torques and reaction force/moments of the arms that make the rehabilitation robot performed on the desired motion. Considering the whole robotic system, this dynamic model creates a redundant structure. In order to realize the desired head-neck motions safely, the set of the inverse dynamic equations is resolved according to the optimization of the reaction force/moments at the gripper point to hold the head and the actuator torques.**

Keywords **- Head-neck rehabilitation robot, Dynamic analysis, Newton-Euler equations, Redundant manipulators.**

I. INTRODUCTION

WITH the technological development, robotic systems are increasingly used in many medical fields. One of these areas is rehabilitation robots [1]. Performing repetitive, long-term, and challenging exercises with robotic systems affects positively the treatment process of the patient as well as increasing the efficiency of the therapist compared to traditional methods. Generally, in literature, rehabilitation robots are used on the lower extremity and upper extremity for the exercises of the arms-hands and legs-feet, respectively. Such robots are currently used commercially in clinics. The most well-known ones are MIT-Manus [2], ARMmin [3], ANYexo [4] for the upper extremity and Locomat [5], ALEX, LOPES [6] for the lower extremity. In addition to these medical robots, a limited number of rehabilitation robots have also been proposed for head-neck exercises [7-9]. However, these proposed head-neck rehabilitation robots are in parallel manipulator structure and generally have three degrees of freedom. This results in a very limited working space and lower dexterity. In another study on head-neck rehabilitation, a six-degree-of-freedom serial dual arm actuated system was proposed. The robotic system will be discussed in this study [10]. The dual arm manipulators are used in many processes such as holding, transporting, and assembling objects. Dynamic equations of robot arms are usually obtained by Lagrange [11] or virtual work method [12]. Thus, reaction forces and moments do not appear in the equations and result in a simplified mathematical model. Although the size of the dynamic equation system increases, if such reaction forces/moments are needed in the solution process, the use of the Newton-Euler method becomes a necessity. In literature, dynamic analyzes of robot manipulators are generally given by the recursive Newton-Euler method [13,14]. However, this method is generally preferred for the inverse dynamic analysis of open-loop serial manipulators. In the dynamic analysis of parallel manipulators or/and multi-arm cooperative manipulators, the classical Newton-Euler method is more useful since it is difficult to define the reaction forces/moments on the end effector of each arm by the recursive Newton-Euler method.

In this study, in addition to the forward and inverse kinematics analysis of a dual arm head-neck rehabilitation robot forming a closed loop, a dynamic equation system was obtained by using the Newton-Euler method. The equation system created is redundant according to reaction force/moments and driving torques. Therefore, the inverse dynamic analysis of the system is resolved for desired motions defined with respect to the head. The solution for a safe motion of the head-neck was based on an optimization. The optimization procedure consists of minimizing only the reaction force/moments at the gripper points of the head and the driving torques of the arms. The procedure also run on some equality and inequality constraints.

II. KINEMATIC AND DYNAMIC ANALYSIS OF THE REHABILITATION ROBOT

In this study, the actuation unit of the rehabilitation robot consists of a dual arm robot manipulator. Each arm with 6 DOF is an underactuated serial manipulator, which only the first four joints of each arm are actuated. The CAD model of the rehabilitation robot with the head-neck model is given in Fig. 1. The connection of the arms with the head is assumed to be rigid. Therefore, the robotic system is in a closed chain structure. As shown in the figure, each arm is designed as RRRRU (R: rotational, U: Universal) structure in order to move without locking during the operations. The head-neck is modeled as a manipulator with four degrees of freedom.

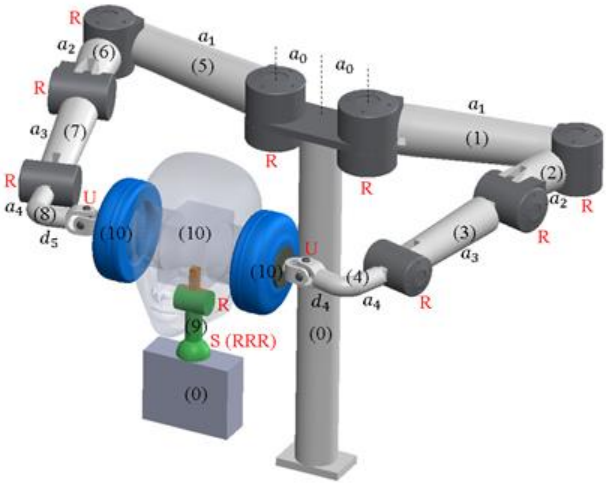

Figure 1: The CAD model of the rehabilitation robot [10].

For dynamic analysis, first of all, the kinematic equations of the head–neck and arms are defined according to the parameters, coordinate systems, and joint variables given in Fig. 1 and Fig.2. The Denavit-Hartenberg parameters were used to generate the calculation of the position and orientation.

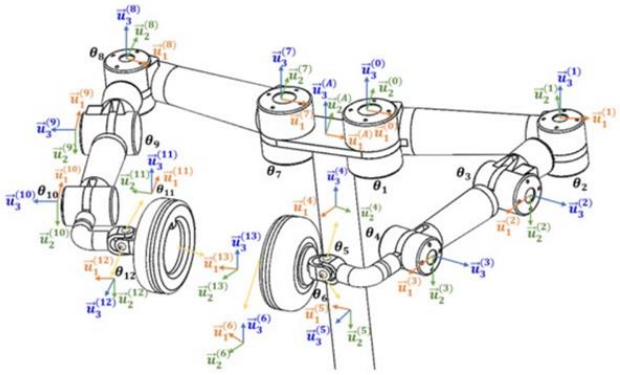

Figure 2: The coordinate systems and joint variables [10].

At first, after some simplifications, the position vector in column matrix and the orientation matrix for the head-neck according to the fixed coordinate system attached to the point-A on the head are given in the forward kinematic equations as follows.

$$\hat{C}_{Head}^{(A,4)} = \hat{C}^{(A,K)} * e^{\tilde{u}_3\theta_1}e^{-\tilde{u}_2\theta_2}e^{-\tilde{u}_3\theta_3}e^{\tilde{u}_2\theta_4}e^{-\tilde{u}_1\pi/2} \quad (1)$$

$$\bar{r}_{Head} = d_k e^{\tilde{u}_3\theta_1}e^{\tilde{u}_1\pi/2}e^{\tilde{u}_3\theta_2}e^{\tilde{u}_1\pi/2}\bar{u}_3 + a_k e^{\tilde{u}_3\theta_1}e^{\tilde{u}_1\pi/2}e^{\tilde{u}_3\theta_2}e^{\tilde{u}_1\pi/2}e^{\tilde{u}_3\theta_3}e^{\tilde{u}_1\pi/2}e^{\tilde{u}_3\theta_4}\bar{u}_1 \quad (2)$$

Here, the expressions, $\vec{u}_1, \vec{u}_2$ and $\vec{u}_3$ represent the unit vectors of the axes. The orientation matrices are written in the exponential form. According to the exponential method; for example, the expression $e^{\tilde{u}_3\theta_1}$ refers to the rotation with θ_1 around the $\vec{u}_3$ axis. Detailed information on this subject can be reviewed from the relevant source [15]. $\hat{C}^{(A,K)}$ represents the orientation of the fixed axis of the head-neck model relative to the world coordinate system axis. The joint angles of the head-neck model can be defined analytically for a given head-neck motion by using the inverse kinematic analysis from Eqn. 1 and Eqn. 2. If the same operations are repeated for the right and left arm manipulators, the following forward kinematic equations are obtained.

$$\hat{C}_{Arm}^{(A,6)} = e^{\tilde{u}_3\theta_{12}}e^{\tilde{u}_2\theta_{34}}e^{\tilde{u}_3\theta_5}e^{\tilde{u}_2\theta_6} \quad (3)$$

$$\bar{r}_L = a_0\bar{u}_1 + a_1e^{\tilde{u}_3\theta_1}\bar{u}_1 + a_2e^{\tilde{u}_3\theta_{12}}e^{-\tilde{u}_1\pi/2}\bar{u}_1 + a_3e^{\tilde{u}_3\theta_{12}}e^{-\tilde{u}_1\pi/2}e^{\tilde{u}_3\theta_3}\bar{u}_1 + a_4e^{\tilde{u}_3\theta_{12}}e^{\tilde{u}_2\theta_{34}}\bar{u}_1 - d_4e^{\tilde{u}_3\theta_{12}}e^{-\tilde{u}_1\pi/2}e^{\tilde{u}_3\theta_3}\bar{u}_3 \quad (4)$$

$$\hat{C}_{Arm}^{(A,12)} = e^{\tilde{u}_3\theta_{78}}e^{\tilde{u}_2\theta_{910}}e^{\tilde{u}_3\theta_{11}}e^{\tilde{u}_2\theta_{12}} \quad (5)$$

$$\bar{r}_R = -a_0\bar{u}_1 - a_1e^{\tilde{u}_3\theta_7}\bar{u}_1 - a_2e^{\tilde{u}_3\theta_{78}}e^{-\tilde{u}_1\pi/2}\bar{u}_1 - a_3e^{\tilde{u}_3\theta_{78}}e^{-\tilde{u}_1\pi/2}e^{\tilde{u}_3\theta_9}\bar{u}_1 - a_4e^{\tilde{u}_3\theta_{78}}e^{\tilde{u}_2\theta_{910}}\bar{u}_1 - d_4e^{\tilde{u}_3\theta_{78}}e^{-\tilde{u}_1\pi/2}e^{\tilde{u}_3\theta_9}\bar{u}_3 \quad (6)$$

The above statements describe the orientation matrix and position vectors of the end effector of the left and right arms relative to the fixed world coordinate system. Here, the indexes "L" and "R" represents the left and right arm respectively. When these expressions are decomposed into their components, the joint variables of each arm for a given desired orientation and position are carried out by semi-analytically. In semi-analytic method, a common variable from the position equations and the orientation equations is considered known. Another common variable for both equation set is calculated in terms of this known variable. The equation sets are reduced to a nonlinear equation with a single variable. As a result, instead of the numerical solution of six variables with six nonlinear equations, the solution performs on one-dimensional search. Then, remaining variables are solved analytically. As seen in Fig.1, there are a total of ten movable links for this robotic system. Newton-Euler equations are applied into all these links, such as the free diagram of an example link shown in Fig.3.

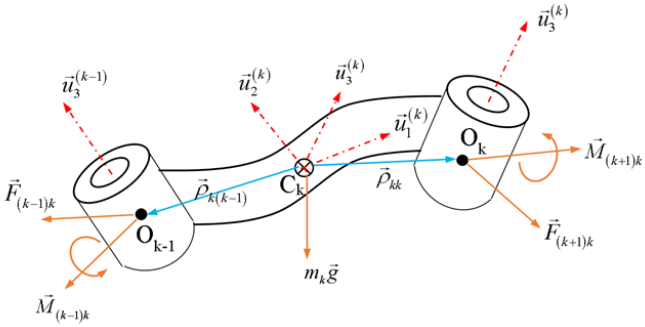

Figure 3: The free body diagram for the k[th] link.

After obtaining the linear and angular accelerations of the centers of gravity of the links from the kinematic analysis, the force and moment equations for each link according to their own coordinate system are defined by Newton-Euler Method as follows, respectively.

$$m_k\bar{a}_{C_k} = \bar{F}_{(k-1)k}^{(k)} - \hat{C}^{(k,k+1)}\bar{F}_{(k-1)k}^{(k)} + m_k\hat{C}^{(k,0)}\bar{g}^{(0)} \quad (7)$$

$$\hat{I}_k\dot{\bar{\omega}}_k + \tilde{\omega}_k \hat{I}_k\bar{\omega}_k = \bar{M}^{(k)}_{(k-1)k} - \hat{C}^{(k,k+1)}M^{(k)}_{(k-1)k} + \hat{\rho}_{k(k-1)}\bar{F}^{(k)}_{(k-1)k} - \hat{\rho}_{k(k-1)}\hat{C}^{(k,k+1)}\bar{F}^{(k+1)}_{k(k+1)} \quad (8)$$

$\bar{F}^{(k)}_{(k-1)k}$ and $M^{(k)}_{(k-1)k}$ represent the column matrices of the reaction force and moment vectors exerted on link k by link k-1, respectively, resolved in their own coordinate systems. The robotic system is considered as a parallel manipulator consisting of two independent loops. The system consists of nine rotational, two universal and one spherical joints. After applying the Newton-Euler equations for the ten movable links, the combined equation of motion of the rehabilitation robot can be written as follows.

$$\hat{M}\begin{bmatrix}\bar{a}_c\\ \bar{\alpha}\end{bmatrix} + \hat{B}\bar{R} + \bar{D} + \bar{G} = \bar{F} \quad (9)$$

The center of gravity accelerations and link angular accelerations can be written in terms of the joint variables.

$$\begin{bmatrix}\bar{a}_c\\ \bar{\alpha}\end{bmatrix} = \hat{\jmath}\ddot{\bar{q}} + \bar{E} \quad (10)$$

Rearranging the force/moment terms and substituting Eqn. 10 into Eqn. 9, the combined equation of motion of the rehabilitation robot is obtained as follows.

$$\tilde{M}\ddot{\bar{q}} + \hat{B}\bar{R} + \bar{Q} = \hat{P}\bar{\tau} \quad (11)$$

$\hat{M} \in \mathrm{R}^{60\times60}$, $\tilde{M} \in \mathrm{R}^{60\times16}$: Mass matrix, reduced mass matrix
$\hat{B} \in \mathrm{R}^{60\times56}$: Generalized reaction force/moment matrix
$\bar{R} \in \mathrm{R}^{56\times1}$: Reaction force/moment unknown vector
$\bar{\tau} \in \mathrm{R}^{8\times1}$: Unknown actuator torques
$\hat{P} \in \mathrm{R}^{60\times8}$: Actuator torque coefficient matrix
$\bar{Q} \in \mathrm{R}^{60\times1}$: Gravity, centrifugal, Coriolis, friction, elastic force/moment vector
$\hat{\jmath} \in \mathrm{R}^{60\times16}$: Generalized Jacobian matrix

$\bar{q} = [\bar{q}_L, \bar{q}_R, \bar{q}_h]^{\mathrm{T}} \in \mathrm{R}^{16\times1}$: Vector of the joint variables

$\bar{q}_L$, $\bar{q}_R$, and $\bar{q}_h$ represent the left arm, right arm, and head-neck joint variables, respectively.

Rearranging Eqn. 11 as follows, a set of equations is obtained for the inverse dynamics of the rehabilitation robot.

$$[\hat{B} \quad \hat{P}]\begin{bmatrix}\bar{R}\\ \bar{\tau}\end{bmatrix} = -\tilde{M}\ddot{\bar{q}} - \bar{Q} \quad (12)$$

In this mathematical model, for a reference head-neck motion, the reaction force/moments and actuator torques will be calculated by the inverse dynamic analysis. $[\bar{R} \quad \bar{\tau}]^{\mathrm{T}}$ is the unknown vector and contains 64 unknowns whereas the total number of equations is 60. Such a situation represents a redundant system and gives an optimization opportunity. In this case, the solution will be based on the optimization of an objective function given in Eqn. 13.

$$Cost = \bar{R}_i\hat{W}_1\bar{R}_i^{\mathrm{T}} + \bar{\tau}_j\hat{W}_2\bar{\tau}_j^{\mathrm{T}} \quad (13)$$

In this objective function, $\bar{R}_i$ is a column matrix containing only the reaction force/moments at the gripper point between the arms and the head, and $\bar{\tau}_j$ includes all the actuator torques. $\hat{W}_1$ and $\hat{W}_2$ are matrices and set the weights of the terms in the objective function. The optimization solution is presented as follows.

$$\begin{bmatrix}\bar{R}\\ \bar{\tau}\end{bmatrix} = \min_{st.\substack{Eqn.12\\ Eqn.15}}(Cost) \quad (14)$$

$$\delta_{min} \le \left|R^h_{L3} - R^h_{R3}\right| \le \delta_{max} \quad (15)$$

Here, R^h_{L3} and R^h_{R3} are the reaction forces acting on the head by the end effector of the arms in the normal directions. Eqn. 15 will provide a rigid gripping between the arms and the head while it also ensures the safety motion.

III. Simulation Study

Although the basic exercise motions for the head-neck have been suggested in literature as flexion, extension, lateral bending and rotation, in this study, a complex reference trajectory was followed for the motion of the head-neck model in order to test the performance of the dynamic model proposed. For this aim, an IMU (inertial measuring unit) was placed on the head in a suitable way and some random complex motions were made to the head for a certain period of time as shown in Fig. 4. The orientation of the head and the position of the center point of the head along the entire trajectory were calculated with the data from the recorded IMU using the 123-Euler angle sequence. Also, the fourth neck angle was given as a sine wave with a large period. Parameters for both arms and head-neck model are selected in accordance with an adult human body. The damping and elastic coefficient terms for the system have been chosen approximately since there is no such study in literature.

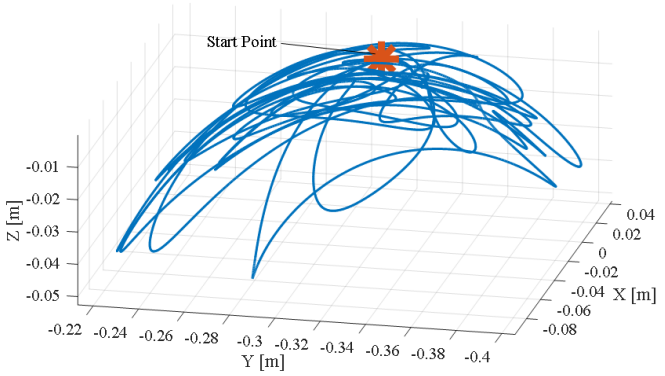

Figure 4: Reference trajectory for the head-neck motion.

For the given reference position and orientation, the solution model was established by taking Eqn. 12 as equality constraint and Eqn. 13 as the objective function. In addition, some restrictions were assigned onto the actuator torques and the reaction force/moments at the grip point between the arms and the head. This redundant dynamic model was numerically

solved for the entire trajectory using the "fmincon" command in MATLAB. As a result, besides the reaction force/moments, the actuator torques that provide the head-neck motion were also calculated. After the simulation, the actuator torques of the left and right arms along the trajectory are given in Fig.5 and Fig.6, respectively. As can be seen from the results, the joint driving torques remained within certain torque values and showed a behavior without excessive oscillations.

In the simulations, each component of the reaction forces at the gripper point is limited to ±50 N while the actuator torques are limited to ±100 Nm. The limits of the force difference in the normal direction were selected as $\delta_{min} = 2\text{N}$ and $\delta_{max} = 6\text{N}$.

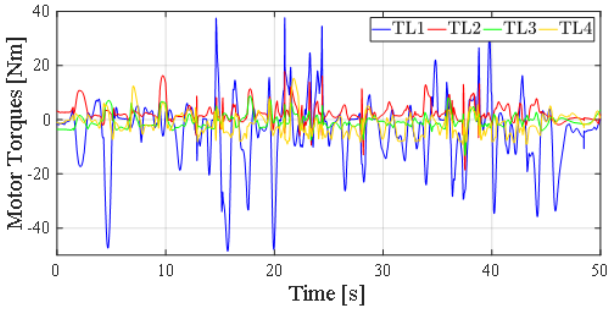

Figure 5: The actuator torques of the left arm.

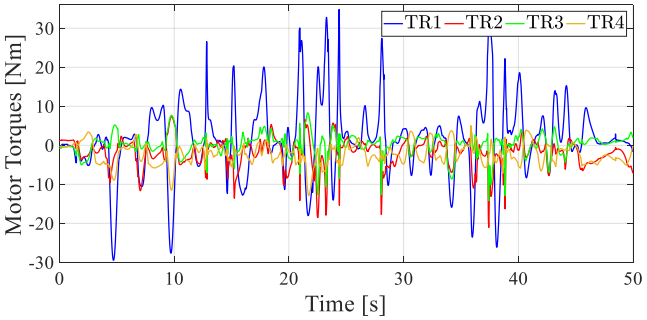

Figure 6: The actuator torques of the right arm.

Likewise, the reaction moment/forces at the grip points between the head and the arms remain within boundary values assigned in the solution procedure. These values seem suitable to grip the head by the arms safely. These outcomes of the reaction moment/forces for the left and right side can be seen in Fig.7 and Fig.8, respectively.

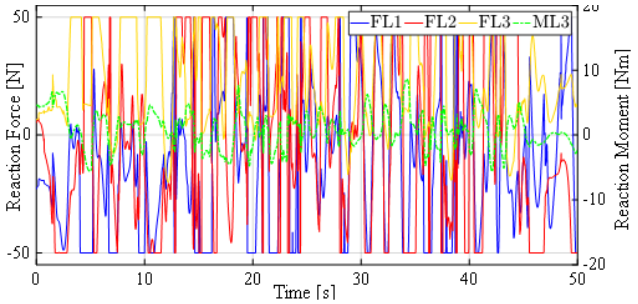

Figure 7: The reaction torque/forces at the left side grip point.

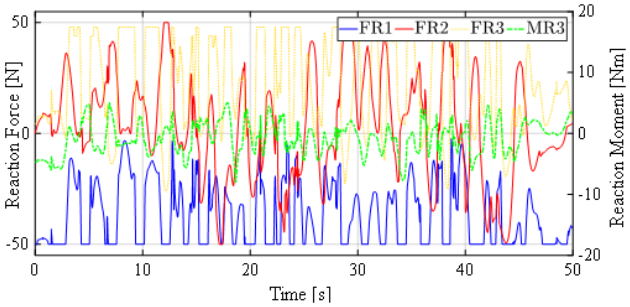

Figure 8: The reaction torque/forces at the right side grip point.

An animation showing the motion of the rehabilitation robot for the given reference trajectory based on these simulations is given as a supplementary material in the Online resource [16].

IV. Conclusion and Discussion

In this study, the dynamic analysis of a rehabilitation robot was carried out using Newton-Euler equations. The system involves a set of redundant dynamic equations. The solution is carried out according to equality constraints, inequality constraints and optimization of an objective function. From the simulation results, the actuator torque values that provide the motion of the head are generated within reasonable values without excessive oscillations. In the meanwhile, the reaction force/moment values between the head and the arms were kept between the appropriate values by the optimization. This ensures that the rehabilitation robot can safely perform the exercise motions on the head-neck.

References

[1] H. I. Krebs, and B. T. Volpe, "Rehabilitation robotics," *Handbook of clinical neurology*, vol. 110, pp. 283-294, 2013.

[2] H. I. Krebs, M. Ferraro, S. P. Buerger, M. J. Newbery, A. Makiyama, M. Sandmann, and N. Hogan, "Rehabilitation robotics: pilot trial of a spatial extension for MIT-Manus," *Journal of Neuroengineering and Rehabilitation*, vol. 1(1), pp. 1-15, 2004.

[3] T. Nef, V. Klamroth-Marganska, U. Keller, and, R.Riener, "Three-dimensional multi-degree-of-freedom arm therapy robot (ARMin),". *Neurorehabilitation Technology*, pp. 351-374, 2016

[4] Y. Zimmermann, A. Forino, R.Riener, and, M. Hutter, "ANYexo: A versatile and dynamic upper-limb rehabilitation robot,". *IEEE Robotics and Automation Letters*, vol. 4(4), pp. 3649-3656, 2019.

[5] M. Bernhardt, M. Frey, G. Colombo, and, R. Riener, "Hybrid force-position control yields cooperative behaviour of the rehabilitation robot LOKOMAT," *in 9th Int. Conference on Rehabilitation Robotics, ICORR IEEE*, pp. 536-539, June 2005.

[6] G. Chen, C. K. Chan, Z. Guo and,H. Yu, "A review of lower extremity assistive robotic exoskeletons in rehabilitation therapy," *Critical Reviews™ in Biomedical Engineering*, vol. 41(4-5), 2013.

[7] D. Wu, L. Wang, and, P. Li, "A 6-DOF exoskeleton for head and neck motion assist with parallel manipulator and sEMG based control," *in Int. Conference on Control, Decision and Information Technologies (CoDIT)*, pp. 341-344, April 2016

[8] P. K. Lingampally, and, A. A. Selvakumar, "A kinematic and workspace analysis of a parallel rehabilitation device for head-neck injured patients," *FME Transactions*, vol. 47(3), pp. 405-411, 2019.

[9] M. E. H. Ibrahem, M. S. El-Mohandes, M. T. El-Wakad, and, S. A. Sami, "Design and analysis of a dynamic neck brace," *in 3rd Novel Intelligent and Leading Emerging Sciences Conference (NILES)*, pp. 236-240, October 2021..

[10] A. Bayram, and, A. S. Duru, "Design and control of a rehabilitation robot manipulator for head–neck orthopaedic disorders," *International Journal of Robotics and Automation*, vol. 37(6), pp. 486-497, 2022.

[11] A. K. Swain, and, A. S. Morris, "Dynamic control of multi-arm cooperating manipulator systems," *Robotica*, vol. 22(3), pp. 271-283, 2004.
[12] S. Pedrammehr, S. Nahavandi, and, H. Abdi, "Closed-form dynamics of a hexarot parallel manipulator by means of the principle of virtual work," *Acta Mechanica Sinica*, vol. 34(5), pp. 883-895, 2018.
[13] X. Jing, H. Gao, Z. Chen, and, Y. Wang, "A recursive dynamic modeling and control for dual-arm manipulator with elastic joints," *IEEE Access*, vol. 8, pp. 155093-155102, 2020.
[14] J. He, H. Zheng, F. Gao, and, H. Zhang, "Dynamics and control of a 7-DOF hybrid manipulator for capturing a non-cooperative target in space," *Mechanism and Machine Theory*, vol.140, pp. 83-103, 2019.
[15] M. K. Ozgoren, "Kinematic analysis of spatial mechanical systems using exponential rotation matrices, Journal of Mechanical Design, vol. 129(11), pp. 1144–1152, 2006.
[16] Online Recourse 1, 2022, https://drive.google.com/file/d/18E8I3v89QhvtspgghuQRvjiEjCBLAytH/view?usp=sharing

Towards an Efficient Maintenance Management Plan

N.E.H. KHANFRI[1], N. OUAZRAOUI[2], A. SIMOHAMMED[3] and H.TOUAHAR[4]

[1.2.3.4]LRPI Laboratory, Health and Safety Institute, Batna 2 University, Batna, Algeria
[1]n.khanfri@univ-batna2.dz
[2]ouzraoui@yahoo.fr
[3]simo.antar@gmail.com
[4]hafedtouahar@gmail.com

Abstract **- Importance measures are used in reliability engineering to prioritize complex system components. The present importance measures did not sufficiently consider the incurred costs as a result of components' failures that differ from one to another. Some component failures result only in their maintenance costs, while others may result in major economic losses. The more realistic the failure cost modeling; the more credible the component classification. This paper proposes the use of a cost-based importance measure to improve both system availability and maintenance plan. When comparing the obtained results to the Birnbaum importance measure, several components that were regarded as less significant in the Birnbaum classification were shown to be important in the cost-based importance classification.**

Keywords **- Cost Importance Measure, Complex System, Failure Costs, Maintenance Management.**

I. INTRODUCTION

Inorder to improve the effectiveness of maintenance activities and to guarantee the high performance of industrial equipment, the identification and prioritization of critical components are crucial, for that purpose, several methods and techniques were suggested in the literature, among of which, the importance measure method that ranks equipment based on its contribution to system's availability, and includes several techniques such as, Birnbaum importance (BI), criticality importance (CI), Fussell-Vesely (F-V) importance, and generalized importance measure (GI)[1]. Generally, the commonly used importance measures in the literature consider the failure probability of a component and its impact on system availability and ignore the severity of failure effects such as repair costs, production losses, loss of lives, damage to health, the release of hazardous materials, etc.[2].

In practice, Importance-measure-based maintenance techniques are used to identify and select the component (s) that should be examined first following system's failure using a previously prepared checklist, to restore system functionality as quickly as possible [3].Additionally, it assists in determining which components should receive specific attention during maintenance schedules.

Further studies have extended the reliability importance measures by measuring the instantaneous importance of the components in relation to their repair costs (including replacement and labor costs, downtime cost), to determine the appropriate time to replace the equipment, i.e., at each random moment they study the cost importance of the component and see when it is advantageous to replace it to improve the system's reliability. Gupta[2]introduced a cost-effective importance measure (CEIM) which is based on the measurement of the general importance of a component and its associated failure costs (repair and production loss costs) to prioritize equipment's inspection and maintenance. The proposed approach was applied to classify the ten components of the belt conveyor system In addition, Kuo et Zhu[3] introduced a cost-importance measure of repairable independent components with negligible repair time that takes into account Birnbaum importance measure and the cost of components maintenance and system failure costs (production loss due to component failure). For better maintenance decision-making Do and Bérenguer [4]presented an extension approach of RIM (Conditional reliability-based importance measure) called RIMc which allows taking into account both the improvement ability and different cost structures (maintenance and benefit costs) of non-repairable components in importance ranking. It is within this category that the present paper fits, in which we aim to compare the Birnbaum importance measure and cost-based importance along the system life length.

The rest of the paper is organized as follows: section 02 presents the importance measures used in maintenance management; the adopted failure cost model is introduced in section 03; section 04 illustrates the applicability of the proposed methodology; and finally, a conclusion is given in section 05.

II. IMPORTANCE MEASURE IN MAINTENANCE MANAGEMENT

The fundamental measures of reliability are highly informative in terms of the system's proper operation, but they do not describe the system's tolerance for its components failures. As a result, importance analysis serves

as a sensitivity analysis to pinpoint system flaws and determine which system components should be upgraded to increase the overall availability, whether through component replacement, component redundancy reallocation, or enforced inspection, test, and maintenance programs [1].

In the design phase, importance measures are used to help engineers minimize maintenance costs and prolong the life of the system [5]. This analysis depends on the reliability of the components and the structure of the system in which the component is located. The importance of an event's contribution to the top-event occurrence may be regarded as an importance measure (IM). There are several methods for assessing the importance of components, including:

A. Birnbaum Reliability Importance Measure:

Birnbaum importance measure or reliability importance of the component helps to determine the change in the system unavailability with the failure of that component. The Birnbaum importance measure is completely dependent on the system architecture and independent of the current probability of the basic event (component failure probability) [6], it is defined by the first derivative of the system reliability function with respect to the component reliability:

$$I_i^B(A) = \frac{\partial R_s(t)}{\partial R_A(t)} \quad (1)$$

Where:$I_i^B(A)$ = Birnbaum importance measure for event A; $R_s(t)$ is the system reliability function; $R_A(t)$:component (A) reliability function.

B. Cost Based Importance Measure:

For the purpose of improving a system's reliability while controlling costs related to system failure and maintaining failed components, the adequate classification of the system's components for improvement with the consideration of maintenance costs can have a significant influence on the final ranking [7]. The cost-based importance of component *k* which is repaired immediately after its failure detection can be defined as follows:

In case of series system: $I_k^C(t) = \frac{(C_k + C_{s,k})}{R_k(t)}$ (2)

In case of parallel system: $I_k^C(t) = \frac{C_k}{R_k(t)}$ (3)

Where:

$R_k(t)$: is the reliability function of component *k*

C_k: is the time independent failure cost of component *k*

$C_{s,k}$: The expectedtimeindependentcost of system failure caused by the failure of component *k.*

III. Failure Cost Modeling

According to IEC 60300 [8], the Life cycle cost of the equipment should be updated and used during the entire equipment life stages to identify areas of significant cost uncertainty and risk, which means most of the costs cannot be predicted until the operational phase of the equipment, where most of the failures with their real consequences occur, three majors' cost categories associated with corrective maintenance are considered:

- Non-recurring costs, such as those for test instruments, tools, initial spare parts, staff training and initial documentation.
- Recurring costs, such as: labor wages, spares and consumables, on-going training, and documentation
- Consequential costs resulting from production loss including compensation costs and lost revenue.

The failure cost model of a component in the operational phase generally modeled as follows:

$$C_{k/Failure} = x_i * C_{Hazard} + x_i * C_{CM} + x_i * C_{Production\ Loss} \quad (4)$$

$$C_{CM} = x_i * C_{MP} + x_i * C_{SP} + x_i * C_{Supp} \quad (5)$$

$$C_{MP} = MTTR_i * N_{MP} * C_{HR} \quad (6)$$

$$C_{Production\ Loss} = MTTR_i * C_{Production\ Loss/hour} \quad (7)$$

$$C_{Hazard} = x_i * C_{Environmental\ Regulation} + x_i * C_{Fatalities/Injuries} \quad (8)$$

where:

C_{SP}	:	The spare parts consumption costs.
$MTTR_i$	:	Time (in hours) it takes to restore faulty equipment with critical failure mode *i* to operating condition.
N_{MP}	:	The required number of persons to do the work.
C_{HR}	:	Person hour rate
C_{MP}	:	Person hour cost.
C_{Supp}	:	Cleaning costs+ transportation costs... etc.
C_{Hazard}	:	It depends on the failure consequences such as the Environmental regulation (Flaring taxes), and cost of fatalities/injuries (medical costs...etc.)
x_i	:	A binary decision variable that takes the value of 1 if the cost is included and the value 0 if it is not.

IV. Case Study

A. System description:

The chosen system for this study, which consists of an oil tank with top-mounted components is installed to ensure the adequate lubrication/sealing (in a matter of oil pressure and temperature) of the Turbo-compressor bearings and seals [9].

We initially performed a failure mode and effect analysis to investigate the potential failure modes and determine the most critical ones on the EHS and production. Failure rates and failure costs are shown in Table 1. Equation (4) is used to obtain the total failure cost for each component.

Table 1: Lube / Seal Oil unit components data: [11, 12].

N°	Component	Failure Rate (/h)	Total Failure costs (Unit)
1	Lube Oil Heater	3.01E-05	50,608.5
2	Lube Oil Pump	3.46E-06	30,043.5
4	Oil Cooler	1.00E-05	500.5
3	Filter	1.00E-6	34,430
4	Seal Oil Pump	3.46E-06	30,043.5
5	Seal Oil Trap	1.75623E-05	42,979
6	Vacuum Pump	4.39059E-05	8,762.5

B. Binary Decision diagram and structure function:

The potential success and failure states for the chosen system are modeled using the binary decision tree:

The architecture function of the lube/seal oil unit is as follows:

$$\varphi(x) = x_1 \times x_{16} \times (x_2 \times x_3 + x_3 \times x_4 + x_2 \times x_3) \times (x_5 \times x_6 + x_6 \times x_7 + x_7 \times x_5) \times (x_8 + x_9) \times (x_{10} + x_{11}) \times (x_{12} + x_{13}) \times x_{14} \times x_{15} \quad (9)$$

C. Results and discussion:

The Birnbaum reliability importance and cost importance measures of the chosen components are illustrated in tables 2 and 3, and their order is presented in Table 4 with their corresponding plots in Figures 2 and 3, respectively.

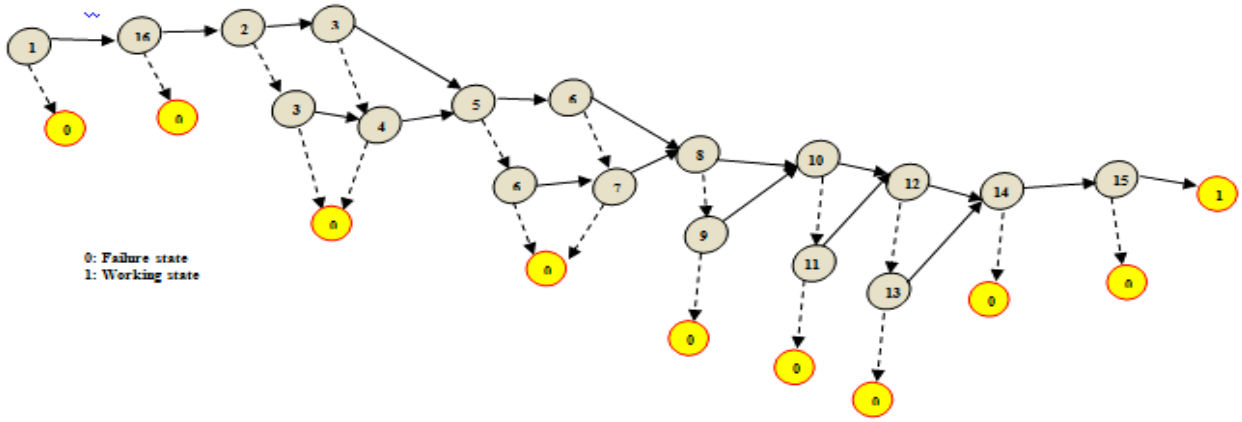

Figure 1: Binary decision diagram of the selected system.

Table 2: Lubrication /sealing unit components importance results according to BRI

Time	Lube Oil Heater (I_1)	Lube Oil Pumps(I_2)	Oil Coolers(I_3)	Filters (I_4)	Seal Oil pumps (I_5)	Oil Traps (I_6)	Vacuum Pump (I_7)
8760	5.92E-01	2.64E-02	7.14E-02	4.59E-01	4.69E-01	6.62E-02	6.69E-01
17520	3.28E-01	2.16E-02	5.61E-02	1.97E-01	2.06E-01	5.51E-02	4.18E-01
26280	1.73E-01	1.27E-02	3.22E-02	8.05E-02	8.59E-02	3.36E-02	2.49E-01
35040	8.79E-02	6.43E-03	1.61E-02	3.17E-02	3.46E-02	1.78E-02	1.43E-01
43800	4.34E-02	2.97E-03	7.48E-03	1.21E-02	1.35E-02	8.76E-03	7.95E-02
52560	2.10E-02	1.29E-03	3.28E-03	4.55E-03	5.18E-03	4.09E-03	4.34E-02
61320	9.96E-03	5.38E-04	1.39E-03	1.67E-03	1.95E-03	1.84E-03	2.32E-02
70080	4.66E-03	2.17E-04	5.72E-04	6.06E-04	7.20E-04	8.02E-04	1.23E-02
78840	2.15E-03	8.51E-05	2.30E-04	2.17E-04	2.63E-04	3.43E-04	6.39E-03
87600	9.82E-04	3.27E-05	9.09E-05	7.68E-05	9.52E-05	1.44E-04	3.29E-03
96360	4.45E-04	1.23E-05	3.54E-05	2.69E-05	3.41E-05	5.97E-05	1.68E-03
105120	2.00E-04	4.60E-06	1.36E-05	9.37E-06	1.21E-05	2.44E-05	8.52E-04
113880	8.91E-05	1.69E-06	5.20E-06	3.24E-06	4.29E-06	9.91E-06	4.29E-04
122640	3.95E-05	6.16E-07	1.97E-06	1.11E-06	1.51E-06	3.98E-06	2.15E-04
131400	1.74E-05	2.22E-07	7.38E-07	3.81E-07	5.26E-07	1.59E-06	1.07E-04

The analysis of the time plot of importance measures revealed a diversification in the component's importance classification, some components that were classified as important by BRI were regarded as less important in CIM, which is the case of the vacuum pump at 8760 hours. The failure rate of vacuum pump was assessed to be the highest among unit's components, and any change in the vacuum pump reliability will engender a large change in the system reliability, which is represented by its highest importance grade with regards to BRI classification, however the incurred costs of its failure are minor compared to heater failure costs, for that heater failure was ranked the first in CIM at 8760 h. Along the system life length, components' reliability decrease over time and the fraction cost of failure over reliability increases especially for those components with a higher failure rate and no redundancy. At the end of the system's lifetime Birnbaum and cost importance measure gave almost the same classification with a difference in lube

and seal oil pumps and oil cooler ranking. Since BRI focuses only on system reliability and its architecture, CIM considers failure costs, making it more applicable to repairable systems.

Table 3: Lubrication /sealing unit components importance results according to CIM

Time	Lube Oil Heater (I_1)	Lube Oil Pumps (I_2)	Oil Coolers (I_3)	Filters (I_4)	Seal Oil Pumps (I_5)	Oil Traps (I_6)	Vacuum Pump (I_7)
8760	6.6E+04	3.1E+04	5.5E+02	3.5E+04	3.1E+04	5.0E+04	1.3E+04
17520	8.6E+04	3.2E+04	6.0E+02	3.5E+04	3.2E+04	5.8E+04	1.9E+04
26280	1.1E+05	3.3E+04	6.5E+02	3.5E+04	3.3E+04	6.8E+04	2.8E+04
35040	1.5E+05	3.4E+04	7.1E+02	3.6E+04	3.4E+04	8.0E+04	4.1E+04
43800	1.9E+05	3.5E+04	7.8E+02	3.6E+04	3.5E+04	9.3E+04	6.0E+04
52560	2.5E+05	3.6E+04	8.5E+02	3.6E+04	3.6E+04	1.1E+05	8.8E+04
61320	3.2E+05	3.7E+04	9.2E+02	3.7E+04	3.7E+04	1.3E+05	1.3E+05
70080	4.2E+05	3.8E+04	1.0E+03	3.7E+04	3.8E+04	1.5E+05	1.9E+05
78840	5.4E+05	3.9E+04	1.1E+03	3.7E+04	3.9E+04	1.7E+05	2.8E+05
87600	7.1E+05	4.1E+04	1.2E+03	3.8E+04	4.1E+04	2.0E+05	4.1E+05
96360	9.2E+05	4.2E+04	1.3E+03	3.8E+04	4.2E+04	2.3E+05	6.0E+05
105120	1.2E+06	4.3E+04	1.4E+03	3.8E+04	4.3E+04	2.7E+05	8.9E+05
113880	1.6E+06	4.5E+04	1.6E+03	3.9E+04	4.5E+04	3.2E+05	1.3E+06
122640	2.0E+06	4.6E+04	1.7E+03	3.9E+04	4.6E+04	3.7E+05	1.9E+06
131400	2.6E+06	4.7E+04	1.9E+03	3.9E+04	4.7E+04	4.3E+05	2.8E+06

Table 4: Lubrication /sealing unit components classification according to BRI and CIM

Classification	
BRI	CIM
$I_7 > I_1 > I_5 > I_4 > I_3 > I_2 > I_6$	$I_1 > I_6 > I_4 > I_5 = I_2 > I_7 > I_3$
$I_7 > I_1 > I_5 > I_4 > I_3 > I_6 > I_2$	$I_1 > I_6 > I_4 > I_5 = I_2 > I_7 > I_3$
$I_7 > I_1 > I_5 > I_4 > I_6 > I_3 > I_2$	$I_1 > I_6 > I_4 > I_5 = I_2 > I_7 > I_3$
$I_7 > I_1 > I_5 > I_4 > I_6 > I_3 > I_2$	$I_1 > I_6 > I_7 > I_4 > I_5 ; I_2 > I_3$
$I_7 > I_1 > I_5 > I_4 > I_6 > I_3 > I_2$	$I_1 > I_6 > I_7 > I_4 > I_5 ; I_2 > I_3$
$I_7 > I_1 > I_5 > I_4 > I_6 > I_3 > I_2$	$I_1 > I_6 > I_7 > I_4 > I_5 ; I_2 > I_3$
$I_7 > I_1 > I_5 > I_6 > I_4 > I_3 > I_2$	$I_1 > I_7 > I_6 > I_5 = I_2 > I_4 > I_3$
$I_7 > I_1 > I_6 > I_5 > I_4 > I_3 > I_2$	$I_1 > I_7 > I_6 > I_5 = I_2 > I_4 > I_3$
$I_7 > I_1 > I_6 > I_5 > I_3 > I_4 > I_2$	$I_1 > I_7 > I_6 > I_5 = I_2 > I_4 > I_3$
$I_7 > I_1 > I_6 > I_5 > I_3 > I_4 > I_2$	$I_1 > I_7 > I_6 > I_5 = I_2 > I_4 > I_3$
$I_7 > I_1 > I_6 > I_3 > I_5 > I_4 > I_2$	$I_1 > I_7 > I_6 > I_5 = I_2 > I_4 > I_3$
$I_7 > I_1 > I_6 > I_3 > I_5 > I_4 > I_2$	$I_1 > I_7 > I_6 > I_5 = I_2 > I_4 > I_3$
$I_7 > I_1 > I_6 > I_3 > I_5 > I_4 > I_2$	$I_1 > I_7 > I_6 > I_5 = I_2 > I_4 > I_3$
$I_7 > I_1 > I_6 > I_3 > I_5 > I_4 > I_2$	$I_1 > I_7 > I_6 > I_5 = I_2 > I_4 > I_3$
$I_7 > I_1 > I_6 > I_3 > I_5 > I_4 > I_2$	$I_7 > I_1 > I_6 > I_5 = I_2 > I_4 > I_3$

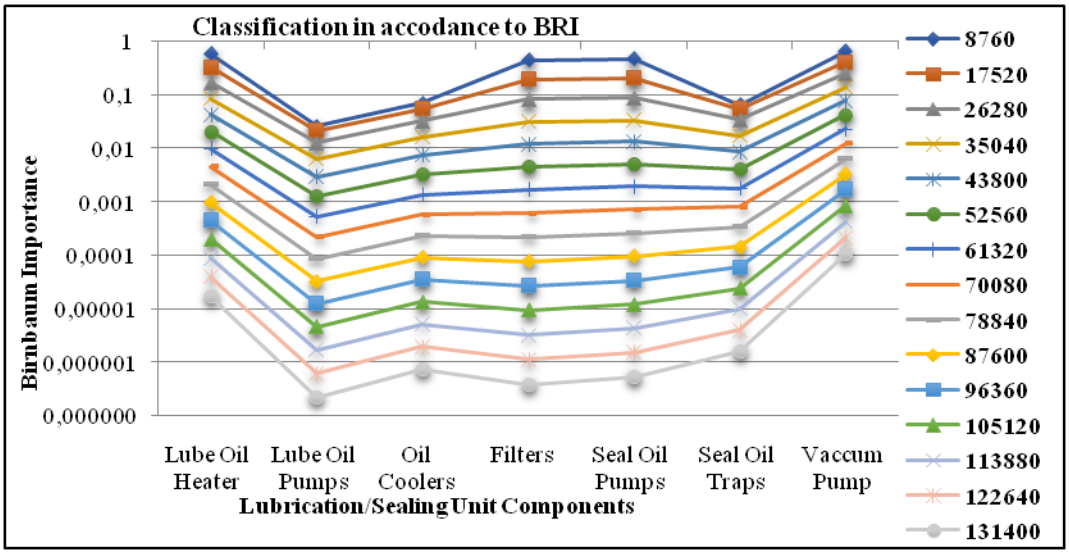

Figure 2: Lubrication/sealing Unit components classification in accordance WITH Birnbaum Reliability Importance BRI.

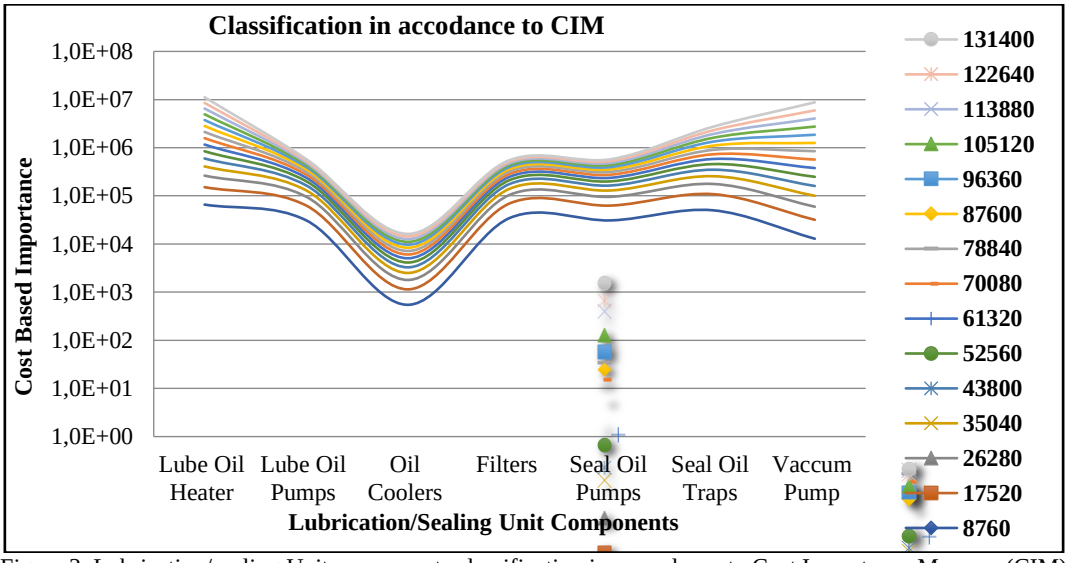

Figure 3: Lubrication/sealing Unit components classification in accordance to Cost Importance Measure (CIM)

V. Conclusion

A successful mix of technical and financial knowledge is necessary for maintenance management, in order to maintain high system reliability at the lowest possible costs. Importance measures combined with real cost modeling assist decision makers in ensuring proper maintenance plan selection and optimal resource allocation by focusing reliability improvement on weak components with high failure costs. To provide a more credible classification it is important to analyze importance measures with regards to system life length and avoid the static ranking, related to a specific point in time of operation.

References

[1] S. Gupta, and U. Kumar, "Maintenance resource prioritization in a production system using cost-effective importance measure". In International Workshop and Congress on eMaintenance: 22/06/2010-24/06/2010, pp. 196-204. Luleåtekniskauniversitet, 2010.

[2] S. Gupta, J. Bhattacharya, J. Barabady, and U. Kumar, "Cost-effective importance measure: a new approach for resource prioritization in a production plant". International Journal of Quality & Reliability Management, 2013.

[3] W. Kuo, and X. Zhu, "Importance measures in reliability, risk, and optimization: principles and applications". John Wiley & Sons, 2012.

[4] P.Do, and C. Bérenguer, "Conditional reliability-based importance measures. Reliability Engineering & System Safety", 106633. doi: 10.1016/j.ress.2019.106633, 2019.

[5] J. Zheng, H. Okamura, and T. Dohi, "Reliability importance of components in a real-time computing system with standby redundancy schemes". International Journal of Mathematical, Engineering and Management Sciences, 3(2), 64, 2018.

[6] M. Van der Borst, and H. Schoonakker, "An overview of PSA importance measures". Reliability Engineering & System Safety, 72(3), 241-245, 2001.

[7] S.Wu, and F. P. Coolen, "A cost-based importance measure for system components: An extension of the Birnbaum importance". European Journal of Operational Research, 225(1), pp.189-195, 2013.

[8] IEC60300-3-3: Life cycle costing, 1996

[9] SIEMENS GT-600 MANUEL. Available: https://essay.utwente.nl/71939/1/Stageverslag_Stefan%20Klooster.pdf

[10] S. P. Ryan, "The costs of environmental regulation in a concentrated industry". Econometrica, 80(3), 1019-1061,2012.

[11] OREDA Participants OREDA handbook (4th ed.). Trondhim: OREDA Participants, 2002.

[12] D.MANNAN, "Lees' Loss Prevention in the Process Industries". 2005. Web Links, 1-3

Rapid and Low Cost Laser Prototyped Microfluidic Devices for On-Chip Emulsion Generation

S. GUCLUER[1]

[1] Aydın Adnan Menderes University, Aydın/Turkey, sgucluer@adu.edu.tr

Abstract **- Microfluidic platforms provide numerous benefits in fluid manipulation for sample preparation, disease diagnostics, and material synthesis. Especially for precise chemical processing and formation of personalized drugs for drug delivery studies, the field of microfluidics offers extremely well-controlled dosing and reagent concentrations. In addition, controlled and closed environment of the microfluidic devices offer contamination-free chemical synthesis and bio-sample analysis. While the microfluidics provides these benefits, current device fabrication methods are costly and time-consuming. The traditional approach for microfluidic device fabrication requires expensive cleanroom fabrication facilities that cannot be found in most of the research institutes. Therefore, more accessible, and simpler means of microfluidic device fabrication is necessary for low-resourced laboratory environments. In this work, rapid laser prototyping is adopted to fabricate microfluidic devices. For this, the microfluidic device is designed as multiple layers, and each layer is fabricated by using CO2 laser cutting. The middle layer of the device contains the fluidic channel. This layer is covered with industrial double-sided tape. Top, middle, and bottom layers are pressed together to obtain a leak-free microfluidic device. For proof of concept, a microfluidic device with three inlets and single outlet is designed for water in oil droplet generation. Various flow rate ratios are tested, and different size droplet generation is studied in the fabricated microfluidic device. Overall, the rapid-laser prototyping is shown to be a suitable method for general purpose microfluidic platform. This approach can be a viable option for various applications in biology, medicine, and engineering.**

Keywords **- microfluidics, emulsions generation, laser prototyping, droplets, microsystems**

I. INTRODUCTION

THE field of microfluidics is rapidly evolving, and have been applied in solving new and more challenging problems in biomedical and engineering research [1]. From a fundamental point of view, the microfluidics deals with the manipulation of very small amounts of fluids ranging from picolitres to milliliters within small network of channels [2], [3]. In a microfluidic device, the size of the channels at least for one dimension should be smaller than 1 mm. The small size of microfluidic channels enables different flow characteristics compared to the bulk fluid motion in bigger scales [4]–[7]. For example, the flow in microfluidics is commonly characterized as laminar flow having Reynolds numbers usually less than 100 [8], [9]. In addition, consumption of very small amount of chemicals in microfluidic devices provide a low-cost alternative to large scale batch chemical processes [10], [11]. Therefore, microfluidic platforms have emerged as low-cost, contamination-free and precise miniaturized reactors [12]. Even though the cost of an individual microfluidic device is low, the method and required facilities for the fabrication of microfluidic devices are expensive and not available in most of the universities in the world. Therefore, new approaches for low-cost microfluidic device fabrication are desired to make the research accessible in this field.

The mainstream method of microfluidic chip fabrication relies on photolithography and cleanroom fabrication including wet processing and dry etching [13]. In the photolithography process, photo resists are UV exposed to form patterns which are defined using either masks or computer-controlled UV illumination [11], [14]. For both cases, the required equipment costs more than 300,000 USD for only one function. In addition to the cost of these systems, process complexity and durations are also important parameters to consider for the standpoint of practicality of microfluidic device fabrication [15]–[17]. For example, a simple microfluidic mold preparation requires multiple steps of spin-coating, baking, UV-exposing, developing, and hard baking using standard negative photo resists. It is even more complicated if deep reactive ion etching is involved to fabricate master molds from silicon wafers directly [8], [18]. As an alternative to the traditional device fabrication approach, 3D printing has recently been applied in fabrication of some microfluidic devices with decent functionalities [19]–[21]. For example, Lee et al. presented 3D-printed Quake-style microvalves and micropumps for variety of microfluidic functions [22]. Even though 3D printing can be a good alternative to photolithography, the process is not currently suitable for fabricating optically clear devices due to the material limitations.

In this study, a simple CO_2 laser cutting system is used to rapidly prototype microfluidic devices using poly (methyl methacrylate) (PMMA). PMMA is a safe, optically transparent, and low-cost material that is suitable for

microfluidic applications. As a proof-of-concept application, water-in-oil droplets are formed in the fabricated microfluidic device. Simplicity and functionality of the laser prototyped microfluidic device can enable researchers in low-resourced laboratories to apply microfluidics in fundamental and applied research.

II. Materials and Methods

For the fabrication of the device, first a strong double-sided tape is applied to both sides of a PMMA sheet that was cut into 20 × 20 cm in size. The tape is 20 cm in width. PMMA sheets of 0.5-, 1-, and 2-mm thicknesses were used for various layers of the microfluidic device. Each layer of the device was designed in computer aided drawing software AutoCAD as shown in Figure 1. Then, the files were uploaded to the laser system and each piece was cut using optimal feed rate and laser powers. The laser system is a CO_2 powered 100W system (Lazerfix, 100W, Konya, Turkey). A separate software called RDWorksV8 was used for the laser cutting system. The drawings were exported as DXF files from the AutoCAD, and these files imported directly into RDWorksV8.

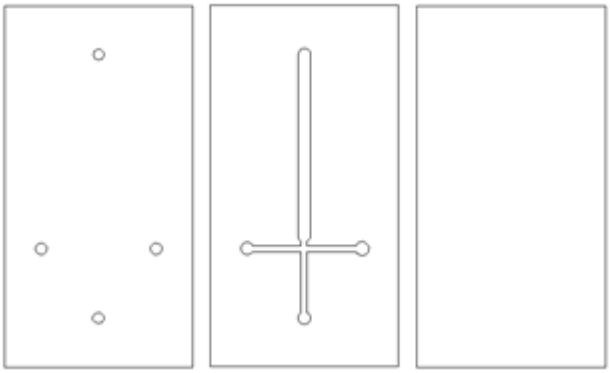

Figure 1: CAD drawing of the layers of microfluidic device.

The microfluidic channel layer which was in the middle PMMA sheet is designed to have three inlets and one outlet. The thickness of this layer was 0.5 mm. The width of the microfluidic channel is 1 mm, and the width of each inlet channel was 0.5 mm as shown in Figure 2. Laser cut layers are shown in Figure 3. The mid layer is different color because of the double-sided tape that was applied to both sides of the layer. Polyethylene tubes were inserted into the inlets and the outlet of the device, and a 5-minute fast curing epoxy (E340, Akfix, Istanbul, Turkey) was used to seal permanently fix the tubes. A Home-built syringe infuser was used to inject mineral oil and deionized water into the fluidic device. An optical microscope (OX.2053-PLPH, Euromex, Arnhem, The Netherlands) with inverted lens geometry was used to observe and record the experiment. FIJI image analysis software was used to analyze the images for the emulsion size measurements.

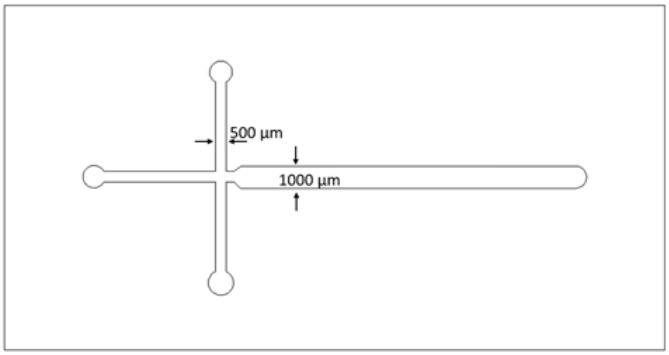

Figure 2: Dimensions of the microfluidic channel.

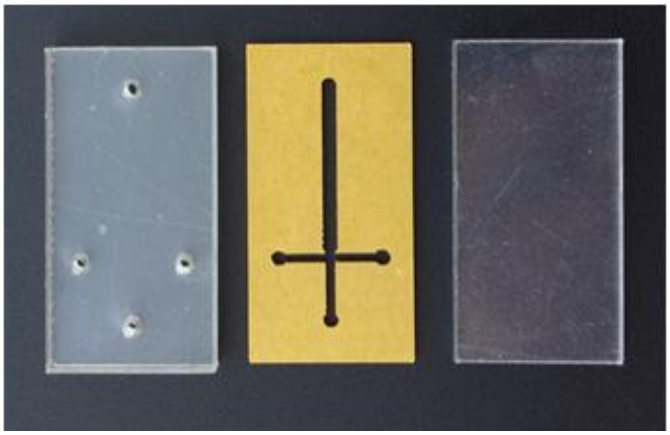

Figure 3: Pictures of the three layers of microfluidic device.

III. Results and Discussion

Completely assembled device schematic and actual image is shown in Figure 4a and b. The assembled device is slightly opaque as seen in the top view in Figure 4b. This is due to the applied double-sided tape. The actual fluidic channel is optically transparent because no adhesive overlaps the channel. The device is tested for the fluid leaks and found to be leak-free. For the leak test, up to 500 µl/min flow rates were applied to the device without any visible leakage. The schematic depiction of the leak testing is shown in Figure 5. Here, the total flow rate was gradually increased until a leak is observed in the device.

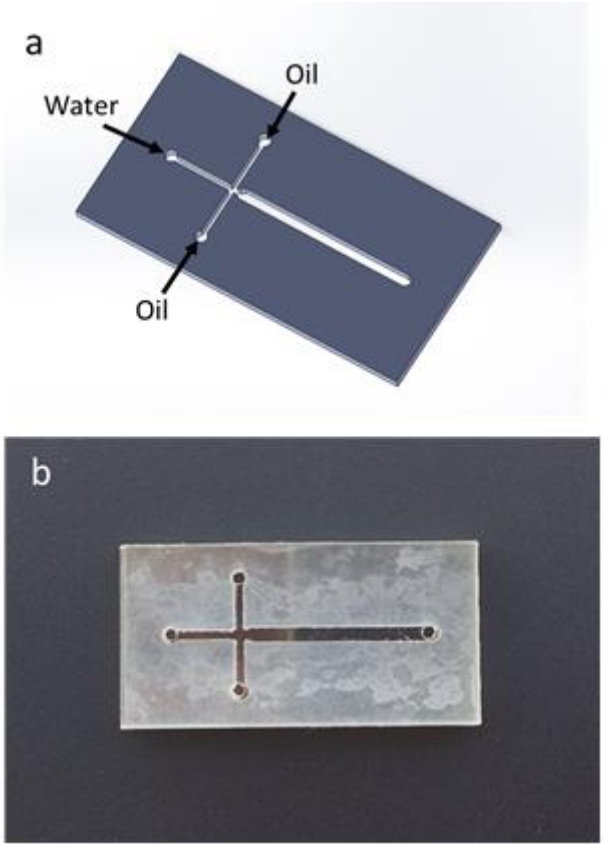

Figure 4: Picture and schematic of the assemble device.

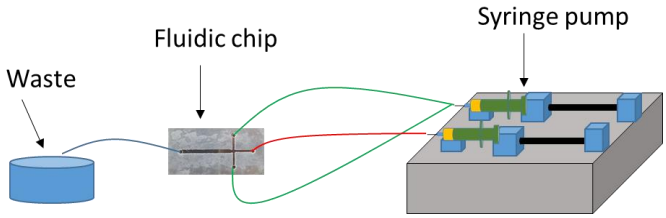

Figure 5: Schematic of the device leak testing using a syringe pump.

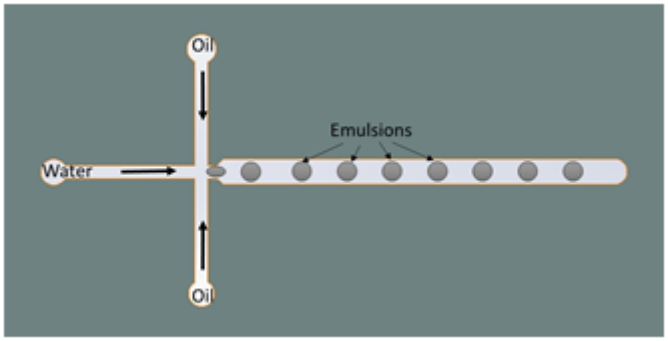

Figure 6: Working principle of the system.

The working principle of the device is shown in Figure 6. This is a well-established and heavily studied emulsion generation channel geometry [23]. This simple example was used to demonstrate operation and suitability of the fabricated microfluidic device. Emulsion (or droplet) generation in microfluidics relies on immiscibility of two fluids such as water and oil. In this example, deionized water and mineral oil were used to form the emulsions. The mineral oil used in this work has a viscosity of 206.89 mPa.s. The oil flows were injected from the side inlets of the device while the water flow was infused from the center inlet. This way, water in oil emulsions were targeted. In this kind of applications, various chemicals or cells can also be enclosed in size controllable emulsions.

For the generation of the emulsions, flow rate of the water stream was set as 20 µl/min, and the total flow rate of the oil flows was gradually increased from 6 µl/min to 40 µl/min. The lowest flow rate of the oil phase corresponds to a flow rate ratio of 0.3 between the oil and water flows. Figure 7 shows the shape of formed emulsions for three different oil phase flow rates. The lowest oil flow rate (Figure 6a) yielded larger and non-uniform emulsions. As the flow rate was increased the droplets got smaller and more uniform in size. For the oil flow rate of 40 µl/min droplets are much smaller (about 60 micrometers in diameter in average) and more uniform in size. Very small droplets that are seen in Figure 6b and c occurred after the collection of the generated emulsions during which unwanted agitation of the fluids occurred. These very small droplets were considered outliers and they were excluded from the calculations of the average emulsion size.

Characterization of the emulsion size as a function of the oil flow rate is given in Figure 8. The larger error bars seen for the emulsions generated at the smaller flow rates demonstrates the non-uniform size distribution at lower flow rates. The experiments were repeated for 5 times for each condition and standard deviation was calculated and used as error bars. As the flow rate of the oil stream was increased, the emulsions got smaller and more uniform as shown in Figure 8. It was possible to obtain emulsions that were less than 100 micrometers in diameter. Further flow rates were not tested in this work. Other than the three-inlet design used in this work, different droplet generation mechanisms and higher flow rates will be studied in the future work.

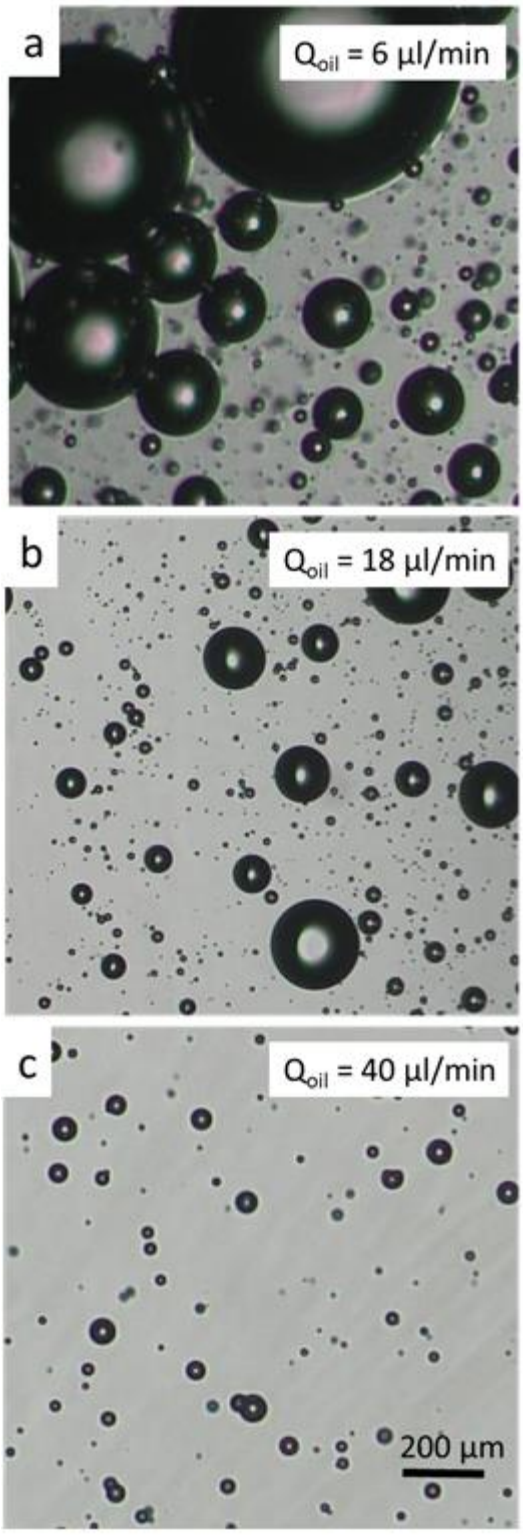

Figure 7: Pictures of the generated emulsions at a) 6, b) 18, and c) 36 µl/min oil flow rates.

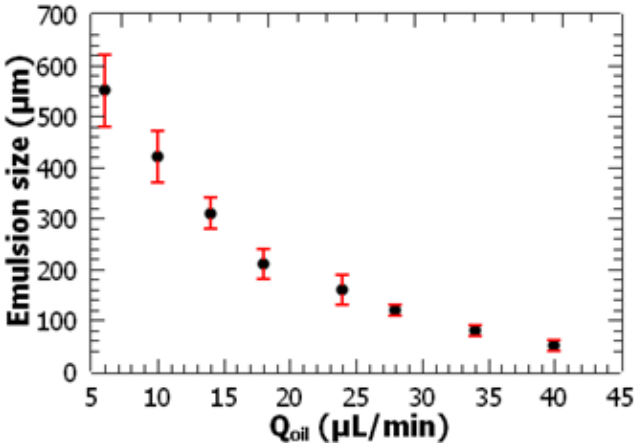

Figure 8: Emulsion size versus oil flow rate characterization.

IV. Conclusion

A simple and low-cost microfluidic device is demonstrated for on-chip emulsion generation. Evolving necessities of medical research and applications require unconventional approaches to produce rapid and simple solutions. For example, during the recent global covid pandemic, 3D printing was adopted to fabricate respirators, face shields and mask holders even in very remote places. In the developing countries, lab-on-a-chip medical device fabrication is still challenging due to required central facilities and costly consumables. In this work, laser rapid prototyping was shown to be a suitable method for lab-on-chip device fabrication. Water in oil droplets were successfully generated using the fabricated device. This demonstration shows the potential of simple device fabrication approaches for biomedical and engineering research.

Acknowledgment

Discussions and feedback received from Dr. Fatih Akkoyun and Osman Guler were greatly appreciated.

References

[1] J. Wu, Q. Chen, and J.-M. Lin, "Microfluidic technologies in cell isolation and analysis for biomedical applications," *Analyst*, vol. 142, no. 3, pp. 421–441, 2017, doi: 10.1039/C6AN01939K.

[2] C.-Y. Lee, C.-L. Chang, Y.-N. Wang, and L.-M. Fu, "Microfluidic Mixing: A Review," *Int. J. Mol. Sci.*, vol. 12, no. 12, pp. 3263–3287, May 2011, doi: 10.3390/ijms12053263.

[3] X. Mao, S.-C. S. Lin, C. Dong, and T. J. Huang, "Single-layer planar on-chip flow cytometer using microfluidic drifting based three-dimensional (3D) hydrodynamic focusing," *Lab Chip*, vol. 9, no. 11, p. 1583, 2009, doi: 10.1039/b820138b.

[4] Y. K. Suh and S. Kang, "A Review on Mixing in Microfluidics," *Micromachines*, vol. 1, no. 3, pp. 82–111, Sep. 2010, doi: 10.3390/mi1030082.

[5] P.-H. H. Huang, M. Ian Lapsley, D. Ahmed, Y. Chen, L. Wang, and T. Jun Huang, "A single-layer, planar, optofluidic switch powered by acoustically driven, oscillating microbubbles," *Appl. Phys. Lett.*, vol. 101, no. 14, pp. 21–25, Oct. 2012, doi: 10.1063/1.4742864.

[6] T. A. Franke and A. Wixforth, "Microfluidics for miniaturized laboratories on a chip.," *Chemphyschem*, vol. 9, no. 15, pp. 2140–56, Oct. 2008, doi: 10.1002/cphc.200800349.

[7] L. A. Kuznetsova and W. T. Coakley, "Applications of ultrasound streaming and radiation force in biosensors," *Biosens. Bioelectron.*, vol. 22, no. 8, pp. 1567–1577, 2007, doi: 10.1016/j.bios.2006.08.023.

[8] A. Ozcelik *et al.*, "An Acoustofluidic Micromixer via Bubble Inception and Cavitation from Microchannel Sidewalls," *Anal. Chem.*, vol. 86, no. 10, pp. 5083–5088, May 2014, doi: 10.1021/ac5007798.

[9] S. Sareh, J. Rossiter, A. Conn, K. Drescher, and R. E. Goldstein, "Swimming like algae: biomimetic soft artificial cilia," *J. R. Soc. Interface*, vol. 10, no. 78, pp. 20120666–20120666, Nov. 2012, doi: 10.1098/rsif.2012.0666.

[10] E. Skerrett *et al.*, "Evaluation of a low-cost, low-power syringe pump to deliver magnesium sulfate intravenously to pre-eclamptic women in a Malawian referral hospital," *BMC Pregnancy Childbirth*, vol. 17, no. 1, p. 191, Dec. 2017, doi: 10.1186/s12884-017-1382-9.

[11] D. Qin, Y. Xia, and G. M. Whitesides, "Soft lithography for micro- and nanoscale patterning.," *Nat. Protoc.*, vol. 5, no. 3, pp. 491–502, Mar. 2010, doi: 10.1038/nprot.2009.234.

[12] F. Akkoyun and A. Özçelik, "A Battery-Powered Fluid Manipulation System Actuated by Mechanical Vibrations," *Actuators*, vol. 11, no. 5, p. 116, Apr. 2022, doi: 10.3390/act11050116.

[13] V. Studer, A. Pépin, Y. Chen, and A. Ajdari, "Fabrication of microfluidic devices for AC electrokinetic fluid pumping," *Microelectron. Eng.*, vol. 61–62, pp. 915–920, 2002, doi: 10.1016/S0167-9317(02)00518-X.

[14] Y. Xia and G. M. Whitesides, "SOFT LITHOGRAPHY," *Annu. Rev. Mater. Sci.*, vol. 28, no. 1, pp. 153–184, Aug. 1998, doi: 10.1146/annurev.matsci.28.1.153.

[15] D. J. Beebe, G. A. Mensing, and G. M. Walker, "Physics and Applications of Microfluidics in Biology," *Annu. Rev. Biomed. Eng.*, vol. 4, no. 1, pp. 261–286, Aug. 2002, doi: 10.1146/annurev.bioeng.4.112601.125916.

[16] N. Blow, "Microfluidics: in search of a killer application," *Nat. Methods*, vol. 4, no. 8, pp. 665–670, Aug. 2007, doi: 10.1038/nmeth0807-665.

[17] J. Ahn, J. Ko, S. Lee, J. Yu, Y. Kim, and N. L. Jeon, "Microfluidics in nanoparticle drug delivery; From synthesis to pre-clinical screening," *Adv. Drug Deliv. Rev.*, vol. 128, pp. 29–53, Mar. 2018, doi: 10.1016/j.addr.2018.04.001.

[18] S. Orbay, A. Ozcelik, H. Bachman, and T. J. T. J. Huang, "Acoustic actuation of in situ fabricated artificial cilia," *J. Micromechanics Microengineering*, vol. 28, no. 2, p. 025012, Feb. 2018, doi: 10.1088/1361-6439/aaa0ae.

[19] T. J. Wallin, J. Pikul, and R. F. Shepherd, "3D printing of soft robotic systems," *Nat. Rev. Mater.*, vol. 3, no. 6, pp. 84–100, Jun. 2018, doi: 10.1038/s41578-018-0002-2.

[20] G. Cai, L. Xue, H. Zhang, and J. Lin, "A Review on Micromixers," *Micromachines*, vol. 8, no. 9, p. 274, Sep. 2017, doi: 10.3390/mi8090274.

[21] V. E. Garcia, J. Liu, and J. L. DeRisi, "Low-cost touchscreen driven programmable dual syringe pump for life science applications," *HardwareX*, vol. 4, p. e00027, Oct. 2018, doi: 10.1016/j.ohx.2018.e00027.

[22] Y.-S. Lee, N. Bhattacharjee, and A. Folch, "3D-printed Quake-style microvalves and micropumps," *Lab Chip*, vol. 18, no. 8, pp. 1207–1214, 2018, doi: 10.1039/C8LC00001H.

[23] S.-Y. Teh, R. Lin, L.-H. Hung, and A. P. Lee, "Droplet microfluidics," *Lab Chip*, vol. 8, no. 2, pp. 198–220, 2008, doi: 10.1039/B715524G.

Investigation of The Effect of the Use of Top Deflectors on Aerodynamic Performance in Vehicles with CFD Analysis

H. KEPEKÇİ[1]

[1]Nişantaşı University, Istanbul/Turkey, haydar.kepekci@nisantasi.edu.tr

Abstract **-** Carbon-containing waste gases from vehicle exhausts are one of the main causes of climatic disasters. This problem is tried to be solved by reducing the amount of energy consumed by vehicles while they are in motion. To reduce fuel consumption, it is necessary to reduce the effect of aerodynamic drag force, which is the resistance on the solid surface in motion. It is known that high aerodynamic drag force increases fuel consumption. Reducing aerodynamic drag force is important not only for fuel consumption but also for wind noise and roadholding. Heavy vehicles such as trucks have high drag forces due to the width of their surface areas. However, this situation can be minimized with changes to be made in vehicle designs. In this study, the effect of the use of top deflectors on the drag force for trucks has been investigated. In this theoretical study, separate calculations have been made for different vehicle velocities and the results have been compared among themselves. In this study, which has been carried out using the computational fluid dynamics method, k-e has been preferred as the turbulence method. As a result, it has been concluded that the use of top deflectors reduces drag force, which in turn reduces fuel consumption.

Keywords **-** Aerodynamics, Computational fluid dynamics, Drag force, Top deflector.

I. INTRODUCTION

With the increasing dependence on technology in the rapidly globalizing world, energy requirement has increased at the same rate. Owing to the recent Covid-19 pandemic, it has been seen that both education and business life can be carried out remotely online. In the post-pandemic period, some schools and workplaces have decided to continue the remote working model. As a result of this situation, many houses have also started to be used as workplaces and the energy consumption of the houses has increased [1]. Most of the electrical energy is produced from oil and natural gas [2]. As a result, the fluctuation in the prices of one of the energy sources spreads to the other. As a result of the disagreements in the political process that started with the invasion of Ukraine by Russia, the world's largest energy exporter, in 2021, natural gas and oil shipments to Europe came to a halt [3]. The industrial production of the European countries, which experienced fluctuations in energy imports, decreased significantly and the prices of products increased. Countries facing the danger of economic instability have started to seek new energy sources for themselves. It is obvious that the use of petroleum will not be abandoned soon, both because renewable energy sources are not as efficient as conventional fuels and because it will take a long time to abandon vehicle engines that are currently in use. What needs to be done in this case is to reduce the amount of oil used. Petrol, which is an energy type with a wide usage area, is mostly used in the fuel needs of vehicle engines [4].

It is known that if the energy consumption of vehicles is reduced, the use of oil will also decrease. There are different studies on this subject. In addition to modifications that will increase the efficiency of vehicle engines, new designs are also made for vehicle body models. One of the changes made in addition to these designs is the part attachment called the deflector [5]. Parts called deflectors, which are designed to reduce aerodynamic drag, which is one of the energy loss causes of vehicles, also increase driving performance. Aerodynamic drag is proportional to the geometry of the vehicle. It is recommended to use deflectors to reduce the amount of energy lost by heavy vehicles such as trucks, tractors, trailers, and lorries from aerodynamic drag. Considering that the aerodynamic drag increases as the vehicle velocity increases, it is concluded that it is a priority to revise the geometric models of the vehicles that are frequently used on intercity roads and highways. As a result of the research, it has been seen that the truck drag forces can be reduced by up to 50%. Considering that the annual fuel cost per truck is 20 thousand dollars, the reduction in energy consumption will provide significant economic savings. Deflector parts can be attached to different parts of vehicles. Examples of these are the underbody, the space between the tractor and the trailer, the vehicle wheels, the side mirror, and the vehicle's upper area [6]. In this study, the effect of the deflector part, which will be used in the upper part of the truck, on the aerodynamic performance has been numerically investigated.

Numerous academic studies have been conducted on the aerodynamic performance of heavy vehicles such as trucks and lorries. Studies in recent years aim to save fuel by reducing the amount of drag in trucks. Most of the studies have been done with the CFD method. The main reason for the widespread use of the CFD method is that it saves time and money. The CFD method, which eliminates the necessity of setting up an experimental setup for any scientific study, is frequently used both in academia and in the sector [7].

Nabutola and Boetcher investigated the effect of underbody flow deflection of conventional and air-jet wheel deflectors on vehicle drag in their study using the CFD method. As a result of their research, they found that conventional wheel deflectors only reduced wheel drag but increased overall drag by close to 10%. They found that air-jet wheel deflectors, on the other hand, reduced drag by up to 1.5% at velocities of 35 m/s and above [8]. Khosravi et al. [9] investigated the effects of the use of deflectors and cabin blades on heavy commercial vehicle drag. For their study, they modeled the vehicle body structure and made a CFD analysis. As a result, they found that the drag coefficient decreased by 20% when the cabin wing was added to both front edges of the cabin. If a suitable deflector is used in addition to the cabin wing, they achieved a 41% drag reduction compared to the simple model.

McCallen et al. [10], modeled the aerodynamic flow using the tractor-trailer model with the CFD method. They used RANS modeling in their work. They also developed a formulation to calculate aerodynamic flow using the LES model [10]. Miralbes and Castejon investigated boat tails to reduce aerodynamic forces in heavy vehicles and compared the results. They used the CFD method in their studies [11]. Chowdhury et al. [12] investigated the aerodynamic effects of various fuel-saving devices used in a commercial heavy vehicle. In their study with experimental methods, they subjected the 1/10 scale model truck to the wind tunnel test to measure the amount of aerodynamic drag. They used different deflection angles and operating velocities during these experiments. As a result, they found that the devices they used, including the deflector, reduced the aerodynamic drag by approximately 26% on the vehicle model. Gao et al. [13] designed different models of rear air deflectors to reduce aerodynamic drag in commercial trucks and compared these models with each other. In their study using the CFD method, they concluded that the base blades are the most effective design among the tail air deflectors and that approximately 7% drag reduction can be achieved with this design. Marks et al. [14] have studied the effective forces in the aerodynamic drag of trucks. In their experimental study, full-scale trucks moving at 50 mph were used. For models with gap seals and top deflectors, they achieved reductions of up to 35% in zero yaw resistance coefficient and up to 25% in wind average drag coefficient. Chilbule et al. [15] investigated the effect of changes in the profile of trucks on fuel consumption. They used the CFD method in their studies. They compared the coefficient of drag, lift coefficient, and pressure contours between the modified and unmodified truck model profiles. A wind deflector and swirl trap modifications were made in the modified truck model. With these modifications, a 21% reduction in aerodynamic drag was observed. Chowdhury et al. [16] made calculations using the CFD method to investigate the aerodynamic effect of various deflectors used in light trucks used in Bangladesh and Pakistan. As a result, they have seen that they can reduce aerodynamic drag by around 22% in local trucks, which are widely used in their country. They also concluded that with the reduction in drag force, fuel consumption can be reduced by around 12%. Chowdhury et al. [17] conducted experiments in a wind tunnel environment to investigate the effect of deflector use on fuel consumption in locally produced trucks in Bangladesh and Pakistan. As a result, they found that the use of deflectors reduced the total aerodynamic drag by 58% and fuel consumption by 13%. The aim of this study is to examine the airflow around a moving truck and to examine the effect of the top deflector on aerodynamic drag. Truck models with and without top deflectors have been used in CFD analyses for three different velocities. Boundary conditions have been assumed to be the same for each analysis. The obtained drag force values from result of the calculations have been compared and interpreted.

II. MATERIAL AND METHODS

2.1. THEORETICAL AND MATHEMATICAL BACKGROUND

The vertical and tangential forces acting on the surface of an object by the air create aerodynamic forces. The most important aerodynamic forces are lift (F_L) and drag (F_d). Lift force is mostly calculated in aviation, while drag force is used in horizontal motion analysis. The drag force acts in the opposite direction to the solid surface moving in the fluid [5]. The calculation of the aerodynamic drag force F_d is shown in Eq. 1.

$$F_d = (1/2) C_d \rho A V^2 \quad \text{..... (1)}$$

where C_d is drag coefficient, ρ is air density, A is the projected frontal area of the body, and V is the truck's velocity [18]. As can be seen from Eq. 1, the drag force is directly proportional to the front area of the vehicle and its velocity. The drag force is especially felt at high velocities. 60% of the fuel of the full truck and 40% of the fuel of the empty truck is spent on drag [6]. Since the front area of the vehicle is directly proportional to the drag force, the effect of this force on fuel consumption in trucks is higher than in automobiles. Another factor affecting the drag force is vehicle roughness. It is necessary to polish the rough surfaces where the drag force is an undesirable force [19]. If the vehicle windshield is inclined, the drag force will decrease. There are academic studies on this subject. The most well-known are the articles on Ahmed body [20]. In this study, analyzes have been made using the computational fluid dynamics (CFD) program. The calculated drag force values have been obtained directly through the codes in the program. There are steps to be done when any analysis is desired in CFD programs. First, the dimensions of the model to be analyzed should be determined and a geometric drawing should be made. Then the drawn geometry is subjected to a meshing process called mesh. The reason for this is to provide the result sensitivity by dividing the structure to be analyzed into smaller parts. Then, the boundary conditions are determined, and the analysis is started. As a result of the analysis, the values and images that are required to be calculated are obtained as output.

2.2. MODEL CONFIRMATION

The truck without the top deflector used in the analysis is given in Figure 1, the truck with the top deflector is given in Figure 2 and the dimensioning of the model is given in Figure 3. These drawings have been made using ANSYS Workbench. The drawn geometry is accepted as a one-piece body.

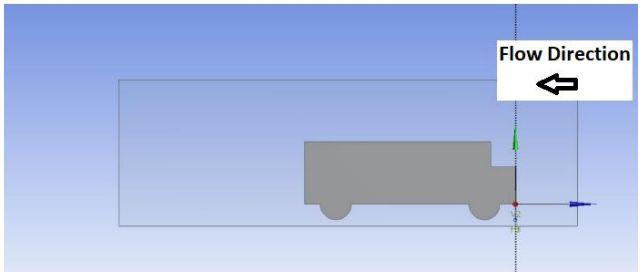

Figure 1. Truck model without deflector

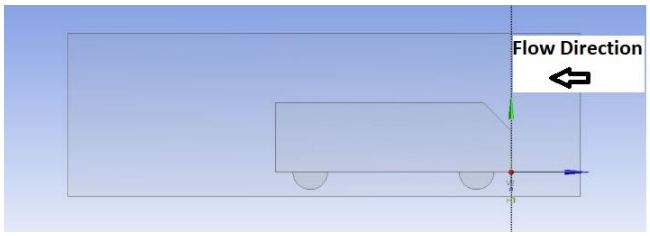

Figure 2. Truck model with deflector

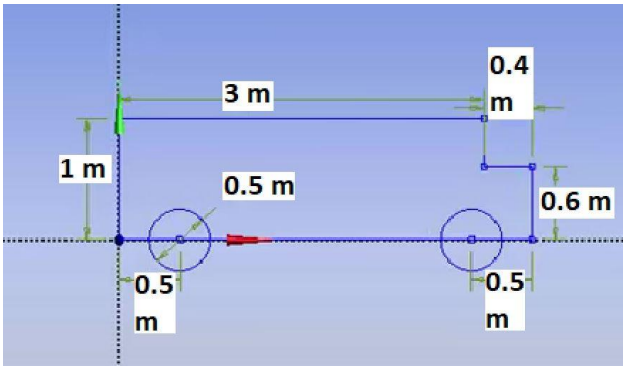

Figure 3. Dimensioning of the truck model

To calculate the drag force on the truck, the domain must be created and the air flow around it must be simulated. The created domain is given in Figure 4.

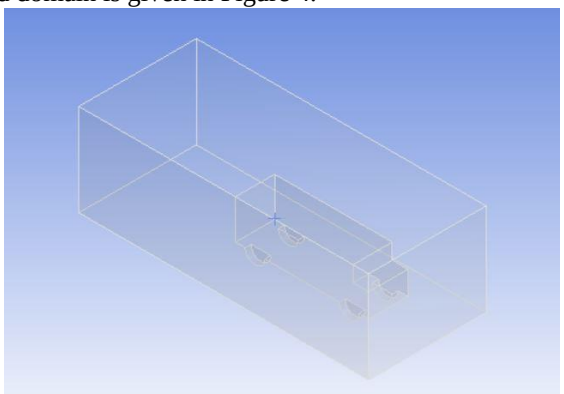

Figure 4. The domain used in the analyzes

Meshing, also called finite element discretization, is required to prepare the created domain for analysis. In the meshing process, the hexahedral and tetrahedral mesh has been used while creating the grids. Different element sizes are used to create a more refined mesh. To increase the accuracy of the results to be obtained from the analysis, the amount of mesh in the front of the truck has been increased and the mesh sizes have been narrowed. The generated mesh file has about 500,000 grid cells. The view of the obtained mesh structure is given in Figure 5.

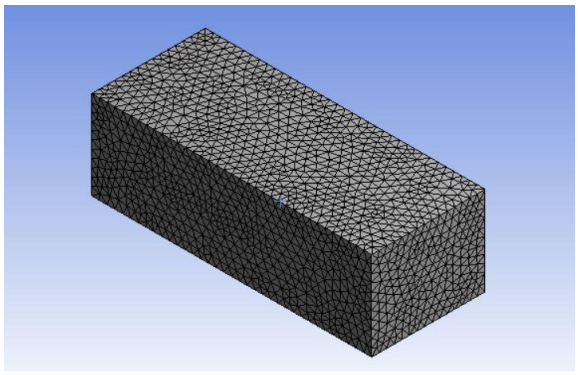

Figure 5. The generated mesh structures

It is assumed that the lateral edges and upper and lower surfaces of the domain are symmetrical. In the analyzes made, the truck velocity has been selected at three different values 50 km/h, 80 km/h, and 100 km/h. The selection of these velocity values is because the trucks have maximum velocity limits in the city, on the intercity roads, and on the highways, respectively. Turbulence intensity and turbulent viscosity ratio have been determined as 1% and 10%, respectively. These values are taken from similar studies in the literature. RANS-based Realizable k-ε model has been chosen as the turbulence method in the analysis. The reason for choosing this model is that it is frequently preferred in aerodynamic force analysis studies in the literature.

III. RESULTS AND DISCUSSION

ANSYS Fluent program has been used in the analysis. The drag force and drag coefficient values obtained from the calculations using three different velocity values for the models with and without top deflector of the truck in motion are given in the table below.

Table 1. Drag forces according to different velocity values

Truck model	Velocity [km/h]	Drag force [N]	Drag coefficient
Without top deflector	50	137.590	0.259
With top deflector	50	104.193	0.196
Without top deflector	80	351.066	0.660
With top deflector	80	259.823	0.489
Without top deflector	100	548.295	1.032
With top deflector	100	394.768	0.743

According to the data in Table 1, the use of top deflectors in trucks reduces the drag forces. This will also reduce fuel consumption. The pressure and velocity contours created by the drag force around the moving vehicle in the front areas of the truck models are given in Figure 6, Figure 7, Figure 8, and Figure 9 for the velocity values of 50 km/h and 80 km/h, respectively.

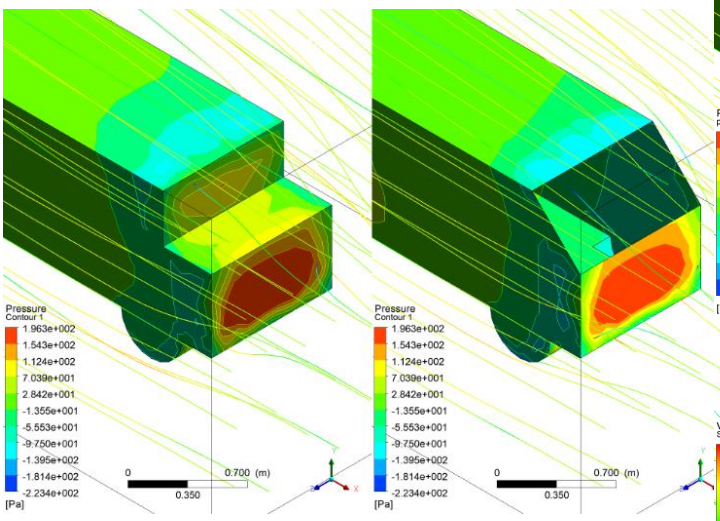

Figure 6. Pressure contours of truck models at 50 km/h

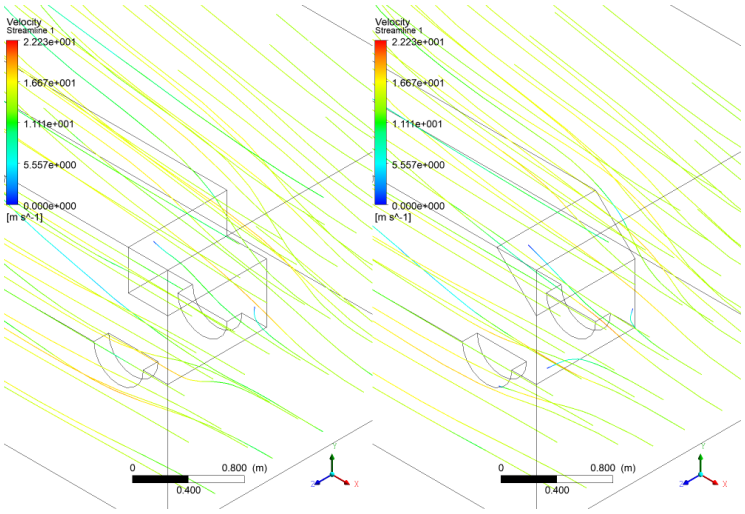

Figure 7. Velocity contours of truck models at 50 km/h

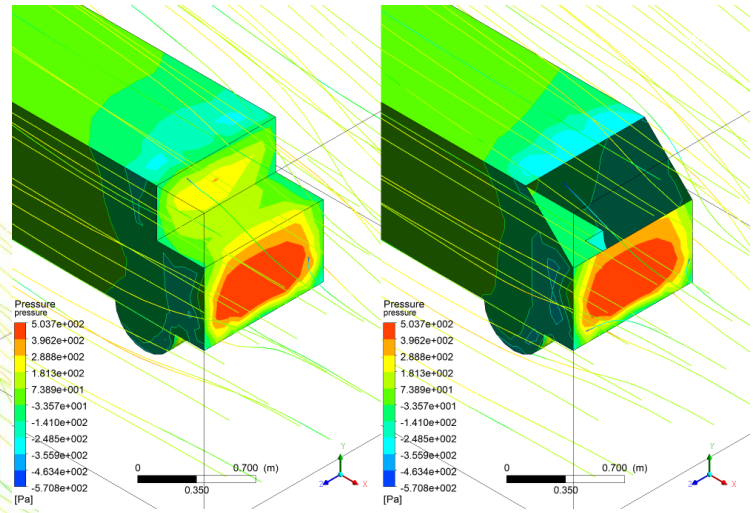

Figure 8. Pressure contours of truck models at 80 km/h

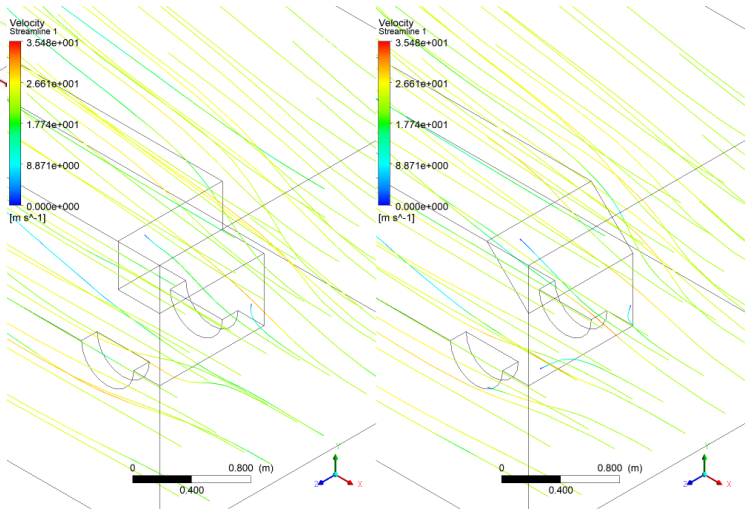

Figure 9. Velocity contours of truck models at 80 km/h

By looking at the contours obtained from the truck models moving at different velocities given in Figure 6, Figure 7, Figure 8, and Figure 9, it can be said that the pressure and velocity values affecting the front area increase with the increase in the velocity of the vehicle. However, it has been observed that increasing pressure and velocity values can be reduced using top deflectors.

IV. CONCLUSIONS

It has been observed that as the velocity of a moving truck increases, the drag force increases with or without the use of a top deflector. While the drag force of a truck moving at 50 km/h without a top deflector is 137.590 N and its Cd value is 0.259, when the truck's velocity reaches 80 km/h, the drag force becomes 351.066 N and the cd value is 0.660. It has been determined because of the analysis that the use of top deflectors reduces the drag force. The drag force of the truck with top deflector has been calculated as 137.590 N and Cd value of 0.259, while the drag force of the truck with top deflector has been calculated as 104.193 N and Cd value of 0.196. The drag force of the truck without top deflector, which moves at 80 km/h, is 351.066N and the Cd value is 0.660, while the drag force of the truck with the top deflector is 259.823 N and the Cd value is 0.489. The drag force of the truck without top deflector, which moves at 100 km/h, is 548,295 N and the Cd value is 1.032, while the drag force of the truck with the top deflector is 394,768 N and the Cd value is 0.743. The effect of the use of top deflectors on reducing the drag force is directly proportional to the velocity, but this effect is not linear. While the use of top deflectors reduced the drag force by 24.27% in the truck moving at 50 km/h, there has been a 26% reduction at 80 km/h and 28% at 100 km/h. Looking at these results, it can be said that the use of top deflectors is more efficient at high velocities. Based on these results obtained from the analysis, it is concluded that the use of top deflectors will reduce fuel consumption. It will be of great benefit to the country's economy if the use of top deflectors is primarily made widespread in commercial trucks and then made compulsory in the future. As a continuation of this study, the prototype of the truck model used in the analysis will be produced and subjected to wind tunnel tests. In the tests to be made, different top deflector geometries will be used, and the ideal top deflector shape will be determined.

REFERENCES

[1] F. Rowe, C. Robinson, and N. Patias, "Sensing global changes in local patterns of energy consumption in cities during the early stages of the COVID-19 pandemic", *Cities*, vol. 129, 103808, 2022

[2] I. Nueza, R. Garcíaa, and J. Osoriob, "A comparative evaluation of CO2 emissions between internal combustion and electric vehicles in small isolated electrical power systems - Case study of the Canary Islands", *Journal of Cleaner Production*, vol. 369, 133252, 2022.

[3] B. Steffen, and A. Patt, "A historical turning point? Early evidence on how the Russia-Ukraine war changes public support for clean energy policies", *Energy Research & Social Science*, vol. 91, 102758, 2022.

[4] K. Kim, J. Lee, and J. Kim, "Can liquefied petroleum gas vehicles join the fleet of alternative fuel vehicles. Implications of transportation policy based on market forecast and environmental impact", *Energy Policy*, vol. 154, 112311, 2021.

[5] W. Hanfeng, Z. Yu, Z. Chao, and H. Xuhui, "Aerodynamic drag reduction of an Ahmed body based on deflectors", *Journal of Wind Engineering and Industrial Aerodynamics*, vol. 148, pp. 34-44, 2016.

[6] Z. Kasim, and A. Filippone, "Fuel savings on a heavy vehicle via aerodynamic drag reduction", *Transportation Research Part D: Transport and Environment*, vol. 15 (5), pp. 275-284, 2010.

[7] H. Kepekci, "Comparative Numerical Aerodynamic Performance Analysis of NACA0015 and NACA4415 Airfoils" *International Journal of Engineering, Science and Information Technology*, vol. 2(1), pp. 144-151, 2022.

[8] K. Nabutola, and S. Boetcher (2021) "Assessment of conventional and air-jet wheel deflectors for drag reduction of the DrivAer model", *Advances in Aerodynamics*, vol.3 (29), pp.1-28, 2021.

[9] M. Khosravi, F. Mosaddeghi, M. Oveisi, and A. Khodayari, "Aerodynamic drag reduction of heavy vehicles using append devices by CFD analysis", International Journal of Heavy Vehicle Systems, vol. 19 (2), pp. 115-127, 2012.

[10] R. McAllen, D. Flowers, T. Dunn, J. Owens, F. Browand, A. Hammache, A. Leonard, M. Brady, K. Salari, W. Rutledge, R. Ross, B. Storms, T. Heinec, D. Driver, J. Bell, S. Walker, and G. Zilliac, "Aerodynamic Drag of Heavy Vehicles Simulation and Benchmarking", SAE Technical Paper, pp. 2000-2209, 2000.

[11] R. Miralbel, and L. Castejon, "Aerodynamic analysis of some boat tails for heavy vehicles", *International Journal of Heavy Vehicle Systems*, vol. 19, pp. 115−120, 2012.

[12] H. Chowdhury, H. Moria, A. Ali, I. Khan, F. Alam, and S. Watkins, "A study on aerodynamic drag of a semi-trailer truck", *Procedia Engineering*, vol. 56, pp. 201 – 205, 2013.

[13] W. Gao., Z. Deng, and Y. He, "A Comparative Study of Tail Air-Deflector Designs on Aerodynamic Drag Reduction of Medium-Duty Trucks", *Aerodynamics of Road Vehicles*, vol. 8 (2-3), pp. 316-333, 2022.

[14] C. Marks, F. Buckley, and W. Walston, "An Evaluation of the Aerodynamic Drag Reductions Produced by Various Cab Roof Fairings and a Gap Seal on Tractor-Trailer Trucks", SAE Transactions, vol.85, pp. 366-374, 1976.

[15] C. Chilbule, A. Upadhyay, and Y. Mukkamala, "Analyzing the profile modification of truck-trailer to prune the aerodynamic drag and its repercussion on fuel consumption", Procedia Engineering, vol.97, pp. 1208-1219, 2014.

[16] H. Chowdhury, R. Juwono, M. Zaid, R. Islam, B. Loganathan, and F. Alam, "An experimental study on the effect of various deflectors used for light trucks in Indian subcontinent", *Energy Procedia*, vol. 160, pp. 34-39, 2019.

[17] H. Chowdhurya, B. Loganathana, I. Mustarya, H. Moriab, and F. Alama, "Effect of various deflectors on drag reduction for trucks", *Energy Procedia*, vol.110, pp. 561- 566, 2017.

[18] H. Kepekci, B. Zafer, H. Guven, and B. Korbahti, "Aeroacoustics Investigation of a Wind Turbine for Different Blade Tip Shapes Using Computational Fluid Dynamics Software", *Fresenius Environmental Bulletin*, vol.30 (11), pp.12037-12047, 2021.

[19] K. Flack, M. Schultz, and R. Volino, "The effect of a systematic change in surface roughness skewness on turbulence and drag", *International Journal of Heat and Fluid Flow*, vol. 85, 108669, 2020.

[20] F. Millan, T. Makela, L. Parras, C. Pino, and C. Ferrera, "Experimental study on Ahmed's body drag coefficient for different yaw angles", Journal of Wind Engineering and Industrial Aerodynamics, vol. 157, pp. 140-144, 2016.

Numerical Analysis of Laminar Heat Transfer for Nanofluids in a Microchannel

I. GOKTEPELI[1] and U. ATMACA[1]

[1] Department of Mechanical Engineering, Konya Technical University, Konya/Türkiye, igoktepeli@ktun.edu.tr
[1] Department of Mechanical Engineering, Konya Technical University, Konya/Türkiye, suatmaca@ktun.edu.tr

Abstract **- Nanoparticles having higher thermal conductivity are added to base fluids for specific volume fractions. Then thermal conductivity of nanofluids containing these nanoparticles is better than that of base fluids. Due to their better thermal properties, nanofluids are used in heat transfer enhancement. For this reason, numerical prediction of heat transfer by using nanofluids is important in engineering applications. In a microchannel exposed to uniform wall temperature, heat transfer problem has been solved for steady laminar nanofluid flow in terms of two-dimensional case. In terms of heating, inlet temperature for fluid is assumed to be lower than wall temperature. Flow is hydrodynamically fully developed and thermally developing while axial conduction and viscous dissipation have been neglected for solution. Finite difference method has been implemented to solve convective heat transfer problem for fluid region. Central difference scheme for radial direction and upwind scheme for axial direction have been implemented for discretization. Peclet number is Pe = 10000 corresponding to laminar flow when Prandtl numbers of base fluid and nanofluids are considered. Alumina (Al_2O_3) as a nanoparticle has been added to base fluid of water for various volume fractions of % $0 \leq \phi \leq$ % 4. Nusselt number for laminar flow under uniform wall temperature is constant and this value is considered for comparison. Different thermophysical models including density, specific heat, thermal conductivity and dynamic viscosity for nanofluids have been utilized from open literature and these numerical results have been compared for same nanofluid. As a result, convective heat transfer for increasing volume fractions has been augmented when compared to that of base fluid.**

Keywords **- Finite Difference Method, Heat Transfer, Microchannel, Nanofluid, Nanoparticle.**

I. INTRODUCTION

DUE to the limited energy resources, heat transfer enhancement for thermal systems is an important issue in terms of various industrial applications. For last decades, significant developments have been observed in electronics, communication and information technologies etc. Since thermal management of hybrid electric vehicles, space technologies and microprocessors are quite challenging, it is desired that fluids used in these fields are high-performance and compact. However, it is important that efficient use of energy resources is to increase heat transfer [1]. Compared to traditional channels, better thermal performance could be obtained by using either mini-channels or microchannels based on situations. Especially, microchannel applications are much considered as a crucial case when dimension and weight of heat transfer equipment determine the design [2]. Nevertheless, use of artificial surface elements or microchannels is limited in terms of heat transfer augmentation. Therefore, new techniques with potential to improve thermal properties of fluids are of intense interest to researchers. For instance, thermal properties of traditional fluids such as water, ethylene glycol, mineral oil are lower. Addition of metallic or non-metallic small particles to these base fluids is another method to improve the thermal properties [1]. Researchers have also studied on adding micro scale or smaller particles in terms of better thermal properties of fluids [3]. By adding nanoparticles to base fluids, nanofluids are obtained after developments in nanotechnology. Nanofluids are utilized since higher thermal conductivity could be provided by less volume fraction [1]. It is known that thermal conductivity of solid particles added is higher than that of fluids [3]. Thus, higher thermal conductivity by uniform dispersion of nanoparticles in the base fluid, cooling of the microchannel without clogging, reducing wear possibility and improving the heat conduction and mixing stability could be achieved with pumping power [1]. Pak and Cho [4] have determined dynamic viscosity values of water-Al_2O_3 and water-TiO_2 nanofluids for $10000 < Re < 100000$ in an experimental study. As a result of the study, they have recommended a correlation of Nusselt number for present conditions. Maïga et al. [5] have numerically studied on forced convection of water-Al_2O_3 and ethylene glycol-Al_2O_3 in a tube exposed to uniform heat flux. Heat transfer has been augmented with increasing volume fractions for laminar and turbulent flows. Lee and Mudawar [6] have added Al_2O_3 nanoparticle having diameter of 36 nm for volume fractions of $0 \leq \phi \leq 2$. For $200 \leq Re \leq 1000$, they have recommended that nanoparticles could be used in microchannel. Nguyen et al. [7] have researched the effect of temperature and particle diameter on dynamic viscosity for water-Al_2O_3 and water-CuO. In terms of experimental study, two different particle diameter values for water-Al_2O_3 and a value of particle diameter for water-CuO have been considered. For higher volume fractions, higher values of dynamic viscosity have been acquired with for water-Al_2O_3 with larger particle diameters. They have recommended a correlation of thermophysical properties which is valid for present conditions. Murshed et al. [8] have added nanoparticle with optimum dimensions and volume fraction to base fluids.

Otherwise, they have explained that there was clogging for duct outlet. Williams et al. [9] have experimentally investigated nanofluids of water-Al_2O_3 and water-ZrO_2 in terms of different volume fractions. For $9000 < Re < 63000$, they have compared the results with the ones of correlations for a horizontal pipe. For calculations of Nusselt number, Prandtl number and Reynolds number, they have reported that correlations were successful to obtain heat transfer and pressure drop, accurately. Mintsa et al. [10] have presented an experimental study to determine effective thermal conductivity values of water-Al_2O_3 and water-CuO by considering the effects of temperature, particle dimension and volume fraction. Effective thermal conductivity values have been enhanced for smaller particles and higher volume fractions. Zhu et al. [11] have added Al_2O_3 nanoparticles having diameters of 15 nm and 50 nm for various weight fractions Thermal conductivity has been enhanced up to %10.1 in the study including water as a base fluid. Chandrasekar et al. [12] have studied on water-Al_2O_3 for volume fractions of $0.33 \leq \phi \leq 5$. Nanoparticle diameter is 43 nm for study including both experimental and theoretical parts at room temperature. By increasing volume fraction, thermal conductivity and dynamic viscosity of nanofluid have been augmented. Ho et al. [13] have experimentally considered nanofluid of water-Al_2O_3 for $\% 0.1 \leq \phi \leq \% 0.4$ in case of thermal performance. Heat transfer has been augmented for nanofluids compared to result of base fluid. Teng et al. [14] have used Al_2O_3 nanoparticles having diameters of 20 nm, 50 nm and 100 nm for $0.5 \leq \phi \leq 2$ in terms of $10\ °C \leq T \leq 50\ °C$. Thermal conductivity has been increased for smaller nanoparticle, higher temperature and higher weight fraction for experimental study. Corcione [15] has used experimental data of open literature to attain values of thermal conductivity and dynamic viscosity for nanofluids. Obtained correlations have been compared in the study. Vajjha and Das [16] have examined density, specific heat, dynamic viscosity and thermal conductivity for metallic (Al_2O_3 and CuO) and non-metallic nanoparticles (SiO_2) which are added to base fluids. Mah et al. [17] have added Al_2O_3 nanoparticles having diameter of 64 nm for $0 \leq \phi \leq 8$ in terms of laminar flow. Heat transfer by convection showed decrement due to increasing volume fraction in case of viscous dissipation. Zhang et al. [18] have added Al_2O_3 nanoparticle to water for volume fractions including $\% 0 \leq \phi \leq \% 0.77$ and maximum %10.6 of heat transfer enhancement has been provided. Ting et al. [19] have investigated the effect of water-Al_2O_3 on axial conduction for $\% 0 \leq \phi \leq \% 10$ in terms of 60.4 m nanoparticle diameter. Trinavee et al. [20] have studied on water-Al_2O_3 nanofluid for volume fractions of $\% 1 \leq \phi \leq \% 4$. Nanoparticle diameter was 38 nm in their study. They have compared thermophysical properties in terms of temperature dependence. Arjun and Rakesh [21] have added Al_2O_3 nanoparticle with 23 nm diameter to water for $\% 0 \leq \phi \leq \% 5$. In the study for $5 \leq Re \leq 11980$, they have observed that heat transfer enhancement is better in case of laminar flow. Ambreen and Kim [22] have numerically studied on heat transfer by nanofluids of water-Al_2O_3 and water-TiO_2 for laminar flow. They have recommended nanoparticles with smaller diameter for their problem. Lodhi et al. [23] have added Al_2O_3 nanoparticle to water in terms of $\% 1 \leq \phi \leq \% 3$. Heat transfer has been augmented up to % 24.5 when compared to value of a case including only water. Loh et al. [24] have numerically examined forced convective heat transfer problem of nanofluids in a parallel-plate microchannel. They have considered water-Al_2O_3 and water-TiO_2 in terms of viscous dissipation effect.

In the present study, heat transfer problem has been solved as a two-dimensional case for steady laminar nanofluid flow. Peclet number is Pe = 10000 corresponding to laminar flow when Prandtl numbers of base fluid and nanofluids are considered. The case is two-dimensional and steady flow has been considered while axial conduction and viscous dissipation have been neglected. Alumina (Al_2O_3) as a nanoparticle has been added to base fluid of water for various volume fractions of $\% 0 \leq \phi \leq \% 4$. Thermophysical property models of two different studies have been implemented.

II. Numerical Method

In a microchannel exposed to uniform wall temperature, heat transfer problem has been solved as a two-dimensional case for steady laminar nanofluid flow. As presented in Figure 1, inlet temperature for fluid (T_0) is assumed to be equal for $-\infty \leq x \leq 0$ but lower than wall temperature (T_1) in terms of heating between $0 \leq x \leq +\infty$. Peclet number is Pe = 10000 corresponding to laminar flow when Prandtl numbers of base fluid and nanofluids are considered. Alumina (Al_2O_3) as a nanoparticle has been added to base fluid of water for various volume fractions of $\% 0 \leq \phi \leq \% 4$.

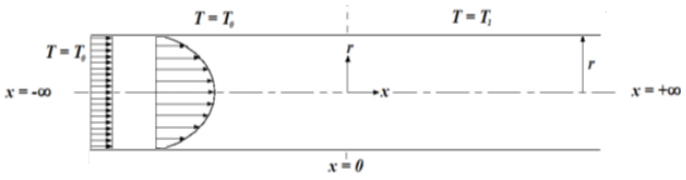

Figure 1: Two-dimensional flow region.

For numerical procedure, general energy equation has been given in (1). Here, velocity components of u, v and w are included for three-dimensional coordinate system. In this equation, t stands for term of "time". Moreover, density (ρ), specific heat (C_p) and thermal conductivity (k) have been presented. An equation for velocity profile has been presented in (2). For this equation, axial velocity component is based on radial coordinate (r), inner radius (r_{wi}) and mean velocity value (u_m).

$$\rho C_p \left[\frac{\partial T}{\partial t} + v\frac{\partial T}{\partial r} + \frac{w}{r}\frac{\partial T}{\partial \theta} + u\frac{\partial T}{\partial x}\right] = \frac{1}{r}\frac{\partial}{\partial r}\left(k\, r\frac{\partial T}{\partial r}\right) + \frac{1}{r^2}\frac{\partial}{\partial \theta}\left(k\frac{\partial T}{\partial \theta}\right) + \frac{\partial}{\partial x}\left(k\frac{\partial T}{\partial x}\right) + \phi \quad (1)$$

$$u = 2\,u_m\left(1 - \frac{r^2}{r_{wi}^2}\right) \quad (2)$$

The case is two-dimensional on x-r plane and steady flow has been considered. Only x-velocity component has been used. Flow is hydrodynamically fully developed and thermally developing while axial conduction and viscous dissipation have been neglected. As indicated in (3), energy equation has been specifically given with respect to assumptions of present study.

$$\rho C_p u \frac{\partial T}{\partial x} = \frac{1}{r}\frac{\partial}{\partial r}\left(k r \frac{\partial T}{\partial r}\right) \quad (3)$$

Using the equation in (3), equation for nanofluid flow has been shown in (4). In this equation, a subscript of "nf" has been used to represent nanofluid region. Furthermore, effective thermal conductivity is symbolized with k_{eff}.

$$\rho_{nf} C_{p_{nf}} \left[u \frac{\partial T_{nf}}{\partial x}\right] = \frac{1}{r}\frac{\partial}{\partial r}\left(k_{eff} r \frac{\partial T_{nf}}{\partial r}\right) \quad (4)$$

Non-dimensional terms have been given as in (5-11).

$$\theta_{nf} = \frac{T_{nf} - T_0}{T_1 - T_0} \quad (5)$$

$$\alpha_{nf} = \frac{k_{nf}}{\rho_{nf} C_{p_{nf}}} \quad (6)$$

$$Pe = \frac{2 u_m r_{wi}}{\alpha_{nf}} \quad (7)$$

$$x' = \frac{x}{Pe\, r_{wi}} \quad (8)$$

$$r' = \frac{r}{r_{wi}} \quad (9)$$

$$u' = \frac{u}{u_m} \quad (10)$$

$$k'_{eff} = \frac{k_{eff}}{k_{nf}} \quad (11)$$

By using the non-dimensional terms, non-dimensional energy equation has also been presented as in (12).

$$(1 - r'^2)\frac{\partial \theta_{nf}}{\partial x'} = \frac{1}{Pe}\frac{1}{r'}\frac{\partial}{\partial r'}\left(k'_{eff}\, r' \frac{\partial \theta_{nf}}{\partial r'}\right) \quad (12)$$

Finite difference method has been implemented to solve convective heat transfer problem for fluid region. Coefficients have been obtained by utilizing discretized equation for non-boundary grid points of Figure 2.

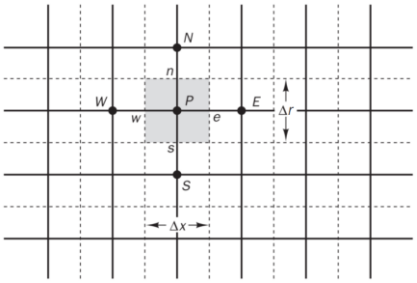

Figure 2: Grid structure on cylindrical coordinates.

Energy equation has been discretized by using non-dimensional energy equation. These coefficients have been presented in (13) and also with their related temperature terms in (14).

$$A_P = A_N + A_S + A_E + A_W \quad (13)$$

$$A_P\, \theta_P = A_N\, \theta_N + A_S\, \theta_S + A_E\, \theta_E + A_W\, \theta_W \quad (14)$$

The coefficients for the nanofluid region have been obtained by discretized equations in terms of appropriate initial and boundary conditions. Temperature values have been determined by using Gauss-Siedel iterative method. Central difference scheme for radial direction and upwind scheme for axial direction have been implemented for discretization. Four different grid structures have been compared for the constant value of Nusselt number in a laminar flow exposed to uniform wall temperature. Only water has been considered as a base fluid. In terms of axial and radial directions, 150 x 30 elements have been chosen for the runs, respectively. Convergence limit has been considered as 10^{-5} for numerical solution.

Maïga et al. [5] have recommended thermophysical property models which are valid for % $0 \leq \phi \leq$ % 5 at 25 °C. Thermophysical property models for density, specific heat, thermal conductivity and dynamic viscosity have been given in (15-18), respectively.

$$\rho_{nf} = (1 - \phi)\rho_f + \phi\rho_p \quad (15)$$

$$C_{p_{nf}} = (1 - \phi)C_{p_f} + \phi C_{p_p} \quad (16)$$

$$k_{nf} = k_f\,(1 + 2.72\,\phi + 4.97\,\phi^2) \quad (17)$$

$$\mu_{nf} = \mu_f\,(1 + 7.3\,\phi + 123\,\phi^2) \quad (18)$$

In a study for addition of the same nanoparticle to water, different thermophysical property models have been proposed by Ho et al. [13]. Thermophysical property models are dependent of temperature in their study. Moreover, these models are valid for % $0 \leq \phi \leq$ % 4. These models for thermal conductivity and dynamic viscosity have been presented in (19-20), respectively. For density and specific heat, the equations in (15-16) have been used.

$$k_{nf} = k_f\,(1 + 2.944\,\phi + 19.672\,\phi^2) \quad (19)$$

$$\mu_{nf} = \mu_f\,(1 + 4.93\,\phi + 222.4\,\phi^2) \quad (20)$$

These models for same nanofluid have been compared in the present study for % $0 \leq \phi \leq$ % 4. In these models, ρ = 3880 kg/m^3, C_p = 773 J/kgK and k = 36 W/mK have been considered for Al_2O_3 nanoparticle with diameter of 13 nm [4].

III. Results and Discussion

Heat transfer problem has been solved as a two-dimensional case for steady laminar nanofluid flow. Peclet number is Pe = 10000 corresponding to laminar flow when Prandtl numbers

of base fluid and nanofluids are considered. Alumina (Al_2O_3) as a nanoparticle has been added to base fluid of water for various volume fractions of % $0 \leq \phi \leq$ % 4. Thermophysical property models of two different studies have been implemented.

Maïga et al. [5] have recommended thermophysical property models which are valid for % $0 \leq \phi \leq$ % 5 at 25 °C. By using these models, solution has been done. Alumina (Al_2O_3) has been added to water for % $0 \leq \phi \leq$ % 4. As a result, variation of Nusselt numbers through the channel has been indicated in Figure 3.

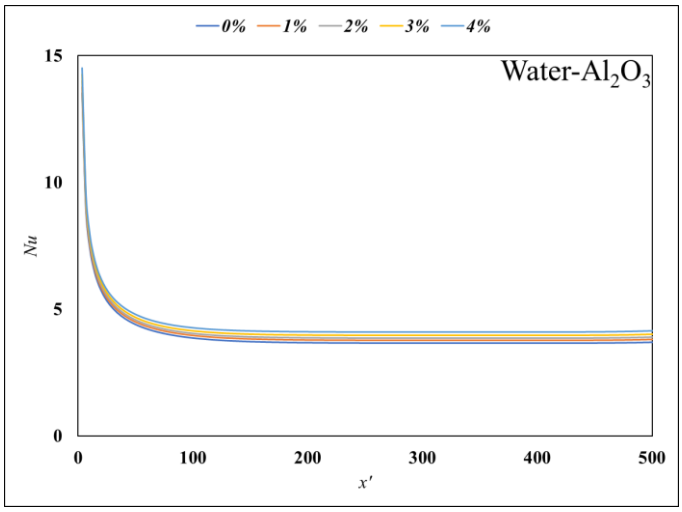

(a)

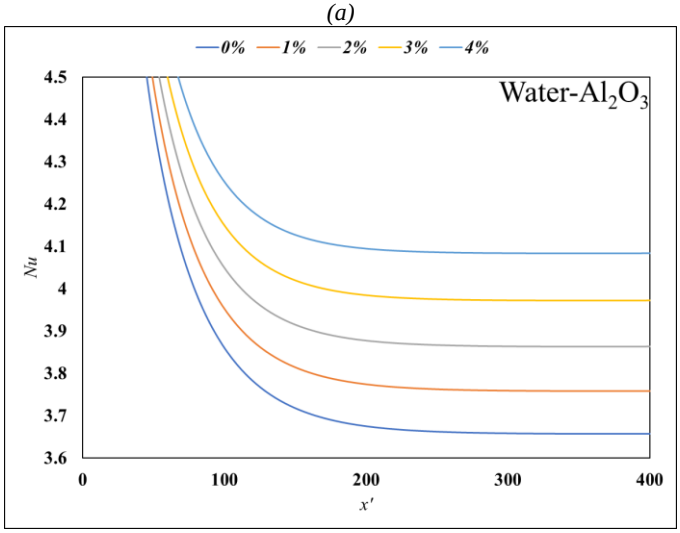

(b)

Figure 3: Effect of volume fractions on Nusselt number variations through microchannel length in terms of a) overall and (b) detailed views for thermophysical property models by Maïga et al. [5].

Heat transfer has been enhanced with respect to Nusselt number values of Figure 3. Heat transfer enhancement has been obtained due to increment of heat conductivity by adding nanoparticle to water. Heat transfer has been augmented by % 2.55 for volume fraction of ϕ = % 1 when compared to the value of water. Similarly, heat transfer has been augmented by % 5.19 for volume fraction of ϕ = % 2. In terms of volume fraction of ϕ = % 3, percentage of heat transfer enhancement is % 7.92 compared to Nusselt number of a case including only water. Heat transfer has been augmented by % 10.75 for volume fraction of ϕ = % 4. Heat transfer tends to increase for ascending volume fractions.

In a study for addition of the same nanoparticle to water, different thermophysical property models have been proposed by Ho et al. [13]. Thermophysical property models are dependent of temperature in their study. Moreover, these models are valid for % $0 \leq \phi \leq$ % 4. Alumina (Al_2O_3) has been added to water for % $0 \leq \phi \leq$ % 4 and solution has been done by using these models. Distribution of Nusselt numbers along the duct has been shown in Figure 4.

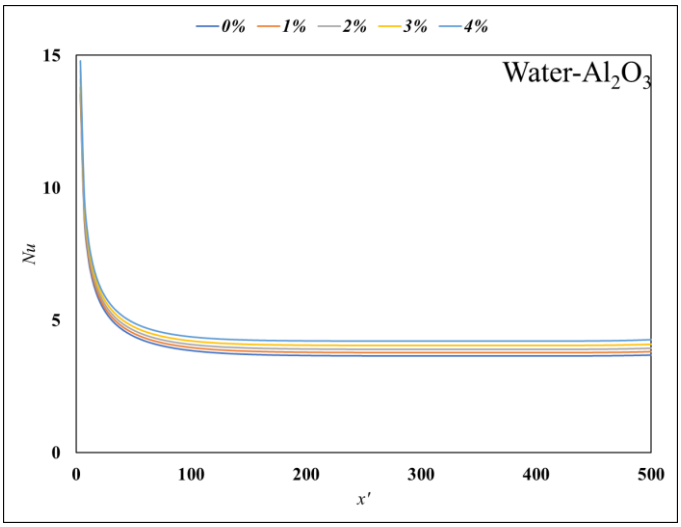

(a)

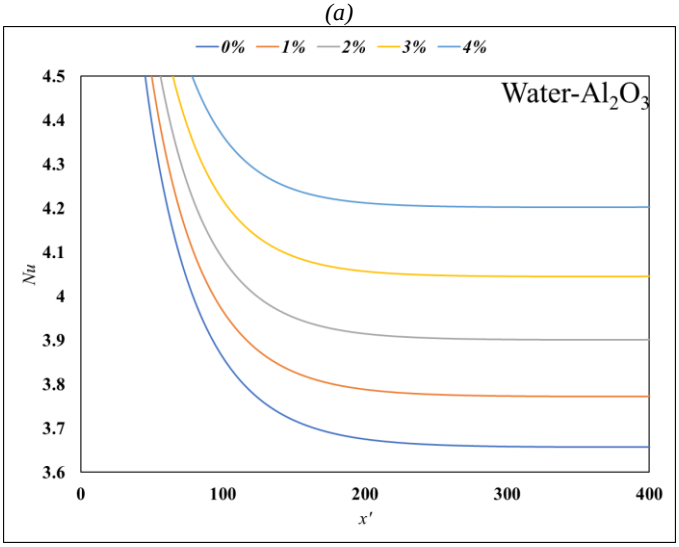

(b)

Figure 4: Effect of volume fractions on Nusselt number variations through microchannel length in terms of a) overall and (b) detailed views for thermophysical property models by Ho et al. [13].

Heat transfer has also been increased as indicated in Figure 4. This result is based on enhancement of Nusselt numbers. By adding nanoparticle to water, heat transfer augmentation has been attained owing to improvement of heat conductivity. Heat transfer has been augmented by % 2.89 for volume fraction of ϕ = % 1. Accordingly, heat transfer has been

augmented by % 6.15 for volume fraction of ϕ = % 2 when compared to the value of water. In terms of volume fraction of ϕ = % 3, percentage of heat transfer enhancement is % 9.78 compared to a case that only water is considered. Heat transfer has been augmented by % 13.77 for volume fraction of ϕ = % 4. As expected, heat transfer has been increased for ascending volume fractions of nanofluids.

For thermophysical property models of different studies, heat transfer has been enhanced by using nanofluids when compared to case of only water used. For increasing volume fractions of nanofluids, effect of heat transfer augmentation also increases as a result of the study. Furthermore, heat transfer increment is a little bit more by using temperature-dependent models.

IV. Conclusions

Heat transfer problem has been solved as a two-dimensional case for steady laminar nanofluid flow. Peclet number is Pe = 10000 corresponding to laminar flow when Prandtl numbers of base fluid and nanofluids are considered. The case is two-dimensional and steady flow has been considered while axial conduction and viscous dissipation have been neglected. Alumina (Al_2O_3) as a nanoparticle has been added to base fluid of water for various volume fractions of % $0 \leq \phi \leq$ % 4. Thermophysical property models of two different studies have been implemented. First of all, the coefficients for the nanofluid region have been obtained by discretized equations in terms of appropriate initial and boundary conditions. Temperature values have been determined by using iterative method and the appropriate grid structure has been determined with respect to Nusselt number value of a case including only water. In order to investigate effect of Al_2O_3 nanoparticle, appropriate thermophysical property models of open literature have been used. These models have been compared. Heat transfer has been increased by nanofluids compared to situation that only base fluid was considered. What is more, it has been augmented with the increasing volume fractions as a result. However, percentage of heat transfer enhancement has also increased via temperature-dependent models.

Acknowledgment

Authors are thankful for the project (2018-OYP-046) of Academic Staff Training Program (OYP). Furthermore, this paper belongs to ongoing PhD study of the first author.

References

[1] R. B. Ganvir, P. V. Walke, and V. M. Kriplani, "Heat transfer characteristics in nanofluid—A review," *Renewable and Sustainable Energy Reviews*, vol. 75, pp. 451–460, August 2017.

[2] S. G. Kandlikar, "History, advances, and challenges in liquid flow and flow boiling heat transfer in microchannels: A critical review," *Journal of Heat Transfer*, vol. 134(3), 034001, March 2012.

[3] X. Q. Wang, and A. S. Mujumdar, "Heat transfer characteristics of nanofluids: A review," *International Journal of Thermal Sciences*, vol. 46(1), pp. 1–19, January 2007.

[4] B. C. Pak, and Y. I. Cho, "Hydrodynamic and heat transfer study of dispersed fluids with submicron metallic oxide particles," *Experimental Heat Transfer*, vol. 11(2), pp 151–170, 1998.

[5] S. E. B. Maïga, C. T. Nguyen, N. Galanis, and G. Roy, "Heat transfer behaviours of nanofluids in a uniformly heated tube," *Superlattices and Microstructures*, vol. 35(3–6), pp. 543–557, March–June 2004.

[6] J. Lee, and I. Mudawar, "Assessment of the effectiveness of nanofluids for single-phase and two-phase heat transfer in micro–channels," *International Journal of Heat and Mass Transfer*, vol. 50(3–4), pp. 452–463, February 2007.

[7] C. T. Nguyen, F. Desgranges, G. Roy, N. Galanis, T. Maré, S. Boucher, and H. A. Mintsa, "Temperature and particle-size dependent viscosity data for water-based nanofluids–hysteresis phenomenon," *International Journal of Heat and Fluid Flow*, vol. 28(6), pp. 1492–1506, December 2007.

[8] S. M. S. Murshed, K. C. Leong, and C. Yang, "Thermophysical and electrokinetic properties of nanofluids–A critical review," *Applied Thermal Engineering*, vol. 28(17–18), pp. 2109–2125, December 2008.

[9] W. Williams, J. Buongiorno, and L. W. Hu, "Experimental investigation of turbulent convective heat transfer and pressure loss of alumina/water and zirconia/water nanoparticle colloids (nanofluids) in horizontal tubes," *Journal of Heat Transfer*, vol. 130(4), 042412, April 2008.

[10] H. A. Mintsa, G. Roy, C. T. Nguyen, and D. Doucet, "New temperature dependent thermal conductivity data for water–based nanofluids," *International Journal of Thermal Sciences*, vol. 48(2), pp. 363–371, February 2009.

[11] D. Zhu, X. Li, N. Wang, X. Wang, J. Gao, and H. Li, "Dispersion behavior and thermal conductivity characteristics of Al_2O_3–H_2O nanofluids," *Current Applied Physics*, vol. 9(1), pp. 131–139, January 2009.

[12] M. Chandrasekar, S. Suresh, and A. C. Bose, "Experimental investigations and theoretical determination of thermal conductivity and viscosity of Al_2O_3/water nanofluid," *Experimental Thermal and Fluid Science*, vol. 34(2), pp. 210–216, February 2010.

[13] C. J. Ho, W. K. Liu, Y. S. Chang, and C. C. Lin, "Natural convection heat transfer of alumina-water nanofluid in vertical square enclosures: An experimental study," *International Journal of Thermal Sciences*, vol. 49(8), pp. 1345–1353, August 2010.

[14] T. P. Teng, Y. H. Hung, T. C. Teng, H. E. Mo, and H. G. Hsu, "The effect of alumina/water nanofluid particle size on thermal conductivity," *Applied Thermal Engineering*, vol. 30(14–15), pp. 2213–2218, October 2010.

[15] M. Corcione, "Empirical correlating equations for predicting the effective thermal conductivity and dynamic viscosity of nanofluids," *Energy Conversion and Management*, vol. 52(1), pp. 789–793, January 2011.

[16] R. S. Vajjha, and D. K. Das, "A review and analysis on influence of temperature and concentration of nanofluids on thermophysical properties, heat transfer and pumping power," *International Journal of Heat and Mass Transfer*, vol. 55(15–16), pp. 4063–4078, July 2012.

[17] W. H. Mah, Y. M. Hung, and N. Guo, "Entropy generation of viscous dissipative nanofluid flow in microchannels," *International Journal of Heat and Mass Transfer*, vol. 55(15–16), pp. 4169–4182, July 2012.

[18] H. Zhang, S. Shao, H. Xu, and C. Tian, "Heat transfer and flow features of Al_2O_3–water nanofluids flowing through a circular microchannel–Experimental results and correlations," *Applied Thermal Engineering*, vol. 61(2), pp. 86–92, November 2013.

[19] T. W. Ting, Y. M. Hung, and N. Guo, "Effects of streamwise conduction on thermal performance of nanofluid flow in microchannel heat sinks," *Energy Conversion and Management*, vol. 78, pp. 14–23, February 2014.

[20] K. Trinavee, T. K. Gogoi, and M. Pandey, "Laminar convective heat transfer characteristic of Al_2O_3/water nanofluid in a circular microchannel," *Journal of Physics: Conference Series*, vol. 759, 012088, 2016.

[21] K. S. Arjun, and K. Rakesh, "Heat transfer enhancement using alumina nanofluid in circular micro channel," *Journal of Engineering Science and Technology*, vol. 12(1), pp. 265–279, January 2017.

[22] T. Ambreen, and M. H. Kim, "Effects of variable particle sizes on hydrothermal characteristics of nanofluids in a microchannel," *International Journal of Heat and Mass Transfer*, vol. 120, pp. 490–498, May 2018.

[23] M. S. Lodhi, T. Sheorey, and G. Dutta, "Single–phase fluid flow and heat transfer characteristics of nanofluid in a circular microchannel: Development of flow and heat transfer correlations," *Proceedings of the Institution of Mechanical Engineers, Part C: Journal of Mechanical Engineering Science*, vol. 234(18), pp. 3689–3708, 2020.

[24] A. K. W. Loh, G. M. Chen, and B. K. Lim, "Viscous dissipation effect on forced convective transport of nanofluids in an asymmetrically heated parallel-plate microchannel," *Case Studies in Thermal Engineering*, vol. 35, 102056, July 2022.

Easy to Carry and Mobile Biogas System Design

R. GÜNDEŞLİ[1] and K. BÜYÜKHAN[1]

[1] Barış Teknolojik Tesisat Sistemleri, Adana/Turkey, rahmi.gundesli@barismuhendislik.com.tr
[1] Barış Teknolojik Tesisat Sistemleri, Adana/Turkey, kubra.buyukhan@barismuhendislik.com.tr

***Abstract* – With the rapidly increasing population on earth, the need for energy is also increasing. With the inadequacy of the energy sources used, the orientation to alternative energy sources has become mandatory. With the increasing population and the increase in urbanization and consumption, a serious solid waste problem has occurred. The elimination of those wastes has gained great importance. In biogas power plants established in fields determined by certain regulations, electricity is obtained by burning the obtained biogas through the engine. The thermal energy need is met by utilizing waste exhaust gas thermal energy using a boiler. In addition, the heating need in the facility is met by using the engine cooling jacket water. Currently, those systems are usually sent to the site in parts and assembled on-site. In addition, a soundproofed steel or reinforced concrete building is required for the installation of the facility. This study conceptualizes a system design that can serve multiple facilities with a single investment. The designed system is easy to implement and mobile. Another feature of the design is the sound-damping feature. The main motivations are limited area conditions and the need for sound insulation. A design of the biogas system that shows the working principle of the system is shown. The design comprises a soundproof container that can carry the equipment in it statically. The sound insulation is designed to have a sound level of 65 dB from 10 m. The container's dimensions are a length of 12.000 mm, a width of 3.000 mm, and a height of 2.855 mm.**

***Keywords* - Biogas; container; silencer.**

I. INTRODUCTION

Biogas systems are recognized as an essential renewable energy source in the world. Many countries such as China, India, and Denmark emphasize this technology and support efforts to increase system efficiency. Biogas obtained from the system can be used as an energy source in heating and electricity production, and fermented waste, which is the other product of fermentation, is used as organic fertilizer to increase soil fertility. The main benefits stated as the reasons for preference for biogas systems can be classified as alternative energy, fermented fertilizers, and economic and social benefits in terms of environment and health.

Biogas is a flammable gas mixture obtained from all kinds of organic waste, such as animal, human and agricultural wastes, by anaerobic fermentation. Biogas is a colorless, odorless, lighter-than-air gas with a density of 0.83 compared to air, an octane number of approximately 110, a combustion temperature of 700 °C, a diesel fuel is 350 °C, and a flame temperature of 870 °C [1]. The composition of the biogas varies depending on the type of organic material from which it is obtained and the type of fermentation. The average heating value of biogas is 4700 - 6000 kcal/m³ [2]. This value depends on the methane gas content.

The heating value of biogas is approximately 23 MJ/m³. This value is greater than the calorific value of quality lignite coal. Considering the simplicity of the combustion systems of gases and the combustion efficiency of about 90%, it is seen that biogas is a fuel that can be easily used in energy production [3].

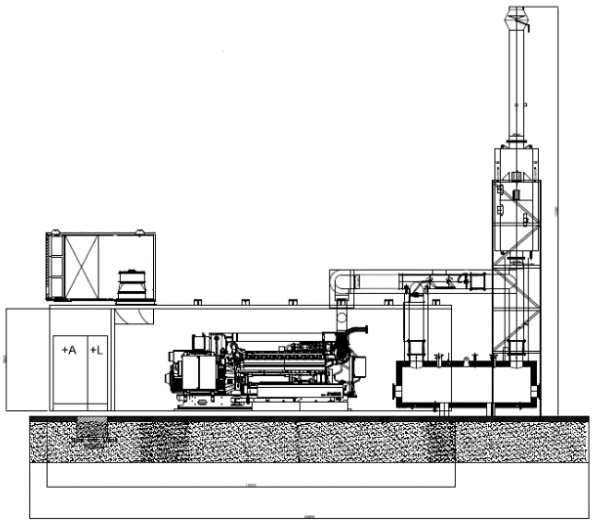

Figure 1: Biogas system design.

There are many advantages of the biogas system as shown in Figure 1. Wastes are generally degraded naturally. Uncontrolled deterioration of the design; cause great soil of water and air. Biogas production is required to use waste as energy raw material. The main purpose of the designed biogas system is to reduce the CO_2 ratio by using exhaust gas heat.

Application areas of wastes used as raw materials and technologies related to the areas required for normal evaluations.

With sustainability and recycling, energy to be redesigned is obtained. With the use of heat and electricity obtained because of biogas production, the need for fossil-based energy is reduced. The sale of heat and electricity strengthens the economy.

Solid fermented wastes produced because of biogas production can be used in the form of fertilizers and soil conditioners in the field, and liquid wastes can be used in irrigation. Thus, the expenditures for fertilizer and irrigation are reduced, and there is no need for the use of mineral fertilizers.

Nitrate pollution in surface and underground waters is reduced. If the resulting fermented waste is sold, the cost is reduced. Compared to other biological methods, less sludge is formed in anaerobic treatment, with higher organic loading rates. Significant reduction in the number of disease-producing organisms in fermented wastes at the exit of the facility and/or complete loss of process is achieved. Healthier and hygienic conditions are provided in waste disposal. The creation of expertise and workforce in the recycling sector is ensured. The image and prestige of the region/city change with the evaluation of waste.

With the small-scale biogas systems that can be used in the fields, additional income is provided to the farmers who cannot get sufficient yield and make a profit with the production of biogas. Fields can become large-scale enterprises with shared biogas systems.

In addition to many advantages, the disadvantages of biogas systems are as follows:

• Biogas generated during plant operation is flammable and explosive [4].

• System operating conditions must be carefully selected and checked regularly [5].

• If the rotted waste generated after fermentation is used as fertilizer, attention should be paid to the nitrogen content so that it does not cause pollution in the water and soil.

In order not to cause visual pollution and noise pollution, the design and operation of the facility should be done appropriately and use the right equipment.

The initial investment costs of biogas systems and the cost of removing waste from landfills may be higher for some regions and waste types. For this reason, the kind of waste to be used in the facility and the location selection should be made appropriately.

Technical knowledge is required for the design and operation of biogas systems. Control of biogas systems is mandatory. Additional costs and labor are required, especially in farm-scale biogas systems.

Benefits of Biogas Production Organic wastes (animal and vegetable origin) are generally burned directly, but some are given as fertilizer for agricultural lands.

Another common application for this type of waste is to use it as heat by burning, but it is not possible to produce heat in the desired way and it is not possible to use it as fertilizer at the same time.

Biogas is a cheap and environmentally friendly renewable energy type. Recycling occurs in various ways from the wastes formed.

Thanks to the production of biogas, the odor of animal manure is reduced to almost non-existent, and the effectiveness of disease elements that threaten human and environmental health arising from these manures will be eliminated.

After the biogas is produced, the wastes are not destroyed while turning into very valuable organic fertilizers.

While energy is gained from wastes by biogas production, it is also ensured that wastes are appropriately returned to the soil.

It provides many different usage areas of biogas (heating, heating, transportation, and steam generation). It provides employment opportunities.

Biogas technology not only meets energy needs but also has many benefits for the farmer, society, and the environment. Compared to the aerobic process, the anaerobic process used in biogas production has some advantages as well as some limitations. Its limitations are as follows:

Biogas is a renewable energy source. Since organic wastes or wastewater are used to produce it, the carbon taken from nature is returned to nature. What is preserved from nature is given back to nature.

The advantages of biogas cogeneration systems are as follows:

• It is a clean fuel: It prevents the environment. At the same time, there is no need for day and night.

• Reduces landfills: Minimizes final waste. easier storage needs.

• Cheap energy: Its raw material is waste. These wastes are converted into electricity, heat, and fertilizer.

• Domestic source: Domestic raw materials instead of imported fossil fuels

• Ease of business: Opportunity to create jobs from human advantage at their convenience. Provides rural technology transfer.

• Greenhouse effect: The greenhouse effect of CH_4 is 21 times simpler than that of CO_2. Unconsciously burned fuels increase greenhouse gas emissions in the atmosphere more. As a result of the emission of carbon dioxide gas from the smokestacks of the factories, significantly increases the greenhouse effect as a type of gas that causes global warming.

II. Design of the Biogas System

A. SILENCER DESIGN

Some boiler designs increase the noise effect. For this reason, silencers are used as shown in Figure 2. They are the elements designed to keep the level of the sound caused by possible excessive speed in the smokestack channels at the level allowed by the standards and to dampen the sound intensity that is more than necessary.

These silencers with round sections are produced in round type. Insulation thicknesses are used at 150mm.

The body, partition, and flanges of all silencers are made of galvanized sheets, and pressed glass wool is used.

The silencer design aims to provide the desired acoustic properties. However, in most instances, the structures used to reduce sound create a resistance to flow. This causes the static pressure to rise.

In silencers, acoustic properties increase in proportion to the volume, while the back pressure decreases with the increase in diameters. Therefore, the silencer volume is another design parameter. Since the volume of the silencers is usually determined before the interior design, the silencer design aims to provide optimum properties for the given volume.

During the design, other requirements such as strength, temperature, corrosion resistance, cost, and spark arrester required from the silencers should also be considered.

In addition to all this, the noise created by the flow and the

noise leaking from the silencer shell should be as small as possible.

There are various definitions for the quantitative determination of the acoustic efficiency of silencers. Transmission loss is the difference between the sound power level entering the silencer and the sound power level leaving the silencer, as shown in equation (1). Transmission loss is the most used parameter in studies on silencers.

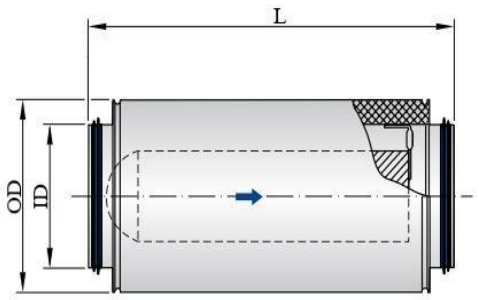

Figure 1: Silencer cross-section.

The equations and parameters used for silencer noise reduction are as follows.

$$TL = 10\,log_{10}(1/a_t) \quad (1)$$

$$1/a_t = C_1^2\,cos^2(\sigma L) + C_2^2\,sin^2(kL) \quad (2)$$

$$C_1 = cosh(\sigma L) + \frac{1}{2}(m + 1/m)\,sinh(\sigma L) \quad (3)$$

$$C_2 = sinh(\sigma L) + \frac{1}{2}(m + 1/m)\,cosh(\sigma L) \quad (4)$$

$$k = \frac{2\pi f}{c} \quad (5)$$

$$\lambda = c/f \quad (6)$$

$$m = \frac{S_2}{S_1} \quad (7)$$

$$\sigma = \frac{\pi f P_w}{2S_2}\left[\frac{\rho_e Y}{2\kappa}\right]^{1/2}\left[(1+\psi^2)^{1/2} - 1\right]^{1/2} \quad (8)$$

$$\frac{S_2}{P_w} = \frac{\frac{1}{4}\pi D_2^2}{\pi D_2} = \frac{1}{4}D_2 \quad (9)$$

$$(\sigma L)_{corr} = \sigma L + \Delta(\sigma L) \quad (10)$$

$$\Delta(\sigma L) = 0 \quad (11)$$

For $0.009 < (S_2)^{1/2}/\lambda < 1.00$:

$$\Delta(\sigma L) = 0.5756\left\{1 + \left[1 + \frac{1.912\,log_{10}(\sqrt{S_2})}{\lambda}\right)\right]^{\frac{1}{3}}\right\} \quad (12)$$

For $(S_2)^{1/2}/\lambda \geq 1.00$:

$$\Delta(\sigma L) = 1.1513 \quad (13)$$

It is desired that the transmission loss value defined by Equation 1 above should be high. However, there is a conflict between high conduction loss and low back pressure. To reduce the back pressure, the path taken by the exhaust gas should be shortened, turns should be avoided, the average flow rate should be reduced, and the body diameter of the silencer cylinder should be enlarged. However, in this case, the cost and volume of the silencer will increase, while the transmission loss (TL) value will decrease. For this reason, optimization should be made between cost, TL, and back pressure criteria during design.

Equations [2-13] stated above represent the sound damping coefficient and the damping correction coefficient, respectively.

Table 1: Mathematical variables for noise reduction

TL	Noise reduction (dB)
S_2	Outside diameter Area (m^2)
S_1	Inside diameter Area (m^2)
k	Number of waves
f	Frequency (Hz)
c	Noise velocity (m/s)
λ	Wavelength (m)
P_w	The perimeter of the flow channel (m)
ρ_e	The density of air in the silencer (kg/m^3)
Y	The porosity of the acoustic material
κ	The coefficient of elasticity of the air in the silencer
ψ	Dimensionless parameter
σ	Sound damping coefficient
$(\sigma L)_{corr}$	Damping correction coefficient

$$\phi_s = 1 + 4.583(1 - Y) \quad (14)$$

$$\psi_1 = \frac{R_1}{2\pi f \rho_m}$$

$$\rho_e = \frac{\rho_o \phi_s \left\{1 + \left[Y + \left(\frac{\rho_m}{\rho_o \phi_s}\right)\right]\psi_1^2\right\}}{1 + \psi_1^2}$$

$$\kappa = [(3\text{-}2\gamma) + (\gamma - 1)\,log_{10}(f)]P_o \quad (15)$$

$$\kappa = \gamma P_o \quad (16)$$

In case the frequency is less than 1000Hz, κ and P_o are taken as equal. Equation 15 is used when the frequency is between 100Hz and 1000Hz. When the frequency is higher than 1000Hz, equation 16 is used.

Table 2: Mathematical variables for structure factor

ϕ_s	Structure factor
γ	Specific heat capacity ratio
ρ_m	The density of acoustic material (kg/m^3)
R_1	Flow resistance of acoustic material (rail/m)
P_o	The absolute pressure of air in the silencer (Pa)
ρ_o	The density of exhaust air (kg/m^3)

$$R_e = \frac{R_1}{1 + \psi_1^2} \quad (17)$$

$$\psi = \frac{R_e}{2\pi f \rho_e} \quad (18)$$

There are pressure losses in the silencer. The fact that the pressure between the pipe and the body is nearly constant across the silencer is a result of the principal pressure loss factor, the obstruction in the holes and mid-chamber creating flow resistance. R_e is the effective flow resistance per unit of thickness

While calculating Equation 17, it is specified which parameters are relevant.

The parameters in the equations used for the silencer sound

reduction calculation are given in Tables 1-2.

B. Container Design

Biogas should not be collected and transported in sealed vehicles or containers.

Vehicles that encounter biogas should be trained with reusable containers and all equipment and designed to transport only certain materials for cross-contamination.

Containers and vehicles should be straightened so as not to prevent contamination if plans of certain plans cannot be allowed. It must be dry and clean before use. After each use, it should be cleaned, washed, and disinfected.

The equipment dimensions to be placed in the container determine the dimensions of the container drawing.

Container body profile places should be designed according to these exit points and the dimensions of the connection pipes or accessories of the main equipment that go out of the container should be drawn.

Container layout drawing and container sizing are designed according to the engine and interior and exterior equipment.

Containers design includes engine, muffler, chimney, ventilation cabinet, radiator etc. should be made according to the portability of the loads.

Chassis profiles will coincide under the engine feet so that adverse conditions such as deflection and vibration will be minimized over time.

The chassis will consist of at least the following materials: Main beams will be UPN 240, intermediate beams will be NPI 140, purlins will be NPI 120, and columns will be composed of UPN 240.

In cases where the air discharge side is required, a double-winged door is used to allow the entrance and exit of the engine.

The container ceiling, ventilation cabinet, and door tops are waterproofed and rain-snow water is prevented from entering.

Insulation works of all necessary pipes in the silencer and container are made with a minimum of 150 mm Rockwool and aluminum plate.

C. Smokestack Design

Calculation of natural draft smokestacks means determining the required smokestack height and cutoff. The section in question here is the net smokestack section and plaster etc. in the smokestack construction. shares must be considered.

The height of the smokestack is the effective height and is the distance between the point where the smoke channel connects to the smokestack and the smokestack cap. The height from the base to the duct connection is not considered for the calculation.

The pressure losses and heat losses in the boiler connection channel–smokestack system is calculated, and it is checked whether the natural draft that occurs, in this case, is sufficient.

The theoretical solution is based on the trial-and-error method. Meanwhile, the state of the system at low loads can be analyzed, except for rated loads.

According to this method, manual smokestack calculation is extremely difficult and tiring. The best way is to use computer programs prepared according to the standard or to use one of the ready-made diagrams given in the standard for various situations.

In addition, another obstacle for Turkey regarding the application of this method is the lack of data on smokestack materials. Therefore, to simplify the calculation, in the smokestack calculation method given below, the heat losses in the smokestack are neglected and the isothermal state is considered. The calculation is based on pressure losses only. This way is also used in smokestack sizing diagrams prepared by many companies in Germany. The smokestack section found according to the calculation method given here is by DIN 4705. If a much larger section is chosen than this section, there is a risk of thermal shrinkage of the smokestack at low loads. Also, in large smokestack sections, smokestack kickback may occur due to reverse wind pressure below the speed value of 2 m/s. If a section smaller than the found section is selected, pressure losses cannot be met, and difficulties in smokestack drafting, especially during the first start-up, may be encountered with noise and vibration. According to DIN 18160, the velocity should never fall below 0.5 m/s at the smallest design power in the smokestack.

III. Conclusion

In this study, the biogas system examination and the advantages and disadvantages of the biogas system, which are necessary for the biogas system design, are discussed. The parameters that affect the biogas system design have been investigated. Parameters that affect the design of the biogas system are container, silencer, and smokestack.

As a result, the mobile biogas system design has been designed according to silencer noise reduction calculations, container dimensions and smokestack design.

References

[1] *C. Turhan, E. Dinç, B. Koçyiğit and F. Koçyiğit.* "Implementation of biogas resources to decrease the energy consumption of village institutes; a case study of Hasanoğlan Village Institute," *Journal of Scientific Perspectives*, 2019

[2] *A. Sasmita, W. Lestari.* "Mitigation of Carbon Dioxide Emissions from Crude Palm Oil Industry in Kampar Regency of Riau Province"*IOP Conference Series: Materials Science and Engineering*, 2019

[3] Anonymous, Biogas Plants and Energy Production Available: http://www.biyogaz.com/bgn.htm

[4] Igoni, A.H., Ayotamuno, M.J., Eze, C.L., Ogaji, S.O.T. and Probert, S.D., "Designs of Anaerobic Digesters for Producing Biogas from Municipal solid waste", Applied Energy, 85: 430-438 (2008).

[5] Bouallagui H., Touhami Y., Cheikh R.B., and Hamdi M., "Bioreactor performance in anaerobic digestion of fruit and vegetable wastes", Process Biochemistry, 40: 989– 995 (2005).

Evaluation of Hemp Seed in the Field of Energy: "Biodiesel Production"

H.OGUZ[1] and M. CELIK TOLU[2]

[1] Necmettin Erbakan University, Konya/Turkey, hidayet@erbakan.edu.tr
[2]Karamanoglu Mehmetbey University, Karaman/Turkey, mervecelik@kmu.edu.tr

***Abstract* - Studies on alternative renewable energy sources continue without slowing down due to the fact that petroleum-derived fuels are exhaustible energy sources, they are not included in the clean energy class, and the problems experienced in their supply due to political relations from time to time. The climatic conditions of our country allow many agricultural products to be grown with the desired yield. Therefore, obtaining this clean energy from vegetable raw material sources grown in our country will contribute to the national economy. By reclamation the hemp plant, it is possible to produce species containing low amount of stimulants, high rates of seeds and fiber. Hemp is also used to obtain vegetable oil. Therefore, hemp oil can be considered as a valuable feedstock that should also be evaluated in the field of energy. In this study, biodiesel production was carried out from hemp oil. Fuel analyzes were carried out in order to examine the energy provided by hemp oil and the performance of the fuel. In this context, the density, viscosity, cetane number, calorific value, flash point and cold flow properties of the fuel were determined. According to the results of the analysis, a biofuel with good performance and suitable for use in cold climate conditions was obtained according to ASTM standards. Promising results have guided new study topics to improve fuel performance.**

***Keywords* – Biodiesel, hemp, fuel properties, renewable energy.**

I. INTRODUCTION

DUE to population growth, industrialization and economic developments, the use of transportation, public transportation and personal vehicles is also increasing. Most of the internal combustion engines used in the transportation industry are compression ignition engines using petrodiesel. Accordingly, oil-based energy demand is increasing day by day in developed and developing countries [1, 2]. However, one of the most important disadvantages of using petroleum-based fuels is that it causes serious greenhouse gas emissions and the other is that it is not renewable and sustainable [3, 4].

The dependency on foreign resources in crude oil and the serious increases in oil prices constitute the basis of the energy crisis that the world has been in recently. In addition, considering the global climate change, environmentally friendly, sustainable, domestic and economic energy resources play a serious role in the development of the country. In addition, when global climate change is taken into account, environmentally friendly, sustainable, domestic and economic energy resources play a great role in the development of the country. In addition, when global climate change is taken into account, environmentally friendly, sustainable, domestic and economic energy resources play a great role in the development of the country. With the norms determined for fuel emissions and clean energy studies, biodiesel has developed and continues to develop as an alternative to diesel fuel over the years [4-6].

The most important advantages of biodiesel are that it is renewable and biodegradable, oxygen content, lower carbon monoxide emission, low sulfur content and high cetane number [7].

II. NON-EDIBLE OIL FOR BIODIESEL

Although the production of biodiesel from edible oils is successful, it is not sustainable in the long term. The rapid increase in the world population and food prices necessitates the production of biodiesel from non-edible oils [8, 9]. Since the use of domestic raw materials will contribute to the national economy, countries are looking for ways to produce efficient biodiesel from the oil of inedible plants that they can grow in their own climate conditions. The fact that we live in a country suitable for agriculture plays an important role in the supply of clean energy [9]. In recent years, energy agriculture has gained speed with the planting of plants that can be grown even in harsh climatic conditions and infertile soils and provide the highest yield per unit area [10, 11]. Despite the high yield these plants provide, the production costs are quite low. Making the necessary infrastructure works for biodiesel production from these raw material sources and switching to large-scale production will enable our country to produce more economical, clean and sustainable energy with its own means [10].

Industrial hemp is a promising renewable and sustainable source for biodiesel production [2, 12]. It is one of hundreds of plants grown and yielding crops for industrial purposes in the world. The cultivation of cannabis is largely banned in many countries, which hinders research into the cannabis plant. It can be cultivated in Turkey subject to permission [1].

Hemp seeds and oil are as in Figure 1.

Figure 1: a) Hemp seed b) Hemp oil

Hemp seeds contain 20-25% protein, 20-30% carbohydrates, 10-15% fiber, minerals and 25-35% oil [1,8]. When the oil content of hemp seed is compared to cotton (15-24%), soybean (17-21%) and olive (20-25%) grown in the United States, Brazil, China and other Asian and European countries, it appears to be an alternative raw material [8]. It can be grown in various climatic conditions water consumption is very low. It is a very economical plant to grow since there is no need for pesticides and fertilization processes [1, 13]. When considered in terms of economic efficiency, the cultivation of hemp plants and the production of biodiesel from its oil are a good alternative in the field of energy.

III. Material and Method

A. Biodiesel Production

It is known that the most suitable method to obtain biodiesel fuel from vegetable oils is the transesterification process. Biodiesel is obtained as a result of the reaction of alcohol with triglycerides of fatty acids in the presence of a suitable catalyst [1, 11, 14].

Glycerin, which is bound to fatty acids, causes vegetable oil to be thicker and sticky. Since the low viscosity of the fuel is an important criterion for engine performance and life, the glycerine is removed from the vegetable oil by the transesterification reaction and the oil is converted into a fuel with lower viscosity and fine structure.

The basis of biodiesel production is the separation of ester and glycerine in the oil [10]. The reaction mechanism is as in Figure 2.

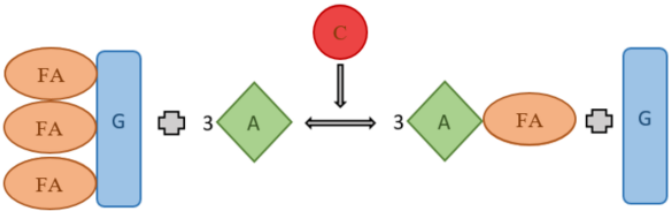

Figure 2: Schematic illustration of transesterification reaction. (FA: Fatty Acid, G: Glycerin, A: Alcohol, C: Catalyst [15]

In this study, cold pressed hemp oil was used for biodiesel production. Experimental parameters were kept constant since it was investigated whether the biodiesel obtained from cannabis oil had physicochemical properties in accordance with the standards.

In the absence of a catalyst, the transesterification reaction between triglyceride and alcohol (methanol or ethanol) is very slow and sometimes the reaction does not occur. For this reason, the reaction is accelerated with the help of an acidic or basic catalyst. The bases used are usually sodium hydroxide (NaOH) and potassium hydroxide (KOH) [16-18]. NaOH (caustic soda) must be pure. KOH has a less toxic effect [10]. The reason why most basic catalysts are preferred today is that they give good results under relatively low temperature and pressure. According to efficiency principles, the economic dimension of production is also very important [15].

Figure 3: Hemp biodiesel

The biodiesel obtained from cannabis oil after the transesterification reaction is shown in Figure 3.

B. Fuel Analysis

1) Density

Density is the key property for biodiesel. The amount of fuel injected into the engine is determined from its volume, so the density of the fuel directly affects the fuel injection process as it changes the air/combustion ratio. This is because the fuel injection pump measures on the basis of the volume of the fuel, not the mass. Therefore, the fuel with high density will be more in mass than the fuel with less density in the same volume [19, 20]. In addition, the density of the fuel is important because it is related to viscosity, calorific value and cetane number [21, 22]. The density of the fuel is also closely related to the amount of particulate matter emitted from the exhaust and NOx emissions. With the increase in density, such emissions will also increase [23, 24]. ASTM D6751 standards did not impose any limitation on density, but according to EN 14214 standard, the density of biodiesel should be in the range of 860-900 kg/m^3 [22, 25]. The density of petroleum diesel is about 0.85 g/cm^3, which is lower than biodiesel with a density of 0.88 g/cm^3. According to the standards, the density of vegetable oil varies between 0.88-0.93 g/cm^3 at 15 ^{o}C, while it decreases to 0.86-0.89 g/cm^3 after the reaction [10, 22].

2) Kinematic Viscosity

Kinematic viscosity, like density, is a characteristic property of biodiesel. The main problem with biodiesel is that its viscosity is higher than petroleum diesel. Compared to petroleum diesel, vegetable oils are 9-17 times more viscous and biodiesel is 1.6 times more viscous [22]. With the decrease in temperature, an exponential increase in viscosity is observed, which adversely affects the flow properties [26]. Except for the viscosity increase caused by cold air, since a high viscosity fuel will mix slowly with the air, complete combustion does not occur, and the exhaust smoke and emission value increase. On the other hand, a low-viscosity fuel cannot provide sufficient lubrication for the fuel injection pumps to be fully seated, so wear and leaks increase [27]. For this reason, optimum viscosity values were determined at certain intervals. According to ASTM D6751 standards, the viscosity value for biodiesel should be in the range of 1.9-6.0 mm^2/s. The EN 14214 standard has determined this range as 3.5-5.0 mm^2/s [22, 25].

3) Cetane Number

Cetane number is a dimensionless parameter related to the ignition delay time of the fuel injected into the combustion chamber in diesel engines [28, 29]. It is an indicator of the self-ignitability of the fuel. The ignition characteristics of the fuel are important in terms of engine performance, noise level and exhaust emissions [22, 26]. The most efficient and high quality combustion of the fuel depends on the high cetane number and low ignition delay time [22]. According to EN 14212 standards, the cetane number should be at least 51. ASTM standards say that this value should be in the range of 48-67 [22, 28].

4) Calorific Value

It is the amount of heat released during the combustion of one unit (one gram) of fuel to produce H_2O and CO_2 at the initial temperature.

This feature characterizes the energy content of the fuel and thus its efficiency [22]. There is no limitation in ASTM D675 and EN 14214 standards regarding the combustion heat or the calorific value of the fuel. However, European standards have determined the lower calorific value for the biodiesel used for heating as 35 MJ/kg [10, 26]. The heating value is important in determining the fuel consumption. The higher the heat obtained as a result of combustion, the lower the fuel consumption will be.

5) Cold Flow Properties

Cold filter plugging point and low temperature flow test can be used to determine the low temperature properties of biodiesel [29, 30]. Cold filter plugging point varies in proportion to the degree of saturation calculated based on the melting point of fatty acids [28]. Biodiesel standards contain conditions related to low temperature properties. The cloud point is take part in ASTM D6751, but no limit has been set. The reason for this is the sharp changes in weather conditions in the USA. The cold filter plugging point is take part in EN 14214 standards. Each country can choose one of these two standards according to its own climatic conditions and seasonal conditions [21].

6) Flash Point

The flash point is the minimum temperature at which a volatile fuel ignites when it comes into contact with fire under a pressure of 101.325 kPa (1 atm). Flash point is a key parameter for safety during storage, transportation, distribution of fuel and in NFPA (National Fire Protection Association) classifications [22]. The flash point is related to the volatility value, which is an important fuel property for the engine to start and warm up. According to ASTM D6751 standards, the flash point should be above 130 ^oC, but according to EN 14214 European standards, this value is a minimum of 120 ^oC [14, 22, 31]. Most vegetable oils have a very high flash point and decrease to the range of 120-220°C at the end of the transesterification reaction. Since these values are higher than petroleum diesel, biodiesel is safer than petroleum diesel during storage and transportation [10, 22].

IV. Results and Discussion

Fuel properties of biodiesel produced from hemp oil are given in Table 1.

Table 1: Fuel properties of hemp biodiesel

Fuel Properties	The Units	Hemp Biodiesel	Test Procedure
Density, (at 15 ^oC)	g/cm^3	0,887	DIN EN ISO 3675 DIN EN ISO 12185
Kinematic Viscosity, (at 40 ^oC)	mm^2/s	6,09	DIN EN ISO 3104
Cetane Number	-	59	process is being evaluated
Calorific Value	cal/g	9230	DIN 51900-3
Cloud Point	^oC	-7,5	-
Pour Point	^oC	-8,8	-
Freezing Point	^oC	-11,1	-
Cold Filter Plugging Point	^oC	-8,0	-
Flash Point	^oC	110	DIN EN ISO 22719
Water content	ppm	481,91	pr EN ISO 12937
Copper Strip Corrosion (3 hours at 50 °C)	1a	1a	-

When the fuel properties are examined in Table 1; Density value of the obtained biodiesel is 0.887 g/cm^3, Kinematic viscosity is 6.09 mm^2/s, Cetane number is 59, Calorific value is 9230 cal/g, Cloud Point, -7.5 ^oC, Pour Point, -8.8 ^oC, Freezing Point, -11.1 ^oC, Cold Filter Plugging Point, -8,0 ^oC, Flash Point, 110 ^oC, Water content 481.91 ppm and Copper Strip Corrosion (3 hours at 50 °C), 1a.

The fuel properties of the produced hemp biodiesel were within the limit values specified in TS EN 14214, excluding the kinematic viscosity and flash point. Limit values specified

in TS EN 14214 are respectively density (860-900 kg/m^3), Copper strip corrosion Class 1, Flash point min. 120 ^{o}C, Cold filter plugging point, temperate climates Type A Max. +5 Type E max. -15, max. Water content 500 mg/kg, max. is in the form. Although the viscosity value is in the range of 3.5-5 mm^2/s in the TS EN 14214 standard, the viscosity value was measured as 6.09 mm^2/s, slightly above the standard in biodiesel.

As a result, it was concluded that biodiesel produced from hemp can be evaluated as a biodiesel raw material.

V. Future Perspective

In this study, biodiesel production was carried out in order to evaluate hemp in the field of energy. The production was carried out with the traditional method and the results showed that hemp is a quite efficient raw material in obtaining energy. It can be considered as a preliminary study on obtaining efficient energy with a raw material that can be grown within the borders of our country and will reduce the production cost. Based on this study, it is planned to carry out new studies in which the test parameters are optimized in order to increase the fuel performance of biodiesel to be obtained from hemp. In addition, the fuel performance of cannabis seeds grown under different conditions or of different types is also worth examining.

References

[1] Z. Yilbaşi, M. K. Yesilyurt and M. Arslan, "The production of methyl ester from industrial grade hemp (Cannabi sativa L.) seed oil: a perspective of Turkey- the optimization study using the Taguchi method," *Biomass Conversion and Biorefinery*, August 2021.

[2] A. R. Gupta,A. P. Jalan and V. K. Rathod, "Solar energy as a process intensification tool for the biodiesel production from hempseed oil,"*Energy Conversion and Management*, vol.171, pp. 126-132, May 2018.

[3] A. M. Parvez, J. D. Lewis and M. T. Afzal, "Potential of industrial hemp (Cannabis sativa L.) for bioenergy production in Canada: Status, challenges and outlook," *Renewable and Sustainable Energy Reviews*, vol. 141, May 2021.

[4] H. Oğuz and M. Çelik Tolu, "A review on biodiesel production using eggshell as catalyst," *International Journal of Energy Applications and Technologies*, vol. 5, pp. 147-152, December 2018.

[5] C. B. John, A. R. Solamalai, R. Jambulingam and D. Balakrishnan, "Estimation of fuel properties and characterization of hemp biodiesel using spectrometric techniques," *Energy Sources, Part A: Recovery, Utilization, and Environmental Effects*, November 2020.

[6] A. Patel, M. Pravez, F. Deeba, V. Pruthi, R. P. Singh and P. A. Pruthi, "Boosting accumulation of neutral lipids in *Rhodosporidium kratochvilovae* HIMPA1 grown on hemp (*Cannabis sativa Linn*) seed aqueous extract as feedstock for biodiesel production," *Bioresource Technology*, vol. 165, pp.. 214-222, April 2014.

[7] H. T. Rheay, E. C. Omondi and C. E. Brewer, "Research Review: Potential of Hemp (*Cannabis sativa* L.) for Paired Phytoremediation and Bioenergy Production," *GCB Bioenergy*, vol. 13, pp. 525-536, 2021.

[8] M. S. U. Rehman, N. Rashid, A. Saif, T. Mahmood and J. Han, "Potential of bioenergy production from industrial hemp (Cannabis s*ativa*): Pakistan perspective," *Renewable and Sustainable Energy Reviews*, vol. 18, pp. 154-164, 2013.

[9] K. Ullah, M. Ahmad, S. Sultana, L. K. Teong, V. K. Sharma, A. Z. Abdullah, M. Zafar anf Z. Ullah, "Experimental analysis of di-functional magnetic oxide catalyst and its performance in the hemp plant biodiesel production," *Applied Energy*, vol. 113, pp. 660-669, 2014.

[10] H. Öğüt, and H. Oğuz, 2006, *Üçüncü milenyumun yakıtı biyodizel*. Ankara: Nobel Yayın Dağıtım, 2006.

[11] H. Oğuz, H. Öğüt and T. Yılmaz, "Investigation of Biodiesel Production, Quality and Performance in Turkey," *Energy Sources, Part A: Recovery, Utilization, and Environmental Effects*, vol. 29, pp. 1529-1535, October 2007.

[12] M. B. Viswanathan, M-H. Cheng, T. E. Clemente, I. Dweikat and V. Singh, "Economic perspective of ethanol and biodiesel coproduction from industrial hemp," *Journal of Cleaner Production*, vol. 299, March 2021.

[13] J. Finnan and D. Styles, "Hemp: A more sustainable annual energy crop for climate and energy policy," *Energy Policy*, vol. 58, pp. 152-162, March 2013.

[14] S-Y. Li, J. D. Stuart, Y. Li and R. S. Parnas, " The feasibility of converting *Cannabis sativa* L. oil into biodiesel" *Bioresource Technology*, vol. 101, pp. 8457-8460, June 2010.

[15] M. B. Uluengin, *Siz de evinizde biyodizel üretebilirsiniz!,* İstanbul: Birsen Yayınevi, 2007.

[16] J. A. Melero, L. F. Bautista, G. Morales, J. Iglesias and R. Sanchez-Vazquez, "Acid catalyzed production of biodiesel over arenesulfonic SBA-15: Insights into the role of water in the reaction network," *Renewable Energy*, vol. 75, pp. 425-432, 2015.

[17] Z. Ö. Özdemir and H. Mutlubaş, "Biyodizel üretim yöntemleri ve çevresel etkileri," Kırklareli University Journal of Engineering and Science, vol. 2, pp. 129-143, 2016.

[18] M. A. A Silva, R. A. Correa, M.G. de O.Tavares and N. R. Antoniosi Filho, "A new spectrophotometric method for determination of biodiesel content in biodiesel/diesel blends," *Fuel*, vol. 143, pp. 16-20, 2015.

[19] E. Alptekin and M. Canakci, "Determination of the density and the viscosities of biodiesel–diesel fuel blends," *Renewable Energy*, vol. 33, pp. 2623-2630, 2008.

[20] A. A. Refaat, "Correlation between the chemical structure of biodiesel and its physical properties," *International Journal of Environmental Science and Technology*, vol. 6, pp. 677-694, 2009.

[21] G. Knothe and K. R. Steidley, "Kinematic viscosity of biodiesel fuel components and related compounds. Influence of compound structure and comparison to petrodiesel fuel coponents," *Fuel*, vol. 84, pp. 1059-1065, 2005.

[22] B. Sajjadi, A. A. A. Raman and H. Arandiyan, "A comprehensive review on properties of edible and non-edible vegetable oil-based biodiesel: compositioni specification and prediction models," *Renewable and Sustainable Energy Reviews*, vol. 63, pp. 62-92, 2016.

[23] J. P. Szybist, J. Song, M. Alam, and A. L.Boehman, "Biodiesel combustion, emissions and emission control," *Fuel Processing Technology*, vol. 88, pp. 679-691, 2007.

[24] M. Canakci and H. Sanli, "Biodiesel production from various feedstocks and their effects on the fuel properties," *Journal of Industrial Microbiology and Biotechnology*, vol. 35, pp. 431-441, 2008.

[25] S. K. Hoekman, A. Broch, , C. Robbins, E. Ceniceros and M. Natarajan, "Review of biodiesel composition, properties and specifications," *Renewable and Sustainable Energy Reviews*, vol. 16, pp. 143-169, 2012.

[26] G. Knothe, ""Designer" biodiesel: optimizing fatty acidcomposition to improvefuel properties," *Energy & Fuels*, vol. 22, pp. 1358-1364, 2008.

[27] S. V. D. Freitas, M. J. Pratas, R. Ceriani, A. S. Limas, and J. A. P Coutinho, "Evaluation of predictive models for the viscosity of biodiesel," *Energy Fuels*, vol. 25, pp. 352-358, 2011.

[28] M. J. Ramos, C. M. Fernandez, A. Casas, L. Rodrigues, and A. Perez, "Influence of fatty acid composition of raw meterials on biodiesel properties," *Bioresource Technology*, vol. 100, pp. 261-268, 2009.

[29] G. Knothe, "Improving biodiesel fuel properties by modifying fatty ester composition," *Energy & Environmental Science*, vol. 2, pp. 759-766, 2009.

[30] R. O. Dunn, and M. O. Bagby, "Low-temperature properties of triglyceride-based diesel fuels: transesterified methyl esters and petroleum middle distillate/ester blends," *Journal of American Oil Chemists' Society,* vol. 72, pp. 895-904, 1995.

[31] J. H. F. Boog, E. L. C. Silveira, L. B. deCaland and M. Tubino, "Determining the residual alcohol in biodiesel through its flash point," *Fuel*, vol. 90, pp. 905-907, 2011.

Large Deflections of Bi-directional Functionally Graded Cantilever Beams

AYHAN HACIOĞLU[1], ADEM CANDAŞ[2], and CEMAL BAYKARA[3]

[1] Faculty of Mechanical Engineering, Istanbul Technical University, Istanbul/Türkiye, hacioglua@itu.edu.tr
[2] Faculty of Mechanical Engineering, Istanbul Technical University, Istanbul/Türkiye, candas@itu.edu.tr
[2] Department of Naval Architecture, Ocean and Marine Engineering, University of Strathclyde, Glasgow/UK
[3] Faculty of Mechanical Engineering, Istanbul Technical University, Istanbul/Türkiye, baykaracem@itu.edu.tr

Abstract **- The large deflections of a bi-directional cantilever beam that obeys modified Ludwick's constitutive law and made of FGM is analyzed as a layered structure in this study. The nonlinearly elastic cantilever beam is subjected to a concentrated force at the free end. The modified Ludwick type of material model and functionally graded material properties are defined by using Marlow's material model in finite element analysis. The results show that the number of layers is one of the most important properties in the evaluation of both normal stress distributions along the thickness direction and deflections of the free ends of slender beams. The effect of the number of layers on the stress distributions on the beam is obvious when compared particularly the single-layered FGM with any of the multi-layered FGMs.**

Keywords **- Large deflections, functionally graded materials, cantilever beams, Ludwick's law, nonlinearly elastic.**

I. Introduction

FUNCTIONALLY graded materials (FGMs) have long been a material of great interest in a wide range of fields. Recent trends in 3-D printing technologies have led to a proliferation of studies that examine FGMs. In addition, recent years have witnessed a growing academic interest in both FGMs and non-linearly elastic materials. Thus, FGMs have been an object of research that examine the behavior of beams subjected to various loads [1]. During the last decade, the combination of FGMs and nonlinearly elastic materials has been at the center of much attention. Many researchers have considered not only geometrical nonlinearity but also material nonlinearity. Much of the literature since the mid-1990s emphasizes the analytical solutions of nonlinear beams subjected to large deflections [2-4].

Lewis and Monasa [5,6] examined a thin cantilever beam under a transverse end load and a moment in terms of large deflections of the free end. Baykara et al. [7] considered nonlinear bi-modulus material behavior to investigate a thin cantilever beam with an end moment. A large buckling analysis in fibrous materials using Ludwick type material model was examined by Jung and Kang [8]. Kang and Li [9,10] took into account large and small deflections of nonlinearly elastic functionally graded beams (FGBs). The large deflections of a slender, non-homogeneous beam under combined loads were studied by Sitar et al. [11]. In that study, the beam was modelled as a functionally graded material and discretized with a certain number of nonlinearly elastic layers that obey generalized Ludwick's constitutive law.

Hacıoğlu [12] examined the variation of Young's modulus relating to power-law and geometrical nonlinearity on the deflection. The results of that study showed that gradient indexes and material constant in Ludwick's law significantly affect the bending strength of an FGM beam. Hacıoğlu and Baykara [13] examined the nonlinear functionally graded beam subjected to concentrated and combined loads. Moreover, Hacıoğlu et al. [14] studied large deflections of a cantilever beam which is made of nonlinearly elastic, modified Ludwick's type of material using FEA. Marlow's material model was used in Ref. [14] to combine direction dependent material properties in the functionally graded material and nonlinearity from modified Ludwick's law.

However, such studies remain narrow in focus dealing only with one-directional functionally graded beams. In all the studies reviewed here, the modelling of the FGM beam which is layered in the thickness direction is recognized as significant. Karamanlı [15,16] investigated the elastostatic behavior of two-directional functionally graded beams under different sets of boundary conditions. A bending analysis study was presented to examine the effects of different sets of boundary conditions on FGM beams [17].

In this study, the large deflections of a nonlinearly elastic bi-directionally functionally graded cantilever beam subjected to end load are presented. A combination of the bi-directional FGM model and nonlinearity of material properties based on modified Ludwick's law is introduced. The material properties vary through both thickness and length directions with respect to the function of FGMs. Firstly, we present the effect of the number of layers in thickness direction on the deflections at the end of the beam. Then, bi-directional layer is applied and the effect of both thickness and length directions are examined.

II. Problem Definition and Modeling

A slender cantilever beam of length, L through x axis and the rectangular cross-section of thickness, h through y axis and width, b is used as seen in Fig. 1. The bi-directional functionally graded beam is composed of several rigidly bonded layers which are named as nh and nl in thickness (h) and length (L) directions, respectively. Layers are assumed to be

incompressible. F_y is the point load applied vertically at the free end of the beam as defined in Fig. 1.

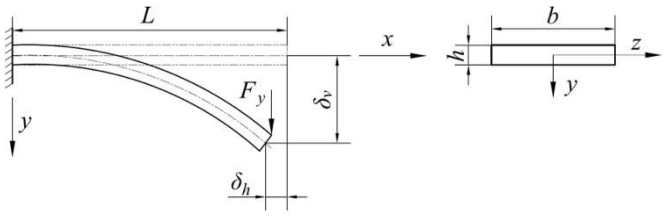

Figure 1: Geometric details of the beam.

The modified Ludwick's constitutive model that governs the stress-strain relationship is given by the following expression [18],

$$\sigma = \text{sign}(\varepsilon) E \left((|\varepsilon| + \varepsilon_0)^{\frac{1}{k}} - \varepsilon_0^{\frac{1}{k}} \right) \qquad \text{for all } \varepsilon, \tag{1}$$

where, σ and ε defines normal stress and strain respectively. E, ε_0, and k are material constants and sign(ε) represents the symbol function which has a value of 1 or -1 in a case of tension or compression. Here, Ludwick's constitutive relation is obtained by setting $\varepsilon_0 = 0$ while Hooke's constitutive law is obtained by setting $k = 1$. In order to define the material model of modified Ludwick type material, Marlow's first-invariant constitutive model was adapted in this study [19]. In Marlow's form, it is assumed that strain energy potential changes only with the first deviatoric invariant. Calculated stress-strain values of generalized Ludwick type material is used by Marlow's model to reproduce stress-strain curve. A commercial finite element analysis software, ABAQUS supports the Marlow strain energy potential form. Plane stress assumption was considered and the geometry was modeled as 2-D shell structure in ABAQUS. The 4-node linear quadrilateral shell elements with reduced integration and hourglass control (S4R) were used to model the mesh geometry.

The effective material properties of a bi-directionally graded FGMs are calculated by [16],

$$E(\bar{x}, \bar{y}) = (E_1 - E_2)\left(1 - \frac{\bar{x}}{2L}\right)^{p_x}\left(\frac{1}{2} + \frac{\bar{y}}{h}\right)^{p_y} + E_2, \qquad -h/2 \le \bar{y} \le h/2 \text{ and } 0 \le \bar{x} \le L, \tag{2}$$

where E_1 and E_2 are Young's modulus at certain points and p_x, p_y are the gradation exponents of the FGM (Fig. 3). In the case of bi-directional gradation, Young's modulus of each layers is calculated as follows,

$$E_{i,j} = \frac{1}{\Delta_i \Delta_j} \int_{(i-1)\Delta_i}^{i\Delta_i} \int_{(j-1)\Delta_j}^{j\Delta_j} E(\bar{x}, \bar{y}) d\bar{x} d\bar{y}, \tag{3}$$

where i and j represent the order of a layer, Δ_i and Δ_j are the thickness and length of each layer. $E_{i,j}$ is the averaged Young's modulus of a certain layer.

III. Numerical Examples

The first set of numerical examples aimed to examine the generalized Ludwick type bi-directional functionally graded beam by dividing it into a finite number of layers through only thickness direction. To compare the difference between one-directional and two-directional partitions, the beam is modelled as a bi-directionally layered structure in the second set of examples. The cantilever beam in Fig. 1 made of bi-directional functionally graded material obeying generalized Ludwick's constitutive law has a length of L = 1000 mm, a thickness of h = 50 mm, and width of b = 100 mm. The effective material parameters are set to E_1 = 300 MPa, E_2 = 70 MPa, k = 1.5, and ε_0 = 0.07. The gradation exponents are taken to be p_x = 5 and p_y = 2. The only load applied to the beam is the concentrated force F_y having magnitudes of 100, 200, 300, 400, and 500 N and acting towards to vertical direction.

A. Generalized Ludwick Type One-directionally Layered Bi-directional Functionally Graded Beam

The effects of the number of vertical layers on the modelling bi-directional FGM beam are examined in this example. The number of layers through the thickness direction is *nt* =1, 5, 10, and 20 while it is constant through the length direction as *nl* = 1. The comparison of deflections and the stress distributions on the beams is given in Fig. 2 in the case that the applied load is 500 N. The maximum tensional normal stresses occur on the top surface of the beam and the magnitudes are 10.8, 8.12, 7.95, and 9.38 MPa for *nt* = 1, 5, 10, and 20, respectively. However, these maximum values are undoubtedly affected due to the presence of singularity points located at the top and bottom corners of the clamped surface of the beam. Considering Saint - Venant's principle, to avoid the misleading effects of singularity points, stress values are measured at a certain point, where the maximum stress values are converged. The normal stresses measured at that point are 8.89, 6.21, 6.05, and 6.04 MPa for *nt* = 1, 5, 10, and 20 respectively.

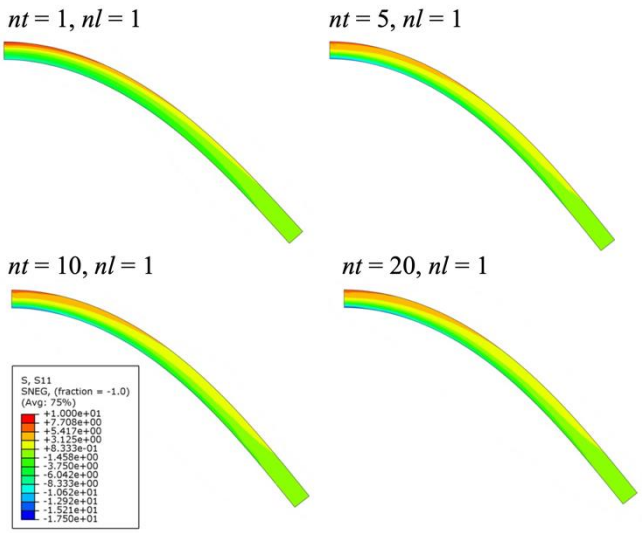

Figure 2: The large deflections and normal stresses on one-directionally layered FGM beam with respect to the number of layers in the thickness direction.

The properly converged normal stress results show that a single layered FGM beam is not capable of representing an actual FGM beam in terms of either stress distributions or large deflections. On the other hand, modeling beams as multi-layered structures are able to simulate the FGM beam accurate enough, regardless of the number of layers.

The vertical (δ_v) and horizontal (δ_h) deflections (in mm) of the beam considering the applied loads are given in Table 1 for each number of layers cases. The maximum vertical and horizontal deflections depend on mostly the applied load. The variation of the number of layers through the thickness direction seems not to affect the deflections significantly. The values for nt = 5, 10, and 20 are very close to each other in this particular example.

Table 1: Deflections of the free end of one directionally layered FGM beam (in mm).

	nt = 1 nl = 1		nt = 5 nl = 1		nt = 10 nl = 1		nt = 20 nl = 1	
F [N]	δ_v	δ_h	δ_v	δ_h	δ_v	δ_h	δ_v	δ_h
100	144.1	17.8	158.1	19.4	157.5	19.3	157.4	19.2
200	274.7	55.7	300.3	62.9	299.4	62.4	299.2	62.3
300	382.8	104.1	415.2	117.9	414.2	117.1	414.0	117.0
400	468.4	154.9	503.6	174.2	502.6	173.3	502.4	173.1
500	535.2	203.5	570.9	226.9	569.9	225.9	569.8	225.7

B. Generalized Ludwick Type Two-directionally Layered Bi-directional Functionally Graded Beam

The analysis of a two-directionally layered, bi-directional functionally graded beam is presented in this section. The number of layers through the thickness is nt = 20 and through the length is nl = 1, 5, 10, and 20. In Fig. 3, the variation of Young's modulus is given over a bi-directional 20×20 layered FGB. Young's modulus in the left and right top corners are the same and equal to E_2.

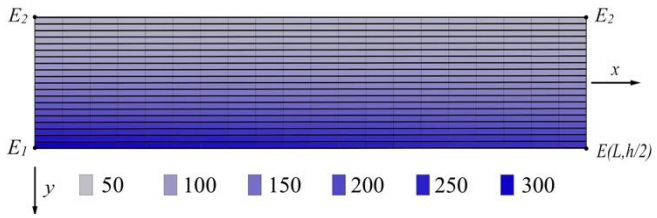

Figure 3: Young's modulus gradient in the bi-directional 20×20 FGB.

The large deflections of the free ends and normal stress distributions on the beams under the effect of concentrated force Fy = 500 N are given in Fig. 4. The converged normal stress values obtained from a specific point far from the singularity regions are 6.04, 5.93, 5.91, and 5.90 MPa for nl = 1, 5, 10, and 20 respectively when nt = 20. The result obtained from a vertically single-layered beam is the most distinctive one with a magnitude of 6.04 MPa. The differences among the multi-layered beams are negligible.

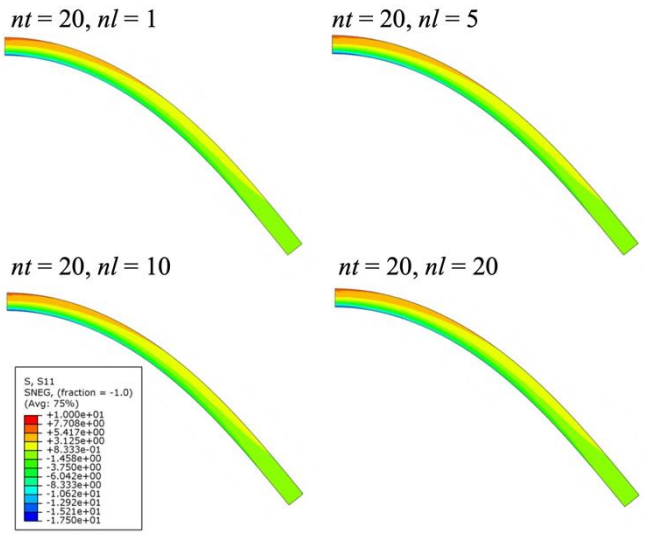

Figure 4: The large deflections and normal stresses of bi-directional FGBs depend on the number of layers in the thickness and length directions.

Table 2 shows the deflections of the end points considering to magnitude of the load and the number of layers. The free end deflection of the 20×1 layered beam is the maximum, while 20×20 layered beam's is the minimum. Besides, the differences in the deflections among two-directionally layered beams are much less than observed between one-directionally layered and the other beams, the same as in the stress distributions.

Table 2: Deflections of the free end of the 2-D FGB (in mm).

	nt = 20 nl = 1		nt = 20 nl = 5		nt = 20 nl = 10		nt = 20 nl = 20	
F [N]	δ_v	δ_h	δ_v	δ_h	δ_v	δ_h	δ_v	δ_h
100	157.4	19.2	153.5	18.4	153.3	18.4	153.3	18.4
200	299.2	62.3	292.4	59.9	292.2	59.8	292.1	59.8
300	414.0	117.0	405.7	112.8	405.5	112.7	405.4	112.6
400	502.4	173.1	493.7	167.5	493.4	167.4	493.3	167.3
500	569.8	225.7	561.1	219.1	560.9	218.9	560.8	218.9

IV. CONCLUSION

Evaluation of both material and geometrical nonlinearities rise from the slender geometry; nonlinearly elastic material behavior and functional gradation of effective material properties is an intensely challenging process. Although there are several analytical studies on FGMs, finite element simulations are limited. In this study, a generalized Ludwick type nonlinearly elastic, bi-directional functionally graded beam is modeled as a layered structure to analyze by commercial FEA software. The effects of the number of layers on the normal stress distribution and end deflections are examined. Since the division of the beam into layers is a laborious process and adding more layers directly increases the CPU time, bi-directional FGB is studied as a one-directionally layered structure. Then the same beam is two-directionally

divided into layers. Results show that a homogenous beam is not capable of representing an FGB. On the other hand, there is no significant difference between one-directionally layered beam models. Two directionally layered beam models are very successful in simulating bi-directional FGBs. The results are converged at a certain number of layers. The stress distribution and large deflection of FGBs show the almost same behavior in 20×10 and 20×20 layered beams. The results presented here should be verified by further studies to increase our ability to understand the effects of the modelling parameters.

ACKNOWLEDGMENT

Adem Candaş is supported by The Scientific and Technological Research Council of Turkey (TÜBİTAK) 2219 International Postdoctoral Research Fellowship Grant (1059B192100891).

REFERENCES

[1] A. Candaş, E. Oterkus, and C. E. İmrak, "Peridynamic Simulation of Dynamic Fracture in Functionally Graded Materials Subjected to Impact Load," *Engineering with Computers*, 2021. doi.org/10.1007/s00366-021-01540-2

[2] S. Chucheepsakul, S. Buncharoen, and C. M. Wang, "Large Deflection of Beams under Moment Gradient," *Journal of Engineering Mechanics*, vol. 120(9), pp. 1848–1860, 1994.

[3] C. M. Wang, K. Y. Lam, X. Q. He, and S. Chucheepsakul, "Large Deflections of an End Supported Beam Subjected to a Point Load," *International Journal of Non-Linear Mechanics*, vol. 32(1), pp. 63–72, 1997.

[4] K. Lee, "Large Deflections of Cantilever Beams of Non-Linear Elastic Material under a Combined Loading," *International Journal of Non-Linear Mechanics*, vol. 37(3), pp. 439–443, 2002.

[5] G. Lewis and F. Monasa, "Large Deflections of Cantilever Beams of Nonlinear Materials," *Computers & Structures*, vol. 14(5–6), pp. 357–360, 1981.

[6] G. Lewis and F. Monasa, "Large Deflections of Cantilever Beams of Non-Linear Materials of the Ludwick Type Subjected to an End Moment," *International Journal of Non-Linear Mechanics*, vol. 17(1), pp. 1–6, 1982.

[7] C. Baykara, U. Güven, and I. Bayer, "Large Deflections of a Cantilever Beam of Nonlinear Bimodulus Material Subjected to an End Moment," *Journal of Reinforced Plastics and Composites*, vol. 24(12), pp. 1321–1326, 2005.

[8] J. ho Jung and T. J. Kang, "Large Deflection Analysis of Fibers with Nonlinear Elastic Properties," *Textile Research Journal*, vol. 75(10), pp. 715–723, 2005.

[9] Y. A. Kang, and X. F. Li, "Bending of Functionally Graded Cantilever Beam with Power-Law Non-Linearity Subjected to an End Force," *International Journal of Non-Linear Mechanics*, vol. 44(6), pp. 696–703, 2009.

[10] Y. A. Kang and X. F. Li, "Large Deflections of a Non-Linear Cantilever Functionally Graded Beam," *Journal of Reinforced Plastics and Composites*, vol. 29(12), pp. 1761–1774, 2010.

[11] M. Sitar, F. Kosel, and M. Brojan, "Large Deflections of Nonlinearly Elastic Functionally Graded Composite Beams," *Archives of Civil and Mechanical Engineering*, vol. 14(4), pp. 700–709, 2014.

[12] A. Hacıoğlu, "Large Deflection Analysis for Functionally Graded Cantilever Beams", MSc Thesis, *Graduate School of Science Engineering and Technology, Istanbul Technical University*, pp. 91, 2017.

[13] A. Hacıoğlu and C. Baykara, "A Non-linear Large Deflection Analysis for FGM Beams Under the Different Boundary Conditions and Different Loads Based on Generalized Ludwick Law," in *MECHCOMP3 3rd International Conference on Mechanics of Composites, University of Bologna, Italy*, pp. 9, 4-5 July 2017.

[14] A. Hacıoğlu, A. Candaş, and C. Baykara, "Large deflections of functionally graded non-linearly elastic cantilever beams," *Journal of Engineering Materials and Technology, Transactions of ASME*, (article in press), 2022.

[15] A. Karamanlı, "Elastostatic analysis of two-directional functionally graded beams using various beam theories and Symmetric Smoothed Particle Hydrodynamics method," Composite Structures, vol. 160, pp. 653-669, 2017.

[16] A. Karamanlı, "Bending Analysis of Two Directional Functionally Graded Beams Using a Four-Unknown Shear and Normal Deformation Theory," *Journal of Polytechnic*, vol. 21, 2018. doi.org/10.2339/politeknik.389616.

[17] M. Turan, "Bending analysis of two-directional functionally graded beams using trigonometric series functions", *Archive of Applied Mechanics*, vol. 92, pp. 1841–1858, 2022.

[18] M. Brojan, T. Videnic, F. Kosel, "Large deflections of nonlinearly elastic non-prismatic cantilever beams made from materials obeying the generalized Ludwick constitutive law", *Meccanica*, vol. 44, pp. 733-739, 2009.

[19] R.S. Marlow, "A General First-Invariant Hyperelastic Constitutive Model," *Constitutive Models for Rubber*, pp. 157–160, 2003.

Experiments and simulations of a liquid contaminant propagation in a vegetated bottom channel

H. ROMDHANE[1] and A. SOUALMIA[1]

[1]National Institute of Agronomy of Tunisia, Tunis, Tunisia, romdhane_hela@yahoo.com

[1]National Institute of Agronomy of Tunisia, Tunis, Tunisia, amel.inat@hotmail.fr

Abstract **- Over the last decades, the Medjerda river, like most rivers, has seen its quality deteriorated. This water resources degradation was due to the development of urbanization, industrial and agricultural activities throughout the basin. In fact, natural watercourses generally receive domestic, industrial and agricultural waste; in some cases, accidental discharges were found in rivers and irrigation networks, such as the Medjerda Cap Bon channel. These discharges were generally punctual, and can cause various problems for water quality, infrastructure, river morphology and they can also lead to hydraulic and road structures damage and also pose a threat to the global environment. This deterioration in water quality is particularly associated to several pollutants input. It is therefore important to know the rivers capacity to mix and transport these contaminants and to determine the pollutant dispersion rate in solution. In this context was leaded this experimental analysis work concerning a pollution propagation in free surface flows, at a laboratory channel over a vegetated or smooth bottom. Then preliminary numerical simulations of these results were carried out. Two experimental scenarios were considered; the first one was leaded with a discontinuous pollution source, and the second one with a continuous pollution source. These experiments were carried out initially over a smooth bed and then over a vegetated bed. The aim is to show the vegetation effect on the pollutant propagation.**

By comparing the two injection types, we see that discontinuous injection best promotes the pollutant mixing in solution compared to continuous injection, where such a pollutant remains in the medium with greater concentration. It can also be seen that the vegetation presence on the channel bottom causes a decrease in the pollutant concentration in water, this is due to the fact that the vegetation presence increases the bed shear stress and subsequently will delay a solution propagation in water. Indeed, vegetation plays a retarding role of these pollutants' types dispersion.

Keywords **- Free surface flow, Liquid contaminant, Experiments, Vegetated Bottom, Dispersion, Simulations.**

I. INTRODUCTION

Water pollution in free surface flows is a topic of great interest to scientists. As a result, more and more researches are being done on water quality. They respond to a demand expressed by environmental protection specialists. [14]

Population explosion, industrial activity and the rate at which new chemicals and products developed and used pose a threat to the global environment. The natural decomposition processes in water bodies are no longer sufficient to overcome these pollutants inputs [11, 12, 13]. Technology can be used in many cases to reduce or eliminate substances that can harm the environment.

But what happens when the contaminants are not removed, even by the most modern water treatment methods? They may be present in only minimal quantities; however, as they are persistent, they can accumulate to form very harmful concentrations. In this case, there is only one way to protect future generations and the entire ecosystem, is to keep chemicals out of the river system. [6, 7]

Water resources have a paramount importance for humans, aquatic life and agriculture. However, the pollutant evolution depends mainly on the flow characteristics that carry it. A precise presentation of all the hydrodynamic phenomena present in the receiving environment is therefore necessary, in particular taking into account turbulence. [3, 5, 10]

The objective of this research work is therefore to experimentally analyze the propagation of such pollution in free surface flows along a laboratory channel.

II. THEORETICAL BACKGROUND

Spectrophotometry is the field that studies the energy measurement carried by electromagnetic radiation in the visible light field. It is a quantitative and qualitative analytical method that measures the absorbance or optical density of a given chemical, usually in solution. The more concentrated the sample, the more light it absorbs within the limits of proportionality set out by the Beer-Lambert law. [7].

The samples optical density is determined by a spectrometer previously calibrated on the absorption wavelength of the studied substance.

A. Beer Lambert's Law

The absorbance A at the solution wavelength λ depends on the solution concentration (C) and the solution length (l) crossed by the light:

$$A = k \times C \quad (1)$$

With A: Absorption (without unit)
C: Molar concentration (mol. L-1)
K= ε * l (L.mol-1): called Proportionality coefficient and is constant for a given chemical species and wavelength.

B. Dilution and Procedure

We try to determine a solution concentration Cx. The determination by calibration will be based on a physical characteristic of this solution: for example, its conductivity for an ionic solution or its absorbance for a colored solution.

Several solutions of the same nature, as the solution to be assayed, are then produced. These solutions will serve as standards: so that their concentration is known with the best possible precision. A "standard range" is thus obtained (also called "tint scale" in the case of a colored solution).

We will now use the absorption spectra in the form of graphs A = f (λ). Such a graph is obtained using a spectrophotometer. Each sample was measured; the calibration curve can then be plotted. It is then sufficient to pass the unknown concentration samples through the measuring device to determine its concentration using the calibration curve.

The pollutant chosen for this study is the potassium permanganate ($KMnO_4$) (0.1 N) having an initial concentration C_0 = 0.02 mol / l, which is a purple-colored, water-soluble chemical compound. It can be seen in the figure opposite that potassium permanganate has an absorption maximum for a wavelength λ = 530 nm and has a second non-negligible absorption peak for λ = 550 nm (Fig. 1).

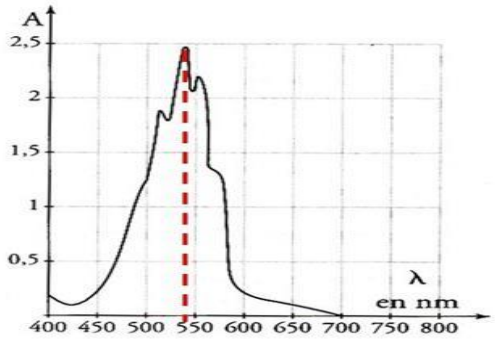

Figure 1: Absorption Spectrum of a Potassium Permanganate solution

After measuring the absorption of the 5 diluted solutions by the spectrophotometer, the calibration curve A (C) was plotted (Fig. 2, Table 1).

Table 1. Concentration and absorbance of standard solutions

C (mol/l)	A
0.00004	0.177
0.0002	0.458
0.0004	0.698
0.001	1.517
0.002	3.179

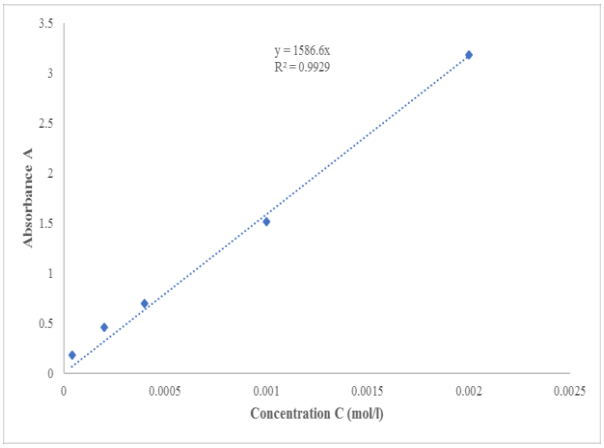

Figure 2: Calibration Curve of a Potassium Permanganate solution

According to the Beer-Lambert law, A is a linear function of C, so the curve A (C) is a line passing through the origin. This curve is the calibration curve which makes it possible to determine the concentrations of various samples taken from the channel, it has a determination coefficient close to the unity (R^2 = 0.9929) and a coefficient K = 1586.6 for this case.

It is therefore sufficient to measure the absorbance of each sample by the spectrophotometer and then project on the curve and read its abscissa which represents the concentration. [1, 2]

III. EXPERIMENTS AND RESULTS

Experiments were carried out in a rectangular channel at the National Institute of Agronomy of Tunisia in the laboratory of water science and technology (Fig. 3). These experiments concern the analyses of a solution pollutants transport phenomenon in two cases, over smooth bed and over a vegetated bed. To do this, a concentrated solution of a tracer (potassium permanganate) was injected upstream at the channel, then water samplings were taken as functions of time and at the channel center and for the different scenarios. This is in order to measure the sample concentrations using a laboratory spectrophotometer. The objective was to analyze the pollutant propagation phenomena, and to understand the dispersion rate of this pollutant in the water, and the effect of the bottom vegetation presence on this phenomenon [15, 16].

The injection and withdrawal operations were carried out through a set of syringes.

Two experimental scenarios were carried out: a discontinuous pollution source case, where the pollutant

injection was carried out upstream the channel for 20 seconds and then it was stopped; and a continuous pollution source case, where the pollutant injection into the channel upstream was done permanently. These two scenarios are carried out over the smooth bed and then over the vegetated bed.

These experiments were carried out initially with several flow rates and a dye fixed concentration. Secondly, this concentration was varied and the flow rate was kept constant. We will therefore analyze the increasing flow rate effect on the mixing rate, and also the varying concentrations effect. The withdrawals were taken at the middle of the channel after 2m from the injection point.

Figure 3: Experimental Setup at the INAT laboratory (Length: 10m; width: 0.8m; Hight: 0.6m)

During the different scenarios carried out, we observe that the pollution dispersion occurs according to two mechanisms which are convection and dispersion phenomenon. In fact, first the pollutant moves longitudinally according to the flow velocity effect; it is the advection process, and afterwards it gains the whole width of the channel and so decreases in concentrations within the cloud, it is the dispersion phenomenon. [1, 2, 9]

A. Continuous injection

In these experiments, the pollutant was injected into the channel permanently for two cases, over smooth bed and over a vegetated bed.

The figures below show the pollutant concentration evolution for the different injected volume and for different flow rates for the two cases, over smooth bed and over a vegetated bed.

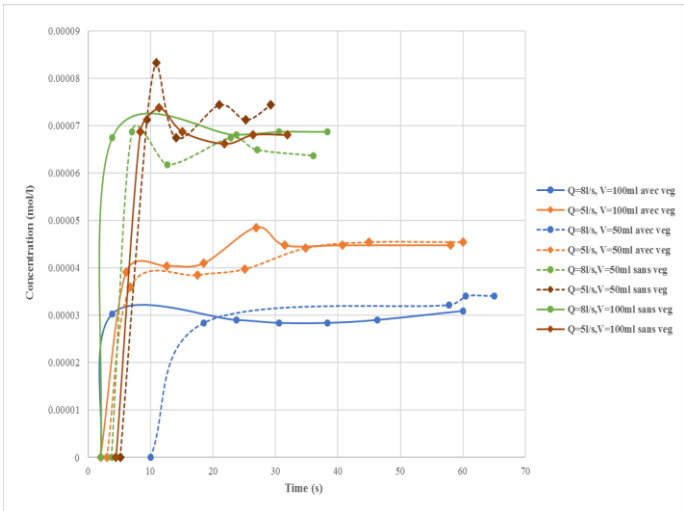

Figure 4: Concentration profile for the different continuous injected pollutant volume of 100 ml and 50 ml and for Q= 8 l/s and Q= 5 l/s, over a vegetated and a smooth bed

From this curve we noticed that for the different cases, the concentration variation was as follows: First a very rapid rise was observed, this is the convective period. The last phase was characterized by a very slow rise, which over time becomes almost constant, this is the diffusive period. On the other hand, the increased flow rate generates a rapid convection period, this is due to the fact that more the velocity flow increases, more the injected quantity diffuses quickly downstream where the mixture will be completed and a stability state is achieved faster.

The increased flow rate accelerates the pollution transport, but in return generates a larger concentrations peak. This can be explained by the turbulence rate which increases with the flow, in fact, the turbulent diffusion will be important and this will increase the mixing rate and in return decreases the time necessary to reach the stability state.

It can also be seen that the vegetation presence on the channel bottom causes a decrease in the pollutant concentration in water, this is due to the fact that the vegetation presence increases the bed shear stress and subsequently will delay the solution propagation in water. Indeed, vegetation plays a retarding role of these pollutants' types dispersion.

B. Discontinuous injection

For these experiments, the pollutant injection into the channel was done during 20 seconds, but the sampling processes were continued even after the injection had been stopped.

The figures below showed the pollutant concentration evolution for the different injected volumes and for different flow rates in the two cases, over smooth bed and over a vegetated bed.

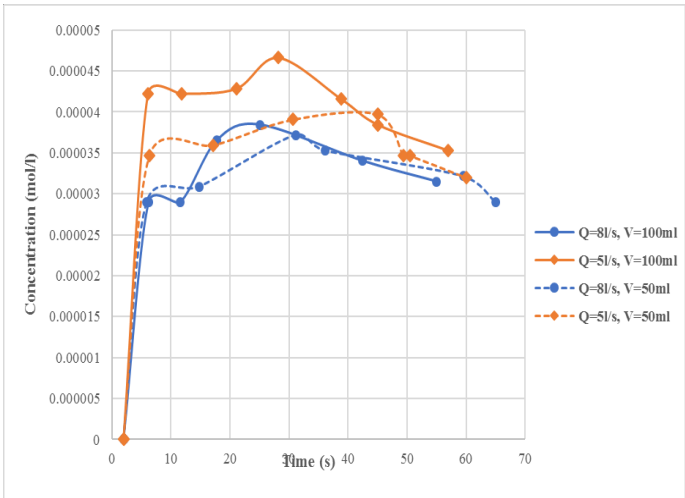

Figure 5: Concentration profile for the different discontinuous injected pollutant volume of 100 ml and 50 ml and for Q= 8 l/s and Q= 5 l/s, over a vegetated bed

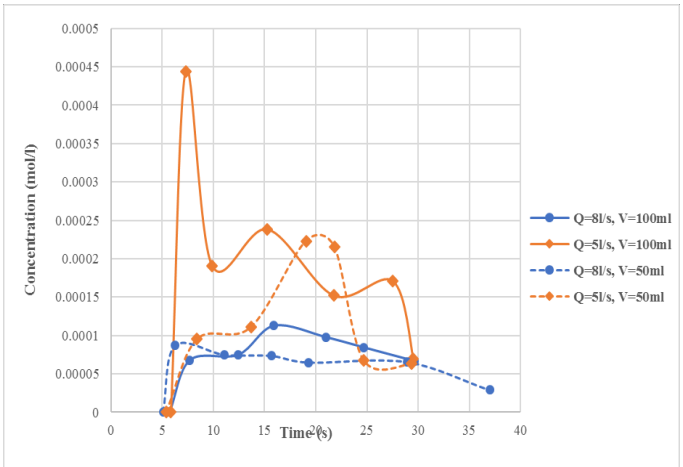

Figure 6: Concentration profile for the different discontinuous injected pollutant volume of 100 ml and 50 ml and for Q= 8 l/s and Q= 5 l/s, over smooth bed

For the different cases we first observe a rise to reach a peak before descending. On the other hand, we note that more the flow rate increases for the same volume injected, the greater the reduction in concentration in the downstream section, this can be explained by the turbulence rate which increases with the flow, the turbulent diffusion will be important which will increase the mixing rate and in return decreases the pollutant propagation time. Also, For the same flow rate, we see that the greater the upstream injected pollutant quantity, the greater the concentration peaks we have during the convective period.

It can also be seen that the vegetation presence on the channel bottom causes a decrease in the pollutant concentration in water, also for the case of discontinuous injection.

IV. Water Quality Simulation

Preliminary simulations of these flows were carried out using the HEC-RAS water quality module, to validate the experimental results.

For this, initial conditions must be precised, such that the pollutant initial concentration corresponding to the concentration found in the channel before the injection. Also, the pollutant discharged masses into the channel as well as the discharge moment must be indicated in the software, as well as the simulation time corresponding to the period for which the monitoring is carried out. At the location where the injection occurs, the pollutant concentration as well as the injection duration must also be indicated for the model.

We present here an example of the fist simulations carried out for the continuous injection case over both a smooth and a vegetated bottom. Note that for the other cases, we found similar results.

In the following, we presented a comparison of the simulated and measured concentration profiles for the continuous injected pollutant volume of 50 ml and for Q= 5 l/s, in the two cases over a vegetated (VB) and a smooth bed (SB).

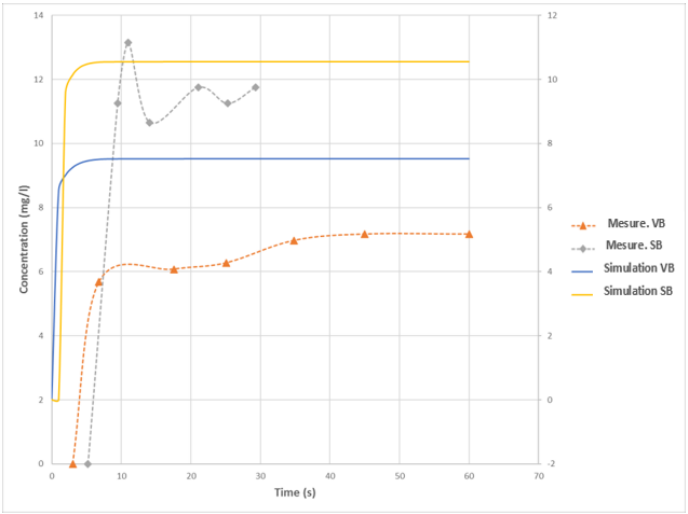

Figure 7: Comparison of the simulated and measured concentration profiles for the continuous injected pollutant volume of 50 ml and for Q= 5 l/s, over a vegetated (VB) and a smooth bed (SB)

This figure showed that for both cases on the smooth or vegetated bottom, the simulations with HEC-RAS overestimated the experiments values. On the other hand, it can also be noted that the simulations showed clearly that the vegetation presence at the channel bottom tends to reduce the propagation of the substance's concentrations in water, which agreed well with experiments.

V. Conclusion

This study concerns laboratory channel experiments and preliminary simulations with the objective of analyzing the

bottom vegetation effect on the propagation rate of a liquid pollutant, the potassium permanganate, and to understand its dispersion rate.

By comparing the two injection types, we see that discontinuous injection best promotes the pollutant mixing in solution compared to continuous injection, where such a pollutant remains in the medium with greater concentration.

It can also be seen that the vegetation presence on the channel bottom causes a decrease in the pollutant concentration in water, this is due to the fact that the vegetation presence increases the bed shear stress and subsequently will delay a solution propagation in water. Indeed, vegetation plays a retarding role of these pollutants' types dispersion.

REFERENCES

[1] S. Benmamar, J. Arrar. "Etude expérimentale de la dispersion d'un polluant passif dans un canal rectangulaire", *Proc of Conférence à l'Université Amar Teldji Laghouat du 19 au 23 novembre 2004.*

[2] E. I. Debol'skaya, I. I. GritsukDebol'skii, V. K. D. N. Ionov. "Effect of Bank Deformations on Pollutant Transport in Rivers in Cryolithozone: Laboratory and Mathematical Modeling", *Water Resources*, vol. 45, pp. 542–552, 2018.

[3] R. Hermann, S. Marc, M. Radmilla. "Particle bound pollutants in rivers: Results from suspended sediment sampling in Globaqua River Basins", *Science of the Total Environment*, vol. 647, pp. 645–652, 2019.

[4] R. Hermann, S. Marc, E. Marius, G. Peter. "Monitoring of event-based mobilization of hydrophobic pollutants in rivers: Calibration of turbidity as a proxy for particle facilitated transport in field and laboratory", *Science of the Total Environment*, vol. 490, pp. 191–198, 2014.

[5] R. Hermann, B. Barbara et al. "Turbidity as a proxy for total suspended solids (TSS) and particle facilitated pollutant transport in catchments", *Environ Earth Sci*, vol. 69, pp. 373–380, 2013.

[6] D. Jabbour. "Etude expérimentale et modélisation de la dispersion en champ lointain suite à un rejet accidentel d'un polluant miscible dans un cours d'eau. Application à la gestion de crise", Thèse de Doctorat de l'université de Provence (Aix Marseille 1), 2006.

[7] H. James, R. Matteo and L. Tom. "An Experimental Investigation of the Hydraulics and Pollutant Dispersion Characteristics of a Model Beaver Dam", *Water*, vol. 12, 2020.

[8] N., Khaldi. "Analyse de la validité des approximations de la couche limite pour un écoulement de type jet pulsé : Application à la dispersion de polluants dans un écoulement à surface libre", Thèse de Doctorat de l'Ecole Nationale d'Ingénieurs de Monastir, 2016.

[9] A. M. Lagoun and S. Benziada. "Experimental Study of Transverse Mixing of Pollutants in Trapezoidal Open Channel, Energy, Transportation and Global Warming", *Green Energy and Technology*, pp. 741-753, 2016.

[10] Z. Roberto, C. Flaviano, Z. Luca, Z. Aleardo. "The effect of floods on the transport of suspended sediments and contaminants: A case study from the estuary of the Dese River (Venice Lagoon, Italy) ", *Environment International*, vol. 31, pp. 948 – 958, 2005.

[11] F. Ulrich. "Sediment dynamics and pollutant mobility in rivers: An interdisciplinary approach", *Lakes & Reservoirs: Research and Management*, vol. 9, pp. 25–40, 2004.

[12] F. Ulrich, S. J~rgen, K. Hans-Diethard. "Metal pollution in the tidal Elbe river", *The Science of the Total Environment*, vol. 97, pp. 347-368, 1990.

[13] L. Yanhong, X. Liquan, S. Tsung-chow. "Bio-Capture of Solid Pollutants by Vegetation Canopy Cave in Shallow Water Flow", *Int. J. Environ. Res. Public Health*, vol. 16, 2019.

[14] V. Yvetta, S. Marek, H. Peter. "Pollutant Spreading in a Small Stream: A Case Study in Mala Nitra Canal in Slovakia", *Environ. Process.*, vol. 1, pp. 265–276, 2014.

[15] H. Romdhane, A. Soualmia, L. Cassan, D. Dartus. "Flow over flexible vegetated bed: Evaluation of analytical models". *Journal of Applied Fluid Mechanics*, 12 (2), pp. 351-359, 2019.

[16] H. Romdhane, A. Soualmia, L. Cassan, G. Belaud. "Effect of vegetation on flows and sediment transport", *E3S Web of Conferences (Environmental sciences, Energy, Earth and planetary sciences), River Flow 2018-Ninth International Conference on Fluvial Hydraulics*, 40(2018) 02017, pp.1-8, 2018.

Determination Of Geometrical Properties of Formed Sheet Metal Parts With 3D Scanning Method

M.AYDIN[1], O. ÖZTÜRK[1] and M. TÜRKÖZ[1]

[1] Konya Technical University, Konya/Turkey, maydin@ktun.edu.tr
[1]Konya Technical University, Konya/Turkey, osmanozturk@ktun.edu.tr
[1]Konya Technical University, Konya/Turkey, mturkoz@ktun.edu.tr

***Abstract* - Many methods are used to determine the formability of sheet metal parts. For example, measuring the radius of curvature of a bulged part or the corner and die entrance radius of a part produced as a cylindrical cup is necessary. Generally, different gauges or measuring instruments are used for each measurement. However, the 3D scanning process can be used to make many measurements such as thickness distribution, curvature radius, corner and die entrance radiuses, wrinkle heights, and wrinkle widths of sheet metal parts. When the 3D scanning method is used, different measuring instruments are not necessary for measurements, and measurements can be taken easily from every desired area of the sheet metal part. In this study, the curvature radii, bulge heights, and thickness distributions of the samples formed with the hydraulic bulge test were measured by the 3D scanning method. In addition, a cup-shaped part was produced with hydroforming, and the corner and die entrance radiuses of the cup-shaped parts and the die-filling ratio were measured using the 3D scanning method. The thickness distributions measured by 3D scanning were compared with the values measured by magnetic ball thickness gauge, and the accuracy of the values measured by 3D scanning was introduced. A minimal difference of 0.6 % was found between the thickness distributions measured by 3D scanning and magnetic ball.**

***Keywords* – 3D Scanning Method, Die-Filling Ratio, Formed Sheet Metal, Thickness Distribution, Corner Radius, Die entrance radius**

I. INTRODUCTION

Sheet metal forming is a famous manufacturing method in many fields in industry. The main purpose of sheet metal forming is to form the sheet into the shape of the mold. The measure of success in sheet metal forming is "formability". There is no single measurement method for formability. These measurement methods may vary according to the forming method and the shape of the formed part. For example, if the forming performance of a hydraulically bulged specimen is to be examined, thickness distribution, bulge height or curvature radii should be measured. Also, thickness distribution is very important for formed cylindrical cups. In addition, the corner and die entrance radii are also measures of formability.

Nowadays, many gauges, mechanical or electronic measuring instruments have been developed to perform the mentioned measurements. In particular, there are many methods for measuring thickness distributions [1]. In one of these, the part is physically cut at a specific cross-section and measured along that cross-section with devices such as profile projection and SEM (Scanning Electron Microscope). These methods have the disadvantages of only being able to take measurements from the cut section, difficulty in sample preparation, susceptibility to personal error, long measurement time and inappropriate cost. In another method, ultrasonic thickness devices can also measure thickness point by point, but without the use of appropriate probes, accurate results cannot be obtained, especially at corner radii. Today, one of the most practical solutions and one of the latest technologies for determining the thickness distribution of sheet metal parts is the three-dimensional (3D) scanning method [2,3]. In Andersonn and Syk's study [4], different geometries such as cone, rectangular parts, and spherical dome were formed by electromagnetic pulse forming. The geometric and strain values of the formed parts were compared with 3D scanning process.

Unlike other methods such as profile projection and SEM, this method can determine thickness distributions along the entire part without cutting the part and more precisely than the ultrasonic method. Since sheet materials exhibit anisotropic behavior, it will be important to determine the thickness distributions along the entire part [5, 6]. Dilmec M. et al. [1] measured the thickness strains of Nakajima test specimens with 3D scanning, SEM and Profile projector and compared the measurement methods. It was observed that the thickness strains obtained by different measurement methods were very close to each other. As a result, it was concluded that thickness measurements of sheet metal parts should be performed with 3D scanning, which can be easily measured across the entire specimen. Önal Ü. [7] compared the geometry of the cylinder cups produced by gradual forming with different angle increments using the incremental forming method with the designed geometry using the 3D scanning process and measured the geometric accuracy. In Sönmez's E. [8] study, the springback performance of DC04 steels with a thickness of 0.7 mm was investigated by using the finite element method. The formed sheets were scanned with an optical scanner and transferred to the computer environment in order to be compared with the geometries to be obtained as a result of finite element analysis.

In this study, it is aimed to make precise geometric measurements of sheet metal parts hydroformed by hydraulic bulging and sheet hydroforming with die with 3D optical scanning. The thickness distributions measured by 3D scanning

were compared with the values measured by magnetic ball thickness gauge, and the accuracy of the values measured by 3D scanning was introduced.

II. Materials and Methods

In this study, geometric measurements of sheet metal specimens formed by hydraulic bulging and sheet hydroforming with die processes were made by 3D scanning process. The material used in this study is Ti-6Al-4V Grade 5 sheet with 0.55 mm thickness. The chemical composition of the material is given in Table 1.

Table 1. Chemical composition of the Ti-6Al-4V Grade 5.

Chemical Composition (%)							
Ti	**Fe**	**C**	**N**	**O**	**H**	**Al**	**V**
89.6	0.049	0.01	0.011	0.044	0.0089	6.15	4.15

In this context, in hydraulic bulging tests, the workpiece diameter and the die cavity were 175 mm and 100 mm, respectively. Also, in sheet hydroforming with die process, the workpiece diameter and the die diameter were 72 mm and 40 mm, respectively. The formed bulged test specimens and cylindrical cup specimens are shown in Figure 1a and Figure 1b, respectively.

a) b)

Figure 1. a) Hydraulic bulged specimen b) Cylindrical cup

After the forming processes, the parts were scanned and geometrical measurements were made on the Breuckmann optoTop-HE 3D optical scanning device shown in Figure 2. For the scanning process, index marks with a diameter of 4 mm were attached to the inner and outer surfaces of the specimens. Thanks to these labels, the optical scanning device can align and combine successive exposures to create a point cloud of the desired object.

Figure 2. 3D Scanning device

After scanning, the point clouds were combined into a whole and saved in .stl format. After the point clouds were created, measurements such as thickness distribution, bulge height, curvature radius, etc. were made using Geomagic Control X software. In order to demonstrate the precision and accuracy of scanning sheet metal parts with the 3D method, the thickness distribution of the sheet metal parts was also measured with a magnetic ball device and a comparison was made. Then, the corner and die entrance radii of the cylindrical cup parts shaped by female hydroforming were measured..

III. Results and Discussion

The thickness distributions obtained by 3D scanning and magnetic ball measurements are shown in Table 2. A total of 18 points were measured from the specimen. The scanning process was performed in two repetitions. According to the results, there is an average deviation of 0.005 mm between the thickness distributions measured by the magnetic ball and the thickness distributions obtained by the 3D scanning process. This result indicates that the 3D scanning process is highly

accurate.

Table 2. Thickness distributions of bulged sheets

Measurement Number	Magnetic Ball	3D Scanning 1	3D Scanning 2	Mean (3D Scanning)	Deviation (mm)
1	0.521	0.519	0.511	0.515	0.006
2	0.503	0.506	0.509	0.508	0.005
3	0.5	0.492	0.489	0.491	0.009
4	0.493	0.486	0.487	0.487	0.007
5	0.486	0.485	0.482	0.484	0.003
6	0.481	0.482	0.478	0.480	0.001
7	0.477	0.476	0.478	0.477	0.000
8	0.468	0.471	0.471	0.471	0.003
9	0.468	0.471	0.464	0.467	0.001
10	0.465	0.468	0.454	0.461	0.004
11	0.469	0.466	0.463	0.465	0.004
12	0.466	0.468	0.468	0.468	0.002
13	0.465	0.469	0.460	0.465	0.000
14	0.473	0.476	0.466	0.471	0.002
15	0.471	0.477	0.483	0.480	0.009
16	0.477	0.481	0.493	0.487	0.010
17	0.492	0.496	0.510	0.503	0.011
18	0.504	0.506	0.515	0.510	0.006
				Mean Deviation	**0.005**

The results are shown graphically in Figure 3.

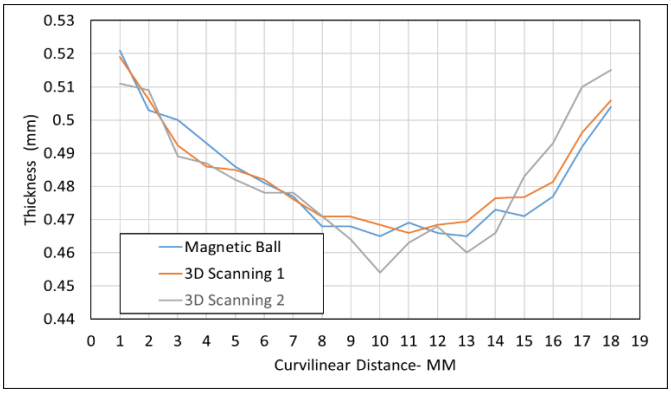

Figure 3. Comparison of thickness distributions of different measurement methods

With the 3D scanning process, thickness distribution can be measured from any section of the part after it has been scanned. In this way, rolling direction-dependent variations seen in anisotropic materials can be easily examined. In addition, measurements that is formability, such as curvature radius or bulge height, can also be made after a single scan. Therefore, 3D scanning is very advantageous compared to other measurement methods. Figure 4 shows the curvature radius measurement obtained from the bulge test specimen. When this measurement is made, a circle is adapted to the curvilinear part of the scanned part and the radius of this circle gives the curvature radius.

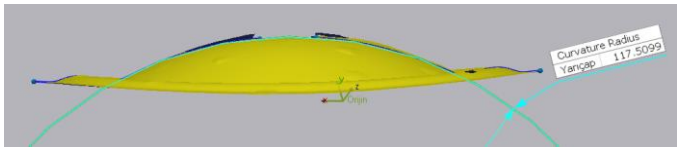

Figure 4. Measurement of curvature radius of bulged sheet

At the same time, precise measurements of the corner and die entrance radii of cylindrical cups can be made with the 3D scanning process. Figure 5 shows the corner radius measurement of a cylindrical cup-shaped sheet metal part. Here, measurements were made at a total of 10 points (36° intervals) and the measurements were averaged. Thus, the average corner radius value can be easily calculated.

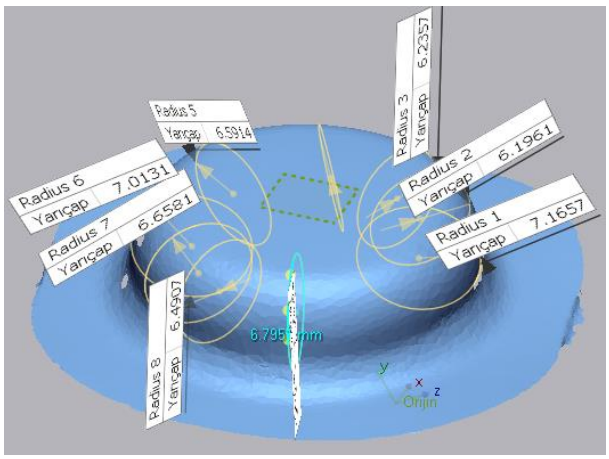

Figure 5. Measurement of corner radius of cylindrical cup

To determine the reliability of the average radius measurement, the same specimen was scanned 4 times and corner radii were measured at 10 different locations. The average corner radii obtained from the four scans are shown in table x. According to the results, the standard deviation between measurements was very small, 0.04 mm. In addition to measuring the base radii of such specimens, the die entrance radii can also be measured with the same method. In addition, die fill ratios can also be calculated by proportioning the volume under the plane passing through the flange surface (shaped part) to the die volume.

Table 3. Deviation analysis of repeated scanning measurements

Scanning Number	Mean Corner Radius
1	8.39
2	8.31
3	8.38
4	8.39
Standard Deviation	**0.04**

As a result, it was concluded that thickness measurements, curvature radii, corner and die entrance radii and die filling ratios of sheet metal parts should be performed with 3D optical scanning.

IV. CONCLUSIONS

In this study, geometric measurements of sheet metal parts shaped by 3D scanning method were investigated. The outputs of the study are summarized below:

(1) According to the thickness distribution results obtained with the magnetic ball and 3D scanning were found to be quite compatible with each other. Therefore, it was determined that the thickness distributions of sheet metal parts can be determined precisely with the 3D method.

(2) 3D scanning was found to be more suitable especially for anisotropic materials.

(3) By scanning the formed sheet once, multiple geometric measurements can be made quickly and easily with 3D scanning.

(4) Very small deviations of 0.005 mm were calculated between repeated radius measurements.

REFERENCES

[1] M. Dilmeç, F. Öztürk, and H.S. Halkacı. "3B Tarama Yöntemiyle Sac Metal Parçaların Kalınlık Dağılımlarının Belirlenmesi." *Düzce Üniversitesi Bilim ve Teknoloji Dergisi* 5.2 (2017): 477-484.

[2] Schneider, M., H. Friebe, and K. Galanulis. "Validation and optimization of numerical simulations by optical measurements of tools and parts." *International Deep Drawing Research Group* (2008): 327-332.

[3] J.H. Vogel, and D. Lee, The automated measurement of strains from three-dimensional deformed surfaces. *JOM*, 1990, 42.2: 8-13.

[4] R. Andersson, and M. Syk. "Electromagnetic pulse forming of carbon steel sheet metal." (2008).

[5] Z. Marciniak, S.J. Hu, J.L. Duncan, *Mechanics of Sheet Metal Forming*, Butterworth-Heinemann, London, 2002.

[6] S. Kohara, "Influence of Strain Path on the Forming Limit Curve in Aluminum," *Metallurgical and Materials Transactions* A, 36A, 1033-1037, 2005.

[7] Ü. Önal, DC04 sacının kademeli artımlı şekillendirme yöntemi ile şekillendirilebilirliğinin araştırılması. *MS thesis.* Sakarya Uygulamalı Bilimler Üniversitesi, 2020.

[8] E. Sönmez,Metal şekillendirme işleminde geri esneme tahmininin deneysel ve sonlu elemanlar yöntemi ile incelenmesi., MS Thesis, 2015.

A Study on Nanobeam with Spring

Burak Emre YAPANMIŞ[1]

[1] Ege University, İzmir/Turkey, burak.emre.yapanmis@ege.edu.tr

Abstract **- Nanobeams is an indispensable element of nano electro-mechanical system. They are fairly common used for connection between two pieces of equipment under a controlled medium. The medium generally has under control by dint of the clean room. In case there are any tiny particles on the air during the manufacturing of nano-size devices in the room, the sensibility and functionality of beams or nano equipment can be broken. From this perspective, there are numerous theoretical studies on nanodevices with different theories for modeling this kind of scenario. One of the fascinating works of nanobeam on natural frequency is present in this study. A spring is settled in the middle position of modeled nanobeam. The linear natural frequencies of nanobeams are obtained theoretically. The effect of the spring's position and the nonlocal coefficient on the naturel frequencies of nanobeam is the biggest motivation for the current work. The results are presented with tables and graphs.**

Keywords **- Continuum theory, Hamilton's principle, Linear vibration, Nanobeam, Perturbation methods.**

I. Introduction

Nano-sized structures have limitations due to some reasons such as the difficulty, cost and time consumption of experimental studies under different conditions. For these reasons, researchers have developed a considerable number of theories in order to carry out their studies on nano size. Some of these theories are strain gradian theory [1,2], micropolar theory [3], modified couple stress theory [4,5], nonlocal elasticity theory [6,7].

II. Equation of Motion and Solving Steps

The nanobeam with spring is shown in figure 1. The equations of motion of the nanobeam are obtained using Hamilton's principle. In order to apply Hamilton's principle, we need to find the Langrangian of the nanobeam. The Langrangian of the system is calculated from the difference between the kinetic and potential energies of the nanobeam in the Eq. (1).

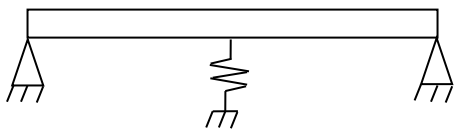

Figure 1: Simple supported nanobeam with spring.

$$\delta\int_{t_1}^{t_2}\left[\begin{array}{l}\frac{1}{2}\int_0^{x_S}\rho A\left(\frac{\partial w_1^*}{\partial t^*}\right)^2 dx^* + \frac{1}{2}\int_{x_S}^{L}\rho A\left(\frac{\partial w_2^*}{\partial t^*}\right)^2 dx^* \\ -\frac{1}{2}\int_0^{x_S}\left(\begin{array}{l} EI\frac{\partial^2 w_1^*}{\partial x^{*2}} + (e_0a)^2 N\frac{\partial^2 w_1^*}{\partial x^{*2}} \\ -(e_0a)^2\rho A\frac{\partial^2 w_1^*}{\partial t^{*2}}\end{array}\right)\frac{\partial^2 w_1^*}{\partial x^{*2}}dx^* \\ -\frac{1}{2}\int_{x_S}^{L}\left(\begin{array}{l} EI\frac{\partial^2 w_2^*}{\partial x^{*2}} + (e_0a)^2 N\frac{\partial^2 w_2^*}{\partial x^{*2}} \\ -(e_0a)^2\rho A\frac{\partial^2 w_2^*}{\partial t^{*2}}\end{array}\right)\frac{\partial^2 w_1^*}{\partial x^{*2}}dx^* \\ -\frac{1}{2}\int_0^{x_S} N\left(\frac{\partial w_1^*}{\partial x^*}\right)^2 dx^* - \frac{1}{2}\int_{x_S}^{L} N\left(\frac{\partial w_2^*}{\partial x^*}\right)^2 dx^* + \frac{1}{2}kw_1^{*2}\end{array}\right]dt^* \quad (1)$$

When the integral is distributed and partial integration is applied for each term separately, the equation of motion is obtained from the double integrals in the final form of the equation, and the boundary conditions are obtained from the single integrals. The spring is divided into nanobeam two different parts. Therefore, it is obvious that two equations for the equation of motion of the nanobeam are obtained because of the spring. The equation of the motions are follows;

$$-\rho A\frac{\partial^2 w_1^*}{\partial t^{*2}} - EI\frac{\partial^4 w_1^*}{\partial x^{*4}} - (e_0a)^2 N\frac{\partial^4 w_1^*}{\partial x^{*4}} + (e_0a)^2\rho A\frac{\partial^4 w_1^*}{\partial t^{*2}\partial x^{*2}} + N\frac{\partial^2 w_1^*}{\partial x^{*2}} = 0 \quad (2)$$

$$-\rho A\frac{\partial^2 w_2^*}{\partial t^{*2}} - EI\frac{\partial^4 w_2^*}{\partial x^{*4}} - (e_0a)^2 N\frac{\partial^4 w_2^*}{\partial x^{*4}} + (e_0a)^2\rho A\frac{\partial^4 w_2^*}{\partial t^{*2}\partial x^{*2}} + N\frac{\partial^2 w_2^*}{\partial x^{*2}} = 0 \quad (3)$$

Here, the axial force is given in Eq. (4).

$$N = \frac{EA}{2L}\int_0^{x_s}\left(\frac{\partial w_1^*}{\partial x^*}\right)^2 dx^* + \frac{EA}{2L}\int_{x_s}^{L}\left(\frac{\partial w_2^*}{\partial x^*}\right)^2 dx^* \quad (4)$$

Nondimensionalization processes have been carried out in order to make the main equations and boundary conditions of the nanobeam independent of the geometric and material properties. Among the variable parameters; the position of spring, time parameters and nonlocal coefficient are

recommended such as $x=\frac{x^*}{L}$, $w_1=\frac{w_1^*}{r}$, $w_2=\frac{w_2^*}{r}$, $t=\frac{1}{L^2}\sqrt{\frac{EI}{\rho A}}t^*$, $\gamma=\frac{e_0 a}{L}$, $\eta=\frac{x_s}{L}$. After the non-dimensional transformation, the necessary mathematical operation has been performed and final version of the main equation is below;

$$w_1^{iv}+\ddot{w}_1-\gamma^2\ddot{w}_1''=\frac{1}{2}\left[\int_0^{\eta}w_1'^2\,dx+\int_{\eta}^{1}w_2'^2\,dx\right]\left[w_1''-\gamma^2 w_1^{iv}\right] \quad (5)$$

$$w_2^{iv}+\ddot{w}_2-\gamma^2\ddot{w}_2''=\frac{1}{2}\left[\int_0^{\eta}w_1'^2\,dx+\int_{\eta}^{1}w_2'^2\,dx\right]\left[w_2''-\gamma^2 w_2^{iv}\right] \quad (6)$$

The boundary conditions of the nanobeam which has spring in mid position are shown in Table 1.

Table 1: Boundary Conditions

First Support	Spring	End Support
$w_1(0,t)=0$	$w_1(\eta,t)=w_2(\eta,t)$	$w_2(L,t)=0$
$w_1''(0,t)=0$	$w_1'(\eta,t)=w_2'(\eta,t)$	$w_2''(L,t)=0$
	$w_1''(\eta,t)=w_2''(\eta,t)$	
	$EI\left(w_1'''(\eta,t)-w_2'''(\eta,t)\right)$	
	$-m\ddot{w}_1(\eta,t)-kw_1(\eta,t)$	

Forcing and damping terms are added to the equations of motion before applying the perturbation method. The expressions $\bar{\mu}$, $\bar{F}$ and Ω in the equations represent damping, forcing force and frequency, respectively. The necessary transform is performed like $\bar{\mu}=\varepsilon\mu$, $\bar{F}=\varepsilon\sqrt{\varepsilon}F$, $w=\sqrt{\varepsilon}y$ to make the equation to ready for the perturbation step.

$$y_1^{iv}+\ddot{y}_1-\gamma^2\ddot{y}_1''=\frac{1}{2}\varepsilon\left[\int_0^{\eta}y_1'^2\,dx+\int_{\eta}^{1}y_2'^2\,dx\right]\begin{bmatrix}y_1''\\-\gamma^2 y_1^{iv}\end{bmatrix}+\varepsilon F\cos(\Omega t)-2\varepsilon\mu\dot{y}_1 \quad (7)$$

$$y_2^{iv}+\ddot{y}_2-\gamma^2\ddot{y}_2''=\frac{1}{2}\varepsilon\left[\int_0^{\eta}y_1'^2\,dx+\int_{\eta}^{1}y_2'^2\,dx\right]\begin{bmatrix}y_2''\\-\gamma^2 y_2^{iv}\end{bmatrix}+\varepsilon F\cos(\Omega t)-2\varepsilon\mu\dot{y}_2 \quad (8)$$

If the straightforward expansion for the displacement is substituted in the main equations, the linear equations of motion will be as follows;

$$Y_1^{iv}(x)-\omega^2 Y_1(x)+\gamma^2\omega^2 Y_1''(x)=0 \quad (9)$$

$$Y_2^{iv}(x)-\omega^2 Y_2(x)+\gamma^2\omega^2 Y_2''(x)=0 \quad (10)$$

III. Research Results And Discussion

By using boundary conditions, the natural frequencies for the nanobeam with spring are found. The spring coefficient is selected as 10 and mass of the beam is 1. The natural frequencies of nanobeam with spring under different nonlocal coefficient and spring position is shown in Table 2. The natural frequencies are verified by drawing the mode shapes.

Table 2: Linear Natural Frequencies.

	γ= 0.1		
η	**0.1**	**0.3**	**0.5**
ω_1	9.507	10.020	10.334
ω_2	33.501	33.623	33.427
ω_3	64.695	64.649	64.723
	γ= 0.3		
η	**0.1**	**0.3**	**0.5**
ω_1	7.251	7.643	7.883
ω_2	18.542	18.611	18.501
ω_3	29.642	29.621	29.656
	γ= 0.5		
η	**0.1**	**0.3**	**0.5**
ω_1	5.351	5.639	5.817
ω_2	12.000	12.045	11.974
ω_3	18.454	18.441	18.462

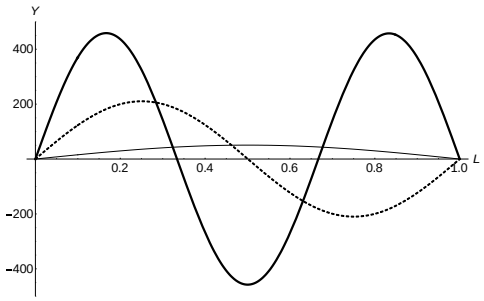

Figure 1: The first three mode shapes of nanobeam with spring for γ= 0.1 and η=0.1 [1st mode (—), 2nd mode (---), 3rd mode (—)]

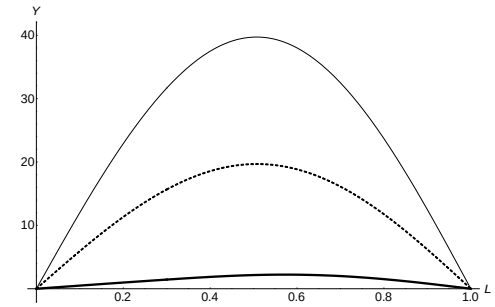

Figure 2: First linear natural frequency mode shapes for different γ [γ= 0.1(—), γ= 0.3(---), γ= 0.5(—)]

IV. Conclusion

In this study, nanobeam with spring which is settled in mid position is researched. The position of the spring and nonlocal coefficient are focused as variable parameters. As a result of changing variable parameters, natural frequency differentiation is investigated. When results examine

generally, it is clearly seen that the natural frequency values of the nanobeams and the amplitudes of the mode shapes decrease when the non-local parameter increase.

REFERENCES

[1] R.D. Mindlin, N.N. Eshel, (1968). On first strain-gradient theories in linear elasticity. International Journal of Solids and Structures. 4(1), pp.109–124.

[2] Dang V. H., Duong T. H. Bui G. P. (2020). Nonlinear Vibration of a Functionally Graded Nanobeam Based on the Nonlocal Strain Gradient Theory considering Thickness Effect. Advances in Civil Engineering. https://doi.org/10.1155/2020/9407673.

[3] M. F. Oskouie, A. Norouzzadeh, R. Ansari, H. Rouhi (2019). Bending of small-scale Timoshenko beams based on the integral/differential nonlocal-micropolar elasticity theory: a finite element approach. Appl. Math. Mech.-Engl. Ed. 40, pp. 767–782. https://doi.org/10.1007/s10483-019-2491-9

[4] N. Togun, S. M. Bağdatlı (2017). Investigation of the Size Effect in Euler-Bernoulli Nanobeam Using the Modified Couple Stress Theory. Celal Bayar University Journal of Science, 13(4) 893-899. doi: 10.18466/cbayarfbe.370362.

[5] E. R. Estabragh, G. H. Baradaran, (2021) Analysis of large deflection of nanobeams based on the modified couple stress theory by using finite element method. Arch Appl Mech 91, pp. 4717–4734. https://doi.org/10.1007/s00419-021-02029-6

[6] A. C. Eringen, (1965), Theory of micropolar continua, in Developments in Mechanics. (T. C. Huang and M. W. Johnson, Jr., eds), 3. Wiley, New York

[7] B. E. Yapanmış, S. M. Bagdatlı (2022). Investigation of the nonlinear vibration behaviour and 3:1 internal resonance of the multi supported nanobeam. Z Naturfr A. https://doi.org/10.1515/zna-2021-0300.

Investigation of Classic and Non-classic Functionally Graded Beams Model

B.E.YAPANMIŞ[1] and S.M. BAĞDATLI[2]

[1] Ege University, İzmir/Turkey, burak.emre.yapanmis@ege.edu.tr
[2] Manisa Celal Bayar University, Manisa/Turkey, murat.bagdatli@cbu.edu.tr

Abstract **- In the presented study, beams made from functionally graded materials (FGMs) are examined. FGMs is clarified in detail and the general information about features, design, application areas, mathematical models of FGMs and literature studies are presented. In addition, general information about different beam theories are given. The governing equations base on Euler-Bernoulli Beam Theory and Timoshenko Beam Theory are shown and discussed respectively. It is indicated that the Euler-Bernoulli beam theory is available for using thin beams owing to neglecting of rotary inertia and shear deformation. However, Timoshenko beam theory proposes more accurate results for thick beam analysis.**

Keywords **– Euler-Bernoulli beam theory, Continuum mechanics, Functionally graded materials, Rayleigh beam theory, Timoshenko beam theory.**

I. Introduction

Nowadays, it is desired that the materials have an inhomogeneous gradual, or constantly changing structure in industrial applications. For this reason, scientists have developed a new generation material called Functionally Graded Materials (FGM). FGMs consists of two or more than two materials combined with each other that having different physical and chemical properties. The thermal stresses are low by dint of their graded structures due to the different thermal expansion coefficients between the two materials. In addition, other negative effects that may occur due to sudden changes in physical and chemical properties between two substances are also minimal. A mixture of metal and ceramic materials can be given as a typical example of FGMs. In this way, the ceramic will be able to resist high temperatures in thermal environments, and the metal will reduce the tensile stresses that will occur on the ceramic surface in the first stages of cooling.

Composite materials have sophisticated material properties. These materials are made of one or more solid materials with distinct physical and chemical properties. Composite material offers excellent property which is not the same properties as used individual materials. In addition, they are popular with their lighter properties. However, connection interface errors, which are known as delamination, commonly arise on the material after extreme working conditions. This error has impulsed scientists to find out new materials. Consequently, the FGMs emerged in a space project in Japan. In the project, the high-temperature atmosphere causes thermal stress in the thermal barrier of the composite material. As a result of thermal stress, the crack occurs on the connection line of the material. In the end, FGMs is discovered to eliminate for delamination.

Generally, FGMs are obtained by gradually changing the volume ratios of the components that make up the material from one surface to another. In this way, the material properties of the structure are also gradually changed along the direction of change. The change in the volume ratios of the components that make up the material can be continuous or stepwise such as in Fig 1. The performance of the FGMs is optimized by changing the proportions, shapes, and orientations of the component phases in according to directions. Typical variables in continuous-grade materials are volume fraction and shape of components, orientation, component diameter, the chemical composition of fibers, changes in porosity, etc. The continuous FGMs figure is shown in Figure 2.

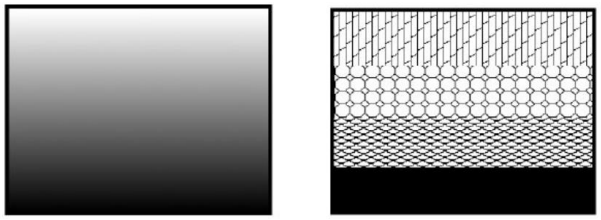

Figure 1: Schematic view of FGMs a) continuously b) stepwise [1]

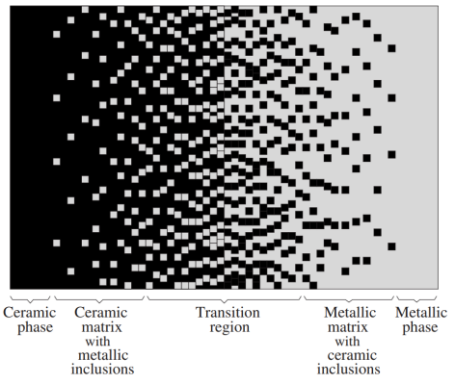

Figure 2: Details view of continuous graded ceramic-metal materials [2]

FGMs is widely used in much different application area. Some of them; automotive, machinery and equipment, biomedical, energy, defense etc. FGMs can be manufactured in different methods such as deposition-based methods, solid-state methods, and liquid-state methods. For more information, it is offered to read Ref. [13].

It can be clearly seen that numerous different beam theories on FDMs in literature. Aydogdu and Taskin [4] searched the free vibration characteristic of FGMs beam with simply supported using various higher-order beam theories. They assumed that the modulus of elasticity is changed according to a force function along the thickness. Hamilton's principle and Navier-type solution method are preferred for having governing equation and solved. Li et. all [5] examine FGMs Timoshenko beam under different load and boundary conditions. Clamped-free, simple-free, clamped-clamped and simple-simple supports are selected as the variable parameter for boundary conditions. Şimşek [6] performed a frequency analysis of FGMs beams with different beam theories like classic, first-order and higher-order shear deformation beam theory. He researched the slenderness ratio and material variational effect on the fundamental frequency. Sina et al. [7] recommend a new theory about the free vibration analysis of FGMs beams. The main equations are obtained with the help of Hamilton's principles by assuming that the lateral normal stresses in the beam are zero. Thai and Vo [8] performed free vibration and bending analyzes of FDM beams using various higher-order shear deformation theories. They examined the effect of shear deformation and power law index on the free vibration and bending behavior. Nguyen et al. [9] developed an analytical solution according to Timoshenko beam theory for static and free vibration analysis of FDM beams under axial load. Hadji et al. [10] developed a new high-order shear deformation model for free vibration and static analysis of FGMs beams. Chen and Chang [11] investigated the free vibrations of FGMs Euler-Bernoulli beams with the transformed section method. Lee and Lee [12] examined the vibration behaviour of FGMs Euler-Bernoulli beams using the transfer matrix method. They stated that this method is very useful in the calculation of mode shapes and the natural frequencies and when the material properties change according to the force function along the height. Kahya ve Turan [13] investigated vibration and bending analysis of FGMs sandwich beam that consists of ceramic and metal based on first-order shear deformation theory. The power law index, thickness ratio and different boundary conditions were considered.

II. Definition of FGMs

The standard rectangular cross-section beam is considered for obtaining the FGMs beam. x, y, x axes are in the same direction with length, width and height, respectively. If it is considered *P* is material properties, it can be defined as;

$$P = P_p V_p + P_c V_c \tag{1}$$

Here, P_p and P_c are material properties, V_p and V_c is the volume of materials. The ratio of volume can be defined as follows;

$$V_p = \left(\frac{z}{h} + \frac{1}{2}\right)^N \tag{2}$$

In Eq. (2), *N* is any number that expresses the material volume fraction coefficient. This expression indicates the proportion of material type. *N* curves are shown in Fig. 3. The left of the graph is represented fully ceramic, right of the graph is represented fully second material in the figure.

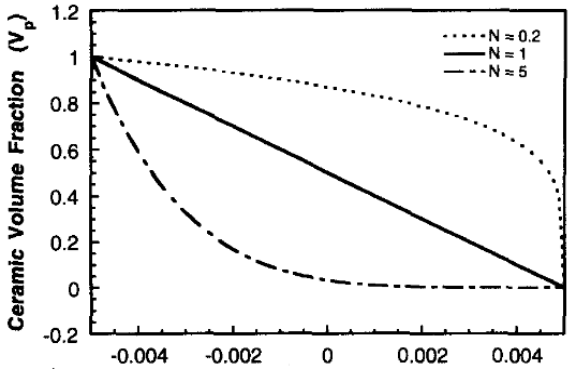

Figure 3: Variation of volume fraction [14]

The sum of the two types of material is equal to 1 as it is shown in Eq. (3). Based on this brief information, when the material volume fraction is substituted in Eq. (1), the new material properties coefficient is obtained in Eq. (4). The Poisson ratio, material density, elasticity modulus, and shear modulus can be defined for material properties.

$$V_p + V_c = 1 \tag{3}$$

$$P = \left(P_p - P_c\right)\left(\frac{z}{h} + \frac{1}{2}\right)^N + P_c \tag{4}$$

It can be understood, if *z* is equal to -h or h, the material properties will be fully a material that is located in up or down. The tension stress and shear stress for FGMs is given in Eq. (5).

$$\sigma_{xx} = E(z)\varepsilon_{xx},\ \tau_{xz} = KG(z)\gamma_{xz} \tag{5}$$

Here, σ represent tension stress and τ represent shear stress. *K* is the correction coefficient that is defined 5/6 for rectangular cross-section, *E* is elasticity, and G is the shear elasticity modulus [15].

III. An Overview of Beam Theories

Beams have a significant position for structural equipment. Beam theories have arisen to understand beam mechanics

easily. There are a lot of different beam theories in the literature such as the Euler-Bernoulli (classic), Rayleigh, and Timoshenko, Reddy–Bickford beam theories etc. Euler-Beornolli and Timoshenko beam theories are the most common used theories among them. The shapes of deformed geometries according to different beam theories are shown in Figure 4. In this study, it is focused on Euler-Bernoulli and Timoshenko's beam theory. When the beam cross-section is large, the Euler-Bernoulli beam theory overestimates the natural frequencies. However, Timoshenko beam theory proposes better results for large scale. Therefore, the Euler-Bernoulli beam is referred to as a thin beam theory, and the Timoshenko beam is known as the thick beam theory.

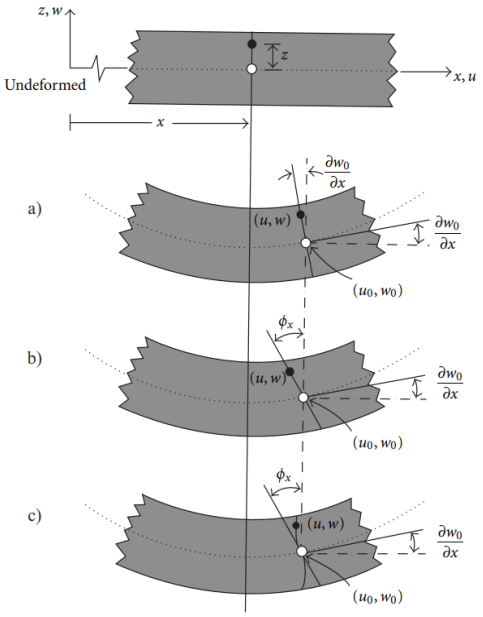

Figure 4: Deformation geometries of Euler-Bernoulli, Timoshenko and Reddy–Bickford beam theories [16]

IV. Governing Equation of Euler-Bernoulli Beam Theory

There are very different methods in literature to obtain the governing equation of beams such as Hamilton's principle, Energy conversation or Newton's second law etc. Newton's method most easy method in terms of applicability. The relation between the deflection of the beam and the applied distributed load on the dynamic equation is as follows.

$$-V+\left(V\frac{\partial V}{\partial x}\right)+qdx=\rho Adx\frac{\partial^2 y}{\partial t^2} \tag{6}$$

Here V is shear force, ρ is density, A is cross-section area, and q is load. It is known that $V=\frac{\partial M}{\partial x}$ from constitutive relation. If the necessary mathematical operation is carried out, the final version of the main equation is below;

$$\frac{\partial^4 y}{\partial x^4}+q=\frac{\rho A}{EI}\frac{\partial^2 y}{\partial t^2} \tag{7}$$

V. Governing Equation of Timoshenko Beam Theory

Timoshenko beam is a different version of the Euler-Bernoulli beam theory. Timoshenko beam theory is considered the effect of shear deformation and rotary inertia. The Governing equation of the Timoshenko beam based on Newton's law is given below.

$$-V+\left(V+\frac{\partial V}{\partial x}\right)+qdx=\rho Adx\frac{\partial^2 y}{\partial t^2} \tag{8}$$

$$-M+\left(M+\frac{\partial M}{\partial x}dx\right)D+\frac{1}{2}Vdx+\frac{1}{2}\left(V+\frac{\partial V}{\partial x}dx\right)=J\frac{\partial^2\phi}{\partial t^2} \tag{9}$$

Here, the shear force is defined as an expression relevant to shear strain (G) and coefficient (κ).

$$V=AG\kappa\left(\frac{\partial y}{\partial x}-\phi\right) \tag{10}$$

After substituting shear force in main equations, the final form of the governing equation is obtained as below:

$$AG\kappa\left(\frac{\partial\phi}{\partial x}-\frac{\partial^2 y}{\partial t^2}\right)+\rho A\frac{\partial^2 y}{\partial t^2}=q(x,t) \tag{11}$$

$$GA\kappa\left(\frac{\partial y}{\partial x}-\phi\right)+EI\frac{\partial^2\phi}{\partial x^2}=\rho I\frac{\partial^2\phi}{\partial t^2} \tag{12}$$

In the equation of the motion of the beam, J is polar inertia moment, I is cross-section inertia moment, and E is elasticity modulus.

Table 1: The comparison of Timoshenko and Euler Bernoulli beam theories [17]

	Euler-Bernoulli Beam Type	Timoshenko Beam Type
Bending moment	+	+
Lateral displacement	+	+
Shear deformation	-	+
Rotary inertia	-	+

VI. Conclusion

In the present study is related to the comparison of thin and thick beam theories. It is stated that the Euler-Bernoulli beam model might be used for slender and micro and nano-beams. However, this theory overestimates natural frequencies for

macro size. Therefore, the Timoshenko beam theory is developed. This theory is considered shear deformation and rotary inertia. In recent years, functionally graded materials are researched often among scientists. The reason for this intensity is explained and the innovation of functionally graded materials is clarified. The basic equations on functionally graded materials are presented in the second section. A lot of different methods can be used to the derivation of governing equations for functionally graded beams. Therefore, the most common and basic method is preferred for the normal beam to increase the understanding of work. It is considered that the presented study will be a fundamental reference for new researchers in this field.

REFERENCES

[1] Y. Miyamoto, W.A. Kaysser, B.H. Rabin, A. Kawasaki, R.G. Ford, *Functionally Graded Materials: Design, Processing and Applications*, Kluwer Academic Publishers, Massachusetts, USA, 1999.

[2] Y. Chan, G. Paulino, A. C. Fannjiang, "Gradient Elasticity Theory for Mode III Fracture in Functionally Graded Materials—Part II: Crack Parallel to the Material Gradation", *J. Appl. Mech*., 75(6), 061015, 2008.

[3] B. Saleh, J. Jiang, R. Fathi, T. Al-hababi, Q. Xu, L. Wang, D. Song, A. Ma, "30 Years of functionally graded materials: An overview of manufacturing methods, Applications and Future Challenges", *Composites Part B: Engineering*, 201,2020.

[4] M. Aydaoğdu, V. Taşkın, "Free vibration analysis of functionally graded beams with simply supported edges", *Materials & Design*, vol. 28(5), pp.1651-1656, 2007.

[5] S. R. Li, D. F. Cao, Z. Q. Wan, "Bending solutions of FGM Timoshenko beams from those of the homogenous Euler–Bernoulli beams", *Applied Mathematical Modelling*, vol. 37, pp 7077-7085, 2013.

[6] M. Şimşek, "Fundamental frequency analysis of functionally graded beams by using different higher-order beam theories", *Nuclear Engineering and Design*, vol. 240 (4), pp.697-705, 2010.

[7] S.A.Sina, H.M.Navazi, H.Haddadpour, "An analytical method for free vibration analysis of functionally graded beams", *Materials & Design*, vol. 30 (3), pp.741-747, 2009.

[8] H. T. Tai, T. P. Vo, "Bending and free vibration of functionally graded beams using various higher-order shear deformation beam theories", *International Journal of Mechanical Sciences*, vol. 62 (1), pp.57-66, 2012.

[9] T. K. Nguyen, T. P. Vo, H. T. Thai, "Static and free vibration of axially loaded functionally graded beams based on the first-order shear deformation theory", *Composites Part B: Engineering*, vol. 55, pp. 147-157, 2013.

[10] L. Hadji, Z. Khelifa, A. B. El Abbes, "A new higher order shear deformation model for functionally graded beams" *KSCE Journal of Civil Engineering*, Vol. 20, pp. 1835-1841, 2016.

[11] W. R. Chen, H. Chang, "Closed-Form Solutions for Free Vibration Frequencies of Functionally Graded Euler-Bernoulli Beams", *Mechanics of Composite Materials*, vol. 53, pp.79-98, 2017

[12] J. W. Lee, J. Y. Lee, "Free vibration analysis of functionally graded Bernoulli-Euler beams using an exact transfer matrix expression", *International Journal of Mechanical Sciences*, vol. 122, pp.1-17, 2017

[13] V. Kahya, M. Turan, "Vibration and stability analysis of functionally graded sandwich beams by a multi-layer finite element", *Composites Part B: Engineering*, vol. 146, pp.198-212.

[14] K.S.Ravichandran, "Thermal residual stresses in a functionally graded material system", *Materials Science and Engineering*: A, vol. 201(1), pp. 269-276, 1995.

[15] M. Turan, V. Kahya, "Fonksiyonel Derecelendirilmiş Kirişlerin Serbest Titreşim Analizi ", *Karadeniz Fen Bilimleri Dergisi* vol. 8(2), pp. 119-130, 2018.

[16] M. Sobhy, M. A. Abazid, F. H. Al Mukahal, "Electro-thermal buckling of FG graphene platelets-strengthened piezoelectric beams under humid conditions", *Advances in Mechanical Engineering*, 14(4), 2022.

[17] S. M. Han, H. Benaroya, T. Wei, "Dynamics of Transversely Vibrating Beams Using Four Engineering Theories", *Journal of Sound and Vibration*, vol. 225(5), pp.935-988, 1999.

Analysis of Position-Level Forward Kinematic Singularities of Planar RPRPR Parallel Robots

Mustafa ÖZDEMİR[1] and Levent KARAKAYA[2]

[1]Department of Mechanical Engineering, Faculty of Engineering, Marmara University, Recep Tayyip Erdoğan Campus, 34854 Maltepe, İstanbul, Türkiye, E-mail: mustafa.ozdemir@marmara.edu.tr, ORCID iD: https://orcid.org/0000-0002-4981-9573

[2]Department of Mechanical Engineering (English), Institute of Pure and Applied Sciences, Marmara University, Göztepe Campus, 34722 Kadıköy, İstanbul, Türkiye, E-mail: leventkarakaya@marun.edu.tr, ORCID iD: https://orcid.org/0000-0002-3896-8194

Corresponding author: Mustafa ÖZDEMİR

***Abstract* - Parallel robots have many advantages over their conventional serial counterparts. High accuracy and high payload-to-weight ratio are the main ones of these advantages. The main factor underlying the success of parallel robots is their closed-loop construction. However, this architectural feature also causes a characteristic singularity problem, which constitutes their biggest disadvantage. Being different than serial robots, singularities known as Type II occur in the forward kinematic solution of parallel robots. Unlike Type I singularities encountered in inverse kinematics, these singularities of second kind are located within the workspace and around them the magnitude of the inverse dynamic solution goes to infinity. Therefore, in the vicinity of Type II singularities, the actuators get saturated and lose the control of the robot. Consequently, the entire available workspace is not usable by the robot. Due to these facts, singularity analysis has been one of the most important research topics in parallel robotics. The aim of this paper is to analyze the forward kinematic position singularities of a commonly used parallel robot, namely the RPRPR-type planar parallel robot. The paper examines the degeneracies of the position-level forward kinematic solution of the said parallel robot and explores the relations of these degeneracies with the forward kinematic motion singularities.**

***Keywords* - Parallel robot, planar parallel robot, forward kinematics, singularity, position singularity.**

NOMENCLATURE

A, B	Centers of base revolute joints
a_1	Length $\|AB\|$
Axy	Fixed Cartesian coordinate system with point B on the x-axis
E	End-effector
s_1, s_2	Prismatic joint variables
θ_1, θ_2	Revolute joint variables

Superscript

-1	Inverse of a matrix

I. INTRODUCTION

PARALLEL robots are composed of closed kinematic chains and are more preferable than their open-chain serial counterparts because of their superiorities in operation speed, acceleration capability, accuracy, precision, rigidity, and loading capacity [1-4]. Their major shortcoming is in that they have a complex singularity problem. Type I singularities [5], also known as inverse kinematic singularities, are common to both serial and parallel robots. The good news is that the singularities of this type are generally encountered at the workspace boundaries [5], and for this reason are not considered to pose a serious limitation in the use of parallel robots. Type II singularities [5] (or forward kinematic singularities), on the other hand, are unique to parallel robots and the critical ones are these singularities. What makes them critical is that they arise inside the workspace [5] and around them the magnitude of the inverse dynamic solution diverges to infinity, which yields the saturation of the actuators. This results in the loss of the control of the robot [6]. The direct consequence of this is that the robot cannot utilize the whole of its workspace. That is why in the parallel robotics literature there has been a great amount of research dealing with Type II singularities.

One condition that is necessary for passing through a Type II singular configuration is the consistency of the dynamic model at that configuration [7-9]. There have been three methods proposed in the literature to have the consistency of the dynamic equations maintained at the singular position. These are:

- Trajectory planning [7-12]
- Balancing [13]
- Payload placement [14, 15]

Exploration of high-order parallel singularities by Özdemir [16-18] is a breakthrough advancement for fully utilizing the workspace of parallel robots. Özdemir [16] developed a complete theory for parallel robots which derives the additional singularity removal conditions required other than the one for consistency.

Another study that has brought a new perspective to the

singularity analysis of parallel robots is by Ozgoren [19], who showed that in addition to motion singularities, parallel robots can also have position singularities just like serial robots do [20, 21]. Based on an analysis focusing on the 5R planar parallel robot, Ozgoren [19] concluded that every position singularity is also a motion singularity, but not vice versa. In the present paper, we examine the position-level forward kinematic singularities of the RPRPR-type planar parallel robot to see whether this conclusion can be generalized to other parallel robots or not. It is worth noting that in accordance with the usual convention in the field of robotics, the uppercase letters R and P are used in the paper to represent revolute and prismatic joints, respectively, and the underlines show the actuated joints.

II. Loop-Closure Equations

The kinematic diagram of a planar RPRPR parallel robot is shown in Figure 1. The robot is a single-loop five-bar mechanism having two degrees of freedom. Point *A* is the origin of the fixed Cartesian coordinate system *xy*. Point *B* is at $(x,y) = (a_1,0)$. Point *E* is the end-effector of the robot. The robot is driven by two revolute motors that are located at joints *A* and *B*. Hence, θ_1 and θ_2 are the actuated joint variables, and $s_1 = |AE|$ and $s_2 = |BE|$ are the unactuated ones.

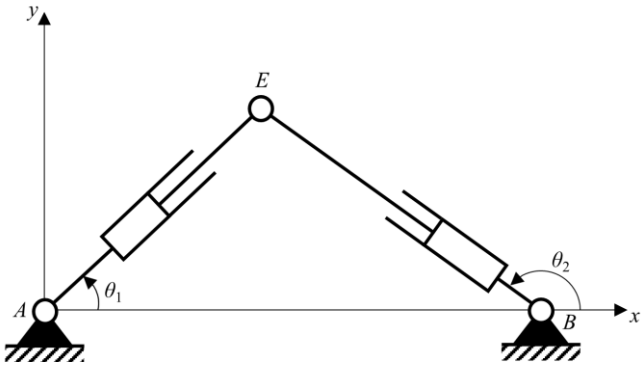

Figure 1: Planar RPRPR parallel mechanism.

The loop-closure constraint equations of the mechanism can be written as follows:

$$s_1\cos(\theta_1) - a_1 - s_2\cos(\theta_2) = 0 \tag{1}$$

$$s_1\sin(\theta_1) - s_2\sin(\theta_2) = 0 \tag{2}$$

Differentiating these equations with respect to time *t* gives the following velocity loop equations:

$$\dot{s}_1\cos(\theta_1) - s_1\dot{\theta}_1\sin(\theta_1) - \dot{s}_2\cos(\theta_2) + s_2\dot{\theta}_2\sin(\theta_2) = 0 \tag{3}$$

$$\dot{s}_1\sin(\theta_1) + s_1\dot{\theta}_1\cos(\theta_1) - \dot{s}_2\sin(\theta_2) - s_2\dot{\theta}_2\cos(\theta_2) = 0 \tag{4}$$

III. Motion Singularities of the Forward Kinematic Problem (Type II Singularities)

Singularities of parallel robots are classically determined in the literature by using the velocity-level kinematic relations between the actuated joint variables and the task variables [5]. For this reason, the so-obtained singularities can be called motion singularities [19].

Instead of using the relationships between the input and output velocities, Type II singularities can be determined more easily using the velocity loop equations [7]. For this purpose, equations (3) and (4) can be rewritten in matrix-vector form as follows:

$$\mathbf{A}\begin{bmatrix}\dot{s}_1\\ \dot{s}_2\end{bmatrix} + \mathbf{B}\begin{bmatrix}\dot{\theta}_1\\ \dot{\theta}_2\end{bmatrix} = \begin{bmatrix}0\\ 0\end{bmatrix} \tag{5}$$

Here **A** and **B** are 2-by-2 matrices that are respectively given by

$$\mathbf{A} = \begin{bmatrix}\cos(\theta_1) & -\cos(\theta_2)\\ \sin(\theta_1) & -\sin(\theta_2)\end{bmatrix} \tag{6}$$

and

$$\mathbf{B} = \begin{bmatrix}-s_1\sin(\theta_1) & s_2\sin(\theta_2)\\ s_1\cos(\theta_1) & -s_2\cos(\theta_2)\end{bmatrix} \tag{7}$$

Equation (5) can be solved for the unactuated joint velocities in terms of the position variables and the actuated joint velocities as

$$\begin{bmatrix}\dot{s}_1\\ \dot{s}_2\end{bmatrix} = -\mathbf{A}^{-1}\mathbf{B}\begin{bmatrix}\dot{\theta}_1\\ \dot{\theta}_2\end{bmatrix} \tag{8}$$

By performing the matrix inversion and multiplications in equation (8), we can get

$$\dot{s}_1 = \frac{s_2\dot{\theta}_2 - s_1\dot{\theta}_1\cos(\theta_1 - \theta_2)}{\sin(\theta_1 - \theta_2)} \tag{9}$$

and

$$\dot{s}_2 = -\frac{s_1\dot{\theta}_1 - s_2\dot{\theta}_2\cos(\theta_1 - \theta_2)}{\sin(\theta_1 - \theta_2)} \tag{10}$$

It can be seen from these equations that the motion singularities of the forward kinematic problem [19] (or Type II singularities) are given for the RPRPR-type planar parallel robot by

$$\sin(\theta_1 - \theta_2) = 0 \tag{11}$$

This singularity condition corresponds to the configurations where point *E* is collinear with points *A* and *B*. Thus, Type II singularities of the planar RPRPR parallel robot occur when point *E* is on the *x*-axis. At these singularities, one of the following three cases holds:

(i) $\theta_1 = \theta_2 = 0$
(ii) $\theta_1 = 0$ and $\theta_2 = \pi$
(iii) $\theta_1 = \theta_2 = \pi$

IV. Position-Level Forward Kinematic Singularities

Equations (1) and (2) can be recast into the following matrix-vector form:

$$\mathbf{A}\begin{bmatrix} s_1 \\ s_2 \end{bmatrix} + \mathbf{b} = \begin{bmatrix} 0 \\ 0 \end{bmatrix} \tag{12}$$

where the matrix **A** is as given in equation (6) and **b** is a 2-dimensional column vector given by

$$\mathbf{b} = \begin{bmatrix} -a_1 \\ 0 \end{bmatrix} \tag{13}$$

Equation (12) can be solved for the unactuated joint positions in terms of the fixed parameter a_1 and the actuated joint positions as

$$\begin{bmatrix} s_1 \\ s_2 \end{bmatrix} = -\mathbf{A}^{-1}\mathbf{b} \tag{14}$$

By carrying out the matrix inversion and multiplication in equation (14), we can obtain

$$s_1 = -\frac{a_1 \sin(\theta_2)}{\sin(\theta_1 - \theta_2)} \tag{15}$$

and

$$s_2 = -\frac{a_1 \sin(\theta_1)}{\sin(\theta_1 - \theta_2)} \tag{16}$$

It follows from these equations that the condition for the occurrence of singularities in the position-level forward kinematics of the RPRPR-type planar parallel robot is also given by equation (11).

V. Discussion

At a position-level forward kinematic singularity of the planar parallel RPRPR robot, one of the loop-closure equations, namely, equation (2), becomes 0 = 0. On the other hand, the other loop-closure constraint, namely, equation (1), reduces to one of the following three equations:

$$\begin{cases} s_1 - s_2 = a_1, & \text{for } \theta_1 = \theta_2 = 0 \\ s_1 + s_2 = a_1, & \text{for } \theta_1 = 0 \text{ and } \theta_2 = \pi \\ s_2 - s_1 = a_1, & \text{for } \theta_1 = \theta_2 = \pi \end{cases} \tag{17}$$

Therefore, we can deduce that at a position singularity of the forward kinematic problem of the RPRPR-type planar parallel robot, there are infinite number of solutions for s_1 and s_2.

VI. Conclusion

The analysis conducted in this paper shows that in the forward kinematics of the planar RPRPR parallel robot, every position singularity is also a motion singularity and vice versa. In other words, it is proved that the position and motion singularities of the forward kinematic problem are identical for the RPRPR-type planar parallel robot. This is the contribution of the present paper to the existing literature.

Acknowledgment

This paper is based on a part of the Master of Science Thesis of the second author (Levent KARAKAYA), which is in preparation in the Department of Mechanical Engineering (English) at Marmara University Institute of Pure and Applied Sciences under the supervision of the first author (Assoc. Prof. Dr. Mustafa ÖZDEMİR).

References

[1] J.-P. Merlet, *Parallel Robots*, 2nd ed. Dordrecht: Springer, 2006.
[2] J.-P. Merlet and C. Gosselin, "*Parallel Mechanisms and Robots*," in: *Springer Handbook of Robotics*, B. Siciliano and O. Khatib, Eds. Berlin, Heidelberg: Springer, 2008, pp. 269–285.
[3] D. Zhang, *Parallel Robotic Machine Tools*. New York, NY: Springer, 2010.
[4] Y. Jin, H. Chanal, and F. Paccot, "*Parallel Robots*," in: *Handbook of Manufacturing Engineering and Technology*, A. Y. C. Nee, Ed. London: Springer, 2015, pp. 2091–2127.
[5] C. Gosselin and J. Angeles, "Singularity analysis of closed-loop kinematic chains," *IEEE Trans. Robot. Autom.*, vol. 6, no. 3, pp. 281–290, Jun. 1990.
[6] P. Choudhury and A. Ghosal, "Singularity and controllability analysis of parallel manipulators and closed-loop mechanisms," *Mech. Mach. Theory*, vol. 35, no. 10, pp. 1455–1479, Oct. 2000.
[7] S. K. Ider, "Inverse dynamics of parallel manipulators in the presence of drive singularities," *Mech. Mach. Theory*, vol. 40, no. 1, pp. 33–44, Jan. 2005.
[8] C. K. K. Jui and Q. Sun, "Path Tracking of Parallel Manipulators in the Presence of Force Singularity," *J. Dyn. Syst. Meas. Control-Trans. ASME*, vol. 127, no. 4, pp. 550–563, Dec. 2005.
[9] S. Briot and V. Arakelian, "Optimal Force Generation in Parallel Manipulators for Passing through the Singular Positions," *Int. J. Robot. Res.*, vol. 27, no. 8, pp. 967–983, Aug. 2008.
[10] S. Briot, G. Pagis, N. Bouton, and P. Martinet, "Degeneracy conditions of the dynamic model of parallel robots," *Multibody Syst. Dyn.*, vol. 37, no. 4, pp. 371–412, Aug. 2016.
[11] M. Özdemir, "Optimization in motion planning for parallel robots passing through singular positions," *J. Fac. Eng. Archit. Gazi Univ.*, vol. 32, no. 4, pp. 1089–1096, Dec. 2017.
[12] V. Muralidharan, T. K. Mamidi, S. Guptasarma, A. Nag, and S. Bandyopadhyay, "A comparative study of the configuration-space and actuator-space formulations of the Lagrangian dynamics of parallel manipulators and the effects of kinematic singularities on these," *Mech. Mach. Theory*, vol. 130, pp. 403–434, Dec. 2018.
[13] M. Özdemir, "Singularity robust balancing of parallel manipulators following inconsistent trajectories," *Robotica*, vol. 34, no. 9, pp. 2027–2038, Sep. 2016.

[14] M. Özdemir, "Singularity-consistent payload locations for parallel manipulators," *Mech. Mach. Theory*, vol. 97, pp. 171–189, Mar. 2016.
[15] M. Özdemir, "Dynamic analysis of planar parallel robots considering singularities and different payloads," *Robot. Comput.-Integr. Manuf.*, vol. 46, pp. 114–121, Aug. 2017.
[16] M. Özdemir, "Removal of singularities in the inverse dynamics of parallel robots," *Mech. Mach. Theory*, vol. 107, pp. 71–86, Jan. 2017.
[17] M. Özdemir, "High-order singularities of 5R planar parallel robots," *Robotica*, vol. 37, no. 2, pp. 233–245, Feb. 2019.
[18] M. Özdemir, "Hypersingularities of 3-RRR planar parallel robots," *Proc. Ro. Acad., Series A*, vol. 22, no. 4, pp. 353–360, Oct.-Dec. 2021.
[19] M. K. Ozgoren, "Kinematic and Kinetostatic Analysis of Parallel Manipulators with Emphasis on Position, Motion, and Actuation Singularities," *Robotica*, vol. 37, no. 4, pp. 599–625, Apr. 2019.
[20] M. K. Özgören, "Kinematic analysis of a manipulator with its position and velocity related singular configurations," *Mech. Mach. Theory*, vol. 34, no. 7, pp. 1075–1101, Oct. 1999.
[21] M. K. Özgören, "Topological analysis of 6-joint serial manipulators and their inverse kinematic solutions," *Mech. Mach. Theory*, vol. 37, no. 5, pp. 511–547, May 2002.

Comparison of Placement Heuristics in Simulated Annealing for the One-Dimensional Cutting Stock Problem

B. İÇMEN ERDEM[1] and R. KASIMBEYLİ[1]

[1]Eskisehir Technical University, Eskisehir/Turkey, bicmen@eskisehir.edu.tr
[1]Eskisehir Technical University, Eskisehir/Turkey, rkasimbeyli@eskisehir.edu.tr

***Abstract* - Placement heuristics are an important part of the solution approach for the solution of the one-dimensional cutting stock problem. We study different placement heuristics for the one-dimensional cutting stock problem in this paper and we use these heuristics in simulated annealing. A novel placement heuristic is proposed and two different placement heuristics are investigated within simulated annealing. The placement heuristics are compared in terms of obtaining better solutions, easy implementation, and computational time. The proposed methods significantly obtained better solutions.**

***Keywords* – cutting problems, packing problems, placement heuristics, simulated annealing.**

I. INTRODUCTION

MANY enterprises that deal with one-dimensional cuts of materials such as pipes, cables, steel shafts, paper, glass, and metal face one-dimensional cutting stock problems. One-dimensional materials, such as steel shafts, or multi-dimensional materials, such as rectangles or prisms, with cuts evaluated in a single dimension, are handled. In terms of computer complexity, the problem is characterized as NP-hard. When examining the larger difficulties, solving this problem is difficult because to the numerous decision variables, data size, and limits.

One-dimensional cutting stock (1DCSP) problems have been studied with many aspects since 1961 [1] in the operations research studies. Gilmore and Gomory developed the famous mathematical model for the problem which includes cutting patterns. In order to solve this problem Column generation method was developed. Kasımbeyli et al. [2] studied one-dimensional cutting stock problems without using previously defined cutting patterns. They proposed a mathematical model that does not require a cutting pattern. Since it approaches the problem's solution from a different angle, it provides a new perspective. For the one-dimensional cutting stock problem, Campello [3] developed a brand-new heuristic technique named the Residual Recombination Heuristic. The aim of the work by Ayres et al. [4] was to offer a new mathematical model for integrated lot sizing, one-dimensional cutting-stock, and two-dimensional cutting-stock problems. Two mathematical models that were presented in the study were based on a one-dimensional multi-period cutting stock problem with new features, such as the numerous production types that can be used to produce the slabs [5]. Cerqueira et al.'s Constructive Greedy Heuristic [6] suggested sorting items of pair or odd length in descending order, prioritizing those that appear more frequently in the problem. Chen et al. [7] formulated the one-dimensional cutting stock problem as an integer linear programming problem, and offered a novel simulated annealing solution. Shen et al. [8] suggested a particle swarm optimization based on simulated annealing approach to solve the problem.

Heuristic and metaheuristic approaches are used in addition to exact approaches to solve one-dimensional intersection problems, especially for large problems. No matter which solution approach is used, a placement heuristic must be incorporated in the method. Also, the success of the proposed method mostly depends on the placement heuristic. If the placement heuristic fails to obtain good solution, the metaheuristic might take so long to converge the good solutions.

This study investigates different placement heuristics and compares them in terms of ability to obtain better solutions, easy complementation and computational times.

The following is how the paper is structured. Section 2 depicts the simulated annealing algorithm. Section 3 discusses the placement heuristics and their algorithm furthermore Section 4 gives the computational results and analyses. Finally Section 5 provides a summary of the work and further research directions.

II. SIMULATED ANNEALING

S. Kirkpatrick et al. [9] and V. Cerny [10] suggested simulated annealing (SA) as a solution to several optimization problems. SA was widely employed as an effective and uncomplicated strategy for solving combinatorial optimization problems in the 1980s. The foundation of SA is the idea that by slowly cooling a substance after it has first been heated, a strong crystal structure can be formed. The rate and duration of metal cooling affect the structure's strength. Defects develop in the material if the starting temperature is low or if a quick cooling plan is used. In this situation, no temperature level allows the cooled solid to achieve fundamental equilibrium. By cooling carefully and slowly, strong crystals can be produced [11].

Starting with a predetermined initial solution and moving through numerous phases, the algorithm considers various

potential solutions. A new solution is developed individually for the problem at each stage. Neighboring ($f(s)$) solutions that improves the value of the objective function are always approved. The probability of selecting non-healing neighbor solutions ($f(s')$) relies on the algorithm's current temperature (T) and how the objective function changes (ΔE). The method avoids being stuck in the local best by accepting candidate solutions that do not improve the objective function. As the algorithm develops, the likelihood of accepting candidate solutions that do not enhance the objective function lowers as the current temperature does. Using the Boltzmann distribution, the likelihood that poor candidate solutions will be accepted is computed as follows:

$$P(\Delta E, T) = e^{-\frac{f(s')-f(s)}{T}}. \quad (1)$$

After a specified number of changes at each temperature level, candidate solutions are generated and analyzed. The equilibrium state is reached and the temperature begins to progressively decrease after a certain number of potential solutions are considered. The temperature is lowered in accordance with a precise cooling schedule.

A permutation of complete items is used to represent possible solutions for 1DCSP in the SA method. This array represents the order in which the chosen placement heuristic distributes items to stocks.

Starting with the initial solution, the algorithm runs. The initial solution can be produced using various methods. The two initial solution methods that are most frequently used are random and decreasing order by length. In this study we used decreasing order by length in order to create initial solution.

To decide the results, the SA algorithm considers various possible solutions. A neighbor solution is a candidate solution that is produced at each iteration. This work uses a 2-opt exchange operator to construct neighbor solutions. We select two items at random from the array of items using the 2-opt exchange operator, and we then swap their positions. Every potential solution is sent to the chosen placement heuristic. The final item placement, which is a cutting pattern, is determined using the placement heuristic, which also calculates the objective function value, the quantity of used stock.

The SA metaheuristic has been shown to be effective in a variety of well-known combinatorial optimization problems. The majority of problems for which SA metaheuristics have proven to be effective fall into the following categories [12]: cutting stock, vehicle routing, and assignment problems.

The flow of the SA is given in Algorithm 1.

Algorithm 1: Algorithm of simulated annealing

Require: Cooling schedule $(g(T))$, Initial temperature (T_{max})
1: Create initial solution (s_0)
Ensure: $T = T_{max}$ $s = s_0$
2: while $T \neq T_{stop}$ **do**
3: **while** $i < N$ **do**
4: Create candidate solution s' of s
5: $\Delta E \Leftarrow f(s) - f(s')$,
6: **if** $\Delta E \leq 0$ **then**
7: $s \Leftarrow s'$
8: **else**
9: **if** $P(\Delta E, T) < \rho$ **then**
10: $s \Leftarrow s'$
11: **end if**
12: **end if**
13: $i \Leftarrow i + 1$
14: **end while**
15: $i \Leftarrow 0$
16: $T \Leftarrow g(T)$
17: **end while**
18: Feasible solution s is found

III. Placement Heuristics for One-Dimensional Cutting Stock Problem

Variety of placement heuristics are utilized in the literature, depending on the metaheuristic or solution approach used and the type of problem being addressed. Placement Heuristics, which are designed to reflect the features of the problem and are specialized to work within the constraints of the problem, are critical to the solution's success.

Candidate solutions can be assigned to stock using the provided placement heuristics based on defined rules. The candidate solutions are subsequently transformed into relevant cutting patterns that show the items' beginning and ending locations, as well as their sequences.

In this paper, we used three different placement heuristics for one-dimensional cutting stock problem and compare the capability to obtain solutions. The following are the placement heuristics we use:

- Sequential placement heuristic
- Controlled and Sequential placement heuristic
- Sequential, controlled and pre-processed placement heuristic

Sequential, controlled and pre-processed placement heuristic is revised and improved version of first two heuristics and proposed in the study.

A. Sequential Placement Heuristics

In the sequential placement (SP) heuristic, as it can be understood from the title, the items in the candidate solution sequence are assigned to the stock materials in given order. When the remaining length of the stock material is zero or the next item does not fit in the remaining length, we continue with the next stock material. SP heuristic is described in Algorithm 2 given below.

Algorithm 2: Algorithm of sequential placement heuristic

Step 1 We choose the first unassigned item in the sequence, place it in stock and update the remaining length. Repeat Step 1 until an item does not fit the given remaining length and then continue with Step 2.

Step 2 Place the item to a new stock and update the remaining length and return to Step 1. If there is no item left in sequence unassigned, terminate the algorithm.

Table 1: Item data for SP.

Item id	Length	Stock id
1	6	1
2	6	1
3	5	2
4	4	2
5	4	2
6	4	3
7	3	3
8	3	3
9	2	3
10	2	3
11	2	4
12	2	4

As it can be seen in the Algorithm 2, this heuristic uses a basic idea and easy to generate. Also, we can say since so little computational process is made, it is a very quick and easy to implement.

We use this heuristic to solve a problem to demonstrate the solution. The data and the result of the problem is explained in Table 1. These items are cut from a stock with a length of 15 units. Table 1 gives the result of the problem in the column stock id. Total 4 identical stock is used.

Even though this is a quick solution approach, this heuristic does not consider the un used spaces of the stocks since when an item does not fit to a stock it continues with the next one. In order to enhance this approach a control mechanism added to the heuristic.

B. Controlled and Sequential Placement Heuristics

In the controlled and sequential placement (CSP) heuristic, we consider the unused parts of the stocks. This heuristic uses a similar approach to the SP heuristic, but once an item does not fit to the remaining length, it does not continue with the next stock automatically. CSP first searches the candidate solution sequence if there is an item that fits to the remaining length. CSP heuristic is described in Algorithm 3 given below.

Algorithm 3: Algorithm of controlled and sequential placement heuristic

Step 1 We choose the first unassigned item in the sequence, place it in stock and update the remaining length. Repeat Step 1 until an item does not fit the given remaining length and then continue with Step 2.

Step 2 We search the candidate solution sequence of unassigned items, and choose the first item that fits to the remaining length and continue with Step 3. If there is no item that fits, continue with Step 3.

Step 3 Place the item to a new stock and update the remaining length and return to Step 1. If there is no item left in sequence un assigned, terminate the algorithm.

We use this heuristic to solve the same problem given in Table 1 to demonstrate the solution of CSP. The data and the result of the problem is explained in Table 2. These items are also cut from a stock with a length of 15 units.

Table 2: Item data for CSP.

Item id	Length	Stock id
1	6	1
2	6	1
3	5	2
4	4	2
5	4	2
6	4	3
7	3	1
8	3	3
9	2	2
10	2	3
11	2	3
12	2	3

Table 2 shows the result of the problem obtained with CSP heuristic in the column stock id. Total 3 identical stock is used. This solution approach obtained a better solution for the same problem. This heuristic also has an easy implementation. But one the number of the total items, CSP might fail to obtain a good solution.

C. Sequential, Controlled and Pre-processed Placement Heuristic

Sequential, controlled, and pre-processed placement (SCPP) heuristic is based on the idea of creating doubles of items with zero trim loss. Because of this pre-processing, the number of items in the sequence reduces by pre-assigning zero-trim loss items to stocks, thereby reducing the sequence. After pre-processing, the remaining items are considered by the given order. Items are assigned to the stock by considering the given length. If an item does not fit the stock, the first item does fit to the remaining length is assigned. SCPP heuristic is described in Algorithm 4 given below.

Algorithm 4: Algorithm of sequential, controlled, and pre-processed placement heuristic

Step 1 The doubles of items with zero trim loss are assigned to the stocks by starting the first item in the items' sequence. These doubles construct a cutting pattern. The remaining items at the end of Step 1 transferred to Step 2.

Step 2 We choose the first unassigned item in the sequence, place it in stock and update the remaining length. Repeat Step 2 until an item does not fit, he given remaining length.

Step 3 If an item does fit the given remaining length, it is placed in the stock. Otherwise, start a new stock and repeat Step 2 and Step 3.

Step 4 If there is no item left in sequence unassigned, terminate the algorithm.

IV. Computational Results

We perform a series of computational experiments to test the performance of our placement heuristics. We use three different placement heuristics in SA and compare the results.

The numerical experiments have been carried out on a PC with Apple Mac Pro with a 3.7 GHz Quad-Core Intel Xeon E5 processor and 12 GB RAM. Different versions of SA are implemented in Python 3.9 which is executed on PyCharm 2020.3.5.

The 20 test problems with the label "binpack1" in OR-LIB are used to test algorithms. Each problem comprises 120 items, which will be cut from stocks with length 150. Table 3 lists the parameters utilized in SA.

Table 3: Parameters used in SA.

Initial Temperature	Cooling ratio	Iteration number	Accepting ratio
100	0.8	100	0.25

The comparison of experimental results obtained by different version of SA are presented in Table 4. Column "Opt" represents the best solution for test problem. Columns z_{sp}, z_{csp} and z_{cspp} shows the objective value of problems with corresponding placement heuristics. Objective value is the number of stocks that is used to cut the demanded items. And finally, columns t_{sp}, t_{csp} and t_{cspp} gives the duration of the corresponding algorithms.

Test Problems	Opt	z_{sp}	t_{sp}	z_{csp}	t_{csp}	z_{cspp}	t_{cspp}
U120_00	48	53	3,59	50	16,2	49	24,725
U120_01	49	55	3,53	50	16,3	**49**	21,235
U120_02	46	51	3,57	47	16,73	47	23,432
U120_03	49	57	3,6	51	16,9	50	21,620
U120_04	50	57	3,53	51	16,9	**50**	24,239
U120_05	48	53	3,6	50	16,9	**48**	21,182
U120_06	48	52	3,56	50	16,71	49	21,340
U120_07	49	54	3,58	51	16,97	50	21,169
U120_08	51	57	3,62	52	16,78	**51**	22,133
U120_09	46	51	3,61	48	16,16	47	23,834
U120_10	52	59	3,6	53	16,83	**52**	20,564
U120_11	49	54	3,6	51	16,55	50	21,871
U120_12	48	52	3,64	50	16,98	49	19,790
U120_13	49	53	3,54	50	16,73	**49**	19,762
U120_14	50	56	3,61	51	16,74	**50**	19,883
U120_15	48	56	3,59	50	16,5	**48**	22,785
U120_16	52	58	3,59	54	16,6	**52**	19,604
U120_17	52	57	3,56	54	16,81	53	20,501
U120_18	49	54	3,56	51	16,6	50	21,394
U120_19	50	57	3,66	51	16,89	**50**	23,478

As we can see, whereas CSP can obtain better solutions than SP, both placement heuristics fail to get the best solutions for the test problems. On the other hand, CSPP can receive half of the optimal solution for the test problem. Among these three placement heuristics, CSPP is more successful but still open to improvement.

V. Conclusion

In order to solve the one-dimensional cutting stock problem, we discuss three different placement heuristic in this paper. Sequential, controlled, and pre-processed placement is a novel approach for the use of one-dimensional cutting stock problems. Sequential, controlled, and pre-processed placement is better in order to obtaining the solution but has a higher computational time. Half of the problems we can obtain the optimal solutions, but in order to solve the whole problems some of improvements will be made and using this placement heuristic with different metaheuristics will be researched.

Appendix

This study is supported by Eskisehir Technical University, Turkey Scientific Research Projects Committee (20DRP013).

References

[1] P. C. Gimore and R. E. Gomory, "A linear programming approach to the cutting-stock problem," *Operations Research*, vol. 9, pp. 849-859, 1961.
[2] N. Kasimbeyli, T. Sarac and R. Kasimbeyli, "A two-objective mathematical model without cutting patterns for one-dimensional assortment problems," *Journal of Computational and Applied Mathematic.*, vol. 235(16), pp. 4663–4674, 2011.
[3] B. S. C. Campello, C. T. L. S. Ghidini, A. O. C. Ayres and W. A. Oliveira, "A residual recombination heuristic for one-dimensional cutting stock problems," *TOP*, vol. 30, pp.194-220, 2021.
[4] A. O. C. Ayres, B. S. C. Campello, W. A. Oliveira, C. T. L. S. Ghidini, "A Bi-Integrated Model for coupling lot-sizing and cutting-stock problems," *OR Spectrum*, vol. 43(4), pp.1047-1076, 2021.
[5] C. D. Signorini, S. A. Araujo and G. M. Melega, "One-dimensional multi-period cutting stock problems in the concrete industry," *International Journal of Production Research*, vol. 60(8), pp. 2386-2403, 2021.
[6] G. R. L. Cerqueira, S. S. Aguiar and M. Marques, "Modified Greedy Heuristic for the one-dimensional cutting stock problem," *Journal of Combinatorial Optimization*, vol. 42(3) pp. 657-674, 2021
[7] C. L. S. Chen, S. M. Hart and W. M. Tham, "A simulated annealing heuristic for the one-dimensional cutting stock problem," *European Journal of Operations Research*, vol. 93(3), pp. 522-535, 1996.
[8] X. J. Shen, Y. X. Li, B. J. Zheng and Z. F. Dai, "General particle swarm optimization based on simulated annealing for multi-specification one-dimensional cutting stock problem", ICCIAS 2006.
[9] S. Kirkpatrick, C. D. Gelatt Jr. and M. P. Vecchi, "Optimization by Simulated Annealing", *Science*, vol. 220(4598) pp. 671-680, 1983.
[10] V. Cerny, "Thermodynamical approach to the traveling salesman problem: An efficient simulation algorithm", *Journal of Optimization Theory and Applications*, vol. 45, pp. 41–51, 1985.
[11] T. El-Ghazali, "METAHEURISTICS From Design to Implementation", New jersey: Wiley, 2009.
[12] B. Suman and P. Kumar, "A survey of simulated annealing as a tool for single and multiobjective optimization", Journal of The Operational Research Society, vol. 57(10), pp. 1143-1160, 2006.

Experimental Study and Grey Correlation Analysis of Unconsolidated-Undrained Triaxial Compression Behavior for Geotextile-Reinforced Clay

M. N. ÖDEMİŞ[1] and M. E. ORAKOĞLU FIRAT[1*]

[1] Fırat University, Elazığ/Türkiye, mnuri.odemis@gmail.com
[*1]Fırat University, Elazığ/Türkiye, morakoglu@firat.edu.tr, Corresponding Author

Abstract **- Geosynthetics is one of the most frequently used materials in geotechnical engineering by showing rapid change and development. Polymer materials, which have a significant effect on the implementation of geotechnical projects by being produced in factories and used with the ground, offer various advantages over traditional methods by increasing soil performance, having an easy land application, and reducing costs. In this study, nonwoven geotextile was used to investigate the unconsolidated-undrained triaxial behavior of clayey soil. The experimental results showed that the strength of the soil was improved by geotextile reinforcements. The maximum deviator stress of unreinforced soil increases as a result of geotextile reinforcements. The reinforced samples had better strength at higher strain. The degree of correlation between the failure strength and other factors, such as confining pressure and the number of geotextile layers, was also evaluated using the Gray correlation analysis. According to Gray correlation analysis, the influence of the number of layers of geotextile and confining pressure on the failure strength was revealed.**

Keywords **- Clay soil, Unconsolidated-Undrained Triaxial test, Number of geotextile layers, Gray correlation analysis**

I. INTRODUCTION

THE low strength of many cohesive soils is the fundamental impediment to soil structure stability. This issue is somewhat resolved by adding geosynthetic reinforcement to the soil. Geotextiles are one of the most often utilized geosynthetic materials for soil reinforcement [1, 2]. Since geosynthetic materials provide both useful and alternative solutions in engineering applications all over the world, their use has become widespread in recent years. It is important to examine the effects of these materials, which have a significant influence on the application phase of geotechnical projects, on soil behavior, to offer solutions for infrastructure problems, and to evaluate alternative reinforcement materials [3].

In general, geosynthetics are of great importance in terms of separation, filtration, and drainage properties in highways [4, 5], in terms of reducing the need for granular filling material, increasing the bearing capacity, and rapidly absorbing pore water pressure in railways [6- 8]. Also, they are extremely significant against deformations that may occur in the dam body due to the elasticity and durability they provide in earth-fill dams [9-10], and both in terms of area and economically, by providing cohesion to the reinforced slopes in retaining structures [11- 12].

Numerous studies have been carried out utilizing various experimental tests, such as direct shear, triaxial, and shear tests, to assess the stress-strain behavior of geotextile-reinforced soils [13-17]. The experiments' findings demonstrated that, in general, reinforcements improve peak shear strength. The apparent cohesion or rise in confining pressure correlates to the reinforced soil's increased strength. The density, shape, and size of the soil's particles as well as the reinforcement's strength, stiffness, and spacing are just a few of the many variables that affect how reinforcement affects the shearing behavior of soil materials. The reinforced soils are strengthened by increasing the stiffness and number of reinforcing layers.

In this study, to analyze the behavior and failure processes of geotextile-reinforced clay specimens, a series of UU triaxial compression tests were conducted and the findings were evaluated using Grey correlation analysis. The evaluation of the impacts of nonwoven geotextile reinforcing layers on the enhancement of clay's shear strength was the main objective of this investigation.

II. MATERIALS

Soil samples were collected from the province of Elazig in Türkiye and are presented with a red dot in Figure 1. A clayey soil designated as CL in the Unified Soil Classification System was used in this study for laboratory experiments. Table 1 presents the characteristics of the soil, and Figure 2 displays the distribution of the soil's grain size.

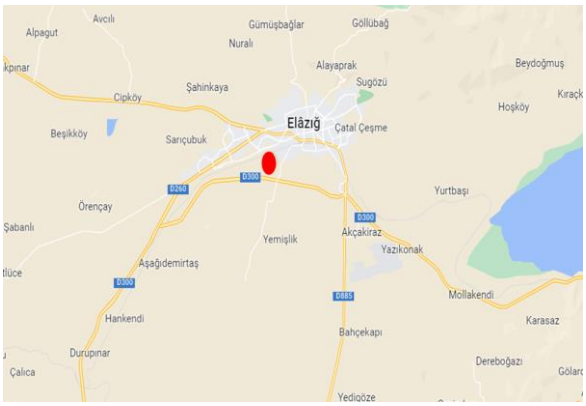

Figure 1: The study location.

Table 1: The characteristics of the soil.

Specific gravity (g/cm³)	2.55
Liquid limit (%)	38.30
Plastic limit (%)	18.60
Plasticity index (%)	19.70
Optimum water content (%)	17.70
Maximum dry density (g/cm³)	1.66

Figure 2: The distribution of the soil's grain size.

The nonwoven fabric used in this study is readily accessible commercially. The various reinforcement configurations used in this investigation, which comprise one layer of geotextile and three layers of geotextile, are shown in Figure 3. Also, Table 2 lists the geotextile's mechanical and physical characteristics as indicated by the manufacturer.

Table 2: The geotextile's mechanical and physical characteristics.

Tensile Strength	12 kN/m
Thickness	1 mm
Tensile Elongation	50 % (min)

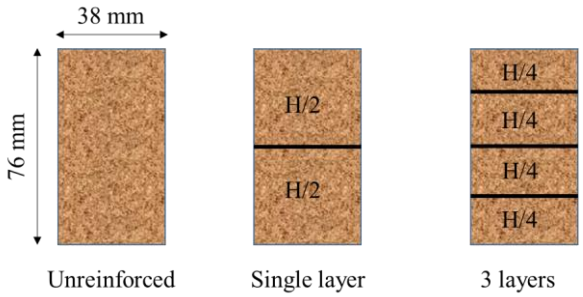

Figure 3: The reinforcement arrangements used in the study.

III. METHODS FOR TESTING

The goal of this study is to determine how different geotextile layers affect the shear strength properties of highly compressible clay that has been compressed to the maximum dry density with the optimum water content. For this purpose, to prepare the sample, the required optimum water content was first calculated, then the soil was mixed with it. The combination was then put in plastic bags and allowed to sit for 24 hours to ensure that the soil mass had a homogenous water content. Before compressing the sample, the water content was verified. During the soil compaction process in the mold, the geotextile layer was inserted when half and one-fourth of the sample were compacted. Each sample was taken out of the mold and immediately wrapped in plastic to preserve its moisture content.

Then, unconsolidated-undrained (UU) triaxial compression tests were performed to assess the soil's shear strength parameters (Figure 4). Throughout the testing procedure, the strain rate remained constant at 0.78 mm per minute in accordance with ASTM D2850-95 [20]. Failure criteria under UU loading are defined by 25% shear deformation. To simulate the actual state of the ground surface, three confining pressures (100, 200, and 300 kPa) had been selected for triaxial experiments.

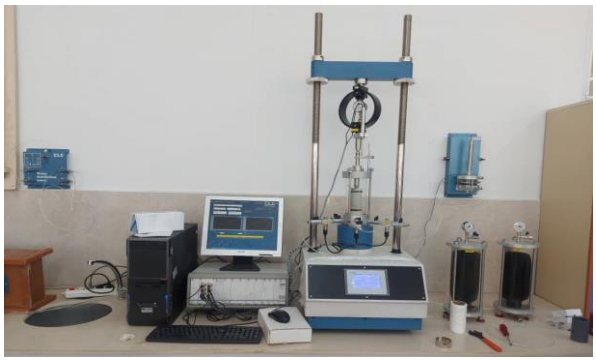

Figure 4: Triaxial test machine.

IV. RESULTS AND DISCUSSIONS

Triaxial compression tests have been carried out on highly compressible clay to examine the impact of various geotextile layers on the shear strength properties of clay that has been compacted to the maximum dry density with the optimum water content.

A. *Impact of the geotextile layers on stress-strain behavior*

Figure 5 presents the stress-strain changes under different confining pressures of pure and reinforced soils with different geotextile layers. In this study, failure criteria under undrained-unconsolidated triaxial compressive test loading were defined with 25% shear deformation. At the same confining pressure, the reinforced clay specimens showed larger peak shear strengths than the pure soil specimens, indicating that the addition of permeable reinforcements can significantly increase the undrained shear strength of clay. Deviator stress values increased for increasing confining pressures and strain values of all soil samples. In addition, the increase in the number of geotextile layers on the soils increased the strength values of the soils. According to this experimental finding, restricted reinforcement spacing or high confining pressure make the clay-geotextile contact stronger. As the number of geotextile layers increased, the stress-strain behavior of soil samples changed from strain softening to strain hardening at increasing deformation values.

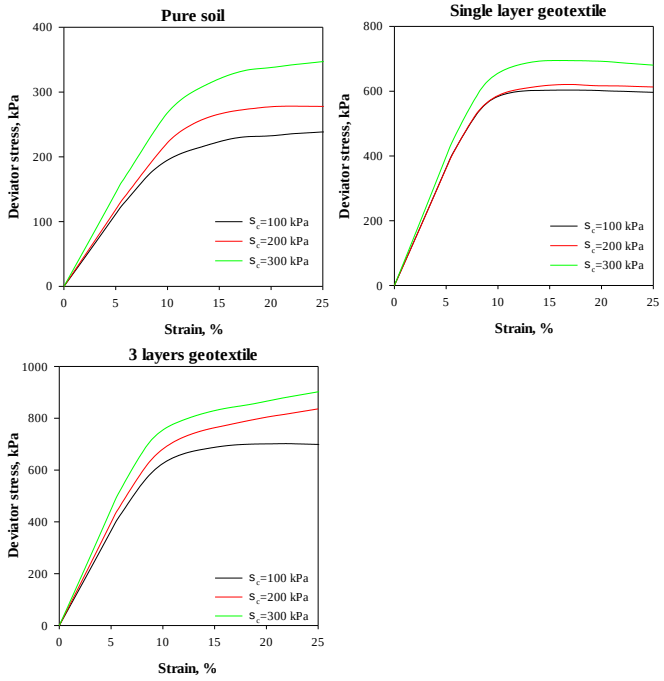

Figure 5: Stress-strain changes under different confining pressures of pure and reinforced soils with different geotextile layers.

B. *Impact of the geotextile layers on the failure strength*

In this study, failure criteria under undrained-unconsolidated triaxial compressive test loading were defined with 25% shear deformation. Until this deformation is reached, there has been no failure in either the pure or reinforced condition of the soils. According to Figure 6, while the failure strength of the pure soil sample was 242.38 kPa under a confining pressure of 100 kPa, this value increased by 148.99% for the geotextile placed in a single layer. On the other hand, it increased by 189.63% for geotextile placed in 3 layers. Upon raising the confining pressure to 200 kPa, the failure strength increased by 123.07% for the single layer geotextile and by 209.25% for the 3 layers' geotextile. Finally, while the confining pressure was increased up to 300 kPa, the failure strength of the pure soil sample increased to 353.870 kPa, while this value increased by 96.32% for the single layer geotextile and by 162.17% for the 3 layers' geotextile. As a result, the geotextile layers induced the soil components' enhanced ductility, which led to the occurrence of failure strength at larger axial strains.

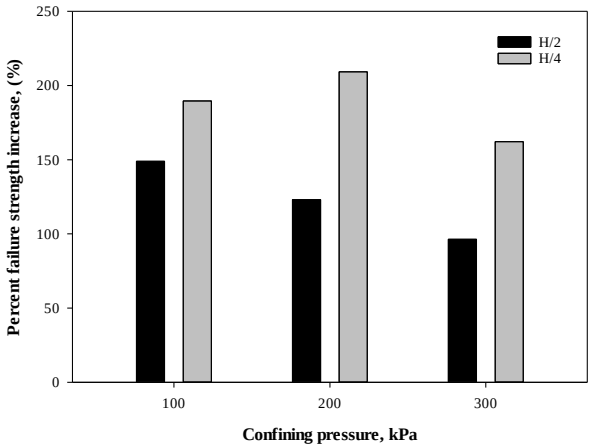

Figure 6: Percent failure strength increase vs. confining pressure.

The following equations illustrate the normalized parameters that are presented to assess how geotextile reinforcement affects the deviator stress of clay soil:

$$f_{q\max} = \frac{f_{\max(reinforced)}}{f_{\max(unreinforced)}} \quad (1)$$

$$f_{q10\%} = \frac{f_{10\%(reinforced)}}{f_{10\%(unreinforced)}} \quad (2)$$

$$f_{q20\%} = \frac{f_{20\%(reinforced)}}{f_{20\%(unreinforced)}} \quad (3)$$

where, correspondingly, f_{qmax}, $f_{q10\%}$ and $f_{q20\%}$ are deviator stress rates for the maximum condition, 10% axial strain and 20% axial strain. In reinforced and unreinforced circumstances, $q_{10\%(reinforced)}$ and $q_{10\%(unreinforced)}$ are deviator stresses at axial strains of 10%, and $q_{20\%(reinforced)}$ and $q_{20\%(unreinforced)}$ are deviator stresses at axial strains of 20%, respectively.

The change of the deviator stress rates in relation to the confining pressure of the clay soils employed in this study is depicted in Figure 7. Geotextile reinforcement is more effective on the maximum failure stress of the studied soil at small strain ratios. On the other hand, it was found that the strength of the soil with 3 layers of geotextile reinforcement was greater at increasing strain ratios compared to a single geotextile layer. On samples with one reinforced layer in clay soil, the f_{qmax} ranged from 2.19 to 2.77; in samples with three reinforced layers, it ranged from 2.62 to 3.10. In all samples, the efficiency of the reinforcement was declined when the confining pressure was raised to its maximum.

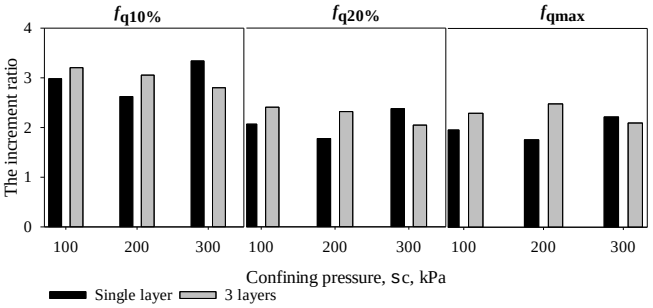

Figure 7: Impact of reinforcement on deviator stress rates.

C. *Impact of the geotextile layers on cohesion and internal friction angle*

The failure envelopes of the clay specimens (unreinforced and reinforced) in the principal stress domain are depicted in Figure 8. In this study, failure strength was defined as the strength at 25% strain value. The failure envelopes of the reinforced clay specimens moved upward as the number of reinforcing layers raised. Unreinforced clay and reinforced clay with one and three layers of geotextiles have failure envelopes that are typically parallel.

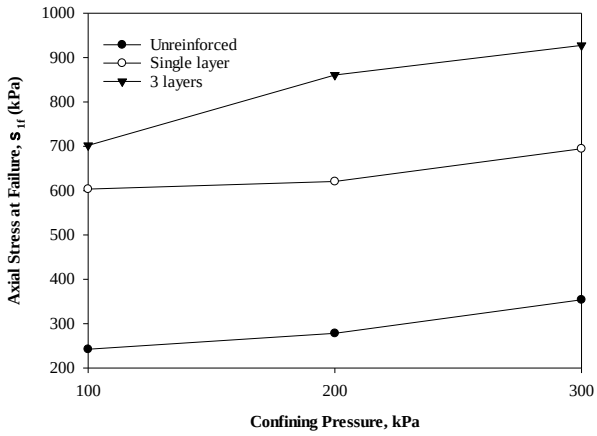

Figure 8: Failure envelopes of clay with and without reinforcement.

To show the impact of the numbers of geotextile layers on the soil shear strength parameters, in this investigation, the cohesion (c) and internal friction angle (ϕ) values, which are the shear strength parameters, were determined by the changes in the p-q graphs. These parameters are calculated with equations (4) and (5) as the following:

$$p=\left[\frac{(\sigma_1+\sigma_3)_f}{2}\right] \quad (4)$$

$$q=\left[\frac{(\sigma_1-\sigma_3)_f}{2}\right] \quad (5)$$

where σ_1 and σ_3 are the axial and lateral stresses of the soil at failure. Also, the general relationship between p and q are given in Equation (6):

$$q=b+p\tan\alpha \quad (6)$$

where α is the slope and the b line intersects the q axis. Taking into account the b and α data, the cohesion (c) of the samples and the internal friction angle (ϕ) are calculated by Equation (7) and (8) [21]:

$$\phi=\sin^{-1}\tan\alpha \quad (7)$$

$$c=\frac{b}{\cos\phi} \quad (8)$$

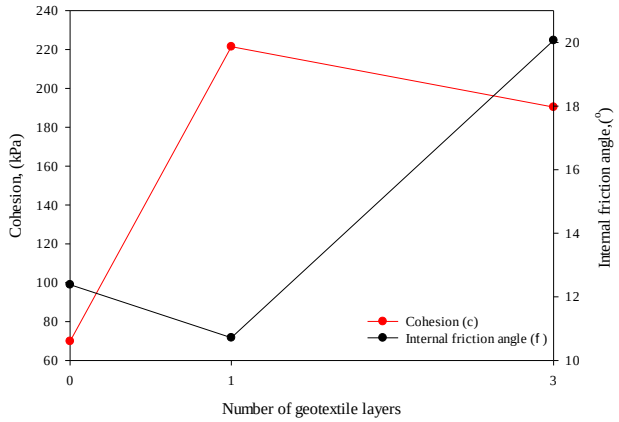

Figure 8: Changes in cohesion and internal friction angles of clay with and without reinforcement.

Figure 8 presents the changes in undrained cohesion (cu) and internal friction angles of clay with and without reinforcement. The increase in cohesion may be the cause of the improvement in shear strength. The cohesion values of the soil samples reinforced with geotextiles showed an increase of 217.03% for the single layer geotextile and 172.55% for the 3-layers geotextile compared to the pure soil. No significant relationship was found on the layer increase in cohesion values. Similar results were observed in the study conducted by Noorzad and Mirmoradi (2010) in the literature [3]. On the other hand, as the number of layers of geotextile rose, the slopes of the failure envelopes steepened, leading to an increase in friction angles.

V. Grey Correlation Analysis (GCA)

The GCA is a method to assess the geometric alignment between various sequences within a structure. To investigate the main factors affecting the maximum deviator stress of the soil (D), the correlations between the confining pressure (A), the numbers of geotextile layers (B) and strain levels (C) at the responsible stress level given in Table 3 was determined based on the grey correlation theory.

Table 3: UU triaxial test results of unreinforced and reinforced soil.

No	A	B	C	D	No	A	B	C	D

1	100	0	25	242.378	15	200	3	20	805.108
2	100	1	25	592.654	16	300	0	20	338.295
3	100	3	25	695.185	17	300	1	20	692.109
4	200	0	25	277.301	18	300	3	20	866.578
5	200	1	25	609.498					
6	200	3	25	860.730	No	A	B	C	D
7	300	0	25	353.870	19	100	0	10	195.890
8	300	1	25	672.349	20	100	1	10	584.289
9	300	3	25	927.734	21	100	3	10	627.816
No	A	B	C	D	22	200	0	10	223.544
10	100	0	20	232.780	23	200	1	10	586.704
11	100	1	20	601.537	24	200	3	10	683.151
12	100	3	20	701.036	25	300	0	10	584.289
13	200	0	20	277.584	26	300	1	10	659.460
14	200	1	20	616.703	27	300	3	10	756.307

The maximum failure strength was chosen as the reference sequence and the confining pressure, the numbers of geotextile layers and strain levels were taken as the comparison sequence. The sequences of reference and comparison can be described in Eqs. (9) and (10), respectively:

$$f_0(x_k) = \{f_0(x_1),\ f_0(x_2),\ldots,\ f_0(x_n)\} \quad (9)$$

$$f_i(x_k) = \{f_i(x_1),\ f_{i0}(x_2),\ldots,\ f_i(x_n)\} \quad (10)$$

where $f_{0(xk)}$ and $f_{i(xi)}$ are the reference and comparison sequences, respectively, and k is the number of reference or comparison sequences.

Due to the fact that the parameters in the reference and comparison sequences had different dimensions, the two sequences were standardized using Eqs. (11) and (12).

$$f_0'(x_k) = f_0'(x_k)/\ f_0(x_1) = \{f_0'(x_1),\ f_0'(x_2),\ldots,\ f_0'(x_n)\} \quad (11)$$

$$f_i'(x_k) = f_i'(x_k)/\ f_i(x_1) = \{f_i'(x_1),\ f_i'(x_2),\ldots,\ f_i'(x_n)\} \quad (12)$$

inhere $f_0'(x_k)$ and $f_i'(x_k)$ the normalized reference and comparison sequences, respectively.

Eq. (13) was used to get the correlation coefficient following the normalizing of the sequences:

$$\xi_i(x_k) = \frac{\min\limits_i \min\limits_k \left|f_0(x_k) - f_i(x_k)\right| + \rho \max\limits_i \max\limits_k \left|f_0(x_k) - f_i(x_k)\right|}{\left|f_0(x_k) - f_i(x_k)\right| + \rho \max\limits_i \max\limits_k \left|f_0(x_k) - f_i(x_k)\right|} \quad (13)$$

where ξ is the correlation coefficient, which in this case is chosen to be equal to 0.50 [22].

Eq. (14) can be used to obtain the grey correlation degree (r_i), which takes into account the correlation coefficient calculated from Eq. (13):

$$r_i = \frac{1}{n}\sum_{k=1}^{n} \xi_{0i}(x_k) \quad (14)$$

The maximum correlation coefficients calculated from Eq. (13) are for maxξi(A) = 0.9732, maxξi(B) = 0.9732, and maxξi(C) = 0.9082. For the stabilization of the soil used in the study, the use of the single layer of geotextile was found to be the highest maxξi in the optimum sequence over the maximum deviator stress. For this context, the use of single geotextile layers will give more optimum results than the use of the maximum number of geotextiles.

Also, the r_i values of the reference and comparison sequences is calculated using of Eqs. (13) and (14), and the outputs were shown in Table 3.

Table 4: Grey correlation degree.

	Grey relational grade		
	A	*B*	*C*
$(\sigma_1-\sigma_3)_{max}$	0.6646	0.7425	0.5209

The grey correlation sequence of various parameters was found to represent the number of geotextile layers > the confining pressure > the strain levels at the responsible stress level. It is clear that the numbers of geotextile layers have the greatest impact on the maximum deviator stress.

VI. Conclusions

To analyze the behavior and failure processes of geotextile-reinforced clay specimens, a series of UU triaxial compression tests were conducted and the findings were evaluated using Grey correlation analysis. The evaluation of the impacts of nonwoven geotextile reinforcing layers on the enhancement of clay's strength was the main objective of this investigation. Following is a summary of the study's findings:

1) The presence of geotextiles increases the peak strength, which suggests that reinforcing enhances the mechanical properties of soil. Additionally, the reinforced samples are less rigid than the ones that are not reinforced. As there are more layers of geotextile, the mechanical properties get better.
2) Clay soil's maximum deviator stress increases as a result of geotextile reinforcements. The strength that was caused by the reinforcement was reduced when the confining pressure was increased. Under cell pressures of 100 and 300 kPa, the maximum deviator stress of the samples reinforced with three layers of geotextile rose by roughly 182.01% and 171%, respectively.
3) The ductility of the soil was improved by geotextile reinforcements. The 3 layers of geotextile-reinforced soil had better strength at higher strain. This result is especially important in projects sensitive to deformations. On samples with three reinforced layers in clay soil, the $f_{q10\%}$ ranged from 2.80 to 3.20 and the $f_{q20\%}$ ranged from 2.56 to 3.01, and f_{qmax} changes between 2.62 to 3.10.
4) The failure envelopes of the reinforced clay specimens migrated upward as the number of reinforcing layers increased. Unreinforced clay and clay reinforced with one and three layers of geotextiles tend to have parallel failure envelopes.

5) In comparison to pure soil, the cohesion values of the soil samples reinforced with geotextiles increased by 217% for a single layer and 172.55% for three layers. The cohesion values increased a little as the number of layers increased, but no correlation was identified. Additionally, as the number of layers of geotextile rose, the slopes of the failure envelopes grew sharper, increasing friction angles.
6) Gray relational analysis revealed that the number of geotextile layers was the most effective parameter on the maximum deviator stress.

ACKNOWLEDGMENT

This study was supported by Firat University (in Turkey) Science Research Projects (FUBAP) (Project no. TEKF.22.03). The authors would like to thank FUBAP for financial support.

REFERENCES

[1] K. Jana, S. Hazari, and S. Ghosh, "Experimental and numerical studies of three-layered unreinforced and geosynthetic-reinforced soil slopes," *Innov. Infrastruct. Solut.*, vol. 6*(1)*. pp. 1-29, November 2021.
[2] K. R. Sreelakshmi, and A. K. Vasudevan, "Study on Performance of Geotextile Reinforced Soils Using Triaxial Compression Test", in *Proceedings of Indian Geotech. Conf.*, pp. 189-200, 2019.
[3] R. Noorzad, S. H. and Mirmoradi, "Laboratory evaluation of the behavior of a geotextile reinforced clay," *Geotext. Geomembr.*, vol. 28*(4)*, pp. 386-392, August 2010.
[4] D. E. Aju, K. C. Onyelowe, and G. U. Alaneme, "Constrained vertex optimization and simulation of the unconfined compressive strength of geotextile reinforced soil for flexible pavement foundation construction," *Clean. Eng. Technol.*, vol. 5, 100287, December 2021.
[5] S. Ramjiram Thakur, B. P. Naveen, and J. P. Tegar, "Improvement in CBR value of soil reinforced with nonwoven geotextile sheets," *Int. Journal Geo-Eng.*, vol. 12*(1)*, pp. 1-10, March 2021.
[6] M. Geng, "A short review on the dynamic characteristics of geogrid-reinforced soil retaining walls under cyclic loading," *Adv. Mater. Sci. Eng*, vol. 2021, 5537912, September 2021.
[7] F. Tatsuoka, "Geosynthetic-reinforced soil structures for railways and roads: development from walls to bridges," *Innov. Infrastruct. Solut.*, vol. 4*(1)*, pp. 1-18, October 2019.
[8] X. Liang, J. Jin, G. Yang, X. Wang, Q. Zhao, and Y. Zhou, "Performance of modular-reinforced soil-retaining walls for an intercity railway during service,". *Sustainability*, vol. 14*(10)*, 6084, May 2022.
[9] K. Jana, S. Hazari, and S. Ghosh, "Experimental and numerical studies of three-layered unreinforced and geosynthetic-reinforced soil slopes," *Innov. Infrastruct. Solut.*, vol. 6*(1)*, pp. 1-29. November 2021.
[10] K. Jana, S. Hazari, and S. Ghosh, "Experimental and numerical studies of three-layered reinforced soil slope under dynamic loading condition,". *In: C. N. V. Satyanarayana Reddy, S. Saride, A. M. Krishna, (eds) Ground Improvement and Reinforced Soil Structures. Lecture Notes in Civil Engineering*, vol. 152. Springer, Singapore. Available: https://doi.org/10.1007/978-981-16-1831-4_57.
[11] R. Hore, S. Chakraborty, A. M. Shuvon, and M. A. Ansary, "Effect of acceleration on wrap faced reinforced soil retaining wall on soft clay by performing shaking table test,". *PETI*, vol. 15, pp. 24-34, April 2020.
[12] H. Alhajj Chehade, D. Dias, M. Sadek, O. Jenck, and F. Hage Chehade, "Pseudo-static analysis of reinforced earth retaining walls," *Acta Geotech.*, vol. 16*(7)*, pp. 2275-2289, February 2021.
[13] R. Rezvani, "Shearing response of geotextile-reinforced calcareous soils using monotonic triaxial tests," *Mar. Georesources Geotechnol.*, vol. 38(2), pp. 238-249, January 2020.
[14] S. C. Tseng, K. H. Yang, Y. K. Tsai, and F. Teng, "Investigation of the blast-resistance performance of geotextile-reinforced soil," *Geosynth. Int.*, pp. 1-60, October 2022.
[15] I. N. Markou, "A study on geotextile—sand interface behavior based on direct shear and triaxial compression tests," *Int. J. Geosynth. Ground Eng.*, vol. 4*(1)*, pp. 1-15, January 2018.
[16] K. Salehi, H. Mohammad Eisa, and K. Badv, "Reinforcement effect of geotextiles on shear strength of peat soil: a case study on Urmia peat," *Bull. Eng. Geol.*, vol. 80(9), pp. 6799-6812, July 2021.
[17] F. Yi, C. Du, "Triaxial testing of geosynthetics reinforced tailings with different reinforced layers," *Mater.*, vol. 13*(8)*, 1943, April 2020.
[18] C. C. Ikeagwuani, J. C.Agunwamba, C. M. Nwankwo, and M. Eneh, "Additives optimization for expansive soil subgrade modification based on Taguchi grey relational analysis,". Int. J. Pavement Res. Technol., vol. 14*(2)*, pp. 138-152, March 2021.
[19] M. Feng, S. Liu, J. Wang, and Y. Hu, "Influence of stabilisers on the unconfined compressive strength of a fine soil," *Geotech. Res.*, vol. 7*(4)*, pp. 209-217, August 2020.
[20] ASTM D2850-95, "Standard Test Method for Unconsolidated-Undrained Triaxial CompressionTest on Cohesive Soils," West Conshohocken, PA, 1999.
[21] D. Wang, W. Ma, Y. H. Niu, X. Chang, Z. Wen, "Effects of cyclic freezing and thawing on mechanical properties of Qinghai-Tibet clay," *Cold Reg. Sci. Technol.*, vol. 48, pp. 34-43, April 2007.
[22] B. Jun-an, Y. Ping, C. Chen, "Research on factors influencing frost heaving and thaw collapsing based on grey relational preponderance analysis", *Subgrade Eng.*, vol. 01, pp. 21-23, 2012.

Microstructure Analysis of Recycled Ferrochrome-Filled Polymer Concretes Containing SWCNT

S. SUBASI[1], F. DOGAN[2], H. DEHGHANPOUR[3] and M. MARASLI[4]

[1] Duzce University, Duzce/Turkey, serkansubasi@duzce.edu.tr
[2] Munzur University, Rare Earth Elements Application & Research Center, Tunceli/Turkey, fatihdogan@munzur.edu.tr
[3] Fibrobeton Company, R&D Center, Duzce/Turkey, heydar.dehghanpour@firobeton.com.tr
[4] Fibrobeton Company, R&D Center, Duzce/Turkey, muhammed@firobeton.com.tr

***Abstract* - In this study, microstructures of a novel polymer concrete samples produced using silica sand and recycled ferrochrome as aggregate, single-walled carbon nanotube (SWCNT) as reinforcement and epoxy resin as the main component material of the mixture were characterized. The morphology and crystal structure effects of the same ratio of SWCNT content on different fillers were evaluated. The use of recycled ferrochrome filler and SWCNT reinforcement component in PC achieved significant results regarding material morphology and structural changes.**

***Keywords* - Microstructure analysis, Polymer concrete, Recycled ferrochrome, SWCNT**

I. INTRODUCTION

The importance of material selection, which is made by considering economic factors and environmental sustainability, is increasing day by day. It is aimed to improve the mechanical, thermal and conductivity properties of the material by adding industrial recycles or recycled materials to the concrete mix [1]. In studies on the use of recycled or recycled materials in polymer concrete mix, low-cost and high-strength concretes are thought to be important in terms of sustainability [2]. Selection is made for certain applications, one of the Portland cement concrete, polymer concrete (PC) and geopolymer concrete, which are widely used in construction applications. PCs with durability, strength, adhesion, sound and heat insulation and fast curing properties are preferred in different applications [3]. The resin used as adhesive material in PC could form a stable matrix network and form strong bonds with aggregates. Epoxy and polyester resins are used as binders together with different aggregates and fillers in PCs. Epoxy resin is one of the most applied polymers in PCs due to its strong bond compatibility with aggregates and mechanical properties [4]. In addition, fillers and aggregates improve the compressive and flexural strengths of PC and reduce the cost of concrete [5]. Different types of aggregates such as quartz, silica sand, river sand and basalt are used in PCs [6]. Different fiber additions are made to improve PC blends. [7]. Materials such as glass fibers and carbon fibers are used as reinforcement elements in PCs. Thus, it is aimed to improve both the mechanical and physical properties of the PC [8]. In this study, microstructural changes in PCs were investigated by using silica sand and recycled ferrochrome fillers as aggregate, epoxy as resin and SWCNT as reinforcement.

II. EXPERIMENTAL METHODS

All Mixture details are given in Table 1. The morphologies of SWCNT reinforced polymer concrete samples filled with recycled ferrochrome and silica sand were analyzed by scanning electron microscopy (SEM) on a FEI model Quanta FEG 250 in secondary electron mode at 10 keV. X-ray spectra of polymer concrete samples were detected on the Rigaku D/MAX 2000 X-ray generator and CuKα radiation diffractometer with a wavelength of 1.54059A° and spectra were obtained by scanning the samples at 10° to 90° (2 θ angle) and 1/min.

Table 1. Mixture details of polymer concrete.

No	Code	SS (%)	FRC (%)	Epoxy (%)	Cobalt (%)	MEK (%)	CNT (%)
1	SS	66.12	0	33.06	0.33	0.49	0
2	FRC	0	66.12	33.06	0.33	0.49	0
3	SS-FRC	33.06	33.06	33.06	0.33	0.49	0
4	SS-CNT	66.12	0	33.01	0.33	0.49	0.05
5	FRC-CNT	0	66.12	33.01	0.33	0.49	0.05
6	SS-FRC	33.06	33.06	33.01	0.33	0.49	0.05

III. RESULTS

Figure 1 shows the morphology surfaces of unreinforced silica sand and SWCNT-reinforced silica sand samples. Low (Figure 1(a)) and high (Figure 1(b)) magnification FE-SEM images of the SS sample show that the surface areas are composed of irregularly shaped particles. The crack growth seen in the low magnification image could be attributed to the insufficient bond strength between silica sand and epoxy resin. However, it is seen that the silica sand aggregate particles are homogeneously dispersed in the epoxy resin matrix phase (Figure 1(b)). Although crack formation is observed in figure 1(a), it could be reported that silica sand particles in high magnification figure 1(b) provide binder adhesion with epoxy resin. On the other hand, it is stated that the particle agglomeration of aggregates in the resin increases the stress strain and reduces the mechanical strength of the concrete material [3]. it could be emphasized that the silica sand particles not being agglomerated in the epoxy resin may contribute to the mechanical properties of the SS polymer concrete sample. It can be declared that the aggregates in the silica sand filled polymer concrete sample are homogeneously dispersed in the epoxy resin matrix and provide good adhesion with the matrix. Figure 1 (c) and (d) show low and high magnification FE-SEM images of the SS-CNT sample, respectively. Compared to the pure silica sand filled polymer concrete sample, the SWCNT reinforcement appears to form a dense microstructure with silica sand aggregate particles in the epoxy resin matrix. As well as, low-magnification micrograph shows a generally homogeneous aggregate distribution, although the silica sand particles are dispersed in different sizes in the epoxy resin. The high magnification morphology picture shows that the SWCNTs begin to disperse in the epoxy resin. In addition, SWCNTs formed a network structure between the gaps formed in the structure. Moreover, deformations on the SWCNT surface allow the formation of stronger adhesion areas on the epoxy resin surface [1]. Additionally, the dispersion of large surface area SWCNTs in the epoxy resin improved the aggregate/resin interfacial adhesion as it increased the contact area in the matrix. It could be said that the structural changes in the morphology may relatively contribute to the compressive and flexural strength results of the polymer concrete sample. On the contrary, observation of SWCNTs in certain regions of the morphology surface can be associated with the formation of agglomeration of SWCNTs. In addition, it has been reported that the increase in the SWCNT content added to the mixture will increase the agglomeration in the matrix [9]. Contrarily, in this study, it could be said that 0.05% SWCNT content contributes to the bonding between polymer mortar and silica sand aggregates and increases the interfacial adhesion. FE-SEM morphologies of recycled ferrochrome filled (FRC) and SWCNT reinforced (FRC-CNT) polymer concrete samples are given in figure 2. The low magnification image of the recycled ferrochrome filled sample shows the formation of hollow structures (Figure 2(a)). It is understood that recycled ferrochrome aggregates are dispersed in epoxy resin in different shapes and sizes.

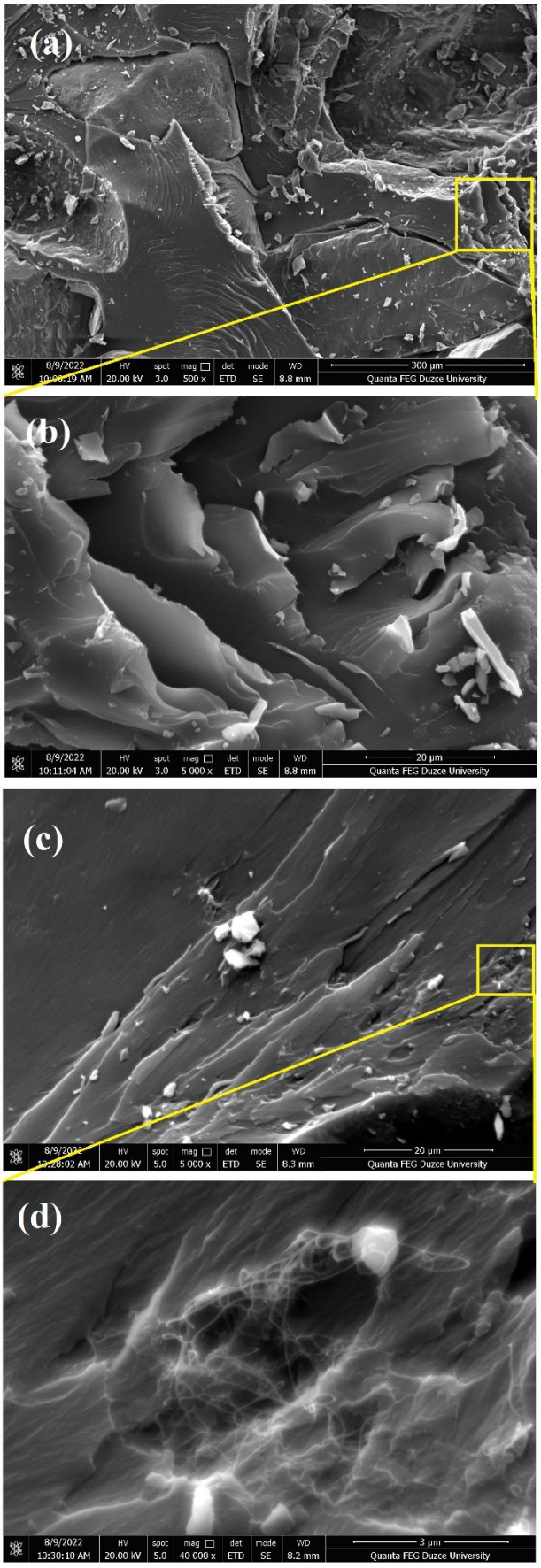

Figure 1. FE-SEM images of SS (a, b) and SS-CNT (c, d).

On the other hand, in the high magnification image of the region shown in yellow in the FRC sample morphology, the compact structure was formed. The greater voids in the FRC sample compared to the morphology of the SS sample can be attributed to reduced adhesion between epoxy resin/recycled ferrochrome. Therefore, it can be said that the contribution of the polymer concrete sample in transmitting the transfer load applied on it is low [10]. On the other hand, a more uniform and dense structure formation is observed in the morphology of the polymer concrete sample reinforced with SWCNT. It can be noted that SWCNTs improve adhesion between epoxy resin/recycled ferrochrome aggregates [11]. The high-magnification image of the area highlighted in yellow in figure 2(c) shows that SWCNTs cluster around the micro-void. It has been observed that SWCNTs are not evenly dispersed in the epoxy resin matrix and do not bridge the recycled ferrochrome/epoxy resin voids. In addition, it has been understood that SWCNTs with large surface area cannot expand the contact area and do not contribute much to the adhesion between resin/aggregate. The low development of adhesion between the components in the polymer mortar mix could be ascribed to the weakening of the bond strength between the materials and the difficulty of load transfer [12]. It could be reported that the use of SWCNT in the polymer mortar mix relatively reduces the damage to the epoxy matrix. Contrariwise, embedded dispersion of SWCNTs in the epoxy resin matrix contributed to the bonding between the recycled ferrochrome aggregates and the resin. Figure 3 shows low and high magnification FE-SEM micrographs of SS-FRC and SS-FRC-CNT polymer concrete samples. The use of both silica sand and recycled ferrochrome aggregates in the polymer mortar mixture reduced the crack formation and porous structures in the surface morphology (Figure 3 (a)). In addition, it was observed that the aggregate particles were dispersed in different sizes and shapes in the epoxy resin matrix. It is understood that the FE-SEM image of the SS-FRC sample has a more dense and compressed structure than the SS and FRC samples. In the high magnification image of the SS-FRC sample, compact structure formation was observed more clearly (Figure 3 (b)). Thus, it can be stated that the compactness increases with the increase of the bonding between the epoxy resin/aggregate [13]. Equal proportions of silica sand and recycled ferrochrome content in the dense structure can be attributed to the strength increase of the polymer concrete sample. Low and high magnification FE-SEM images of the SS-FRC-CNT sample obtained by adding SWCNT reinforcement components to the SS-FRC sample are shown in figures 3 (c) and (d), respectively. As seen in the low magnification picture, combining two different aggregates in the polymer mortar mixture, and adding SWCNTs made the sample morphology denser. Although aggregates of different shapes and sizes form agglomeration in a certain region of the epoxy matrix surface, it is understood that they are generally dispersed in the resin.

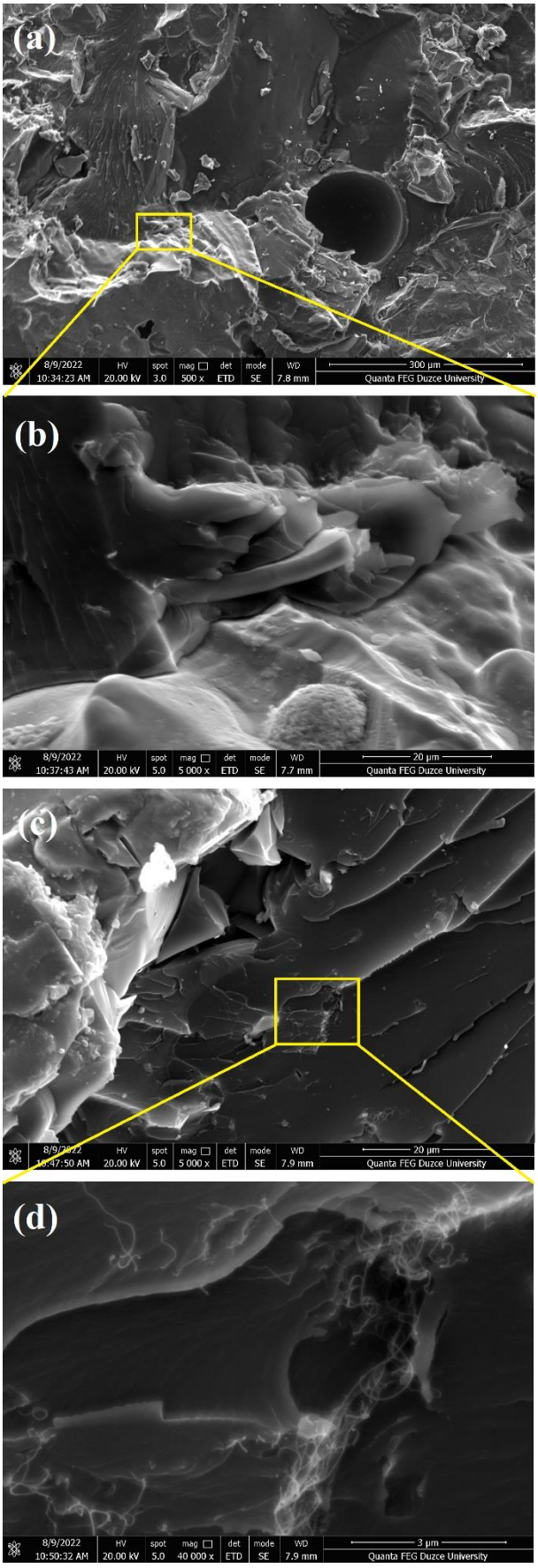

Figure 2. FE-SEM images of FRC (a, b) and FRC-CNT(c, d).

This could be related to the fact that the load applied to the sample contributes to the strength of the aggregates adhering to the matrix. In addition, the morphology of the SS-FRC-CNT sample was less porous compared to the other samples, which contributed to the formation of homogeneous matrix in the structure. It has been reported that the well-dispersed carbon nanotube retards the formation and propagation of microcracks in the epoxy matrix [14]. It is seen in figure 3 (d) that SWCNTs well dispersed in the polymer concrete matrix form a denser microstructure, preventing crack propagation and bridging between particles. Also, it can be stated that the low amount of SWCNT content reduces the formation of agglomeration in the matrix. Compared to SS, FRC and SS-FRC samples, it can be emphasized that the SWCNTs in the SS-FRC-CNT sample provide better adhesion with the epoxy resin, improving the interfacial bonding and contributing to the charge transfer process. As mentioned above, in the micrograph of the SS-FRC sample, the binding of more aggregate to the epoxy resin confirms that the adhesion between the epoxy/aggregate is increased and is therefore associated with improved charge transfer. However, it is expected that the SWCNT modification in the SS-FRC sample will contribute to the mechanical properties of the material. In Figure 3 (d), it acts as a bridge connecting the SWCNT epoxy resins. In addition, SWCNTs strengthened the epoxy resin matrix, limiting crack propagation. It can be noted that SWCNTs within the PC increase the energy dissipation [15]. EDS analysis results of PC samples are shown in figure 4. Oxygen element detected in SWCNT supplemented samples can be associated with hydroxyl and carboxyl groups formed by SWCNTs in the matrix. The high carbon peak intensity in the SWCNT added samples proves that the SWCNT reinforcement component is dispersed in the resin matrix. Mineralogical composition and crystal phases of polymer concrete samples determined by XRD analysis are shown in figure 5. Quartz, spinel, forsterite ($MgSi_2O_4$), $MgFe_{0.2}Al_{1.8}O_4$ and, Al_2CuO_4 peaks were detected in the XRD diffractogram and the crystal phase peaks of the other samples did not form broad humps, except for the FRC-CNT sample. It is seen that all samples have almost similar curves and although amorphous structures appear in the FRC-CNT sample, distinct crystalline phases are formed in the other samples. The peak peaks that appear in the range of 15-25 in the XRD models of the samples containing the SWCNT additive compound can be associated with the strong covalent bonding of the SWCNTs in the cement matrix [16]. The diffraction peak at ~21.06◦ can be attributed to the graphite structure of SWCNTs, and it can be said that SWCNTs carry out a chemical reaction with the resin matrix [17]. The almost similar overlapping peaks of the crystalline phases with and without SWCNT in the silica-filled samples can be explained by the fact that SWCNT does not interfere with the polymerization process. On the other hand, the semi-crystalline phase formations of the SWCNT additive in ferrochrome filled samples can be attributed to the poor chemical coupling of the SWCNT and the resin. Compared to the pure samples, the SWCNT addition improved the crystal phase formation, contributing to the compactness of the microstructure as mentioned above. Thus, new nucleation sites were formed, and the reactive surface area increased [18].

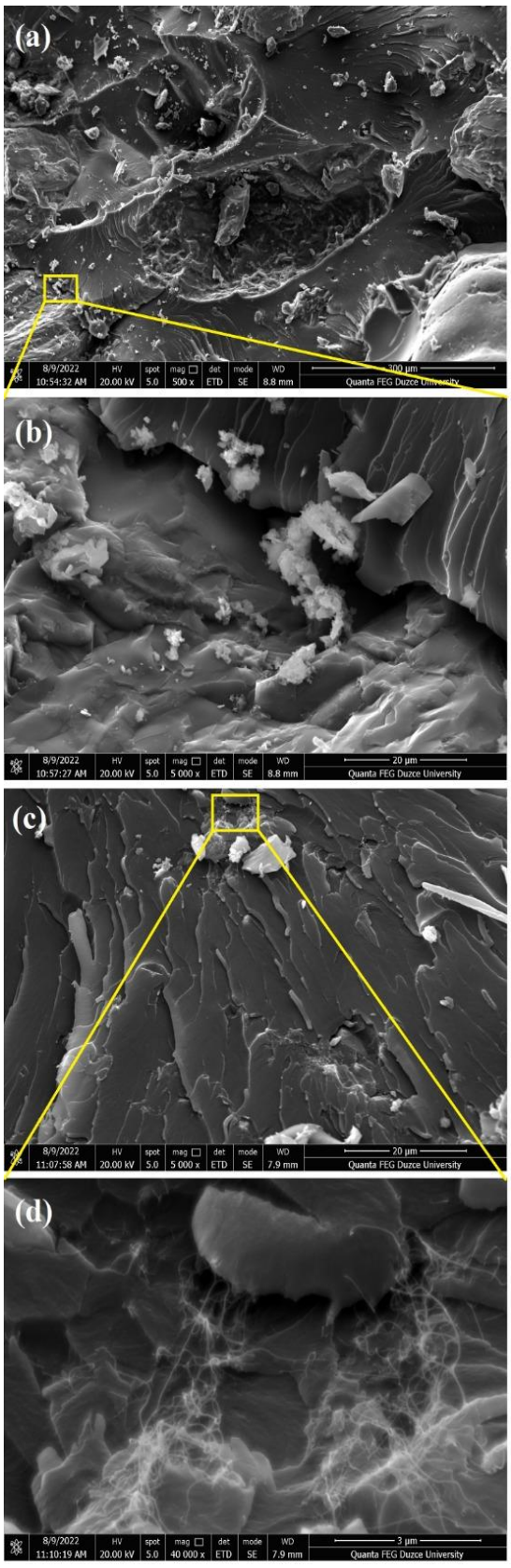

Figure 3. FE-SEM images of SS-FRC (a, b) and SS-FRC-CNT(c, d).

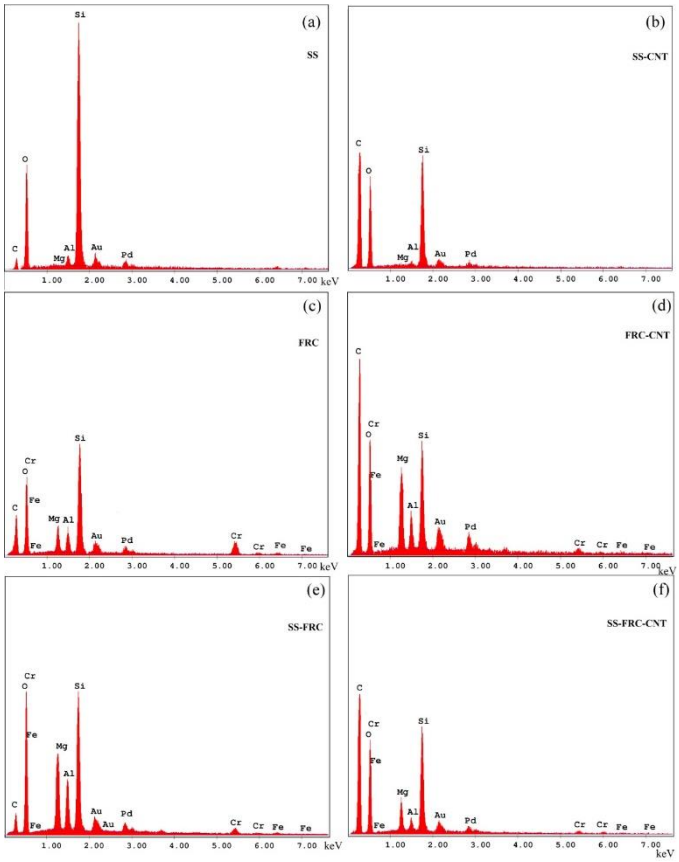

Figure 4. EDS results of polymer concrete samples.

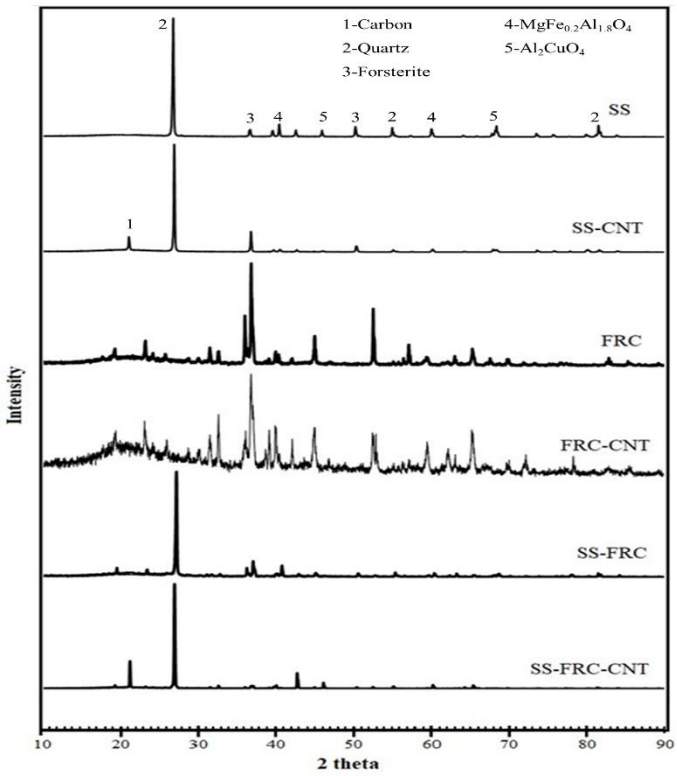

Figure 5. XRD analysis results of polymer concretes.

IV. CONCLUSIONS

FE-SEM images of polymer concrete samples were associated with increased adhesion strength of SWCNT-modified silica sand and recycled ferrochrome aggregates with epoxy resin. The silica sand particles were more effective in filling the voids in the epoxy resin matrix compared to the recycled ferrochrome particles. Silica sand aggregates of different sizes and irregular shapes can improve the tensile strength of polymer concrete. It was concluded that low concentration SWCNTs well dispersed in the epoxy resin increased the adhesion strength at the matrix interfaces. SWCNTs are expected to contribute to the void-filling effect and strong bond formation between resin/aggregate in porous structures and to the mechanical properties of the polymer concrete sample. EDS and XRD analysis results showed that SWCNTs exhibited potential behavior in resin matrix by increasing the physical interaction in reinforced polymer concretes.

ACKNOWLEDGMENT

This study was carried out within the scope of the project coded STB-072161 of Fibrobeton R&D Center. Thank you to Fibrobeton Company for their support. We also thank Eti Krom Inc. for their support of ferrochrome materials.

REFERENCES

[1] G. Martínez-Barrera, J.J. del Coz-Díaz, E. Martínez-Cruz, M. Martínez-López, M.C.S. Ribeiro, C. Velasco-Santos, H.E.H. Lobland, W. Brostow, Modified recycled tire fibers by gamma radiation and their use on the improvement of polymer concrete, *Constr. Build. Mater*. 204 (2019) 327–334.

[2] I. Tekin, M. Yasin Durgun, O. Gencel, T. Bilir, W. Brostow, H.E. Hagg Lobland, Concretes with synthetic aggregates for sustainability, *Constr. Build. Mater.* 133 (2017) 425–432.

[3] M.H. Niaki, A. Fereidoon, M.G. Ahangari, Effect of basalt, silica sand and fly ash on the mechanical properties of quaternary polymer concretes, *Bull. Mater. Sci.* 41 (2018) 69.

[4] M.G. Ahangari, A. Fereidoon, Micromechanical properties and morphologies of self-healing epoxy nanocomposites with microencapsulated healing agent, Mater. *Chem. Phys*. 151 (2015) 112–118.

[5] M.R.M. Aliha, H. reza Karimi, M. Abedi, The role of mix design and short glass fiber content on mode-I cracking characteristics of polymer concrete, *Constr. Build. Mater*. 317 (2022) 126139.

[6] H. Haddad, M. Al Kobaisi, Optimization of the polymer concrete used for manufacturing bases for precision tool machines, *Compos. Part B Eng*. 43 (2012) 3061–3068.

[7] B. Hu, N. Zhang, Y. Liao, Z. Pan, Y. Liu, L. Zhou, Z. Liu, Z. Jiang, Enhanced flexural performance of epoxy polymer concrete with short natural fibers, Sci. *China Technol. Sci.* 61 (2018) 1107–1113.

[8] J.M.. Reis, A.J.. Ferreira, Assessment of fracture properties of epoxy polymer concrete reinforced with short carbon and glass fibers, *Constr. Build. Mater.* 18 (2004) 523–528.

[9] H.S. Lee, B. Balasubramanian, G.V.T. Gopalakrishna, S.-J. Kwon, S.P. Karthick, V. Saraswathy, Durability performance of CNT and nanosilica admixed cement mortar, *Constr. Build. Mater*. 159 (2018) 463–472.

[10] J.M. Wernik, S.A. Meguid, On the mechanical characterization of carbon nanotube reinforced epoxy adhesives, *Mater. Des.* 59 (2014) 19–32.

[11] B. Ashrafi, J. Guan, V. Mirjalili, Y. Zhang, L. Chun, P. Hubert, B. Simard, C.T. Kingston, O. Bourne, A. Johnston, Enhancement of mechanical performance of epoxy/carbon fiber laminate composites using single-walled carbon nanotubes, *Compos. Sci. Technol.* 71 (2011) 1569–1578.

[12] M.R. Irshidat, M.H. Al-Saleh, Effect of using carbon nanotube modified epoxy on bond–slip behavior between concrete and FRP sheets, *Constr. Build. Mater.* 105 (2016) 511–518.

[13] S. Jena, R. Panigrahi, Performance assessment of geopolymer concrete with partial replacement of ferrochrome slag as coarse aggregate, *Constr. Build. Mater.* 220 (2019) 525–537.
[14] M. Tehrani, A.Y. Boroujeni, T.B. Hartman, T.P. Haugh, S.W. Case, M.S. Al-Haik, Mechanical characterization and impact damage assessment of a woven carbon fiber reinforced carbon nanotube–epoxy composite, *Compos. Sci. Technol.* 75 (2013) 42–48.
[15] S.M. Daghash, E.M. Soliman, U.F. Kandil, M.M. Reda Taha, Improving Impact Resistance of Polymer Concrete Using CNTs, Int. J. *Concr. Struct. Mater.* 10 (2016) 539–553.
[16] K.M. Liew, M.F. Kai, L.W. Zhang, Mechanical and damping properties of CNT-reinforced cementitious composites, *Compos. Struct.* 160 (2017) 81–88.
[17] L. Liu, J. Xu, T. Yin, Y. Wang, H. Chu, Improved conductivity and piezoresistive properties of Ni-CNTs cement-based composites under magnetic field, *Cem. Concr. Compos.* 121 (2021) 104089.
[18] M.A. Mousavi, A. Sadeghi-Nik, A. Bahari, C. Jin, R. Ahmed, T. Ozbakkaloglu, J. de Brito, Strength optimization of cementitious composites reinforced by carbon nanotubes and Titania nanoparticles, *Constr. Build. Mater.* 303 (2021) 124510.

Real Estate Valuation with Regression Analysis: The Case of Meram District of Konya Province

T. ALKAN[1], O. F. ATIZ[1], S. S. DURDURAN[1], and M. I. BAYRAKDAR[1]

[1]Necmettin Erbakan University, Konya/Turkey, tansualkan93@gmail.com
[1]Necmettin Erbakan University, Konya/Turkey, oatiz@erbakan.edu.tr
[1]Necmettin Erbakan University, Konya/Turkey, durduran2001@gmail.com
[1]Necmettin Erbakan University, Konya/Turkey, mhmmdbrkdr@gmail.com

Abstract **- Real estate valuation is the estimation of the value of a real estate by taking into account the factors affecting the value and market conditions. Real estate valuation procedures should be carried out in an impartial and scientific manner using accurate data. In this study, Meram district of Konya province was determined as the study area. The data of one hundred real estates in the study area were obtained with the help of online real estate sites. The factors affecting the value of the real estate were determined as area, number of rooms, age of the building, floor location, number of floors, building type and bathroom. Multiple linear regression analysis was used to determine the real estate value. The performance analysis of the method used was tested with the R^2 value and this value was calculated as 0.85.**

Keywords **- Real estate valuation, factors affecting real estate value, multiple linear regression.**

I. INTRODUCTION

Valuation is a concept that arises with the desire to know the value of real estate owned by people. Real estate valuation is explained as the determination of real estate value according to objective criteria in accordance with market conditions, taking into account the rights and benefits associated with the real estate [1]. Real estate valuation is a field that is gaining importance day by day. This is because real estate valuation is required for public actions such as urban and rural land readjustment, expropriation, urban transformation, easement establishment, taxation, registration-based transactions, as well as for private and individual actions such as insurance, banking, lending, and capital market [2].

Many methods, defined as traditional, statistical and modern methods, are used in real estate valuation. It is not possible to speak of a precise model or mathematical method. There are differences between the values resulting from the methods used in real estate valuation and the market values, and, moreover, the values obtained for the same real estate by different methods may differ from each other [3]. Moreover, although there are provisions related to real estate valuation in laws such as the Expropriation Act, the Cadastre Act, and the Real Estate Tax Act, there is no general legal regulation on this subject.

Determining the factors that affect real estate value is the most important step in the application of real estate valuation. The factors that affect real estate value have different characteristics, and the extent to which these factors affect the real estate may vary [4]. Each real estate differs from others by its physical, location, structural, legal, and environmental characteristics. These characteristics that affect the value of the real estate change from person to person in terms of quantity and quality. The type of real estate being valued also changes the factors being determined. The fact that the number of factors is high, differs from region to region, and changes according to time and person, leads to the fact that the value of the real estate cannot be accurately determined [5].

There are many methods used in the valuation of real estate. Reviewing the literature, various methods are applied for real estate valuation, such as nominal valuation method [6], multiple regression [7], hedonic pricing model [8], artificial neural networks [9], fuzzy logic [10], machine learning [11], and analytical hierarchy process [12].

In this study, the data of one hundred real estate in Meram district of Konya province were obtained by using online real estate sites. The factors that affect the real estate value were determined. The method of multiple linear regression was applied to determine the real estate valuation.

II. MATERIAL AND METHOD

In this study, Meram district of Konya province is the study area. Meram district is one of the central districts of Konya province and is located in the southwestern part of the city (Figure 1).

The data used in this study were obtained from online real estate sites. Advertisements published for Meram district were studied and data on one hundred residential real estate were collected. The physical and structural features of the real estate were taken into account in determining the factors that affect the real estate value. The factors that affect real estate value obtained using online real estate sites are as follows: Area, number of rooms, age of the building, floor location, number of floors, building type, and bathroom. The building type factor was based on whether or not it was a luxury real estate, and it was assigned points and included in the analysis. The sample data of ten real estate are shown in Table 1.

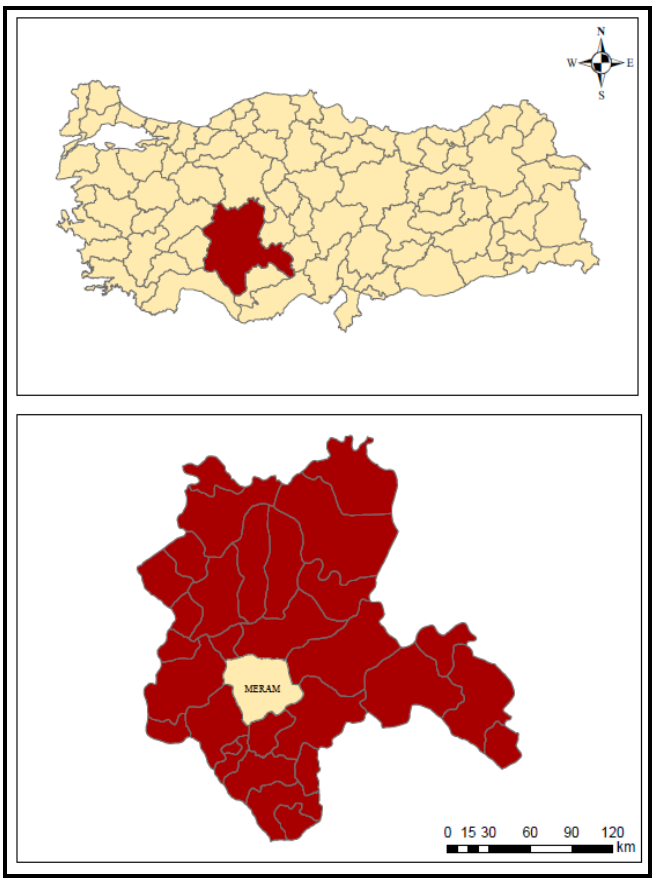

Figure 1. Study area

Table 1. The sample data of real estate in the study area

Area (m^2)	Rooms	Age	Floor	∑Floor	Bathroom
150	3+1	21+	1	4	1
60	1+1	16-20	2	4	1
170	4+1	16-20	1	4	1
170	4+1	16-20	8	8	2
80	2+1	4	3	3	1
200	4+1	5-10	3	3	2
88	2+1	5-10	5	6	1
160	3+1	11-15	4	5	1
135	3+1	4	2	8	1
145	3+1	3	2	8	2

In this study, multiple linear regression analysis between statistical valuation methods was used. In statistical problems, an important problem is to determine if there is a relationship between variables, and if so, to determine the degree of that relationship. Regression analysis is used to examine the relationship between variables. If the value of one variable changes and the value of another variable changes accordingly, it can be said that there is a relationship between them [13]. It is based on the rule of keeping one of the variables or category of variables at a predetermined level and studying how the other variable changes depending on this level [7].

In regression analysis, variables are divided into two groups: dependent, and independent variables. The dependent variable is described by independent variables.

One of the most frequently used methods in real estate valuation is regression analysis. The factors affecting the real estate value can be analyzed simultaneously and their effects on the valuation can be determined with this method [14]. For example, in the valuation of residential real estate, it is possible to calculate the extent to which factors such as area, age, and floor affect the value.

In multiple linear regression analysis with more than one independent variable, the most general equation (1), where x_i represents the independent variables and y represents the dependent variable is as follows:

$$y = b_0 + b_1 x_1 + b_2 x_2 + \dots + b_n x_n + u \quad (1)$$

y: Dependent variable,
$x_1, x_2, \dots, x_n$: Independent variables,
b_0: Constant coefficient,
$b_1, b_2, \dots, b_n$: Variable coefficients,
u: Error term.

III. Results

In the implementation phase, data collected through online real estate sites were first organized. Area, number of rooms, age of the building, floor location, number of floors, and bathroom factors affecting real estate value were used as quantitative data. The building type factor was categorized as 1 if it is luxury real estate and 0.5 for other cases.

Regression analysis was performed using Microsoft Excel. The real estate price is the dependent variable, and the factors that affect the value of the real estate are the independent variables. The coefficients obtained are shown in Table 2.

Table 2. Coefficients Table

	Coefficients	Standard Error	t-value	P-value
Intersection	-999269,19	90000,5	-3,21	0,0018
Area	4365,56	1642,85	2,66	0,0093
Rooms	54624,85	81167,66	0,67	0,5026
Age	-18153,77	6416,30	-2,83	0,0057
Floor	-49696,89	39937,65	-1,24	0,2165
∑Floor	72540,47	140755	2,38	0,0193
Type	1408964,04	100555	3,17	0,0021
Bathroom	289470,91	111096,44	2,61	0,0107

Multiple linear regression equation:

Value: -999269.19 + 4365.56 Area + 54624.85 Rooms – 18153.77 Age – 49696.89 Floor + 72540.47 ∑Floor + 1408964.04 Type + 289470.91 Bathroom

In the coefficients of the obtained multiple linear regression equation, the positive sign (+) has an increasing effect on the real estate value, while the negative sign (-) has a decreasing effect. The factors area, number of rooms, age of the building, number of floors, building type, and bathroom have a positive effect, while the factors age and floor location have a negative effect.

The distributions of the predicted values resulting from the regression analysis were examined and the curve equation was generated (Figure 2).

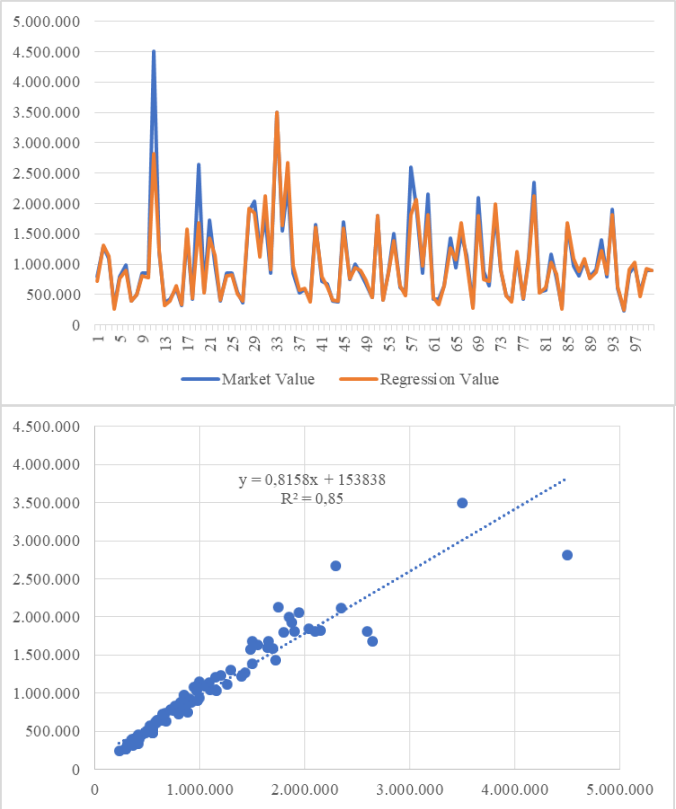

Figure 2. Distribution of values and performance analysis

The R^2 value must be in the range of 0 to 1, and a value close to 1 means that the results obtained are significant. It was determined that the values obtained as a result of the study with the R^2 value (0.85) were significant. In addition, the average approximation rate was calculated to study the relationship between the values obtained from the regression analysis and the market values (Equation 2).

$$\text{Average Approximation } \% = \frac{\sum_{i=1}^{n} 1 - \left[\frac{|x_p - x_i|}{x_i}\right]}{n} * 100 \quad (2)$$

x_p: market value, x_i: regression value,
n: number of real estate,
i:1,2,3,…,n.

The average approximation rate of real estate values and sales values obtained by the regression analysis is 91.33%. This shows that the values determined by the regression analysis and the market values overlap.

IV. Conclusion

Real estate valuation is an area that is very important today. It is important to create a reliable market environment in the real estate sector and to determine the value objectively. For this purpose, regression analysis is a method that is widely used in real estate valuation and mathematically meaningful results.

In this study, data on the physical and structural and features of one hundred residential real estate in Meram district of Konya province were used. The real estate valuation study was conducted using multiple linear regression method. In examining the obtained results, the R^2 value was calculated as 0.85 and the results were found to be significant. In addition, the average approximation rate was calculated as 91.33%. These results show that the regression analysis method used can be used in real estate valuation studies.

References

[1] A. Açlar, and V. Çağdaş, *Taşınmaz (Gayrimenkul) Değerlemesi*, HKMO, ISBN 975-395-551-0, Ankara, 2008.

[2] N. Erdem, "An evaluation on scientific study and recommendations for restructuring the Turkish immovable valuation system", *Niğde Ömer Halisdemir University Journal of Engineering Sciences*, vol. 7(1), pp. 159-170, 2018.

[3] Ş. Yalpır, "The development and application of a real-estate valuation model with fuzzy logic methodology: Konya case study", Ph.D. dissertation, Selcuk University, Konya, 2007.

[4] A. Bozdağ, and E. Ertunç, "Real Property Valuation in the Sample of the City of Niğde through GIS and AHP Method", *Journal of Geomatics*, vol. 5(3), pp. 228-240, 2020.

[5] M. Girgenç, T. Alkan, and S.S. Durduran, "Examination of real estate value maps by fuzzy logic method in Ankara / Mamak district", *Niğde Ömer Halisdemir University Journal of Engineering Sciences*, vol. 11(3), pp. 681-688, 2022.

[6] M. Doldur, and R.M. Alkan, "Producing GIS-based Land Value Maps by Using Nominal Valuation Method: Case Study in Avanos/Nevşehir", *Afyon Kocatepe University Journal of Science and Engineering*, vol. 21(4), pp. 846-863, 2021.

[7] M.E. Tabar, A.C. Başara, and Y. Şişman, "Housing valuation study in Tokat province with multiple regression and artificial neural networks", *Turkish Journal of Land Management*, vol. 3(1), pp. 01-07, 2021.

[8] İ. Güler, U. Başer, and M. Bozoğlu, "Valuation of house prices in the central district of Rize province using an hedonic price model", *Journal of the Institute of Science and Technology*, 9(4), pp. 2294-2302, 2019.

[9] A.T. İlhan, and N.S. Öz, "Applicability of artificial neural networks on mass valuation of real estates: The case of Gölbaşı district", *Hacettepe University Journal of Social Sciences*, vol. 2(2), pp. 160-188, 2020.

[10] F.T. Özcan, and A. Eldem, "Approach of fuzzy logic based model for house price valuation", *Nevsehir Journal of Science and Technology*, vol. 9(2), pp. 194-205, 2020.

[11] T. Dimopoulos, and N. Bakas, "Sensitivity analysis of machine learning models for the mass appraisal of real estate. Case study of residential units in Nicosia, Cyprus", Remote Sensing, vol. 11(24), 3047, 2019.

[12] T. Alkan, and S.S. Durduran, "Analysis of real estate in tourism cities by GIS and AHP method: The case of Alanya city", *Niğde Ömer Halisdemir University Journal of Engineering Sciences*, vol. 10(1), pp. 178-187, 2021.

[13] C. Karaca, and H. Karacan, "Investigation of factors affecting demand for electricity consumption with multiple regression method", *Selcuk University Journal of Engineering, Science and Technology*, vol. 4(3), pp. 182-95, 2016.

[14] S. Çinar, and F. B. Ünel, "Mass valuation of real properties transformed from forest to agricultural land", *Journal of Geomatics*, vol. 7(2), pp. 112-127, 2022.

Developing a Novel Photogrammetry Methodology in Cultural Heritage Documentation: Mardin Melik Mahmut Mosque

İ.KUTLU[1], A.SOYLUK[2] and A.İ.ÜNAY[3]

[1] Mardin Artuklu University, Mardin/Turkey, izzettinkutlu@artuklu.edu.tr
[2]Gazi University, Ankara/Turkey, asenad@gazi.edu.tr
[3]Gazi University, Ankara/Turkey, unay@gazi.edu.tr

Abstract **- Preservation, documentation, and dissemination of historical buildings as the tangible examples of cultural heritage have never been more significant than today in the Information Age. Yet, historical buildings are under the constant threat of damage and destruction due to many factors, such as deterioration of materials and structure, natural disasters, misuse, and vandalism. To reduce the risk of the loss of historical buildings, it is highly essential and required to develop a robust research methodology about the effective documentation of tangible heritage. The design of practical documentation processes, which are cost-effective and time-saving, is one of the challenges of the most recent research in the field in which the use of photogrammetry increases. Although photogrammetry has been in use for a long time, there has been recent advancements and improvements in the methods and the tools deployed to digitally record 3D data from physical environments, such as historical sites. The recent improvements solve the issues of computationally expensive processes of photogrammetry while preserving the level of accuracy and detail. This research applies one of the recent photogrammetry techniques available in the field in the context of the documentation of a historical building in Mardin, which is the Melik Mahmut Mosque constructed in the Artuklu period in the 14th century. One of the objectives is to disseminate the use of the novel photogrammetry methods integrated into the studies of the preservation, documentation and conservation of historical buildings as cultural heritage. The methodology is built on the use of mobile recording techniques that guarantee the required level of accuracy with visual and geographical data based on high-definition images. The research shows how effective the used photogrammetry technique is in surveying on site to record necessary data in limited time. The paper demonstrates how the representation of the 3D models are processed in the photogrammetric modeling software of Agisoft's Metashape following the steps of recording on site. The results present how the used photogrammetry technique generates computational inexpensive, practical, fast and comprehensible digital data for the 3D representation and visualization in the context of cultural heritage documentation. With the use of an effective and contemporary method that produces satisfactory accurate results, the research contributes to the knowledge production about the understanding of the conditions that impact the preservation of historical buildings.**

Keywords **– Cultural heritage, documentation, historical building, photogrammetry, Artuklu.**

I. INTRODUCTION

Cultural heritages should be preserved due to they include the traditions, beliefs, lifestyle, art style and socio-cultural characteristics of the period [1]. As a consequence of their features, they provide a connection between the past, the present, and the future. So, it is significant for societies to notice their cultural heritage as a complementary element. Since it includes the past of societies and provides a connection with the future, cultural heritages require preservation, maintenance, and passing on to future generations [2]. UNESCO (United Nations Educational, Scientific and Cultural Organization) established in 1954 and ICOMOS (International Council on Monuments and Sites) established in 1965 have published international conventions for the preservation of cultural heritage, improvement of intercultural understanding, and emphasizing the significance of international cooperation. In these conventions, which determine the basic theoretical approaches to the preservation and conservation of cultural heritage, the importance of passing on these heritages to future generations were emphasized [3]. To pass on and preserve these values to future generations, it has become a necessity to conduct documentation studies [4]. Documentation of cultural heritage is the measurement, recording, and presentation processes necessary for the evaluation of the current state (size, shape, and location) of historical or cultural structures [5].

Cultural heritages inherited from past generations are values that need to be passed on to future generations in an original situation [6]. Cultural heritages are generally defined as tangible or intangible [7] and one of the most important examples is architectural buildings. Architectural and structural features of cultural heritage are important for restorations. Cultural architectural heritages may need restoration and reuse due to natural or artificial reasons as a result of time-dependent deformation [8,9]. Restoration and reuse studies must be carefully documented to realize interventions that are compatible with the original condition of the buildings. Documentation physically or digitally ensures that the architectural buildings are archived and allows deductions about the past.

There are different documentation methods used in the

documentation of historical and cultural heritage. These methods, which are indispensable for the preservation of cultural heritage, are the classical manual documentation method, topographic methods, photogrammetric methods, and scanning methods [10]. The classical manual documentation method causes a great disadvantage in terms of time and cost. The probability of mistakes increases because the documentation of the buildings is usually conducted by human hands [2]. Many methods from different professional disciplines are used in the documentation and survey studies with the developing technology. Today, documentation studies containing photographs and visual details are noticeable among these methods [11]. Photogrammetry is one of the most frequently used methods as it allows the production of 3D models from two-dimensional (2D) photographs taken with digital cameras. With the photogrammetry method, 3D modeling and documentation of structures can be implemented without risk and at low costs [12]. For this reason, documentation studies conducted with the photogrammetric method can be the basis for restoration projects of deformed historical architectural buildings [4].

Varol et al. [1], Yakar et al. [13], Şasi and Yakar [14] produced 3D models of cultural architectural buildings from images obtained by the photogrammetry method. Aydın [15] built 3D models from 2D photographs taken from narrow streets in the old city of Kashgar, China. Ulvi and Yiğit [16], Yakar and Bilgi [17] produced 3D models of two different historical fountains using the photogrammetric model. As the number of digital tools that take high-resolution photos increases, the number and variety of studies are also increasing.

Turkey contains lots of historical values in terms of its geographical, historical, and cultural features. Mardin is located in the southeast of Turkey and the Mesopotamian region. It is one of the most important cities in the region and has hosted many different civilizations. The fact that the city is on trade routes such as the Silk Road and has important agricultural areas such as the Mesopotamian Plain has made it an important city from the past to the present. Today, its cultural features have attracted great attention. This study aims to emphasize the importance of documenting valuable and rare historical buildings with the example of *Mardin Melik Mahmut Mosque*. In the documentation of Melik Mahmut Mosque, the photogrammetric modeling method was used and the stages in the process were discussed. To built a photogrammetric model, photographs can be taken with many different tools today. The images used in the study were taken with smartphones that can produce high-resolution photographs (Iphone 13 Pro Max by Apple). As a result of qualified field planning, photogrammetric models can be built without the need for workload and time. After obtaining the photographs, Metashape (company Agisoft) software was used for the three-dimensional (3D) model. The model built as a result of the alignment of the photographs was scaled with the measurements obtained from the building and the digital documentation process was completed.

II. METHODOLOGY

Photogrammetry is the method that allows the built of 3D models at close or far range. With the developing technology, many photogrammetric models can be built using different techniques. Based on these techniques, some processes are conducted using cameras with different focal lengths and special software, and 3D models are built from the photographic surface [18]. Photogrammetry is the technique of measuring objects and the metric interpretation of image data. The process is conducted with the special modeling algorithm of the software used. The software's modeling algorithm was shown below (Figure 1):

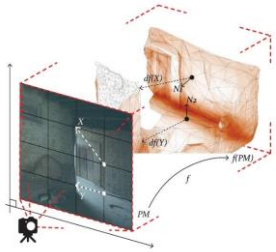

Figure 1: Diagram of a 3D model produced from 2D photographs [15].

Classification of photogrammetry can be found in different sources according to various situations, technologies, and application areas. As a result of the examinations in the literature, photogrammetry was classified generally in 5 different ways; (1) to the application area, (2) to the location of the pictures, (3) to the number of photographs used, (4) to the size of the object and (5) to the evaluation method [19-21]. In this study, only the term "photogrammetry" was used in terms of subject integrity.

Photogrammetric methods are frequently used in many areas from the past to present. Photogrammetry has developed in parallel with the development of technology and has become a preferred method in documentation studies. Before the photogrammetric documentation method, different traditional methods were used in similar fields and are still used when necessary. Traditional measuring methods can sometimes be inadequate, especially due to the complex geometries of masonry structures [19].

III. CASE STUDY: MARDIN MELIK MAHMUT MOSQUE

Melik Mahmud Mosque is located on First Street in Savur Kapı Neighborhood in Artuklu, the central district of Mardin. It was built during the Artuqid period, which ruled in the Southeastern Anatolia Region between the twelfth and fifteenth centuries. During the Artuqid period, especially mosques and madrasas had an important place in terms of their development in early Anatolian architecture [23,24].

The mosque was built in the fourteenth century. This situation can be seen from the inscription on the portal niche, which includes the date of construction *"…ed din Ahmed bin Sultan el-Melik es Salih Şems ed Dünya veddin bin Artuk adını ve sonunda…sene 7…"* [25]. In the niche of the mihrab on the

south wall, there is another inscription with Ayet-el Kürsi. (Figure 2).

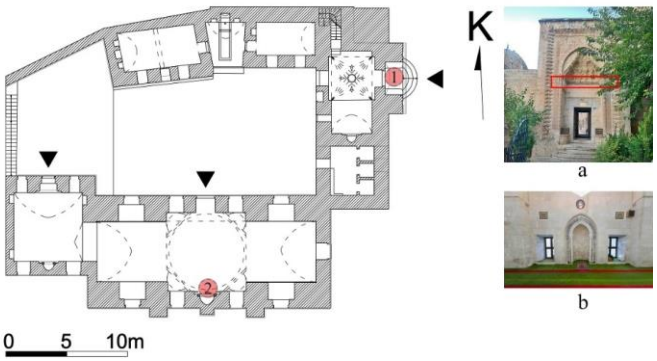

Figure 2: Melik Mahmut Mosque – a) the inscription on the portal niche 1, b) the inscription in the mihrab niche (Plan was retrieved from Promim Architecture Office.)

The mosque has remained standing with various restorations from the first years it was built. In its current state, it has the characteristics of a mosque of the Artuqid period with its rectangular-planned sanctuary, courtyard, and dome in front of the mihrab.

A. Spatial Organization

Today, the mosque consists of a rectangular-planned sanctuary, a courtyard, a public fountain, an entrance iwan, and spaces of different sizes (imam room, etc.).

The mosque is accessed through the monumental portal gate, which is located on the east side and is the only entrance to the mosque. The portal gate is located both higher than the main masonry walls of the mosque and protrudes forward (Figure 3a). The portal was built entirely of cutting lime-stone and has a rectangular form. There are many original stone-ornamentations on the portal.

The iwan, which provides the entrance to the mosque courtyard, has a square plan type. There is a minaret entrance door to the right and two spaces of different sizes to the left of the entrance iwan. In addition, in the center of the vault on the ceiling of this iwan, there is an ornamented rosette with original stone (Figure 3b).

After the entrance iwan, on the north side of the courtyard, the fountain was located in traditional Mardin religious buildings and two rooms on both sides of the fountain; to the south is the sanctuary, and to the west is the staircase that accesses the dome. The flooring of the courtyard is cutting lime-stone. The sanctuary is accessed through two doors in the courtyard.

Figure 3: Melik Mahmut Mosque - a) The portal in the east, b) The vault of the entrance iwan.

The sanctuary consists of a single nave parallel to the mihrab. The sanctuary is approximately 27 x 9 m in dimensions and is located in an east-west direction. The mosque, which has a dome in front of the mihrab, has barrel vaults in the east and west directions of the dome. Consequently, Melik Mahmut Mosque has the characteristics of the sanctuary type and a dome in front of the mihrab which was built in the Artuqid period (Figure 4).

B. Material Properties

Melik Mahmut Mosque was built entirely of cutting lime-stone extracted from the region. The height of the cut stones used is mostly 50-55 cm, and the depth is between 20-25 cm.

C. Construction Technique and Structural Features

In the mosque, the dome in front of the mihrab and the barrel vaults in the naves transfer the loads to the masonry walls. Apart from the masonry walls, there is no other vertical structural element in the sanctuary. The masonry wall with the least depth is 70 cm in the women's sanctuary, and the masonry wall with the greatest depth is 212 cm on the south facade wall. Similar features are obtained for the entrance iwan, imam rooms, and courtyard. Today, in the northeast of the mosque, there is a minaret starting with a square pulpit and with an ornamented circular body, measuring approximately 2.80 x 2.80 m. The pulpit was constructed adjacent to the walls of the mosque.

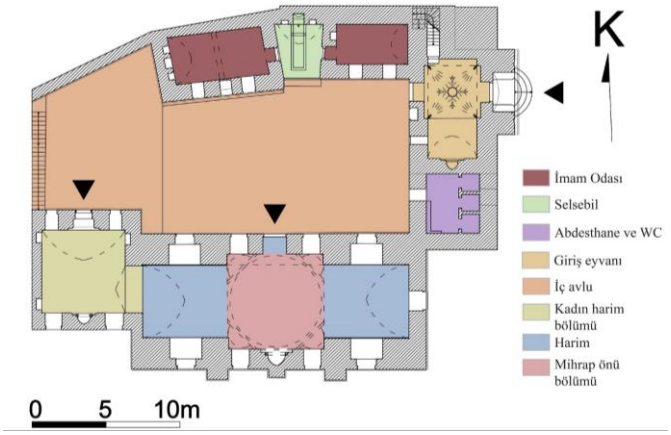

Figure 4: Melik Mahmut Mosque – Spatial organization diagram.

IV. FINDINGS: 3D MODEL

Documentation of historical buildings with the photogrammetric method includes a two-stage process containing field and office studies (Figure 5). During field studies, photographs of the building are taken. Camera calibration, transferring images to computer, evaluation, and drawing processes are applied with photogrammetric software in office studies. Field and office studies were also conducted in the study, in which a 3D photogrammetric model of the historical Mardin Melik Mahmut Mosque was built.

During the field study, photographs were taken from Melik Mahmut Mosque. The process of taking photographs of the field with a planned organization accelerated the modeling process. Photographing is the most important stage of the photogrammetric model-built process. During photography, a suitable time, high-resolution camera, and appropriate editing technique should be chosen. To built the photogrammetric model, 815 photographs were taken with a smartphone (Iphone-13 Pro Max) during the field study for Melik Mahmut Cami. Field studies were completed in 3 hours with a planned study.

During the office study, the photographs taken of the mosque were evaluated and the model-built process was started. The process was applied with photogrammetric software. Metashape photogrammetric software was used in this study. Developed by Agisoft, Metashape is defined by the company as: *"Agisoft Metashape is a stand-alone software product that performs photogrammetric processing of digital images and generates 3D spatial data to be used in GIS applications, cultural heritage documentation, and visual effects production as well as for indirect measurements of objects of various scales."* [26]. This software is used to make a three-dimensional model and metric measurements of an object from digital images. 815 photos of Melik Mahmut Mosque were added to the program. The software identified and aligned all these photos. These photos taken via smartphone have a 3024 x 4032 pixel size and 72 dpi (dots per inch) horizontal and vertical resolution. Identifying and aligning all photographs is not a one-time process. In the identification processes of the 815 photographs taken, unidentified photographs were detected and the surfaces of the bright objects on the photograph were edited and covered with black, and transferred to the program again. These surfaces can be included vehicles passing over the road or photo frames with sunshine. In this way, the photogrammetric model of Melik Mahmut Mosque was built for about 10 hours.

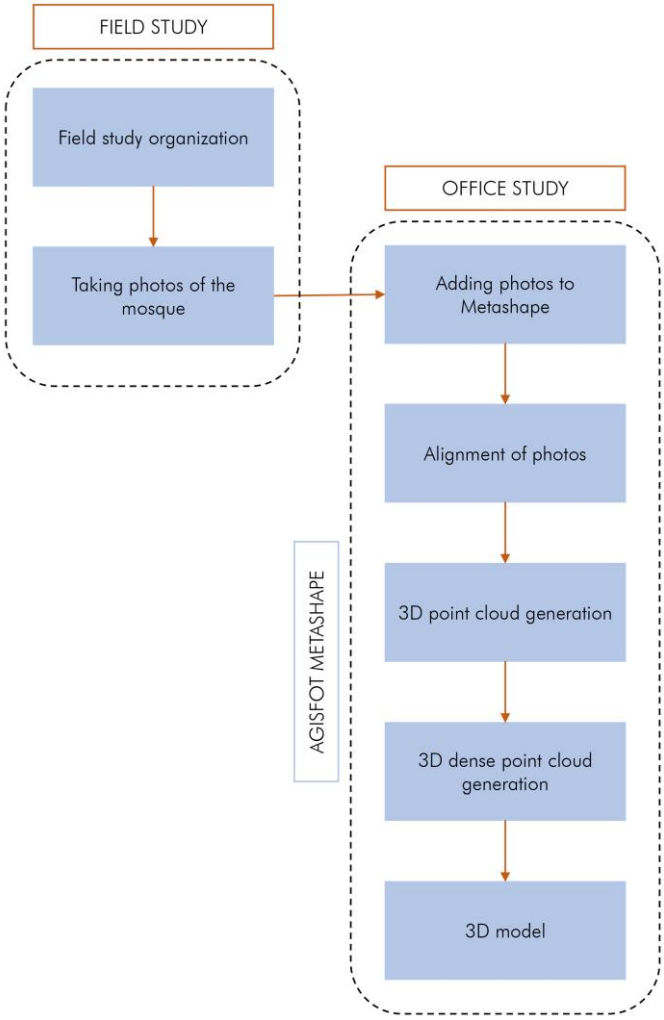

Figure 5: Work-flow diagram.

After the photos were added to Metashape, the process of definition and model-built began. All 815 photographs taken in the first process of the photogrammetric model were aligned by the Metashape software. As a result of this process, a model consisting of point clouds and camera angles was built. With the alignment of 815 photographs, the 3D dense point cloud of Melik Mahmut Mosque was created. After the dense point cloud process, the process of transforming the point clouds into meshes was conducted. Cleaning up unnecessary point clouds in the meshing process simplifies the process. With the obtained meshes, unnecessary data other than the required model can be cleaned. With the editing of geometry and mesh, the textures on the photograph were visible on the model. With this process, the digital 3D photogrammetric model-built process was completed (Table 1).

Table 1: Melik Mahmut Mosque photogrammetric model process.

Align photos
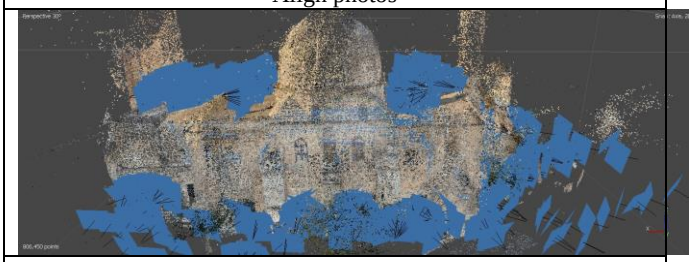
Build dense cloud

Build mesh
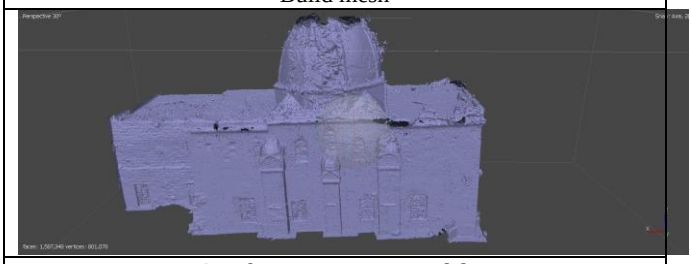
3D photogrammetric model
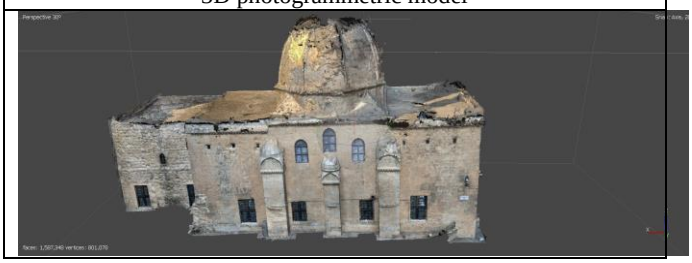

The numerical data of the photogrammetric model in Table 2 were presented. The data generated in the model is directly related to the resolution of the aligned photos, depending on the number of photos. In addition, Metashape provides the opportunity to choose the density, such as "highest, high, medium, low, lowest" during the model-built process. For a high-quality model, the model should be built with the highest density. Melik Mahmut Mosque, whose 3D model has been produced in this study, was produced with high density.

Table 2: Numerical data of the photogrammetric model

Number of Photos	815
Dense Point Cloud	70,733,757.00
3D Model Number of Triangles (Meshes)	1,587,348.00

V. EVALUATION

The photogrammetric modeling technique used in the study was conducted with a process that can be routinely performed everywhere thanks to smartphones. Photogrammetric models that can be built from photographs taken with smartphones can greatly reduce the modeling time of historical buildings. These models can be used in digitally documenting historical buildings, preserving their current condition, and creating survey drawings on the model. In addition, the 3D models produced in the study can be exported to different software formats. In this way, it can be used as reference data in restoration and conservation works.

In photogrammetric models via smartphones, it is not possible to built the points where the phone camera cannot reach and the image cannot be taken. In this study, it can be seen that the spire of the dome of Melik Mahmut Mosque could not be built by the software. Because there were few or no photos for which the software could identify and align the points. In this case, it is possible to add the photos obtained from online resources to Metashape by making them the same size as the photo sizes taken with smartphones. The software can identify and align photos obtained from different sources, provided that the resolution of the photo obtained online is high and the ambient light is similar. In addition, it can conveniently create a 3D digital model with photographs obtained from unmanned aerial vehicles. A more accurate model of the building can be built as a result of transferring aerial images and photographs such as the dome frames. However, there are high costs and many procedures to be applied for the use of these tools. In this case, alternatives can be produced by making an evaluation between cost and model quality.

VI. CONCLUSION

Today, the preservation of cultural heritages and their passing on to future generations is very significant in terms of preserving the socio-cultural values of societies. Due to natural and artificial reasons, cultural heritages can be destroyed or completely demolished over time. For this reason, it is important to document, preserve and pass on the existing cultural heritage structures to future generations. Documentation studies conducted with traditional methods in the past, sometimes both require a large workload and pose a disadvantage in terms of precision and accuracy. The photogrammetry method, whose use is increasing rapidly in parallel with technological developments, can be successfully applied in the preservation, conservation, and documentation of the 3D model of cultural heritage. Many data obtained in traditional methods are also accessed through the 3D digital photogrammetric model. This process can be completed in a short time and low-cost, as the current status of the cultural heritages is documented with the photogrammetry. This method includes automatically calculated mathematical equations and photographs of buildings within the software. Traditional methods may require field and office studies for a long time. But the photogrammetric method can be more practical. Although the buildings are documented in 2D with classical methods, it is possible to document the buildings in 3D in photogrammetric models. With all these features, photogrammetry is a method that can be easily used in such

documentation and three-dimensional modeling studies and can provide great advantages in lots of areas.

As a result, within the developing technology, many software, and imaging techniques can also be used in architectural heritage inventory. In this context, historical heritages pass on to future generations will be more accurate and permanent with the photogrammetry method. With this user-friendly digital method, many processes that need to be carefully applied in conservation studies and that sometimes encounter difficulties will be certainly achieved.

REFERENCES

[1] F. Varol, A. Ulvi, and M. Yakar, "Kültürel Mirasın Dokü mantasyonunda Yersel Fotogrametri Tekniğinin Kullanılması: Sazak Köprüsü ÖrneğI," *Uluslararası Sosyal Araştırmalar Dergisi, 11(57)*, pp. 986-991, 2018. http://dx.doi.org/10.17719/jisr.2018.2508

[2] Y. Kaya, and D. Temel, "Cep Telefonu Kameralarından Elde Edilen Görüntüler ile Kültürel Miras Eserlerinin Modellenmesi," *Türkiye Fotogrametri Dergisi*, 4(1), pp. 17-22, 2022.

[3] Z. Ahunbay, *Tarihi Çevre Koruma ve Restorasyon*. İstanbul: Yem Publishing, 2009.

[4] E. Candaş, K. Öztürk, and Ç. Eren, "Kültürel Mirasın Belgelenmesi: Katip Mustafa Çelebi Mahallesi Örneği," *TMMOB Harita ve Kadastro Mühendisleri Odası 12. Türkiye Harita Bilimsel ve Teknik Kurultayı*, 11-15 May 2009, Ankara.

[5] A. Georgopoulos, and C. Ioannidis, "Photogrammetric and surveying methods for the geometric recording of archaeological monuments," *FIG Working Week*, vol. 22, pp. 27, May, 2004.

[6] Z. Duran, and G. Toz, "Tarihi Eserlerin Fotogrametrik Yöntemle 3D Modellenmesine Örnek," *Selçuk Üniversitesi Jeodezi ve Fotogrametri Mühendisliği Öğretiminde 30. Yıl Sempozyumu*, Konya, 16-18 Oct 2002.

[7] ICOMOS, *International Cultural Tourism Charter*. Principles And Guidelines for Managing Tourism at Places of Cultural and Heritage Significance. ICOMOS International Cultural Tourism Committee, 2002.

[8] P. Castellini, V. Abaskin, and E. Achimova, "Portable electronic speckle interferometry device for the damages measurements in veneered wood artworks," *Journal of Cultural Heritage*, 9(3), pp. 225-233, 2008.

[9] H. İ. Şenol, N. Polat, Y. Kaya, A. Memduhoğlu, and M. Ulukavak, "Digital documentation of ancient stone carving in Şuayip City," *Mersin Photogrammetry Journal*, 3(1), pp. 10-14, 2021.

[10] W. Böhler, and G. Heinz, "Documentation, surveying, photogrammetry," *XVII CIPA Symposium*, Recife, Olinda. Brazil, 1999.

[11] M. Yakar, A. Ulvi, F. Varol, A. Y. Yiğit, Y. Kaya, A. Kabadayı, K. Çıkıkçı, and S. S. Catin, "Kültürel Miras Çalışmalarında Yersel Fotogrametri Yönteminin Uygulanması: Fetih Camii Örneği," Uluslararası Kültürel Miras ve Turizm Kongresi, pp. 175-185, May 2018.

[12] A. Ozimek, P. Ozimek, K. Skabek, and P. Łabędź, "Digital modelling and accuracy verification of a complex architectural object based on photogrammetric reconstruction," *Buildings*, 11(5), pp. 206, 2021.

[13] M. Yakar, A. Kabadayı, A. Y. Yiğit, K. Çıkıkcı, Y. Kaya, and S. S. Catin, "Emir Saltuk Kümbeti fotogrametrik rölöve çalışması ve 3 boyutlu modellenmesi," *Geomatik*, 1(1), pp. 14-18, 2016.

[14] A. Şasi, and M. Yakar, "Photogrammetric modelling of hasbey dar'ülhuffaz (masjid) using an unmanned aerial vehicle," *International Journal of Engineering and Geosciences*, 3(1), pp. 6-11, 2018.

[15] S. Aydın, "Decoding Kashgar: A digital design approach to steer and diversify creative engagement in digital heritage," Ph.D. dissertation, Victoria University of Wellington, New Zeland, 2018.

[16] A. Ulvi, and A. Y. Yiğit, "Kültürel Mirasın Dijital Dokümantasyonu: Taşkent Sultan Çeşmesinin Fotogrametrik Teknikler Kullanarak 3b Modelinin Yapılması," *Türkiye Fotogrametri Dergisi*, 1(1), pp. 1-6, 2019.

[17] İ. Yakar, and S. Bilgi, "Mobil Telefonlar Kullanılarak Elde Edilen 3 Boyutlu Modellerin Kültürel Mirasın Korunması Kapsamında Kullanılabilirliği: III. Ahmet Çeşmesi Örneği," *Türkiye Fotogrametri Dergisi*, 1(1), pp. 25-29, 2019.

[18] İ. Şanlıoğlu, M. Zeybek, and G. Karauğuz, "Photogrammetric Survey and 3D Modeling of Ivriz Rock Relief in Late Hittite Era," *Mediterranean Archaeology and Archaeometry*, 13(2), pp. 147-157, 2013.

[19] H. Kıvanç, "Kültürel Miras Belgeleme Çalışmalarında Fotogrametrik Yöntem İle Yersel Lazer Tarama Yönteminin Karşılaştırılması,"Master thesis, Konya Technical University, Konya, 2019.

[20] E. Ö. Avşar, "Tarihi köprülerin digital fotogrametri tekniği yardımıyla modellenmesi," Master thesis, Istanbul Technical University, İstanbul, 2006.

[21] S. M. Gül, "Sualtı Kültür Mirası'nın belgelenmesinde güncel fotogrametri yöntemleri," Master thesis, Akdeniz University, Antalya 2021.

[22] A. Ulvi, M. Yakar, A. Y. Yiğit, and Y. Kaya, "İHA ve Yersel Fotogrametrik Teknikler Kullanarak Aksaray Kızıl Kilise'nin 3 Boyutlu Nokta Bulutu ve Modelinin Üretilmesi," *Geomatik Dergisi*, 5(1), pp. 22-30, 2020.

[23] O. Aslanapa, *Anadolu'da ilk Türk mimarîsi: başlangıcı ve gelişmesi*. Ankara: Atatürk Kültür Merkezi Yayınları, 1991.

[24] M. Güler, and İ. Aktuğ Kolay, "12. yüzyıl Anadolu Türk camileri," *İTÜDERGİSİ/a*, 5(2), 83-90, 2006.

[25] A. Altun, *Anadolu'da Artuklu devri Türk mimarisi'nin gelişmesi*. İstanbul: Kültür Bakanlığı, 1978.

[26] Agisoft. [Online] Available: https://www.agisoft.com

Determination of G_0 Shear Modulus of Sandy Pumice Soil

I.YIGIT[1], E. SAKALAK[1], A.USAL[1]

[1]Isparta University of Applied Science, Isparta/Turkey, ibrahimyigit@isparta.edu.tr
[1]Isparta University of Applied Science, Isparta/Turkey, elifnursakalak@isparta.edu.tr
[1]Isparta University of Applied Science, Isparta/Turkey, ausal.usal@gmail.com

Abstract **- In order to analyze behaviour of soils under static or dynamic loading, the shear strain level has to be considered. The engineering parameters needed for large and small strain regions are obtained by different laboratory tests. The small strain shear modulus, which is important in the analysis of small strains of soil under dynamic loading, can be obtained from resonant column and piezoelectric bender elemen laboratory tests. In this context, a study was carried out on the small deformation behavior of the sandy pumice soil by using the piezoelectric bender elements in unconsolidated undrained triaxial test. The test results showed that as the cell pressure increases, the shear modulus also increases at the very small shear strain levels.**

Keywords **- Bender elements, Shear modulus, Shear wave velocity, Pumice Soil**

I. INTRODUCTION

SOILS generally exhibit shear strain in the range of 10^{-1}% to 10^{-6} % according to loading type and level. Shear strains above 10^{-1} %, among 10^{-1} to 10^{-4} % and below 10^{-4} % are called large, small and very small shear strains respectively. Very small shear strains usually not encountered in statically loaded geotechnical field problems but they are important in the view of dynamic loading. In the range of very small shear strains, shear modulus of soil can be determined piezoelectric bender elements and resonant column tests in the laboratory. Former mentioned is used in this study.

There are lots of study in the literature which are conducted to determine shear modulus of granular or fine soils in the very small shear strain range by bender elements. Nevertheless, few studies can be found in the literature which are fulfilled to determine shear modulus of pumice soil by bender elements.

Due to the lower unit weight and enormous intra voids, pumice is a very useful construction material in civil engineering, hence huge amount of study can be found in literature in this discipline. However, geotechnical properties of pumice soil are not known very well. But has to be highlighted. Because, in some regions, cities are positioned near to dormant volcanos as city of Isparta which is next to Gelincik dormant volcano. Pumice is a significant soil stratum in the soil profile of Isparta. Depending on the distance from the volcanic vent, pumice content varies. In this study, shear modulus of pumice soil is determined in the small shear strain region by using bender elements.

II. MATERIAL AND METHODS

A. Pumice

Pumice is formed by rapid cooling of the magma that comes to the surface as a result of volcanic activities. It has a glassy appearance and numerous porous structures from micro to macro scale. Usually there is no connection between the pores. With its pumice color and porous structure, it can be easily distinguished from other volcanic glassy rocks such as perlite, obsidian, etc. [1].

Pumice found in Isparta - Gelincik region is usually off-white or yellowish in color, containing approximately 7-10% gangue by weight [2].

In-hole seismic studies carried out around Isparta, it was observed that the Vp wave velocity was between 184 - 395 m/s and the Vs wave velocity was between 129 - 285 m/s. The Vp/Vs ratio is around 1.5, indicating that the pumice is porous and gas-saturated [3].

The porosity of the pumice is between %69-71 and the void ratio is between 2.3 and 3.1. Generally if the grain size increases, the unit volume weight decreases. This shows that the grain size of pumice and the unit volume weight are inversely proportional. The voids and pores of the pumice may show volumetric and physical changes as well as changes in the ground behavior. If the geotechnical or dynamic behavior of the pumice is in question, the void structure should be taken into account [4].

B. Piezoelectric Bender Elements

The word piezo is of Greek origin and means to compress or to exert pressure. The ability to generate electricity in proportion to the amount of pressure applied to an object of crystalline structure is called piezoelectric. Piezoelectric property can convert a mechanical energy to electrical energy or electrical energy to mechanical energy. The production of electricity from mechanical energy is called piezo, the production of mechanical energy from electrical energy and the production of vibration is called reverse piezo.

Piezoelectric Ceramics is an electro-mechanical transducer that bends as the applied voltage changes, or generates voltage as it bends.

The bender elements, which are in the form of double consoles and a polarized thin plate, are obtained from piezoelectric ceramics. When the load is applied to the piezoelectric ceramics, while the distance between the poles decreases, the charge accumulated on the surface increases, so

a voltage difference occurs between the two ends. If the direction of the electric field changes, charges of the same sign repel each other and the crystal becomes shorter [5]. Electrical energy is converted into mechanical energy as shown in Figure 1. The bender elements used in the study are PZT-5A type bender elements.

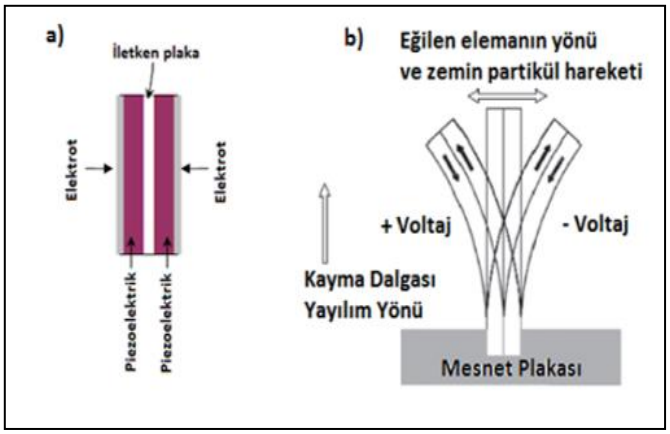

Figure 1: a) Bender element structure b) Bender element operation[6]

C. Obtaining the shear modulus of sandy pumice soil

Bender element tests were performed by mounting bender elements to triaxial test loading caps. Transmitter and receiver bender element was placed top and bottom cap respectively (Figure 2). Cylindrical triaxial test specimens was used with 50mmx100mm in size and height to diameter ratio is two.

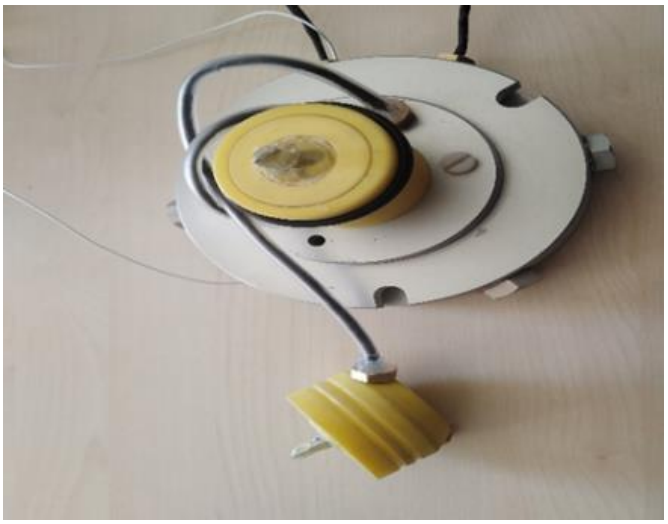

Figure 2: Triaxial test top and bottom cap with bender elements.

The shear modulus is obtained by Equation 1 when the strains are less than % 10^{-4} [7].

$$G = \rho V_s^2 \quad (1)$$

G: shear modulus (kPa)
ρ: density (gr/cm^3)
Vs: shear wave velocity (m/sn)

In order to obtain the shear modulus, the shear wave velocity must be determined, through Equation 2 with the measurement of specimen lenth and travel time.

$$Vs = \lambda f = \frac{L_{tt}}{t} \quad (2)$$

V_s: shear move velocity
λ: wave length,
f: frequency
L_{tt}: length
t: travel time

The total travel time is obtained from Equation 3. An example measurement of total travel time is given in Figure 3.

$$t = t_s - t_i \quad (3)$$

t: total travel time
ts: time of the signal in the receiving bender element
ti: the time of the signal at the transmitter bender element

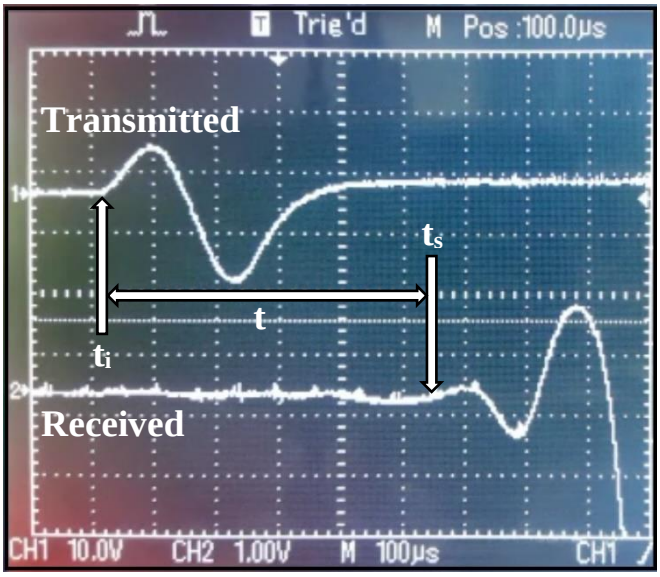

Figure 3: Measurement of total travel time in soil sample.

The most important factor in changing the shape of the signal to be formed in the receiving bender element is the frequency value applied to the source bender element. This effect, known as the Near-Field Effect in the literature, makes it difficult to determine the arrival time of the shear wave in bender element experiments. The near field effect is defined as the ratio of wavelength to wavelength [8, 9, 10]. In this study 4 kHz sine wave pulse signal was used. The sine wave generated from specially designed function generator was send from transmitter to receiver through soil sample. Vpp of sine wave was 20V. Received weak signal was amplified with a linear amplifier and both signals measured with the oscilloscope [11]. The maximum and minimum values of the sine wave are defined as the peak points. The wave travel time, is the time elapsed between the signal emitted from the transmitter and the signal obtained from the receiver.

Factors affecting the total travel time; It depends on the type and shape of the test sample, electronic devices, bender elements and the embedding depth in the sample, cables and

their coating. The wave type, amplitude, and frequency of the electrical signal delivered to the source bender element affect the quality of the signal at the receiving bender element [8].

After bender element test, unconsolidated undrained triaxial tests was conducted to determine strength parameters of the pumice soil sample. Triaxial test specimens at the beginning of the test and at the final stage of the test are shown in Figure 4.

Figure 4: Uncosolidated undrained triaxial test sample

III. Results and Conclusions

Unconsolidated undrained triaxial compression tests were conducted on loose sandy pumice soil samples. Triaxial tests was carried out under confining pressures of 100-150 and 200 kPa. Between cell pressure application and loading stages bender element tests were performed.

Measured shear wave velocity and maximum shear modulus according to different confining pressures given in Table 1. According to table shear wave velocity and maximum shear modulus increase as the confining pressure increases. The increase in the maximum shear modulus is not linear.

Table 1: Shear wave velocities and maximum shear modulus at different confining pressure

Confining pressure (kPa)	Shear wave velocities (m/sn)	Maximum shear modulus (Mpa)
100	132	13.6
150	158	20.3
200	202	34.3

Unconsolidated undrained triaxial compression test results were given as deviator stress axial strain graph in Figure 5. Sandy pumice soil strength parameters were obtained as cohesion 0 and internal friction angle 29°.

According to the results of the triaxial tests, it was observed that as the confinement pressure applied to the sandy pumice sample increased, the shear wave velocity, the maximum shear modulus and the strength of the pumice sample increased. In the low confinement pressure levels such as 100 and 150 kPa initial young modulus seems to be constant but under the 200 kPa loading level it shows an increase.

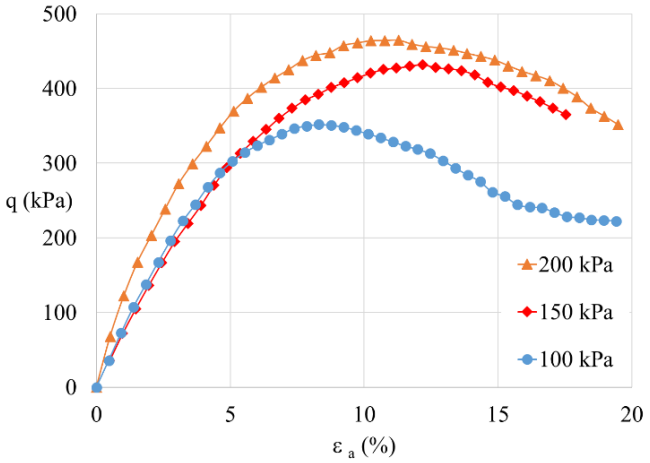

Figure 5: Axial strain and deviator stress graph

ACKNOWLEDGMENT

This study is supported by Isparta University of Applied Science Administration of Scientific Research Projects with project number 2021-YL1-0130.

REFERENCES

[1] İ. Dinçer, O. Ahmet, and S. Çoban, ''*Pomza Araştırma ve Uygulama Merkezi Fizibilite Raporu''*. Nevşehir Hacı Bektaş Veli Üniversity. Faculty of Engineering and Architecture Department of Geological Engineering. Nevşehir. Turkey, 2015.

[2] Y. Kavlak, ''*Isparta Gelincik Pomzasının Karayolu Esnek Üstyapıları Taban Zemini Stabilizasyonunda Kullanımı''*. MSc Thesis. Süleyman Demirel Üniversity, Isparta, Turkey, 2008.

[3] V. Çekmen, ''*Kayma Direnç Parametrelerinin Sismik Hızlar ile Belirlenmesi''*. MSc Thesis. Süleyman Demirel Üniversity. Isparta, Turkey, 2009.

[4] L. Esposito and F. Guadagno, ''Some special geotechnical properties of pumice deposits''. *Bulletin of Engineering Geology and the Environment,* 57, 41–50, 1998.

[5] O'Donovan, John. "Micromechanics of wave propagation through granular material." PhD diss., Imperial College London, 2014.

[6] L. Öner. ''*Determinatıon of Maximum Shear Modulus of Dry Sands Using Piezoelectric Bender Elements''*. MSc Thesis. Yıldız Technical University, Istanbul, Turkiye, 2013.

[7] K.M. Lech. ''The Determination Of Shear Modulus In Overconsolidated Cohesive Soils''. *Foundation of Civil and Environmental Engineering*, 12, 61- 71, 2008.

[8] Rio J.F.M.E. ''*Advances in Laboratory Geophysics Using Bender Elements''*, PhD. Thesis, University College London Department of Civil & Environmental Engineering, London, England, 2006.

[9] E. Brignoli, M. Gotti and K.H. Stokoe, '' Measurement on Shear Waves in Laboratory Specimens by Means of Piezoelectric Transducers''. *Geotechnical Testing Journal*, 19(4), 3384-397, 1996.

[10] Jovicic V. Coop M.R. Simic M. ''Objective criteria for determining Gmax from bender element test''. *Geotechnique*, 46 (2), 357-362, 1996.

[11] G. Viggiani and J.H. Atkinson, ''Interpretation of bender element tests''. *Géotechnique*, 45(1), 149 –154, 1995.

Fundamental Periods of Isolated Bridges with Tall Column Bents and Soil Interaction

A.I. KARAKAS

Karadeniz Technical University, Trabzon/Turkey, aliihsan.karakas@ktu.edu.tr

Abstract **- This study examines the effect of different bent column heights on bridge fundamental period analytically to have an excellent insight into the behavior of isolated bridge structures with substructure flexibility. Also, the influences of integral or rigid and isolated support between bridge superstructure and substructure are investigated. Moreover, soil interaction is taken into account in the calculation of bridge substructure flexibility and the effect of various soil shear modulus are studied. As a result of these studies, it is observed that the flexibility of the bridge substructure causes the bridge fundamental period to increase up to a certain bent column height. Integrated or rigidly connected bridge bent columns reduce the bridge period, but after a certain column height, it reaches to the period of isolated bridges. Thus, it can be stated that the effectiveness of seismic isolators reduces beyond this particular column height. As far as various soil types are considered, it is recognized that the bridge period decreases with increasing shear modulus in relatively short column bridges while there is no significant change for bridges with longer bent columns. In other words, soft soils with small shear modulus have significant impacts on the periods of bridges with slightly tall columns, but none of the soil types has a remarkable effect for bridges with extremely tall column heights.**

Keywords **–Seismic Isolation, box-girder bridge, lead-rubber bearing, soil interaction.**

I. INTRODUCTION

After devastating earthquakes, it is definitely crucial to be able to continue utilizing from some important structures for post-earthquake emergency response and recovery. Bridges are one of these important structures. The presence of a damaged bridge on the route where relief works are obligatory is an important situation to be avoided after an earthquake as it prevents the delivery of emergency aid as well as transportation [1]. Many bridges designed in accordance with traditional strength-based methods damaged after various earthquakes and became unable to function [2]. Therefore, innovative design methods have been developed to ensure that bridges can be utilized uninterruptedly after earthquakes. One of these methods is the use of seismic isolation devices on bridges. Seismic isolation devices that can be used in bridges and various types of structures are generally divided into two categories as friction-based and rubber-based isolators [3]. Friction pendulum and lead-rubber bearing devices are frequently used in bridges [4]. The main features of these isolation devices are reducing the earthquake forces that will occur in the structure by increasing the natural period of the structure and providing additional damping. Many researches have been conducted on these types of isolation devices. For instance, Fenz and Constantinou [5,6] studied on the numerical modeling of sliding friction isolators with different sliding surfaces as well as experimental verifications. Similarly, Deringöl [7] investigated the seismic performance of steel moment frames with variable friction pendulum systems subjected to real ground motions. As far as lead rubber bearings are considered, Turkington et al. [8,9] conducted studies on the design of bridges isolated with such bearings. Also, Chen and Li [10] studied on the seismic performance of tall pier bridges retrofitted with lead rubber bearings and rocking foundation. Moreover, the effect of lead rubber isolators on high-rise buildings was investigated by Fakih et al. [11] and on bridges by Edalati and Tahghighi [12].

Structural analysis methods that can be used in isolated bridge design according to bridge importance class are simplified analytical analysis, response spectrum and time history analysis methods. In this study, the fundamental bridge period to be used in the response spectrum analysis method is investigated parametrically using analytical formulas given in AASHTO 2010 [13] design specifications for simple bridges. The damping of the isolation system on the structure is taken into account with an alteration in the acceleration spectrum in response spectrum analysis. This alteration is the reduction of the spectral acceleration values by dividing a damping coefficient beyond a portion of bridge fundamental period. The fundamental period depends on the effective stiffness of the isolation devices and the stiffness of the substructure depending on column stiffnesses and foundation soil stiffnesses. For this reason, in this study, the effect of different column heights and soil stiffnesses on the bridge fundamental period is investigated in detail as well as the cases without seismic isolation and substructure stiffnesses are considered.

II. METHODOLOGY

In this study, a multi-cell box girder isolated balanced bridge with varying equal column heights is analyzed analytically to obtain the fundamental period. A MATLAB [14] code is developed for the simplified analytical solutions in accordance with AASHTO 2010. The dimensions of multi-cell box girder deck, cap beam, columns and footings are depicted in Figure 1. The rectangular cross section of the cap beam is assumed to be uniform through the length with 1.82 m x 1.5 m dimensions.

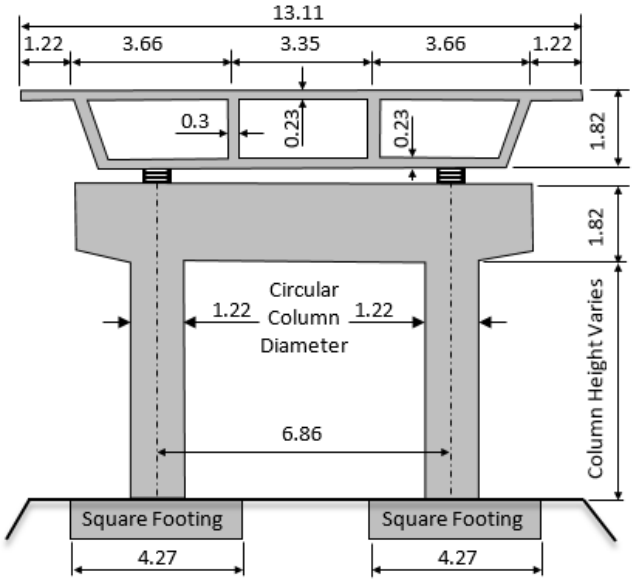

Figure 1: Transverse typical bent layout of the isolated bridge.

The balanced bent column heights to be investigated in the context of this study is varied from 6 m to 60 m height. The longitudinal layout of the bridge is shown in Figure 2.

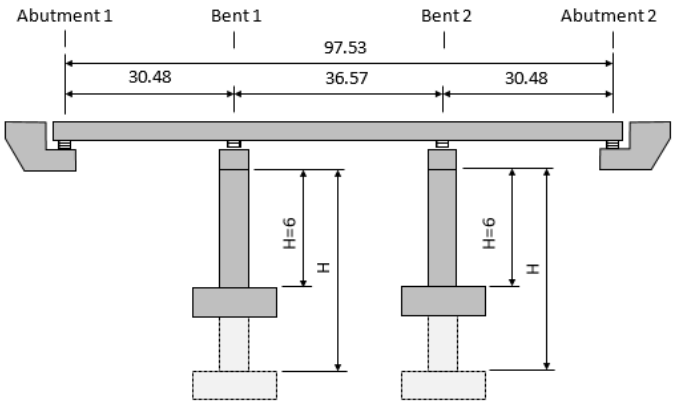

Figure 2: Longitudinal layout of the balanced isolated bridge.

The dimensions of the lead-rubber isolator unit used between the superstructure of the bridge and the cap beam as an isolation device is depicted in Figure 3. The isolator is composed of lead core, upper and bottom connecting and sealing steel plates, laminated steel reinforcing shims and rubber layers.

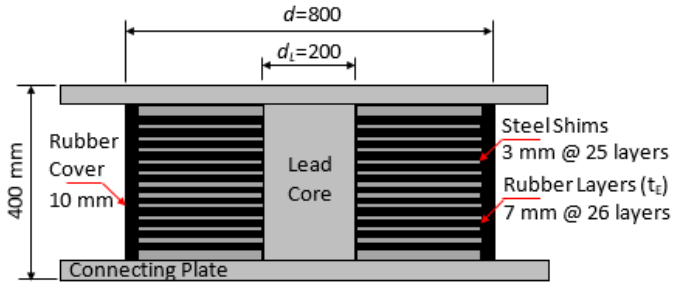

Figure 3: Geometrical details of the lead-rubber isolator unit.

The simplified method can be used for bridges behave as a single degree freedom system. This method can be applied for longitudinal and transverse axes of the bridges independently for different directional periods. In this method, the fundamental effective period, $T_{eff}(s)$, is calculated as:

$$T_{eff} = 2\pi\sqrt{\frac{W}{K_{eff}\cdot g}} \quad (1)$$

where W is the weight of the superstructure, g is the acceleration due to gravity and K_{eff} is the total effective stiffness of the bridge. The stiffnesses of all isolators and substructures are taken into account to obtain the total effective stiffness.

$$K_{eff} = \sum_j K_{eff\,j} \quad (2)$$

where j is the index of each support of the bridge as abutment or bent and $K_{eff\,j}$ is the effective stiffness of the j^{th} support including stiffnesses of the isolator units and columns with soil interaction. The effective stiffness of j^{th} support of the bridge can be calculated as:

$$K_{eff\,j} = \frac{k_{sub\,j} \times (\sum_i k_{eff\,i})_j}{k_{sub\,j} + (\sum_i k_{eff\,i})_j} \quad (3)$$

where $k_{sub}\,j$ is the stiffness of the j^{th} substructure including soil interaction and $k_{eff\,i}$ is the effective stiffness of the i^{th} isolator unit at j^{th} support. The substructure stiffness with soil interaction can be obtained for a single column shown in Figure 4 as:

$$k_{sub} = \left(\frac{1}{K_F} + \frac{h\,x\,L}{K_R} + \frac{1}{K_C}\right)^{-1} \quad (4)$$

where K_F is the longitudinal stiffness and K_R is the rotational stiffness of the soil, h and L are the dimensions shown in Figure 4, and K_C is the stiffness of the single column assumed to be fixed at the base. The column stiffness with rigid regions (half depths) shown in Figure 4 is derived from the first moment area of curvature diagrams about the axis of displacement as shown in Figure 5. The substructure stiffness of each abutment is assumed to be nearly rigid and its value is taken as 10^{11} N/mm. The elasticity modulus (E) and unit weight of the column concrete are taken as 24821 MPa and 24 kN/m^3, respectively.

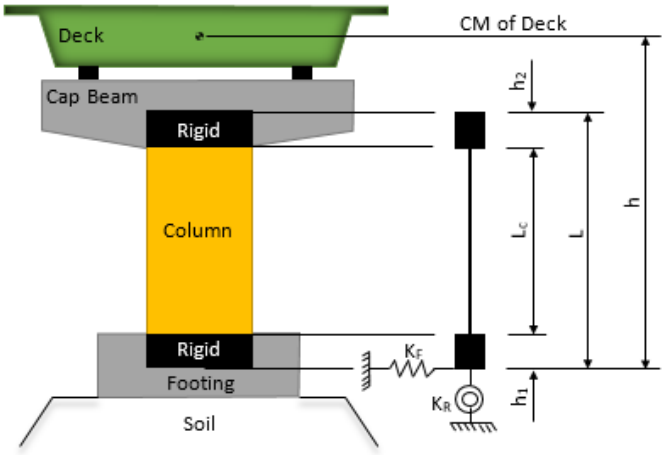

Figure 4: Single column bent for the simplified method.

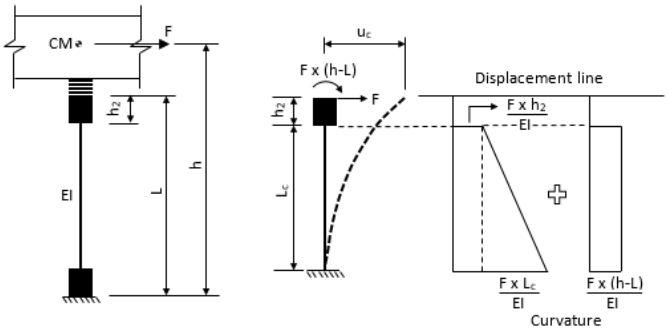

Figure 5: Simplified single column bent with fixed base for curvature diagrams

$$u_c = \frac{F \text{ x } h_2}{EI} \text{x } L_c \text{ x } \left(\frac{L_c}{2} + h_2\right) + \frac{F \text{ x } L_c}{EI} \text{x} \frac{L_c}{2} \text{x} \left(\frac{2 \text{ x } L_c}{3} + h_2\right) + \frac{F \text{ x (h} - \text{L)}}{EI} \text{ x } L_c \text{ x} \left(\frac{L_c}{2} + h_2\right) \quad (5)$$

$$K_C = \frac{F}{u_c} = EI \text{ x} \begin{bmatrix} \frac{{L_c}^2 \text{x } h_2}{2} + L_c \text{ x } {h_2}^2 \\ + \frac{{L_c}^3}{3} + \frac{{L_c}^2 \text{x } h_2}{2} \\ +(h - L) \text{ x } (\frac{{L_c}^2}{2} + L_c \text{ x } h_2) \end{bmatrix}^{-1} \quad (6)$$

$$K_C = EI \text{ x} \begin{bmatrix} {L_c}^2 \text{x } h_2 + L_c \text{ x } {h_2}^2 + \frac{{L_c}^3}{3} \\ +(h - L) \text{ x } (\frac{{L_c}^2}{2} + L_c \text{ x } h_2) \end{bmatrix}^{-1} \quad (7)$$

The effective stiffness of an isolator unit is the equivalent (linearized) property of the isolator in elastic analysis methods. It is gathered from the idealized bilinear force-displacement (hysteretic) behavior of an isolator shown in Figure 6 as:

$$k_{eff} = \frac{Q_d}{D} + k_d \quad (8)$$

where Q_d is the characteristic strength, D is the design displacement and k_d is the post-elastic stiffness of the isolator.

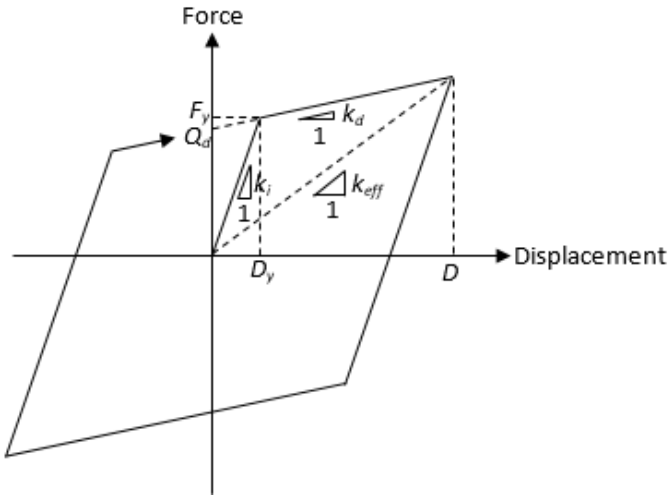

Figure 6: Bilinear force-displacement behavior of a lead-rubber isolator unit.

The characteristic strength can be obtained as:

$$Q_d = F_y(1 - \frac{k_d}{k_i}) \quad (9)$$

where F_y is the yield strength and k_i=10k_d is the assumed elastic stiffness of the isolator. The yield strength is calculated by:

$$F_y = f_{yL} \frac{\pi {d_L}^2}{4} \quad (10)$$

where f_{yL}=11. 4 MPa is the shear yield stress of the lead and d_L is the diameter of the lead core. The post-elastic stiffness is the stiffness of the rubber and it is given by:

$$k_d = \frac{GA_b}{T_r} \quad (11)$$

where G=0.62 MPa is the shear modulus, A_b is the net bonded area and T_r is the total thickness of the rubber. The net bonded area is the gross area without the lead core area. Thus:

$$A_b = \frac{\pi({d_b}^2 - {d_L}^2)}{4} \quad (12)$$

where d_b is the diameter of the bonded rubber without rubber cover.

The superstructure displacement depends on both substructure stiffness and isolator effective stiffness. The substructure stiffness changes with changing column heights and so the superstructure displacement changes. As the superstructure displacement changes the isolator design displacement (D) alters. An iterative procedure is applied to obtain the value of superstructure displacement since the

isolator effective stiffness depends on the isolator design displacement and vice versa.

The stiffness coefficients of the springs representing the footing-soil system are obtained in accordance with Gazetas formulas [15] given in Table 1 ignoring embedment correction factors. In Table 1, G is the shear modulus, v=0.3 is the Poisson's ratio of the soil and B is the half width of the footing. The shear modulus depends on the type of the underground soil as given in Table 2 [16].

Table 1: Directional stiffness coefficients of shallow foundations.

Stiffness Coefficient	Square Shape Foundation (2Bx2B)
Horizontal Longitudinal or Transverse Direction, K_F	$\frac{9 * G * B}{2 - v}$
Rotation about Longitudinal or Transverse Direction, K_R	$\frac{3.6 * G * B^3}{1 - v}$

Table 2: Typical shear modulus values for different soil types

Soil Type	Shear Modulus (MPa)
Dense Sands and Gravel (DS)	69-345
Silty Sand (SS)	27.6-138
Medium Stiff Clays (MC)	6.9-34.5
Soft Clays (SC)	2.75-13.75

III. RESULTS AND DISCUSSIONS

The design displacements of the isolators located at the bents and abutments of the bridge as a result of the iterative process are shown in Figure 7. They are taken into account in the calculation of the effective periods of the isolators for different bent column heights. The design displacement of the bent isolators decreases with increasing column height and approaches to zero at approximately 20 m height. In this case, it can be said that the efficiency of the bent isolators reduces considerably for a column height of 20 m or above. Bent column stiffnesses provide the desired bridge period level without bent isolators. In other words, the bridge bent columns are able to cover the superstructure displacement themselves. In such a case, there will be no significant difference between the use of isolators and the integral connection of the bent. As far as the abutment isolators are considered, the design displacement increases up to a certain value of 42 m and remains almost constant after this value. This corresponds to the constant displacement region of the spectral displacement considered in the analytical solution.

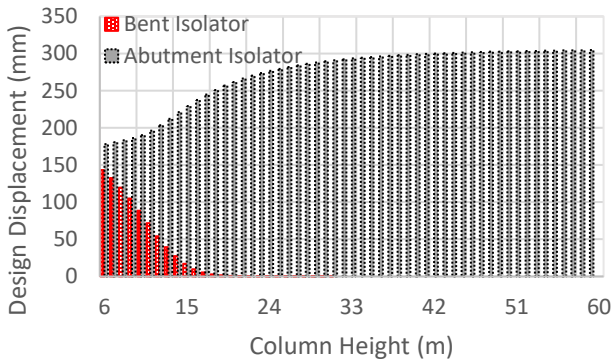

Figure 7: Design displacements of bent and abutment isolators.

Figure 8 depicts the variation of the fundamental period of the bridges with integrated and isolated bents for different bent column heights. It can be seen from the figure that the two curves intersect at a column height of approximately 20 m. That is, the bridge with integrated or isolated bents has the same effect on the bridge period for 20 m and greater column heights. However, it is observed that there are significant changes in the period value, especially up to 10 m height. For example, for a column height of 6 m, the bridge period is 0.88 s in the case of the integrated bents, while this value rises to 1.60 s in the case with isolators. Similarly, for 10 m height, the period which is 1.40 s in the integrated case becomes 1.69 s in the isolated case. So, the use of isolators for bents with 6 m and 10 m column heights increases the bridge period approximately 82% and 21%, respectively. Therefore, it can be concluded that isolators have great efficiency on the period value for the bridges with relatively short column heights.

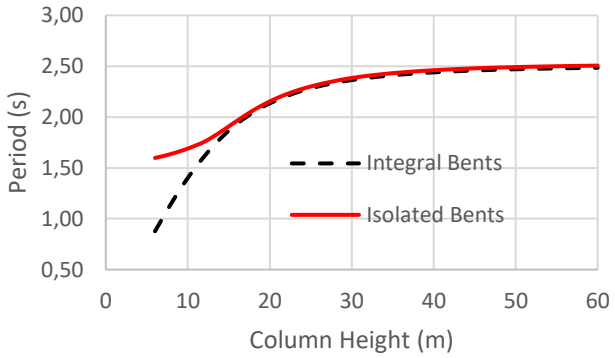

Figure 8: Fundamental periods of the bridges with integral and isolated bents.

Figure 9 illustrates the change in the bridge fundamental natural period when the flexibilities of the bridge bent substructures are taken into account or not. If the substructure flexibility is not considered, it is expectedly observed that the bridge period remains constant at the value of 1.50 s. However, an increase in column height up to nearly 50 m enlarges the bridge period to 2.5 s when the flexibility is taken into account. Also, the period value decreases by approximately 8% for 10 m height and 38% for 50 m height. Therefore, it can be stated that

it is very important to consider the flexibility of the substructure, especially for bridges with column heights of 10 m and higher.

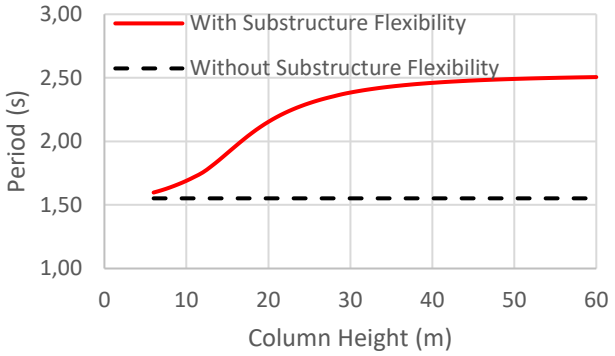

Figure 9: Fundamental periods of the bridges with and without substructure flexibility.

The variation of the period of bridges with different column heights for varying soil shear modulus is depicted in Figure 10. The soil shear modulus is varied between 2.75 MPa and 350 MPa to cover all the soil types given in Table 2. According to Figure 10, it is observed that increasing soil shear modulus decreases the bridge period for all column heights. Also, as the bridge column height increases, the effect of the soil shear modulus on the period decreases. In order to recognize this effect better, the values obtained for the lower and upper limit shear modulus values of the relevant soil type for some particular column heights are given in Table 3. The maximum variation between the periods of bridges considering all soil types decreases from 17.5 % to 0% as the column height increases. Additionally, it can be observed that the SC soil has the largest variation as 11.7 % in the periods of bridges with relatively short columns when the lower and upper shear modulus limit values of each soil type are considered. Therefore, it can be concluded that softer soils have larger effects on relatively short bridges while denser soils have almost no effects on the bridges with any column heights.

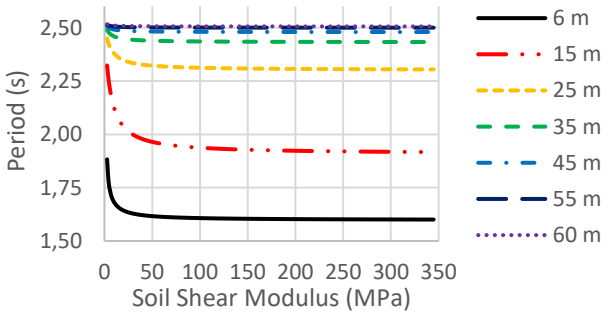

Figure 10: Fundamental periods of the bridges with altering soil shear modulus.

Table 3: Fundamental periods for different soil types and column heights.

Column Heights (m)	Soil Type	Fundamental Periods (s)	Maximum Variation (%)
6	DS	1.61-1.60	17.5
	SS	1.63-1.60	
	MC	1.72-1.62	
	SC	1.88-1.66	
18	DS	2.10-2.07	15
	SS	2.15-2.09	
	MC	2.28-2.13	
	SC	2.38-2.20	
30	DS	2.39-2.39	3.3
	SS	2.41-2.39	
	MC	2.44-2.40	
	SC	2.47-2.42	
42	DS	2.47-2.47	1.2
	SS	2.47-2.47	
	MC	2.49-2.47	
	SC	2.50-2.48	
60	DS	2.51-2.51	0
	SS	2.51-2.51	
	MC	2.51-2.51	
	SC	2.51-2.51	

IV. Conclusion

Isolator systems on a structure provide an increased fundamental period and damping ratio. Thus, internal forces to be occurred in the structure are reduced by decreasing the spectral acceleration depending on both period and damping ratio in response spectrum analysis. Bridge fundamental period is of great importance in design of bridges with seismic isolators in the case of response spectrum analysis method. For this reason, in this study, fundamental periods of isolated bridges with different bent column heights and soil shear modulus values are investigated analytically in detail. In addition, the effects of bridge substructure flexibility and integrated or isolated bents on the fundamental period are examined. As far as the numerical results are considered some important conclusions are drawn. Accordingly, the design displacement values to be taken into account in the calculation of the effective stiffness of the isolators decrease and approach to zero at the bents but increase and reach a constant value at the abutments for increasing bent column heights. Therefore, the effectiveness of the bent isolators reduces with increasing column height and nearly disappears for highly tall bridges. In other words, the bent isolators increase the fundamental periods of slightly and moderately tall bridges when compared to bridges with integral bents. Integral or isolated bents do not change the fundamental period for highly tall bridges. The flexibility of the bridge substructure may not be taken into account during the isolator design process for the simplicity. However, this assumption may result in significantly incorrect results especially for tall bridges according to the results of this study. Finally, when the effects of the soil shear modulus are examined, it can be concluded that the increased shear modulus

significantly reduces the bridge period for short column bridges while it does not cause a significant change in tall column bridges. Also, this significant reduction in the fundamental period is especially noticeable for soft soils such as silty clay soil but this reduction remains too small with increasing column heights for denser soils.

REFERENCES

[1] H. Murat, "Tanarslan deprem sonrasında hasar görmüş veya görmesi muhtemel betonarme köprü rehabilitasyonu için öneriler," *İnşaat Muhendisleri Odası 6. Kentsel Altyapı Sempozyumu 2011*, pp. 39-46.

[2] Wm. H. Hobbs, "A Study of the Damage to Bridges during Earthquakes," *The Journal of Geology*, vol. 16, no. 7, pp. 636-653, 1908.

[3] I.G. Buckle, M.C. Constantinou, M. Dicleli, and H. Ghasemi, "Seismic Isolation of Highway Bridges," *Special Report MCEER-06-SP07*, 2006.

[4] A. Ghobarah, "Seismic behaviour of highway bridges with base isolation," *Journal of Civil Engineering*, pp. 72-78, 1988.

[5] D.M. Fenz and M.C. Constantinou, "Modeling triple friction pendulum bearings for response-history analysis," *Earthquake Spectra*, vol. 24, no. 4, pp. 1011–1028, 2008a.

[6] D.M. Fenz and M.C. Constantinou, "Spherical sliding isolation bearings with adaptive behavior: Experimental verification," *Earthquake Engineering and Structural Dynamics*, vol. 37, no. 2, pp. 185–205, 2008b.

[7] A.H. Deringöl, "Seismic performance of steel moment frames with variable friction pendulum systems under real ground motions," *International Advanced Researches and Engineering Journal*, vol. 02, no. 03, pp. 208–216, 2018.

[8] D. Turkington, A. Carr, N. Cooke, and P. Moss, "Design method for bridges on lead-rubber bearings," *Journal of Structural Engineering*, pp. 3017-3030, 1989a.

[9] D. Turkington, A. Carr, N. Cooke, and P. Moss, "Seismic design of bridges on lead-rubber bearings," *Journal of Structural Engineering*, pp. 3000-3016, 1989b.

[10] X. Chen, and C. Li, "Seismic performance of tall pier bridges retrofitted with lead rubber bearings and rocking foundation," *Engineering Structures*, pp. 1-15, 2020.

[11] M. Fakih, J. Hallal, H. Darwich and H. Damerji, "Effect of lead-rubber bearing isolators in reducing seismic damage for a high-rise building in comparison with normal shear wall system," *Structural Durability & Health Monitoring*, vol.15, no.3, pp.247-260, 2021.

[12] A. A. Edalati and H. Tahghighi, "Investigating the performance of isolation systems in improving the seismic behavior of urban bridges: a case study on the hesarak bridge," *Archives of Civil Engineering*, vol. LXV, no. 4, pp. 155-175, 2019.

[13] American Association of State Highway and Transportation Officials "Guide Specifications for Seismic Isolation Design", Washington, D.C.

[14] MATLAB, 2021. The language of technical computing. Mathworks, Massachusetts, ABD.

[15] G. Gazetas, "Analysis of Machine Foundation Vibrations: State of the Art," *Soil Dynamics and Eartquake Engineering*, vol.2, no.1, pp.2-43, 1983.

[16] M. İ. Onur, M. Tuncan and A. Tuncan, "An experimental study for determining the shear modulus of toyoura sand," *Second European Conference on Earthquake Engineering and Seismology 2014*, İstanbul, pp.1-7.

Economic Feasibility Assessment in Design of Sustainable Prefabricated Industrial Buildings/ Agriculture and The Case Study of Demir Ekosan

D.C.BAL[1] and S. KOCA[2]

[1] Tekirdağ Namık Kemal University, Tekirdağ/Turkey, dcturan@nku.edu.tr
[2] Istanbul Technical University, Istanbul/Turkey, kocas18@itu.edu.tr

Abstract **- Sustainability is a defining element in the design of the new generation of industrial structures. The increasing need for energy necessitates the use of sustainable energy sources such as solar and wind. The use of new technologies and approaches in the structural and architectural design of the next generation of sustainable industrial structures closely impacts the sales and usage performance of the project. Within the scope of this study, the efficiency of structural design, architectural design and economic feasibility studies of new generation multi-purpose industrial sites that produce their own energy by using sustainable energy sources such as solar and wind energy were evaluated in the case study of Demir Ekosan project. Demir Ekosan industrial site is a multi-purpose industrial site built on an area of 300.000 m2 in Çorlu, Tekirdağ, where agriculture and industry develop together. Details developed in SAFECAST, a European Union project, were used in the design and connection of the structural systems of the buildings. Struc-tural and architectural design studies have been carried out and economic feasibility processes have been assessed, considering the impact of the project's agricultural and environmental impact, which will ensure sustainability by producing its own energy and water. In the economic feasibil-ity study, the difference in structural and architectural design, the use of sustainable energy re-sources, and environmental impacts were examined in comparison. General principles have been proposed for the design of sustainable multi-purpose industrial sites through the case study of the Demir Ekosan.**

Keywords **- economic feasibility, sustainability, prefabrication, industrial structures, energy**

I. INTRODUCTION

Energy that can be obtained from natural resources and can always be found in nature is termed renewable energy. This energy takes its source completely from nature. For this reason, it is not possible to completely consume renewable energy. The demand for renewable energy, which offers environmentally friendly, less costly, and sustainable energy when used efficiently with the right systems, is increasing day by day.

Renewable energy sources are more advantageous than fossil fuels because their quantities are not limited, they cause less damage to the environment, and they are safe.

Renewable energy and energy efficiency are given great importance in many countries of the world for the widespread use of clean energy. To ensure sustainable development and to protect the natural balance, it is extremely important to provide energy from continuous, reliable, cheap, clean, high quality and local renewable energy sources and to use it efficiently. In order to create a sustainable development stage in energy, it is necessary to support the transition to a low-carbon energy system.

In Turkey, as in other developing countries, population growth, the effort to increase industrialisation and the support of investments for the development of technology increase the demand for energy day by day. The fact that the majority of Turkey's current energy supply is provided from outsourced brings up the issue of utilising the potential of renewable energy resources.

Within the scope of the study, the use of renewable energy sources in industry, construction, agriculture, etc. has been investigated and evaluated through existing examples. The performance of the use of renewable energy sources in the Demir Ekosan project, which is a new generation industrial site under construction in Tekirdağ/Çorlu, where agriculture and industry develop together in the Thrace region, has been evaluated. General principles for the design of multi-purpose sustainable industrial sites are recommended by examining the use of renewable resources with the ever-growing energy need through the example of Demir Ekosan.

II. RENEWABLE ENERGY

Today, the terms of sustainability and renewable energy are more important due to the fact that natural resources are facing the danger of extinction. Energy obtained from clean and natural sources stands out as much more preferable options for the protection of our world compared to other types of energy.

The International Energy Agency estimates that [1], global energy demand will be approximately 8% less than today in 2050 and that 90% of energy production will be met by renewable energy sources which are solar, wind, biomass, hydrogen and hydroelectric, geothermal, wave and fusion. The

most well-known renewable energy sources are solar and wind energy. The renewable power sector took a large step forward, driven by record expansion in solar photovoltaic (PV) and wind power[2].

The main advantages of using renewable energy sources are [3];

• Increasing energy efficiency while saving money,

•Implement agricultural practices that both save energy and conserve natural resources,

•Generating and using renewable energy.

The agriculture sector accounts for around 4.3% of global GDP.

Energy is required at all stages from the production of food and agricultural products as fertilization, irrigation, processing, storage, and distribution. So, it is one of the most important inputs of agricultural production. Around 30% of the world's energy is consumed within agri-food systems [2].

Between 2009 and 2019, the increase in the use of renewable energy in the power, buildings, agriculture, and transport sectors is shown in Figure 1.

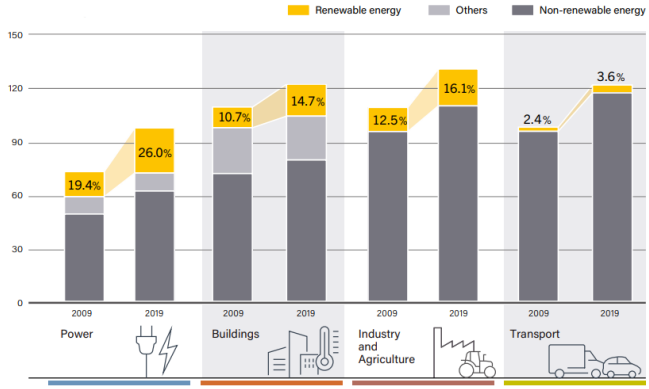

Figure 1: Evolution of Renewable Energy Share in Total Final Energy Consumption, by Sector, 2009 and 2019 [2]

In the construction sector, the use of renewable energy sources has increased by 4% from 10.7% to 14.7% and in the industry/ agriculture sector, by 3.6% from 12.5% to 16.1% in the last decade. This increase has continued in every sector and is pleasing in terms of protecting the global balance and less pollution of nature.

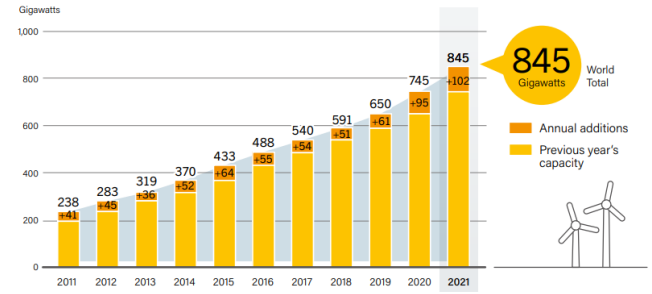

Figure 2: Wind Power Global Capacity and Annual Additions, 2011~2021 [2]

Wind energy, which is among the renewable energy sources and adapts to technological development in the fastest way, has attracted considerable importance in recent years among other alternatives. Many countries in the world prioritise incentive policies to increase the use of renewable energy resources and to develop energy production technologies in this direction. Among the renewable energy sources in the world, wind energy is one of the most developed and commercially favourable energy types. Figure 2 shows the increase in total wind energy capacity in the world between 2011 and 2021. By 2021, the global wind power capacity had reached 845 GigaWatts [2].

The first thing that comes to mind in wind energy technologies is wind turbines. Wind turbines are the main structural element of wind power plants and are machines that convert the kinetic energy of moving air into mechanical energy and then into electrical energy.

The fact that the turbines installed to obtain wind energy have low maintenance and operating costs, no harmful gas is emitted to the atmosphere during the energy production phase, saving oxygen in the atmosphere, and simple technology is sufficient for its installation makes this energy source more attractive against other alternatives.

The fact that large percentage of the world's energy consumption is used in the construction and use of buildings shows the serious role played by the architecture and construction sector in this context [4]. As a result of this situation, it becomes more important to ensure and develop sustainability (energy efficient buildings, green and sustainable buildings, passive houses, etc.) to minimise environmental damage in architecture[5,6]. It causes high energy consumption not only during construction but also in all phases starting from the production of building materials to the utilisation of structures.

Wind energy is a clean, abundant, and renewable resource that can be utilised in most regions with agricultural activities. When there is sufficient wind speed, the energy requirement in the agricultural sector can be easily met through windmills used in small farms and wind turbines that meet larger energy requirements.Wind turbines are a more economical energy source compared to fossil fuel power plants due to their low operating costs other than labour [7,8].

Small wind systems can serve many agricultural processes on farms where there is a need for mechanical energy utilisation, such as electricity generation, water pumping, storage, cooling or grain milling.

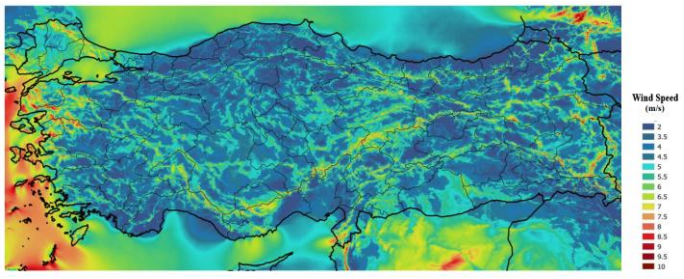

Figure 3: Wind Power Potential Map of Turkey,100 meters (REPA) [9,10]

Figure 3 shows Turkey Wind Energy Potential Map for 100 metres. When the Wind Energy Potential Atlas of Turkey is analysed, especially in the Aegean, Marmara, Mediterranean and Central Anatolia Regions, regions with an average speed of 7 m/s and above, which are required to generate wind

energy economically, stand out [11].

Tekirdağ city is one of the leading cities in Turkey in terms of wind energy potential due to its geographical location. When the Wind Energy Potential Map (REPA) [10] of Tekirdağ province is examined, it is seen that the average wind speeds, especially in the south-western parts, are higher than the minimum average speed of 7 m/s required to generate wind energy economically. Wind energy potential map of Tekirdağ is given in Figure 4.

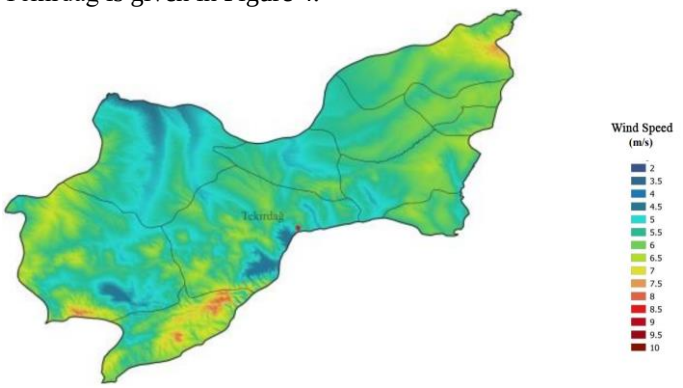

Figure 4: Wind Power Potential Map of Tekirdağ,100 meters [10]

The use of wind turbines in the Tekirdag region, where industry and agriculture sectors develop together, is becoming increasingly widespread. The fact that a large part of the industrial and production density in Turkey is in this region and with the increasing energy crisis, it has become inevitable for producers to turn to renewable energies. Figure 5 shows the wind turbines installed in the industrial facilities in the Çorlu region and the agricultural areas in the near surroundings.

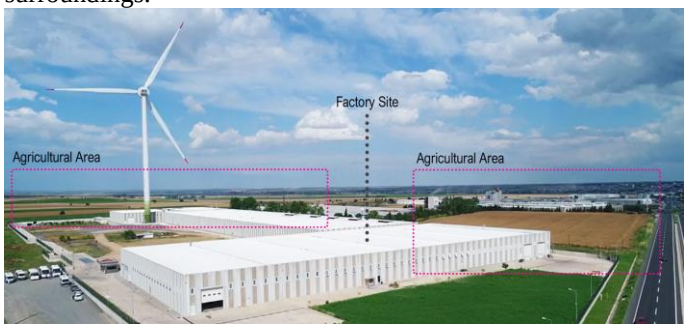

(a)

(b)

(c)

Figure 5: The Relationship Between Industry and Agricultural Areas in Corlu and The Use of Wind Turbines (a) Ucler Textile Factory Site (b) Saray Aluminium Assembly of Prefabricated Factory (c) Borusan Balabanlı Wind Energy Power Plant [12]

As of 2021, the number of wind power plants in operation in Turkey is 273 and has an installed capacity of 11,101 MWm. The rate of electricity generation from wind energy is 9.84% and 20 wind power plants are under construction [13]. Table 1 shows the installed wind power plants in Tekirdag province, their opening dates, and their installed power capacities. Annual production for Tekirdag province is totalled 187 MWm.

Table 1: Wind power plants in Tekirdag

Location	Opening Date	Installed Capacity (MWm)
Balabanlı	2014	61,40
Kıyıköy	2015	45,00
Sarköy	2009	56,65
Karatepe	2021	16,10
Saray	2012	4,60
Malkara	2019	3,40
TOTAL		187,15

Solar energy is a renewable energy source with features such as ease of installation and use, as well as not polluting the environment and not creating harmful waste. Especially being a clean energy source and working at low cost after installation increases the importance of solar energy.

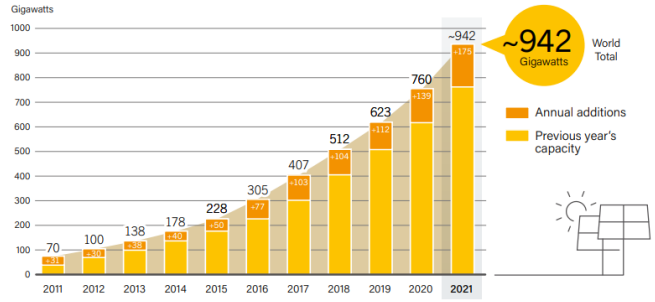

Figure 6: Solar PV Global Capacity and Annual Additions, 2011~2021 [2]

The solar photovoltaics market maintained its record-breaking streak, with new capacity installations totalling an estimated 175 GigaWatts in 2021 compared to 2020. This was the largest annual capacity increase ever recorded and brought the cumulative global solar PV capacity to 942 GW [2]. Figure 6 shows the increase in total solar energy capacity in the world between 2011 and 2021.

Turkey has a very advantageous position in terms of benefiting from solar energy geopolitically, and the sun's rays are effective with high efficiency in many geographical regions throughout the year. With the ever-growing energy demand, the importance of the installation of solar power plants is increasing. Unlike other sources, the use of solar power plants is becoming widespread in Turkey due to its renewable and sustainable nature. Solar power plants can be installed on large areas of land or can be used by mounting them on the roofs of existing buildings [2].

The use of solar energy at roof level in new buildings is evaluated during design and structural calculations. Panel

carrier systems and panel weights varying according to the type of roof covering selected are included in the design loads. In existing buildings, the addition of such elements to the structure without calculations in some roof beams that do not have bearing capacity causes problems [14]. Figure 7 shows solar energy systems mounted on existing industrial buildings in Çorlu/Tekirdağ.

Figure 7: Solar Energy Systems Mounted at Roof Level [15,16]

It is also possible to apply solar energy systems in building facade systems. Solar energy systems mounted as wall panels provide the heat energy required for production and realise the conversion of solar energy into thermal energy with high efficiency.

Figure 8: Solar Wall Systems Mounted at Facade, Inan Makina [17]

Solar wall panels are one of the new generations of renewable energy technologies that provide solar heating and passive cooling. This system was used in the Inan Makina factory with a closed area of 43.000 m^2 in Çorlu/Tekirdağ region and is shown in Figure 8. The estimated payback system of the system installed in the facility, which has a total of 2100 m2 solar wall panels on 3 facades, is calculated as 2.7 years [17].

III. The Case Study of Demir Ekosan

Demir Ekosan Industrial Site is being built in Çorlu 1_{st} Organised Industrial Zone in Tekirdağ, which will become the production and logistics centre of the region. It is the most comprehensive industrial site built in the region with 7 blocks including 362 manufactories, 65 shops, 3000-person fair/convention hall and meeting halls included in an area of 243.292 m2.

In regions where agricultural and industrial areas have developed together, the construction of sustainable industrial structures is very important and the damage to the environment should be minimised. Thanks to the rapid construction technique, prefabrication technology is proposed for the Demir Ekosan Industrial Site and the manufacturing blocks are designed as reinforced concrete prefabricated buildings. Demir Ekosan site layout (names of blocks), production area settlements and perspective view and its relationship with agricultural areas are shown in Figure 9.

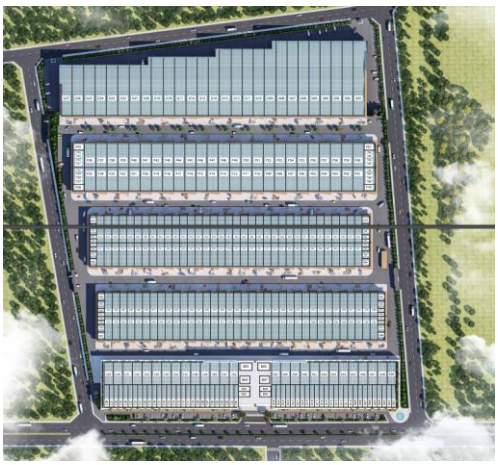

(a)

(b)

Figure 9: Demir Ekosan (a)Layout (b) Perspective View [18]

The blocks are designed in different sizes and divided into units in order to serve different organisations (chemistry, logistics, production, storage, packaging, etc.). In the industrial site where all kinds of sectoral activities can be carried out, the floor height from the ground floor is determined as 12m. Partial mezzanine floors that can be used as office units are also included in the project. Block layouts and sample sections are given in Figure 10.

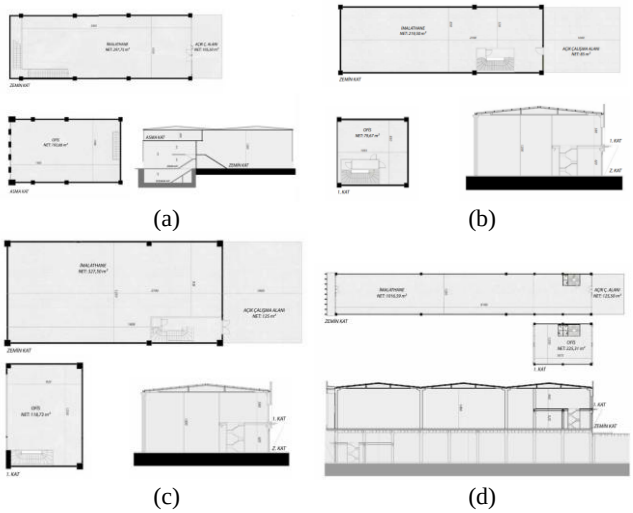

(a) (b) (c) (d)

Figure 10: Different Block Layouts and Sections (a) A-C Bloks (b) D-E Bloks (c) F Bloks (d) G Bloks [18]

Because of the natural slope on the land, 2 of the blocks (F,G) have basement floors and there is a bridge structes

connecting these two blocks. blocks A, B, and C also have basement floors for car parking purposes, and block B is designed as 18m from the ground floor (Figure 11). All buildings are constructed with prefabricated reinforced concrete method except for block B where social units are located.

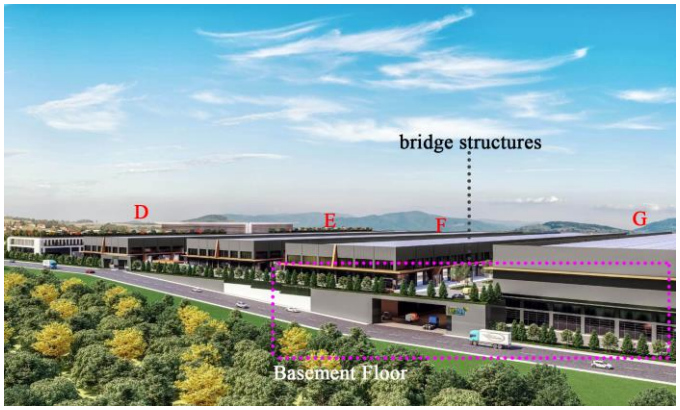

Figure 11: Natural Slope, Basement Floors and Bridge Structures

Prefabricated reinforced concrete buildings are buildings in which the structural system elements are specially manufactured at high standards in production facilities, transported to the construction site and assembled. In Turkey, prefabricated reinforced concrete buildings are constructed especially for industrial buildings, trade centres, sports halls, depot/storage structures, less frequently for housing, schools, hospitals and car park structures. The fact that the production is serial and controlled, pre or post-tensioning methods can be used, and the fast construction technique makes prefabricated buildings superior in many respects compared to buildings constructed by traditional methods.

Studies to increase the earthquake safety of prefabricated reinforced concrete structures are also continuing.SAFECAST Project (Performance of Innovative Mechanical Connections in Precast Building Structures under Seismic Conditions) is a European Union project in which the earthquake safety of joint details in prefabricated buildings is investigated and theoretical and experimental studies are carried out on this subject. Within the scope of the project, the project partners have investigated the joint details and earthquake safety of different prefabricated structural elements. In the project, in which ITU and TPB from Turkey are partners, the earthquake safety of moment transmitting column beam joints has been focused on. Within the scope of full-scale experimental studies carried out at ITU Structural and Earthquake Engineering Laboratory, one moment transfer joint detail for industrial buildings and one moment transfer joint detail for house buildings were developed and tested [19,20]. The details developed in SAFECAST were used in the structural system design and joints of the structures in such a large-scale industrial site. Figure 12 shows the use of the developed joint details in the construction of Demir Ekosan.

Figure 12: Column-Beam Joints Details

By following the principles of sustainable architecture in the design of Demir Ekosan industrial site, the buildings are more environmentally friendly. By using the prefabrication technique, the construction phase was shortened, and it was planned to complete the construction with minimum on-site intervention. In Demir Ekosan industrial site, water recycling is aimed and rainwater harvesting systems are designed. With rainwater harvesting systems, it is aimed to reduce the dependence of users on the city's water resources. By collecting rainwater in water tanks, the water needed during production is provided. It is aimed to collect water by using roof and natural slopes.

Today, solar energy systems that can be easily mounted on the roof, which enable the utilisation of solar energy, are among the most common projects. The advantages of the solar energy system on the roof; minimising the costs incurred in the use of fuel and contributing to economy. It provides cheaper electricity generation as it can be used for many years as it offers installation cost suitability. Solar energy systems provide cleaner and harmless energy use in the structuring process caused by fossil fuels that do not allow recycling. All the efficiency obtained from the sun, which is an unlimited energy source in raw form in nature, finds active use with the help of these panels on the roof. It provides benefits as national economic income in the country where you live. Meeting the needs obtained from energy with less costs, activating renewable energy sources also benefits the national economy.

It is planned to use solar energy systems on almost all blocks in the Demir Ekosan industrial site built in a large area, and the design and calculations have been completed accordingly. Table 2 shows the roof area, planned panel area, panel power and number of panels according to the blocks in the Demir Ekosan. In Table 3, the solar energy generation analysis for the Demir Ekosan industrial site is given. The energy generated from the sun is given according to the months and the 10-year production calculation is added.

Table 2: Solar Energy Data

Blok	Roof Area (m^2)	Panel Area (m^2)	Panel Power (kWp)	Number of Panels
D	11.947	9.602	2.393	7.144
E	11.629	9.346	2.330	6.954
F	13.987	11.241	2.802	8.364
G	16.919	13.597	3.389	10.117
B	5.128	4.102	1.027	3.066
Total	59.610	47.888	11.941	35.645

Table 3: Solar Energy Data by Years and Months

Months	Power Generated from Solar System (kWp)	Years	Annual Generated Energy (kWh)
January	444.330	1.	11.671.600
February	539.900	2.	11.508.198
March	871.400	3.	11.438.168
April	1.244.500	4.	11.368.138
May	1.354.900	5.	11.298.109
June	1.505.300	6.	11.228.079
July	1.584.200	7.	11.158.050
August	1.389.800	8.	11.088.020
September	1.080.800	9.	11.017.990
October	761.300	10.	10.947.961
November	502.200		
December	393.000		
Total	11.671.600		

As can be seen in Table 3, the total production from the sun in the first year when solar energy systems will be installed is analysed as 11.671.600 kWp. When the 10-year period is considered, the system capacity is capable of producing 10.947.961 kWp. tekirdağ region is suitable for solar energy systems in all months of the year due to its location and gives maximum efficiency between April and September.

IV. CONCLUSION

The concept of sustainable architecture emerges as an essential point for building design processes today. In order to struggle against global warming and climate change, realising sustainable building and urbanisation projects is not a choice but a necessity for human beings. Energy efficiency of buildings is not the only goal in sustainable architectural design. Beyond energy and water consumption savings, the principles of sustainable architecture define buildings that are resistant to climate change, have high indoor environmental quality, protect and renew nature, and take into account the health of human and nature.

The goal of sustainable architecture is to design buildings that are self-sufficient for future generations in the long term by using local materials, infrastructure, climate, technology and natural resources in the design process from large scale to mini scale.

Renewable energies should be used in a wider area, as they will not be exhausted and cause the least harmful consequences in terms of the effects they will create on the environment.

In order to ensure sustainable development, it is recommended to organize policies that support the dissemination of renewable energy sources.

Attempts to obtain renewable energy sources require expensive infrastructure investments at the beginning. Government's leadership and incentives are important in the dissemination and financing of such services, whose social and private benefits outweigh the costs. With the legal regulations and incentives to be made, the country's renewable resources can be used to contribute to economic development.

Employment can increase thanks to investments in the renewable energy sector. The creation of a qualified workforce will be supported by training and various regulations in this field. The increase in the number of facilities can lead to positive developments in the labor and industry sectors, thanks to the provision of equipment and services.

REFERENCES

[1] A. Chel, G. Kaushik. (2011). Renewable energy for sustainable agriculture. Agron. Sustain. Dev. 31:91–118. DOI: 10.1051/agro/2010029

[2] Renewables Global Status Report. (2022). REN21. http://www.ren21.net/status-ofrenewables/global-status-report/

[3] International Energy Agency (2021). Not zero by 2050: A roadmap for the global energy sector; International energy agency: Paris, France. Pp.18-19

[4] N. Yanar, "Understanding of Sustainability and Ecology in Architectural Design in Context of Konya." M.Sc. Thesis, Selcuk University, Konya, 2017.

[5] G. Uşma, and N. F. Akinci. "Yenilenebilir Enerji Kullanimi ve Konutlarda Enerji Etkinliği: Türkiye'deki Duruma Genel Bir Bakış." *Vii. Umteb International Congress on Vocational & Technical Sciences.*2019.

[6] C. Ozburak, "Mimari Yaklaşimda Binaya Entegre (Bütünleşik) Yenilenebilir Enerji Kaynaklari Kullaniminin Kent Kimliğine Olan Etkileri." *SBE16 İstanbul-Uluslararası Sürdürülebilir Yapılı Çevre Konferansı*. 2016.

[7] S. Turan, "Yenilenebilir Enerji Kaynakları." *Konya Ticaret Odası Dergisi* 2006. Available: www.kto.org.tr/tr/dergi/dergiyazioku.asp?yno=700&ano=61,

[8] H.H. Öztürk, " Tarımda Yenilenebilir Enerji Kaynaklarının Kullanımı." Available: http://www. emo. org. tr/ekler/85e48a43c7f63ac_ek. pdf.

[9] T.C. Enerji ve Tabii Kaynaklar Bakanlığı. 2022. Avaible: http://www.enerji.gov.tr/tr-TR/Sayfalar/Ruzgar

[10] REPA Avaible: https://repa.enerji.gov.tr/REPA/bolgeler/TURKIYE-GENELI.pdf

[11] A. D. Çelik, T. Kızıltuğ, and E. Dağıstan, "Dünya'da ve Türkiye'de Rüzgar Enerjisi Üretimi ve Tarımda Kullanım Olanakları. " *2nd International Mediterranean Science and Engineering Congress (IMSEC 2017).* 2017

[12] Avaible:https://www.borusanenbw.com.tr/kurumsal/santraller/1/3/balabanli-res

[13] Avaible: https://www.tureb.com.tr/

[14] S. Koca, A. Bal, and O. Ç. Çelik "Evaluation of Sloped Roof Beam/System Alternatives in Precast Reinforced Concrete Industrial Buildings." *Precast Concrete Journal,* vol.144, pp.7-27,2022.

[15] Avaible: https://goktekinenerji.com/projeler/ran-tekstil

[16] Avaible: https://dalelektriksolar.com/portfolio/486-kw-cati-uzeri-ges-projesi-corlu-tekirdag/

[17] Avaible: https://www.solarwall.com.tr/

[18] Avaible: https://www.demirekosan.com/

[19] Karadoğan F., Yüksel E., Bal İ.E. (2012). Safecast Araştırma Projesinin Bir Parçası Olarak İki Tip Prefabrike Dış Kolon – Kiriş Birleşim Bölgesi, Beton Prefabrikasyon Dergisi, 102, 7-62.

[20] Yüksel E., Karadoğan H. F., Bal İ. E., İlki A., Bal A., İnci P. (2015). Seismic behavior of two exterior beam column connections made of normal strength concrete developed for precast construction, Engineering Structures, vol. 99, pp. 157-172.

MODAL ANALYSIS OF THE STEEL INDUSTRY STRUCTURE BY FINITE ELEMENT METHOD ACCORDING TO TBDY 2018 REGULATION

H. AYDIN[1]

[1] Construction Technology, Kavak Vocational School, Samsun University, Turkey

hakan.aydin @ samsun.edu.tr

Abstract **- In this research, an exemplary steel industry structure to be designed in the city of Samsun was used. For this purpose, the behavior of the steel structure under different loads according to the principles of the TBDY 2018 regulation was examined. It is aimed to investigate the effect of steel wind rod elements on dynamic parameters. For this reason, two different model experimental structures, with wind rod connection and without rod connection were analyzed. In the analysis, the effects of the steel structure on the dynamic behavior of the structure were revealed by using the finite element method (SAP2000) program. These dynamic parameters consist of natural frequency, period and mode shapes. With the comparison of the results obtained it is seen that the effect of the steel test structure of the wind tension rod on the dynamic parameters provides a 32,58 % decrase in the dominant period and a 48,32 % increase in the dominant frequency. When the mode shapes of the model structure in both wind tension rod connected and unconnected cases are examined in general, the wind tension rod in the steel test structure reinforced with wind tension rod have been replaced by the torsional mode shapes compared to the model steel industry test structure. In the mode shapes on the other hand, with the addition of wind tension rod more balanced and smaller deformations were observed in other directions instead of the displacement values in the y direction. With this study, the author aimed to reveal the effects of the use of wind tension rod in the system in steel industry structures on the dynamic behavior of the structures (period, frequency, mode shapes). As a result, it has been seen that with the addition of wind tension rod in the steel industry structure, our structure has become more rigid and stable. It has been concluded that the model steel structure is made safer against dynamic effects by using steel wind tension rod element.**

Keywords **- Steel Industry Structure, Period, TBDY2018, Finite Element Method (FEM), Modal Analysis**

I. INTRODUCTION

TBDY2018, which started to be used in Turkey with effect from 2019, includes the necessary rules for the design and construction of all or parts of all official and private buildings and building-type structures to be rebuilt, modified, enlarged, and for the evaluation and strengthening of the performance of existing buildings under the influence of earthquakes. This regulation also determines the minimum conditions [23]. It is understood from the researches that earthquakes can have devastating effects on all kinds of structures forms [20,1,2,7,11,12,18,19]. In addition to the different factors affecting the structure the harmful effects of environmental vibration should not be ignored. By environmental factors, the environmental loads that the buildings are exposed to almost every day come to mind. (Vehicle, wind, etc.) and it is known that it causes rapid changes and developments in steel structure designs [9,20,12,3] There are various studies and practices to minimize the effects that will affect the structure [21,22,20,7] It is known that steel industry structures are adversely affected by these environmental movements due to both large spans and height [9,12,3,1,21,18]. The new earthquake regulation TBDY 2018 includes significant changes in the calculation of earthquake loads and calculation approaches to be used in all kinds of building design (steel, reinforced concrete, masonry, etc.) compared to the previous regulations [4,5,22].

Chapter 9 of the TBDY2018 regulation – Special rules for the design of steel building support systems under the impact of earthquake includes the conditions to be complied with in the design of steel structure systems [10,23]. TBDY 2018 new

regulation design rules for pre-engineered reinforced concrete, light steel and wooden building carrier systems are also examined in a separate section. With this regulation, serious innovations to be taken into account in designs have come. The first major change regarding the calculation of earthquake ground motion is the updated Turkey Earthquake Hazard Maps, which will be used with TBDY 2018. With the new earthquake hazard maps, the concept of earthquake zones has completely disappeared. Instead, S_S and S_1 values can be read from the map for every point in Turkey.

With the new change, S_S and S_1 values can be read from the map for every point in Turkey. These are the map spectral acceleration coefficients corresponding to the T = 0.2 second short period and T = 1.0-second-long period regions, respectively. These values are converted into design spectral acceleration coefficients (S_{DS} and S_{D1}) by multiplying with the coefficients reflecting the soil properties, and the design acceleration spectrum is formed based on these values. Thus, the spectral acceleration coefficient, which takes a single value depending on the earthquake region in which the structure is located, will be determined separately for the short and long period regions. In this research article, Samsun province conditions were used in the design. (Figure 2,3) The Steel Industry Structure model is located at Latitude: 41.278308 and Longitude: 36.303740. Local Soil Class: ZD, Earthquake Ground Motion Level: DD-2, Turkey Earthquake Hazard Map was taken from Interactive Web application (AFAD) (figure 2). In recent years, many earthquakes have occurred in the world and as a result, heavy losses have been given. By looking at the results, it has been understood that this situation creates various problems for the countries that have suffered heavy losses, and how important it is for the structure to be informed about the current status of the structures. Knowing the dynamic parameters of the structures provides us with information about the situation that may occur before or after the structure. Experimental behavior of structures is investigated with experimental studies in structures vibrating with various factors. In these studies, primarily analytical models of the structures are created. The dynamic behavior of buildings, bridges and other structural systems when exposed to earthquakes is generally studied with analytical and experimental models. Investigation of the dynamic behavior of any structure can be investigated theoretically by constructing a finite element model and experimentally by using modal analysis methods. In the literature review related to this publication, many studies using the finite element method have been reached. In some studies, such as some of the publications using the finite element method and guiding the author's work are as follows on the use of the finite element method were used [14,15,16,17]. With all this knowledge, this new study has been carried out. Researchers have conducted many studies using the Finite Element Method (FEM) on steel structures [21,22,11,12,20,9,19,18,15,3]. The author also refers to these studies about the steel structures made. Looking at the literature studies, the researchers carried out a different number of studies using the finite element method [1,2,7,11,12,18,19,20].

With this study, the author aimed to reveal the effects of the use of wind tension rod in the system in steel industry structures on the dynamic behavior of the structures (period, frequency, mode shapes). The use of fasteners in steel structures can be presented as an economical and practical method of structural strengthening. In this study, the steel industry structure model created with the SAP2000 [13] program was used. The variable factor was chosen as wind tension rob in the structure design. In the analysis of the steel industry structure, earthquake, snow, self-weights of the steel structure and wind conditions are included in the analysis. Analysis results are given comparatively at the end of the study. As a result, the design of the steel structure was carried out. In this research, which was analyzed according to the TBDY 2018[10,23] regulation data, it was evaluated as an original study in terms of being a resource for researchers related to this subject, since the design was made according to the SAMSUN conditions (figure 2) required by the regulation.

II. MATERIALS AND METHOD

In this study, a model steel industry structure was created and modal analysis was carried out with the finite element method. In the application of the finite element method, the SAP2000 package program, which is used in the field of academic and engineering applications all over the world, was used.

A) Description of Model Steel Industry Structure

In this study, a model steel industry structure with a length of 20 m, an opening of 10 m and a height of 9,36 m was used. The structure modeled as a industry structure geometry. Steel structure is modelled as a single storey. The steel industry structure consists of equal length spans in the range of 5 meters. The roof strut is designed as 2,06 meters. In the designed steel industry structure, the pre-sizing was made with the SAP2000 program without making the pre-analysis design. Preferred profiles are respectively: IPE in the columns, UPN steel profile in the purlins and cross connection elements, a 0,018m circular bar element in the steel tension connections, and UPN80 profiles in the 2L Cornier Wind tension rod in the roof trusses.

After the analysis, optimum profile thicknesses were obtained in the program without any problems and the structure was designed with appropriate profiles. The model steel structure finite element model was created using the SAP 2000 program. The finite element model of the steel industry structure is given in (Fig.1,4)

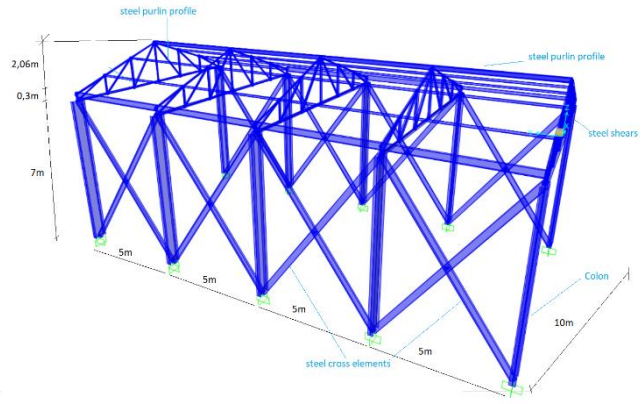

Figure 1: Finite element model of the steel industry structure without steel wind tension rod with Sap2000

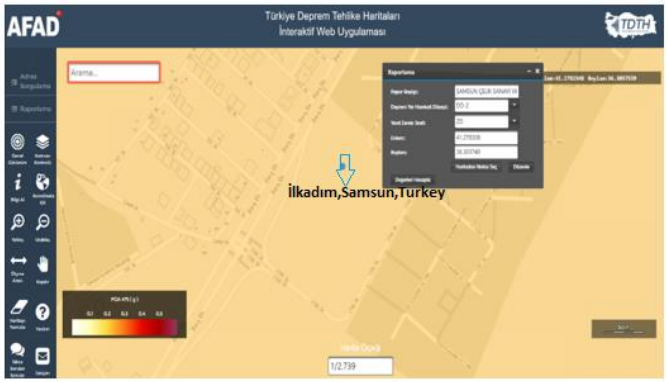

Figure 2: Turkey Earthquake Hazard Map was taken from Interactive Web application. Ground conditions of the steel industry structure to be designed in Samsun

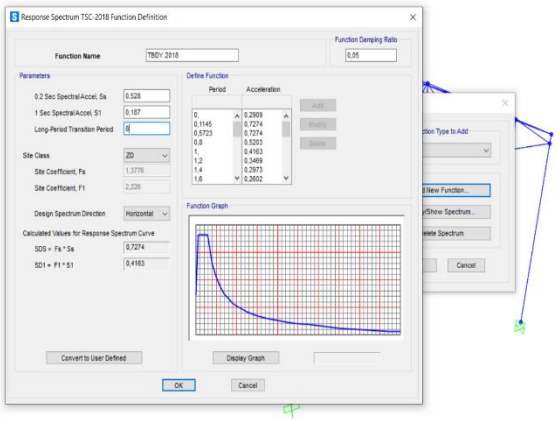

Figure 3: Transferring the design values such as S_S , S_1 etc., used for Samsun province conditions in the design to the SAP2000 program.

B) Description of Tension Rod and Wind Tension Rod

The diameter of the steel tension rod to be used in the structure model is designed as 0.018 meters. Steel tension rods are designed to be connected to the truss corner points by passing through the middle points of the purlin in the roof truss. UPN80 profile is used as steel profile connection in wind tension rod. Wind connectors are designed in a diagonal manner at the roof truss corner points.

III. RESULT AND DISCUSSION

The model steel industry structure was first analysed with the finite element method using SAP2000 (V24) [13], then wind tension rods were added to the system and the same analyses were repeated and the results were compared. In this study, the following were taken as material properties in the analysis; Material grade: S235 steel; the modulus of elasticity as E = 2.0x105MPa, material density ρ = 7.85kg / m3 and Poisson ratio υ = 0.3. The Author preferred Aisc360-Asd89 American Institute of Steel Construction Regulation in the Analysis [8].

C) Results of The Model Steel Structure with Wind Tension Rod

The steel industry structure was analysed with wind tendon rob. The first 5 modes were taken into account in the analysis. Obtained results are presented in figures 5,6,7,8,9 as periods and mode shapes (Table 1) After design check control on steel industry structure with wind tension rod all steel frames passed the stress capacity check (figure 10).

Table 1: Modal period and frequencies of steel industry structures with wind tension rod.

TABLE: Modal Periods And Frequencies				
OutputCase	**StepType**	**StepNum**	**Period**	**Frequency**
Text	Text	Unitless	Sec	Cyc/sec
MODAL	Mode	1	0,2655	3,7663
MODAL	Mode	2	0,2601	3,8443
MODAL	Mode	3	0,2428	4,1190
MODAL	Mode	4	0,2339	4,2761
MODAL	Mode	5	0,2179	4,5886

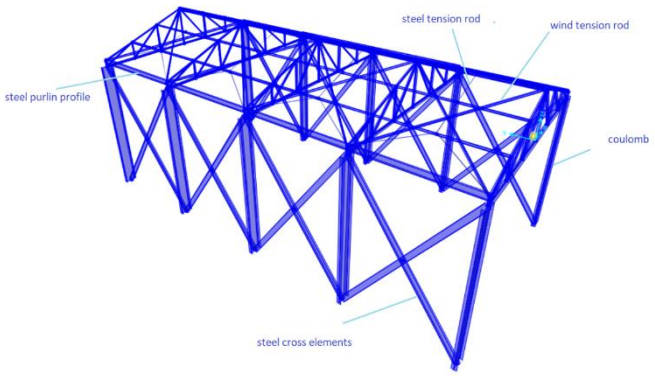

Fig. 4. Sap2000 anaylsis model of the steel industry structure with wind tension rod

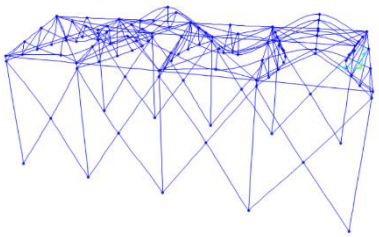

Fig. 5. Mode 1 shape (Period value = 0.2655s)

Mode 1 is torsional mode shape

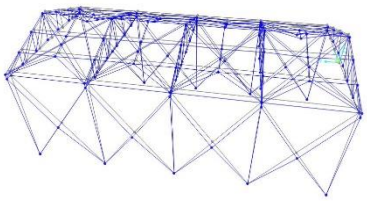

Fig. 6. Mode2 shape (Period value = 0.2601s)

Mode 2 is translational mode shape

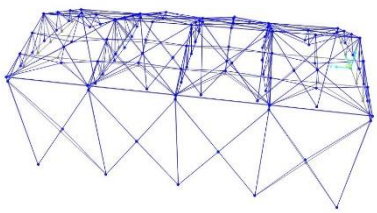

Fig. 7. Mode3 shape (Period value = 0.2428s)

Mode 3 is torsional mode shape

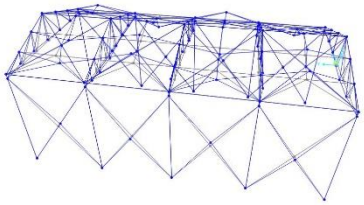

Fig. 8. Mode4 shape (Period value = 0.2339 s)

Mode 4 is torsional mode shape

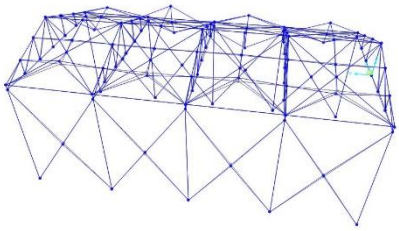

Fig. 9. Mode5 shape (Period value = 0.2179 s)

Mode 5 is torsional mode shape

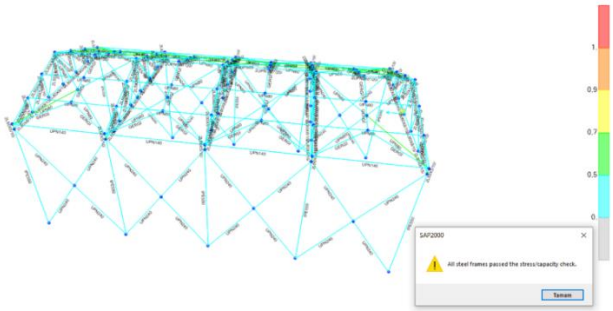

Figure 10: After design check control on steel industry structure with wind tension rod all steel frames passed the stress capacity check.

D) Results of the Model Steel Industry Structure without wind Tension Rod

The model steel industry structure tension rod was the only analysed in Fig.11. In this analysis, only the tension connection rod system was analysed. Wind connection rods were not included in the analysis. In this study, the following were taken as material properties in the analysis; Material grade: S235 steel material, the modulus of elasticity as E = 2.0x105MPa, material density ρ = 7.85kg / m3 and Poisson ratio υ = 0.3. The Author preferred Aisc360-Asd89 American Institute of Steel Construction Regulation in the Analysis.As a result of the analysis, although the analyses of the steel model structure were made for 12 different modes, the author has taken into account the first 5 modes of the structure. The results are presented for 5 modes at 12,13,14,15,16,17 figures. Table 2 Modal period

and frequencies of steel industry structures by tendon rob analysis results. After design check control on steel industry structure with non-wind tension rod all steel frames passed the stress capacity check (Figure 18)

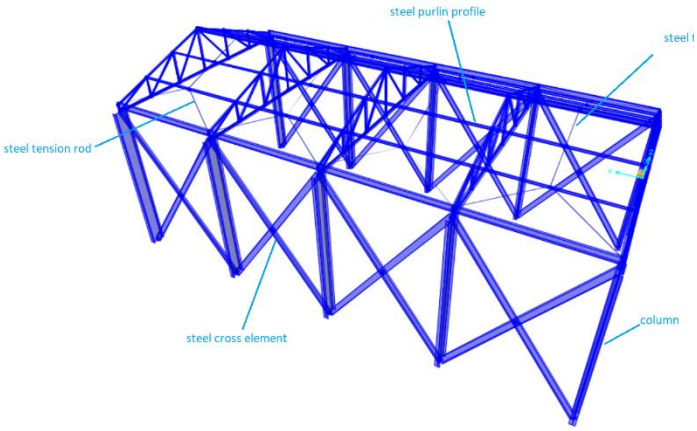

Fig. 11. Model steel industry structure with tension rod by Sap2000

E) Description of Tension Rod

The diameter of the steel tension rod to be used in the structure model is designed as 0.018 meters. Steel tension rods are designed to be connected to the truss corner points by passing through the middle points of the purlin in the roof truss. The tension rods will be passed through the center of the purlins in such a way as to center the purlins. (fig.11)

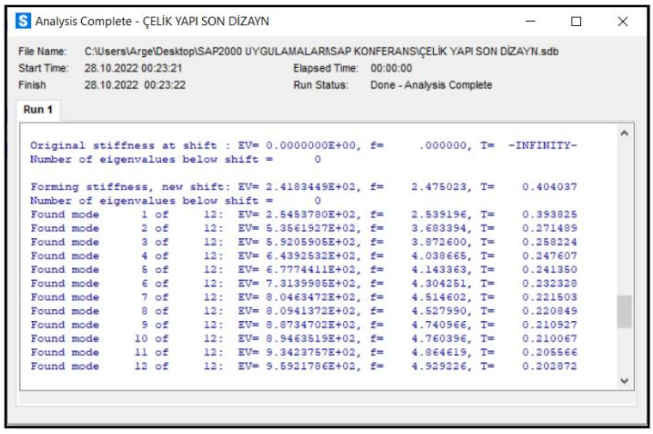

Fig. 12. Sap2000 analysis results of the steel industry structure with tension rod

Table 2: Modal period and frequencies of steel industry structures by tendon rob analysis results

TABLE: Modal Periods And Frequencies				
OutputCase	**StepType**	**StepNum**	**Period**	**Frequency**
Text	**Text**	**Unitless**	**Sec**	**Cyc/sec**
MODAL	Mode	1	0,3938	2,5392
MODAL	Mode	2	0,2715	3,6834
MODAL	Mode	3	0,2582	3,8726
MODAL	Mode	4	0,2476	4,0387
MODAL	Mode	5	0,2414	4,1434

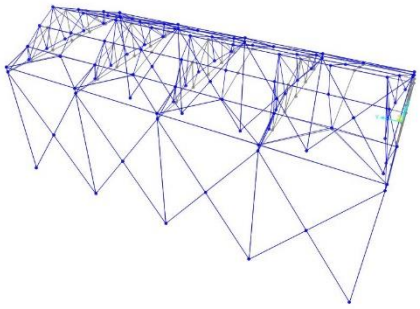

Fig. 13. 1. Mode shape (Period value = 0.3938 s)

Mode 1 is translational mode

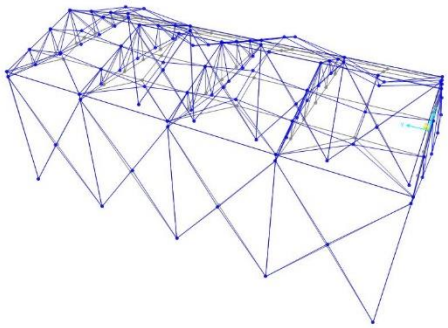

Fig. 14 2. Mode shape (Period value = 0.2715 s)

Mode 2 is torsional mode shape

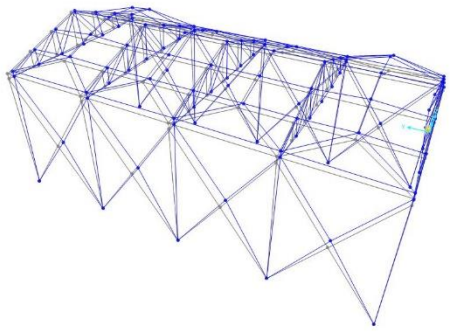

Fig. 15. 3. Mode shape (Period value = 0.2582 s)

Mode 3 is translational mode shape.

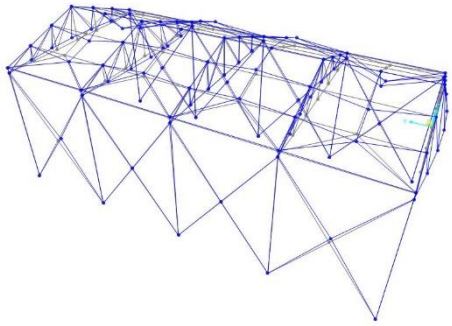

Fig. 16. 4. Mode shape (Period value = 0.2476 s)

Mode 4 is torsional mode shape.

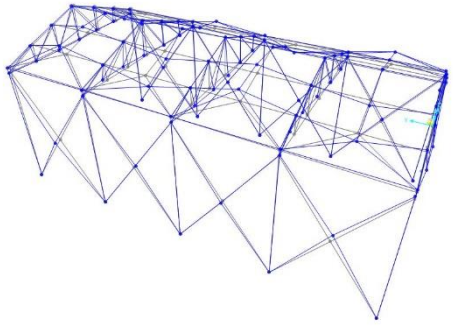

Fig. 17. 5. Mode shape (Period value = 0.2414 s)

Mode 5 is torsional mode shape in Y side

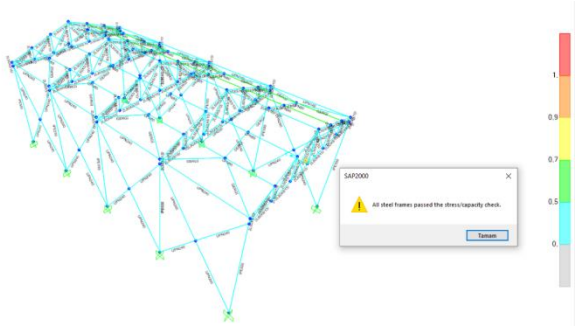

Figure 18: After design check control on steel industry structure with non-wind tension rod all steel frames passed the stress capacity check.

IV. COMPARISION AND RESULT

The comparison of model steel industry structure with wind tension rod and without tension rod of the model is given in Table 4. The first 5 mode shapes of the model steel industry structure were used in this study, which was done by connecting the tension rod and removing the tension rods. When the mode shapes are examined, Y translational mode shapes and torsion mode shapes are also seen in the model steel industry structure whose wind tension elements have been removed. Table.3.

Table 3: Comparison of mode shape type of steel industry structure

Mode	**1**	**2**	**3**	**4**	**5**
Non- wind tension rob	Translational	Torsional	Translational	Torsional	Torsional
Wind tension rob	Torsional	Translational	Torsional	Torsional	Torsional

Table 4. Comparison of period value between wind tension rod and without wind tension rod systems

	Wind Tension Rod		**Without wind Tension Rod**			
MOD	**FREQUENCY**	**PERIOD**	**FREQUENCY**	**PERIOD**	**DIFFERENCE**	**PERIOD DIFFERENCE %**
1	**3,7663**	**0.2655**	**2,5392**	**0.3938**	**0.1283**	**32,58**
2	**3,8443**	**0.2601**	**3,6834**	**0,2715**	**0.0114**	**4,201**
3	**4,1190**	**0.2428**	**3,8726**	**0,2582**	**0.0154**	**5,964**
4	**4,2761**	**0.2339**	**4,039**	**0,2476**	**0.0137**	**5,533**
5	**4,5886**	**0.2179**	**4,1434**	**0,2414**	**0.0235**	**9,735**

The difference between **wind tension rod** and non- **tension rod** systems in the dominant period is **32,58** %.

V. CONCLUSION

In the model steel industry structure, the effect of wind tension rod on the dominant period was obtained as 32,58 %. As a result, it can be said that the rigidity of the structure increases as the addition of wind tension rod affects the reduction of the structure period. In the model steel industry structure, the effect of wind tension rod on the dominant frequency was obtained as 48,32 %. With the addition of wind tension rod, more stable and smaller deformations were observed in other directions instead of the displacement values in the y direction. As a result, it is clearly seen that wind tension rod play a positive role in the balanced distribution of horizontal loads on the steel test industry structure.

In the mode shapes, on the other hand, with the addition of wind tension rod, more balanced and smaller deformations were observed in other directions instead of the displacement values in the y direction. Looking all these results, it is clearly seen that the rigidity of the structure increases by strengthening the model steel industry structure with wind tension rods. According to the results, it is clearly seen that the rigidity of the structure increases by strengthening the model steel structure with wind tension rod.

With the use of tension rod in the model steel industry structure, it was concluded that the model steel structure was made safer against dynamic effects.

REFERENCES

[1] Wei-Xin Ren; Tong Zhao; and Issam E. Harik, M. ASCE (2004) Experimental and Analytical ModalAnalysis of Steel Arch Bridge,Journal of Structural Engineering Volume 130 Issue 7 - July

[2] Tuhta S., GUNDAY F., AYDIN H.,2020, Modal analysis of steel test structure reinforced with cable elements by finite element method, 2nd International Eurasian Conference on Science, Engineering and Technology (EurasianSciEnTech 2020), October 07-09, 2020www.EurasianSciEnTech.org

[3] Naimi S, Peker Ö, 2022. Comparison of Different Types of Steel Structures Under Earthquake Forces Using StaSTEEL and SAP2000. Journal of the Institute of Science and Technology, 12(3): 1577 – 1591

[4] Öztürk M.,2018, An Evaluatıon About 2018 Turkey Buıldıng Earthquake Regulatıons And Turkey Earthquake Hazards Map Based On Central Anatolıa Regıon, *Selçuk-Teknik Dergisi Issn 1302-6178 Journal Of Selcuk-Technic Cilt 17, Sayı:2-2018 Volume 17, Number:2-2018*

[5] Akansel V.H., Soysal B.F., Kadas K., And Gulkan H.P, 2020, An Evaluation of the 2018 Seismic Hazard Map of Turkey on The Basis of Spectrum Intensity Akansel Et Al. / Turkish Journal of Earthquake Research 2 (2), 115-137, December 2020

[6] Turkey Earthquake Hazard Maps Interactive Web Application, https:// tdth.afad.gov.tr/, 2018.

[7] Hsiao P. C., Lehman D. E.and Roeder C. W. (2012). Improved Analytical Model for Special Concentrically Braced Frames. Journal of Constructional Steel Research, (73), 80-94.

[8] ANSI/AISC 360-ASD89 (2016). Specification for Structural Steel Buildings, American Institute of Steel Construction, Chicago, Illinois, USA.

[9] Günday F., 2022, Modal Analysis of Steel Hangar Retrofitted with Cable Element Using Finite Element Method, ICEANS 2022, Konya,Turkey

[10]https://www.resmigazete.gov.tr/eskiler/2018/03/20180318M1 2.htm,TBDY 2018

[11] Kasimzade, A. A., Tuhta, S., Günday, F., Aydın, H. "Obtaining Dynamic Parameters by Using Ambient Vibration Recordings on Model of The Steel Arch Bridge", Periodica Polytechnica Civil Engineering, 65(2), pp. 608–618, 2021. https://doi.org/10.3311/PPci.16422

[12] Günday, F., Dushimimana, A., & Tuhta, S. (2018). Analytical a nd Experimental Modal Analysis of a Model Steel Structure Using Blast Excitation. Presented at the International Conference on Innovative Engineering Applications.

[13] SAP2000 (2024), Integrated Finite Element Analysis and Design of Structures, Computers and Structures Inc., Berkeley, California, USA.

[14] Oden, J. T., & Reddy, J. N. (1976). An introduction to the mathematical theory of finite elements. Wiley, New York.

[15] Tekkaya A.E., & Soyarslan C. (2019). Finite Element Method. In: Chatti S., Laperrière L., Reinhart G., Tolio T. (eds) CIRP Encyclopedia of Production Engineering. Springer, Berlin, Heidelberg.

[16] Sewell, G. (1985). Analysis of a Finite Element Method. Springer, New York, NY.

[17] Bathe, K.-J. (2008). Finite Element Method. In Wiley Encyclopedia of Computer Science and Engineering, B.W. Wah (Ed.).

[18] Tuhta, S., & Günday, F. (2020). Analytical Modal Analysis of RC Building Retrofitted with CFRP using Finite Element Method. International Journal of Latest Technology in Engineering, Management Applied Science, 9(2), 78–82.

[19] Sertaç Tuhta,Furkan Günday, Hakan Aydın ,Mohammad ALALOU (2020), Modal analysis of model steel bridge by finite element method, 2nd International Eurasian Conference on Science, Engineering and Technology (EurasianSciEnTech 2020), October 07-09, 2020

[20] Aydın, H. (2022). Determination of the Effect of bridges on Dynamic Parameters of Model Steel Bridge with Finite Elements. 2ndInternational Congress of Engineering and Natural Sciences Studies ISBN: 978-605-71156-5-2 *Ankara/Turkey*, 296.

[21] Kocabaş S., Analysis and Design of Steel Constructions with The Aid of Sap2000, Msc Thesis, Department of Civil Engineering Institute of Naturel and Applied Science University of Cukurova,2005

[22] Jamal R., Yüksel S.B., Comparison of Performance Analysis of a Moment Resisting Framed Structure According to TBDY 2018 and ASCE 41-17, El-Cezeri Journal of Science and Engineering Vol:8, No: 1,2021, (432-444) DOI: 10.31202/ecjse.808585

[23] Disaster and Emergency Management Presidency, Turkey Building Earthquake Regulation (TBDY2018), Ankara, Turkey. https://en.afad.gov.tr/head-of-afad

A Case Study for Validation of KP505 Propeller Open-Water Characteristics Via Computational Fluid Dynamics

M.CINAR[1], H. UCAR[2] and F. DIKMEN[3]
[1]Yildiz Technical University, İstanbul/Turkey, muhammeddcinar@gmail.com
[2]Piri Reis University, İstanbul/Turkey, hkucar@gmail.com
[3]Yildiz Technical University, İstanbul/Turkey, frhtdkmn@gmail.com

Abstract **- In this paper, the validation study of open water characteristics (thrust coefficient; K_T, torque coefficient; K_Q, efficiency; η) of the KP505 propeller for KRISO container ship KCS was presented by using computational fluid dynamics(CFD). The validation aimed at verifying the correctness of results of numerical simulations performed in the model scale were confronted with those measured in the experiment. There are many studies in the literature on this subject, and in this study, considering the effect of the number of mesh elements on the thrust and torque values, the optimum mesh size to be used was determined by performing mesh sensitivity analysis during mesh generation. The computational analysis was carried out for advance coefficients in the range from J=0.1 to J=0.8 and the mean errors was calculated 6,43% for K_T and 0,73 % for K_Q. So, it was evaluated that CFD results show a good agreement with the experimental results. In future study, self propulsion validation analysis will be performed to identify the self propulsion coefficients K_T (thrust coefficient) and K_Q (torque coefficient) pressure distribution on the ship hull, nominal and effective wake field around the KP505 propeller disk which are essential for ship and propeller design.**

Keywords **- CFD, open water, propeller, validation.**

List of Abbreviations and Symbols

CFD	:	Computational Fluid Dynamics
KCS	:	Kriso Container Ship
SRI	:	Ship Research Institute
F_N	:	Froude Number
ITTC	:	International Towing Tank Conference
SRI	:	Ship Research Institute
J	:	Advance Coefficient
K_Q	:	Torque Coefficient
K_T	:	Thrust Coefficient
Lwl	:	Length at Load Water Line [m]
Lpp	:	Length Between Perpendiculars [m]; L
RANS	:	Reynolds Averaged Navier Stokes
R	:	Convergence Rate
rpm	:	Rate Per Minute (rev/min)
rps	:	Rate Per Second (rev/sec)
ρ	:	Density [$kg*s^2/m^4$]
Ŋ	:	Efficiency
n_p	:	Propeller Revolution Rate [1/s, Hz]
P	:	Pressure [kg/m^2]
Re	:	Reynolds' Number
ν	:	Kinematic Viscosity [m^2/s]

I. INTRODUCTION

Determination of the propeller open water characteristics is a compulsory step in the early stage of ship design. Therefore, the open water towing tank tests are generally used to identify the open water characteristics of the propeller. However, as a result of intensive development of advanced numerical methods, the ship propeller design process has recently reduced in terms of computational and time cost. Thus, ship hydrodynamic problems have been rapidly investigated by researchers. Within this context, it can be stated that the vast majority part of towing tank tests have been replaced by the advanced CFD (Computational Fluid Dynamics) simulations to investigate the propeller open water performance characteristics. CFD analysis can also be used as a practical and much less costly tool in evaluating the design with an iterative approach. For this purpose, in cases where the ship thrust is insufficient or more than the predicted value, the propeller geometry is redesigned in a way that will improve or reduce the thrust by modifying the propeller design. In this study, the open water characteristics of KCS KP505 propeller are determined by applying a numerical study based on CFD. In the numerical analysis, mesh sensitivity analysis ignored in the literature was performed to identify the optimum mesh element size due to the fact that the number of mesh elements used in numerical analysis greatly affects the thrust and torque values, but also directly changes the analysis time and cost. At the end of the analysis, the computed results were compared with the open water test results of the KCS KP505 test propeller on the 1/31,5994 model scale ratio. The RANS (Reynold Averaged Navier Stokes) governing equations are used for numerical calculation and standart k-ω was used for turbulence modeling. K_T, K_Q and η_0 parameters were calculated using the open water performance values (torque and thrust) obtained from the

numerical calculation.

II. KCS KP505 PROPELLER CFD ANALYSIS

A. Basic Characteristics

The propeller open water verification analysis is performed by comparing certain dimensionless coefficients of the propeller obtained in computational fluid dynamics with the values obtained in the experimental environment.

The dimensionless performance coefficients specifying the general performance characteristics of the propeller are thrust coefficient (K_T), torque coefficient (K_Q) and advance coefficient (J) values. These dimensionless coefficients are calculated as follows depending on the inputs of propeller thrust (T), propeller torque (Q), fluid density (ρ), rate of revolutions of the model propeller (n), propeller diameter (D) and propeller advance speed(V_a). Based on these coefficients, the propeller open water efficiency (μ0) is obtained. [2]

$$K_Q = \frac{Q}{\rho n^2 D^4} \tag{1}$$

$$K_T = \frac{T}{\rho n^2 D^5} \tag{2}$$

$$J = \frac{V_a}{nD} \tag{3}$$

$$\eta = \frac{K_T}{K_Q}\frac{J}{2\pi} \tag{4}$$

B. The Numerical Theory

The Reynolds Averaged Navier-Stokes (RANS) solver equations is employed in the present study. When the Reynolds averaging approach for turbulence modeling is applied, the governing equations (Navier–Stokes equations) are written for the mass(continuity) and momentum conservation in cartesian tensor form;

$$\frac{\partial \rho}{\partial t} + \frac{\partial u_i}{\partial x_i} = 0 \tag{5}$$

$$\frac{\partial}{\partial t}(\rho u_i) + \frac{\partial}{\partial x_j}(\rho u_i u_j) = -\frac{\partial p}{\partial x_i} + \frac{\partial}{\partial x_j} \left[\mu\left(\frac{\partial u_i}{\partial x_j} + \frac{\partial u_j}{\partial x_i}\right) - \left(\frac{2}{3}\mu \frac{\partial u_i}{\partial x_i}\right)\right] + \frac{\partial}{\partial x_j}\left(-\rho \overline{u_i}' \overline{u_j}'\right) \tag{6}$$

where x_i are Cartesian coordinates, u_i are the corresponding velocity components, p is the pressure, ρ is the density, and μ is the viscosity. Also, $-\rho \overline{u_i}' \overline{u_j}'$ is the Reynold stress term which has been closed by using the k–ω standart turbulence model. This model solves for the transport variables; turbulence kinetic energy (k) and turbulence dissipation rate (ω). In this model it is assumed that the turbulence viscosity is associated with turbulence kinetic energy and turbulence dissipation rate by the expression;

$$\mu_t = \rho \frac{k}{\omega} \tag{7}$$

The transport equations used for solving the transport variables k and ω are as follows:

For turbulent kinetic energy *k*,

$$\frac{\partial(\rho k)}{\partial t} + \frac{\partial}{\partial x_j}(\rho u_i k) = \frac{\partial}{\partial x_j}\left[\left(\mu + \frac{\mu_t}{\sigma_k}\right)\frac{\sigma_k}{\partial x_j}\right] + P_K - \beta' \rho k \omega \tag{8}$$

For turbulence dissipation rate *ω*,

$$\frac{\partial(\rho \omega)}{\partial t} + \frac{\partial}{\partial x_j}(\rho u_i \omega) = \frac{\partial}{\partial x_j}\left[\left(\mu + \frac{\mu_t}{\sigma_\omega}\right)\frac{\sigma_\omega}{\partial x_j}\right] + a\frac{\omega}{k}P_K - \beta' \rho \omega^2 \tag{9}$$

P_K is the turbulence production rate due to the viscous forces and is presented by

$$P_K = \tau_{ij}\frac{\partial u_i}{\partial x_j} a \tag{10}$$

The convergence criterion of 10^{-6} was used for this analysis.

C. Model Geometry

The KP505 test propeller of the KCS ship was designed and manufactured by KRISO (Korea Research Institute of Ships and Ocean Engineering) in model scale and sent to the Ship Research Institute (SRI) to be used in open water test tests. KP505 standard test propeller (SRI MP No.460) basic parameters are given in Table 1 and Figure 1, and the parameters used in the analyzes were kept the same as those used in the open water performance test carried out by The Ship Research Institute (SRI) in order to compare the analysis results. The propeller geometry is officially provided in [12]. The 3D model of the propeller to be used in the analysis is shown in Figure 2.

Table 1. Principal Particulars of Tested Propeller [1]

Characteristics	Value
Diameter	0.2500
Boss Ratio	0.1800
Pitch Ratio at 0.7R	0.9967
Expanded Blade Area Ratio	0.800
Rake Angle	0.000
Skew Angle	32.0
Number of Blade	5
Direction of Rotation	Right
Blade Section	NACA66 Thickness +a=0.8 Camber

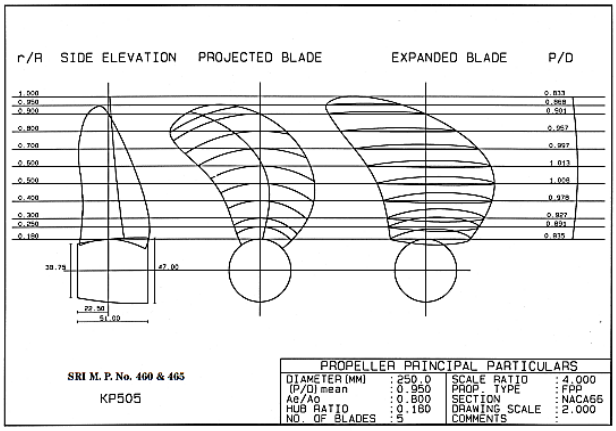

Figure 1. KP505 Propeller Principal Particulars [1]

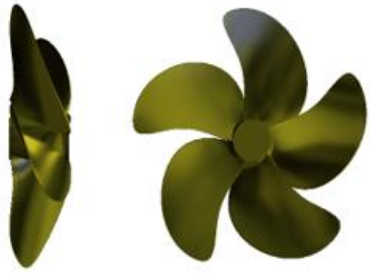

Figure 2. KP505 Propeller Solid Model

D. Flow Volume Geometry

For the propeller analysis, two solution geometries (control volumes) were created flow simulation. The moving control volume is located inside of the external control volume and is defined as rotor. The external control volume is stationary and defined as stator. The CFD solver used keeps the surfaces in the moving control volume stable and rotates the fluid around the surface. For the analysis performed using the five-bladed model, the solution volume height was determined as 5 times the propeller diameter, and the solution volume length was determined as 12 times the propeller diameter as shown in Figure 3.

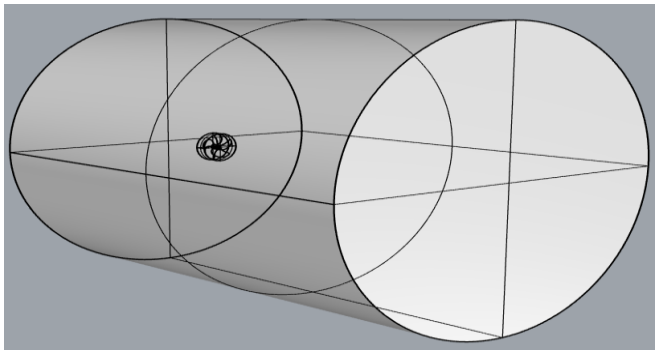

Figure 3. Computational Domain

E. Mesh Sensitivity Analysis

Mesh sensitivity analysis was performed to determine the optimum mesh element size to be used in the control volumes for the wide advance coefficient (J) range. Sensitivity analysis for thrust and torque values was performed at the condition of advance coefficient J=0.5 (V_a=1.5 m/s), the variation of thrust and torque values according to number of mesh elements are given in Figure 4 and Figure 5 respectively.

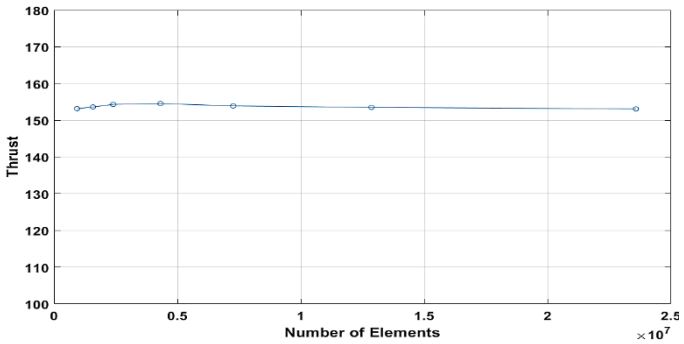

Figure 4. Change of thrust with number of elements

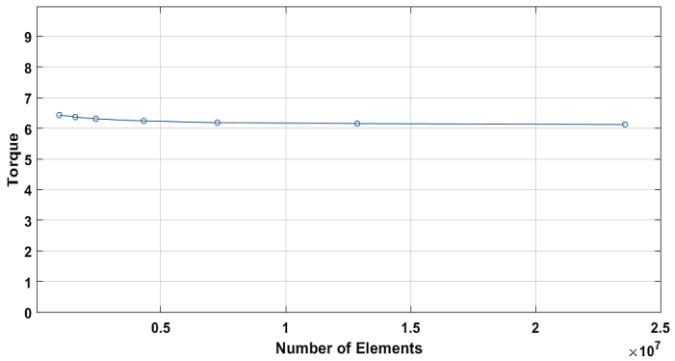

Figure 5. Change of torque with number of elements

Seven different meshes were used in the study and the cell numbers ranged from 932.485 to 23.582,780. In order to determine the optimum mesh size for the propeller blades, the analysis was repeated by reducing the mesh size by √2 times the previous one[3]. It was observed that the torque and thrust values obtained from the propeller did not change after a certain mesh size, and the mesh size at this point was applied for the propeller blades.As stated in [3], convergence evaluation is made over the ratios of differences between the results obtained for the mesh created using different cell sizes.When the result of the analysis with fine mesh parameter is S_1, the result of the analysis with medium mesh parameter is S_2, and the result of the analysis with coarse mesh parameter is S_3, the differences between the analysis results are as follows:

$$E_{21}=S_2-S_1 \quad (11)$$

$$E_{32}=S_3-S_2 \quad (12)$$

Changes between medium-fine (E_{21}) and coarse-medium (E_{32}) solutions are used to define the convergence ratio(R). The convergence ratio is expressed as:

$$R= E_{21} / E_{32} \quad (13)$$

According to this definition, three convergence conditions are possible:

Monotonic convergence: 0 < R< 1
Oscillatory convergence: R< 0
Divergence: R> 1

Table 2. Mesh Sensitivity Analysis

CASE	Blade Mesh Element Size(mm)	S	Thrust	Torque	Thrust		Torque		R_{Thrust}	R_{Torque}
					E_{21}	E_{32}	E_{21}	E_{32}		
1	2,83	S_3	153,17	6,43	-0,47	-0,44	0,057	0,068	1,07	0,83
	2,00	S_2	153,61	6,37						
	1,41	S_1	154,08	6,31						
2	2,00	S_3	153,61	6,37	-0,45	-0,47	0,072	0,057	0,96	1,27
	1,41	S_2	154,08	6,31						
	1	S_1	154,53	6,23						
3	1,41	S_3	154,08	6,31	0,63	-0,45	0,053	0,072	-1,4	0,74
	1	S_2	154,53	6,23						
	0,71	S_1	153,90	6,19						
4	1	S_3	154,53	6,24	0,39	0,63	0,033	0,053	**0,62**	**0,63**
	0,71	S_2	153,90	6,19						
	0,5	S_1	153,51	6,15						

The final thrust and torque values obtained by systematically reducing the element size of the mesh on blade are given in Table 2 and the convergence analysis data is given in Table 3.

Table 3. Thrust and torque values obtained as a result of mesh independence study

		J	Thrust	Torque	Blade Element Size (mm)	Number of Elements	R_{Thrust}	R_{Torque}
S_3	COURSE MESH	0,5	154,53	6,2384	1	4314265		
S_2	MEDIUM MESH	0,5	153,9	6,1855	0,71	7263292	**0,62**	**0,63**
S_1	FINE MESH	0,5	153,51	6,1524	0,5	12866127		

Since the monotonic convergence condition(0<R<1) was provided for both thrust and torque parameters, convergence was obtained and the mesh cell size to be used in the propeller blade was determined as 0,5 mm. Thus, the total number of mesh elements on the propeller blades is 12866,127.

Quality criteria that determine the mesh element quality during the process of creating the mesh structure; the y+ value, skewness and orthogonal quality. In order to accurately model the fluid motion around the propeller, a boundary layer structure was created on the propeller blade. The mean boundary layer is divided into 12 layers. The total boundary layer thickness was determined by increasing 1,2 times from the inside out for each layer. The *y+* value is the quality criterion for the boundary layer (inflation) that determines the quality of the mesh elements and enables it to be evaluated. In the boundary layer process, first the relevant control volume and then the non-slip wall will be examined in that control volume are selected, and a boundary layer thickness is created between the geometry and the fluid. The boundary layer thickness is determined by the formula below.

$$\nabla y1 = \frac{(y+)\mu}{\rho V} \tag{14}$$

In the above formula, *"Δy1"* is the boundary layer thickness, *"μ"* is the kinematic viscosity of the fluid, *"ρ"* is the fluid density, and *"V"* is the fluid velocity. By selecting the dimensionless *"y+"* value in the formula, the total boundary layer thickness of the geometry is calculated and the boundary layer thickness value is entered in the mesh module. One of the most important parameters of mesh element quality is the skewness value. This value shows how close the geometric dimensions of the mesh elements to the ideal dimensions (equilateral triangle or square). The fact that the skewness value is below 0.95 shows that the error rate in the solution of the established mathematical model is an acceptable value for the solver. Keeping this value as low as possible will improve mesh element quality.

Finally, the mesh structure was created as shown in Figure 6.

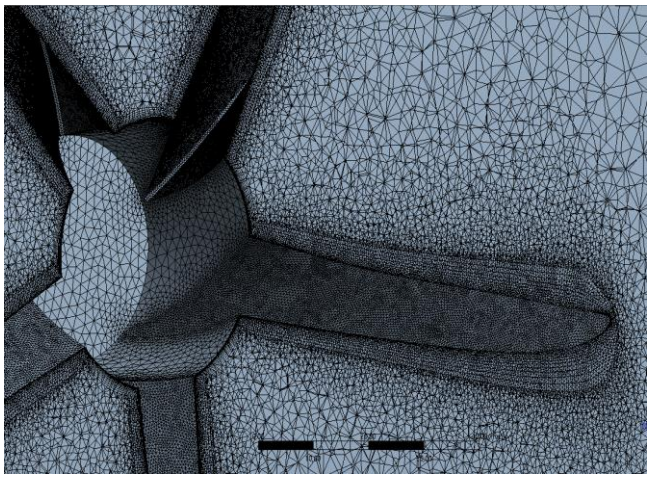

Figure 6. Propeller mesh structure and inflation

F. Boundary Conditions

In the open water CFD analyzes the k-ω Standard method was employed for the turbulence model. Second order and high resolution methods were used in turbulence model and solver algorithms. Analyzes were performed with steady state condition. The limits of the boundry conditions are shown in Table 4.

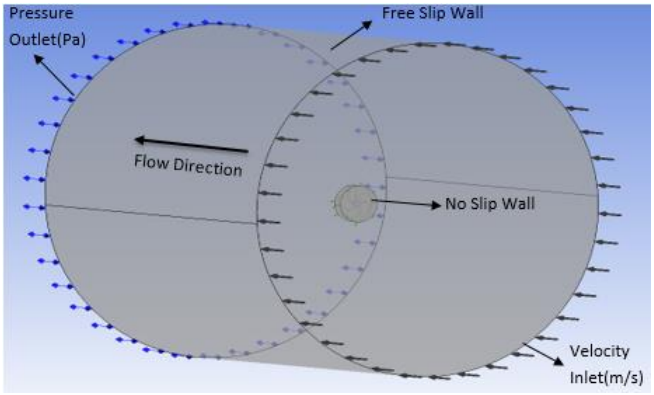

Figure 7. Boundary Conditions

The computational domain of the propeller and the cylindrical boundary around its shown in Figure 7. No-slip wall condition was applied on the propeller and its hub. On the inlet boundary, velocity values obtained from the formula given by Table 5 were imposed, while the static pressure was set to zero on the exit boundary. On the outer cylindrical boundary, free slip condition was employed.

Table 4. KP505 Propeller Boundary Conditions

	Boundary Condition
Fluid Type	Sea water(999,4428kg/m^3)
Inlet	Velocity Inlet; V_A
Outlet	Pressure Outlet (0 Pa)
Propeller	No Slip Wall
Stator	Free Slip Wall

III. OPEN WATER ANALYSIS AND EVALUATIONS

In order to create the KP505 propeller open water performance graph as a result of the CFD analysis, the computational simulation was carried out by means of varying the inlet velocity with a constant rotating speed of n=12 rps for each propeller advance coefficient(J) from 0,1 to 0,8. V_A is the velocity of suction side of the propeller (propeller advance speed) which is the value to be entered as an inlet velocity value to the solver. The velocity value required to be entered in each advance coefficient was determined and presented in Table 5.

$$V_A = JnD \quad (15)$$

Table 5. Advance Velocity (Velocity Inlet) Values Based on the Propeller Advance Coefficients

J	V_A
0,100	0,3000
0,200	0,6000
0,300	0,9000
0,400	1,2000
0,500	1,5000
0,600	1,8000
0,700	2,1000
0,800	2,4000

Table 6. Propeller Open Test Results in SRI 400 m Towing Tank

J	K_T	$10K_Q$	Eta0
0,100	0,4820	0,6770	0,1130
0,200	0,4350	0,6220	0,2230
0,300	0,3870	0,5570	0,3320
0,400	0,3360	0,4970	0,4310
0,500	0,2850	0,4370	0,5190
0,600	0,2350	0,3760	0,5970
0,700	0,1850	0,3110	0,6650
0,800	0,1370	0,2470	0,7050
0,900	0,0830	0,1810	0,6540
1,000	0,0220	0,0960	0,3730

Open water analyzes were performed on the model scale (λ=31.6) for the range of 0,1<J<0,8 advance coefficients. The comparison of propeller open water characteristics obtained from CFD and test is shown in Table 7 and Figure 8.

Table 7. Comparing of CFD and Test Results

		Thrust Coefficient			Torque Coefficient			Efficiency(η)		
J	V_{inlet}	CFD K_T	Open Water K_T	Error [%]	CFD $10K_Q$	Open Water $10K_Q$	Error [%]	CFD	Open Water	Error [%]
0,1	0,3	0,46	0,48	-3,88	0,67	0,68	-0,50	0,11	0,11	3,12
0,2	0,6	0,42	0,44	-3,02	0,62	0,62	-0,17	0,22	0,22	3,03
0,3	0,9	0,37	0,39	-3,22	0,56	0,56	0,97	0,32	0,33	4,22
0,4	1,2	0,32	0,34	-3,48	0,50	0,50	0,75	0,41	0,43	4,33
0,5	1,5	0,27	0,29	-4,44	0,44	0,44	0,02	0,50	0,52	6,99
0,6	1,8	0,22	0,24	-6,52	0,37	0,38	-1,00	0,56	0,60	5,60
0,7	2,1	0,17	0,19	-9,91	0,31	0,31	-1,71	0,61	0,67	8,66
0,8	2,4	0,11	0,14	-16,9	0,24	0,25	-4,17	0,61	0,71	13,24

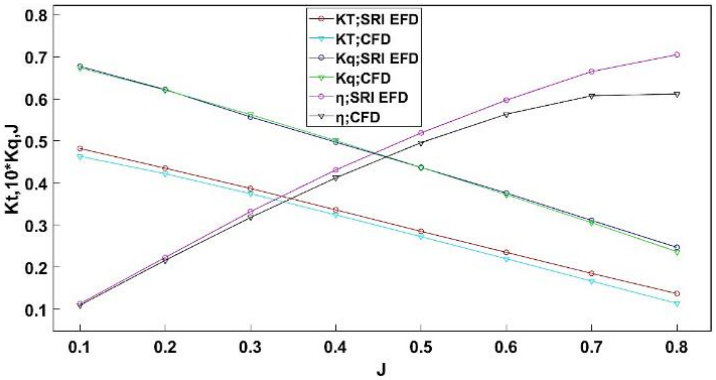

Figure 8. Comparison of thrust coefficient, torque coefficient, and open water efficiency between the experimental and computational results.

The average error rates between calculated and measured results for thrust and torque coefficients are shown in Table 7.

Table 7. Percentage differences between CFD and experimental results

Error(%)		
J	Kt	10Kq
0,100	-3,88	-0,50
0,200	-3,02	-0,17
0,300	-3,22	0,97
0,400	-3,48	0,75
0,500	-4,44	0,02
0,600	-6,52	-1,00
0,700	-9,91	-1,71
0,800	-16,99	-4,17
Average	**-6,43**	**-0,73**

IV. CONCLUSIONS

This paper presents a numerical calculation of open water characteristics of KP505 propeller in model scale using a RANS method. The mesh sensitivity analysis demonstrates that there is an important influence of the mesh size on the calculated open water characteristics of the propeller. The computational analysis was carried out for advance coefficients in the range from J=0.1 to J=0.8 and the mean errors was calculated 6,43% for K_T and 0,73 % for K_Q. Therefore, the numerical open water performance prediction of KP505 propeller is considered to have a very good agreement with experiment. Thus, the present paper approved that computational fluid dynamics analysis can be used for the validation of propeller open water characteristics instead of using towing tank that is more expensive and impractical method. In addition, it was evaluated that in high advance ratios the differences between the measured and calculated results are relatively large due to the very small thrust and torque coefficient values.

In future study; the self propulsion validation analysis which allows to simulate the velocity wake field around the propeller and pressure distribution on the ship hull surface for with/without propeller condition and identify the self propulsion performance characteristics torque coefficient(K_Q), thrust coefficient(K_T) and effective and nominal wake fraction (ω_T, ω_N) will be performed.

REFERENCES

[1] Surface Pressure Measurements on the KCS Model(SRI M.S.No.631) in the SRI 400M Towing Tank, Report of Ship Performance Division, Tokyo, Japan
[2] CARLTON, J.S., Marine Propellers and Propulsion, Second Edition, Butterworth-Heinemann Ltd, 2006
[3] ITTC Quality System Manual Recommended Procedures and Guidelines "Uncertainty Analysis in CFD Verification and Validation Methodology and Procedures",2017
[4] ITTC Quality System Manual Recommended Procedures and Guidelines "Open Water Test",2014
[5] Paik Kwang J. ,Numerical Study on the hydrodynamic characteristics of a propeller operating beneath a free surface, Department of Naval Architecture and Ocean Engineering, Inha University Incheon, South Korea, 2017
[6] Lungu A, Numerical simulation of the cavitating KP505 propeller working in open water conditions, Department of Naval Architecture, Dunarea de Jos University of Galati, Romania
[7] ITTC Quality System Manual Recommended Procedures and Guidelines" Practical Guidelines for Ship Self-Propulsion CFD", 2014
[8] Seok W., Lee S.B.,Rhee S.H.,Computational Simulation of turbulent flows around a marine propeller by solving the partially averaged Navier-Stokes equation,Department of Naval Architecture and Ocean Engineering,Seoul National University,Seoul,Korea
[9] Krasilnikov V.I., Self propulsion RANS computations with a single skrew container ship,Norwegian Marine Technology Research Institute(MARINETEK), Trondheim, Norvey
[10] Baek Dong G.,Yoon Hyun S. , Jung Jae H., Kim Ki S., Paik Bu G., Effects of the advance ratio on the evolution of a propeller wake, Korea, 2015
[11] Gaggero S., Villa D., Viviani M., The Kriso Container Ship (KCS) Test Case: An Open Source Overview, Department of Electric, Electronic, Telecommunication Engineering and Naval Architecture, University of Genoa Via Montallegro, Genoa, Italy
[12] National Maritime Research Institute (NMRI) 2015 Tokyo 2015: A Workshop on CFD in Ship Hydrodynamics, http://www.t2015.nmri.go.jp

Architectural Research of the Interaction Between the Structural System of Buildings and Curtain Wall: An Analysis on Selected Buildings in Ankara

T. ERARTSIN[1] and A. İ. ÜNAY[2]

[1] Gazi University, Ankara/Turkey, tugce.erartsin@gazi.edu.tr
[2] Gazi University, Ankara/Turkey, unay@gazi.edu.tr

Abstract **- In recent years, with the engineering technology developing day by day, the building typology which is a form of expression of prestige and power is high-rise buildings. In these structures, curtain walls, which act as a shell, are used to separate the building from the outside atmosphere. Curtain walls are self-supporting systems, which can be opaque or transparent depending on their location and function, can be composed of different materials, but mostly glass is used and formed by the combination of building elements. The height of the building, its location, the purpose of use and the structural system of the building are the factors affecting the design of façades in high-rise buildings. The most important of these factors in high-rise buildings is the type of the structural system. In this study, the structural systems of high-rise buildings were examined and the façade-structure interaction was discussed on some buildings in Ankara, taking into account the structural system-curtain wall diversity. As in the examples in the world, the evaluation has been made by considering the compatibility of a curtain wall with the texture of the city, its safety, ease of use, its technological form, its efficiency, interaction with the environment, and insulation status. This study will strengthen the façade-structure perception of the designers by considering the high-rise buildings with different load-bearing systems together with the curtain wall and their diversity.**

Keywords **- Structural analysis, High-rise buildings, Façade, Curtain wall, Structural system**

I. Introduction

THE word façade comes from the word "facies", which means face in Latin, and is the first perceived element in every building, regardless of location. It acts as a shell between the inside and the outside of the building, and with the design decision, it shows the feature of a wall that takes the outdoor conditions of the building inside at the desired rate.

Façades, which have a design determined by the structural system diversity and material of the buildings, are sometimes applied to the façades that help the structural system, and sometimes curtain wall systems are preferred in terms of aesthetics. A comprehensive planning method is also essential in façade designs, especially when determining the heights and building masses of multi-storey high-rise buildings. Curtain walls are systems that transfer external loads (self-load, earthquake and wind loads) to the building structural system with a certain safety [1].

Factors affecting façade formations in high-rise buildings; height of the building, environment, purpose of the project (hotel, airport, business or cultural center) and structural system. Among these factors, the most important factor affecting the façade formation in high-rise buildings is the structural system. Structural system behavior in high-rise buildings and the stylistic variations it brings affect façade alternatives.

II. Classification Of Structural Systems In Architecture

In reinforced concrete structures, load-bearing systems can be designed as framed, curtain walled and curtain-framed. The behavior of these three carrier systems under the influence of horizontal loads is different. In Figure 1, the curves showing the displacements of these three systems under horizontal loads are given. The earthquake resistance of curtain wall or curtain-frame building systems is higher than framed structures [2]. Structural systems in high-rise buildings vary according to the material used, the height of the building, the number of floors and the function of the building. The types of structural systems used in the transfer of horizontal and vertical forces acting on high-rise buildings can be classified as frame system, curtain wall (shear wall) system, frame and curtain wall system, core system, tubular system [3].

A. Shear Wall Systems

Shear walls are the systems most used in the past to stabilize the structure to resist horizontal loads created by winds and earthquakes. With the developments in reinforced concrete; shear wall systems are also used in the tallest buildings.

The structural system of a shear wall structure is formed by shear walls parallel to each other in various directions, providing sufficient rigidity against horizontal loads and carrying vertical loads at the same time. Cores or other shear walls enclosed in the framing of elevator and stairwells provide their stability in their plane.

B. Frame Systems

Frame systems in high-rise buildings commonly consist of vertical columns and horizontal beams formed with rigid connections. The strength of these structural systems, in which reinforced concrete and steel materials can be used, against horizontal loads depends on the rigidity of the connection points. The main advantage of the frame system is that it provides freedom in the arrangement of spaces such as windows and doors in planning [4].

C. Frame-Shear Wall Systems

In multi-storey buildings formed only with frames, as the height of the building increases, especially in the lower floors, the column sections become very large. The main reason for this is that the frames are insufficient to meet the horizontal loads for increasing building heights. For this reason, curtain and frame systems are used together. In this way, insufficient ductility rates arising from the great stiffness of the shear walls are increased by adding frames to the building [5]. Thus, if only frames are used, the displacements caused by horizontal loads are prevented to some extent by adding shear walls to the system. Figure 1 shows a graph of the displacements of the frame, shear wall and frame-shear wall systems against lateral loads.

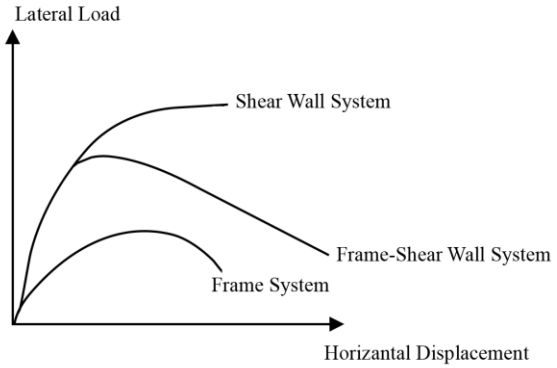

Figure 1: Behavior of structural systems under horizontal loads [2].

D. Core Systems

Cores are large beams that cantilever out of the ground against horizontal loads. The bending and shear stresses in the core are similar to those of a box-section beam, assuming no torsion in the section. Since this system also carries vertical loads, the pressure forces acting on it have a prestressing effect [5].

In high buildings with a core system, all or most of the loads are carried by a single core or by cores in various parts of the building. In these structures, frame, curtain wall or cable hanging systems can be used to assist the core.

E. Tubular Systems

The tube is formed by tightly spaced columns around the structure. This façade structure looks like a perforated wall. The tube is very rigid and resists horizontal loads similar to a cantilever beam. Since the outer walls meet all or most of the wind and earthquake loads, there is no need for diagonal crossings and shear walls inside the building. Tubular systems not only increase the structural efficiency compared to the framed systems, but also save 50% from the structural material. Thus, it allows the construction of lighter buildings [6].

III. Classification Of Curtain Wall Systems In Architecture

Curtain walls are systems that do not carry a load except their own loads and transfer their own loads to the main structural systems of the buildings. It is designed using different materials as well as being opaque or transparent. The most commonly used material is glass in curtain wall systems. Curtain walls are classified in 2 different groups depending on the weight of the panels used on the façade.

A. Heavy Curtain Walls

It is a curtain wall system consisting of concrete-based panels. Heavy cladding elements are generally precast concrete. With the wide possibilities in the use of molds, desired shapes and desired surface texture can be given to concrete [7].

B. Lightweight Curtain Walls

Lightweight curtain wall system is a type of curtain wall formed by transparent or opaque panels, in which the façade elements are placed on a carrier frame. Lightweight curtain wall cladding elements; glass, precast concrete, ceramic, ceramic, metal composite, wood, stone [8].

Curtain walls are classified as single skin and double skin according to the number of façades. In Turkey, approximately 20% of the total energy is used in transportation, 43% in industry and 37% in buildings [9]. This makes it necessary to design buildings as less energy consuming buildings throughout their life stages. Double skin façades, which are widely used in Europe and North America, have almost no application area in our country [10]. Double-skinned façade systems, which play an effective role in increasing the energy performance of the building when applied in cold climate regions, do not have much application area in warm and temperate climate regions as in some regions of our country.

IV. An Analysis On Selected Buildings In Ankara

A. Ankara High Speed Train Station

Although curtain walls are associated with high-rise buildings, Ankara High Speed Train Station, which can be an example for large-scale buildings, has been examined in this part of the research, as it is an indispensable element for large-scale structures such as airports, business and cultural centers.

Reinforced concrete shear walls and curvilinear steel carriers to carry the façade and roof are used in the building as a basis. With the integration of steel and glass panels with each other, Ankara High Speed Train Station has a façade character reminiscent of the abstracted state of a high-speed train in three dimensions as shown in Figure 2 [11]. The organic outer shell character, which becomes transparent from time to time, draws attention in the building entrances and terrace areas.

Figure 3: General view of Ankara High Speed Train Station [12]

In the roof structure of the station building (see Figure 3), the details of the curtain wall system, where the strong steel carriers required by the technology, globalization and competitive environment, are combined with composite coatings, and the openings opened in order to increase the use of daylight inside the building are seen. The curtain wall system used is supported by steel joints forming the roof structure of the building, and high steel reinforced columns forming the main building structure as shown in Figure 3.

Figure 3: Roof and building structure details [12]

Figure 4: Terraces and façade details [12]

Another factor in the façade and shell design of the project is that the steel structure, which carries the large glass façade, facing Celal Bayar Boulevard, that is, facing southwest and designed as vertically inclined, continues on top and becomes the structure that carries the roof. Terrace spaces, which visually look like double skin curtain walls, also emphasize the structure and façade of the building seen in Figure 4.

Since it is possible to see the structural system of the building in some parts of the façade and on the roof, it is possible to say that their interactions have a language in terms of design decision.

B. YDA Center

YDA Center the biggest building complex in the area- has not yet been activated located in Çukurambar region in Dumlupınar Boulevard, Eskişehir road axis. YDA Center, a recently constructed high-rise architectural project. With its height (166 meters) and unusual shape (see Figure 5), YDA Center is the strongest and the most external landmark that can be seen from a distance and is apparent in the city silhouette.

As seen in Figure 6, the building is built with reinforced concrete and the core system and shear walls are used as the load-bearing system.

Figure 6: YDA Center general view [13]

Figure 6: YDA Center under construction [14, 15]

The building itself is positioned as a large mass and the construction of the building, which prevents the air circulation of Çukurambar due to its location, was completed despite the court orders. Reflective glasses are used on the façade so that the temperature level of the interior does not increase too much. Since there is no building to be shown as a precedent for this building in Ankara, the fact that its façade is so massive has been the subject of discussion. The structural system of the building has been chosen as the most suitable system in terms of price and benefit and does not have a direct interaction with its façade.

Figure 7: YDA Center façade construction [15]

V. CONCLUSION

Within its limited framework, this study has tried to put forth the interaction between structural system and curtain walls basically façades while examining with selected projects in Ankara.

In addition to the analysis about the selected buildings, it is also possible to conduct research by examining the geometric shapes of buildings with different or the same structural systems in order to detail the interaction of the structural systems of the buildings with their facades.

REFERENCES

[1] E. İrtem and G. Tığ, "Giydirme Cephe Taşiyici Sistem Profilleri için Optimum (Ekonomik) Kesit Boyutlarının Geliştirilmesi, 3," *Ulusal Çati & Cephe Kaplamalarinda Çağdaş Malzeme Ve Teknolojiler Sempozyumu*, pp. 17-18, 2006.

[2] M. S. Döndüren and A. Karaduman, "Deprem Bölgelerindeki Yüksek Katlı Betonarme Yapılarda Taşıyıcı Sistem Seçiminin Kesit Tesirlerine Etkisi," *Selçuk-Teknik Dergisi*, vol. 9, no. 2, pp. 131-143, 2010.

[3] H. Kasap, M. Necati, E. Sevim, and B. Şeber, "Perdeli-Çerçeveli Taşıyıcı Sistemli Binalarda Taşıyıcı Sistem Seçiminin Yapı Davranışı Üzerindeki Etkisinin İncelenmesi," *Academic Platform-Journal of Engineering and Science*, vol. 3, no. 1, pp. 48-55, 2015.

[4] Y. Koç, A. B. Gültekin, G. Durmuş, and Ç. B. Dikmen, "Yüksek yapı tasarımının malzeme ve taşıyıcı sistem kapsamında incelenmesi - Examination of high-rise building design in the context of material and carrier system," in *5. Uluslararası İleri Teknolojiler Sempozyumu (IATS'09)*, Karabük, Turkey, 2009.

[5] İ. T. Beyazoğlu, "Yüksek binalarda tübüler taşıyıcı sistemler ve uygulama örnekleri," [yy], 1997.

[6] F. Yılmaz, "Yüksek Binalarda Taşıyıcı Sistem Etkinliği," Fen Bilimleri Enstitüsü, 1998.

[7] F. Ş. Sezer, "Türkiye'de Metal Çerçeveli Giydirme Cephe Sistemlerinin Üretim Ve Uygulama Aşamalarının İncelenmesi," 2005.

[8] A. Ağdemir, "Giydirme cephe sistemleri ve kaplama elemanlarının incelenmesi," M. Sc. Thesis, Fen Bilimleri Enstitüsü, 2017.

[9] Z. Yilmaz, "Akilli binalar ve yenilenebilir enerji," *Tesisat Muhendisligi Dergisi,(91)*, vol. 7, p. 15, 2006.

[10] T. İnan and T. Başaran, "Çift cidarlı cepheler üzerine bir araştırma," *Megaron*, 2014.

[11] T. Özdemir and P. D. Kalaycı, "Tüketim Toplumu Bağlamında Terminal Mimarisi Ankara Yüksek Hızlı Tren Garı Örneği," *ISAS, Ankara, Turkey*, 2019.

[12] "Ankara Yüksek Hızlı Tren Garı." Arkiv. https://www.arkiv.com.tr/proje/tcdd-ankara-hizli-tren-gari/7255 (accessed Oct 18, 2022).

[13] "Konut & Ofis Projeleri." https://www.yda.com.tr/ydagroup/yda-center/ (accessed Oct 19, 2022).

[14] "YDA Center." Sektör Ankara. https://www.sektorankara.com/yda-center-ankara-trafigini-kitleyecek-iste-ayrintilar-24674h.htm (accessed Oct 19, 2022).

[15] Y. Group. "YDA Center Şantiyesi - 15 Aralık 2017." https://www.youtube.com/watch?v=W5kQDxEpqKo&ab_channel=YDAGroup (accessed Oct 19, 2022).

Design of a CMOS Operational Transconductance Amplifier for Current Controlled 2nd Order Active Filter Design

S. YAMACLI

Nuh Naci Yazgan University, Dept. of Electrical-Electronics Eng., Kayseri/Turkey, syamacli@nny.edu.tr

***Abstract* - In this work, a CMOS operational transconductance amplifier is designed for use in 2nd order controlled active filters. The developed operational transconductance amplifier employs a differential pair and a cascode current mirror in which the cascode current mirror at the output stage guarantees high output impedance. 0.35µm CMOS technology parameters are used for the verification of the designed operational transconductance amplifier in PSPICE. The results show that the gain of the operational transconductance amplifier can be varied in a wide range using the control current. After the verification of the proper operation of the operational transconductance amplifier, a 2nd order Butterworth type lowpass filter is implemented using the proposed OTA structure. The PSPICE simulation results of the active filter demonstrates the variability of its cutoff frequency easily using the control current of OTAs.**

***Keywords* – Operational transconductance amplifier, active filter design, electronically controlled.**

I. INTRODUCTION

VOLTAGE mode amplifiers are widely used for the implementation of various analogue mode circuits such as active filters, oscillators and signal processing blocks. Transistors as well as operational amplifier are used as the active element in these conventional circuits. Conventional voltage-mode operational amplifiers are utilized as a standard gain block with well-known predefined properties as having infinite input resistance, infinite voltage gain and zero output impedance at the ideal limit. The advances in integrated circuit technology enables us to have almost rail-to-rail ultra low power operational amplifiers for use in mobile devices and microwave equipment such as tablet computers and mobile phones.

The advantages of the current-mode design has also been widely studies in the literature as summarized in [1]. The main point in current-mode design stems from the utilization of low-impedance nodes in current-mode to have a much higher cutoff frequency especially in active filter designs. The importance of this wide bandwidth is also demanded by the needs of microwave or other high frequency equipment used in telecommunication devices.

The main active components used in electronics are bipolar junction transistors (BJTs) and field effect transistors (FETs). These components are current controlled current sources and voltage controlled current sources, respectively. This means that BJTs and FETs are originally employ current-mode operation. Despite this fact, circuit design is oriented towards the voltage-mode realm for a long time due to the practical voltage-mode nature of sensor and transducer elements such as microphones and antennas. However, as mentioned above, the needs of wide bandwidth circuits gives momentum for new designs and implementations of current-mode systems.

A typical analogue amplifier block can be shown as in Figure 1 where input and output can have voltage-mode or current-mode signals. The possible combinations of these modes imply the amplifier types as given in Table 1.

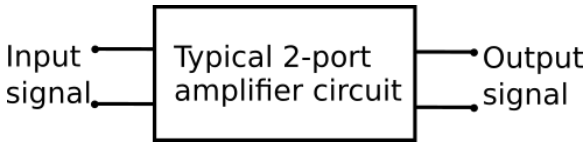

Figure 1: Typical 2-port amplifier block

Table 1: Amplifier types

Input signal	Output signal	Amplifier type
Voltage-mode	Voltage-mode	Voltage amplifier
Voltage-mode	Current-mode	Transconductance amplifier
Current-mode	Voltage-mode	Transresistance amplifier
Current-mode	Current-mode	Current amplifier

A typical operational amplifier (Opamp) block is a voltage-mode amplifier circuit per its description. The other operational type amplifier are the current operational amplifier (COA), operational transconductance amplifier (OTA) and operational transresistance amplifier (OTRA) [2-4]. Among these least known operational type amplifier, COA is the current-mode analogue of the conventional well-known voltage-mode opamp where the its definitions include an infinite current gain, zero input impedance and infinite output resistance. On the other hand, OTA and OTRA blocks differ from opamp and COA such that the gains of OTA and OTRA are not infinite but a finite, and usually controllable, value. In ideal OTA, the input impedances are again infinite and output resistance is zero. Conversely, the input impedance of OTRA

is zero while its output impedance is infinite. The finite gains and voltage to current and current to voltage conversion capabilities of OTA and OTRA blocks make them popular for the implementation of resistorless active filters and oscillators which are suitable for use inside integrated circuits. The aim of this work is the design of a high performance OTA block in complementary metal oxide semiconductor (CMOS) technology and the implementation of an electronically controlled 2nd order active filter using the designed OTA circuit. The designed OTA circuit uses a differential amplifier at the input stage and a cascode current mirror at the output stage for achieving high impedance at the output stage. The variation of the gain of the OTA with the control current is demonstrated and it is also shown that the cutoff frequency of the active filter employing the designed OTA can be changes in a wide range.

II. CMOS OPERATIONAL TRANSCONDUCTANCE AMPLIFIER (OTA) DESIGN

Operational transconductance amplifiers are required to generate output current signal proportional to the difference at its input signals. The circuit symbol and the defining equations of the operational transconductance amplifier is given in Figure 2 and Equation (1), respectively.

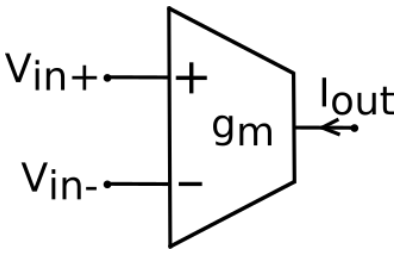

Figure 2: Circuit symbol of OTA

$$I_{out} = g_m(V_{in+} - V_{in-}) \quad (1)$$

The transconductance of the operational amplifier, denoted by gm in Equation (2), can be electronically controlled in most designs therefore enabling the circuit designer to implement electronically controllable circuits.

The operational transconductance amplifier circuits usually contain a differential amplifier as the input stage while some form of current source as the output stage. In this study, a standard CMOS differential pair is used at the input stage while a high performance cascode class-AB current mirror is utilized at the output stage for achieving high output resistance to make the operational transconductance amplifier drive moderate level loads.The designed CMOS operational transconductance amplifier is shown in Figure 3.

The designed operational transconductance amplifier circuit consists of two main stages: the differential amplifier at the input stage and a class-AB cascode current mirror. The circuit is meant to operate with symmetrical power supply denoted by V_{DD} and V_{SS} in Figure 3.

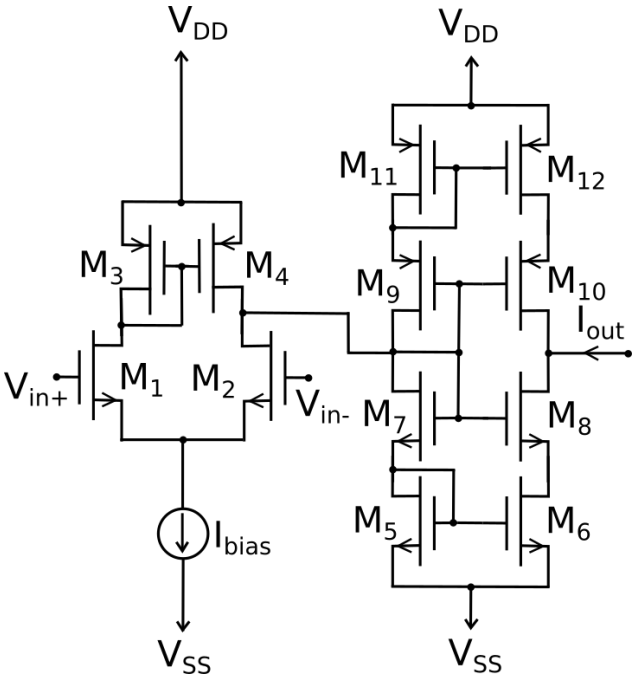

Figure 3: Designed CMOS OTA circuit

The transistors M_1 and M_2 are the input transistors while M_3 and M_4 form active loads for M_1 and M_2. I_{bias} provides the quiescent current for setting the operating point for the input stage. The gain of the operational transconductance amplifier can be varied using I_{bias}. The output current of the input stage is taken from the drain node of M_2 and fed to the class-AB cascode current mirror consisting of the transistors M_5-M_{12}. The reason for the utilization of the cascode current mirrors is to increase the output impedance of the operational transconductance amplifier.

The gain of the operational transconductance amplifier can be expressed as follows [5]:

$$g_m = \sqrt{k_n . I_{bias} . \left(\frac{W}{L}\right)_1} \quad (2)$$

In Equation (2), k_n is the gain parameter and $(W/L)_1$ is the aspect ratio of the input transistor M_1.

The designed operational transconductance amplifier circuit is simulated in PSPICE environment using the 0.35μm process parameters. The aspect ratios of the PMOS transistors are taken as 2.5 times higher than those of the NMOS transistors considering that the mobility of negative charge carriers is approximately 2.5 times higher than the mobility of positive charge carriers in silicon processes [5].

The device characteristics of the operational transconductance amplifier are shown in Figures 4, 5, 6 and 7. The DC input-output gain characteristic is given in Figure 4. In Figure 5, the AC response of the input-output transfer curve is shown. Figure 6 and Figure 7 show the frequency dependent impedance characteristics of the input and output terminals of the operational transconductance amplifier.

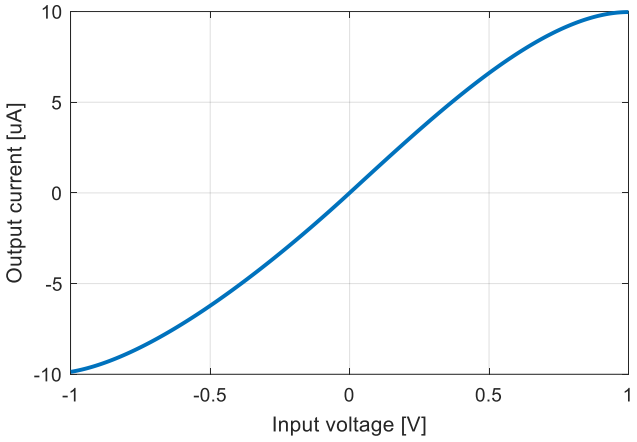

Figure 4: Input-output DC characteristic of the designed OTA

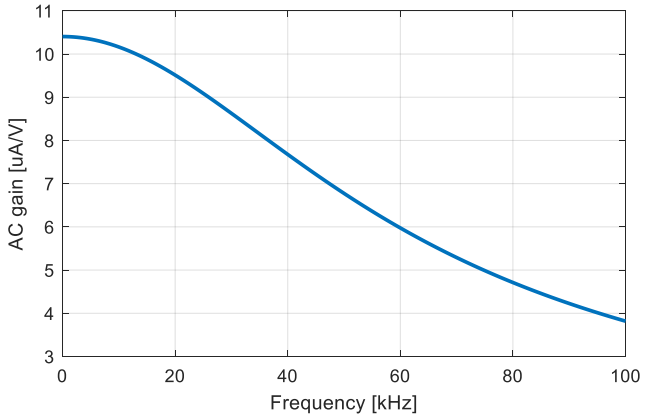

Figure 5: AC gain-frequency variation of the designed OTA

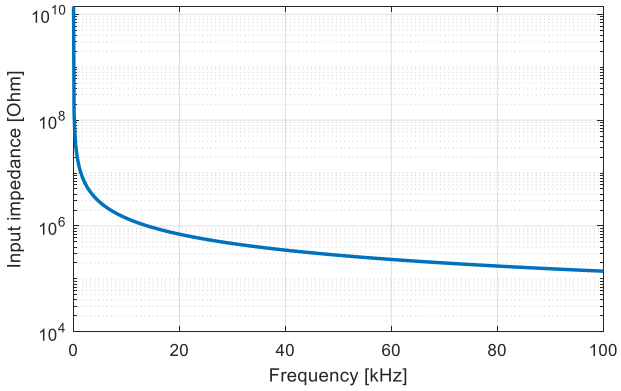

Figure 6: Input impedance-frequency variation of the OTA

Figure 4 shows that the designed OTA has a quite well linear input-output characteristics in the [-1V, 1V] input voltage range. The AC gain of the OTA has the value of g_m=11.38µA/V and the bandwidth of this gain is 42kHz, as observed from Figure 5, which makes this design suitable for audio applications. Figure 6 shows the variation of the input impedance with the frequency. The input stages has the gate nodes of the input transistors M_1 and M_2 therefore it is expected to have high resistance. Figure 6 demonstrates that the input impedance has the value of R_{inp}=138.46MΩ at f=100Hz indicating the verification of the high input impedance. The output resistance of the designed OTA has the value of R_{out}=1.42MΩ indicating that the employed cascode current mirrors at the output stage enables to drive relatively higher impedance loads. It is worth noting that these gain values are for the control current value of I_{bias}=10µA. As it was indicated before, the main advantage of an operational transconductance amplifier is the ability to control its gain using the control current, which is denoted by I_{bias} in our circuit. Therefore, the AC gain of the designed operational transconductance amplifier is simulated in PSPICE for different I_{bias} values as shown in Figure 7. Figure 7 implies that the AC gain of the operational transconductance amplifier can be varied using the control current I_{bias} as expected.

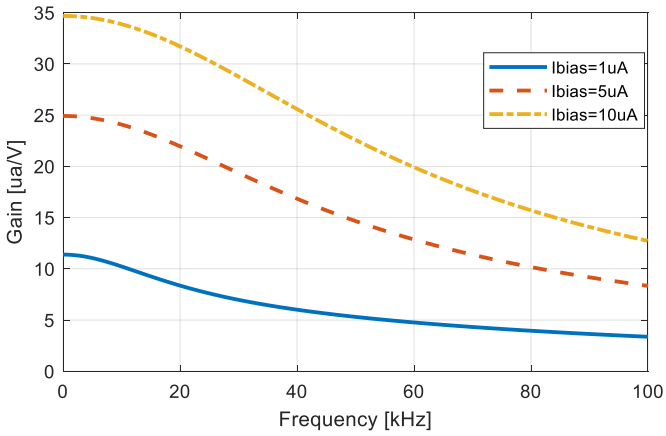

Figure 7: Gain-frequency characteristics of the designed OTA for different control (bias) current values

III. IMPLEMENTATION OF A 2ND ORDER ELECTRONICALLY CONTROLLED LOWPASS FILTER USING THE DESIGNED OTA

A generic 2nd order lowpass filter is implemented using the designed operational transconductance amplifier in this section. The designed filter employs two operational transconductance amplifier and two capacitors as shown in Figure 8 [5]. The filter does not contain any resistor or inductor components making it suitable for realization inside integrated circuits depending on the value of the capacitors.

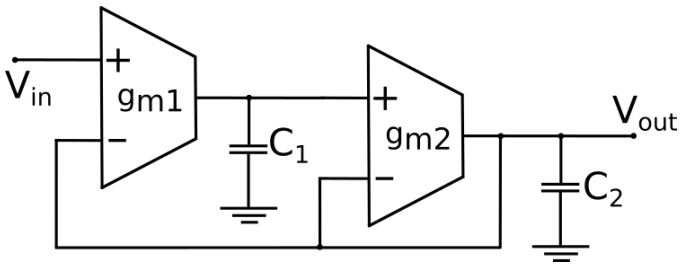

Figure 8: A 2nd order active lowpass filter using OTAs [5]

The transfer function of the filter shown in Figure 8 can be expressed as follows:

$$T(s)=\frac{V_{out}(s)}{V_{in}(s)}=\frac{b_0}{s^2+b_1 s+b_0} \tag{3}$$

It is worth noting that the constant term in the numerator is equal to the constant term of the denominator. The coefficients of the denominator polynomial is expressed as follows [5]:

$$b_1=\frac{g_{m2}}{C_2} \tag{4}$$

$$b_0=\frac{g_{m1}g_{m2}}{C_1C_2} \tag{5}$$

The cutoff frequency and the quality factor of the filter can be derived from b_1 and b_2 as in Equations (6) and (7), respectively.

$$f_c=\frac{1}{2\pi}\sqrt{\frac{g_{m1}g_{m2}}{C_1C_2}} \tag{6}$$

$$Q=\sqrt{\frac{g_{m1}C_2}{g_{m2}C_1}} \tag{7}$$

The cutoff frequency and the quality factor of the filter can be varied using g_{m1} and g_{m2} which in turn are controlled by I_{bias1} and I_{bias2}, respectively.

The implemented filter is also simulated in PSPICE with the control currents of operational transconductance amplifiers adjusted as $I_{bias1}=I_{bias2}=1\mu A$, $I_{bias1}=I_{bias2}=5\mu A$ and $I_{bias1}=I_{bias2}=10\mu A$. The values of the capacitors are taken as $C_1=10nF$ and $C_2=20nF$ therefore the quality factor of the filter is set as Q=0.707 making it a Butterworth type 2nd order filter. It is worth noting that the quality factor of the filter and the cutoff frequency can be adjusted independently using the capacitor values and the gains of the OTAs. The gain-frequency characteristics of the filter for different control currents are plotted in Figure 9 in the same axis pair.

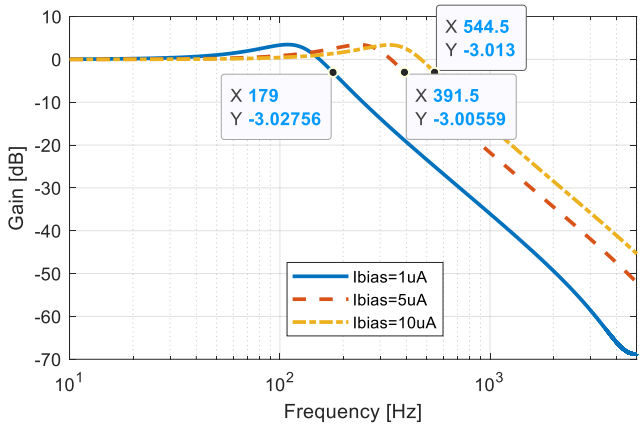

Figure 9: Gain-frequency response of the implemented filter for the control currents of 1μA (–), 5μA (--) and 10μA(-.-)

The -3dB cutoff frequencies for different control currents are also shown on the curves of Figure 9. As it can be seen from Figure 9, the cutoff frequency of the filter can clearly be adjusted using the control (bias) currents of the operational transconductance amplifiers. The -3dB cutoff frequencies for $I_{bias}=1\mu A$, $I_{bias}=5\mu A$ and $I_{bias}=10\mu A$ are obtained as $f_c=179Hz$, $f_c=391.5Hz$ and $f_c=544.5Hz$, respectively. Combining Equation (2) and Equation (6) for the same control (bias) currents for OTAs, in other words $I_{bias1}=I_{bias2}$ leads the cutoff frequency dependent on the control (bias) currents of the OTAs as follows:

$$f_c=\frac{1}{2\pi}\sqrt{\frac{k_n.\left(\frac{W}{L}\right)_1}{C_1C_2}}.\sqrt{I_{bias1}} \tag{8}$$

Therefore, theoretically the cutoff frequency is proportional to the square root of the control current. The cutoff frequencies obtained from the PSPICE simulations follow this expectation as it is shown in Table 2, which shows theoretical and observed cutoff frequencies.

Table 2: Theoretical and observed cutoff frequencies of the filter dependent on the control currents of OTAs

Control current	Theoretical cutoff frequency	Observed cutoff frequency
$I_{bias}=1\mu A$	174Hz	179Hz
$I_{bias}=5\mu A$	389Hz	391.5Hz
$I_{bias}=10\mu A$	548.5Hz	544.5Hz

As it can be seen from Table 2, the obtained cutoff frequencies for different control currents are compatible with the expected theoretical values. On the other hand, the designed 2nd order active filter can be used as an audio filter which require electronically tunable cutoff frequencies such as required in equalizer applications.

IV. CONCLUSIONS

A CMOS operational transconductance amplifier circuit is designed in this study for the implementation of current controlled active filter design. The CMOS operational transconductance amplifier consists of a differential amplifier as the input stage and a class-AB cascode current mirrors at the output stage. The reason for the utilization of cascode current mirrors is to increase the output impedance since the operational transconductance amplifier is a current-output device whose output impedance is ideally infinite according to the Norton equivalent circuit. The output impedance of a typical differential pair is on the order of a few kΩ while the utilization of the cascode current mirrors in the designed OTA has the value of R_{out}=1.42MΩ. Moreover, the designed OTA includes a biasing current which can be used as a control current for adjusting its gain. The PSPICE simulations of the designed OTA shows that its gain can be controlled in a wide range and the gain value has the values of g_{m1}=11.38µA/V, g_{m2}=24.91µA/V and g_{m3}=34.68µA/V for the control (bias) currents of I_{bias1}=1µA, I_{bias2}=5µA and I_{bias3}=10µA, respectively. Then, a 2nd order active lowpass filter is implemented using the designed operational transconductance amplifier. The quality factor of the filter is set as Q=0.707 for having a Butterworth type characteristic. The frequency-domain SPICE simulations of the filter shows that the filter operates as expected and that the cutoff frequency of the filter can be adjusted using the control (bias) currents of the OTAs. The filter is shown to have the cutoff frequency values of f_c=179Hz, f_c=391.5Hz and f_c=544.5Hz for the control (bias) currents of I_{bias1}=1µA, I_{bias2}=5µA and I_{bias3}=10µA, respectively. It is observed that these cutoff frequencies are close to the theoretically expected values.

REFERENCES

[1] C. Toumazou, *Analogue I.C.Design: The Current-mode Approach*. New York: IEEE Press, 1993.

[2] H. Kuntman, and D. Ozenli, "Current Operational Amplifiers" in *Trends in Circuit Design for Analog Signal Processing*. New York: Springer, 2022.

[3] M.N. Sabry, H. Omran, and M. Dessouky, "Systematic design and optimization of operational transconductance amplifier using gm/ID design methodology", *Microelectronics Journal*, vol. 75, pp. 87-96, 2018.

[4] G. Komanapalli, R. Pandey, and N. Pandey, "New sinusoidal oscillator configurations using operational transresistance amplifier", *International Journal of Circuit Theory and Applications*, vol. 47, pp. 666-685, 2019.

[5] H. Kuntman, *Analog MOS Tümdevre Tekniği*, Istanbul: İTÜ Yayınları, 1998.

Biomass Energy Potential, Its Current Usage Status, and Developments in Biomass Energy Production Systems in Turkey

Faruk KÖSE[1] and Suleyman KOSE [2]

[1] Department of Mechanical Engineering, Konya Technical University, Konya, Türkiye, fkose@ktun.edu.tr
[2] Energy 2050, Department of Mechanical Engineering, Faculty of Engineering, University of Sheffield, Sheffield, UK, skose1@sheffield.ac.uk

Abstract **- Among renewable energy sources, biomass energy is the most widespread and has the highest capacity in the world. Even at the poles, which receive the least amount of sunlight in the world, some plants that are a source of biomass can be grown during a short period of the year. In addition, animal and human wastes living in these regions also constitute biomass energy sources. Therefore, it is possible to access biomass energy sources in all regions of the world where people can live. Since Turkey is located in the middle climate zone such as 36-42 latitudes in the northern hemisphere, it has more biomass energy resources than the cold climate countries located further north of Turkey and the desert climate countries located further south of Turkey. In this study, the total biomass potentials of the world and Turkey are given and Turkey's current utilization status is considered. The types of biomass from which energy is produced in Turkey and the installed, licensed and planned power generation values are given. Finally, the systems used in energy production from biomass, the efficiency improvement methods applied on these systems, and domestic biomass energy production practises are included in this current study.**

Keywords: Biomass energy, Biomass energy systems, Energy, Turkey biomass energy potential.

I. INTRODUCTION

Biomass is defined as the total mass of living organisms belonging to a species or a community of several species at a given time. Biomass is also recognized as an organic carbon in the sense of fuel. The world's bioenergy capacity (installed capacity) in 2021 is 143,371 MW and Turkey's is 1,641 MW. The world's total installed capacity for solid biofuels and renewable waste in 2021 is 119,213 MW, while Turkey's is 622 MW. The total renewable municipal waste capacity in the world is 19,520 MW and in Turkey it is 17 MW. The world total power value for other solid fuels is 79,043 MW and for Turkey this biofuels power is 605 MW. While the world's total power capacity of liquid biofuels is 2,584 MW, in Turkey it is 19 MW. The world total biogas plant power is 21,574 MW and Turkey's total power is 1,000 MW [1]. In Turkey, the Energy Market Regulatory Authority (EMRA), which is the official institution responsible for the licensing of electricity generation plants, the installation and commissioning of the power plant, the delivery of the generated electricity to the system and the termination of the license, also publishes annual reports on this subject [2]. Köse et al. [3] investigated the effect of different binder materials on the properties of biofuel pellets produced from MDF and pine wood sawdust waste. Kazaz [4] investigated Turkey's agricultural and animal-based biomass energy potential. According to 2017 data in this study, the total cultivated area is 15,856,351 hectares and an average of 436,049,652.5 tons of dry biomass can be obtained from this area, which is 176,600,109.3 Tons of Oil Equivalent (TOE) and biomass, equivalent to 2,053,859 MW of energy. The current amount of animal waste in Turkey is 96,655,868.2 tons and 4,309,771,357 m^3/year of biogas can be obtained from these wastes and this biogas is equivalent to $2.03x10^{10}$ kWh/year of electrical energy [4]. Köse [5] investigated the effect of co-fermentation (co-fermentation of multiple substances) and thermal insulation on biogas production and noted that co-fermentation can increase biogas production up to 2-3 times of the normal single product dependent system. Thermal insulation is also important to keep the biogas-producing bacteria at the optimum operating temperature so that production is economical, does not decrease and is not interrupted [5].

Vural [6] obtained a 30 percent increase in the specific energy value of total biogas production by applying ultrasound for various durations to the sludge taken from the secondary digestion tank of the agricultural biogas production plant. Çilingir [7] applied microwave pre-treatments to chicken manure prepared under three different acidic conditions and two different alkaline conditions (pH values of 10 and 12) at three different powers (300, 450 and 600W) and three different application times (2, 4 and 6 minutes). According to the results obtained from only microwave treated wastes, the maximum yield was obtained at 300 W microwave power at 6 minutes application time with a 50% increase in the amount of bio methane potential.

Köse [8], by designing a biogas production system to be heated with solar energy, stated that the required heating energy for the biogas plant to be established in rural areas, especially in winter months, can be met with hot water provided by solar collectors. In the system, in addition to the solar collectors that can be sufficient in winter months, there is also a boiler where the biogas produced can be burned, and the whole system will be able to meet the house's hot water, heating, kitchen gas and heating needs of the biogas fermenter throughout the year when solar energy is not sufficient [8].

The potential values of biomass energy resources in Turkey and the amount of energy that can be produced from these resources can be determined by utilizing the Biomass Energy Potential Atlas (BEPA) data of the Ministry of Energy and Natural Resources (MENR) [9]. Turkey's electricity generation values from different sources, their ratios to total generation and their annual comparisons are taken from the

data of Turkish Electricity Transmission Corporation (TEIAS) [10].

II. BIOMASS ENERGY

Biomass energy is an important energy source for renewable energy sources. It is a type of energy obtained from all kinds of organic waste (plants, grasses, algae, animal manure, sewage water, organic garbage waste and industrial waste). Biomass is a plant organism that stores solar energy through photosynthesis. Organic matter consumes carbon dioxide through photosynthesis and releases oxygen into the atmosphere necessary for the respiration of living organisms. The carbon dioxide produced by the burning of this organic matter replaces the carbon dioxide consumed during photosynthesis. The main characteristic of classical biomass energy utilization is that energy from biomass is obtained by direct combustion technique with various combustion devices. Modern biomass sources are energy forestry products (poplar, willow, eucalyptus) and forest and wood industry waste. The capacity factor (Cp) value, which indicates the efficiency of power generation systems, can be calculated by expression (1) [4].

$$C_p = \frac{Existing\ generated\ energy}{Therotical\ energy\ to\ be\ generated} \qquad (1)$$

At the end of 2021, when Turkey's biomass installed capacity is compared to solar installed capacity, biomass is 4.75 times smaller than solar power, but its contribution to the electricity generation is 1.74 times less. The capacity factor of biomass is quite high with Cp=52.8%, which is 2.72 times higher than the solar Cp=19.4% [2]. Table 1 shows the number of power plants, installed capacity and the ratio of installed capacity to total capacity by source in Turkey in September 2022. Accordingly, the natural gas power plant has the highest power and share of 25,295.1 MW and 24.73%, while the biomass power plant ranks 8th with 1,822.9 MW and 1.78%, respectively. The total number of power plants is 11,142 and the total installed capacity is 102,280.9 MW [8].

Table 1: Turkey's September 2022 power plant numbers, installed capacity and ratios of installed capacity to total value by energy source [8]

Primary Source	Number of Plant	Installed Power (MW)	Installed Power Rate, %
River Hydro	609	8,293.00	8.11
Dam Hydro	141	23,275.20	22.76
Wind	357	11,199.20	10.95
Solar	9,071	8,961.70	8.76
Biomass	383	1,822. 90	1.78
Geothermal	63	1,686.30	1.65
Natural Gas	344	25,295.10	24.73
Lignite	46	10,136.50	9.91
Imported Coal	16	9,713.80	9.50
Hard Coal	4	840.8	0.82
Asphalte, Coal	1	405	0.40
Waste Heat	95	391.8	0.38
Fuel Oil	9	251.9	0.25
Naphtha	1	4.7	0.00
LNG+Diesel	2	3	0.00
Total	11,142	102,280.90	100.00

Figure 1 and Table 2 shows the 10-year total biomass electricity production and power capacity values of the world countries between 2011 and 2020, and the production of approximately 330,000 GWh in 2011 increased to 580,000 GWh in 2020, an increase of 75% in 10 years [1].

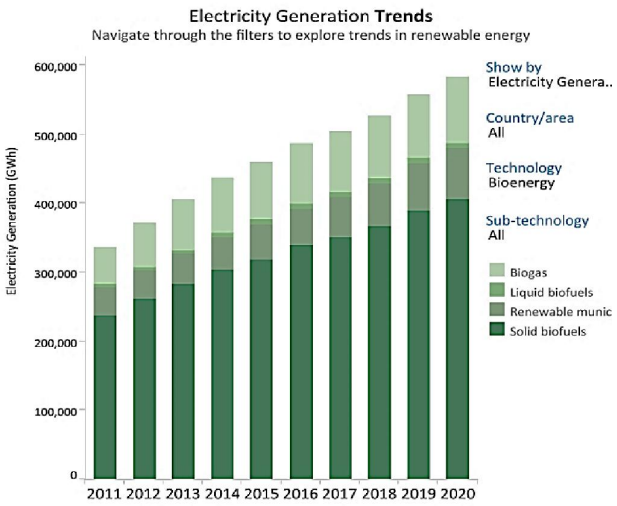

Figure 1: Total electricity production from biomass in the world for the 10-year period between 2011 and 2020 [1]

III. MAIN SOURCES OF BIOMASS

Biomass energy sources are not unified like fossil energy sources, but are spread across the earth. Therefore, harvesting large quantities of biomass resources for energy production significantly increases the cost. According to the Biomass Energy Potential Atlas (BEPA) prepared by the Ministry of Energy and Natural Resources to determine the biomass energy potential, the total economic energy equivalent of only our wastes is around 3.9 MTOE/year (MTOE: Million Tons of Oil Equivalent) [2].

Table 2: Turkey and world biomass installed capacity values in 2021 [1]

Biomass variety	Türkiye, MW	World, MW
Solid biofuels + Renewable waste	622	119,213
Municipal wastes	17	19,520
Other solid fuels	505	79,043
Liquid biofuels	19	2,584
Biogas	1,000	21,574
Bioenergy	1,641	143,371
Total	3.804,0	367.737,0

Bioenergy is currently the largest contributor to the global renewable energy mix and its share is expected to more than double by 2030 according to the International Energy Agency-World Energy Outlook (IEA-WEO) (Figure 2). Thus, in relation to the 2030 Agenda for Sustainable Development, bioenergy is expected to make critical contributions to the Sustainable Development Goals (Climate Action and Clean and Accessible Energy) [11].

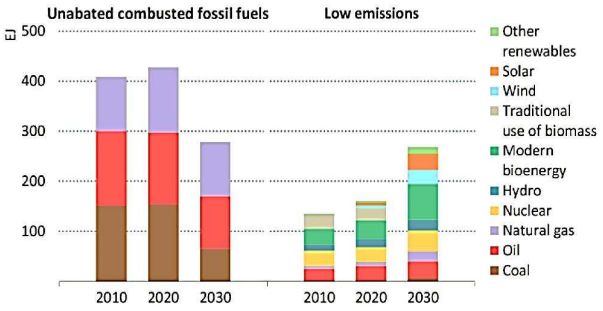

Figure 2: Changes in world energy consumption (EJ) in 2010, 2020 and 2030 according to the current use of fossil resources and the use of low emission resources [11]

A. Turkey's Biomass Potential

The total cultivated area in Turkey is 15,856,351 hectares and the average amount of dry biomass that can be obtained from this area is 436,049,652.5 tons. The average dry biomass energy value of this area is 176,600,109.3 TOE (Tons of Oil Equivalent). This dry biomass is equivalent to 2,053,859 MW of energy. The total number of animals used for biomass resource is 408,561,087. The amount of animal waste in Turkey is 96,655,868.19 tons. Only 4,309,771,357 m^3/year of biogas can be obtained from these wastes. This biogas is equivalent to $2.03x10^{10}$kWh/year≅20 Billion kWh of electrical energy [4].

Turkey's total biomass installed power capacity between 2011 and 2021 is given in Figure 3, which is approximately 90 MW in 2011 and reached 1,600 MW in 2021 [1]. Figure 4 shows Turkey's total biomass electricity production values between 2011 and 2020, which increased 15 times in 10 years from approximately 300 GWh/year in 2011 to 4,500 GWh/year in 2020 [1].

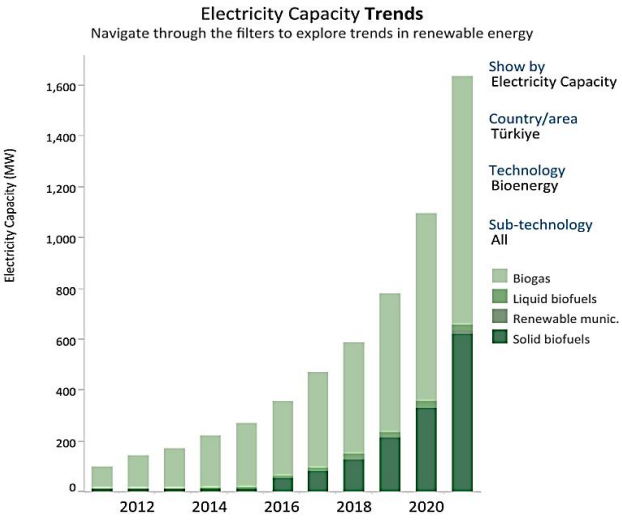

Figure 3: Total annual biomass electricity installed capacity values between 2011 and 2020 in Turkey [1]

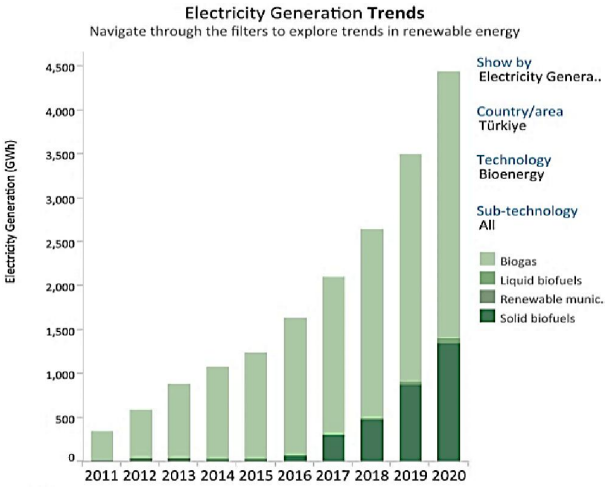

Figure 4: Turkey's total annual biomass electricity generation values between 2011 and 2020 [1]

According to the Biomass Energy Potential Atlas (MENR-BEPA) prepared by the Ministry of Energy and Natural Resources, the total gross biomass potential of Turkey is 34,002,549.6 TOE/year [9]. Plant and animal wastes contribute the highest amount to this total value with 29,769,639.50 TOE/year. Municipal waste (municipal garbage and sewage) is the second potential waste with 2,906,130.1 TOE/year and forestry waste is the third potential waste with 859,898.70 TOE/year. When we convert these annual TEP potential values to kWh/year with a conversion rate of 1TEP=11,628 kWh, we find that the total biomass potential is 395,381,646,748.8 kWh/year ($39.5x10^{10}$kWh/year or 395,381.65 GWh/year). This biomass potential value is 23% higher than Turkey's total approximate electrical energy consumption value of 320 billion kWh/year in recent years [9].

IV. BIOMASS ENERGY PRODUCTION SYSTEMS

The systems and technologies used in energy production from biomass vary according to the type and content of the biomass material to be produced are given in Figure 5.

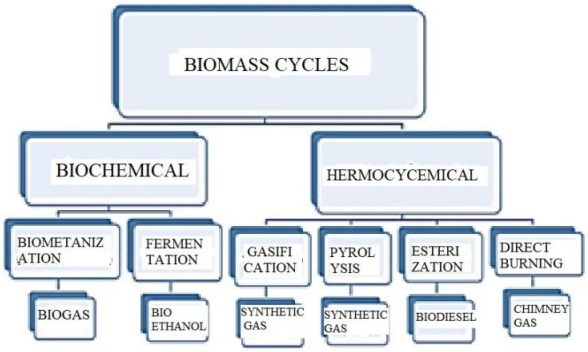

Figure 5: Classification of biomass energy production systems

A. Energy Generation Systems by Burning Biomass

The process of burning biomass is different from burning fossil fuels. Therefore, environmental pollution and CO_2 emissions from the combustion of biomass are lower than when fossil fuels are burned [4]. City garbage, sewage waste and animal manure are not suitable for energy production through incineration, but are more suitable for biogas production. Various agricultural products and wastes can be used for pellet production as raw material, towards the purpose of biomass fuel production [12]. Pelletizing and briquetting and incineration systems for forest products are given in Figures 6 and 7.

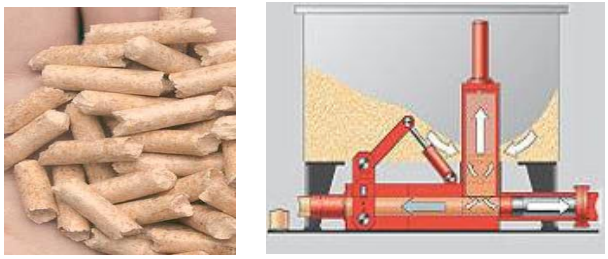

Figure 6: Pellet (left) and briquette making machine (right) for burning biomass

Figure 7: Pellet biomass combustion system (left), and fluidized bed combustion system (right)

B. Liquid Bio Fuel (Bio benzene, Biodiesel, Ethanol) Production Systems

The liquid fuel production cycle from biomass is carried out in liquid biofuel production plants with coal, biomass and algae. Figures of these production systems are given in Figure 8.

Figure 8: Fuel production cycle from biomass and liquid biofuel production plants from coal, biomass and algae

"Ethanol", a liquid biofuel, is produced from sugar, starch or cellulose residues (wood, crops, city garbage, etc.). In the US and Brazil, ethanol production by fermentation from corn is widespread. In this industry, corn mills produce corn oil, animal feed and ethanol. "Methanol" is a biofuel derived from biomass (distillation of wood, etc.) and is used in diesel engines (Figure 9).

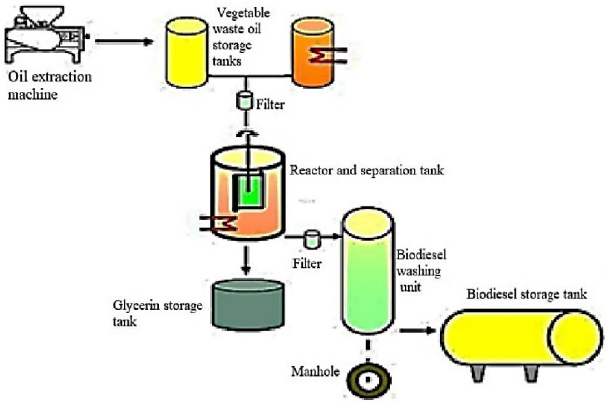

Figure 9: Process flow chart of biodiesel plant with 100 lt/batch capacity

C. Systems for Biogas Production

Biogas is a gas mixture resulting from the fermentation of organic-based residues in an oxygen-free (anaerobic) environment and is lighter than air, colourless, odourless, burning with a bright blue flame. It is a gas mixture containing 50-75% methane, 25-50% carbon dioxide, 0-3% hydrogen sulphide and very small amounts of nitrogen and hydrogen depending on the structure of the organic materials in its composition. The formation of biogas takes place in the following stages: 1-Fermentation and Hydrolysis, 2-Formation of Acetic Acid, 3-Formation of Methane Gas.

Reactor (fermenter) temperature has a great impact on the biogas production process. Methane bacteria, which are activated in the third stage of anaerobic fermentation and lead to methane formation, are divided into three groups according to the temperature of the fermentation environment:

1-Sacrophilic (psychrophilic) bacteria; (5-30)^{o}C,
2-Mesophilic (mesophilic) bacteria; (30-40)^{o}C,
3-Thermophilic (thermophilic) bacteria; (50-60)^{o}C.

Co-fermentation (fermentation of multiple substances together) can increase biogas production up to 2-3 times that of a normal single-product system [5]. For example, adding frying oil, stubble and hay to cattle manure. The size and design of biogas production facilities can be in three different forms according to the user purpose;

1-Family type (6 -12 m^3),
2-Farm and village type (50-100-150 m^3), and
3-Industrial scale facility (1,000-10,000 m^3).

Figure 10 shows a small family type biogas production system [5, 8]. This system has been designed with hand filling and mixing so that it can be operated very economically. In the large industrial biogas production systems shown in Figure 11,

the biogas generators (fermenters) consist of two parts and are called primary and secondary fermenters (digestion tanks).

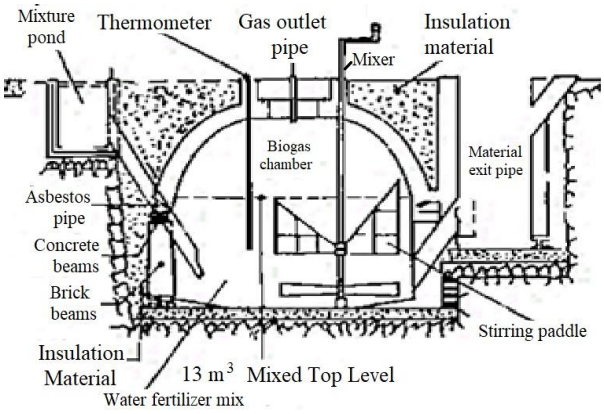

Figure 10: A small family type biogas production system

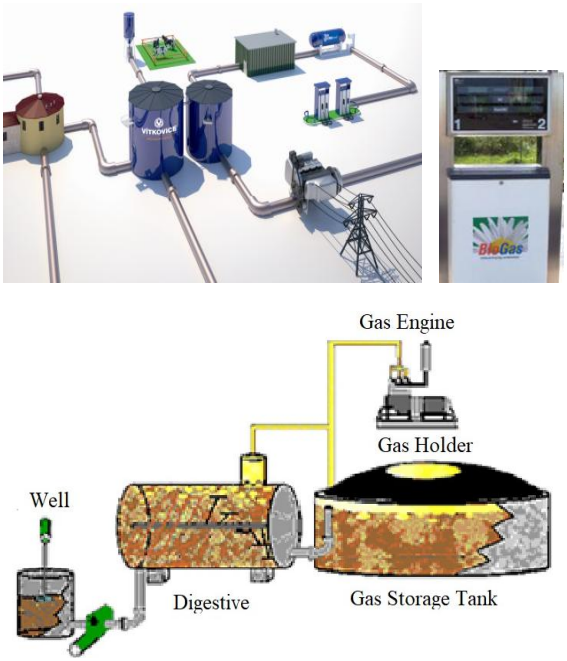

Figure 11: Large biogas production systems from biomass and biogas vehicle fuel filling station (top)

1) Systems and methods for increasing the efficiency of biogas production systems

The application of ultrasound to the sludge from the secondary digestion tank of the agricultural biogas production plant for various durations also showed that the anaerobic digestion efficiency of the biogas production plant residual biomass increased with increasing ultrasound specific energy. A 21% per cent increase in total biogas production was observed with a specific energy of 2334 kJ/kgTS (TS: Total Solid). As a result of the experiment with the residual biomass taken from anaerobic digestion process of the wastewater treatment plant, it was observed that ultrasonic pre-treatment has a greater effect on the digestion efficiency of this biomass and the anaerobic digestion rate of this biomass is higher. It was observed that by applying specific energy of 1122 kJ/kgTS and 5413 kJ/kgTS to this sludge, 90 percent of the biogas production was completed in 13 and 10 days, respectively, and the total biogas production increased by 30 percent at a specific energy value of 5413 kJ/kgTS [6]. In another study, microwave pretreatments has been applied to chicken manure prepared under three different acidic conditions and two different alkaline conditions (pH values of 10 and 12) at three different powers (300, 450 and 600W) and three different application times (2, 4 and 6 minutes) [7]. According to the results obtained from only microwave treated wastes, the maximum yield was obtained at 300 W microwave power at 6 minutes application time with a 50% increase in the amount of bio methane potential [7]. Biogas production increases 2-3 times by co-fermenting different organic products such as animal manure, cooking oil waste and dry grass.

V. CONCLUSION

The current study presented that Turkey's biomass energy potential is 23% higher than the its current electricity consumption and the installation of biomass electricity generation systems is continuously increasing year by year. It is also highlighted that more energy has been produced from biomass in recent years with new methods and systems developed with the contribution of scientific studies.

REFERENCES

[1] IRENA (2022), Renewable Energy Statistics 2022, The International Renewable Energy Agency, Abu Dhabi. ISBN: 978-92-9260-428-8
[2] EPDK, Enerji Piyasası Düzenleme Kurumu 2021 Yılı Faaliyet Raporu, 15 Nisan 2022, Ankara.
[3] Kose, F., Kaya, M.N., Aksoy, M.H., Tuplek, A., 2015, Effect of Different Binding Materials on The Properties of Biofuel Pellets Produced From MDF and Dush Pine Wood Sawdust Waste, 2nt International Conference on Energy and Enwronment, 18-19 June 2015, Guimaraes, Portugal.
[4] Kazaz, O., 2018, Biomass Energy Potentıal of Turkey, Yüksek Lisans Tezi, Çukurova Üniversitesi F.B.E., Makine Müh. Anabilim Dalı, Adana.
[5] Köse, F., 2007, Biyogaz Üretim Tesisi Tasarımında Kofermantasyon ve Isı Yalıtımının Etkisi, IV. Yeni ve Yenilenebilir Enerji Kaynakları Sempozyumu, 23-24 Kasım 2007, Kayseri.
[6] Vural, M., Ultrasonik Ön Aritmanin Tarımsal Biyogaz Tesislerinden Çıkan Artik Biyokütlenin Anaerobik Çürütme Verimine Etkisi, Y.Lisans Tezi, İ.T.Ü. F.B.Enstitüsü, Çevre Müh. Anabilim Dalı, 2011. İstanbul.
[7] Çilingir, E.Ç., Mikrodalga Destekli Asit ve Alkali Ön Arıtımın Tavuk Atıklarından Biyogaz Üretimine Etkisi, Yük. Lisans Tezi, Hacettepe Üniversitesi F.B.Enstitüsü, Çevre Müh. Anabilim Dalı, 2018. Ankara.
[8] Köse, F., "Güneş Isıtmalı Biyogaz Uretimi", Enerji Workshop-1 Alternatif Enerji Kaynakları, Bildiriler Kitabı Sayfa, 94-100, 15-16 Ekim 1998, Konya.
[9] ETKB, Enerji ve Tabii Kaynaklar Bakanlığı, url: https://enerji.gov.tr/eigm-yenilenebilir-enerji-kaynaklar-biyokutle
[10] TEİAŞ, Türkiye Elektrik İletim A.Ş., Url: teias.gov.tr.
[11] IEA, International Energy Agency Bioenergy Annual Report 2022. Url: Bioenergy - Fuels & Technologies - IEA
[12] Acaroglu, M., Baser, E., Aydogan, H., Canli, E., A new energy crop onopordum spp.: A research on biofuel properties, Energy 261 (2022) 125305.

Investigation of Energy Supply of a Residential Area from Renewable Energy Sources: The Case of "Our City-Konya Project"*

Faruk KÖSE[1] and İlhan KOÇ[2]

[1] Department of Mechanical Engineering, Konya Technical University, Konya, Türkiye, fkose@ktun.edu.tr
[2]Department of Architecture, Konya Technical University, Konya, Türkiye, ikoc@ktun.edu.tr

Abstract **- Approximately 25% of the total energy consumed in the world is used in residences. Considering that approximately 80% of the total energy consumption is from fossil fuels polluting the environment, it is seen that the energy sources used in settlements have an effect of 20% on environmental pollution and greenhouse effect. In this article it has been investigated whether the entire energy of the settlements can be produced by using renewable energies, mainly solar and wind energy. This research was carried out in an exemplary settlement in Konya within the scope of the "Our City-Konya" project completed in November 2019, which was prepared for the Ministry of Environment Urbanization and Climate Change. Developing designs within the framework of environmentally sensitive and sustainable approaches in urban planning are the goals and basic principles of the strategy plan. Within the framework of these principles, it is important to reduce the deteriorating global climate effects by providing renewable energy production and efficiency in settlements. In this context, measures have been taken in design studies of the field in order to provide energy efficiency in urban design work and to reduce the negative effects of climate change. Within the scope of the study targeting the concepts of ecological (environmental) and sustainable cities it is aimed to set an example for new applications to be made in the project concept. Türkiye has a very good potential in terms of solar and wind energy capacity from renewable energy sources. Especially in Konya, in which the research area is existed, the potential for solar energy is quite high. In the area planned to have a population of 20,000, buildings are designed as detached block of 2, 4 and 6 storey. It has been determined that it may be possible to meet the heating energy of the settlement with soil and solar heat pumps in winter, but the cost will be very high in today's conditions. It has been designed that the electrical energy and hot water needs of all residences, including official and social facilities in the planning area, can be met with solar PV-T and wind energy systems suitable for the settlement.**

Keywords **- Energy, Renewable energy, Ecological design, Urban design, Buildings producing their own energy.**

I. INTRODUCTION

In 2017, despite a 70% increase in renewable energy generation worldwide, energy-related carbon dioxide (CO_2) emissions globally increased by 1.4%, after three years of stagnation. The reasons for this increase are the large global economic growth (3.7%) combined with low fossil energy prices and weak energy efficiency efforts [1]. But despite this poor outlook, renewable power generation capacity saw the largest annual increase ever (9%), at around 178 GW per year. New solar photovoltaic generation capacity alone increased by 55%. The increase was 29% for wind and 11% for hydropower [1].

As in 2016, renewable energy accounts for around 18.2% of total global final energy consumption. Of this amount, 10.4% is provided by renewable clean energies (solar, wind, wave, etc.) [1]. According to 2015 calculations, Turkey produces approximately 25% of the total energy it consumes and imports 75% of it. As a country that imports a large amount of the energy it uses, it is a fact that it has to spend a large portion of its gross national product on energy. The types of energy it supplies as total primary energy consist of fossil energy sources (oil 31%, coal 27%, natural gas 28%), which cause global warming and thus human health and environmental pollution. Although these constitute the majority, the total proportion of fossil energy sources offered in the country is 87.6% [2]. Renewable energy sources constitute 12.1% of the total supply. Of this, 2.5% is made up of biofuels and wastes, which also produce dirty gases and waste. The remaining 9.6% is made up of water (hydroelectric) (4.4%), geothermal (3.7%), wind (0.8%) and solar (0.7%) energies known as renewable and clean energy (Figure 1) [2].

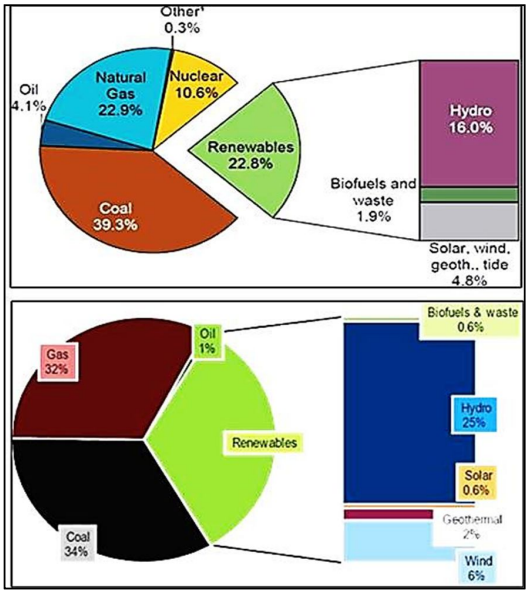

Figure 1: Proportion of energy sources used for electricity generation in the world (top) and Turkey (bottom) [2]

* This article is based on the "Our City Konya Project" report designed for the Ministry of Environment, Urbanization and Climate Change of the Republic of Turkey.

As can be seen from the above data, fossil-based energy sources constitute the majority of energy sources that cause human health and environmental pollution both in the world and in Turkey. Of course, these fossil energy sources are directly used as primary energy in the main sectors mentioned above, but the electrical energy obtained as secondary energy is also produced from primary energy sources at large rates. It is understood that electricity, which is known as clean energy, is actually one of the most important factors in the release of CO_2 gas into the atmosphere (Figure 1). The share of electricity generated from renewable energy sources in Turkey is 33%. The largest share in this ratio is water (hydroelectric) energy with a rate of 25%. Considering the economic realities of our country, wind energy is also close to ideal (6%). However, electricity generation from solar energy, which is known as the most important renewable and clean energy source, has a very low rate (0.6%) [2].

II. ENERGY NEEDS OF SETTLEMENTS

In the study, developing designs within the framework of environmentally sensitive and sustainable approaches are the objectives and basic principles of the strategy plan. Within the framework of these principles, the main topics of this section are the provision of renewable energy recovery and efficiency and mitigating the effects of global climate change. In this context, measures have been taken in the urban design architectural project studies to reduce the negative effects of energy efficiency and climate change. In the study, it is emphasized that all of the electricity and hot water needs of the settlement can be met from renewable energy sources. The average daily electricity consumption of an apartment in Konya is determined as 6 kWh [3].

III. UTILIZATION OF RENEWABLE ENERGY RESOURCES FOR ENERGY NEEDS

In the "Bizim Şehir-Konya" project, it is aimed to set an example for new applications to be made in the project concept of ecological city, sustainable city concepts. It is thought that this can be achieved by using all natural resources underground and above ground in the most efficient way. The most important of these resources are undoubtedly energy resources. When fossil-based mineral natural resources, which have been formed over millions of years, are depleted, it takes millions of years to form again. In addition to being the most basic substance of life, water is among the most important energy resources in terms of its ability to produce energy (hydroelectric energy). In addition to the depletion of non-renewable natural energies (fossil fuels), the formation of chemical gases and wastes harmful to life and the physical environment that arise in the use of energy causes significant damage to human health and the built environment and leads to global warming. Measures have started to be taken all over the world to avoid these damages. One of these measures is to use clean, inexhaustible, renewable energy sources (solar, wind, geothermal, biomass, etc.) that do not produce greenhouse gases.

It is planned that the electrical energy and hot water to be used in the residences, workplaces and buildings belonging to state institutions in the project area can be produced with panel type PV modules (Photovoltaic solar panel) placed on the roofs of the buildings within the site. In addition, electricity will be generated by a PV power plant to be installed in an empty field with no settlement and common use area in the region, special tree-type PV modules and small wind turbine units to be placed in public areas (roadsides and parks), and PV panels and small wind turbine units to be placed on street lighting poles. The power of these systems, their electricity generation capacities and their implementation (operation) models according to the relevant legislation (laws and regulations) in the project area are explained below.

PV and wind turbine systems to be installed in the project area for electricity generation are not systems that generate electricity continuously 24 hours a day, every day, depending on the solar and wind energy regime of the region, so they have to work in connection with the local electricity distribution network. Therefore, they must be installed and operated according to the "Regulation on Unlicensed Electricity Generation in the Electricity Market" prepared by the Energy Market Regulatory Authority (EMRA) and published in the Official Gazette dated 02.10.2013 and numbered 28,783 [4]. According to this regulation, in order to install an electricity generation system, you must be an electricity user (consumer) and use some of your production in this facility. The size of the facility you can install can be at most 30 times larger than the power of your consumption facility.

A. Use of Solar Energy

1) Calculation of the amount of solar radiation required in the project area

For "Bizim Şehir Konya" project, the average solar radiation values of Konya center (Selçuklu, Meram and Karatay average) were taken as appropriate due to its location (adjacent to Meram district within the borders of Selçuklu district) (Figure 2).

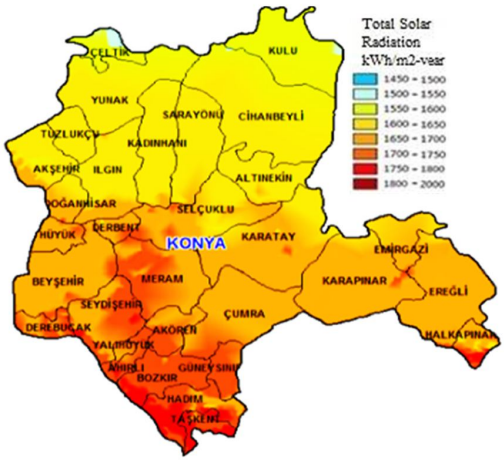

Figure 2: Total annual solar radiation per m^2 of Konya [5]

In this context, the Solar Energy Potential Atlas (SEPA) data of the General Directorate of Renewable Energy of the Ministry of Energy and Natural Resources, which are compatible with the measurement data of Konya Meteorology Regional Directorate, were taken as representative data for the region (Figure 2) [5]. According to the solar energy potential atlas (SEPA) data and monthly irradiance values (Figure 3), the average daily sunshine duration of the project region is 7.2 hours/day and the average unit energy production value is 3.6 kWh/m^2-day [5]. Figure 4 shows the daily unit solar radiation (kWh/m^2-day), daily sunshine hours and annual electricity production amounts (kWh/year) with different PV types obtained from Konya SEPA.

2) Photovoltaic systems, their use and operation in buildings

Two types of PV panels are used in the market; the first is the polycrystalline PV type, which, according to SEPA data, has an annual electricity generation value of approximately 24,000 kWh/year for a 100 m^2 area. The second is the monocrystalline PV-T type, which is 25% more expensive. These modules are capable of producing hot water as well as electricity. The additional cost of this system compared to PV that only produce electricity is the installation of plumbing up to the PV-T panels and the installation of heat sink pipes under the panels. This is similar to the rooftop solar hot water collectors used today. The electricity production value of these is 27,000 kWh/year for an area of approximately 100 m^2, which is 12.5% more efficient than the others. In addition, since the PV panels are cooled while hot water is being produced, their efficiency increases by another 12.5% and the total efficiency increases by about 25%. Of course, this efficiency increase compensates for the 25% cost overrun of monocrystalline PV-T (with hot water production) [6].

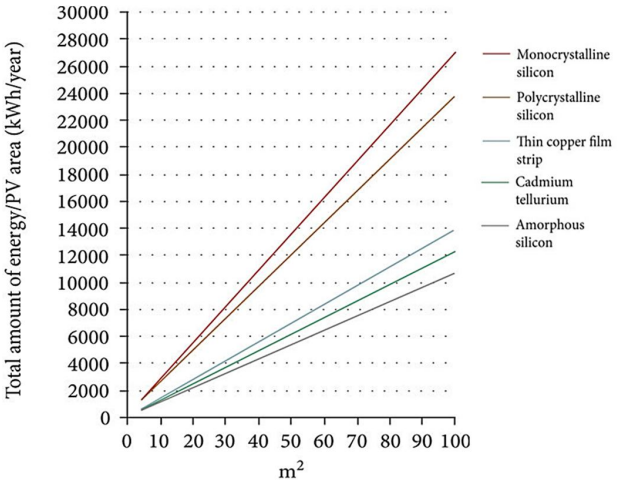

Figure 3: Annual electricity production amounts with different PV types [5]

The area of 1 PV panel (1.00m x1.62m) is approximately 1.62m^2 and its power (polycrystalline PV) is 250W. According to the calculations made from the graphs below (Figure 4-5), an average of 1,500,000 kWh/year of electrical energy can be produced with a 1,000 kW Polycrystalline PV power plant under Konya conditions. From here, 1,500 kWh/year electricity is produced from 1 kW PV module. In contrast, monocrystalline PV-Ts with hot water production, which have a 25% higher electricity generation efficiency, generate an average of 1,875,000 kWh/year from a 1,000 kW plant.

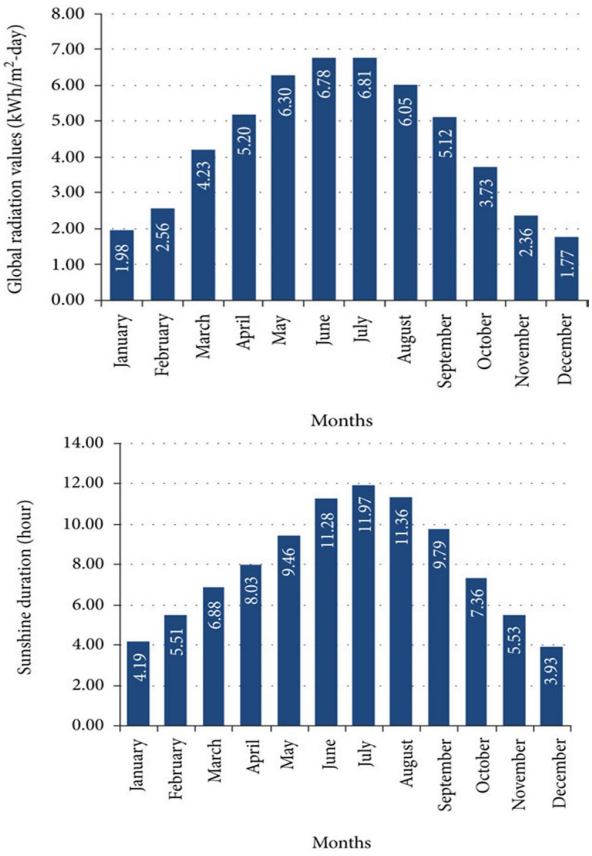

Figure 4: Konya solar energy potential map daily unit solar radiation (top) and sunshine hours (bottom) [5]

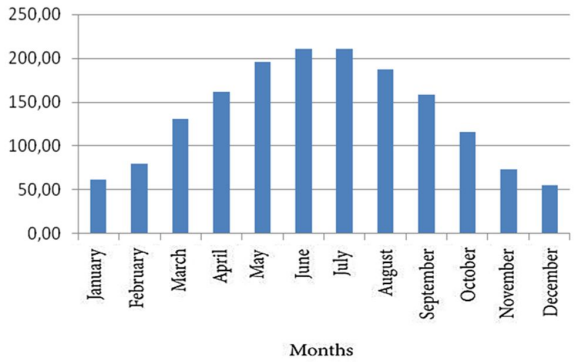

Figure 5: Konya monthly average solar electricity generation values, kWh/m^2-month

3) Business model for electricity generation with PV panels in residential buildings

Three-phase connection is required according to the "Connection Principles" of the Communiqué on the Implementation of the Regulation on Unlicensed Electricity Generation in the Electricity Market [4].

Production with polycrystalline PV:

According to this situation, the most appropriate way of operation would be to install 5 kW for each household (apartment) where the roof area is sufficient, to connect to single-phase medium voltage and to use it for the independent needs of each residence and to generate income by selling the excess production. The roof areas of a total of 1000 (block + detached + villa) residential buildings planned in the project area are approximately 170,000m^2. Based on the assumption that the PV panels will be placed only on the sun-facing surfaces of the roofs (south east, south and south west) for efficient operation; as a result of the drawings and calculations, it is predicted that the panels will cover at least 1/3 (33.3%) of the roof surfaces in the project area. The total Polycrystalline PV installed power on the roofs of the residential buildings (blocks) is estimated to be approximately 8,657 kW.

The total number of dwellings (households) in the Project area is 4,195. When the total power that can be installed on the roofs of the houses is divided by the number of households (8,657/4,195), there is approximately 2.0 kW installed power per house (household). 3,000 kWh/year of electricity can be generated per household. When monocrystalline PV-T panels are used, the annual electricity generation is 25% higher (3,000x1.25) at 3,750 kWh/year.

Thus, approximately 12,985,500 kWh/year with polycrystalline photovoltaic panels (8,657kW x1,500,000) and 16,231,875 kWh/year with monocrystalline PV-T panels placed on the roofs of residential buildings in the project area.

The amount of energy required by all residences in the project area, the average household size is assumed to be 4, and the total number of residences (households) is 4,195. Considering the average household electricity consumption as 3,000 kWh/year, the annual energy requirement of all houses in the project area is calculated as (4,195x3,000) 12,585,000 kWh/year.

When polycrystalline PV panels are installed on one third of the roof surfaces of the residential blocks in the project area, it is revealed that it will meet the annual electricity consumption of the entire housing. In other words, the consumption amount (12,585,000 kWh/year) was determined to be smaller than the production amount (12,985,500 kWh/year). When monocrystalline PV-T panels are used, production of 16,231,875 kWh/year is much higher than consumption (28.9% more). The ability to produce hot water as well as electricity with monocrystalline PV-T was explained above. The total electrical energy obtained from PV-T panels is 16,231,875 kWh/year, 25% more than normal polycrystalline PV. In addition, 50 liters of hot water with an average daily temperature of 45^{o}C can be obtained from 1 m^2 area of PV-T panels. A total of 1,022,000m^3 of hot water can be obtained daily from 56,000 m^2 of PV-T panels to be installed on the roofs of all housing blocks. The amount of hot water per household will be approximately 244m^3 per year and 20m^3 per month, which will more than meet the monthly hot water needs of 4-5 people.

Figure 6: Tree and rooftop solar PV systems used in the project

4) Electricity generation with PV panels in commercial and public buildings

By applying the business models described above for residential buildings, PV (polycrystalline) or PV-T (monocrystalline) panels will be installed on the sloping or flat terrace roofs of commercial and public (educational, administrative, health, social, etc.) buildings in the project area to meet only the electricity or both electricity and hot water needs of these buildings. With the power that can be installed here, if the electricity system in these buildings is three-phase, it can go up to 11 kW and above. If the electricity network is single phase, 5 kW systems can be installed.

The total roof area of commercial and public buildings in the project area is approximately 53,000 m^2. The area of the panels is calculated as approximately 17,500 m^2 (53,000m^{2}x0.33), assuming that they will cover at least 1/3 (33.3%) of the roof surfaces. The area of a 250W polycrystalline panel (1.00m x1.62m) is 1.62m^2, therefore the total number of panels that can be placed on the roofs of the buildings in question (17,500 m^2/1.62 m^2) is determined as approximately 10,800 panels. With a total installed capacity of 2,700 kW, approximately 4,050,000 kWh/year (4.05 million kWh/year) of electrical energy can be generated from PV panels placed on the roofs of commercial and public buildings. The total electrical energy generated from monocrystalline PV-T panels is 25% more than normal polycrystalline PVs (2,700kW), amounting to 5.06 million kWh/year.

The total installed capacity of polycrystalline PV panels on the roofs of all (residential+commercial+public) buildings in the project area is 11,357 kW and the total electricity generated is 17.03 million kWh/year. The total installed capacity of monocrystalline PV panels is 11,357 kW and the total electricity generated is 21.3 million kWh/year.

5) Electricity generated by solar power plants

The characteristics of the land where the SPP will be installed have been selected in accordance with the regulation

[3]. PV panels with a size of 20,412m^2 are placed on the 50,000 m2 area designated as the Solar Power Plant (SPP) field in the southwest of the project area, taking into account the circulation areas. By placing a total of 12,600 polycrystalline panels in the area, the solar power plant with an installed power of 3,150 kW can be operated according to the unlicensed electricity generation regulation. With 3.150x1,500,000 kWh/year, a total of 4,725,000 kWh/year (4.725 million kWh/year) electricity can be generated from this power plant.

Within the scope of this study, the total installed power of Polycrystalline PV panels that can be placed in all buildings and solar power plant in the area is Buildings + Solar power plant Total Power: 8,657+2,700+3,150=14,507 kW. The total electricity generated from the Buildings + Solar power plant is 21,750,000 kWh/year.

B. Use of Wind Energy

The wind speed map of Konya province is given in Figure 6 and the annual average wind speed of the center and its vicinity is 5-7 m/s for 50 m. Electricity can be generated with tree-type PV panels and wind turbines for lighting public areas [6, 7]. For the illumination of public areas (roads, squares, parks, etc.), it is planned to place tree-type PV panels every 200 m in the refuges of main roads and tree-type vertical axis wind turbine systems in public areas with sufficient wind (main road refuges, parks, etc.). These systems will be operated by the local authorities responsible for lighting these areas and providing the necessary electrical energy.
Tree type PV system: In this system, a total of 20 5 kW panels of 250 W (0.25 kW) PVs can be placed on 1 tree. This type of layout occupies 40% less area than the common flat, side-by-side layout in buildings or areas, and larger power can be installed per unit area. A 1 MW PV plant requires 5 hectares of land for the common layout, while the tree layout requires 3 hectares (Figure 7).

The tree-type PV system is 5% more expensive than common panels and construction, but its efficiency is 10% higher by placing it higher, and the floor area it covers is much smaller, so that the bottom of the system can be used for green areas, car parks and agriculture. In the project area, a total of 200 tree-type PV systems (200*5kW) are installed every 200m in suitable locations such as the median of the main roads, main pedestrian axes, etc., resulting in a total installed capacity of 1,000 kW. Since it is 10% efficient, a total of 1,650,000 kWh/year (1.65 million kWh/year) of electricity can be generated from 1,000 kW in a year. In this system, the energy of 15 street lamps can be met with 1 tree type PV and 3,000 street lamps with 200 tree type PVs. It is planned to generate electricity by installing 200 tree-type vertical axis wind turbine systems at 100 m intervals of tree-type PVs in the project area. A total of 50 turbines of 100 W are placed in a tree, so that the total turbine power of each tree is at least 5,000W (5.0 kW). The total installed power of all trees is 1,000 kW. All turbines in trees of this power will be able to generate an average of 1,500,000 kWh/year of electricity. Since the tree-type turbines will be placed on the sides of the main roads where vehicle traffic is continuous, the wind current generated by the traffic will also be utilized. In parks and walking path areas where tree-type PV and wind turbines are not installed, the lighting lamps will be PV panels with storage and small wind turbine systems placed on each lamp post.

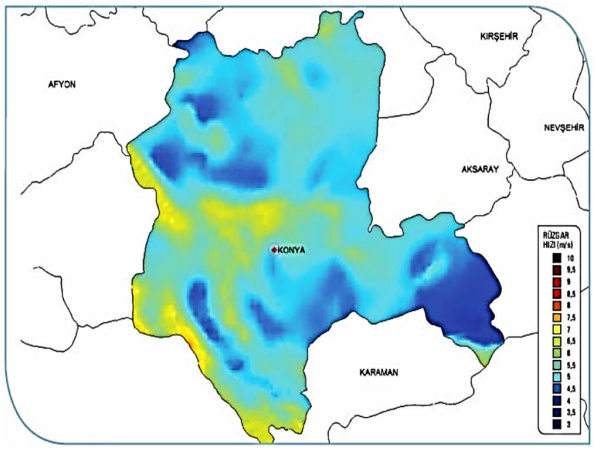

Figure 6: Wind speed distribution map at 50 m in Konya province [7]

Figure 7: Tree type PV panel (left) and wind turbine (right) systems in parks etc.

C. Ground Source Heat Pump Utilization

Ground source heat pump application is not recommended in the project area due to the high initial investment cost of these systems as well as the damage caused by landscape elements such as deep-rooted and shade-forming trees in the gardens of the houses, especially to the pipes of the horizontal tube heat pump that draw heat from the soil.

D. Impact of the Use of Energy Efficient Materials İn Buildings on Energy Consumption

In the urban design project being carried out in the project area, while deciding on the settlement of the main center, sub-centers, residential areas and other areas such as recreation parks, etc. in accordance with the public transportation system designed to be integrated into the city's transportation network, the solution regarding the energy consumption or gain of open and closed spaces is prioritized. The main objective of layout planning and micro-climate control in terms of ensuring energy efficiency is to reduce the need for active energy support in air conditioning by helping to provide heating, cooling and ventilation with passive methods. In this framework, since the most appropriate orientation for the region is south-east, the buildings are oriented in a way that maximizes the sun's maximum utilization in their positioning on the land. The buildings within the scope of the project are designed as "energy efficient buildings". It is estimated that the initial construction costs will increase by 5-10% if the project is implemented as a Green Building according to the international Leadership in Energy and Environmental Design (LEED) criteria. However, since the energy savings in green buildings are 50-70%, this cost increase is not seen much [8, 9]. In addition, green buildings offer significant gains in the long term with their low operating costs. Natural ventilation is provided by utilizing the pressure difference created by the outdoor wind flow between indoor and outdoor and the pressure difference created by the temperature difference between indoor and outdoor.

IV. CONCLUSION

In the urban design study, measures to reduce energy demand were taken first, followed by the use of efficient systems and finally the addition of renewable energy systems. Within the scope of the project area, as explained in detail in the following sections, it is calculated that the area has a great solar energy potential due to the geography of the area, and tree-type PV panels are placed in the area allocated in the south-west of the area as a solar field and in the refuges of the main roads as well as on the roofs of the buildings in the project area to meet the electricity needs of the area and to meet the low solar energy in the winter season by selling to the national grid. As renewable energy, tree-type vertical axis wind turbines are also installed in public areas with sufficient wind (main road medians, parks, etc.). Table 1 below summarizes the electricity gains from renewable energy sources in terms of area and number of units.

As can be seen from Table 1, the electrical energy produced by solar and wind energy systems in our city Konya region meets the electricity and hot water needs of the region and produces more than 4,000 kWh per year.

Table 1: Amounts of electricity generated as renewable energy from solar power plants and tree-type energy systems in buildings in the project area

Energy Type	Device Location Area	Panel Area, m^2	Panel / Number of turbines	Installed Power, kW	Electricity Generated kWh/year
PV Panels	Housing Roofs	170,000	34,630	8,657	12,985,500
	Commercial and Public Buildings	53,000	10,800	2,700	4,050,000
	Solar PV Power Plant	50,000	12,600	3,150	4,725,000
	Tree Type PV Panels	200	4,000	1,000	1,650,000
Wind Turbine	Tree Type Wind Turbines	200	10,000	1,000	1,500,000
TOTAL	Panels	273,000	62,030	15,507	23,410,500
	Turbines	400	10,000	1,000	1,500,000
Used Electricity MWh/yıl		12,585	Excess Electricity Generated kWh/yıl		4,000

ACKNOWLEDGMENT

This article is based on the report of "Our City Konya" project supported by the Republic of Turkey Ministry of Environment, Urbanization and Climate Change.

REFERENCES

[1] IRENA (2018), Renewable Energy Statistics 2018, The International Renewable Energy Agency, Abu Dhabi. ISBN 978-92-9260-077-8

[2] IEA, (2016), Energy Policies of IEA Countries, Turkey 2016 Rewiev, International Energy Agency 9 rue de la Fédération 75739 Paris Cedex 15, France. www.iea.org,

[3] F. Köse, Kaya M. N., Gemi, D. S., "Yenilenebilir Enerji Kaynakları İle Konya Şartlarında Müstakil Bir Evin Enerji İhtiyacının Karşılanma Çalışması", Akıllı ve Yeşil Binalar Kongresi ve Sergisi, 209-216, 23-24 Mayıs 2013, Ankara.

[4] EPLEÜY, Elektrik Piyasasında Lisanssız Elektrik Üretim Yönetmeliği, Resmî Gazete Tarihi: 12.05.2019 Resmî Gazete Sayısı: 30772.

[5] ETKB, T.C. Enerji ve Tabii Kaynaklar Bakanlığı Bilgi Merkezi, URL: https://enerji.gov.tr/bilgi-merkezi-enerji-gunes, Erişim Tarihi: 14.10.2022.

[6] M. Öksüz, F. Köse, "Hibrit Fotovoltaik Isıl PV-T-su ve PV-T-hava Güneş Kollektörlerinin İncelenmesi", Ulusal Çevre Bilimleri Araştırma Dergisi, Sayı 2(3): 95-102, 2019.

[7] ETKB, T.C. Enerji ve Tabii Kaynaklar Bakanlığı Bilgi Merkezi, URL: https://enerji.gov.tr/bilgi-merkezi-enerji-ruzgar, Erişim Tarihi: 14.10.2022.

[8] A.Ç. Karademir, A. Dağ, "Sürdürülebilirlik Uygulaması Olarak Yeşil Bina ve LEED Sertifikasyonu Üzerine Türkiye İnşaat Sektöründe Bir Çalışma", Academia Journal of Nature and Human Sciences, Sayı: 7(1), 63-83, 2021. e-ISSN: 2717-8528.

[9] İ. Erol, G.Ç. Kıasıf, "LEED Sertifikalı Ofis Binalarının Enerji ve Atmosfer Kriteri Açısından Değerlendirilmesi: Maslak Bölgesi Örneği", BŞEÜ Fen Bilimleri Dergisi Sayı: 8(1), 322-335, 2021. https://doi.org/10.35193/bseufbd.887581

Pulsating Performance Tests of Hydroforming Press

Ö.F.GÖKCEPINAR[1], M.AYDIN[1], H.M. İLBEYLİ[1], M.TÜRKÖZ[1], M.DİLMEÇ[2], H.S.HALKACI[1]

[1] Konya Technical University, Konya/Turkey, ofgokcepinar@ktun.edu.tr
[1] Konya Technical University, Konya/Turkey, maydin@ktun.edu.tr
[1] Konya Technical University, Konya/Turkey, mertolino.ilbeyli@gmail.com
[1] Konya Technical University, Konya/Turkey, mturkoz@ktun.edu.tr
[2] Necmettin Erbakan University, Konya/Turkey, muratdilmec@erbakan.edu.tr
[1] Konya Technical University, Konya/Turkey, halkaci@ktun.edu.tr

Abstract **- Hydraulic systems are widely preferred in the industrial field today. The cause for this is that the cost is economical, and the life of the system is long. It can also be used efficiently in many production methods. Hydraulic systems are widely used especially in press machines and test systems. Today, with the need for new production methods, productions are made by hydroforming method using high pressure fluids in hydraulic presses. Pressure intensifiers are used to increase the fluid pressure to the desired value. The low pressure taken from the pump can be increased to remarkably high pressures thanks to the pressure intensifiers. By integrating computer control to hydroforming presses, desired pressure profiles can be applied.**

A new way in hydroforming to increase formability of materials is applying pressure in a pulsating manner. This process named as pulsating hydroforming. The success of the process depends on to apply the pressure at desired frequencies and amplitudes. Therefore, it is important to control the pressure values in hydroforming press momentarily and to apply these values at the intended level. In this study, performance tests were carried out on a hydroforming test system working with a pressure intensifier. Experiments were performed in triplicate. These experiments were applied at different frequencies and amplitudes. The amplitude limit of the system was determined as 2.5 MPa and 10 MPa. The frequency limit is determined as 1 Hz and 3 Hz. The system was able to apply all frequency values with 90% accuracy. The error rate of the system is 0.33% at the lowest 5 MPa and 2 Hz frequency values, and the highest error rate is 39.67% at 10 MPa amplitude and 3 Hz frequency.

Keywords **– Amplitude, Frequency, Hydroforming, Performance Test, Pressure Intensifier**

I. INTRODUCTION

One of the alternatives forming methods is the forming process with pulsating loading, which has increased in recent years. Pulsating loading is the application of selected parameters in shaping processes as increasing, decreasing, and then increasing again at a certain amplitude and frequency, instead of monotonically increasing according to time [1]. This process, which will contribute to formability, has emerged in recent years and there are limited studies on the subject in the literature. In the literature, it has been determined that pulsating loading is used in manufacturing methods such as hydroforming, deep drawing and forging, and the studies mostly focus on pulsating hydroforming. In the pulsating hydroforming method, the fluid pressure is given as pulsating instead of monotonically increasing over time. It is stated that pulsating application of pressure increases formability.

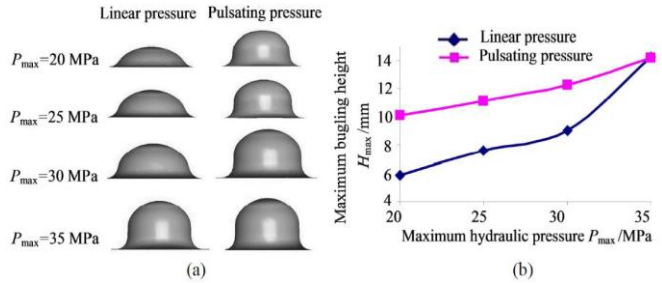

Figure 1: Curves of maximum bulging heights under two loading paths: (a) comparison of formed parts; (b) variation curve of maximum bulging height [1].

It is not possible to attain the loading profile used in pulsating hydroforming processes in materials shaped at high pressures, only with hydraulic pumps. For this reason, pressure intensifier that increase the pump pressure are used. A pressure of 138 MPa is required in high pressure sheet hydroforming processes [2].

In the study by Suzuki, the performance of the pressure intensifier was tested. It has been revealed that the pressure obtained from the pressure intensifier is six times higher than the pressure obtained from the hydraulic system. The pressure intensifier was controlled via a solenoid valve without an analog circuit. In this way, the pressure intensifier can be controlled without using complex electrical circuits [3].

In his study, Urmamen transformed the hydromechanical deep drawing press into a double-sided hydroforming press and performed performance tests [4]. Consequently, the distinction between the pressures measured and applied with the pressure intensifier in the double-sided hydroforming press were calculated. When the difference and errors were evaluated for the pressure formed, the difference and error increased as the slope of the applied curve increased. In a curve without slope, the difference is quite low. As a result, it turns out that the overall error is acceptable even if the corresponding pressure difference is high, especially at the end stages of the process.

In another study, the performance of the pressure intensifier was tested with the high-speed on-off valve. Steady and fluctuating tests of the pressure intensifier were carried out. It

has been shown that the output pressure can be adjusted by changing the pulse width modulation (PWM) signal sent to the on-off valve. It was observed that the output pressure increased from 5 MPa to 11.6 MPa when the PWM signal was 0.7 (Figure 2) [5].

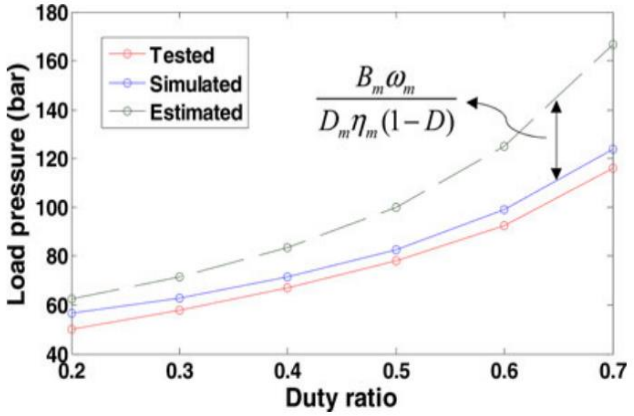

Figure 2: Load pressure at different pulse width modulation

In the study of Kim et al. a test setup was established for systems requiring high impact pressure. The components of the test setup, the accumulator, hydraulic hoses, are designed to withstand high pressures. Thus, it was possible to test products that require high pressure capacity (Figure 3) [6].

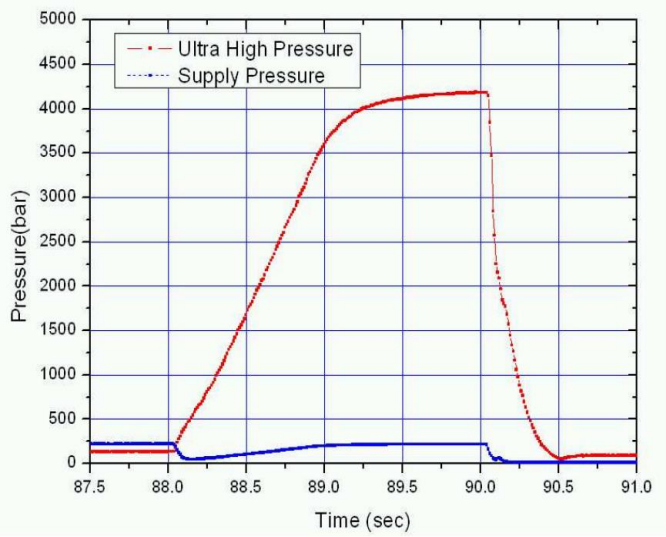

Figure 3: 420 MPa wave in the intensifier system

As it can be understood from the studies, it has been observed that a pulsating loading profile should be applied to increase the formability in hydroforming processes. There are also many studies in the literature in which pulsating loading increases formability [7-17]. It is not possible to apply the pressure profile pulsating at the desired pressure and time with hydraulic pumps. Therefore, pressure intensifiers are used. It is important to determine the performance of pressure intensifiers and to determine their working intervals. This study includes performance tests of pulsating loading in hydroforming processes used in the literature.

II. Materials and Methods

In this study, the performance tests of the pressure intensifier connected to the hydroforming press were carried out. The hydroforming press can reach a pressing force of 60 tons. The press is controlled by HNC (Hydraulic Numerical Control) control. The hydroforming press in Konya Technical University was used in the experimental studies (Figure 4).

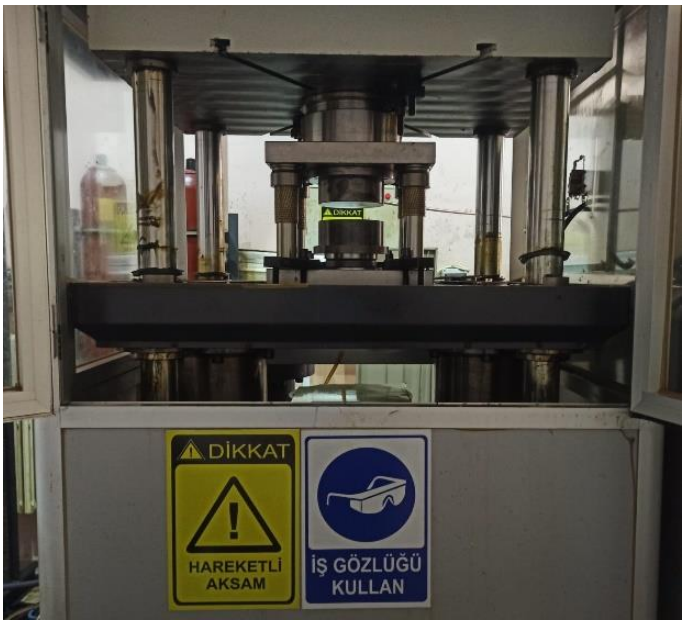

Figure 4: Hydroforming press.

The pulsating loading profiles of the pressure intensifier were examined, and the applied and measured amplitude and frequency values were investigated. In the experiments, pressure, amplitude, frequency, blank holder force, pressure intensifier position, battery pressure is recorded instantaneously. Measurements were recorded with the controller (Figure 5).

Figure 5: Hydraulic numerical control.

The experiments were carried out by hydroforming. In the experiments, the pressure profile was carried out using a pressure intensifier with a capacity of 450 MPa (Figure 6).

Figure 6: Pressure intensifier.

The amplitude and frequency values obtained after each experiment were recorded. Data from the controller were recorded with 100 ms precision. Initial pressure constant 35 MPa was applied. The experimental design is given in Table 1.

Table 1. Design of experiment

Exp. No/Parameters	Amplitude (MPa)	Frequency (Hz)	Initial Pressure (MPa)
1	2.5	1	35
2	2.5	2	35
3	2.5	3	35
4	5	1	35
5	5	2	35
6	5	3	35
7	10	1	35
8	10	2	35
9	10	3	35

III. Results and Discussion

As the frequency increases, the pressure intensifier is forced to provide the amplitude value. The data given to and recorded from the system at 5 MPa amplitude and 1 Hz frequency values are indicated in Figure 7. The frequency and amplitude values are shown in Figure 8 by enlarging the scale of the graph.

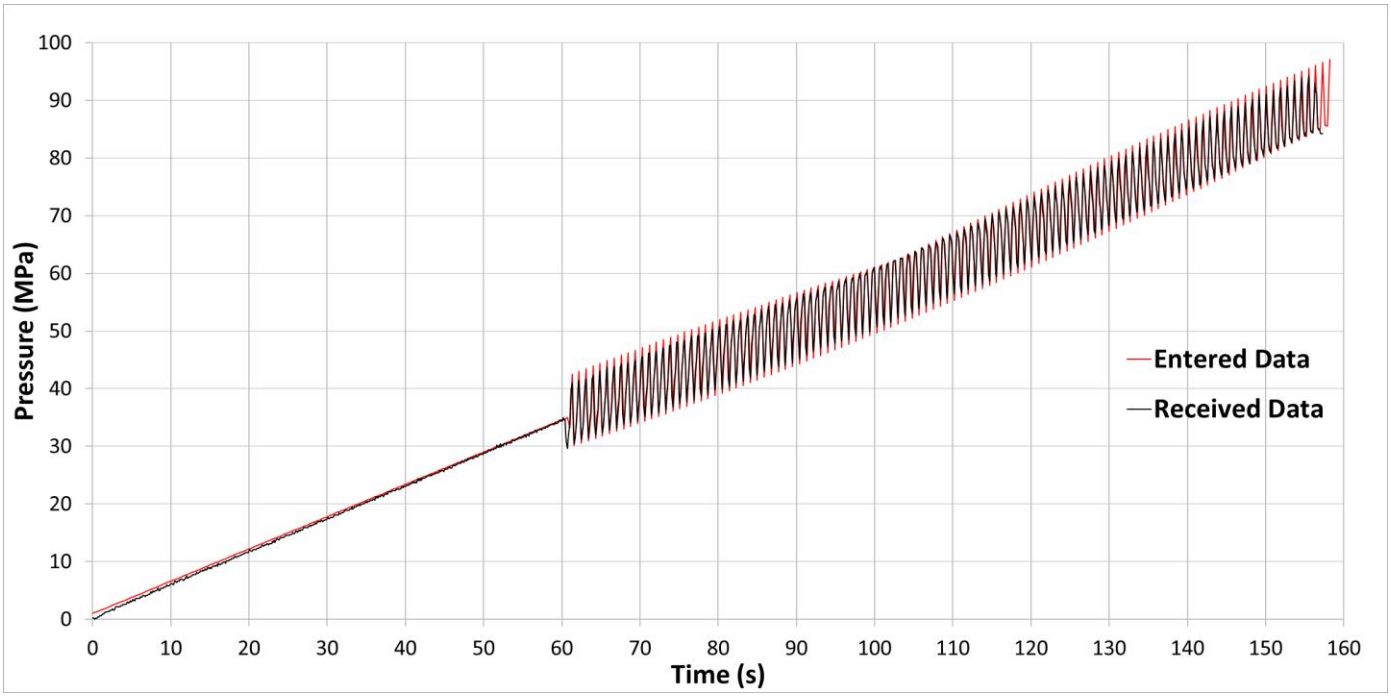

Figure 7: Curve measured by applying 5 MPa amplitude, 1 Hz frequency.

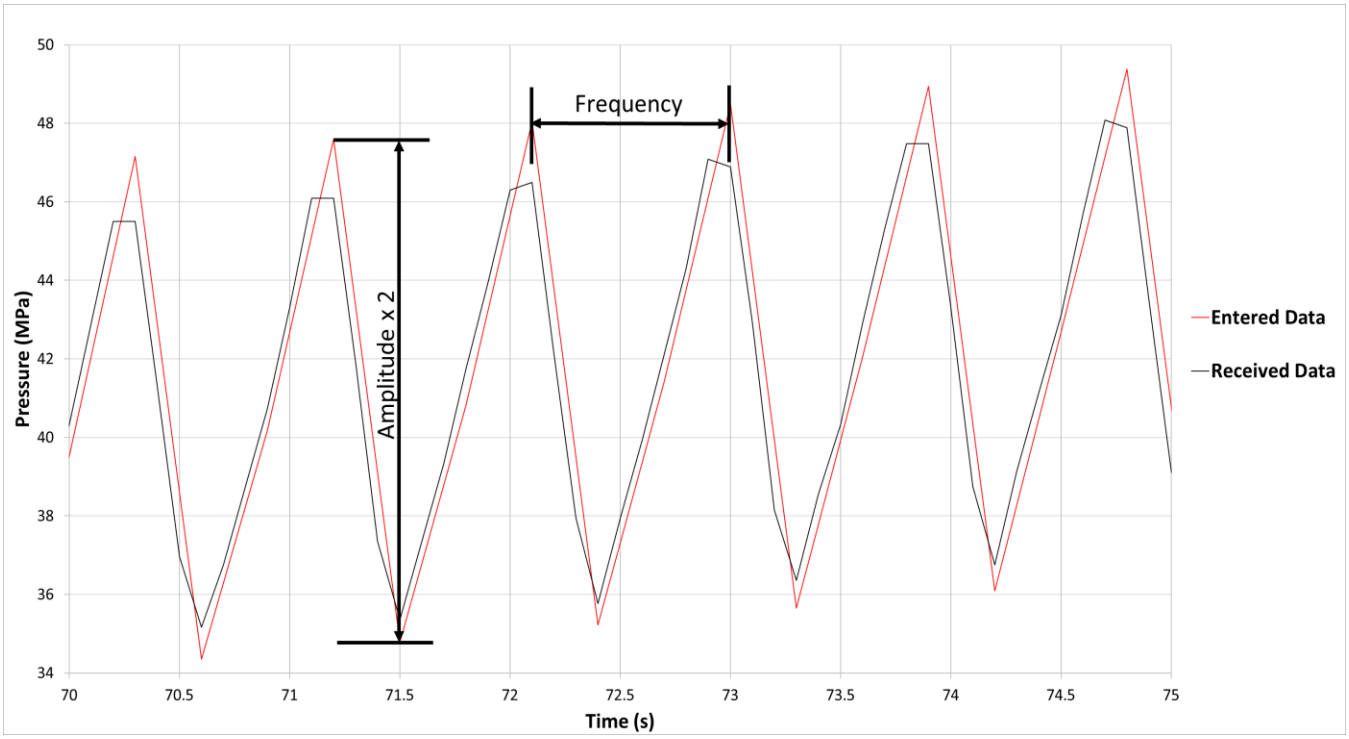

Figure 8: Amplitude and frequency values.

The results of the amplitude values obtained from the experiments are given in Table 2. Error rates were calculated for each experiment. It is clearly seen that when the frequency increases, the system has difficulty in meeting the given amplitude values. However, at low frequencies, the system can operate with low error.

Table 2: Received amplitude and entered amplitude

Exp. No	Exp. 1 (MPa)	Exp. 2 (MPa)	Exp. 3 (MPa)	Mean	Entered Amplitude	Error %
1	2.50	2.35	2.50	2.45	2.5	2.00
2	2.00	1.80	1.80	1.87	2.5	25.33
3	1.80	2.05	1.80	1.88	2.5	24.67
4	5.50	5.25	5.45	5.40	5	8.00
5	4.85	5.05	5.15	5.02	5	0.33
6	4.70	4.70	4.95	4.78	5	4.33
7	9.00	8.95	9.65	9.20	10	8.00
8	8.15	8.60	8.50	8.42	10	15.83
9	5.70	6.35	6.05	6.03	10	39.67

The system can meet the given frequency with 90% accuracy in all experiments. It has been measured that the amount of 1, 2 and 3 waves that should occur per one second at frequencies of 1 Hz, 2 Hz, 3 Hz occurs in 0.9 s.

IV. CONCLUSIONS

1. Performance tests were carried out to create pulsating loading conditions in the hydroforming process. In these tests, the initial pressure was kept constant, and the amplitude and frequency values were changed. As these values change, the performance of the system also changes. Especially as the frequency value changes, the amplitude value that the system can give has been significantly affected.

2. The pressure amplifier was able to apply the desired frequency with 90% accuracy at all amplitude values.

3. The pressure intensifier can be applied with high accuracy with a frequency of 2 Hz and an amplitude of 5 MPa with an error rate of 0.33%.

4. The system had difficulty in meeting the amplitude values as the frequency increased. It was not possible to obtain an amplitude value of 10 MPa at a frequency of 3 Hz. The error rate at these levels was calculated as 39.67%.

5. The limit of the system was determined as greater than 2.5 MPa and less than 10 MPa for amplitude values. It is seen that the frequency value can also be applied in the range of 1 Hz and 3 Hz.

6. It has been determined that a frequency lower than 1 Hz should be used in order to obtain amplitude values greater than 10 MPa in the system.

REFERENCES

[1] Y. Lianfa, *Formability of AZ31B Magnesium Alloy Sheet in Hydro-bugling by Pulsating Hydraulic Pressure*, Manufacturing Science and Technology, 1-7, 2011.

[2] A. Saifullah, A. Rasel, M. Halder, *Design, Construction and Performance Test of a Hydraulic Pressure Intensifier*, The Experiment 1268-1283, 2014.

[3] K. Suzuki, *Application of a New Pressure Intensifier Using Oil Hammer to Pressure Control of a Hydraulic Cylinder*, Journal of Dynamic Systems, Measurement, and Control, 1989.

[4] M. K. Urmamen, G. Atas, M. Dilmec, M. Türköz, O. Ozturk, H. S. Halkaci, *Design, Fabrication and Performance Tests of a Double-Sided Sheet Hydroforming Test System*, Metrology and Measurement System, 33-38, 2017.

[5] F. Wang, L. Gu, Y. Chen, *A Hydraulic Pressure-Boost System Based on High-Speed On-Off Valves*, IEEE/ASME Transactions on Mechatronics, vol. 18, April 2013.

[6] H. E. Kim, G. C. Lee, J. H. Kim, *System Design and Performance Test of Hydraulic Intensifier*, Transactions of the Korean Society of Mechanical Engineers A, vol. 34, pp. 947-952, August 2010.

[7] Y.F. Yapan, O. Öztürk, M. Türköz, M. Dilmeç, H. Livatyalı, H. S. Halkacı, H. Kotan, *Microstructural Characterization of Improved Formability of Ti-6Al-4V Sheet by Pulsating Hydraulic Bulging at Room Temperature*, Journal of Materials Engineering and Performance, 2022.

[8] A. Mostafapour, A. Akbari and M.R. Nakhaei, *Application of Response Surface Methodology for Optimization of Pulsating Blank Holder Parameters in Deep Drawing Process of Al 1050 Rectangular Parts*, Int. J. Adv. Manuf. Technol, 2017, 91, p 731–737.

[9] M. Loh-Mousavi, M. Bakhshi-Jooybari, K. Mori and K. Hyashi, *Improvement of Formability in T-shape Hydroforming of Tubes by Pulsating Pressure*, Proc. Inst. Mech. Eng. Part. B. J. Eng. Manuf, 2008.

[10] J. Ma, L. Yang, J. Liu, Z. Chen, and Y. He, *Evaluating the Quality of Assembled Camshafts Under Pulsating Hydroforming*, J. Manuf. Process, 2021.

[11] A. Talebi Anaraki, M. Loh-Mousavi and L.L. Wang, *Experimental and Numerical Investigation of the Influence of Pulsating Pressure on Hot Tube Gas Forming Using Oscillating Heating*, Int. J. Adv. Manuf. Technol, 2018.

[12] A. Ashrafi and K. Khalili, *Investigation on the Effects of Process Parameters in Pulsating Hydroforming Using Taguchi Method*, Proc. Inst. Mech. Eng. Part. B. J. Eng. Manuf, 2015.

[13] K. Mori, T. Maeno and S. Maki, *Mechanism of Improvement of Formability in Pulsating Hydroforming of Tubes*, Int. J. Mach. Tools. Manuf, 2007.

[14] G. Hu, C. Pan and Z. Liu, *Investigation on Wrinkling Behaviors of Metal Thin-walled Tube in Pulsating Hydroforming with Axial Feeding*, J. Strain. Anal. Eng. Des, 2020.

[15] G. Hu and C. Pan, *Investigation on Deformation Behavior of Magnesium Alloy Sheet AZ31B in Pulsating Hydroforming*, Proc. Inst. Mech. Eng. Part. B. J. Eng. Manuf, 2021.

[16] S. Zhang, A. Yuan, B. Wang, H. Zhang and Z. Wang, *Influence of Loading Path on Formability of 304 Stainless Steel Tubes*, Sci. China. Ser. E. Technol. Sci, 2009.

[17] F.Q. Li, J.H. Mo, J.J. Li, L. Huang and H.Y. Zhou, *Formability of Ti–6Al–4V Titanium Alloy Sheet in Magnetic Pulse Bulging*, Mater. Des, 2013.

PCA-SVM-Random Search Optimization Based Application for Classification of Date Fruits According to Physical Properties

Muhammet Fatih Aslan

Electrical and Electronics Engineering, Karamanoglu Mehmetbey University, Karaman, Turkey

***Abstract* - Date fruit, which is an important source of income especially for African and Middle Eastern countries, has a religious and cultural importance for Muslims as well. Only a few (10%) of the date fruit, of which there are many species worldwide, are known. Therefore, it is necessary to distinguish between different types of date fruit. However, manual methods are slow and risky. This study uses a dataset containing physical properties of date fruits for date fruit classification. Experimental implementation includes two steps. In the first step, the Support Vector Machine (SVM), whose hyperparameters are adjusted by random search optimization, classifies the normalized features. In the second step, the normalized features are reduced by Principal Component Analysis (PCA). These reduced features are fed into the SVM whose hyperparameters are optimized. At the end of the study, the results obtained from both applications were 89.9% and 92.2%, respectively. As a result, features reduced and enhanced by PCA provide more successful date fruit recognition.**

***Keywords* – Date Fruit, Machine Learning, SVM, Random Search Optimization, PCA**

I. INTRODUCTION

Increasing world population, global warming and climate change necessitate fast and high quality production for the future. The worldwide population growth is expected to reach 10 billion by 2050. Agriculture is one of the sectors that will be most affected by this situation. Fast and high quality production is essential to meet the increasing demands [1, 2]. Date fruit, also known as *Phoenix dactylifera*, is a nutritious fruit that has played an important role in the nutrition of human beings since ancient times. The most prominent countries in date cultivation are the Middle East and African countries. Among these, the countries that produce the most are Egypt, Iran, Algeria and Saudi Arabia, respectively [3]. Today, 100 million date palm trees are grown worldwide and 7.5 million tons of date fruit are produced annually. Date fruit with such a high production has soft, hard, fresh and dry types [4]. As far as is known, only about 10% of the date fruit, of which there are more than 2500 species worldwide, has been identified. Date fruit is also consumed by people for dietary purposes, as it has a high nutritional value and is rich in calcium, iron and vitamin C [5]. However, different types of date fruit have different amounts of nutrients. However, insufficient information on the type of date fruit prevents a comprehensive classification of dates. Recently, the importance of computer-based systems in the classification of date fruit has increased due to the difficulty and cumbersomeness of classical discrimination methods.

Thanks to computer-based systems, agricultural products can be classified automatically and quickly, instead of resorting to expert knowledge or discriminating in the laboratory and with different sensors. In such applications, the species recognition decision must be automatically generated by the computer. Therefore, such solutions are based on artificial intelligence. Machine learning and deep learning methods developed after expert systems are used to solve many classification and regression problems today. Machine learning is still indispensable for small size data. Examples of machine learning methods commonly used by researchers are Naive Bayes (NB), Support Vector Machine(SVM), Linear Discriminant Analysis (LDA), Logistic Regression (LR), Artificial Neural Network (ANN), K-Nearest Neighbor (k-NN) and Decision Tree (DT) algorithms [6, 7]. In order to perform classification or regression applications with machine learning methods, features must be extracted from the data. In addition, these features need to be strongly representative of different classes. Therefore, feature selection and feature extraction before the machine learning algorithm is very effective in machine learning performance [8].

Recently, the number of studies [9-13] developing artificial intelligence-based solution methods for the differentiation of agricultural products has increased considerably. Due to the large number of different species of the date fruit as an agricultural product, researchers have recently proposed different artificial intelligence-based methods to distinguish these species. Koklu, et al. [14] used LR, ANN and the stacking model formed by combining these two models for date fruit classification. The dataset used in the study was created by the authors, and this data included a total of 898 date fruit samples and seven different species. They produced a total of 34 features, including shape, color and morphological features, from each date fruit image. As a result of the study, the ANN, LR and stacking model provided 92.2%, 91% and 92.8% accuracy, respectively. Muhammad [15] classified date fruits using the features of texture, shape, and size. He used the Local Binary Pattern (LBP) or Weber Local Descriptor (WLD) feature descriptor for texture features. He then combined these texture features. Also, feature selection was performed with Fisher Discrimination Ratio (FDR) before classification. As a result of the classification performed with the SVM, he

distinguished four different types of date palm fruit with an average accuracy of 98.1%. Color, texture and size attributes were used in the date fruit classification study by Sen, et al. [16]. These features extracted from the Mabroom, Sagai, Ajwa and Sukkary types were fed into the SVM, DT, RF and ANN machine learning algorithms. At the end of the study, SVM provided the most successful classification with 73.8% accuracy. Finally, Alzu'bi, et al. [17] extracted features from the date fruit images with the Scale Invariant Feature Transform (SIFT) feature extraction method. These features were then classified with SVM. At the end of the study, up to 100% accuracy was obtained.

More examples can be given to artificial intelligence-based studies for differentiating date fruit types. The generally adopted method is to extract shape, texture, color, etc. features from the date fruit and classify these features with different algorithms. In this study, shape, color and morphological features created by Koklu, et al. [14] and extracted from seven different date fruit species are used. In practice, these features in different value ranges are first normalized. These normalized features are then fed to the SVM with hyperparameters adjusted by the random search optimization algorithm. At the last stage, the number of features is reduced with the Principal Component Analysis (PCA) method and these features are fed to the SVM, whose hyperparameters are again optimized. At the end of the study, the effect of PCA on the date fruit classification performance is clearly seen.

II. Material and Methods

A. Dataset

The dataset used in this study was created by Koklu, et al. [14]. The dataset includes 98, 65, 204, 72, 199, 94 and 166 samples from Deglet Nour, Barhee, Sukkary, Rotab Mozafati, Safawi, Sagai and Ruthana date fruit species, respectively. The authors designed a conveyor system to generate a dataset from these date fruit images, containing a total of 898 samples. Moreover, this mechanism was resistant to lighting changes and therefore suitable for computer vision applications. The researchers acquired date fruit images with a resolution of 1280 × 1024 with this mechanism they designed. They then extracted 34 different features, including shape, color, and morphology, from each image. Table 1 shows some of these features. As can be seen in Table 1, the value ranges of some extracted features are very different from each other.

Table 1: Some values of the dataset

Perimeter	Convex Area	Shape Factor 1	EntropyRR
2378,908	424428	0,002	-59191263232
2275,7791	385277	0,0021	-29873577984
2216,49	366374	0,0022	-41679380480
2040,285	316111	0,0023	-23896397824
2015,198	308043	0,0023	-23275982848
2647,394	528876	0,0018	-93948354560

B. Normalization

The dataset raw values seen in Table 1 have different lower and upper limit values. This causes different features to have different importance levels during training. To avoid this, feature types are normalized to ensure that each feature type is of equal importance. In this way, more accurate learning of the network is provided in artificial intelligence training [18]. With the normalization applied to the raw data, all the features are constrained to an equal range. There are different feature scaling methods to limit the range. In this application, feature scaling normalization called min-max is used. As seen in (1), with this normalization method, new features ($\hat{x}$) are calculated according to the maximum (x_{max}) and minimum (x_{min}) values. As a result of min-max normalization, all newly calculated features are normalized in the range of 0-1.

$$\hat{x} = \frac{\mathrm{x} - x_{min}}{x_{max} - x_{min}} \quad (1)$$

C. Classification with Optimized SVM

Normalized shape, color and morphological features are ready to be fed into the machine learning algorithm. However, each machine learning method has hyperparameters that significantly affect performance. Most previous work only performs hyperparameter tuning at the beginning of the application. However, if these parameters are adjusted according to the data, more successful results can be produced. Different hyperparameter optimization techniques can be used for this. Random Search optimization differs from many other optimization methods with its low computational cost and simplicity [19]. In addition, in the SVM hyperparameter optimization study conducted by Czarnecki, et al. [20], it was stated that the random search algorithm was more successful than the grid search and heuristic-based approaches.

D. Classification with Optimized PCA-SVM

Classifying hyperparameters with SVM optimized by random search is the first application of this study. The available features in the dataset have different significance values for the date fruit type. Therefore, in artificial intelligence applications, a new feature vector is created by selecting or transforming some features. This also reduces the computational cost and provides more reliable results. In this context, in the second application, the PCA method is used to reduce the raw features in the dataset. PCA is a frequently used statistical method for feature reduction. In the PCA method, correlations between features are determined and an orthogonal transformation is applied for newly created features. As a result of the transformation, there are fewer features and the variance value between new features is higher. Thus, redundant features are removed.

III. Results

In this section, a comparative analysis is made for the results of Optimized SVM and Optimized PCA-SVM applications.

A. *Classification with Optimized SVM*

Before classifying the raw data with SVM, first of all, the hyperparameters that will give the optimum value are determined with the random search algorithm. Figure 1 shows the classification error graph obtained over 30 iterations with the random search algorithm. According to Figure 1, the error rate has been gradually reduced by changing the hyperparameters.

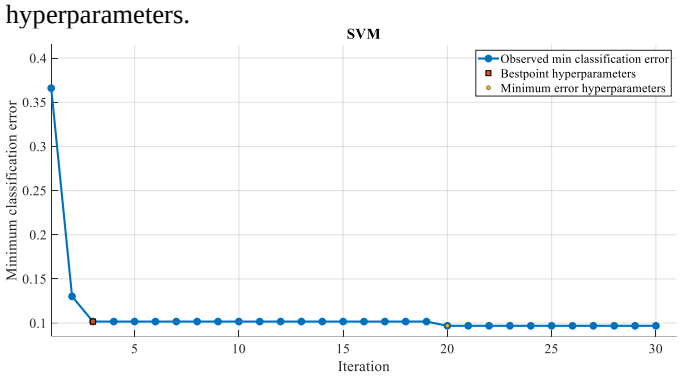

Figure 1: Minimum classification errors according to the iteration obtained as a result of random search optimization

Table 2: SVM hyperparameter values determined by random search optimization

Hyperparameter	Multiclass Method	Box Constraint	Kernel Function
Value	One-vs-One	361.9627	Gaussian

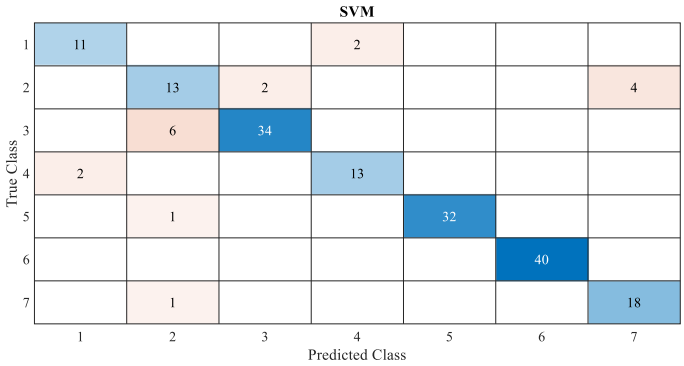

Figure 2: Confusion matrix of optimized SVM

The hyperparameters of the SVM that provided the least error among the iterations shown in Figure 1 are shown in Table 2. Training and testing steps are performed using the SVM with these values. 80% of 898 data is reserved for train and 20% for testing. Random search optimization, which determines the hyperparameters of normalized features containing 34 features, takes 58.16 seconds. After training, the average accuracy obtained from the test data is 89.9%. The confusion matrix showing the number of correct and incorrect classifications between different classes in the test data is shown in Figure 2. The class indices shown in the confusion matrix represent the classes Barhee, Deglet Nour, Sukkary, Rotab Mozafati, Ruthana, Safawi, and Sagai, respectively. Accordingly, only Safawi types are classified with 100% accuracy with the optimized SVM. The classification for other species shows that the proposed application is of sufficient accuracy.

B. *Classification with Optimized PCA-SVM*

In the first approach, which classifies the raw data with the SVM optimized by the random search method, all normalized features are used. However, this section reexamines the results using feature reduction with PCA. For PCA, the number of principal components is determined as 20, so random search optimization and SVM steps are performed by using 20 features instead of 34. Figure 3 is the graph obtained as a result of the random search optimization algorithm showing the classification errors after applying PCA to the features.

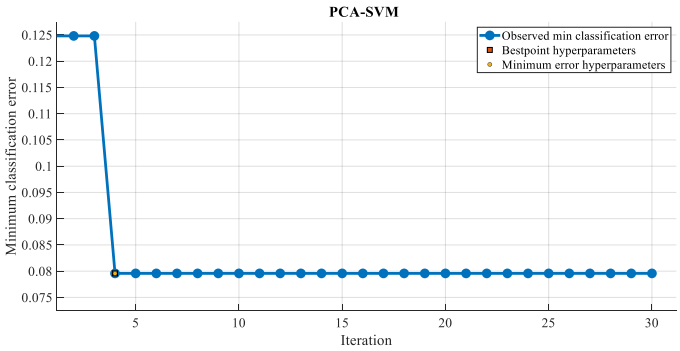

Figure 3: Minimum classification error graph according to iteration obtained with Random Search optimization after PCA

Table 3: SVM hyperparameter values adjusted with random search optimization after PCA

Hyperparameter	Multiclass Method	Box Constraint	Kernel Function
Value	One-vs-One	40.3621	Cubic

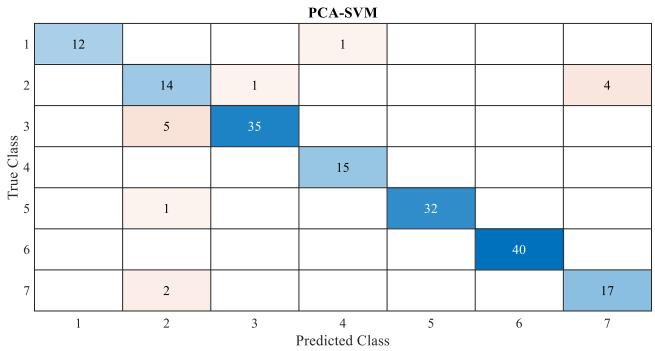

Figure 4: Confusion matrix obtained as a result of classification of features reduced by PCA with optimized SVM

It can be seen that the minimum classification error obtained in Figure 3 is less than that of Figure 1. The hyperparameter values that provide the least error are shown in Table 3. Of the new data with 20 features obtained after PCA, 80% is used for training and 20% for testing. The time spent optimizing these features is only 19.49 seconds. As a result of the training and testing steps performed after the hyperparameters adjustment, the accuracy of the model in the test data is 92.2%. Figure 4 shows the confusion matrix obtained after classifying the test data. This confusion matrix contains less errors than the confusion matrix obtained in the first application (Figure 2).

IV. Discussion

When the results of the study are examined, SVM, whose hyperparameters are adjusted with the random search optimization method, provides a more accurate classification for the features reduced by PCA. This shows that the features of the used dataset are more distinguishable after orthogonal transformation. Moreover, with fewer features, classification is less costly and therefore takes less time to optimize. However, an optimization algorithm can be used to determine the optimum number of principal components. In this way, more successful classification can be achieved.

V. Conclusion

This study develops an application based on machine learning, optimization and feature reduction for a dataset of date fruits containing seven different species. After normalizing the raw features in the dataset, they are classified with SVM. Before classification, optimum hyperparameters of SVM are determined by random search optimization. Then PCA is applied to the raw features and the number of principal components is reduced to reduce computational cost and increase accuracy. The last application with fewer features provides more accurate date fruit recognition. These results show the importance of PCA for the classification of color, shape and morphological characteristics of date fruits with both lower cost and higher accuracy.

References

[1] M. F. Aslan, A. Durdu, K. Sabanci, E. Ropelewska, and S. S. Gültekin, "A comprehensive survey of the recent studies with uav for precision agriculture in open fields and greenhouses," *Applied Sciences*, vol. 12, no. 3, p. 1047, 2022.

[2] M. C. Hunter, R. G. Smith, M. E. Schipanski, L. W. Atwood, and D. A. Mortensen, "Agriculture in 2050: recalibrating targets for sustainable intensification," *Bioscience*, vol. 67, no. 4, pp. 386-391, 2017.

[3] H. Altaheri, M. Alsulaiman, and G. Muhammad, "Date Fruit Classification for Robotic Harvesting in a Natural Environment Using Deep Learning," *IEEE Access*, vol. 7, pp. 117115-117133, 2019, doi: 10.1109/ACCESS.2019.2936536.

[4] A. Kamal-Eldin and S. Ghnimi, "Classification of date fruit (Phoenix dactylifera, L.) based on chemometric analysis with multivariate approach," *Journal of Food Measurement and Characterization*, vol. 12, no. 2, pp. 1020-1027, 2018/06/01 2018, doi: 10.1007/s11694-018-9717-4.

[5] K. Albarrak, Y. Gulzar, Y. Hamid, A. Mehmood, and A. B. Soomro, "A Deep Learning-Based Model for Date Fruit Classification," *Sustainability*, vol. 14, no. 10, p. 6339, 2022. [Online]. Available: https://www.mdpi.com/2071-1050/14/10/6339.

[6] P. P. Shinde and S. Shah, "A review of machine learning and deep learning applications," in *2018 Fourth international conference on computing communication control and automation (ICCUBEA)*, 2018: IEEE, pp. 1-6.

[7] A. Sarkar, A. Singh, and R. Chakraborty, "A deep learning-based comparative study to track mental depression from EEG data," *Neuroscience Informatics*, p. 100039, 2022.

[8] O. Attallah, "MB-AI-His: Histopathological Diagnosis of Pediatric Medulloblastoma and its Subtypes via AI," *Diagnostics*, vol. 11, no. 2, p. 359, 2021. [Online]. Available: https://www.mdpi.com/2075-4418/11/2/359.

[9] E. Ropelewska, K. Sabanci, and M. F. Aslan, "Discriminative Power of Geometric Parameters of Different Cultivars of Sour Cherry Pits Determined Using Machine Learning," *Agriculture*, vol. 11, no. 12, doi: 10.3390/agriculture11121212.

[10] E. Ropelewska, X. Cai, Z. Zhang, K. Sabanci, and M. F. Aslan, "Benchmarking Machine Learning Approaches to Evaluate the Cultivar Differentiation of Plum (Prunus domestica L.) Kernels," *Agriculture*, vol. 12, no. 2, p. 285, 2022.

[11] A. Ali *et al.*, "Machine learning approach for the classification of corn seed using hybrid features," *International Journal of Food Properties*, vol. 23, no. 1, pp. 1110-1124, 2020.

[12] M. Koklu and I. A. Ozkan, "Multiclass classification of dry beans using computer vision and machine learning techniques," *Computers and Electronics in Agriculture*, vol. 174, p. 105507, 2020.

[13] D. Singh *et al.*, "Classification and Analysis of Pistachio Species with Pre-Trained Deep Learning Models," *Electronics*, vol. 11, no. 7, p. 981, 2022. [Online]. Available: https://www.mdpi.com/2079-9292/11/7/981.

[14] M. Koklu, R. Kursun, Y. S. Taspinar, and I. Cinar, "Classification of Date Fruits into Genetic Varieties Using Image Analysis," *Mathematical Problems in Engineering*, vol. 2021, p. 4793293, 2021/11/10 2021, doi: 10.1155/2021/4793293.

[15] G. Muhammad, "Date fruits classification using texture descriptors and shape-size features," *Engineering Applications of Artificial Intelligence*, vol. 37, pp. 361-367, 2015/01/01/ 2015, doi: https://doi.org/10.1016/j.engappai.2014.10.001.

[16] A. A. A. Sen, N. M. Bahbouh, A. B. Alkhodre, A. M. Aldhawi, F. A. Aldham, and M. I. Aljabri, "A Classification Algorithm for Date Fruits," in *2020 7th International Conference on Computing for Sustainable Global Development (INDIACom)*, 12-14 March 2020 2020, pp. 235-239, doi: 10.23919/INDIACom49435.2020.9083706.

[17] R. Alzu'bi, A. Anushya, E. Hamed, E. A. Al Sha'ar, and B. A. Vincy, "Dates fruits classification using SVM," in *AIP Conference Proceedings*, 2018, vol. 1952, no. 1: AIP Publishing LLC, p. 020078.

[18] M. F. Aslan, K. Sabanci, and A. Durdu, "A CNN-based novel solution for determining the survival status of heart failure patients with clinical record data: numeric to image," *Biomedical Signal Processing and Control*, vol. 68, p. 102716, 2021/07/01/ 2021, doi: https://doi.org/10.1016/j.bspc.2021.102716.

[19] A. C. Florea and R. Andonie, "A Dynamic Early Stopping Criterion for Random Search in SVM Hyperparameter Optimization," in *Artificial Intelligence Applications and Innovations*, Cham, L. Iliadis, I. Maglogiannis, and V. Plagianakos, Eds., 2018// 2018: Springer International Publishing, pp. 168-180.

[20] W. M. Czarnecki, S. Podlewska, and A. J. Bojarski, "Robust optimization of SVM hyperparameters in the classification of bioactive compounds," *Journal of Cheminformatics*, vol. 7, no. 1, p. 38, 2015/08/14 2015, doi: 10.1186/s13321-015-0088-0.

A Design Study for MEMS Comb-Drive Resonator

Serdar TEZ

Pamukkale University, Department of Electrical and Electronics Engineering, Denizli, Turkey, stez@pau.edu.tr

***Abstract* – This paper presents a design study for the MEMS comb-drive resonator with a resonance frequency of approximately 532 kHz. The theoretical calculation of the MEMS comb-drive resonator is performed by considering the second-order spring-mass-damper model. On the other hand, the simulation study based on the finite element method (FEM) is also performed by using open-source Elmer FEM software to obtain both values of the eigenfrequency and the capacitance of the designed resonator. A comparison table is also given to compare the theoretical values to the simulation results. The designed resonator can be used as a mass sensor mainly depending on the resonance frequency shift after integrating a sensing layer. Furthermore, the main benefits of the presented comb-drive resonator are to have independent mechanical springs and proof mass regions compared to the examples of the mass sensors given in the literature. Therefore, this can contribute to the improvement of the sensing features.**

***Keywords* – MEMS, comb-drive resonator, FEM analysis.**

I. INTRODUCTION

Microelectromechanical systems (MEMS) resonators have been used for frequency control, timing, filtering, and sensing, applications [1] in various research areas. Nowadays, resonant devices have also attracted attention in the literature as they offer to digitize frequency output, which is an advantage over traditional analog sensors [2]. Furthermore, the fundamental unit of MEMS gyroscopes and accelerometers is mainly related to the resonator structure [3]. Therefore, the design and fabrication of MEMS resonators have been ongoing research interest in the literature. Mass sensor applications have attracted attention due to the compact and high-performance device systems presented by MEMS technology. The favourite structure used in these implementations is a cantilever [4-6]. However, there are some drawbacks observed in the literature for this structure like the effect of the thickness [7] and the position of the sensing layer [8] on the output signal.

The current paper presents both theoretical and simulation results for designing a MEMS comb-drive resonator with a resonance frequency of nearly 532 kHz. The characteristic features of the resonator are theoretically determined by using the second-order spring-mass-damper system. Furthermore, the conceptual model of the designed MEMS resonator is formed by using the FreeCAD software [9], and this model is transferred to Elmer FEM [10] to implement the FEM simulation. The FEM simulation results are visualized by using ParaView [11] software. A comparison table is also provided for the obtained results.

II. COMB-DRIVE RESONATOR DESIGN

The primary elements of the MEMS comb-drive resonator are the mechanical spring, the proof mass, and the electrode regions. Figure 1 shows the layout of the designed MEMS comb-drive resonator. There are six mechanical spring structures, which are attached to the proof mass part. The length and the width of mechanical spring structures are 55 and 6.5 microns, respectively. The structural thickness is also selected as 35 μm. Moreover, the drive and sense electrodes are formed by placing capacitive fingers side by side with a 2 μm-gap. There are 25 capacitive fingers, of which length and width are 70 μm and 4 μm, respectively. The overlap length of the capacitive fingers is 60 μm. Table 1 summarizes some of the design parameters of the resonator.

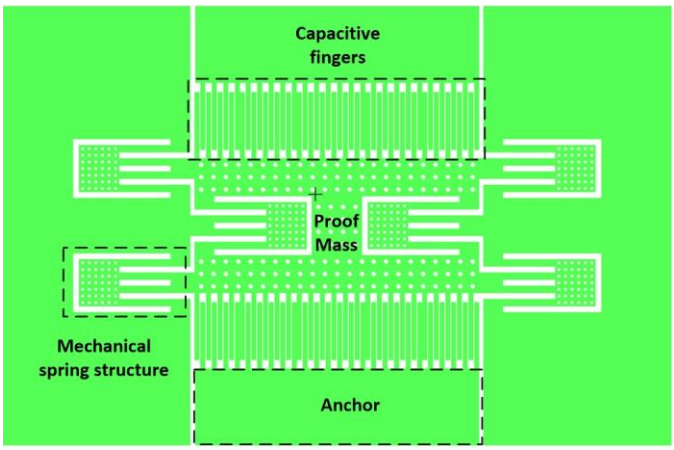

Figure 1: The layout of the MEMS comb-drive resonator

Table 1: The parameters used during the design of the MEMS comb-drive resonator

Design Parameters	Value
Spring Width (μm)	6.5
Spring Length (μm)	55
Number of Spring	6
Spring Constant (N/m)	58581
Finger Width (μm)	4
Finger Length (μm)	70
Finger Overlap (μm)	60
Capacitive Gap (μm)	2
Number of Fingers per side	25
Proof Mass Amount (kg)	4.7729×10^{-9}
Resonance Frequency (kHz)	557.58
Rest Capacitance (pF)	0.455

III. Theoretical Analysis

During the design study, the spring-mass-damper system, a well-known model in the literature, is used to theoretically analyze the MEMS capacitive resonator [12]. The transfer function of the mechanical model of the MEMS capacitive resonator can be given with the following equation:

$$\frac{X(S)}{F(S)} = \frac{1}{s^2 + \frac{b}{m}s + \frac{k}{m}} \tag{1}$$

where F is the electrostatic force, X is the displacement, k is the spring constant, b is the damping coefficient, and m is the proof mass amount. The natural angular frequency ω_0 and the quality factor Q can also be defined with the following equation (2):

$$\omega_0 = \sqrt{\frac{k}{m}} \qquad Q = \frac{\omega_0 m}{b} \tag{2}$$

The spring constant k is another factor affecting the characteristics of the resonator, and it can be given for the folded spring structure with the following equation (3) [13]:

$$k = \frac{Ehw^3}{l^3} \tag{3}$$

where E is young's modulus, h is the structural thickness, and w and l are the width and length of the folded spring structure. If the system is actuated with an external force, the amplitude of the displacement starts increasing until it is limited by losses known as damping. The electrostatic force given with the following equation is used to drive the system [14]:

$$F = \frac{1}{2}\frac{dC}{dX}V^2 \tag{4}$$

where V is potential including the DC and AC terms, and C is the capacitance formed among the fingers. The capacitance expression can also be given in the following equation:

$$C = \frac{\varepsilon_0 A}{g} \tag{5}$$

where ε_0 is the permittivity of the free space, A is the area of the capacitive fingers, and g is the capacitive gap. As one can see from Eq. (2), the damping coefficient and the quality factor are closely related to each other. Figure 2 (a-c) shows the graphs obtained during the theoretical analysis. Eq. (1) is utilized during the theoretical analysis, where the design parameters given in Table 1 are considered. Moreover, the DC and AC voltage values used during the analysis are selected as 70 V and 2 V, respectively. On the other hand, the quality factor Q value is chosen as the variable. The real and imaginary parts of the displacement are obtained with respect to frequency (Figure 2 (a)).

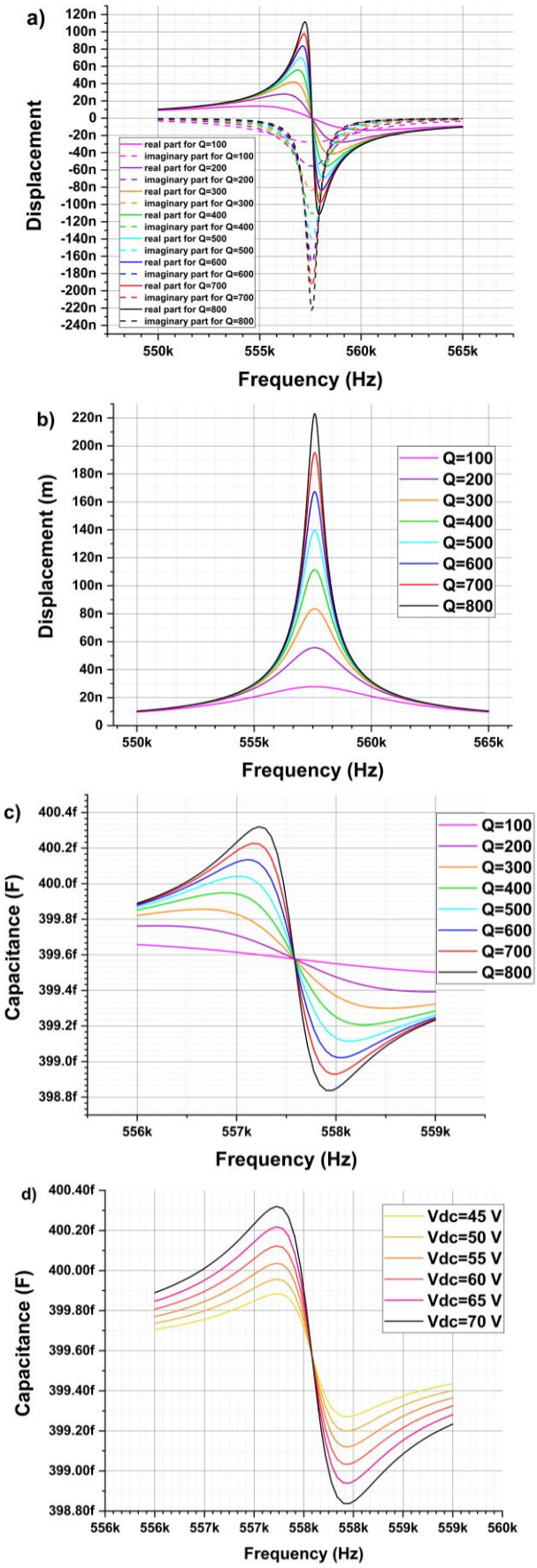

Figure 2: (a-b-c) Theoretical results of the resonator with respect to Q and (d) the DC potential

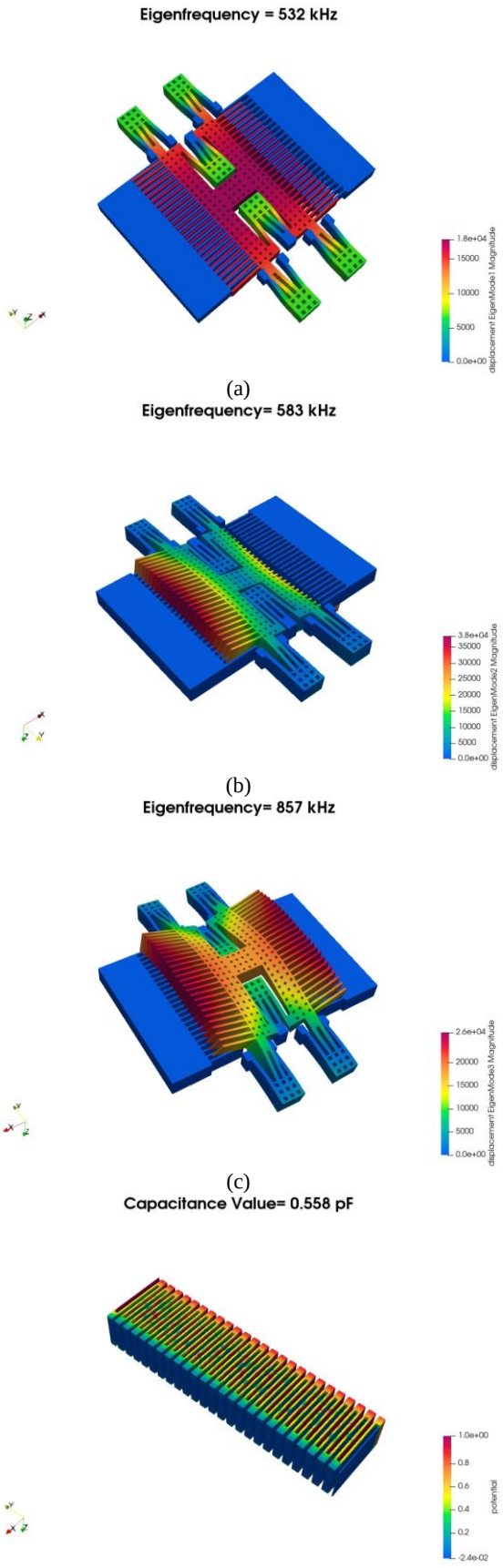

Figure 3: (a-b-c-) The simulation results of the modal analysis in Elmer FEM (d) The capacitance value obtained in Elmer FEM

Furthermore, the amplitude of the displacement is also presented with respect to the frequency (Figure 2 (b)), where the resonance frequency can be determined from the maximum amplitude value. The capacitance graph is also theoretically provided with respect to frequency (Figure 2 (c)). Another analysis is also performed by using the same model. However, this time DC voltage value is selected as the variable while the AC voltage and Q values are 2 V and 800, respectively. Figure 2 (d) shows the capacitance vs frequency graph for the case Q=800 and 2V AC.

IV. FEM SIMULATION

A Three-dimensional (3D) design model is formed using FreeCAD [9]. The analysis of the formed 3D model is performed by using open-source Elmer FEM [10]. The obtained result is visualized by using ParaView [11]. During the simulation study, the 3D model is first fixed in certain regions, and then the mesh size is determined. Finally, the modal analysis is completed, and the obtained result is given in Figure 3 (a-b-c). The resonance frequency of the first mode is 532 kHz, and this value is highly different from the other modes, which guarantees safe operation. The simulation study is also performed for determining the capacitance value of the design. Therefore, a 3D model of the region among the fingers is formed. Next, the potential difference is applied among the plates in the formed 3D model, where the air medium is selected as a dielectric in Elmer FEM. Next, the rest capacitance value in the simulation is determined as 0.558 pF (Figure 3 (d)). Table 2 gives a comparison of the values obtained in the theoretical calculations and simulation.

Table 2: The comparison of the theoretical calculation and the simulation result for the designed MEMS resonator

	Theoretical Results	**Simulation Results**
Resonance frequency (kHz)	557.58	532
Rest capacitance (pF)	0.455	0.558

V. CONCLUSION

This study presents the design of a MEMS comb-drive resonator and gives theoretical and simulation results. Theoretical and simulation results are in good agreement with each other. On the other hand, the reason for the difference in the resonance frequency values is related to the effective mass of the resonator, which corresponds to the whole moving mass. The fringing field is responsible for the slight difference observed in the capacitance value of the resonator.

As the designed MEMS comb-drive resonator has independent mechanical springs and proof mass regions, the problems observed in the literature can be minimized with the designed resonator. Moreover, this structure can be used to measure the quantity of volatile organic chemicals (VOCs) after the integration of the sensing elements.

ACKNOWLEDGEMENT

This study is supported by the Scientific and Technological Research Council of Türkiye (TUBITAK) under the grant number 116E231. The author would like to thank TUBITAK.

REFERENCES

[1] S. -S. Li, "CMOS-MEMS resonators and their applications," 2013 Joint European Frequency and Time Forum & International Frequency Control Symposium (EFTF/IFC), 2013, pp. 915-921, doi: 10.1109/EFTF-IFC.2013.6702098.

[2] P. Hauptmann, "Resonant sensors and applications", Sensors and Actuators A: Physical,Volume 26, Issues 1–3,1991, Pages 371-377, https://doi.org/10.1016/0924-4247(91)87018-X.

[3] F. Chen, Z. Wen, D. Xu, W. Zhou and X. Li, "An Anti-Aliasing and Self-Clocking ΣΔM Cobweb-Like Disk Resonant MEMS Gyroscope with Extended Input Range", 2021 IEEE 34th International Conference on Micro Electro Mechanical Systems (MEMS), 2021, pp. 334-337, doi: 10.1109/MEMS51782.2021.9375143.

[4] M. Villarroya *et al*., "Cantilever based MEMS for multiple mass sensing," *Research in Microelectronics and Electronics, 2005 PhD*, 2005, pp. 197-200 vol.1, doi: 10.1109/RME.2005.1543038.

[5] Toky Rabenimanana, Vincent Walter, Najib Kacem, Patrice Le Moal, Gilles Bourbon, Joseph Lardiès, "Mass sensor using mode localization in two weakly coupled MEMS cantilevers with different lengths: Design and experimental model validation", Sensors and Actuators A: Physical, Volume 295, 2019, pp: 643-652,https://doi.org/10.1016/j.sna.2019.06.004.

[6] C. Kim, P. Getz, M. -g. Kim and O. Brand, " Room-tempearutre CO2 sensing based on interdigitated capacitors and resonant cantilevers," 2017 19th International Conference on Solid-State Sensors, Actuators and Microsystems (TRANSDUCERS), 2017, pp. 1532-1535, doi: 10.1109/TRANSDUCERS.2017.7994351.

[7] McFarland, W. A. and Colton, S.J., 2005. "Role of material microstructure in plate stiffness with relevance to microcantilever sensors", Journal of Micromechanics and Microengineering, 15, 1060-1067.

[8] Johnson, B.N., Mutharasan, R., 2012. "Biosensing using dynamic-mode cantilever sensors: A review", Biosensors and Bioelectronics, 32, 1-18.

[9] J. Riegel, W. Mayer, Y. Havre: FreeCAD (Version 0.18.4R) http:// www.freecadweb.org (2022). Accessed 10.25.2022.

[10] P. Raback, M. Malinen, J. Ruokolainen, A. Pursula, T. Zwinger, Eds. (May, 2019). Elmer Models Manual. CSC-IT Center for Science.

[11] J. Ahrens, B. Geveci, C. Law: ParaView: An End-User Tool for Large Data Visualization, Visualization Handbook, 1st Ed., Elsevier, ch. 36, 717-31, (2005).

[12] M.I. Younis, (2011). Vibrations of Lumped-Parameter Systems. In: MEMS Linear and Nonlinear Statics and Dynamics. Microsystems, vol 20. Springer, Boston, MA. https://doi.org/10.1007/978-1-4419-6020-7_2

[13] İ.E. Ocak, "A Tactical Grade Mems Accelerometer", PhD, Dissertations, 2010, METU, Ankara.

[14] M. Bao, H. Yang, H. Yin, S. Shen: "Effects of electrostatic forces generated by the driving signal on capacitive sensing devices", Sens. Actuator A Phys. 84, 213-219, (2000) https://doi.org/10.1016/S0924-4247(00)00312-5

Low-cost Energy Management System in Homes

F ACUN[1] and M ÇUNKAŞ[2 *]

[1] ERG Operation Transportation and Maintenance Inc. Ankara, Turkey. furkanacun42@gmail.com
[2]Selçuk University, Faculty of Technology, Department of Electrical & Electronics Engineering, 42031, Konya, Turkey. mcunkas@selcuk.edu.tr

Abstract **- Energy management in homes has attracted the attention of many researchers in recent years since houses consume a high amount of energy produced by different energy sources. Energy management in residential buildings is a complex procedure due to the number of interconnected variables in the system. To effectively manage the energy in the residences, an efficient energy control system is required that can reduce the total energy consumption without going too far from the comfort level requested by the user inside the residence. In this study, a low-cost alternative method for energy management in residences has been developed using fuzzy logic. Light, motion, temperature, and sound sensors are used as system inputs. Three different fuzzy logic inference engines were used. Lighting, heating, and cooling output powers were controlled according to sensor data, lighting conditions, ambient temperature, and consumer conditions. The control of the system is provided by a microcontroller, sensors, and Nextion HMI display. As a result of this study, electricity consumption has been reduced to a minimum effect on consumer comfort. Electricity, water, and natural gas consumption were controlled when the consumers were not in the residences, unnecessary consumptions were prevented, and water and natural gas savings were achieved.**

Keywords: Energy consumption, Energy management, Home automation, Consumer electronics, Smart home

I. INTRODUCTION

Energy management is concerned with planning, monitoring, and controlling energy-related processes to protect energy resources, energy cost management and the environment. The purpose of energy management in residences is energy efficiency or energy saving. Although energy efficiency and energy saving may seem the same, they are different terms. Energy efficiency is directly related to sustainable development, the choice of ideal fuel, the choice of renewable energy sources, the continuation of environmental awareness and safety. Energy efficiency in residences refers to the reduction of energy consumption per unit service and consumption-generating device without reducing the living standard and service quality.

Energy efficiency serves to reduce consumption while meeting daily needs. Energy saving is based on reducing energy consumption activities by people using less energy-consuming devices [1]. According to the data obtained after August 2022, the installed power of electricity in Turkey has reached 102,043 MW. Distribution of this installed power by production resources 30.9% is hydraulic energy, 24.8% is natural gas, 20.7% is coal, 10.9% is wind, 8.6% is solar, 1.7% is of which is composed of geothermal, and 2.4% of other resources [2]. Increasing water demands in proportion to the population in the world, the limited water supply of water resources, and the difficulties that will be caused by the climate changes expected in the coming years show that studies will be developed to support water management in houses [3]. This and similar studies on reducing or eliminating water leaks in houses [4] and controlling water consumption [5] are important for water conservation.

Hundreds of chemicals used to drill and break natural gas wells in regions with natural gas, drilling muds during drilling, and diesel emissions during operation show how laborious and costly natural gas is. It shows that studies will be developed to support natural gas management in residences in line with the economical use of natural gas reserves.

Due to the increase in the population of some countries, energy consumption in houses is increasing every year. Each country has developed energy management systems for its benefit. While doing this, it has developed the management techniques of lighting, heating, cooling, ventilation, and household appliances, which are the lowest consumption units that provide energy consumption. In the literature, there are energy and electricity management studies in houses where fuzzy logic [6-13] and neural network [14-15] techniques are used.

In this study, a low-cost energy management system has been developed. Unlike other studies, unnecessary water and natural gas consumption were also controlled, and even if there are leaks in the water line, these leaks are prevented in cases where there is no consumer. Maximum energy savings and optimum comfort management are achieved with three different inference engines and electricity price inputs that can be changed according to Electricity Distribution Company electricity prices and tariffs.

The remainder of this article is organized as follows. Chapter 2 provides information on energy management in residential buildings. Section 3 gives information about the proposed fuzzy logic-controlled system, Section 4 is about the experimental results and Section 5 concludes with the study.

II. Energy Management In Housings

The devices that provide the highest energy consumption in residences are heaters, coolers, lighting systems, and electrical household appliances. The management of these devices should be carried out by maintaining the comfort level at the optimum level according to the consumer situation in the houses. The most common sensors that can be used to detect consumers in residences are motion, light, and sound sensors. The time factor should also be considered when determining the consumer. Consumer identification based on sensor data and instantaneous time will facilitate consumer status estimation. There may be no consumers in the houses, there may be people or pets.

The purpose of energy management in residences is to control the heating, cooling, and lighting systems while maintaining the optimum comfort level of the consumer. The most important parameters when controlling the heating-cooling system are the consumer in the house at the time of consumption, the electricity price determined by the distribution company, and the instantaneous ambient temperature. The most important parameters when controlling the lighting system are the instantaneous illumination of the environment, the brightness level of the outdoor environment, and the electricity price determined by the distribution company. Considering all these parameters, it is possible to determine the consumer status and to change the heating-cooling and lighting output powers. The general scheme for the proposed energy management is given in Figure 1.

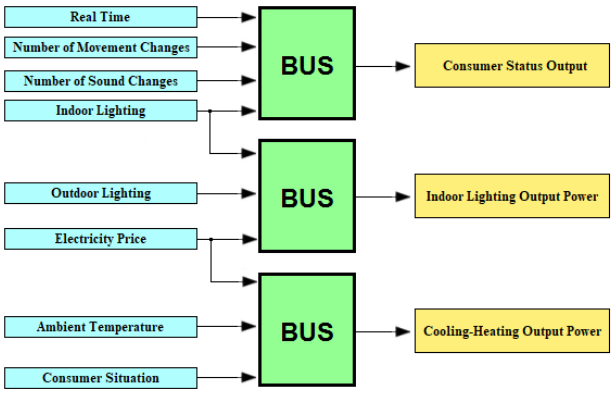

Figure 1: Proposed energy management

III. Proposed System

Fuzzy logic is the human ability to make logical decisions in different situations with uncertain degrees that play a role in reasoning. In this study, Fuzzy logic is used because classical logic cannot produce solutions to incomprehensible and imprecise expressions and does not focus on a single result, such as present or absent, in cases where a variable has different degrees [16]. In the proposed system for energy management in houses, fuzzy logic is used as a method. The energy management system consists of a motion sensor, sound sensor, light sensor, temperature sensor, and real-time clock. Three different inference engines were used in the system. When the system is started, the data received from the motion sensor, sound sensor, light sensor, and real-time clock are analyzed with the 1st fuzzy inference engine and the consumer situation is obtained. The obtained consumer output is analyzed with the second fuzzy inference engine according to the ambient temperature and the instant electricity price determined by the distribution company, and the cooling-heating output powers are obtained. Outdoor lighting, indoor lighting, and the instantaneous electricity price are analyzed with the third fuzzy inference engine and the lighting output powers are determined.

Fuzzy membership sets are calculated with triangular and trapezoidal membership functions. The mathematical expressions for the triangle and the trapezoidal membership functions in Figure 2 and Figure 3 are given in Equation (1) and Equation (2), respectively.

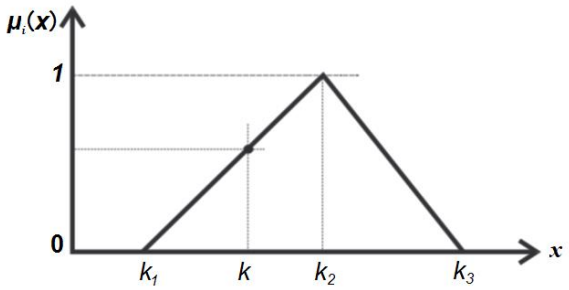

Figure 2: Triangular membership function

$$\mu_i(x;k,k_1,k_2,k_3)=\begin{cases}\dfrac{|k|-|k_1|}{|k_2|-|k_1|}, k_1\le k\le k_2\\ \dfrac{|k_3|-|k|}{|k_3|-|k_2|}, k_2\le k\le k_3\\ 0 \quad for\ other\ situations\end{cases} \tag{1}$$

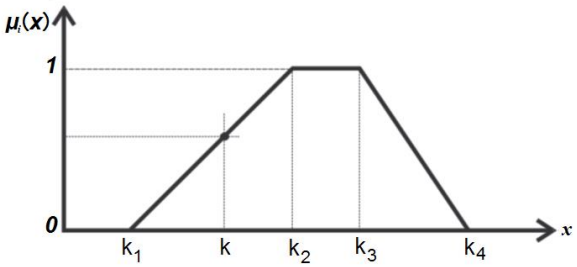

Figure 3: Trapezoidal membership function

$$\mu_i(x;k,k_1,k_2,k_3,k_4)=\begin{cases}\dfrac{|k|-|k_1|}{|k_2|-|k_1|}, k_1\le k\le k_2\\ \dfrac{|k_4|-|k|}{|k_4|-|k_3|}, k_2\le k\le k_3\\ 1 \qquad k_2\le k\le k_3\\ 0 \quad for\ other\ situations\end{cases} \tag{2}$$

Figures 4 -8 shows the input and output membership functions of the first fuzzy logic inference engine.

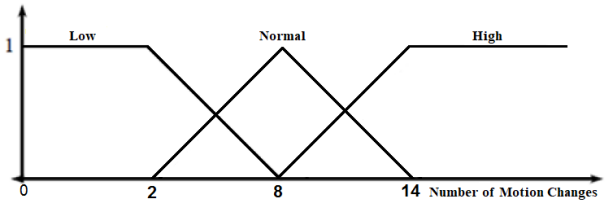

Figure 4: Input membership function for motion change

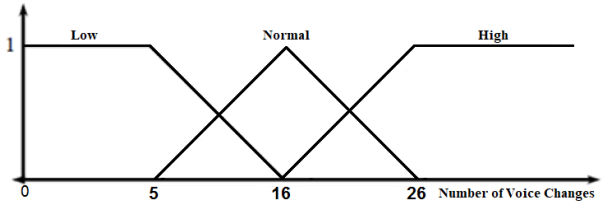

Figure 5: Input membership function for voice change

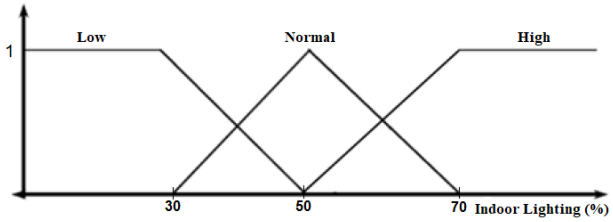

Figure 6: Input membership function for indoor lighting

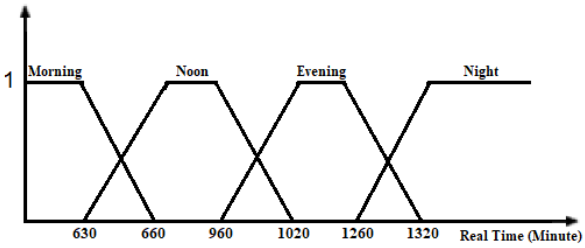

Figure 7: Input membership function for real-time clock

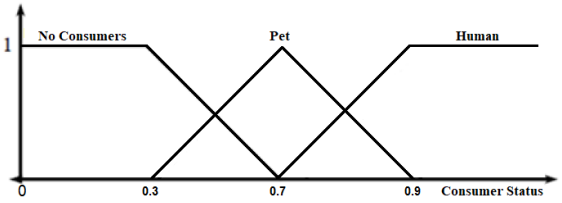

Figure 8: Output membership function for consumer state

Figures 9 -12 shows the input and output membership functions of the second fuzzy logic inference engine.

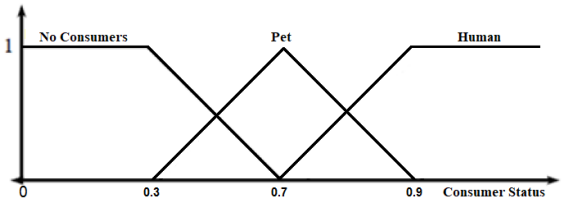

Figure 9: Input membership function for consumer status

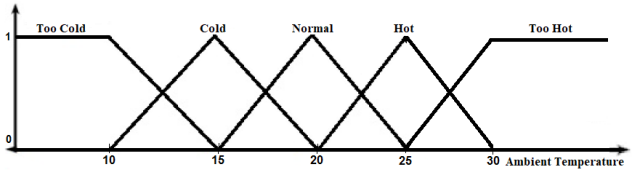

Figure 10: Input membership function for ambient temperature

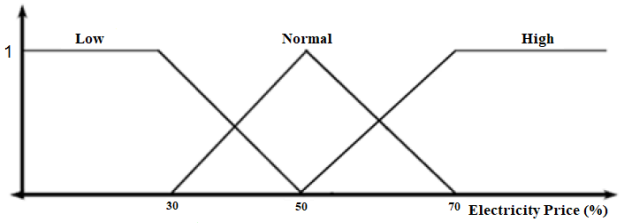

Figure 11: Input membership function for electricity price

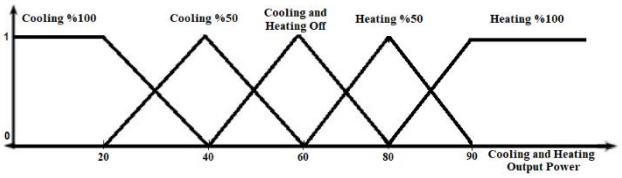

Figure 12: Output power output membership function for cooling and heating

Figures 13-16 shows the input and output membership functions of the third fuzzy logic inference engine.

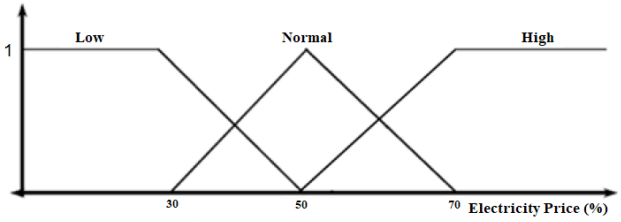

Figure 13. Input membership function for electricity price

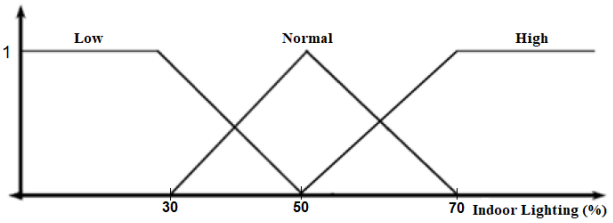

Figure 14. Input membership function for indoor lighting

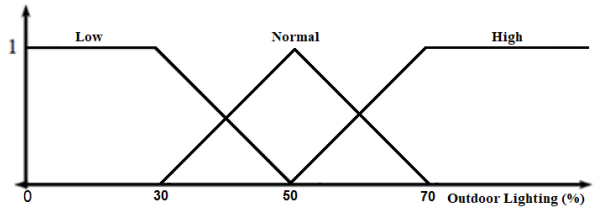

Figure 15: Input membership function for outdoor lighting

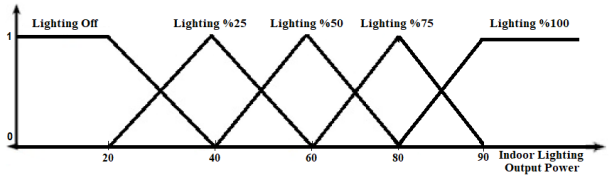

Figure 16: Output power membership function for indoor lighting

There are 108 rules for the first inference engine, 45 rules for the second inference engine, and 27 rules for the third inference engine. Mamdani minimum inference method was used as the inference method. Centroid defuzzification method given in Figure 17, Equation (3) was applied in the clarification process of the data processed according to these three separate rule bases.

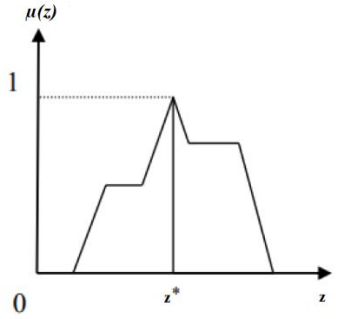

Figure 17: Centroid defuzzification method

$$(z^*) = \frac{\sum_{i=1}^{n} z_i \cdot \mu_C(z_i)}{\sum_{i=1}^{n} \mu_C(z_i)} \quad (3)$$

The names, abbreviations, linguistic variables, and explanations of the input-output variables of the membership function are given in Table 1.

Table 1: Linguistic variables and descriptions.

Description	Linguistic Variables
Motion Change Low	MCL
Motion Change Normal	MCN
Motion Change High	MCH
Voice Change Low	VCL
Voice Change Normal	VCN
Voice Change High	VCH
Indoor Lighting Low	ILL
Indoor Lighting Normal	ILN
Indoor Lighting High	ILH
Time Morning	TM
Time Noon	TNO
Time Evening	TE
Time Night	TN
No Consumers	NC
Consumer Pet	CP
Consumer Human	CH
Electricity Price is Low	EPL
Electricity Price is Normal	EPN
Electricity Price is High	EPH
Ambient Temperature Too Cold	ATTC
Ambient Temperature Cold	ATC
Ambient Temperature Normal	ATN
Ambient Temperature Hot	ATH
Ambient Temperature Too Hot	ATTH
Cooling Power %50	CP %50
Cooling Power %100	CP %100
Cooling and Heating Off	CHO
Heating Power %50	HP %50
Heating Power %100	HP %100
Outdoor Lighting Low	OLL
Outdoor Lighting Normal	OLN
Outdoor Lighting High	OLH
Indoor Lighting Off	ILO
Indoor Lighting Output Power %25	ILOP %25
Indoor Lighting Output Power %50	ILOP %50
Indoor Lighting Output Power %75	ILOP %75
Indoor Lighting Output Power %100	ILOP %100

According to the instantaneous data obtained from the light sensor, sound sensor, motion sensor, and real-time clock, the consumer is detected with the first fuzzy logic inference engine. An 'IF THEN' process for this is defined as follows.

- IF indoor lighting is low AND voice change is low AND movement change is low AND the time is morning then consumer status is no consumers
- IF indoor lighting is normal AND voice change is normal AND movement change is low AND the time is noon then consumer status is consumer pet
- IF indoor lighting is low AND voice change is high AND movement change is normal AND the time is evening then consumer status is consumer human

  .
  .
  .
- IF indoor lighting high AND voice change high AND movement change high AND the time is night then consumer status is consumer human

If the consumer output is "human exists", no shutdown has been made for electricity, water, and natural gas. If the consumer output is "pet exists", electricity and water consumption has not been shut down, and only natural gas has been turned off.

With the second fuzzy logic inference engine, cooling or heating was operated at 50% or 100% power according to the consumer situation in the house, instant electricity price, and ambient temperature. In cases where the ambient temperature is maintained and the consumer output is "no consumer", heating and cooling are turned off. The examples of 'IF THEN' process for this is below.

- IF consumer status is no consumers AND electricity price is high AND the ambient temperature is too hot then cooling and heating power is off
- IF consumer status is consumer pet AND electricity price is low AND ambient temperature is too cold then cooling and heating power is 50%
- IF consumer status is consumer human AND electricity price is low AND ambient temperature too cold then cooling and heating power is 100%
- IF consumer status is consumer human AND electricity price is normal AND ambient temperature is too hot then cooling and heating power is 50%

.
.
.

- IF consumer status is consumer human AND electricity price is high AND ambient temperature is hot then cooling and heating power is off
- IF consumer status is consumer human AND electricity price is high AND ambient temperature is too cold then cooling and heating power is 50%

With the third fuzzy logic inference engine, the lighting output powers are set as 25%, 50%, 75%, 100% or off according to the electricity price, indoor lighting level and outdoor lighting level. The examples of 'IF THEN' process is below.

- IF the electricity price is low AND indoor lighting low AND outdoor lighting is low then indoor lighting output power is 100%
- IF the electricity price is normal AND indoor lighting is low AND outdoor lighting is high then indoor lighting is off
- IF the electricity price is normal AND indoor lighting is high AND outdoor lighting is normal then indoor lighting power is 25%
- IF the electricity price is high AND indoor lighting is low AND outdoor lighting is low then indoor lighting power is 50%

.
.
.

- IF the electricity price is high AND indoor lighting is high AND outdoor lighting is low then indoor lighting power is 50%
- IF the electricity price is high AND indoor lighting is high AND outdoor lighting is high then indoor lighting is off

IV. Experiment Results

All the data received from the sensors in the system are read by the microcontroller, processed in three different fuzzy logic inference engines according to three separate rule bases, and the result is found by defuzzification. Nextion HMI screen was used for the control of the system and the proposed method was tested on a model house. The Nextion HMI interface of the developed control system is shown in Figure 18.

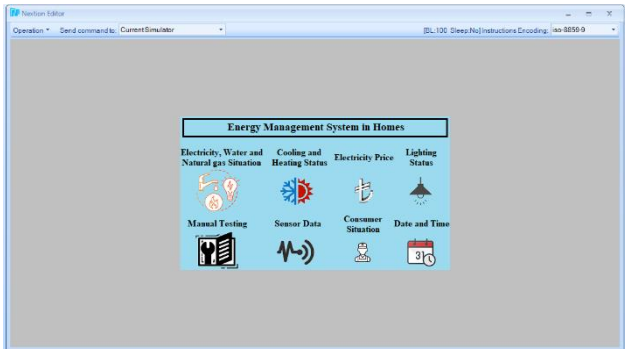

Figure 18: Interface of the proposed system

A manual test section has been added so that we can test the study results separately. The operating status of the system was tested according to the selected parameters instantly. Figure 19 and Figure 22 are examples showing the interface where parameters are entered. In the figures, the consumer status, cooling-heating output powers, interior lighting output powers, and output values obtained because of clarification are shown on the right. Depending on the consumer status, the on and off states of electricity, water, and natural gas are also added. Figure 20 and Figure 23 show the mathematical results obtained because of the Centroid defuzzification method. In Figure 21 and Figure 24, the values of the output membership functions are shown according to the defuzzification result.

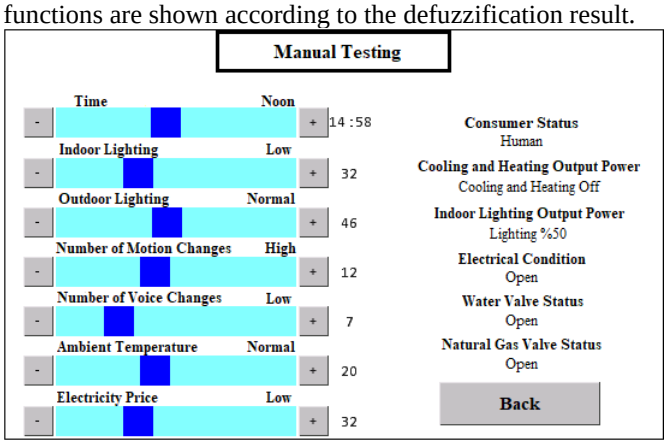

Figure 19: Test parameters and results for case-1

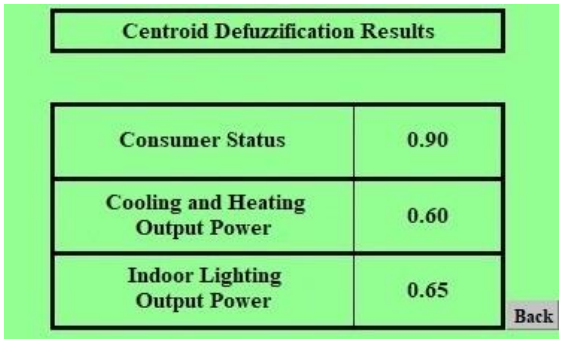

Figure 20 Centroid defuzzification for case 1

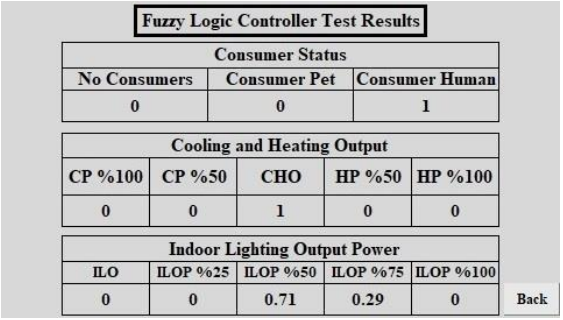

Figure 21: Test results for case 1

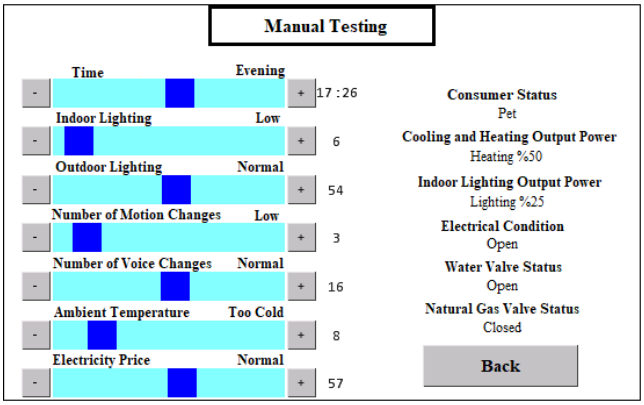

Figure 22: Test parameters and results for case-2

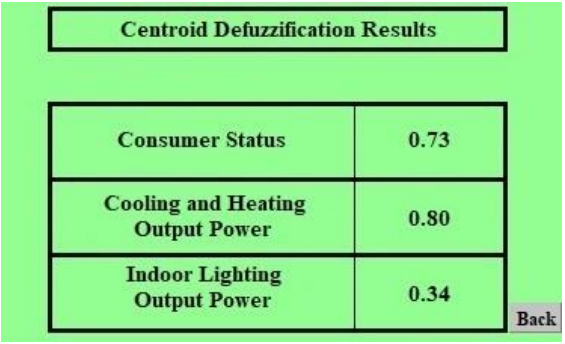

Figure 23: Centroid defuzzification for case 2

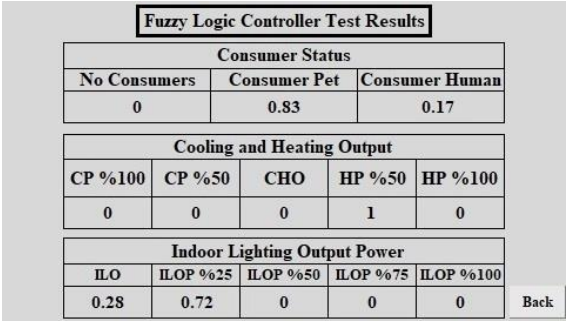

Figure 24: Test results for case 2

V. CONCLUSION

This study has presented low-budget energy management with fuzzy logic control in residences. The cooling and heating output powers of the residences were controlled according to the instantaneous state of the electricity price, the state of the consumer, and the ambient temperature. In addition, lighting output powers were adjusted according to indoor lighting level, outdoor lighting level, and instant electricity price. Thus, fuzzy logic inference engines have been used efficiently in the energy management system and unnecessary consumptions that may occur in electricity, water, and natural gas have been saved in the absence of consumers.

For future studies, the control system can be monitored remotely via an application using the wi-fi module. Through the manual test section, special settings can be made for natural gas, water, and electricity. Smart home appliances in residences such as washing machines and ovens etc. can be remotely controlled. The energy of household appliances can be turned on and other energies turned off, the consumptions needed at that moment can be protected and unnecessary consumptions can be saved.

REFERENCES

[1] L. Shinn. (2018, August). Energy Efficiency: The Clean Facts. [Online]. Available: https://www.nrdc.org/stories/energy-efficiency-clean-facts

[2] T.C. Enerji ve Tabii Kaynaklar Bakanlığı (2022, September). Elektrik. [Online]. Available: https://enerji.gov.tr/bilgi-merkezi-enerji-elektrik

[3] A. Cominola, M. Giuliani, D. Piga, A. Castelletti, and A. E. Rizzoli "Benefits and challenges of using smart meters for advancing residential water demand modeling and management: A review" *Environmental Modelling & Software*, vol.72, pp. 198-214, October 2015.

[4] J. O. Nelson, *Home Water Savings Project*. United States of America: Journal of Contemporary Water Research and Education, 1990.

[5] A. J. R. Alves, L. T. Manera, and M. V. Campos. (September 2019). Low-cost wireless sensor network applied to real-time monitoring and control of water consumption in residences. *SciELO - Scientific Electronic Library* [Online]. *14(6)*. Available: https://www.scielo.br/j/ambiagua/a/Lq3MpKpYvRcvvCPJ8PWj9qC/?lang=en

[6] S. Atef, N. Ismail, and B. Eltawil, "A new fuzzy logic based approach for optimal household appliance scheduling based on electricity price and load consumption prediction," *Advances in Building Energy Research*, vol. 16, pp. 262-280, January 2021.

[7] D. Kontogiannis, D. Bargiotas, and A. Daskalopulu, *Fuzzy Control System for Smart Energy Management in Residential Buildings Based on Environmental Data*. Greece: Energies, 2021

[8] M. Fayaz, and D. Kim, *Energy Consumption Optimization and User Comfort Management in Residential Buildings Using a Bat Algorithm and Fuzzy Logic*. Korea: Energies, 2018

[9] K. Christopoulos, A. Raptis, C. Antonopoulos, T. Orfanoudakis, and N. S. Voros, "A Scalable Approach to Efficient House Power Consumption and CO_2 Management Through Fuzzy Logic," in *2018 IEEE International Conference on Industrial Technology (ICIT)*.

[10] A. Garrab, A. Bouallegue, and R. Bouallegue, "An Agent Based Fuzzy Control for Smart Home Energy Management in Smart Grid Environment," *International Journal of Renewable Energy Research*, vol. 7, No.2 December 2016.

[11] J. I. Méndez, P. Ponce, O. Mata, A. Meier, T. Peffer, A. Molina, and M. Aguilar, "Empower saving energy into smart homes using a gamification structure by social products," *2020 IEEE International Conference on Consumer Electronics (ICCE)*.

[12] K. T. Prajwal, and V. S. Gupta, "Smart Home Energy Management System using Fuzzy Logic for Continuous Power Supply with Economic Utilisation of Electrical Energy," *Proceedings of the Second International Conference on Inventive Systems and Control (ICISC 2018)*.

[13] R. Zhang, V. Sathishkumar, and R. D. J. Samuel, *Fuzzy Efficient Energy Smart Home Management System for Renewable Energy Resources*, Sustainability, 2020.
[14] C. Mahapatra, A. K. Moharana, and V. C. M. Leung, *Energy Management in Smart Cities Based on Internet of Things: Peak Demand Reduction and Energy Savings.* Canada: Sensors, 2017
[15] M. S. Ahmed, A. Mohamed, R. Z. Homod, and H. Shareef, *Hybrid LSA-ANN Based Home Energy Management Scheduling Controller for Residential Demand Response Strategy*, Energies, 2016.
[16] L. A. Zadeh, "Fuzzy logic," *IEEE*, vol. 21, pp. 83-93, April 1988.

The Role of Thickness and Position of Partial Metal Foam in Jet Impingement Cooling

M. ALBAYRAK[1], K. DAĞIDIR[1] and B. SARPER[1]

[1] Tarsus University, Mersin/Turkey, kayhandagidir@tarsus.edu.tr
[1]Tarsus University, Mersin/Turkey, melisa_albayrak@tarsus.edu.tr
[1]Tarsus University, Mersin/Turkey, bugrasarper@tarsus.edu.tr

***Abstract* - In this study, the effects using partial metal foam in electronics cooling are analyzed numerically. The focus is on the role of thickness and location of the partial metal foam on convective heat transfer, while porosity ($\varepsilon = 0.9005$), pore density ($\omega = 20$ PPI), permeability ($K = 0.9 \times 10^{-7}$) and jet Reynolds number ($Re_J = 50$) do not change. The jet flow is considered to be two-dimensional and laminar, and the flow and heat transfer in the porous media are modeled using the Brinkman-Darcy-Forchheimer and local thermal non-equilibrium (LTNE) models, respectively. As a result of the study, it is determined that convective heat transfer improves by up to 36.26% in the use of metal foam compared to the case without metal foam.**

***Keywords* – Electronics Cooling, Jet Impingement, Partial Metal Foam, Porous Media.**

I. INTRODUCTION

NOWADAYS, researchers make an effort to develop innovative methods for the improvement of technologies based on energy efficiency. Applications related to porous materials, also called foam, can also be considered as one of these innovative methods. Porous materials are used extensively in heat transfer applications due to properties such as light weight, high thermal conductivity, high permeability, and large heat transfer surface areas. Metal foams are frequently preferred in various industrial applications such as electronics cooling, battery cooling and heat recovery [1, 2].

It is predicted that the use of metal foam may be beneficial in the jet impingement applications, primarily used in the electronics cooling. Wong and Saeid [3] numerically investigated the effects of the porous material completely covering the flow domain in a heated channel in laminar jet impingement. In that study, it was stated that the average Nusselt number augmented with increasing porosity. Dorea and Lemos [4] numerically investigated the heat transfer characteristics of a heated surface covered with porous material in laminar jet impingement. In that study, it was noted that the porous medium affected the temperature distribution in the stagnation zone. Buonomo et al. [5] experimentally investigated the effects of the use of porous material on the heat transfer behavior of a wall heated by constant heat flux and cooled by a laminar jet. The study reported that the use of metal foam improved heat transfer from the heated wall. Buonomo et al. [6] numerically investigated the heat transfer characteristics of the laminar impinging jet in a parallel plate channel partially covered with a porous medium. The study emphasized that the use of metal foam provided an improvement in heat transfer. Hosseinalipour et al. [7] numerically investigated the influence of a porous block placed on a heated surface on the heat transfer characteristics in the laminar impinging jet. In the study, it was observed that the use of porous material could change the Nusselt number distribution on the heated plate.

The position and thickness of the metal foams placed in the flow domain are fixed in the recent studies. It is known that metal foams are used in different positions and thicknesses as applied in different application areas [8]. It is anticipated that the use of metal foams in different positions and thicknesses in impinging jets can improve heat transfer rate. Thus, in this study, the use of a partial aluminum foam at different locations for various thicknesses with the constant values of porosity, pore density, permeability and Reynolds number is investigated numerically.

II. NUMERICAL METHOD

A. Problem Description and Mathematical Model

Schematic representation of the impinging jet geometry investigated in this study is given in Fig. 1a. Since the problem is symmetrical, only the half of the geometry is taken into account and the symmetrical solution is realized. In the schematic representation, W, L, s, H, and g represent half of the nozzle width, half of the heated surface length, half of the adiabatic surface length, nozzle-to-heated surface distance and gravitational acceleration, respectively. The target plate is heated locally and has a constant temperature (T_H). Other parts of the target plate and upper surfaces are adiabatic. The air at the inlet of the jet nozzle has uniform velocity (u_0) and temperature (T_0). At the outlet, the outflow boundary condition is applied. The Reynolds number used in the study is 50 and the flow is laminar and steady-state.

The configurations of the aluminum foam are given in Fig. 1b. The aluminum foam used in the study is first placed on the upper surface and then positioned on the heated surface. Except for the Case 0 and Case 1, the aluminum foam length (L_p) is fixed and is 27 mm. W, L, H and s are 3 mm, 30 mm, 30 mm and 180 mm, respectively. In Case 0, no metal foam is used, and in Case 1, the metal foam covers the whole area except the

underneath of the jet nozzle. The thickness of the aluminum foam (t_p) is gradually changed and its effect on convective heat transfer is evaluated for other cases.

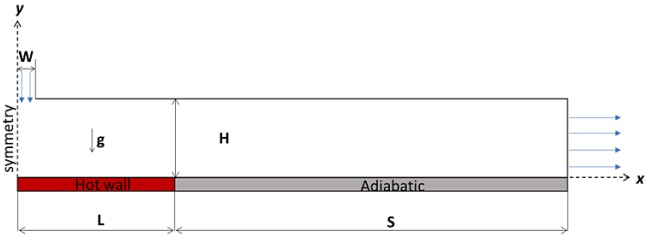

a) Schematic representation of the symmetrical flow domain.

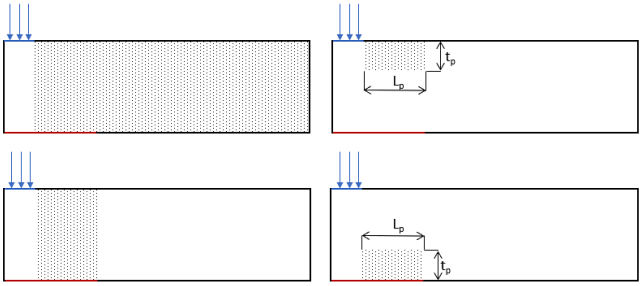

b) Position and thickness of porous region.

Figure 1: Schematic representations of the flow domain considered cases.

All thermophysical properties of air does not change with temperature. It is considered that the metal foam has uniform, homogeneous and isotropic porous medium properties. In numerical analyses, the Brinkman-Darcy-Forchheimer flow and Local Thermal Nonequilibrium (LTNE) energy models are used together [9]. Conservation equations for the clear zone and porous zone are expressed separately [10].

Navier-Stokes and energy equations for the flow region without metal foam are given in Equations from (1) to (4).

Continuity equation:

$$\frac{\partial u}{\partial x}+\frac{\partial v}{\partial y}=0 \tag{1}$$

x-momentum equation:

$$\rho_f\left(u\frac{\partial u}{\partial x}+v\frac{\partial u}{\partial y}\right)=-\frac{\partial P}{\partial x}+\mu_f\left(\frac{\partial^2 u}{\partial x^2}+\frac{\partial^2 u}{\partial y^2}\right) \tag{2}$$

y-momentum equation:

$$\rho_f\left(u\frac{\partial v}{\partial x}+v\frac{\partial v}{\partial y}\right)=-\frac{\partial P}{\partial y}+\mu_f\left(\frac{\partial^2 v}{\partial x^2}+\frac{\partial^2 v}{\partial y^2}\right) \tag{3}$$

Energy equation:

$$\left(\rho c_p\right)_f\left(u\frac{\partial T_f}{\partial x}+v\frac{\partial T_f}{\partial y}\right)=k_f\left(\frac{\partial^2 T_f}{\partial x^2}+\frac{\partial^2 T_f}{\partial y^2}\right) \tag{4}$$

Here, the terms u and v represent the velocities in the x and y directions, respectively. T and P represent the fluid temperature and pressure, respectively. The subscript f represents the fluid. Density, viscosity, specific heat and thermal conductivity are represented by the symbols ρ, μ, c_p and k, respectively.

Terms in the Navier-Stokes and energy equations given for the porous media are obtained by applying the representative elementary volume approach and the volume average technique [11,12]. Thus, these terms are expressed with the subscript of p.

Navier-Stokes and energy equations for the porous media are given in Equations from (5) to (9).

Continuity equation:

$$\frac{\partial u_p}{\partial x}+\frac{\partial v_p}{\partial y}=0 \tag{5}$$

x-momentum equation:

$$\frac{\rho_f}{\varepsilon^2}\left(u_p\frac{\partial u_p}{\partial x}+v_p\frac{\partial u_p}{\partial y}\right)=-\frac{\partial P_p}{\partial x}+\underbrace{\frac{\mu_f}{\varepsilon}\left(\frac{\partial^2 u_p}{\partial x^2}+\frac{\partial^2 u_p}{\partial y^2}\right)}_{Brinkman\ term}-\underbrace{\frac{\mu_f}{K}u_p}_{Darcy\ term}-$$

$$\underbrace{\frac{C_F}{\sqrt{K}}\rho_f\sqrt{{u_p}^2+{v_p}^2}\,u_p}_{Forchheimer\ term} \tag{6}$$

y-momentum equation:

$$\frac{\rho_f}{\varepsilon^2}\left(u_p\frac{\partial v_p}{\partial x}+v_p\frac{\partial v_p}{\partial y}\right)=-\frac{\partial P_p}{\partial y}+\underbrace{\frac{\mu_f}{\varepsilon}\left(\frac{\partial^2 v_p}{\partial x^2}+\frac{\partial^2 v_p}{\partial y^2}\right)}_{Brinkman\ term}-\underbrace{\frac{\mu_f}{K}v_p}_{Darcy\ term}-$$

$$\underbrace{\frac{C_F}{\sqrt{K}}\rho_f\sqrt{{u_p}^2+{v_p}^2}\,v_p}_{Forchheimer\ term} \tag{7}$$

In equations given for porous media, ε, K and C_F express the porosity, permeability and Forchheimer coefficient, respectively.

The energy equation is separately considered for both the fluid (air) phase and the solid (aluminum foam) phase.

Fluid phase:

$$\left(\rho c_p\right)_f\left(u_p\frac{\partial T_f}{\partial x}+v_p\frac{\partial T_f}{\partial y}\right)=\varepsilon k_f\left(\frac{\partial^2 T_f}{\partial x^2}+\frac{\partial^2 T_f}{\partial y^2}\right)+h_{sf}\,a_{sf}\left(T_s-T_f\right) \tag{8}$$

Solid phase:

$$(1-\varepsilon)\,k_s\left(\frac{\partial^2 T_s}{\partial x^2}+\frac{\partial^2 T_s}{\partial y^2}\right)-h_{sf}\,a_{sf}\left(T_s-T_f\right)=0 \tag{9}$$

In the LTNE energy model, h_{sf} and a_{sf} are calculated using the Eqs. (10) and (11) [13].

$$h_{sf} = \begin{cases} 0.75\, Re_{d_b}^{0.4}\, Pr_{air}^{0.37} \left(\frac{k_f}{d_b}\right), & 1 \le Re_{d_b} \le 40 \\ 0.51\, Re_{d_f}^{0.5}\, Pr_{air}^{0.37} \left(\frac{k_f}{d_b}\right), & 40 \le Re_{d_b} \le 1000 \\ 0.26\, Re_{d_f}^{0.6}\, Pr_{air}^{0.37} \left(\frac{k_f}{d_b}\right), & 1000 \le Re_{d_b} \le 2 \times 10^5 \end{cases} \quad (10)$$

$$\alpha_{sf} = \frac{3\pi d_b}{(0.59\, d_p)^2}\left(1 - e^{-\frac{1-\varepsilon}{0.04}}\right) \quad (11)$$

Here, subscript s represents the solid phase, α_{sf} and h_{sf} represent the specific surface area density and the heat transfer coefficient of porous media, respectively.

$$\frac{K}{{d_p}^2} = 0.00073(1-\varepsilon)^{-0.224}\left(\frac{d_b}{d_p}\right)^{-1.11} \quad (12)$$

$$c_f = 0.00212(1-\varepsilon)^{-0.132}\left(\frac{d_b}{d_p}\right)^{-1.63} \quad (13)$$

Here, d_b and d_p represent fiber and pore diameters, respectively.

The related dimensionless numbers are calculated by the following equations.

The jet Reynolds number is:

$$Re_j = \frac{\rho_f u_o 2W}{\mu_f} \quad (14)$$

The Prandtl number is:

$$Pr_{air} = \frac{\mu_f c_p}{k_f} \quad (15)$$

The local Nusselt numbers for fluid and solid zones are:

$$Nu_f = \frac{h_f 2W}{k_f} \quad (16)$$

$$Nu_s = \frac{h_s 2W}{k_f} \quad (17)$$

The local and average total Nusselt numbers are:

$$Nu_{tot} = \frac{h_{tot} 2d}{k_f} = \frac{(h_f + h_s)2d}{k_f} \quad (18)$$

$$Nu_{tot,ave} = \frac{h_{tot,ave} 2W}{k_f} = \frac{(h_{f,ave} + h_{s,ave})2W}{k_f} \quad (19)$$

The metal foam properties used in the analyses are given in Table 1. Investigations are performed at a constant jet Reynolds number of 50.

Table 1. Aluminum foam properties [14].

ω [PPI]	ε	Kx10^7 [m^2]	C_F
20	0.9005	0.90	0.088

B. *Numerical Solution Procedure*

Numerical analyses are performed using the ANSYS Fluent 2021 R2, a commercial computational fluid dynamics software. The SIMPLE algorithm is applied for the coupling of velocity and pressure, and the PRESTO scheme is used for interpolation of the pressure. The momentum equations are discretized by the 2nd order upwind scheme. The convergence criteria are met with an approximation of 10^{-5} for the velocity components and 10^{-8} for the temperature components.

C. *Grid structure*

In the simulations, a rectangular grid structure is used, which is concentrated towards the heated plate and the adiabatic upper surface. For the grid independency study, solutions are performed on four different grids, and the total average Nusselt numbers are calculated on the heated surface for each grid. When the results in Table 2 are examined, it is considered that the number of 25200 cells is sufficient for final simulations.

Table 2. Results of the grid independency.

Cell no.	$Nu_{tot,ave}$	Error (%)
6240	4.066	-
11200	4.098	0.799
25200	4.128	0.736
99360	4.154	0.623

D. *Validation of the Solution Algorithm*

The numerical model applied in this study is validated using a similar study in the literature [9]. The average Nusselt numbers obtained as a result of the validation performed for three different Peclet numbers (350, 750, and 1500) as shown in Fig. 2. As seen in Fig. 2, the numerical model agrees with the literature [9], especially at low Peclet numbers, and these results are considered to be sufficient in terms of validation of the solution algorithm.

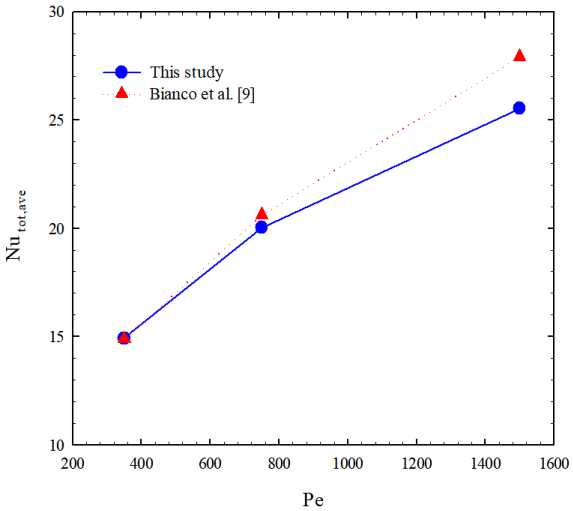

Figure 2: Results of the validation study.

III. Results and Discussion

In this study, the role of partial aluminum foam thickness and location on the jet impingement cooling characteristics of a heated plate is numerically investigated. The focal point of the study is on the influence of the thickness and location of the partial metal foam on the convective heat transfer characteristics, while porosity ($\varepsilon = 0.9005$), pore density ($\omega = 20$ PPI), permeability ($K = 0.9 \times 10^{-7}$) of the aluminum foam and jet Reynolds number ($Re_J = 50$) are held constant.

Velocity and temperature contours are given in Fig. 3 for all studied cases. In Case 0, there is no aluminum foam in the flow domain. In Case 1, the aluminum foam covers the entire flow domain except for the stagnation region, while in Case 2, the top of the heated plate is completely covered with aluminum foam, except for the stagnation region. In Case 0, the air coming out of the nozzle impinges the heated plate and then flows to the outlet where the pressure is lower. In the wall jet region, the boundary layer thickness gradually increases, and at about x=0.04'm, the fluid separates from the surface. In addition, a large secondary flow zone arises next to the jet nozzle. Parallel to the hydrodynamic boundary layer, the thermal boundary layer thickness also increases in this case, as expected. In Case 2, the velocity and temperature fields are almost the same as in Case 1. From Case 3 to Case 7, the thickness of the partial aluminum foam is gradually increased towards the heated plate in 5 mm increments. In Case 3, it is seen that a large secondary cell is formed in the vicinity of aluminum foam, and this cell is divided into two with an increase in the thickness of the foam. In Cases 6 and 7, the cells downstream of the foam appear, while the cells underneath the foam disappear. When examining the temperature contours, it is seen that the cold air leaving the nozzle significantly affects the aluminum foam from the Case 3 to Case 5. In these cases, the temperature of the air inside the foam is almost equal to the jet temperature. Further increase in the foam thickness increases the interaction of the heated plate with the foam, causing the foam to heat up slightly. In Case 8 and beyond, the foam is in contact with the heated plate, while the foam thickness is reduced by 5 mm decrements. When the velocity contours are examined, the air penetrates into the aluminum foam in Case 8, but a secondary cell is formed at about x=0.04 m. The gradual reduction in foam thickness causes the formation of another cell downstream of the jet nozzle, and the width of the secondary cell increases as the foam thickness decreases. This indicates that the aluminum foam exhibits an obstacle behavior. When the temperature contours are examined, it is seen that the aluminum foam is heated by absorbing the heat from the heated plate, and the air temperature in the foam is uniform.

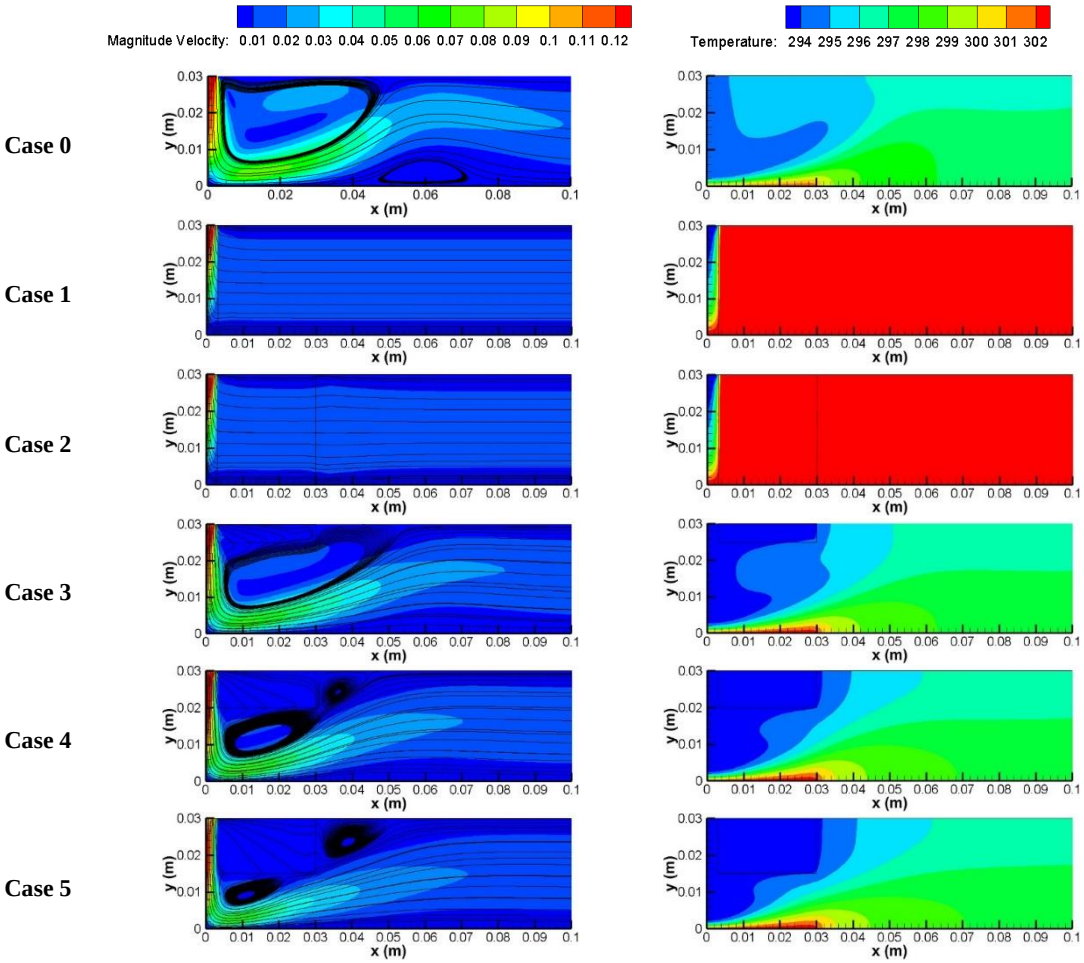

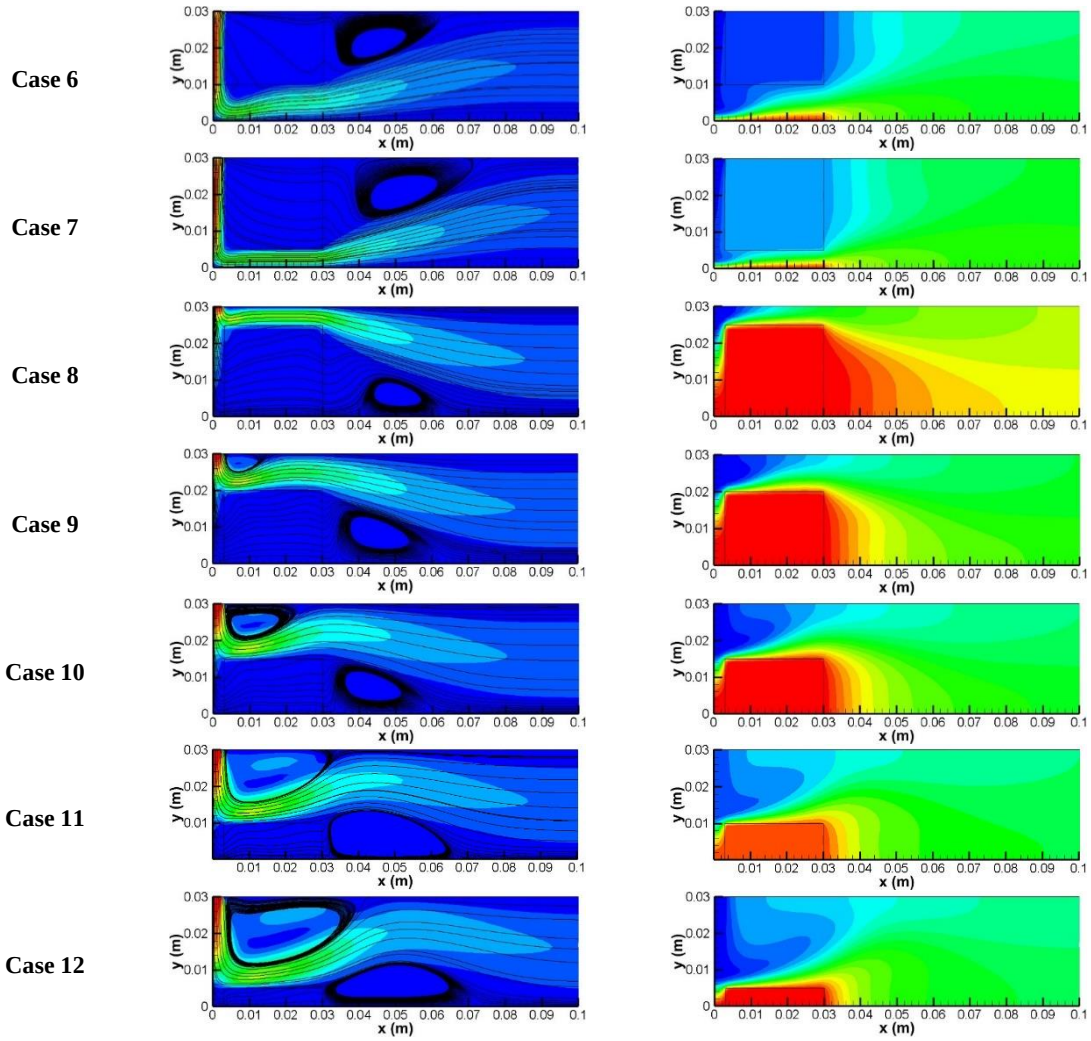

Figure 3: Velocity and temperature contours for different cases.

The total local Nusselt number variation on the heated plate for all cases is shown in Fig. 4. In Cases 1 and 2, the local Nusselt number values are close to each other and higher than in other cases studied. In contrast to Case 2, the local Nusselt number increases towards the outlet in Case 1. This is due to the fact that the aluminum foam fills the flow region up to the outlet in Case 1. In Cases 1 and 2, the local Nusselt number values are very low in the stagnation region, since the aluminum foam fills the flow region. When the aluminum foam is placed on top, the local Nusselt number values are higher in the stagnation region due to the cross-sectional narrowing with the increase of the foam thickness. When the foam is placed on the heated plate, the local Nusselt number values in the stagnation region are very close to zero, similar to the Cases 1 and 2. At this point, the increase in foam thickness increases the local Nusselt number, especially in the wall jet region.

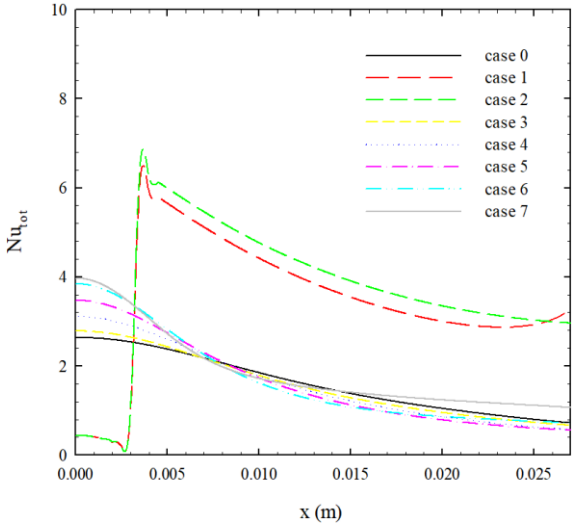

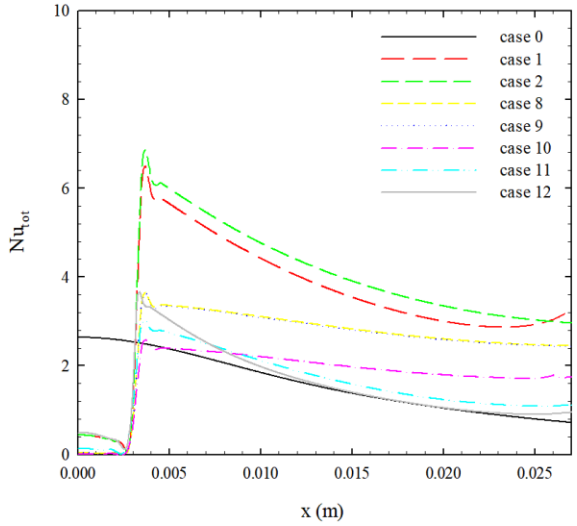

Figure 4: Total local Nusselt number variation at the heated plate for different cases.

The total average Nusselt number variation on the heated plate due to the change in aluminum foam thickness is shown in Fig.5. The use of aluminum foam improves convective heat transfer, while the increase in foam thickness promotes this improvement. In addition, it is seen that aluminum foam affects the Nusselt number more when it is in contact with the heated plate than when it is not, and the Nusselt number is the highest when the top of the heated plate is completely covered with aluminum foam.

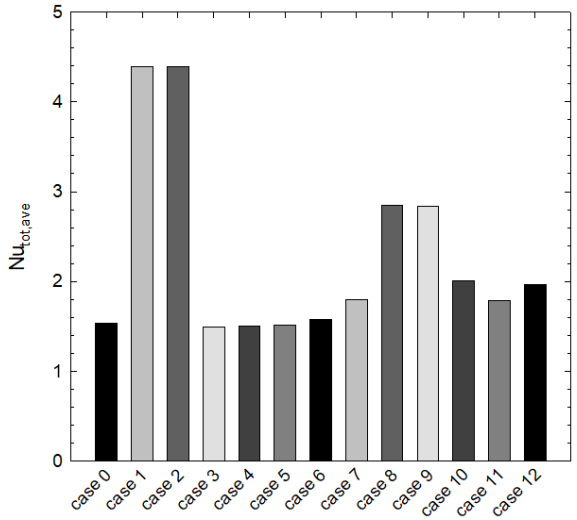

Figure 5: Total average Nusselt numbers for different cases.

IV. Conclusion

In this study, the role of thickness and location of the partial metal foam on jet impingement cooling of a heated plate is numerically investigated. The important findings of the study are as follows:

- The location and thickness of the partial metal foam significantly affect the temperature and velocity fields.
- In all cases except Cases 1 and 2, secondary flows occur within the flow domain.
- Temperature fields are significantly affected by the velocity distribution.
- Secondary flows occurring near the jet nozzle and in the vicinity of aluminum foam are affected by foam location and thickness.
- Increasing the foam thickness while the foam is on top improves convective heat transfer. Similar results are valid for cases where the foam is on the heated plate, but the results obtained for Case 10 and 11 are quite close to each other.
- While convective heat transfer is highest in Cases 1 and 2, the heat transfer rate is also higher when aluminum foam comes into contact with the heated plate.
- When the results are evaluated, it is considered that the aluminum foam is a good alternative to improve convective heat transfer in impinging jet applications.

References

[1] A. T. W. Kuruneru, K. Vafai, E. Sauret, and Y. T. Gu, "Application of porous metal foam heat exchangers and the implications of particulate fouling for energy-intensive industries," *Chemical Engineering Science*, vol. 228 (115968), 2020.

[2] S. Rashidi, M. H. Kashefi, K. C. Kim, and O. Samimi-Abianeh, "Potentials of porous materials for energy management in heat exchangers - A comprehensive review," *Applied Energy*, vol. 243, pp. 206–232, 2019

[3] K. C. Wong and N. H. Saeid, "Numerical study of mixed convection on jet impingement cooling in a horizontal porous layer under local thermal non-equilibrium conditions," *International Journal of Thermal Sciences*, vol. 48:5, pp. 860-870, 2009.

[4] F. T. Dorea and M. J. S. Lemos, "Simulation of laminar impinging jet on a porous medium with a thermal non-equilibrium model," *International Journal of Heat and Mass Transfer*, vol. 53:23–24, pp. 5089-5101, 2010.

[5] B. Buonomo, L. Cirillo, O. Manca, N. Mansi, and S. Nardini, "Confined impinging jets in porous media," *Journal of Physics: Conference Series*, vol. 745(032142), 2016.

[6] B. Buonomo, O. Manca, S. Nappo, and S. Nardini, "Numerical investigation on laminar slot-jet impinging on a surface at uniform heat flux in a channel partially filled with a porous medium," *Energy Procedia*, vol. 148, pp. 790-797, 2018.

[7] S. M. Hosseinalipour, S Rashidzadeh, M. Moghimi, and K Esmailpour, "Numerical study of laminar pulsed impinging jet on the metallic foam blocks using the local thermal non-equilibrium model," *Journal of Thermal Analysis and Calorimetry*, vol. 141, pp. 1859-1874, 2020.

[8] K. Dağıdır, B. Sarper and MT Erdinç , "The numerical investigation of the effects of porous material pore density and thickness on heat transfer and pressure drop in in-line type pipe bundles," *Dokuz Eylul University Faculty of Engineering Journal of Science and Engineering*, vol. 24:71, pp. 447-461. 2022.

[9] V. Bianco, B. Buonomo, A. Pasqua, O. Manca, "Heat transfer enhancement of laminar impinging slot jets by nanofluids and metal foams," *Thermal Science and Engineering Progress*, vol. 22: 100860, 2021.

[10] S. Akar, S. Rashidi, and J.A. Esfahani, "Appropriate position of porous insert in a heat exchanger by thermohydraulic analysis", *Heat Transfer-Asian Res.*, vol. 46, pp. 1363-1379, 2017.

[11] S. Whitaker, "The Method of Volume Averaging," Springer, Netherlands, 1998.

[12] D. A. Nield, A. Bejan, "Convection in Porous Media," Fourth Ed., Springer, New York. 2013.

[13] A. Bhattacharya, V. V. Calmidi, R. L. Mahajan. Thermophysical properties of high porosity metal foams, *International Journal of Heat and Mass Transfer*, vol. 45, pp. 1017-1031, 2002.

[14] V. Calmidi, R. L. Mahajan, "Forced convection in high porosity metal foams," *Asme J. Heat Transfer*, vol. 122, pp. 557-565, 2000.

The Impact of Geometrical Parameters of Stenosis on Blood Flow Modeling

A. MUFTUOGULLARI[1], M. ALBAYRAK[1], M. SUNER[1] and B. SARPER[1]

[1] Tarsus University, Mersin/Turkey, ali_muftuogullari@tarsus.edu.tr
[1] Tarsus University, Mersin/Turkey, melisa_albayrak@tarsus.edu.tr
[1] Tarsus University, Mersin/Turkey, msuner@tarsus.edu.tr
[1] Tarsus University, Mersin/Turkey, bugrasarper@tarsus.edu.tr

***Abstract* – The aim of the study is to investigate the role of stenosis degree and corner rounding on the alteration of pressure, velocity and wall shear stress in intravascular flow. Three-dimensional simulations are performed with the ANSYS Fluent software in the steady-state regime. The flow rate of the blood is kept constant throughout the studies, and the blood is modeled both as Newtonian and non-Newtonian for four stenosis degrees (%20, %40, %60 and %80) and two corner rounding values (r_c/r_a =0.0 and 0.5). Non-Newtonian behavior is modeled using the Carreau model. The flow structures, the peak values of the velocity, wall pressure and wall shear stress alterations are scrutinized in the stenotic and post-stenotic areas, and it is found that the peak values increase as the stenosis degree increases and the recirculation lengths in the post-stenotic region are found to be shorter for both sharp corner and rounded corner in the non-Newtonian model.**

***Keywords* - Atherosclerosis, Carreau Model, Corner Rounding, Intravascular Flow, Stenosis Degree**

I. INTRODUCTION

ATHEROSCLEROSIS, the most common type of cardiovascular disease, is a leading reason of many deaths globally. This disease, which is a pathological circumstance, is the result of stenosis caused by the accumulation of factors such as fat, inflammation and cholesterol on the vessel wall [1,2]. In addition to the fact that stenosis is associated with the risk factors mentioned above, it is more likely to occur in the curved and bifurcated areas in the vessel [3]. The stenosis in the vessels leads to significant increases in blood and wall pressure, a sudden rise in wall shear stress and the formation of secondary flows in the post-stenotic region. Wall shear stress causes fat, cholesterol and inflammation in the blood to attach to the vessel wall, and this is more likely to occur in areas where wall shear stress is low and oscillating. This in turn is a key factor in the development of atherosclerosis. For this reason, stenotic artery hemodynamics is designated by wall shear stress descriptors [4-7].

Numerous studies in the literature, including in vivo and in vitro, address the role of stenosis degree and different factors on the wall shear stress descriptors in steady-state regime or transient periodic flow. He et al. [8] investigated that branch geometry has a significant risk factor for the formation of atherosclerosis and executed numerical analyzes to assess hemodynamics in three different 90° T-shaped geometries with respect to Reynolds numbers ranging from 15 to 350. Sung et al. [9] studied the impact of the catheter tip on the pressure measurement in aortic dilatation. On the other hand, they also scrutinized the flow field in the vicinity of dilatation zones by experimental method. Ryval et al. [10] worked on a three-dimensional straight tube, that exhibits 50% diameter reduction for both steady and pulsed flows. In their study, they examined the straight tube in the Reynolds number range from 200 to 1000. Petkova et al. [11] examined the blood flow in two models of a healthy hepatic vein and a stenotic vein respectively. Ryval et al. [12] performed analyzes on 75% and 90% stenotic arteries in steady and periodically pulsatile flows implementing standard and transitional *k-ω* turbulence models. Sun et al. [13] analyzed the effect of plaques on some parameters such as flow structure, pressure, shear stress and velocity distribution in healthy and calcified artery models. Chaichana et al. [14] worked on four realistic, eight simulated left coronary artery models. They investigated the hemodynamic influence of the branching angle numerically. Chaichana et al. [15] observed the alterations in pressure, velocity and shear stress in a left coronary artery. Malve et al. [16] performed analyzes on reconstructed tomography scans of the left coronary artery. They perused the velocity distribution of blood flow in transient regime and compared the results of FSI (Fluid Solid Interaction) and rigid-wall models. Linge et al. [17] worked on three-dimensional arterial stenosis with 75% cross-sectional reduction in area and studied the influence of pulsatile and steady blood flow through this model. Moreover, they figured out that the spiral velocity component reduces the turbulence intensity and wall shear stress found in the post-stenosis region. Wu et al. [18] performed numerical simulations to identify the influence of stenosis and dilatation at various degrees of stenosis and they investigated the hemodynamic parameters of wall shear stress (WSS), wall pressure gradient and pressure drop. Mahalingam et al. [19] worked on arteries with different degrees of stenosis (0%, 30%, 50% and 70%) and analyzed the pulsatile flow through the arteries and quantified hemodynamic parameters such as wall shear stress and oscillatory shear index. Tabe et al. [20] performed studies on arteries with 50% and 75% stenosis degrees in the Reynolds numbers range from 500 to 2000. Kamangar et al. [21] worked on the left coronary artery and investigated hemodynamic parameters on this model with and without stenosis. Buradi and Mahalingam [22] investigated the effect of the stenosis degree

on wall shear stress and motion of red blood cells (RBCs) using multiphase mixture-theory model. Choi et al. [23] studied on a deformable stenosis and two different rigid stenosis models and investigated the flow characteristics around them. Kabir et al. [24] carried out numerical analyses with different Reynolds numbers to figure out the influence of stenosis in arteries with using *k-ω* turbulence model. Tado et al. [25] analyzed the influence of the presence of stenosis at bifurcation zones of the coronary artery. They carried out analyzes on some hemodynamic parameters such as WSS, velocity and wall pressure distribution. Biglarian et al. [26] performed a computational study to see the effects of 30% and 50% stenosis degrees in dynamic curvature of a coronary artery and they analyzed WSS profiles in pulsatile flow numerically. Carvalho et al. [27] investigated a 3D printed stenotic coronary artery with 70% stenosis degree in both steady and pulsatile blood flow conditions numerically and experimentally. To obtain flow patterns, they used dimethyl sulfoxide, which has transfer properties quite similar to blood. Carvalho et al. [28] worked on both healthy and stenotic coronary arteries with four different stenosis degrees 50%, 60%, 70% and 80%. Laminar and turbulent regimes were used to model blood flow. Multiphase and single-phase methods were applied on laminar flow. On the other hand, in turbulent regime, the blood was considered non-Newtonian. According to their results, the modeling of turbulent pulsatile flow is of great importance of hemodynamic studies. Canlı et al. [29] performed a parametric study to investigate the velocity and turbulence characteristics in hydrodynamic entrance region in a pipe. The study was carried out for four different Reynolds numbers, k-ε turbulence model was used, and hydrodynamic entrance length, velocity and turbulence distribution are analyzed at various positions.

II. NUMERICAL STUDY

The role of the stenosis degree and the corner rounding on the velocity fields, alteration of the values of peak pressure, velocity and wall shear stress in intravascular flow is studied three-dimensionally in the steady state regime. For this purpose, numerical simulations for four different degrees of stenosis (%20, %40, %60 and %80) and two different dimensionless corner radii (r_c/r_a =0.0 and 0.5) are carried out using the ANSYS Fluent software. The simulations were performed for two scenarios. In the first scenario, blood is considered Newtonian, while in the second scenario, it is considered non-Newtonian. Non-Newtonian behavior is modeled using the Carreau model [28]. In both scenarios, the blood is assumed to be homogeneous while the flow is laminar.

In accordance with these assumptions, the governing equations are as follows:

$$\nabla.\vec{u} = 0 \quad (1)$$

$$\rho(\vec{u}.\nabla)\vec{u} = -\nabla p + \nabla.\mu\nabla\vec{u} \quad (2)$$

In Eqs. (1) and (2), ρ, μ, $\vec{u}$, p represent the density and dynamic viscosity of the fluid, the velocity vector and the pressure, respectively [30].

Schematic representation of a stenosed coronary artery is presented in Fig. 1. The total length of the coronary artery with a circular cross-section of 3 mm in diameter (D_a) is 50 mm. The length of the stenosis located in the middle of the artery is twice the diameter of the artery. The study focuses on the stenosis degree and the corner rounding (r_c) on the change in peak values of the wall shear stress, pressure and velocity in the stenotic and post-stenotic regions. The stenosis degree is described as follows [28]:

$$SD\ (\%) = \left(1 - \frac{D_s}{D_a}\right) \times 100 \quad (3)$$

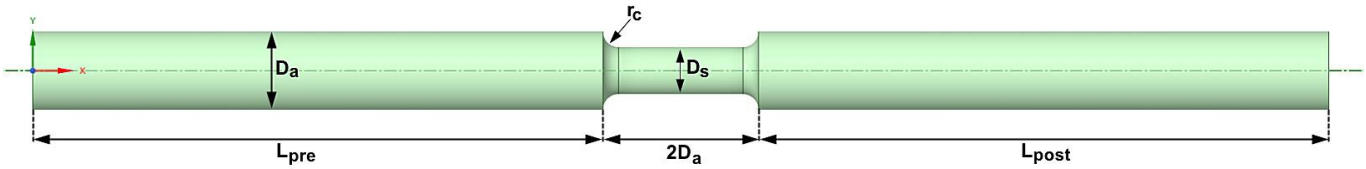

Figure 1: Schematic representation of a stenosed coronary artery.

The flow rate at the arterial entrance is uniform, does not change over time and corresponds to 5 ml/min. The gauge pressure at the outlet of the artery is zero, while the blood velocity at the walls of the rigid artery and stenosis is zero.

In the numerical simulations, the SIMPLE algorithm is implemented for the coupling of pressure and velocity, and the 2nd order upwind scheme is employed for interpolation of the pressure. The momentum equations, on the other hand, are discretized by the 2nd order upwind scheme.

While a polyhedral mesh is used in the simulations, the frequency of the mesh is higher in areas close to stenosis and arterial walls. The mesh independence study is performed between five different cell numbers and the details of the mesh independence study are given in Table 1. The area-weighted average values of the dimensionless velocity in the stenosis center (at 25 mm) are calculated and compared each other for consecutive cell numbers. As can be seen from Table 1, the 800667 cells are preferred in the final simulations because the difference between the dimensionless velocity values calculated for the last two consecutive meshes is less than 1%.

Table 1: Results of the mesh independence study.

Cell Number	Dimensionless Velocity (u/u_{in})	Relative Error (%)
104681	2.583	1.642
201493	2.625	1.027
429357	2.652	1.019
800667	2.679	0.899
1906958	2.703	-

The accuracy of the solution algorithm is confirmed by the experimental and numerical results of Carvalho et al. [27] for a healthy artery and an artery with a 50% stenosis degree, and the results of the study show a high agreement with the results of Carvalho et al. [27].

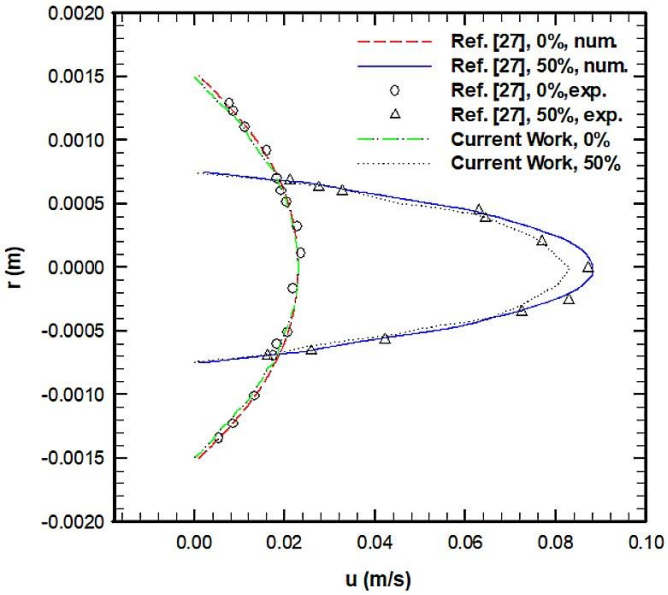

Figure 2: Schematic representation of a stenosed coronary artery.

III. RESULTS AND DISCUSSION

In this study, the role of the stenosis degree and corner rounding on the variation of the peak values of wall pressure, velocity and wall shear stress in intravascular flow is studied three-dimensionally in the steady-state regime. Numerical studies are performed for two scenarios for stenosis degrees of 20, 40, 60, 80% and dimensionless corner radius values of 0.0 and 0.5. In the first scenario, the blood is considered Newtonian, and in the second scenario, it is non-Newtonian.

Figure 3 shows the flow structure in the stenotic and post-stenotic areas. As seen in Fig. 3, high velocities occur in the stenotic area in all scenarios due to cross-sectional narrowing, while secondary flows occur in the post-stenotic area. The sizes of the cells are smaller at r_c/r_a=0.5 and the blood reattaches to the arterial wall again earlier. Also, in the non-Newtonian modeling of blood, the intensity of the secondary flow is weaker and the cell sizes are smaller in the post-stenotic area both at r_c/r_a=0.0 and r_c/r_a=0.5.

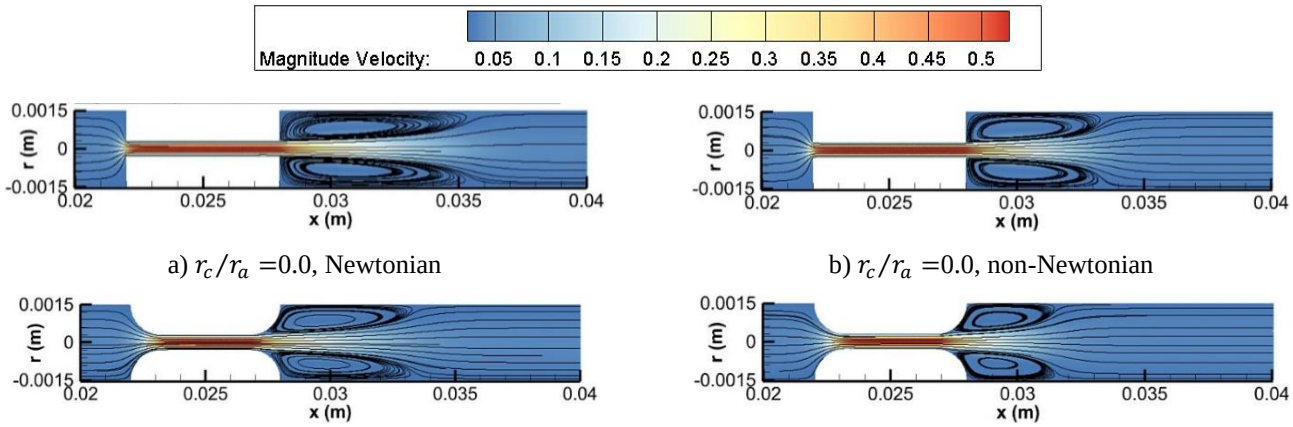

a) r_c/r_a =0.0, Newtonian

b) r_c/r_a =0.0, non-Newtonian

c) r_c/r_a =0.5, Newtonian

d) r_c/r_a =0.5, non-Newtonian

Figure 3: Superimposed velocity contours and streamlines at the mid-plane of the artery.

Figure 4 shows the peak velocity values in the stenotic area. As seen in Fig. 4, the peak velocities are less for all stenosis degrees, in non-Newtonian blood modeling at r_c/r_a =0.5. However, the peak velocities are higher in Newtonian modeling of blood at r_c/r_a =0.0. As expected, the peak velocities increase significantly due to the cross-sectional narrowing in the stenotic area, especially from 60% of stenosis degree.

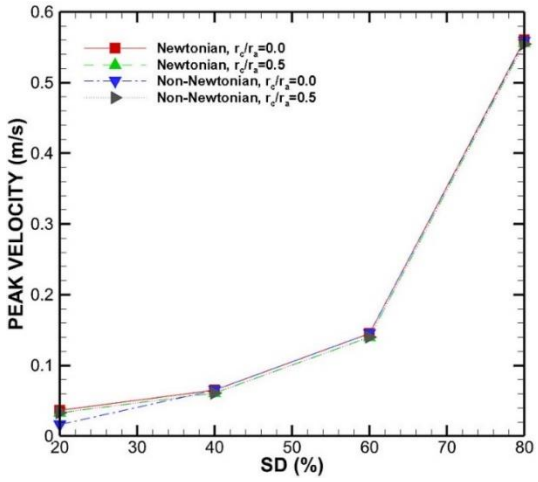

Figure 4: The peak velocity values in the stenotic area.

Figure 5 shows the peak pressures at the arterial walls. As seen in Fig. 5, the peak pressure values at the arterial wall are very close to each other at low stenosis degrees, and the difference between the calculated wall pressures for different scenarios increase with the increase in stenosis degree. At r_c/r_a =0.5, the peak pressure is higher at all stenosis degrees, and the peak pressure is higher in computations made with Newtonian model.

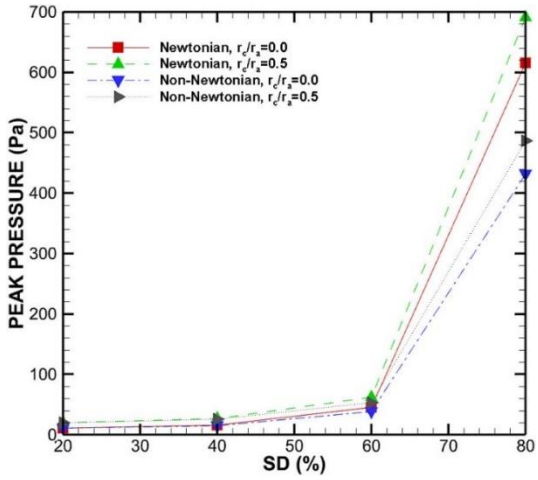

Figure 5: The peak pressure values at the arterial wall.

Figure 6 shows the peak WSS values at the arterial walls. As seen from Fig. 6, the peak values of WSS are almost constant at low stenosis degrees. However, after the 40% stenosis degree, the results of computations performed with Newtonian and non-Newtonian models differ. The peak WSS values calculated with the Newtonian model increases after 40% stenosis degree, while the WSS values of the non-Newtonian model remain almost constant at 60% stenosis degree. Beyond the 60% stenosis degree, the WSS values obtained with both models show a rapid increase. In addition, at r_c/r_a =0.5, the peak WSS values are higher than the values obtained for r_c/r_a =0.0.

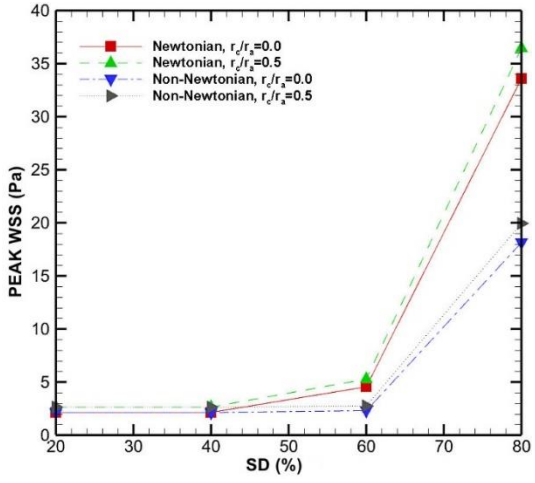

Figure 6: The peak WSS values at the arterial wall.

IV. CONCLUSION

In this study, the role of stenosis degree and corner rounding on the flow structure in the stenosis area, the peak values of velocity, wall pressure and wall shear stress are numerically investigated. Numerical simulations are performed for both Newtonian and non-Newtonian fluids, and the important findings of the study are presented below:

- The values of peak velocity, wall pressure and wall shear stress increase significantly as the stenosis degree increases.
- Rounding corners instead of sharp corners reduces the recirculation length in the post-stenotic area.
- The recirculation length is less in the non-Newtonian Carreau model than in the Newtonian model.
- The results for both the Newtonian and non-Newtonian models are fairly close up to the 60% stenosis degree, while the peak wall pressure and peak wall shear stress values differ from each other in constrictions beyond 60%.

REFERENCES

[1] F. Abdolmaleki, S.M.G Hayat, V. Bianconi, T.P. Johnston, and A. Sahebkar, "Atherosclerosis and immunity: A perspective," *Trends in Cardiovascular Medicine*, vol.29, pp. 363–371, September 2019.

[2] A. Haverich and E.C. Boyle, *Atherosclerosis Pathogenesis and Microvascular Dysfunction*, Springer, 2019.

[3] J. Huston, D. A. Nichols, P. H. Luetmer, C. H. Rydberg, B. D. Lewis,F. B. Meyer, R. D. Brown, and C. D. Schleck, "MR Angiographic and Sonographic Indicationsfor Endarterectomy," *American Journal of Neuroradiology*, vol.19, pp. 309-315, February 1998.

[4] A.M Malek, and S.L Alper, "Hemodynamic shear stress and its role in atherosclerosis," *The Journal of the American Medical Association*, vol. 282, pp. 2035-2042, December 1999.

[5] S. I. S. Pinto and J. B. L. M. Campos, "Numerical study of wall shear stress-based descriptors in the human left coronary artery," *Computer Methods in Biomechanics and Biomedical Engineering*, vol. 19, pp. 1443-1455, February 2016.

[6] T. Barber, "Wall shear stress and near-wall flows in the stenosed femoral artery," *Computer Methods in Biomechanics and Biomedical Engineering*, vol.20, pp. 1048-1055, May 2017.

[7] F. Gijsen, Y. Katagiri, P. Barlis, C. Bourantas, C. Collet, U. Coskun, J. Daemen, J. Dijkstra, E. Edelman, P. Evans, K. Heiden, R. Hose, B.K. Koo, R. Krams, A. Marsden, F. Migliavacca, Y. Onuma, A. Ooi, E. Poon, H. Samady, P. Stone, K. Takahashi, D. Tang, V. Thondapu, E. Tenekecioglu, L. Timmins,

R. Torii, J. Wentzel, and P. Serruys, "Expert recommendations on the assessment of wall shear stress in human coronary arteries: existing methodologies, technical considerations, and clinical applications," *European Heart Journal*, vol.40, pp. 3421-3433, September 2019.
[8] X. He, and D. N. Ku, "Flow in t-bifurcations: Effect of the sharpness of the flow divider," *Biorheology*, vol.32, pp.447-458, March 1995.
[9] H.W. Sung, P.S. Yu., C. H Hsu., and J. C Hsu, "Can cardiac catheterization accurately assess the severity of aortic stenosis? An in vitro pulsatile flow study," *Annals of Biomedical Engineering*, vol.25, pp. 896-905, February 1997.
[10] J. Ryval, A.G. Straatman, and D.A. Steinman, "Low Reynolds Number Modeling of Pulsatile Flow in a Moderately Constricted Geometry," in *Conf. Rec. 2003 11th annual conference of the CFD Society of Canada*.
[11] S. Petkova, A. Hossain, J. Naser, and E. Palombo, "CFD Modeling of Blood Flow in Portal Vein Hypertension with and without Thrombosis," in *Conf. Rec. 2003 Third International Conference on CFD in the Minerals and Process Industries CSIRO*, Melbourne, pp 527-530.
[12] J. Ryval, and D.A. Steinman, "Two-equation Turbulence Modeling of Pulsatile Flow in a Stenosed Tube," *Journal of Biomechanical Engineering*, vol.126, pp. 625-635, October 2004.
[13] Z. Sun, B. Mwipatayi, T. Chaichana, and C. Ng, "Hemodynamic Effect of Calcified Plaque on Blood Flow in Carotid Artery Disease: A Preliminary Study, *Conf. Rec. 2009 3rd International Conference on Bioinformatics and Biomedical Engineering*, pp 1-4.
[14] T. Chaichana, Z. Sun, and J. Jewkes, "Computation of hemodynamics in the left coronary artery with variable angulations," *Journal of Biomechanics*, vol.44, pp.1869-1878, July 2011.
[15] T. Chaichana, Z. Sun, and J. Jewkes, "Computational Fluid Dynamics Analysis of the Effect of Plaques in the Left Coronary Artery," *Computational and Mathematical Methods in Medicine*, vol. 2012, pp. 1-9, May 2014.
[16] M. Malvè, A. García, J. Ohayon, and M. Martínez, "Unsteady blood flow and mass transfer of a human left coronary artery bifurcation: FSI vs. CFD," *International Communications in Heat and Mass Transfer*, vol. 39, pp. 745-751, April 2012
[17] F. Linge, M. A. Hye, and M. C. Paul, "Pulsatile spiral blood flow through arterial stenosis," *Computer Methods in Biomechanics and Biomedical Engineering*, vol. 17, pp. 1727-1737, March 2013.
[18] J. Wu, G. Liu, W. Huang, D. N. Ghista, and K. K. L. Wong, "Transient blood flow in elastic coronary arteries with varying degrees of stenosis and dilatations: CFD modelling and parametric study," *Computer Methods in Biomechanics and Biomedical Engineering*, vol.18, pp. 1835-1845, November 2014.
[19] A. Mahalingam, U. U. Gawandalkar, G. Kini, A. Buradi, T. Araki, N. Ikeda, A. Nicolaides, J. R. Laird, L. Saba, and J. S. Suri, "Numerical analysis of the effect of turbulence transition on the hemodynamic parameters in human coronary arteries," *Cardiovascular Diagnosis and Therapy*, vol.6, pp. 208-220, January 2016.
[20] R. Tabe, F. Ghalichi, S. Hossainpour, and K. Ghasemzadeh, "Laminar-to-turbulence and relaminarization zones detection by simulation of low Reynolds number turbulent blood flow in large stenosed arteries," *Bio-Medical Materials and Engineering*, vol. 27, pp. 119-129, February 2016.
[21] S. Kamangar, I. A. Badruddin, A. Badarudin, N. N. Ghazali, K. Govindaraju, N. J. Salman Ahmed, and T. M. Y. Khan, "Influence of stenosis on hemodynamic parameters in the realistic left coronary artery under hyperemic conditions," *Computer Methods in Biomechanics and Biomedical Engineering*, vol.20, pp. 365-372, September 2016.
[22] A. Buradi and A. Mahalingam, "Effect of Stenosis Severity on Wall Shear Stress Based Hemodynamic Descriptors using Multiphase Mixture Theory, *Journal of Applied Fluid Mechanics*, vol.11, pp. 1497-1509, June 2018.
[23] W. Choi, J. H. Park, H. Byeon, and S. J. Lee, "Flow characteristics around a deformable stenosis under pulsatile flow condition," *American Institute of Physics*, vol.30, pp. 1-11, January 2018.
[24] M. A. Kabir , M. F. Alam, and M. A. Uddin, "A Numerical Study on the Effects of Reynolds Number on Blood Flow with Spiral Velocity Through Regular Arterial Stenosis," *Chiang Mai Journal of Science*, vol. 45, pp. 2515-2527, April 2018.
[25] R. Tado, A. B. Deoghare, and K. M. Pandey, "Computational Study of Blood Flow Analysis for Coronary Artery Disease," *International Journal of Biomedical and Biological Engineer*, vol. 12, pp. 35-39, 2018.
[26] M. Biglarian, M. M. Larimi, H. H. Afrouzi, A. Moshfegh, D. Toghraie, A. Javadzadegan, and S. Rostami, "Computational investigation of stenosis in curvature of coronary artery within both dynamic and static models," *Computer Methods and Programs in Biomedicine*, vol. 185, pp. 1-11, October 2019.
[27] V. Carvalho, N. Rodrigues, R. Ribeiro, P. F. Costa, J. C. F. Teixeira, R. A. Lima, and S. F. C. F. Teixeira, "Hemodynamic study in 3D printed stenotic coronary artery models: experimental validation and transient simulation," *Computer Methods in Biomechanics and Biomedical Engineering*, vol. 24, pp. 623-626, October 2020.
[28] V. Carvalho, N. Rodrigues, R. Ribeiro, P. F. Costa, R. A. Lima, and S. F. C. F. Teixeira, "3D Printed Biomodels for Flow Visualization in Stenotic Vessels: An Experimental and Numerical Study," *Micromachines*, vol. 11, pp. 1-14, May 2020.
[29] E. Canli, A. Ateş, and Ş. Bilir, "Developing Turbulent Flow in Pipes and Analysis of Entrance Region," *Academic Platform Journal of Engineering and Science*, vol.9, pp. 332-353, March 2021.
[30] J.H. Ferziger and M. Perić, *Computational Methods for Fluid Dynamics*, Springer, 2002.

Investigation and Optimization of The Effect of Anhydrous Borax Mineral on The Vickers Hardness and Indentation Modulus Values of Iron Material

Şenol ŞAHİN[1], Ayşegül BODUR YILMAZ[2], Talha Tunahan KESEMENLİ[3]
[1] Kocaeli University, Kocaeli/Türkiye, sensah@kocaeli.edu.tr
[2] Kocaeli University, Kocaeli/Türkiye, aysegul.bodur@kocaeli.edu.tr
[3] Paktaş Platform A.S., Kocaeli/Türkiye, talha.kesemenli@gmail.com

Abstract **- In this study, 5% and 10% by weight of anhydrous borax (AHB) was added to the iron (Fe) matrix material by powder metallurgy method and the effects of the additive ratio on the Vickers hardness (HV), Brinell hardness (HB) and Indentation modulus (E_{IT}) values of the composites (Fe/AHB) were investigated. In the productions carried out using Taguchi experimental design method, AHB additive ratio, and sintering temperature parameters were selected as control parameters that were thought to affect the physical and/or mechanical properties of the Fe/AHB composite materials. The productions were carried out according to the Taguchi L4 orthogonal array, which was created depending on the control parameters and levels. Vickers hardness and indentation modulus measurements of pure iron and Fe/AHB composite materials were performed in accordance with BS EN ISO 14577-1 standard and Brinell hardness measurement was performed in accordance with TS EN ISO 6506-1 standard. According to the signal-to-noise ratio (S/N) analysis performed with the experimental data, it was determined that the 10% AHB additive ratio and 950ºC sintering temperature optimized all the investigated properties of the Fe/AHB composite material. It was determined that the values for Vickers hardness, Brinell hardness and indentation modulus increased by 142.03%, 69.32% and 144.11%, respectively, in the levels where the properties of the composite material were optimized compared to pure Fe material. As a result of the qualitative examination of all samples after storage in a comfortable environment without daylight, it was also observed that the anhydrous borax additive delayed the corrosion time of pure iron material.**

Keywords **- Anhydrous borax, composites, hardness, iron, powder metallurgy**

I. INTRODUCTION

Composites are a group of advanced technological materials formed by the combination of at least two different materials, where the components called matrix and reinforcement come together by creating an interface and behave as a single material. As technology has evolved, the properties expected from materials have changed and the increasing demand for lightweight materials with high chemical and mechanical strength in many sectors has increased the interest in composites [1,2].

Metal matrix composites (MMCs) with continuous fibers and whiskers as reinforcement were developed in the 1970s and proposed for applications requiring high performance. [3]. These materials have attracted great interest from industry due to their unique mechanical and structural properties [3,4].

The improved mechanical strength, wear resistance, hardness, stiffness, damping capacity, thermal stability, ductility of metal matrix composites have attracted attention for a wide range of applications [3,5]. MMCs are ideally suited for use in ground transportation and aviation in the reduction of structural weight and related fuel consumption. [5]. When the reinforcement materials preferred in the production of metal matrix composites, which can be produced by different techniques [7] such as powder metallurgy, spray deposition technique, and stir casting, are examined; silicon carbide (SiC) with high hardness, wear resistance, toughness, fatigue resistance properties and boron carbide (B_4C) with high melting point, low density, great resistance to chemical substances are frequently preferred materials [5]. Boron carbide (B_4C), an important reinforcement material, is the hardest known material after diamond and cubic boron nitride (cBN) [6].

When the materials used in the production sector do not perform as expected, situations such as production inefficiencies, quality problems and consequently customer dissatisfaction inevitably arise. In this context, there are different methods developed to improve both expected material properties and product quality. The Taguchi method is one of the methods developed to obtain the most information with the least amount of time, cost, and energy by designing experimental studies. It has proven to be an effective tool to create optimal production conditions in a wide range of production environments, especially in achieving more efficient results with reduced trials [8,9].

In this study, a metal matrix composite was produced with iron (Fe) as the matrix material and anhydrous borax (AHB), a type of boron mineral, as an additive.

By evaluating the effects of anhydrous borax and/or anhydrous borax additive ratio and sintering temperature factors on the mechanical properties of the final product (composite material), it is aimed to determine the most effective additive ratio and sintering temperature to increase Brinell hardness, Vickers hardness and indentation modulus values and to develop Fe/AHB composite material. The experimental study was carried out by Taguchi experimental design method and Fe/AHB composites were produced by powder metallurgy

method according to the obtained Taguchi orthogonal array.

II. MATERIAL AND METHOD

A. Iron (Fe)

Pure iron with a density of 7.87 g/cm^3, a melting temperature of 1535ºC and a grain size of 3 µm was used as matrix material for the production of composite materials.

B. Anhydrous Borax

Anhydrous borax mineral with the trade name Etibor-68 purchased from Eti Maden Operations, with a density of 2.37 g/cm^3 and a melting temperature of 742.5ºC, was ground and used under a sieve size of 20 µm as an additive material for the production of composite materials.

C. Implementation of Taguchi Method

Taguchi experimental design method was used to optimize the Brinell hardness, Vickers hardness and Iz modulus values of the composites produced and to determine the optimum levels of the factors. In addition to the control factor of sintering temperature, which is thought to affect the quality and mechanical properties of the composite products by powder metallurgy method, the AHB additive ratio was also specified as a control factor in order to investigate the effect of different weight percentages of AHB additive. (see Table 1).

Table 1: Control factors and their levels

Factors	Level 1	Level 2
AHB additive ratio (wt. %)	5	10
Sintering temperature (ºC)	850	950

Depending on the factors and their levels, Taguchi L4 orthogonal array was selected (see Table 2) and the productions were carried out in accordance with the orthogonal array. At least 3 specimens were produced for each test set-up and Brinell hardness, Vickers hardness values and indentation modulus values were determined by taking 5 different measurements on the specimens.

Table 2: Experimental conditions for L4 orthogonal array

Trials	AHB additive ratio (wt. %)	Sintering temperature (ºC)
1	5	850
2	5	950
3	10	850
4	10	950

Using the experimental data obtained after the measurements of Brinell hardness, Vickers hardness and indentation modulus values, signal-to-noise ratios (*S/N*) were examined in accordance with the "larger is better" method (see Equation 1) to determine the parameters that optimize these values.

$$S/N = -10 \cdot \log\left(\frac{1}{n}\sum_{i=1}^{n}\frac{1}{y_i^2}\right) \quad (1)$$

Where, y_i = i. measured observation value, n = number of observations.

D. Composite Material Production

In the preliminary preparation stage before production, AHB was first subjected to grinding in RETSCH brand SK100 model device to reduce the grain size and then to sieving in RETSCH brand AS200 model device to separate the particles according to grain size. In order to obtain a homogeneous mixture, Fe/AHB composites with different weight percentages were prepared in a glass jar with a nickel ball inside using MSE-TEC brand ball mill machine at grinding speed of 200 rpm and grinding time of 30 minutes. Then, Fe/AHB composite materials were obtained (see Figure 1) in a DIEX model induction furnace, in a graphite mold with an inner diameter of 20 mm, at a constant heating rate of 45ºC/min to the sintering temperature, under a constant 15 min holding time at sintering temperature, and at different sintering temperatures (850ºC – 950 ºC). Since the sintering temperature was higher than the melting temperature of AHB used as an additive, AHB liquefied in the mold and caused fractures in the mold when pressure was applied. For this reason, the productions were carried out under a constant pressure of 2 MPa to prevent damage to the mold.

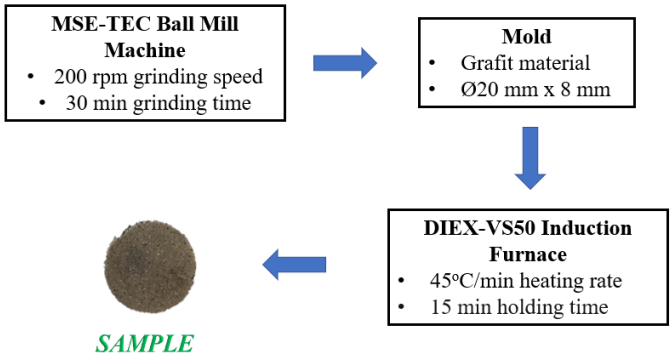

Figure 1: Sample production steps

E. Brinell Hardness, Vickers Hardness and Indentation Modulus Measurement

Vickers hardness and indentation modulus measurements were carried out under 1 kg load according to BS EN ISO 14577-1 standard on Zwick BZ2.5/TS1S instrumented hardness tester at Tübitak National Metrology Institute. Brinell hardness measurement was carried out under 31.25 kg load according to TS EN ISO 6506-1 standard in WOLPERT brand hardness tester in Kocaeli University Mechanical Engineering Department.

III. FINDINGS AND DISCUSSION

A. *Brinell Hardness Value*

The Brinell hardness values of the materials are comparatively graphed in Figure 2, which was prepared using the experimental data obtained. When Figure 2 is examined, it is determined that the hardness value of the composite material produced at 850ºC sintering temperature with 5 wt% AHB additive increased by 25.40% compared to the reference pure Fe material produced at 850ºC sintering temperature. It was also found that the hardness value of the composite material produced at 950ºC sintering temperature with 10% AHB additive increased by 69.32% compared to the reference pure Fe material.

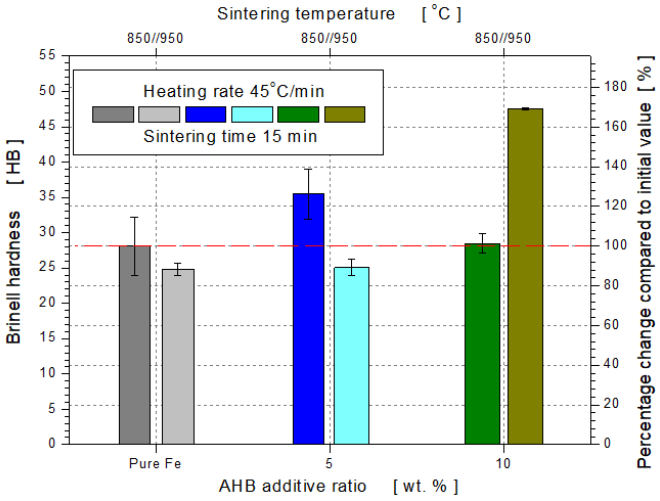

Figure 2: Graph of the change in Brinell hardness values

When the *S/N* ratio table (see Table 3) and graph (see Figure 3) are examined, it was determined that the most effective factor on Brinell hardness is the AHB additive ratio, which is the factor with the largest delta value. It was determined that the factor levels that optimized (maximized) the Brinell hardness value were 10% AHB additive ratio and 950ºC sintering temperature.

Table 3. S/N ratio response table of Brinell hardness values of composites

Level	AHB additive ratio	Sintering temperature
1	29.27	29.74
2	**31.08**	**30.61**
Delta	1.82	0.88
Rank	1	2

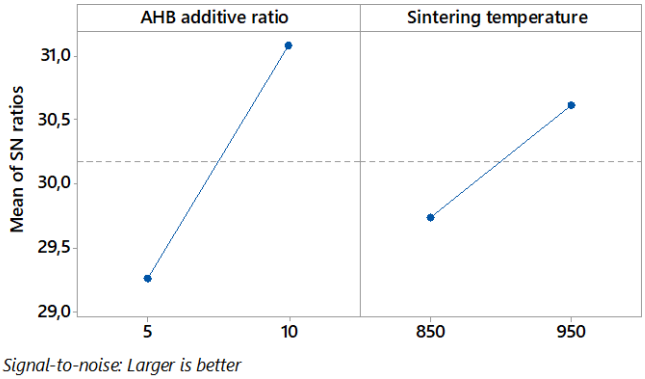

Figure 3: Main effects plot of S/N ratios of Brinell hardness values of composites

B. *Vickers Hardness Value*

The Vickers hardness values of the materials are comparatively graphed in Figure 4, which was prepared using the experimental data obtained. When Figure 4 is examined, it is determined that the hardness value of the composite material produced at 850ºC sintering temperature with 5 wt% AHB additive increased by 36% compared to the reference pure Fe material produced at 850ºC sintering temperature. It was also found that the hardness value of the composite material produced at 950ºC sintering temperature with 10% AHB additive increased by 142.03% compared to the reference pure Fe material.

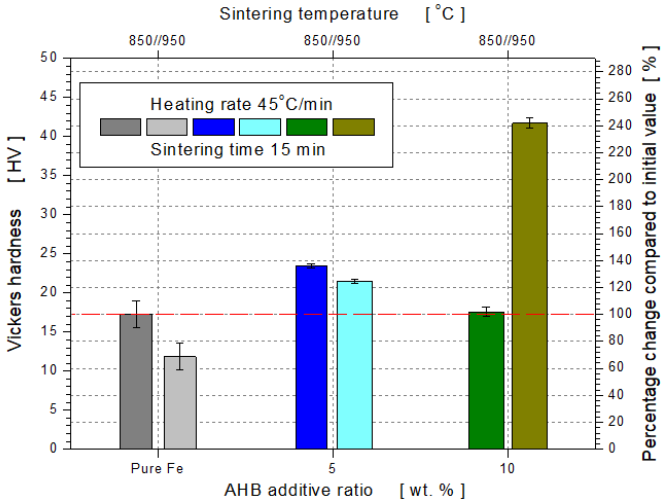

Figure 4: Graph of the change in Vickers hardness values

When the *S/N* ratio table (see Table 4) and graph (see Figure 3) are examined, it was determined that the most effective factor on Vickers hardness is the sintering temperature, which is the factor with the largest delta value. It was determined that the factor levels that optimized (maximized) the Vickers hardness value were 10% AHB additive ratio and 950ºC sintering temperature.

Table 4: S/N ratio response table of Vickers hardness values of composites

Level	AHB additive ratio	Sintering temperature
1	27.10	26.35
2	**29.07**	**29.81**
Delta	1.97	3.46
Rank	2	1

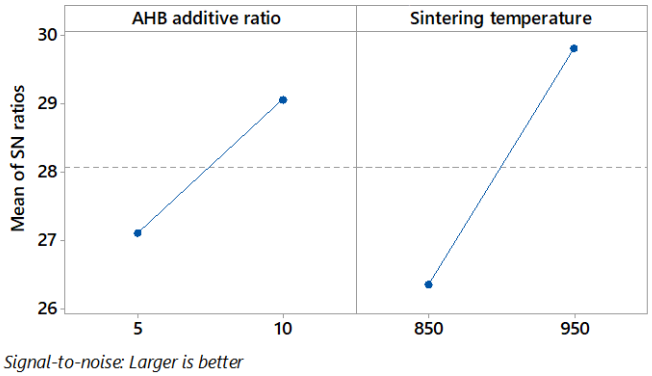

Figure 5: Main effects plot of S/N ratios of Vickers hardness values of composites

C. *Indentation Modulus Value*

The Indentation modulus values of the materials are comparatively graphed in Figure 6, which was prepared using the experimental data obtained. When Figure 6 is examined, it is determined that the hardness value of the composite material produced at 850ºC sintering temperature with 5 wt% AHB additive increased by 43.84% compared to the reference pure Fe material produced at 850ºC sintering temperature. It was also found that the modulus value of the composite material produced at 950ºC sintering temperature with 10% AHB additive increased by 144.11% compared to the reference pure Fe material.

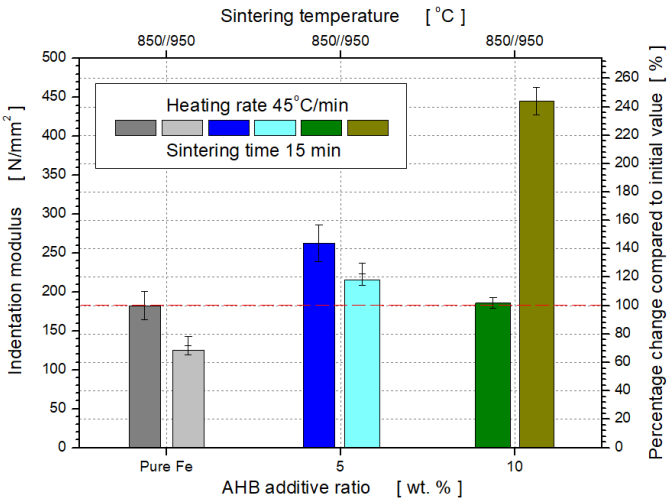

Figure 6: Graph of the change in Indentation modulus values

When the *S/N* ratio table (see Table 5) and graph (see Figure 7) are examined, it was determined that the most effective factor on Indentation modulus is the sintering temperature, which is the factor with the largest delta value. It was determined that the factor levels that optimized (maximized) the Indentation modulus value were 10% AHB additive ratio and 950ºC sintering temperature.

Table 5: S/N ratio response table of Indentation modulus values of composites

Level	AHB additive ratio	Sintering temperature
1	47.47	46.94
2	**49.53**	**50.05**
Delta	2.06	3.11
Rank	2	1

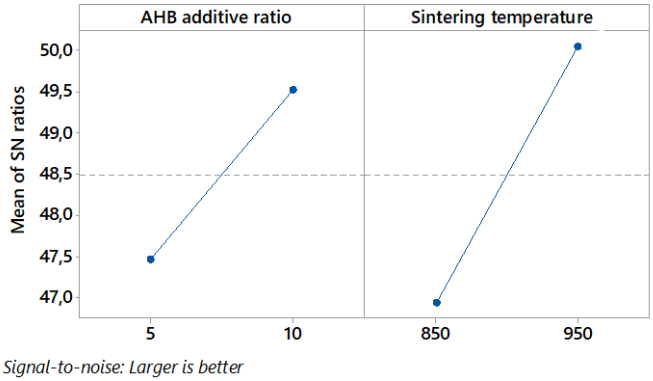

Figure 7: Main effects plot of S/N ratios of Indentation modulus values of composites

D. *Qualitative Examination*

As a result of the qualitative examination of all samples after storage during 12 months in a comfortable environment without daylight, it was observed that the anhydrous borax additive delayed the corrosion time of pure iron material (see Figure 8 and 9)

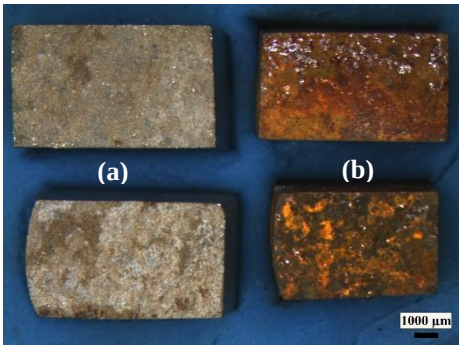

Figure 8: Macro image of produced at 850ºC sintering temperature (a) Fe/AHB composite with 5% AHB additive and (b) pure Fe materials

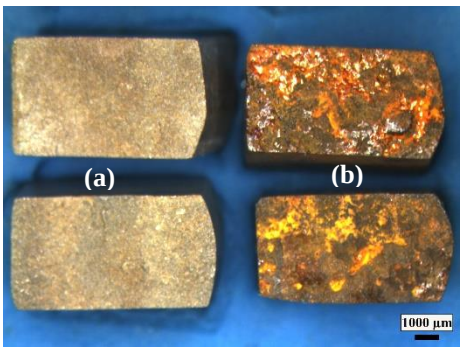

Figure 9: Macro image of produced at 950°C sintering temperature (a) Fe/AHB composite with 10% AHB additive and (b) pure Fe materials

IV. RESULTS

The Brinell hardness, Vickers hardness and indentation modulus were strongly affected by the AHB additive.

Compared with the pure reference material (850°C), the composite sample with 10% AHB additive, prepared at a sintering temperature of 950°C, showed the best results with an increase in Brinell hardness, Vickers hardness and indentation modulus of 69.32%, 142.03% and 144.11%, respectively.

The factors that optimize the Brinell hardness, Vickers hardness and indentation modulus together are the ratio of 10% SB additive and the sintering temperature of 950°C.

As a result of the qualitative examination of all samples after storage during 12 months in a comfortable environment without daylight, it was observed that the anhydrous borax additive delayed the corrosion time of pure iron material.

In future studies on the related subject, it is recommended to decrease/increase the particle size of anhydrous borax and to decrease/increase the anhydrous borax additive ratios and to examine the effect of different production parameters.

ACKNOWLEDGMENT

This study was prepared within the scope of the master's thesis titled "*Production of anhydrous borax added iron material by powder metallurgy and optimization of tribological and mechanical properties by experimental design method*" with the thesis number 651237 of the Council of Higher Education.

REFERENCES

[1] Petersson, H., "Carbon Fiber Composite Materials in Modern Day Automotive Production Lines: A Case Study", *Proceedings of the ASME 2013 International Mechanical Engineering Congress & Exposition IMECE2013*, San Diego, California, USA, 2013.

[2] V. V. Reddy, R. K. Mandava, V. R. Rao, S. Mandava, "Optimization of dry sliding wear parameters of Al 7075 MMC's using Taguchi method", *Materials Today: Proceedings*, Vol 62, pp. 6684–6688, 2022

[3] V. Rana, H. Kumar, A. Kumar, "Fabrication of hybrid metal matrix composites (HMMCs) –A review of comprehensive research studies", *Materials Today: Proceedings*, Vol 56 pp. 3102–3107, 2022

[4] P.D. Mangalgiri, "Composite materials for aerospace applications", *J. Bull. Mater*. Sci. 22 (3) 657–664, 1999

[5] S. Seetharaman, J. Subramanian, R. A. Singh, W. L. E. Wong, M. L. S. Nai, M. Gupta, "Mechanical Properties of Sustainable Metal Matrix Composites:A Review on the Role of Green Reinforcements and Processing Methods", *Technologies*, https://doi.org/10.3390/technologies10010032, 2022

[6] E. Karacay, "Production of boron carbide and its characterization", Gazi University, Institute of Science and Technology, Master Thesis, Ankara, Türkiye, 2008.

[7] M.K. Surappa, "Microstructure evolution during solidification of DRMMCs (Discontinuously reinforced metal matrix composites): State of art", *Journal of. Material Process Technology*, vol 63 (1-3) pp. 325–333, 1997

[8] M. Inal, S. Sahin. ve Y. Sahin, "Optimization of the Young's Modulus of Low Flow Polypropylene Talc/Colemanite Hybrid Composite Materials with Artificial Neural Networks", IFAC-PapersOnLine Volume 51, Issue 30, Pages 277-281, 2018

[9] A. Bodur., S. Sahin. ve Y. Sahin, M. Inal, "Modelling of the Flexural Strength of Low Flow Polypropylene Talc/Colemanite Hybrid Composite Materials with Taguchi and ANFIS Methods", IFAC-PapersOnLine Volume 51, Issue 30, Pages 271-276, 2018

Investigation Of Different Air Curtain Design In Industrial Type Vertical Refrigerator Cabinets

M.H. ERDOGAN[1], S. DOGAN[2], S. YAGMUR[2], A.H. ALTUN[3]

[1] Çağlayan Soğutma A.Ş., Konya/Turkey, mh.erdogan@caglayansogutma.com
[2]Konya Technical University, Konya/Turkey, sercandogan@ktun.edu.tr
[2]Konya Technical University, Konya/Turkey, syagmur@ktun.edu.tr
[3]Selcuk University, Konya/Turkey, ahaltun@selcuk.edu.tr

***Abstract* - Industrial type vertical refrigerator cabinets designed as open and closed are widely used in the world. While there is a physical barrier between the environment and the inside of the cabinet in closed refrigerator cabinets, air curtains are used in open refrigerator cabinets. Air curtains used in open refrigerator cabinets allow minimizing the air exchange between the two environments. This reduces heat transfer and ensures that the humidity balance in the environment remains constant. It also reduces the energy required to cool products down to optimal storage temperatures. In this study, numerical analyzes were carried out by the CFD method to observe the effect of air curtains with different velocity profiles caused by the angles of the baffler plate on the average shelf temperatures in a typical open-cooled vertical refrigerator cabinet. In CFD studies, solutions were made with Realizable k-epsilon turbulence model. In the analyses, the boundary conditions of the outdoor conditions are defined by considering the ISO 23953-2-89 Class-3 standard. As a result of all CFD analyzes, it was determined that the velocity profiles in the air curtain had a significant effect on the average shelf temperature. It has been observed that the average shelf temperature values obtained in air curtains with high vertical velocity inside the cabin are lower than those with parabolic velocity profile.**

***Keywords* - air curtain, cooling, refrigerator, vertical display cabinet**

I. INTRODUCTION

FOOD reach the consumer from the producer through very long processes. Some of this long time is spent in the storage phase. In this process, some products need to be kept in the cold chain. Almost half of the food products sold in supermarkets are sold frozen or refrigerated [1]. Some of these products are stored at positive temperatures, while others are stored at negative temperatures. In the face of this situation, especially the retail sector makes demands from the cooling industry to meet the mentioned demands. The cooling industry offers solutions to these demands with many different ideas. Industrial refrigerator cabinets are classified as negative and positive according to the interior temperature of the cabinet, and open and closed according to the physical barrier separating the interior and exterior of the cabinet.

Managing energy efficiency for the retail industry is a great paradox [2]. In general, a refrigerator to be used in the retail sector should have high energy efficiency and be able to display the product easily. In refrigerators, all effects that cause energy loss should be at a minimum level to have high energy efficiency. However, refrigerator cabinets are generally designed with an open front for easy display. This contradicts the first claim. The removal of the barrier causes the contact of the hot air outside the cabin with the cold air inside the cabinet. In order to eliminate all these effects, air curtains are often used in open cabinets [3].

The air curtains used in the cooling cabinets can be defined as the air sucked from the bottom opening of the cabinet by a fan positioned behind the evaporator, first passing it through the evaporator and then through the limited volume behind the cabinet and blowing it through the top opening of the cabinet. Thanks to the air curtains, the outside hot air is prevented from entering the cabinet and it is ensured that the product and shelf temperatures are kept within the prescribed temperature range.

As it is known, the air moves from the hot environment to the cold environment. In this case, it creates a negative effect on the air curtain. At the same time, hot air participates in the air curtain circulation. This causes an increase in the cooling load. According to the studies of Howell and Adam (1991), approximately 75% of the cooling load in refrigerator cabinets is due to the air curtain [4].

Navaz et al. (2002) conducted a study using DPIV technique and CFD method together to examine the air curtain and performance of open refrigerator display cabinets used in supermarkets. As a result of the study, they were able to accurately predict the leakage rate and prepared the infrastructure for open showcase designs that would consume less energy [5]. Giovonni et al. (2001) analyzed the vertical multi-deck refrigerator display cabinet under different operating conditions using the LES turbulence model. These analyzes were carried out by the EN-441 standard. They confirmed the analysis results with experimental results [6]. D'agaro et al. (2006) simulated airflow and temperature distribution in open display cabinets using CFD method. In this study, which was carried out using 2D and 3D modeling, it was revealed that the analyzes of refrigerator cabinets with 2D modeling may be insufficient in simulating the effects that develop depending on the cabinet length and ambient air movements. They also proved that 3D simulations are the reliable tool for finding the cooling power and air curtain flow model [7]. Navaz et al. (2005) confirmed that CFD modeling would be a reliable tool for estimating the amount of leakage. They also determined that turbulence in the discharge air grid

(DAG) should be minimized and it should have a value in the range of Re = 3200-3400 for optimal air curtain [8]. Navaz et al. (2006) conducted a study to address the effects of the velocity profile at the DAG outlet on the amount of air entrained in the open display cabinet. They determined that significant changes can be experienced in the drift rate with the changes to be made in the velocity profiles at the DAG output. It also revealed the fact that the velocity profile depends on the surface shapes the air comes into contact with before coming to DAG [9]. Hawadey et al. (2012) examined in detail the design parameters that affect the performance of refrigerated display cases. These parameters were determined as air curtain velocity and width, evacuation angle and vertical distance of DAG and rack. In addition to these, in the study, the case of a lateral flow affecting the showcase was analyzed in 3D using CFD. The obtained results were compared with the experimental results and a high level of similarity was found. The most important result obtained in the CFD analysis results is that the air curtain is optimally formed when one third of the total mass flow rate in the showcase is caused by the air curtain. Another important result is that maximum air curtain efficiency can be achieved if the DAG width is positioned in the range of 90-110 mm and angled 5-10 degrees outward [10].

In this study, CFD modeling of three different versions of a typical open refrigerator cabinet based on different baffler plate geometry will be made. The effect of the different air curtains to be formed depending on the geometry of the directional plate on the shelves will be observed. The obtained data will form the basis of future studies.

II. Material and Methods

Continuity and momentum equations are used to analyze turbulent flows. In the presence of turbulent flow, times averaging of the continuity and momentum equations as well as the incompressible unsteady Reynolds Averaged Navier-Stokes equations are used. Equations 1 and 2 express the continuity and momentum equations for incompressible flow, respectively.

$$\frac{\partial \rho}{\partial t} + \frac{\partial}{\partial x_i} + (\rho u_i) = 0 \quad (1)$$

$$\frac{\partial \rho U_i}{\partial t} + \frac{\partial}{\partial x_i} + \left(\rho u_i u_j - \tau_{ij}\right) = \frac{\partial P}{\partial x_j} + S_{ij} \quad (2)$$

If τ_{ij} is the viscous stress tensor:

$$\tau_{ij} = 2\mu S_{ij} - \frac{2}{3}\mu \frac{\partial u_k}{\partial x_k}\delta_{ij} \quad (3)$$

$$S_{ij} = \frac{1}{2}\left(\frac{\partial u_i}{\partial x_j} + \frac{\partial u_j}{\partial x_i}\right) \quad (4)$$

$$\frac{\partial}{\partial x_i}\left(\rho u_i h - \lambda \frac{\partial T}{\partial x_i}\right) = u_i \frac{\partial P}{\partial x_i} + \tau_{ij}\frac{\partial u_i}{\partial x_i} \quad (5)$$

u_i and u_j express the velocity components. These velocity components are located on the x_i and x_j cartesian coordinates.

The energy equations should be used in addition to the continuity and momentum equations. The heat transfer solution can be solved with the following Equation 6:

$$\frac{\partial}{\partial t}(\rho E) + \frac{\partial}{\partial x_i}[u_i(\rho E + p)] = \frac{\partial}{\partial x_j}\left[\left(k + \frac{C_p \mu_t}{Pr_t}\right)\frac{\partial T}{\partial x_j} + u_i\left(\tau_{ij}\right)_{eff}\right] + S_h \quad (6)$$

In the energy equations, k is used to express the coefficient of thermal conductivity, E is the total energy, and $\left(\tau_{ij}\right)_{eff}$ is used to express the tensile tensor.

In the analyzes, the k-epsilon Realizable was used as the turbulence model. The transport equations for k-epsilon Realizable are given below.

$$\frac{\partial}{\partial t}(\rho k) + \frac{\partial}{\partial x_j}(\rho k u_j) = \frac{\partial}{\partial x_j}\left[\left(\mu + \frac{\mu_k}{\sigma_k}\right)\frac{\partial k}{\partial x_j}\right] + G_k + G_b - \rho\epsilon + S_k \quad (7)$$

$$\frac{\partial}{\partial t}(\rho \epsilon) + \frac{\partial}{\partial x_j}(\rho \epsilon u_j) = \frac{\partial}{\partial x_j}\left[\left(\mu + \frac{\mu_t}{\sigma_\epsilon}\right)\frac{\partial \epsilon}{\partial x_j}\right] + \rho C_1 S\epsilon - \rho C_2 \frac{\varepsilon^2}{k+\sqrt{\nu\varepsilon}} + C_{1\varepsilon}\frac{\varepsilon}{k}C_{3e}G_b + S_e \quad (8)$$

G_k represent the generation of turbulent kinetic energy resulting from the velocity gradient. G_b is the generation and the contribution based on buoyancy used for k-epsilon models, where gravity and temperature gradients are present simultaneously. σ_k is the turbulent Prandtl number for k and σ_ϵ is the turbulent Prandtl number for ϵ. Sk and $S\epsilon$ are user-defined source terms. C_2 and $C_{1\varepsilon}$ are constants [11].

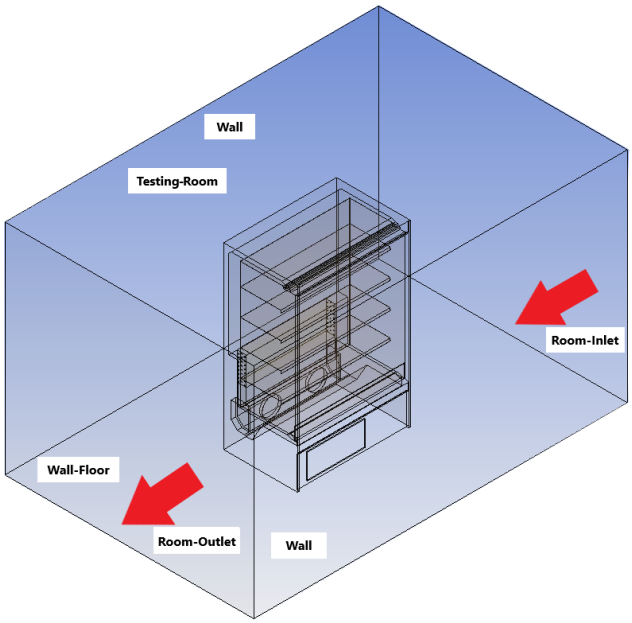

(a)

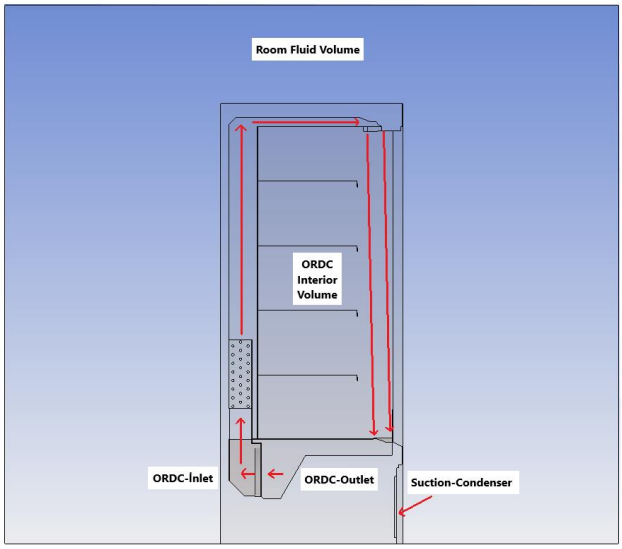

(b)

Figure 1. (a) Position of ORDC fluid volume in test room flow volume (b) boundary conditions

Table 1. Boundary conditions for the present numerical analysis.

Location	Boundary Condition	Value
Room-Inlet	Velocity Inlet	0.15 m/s at 298 K
ORDC-Inlet	Mass Flow Inlet	0.055 kg/s at 271 K
Room-Outlet	Pressure Outlet	A gauge pressure of zero
Wall/Wall-Floor/Refrigerator	Wall	No-slip adiabatic wall

The location and boundary conditions of the ORDC (Open Refrigeration Display Cabinet) in the test room are given Figure 1. The test room is conditioned in accordance with climate class 3 in ISO 23953-2. Inlet of the test room boundary condition was defined as the velocity inlet where the uniform velocity was 0.15 m/s at a temperature of 298K [12]. The outlet of the test rom can be considered a zero-gauge pressure outlet boundary condition.

In the analyzes, the ORDC consists of three fans. One of these fans is located in the condenser suction and the other two are located in the evaporator which are placed symmetrically in the cabinet. Boundary conditions for ORDC are detailed in Table 1.

The baffle plate geometry to be used in the ORDC is given in Figure 2. Five different baffle first step angles ß as 22°, 45°, 57°, 75° and 90° are set as a parameter for CFD analysis. Then the effects of the ß angle were investigated by comparing them with the shelf temperature and velocity distributions.

The structured mosaic (poly-hexacore) mesh cells were formed in the flow volume. Approximately a total of 7.5 million cells were used for the ORDC and test room flow volume.

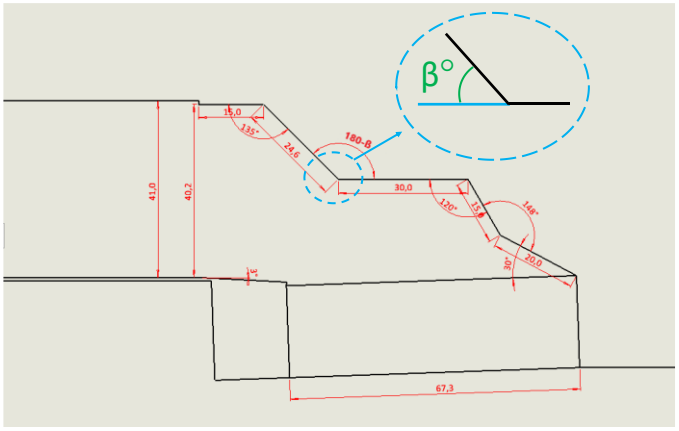

Figure 2. Baffle plate geometry

III. Results and Discussions

The effects of ORCD's five different baffle plate geometries on the cabinet interior volume were analyzed using steady state CFD analyses.

The results are shown in Figures 3 to 5 and include temperature and velocity contours projected onto three different planes. The distributions of the temperature and the velocity contours are limited to 271 to 298 K and 0-2 m/s, respectively.

The three planes on which the results are projected are numbered from 1 to 3. Plane 1 is a cross-section of the refrigerator cabinet, taken from a point close to the test room suction plane. Plane 2 splits the ORDC straight down the middle. Similarly, Plane 3 is the section taken from the side close to the test room blowing plane.

The analyzed ORDC has 5 shelves. The average temperature values of the upper 3 shelves were not change with the change of ß angles. However, with the increasing of ß angles from 22° to 90°, the average temperature distributions of the fourth and the fifth shelves decreased. In addition, as the angle value increased, the average temperature value decreased in the suction region which is clearly seen at Figure 5. The evaporator suction temperature also effects the cooling load of the refrigerator. As the average temperature at the suction region was high, the cooling load of the system increased.

The velocity distributions in the three planes are demonstrated in Figure 3 to 5. It is seen in the velocity contours that some of the air coming out of the DAG (Discharge Air Grill) goes toward the shelves, while the remaining part reaches the evaporator suction area.. As the angle decrease, the velocity distribution was getting similar in each the shelves, which was an indication that less air reaches the shelves. In fact that less cold air reached the shelves is evidence that higher average temperatures can occur in this region. As the angle increased, the velocity of the air coming out of the DAG was higher toward the shelves.

When plane 1 to 3 was examined, it can be observed that some of the cold air in the cabinet volume leaks out of the cabinet. This leakage increased as the baffle plate angle decreases. This is a parameter that should be considered when comparing baffler plate at different angles. In Plane 2 and 3, the leak was seen more clearly. However, in 3-D analysis performed in a conditioned test room, vortex formation is

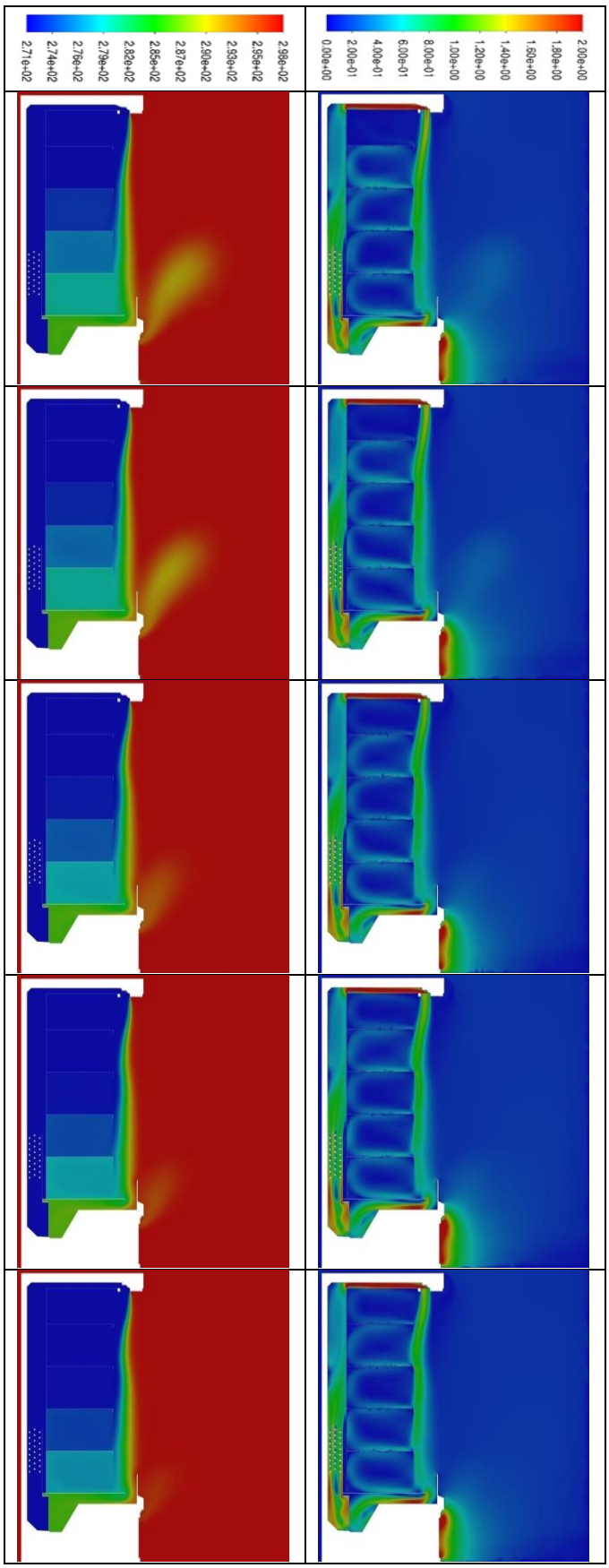

Figure 3. Temperature (K) and velocity (m/s) contour at ß = 22°, 45°, 57°, 75° and 90°, respectively from top to bottom in Plane-1

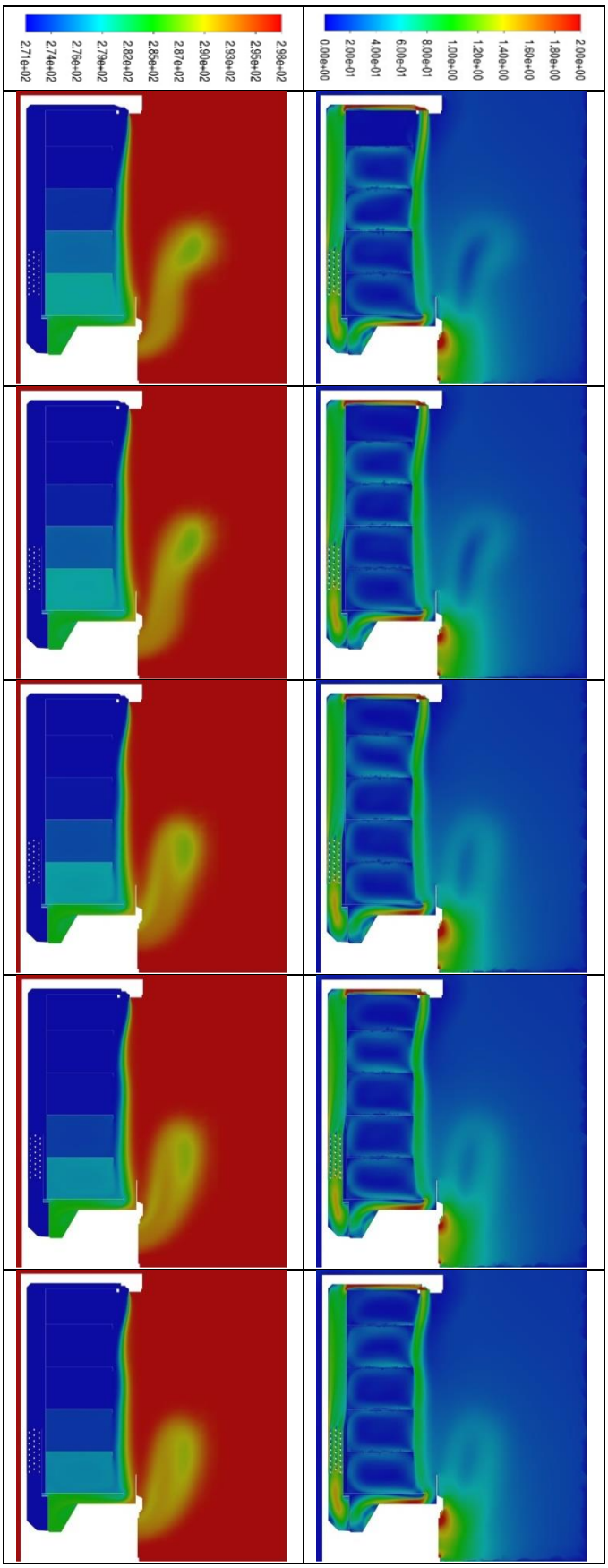

Figure 4. Temperature (K) and velocity (m/s) contour at ß = 22°, 45°, 57°, 75° and 90°, respectively from top to bottom in Plane-2

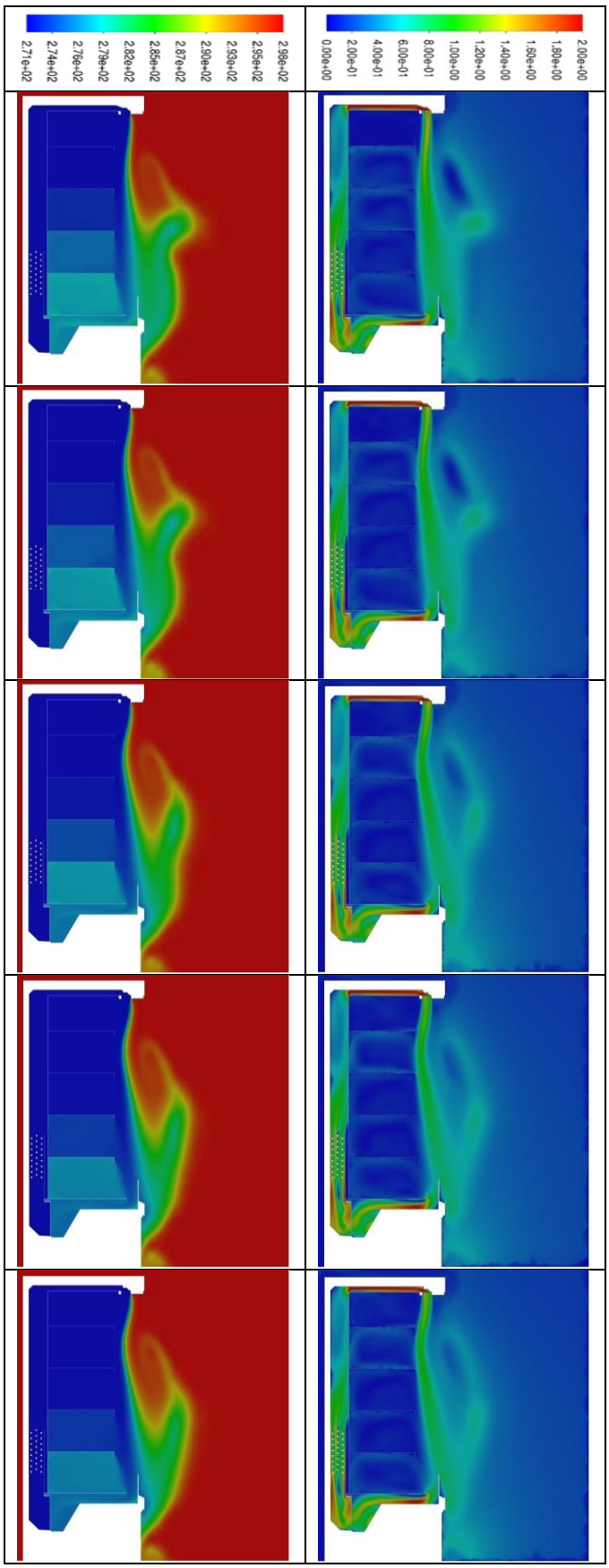

Figure 5. Temperature (K) and velocity (m/s) contour at ß = 22°, 45°, 57°, 75° and 90°, respectively from top to bottom in Plane-3

expected in the part of the ORDC close to the blower plane of the test room. This situation is characteristic and expected in all the 3-D analysis.

IV. Conclusions

According to the CFD results, the average shelf temperatures were investigated for three planes of the cabinet. The lowest average shelf temperatures obtained at the 90° baffle plate in all planes. As the angle decreases, the average inner temperature increase in the cabinet. The velocity profile of the leaving air from the DAG changes depending on the baffle angle. For the plate with an angle of 90° baffle, the velocity distribution towards the cabinet is high, but for 22°, this situation turns to the opposite. Air curtain with high velocity towards the interior of the cabinet reveals a better performance than air curtains with high velocity towards the outside.

This study has been a fundamental study in term of understanding the behavior of the air curtain.

Acknowledgment

The authors would like to thank Çağlayan Soğutma A.Ş for their contributions.

References

[1] Z. Muranko, D. Andrews, I. Chaer, E.J. Newton, P. Proudman, Encouraging remanufacturing in the retail refrigeration industry, Energy Proced 161, 283-291, 2019.
[2] U. Lindberg, Research for the retail grocery context: A systematic review on display cabinets, Trends in Food Science & Technology, 100, 19-34, 2020.
[3] N.J. Smale, J. Moureh, G. Cortella, A review of numerical models of airflow in refrigerated food applications, International Journal of Refrigeration, 29 (3), 911-930, 2006.
[4] R.H. Howell, P.A. Adams, Effects of indoor space conditions on refrigerated display case performance, ASHRAE-596RP, Department of Mechanical Engineering, University of South Florida, Tampa, FL, 1991.
[5] H.K. Navaz, Faramarzi, Ramin, D. Daribi, M.Modarress, The application of advanced methods in analyzing the performance of the air curtain in a refrigerated display case, ASME J. of Fluid Engineering, Vol. 124, 2002.
[6] G. Cortella, M. Manzan, G. Comini, CFD simulation of refrigerated display cabinets, International Journal of Refrigeration, 24(3), 250-260, 2001.
[7] P. D'Agoro, G. Cortella, G. Croce, Two- and three- dimensional CFD applied to vertical display cabinets simulation, International Journal of Refrigeration, 29(2), 178-190, 2006.
[8] H. K. Navaz, B. S. Henderson, R. Faramarzi, A. Pourmovahed, F. Taugwalder, Jet entrainment rate in air curtain of open refrigerated display cases, International Journal of Refrigeration, 28(2), 267-275, 2005.
[9] H.K. Navaz, M. Amin, S. C. Rasipuram, R. Faramarzi, Jet entrainment minimization in an air curtain of open refrigerated display case, International Journal of Numerical Methods for Heat and Fluid Flow, 16(4), 417-430, 2006.
[10] A. Hawadey, T. Jaber, W. A. Ghaffar, A. H. A. M. Hasan, Air curtain design optimization of refrigerated vertical display cabinet using CFD, International Journal of Scientific Engineering and Technology, 1(4), 76-88, 2012.
[11] The FLUENT Theory Guide, Fluent Inc., November 2013.
[12] Refrigerated display cabinets – part 2: classification, requirements and test conditions, TS EN ISO 23953-2, 2017.

DEEP LEARNING RESEARCH IN DAMAGE DETECTION OF RC STRUCTURES

Beyza GÜLTEKİN[1] and G. DOĞAN[2]

[1]Konya Technical University, MsC, Konya/Turkey, beyzagltkn42@gmail.com
[2]Konya Technical University, Asist. Prof. Dr., Konya/Turkey, gdogan@ktun.edu.tr

Abstract **- The concept of artificial intelligence, which has entered our lives with the advancement of technology, is divided into many areas within itself. Deep Learning method is also an artificial intelligence algorithm. This method, which imitates the learning mechanism of people, makes predictions on new data groups with the features learned by learning with data. Convolutional Neural Networks, which are used in the field of computer vision from Deep Learning models, which have found different applications in every conceivable sector in recent years, are especially preferred in image classification processes. In structural engineering, damage assessment studies, the process of grouping the damage level according to the nature of the damage is a classification problem. From this point of view, in this study, the use of this innovative technology in structural damage assessment studies, which is very important in the field of structural engineering, has been investigated. The researchers used the Convolutional Neural Networks algorithm in this field in order to minimize the risks in structural damage detection field studies and to make the right decisions about the structural damage situation. All the studies examined showed that using the Deep Learning method in structural damage detection gave very successful results and was found suitable to be developed as an innovative method.**

Keywords **- Deep learning, convolutional neural networks, structural damage detection, reinforced concrete (RC) structures.**

I. INTRODUCTION

Structural damage and resulting cracks are a potential threat to the safety and durability of structures. For this reason, it is necessary to regularly and carefully inspect for structural cracks during the service life of any structure by experts in the field. Especially after natural disasters such as earthquakes, rapid damage assessment studies are extremely important in the field of civil engineering. After a possible earthquake, rapid inspections are required so that citizens can return to their homes and workplaces in a safe and timely manner. Inspections in field work are not only dangerous, but also time consuming and laborious. In addition, one of the disadvantages of damage assessment studies is that the number of damaged structures after large magnetized earthquakes is high, but the number of experts who can determine damage is not sufficient. For all these reasons, methods are being developed by researchers to help speed up and increase the automation of the whole process. Deep Learning (DL) model, which is one of the artificial intelligence methods; It is used in many fields such as medicine, engineering, and defense industry. DL algorithms, which basically aim to make a good generalization, left their mark on the scientific world in the Large-Scale Visual Recognition Competition held in 2012. In fact, the reason why this method, which has its roots in the past, has become so popular in recent years is that with the development of technology, the quality of computer hardware has increased and it has become easier to access large data groups.

In this study, DL models in the field of structural engineering are mentioned and DL model research developed for damage assessment studies in reinforced concrete (RC) structures after earthquakes are examined. The importance of these studies in the literature in the field of structural engineering was emphasized and their achievements were discussed within the scope of the future of structural engineering.

II. DEEP LEARNING

One of the methods used to automate damage assessment studies is the algorithms developed using the DL method. DL, which is a Machine Learning (ML) method, is a model that can predict outputs by learning from any dataset introduced to the system as input. What makes it different from ML is that it learns the features extracted from the data by itself, not manually. Increasing the amount of data in question will enable the algorithm to make more successful predictions. This method, which has been mentioned frequently in recent years, is used in many areas such as object recognition, natural language processing, image classification [1].

DL; There are network models such as Convolutional Neural Networks (CNN), Recurrent Neural Networks (RNN), Long-Short-Term Memory Networks (LSTM), Restricted Boltzmann Machines (RBM), Deep Belief Networks (DBN), Deep Autoencoders (DOC). Since the classification technique is applied over images in the detection of structural damage, the CNN model is frequently used as a computer vision method, which is used in processes such as image recognition and classification. At the same time, in a study conducted by Akinosho et al. in 2020, it was suggested that CNN is the most

widely used DL method in the construction industry [2].

A. Convolutional Neural Network

With its architecture inspired by the visual cortex organization of animals, CNN successfully performs image classification processes. This model, which was first proposed in the 1980s, has become much more popular with the development of graphics processing unit technology [3]. CNN has many layers as shown in Figure 1. Layer descriptions are given in Table 1.

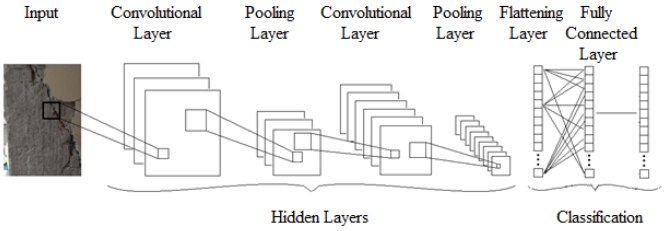

Figure 1: CNN layers

Table 1: CNN layers and descriptions

Layers	Description
Convolutional Layer	It is the layer from which certain features are extracted from the images. At this stage, the images are divided into pixels and various filters are moved over the image matrix with a certain number of steps, the matrix value of the input image and the matrix values of the filters are multiplied in each shift. By summing the product values, feature matrices are obtained [4].
Activation Layer	It is the layer applied to convert the linear structure to a nonlinear structure. There are various types of activation functions such as ReLU, Step, Sigmoid, Linear, Hyperbolic Tangent, Leaky ReLU, Softmax.
Pooling Layer	In order to reduce the calculation amounts, the pooling process is divided into two as maximum pooling and average pooling. In maximum pooling, the highest matrix values are taken, while in average pooling, the average value is selected. The features obtained from the images are not lost while the matrix size is reduced. [5].
Flattening Layer	For the next layer, the Fully Connected Layer, it is the layer where the image features that come in the form of a matrix are turned into a one-dimensional matrix.
Fully Connected Layer	It is the last layer of the CNN, where each neuron that transmits information to the result layer is connected to every other neuron.

The transfer learning (TL) method was created in DL models by inspiring people to apply the knowledge they had learned before on similar problems they encountered later, that is, by inspiring the experience feature. When working with small datasets, using an architecture that was previously trained to solve a similar problem by fine-tuning it according to the course of the work will provide much more successful results. At the same time, starting to train a model with randomly assigned weight values is a very time-consuming application, so it is quick and practical to use the DL technique [6]. Table 2 presents some of the CNN architectures for TL that were previously trained by researchers using very large datasets.

CNN also has different varieties within itself. One of them is Faster R-CNN, developed by adding the Regional Bid Network (RBN) to the Fast R-CNN created by Ross Girshick. It is a deep learning algorithm that can be used in object detection systems. The object detection system is a system that has the function of determining the location of objects in the image so that the classification process can get better results [7]. This method, developed by Shaoqin Ren, consists of 2 separate modules. The first module is the fully convolutional network used to create a RBN. The second module accelerates the computation by helping the Fast R-CNN find the region of interest [8].

Fully Convolutional Networks (FCN) are another type of CNN. Long et al. This method proposed by CNN is the result of replacing fully connected layers with convolution layers. It has an easier application than CNN [9].

Many software languages are used in DL studies. The most commonly used programming languages are MATLAB and Python. Especially open source TensorFlow and Keras libraries working on Python are frequently preferred in image classification processes.

III. Deep Learning Applications in Detection of Structural Damages

Many studies have been conducted using the DL method to classify images in structural damage detection. For example, Patterson et al. study was conducted by in 2018. The aim of the study is to classify each damage occurrence according to the building material and structural element type and to automate the damage assessment studies made after the earthquake. Setting out for this purpose, the authors created a DL algorithm to automatically identify multiple damage types and their associated structural members in a single image by adapting a pre-trained deep neural network. In the study, they stated that the training of the DL algorithm requires approximately 200 images per damage-structural member match. Considering that approximately 20 structural element types and 10 associated damage types are defined for the assessment of post-earthquake damage, according to the building material category (concrete, steel, masonry, wood, etc.), at least 40,000 images must be correctly labeled and then processed by an expert team. calculated to be verified. For this reason, it was stated that the most important and most important part of the study was the data collection part and this process progressed very slowly.

Table 2: CNN architectures

Artchitectures	Designers	Filter Size	Number of Layers	Error Rate
AlexNet	Alex Krizhevsky	11x11, 5x5, 3x3 size filters are used [10].	It consists of 8 layers.	%15,3
VGG16	Simonyan and Zisserman	3x3 size filters are used [11].	It consists of 16 layers.	%7
Inception v2	Szegedy et al.	1x1, 3x3 size filters are used [12].	It consists of 64 layers.	%6,67
ResNet	He at al.	7x7, 3x3 size filters are used [10].	It consists of 152 layers.	%3,57
Ci-Net	Ronneberger and Shelhamer	3x3, 2x2 size filters are used	It consists of 18 layers.	
ResNet-50		1x1, 3x3 size filters are used [13].	It consists of 18 layers.	
ResNet-101			It consists of 101 layers.	
Inception-ResNet v2	He et al.	1x1, 3x3 size filters are used [14].		

In the study, Python programming language and Keras library running on TensorFlow were used. AlexNet and ResNet were preferred among DL architectures. In addition, a graphical user interface (GUI) wrapper is used for the DL solution. The aim here is to enable engineers or researchers who do not have knowledge about programming to use this classification system [15].

The working steps are listed as follows;

• Collecting the input images: The higher the number of images, the higher the success of the algorithm.

- Manually labeling the images: The authors use the software to draw a rectangular bounding box around the damage that has occurred.
- Separating the labeled images into two groups as training and test sets
- Training phase: Training starts with assigning a specific weight value to each neuron and iterates until optimum weight values are obtained.
- Validation phase: Experts check whether the algorithm can identify the correct image features.
- Implementation phase: A completely new image is given as input to the algorithm and the classification process is applied. The workflow of DL is shown in Figure 2.

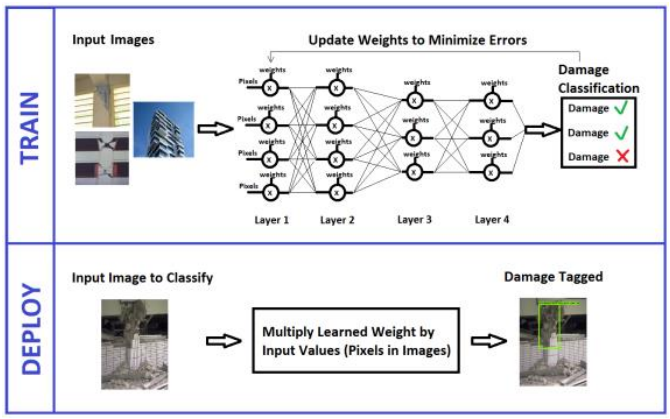

Figure 2: Workflow of DL [15]

The classifier algorithm created in the study was first used to group the images with or without damage (1), then to draw a bounding rectangle around the damages (2), and then to draw a bounding rectangle around the columns exposed to shear damage by showing short column behavior. (3) has been tested. As a result of the test, the accuracy rate obtained from the 1st classification was 88.3%; The accuracy rate obtained from the 2nd process was 85% and finally the accuracy rate from the 3rd process was 77%. The accuracy obtained from the 1st process is the most, as simple classification on images is easier than accurately identifying the target region. The authors noted that the current level of accuracy is very promising on damage to seismic damaged RC structures. Another study focusing on the damage caused by seismic movements is Xu et al. Made by in 2018 [4]. In the study, automatic damage identification from images of RC columns was made with the help of deep CNNs. The aim of the study is to automatically identify and localize multi-type seismic damage (concrete cracking, concrete pouring, reinforcement exposure and reinforcement buckling) from images of exposed RC columns. For this, the authors proposed a faster region-based convolutional neural network (faster R-CNN).

The images used as data in the study were captured by a consumer-grade camera at various locations and arbitrary perspectives to simulate situations where post-earthquake structural damage was taken by non-professionals. With the help of the MATLAB program, the surface cracks on the RC columns are enclosed in the red rectangular bounder, the concrete spills in the blue rectangular delimiter, the areas where the reinforcement is exposed are in the green rectangular box, and the areas with reinforcement buckling are in the yellow rectangular bounding box. Figure 3 shows the application in question.

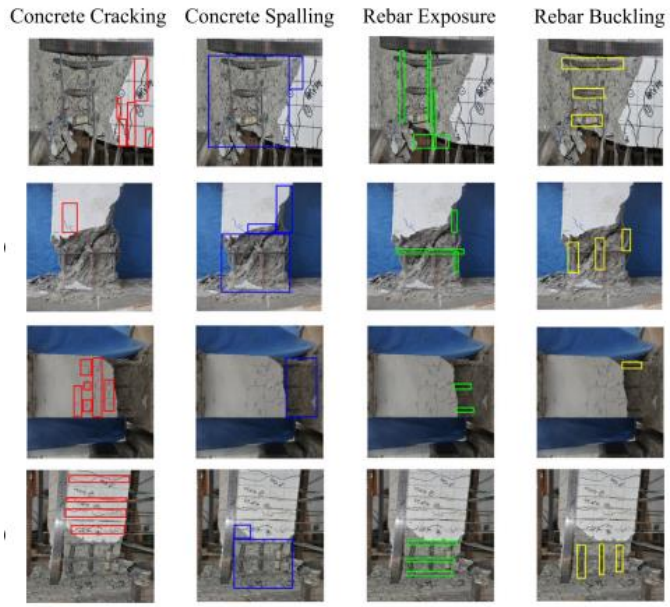

Figure 3: Several representative raw images and labeling of damage regions [4]

A total of 400 raw images were collected within the scope of the study. The data augmentation method was used and these images were rotated 90˚ and rotated horizontally and vertically. 90% of the 2400 images obtained as a result of these processes are allocated as training and 10% as a test set. As a result of the study, the accuracy obtained by the algorithm was 86.7% in concrete cracks; 89.9% in concrete spills; It is 94.4% in reinforcement exposure and 94.4% in reinforcement buckling. The test results show that the trained network can automatically identify and localize multi-type seismic damages, and the average accuracy of the definitions reaches 80%. Mondal et al. In their 2019 study, Xu et al. classified the damages under the same four headings as in the study by A method based on the deep learning method has been studied for the timely evaluation of the damages in buildings due to earthquakes [16]. Region-based convolutional neural network (Faster R-CNN); It was used to detect four different types of damage: surface cracking, swell (including façade and concrete spillage), exposed rebars and severely bent rebars. Damage images used as data in the study are included in Nepal (2015), Taiwan (2016), Ecuador (2016), Erzincan (1992), Düzce (1999), Bingöl (2003), Peru (2007), Wenchuan (2008) and Haiti (2010) obtained from earthquakes. While the images obtained after the Taiwan earthquake were collected by the authors, the data obtained from other earthquakes were taken from "datacenterhub.org".

The CNN architectures used in the study; Inception v2 is ResNet-50, ResNet-101, and Inception-ResNet-v2. 90% of the collected image data to train the network; the remaining 10% was used for testing. 962 images containing superficial cracks characterized as the first type of damage, 2023 images containing the swelling and spilling of the second type damage, 702 images containing the exposure of the reinforcements characterized as the third type of damage, and 599 images containing severely buckled reinforcements, which are described as the fourth type of damage, as data in the study. used. Example images of these classes are given in Figure 4.

(a) (b) (c) (d)

Figure 4: Damage categories considered for fixation (a) Damage 1, surface cracking (b) Damage 2, fragmentation (c) Damage 3, exposed reinforcement (d) 4 damage, severely twisted reinforcement [16]

The accuracy rates obtained from the four different CNN architectures used in the study are Inception v2 51%, ResNet-

50 54%, ResNet-101 55% and Inception ResNet v2 61%. As it can be understood from here, Inception ResNet v2 architecture gave the highest accuracy rate. When the mentioned CNN architectures are evaluated in terms of time, it has been revealed that the architecture that gives the fastest results is the Inception v2 architecture with a value of 0.144 seconds/image. Then, ResNet-50 with 0.167 seconds/image value and ResNet-101 with 0.245 seconds/image value come in order. The slowest architecture, on the other hand, was the Inception ResNet v2 architecture, with the 0.8 second/image value, which also achieved the most successful accuracy.

As a result of the study, when the classification success according to damage types is evaluated, it has been seen that the damage images, which are defined as Type 1 damage, containing only surface cracks, can be easily detected and distinguished by the algorithm. In addition, since other damage types consist of images close to each other, they could not be distinguished very successfully by the algorithm and classification errors occurred. Another study using structural damage during the 2010 Haiti earthquake, 2015 Nepal earthquake, 2016 Taiwan earthquake and 2016 Ecuador earthquakes as a dataset is Nahata et al. this is the study done in 2019 [17]. In the study, the DL method was used to evaluate the post-earthquake building conditions. Damage images used as data were obtained from "datacenterhub.org" and "design-safe" addresses. The aim is to classify the images in 4 groups as no damage, little damage, major damage and collapse. While performing the classification process, images with no damage were assigned to the no damage class, images with damage only in non-structural elements were assigned to the minor damage class, images with damage to both structural and non-structural elements but no collapse were assigned to the major damage class, and collapsed building images were assigned to the collapse class. Within the scope of this purpose, 1000 of the 1200 images collected were allocated as training sets and 200 as test sets. In order to avoid data imbalance between classes, 300 images were obtained from each class.

The authors, who preferred VGG 16 as the CNN architecture, wanted to test the algorithm by changing the learning rate. Therefore 0.00001; 0.0003; Three different algorithms were created using three different learning rates, 0.0001. When the results obtained after testing the models were compared, it was seen that the most successful algorithm was the one in which the learning rate of 0.00001 was used. As a result, it has been proven that a success rate of over 92% is achieved in model damage classification and the usability of CNN-based algorithms in this area. Another work that still prefers VGGNet architecturally was done by Gao and Mosallam in 2018 [18]. The authors aimed to create an DL-based model to perform structural damage detection automatically and quickly. Inspired by the founding of ImageNet and the idea of transfer learning (TL), it has been used to create buildings, bridges, substations, railways, etc. It has been proposed to create a Structural ImageNet containing both structurally damaged and undamaged images related to civil engineering, such as Installing this type of Structural ImageNet can be used for recognition and vision problems in civil engineering. Because civil engineering is a broad discipline, this article has been narrowed down to remain within structural engineering for simplicity. Therefore, the Structural ImageNet proposed here is intended to be used only for detection and recognition of structural features. Figure 5 shows the hierarchy tree of Structural ImageNet.

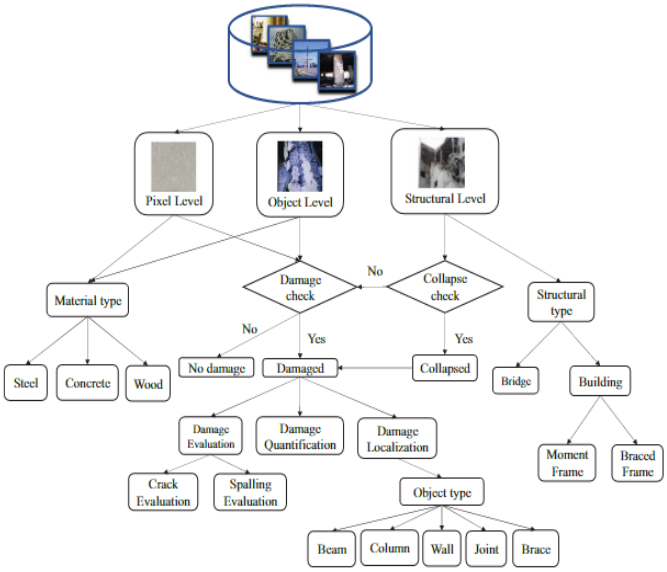

Figure 5: Hierarchy tree of structural ImageNet [18]

Dual classification task, column/beam or wall, for component type identification in the study; dual classification task with or without spill for case of concrete pouring; triple classification task for damage level assessment as no damage, minor damage or moderate/heavy damage; In order to determine the damage type, four classification tasks are defined as no damage, bending, shear or combined damage. A few examples of images assigned for these tasks described in Figure 6 are shown.

(a)

(b)

(c)

(d)

(e) (f)

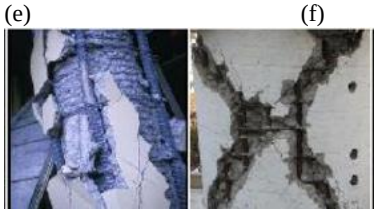

(g)

(h)

(i)

(j)

(k)

Figure 6: Examples of (a) column/beam, (b) wall damage for component type classification; examples of (c) no spillage, (d) spillage for concrete erection status classification; for damage level assessment, examples of (e) no damage, (f) minor damage, (g) moderate/heavy damage; (h) no damage, (i) bending, (j) shear, (k) combined damage examples for damage type classification [18]

Data rates for binary classifications are evenly distributed as 55/45% and 53/47%. In the other multi-class tasks performed in the study, the number of balanced distributions could not be obtained, as there was a limited amount of data for the undamaged classes. However, although it is not acceptable to classify an undamaged structure as damaged, it is absolutely unacceptable to do the opposite, that is, to classify a damaged structure as undamaged. Therefore, the imbalance in the number of data in the study is an acceptable situation. The number of images used as data is 2000. Of these, 80% are grouped as training and 20% as test set.

As a result of the study, 94.5% test accuracy in component type classification, 91.5% test accuracy in dispersion state classification, 89.7% test accuracy in damage level classification, and finally 68.8% test accuracy in damage type classification were achieved from dual classification tasks. While 90% success was achieved in binary and triple classification tasks, 68% accuracy was achieved in the quadruple classification task because as the difficulty of the task defined to the algorithm increases, the case of excessive memorization increases. A multi-class structural damage assessment study like this was conducted in 2019 by Feng et al. implemented by [5]. During long-term use of hydro-connection infrastructure, water flow erosion causes cracking and splintering on concrete surfaces and exposed reinforcement. In order to ensure infrastructure security, a damage assessment method has been proposed in this study. Deep CNN, DL methods and Inception v3 CNN architecture are used. Some changes have been made on the output layer of the model in order to detect multiple damage types. Since there is currently no dataset containing high-quality images of the hydro-link infrastructure, UAVs equipped with HD cameras were used to collect data. As a result of the process, 435 usable resolution raw images were obtained. By using the data augmentation method, the number of images reached 18,605. In order to assign these images, which will be used as data, to 5 different classes as sound, crack, leakage, reinforcement exposure and fragmentation, support was received from experts in the field. Of the 18,605 images, 3,742 were assigned to the crack class, 3,705 to the intact class, 3,716 to the fragmentation class, 3,735 to the leakage class, and the remaining 3,707 to the reinforcement exposure class. Data labeling is shown in Figure 7. 14,873 image training, which corresponds to approximately 80% of the total 18,605 images; 1903 images, corresponding to approximately 10%, and 1829, corresponding to the remaining approximately 10% slice, were used as test data.

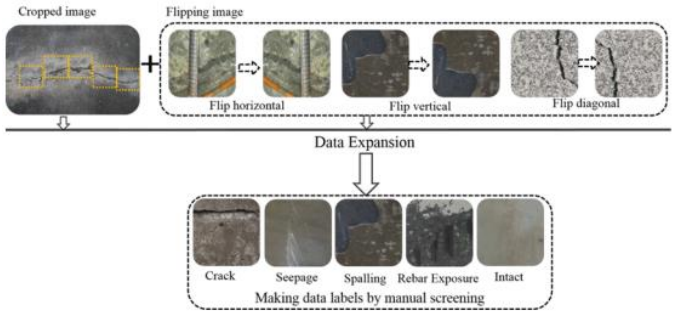

Figure 7: Data expansion and data labeling [5]

As a result of testing the algorithm created using the TensorFlow deep learning framework in the Python program, only 59 images were wrong. has been classified. This proves that the model has achieved an accuracy rate of 96.8%. In the study, the same classification system was created with Support Vector Machines (SVM), which is an ML model, in order to compare the DL and ML methods. Although the accuracy rate of the model created with SVM in cracks and intact classes is high, the low accuracy rate in degraded classes such as fragmentation and leakage reduced the success of the algorithm to 61.2%. The authors have proven that the proposed damage detection model gives much more successful results than the SVM model. Considering that entering buildings after an earthquake can have very dangerous consequences, another study suggesting that data collection be done by UAVs is the 2018 study by Hoskere et al [19]. The researchers preferred UAVs for data collection and an DL-based model for data processing. In the study, fully convolutional networks (FCN) were used and ResNet was preferred as the architecture.

Within the scope of the study, three networks were trained in parallel. The first of these includes building information. What is intended here is; The aim is to introduce objects such as doors, windows, pavements, paths, people, vehicles, trees, debris, and the sky to the network to prevent them from being removed, to perceive them as damage and to produce false results. The second network, to detect the presence of damage; the third mesh was created to determine the type of damage (concrete crack, concrete spillage and reinforcement exposure). Figure 8 shows the results from the networks mentioned.

A total of 1000 images from datacenterhub.org were used for the first network, and a total of 665 images from the authors' own archives were used for the other two networks. 80% of the data were grouped for training and 20% for validation purposes. 1997 images collected after the 2017 Mexico earthquake were used to measure the success of the algorithm. The results showed that the first network reached an accuracy of 88.8%, while the accuracy of the other two combined networks was 91.1%.

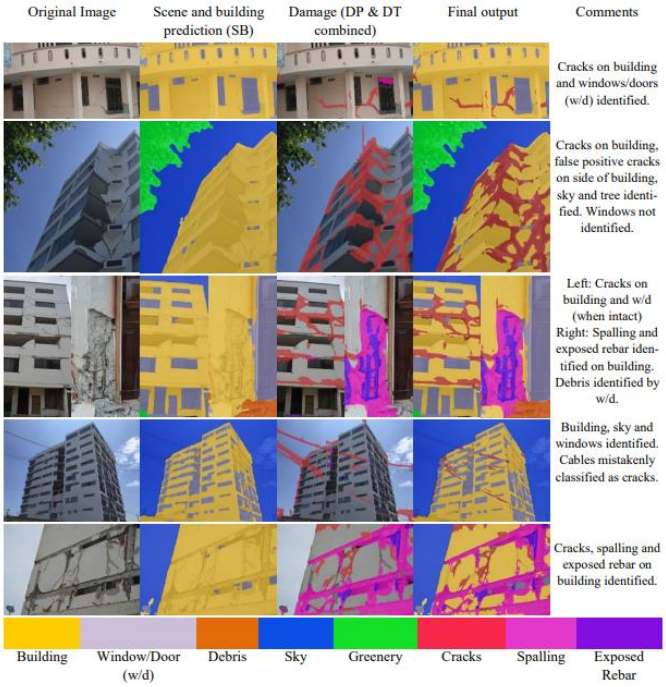

Figure 8: Qualitative results from the proposed networks [19]

Ye et al., in 2019, conducted a study on structural damage detection using CNN, one of the methods of DL. The authors proposed a FCN, Ci-Net [20].

The dataset used as input in the study are crack images from CrackForest and TITS 2016. The total number of raw training images is 762. These raw training images were cropped at 80x3x80 pixel resolution to create the training dataset. A total of 14,000 cracked images were obtained from the data set, which was subjected to various operations with clipping. 70% of the obtained images were allocated as training set and 30% as test set. In the study, concrete beam loading test was also carried out to verify the structural damage recognition capacity of the algorithm. In the indoor concrete beam test performed to create cracks on the concrete structure, a standard size beam was produced using concrete with a compressive strength of 30 MPa. Then, cracks formed on the surface were tried to be detected by Ci-Net and edge detection method. Figure 9 shows the crack image obtained from the beam test and the recognition result in Ci-Net.

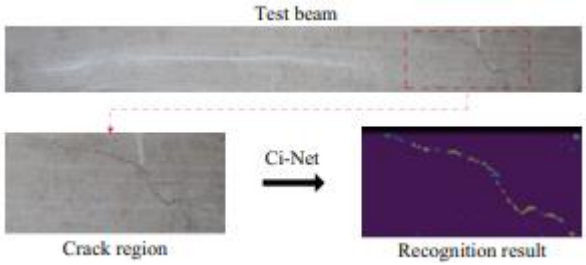

Figure 9: Structural damage detection [20]

It was revealed that the Ci-Net algorithm, which was created as a result of the study, achieved a success rate of 93.6%. In addition, it was stated by the authors that the Ci-Net algorithm produced more successful results when compared to the edge detection method.

IV. Research Results

Considering the studies using the DL method by classifying structural damage images, it has been revealed that the method in question produces very successful results and can be developed with much larger data sets. Table 3 presents various characteristics of all the studies covered.

Table 3: Parameters of all studies reviewed

Studies	Researchers	DL method	CNN architecture	Programming language	Data (Number of images)	Success Rate
Automatic Image Classification of Seismic Damages	Patterson et al., 2018	CNN	AlexNet and ResNet	Python	40.000	%88,3
Automatic Seismic Damage Identification from Images of RC Columns	Xu et al., 2018	Faster R-CNN	-	MATLAB	24.000	%94,4
Multi-Class Damage Detection for Post-Disaster Autonomous Reconnaissance	Mondal et al., 2019	Faster R-CNN	Inception v2, ResNet-50, ResNet-101, Inception-ResNet v2	Python	4.286	%60,8
Post-earthquake Evaluation of Buildings	Nahata et al., 2019	CNN	VGG16	Python	1.200	%92
Image Based Structural Damage Recognition	Gao and Mosallam, 2018	CNN	VGGNet	Python	2.000	%90
Structural Damage Detection	Feng et al., 2019	CNN	Inception v3	Python	18.605	%96,8
Automated Post-earthquake Inspections	Hoskere et al., 2018	FCN	ResNet	Python	1.665	%91,1
Structural Crack Detection	Ye et al., 2019	FCN	Ci-Net	Python	14.000	%93,6

V. Conclusions and Recommendations

Timely and accurate detection of structural damage that may occur during the normal use of reinforced concrete structures or as a result of natural disasters has a very important place in terms of life and property safety. Today, researchers have taken some technological steps to automate this process, due to the danger of aftershocks in field observations in the detection studies carried out by experts in the field, and the time and speed factor for evaluation in cases where the number of damaged buildings is high. One of them, the DL-based CNN method, can make different inferences from the images taken during damage assessment studies, and can divide the images into classes such as there is damage or not, and even into classes such as cracks, spills, reinforcement exposure, reinforcement buckling. Studies have shown that CNN algorithms can achieve a very high success rate in this classification. From this point of view, working with quality datasets in future studies will provide better results.

References

[1] B. Gültekin, 2022. Yapısal ve Yapısal Olmayan Hasarların Derin Öğrenme ile Tespiti, Master Thesis, Konya Technical University Graduate Education Institute, Konya.

[2] Akinosho, T. D., Oyedele, L. O., Bilal, M., Ajayi, A. O., Delgado, M. D., Akinade, O. O., & Ahmed, A. A. (2020). Deep learning in the construction industry: A review of present status and future innovations. Journal of Building Engineering, 32, 101827.

[3] Dong, S., Wang, P., & Abbas, K. (2021). A survey on deep learning and its applications. Computer Science Review, 40, 100379.

[4] Xu, Y., Wei, S., Bao, Y., & Li, H. (2019). Automatic seismic damage identification of reinforced concrete columns from images by a region-based deep convolutional neural network. Structural Control and Health Monitoring, 26(3), e2313.

[5] Feng, C., Zhang, H., Wang, S., Li, Y., Wang, H., & Yan, F. (2019). Structural damage detection using deep convolutional neural network and transfer learning. KSCE Journal of Civil Engineering, 23(10), 4493-4502.

[6] Azimi, M., Eslamlou, A. D., & Pekcan, G. (2020). Data-driven structural health monitoring and damage detection through deep learning: State-of-the-art review. Sensors, 20(10), 2778.

[7] Adiwinata, Y., Sasaoka, A., Bayupati, I. A., & Sudana, O. (2020). Fish species recognition with Faster R-CNN Inception-v2 using QUT FISH dataset. Lontar Komputer: Jurnal Ilmiah Teknologi Informasi, 11(3), 144-154.

[8] Halawa, L. J., Wibowo, A., & Ernawan, F. (2019, October). Face recognition using faster R-CNN with inception-V2 architecture for CCTV camera. In 2019 3rd International Conference on Informatics and Computational Sciences (ICICoS) (pp. 1-6).H. Poor, *An Introduction to Signal Detection and Estimation*. New York: Springer-Verlag, 1985.
[9] Fu, G., Liu, C., Zhou, R., Sun, T., & Zhang, Q. (2017). Classification for high resolution remote sensing imagery using a fully convolutional network. Remote Sensing, 9(5), 498.
[10] https://frightera.medium.com/alexnet-vggnet-inception-ve-resnet-nedir-bddc7482918b
[11] https://ichi.pro/tr/vgg16-nedir-vgg16-ya-giris-267001881294357
[12] https://ayyucekizrak.medium.com/deri%CC%87n-bi%CC%87r-kar%C5%9Fila%C5%9Ftirma-inception-res-net-versiyonlar%C4%B1-f5cfb83df131
[13] Talo, M. (2019). Meme Kanseri Histopatalojik Görüntülerinin Konvolüsyonal Sinir Ağları ile Sınıflandırılması. Fırat Üniversitesi Mühendislik Bilimleri Dergisi, 31(2), 391-398.
[14] Baldassarre, F., Morín, D. G., & Rodés-Guirao, L. (2017). Deep koalarization: Image colorization using cnns and inception-resnet-v2. arXiv preprint arXiv:1712.03400.
[15] Patterson, B., Leone, G., Pantoja, M., & Behrouzi, A. A. (2018). Deep learning for automated image classification of seismic damage to built infrastructure. In Eleventh US National Conference on Earthquake Engineering.
[16] Ghosh Mondal, T., Jahanshahi, M. R., Wu, R. T., & Wu, Z. Y. (2020). Deep learning-based multi-class damage detection for autonomous post-disaster reconnaissance. Structural Control and Health Monitoring, 27(4), e2507.
[17] Nahata, D., Mulchandani, H. K., Bansal, S., & Muthukumar, G. (2019). Post-Earthquake Assessment of Buildings Using Deep Learning. arXiv preprint arXiv:1907.07877.
[18] Gao, Y., & Mosalam, K. M. (2018). Deep transfer learning for image-based structural damage recognition. Computer-Aided Civil and Infrastructure Engineering, 33(9), 748-768.
[19] Hoskere, V., Narazaki, Y., Hoang, T. A., & Spencer Jr, B. F. (2018). Towards automated post-earthquake inspections with deep learning-based condition-aware models. arXiv preprint arXiv:1809.09195.
[20] Ye, X. W., Jin, T., & Chen, P. Y. (2019). Structural crack detection using deep learning–based fully convolutional networks. advances in structural engineering, 22(16), 3412-3419.

AHP and GIS Based Site Selection for Medical Waste Disposal Facility: Kahramanmaras Turkoglu District

O. F. ATIZ[1], T. ALKAN[1], S. S. DURDURAN[1], and S. KAPUKAYA[1]

[1]Necmettin Erbakan University, Konya/Turkey, oatiz@erbakan.edu.tr
[1]Necmettin Erbakan University, Konya/Turkey, tansualkan93@gmail.com
[1]Necmettin Erbakan University, Konya/Turkey, durduran2001@gmail.com
[1]Necmettin Erbakan University, Konya/Turkey, kapukayasevim@gmail.com

***Abstract* – The selection of medical waste disposal (MWD) facilities is crucial for public health and the environment. In this study Multi-Criteria Decision Making (MCDM) is used as integrated with Analytic Hierarchy Process (AHP) to find optimum sites for the MWD facility in Turkoglu district. Six factors were selected and weighted with AHP for suitability criteria. The Geographical Information System (GIS) was used for the spatial analyses and visualization of results. According to the final suitability map, the most suitable, suitable, less suitable, and protected areas were found. As a result of the study, three alternative sites were proposed for the MWD facility in the Turkoglu district, Kahramanmaras (Turkey).**

***Keywords* – AHP, GIS, MCDM, Site selection.**

I. INTRODUCTION

TODAY medical waste disposal (MWD) is one of the challenging processes especially after COVID-19 pandemic to preserve public health and to prevent environmental pollution. During the pandemic the number of infected wastes was increased, and some countries built new MWD sites [1].

The suitable site selection is a major urban planning problem. The decision makers have some challenges due to large number of factors and the complex relations between them. They need some Decision Support Systems (DCS) for modelling the real-world scenarios [2]. Multi-Criteria Decision Making (MCDM) incorporation with Analytical Hierarchy Process (AHP) is extensively used in many studies. Moreover, the Geographical Information System (GIS) is a necessity to handle spatial analyses.

There are some studies conducted over AHP-GIS suitable site selection of varying urban facilities. In Reference [3], the distribution and selection of hospital sites was investigated using an AHP-GIS based approach, in Egypt. In Reference [4], the suitable site selection for rainwater harvesting areas was assessed with the remote sensing and AHP-GIS based decision support systems. They found that MCDM systems are a powerful tool for selection of suitable sites for rainwater harvesting. In Reference [5], an AHP-GIS integrated strategy is proposed for agricultural land suitability analyses. They showed that AHP-GIS based method is successfully applied for determining the sustainable agricultural zones.

In this study, the site selection of MWD facility in Turkoglu District, Kahramanmaras (Turkey), was investigated using MCDM approach. The AHP was used to determine weights of six criteria below:

- Distance to residential and industrial areas
- Geology
- Land use
- Slope
- Distance to roads
- Distance to wetlands.

Moreover, GIS was used to conduct spatial analyses. As result, three suitable sites for MWD facility in Turkoglu were proposed to decision makers.

The manuscript is organized as follows: Section 2 describes the material and methods. In Section 3, the results are given. In Section 4, the study is concluded.

II. MATERIAL AND METHODS

Turkoglu is a district in Kahramanmaras city that is at the eastern side of Turkey. According to the TURKSTAT (Turkish Statistical Institute) population data in December 2021, there are 78,588 people living in Turkoglu district [6]. The location of Turkoglu district is showed in Figure 1.

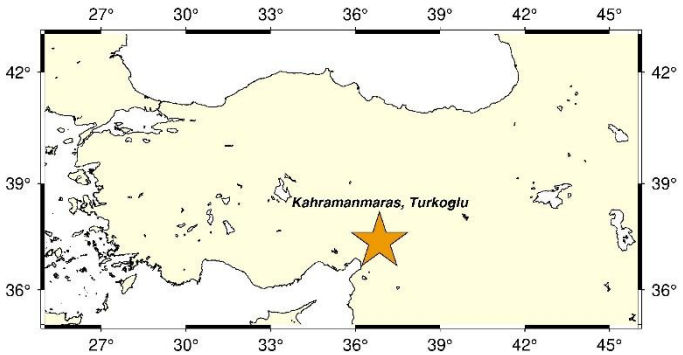

Figure 1: The location of Turkoglu district.

During the COVID-19 pandemic the medical waste amount was increased about 35% in Kahramanmaras city (private

communication). Therefore, emergence MWD sites should be planned. The site selection phenomenon is complicated for the decision makers. When the number of criteria is increased, the decision making becomes more complex. There are different MCDM systems such as AHP, TOPSIS (Technique for Order Performance by Similarity to Ideal Solution), ELECTRE (Elemination and Choice Translating Reality English) etc.

AHP is one of the popular MCDM methods that have been widely used in optimum site selection problem as integrated with GIS software [7, 8, 9]. The AHP method was first proposed by Myers and Alpert in 1968 and developed by Saaty in 1977. AHP method can be used in MCDM problems. AHP consists of four steps below [10]:

1. First, the decision criteria and alternatives are defined.
2. The pairwise comparison matrices are created. After a hierarchical structure consisting of the target, criteria and alternatives of the problem is determined, a pairwise comparison matrix of nxn size of the criteria is created.

Table 1: AHP pairwise comparison scale [11].

Importance	Definitions
1	Equal
3	Moderate
5	Strong
7	Very strong
9	Extreme
2, 4, 6, 8	Between the above values

3. The weights of criteria are calculated. A pairwise comparison matrix is created (1) and each value is divided by its corresponding column sum (2).

$$A = \begin{bmatrix} 1 & a_{12} & \dots & a_{1n} \\ 1/a_{12} & 1 & \dots & a_{2n} \\ \vdots & \vdots & \ddots & \vdots \\ 1/a_{1n} & 1/a_{2n} & \dots & 1 \end{bmatrix} \quad (1)$$

$$b_{ij} = \frac{a_{ij}}{\sum_{i=1}^{n} a_{ij}} \quad (2)$$

$$W_i = \frac{\sum_{j=1}^{n} b_{ij}}{n} \quad (3)$$

4. The consistency ratio (CR) is computed. The upper limit for the CR recommended by Saaty is 0.10. If the calculated CR is greater than 0.10, the pairwise comparison is re-evaluated. The basis of the CR is based on the comparison of the number of criteria with a coefficient (λ). After calculating the λ value (4, 5), the consistency ratio is calculated (6). Random consistency indices (RI) are given in Table 2 depending on the number of criteria.

$$|d_i| = |a_{ij}| * |w_i| \quad (4)$$

$$\lambda = \frac{\sum_{i=1}^{n} (d_i / w_i)}{n} \quad (5)$$

$$CR = \frac{\lambda - n}{RI * (n-1)} \quad (6)$$

Comparisons are consistent if CR ≤ 0.10. The closer the CR is to zero, the more consistent the comparison results will be. If CR > 0.10 the results are inconsistent.

Table 2: Random consistency index (RI) [10].

n	1	2	3	4	5	6	7	8	9	10
RI	0	0	0.58	0.90	1.12	1.24	1.32	1.41	1.45	1.49

III. RESULTS

In this study, the AHP was used among MCDM methods for MWD facility sitting problem in Turkoglu district. In Turkey, the relevant regulations define some factors for MWD facilities. The factors below were considered in this study:

- Distance to residential and industrial areas
- Geology
- Land use
- Slope
- Distance to roads
- Distance to wetlands.

According to the legislation in Turkey, there are some limitations in the selection of MWD sites.

Table 3: MWD site selection criteria and weights.

Main criteria	Sub-criteria	Sub-criteria weights
Distance to residential and industrial areas (W=0.27)	0-1000 m	0.06
	1000-2000 m	0.10
	2000-3000 m	0.16
	3000-4000 m	0.26
	>4000 m	0.42
Slope (W=0.04)	0-10	0.63
	10-20	0.26
	>20	0.11
Land use (W=0.42)	Irrigated agriculture	0.10
	Dry farming	0.16
	Forest, pasture	0.28
	Settlement, rocky	0.47
Distance to wetlands (W=0.14)	0-500 m	0.09
	500-1000 m	0.11
	1000-1500 m	0.16
	1500-2000 m	0.25
	2000+ m	0.39
Distance to roads (W=0.04)	0-250 m	0.45
	250-500 m	0.42
	500-750 m	0.28
	750-1000 m	0.18
	>1000 m	0.16
Geology (W=0.09)	Alluvium	0.06
	Sedimentary	0.10
	Magmatic	0.17
	Melange	0.27
	Metamorphic	0.45

The MWD sites must be 1 km away from the residential and industrial areas. Land use is also crucial due to the negative environmental impacts of MWD facilities. The pairwise comparison matrix and weights of main criteria were constructed according to Reference [12]. The pairwise comparison matrices of sub-criteria were formed considering expertise views. The MWD site selection criteria and weights are showed in Table 3. CR was calculated for the created pairwise comparison matrices and this value is expected to be at most 0.10. If the CR is less than 0.10, the results obtained are consistent, whereas if it is greater than 0.10, the results obtained are inconsistent. In this study, the CR was calculated as 0.06 for the main criteria. The CR for sub-criteria were also found to be less than 0.10. This shows that the obtained results are consistent.

For the suitable site selection of MWD facilities GIS software (ArcGIS) were used. The spatial analyses were conducted using the criteria and weights from AHP above. For each criteria suitability maps were created as illustrated in Figure 2-7.

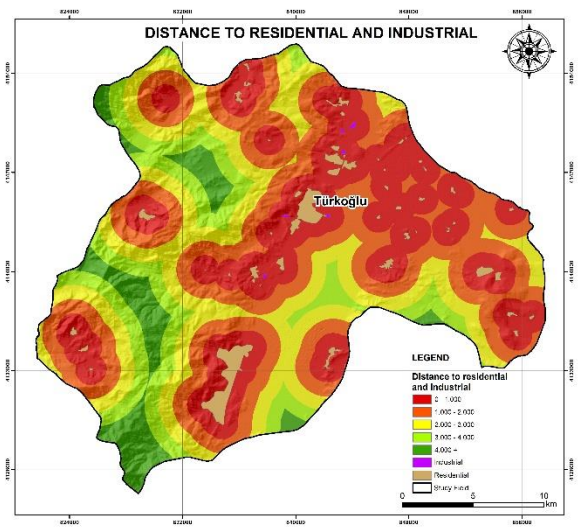

Figure 2: Distance to residential and industrial areas.

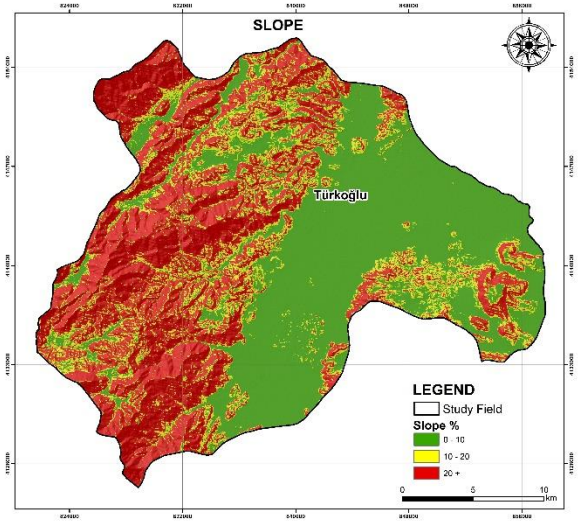

Figure 3: Slope.

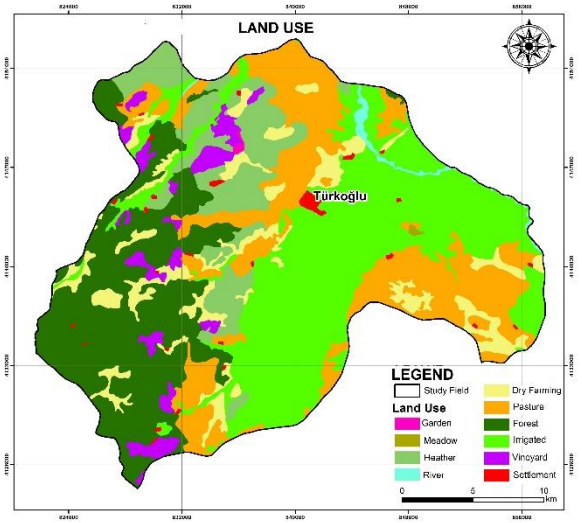

Figure 4: Land use.

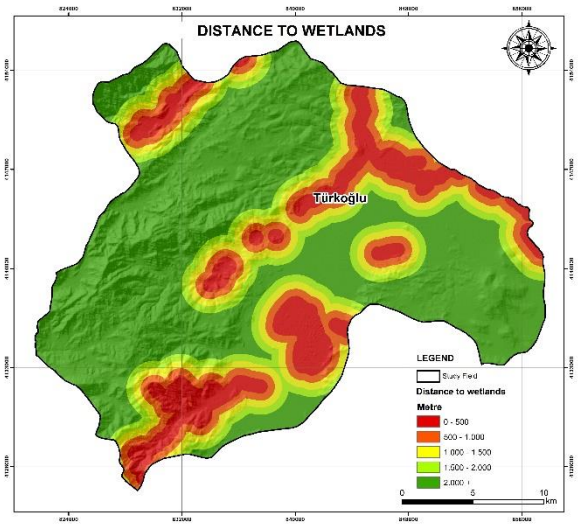

Figure 5: Distance to wetlands.

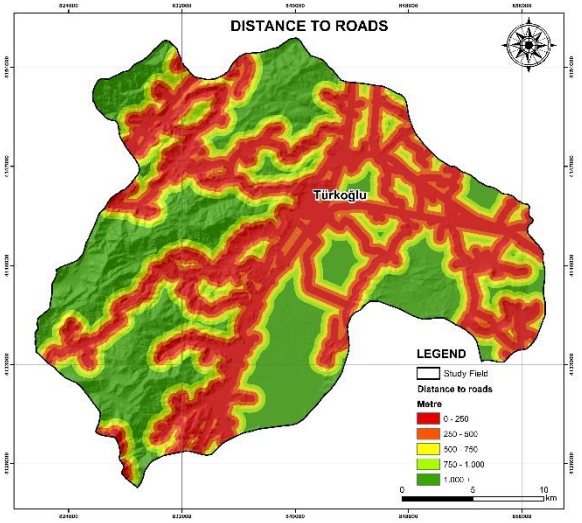

Figure 6: Distance to roads.

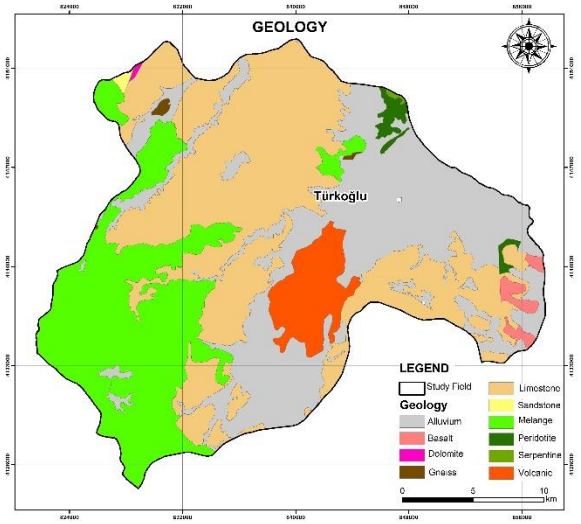

Figure 7: Geology.

The geologic features in Figure 7 are categorized as alluvium, sedimentary, magmatic, melange, and metamorphic to be more consistent with AHP. According to the Figure 2-7 the final suitability map was created. From the suitability map, the most suitable, suitable, less suitable, and protected areas were found. The suitability map is depicted in Figure 8. Between the suitable areas three alternative sites were proposed to decision makers.

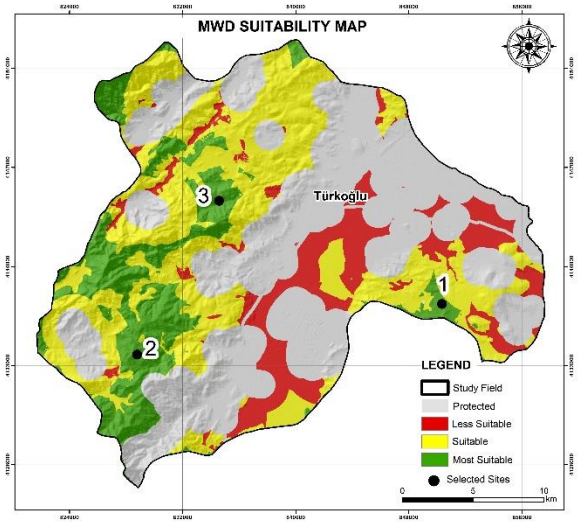

Figure 8: Suitability map.

IV. Conclusion

In this study the AHP-GIS method was used among the MCDM methods for the site selection of MWD facility in Turkoglu district, Kahramanmaras (Turkey). Using the AHP five factors were weighted that are important in the site selection of MWDs. The weighted criteria were used to spatial analyses with GIS. As a result of the study, three alternative sites were proposed to the decision makers for MWD facility in the Turkoglu district, Kahramanmaras (Turkey). The AHP-GIS site selection methodology is convenient when there is a need for rapid decision-making, such as during a pandemic.

References

[1] Sangkham, S. (2020). Face mask and medical waste disposal during the novel COVID-19 pandemic in Asia. Case Studies in Chemical and Environmental Engineering, 2, 100052. https://doi.org/10.1016/j.cscee.2020.100052

[2] Baizyldayeva, U., Vlasov, O., Kuandykov, A. A., & Akhmetov, T. B. (2013). Multi-criteria decision support systems. Comparative analysis. Middle-East Journal of Scientific Research, 16(12), 1725-1730.

[3] Ahmed, A. H., Mahmoud, H., & Aly, A. M. M. (2016). Site suitability evaluation for sustainable distribution of hospital using spatial information technologies and AHP: A case study of Upper Egypt, Aswan City. Journal of Geographic Information System, 8(05), 578. http://dx.doi.org/10.4236/jgis.2016.85048

[4] Radwan, F., & Alazba, A. A. (2022). Suitable sites identification for potential rainwater harvesting (PRWH) using a multi-criteria decision support system (MCDSS). Acta Geophysica, 1-20. https://doi.org/10.1007/s11600-022-00895-4

[5] Bozdağ, A., Yavuz, F., & Günay, A. S. (2016). AHP and GIS based land suitability analysis for Cihanbeyli (Turkey) County. Environmental Earth Sciences, 75(9), 1-15. https://doi.org/10.1007/s12665-016-5558-9

[6] Turkish Statistical Institute, https://www.tuik.gov.tr/indir/duyuru/favori_raporlar.xlsx (Access date 16.08.2022)

[7] Uyan, M. (2014). MSW landfill site selection by combining AHP with GIS for Konya, Turkey. Environmental earth sciences, 71(4), 1629-1639. https://doi.org/10.1007/s12665-013-2567-9

[8] Al Garni, H. Z., & Awasthi, A. (2017). Solar PV power plant site selection using a GIS-AHP based approach with application in Saudi Arabia. Applied energy, 206, 1225-1240. https://doi.org/10.1016/j.apenergy.2017.10.024

[9] Messaoudi, D., Settou, N., Negrou, B., Rahmouni, S., Settou, B., & Mayou, I. (2019). Site selection methodology for the wind-powered hydrogen refueling station based on AHP-GIS in Adrar, Algeria. Energy Procedia, 162, 67-76. https://doi.org/10.1016/j.egypro.2019.04.008

[10] Saaty, T. L. (2008). Decision making with the analytic hierarchy process. International journal of services sciences, 1(1), 83-98.

[11] Saaty, T. L. (1990). How to make a decision: the analytic hierarchy process. European journal of operational research, 48(1), 9-26. https://doi.org/10.1016/0377-2217(90)90057-I

[12] Uyan M., & Yalpir, S. (2016). Site Selection for Medical Waste Sterilization Plants by Integration of Multi Criteria Decision Making Model with GIS. Afyon Kocatepe University Journal of Science and Engineering Sciences, 16 (3), 642-654. (In Turkish). https://www.doi.org/10.5578/fmbd.36294

Performance of an Upstream Cofferdam at Dam Construction Site During a Flood Event: Berdan Dam Case Study

Ş. Pınar GÜVEL[1], M. Ali AKGÜL[2], Ş. Duygu BABACAN[3], Seda SEVER[4] and Recep YURTAL[5]

[1] General Directorate of State Hydraulic Works, 6th Regional Directorate, Information Technologies Department, Geographic Information Systems Section, Adana/Turkey, spinar.guvel@dsi.gov.tr

[2] General Directorate of State Hydraulic Works, 6th Regional Directorate, Information Technologies Department, Geographic Information Systems Section, Adana/Turkey, mali.akgul@dsi.gov.tr

[3] General Directorate of State Hydraulic Works, Ankara/Turkey, dbabacan@dsi.gov.tr

[4] Çukurova University, Faculty of Engineering, Department of Civil Engineering, Adana /Turkey, ssever@cu.edu.tr

[5] Çukurova University, Faculty of Engineering, Department of Civil Engineering, Adana /Turkey, ryurtal@cu.edu.tr

***Abstract* - – Due to the limited availability of water resources in nature, development plans are being prepared for sustainable and effective use of water resources. Water structures are constructed in order to develop and control water resources in line with needs. Specialized engineering units work in coordination during the surveying, planning, project design and construction phases of water structure projects.**

Dam design and construction works depend on several technical, economic, environmental and social factors and dam project implementation is a complex task. The details of project elements regarding hydraulic, geotechnical, structural issues, operation-maintenance works, monitoring, providing dam safety are specified in dam design and construction guidelines. Dams are structures that control large volumes of water and have a long service life. Sustainable water resources management and dam safety effects the performance of the project. The design flood criteria in dam projects depends on safety principles. Flood risk assessments and future projections are essential in flood management.

Flood control during dam construction is essential to prevent damages of flood disasters. Upstream cofferdams are built as temporary structures to provide safety, flood protection, diversion and dry environment during construction of permanent structures. It is an important task to find solutions to flood problems in dam construction sites in order to ensure dam safety.

Berdan Dam was constructed between 1975 and 1984. The dam is located in Mersin City in the Eastern Mediterranean Basin in the southern of Turkey. In this study, the performance of upstream cofferdam of Berdan Dam during 1980 flood event when the dam was under construction stage, was investigated by using ground measurements and satellite-based remote sensing data. As a result, flood inundated areas up to the Berdan Dam site in 1980 flood, calculated as 271 hectares by using remote sensing data. It is evaluated that the dam structures built at the Berdan dam construction site at the 1980 flood event held the flood flow and contributed flood control works of downstream areas.

***Keywords* - Dam safety, Cofferdam, Flood control, Berdan Dam.**

I. INTRODUCTION

THE negative effects of flood events make it essential to take necessary measures to control floods. These measures are considered as structural and non-structural measures. There are many studies on flood-related issues such as flood measures [1-3], flood history [4], detection of flood damages [5], causes of floods [6-7], flood risk [8-9] and flood prediction [10]. Evaluation of flood events in terms of dam safety is also one of the remarkable issues. In this context, investigating the effects of flood events during dam construction sites encountered in previous years can be beneficial in terms of developing necessary precautions during the construction of future water structures.

The risks and safety issues that may be encountered during the construction of a dam were explained in several researches [11]. Flood control standards for reservoir engineering between different countries were presented in the study conducted by Ren et al. (2017) [12]. In the study carried out by Lempérière (2017), lessons from dam accidents related to floods over the past two centuries were reviewed, new solutions were assessed and the risk from floods during construction of embankments was pointed out [13].

The aim of this study is to investigate the performance of upstream cofferdam during the April 1980 flood in Berdan Dam which was under construction, in the Mediterranean Region of Turkey. Satellite-based remote sensing technique

was used to determine the flooded reservoir areas during the April 1980 flood event.

II. Material and Method

Berdan Dam is located in Mersin City in the Eastern Mediterranean Basin in the southern of Turkey. The dam was put into operation in 1984 and the purposes of the dam are irrigation, flood control, energy production, drinking water supply and industrial water supply. Mediterranean climate characteristics are effective in the study area, summers are hot and dry, winters are warm and rainy. The location of the dam is given in Figure 1.

Berdan Irrigation Project areas have fertile agricultural areas between Mediterranean coastal regions and Berdan Dam. Flood prevention and flood control works have been implemented since long years in the region [5]. In this study, different from previous studies, the effect of the 1980 flood event during the construction of the Berdan dam and the flood inundated areas upstream of the cofferdam and the dam body were investigated by using remote sensing technique.

Landsat 3 satellite data were used to detect flood inundated areas, the image of date 01 April 1980 was selected depending on the cloudiness conditions. NDWI index was used for determining flooded areas. The NDWI formula is given in Equation (1) [14]. The NDWI image of the flood inundated areas in the Berdan dam site on 01.04.1980 is given in Figure 2.

$$\mathrm{NDWI} = \frac{\mathrm{Green}-\mathrm{NIR}}{\mathrm{Green}+\mathrm{NIR}} \quad (1)$$

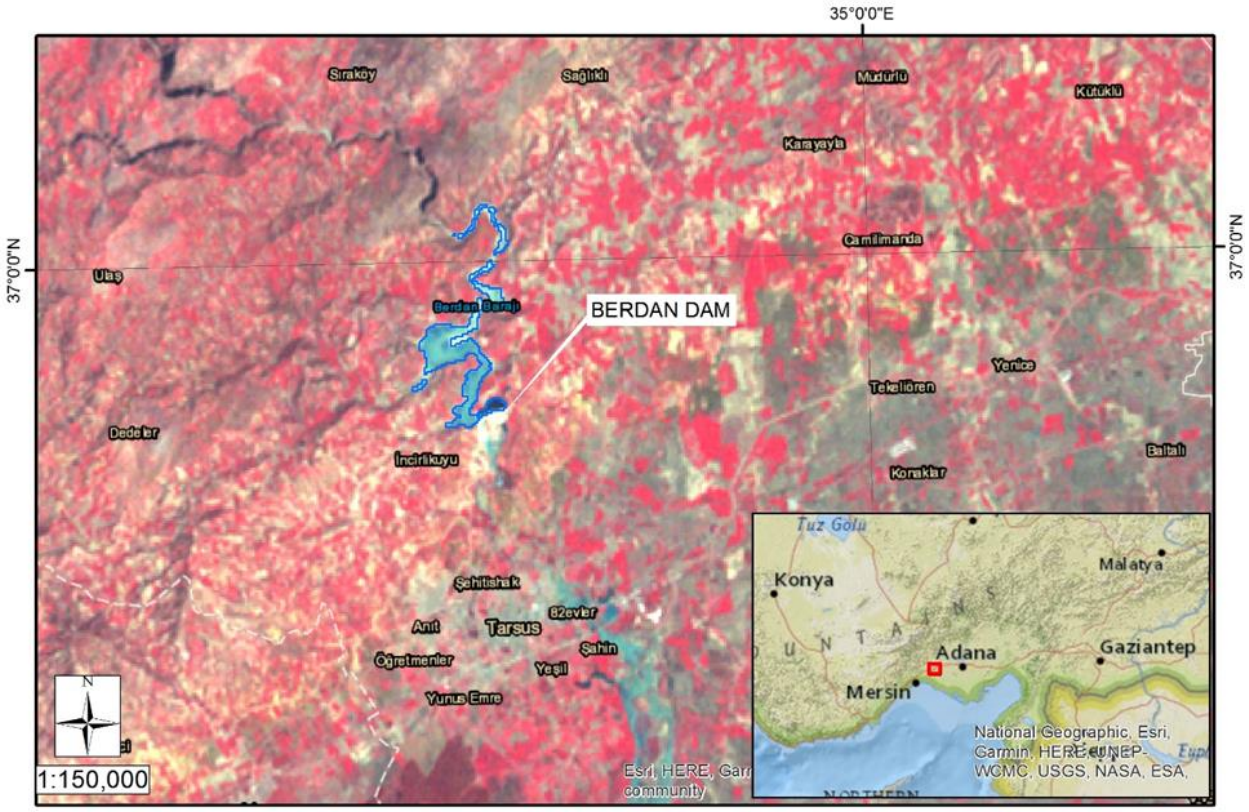

Figure 1: The location of Berdan Dam in Turkey.

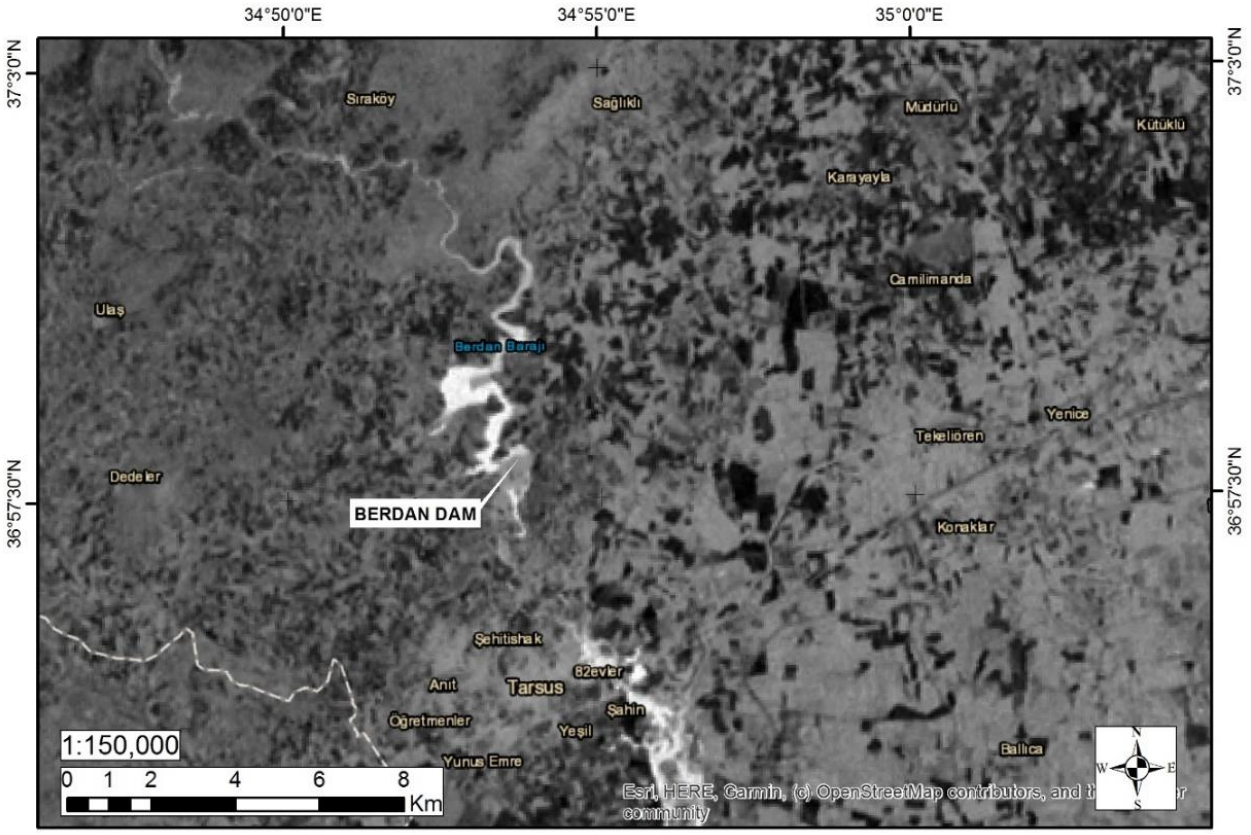

Figure 2: The NDWI image of the flood areas in Berdan dam site on 01.04.1980.

I. Results and Discussion

In this study, the performance of upstream cofferdam in Berdan Dam during 1980 flood was investigated. The 1980 flood extent and the elevations of the flood were investigated by using both the terrestrial measurements before the dam construction and the remote sensing data of 1980. The satellite image of the flood areas in Berdan dam reservoir area on 01.04.1980 is given in Figure 3.

The flood area determined using remote sensing technique and GIS data were analyzed to examine the flood effects on the dam body which was under construction and not completed yet. The flood elevation was calculated using volume-elevation-area data of official reports of General Directorate of State Hydraulic Works (DSİ).

The flood inundated area up to the Berdan dam site in 1980 flood, as given in Figure 2, was analyzed and calculated as 271 hectares by using remote sensing data. The flood elevation and volume corresponding to the flood inundated area of 271 ha, and the flood elevation was estimated to be 40.4 meters and the flood volume to be 14 hm^3 according to area-elevation graph and volume-elevation graph.

In the "Dam Hydraulic Structures Design Guide" published in 2014 by the General Directorate of State Hydraulic Works (DSİ), it is pointed out that it is a general application for diversion facilities in dam projects to design with 25-year flood frequency criteria (with freeboard) and 50-year flood frequency criteria (without freeboard) [15].

The discharge capacity of the Berdan Dam diversion tunnel has been determined according to Q_{25}. The water discharge for Q_{10} is 76.4 hm^3 in 10-year flood hydrograph for the Berdan Dam. It is evaluated that the flood volume of 14 hm^3 was held by the cofferdam and dam structures on the site at the flood event.

In this case, since the construction of Berdan dam structures continued on the flood date of 1980, it is evaluated that the dam structures built up to that date held the flood volume and provided significant benefit to the flood control. The flood event that took place on 01.04.1980 is a regional disaster in the Mediterranean Region with devastating effects on the agricultural areas, the settlements, the environment, and the water structures. Berdan and Aslantaş dams were both under construction on this date (Figure 4).

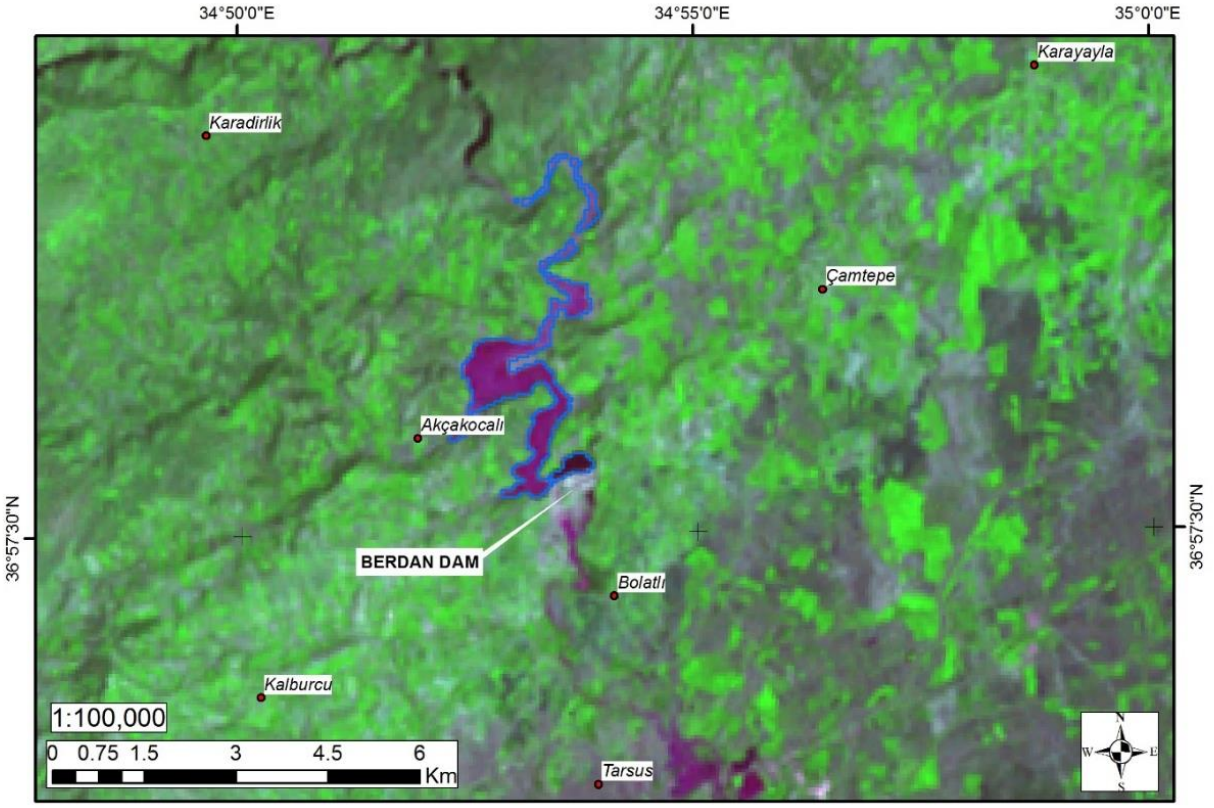

Figure 3: The image of the flood areas in Berdan dam reservoir area on 01.04.1980.

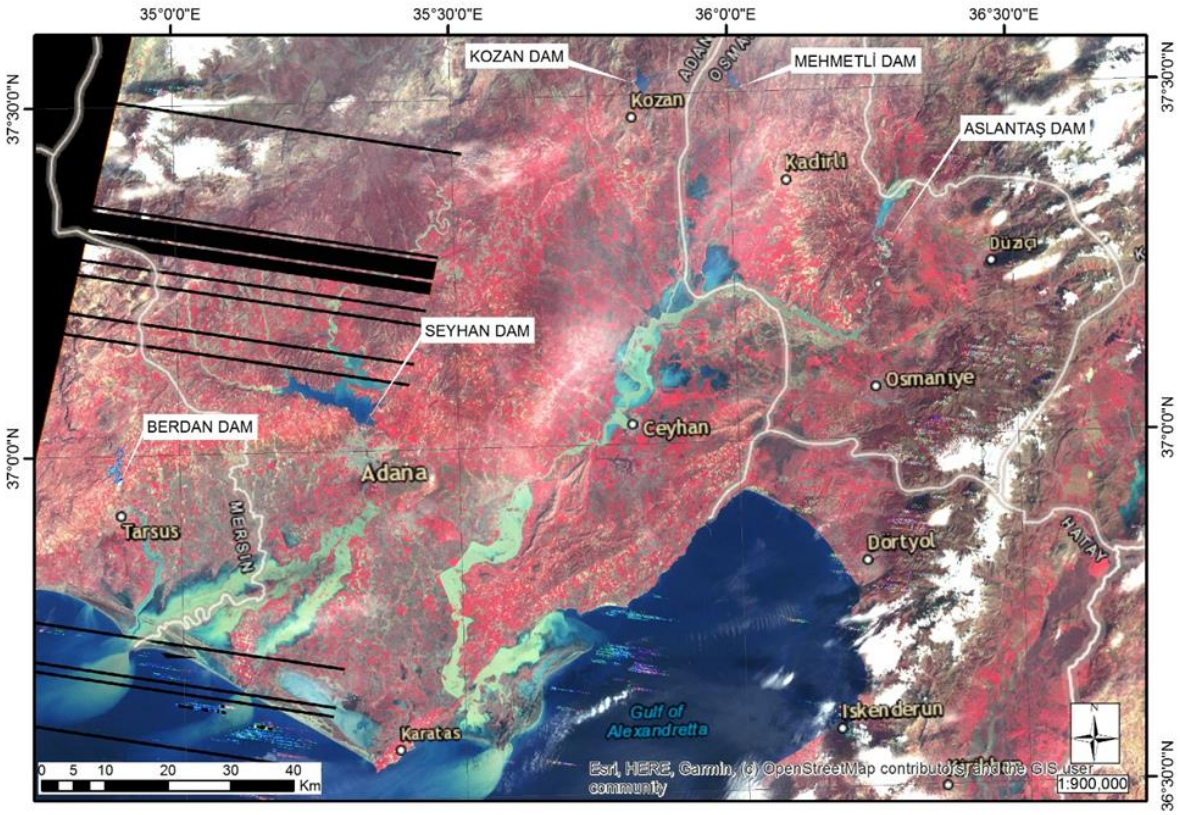

Figure 4: The image of the flood areas in the Mediterranean Region on 01.04.1980.

I. Conclusion

In the project design of the cofferdams, the criteria in the relevant regulations are followed in the selection of the flood flow rate. In this study, the contribution of using remote sensing data in evaluating historical flood effects on Berdan dam construction sites and assessment of performance of upstream cofferdam during flooding was investigated.

As a result, the construction of Berdan Dam structure was continuing on 1980 flood and is it evaluated that the constructed structures of the dam held the flood volume and contributed flood prevention works in downstream areas.

References

[1] Zhang, J., Liu, Z. (2006) Hydrological monitoring and flood management in China, Frontiers in Flood Research, (IAHS Publ. 305, 2006).

[2] Tariq, M.A.U.R., Farooq, R., Van De Giesen, N. (2020) A Critical Review of Flood Risk Management and the Selection of Suitable Measures, Appl. Sci. 2020, 10, 8752; doi:10.3390/app10238752.

[3] Itagaki O, Bermudez DBS, Zemmoto T, Ohara M. (2021) Proposal of a method for assessing combined flood risk reduction effect by hazard control measures and exposure reduction measures based on limited data. J Flood Risk Management. 2021;14:e12714. https://doi.org/10.1111/jfr3.12714.

[4] Caporali, E., Rinaldi, M., Casagli, N. (2005) The Arno River Floods, Giornale di Geologia Applicata 1 (2005) 177 –192, doi: 10.1474/GGA.2005-01.0-18.0018.

[5] Güvel, Ş.P., Akgül, M.A., Aksu, H. (2022). Flood inundation maps using Sentinel-2: a case study in Berdan Plain, Water Supply, Vol 22 No 4, 4098 doi: 10.2166/ws.2022.039.

[6] Spreafico, M. (2006) Flash floods in mountain areas, Climate Variability and Change—Hydrological Impacts (Proceedings of the Fifth FRIEND World Conference held at Havana, Cuba, November 2006), IAHS Publ. 308, 2006.

[7] Van den Honert, R.C., McAneney, J. (2011) The 2011 Brisbane Floods: Causes, Impacts and Implications, Water 2011, 3, 1149-1173; doi:10.3390/w3041149.

[8] Büchele, B., Kreibich, H., Kron, A., Thieken, A., Ihringer, J., Oberle, P., Merz, B., Nestmann, F. (2006) Flood-risk mapping: contributions towards an enhanced assessment of extreme events and associated risks, Nat. Hazards Earth Syst. Sci., 6, 485–503.

[9] Ridolfi, ., Di Francesco, S., Pandolfo, C., Berni, N., Biscarini, C., Manciola, P. (2019) Coping with Extreme Events: Effect of Different Reservoir Operation Strategies on Flood Inundation Maps, Water, 2019, 11, 982; doi:10.3390/w11050982.

[10] Dai, W., Cai, Z. (2021) Predicting coastal urban floods using artificial neural network: The case study of Macau, China, Applied Water Science (2021) 11:161.

[11] Wardahni, N.I., Latief, Y., Machfudiyanto, R.A. (2020) Development of safety plan to improve OHS (occupational health and safety) performance for construction of dam (supporting infrastructure) based on WBS (work breakdown structure), IOP Conf. Series: Earth and Environmental Science 426 (2020) 012017.

[12] Ren, M., He, X., Kan, G., Wang, F., Zhang, H., Li, H., Cao, D., Wang, H., Sun, D., Jiang, X., Wang, G., Zhang, Z. (2017) A Comparison of Flood Control Standards for Reservoir Engineering for Different Countries, Water, 2017, 9, 152; doi:10.3390/w9030152.

[13] Lempérière, F. (2017) Dams and Floods, Engineering, 3, (2017) 144–149.

[14] McFeeters, S., "The use of normalized difference water index (NDWI) in the delineation of open water features.", International Journal of Remote Sensing, Vol. 17, No. 7: 1425-1432, 1996.

[15] DSİ (2014) Dam Hydraulic Structures Design Guide (Baraj Hidrolik Yapılar Tasarım Rehberi), February 2014, Ankara (in Turkish)

Thermal Behavior of Radiator in Passive Liquid Cooling Systems for Spring Season

Gulenay A. KILIC

Yalova University, Yalova/Turkiye, gulenay.kilic@yalova.edu.tr

***Abstract* - Comparing the 2021 electric vehicle (EV) sales in Europe and China, it is seen that there is more demand in Europe relative to population than in China. Although these sales figures show that environmental awareness has increased in the society, an electric vehicle offered to the consumer is produced with the same battery thermal management system (BTMS) in all European countries, regardless of geography and climate conditions. However, the right battery thermal management design should be presented to the consumer according to the geographical location and climatic conditions where the vehicle will be used. Therefore, although these legal regulations constitute the necessary condition, they do not carry the sufficient condition. In this study, it is aimed to prevent catastrophic damage caused by overheating of batteries, which has been mentioned numerous times in the literature. In this experimental study, the thermal responses of the radiator, which is a passive liquid cooling system element, which is one of the BTMS, to different ambient temperature (T_{amb}). changes were investigated. Experiment boundary and acceptance conditions were selected according to the Mediterranean climate spring season. Experiments were made for 2 different cases. The cases are applied for two T_{amb}. Ambient temperatures are 17ºC and 20ºC, heat transfer fluid (HTF) inlet/outlet temperatures are monitored. Experimental results showed that the positive effect of PCM increased the HTF return temperature at T_{amb} 20°C by only 2.2°C within 2 hours.**

***Keywords* - *passive liquid cooling system, battery management system, radiator, electric vehicles*.**

I. INTRODUCTION

In the electric vehicle sales reports in the world in 2021, it is seen that the demand in Europe according to the population is twice as high as in China. In order to ensure high performance and long service life in electric or hybrid vehicles, it is necessary to analyze the battery thermal management system well.

Jouhara et al. (2019) studied the operation and functionality of batteries used in industrial applications [1]. It has been discussed how and why batteries deteriorate and lose efficiency due to improper use. In the obtained data, it is concluded that the development of the battery thermal management system is of vital importance. At the same time, it was stated that the temperature difference between cells should be kept at minimum values. However, different thermal management techniques and configurations have been shown to offer different efficiencies and performances.

Sabbah et al. (2008), active and passive cooling systems were compared with experimental and numerical analysis [2]. Active cooling uses air blown through spaces between cells in the same array (Fig.1) while passive cooling uses a micro-composite matrix surrounding the cell array. It has been stated that active cooling is not a suitable thermal management system to maintain cell temperature under stress with high discharge rates and ambient temperatures (40–45 ◦C) if high fan power is not used. Liquid systems can also be classified as passive systems and active systems. In the passive liquid system, the heat sink used for cooling is a radiator. The radiator is usually located at the front of the vehicle. In passive liquid cooling system, heat transfer liquid, pump is circulated by a closed system [3].

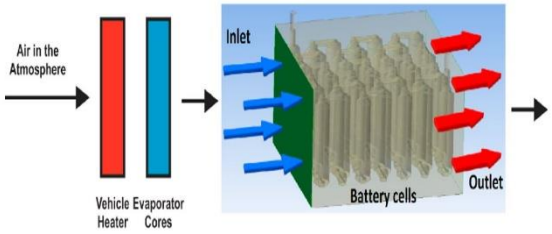

(a)

Figure 1: Active system using air [2]

They focused on the importance of thermochemical energy storage, phase change materials (PCM) to increase the energy efficiency of a system. They classified PCMs as organic, inorganic and eutectic according to their chemical structures and mentioned their advantages and disadvantages. In addition, they mentioned the importance of using a cascade latent heat thermal energy storage system. In addition, automotive applications of PCM materials were presented and the functionality of PCM materials was analyzed. Therefore, using PCM (Fig.2) in a passive liquid-cooled system offers good thermal management performance.

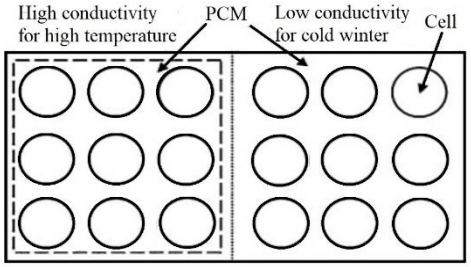

Figure 2: Passive system using PCM in batteries. [2]

For an ideal PCM; long-term thermal performance, small footprint and wide phase change temperature range in the

melting/solidification process should be preferred. During the storage of heat energy, the PCM first acts as an ordinary heat storage material, increasing its temperature as it absorbs the heat. But unlike other materials, when it reaches the phase change temperature, it absorbs much larger amounts of energy without showing a significant temperature change. While the temperature around the material decreases, the material behaves in the opposite direction and releases the latent heat within it to the environment. Such materials can store much more heat per unit mass [3-5].

When the literature is examined, it is observed that the focus is on active and passive cooling for the thermal management system of the batteries. However, it has not been mentioned that the passive liquid cooling system should start at the radiator first. In this study, it is aimed to prevent the catastrophic damage caused by the overheating of the battery, which has been mentioned numerous times in the literature but does not offer a solution. In the study, a new radiator design was made and air was used as HTF, and an alcohol-based fluid was used for PCM. Thus, by using both HTF and PCM, overheating on the battery was prevented and a stable temperature distribution was ensured. By analyzing the data obtained, solution proposals were presented with tables and figures.

II. EXPERIMENTAL FACILITY AND PROCEDURE

A. Geometrical design

In the study, a hexagonal radiator made of aluminum (Al) was designed. Fig. in radiator design. As seen in Figure 3, the heat transfer surface area has been increased with HTF and PCM has been integrated.

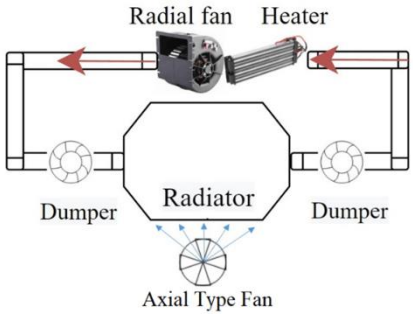

(a)

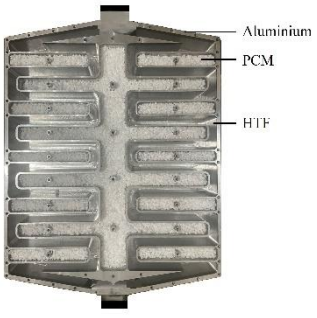

(b)

Figure 3: a) schematic of experiment set up b) inside of radiator.

Radiator dimensions used in the study are 450x355x65 cm, HTF volume is 3.74x10-3 m^3, PCM volume is 4.1158 $x10^{-3}$ m^3. In the experiments, experimental data taken from 10 points including HTF inlet/output temperatures to the radiator, temperature values from 3 different points of the PCM, differential pressure values, HTF velocity in the system, mass flow rate of the HTF, ambient temperature and different wind speeds passed over the radiator were evaluated.

B. Acceptance criterias and boundary conditions

The thermophysical properties of the PCM used for the experiments are presented in Table 1 and the scenario assumptions are presented in Table 2. In the scenarios, assumptions are made by assuming that the Mediterranean climate prevails in the geography where EVs are offered for sale. Thus, transitional season conditions were applied in the climatization of the laboratory. Therefore, the laboratory was set for three different T_{amb} respectively; 17ºC (±0.5), 18ºC (±0.5) and 20ºC (±0.5).

Table 1. Thermophysical properties of PCM.

Properties, Unit	Value
Melting temperature range, °C	22/36
Boiling temperature, °C	260
Latent heat of fusion, kJ/kg	218.40
Specific heat capacity, kJ/kg K	2.407
Density, kg/m^3 (25ºC)	824
Thermal conductivity of solid/liquid (W/m K)	0.2
Dynamic viscosity, kg/m s (25ºC)	10

While changing T_{amb}, a break of 6 hours was given between the experiments in order to remove the thermal loads on the radiator wall. Findings are presented in graphics and tables.

Table 2: Boundary conditions of experimental analysis.

Scenarios	1	2
Ambient air temperature, ±0.5 °C	17°C	20°C
Wind speed velocity	6 m/s	
HTF speed	1.64 m/s	
HTF average volume flow rate	12.8 m^3/h	
Static/total avg. pressure	0.03 mbar	

III. RESULTS AND DISCUSSIONS

Active and passive mechanical cooling applications used in the thermal management system of batteries should be removed during the more effective use of EVs, which limit the charge/discharge times. To solve one of these problems, the liquid volume fraction (β) of the PCM should be around 0.40 at critical operating temperatures [6-8]. In the experimental results, the effect of T_{amb} on HTF inlet/outlet temperatures was investigated by comparing case 1 and case 2. In addition, HTF temperatures were increased in two stages, low and high, by

using a heater. These stages are named A and B. T_{amb} was maintained at 17 °C±0.5 °C for stages A and B in Case 1 (Fig. 4). In Case 2, T_{amb} was kept at 20 °C ±0.5 °C for stages A and B (Fig. 5).

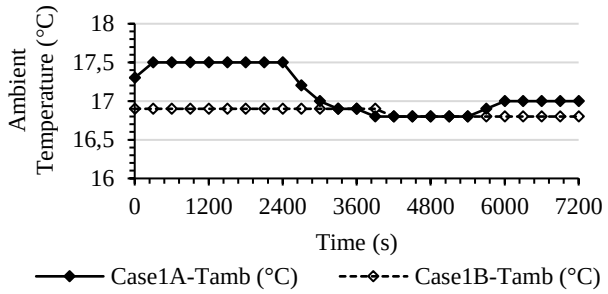

Figure 4: Ambient temperatures of A and B stages in case 1.

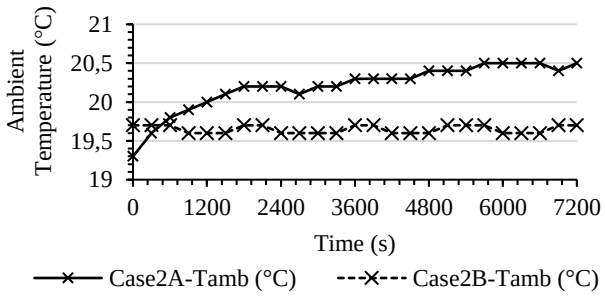

Figure 5: Ambient temperatures of A and B stages in case 2.

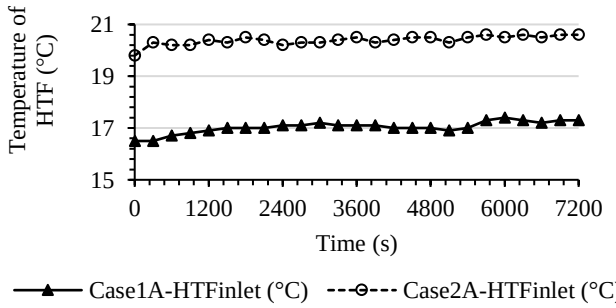

Figure 6: HTFinlet temperature; comparison of time dependent distributions for case 1 and case 2 in stage A.

As seen in Figure 6, the A stages of Case 1 and Case 2 were compared. HTFinlet did not show sudden temperature fluctuations in both scenarios, as the heater was operating at low stage in stage A. This indicates that the PCM is not yet in the phase change region. The time-dependent comparative distribution of HTFoutlet is presented in Figure 7. In this distribution, a behavior similar to the character of the same HTFinlet was observed.

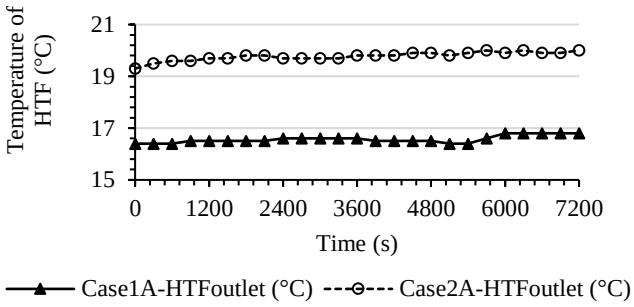

Figure 7: HTFoutlet temperature; comparison of time dependent distributions for case 1 and case 2 in stage A.

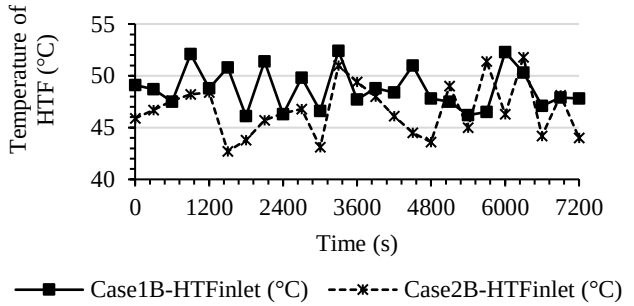

Figure 8: HTFinlet temperature; comparison of time dependent distributions for case 1 and case 2 in stage B.

T_{amb} in Figure 8; At 17°C and 20°C, it was investigated whether the PCM helps cooling when the HTFinlet temperature is increased. Under these conditions, temperature fluctuations were observed in both case 1 and case 2 to switch to PCM melting phase. The time dependent temperature distribution of the HTFoutlet is given in Figure 9. Here, when T_{amb} was at 17°C, the return temperature was stable. In addition, at T_{amb} 20°C, the return temperature increased by only 2.2°C in 2 hours. However, this slight temperature increase followed a slow course.

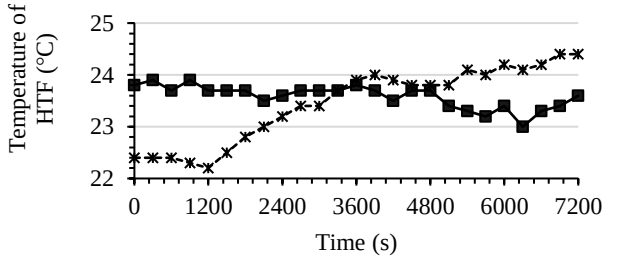

Figure 9: HTFoutlet temperature; comparison of time dependent distributions for case 1 and case 2 in stage B.

IV. CONCLUSIONS

This article presented the inlet and outlet temperature profile of a radiator using PCM for latent heat storage.

The following conclusions were made:

• Thanks to PCM, HTFoutlet was able to maintain a stable temperature while T_{amb} was at 17°C.
• Return temperature increased by only 2.2°C in 2 hours while T_{amb} was at 20°C.
• Thanks to the positive effect of PCM, unstable temperature fluctuations were not observed in the radiator.

Further development and future work on the current topic; it involves connecting the radiator to BTMS with a heat exchanger.

REFERENCES

[1] H. Jouhara, N. Serey, N. Khordehgah, R. Bennett, S. Almahmoud, S.P. Lester, "Investigation, development and experimental analyses of a heat pipe-based battery thermal management system," *International Journal of Thermofluids*, vol. 1–2, 2020.

[2] Z. Rao, S.A. Wang, "A review of power battery thermal energy management," *Renewable and Sustainable Energy Reviews*, vol. 15, pp. 4554-4571, 2011. https://doi.org/10.1016/j.rser.2011.07.096.

[3] R. Sabbah, R. Kizilel, J.R. Selman, S. Al-Hallaj, "Active (air-cooled) vs. sassive (phase change material) thermal management of high power lithium-Ion packs: limitation of temperature rise and uniformity of temperature distribution", *Journal of Power Sources*, vol. 182 (2), pp. 630-638, 2008. https://doi.org/10.1016/j.jpowsour.2008.03.082.

[4] H. Zou, B. Jiang, Q. Wang, C. Tian, and Y. Yan, "Performance analysis of a heat pump air conditioning system coupling with battery cooling for electric vehicles." *Energy Procedia*, vol. 61, pp. 891-894, 2021.

[5] S.A. Khateeb, M.M. Farid, J.R. Selman, S. Al-Hallaj, "Design and simulation of a lithium-ion battery with a phase change material thermal management system for an electric scooter," *Journal of Power Sources* vol. 128, pp. 292–307, 2004. https://doi.org/10.1016/j.jpowsour.2003.09.070.

[6] G.A. Kilic, E. Yalcin, A.A. Aydin, "Optimum operating temperature range of phase change materials used in cold storage applications: A case study," *Environmentally-benign energy solutions, Green Energy and Technology*, pp. 711-726, New York: Springer, 2020. doi: 10.1007/978-3-030-20637-6_35.

[7] A.J. Patel, R.M. Dadhaniya, G.A. Kilic, R. Guduru, "A new approach of li-ion battery thermal management system for electric vehicles", *3rd International Conference on Data Science and Applications 2020*.

[8] G.A. Kilic, E. Yalcin and A.A, "Aydin, Experimental analysis of a cold store integrated with phase change material: a case study", *Bulgarian Chemical Communications*, vol. 48, pp. 195-198, 2016. https://doi.org/10.1016/j.ijft.2019.100004.

Development of a Surrogate Model for Design of a Passive Vibration Isolator Used for an Inertial Measurement Unit

C.VARDALLI[1,2], C.TOLA[1], O.T.SEN[2]

[1] Aselsan Inc, Microelectronics, Guidance & Electro-Optics Sector Division, Turkey
[2] Istanbul Technical University, Department of Mechanical Engineering, Turkey

Abstract **- Inertial measurement units are electronic devices utilized for the measurement of acceleration, angular velocity etc. in various vehicles such as motorcycles, cars, airplanes and missiles. The measurement quality of such devices is quite sensitive to the environmental effects under the operating conditions. One of the most important environmental effect is vibration which could arise due to air friction, turbulence, periodic pressure fluctuations or operating mechanical device within the structure of the vehicle. The passive vibration isolators are commonly used to isolate the inertial measurement units from the unwanted vibrations. Moreover, natural frequency and mode shape of the isolating system is crucial in terms of measurement and isolation efficiency. The chief objective of this study is to construct a surrogate model that will guide design engineers during the geometric design process of a ring type passive vibration isolator used for an inertial measurement unit. Furthermore, the effects of geometric parameter variations, such as changes of gap sizes and angular configurations of the isolator, on natural frequencies of the system are investigated via the response surface method. Finite element models are prepared and parametrized on a commercial FEM solver to determine the natural frequencies of the system. Furthermore, a statistical analysis code is utilized to construct the response surfaces. Consequently, the mathematical relations that can be used during the virtual optimization process of the isolator geometry are determined. Additionally, the geometric parameters that are significantly affecting the mode shapes are determined.**

Keywords - Finite Element Method, IMU Isolator, Response Surface Method, Vibration Isolation

I. INTRODUCTION

PAYLOAD carrying naval and airborne systems such as ships, warplane, and missiles contain inertial measurement units (IMU) to resolve the attitude of the general system by measuring linear acceleration and angular rates. Correct and unbiased measurement of this information is vital in navigation systems and related calculations. However, vibrations engendered via environmental and operating conditions deteriorate the measurement quality and affects the system as a significant noise input. For instance, a missile must endure a wide band random vibration resulting from the turbulent air flow and pressure variations across the route that can significantly disturb the measurement quality. As such, performing engineering calculations with those significantly distorted measurements could lead to biased and misleading results.

Passive vibration isolators are widely used with IMUs to reduce the effects of unwanted vibration on measurements. The structure and configuration of an isolator directly determines the isolation performance of the isolator hence the measurement quality of the IMU. The response surface method is beneficial to design the structure of the isolator so that one can achieve optimal isolation and understand the effect of structural parameters and shapes on the isolation performance of the isolator.

The response surface method is a commonly used statistical regression method in engineering for the investigation of the relationship between inputs and outputs to observe the behavior of a system. Pandya et al. used the response surface method with experimental data to determine vibration response for rolling element bearing [1]. Setubal et al. applied the response surface method to the results of the finite element simulation to predict the external forces and validated the results by performing a modal test and modal assurance criterion value calculation [2]. Huang takes the advantage of response surface method with finite element analysis to optimal *xy* positioning of a platform. [3] Yuvaraju et al. applied this method to estimate the effects of various inputs on the vibration response of a boring bar. [4]

Within the context of this research, the response surface method is used with a commercial finite element solver to understand how the geometric parameters of the isolator structure affect the isolation performance, natural frequency, and mode shapes of the isolation system.

For the ring-shaped passive vibration isolator, the finite element model is constructed in the Abaqus environment and is parametrized by a generated Python script. Additionally, commercial software Minitab is utilized to define the response surface, and the design parameters' boundaries are entered. Finite element analyses are performed and the effect of the geometric parameters of the vibration isolator on the natural frequency of a pre-selected mode shape is obtained. Vibration isolation and parametrization of the structure are explained in the second section, and the finite element modeling strategy is given in the third section of the study. The fourth section explains the response surface methodology and its application within the content of this research, and the concluding remarks are explained in the last section of this work.

II. Transmissibility and Vibration Isolation

A single degree of freedom spring-mass-damper system under harmonic base excitation is shown in Figure 1, where $x(t)$ and $y(t)$ are the time dependent displacement of the mass and the base, respectively.

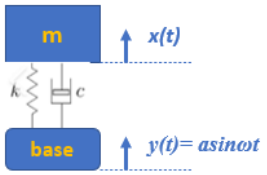

Figure 1: Spring mass damper system

The governing equation of the mass-spring-damper system can be obtained from the free body diagram of the system as shown in Figure 2, and it is given with in (1).

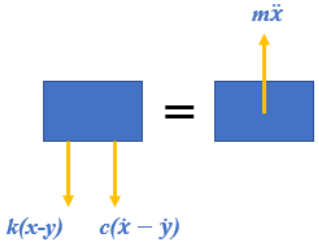

Figure 2: Free body diagram of the spring mass damper system

$$m\ddot{x} + c\dot{x} + kx = ka\sin(\omega t) + ca\omega(\cos\omega t) \qquad (1)$$

where, m, c, k represents mass, damping and stiffness parameters, respectively. Furthermore, the terms x, $\dot{x}$, $\ddot{x}$ correspond to displacement, velocity and acceleration of the mass, respectively. The amplitude of the base excitation is represented with a, t is time coordinate and ω is the excitation frequency.

Transmissibility is a term that explains how input is transmitted to the output, defining the isolation efficiency of a system and the ratio of response to the excitation. A sample transmissibility curve without damping is depicted in Figure 3.

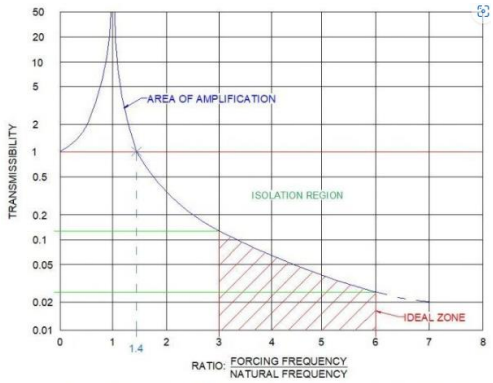

Figure 3: Transmissibility curve of 1-D system [5].

The natural frequency of a system is the most dominant parameter for a passive vibration isolator since it is directly related to the isolation performance. The transmissibility graph given above is divided into 3 regions in the frequency ratio axis. The range between 0 and $\sqrt{2}\omega_n$ *Hz* is called the area of amplification where the natural frequency is denoted by f_a. System operates under the effects of resonance in this region. Moreover, the isolation region starts at $\sqrt{2}\omega_n$ Hz and continues at higher excitation frequencies. Thus, the lower the natural frequency, the larger the isolation region. On the other hand, lowering the natural frequency means having larger transmissibility values in the low-frequency region where the IMU used in missiles usually operates. Therefore, the importance of the natural frequency in an isolation system has a great influence on the isolation efficiency and measurement quality.

Within the scope of this work, an IMU utilized in a missile is considered. Vibrations that affect missiles are in random nature and occur in a wide band frequency spectrum. Similar to the single degree of freedom system example given in Figure 1, the vibration due to environment could be treated as base excitation having wide range frequency spectrum. Moreover, the six degrees of freedom that an IMU operates can be reduced to a single degree of freedom system for the passive vibration isolator. An IMU makes measurements in six degrees of freedom which are linear displacements in the x, y, and z axes and angular displacements about the x, y, and z axes. Each of these six degrees of freedom could be treated as a single degree of freedom system respectively in an isolator design as it is modeled in Figure 1. For each degree of freedom, there is a natural frequency that mode shape of the system dominantly moves in IMU's degree of freedom which is also IMU's measurement axis. Therefore, vibration isolation in six degrees of freedom should be performed by a designed passive vibration isolator. Note that this approach relies on the assumption of weak coupling between all degrees of freedom. In general, the frequency range of the measurements by IMU is limited to 0-50 Hz band for control purposes in missile applications. Thus, the IMU should be isolated from random excitations, which have frequencies above 50 Hz. On the other hand, the natural frequency of the vibration isolator should be high enough such that the measured frequency band should not be amplified by resonance conditions. As a result, optimal natural frequency value which is mainly dictated by the stiffness and mass of the structure should be found for the measurement quality of IMU and isolation efficiency of the vibration isolator.

III. Finite Element Model

A parametric finite element model of the isolator geometry is developed in a commercial software (Abaqus) through a home-written Python script. Details of the parametric finite element model are explained in this section.

A. Isolator Geometry and Parametrization

Ring-shaped vibration isolator as shown in Figure 4 has a fixed inner ($r_i = 40.75\ mm$) and outer radius ($r_o = 49.2\ mm$) due to limited available space in a missile. Furthermore, the depth of the isolator is $14\ mm$. The natural frequency of the vibration isolator will be adjusted by three rows of radially

patterned gaps. Hence, eight parameters are defined which are n_r $(r = 1,2,3 \ldots)$, β, tf_1, tf_2, tf_3, ts_1, ts_2, ts_3. The parameter n_r is the number of three rows of gaps in the radial direction. The parameter β corresponds to the angle between two different rows of gaps (Figure 4). The thicknesses and distance between the three rows of gaps are defined by tf_1, tf_2, tf_3, ts_1, ts_2, and ts_3 and these parameters are depicted in Figure 5. The angle of the gaps, which is denoted by α, depends to β and n_r by (2).

$$\alpha = \frac{360}{n_r} - \beta \qquad (2)$$

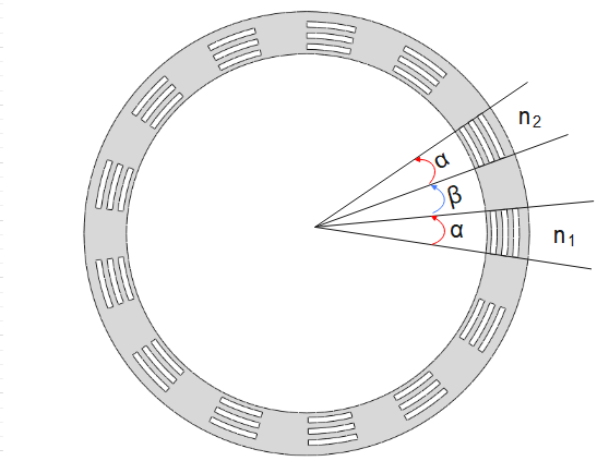

Figure 4: Circumferential parameters of the isolator geometry.

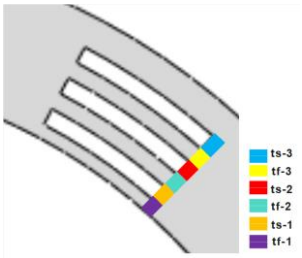

Figure 5: Thickness parameters of the isolator geometry.

B. *Material Properties*

Considering its isolation capability, the isolator geometry will be produced from Thermoplastic Polyurethane (TPU) material. The mechanical properties of the Ultrafuse TPU 85A are tabulated in Table 1.

Table 1: Mechanical properties of Ultrafuse TPU 85A [6].

Young's Modulus	27 *MPa*
Poisson's Ratio	0.495 (assumed)
Density	1082 kg/m^3

C. *Boundary Conditions and Interactions*

The isolator is fixed at its outer surface where it is assumed to be fixed on the missile's almost rigid fuselage. A point mass containing the inertial properties of the IMU is connected to the inner surface of the isolator via kinematic coupling. The boundary conditions and the interactions are illustrated in Figure 6.

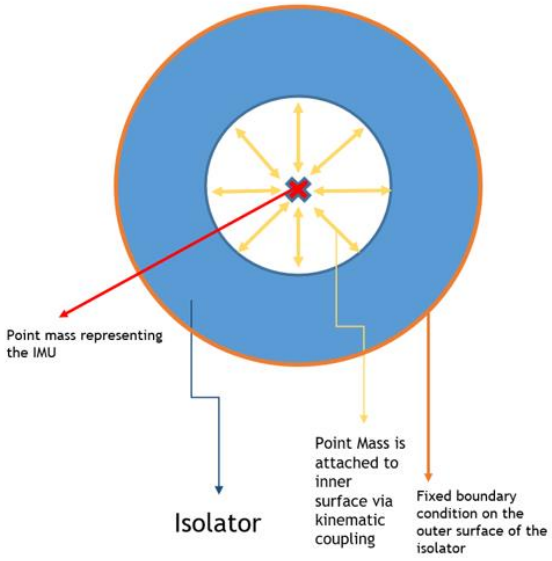

Figure 6: Boundary conditions and interactions.

D. *Mesh Structure*

Linear hexagonal elements having 8 nodes (C3D8R) used for the mesh structure. The average element edge size is taken as 0.5 mm. The mesh structure of a sample isolator design is shown in Figure 7.

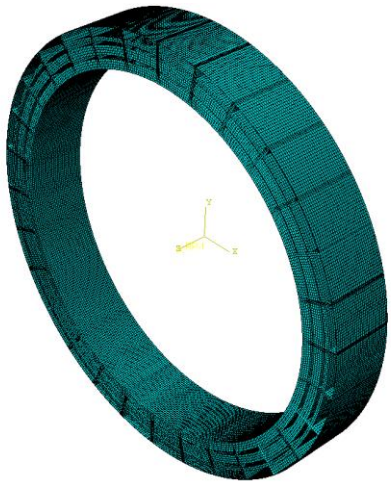

Figure 7: Mesh structure of a sample isolator design

E. *Sample Results*

In this subsection, sample modal analysis results shared to illustrate the mode shapes and corresponding natural frequency values.

The geometric dimensions of the sample design are listed in Table 2, which is modeled and solved using the parametric Python script. Figure 8 illustrates six mode shapes whose motion is in IMU's measurement directions. Mode shapes and corresponding natural frequencies are critical in terms of isolation efficiency as explained before.

Table 2: Geometric parameters used in sample results

n_r	10
β	1 *degree*
tf_1	0.8 *mm*
tf_2	1.3 *mm*
tf_3	0.8 *mm*
ts_1	1.3 *mm*
ts_2	0.8 *mm*
ts_3	1.3 *mm*

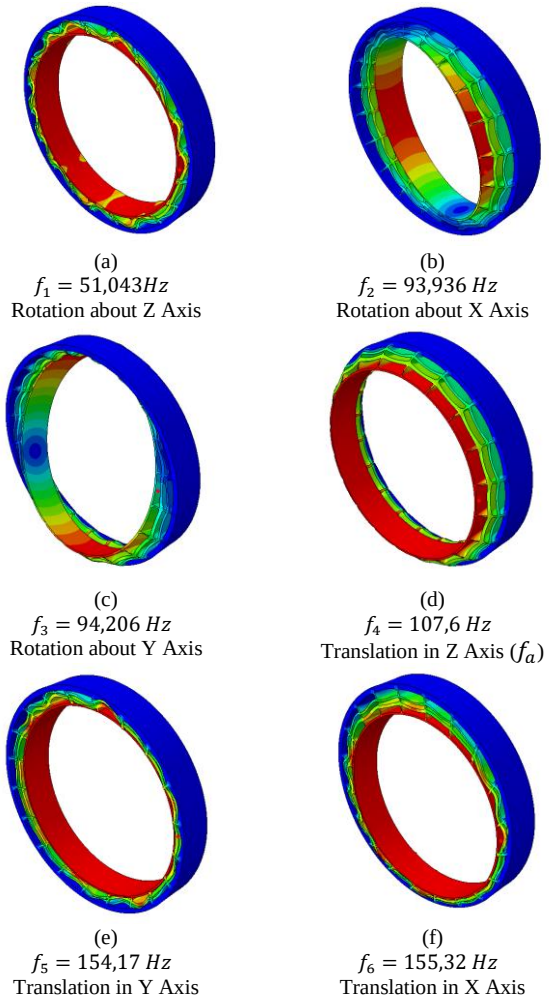

(a) $f_1 = 51{,}043 Hz$ Rotation about Z Axis

(b) $f_2 = 93{,}936\ Hz$ Rotation about X Axis

(c) $f_3 = 94{,}206\ Hz$ Rotation about Y Axis

(d) $f_4 = 107{,}6\ Hz$ Translation in Z Axis (f_a)

(e) $f_5 = 154{,}17\ Hz$ Translation in Y Axis

(f) $f_6 = 155{,}32\ Hz$ Translation in X Axis

Figure 8: Modal analysis results of a sample isolator geometry.

IV. Application and Results of Response Surface Method

Response surface method is a mathematical model that examines the response of certain variables (called response variable) to variation of the design variables.

The aforementioned eight design variables and their variation range of them are introduced into a commercial software (Minitab) to obtain response surfaces. Considering the manufacturability of the product, minimum and maximum values of the parameters are defined and listed in Table 3.

Table 3: Minimum and Maximum Values of Design Parameters

Parameter	Minimum Value	Maximum Value
n_r	10	30
β	1 *degree*	5 *degree*
tf_1	0.8 *mm*	1.3 *mm*
tf_2	0.8 *mm*	1.3 *mm*
tf_3	0.8 *mm*	1.3 *mm*
ts_1	0.8 *mm*	1.3 *mm*
ts_2	0.8 *mm*	1.3 *mm*
ts_3	0.8 *mm*	1.3 *mm*

In order to construct the response surface using face centered model, 145 different designs are prepared and solved via an in-house parametric Python script that is used to parametrize the finite element modeling and the solution process performed in finite elements model. For the scope of this work, the effects of the geometrical parameters on the natural frequency of the Z-axis translational mode shape of the vibration isolator denoted as f_a, which coincides with the forward motion of the missile is considered, and the response surface is constructed via Minitab.

The percent effects of the design variables and their interactions on the response variable (f_a) are also illustrated in a pie chart shown in Figure 9.

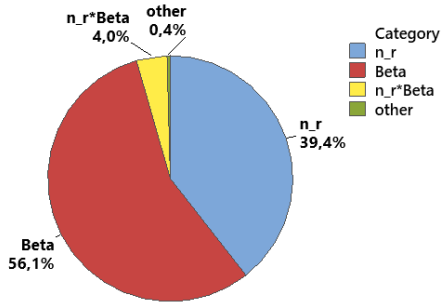

Figure 9: Percentage Effects of Design Variables and Interactions on the Response Variable f_a

As seen in Figure 9, β and n_r has significant effect on the eigenvalue of the Z-axis translation mode shape. Moreover, the product of β and n_r has a contribution of 4% on the value of f_a. Other terms such as ts_1, ts_2, ts_3, tf_1, tf_2, tf_3 and cross products of those have an effect of 0.4%.

To see the change in parameters on the Z-axis translation mode shape of the vibration isolator, 3D response surfaces, and 2D contour plots are obtained and given in Figures 10 and 11, respectively.

The dominant effect of the n_r and β could be understood from Figure 10, whereas a change in thickness parameters in the circumferential direction (ts_1, ts_2, ts_3, tf_1, tf_2 and tf_3) resulted in a relatively small frequency difference on f_a. Similarly, for constant β or n_r values, varying ts_1, ts_2, ts_3, tf_1, tf_2 and tf_3 do not change f_a drastically, which could clearly be seen in Figure 11-b to Figure 11-k.

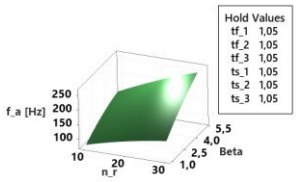

a) Effect of n_r and β on f_a

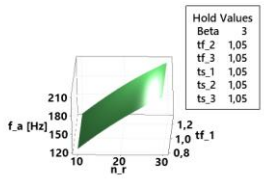

b) Effect of n_r and tf_1 on f_a

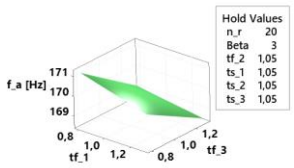

o) Effect of tf_1 and tf_3 on f_a

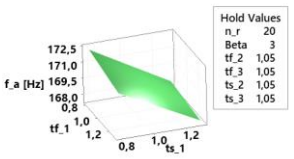

p) Effect of tf_1 and ts_1 on f_a

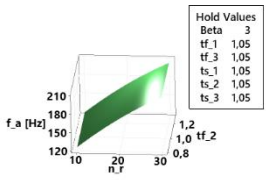

c) Effect of n_r and tf_2 on f_a

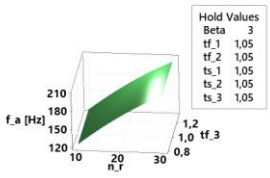

d) Effect of n_r and tf_3 on f_a

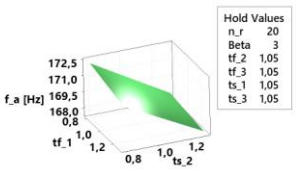

q) Effect of tf_1 and ts_2 on f_a

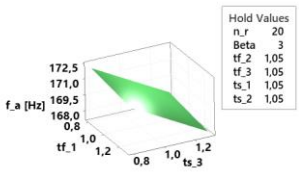

r) Effect of tf_1 and ts_3 on f_a

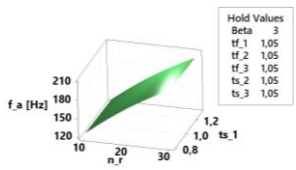

e) Effect of n_r and ts_1 on f_a

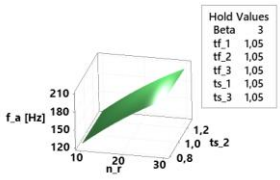

f) Effect of n_r and ts_2 on f_a

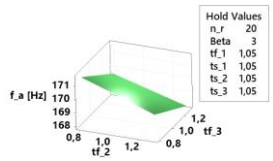

s) Effect of tf_2 and tf_3 on f_a

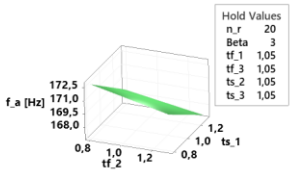

t) Effect of tf_2 and ts_1 on f_a

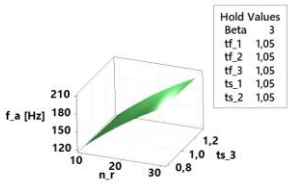

g) Effect of n_r and ts_3 on f_a

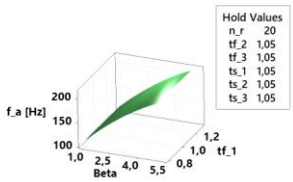

h) Effect of β and tf_1 on f_a

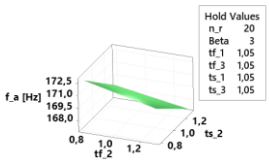

u) Effect of tf_2 and ts_2 on f_a

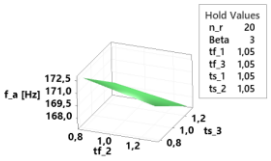

v) Effect of tf_2 and ts_3 on f_a

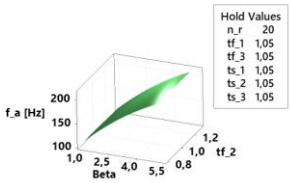

i) Effect of β and tf_2 on f_a

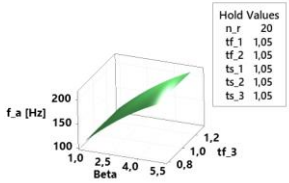

j) Effect of β and tf_3 on f_a

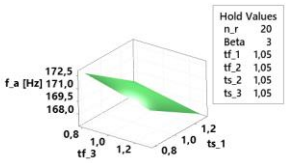

w) Effect of tf_3 and ts_1 on f_a

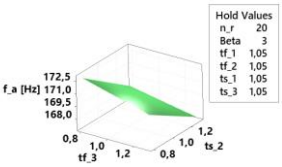

x) Effect of tf_3 and ts_2 on f_a

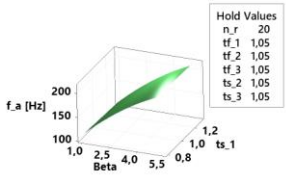

k) Effect of β and ts_1 on f_a

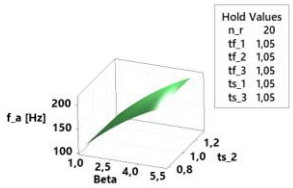

l) Effect of β and ts_2 on f_a

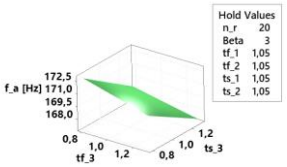

y) Effect of tf_3 and ts_3 on f_a

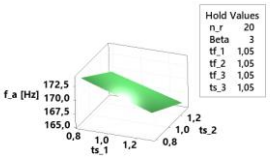

z) Effect of ts_1 and ts_2 on f_a

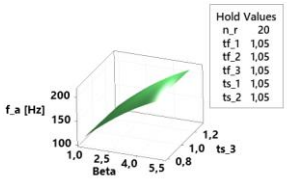

m) Effect of β and ts_3 on f_a

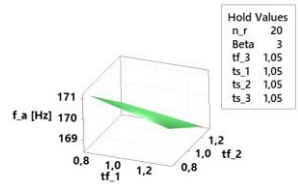

n) Effect of tf_1 and tf_2 on f_a

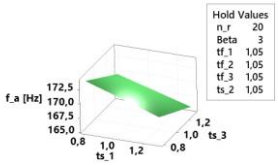

aa) Effect of ts_1 and ts_3 on f_a

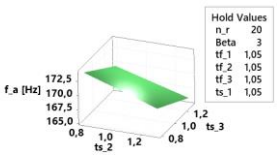

ab) Effect of ts_2 and ts_3 on f_a

Figure 10: Response Surfaces

From another point of view, for constant values of ts_1, ts_2, ts_3, tf_1, tf_2 and tf_3, varying n_r and β influence eigenvalue of the Z-axis translational mode shape in almost linear fashion. On the other hand, Figure 11-a illustrates that keeping n_r constant and changing β or vice versa alters f_a nonlinearly.

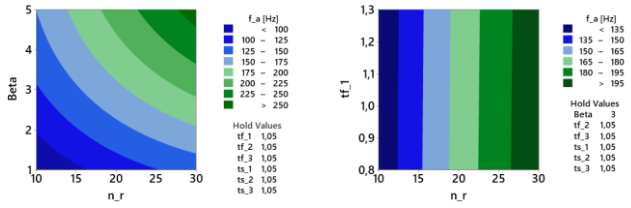

a) Effect of n_r and β on f_a

b) Effect of n_r and tf_1 on f_a

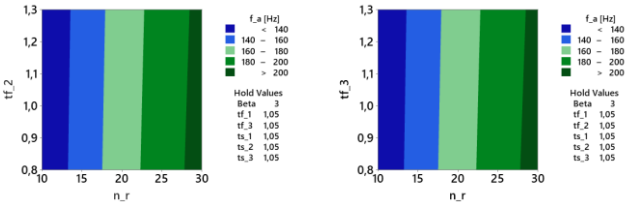

c) Effect of n_r and tf_2 on f_a

d) Effect of n_r and tf_3 on f_a

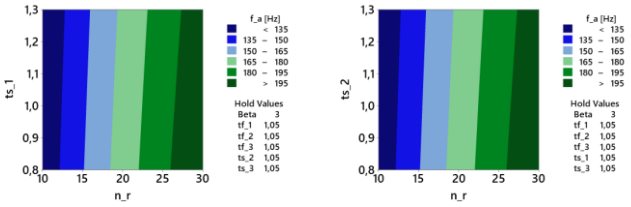

e) Effect of n_r and ts_1 on f_a

f) Effect of n_r and ts_2 on f_a

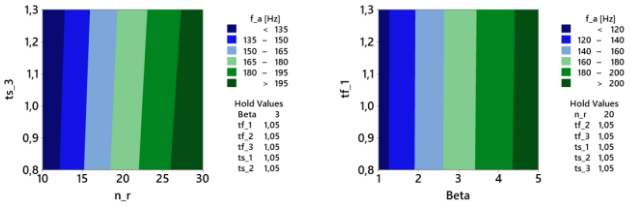

g) Effect of n_r and ts_3 on f_a

h) Effect of β and tf_1 on f_a

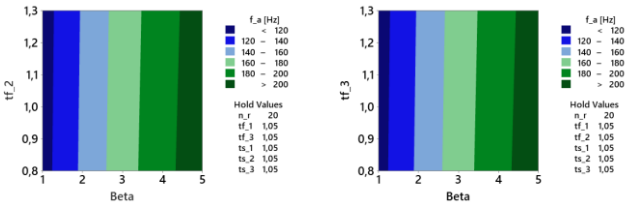

i) Effect of β and tf_2 on f_a

j) Effect of β and tf_3 on f_a

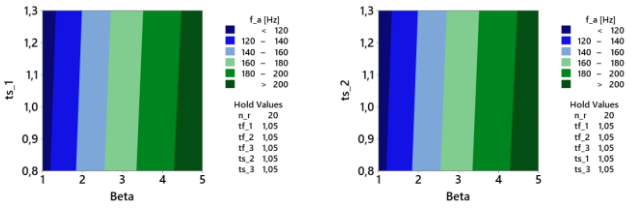

k) Effect of β and ts_1 on f_a

l) Effect of β and ts_2 on f_a

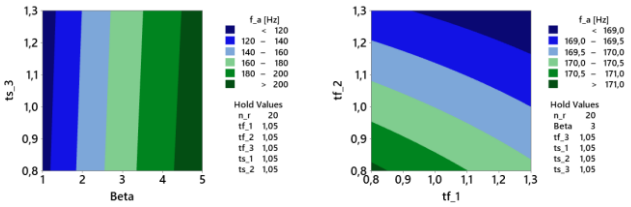

m) Effect of β and ts_3 on f_a

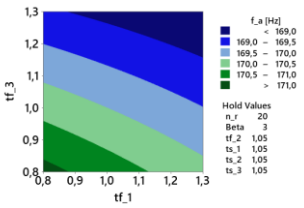

n) Effect of tf_1 and tf_2 on f_a

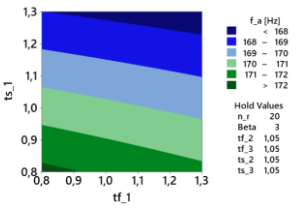

o) Effect of tf_1 and tf_3 on f_a

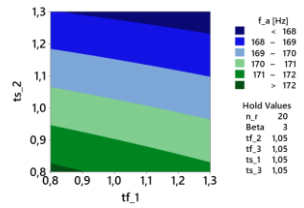

p) Effect of tf_1 and ts_1 on f_a

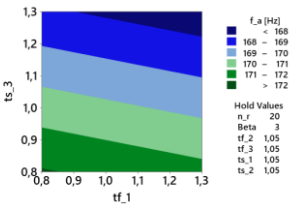

q) Effect of tf_1 and ts_2 on f_a

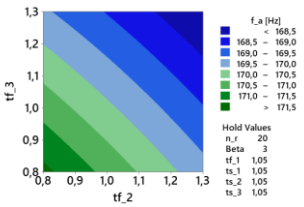

r) Effect of tf_1 and ts_3 on f_a

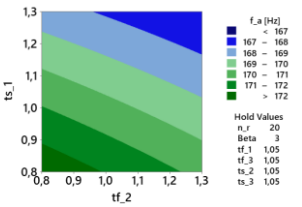

s) Effect of tf_2 and tf_3 on f_a

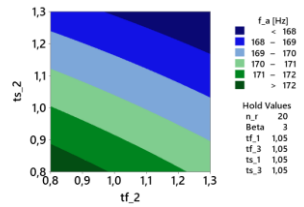

t) Effect of tf_2 and ts_1 on f_a

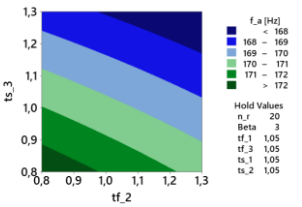

u) Effect of tf_2 and ts_2 on f_a

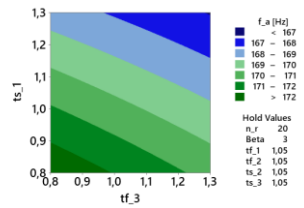

v) Effect of tf_2 and ts_3 on f_a

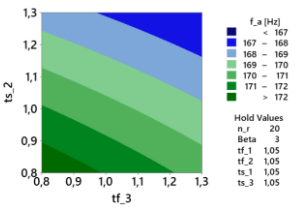

w) Effect of tf_3 and ts_1 on f_a

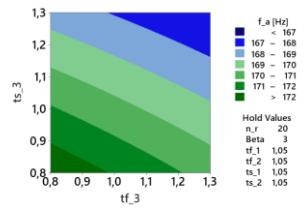

x) Effect of tf_3 and ts_2 on f_a

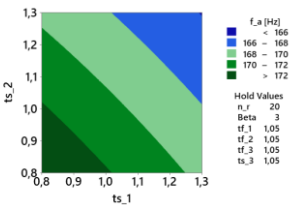

y) Effect of tf_3 and ts_3 on f_a

,

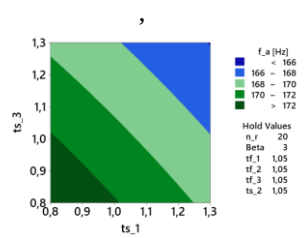

z) Effect of ts_1 and ts_2 on f_a

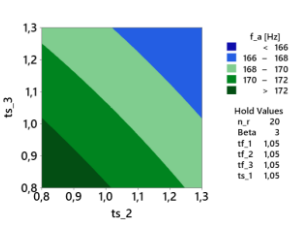

aa) Effect of ts_1 and ts_3 on f_a

ab) Effect of ts_2 and ts_3 on f_a

Figure 11: Contour Plots

Examining Figures 10 and 11, there is a nonlinear relationship among n_r, β, and f_a. This is attributed to the increase of the stiffness of the isolator in Z direction with an increase in n_r and β. Furthermore, the response surface model results show that the thickness parameters of three rows of gaps in circumferential direction has limited influence on this mode shape's eigenvalue as mainly presented in Figures 9, 10 and 11. Though, this parameter may become important if the response variable was selected as X-axis translational mode shape as given in Figure 8, probably due to the significance of these parameters on the stiffness of the isolator in X direction. One can make such inferences easily by taking the advantage of response surface method.

The eigenvalue of Z-axis directional mode shape increases with the increase of n_r, and β. This situation can also be illustrated in the main effects plot shown in Figure 12.

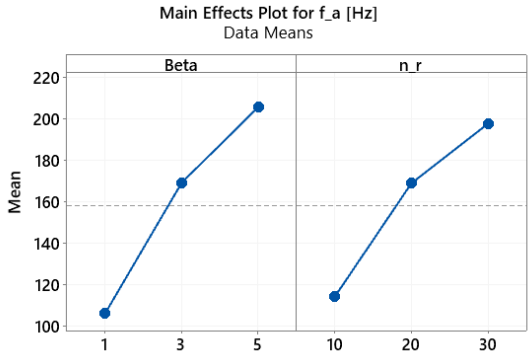

Figure 12: Main Effects Plot

V. CONCLUSION

Engineers should be aware of the effects of the environment on the designing product so that precautions should be taken in the design process. For aerial systems such as a missile, wide band random vibration due to air friction, and pressure fluctuations could be dangerous for using measuring systems like IMUs whose output is directly used by the controller unit. Moreover, passive vibration isolators are used with IMUs to have high quality measurements for navigation of the missile in general application. The natural frequency of the isolator has a significant impact on the IMU's measurement quality so isolator design should be performed properly. The response surface method application on passive vibration isolation is not only limited to the IMU isolator design but also any critical component in a system that is desired to be isolated from vibration such as cameras, gimbals etc.

In this work, a surrogate model for a passive vibration isolator that is commonly used with an IMU utilized on a missile is generated by taking advantage of response surface methodology. In this way, contributions of defined parameters of the vibration isolator geometry on the eigenvalue of the selected mode shape of the isolator are determined. Selected mode shape corresponds to missile's longitudinal direction so the acceleration measurement of the IMU in Z-Axis will be enhanced by passive vibration isolator, where it is resulted that the geometric parameters n_r and β are the most significant parameters in the geometry for the natural frequency of the isolator in the Z-axis according to response surface results since the stiffness of the system in that axis is mostly controlled by those parameters. Changing those parameters would be helpful to match the desired eigenvalue of the isolator for better isolation efficiency and proper transmissibility values for the frequency band that the measurements are made and utilized by the controller of the missile. Thanks to the response surface method, the design engineer could decide the most important parameters that should be focused on in the geometry during the development process. In other words, it helps designers to make decisions much faster and more accurate way.

REFERENCES

[1] A. Misra, D.H. Pandya, S.H. Upadhyay and S.P. Harsha, "*Application of Response Surface Methodology for Determining Vibration Response for Rolling Element Bearing*", 56th Congress of Istam, August 2018.

[2] Setúbal FAdN, Custódio Filho SdS, Soeiro NS, Mesquita ALA and Nunes MVA. *"Force Identification from Vibration Data by Response Surface and Random Forest Regression Algorithms", Energies*. 2022; 15(10):3786. https://doi.org/10.3390/en15103786

[3] Huang, S.-C., and Dao, T.-P. *"Design and computational optimization of a flexure-based XY positioning platform using FEA-based response surface methodology".* In International Journal of Precision Engineering and Manufacturing (Vol. 17, Issue 8, pp. 1035–1048). Springer Science and Business Media LLC. 2016. https://doi.org/10.1007/s12541-016-0126-5.

[4] Yuvaraju, B.A.G. and Nanda, B.K. *"Prediction of Vibration Amplitude and Surface Roughness in Boring Operation by Response Surface Methodology"*, Mater. Today Proc. 2018, 5, 6906–6915. https://doi.org/10.1016/j.matpr.2017.11.352

[5] "Transmissibility Curve of 1-D System" [Online] Available: https://www.mason-uk.co.uk/mechanical-vibration-isolation/transmissibility-graph/

[6] "Ultrafuse Thermoplastic Polyurethane 85A" Material Datasheet. [Online] Available: https://www.ultrafusefff.com/wp-content/uploads/2019/01/Ultrafuse_TPU_85A_TDS_EN_v2.3.pdf [Accessed: 13-Nov-2022].

Structural Analysis for Topology Optimization of a Jet Engine Bracket

A. T. KOÇAK[1] and İ. SARAÇ[1]

[1] Aksaray University, Aksaray/Turkey, timucinalp@gmail.com
[1]Aksaray University, Aksaray/Turkey, isarac2009@gmail.com

***Abstract* - In this study, structural analysis of a bracket used as a fastener in jet engine was performed using ABAQUS software. Required geometry, load conditions and material information were gathered from an online design challenge announced by General Electric in 2013. As requested, Ti-6Al-4V titanium powder material properties were defined for the bracket material. Static analysis has been performed on a bracket with pre-defined load cases and bracket geometry. As a result of the analysis, the load paths inside the jet engine bracket were determined and the bracket was prepared for a topology optimization to minimize mass and maximize rigidity.**

***Keywords* – Additive manufacturing, bracket, structural analysis, TiAl6V4 powder, topology optimization,**

I. INTRODUCTION

Parts that are being used to fix the load carrying parts at the land, sea and air vehicles are called as brackets or fittings. Aircraft brackets are different types of structural components which stands for carrying the manuever loads of the aircraft when flight control surfaces (aileron, flap, elevator etc.) axises are attached and engine structure is mounted.

There exists compression, tension, shear and combined loads at the aircraft brackets. Aircraft brackets are usually manufactured from 7000 series aluminum alloys like 7050-T7451 or 7010-T7651, by forging or NC machining methods. Those aluminum alloys are able to carry heavy loads with their excellent strength values being much lighter than steel. Titanium alloys are extremely expensive but in case of very high strength and light structure is both required at the same time, TiAl6V4 material is preffered for the brackets.

A bracket, manufactured from titanium alloy may be heavy if it's not optimized. Plastics, composites and ceramic materials cannot always be used in those kind of structures because of their properties (being soft, brittle, having low strength etc.). It's important in aviation to design light structures without ignoring the safety. With topology optimization, it's possible to get lighter structures without reducing the strength. Topologically optimized parts cannot usually be produced with conventional manufacturing techniques because of their complex shapes. But with recently used 3d printing methods like SLM (selective laser melting i.e.) help us to maufacture these kind of metal parts.

Additive Manufacturing (e.g., AM, 3D Printing) is a process that involves layer by layer manufacturing. This feature allows manufacturing even complex structural shapes that cannot be produced by conventional manufacturing techniques such as lathe or milling. Because of the lesser cycle dynamic load, lesser mass production demand, unaffected by long production time, AM of an aerospace structure is the best option. Topology optimization leads lesser weight but more complex geometry, which is the best condition for AM.

At optimization time, the loads that are applied to aircraft are cascaded from the outboard to the inboard brackets and so the loading conditions of the bracket is gained. These loads are simulated separately for all load cases. The initial loads are gained from a method called G-FEM (global finite element method) and the detailed part loads are gained from D-FEM.(detail FEM) The loads in the study are taken from a design challenge called ' GE jet engine bracket challenge' of General Electric firm, that hold place at GrabCad designer site [1].

Topology optimization is an efficient way of sizing for the brackets whose loading maps are exactly known. Topology optimization helps to get an ideal geometry by deleting the functionless volume elements that are not carrying load. The data entrance absoluteness and defining the required constraints make the optimization effective. There are lots of analysis software that are used for structural analysis and topology optimization and they have their own data bases for logical and mathematical algorithms (Ansys, TOSCA, Abaqus etc.).

Additive manufacturing is a method develepoed at the end of 80's and had been used for rapid prototyping until the last 10 years. But nowadays it has been a part of series production processes. With the help of this method, the production of polymers, metallic alloys and even metal matrice composites is available [2-5].

In this study, an aircraft engine-bracket, whose loading map is known, has been worked in the concept of topology optimization after structural analysis as the 1st step with Abaqus software, and its manufacturibility with additive manufacturing techniques has been investigated. The result that will be gained from the study is later going to be used for the topology optimization as 2nd step.

II. MATERIAL AND METHOD

Required geometry (Figure 1), load conditions and material information were gathered from an online design challenge

announced by General Electric in 2013. As requested, Ti-6Al-4V titanium alloy was defined for the bracket material and online available material properties were employed [1, 2]. The Arcam Titanium Ti64AlV Grade 5 powder material properties, which has between 45 and 100 microns particle size, were given in the table below.

Figure 1: Bracket geometry.

Table 1: Material properties of Ti-6Al-4V

Parameter	Magnitude	Unit
Young's Modulus	113800	MPa
Poisson's Ratio	0.33	
Yield Stress	903	MPa

For the static analysis, the ABAQUS finite element software was used. Following units were used during the study in the ABAQUS software (Table 2).

Table 2: Employed unit system

Quantity	SI
Length	m
Force	N
Mass	kg
Time	s
Stress	Pa (N/m^2)
Energy	J
Density	kg/m^3

In the case study description, besides the material and geometry, four discrete load conditions that the bracket is encountered were stated. Also, it is declared that the bracket is attached with 4 rigid fasteners to a structure and loads are applied to the rigid pin, which is in contact with the clevis arms of the bracket. In Figure 2, four discrete load conditions are depicted and rigid pin is shown in purple [1].

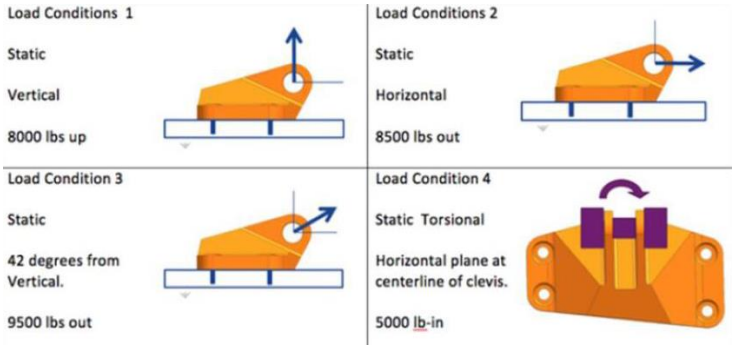

Figure 2: Load conditions.

III. STATIC ANALYSIS

Before performing a topology optimization, static analysis should be done to define the load paths. While preparing the simulation, following parameters have been considered.

To simulate the rigid pin, an analytical or discrete rigid cylindrical surface, which has the same diameter with clevis arms holes, could be created. However, in that case, a contact definition would be required between the bracket clevis arms and the pin. Therefore, this would make the analysis non-linear, increase the computational time and decrease the solution accuracy.

In this study, to simulate the rigid pin, a reference node (i.e., constraint control point) was created right in the middle of the clevis arms of the bracket. Then, depending on the load conditions, a kinematic and continuum distributing coupling constraint were defined between the reference node and the clevis arm hole surfaces. In this method, applied forces or moments on the reference node are distributed onto specified group of node or surfaces as can be seen in Figure 3. Since a typical application of coupling constraints stated as defining a rigid body motion of a group of nodes with a single reference node, aforementioned method were employed in this study [3]. In Figure 4, a typical application of coupling constraints for the twisting motion can be seen.

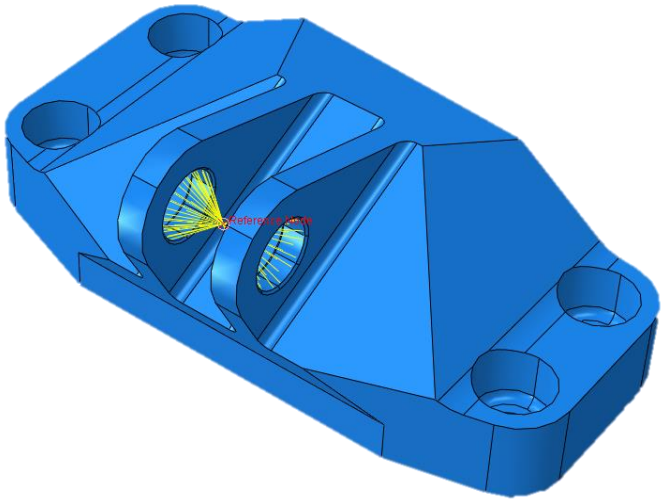

Figure 3: Reference node and coupling constraints.

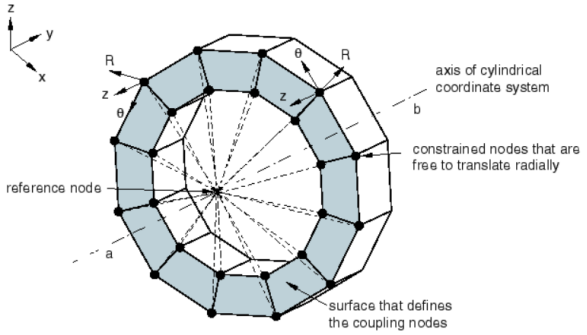

Figure 4: An example of coupling constraint [3].

By employing coupling constraint, since the analysis remained linear, not only the solution accuracy increased, but also the computational time decreased significantly.

After defining a reference node and coupling constraints to simulate rigid pin, given load conditions in Figure 2 were applied to the reference node individually. To simulate given load conditions, four separate static analysis were performed.

It was stated that the bracket was mounted to the structure with 4 rigid fasteners [1]. Therefore, for all load conditions, the all six Degrees Of Freedoms (DOF) of fastener surfaces of the bracket were fixed by encastred boundary conditions as illustrated in Figure 5.

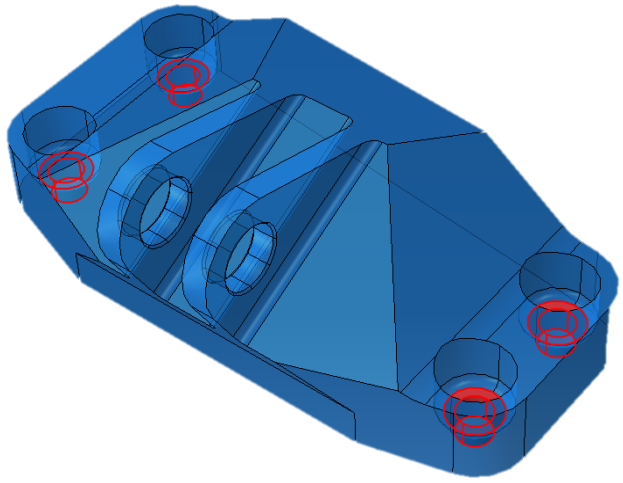

Figure 5: Encastred constraint surfaces

Then, given loads and moment in Figure 2 were applied to the reference node as following. While applying loads and the moment, depending on the load condition, all DOF of the reference node were constrained except for the load or moment direction to make sure that loads or the moment applied through only the given direction. Also, please note that units were converted into SI system.

To simulate given vertical static 8000 lbs. load, 35586 N concentrated force was applied in the positive z-direction for the 1st Load Condition. All DOF of the reference node were constrained except for z-direction. To simulate given horizontal static 8500 lbs. load, 37810 N concentrated force was applied in the negative y-direction for the 2nd Load Condition. All DOF of the reference node were constrained except for y-direction. To simulate given angled static 9500 lbs. load, 31404 N concentrated force was applied in the negative y-direction and 28276 N concentrated force was applied in the positive z-direction for the 3rd Load Condition. All DOF of the reference node were constrained except for y-direction and z-direction. To simulate given static 5000 lbs.in moment, 564924 Nmm concentrated moment was applied in the negative z-direction for the 4th Load Condition. All DOF of the reference node were constrained except for translational and rotational z-direction.

Since the bracket geometry is complex enough, the tetrahedral elements were used instead of the hexahedral elements in this analysis. Although the hexahedral element demands less computational time than the tetrahedral element, it can be used for more simple geometries. Also, although the quadratic geometric order lasts longer, rather than the linear geometric order, quadratic geometric order was preferred, since it is stated in the literature that quadratic geometric order is more convenient than linear geometric order for the topology optimization [4]. Therefore, a C3D10: A 10-node quadratic tetrahedron element type in ABAQUS was employed for the whole analysis cases. The defined finite element mesh is illustrated in

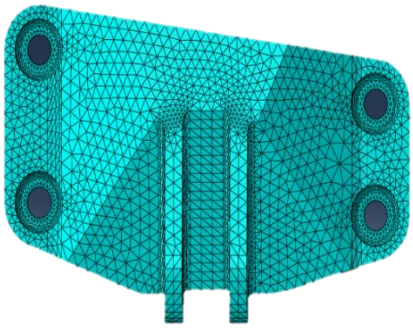

Figure 6: Finite element mesh.

IV. Results and Discussion

All four static analysis results are shown in Figure 7 as Von Mises stress distribution. It can be understood from the results that the majority of the bracket structure remained undeformed for all load conditions and the maximum Von Mises stresses were calculated in the adjacent of either the rigid pin contact surfaces or the four fastener contact surfaces. Therefore, it can be concluded that the case study with the load conditions is very much convenient for topology optimization since the bracket has unnecessary and unused volume and mass for the load conditions.

In an acceptable deviation range

Hata! Başvuru kaynağı bulunamadı., the maximum Von Mises stresses for each load conditions are summarized. The maximum Von Mises stresses are calculated as 700.4 MPa, 533.2 MPa, 463.4 MPa, and; 878.1 MPa for the load condition 1, 2, 3, and 4, respectively. Also, the results were compared with a study in the literature [7] and percentage errors were calculated. Except for the load condition-1, the results are very consistent with an error between 0.3 percent and -8 percent, which is in an acceptable deviation range

Table 3: Maximum Von Mises stresses of both study and error rates

Load Case	Base Study (MPa)	Analysis Result (MPa)	Error (%)
LC-1	628	700.4	-11.53
LC-2	494	533.2	-7.94
LC-3	468	463.4	0.98
LC-4	881	878.1	0.33

In conclusion, since the given yield stress of the material in Table 1 is higher than the whole maximum Von Mises stresses and high local contact stress may not always contribute to the failure of the whole structure [4], analysis results were regarded as convenient and consistent with the literature. Also, the case study is suitable for the topology optimization because most of the bracket was not effected by the applied stresses and moments. This means significant percentage of the bracket material can be removed by topology optimization. To understand the stress distribution better within the bracket, the vectors of maximum principal stresses were illustrated in Figure. As the material removal from the bracket by topology optimization was performed in accordance with load paths, Figure gives an idea about how the final product looks like after optimization

Although the error percentage is more than 10 percent for the load condition-1, this may not be very important because for the both cases, stresses are concentrated in an infinitesimal region, which may decrease the solution accuracy and increase the error rate. Also as another factor, there may be a difference between two cases in terms of contact or coupling constraint definition.

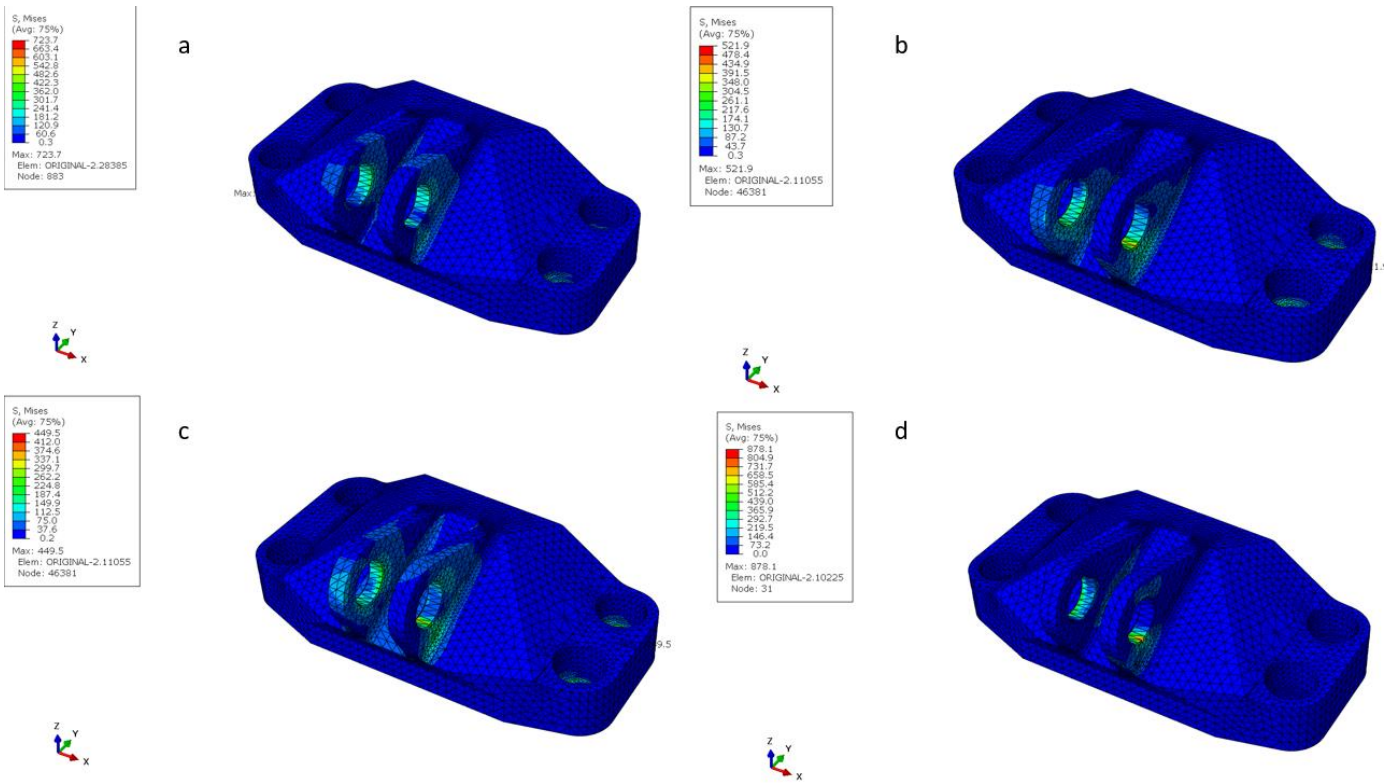

Figure 7: Von Mises stress distribution of (a) LC-1, (b) LC-2, (c) LC-3, (d) LC-4.

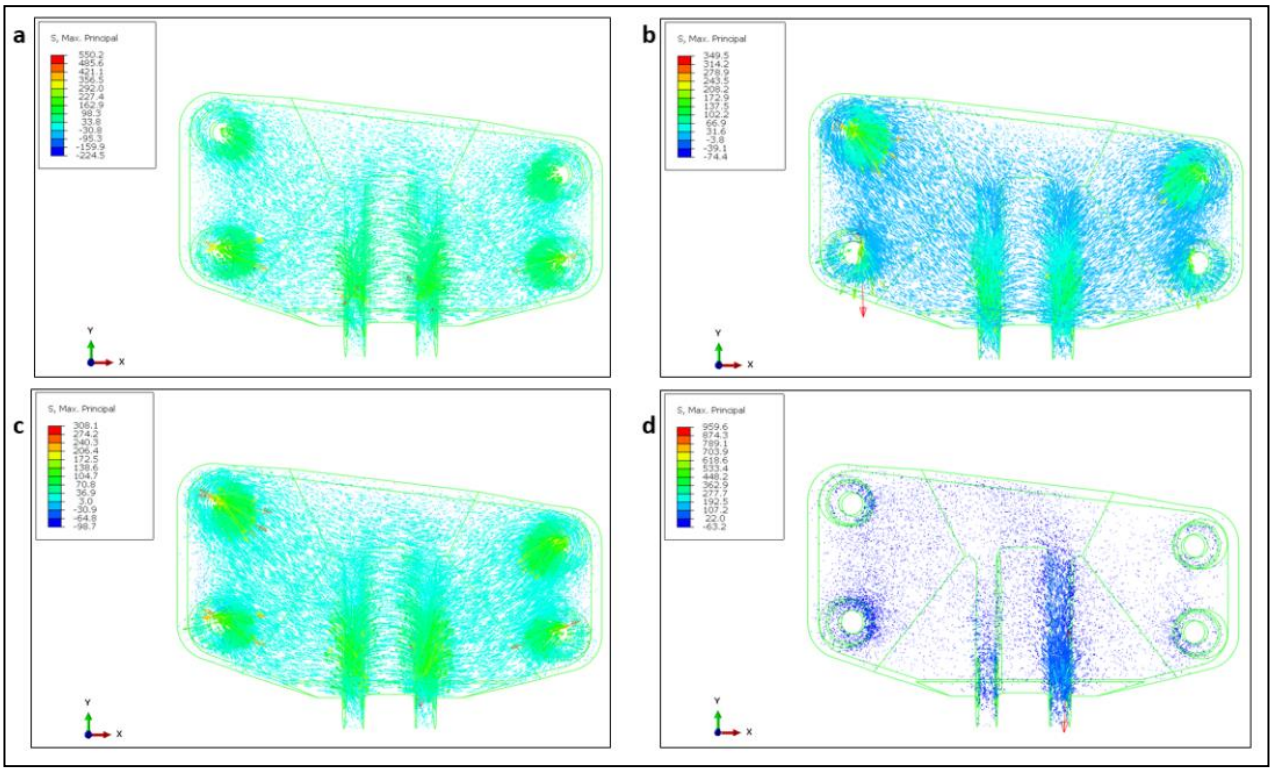

Figure 8: Vectors of maximum principal stresses of (a) LC-1, (b) LC-2, (c) LC-3, (d) LC-4.

I. Conclusion

In this study, structural analysis of a bracket used as a fastener in jet engine was performed using ABAQUS software. Static analysis has been performed on a bracket with pre-defined load cases and bracket geometry. As a result of the analysis, the load paths inside the Jet engine bracket were determined and the bracket was prepared for a topology optimization to minimize mass and maximize rigidity.

As a result of the study, it can be concluded that the case study with load conditions is very suitable for topology optimization, since the bracket has unnecessary and unused volume and mass for the load conditions.

References

[1] Available: https://grabcad.com/challenges/ge-jet-engine-bracket-challenge

[2] M. Attaran, "The rise of 3-D printing: The advantages of additive manufacturing over traditional manufacturing," *Business Horizons*, vol.60, pp. 677–688, (May,2017).

[3] S. Saleh Alghamdi, S. John, N. Roy Choudhury, and N. K. Dutta, "Additive Manufacturing of Polymer Materials: Progress, Promise and Challenges," *Polymers*, vol.13, pp. 753, (February,2021).

[4] R. Brighenti, M.P. Cosma, L. Marsavina, A. Spagnoli and M. Terzano, "Laser-based additively manufactured polymers: a review on processes and mechanical models," *Journal Of Materials Science*, vol. 56, pp. 1–38, (September,2020).

[5] T.T.Wohlers, I. Campbell, O. Diegel, R. Huff, J. Kowen and N. Mostow. (2021). 3D Printing and Additive Manufacturing Global State of the Industry, *Wohlers Associates*.[Online]. Available: https://wohlersassociates.com/product/wohlers-report-2021/

[6] T.T.Wohlers, I. Campbell, O. Diegel, R. Huff, J. Kowen and N. Mostow. (2020). 3D Printing and Additive Manufacturing Global State of the Industry, Wohlers Associates.[Online]. Available: https://wohlersassociates.com/product/wohlers-report-2020/

[7] Available:http://sffsymposium.engr.utexas.edu/sites/default/files/2014-110-Carter.pdf

An Investigation of Hyperspectral Image Fusion Strategies on Real Datasets

V. YILMAZ

Karadeniz Technical University, Trabzon/Turkey, volkanyilmaz.jdz@gmail.com

***Abstract* – Owing to their abilities to discern land cover objects, hyperspectral satellite imageries are used in many remote sensing applications. Despite their high spectral content, hyperspectral imageries suffer from coarse spatial resolution due to some technical sensor limitations, which restricts their use in applications where high spatial detail content is required. Image fusion is a method that is frequently used to improve the spatial structure of hyperspectral images. Such a fusion concept aims to produce spatially enhanced hyperspectral images with the aid of the spatial information of higher spatial resolution imageries. Many image fusion strategies have been introduced for this purpose to date and the developed strategies have been tested mostly on simulated hyperspectral imageries since they provide full reference. The main goal of the current study is to assess the performances of nine widely-used hyperspectral image fusion strategies on real hyperspectral datasets. The evaluated fusion strategies include the maximum a posteriori with stochastic mixing model (MAPSMM), coupled nonnegative matrix factorization (CNMF), Lanaras, guided filter principal component analysis (GFPCA), generalized Laplacian pyramid-based hypersharpening (GLP-HS), hyperspectral super-resolution (HySure), fast fusion based on Sylvester equation with naïve Gaussian prior (FUSE-G), coupled sparse tensor factorization (CSTF) and learning a low tensor-train rank-based method (LTTR). The evaluations showed that the GLP-HS outperformed the others in the study area.**

***Keywords* - image fusion, hyperspectral imagery, image enhancement, digital image processing.**

I. INTRODUCTION

MANY remote sensing satellites are currently orbiting the Earth in order to provide useful information about the land features. Some of these satellites offer coarse resolution-hyperspectral images with considerable object discrimination capabilities, whereas some of them provide higher-resolution multispectral images with less spectral information. Due to the intrinsic limitations of imaging sensors, there is an inverse ratio between the spectral and spatial resolution [1,2]. Hence, it is necessary to select the method that best serves to the purpose of the application. The analysts need hyperspectral imageries with high spatial resolution in many real-world remote sensing applications such as identification of individual trees, monitoring the vegetation health, invasive weed mapping, yield estimation of agricultural products etc. However, the coarse resolution of hyperspectral images limits their use in applications that require high spatial resolution. At this point, image fusion comes to the analysts' rescue by its ability to increase the spatial resolution of hyperspectral images through spatial information obtained from some other higher spatial resolution imageries. The spatial detail content of hyperspectral imageries can be improved through strategies devoted for the fusion of multispectral images. However, these methods are likely to present relatively poor performance due to their incapability of dealing with the high dimensionality of such imageries [3]. In the recent years, many fusion strategies have been developed to enhance the spatial detail quality of hyperspectral images. The hyperspectral image fusion techniques developed to date can be categorized into five classes as component substitution-based techniques, multiresolution analysis-based techniques, spectral unmixing-based techniques, Bayesian-based techniques, and deep learning-based techniques [3]. All these methods have their own merits and drawbacks, which should be considered when selecting the best fusion strategy for the purpose of the application to be conducted.

An important step in hyperspectral image fusion is the investigation of the fidelity of the fusion outcome. The fused data should be assessed properly to understand to what degree the employed fusion algorithm is successful. The quality of fused hyperspectral images can be evaluated visually and quantitatively [4]. The visual evaluation consists in visually comparing the fused data and a reference data, whereas the quantitative evaluation measures the quality of a fused image through some quality indices computed between the fused data and a reference data. Hence, a reference images is needed to investigate the quality of a fused image. However, it may not always be possible to find a reference data, which is why many studies used the original hyperspectral images to simulate a lower-resolution hyperspectral imagery and a higher-resolution multispectral imagery. The simulated images were fused to calculate the fused image, which was then evaluated by using the original hyperspectral image as the reference image [3-7]. The performance of the hyperspectral image fusion methods should also be evaluated on real datasets to have a better idea on how these methods perform. Hence, the aim of this study is to examine the performances of a total of nine hyperspectral image fusion methods on a real dataset. The following section provides further details on the hyperspectral image fusion techniques employed in this study and how their results were evaluated.

II. Material and Methodology

A. Test Site and Dataset Used

The test site was chosen in Rieti, Italy. The hyperspectral and multispectral imageries of the test site were acquired by the Hyperion sensor of the Earth Observing-1 satellite and Sentinel-2 satellite in 2016, respectively. The hyperspectral image consisted of 198 spectral bands at a spatial resolution of 30 m. The Sentinel-2 satellite offers twelve spectral bands, four (i.e., bands 2, 3, 4 and 8) of which have a spatial resolution of 10 m. These four bands were stacked to obtain the multispectral image used for fusion. Both the hyperspectral and multispectral images were downloaded from Google Earth Engine cloud computing platform.

B. Image Fusion

This study investigated the performances of a total of nine hyperspectral image fusion techniques including the maximum a posteriori with stochastic mixing model (MAPSMM) [8], coupled nonnegative matrix factorization (CNMF) [9], Lanaras [10], guided filter principal component analysis (GFPCA) [11], generalized Laplacian pyramid-based hypersharpening (GLP-HS) [12], hyperspectral super-resolution (HySure) [13], fast fusion based on Sylvester equation with naïve Gaussian prior (FUSE-G) [14,15], coupled sparse tensor factorization (CSTF) [16] and learning a low tensor-train rank-based method (LTTR) [17].

The MAPSMM method minimizes a cost function that considers the spectral features of the hyperspectral imagery in the principal component analysis domain [8]. The CNMF strategy improves the spatial quality of hyperspectral imageries using the abundance and endmember information extracted from the hyperspectral and multispectral images via nonnegative matrix factorization [9]. The Lanaras technique also uses the abundance and endmember information that is alternately updated within a gradient-based strategy [10]. The GFPCA strategy uses the first few principal components of the hyperspectral data for guided filtering. The other principal components are used for denoising [11]. The GLP-HS method obtains the spatial features as the difference between the source multispectral data bands and smoothed versions of them. The result is multiplied by a gain factor to compute the spatial features injected into the hyperspectral imagery [12]. The HySure method minimizes an objective function that considers the subspace coefficients derived with the vertex component analysis [13]. The FUSE-G technique employs the Sylvester equation to solve the problem of likelihoods, considering a naïve Gaussian prior [14,15]. The CSTF algorithm uses a core tensor and the dictionaries of three modes to compute the fused image as a third-order tensor [16]. The LTTR method computes the fused image through a LTTR prior obtained by subdividing the source image into equal-sized cubes [17].

C. Quality Evaluation

The qualities of the fused images were assessed qualitatively and quantitatively. The quantitative evaluation was done with quality indices peak signal-to-noise ratio (PSNR) [18], erreur relative globale adimensionnelle de synthèse (ERGAS) [19], spectral angular mapper (SAM) [20] and $Q2^n$ [21].

III. Results

Figure 1 shows the source hyperspectral image and calculated fused images. All images presented in this figure are displayed in 20-15-5 band combination without any contrast stretch.

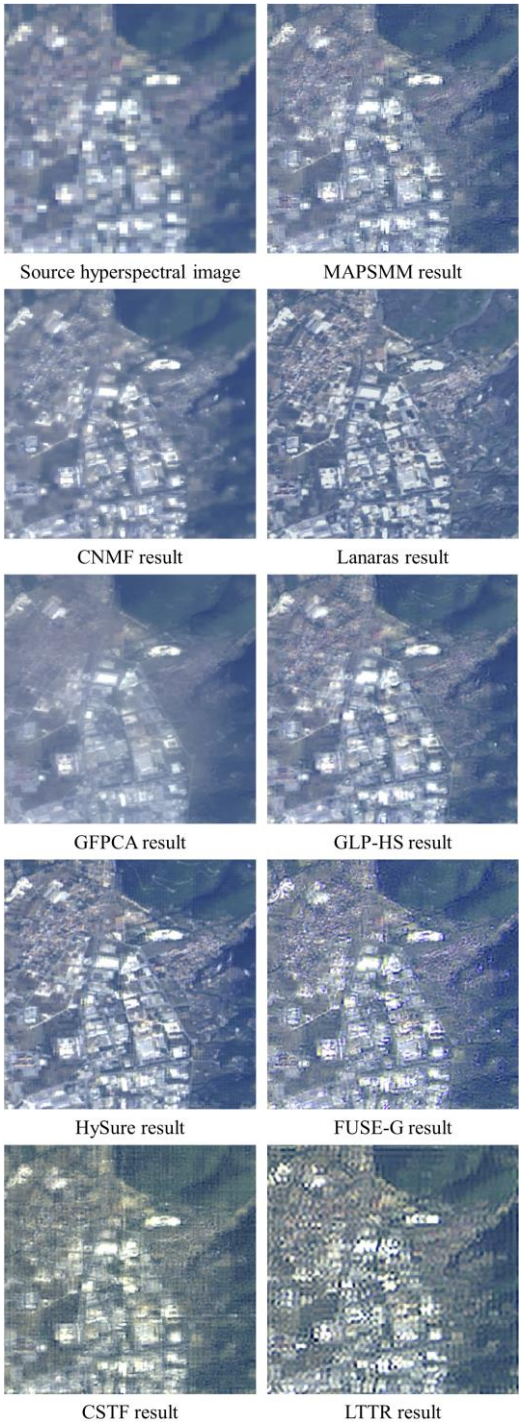

Figure 1: Fusion results.

As seen in Figure 1, all fused imageries except for those generated by the CSTF and LTTR algorithms kept the global radiometric quality to a certain degree. The CSTF and LTTR methods caused severe color distortion on the vegetated areas. The MAPSMM, GLP-HS and CNMF resulted in consistent colors. Another important conclusion drawn from Figure 1 is that all fusion methods caused spatial distortion to some extent, which was expected. The sharpest fused images were produced by the Lanaras and HySure methods. The FUSE-G, CSTF, LTTR and MAPSMM strategies produced images with severe spatial artefacts. The GLP-HS, GFPCA and CNMF methods produced blurry images, which can be seen in Figure 1. Since visual assessment is subjective, it cannot be used for the only evaluation criterion. Hence, quantitative evaluation is also needed for a more impartial quality assessment. Table 1 presents the quality indices calculated from the fused images. In the table, the best value for each index is shown bold and the second-best value for each index is italicized. The poorest index value is also underlined in the table.

Table 1: Quality index values computed from the fused images.

Fusion method	**PSNR**	**SAM**	**ERGAS**	**$Q2^n$**
Optimum value	↑	↓	↓	↑
MAPSMM	**37.0066**	*0.9001*	*3.5466*	**0.8952**
CNMF	23.6309	2.9210	16.6295	0.4539
Lanaras	21.5683	4.0471	17.1415	<u>0.2034</u>
GFPCA	24.1628	3.3366	14.7872	0.4044
GLP-HS	*36.9856*	**0.7603**	**3.0794**	*0.8918*
HySure	23.1162	3.3917	16.3887	0.4724
FUSE-G	29.8047	2.1942	15.8674	0.8091
CSTF	<u>20.2301</u>	<u>9.4510</u>	<u>38.6214</u>	0.2629
LTTR	22.9313	3.8654	24.8170	0.5543

Table 1 shows that the MAPSMM and GLP-HS techniques produced images with the optimum index values. The best PSNR and $Q2^n$ values were obtained by the MAPSMM outcome, whereas the optimum SAM and ERGAS values were achieved by the GLP-HS result. On the other hand, the poorest PSNR, SAM and ERGAS values were obtained by the CSTF algorithm, which justifies the visual findings obtained from the fused image produced by this algorithm. The worst $Q2^n$ value was received by the Lanaras result.

Some inconsistencies were also observed between the findings obtained from qualitative and quantitative evaluation. Despite the fact that the MAPSMM result provided the best PSNR and $Q2^n$ values, its result suffers from serious spatial deterioration. On the other hand, although the Lanaras result seems to have successfully preserved the spectral and spatial quality (see Figure 1), its outcome resulted in poor index values. More examples can be given for such inconsistencies. These inconsistencies arise from the fact that each quality index quantifies the quality with a different strategy and different strategies may, of course, have different merits and drawbacks. So, this study advises to use a number of different quality indices to decide whether or not a fusion technique performs successfully. In this way, factors not taken into account by some quality metrics can be considered by others, providing a more robust quality assessment.

IV. Conclusion

The main goal of this study to compare the performances of some of the most widely-used hyperspectral image fusion methods on real datasets with the hope to inform the interested analysts about how these methods perform on such datasets. To this aim, A Hyperion hyperspectral image and a Sentinel-2 multispectral image was fused with the MAPSMM, CNMF, Lanaras, GFPCA, GLP-HS, HySure, FUSE-G, CSTF AND LTTR methods. The quantitative evaluation revealed that the MAPSMM and GLP-HS methods provided the optimum color and spatial detail quality. However, as can be seen from visual findings, the MAPSMM algorithm caused spatial distortion, which could not be identified by quality indices. Therefore, the GLP-HS technique is recommended for the fusion of hyperspectral and multispectral imageries.

References

[1] C. Serifoglu Yilmaz, V. Yilmaz, O. Gungor, and J. Shan, "Metaheuristic pansharpening based on symbiotic organisms search optimization," *ISPRS J. Photogramm. Remote Sens.*, vol. 158, pp. 167-187, 2019.

[2] C. Serifoglu Yilmaz, V. Yilmaz, and O. Gungor, "A theoretical and practical survey of image fusion methods for multispectral pansharpening," *Inf. Fusion*, vol. 79, pp. 1-43, 2022.

[3] V. Yilmaz, "A comprehensive investigation of image fusion methods for spatial enhancement of hyperspectral images," *Int. J. Remote Sens.*, vol. 43, no. 11, pp. 4151-4186, 2022.

[4] R. Dian, S. Li, B. Sun, and A. Guo, "Recent advances and new guidelines on hyperspectral and multispectral image fusion," *Inf. Fusion*, vol. 69, pp. 40-51, 2021.

[5] X. Tian, W. Zhang, Y. Chen, Z. Wang, and J. Ma, "Hyperfusion: A computational approach for hyperspectral, multispectral, and panchromatic image fusion," *IEEE Trans. Geosci. Remote Sens.*, vol. 60, pp. 1-16, 2021.

[6] Q. Xie, M. Zhou, Q. Zhao, Z. Xu, and D. Meng, "MHF-Net: An interpretable deep network for multispectral and hyperspectral image fusion," *IEEE Trans. Pattern Anal. Mach. Intell.*, vol. 44, no, 3, pp. 1457-1473, 2022.

[7] J. Gao, J. Li, and M. Jiang, "Hyperspectral and Multispectral Image Fusion by Deep Neural Network in a Self-Supervised Manner," *Remote Sens.*, vol. 13, no. 16, pp. 3226, 2021.

[8] M. T. Williams, "Resolution enhancement of hyperspectral imagery using maximum a posteriori estimation with a stochastic mixing model" Ph.D. thesis, University of Dayton, 2004.

[9] N. Yokoya, T. Yairi, and A. Iwasaki, "Coupled nonnegative matrix factorization unmixing for hyperspectral and multispectral data fusion," *IEEE Trans. Geosci. Remote Sens.*, vol. 50, no. 2, pp. 528-537, 2012.

[10] C. Lanaras, E. Baltsavias, and K. Schindler, "Hyperspectral super-resolution by coupled spectral unmixing," in *IEEE International Conference on Computer Vision*, pp. 3586-3594, 2015.

[11] W. Liao, X. Huang, F. Van Coillie, S. Gautama, A. Pižurica, W. Philips, H. Liu, T. Zhu, M. Shimoni, G. Moser, and D. Tuia, "Processing of multiresolution thermal hyperspectral and digital color data: Outcome of the 2014 IEEE GRSS data fusion contest," *IEEE J. Sel. Top. Appl. Earth Obs. Remote Sens.*, vol. 8, no. 6, pp. 2984-2996, 2015.

[12] M. Selva, B. Aiazzi, F. Butera, L. Chiarantini, and S. Baronti, "Hyper-sharpening: A first approach on SIM-GA data," *IEEE J. Sel. Top. Appl. Earth Obs. Remote Sens.*, vol. 8, no. 6, pp. 3008-3024, 2015.

[13] M. Simões, J. Bioucas-Dias, L. B. Almeida, and J. Chanussot, "A convex formulation for hyperspectral image superresolution via subspace-based regularization," *IEEE Trans. Geosci. Remote Sens.*, vol. 53, no. 6, pp. 3373-3388, 2014.

[14] Q. Wei, N. Dobigeon, and J. Y. Tourneret. "Fast Fusion of Multi-Band Images Based on Solving a Sylvester Equation." *IEEE Trans. Image Process.*, vol. 24, no. 11, pp. 4109-4121, 2015.
[15] Q. Wei, N. Dobigeon, and J. Y. Tourneret, "Bayesian Fusion of Multi-Band Images," *IEEE J. Sel. Top. Signal Process.*, vol. 9, no. 6, pp. 1117-1127, 2015.
[16] S. Li, R. Dian, L. Fang, and J. M. Bioucas-Dias, "Fusing hyperspectral and multispectral images via coupled sparse tensor factorization," *IEEE Trans. Image Process.*, vol. 27, no. 8, pp. 4118-4130, 2018.
[17] R. Dian, S. Li, and L. Fang, "Learning a Low Tensor-Train Rank Representation for Hyperspectral Image Super-Resolution," *IEEE Trans. Neural Netw. Learn. Syst.*, vol. 30, no. 9, pp. 2672-2683, 2019.
[18] N. Yokoya, C. Grohnfeldt, and J. Chanussot, "Hyperspectral and Multispectral Data Fusion: A Comparative Review of the Recent Literature," *IEEE Geosci. Remote Sens. Mag.*, vol. 5, no. 2, pp. 29-56, 2017.
[19] L. Wald, "Quality of High Resolution Synthesised Images: Is There a Simple Criterion?" in *3rd conference" Fusion of Earth data: merging point measurements, raster maps and remotely sensed images*, Sophia Antipolis, France, pp. 99-103, 2000.
[20] F. A. Kruse, A. B. Lefkoff, J. W. Boardman, K. B. Heidebrecht, A. T. Shapiro, P. J. Barloon, and A. F. H. Goetz, "The Spectral Image Processing System (Sips)—interactive Visualization and Analysis of Imaging Spectrometer Data," *Remote Sens. Environ.*, vol. 44, no. 2-3, pp. 145-163, 1993.
[21] A. Garzelli, and F. Nencini, "Hypercomplex Quality Assessment of Multi/hyperspectral Images," *IEEE Geosci. Remote Sens. Lett.*, vol. 6, no. 4, pp. 662–665, 2009.

Examination of the Vertical Earthquake Force on a Sample Building with Different Outputs According to TEC 2018

B. S. AKAY[1], A. ÜNAL[1], M. KOÇER[1]

[1] Konya Technical University, Konya/Turkey, selvibusra42@gmail.com
[1] Konya Technical University, Konya/Turkey, aunal@ktun.edu.tr
[1] Konya Technical University, Konya/Turkey, mkocer@ktun.edu.tr

***Abstract*- The concept of vertical spectrum started to be implemented in Turkey with the Turkish Building Earthquake Code 2018 (TEC 2018) regulation. Before this regulation, earthquake analysis was carried out under horizontal loads with only the horizontal spectrum in buildings and it was predicted to stay on the safe side with the axial load limitation made on the columns. In TEC 2018, vertical earthquake analysis is performed depending on the structural defects in the structures. In this study, vertical earthquake analyzes were carried out on building samples with different ratios of cantilever overhangs. During these analyses, the vertical earthquake acceleration assumption made in the earthquake code and the analysis results obtained from the vertical earthquake spectrum were examined. For this purpose, firstly, horizontal earthquake forces under equivalent earthquake force, axial load levels on the columns and sectional effects and displacements on the cantilever supports were obtained on the structures. These results were compared with the data obtained from the vertical spectrum analysis with the response spektrum method, which is the dynamic analysis. The results obtained show that the assumptions made in the equivalent earthquake load method are on the safe side.**

***Keywords*- TEC 2018, equivalent earthquake load, design spectrum, response spektrum method, vertical design spectrum.**

1.INTRODUCTİON

Calculations related to "Earthquake Analysis of Structures", which is one of the most important subjects of civil engineering today, were included in the 1949 Earthquake Code for the first time, albeit very simple, and earthquake calculations became more and more detailed in later codes. The most important difference of the 1968 Earthquake Code from the previous ones is that the earthquake calculation was handled in more detail. In the 1975 Earthquake Code, it is seen that earthquake forces are calculated in much more detail than many parameters. Calculation methods are mentioned in the 1998 and 2007 regulations and these are; Equivalent Earthquake Load has been grouped under three headings as Response Spektrum and Time History Calculation methods, and the application conditions for each calculation method have been determined. Finally, Turkey Building Earthquake Regulation was updated in 2018 and entered into force in 2019 with its publication in the official gazette. In addition, Turkey Earthquake Hazard Map was updated in 2018 by the Disaster and Emergency Management Presidency (AFAD).

Earthquake ground motion affects structures with serious forces both vertically and horizontally. Although there are many studies on the effect of the horizontal effect of the earthquake on the structure, there are limited studies on the vertical effect of the earthquake. The reason for this is that a large factor of safety applied under vertical load in the designed structures is thought to leave the structure on the safe side sufficiently. However, in the 17 August 1999 Kocaeli Earthquake and the 12 November 1999 Düzce earthquake in Turkey, it was observed that the earthquake caused serious damage to the structure caused by direct vertical components that were much heavier than the horizontal effects. In addition, when the earthquakes experienced throughout the world are examined, it is seen that vertical earthquake accelerations were recorded to a large extent in the 1994 Northridge (USA) and 1995 Kobe (Japan) earthquakes.

In general, the vertical component of the earthquake is ignored when dimensioning the building-type structures, since the vertical component of the earthquake is smaller than the horizontal components and the vertical component of the earthquake is effective in the arrangement of the structural system. However, the effect of the vertical component of the earthquake can sometimes be significant in large cantilevered structures and structures where the vertical elements of the structural system are discontinuous. Due to the vertical earthquake effect, dynamic vertical load effects on columns and shear walls, bending effect on beam support regions, second order effects and displacements can cause.

Thanks to the package programs that we use quite widely today, the construction of projects is very fast and practical. By using these possibilities of technology, earthquake resistant structures can be designed, especially in countries such as Turkey, which are in an earthquake zone, taking into account the effects of earthquakes. When analyzes are made on the same structure according to different regulations with real acceleration records, the earthquake forces on the structure and the resulting displacements are different [1,2].

The aim of this study; The aim of this study is to examine the vertical component effect of the earthquake in buildings with different overhang rates in Izmir, Istanbul, Italy, Mexico and California.

With the help of ETABS program, using equivalent earthquake and response spektrum earthquake calculation methods, horizontal and vertical loads acting on the structures were calculated with static and dynamic calculation methods. As a result of the analyses, the effect of the vertical earthquake on the cantilever overhangs and the axial load values of the columns has been examined by comparing the regulatory acceptances with the dynamic effects. In addition, the earthquake calculations of the structures built in different regions were carried out with the regulations in force in the region. Thus, in the results obtained, a comparison was made with regulations such as TEC 2018, EC8-4 and ASCE7-16 in terms of regulation approaches.

2. EFFECT OF VERTICAL GROUND MOVEMENT ACCORDING TO DIFFERENT EARTHQUAKE REGULATIONS

Figure 1 shows the vertical elastic design acceleration spectrum defined for 5% damping. Vertical elastic design spectral accelerations $S_{ae}D(T)$ are defined in terms of gravitational acceleration [g] based on the short period design spectral acceleration coefficient defined for horizontal earthquake ground motion and the natural vibration period. The corner periods T_{AD} and T_{BD} shown in the figure and the T_{LD} transition period (1.1) are calculated by the equations.

$$T_{AD} = T_A / 3$$
$$T_{BD} = T_B / 3$$
$$T_{LD} = T_L / 2 \quad (1.1)$$

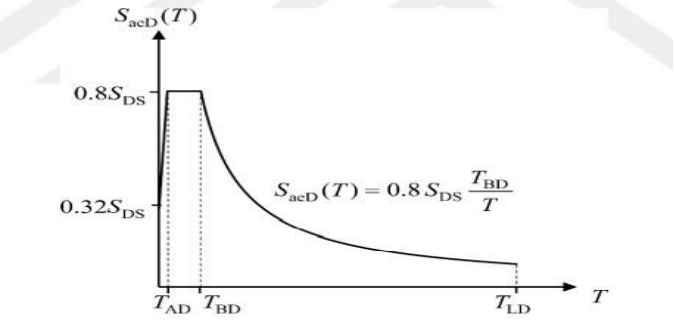

Figure 1: Vertical elastic design acceleration spectrum according to TEC-2018

The equations constituting the vertical elastic design acceleration spectrum curve shown in Figure 1 are obtained by the equations 1.2 to 1.4 below.

$0 \le T \le T_{AD}$ ise $S_{aeD} = [0.32 + 0.48\ T/T_{AD}]\ S_{DS}$ (1.2)

$T_{AD} \le T \le T_{BD}$ ise $S_{aeD} = 0.8\ S_{DS}$ (1.3)

$T_{BD} \le T \le T_{LD}$ ise $S_{aeD} = 0.8\ S_{DS}\ T_{BD}/\ T$ (1.4)

$S_{aeD}(T)$ in the equations represents vertical elastic design spectral accelerations, S_{DS} short period design spectral acceleration coefficient, T natural vibration period, T_{AD} and T_{BD} corner periods, T_{LD} long period.

The short period design spectral acceleration coefficient required to calculate the vertical elastic design spectral accelerations is obtained by multiplying the map spectral acceleration coefficient S_S and the local ground effect coefficient F_s for the short period region.

$$S_{DS} = S_S\ F_S \quad (1.5)$$

Local soil impact coefficient Fs values are given in Table 1 depending on local soil classes.

Table 1: Short period region ground effect coefficients (TEC, 2018)

Local ground class	Local Ground Effect Coefficient for Short Period Region (Fs)					
ZA	0,80	0,80	0,80	0,80	0,80	0,80
ZB	0,90	0,90	0,90	0,90	0,90	0,90
ZC	1,30	1,30	1,20	1,20	1,20	1,20
ZD	1,60	1,40	1,20	1,10	1,00	1,00
ZE	2,40	1,70	1,30	1,10	0,90	0,80
ZF	Site-specific ground behavior analysis will be performed.					

Except for the special conditions specified in the regulation, Ed(z), which is defined as the vertical earthquake effect, will be made approximately as shown below without making any special calculations.

$$Ed(z) \approx (2/3)\ S_{DS}\ G \quad (1.6)$$

The S_{DS} value here is taken from the Turkey Earthquake hazards map from AFAD. In Eurocode 8, the formation of the elastic spectrum of the vertical earthquake component is done with the help of the following equations.

$0 \le T \le T_B$ ise $S_{ve}(T) = a_{vg}\ [1 + T/\ T_B\ (\eta\ 3.0 - 1)]$ (1.7)

$T_B \le T \le T_C$ ise $S_{ve}(T) = 3.0\ a_{vg}\ \eta$ (1.8)

$T_C \le T \le T_D$ ise $S_{ve}(T) = 3.0\ a_{vg}\ \eta\ [T_C/T]$ (1.9)

$T_D \le T \le 4s$ ise $S_{ve}(T) = 3.0\ a_{vg}\ \eta\ [T_C T_D/\ T^2]$ (1.10)

Table 2: Recommended parameter values describing the vertical elastic response spectra according to EC8

Spektrum	a_{vg}/a_g	T_B(s)	T_C(s)	T_D(s)
Type 1	0,90	0,05	0,15	1,00
Type 2	0,45	0,05	0,15	1,00

Recommended spectrum types are: Type 1 and Type 2. In our study, type 1 was chosen because the earthquake magnitudes were greater than 5.5 (Table 2). Since the period value is in the range of 1-4 s, the $S_{ve}(T)$ value, which was substituted in equation 1.10, was calculated (a_{vg}=0.3, taken from the Etabs program). The $S_{ve}(T)$ value found was multiplied by the dead load and the vertical load was applied to the structure.

In the regulations before ASCE 7-16, 2/3 of the size of the horizontal component was assumed in the calculation of the vertical component. However, as a result of studies conducted in recent years, it has been seen that this simple approach used in calculation is not valid in many conditions [3,4]. The main reasons for these are that the vertical ground component has a greater effect than the horizontal ground component in the short period region (in the high frequency range), and this effect increases as the ground deteriorates and the vertical ground motion spreads faster than the horizontal ground component, and the difference increases as the distance to the earthquake decreases.

In addition to the horizontal response spectrum, the vertical response spectrum is also created in ASCE 7-16.

$0 \le T_v \le 0.025s$ ise $S_{aMv} = 0.3\ C_v\ S_{MS}$ (1.11)

$0.025s \le T_v \le 0.05s$ ise

$S_{aMv} = 0.3\ C_v\ S_{MS}(T_v - 0.025) + 0.3\ C_v\ S_{MS}$ (1.12)

$0.05s \le T_v \le 0.15s$ ise $S_{aMv} = 0.8\ C_v\ S_{MS}$ (1.13)

$0.15s \leq T_v \leq 2.0s$ ise

$S_{aMv} = 0.8\ C_v\ S_{MS}\ (0.15/\ T_v\ )^{0.75}$ (1.14)

The coefficient depending on the short period value in the equations, Cv, is shown in Table 3, the value S_{MS} denotes the short period spectral response acceleration value and T_V the vertical vibration period.

Table 3: Vertical coefficient value Cv (ASCE 7-16)

Short Period Region MCER Value	Ground Class A, B	Ground Class C	Ground Class D, E, F
$S_s \geq 2.0$	0,90	1,30	1,50
$S_s = 1.0$	0,90	1,10	1,30
$S_s = 0.6$	0,90	1,00	1,10
$S_s = 0.3$	0,80	0,80	0,90
$S_s \leq 0.2$	0,70	0,70	0,70

When calculating Sav, which is defined as the vertical design response spectrum in ASCE 7-16; The vertical response spectral acceleration S_aM_v is formed by dividing it by 2/3 of its value. The generated earthquake spectrum is shown in Figure 2.

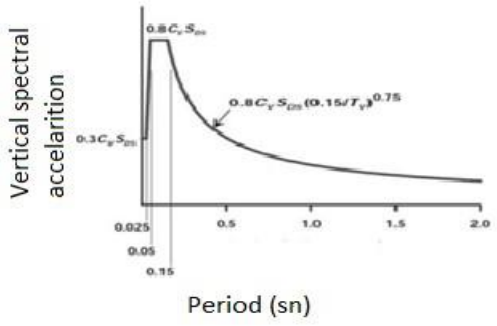

Figure 2: Vertical spectral acceleration spectrum (ASCE 7 - 16).

While calculating the earthquake effect in ASCE 7-16 earthquake code, the vertical earthquake effect is calculated approximately with the equations given below.

$$E_v = 0.2\ S_{DS}\ D \quad (1.30)$$

In the study, as the vertical earthquake load, the Sds value was taken from the OSHPD earthquake hazard map and replaced in equation 1.30, and the vertical load was effected in the Etabs program.

When determining Building Structural System Behavior Coefficient, Excess Strength Coefficient and Building Height class, BYS=5 as our building has a total height of 24 m according to DTS=1 determined for Istanbul and Izmir, according to TEC-2018. Since all of the earthquake effects in our building are covered by reinforced concrete frames, the Structural system behavior coefficient is R=8, and the Excess Strength Coefficient is D=3.

The values of the response coefficient q used for earthquake load reduction in EC8-4 are calculated as in equation 1.31.

$q = q_o\ k_w \geq 1.5$ (1.31)

Since we chose a structure with frame system with high ductility, 4.5 αu/α1 ratio was obtained from the table in the figure, and αu/α1 ratio was 1.3 for multi-storey multi-span frames and frame equivalent binary systems, and q=5.85 was obtained. (kw=1 is taken.)

Since our model is a moment-transmitting framed system in ASCE7-16, the R response coefficient is 8, omega 3, Cd 5.5.

3.ANALYTICAL STUDY

In this study, the same type of housing structure was designed as a reinforced concrete frame system with different protrusion rates (1-3-5 m) (Figure 3 and Figure 4), in Istanbul, Izmir, Italy, Mexico, California, taking into account the vertical component of the earthquake. According to the earthquake regulations of each country, the effect of the vertical earthquake effect on the behavior of the cantilever and overhangs was investigated by using the Etabs V-20 program and analyzing with the equivalent and response spektrum method. The results were also examined according to the TEC 2018, EUROCODE8-2004, ASCE7-16 Earthquake Regulations. In order to better detect the vertical effect, a regular 8-storey structure with no irregularities and symmetrical from both directions was preferred. In the comparisons, the residential building designed in Istanbul, Izmir, Italy, Mexico and California was compared in the ZA floor class. The structural features are given in Table 4.

Dead and live loads on the floor are taken as g=2 kN/m2 and q= 2.0 kN/m2, respectively, to be constant at each floor. In addition, Wall (wall load) (13 cm brick): 6.25 kN/m, on the top floor of the building, Snow (snow load): 1 kN/m2 was also effected.

Table 4: Structure Properties

NO	Building Features	1 m coving	3 m coving	5 m coving
1	Number of floors	8	8	8
2	Plan dimensions	22m*22m	26m*26m	30m*30m
3	Slab Thickness	12cm	12cm	12cm
4	Beam dimensions	30cm * 50cm	30cm * 50cm	30cm * 50cm
5	Column dimensions	40cm * 50cm	40cm * 40cm	40cm * 40cm
6	Concrete and steel grade	30MPa/ B420C	30MPa/ B420C	30MPa/ B420C
7	Floor loads	Cladding + parget 0,2 t/m^2,	Cladding + parget 0,2 t/m^2,	Cladding + parget 0,2 t/m^2,
8	Floor loads	Live load 0,2 t/m^2	Live load 0,2 t/m^2	Live load 0,2 t/m^3
9	Wall load	0,625 t/m^2	0,625 t/m2	0,625 t/m3
10	Building importance coefficient	1	1	1
11	Ground class	ZA	ZA	ZA
12	Building behavior coefficient	8	8	8
13	Floor height	3 m	3 m	3 m

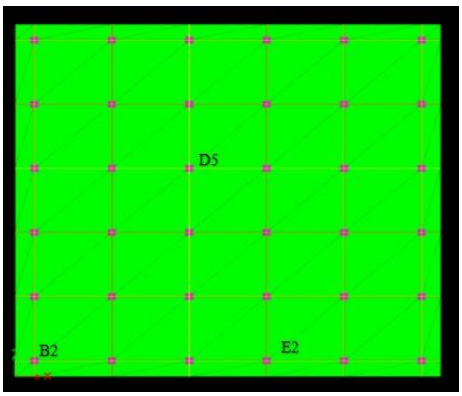

Figure 3: Plan of the building for 1 m

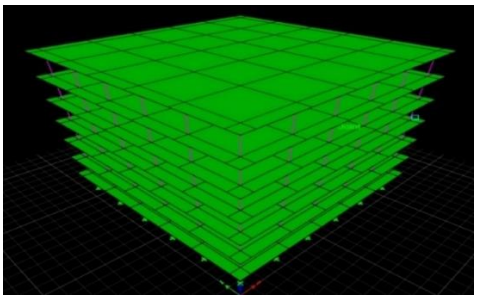

Figure 4: 3D view of the structure for 1 m

4. CONCLUSIONS AND RECOMMENDATIONS

Analysis results were examined in terms of comparison of dynamic and static vertical loads, column axial load comparison and beam section effects.

In Figure 5-6-7-8-9-10, the vertical earthquake effect results of buildings with 1m, 3m and 5m elevations are shown dynamically and statically.

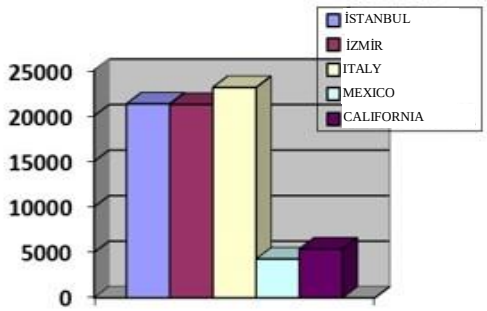

Figure 5: Ez vertical earthquake effect for 1 m overhang (Kn)

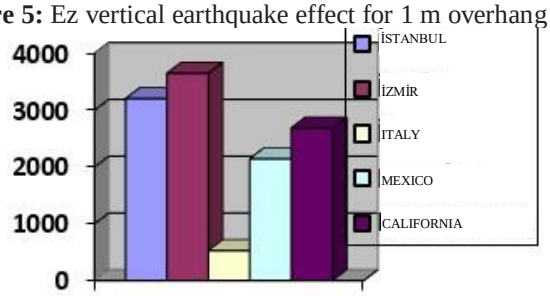

Figure 6: SPECZ vertical seismic effect for 1 m overhang (kN)

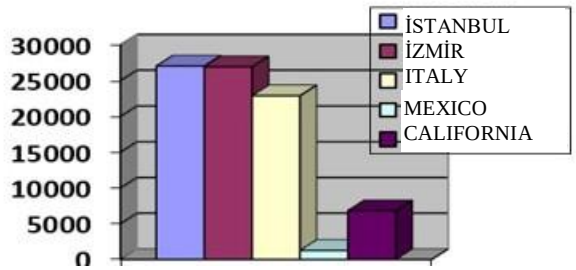

Figure 7: Ez vertical earthquake effect for 3 m overhang(kN)

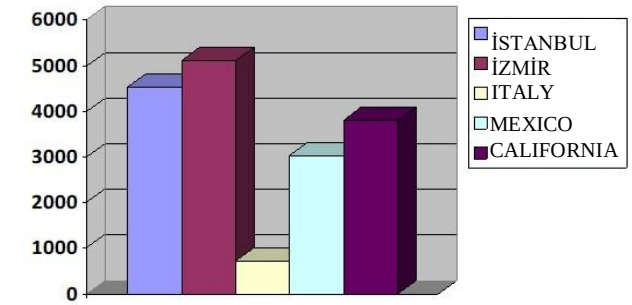

Figure 8: SPECZ vertical seismic effect for 3 m overhang (kN)

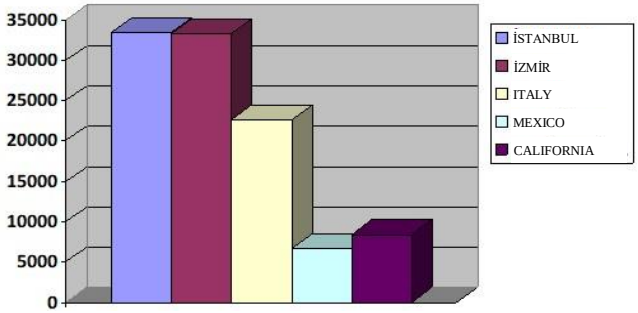

Figure 9: Ez vertical earthquake effect for 5m overhang (kN)

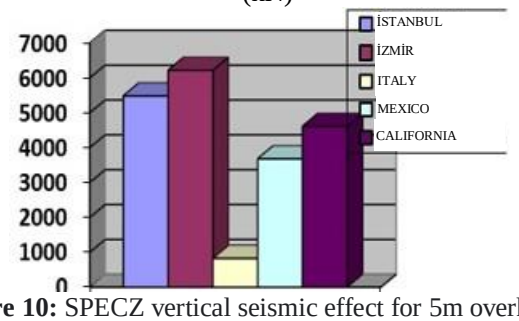

Figure 10: SPECZ vertical seismic effect for 5m overhang (kN)

As the protrusion rate increased, there was a 20-30% increase in the base shear forces from 1m to 3m, from 3m to 5m. In the calculation with the equivalent earthquake load method, it was seen that the base shear force value depending on the vertical component of the earthquake yielded lower results than the 0.2Sve(T)D approach applied in ASCE7-16 for Mexico and California. As a result of the base shear force due to Specz, a lower value was obtained for Italy, which was calculated according to the EC8-4 regulation, compared to other results due to the spectrum differences used. As the protrusion rate increases, the mass of the structure also increases, so it is considered normal to increase the base shear force values.

While examining the beam displacement results, separate examinations were made according to the 1-3-5m rise rates on the seventh floor (the most critical), and they were also examined comparatively

Figure 11: B2 cantilever left endpoint beam Uz displacement of G+Q+0.2S+EX+0.3EY+0.3EZ combination (mm)

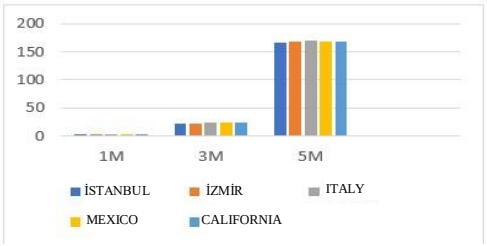

Figure 12: B2 console left endpoint beam Uz displacement of G+Q+0.2S+SPECX+0.3SPECY+0.3SPECZ combination (mm)

When the beam displacement tables and graphs are examined, it is seen that when the overhang rates change from 1 m to 3 m, from 3 m to 5 m, a huge increase of 80-100% in the beam cantilever end area. The beam displacements, which were almost non-existent when the cantilever beam length was 1 m, showed a great change when the overhang rate was 5 m. It has been seen that these change-out rates have a very large effect on the beam, cantilever end displacement, and this result is close to the selected Istanbul, Izmir, Italy, Mexico and California in our analysis. In column B2, the cross-sectional effects on the first floor are given in figures 16 to 21, comparatively.

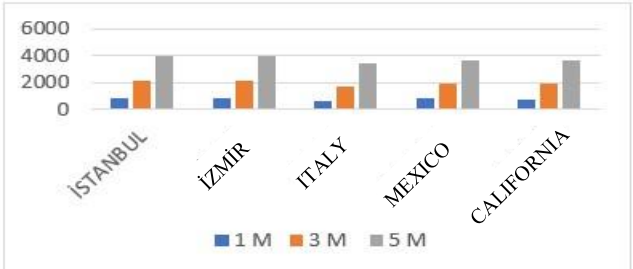

Figure 13: B2 column N comparison of G+Q+0.2S+EX+0.3EY+0.3EZ combination (kN)

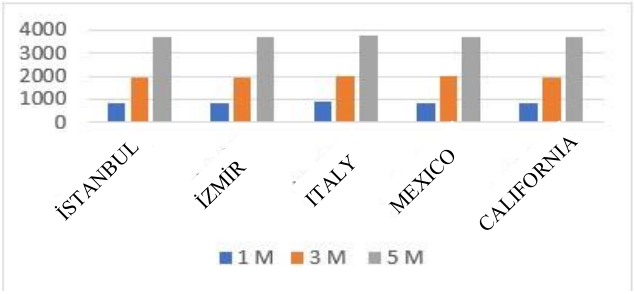

Figure 14: B2 column axial force comparison of G+Q+0.2S+SPECX+0.3SPECY+0.3SPECZ combination(kN)

In Istanbul, Izmir, Italy, Mexico and California, it was determined that the axial force increased between 50% and 60% from 1 m to 3 m, from 3 m to 5 m. As the reason for this, it can be said that the vertical load is affected by 30%. In the bending moment, certain percentage increases were observed in the B2 corner column in the earthquake direction at the top floor due to the total horizontal equivalent earthquake force being excessive, the effective section rigidity of the column/beams and the vertical earthquake effect. It was observed that as the overhang rates increased from 1 m to 3 m, from 3 m to 5 m, the bending moment values increased between 40% and 50%. In the shear force, it has been determined that the increase in the B2 column in the earthquake direction at the top floor can be up to 70-80% due to the high total horizontal equivalent earthquake force and the effective cross-sectional rigidity of the columns/beams, and increases in varying percentages have been observed in the other floors and interior columns. It was observed that the base shear forces increased by 50-60% for the first floor.

Similar results are available for Izmir, Italy, Mexico and California. The axial force was the most affected by the vertical earthquake force in the columns. The M, N, T cross-section effect values obtained for the first floor from the B2 cantilever beam end point are given comparatively.

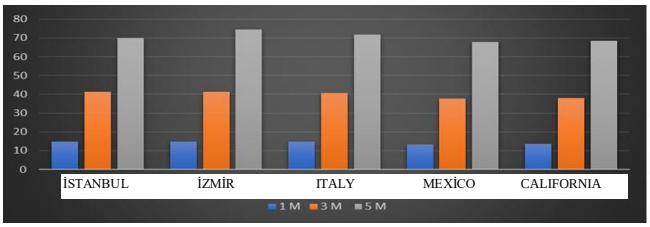

Figure 15: Comparison of B2 cantilever beam end shear force of G+Q+0.2S+EX+0.3EY+0.3EZ combination (kN)

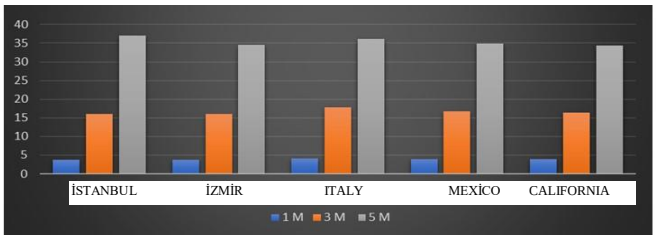

Figure 16: Comparison of B2 cantilever beam end bending moment of G+Q+0.2S+EX+0.3EY+0.3EZ combination (kNm)

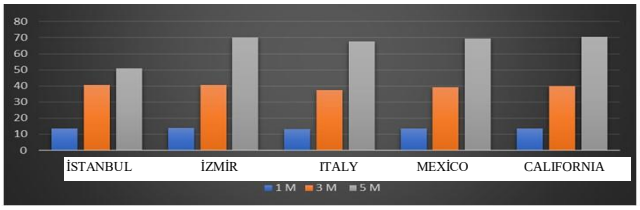

Figure 17: B2 cantilever beam end shear force comparison of G+Q+0.2S+SPECX+0.3SPECY+0.3SPECZ combination(kN)

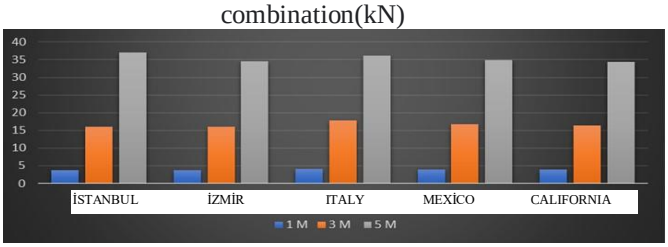

Figure 18: B2 cantilever beam end bending moment comparison of G+Q+0.2S+SPECX+0.3SPECY+0.3SPECZ combination(kNm)

In TEC 2018, it was determined that up to 50% increase in shear force occurred in cantilever beams due to the fact that 30% of the vertical earthquake effect was taken into account, the total horizontal equivalent earthquake force was excessive and the effective sectional rigidity of the columns/beams. As for the bending moment, an increase of 50-70% is observed as the rate of going from 1 m to 3 m and from 3 m to 5 m increases. When the bending moments and shear forces results are examined, it has been determined that the results in the response spektrum method are lower than the results in the equivalent earthquake load method. It has been observed that there are serious increases in loads on beams and columns with the effect of vertical earthquake load.

Although the calculation steps applied in ASCE 7/16 and TEC-2018 are the same, it has been seen that the results from the two regulations are different and the results in TEC 2018 are greater than ASCE7-16. The reason for this is that although the spectral information taken into account in the earthquake calculation in ASCE 7/16 is reduced by 2/3, there is no such reduction in TEC 2018. The obtained Sds spectral acceleration is calculated with the 2/3 Sds approach for TEC 2018 while calculating the vertical earthquake load, while it is included in the calculation with the 0.2 Sds formula for ASCE7-16. Since the earthquake load acting on the structure is higher in TEC 2018, it is quite normal for the base shear force results to be like this.

It has been observed that the results obtained by the response spektrum method are less than the results obtained by the equivalent earthquake load method in all cases. The reason for this is that only the 1st natural vibration period is used in the equivalent seismic load method and the structure periods are used close to 100% in the response spektrum method.

With the effect of the vertical earthquake, great increases were obtained in the base axial force in the structures. Likewise, depending on the direct relationship between the vertical displacement of the top floor and the axial force of the base, large increases were observed in the values of the vertical displacement of the top floor with the effect of the vertical earthquake movement.

Obtained results; revealed the effect of the vertical component of the earthquake on the building elements and building performance. For this reason, the vertical earthquake effect must be evaluated in the structural design calculations.

KAYNAKLAR (REFERENCES)

[1] C. Aksoylu, M.H. Arslan / BEÜ Journal of Science 8 (2), 569-581, 2019

[2] C. Aksoylu, M.H. Arslan Empirical Evaluation of Period Calculations of frame+reinforced concrete type buildings according to TBDY-2019 Regulation, Uludağ University Journal of Engineering Faculty 365-380,2019

[3] Y.Bozorgnia, K.N.Campbell (2016) Ground Motion Model for the Vertical-to-Horizontal (V/H) Ratios of PGA, PGV, and Response Spectra

[4] Peer Ground Motion Database

[5] Turkey Building Earthquake Regulation, Disaster and Emergency Management Presidency, Ankara, 2018.

[6] Turkey Earthquake Hazard Maps Interactive Web Application,https://tdth.afad.gov.tr/,2018.

[7] EC8. 2004. Design of structures for earthquake resistance in Part 1: General rules, seismic actions and rules for buildings.

[8] ASCE7-16. 2017. Minimum Design Loads and Associated Criteria for Buildings and Other Structures in Seismic Design Requirements for Building Structures Structural Engineering Institute.

[9] Özmen İ.G. (2008) Conversion of Mode Combination Method Results to Equivalent Seismic Loads, Technical Journal, 19(94):4509-20

[10] Nemutlu, Ö.F. and Sarı, A. (2018) Comparison of Turkish Earthquake Code in 2007 With Turkish Earthquake Code in 2018, International Engineering and Natural Sciences Conference (IENSC 2018), Diyarbakır. 568-76.

[11] Etabs, Evaluation Version,Computers and Structures, 2020

[12] G.Özmen, E. Orakdöğen, K. Darılmaz (2015). With Examples Sap2000 v17, v17 ed., Birsen Publisher, İstanbul.

[13] Arslan M. (Kasım 2018), The Effects of Different Soil Types on the Behaviors of Curtain Framed Buildings Exposed to Horizontal Earthquake Accelerations and Vertical Earthquake Accelerations

[14] Doğan O.,Genç Y.(2019), The Effect of Vertical Earthquake Force on Second Order Base Moments According to Turkish Building Earthquake Code

[15] Genç Y. (2019), Investigation of Vertical Earthquake Load Effects in the Analysis of Reinforced Concrete Buildings According to Turkish and Some Foreign Earthquake Regulations, Kırklareli University

[16] https://www.seismicmaps.org/, OSHPD

Geometric Measurement System for Engine Valve Parts via Machine Vision

M. AKDOĞAN[1], İ.BAYRAM[1], A.DÜZYOL[1] and M.A. ARI[1]

[1]Adil Karaagac Vocational and Technical Anatolian High School, Konya/Turkey,
akdoganmurat@hotmail.com-israfilbayram@gmail.com-duzyol_ahmet@hotmail.com-maliari42@hotmail.com

Abstract **- Today, machine vision systems are widely used in the mass production factories. The present work focuses on measurement of critical valve sizes using image processing techniques. For this, a experimental setup has been prepared to hold digital camera in a fixed plane to capture the images of valve. This work has been done for measurement of valve stem diameter, head diameter and overall length. The images are captured by using high resolution digital camera which are fixed in the experimental setup. OpenCV programming function was utilized in Python scripting language to perform image processing. High resolution captured images of valve are processed a sequential operations which are correcting defective images caused by working environment. Developed image processing algorithms are applied to measurement of valve sizes. The acquiring results are compared with the results obtained by conventional systems. Dimension Control system decrease faulty production and minimize the unnecessary consumption of raw materials. Experimental results show that the system can quickly measure the dimension of valve parts within the allowable range of error.**

Keywords **- Image Processing, Quality Control, Measurement.**

I. INTRODUCTION

Machine vision technology has been widely applied in the industries such as automobile, electronics, and electrical industry [1]. At present, the application of industrial vision systems can be roughly divided into three directions: automatic detection, intelligent assembly, and visual servo system [2]. Among them, the application of machine vision in automatic detection includes geometric measurement test and automatic visual recognition test [3], and the geometric measurement test technology is an indispensable part of manufacturing technology. Valve parts are one of the most common parts in the automotive industry. Valves are generally used in an internal combustion engine to control the flow of combustible fuel into the engine and burnt fuel out of the engine. The valves in an internal combustion engine play a significant role in engine performance [4].

Valve geometric dimension and precision directly affect the engine performance and life. In the manufacturing stage, quality control of valves both a serious and time-consuming process. Today the operator collects the manufactured valves and manually control one by one using comparator gauge. And then classifies them using their sizes. Worker controlling of valve critical sizes which is stem diameter, head diameter and overall length by manually.

II. OBJECTIVE

The main objectives of this study are to measure valve critical sizes for decrease worker faults and and minimize to controlling time. Camera based measurement system reduce the human involvement in the process. If we use a machine instead of the person the person can do another job by this time. In order to improve the quality and efficiency of the valve measurement, a new method based on machine vision is proposed. For this purpose, a special valve measurement apparatus designed. Visual measurement system was designed to replace manual measurement of valve.

III. SYSTEM OVERVIEW

This vision measurement system is mainly composed of an image acquisition and image processing system. The Figure1. shows the detected target engine valve object.

Figure 1: Engine valves

Valve parameters specified in a technical drawing, are to be measured with this image acquisition system. Figure 2. shows valve size parameters.

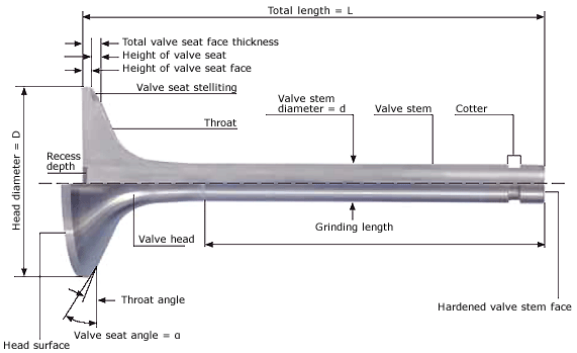

Figure 2: Valve size parameters

A. *Traditional Manually valve measurement method*

Valve critical sizes which is *stem diameter*, *head diameter* and *overall length* direct impact on valve quality. So, quality responsible personal must be measure all manufactured valves one by one using traditional methods. It is generally used Comparator gauge for these measurements. These type measurements may not always give accurate results because of worker, lack precision or not good calibrated measurement device and so on. Figure 3. shows traditional measurement methods.

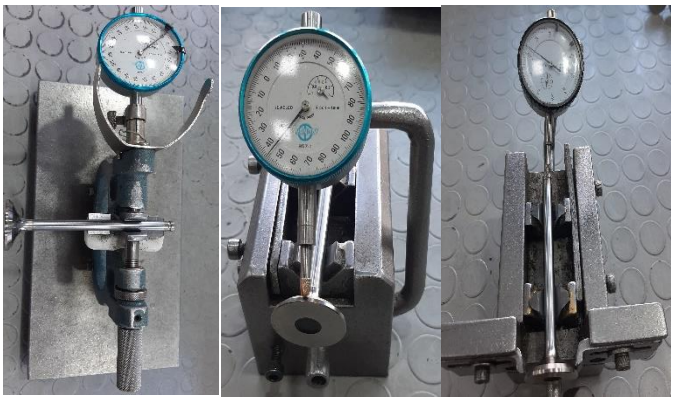

Figure 3: Valve size traditional measurement methods

B. *Camera based image acquisition system*

CCD camera (Elp-Usb 8MP 5-50 mm varifocal lens, Sony IMX179 sensor camera) are placed across to target object. To increase image contrast, an illuminator placed behind of the object. It can ensure image clearer and brighter in case of dark condition. Experiments were conducted under different lighting conditions. Figure 4. shows the image acquisition system.

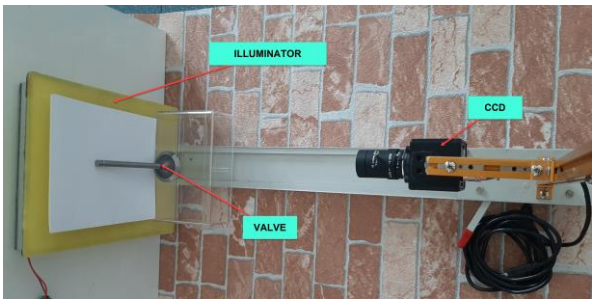

Figure 4: Image acquisition system

C. *Used software and library*

PyCharm

- It is an IDE (integrated development environment) specifically used for the python language.
- PyCharm is easy to use. It supports OpenCV and all its libraries once dependencies are installed.
- Supports all frameworks.

OpenCV

- It is an open-source library used in computer vision, machine learning, image processing.
- There are various applications and functionality of OpenCV which makes it versatile.

NumPy

- It is a python library. It is basically used to do mathematical operations and it is easy to work with arrays.
- It is easy to use and gives excellent results. It can perform great mathematical operations.

IV. DEVELOPED MEASUREMENT SYSTEM

The measurement system of engine valves is composed of two parts: hardware system and software system. The hardware system mainly completes image acquisition and output image. The software system mainly completes the function of image preprocessing and size measurement. Figure 5. shows the block diagram represents the basic working of the valve measurement system.

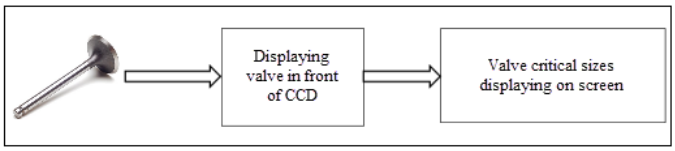

Figure 5: Block diagram

To obtain valve image used high resolution CCD (Charge coupled device) camera used. Valve boundaries fundamental importance in image processing so edge detection significantly reduces the amount of data and filters out useless information. Edge detection is in the forefront of image processing for valve detection. Firstly, getting image from CCD and then some noise removes operations performed. Afterwards image thresholding applied to achieve interested image region. Later OpenCV contours finding algorithm used. Lastly, improved algorithm used finished image and measured critical sizes of valve object. Figure 6. shows the flowchart of developed measurement system.

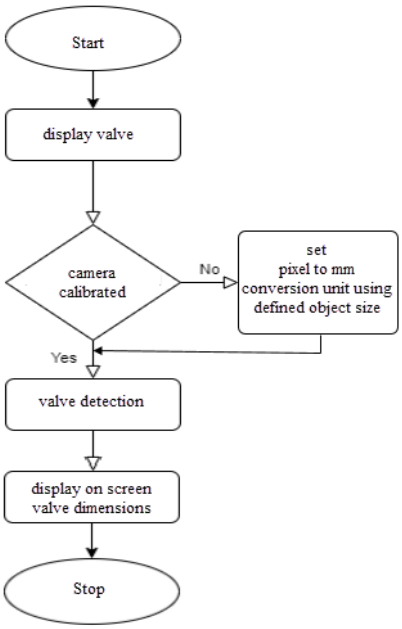

Figure 6: Flowchart

Two-dimensional valve size measurement method includes three steps.

- Camera calibration, Acquiring image and pre-process.
- Extract the contour region of valve.
- Using contours of valve measuring stem diameter, head diameter and total length via improved algorithm.

A. *Camera calibration*

The purpose of camera calibration is to determine the size relationship between the images obtained from the camera and the target objects. For calibration used known references of paper's horizontal and vertical dimensions.

B. *Image pre-process: Filtering, Thresholding and Contour extracting*

Firstly getting image from CCD and applied the image some filters for extract the noise. This process is very important section before contour extracting. In image processing most suitable filter must be selected among the many filter [5]. Median filter is used some kind of noise reduction on an image. Median filtering is very widely used in digital image processing because, under certain conditions, it preserves edges while removing noise. Thresholding is the simplest method of image segmentation. From a grayscale image. Thresholding can be used to create binary images [6]. Figure 7. shows a thresholding view of object. For this operation used equation is shown (1).

Figure 7: Threshed image of valve.

$$G_{x,y} = \begin{cases} 1, f(x,y) \geq T(x,y) \\ 0, f(x,y) < T(x,y) \end{cases} \quad (1)$$

OpenCV uses the Suzuki algorithm to perform contour tracing [7]. In this algorithm, firstly the upper left contour pixel is found. Then, the neighborhood of the first pixel is checked in clockwise direction to find the next pixel of the contour. From now on, the search for the other pixels of the contour is done in anti-clockwise direction and ends when the first two pixels of the contour are found again. Figure 8. shows of object contour. Opencv command;

cv2.drawContours (object name, contour name, 0, (0,0,255), 2). 0 is contour number, (0,0,255), color of contour, 2 is thickness.

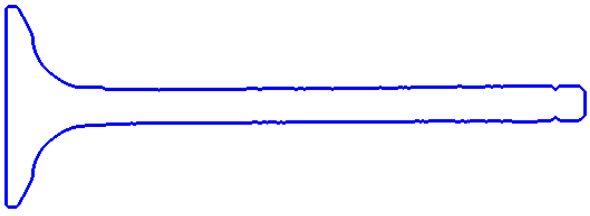

Figure 8: Image Contours

C. *Measurement results*

The algorithm were implemented by Python 2.7. and performed on a Windows 10 Professional operation system. To generate the rules, one of valve object used. Figure 9. shows technical drawing of Valve cross section view.

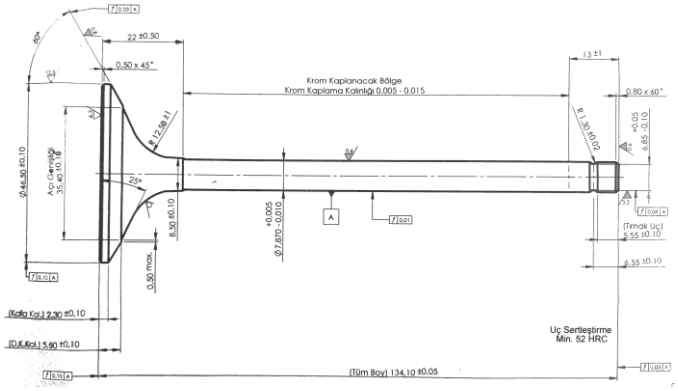

Figure 9: Technical Drawing of valve

Figure 10 shows the real image of valve product.

Figure 10: Real Image of valve

Algorithm firstly find starting point of contours, and than calculate next point difference. If difference is plus, continue otherwise stop and store that point. This is first corner, For tip length of valve contours's specific region decided and calculated the between two point pixel sizes. All pixels scaling, according to the defined object size. Finally, the size of the valve part is displayed through the monitor. Figure 11. presents the result of the valve image,

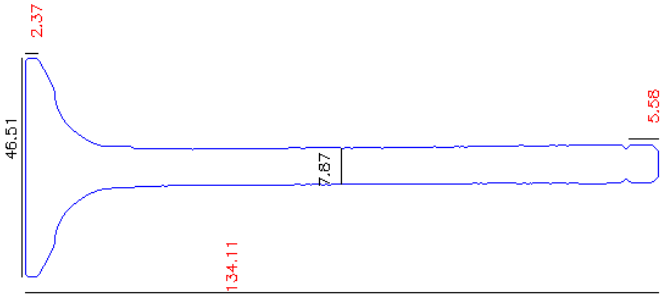

Figure 11: Measured image via image processing

Figure 13. Shows some parts of program written in Pycharm integrated development environment.

```
"---KONTUR CIZME---"
(_, contours, hierarchy) = cv2.findContours(esikleme.copy(), cv2.RETR_LIST, cv2.CHAIN_APPROX_NONE)
for i, cnt in enumerate(contours):
    if hierarchy[0, i, 3] == -1 and cv2.contourArea(cnt) > 1000:
        cv2.drawContours(blank_image, cnt, -1, (255, 0, 0), 2)
        x, y, w, h = cv2.boundingRect(cnt)
        # cv2.putText(blank_image, "{}".format(i), (int(x + 20), int(y + 60)),
        #             cv2.FONT_HERSHEY_SIMPLEX, 2, (0, 0, 255), 1)
kont=contours[0]
liste = noktalama(0, len(kont) - 1, kont)
```

Figure 13: Program parts of measurement system

Valve dimensions is shown in Table 1. If we examine table 1, we can say image based measurement method results is nearly same as traditional measurement method's. Maximum difference equal to -0.14 mm is measured, without total length other dimensions confirming all results is in the tolerances.

Table 1: Result of Measurements

	Std.	Min.	Max.	Real Measure	Image Based Measure	Difference
Stem Diameter (mm)	7.870	7.875	7.860	7.84	7.87	0.03
Head Diameter (mm)	46.50	46.40	46.60	46.45	46.51	0.06
Tip Length (mm)	5.55	5.45	5.65	5.77	5.85	0.08
Head Thickness (mm)	2.30	2.40	2.20	2.49	2.58	0.09
Total length (mm)	134.10	134.05	134.15	134.25	134.11	-0.14

V. CONCLUSIONS

A large number of studies show that the measurement system based on machine vision technology can measure parts effectively and quickly with high measurement accuracy. This study presents a manufactured valve products measurement method using image processing technics. The proposed method can measure stem diameter, head diameter and total length of valve with a high accuracy.

The experimental results show that the proposed method is suitable for 2D products comparing to traditional measurement methods. It can be used to continuously monitor the dimensional quality of any valve. This work is easily applicable for the companies that produce valve.

Future research focuses are concentrated on improve the more robust algorithm for valve's other dimensions.

ACKNOWLEDGMENT

Thanks to "Elzem Automotive" company who has helped us in completing our project work successfully.

REFERENCES

[1] R.S. Lu, Y.F. Li, Q. Yu, On-line measurement of the straightness of seamless steel pipes using machine vision technique[J]. Sens Actuators A 94(1), 95–101 (2001)

[2] R.S. Lu, Y.F. Li, Q. Yu, On-line measurement of the straightness of seamless steel pipes using machine vision technique[J]. Sens Actuators A **94**(1), 95–101 (2001)

[3] M. Brown, D.G. Lowe, Automatic panoramic image stitching using invariant features[J]. Int. J. Comput. Vis. **74**(1), 59–73 (2007)

[4] N. K. Raghuwanshi, A. Pandey, and R. K. Mandloi, "failure analysis of internal combustion engine valves: a review," *International Journal of Innovative Research in Science, Engineering and Technology*, vol. 1, no. 2, pp. 173–181, 2012.

[5] Demigny D., On Optimal Linear Filtering for Edge Detection, IEEE Transactions On İmage Processing, 2002, 11, 728-737

[6] Shapiro, Linda G. & Stockman, George C. (2002). "Computer Vision". Prentice Hall. ISBN 0-13-030796-3

[7] Suzuki, S. and Abe, K., Topological Structural Analysis of Digitized Binary Images by Border Following. CVGIP 30 1, pp 32-46 (1985)

A REVIEW OF POWER LINE DISTURBANCES AND THEIR MITIGATION DEVICES

H.Y. USTUNEL[1] and O. TIMUR[2]

[1] Cukurova University, Adana/Turkey, halilyasarustunel@gmail.com
[2]Cukurova University, Adana/Turkey, otımur@cu.edu.tr

***Abstract* - The developments in industrialization and automation technologies have been increasing in recent years. Along with these developments in these fields, the device Technologies also change and become more sensitive than before. Programmable logic controllers (PLC), variable speed drives (VSDs), microprocessors are just a few of these devices where significant developments have taken place and, these devices are vulnerable to the power quality issues. To keep the progress in industrialization and automation uninterrupted, the term of power quality parameters and their effects become more significant. Voltage fluctuation, flicker, harmonics, voltage imbalance are the just some of the power quality problem that is ability to lead enormous failures and serious economic losses. To alleviate the adverse impact of power quality and improve it, various equipment-based methods are developed. Some of methods improved to ameliorate the power quality, various power quality problems and their characteristics are examined in this paper. Unified power quality conditioner (UPQC), uninterruptible power supply (UPS), distribution static synchronous compensator (D-STATCOM), dynamic voltage restorer (DVR) and filters are evaluated in this study.**

***Keywords* -: Power Quality (PQ), Power Quality Mitigation Devices**

I. INTRODUCTION

The breakthroughs in technology in the last two decades have opened the door to innovations in many fields, especially in automation, microprocessor and power electronic technologies. With these developments, the concept of power quality and its importance have become even more valuable. Since the concept of power quality is considered different aspects, there is no clear definition agreed upon. To define it briefly, power quality refers to changes in the operation of the equipment and the system due to non-ideal conditions in current, voltage and frequency [1-2].

Industrial facilities are modified their systems to the developing automation systems due to important reasons such as the increase in efficiency brought by technology, energy saving, precision in process control, and reduction of error rate by eliminating the human factor. Programmable Logic Controllers (PLC), variable speed drives (VSDs), microprocessors are key elements of these automation systems that are sensitive to power quality. Each of these equipment has extremely important tasks such as managing the processes in which they are located. These devices need high quality electrical power in order not to affect critical processes. An unusual situation due to electrical power quality in systems that contains sensitive equipment; it can cause problems with serious economic problems such as loss of production, production stoppage, loss of income, reduction in equipment life and wasted energy. According to the research that is studied in 25 EU countries, it has been revealed that the annual losses due to power quality is $151 billion dollars per year, and approximately 90% of this loss belongs to the industry [3]. In the following of this study, the types of power quality problems that cause serious problems and the devices developed to reduce their effects will be examined.

II. POWER LINE DISTURBANCES

Under ideal conditions, electrical systems are designed to operate with a sinusoidal voltage and current waveform of constant magnitude and frequency [4]. Abnormalities in these predetermined limits of waveform of electrical quantities such as voltage; are called as power quality problems. Power quality problems are divided into various groups according to their effects and causes, and these groups are shown in below. In this part of the study, power quality problems are examined.

- Frequency Variations
- Flicker and Voltage Fluctuations
- Harmonics (Waveform Distortion)
- Long Duration Voltage Variation
- Short Duration VoltageVariation
- Voltage Imbalance (Unbalance)
- Transients

Frequency Variations: Frequency variation refers to the deviation in the fundamental frequency value (50 Hz or 60 Hz) in the electrical power system. The primary reason of the frequency variation is the deterioration of the balance between the active power demand and power generation. To avoid the frequency variation, there must be balance between active power demand and power generation [5]. To maintain the electrical power grid stable, frequency value must be kept certain limits. In Turkey, national grid frequency is 50 Hz. The minimum and maximum limit of frequency is 49.8 and 50.2, respectively [21].

Flicker and Voltage Fluctuations: Instant and continuous changes in load current. These changes can also cause voltage fluctuations. Flickers can have perceptibility level by the

human eye in the illumination. The operation of the arc furnaces in industrial facilities is one of the most important causes of flickers that is experienced in power distribution systems. Voltage fluctuations can be interpreted as change in the magnitude of the voltage due to the instantaneous variations in the power drawn by the load from the system. Characteristic of voltage fluctuations are closely related with the types and size of connected loads and system capacity. Arc welders, arc furnaces, motor drives with cyclic operation are the main causes of voltage fluctuations [5].

Voltage Imbalance (Unbalance): Voltage imbalance (unbalance) is defined as the ratio of the magnitudes of the negative components of voltage and current to the positive components of their magnitudes. According to its severity voltage balance is split into the two groups as minor (below 2%) and major (above 5%). Single phase loading in three-phase systems, untransposed over headlines, fuse blown in one phase of the reactive power compensation capacitor cell is some reasons of the voltage imbalance [6].

Transients: Transients are the instantaneous, undesirable, short duration, and high-power events in power systems. Transients are also called surge and two subcategorized as the impulsive and oscillatory according to the amplitude, occurrence frequency and rise time. Oscillatory transients can be defined as the frequency changes that occur at a steady state condition in current, voltage, or both, that contains values in both positive and negative polarization. It is possible to divide into groups according to the dominant frequency, duration, and magnitude. The main reasons of the oscillatory transients are listed as follows, capacitor, transformer and transmission line energization, capacitor, and cable switching [4-6]. Impulsive transients can be defined as the frequency changes that occur at a steady state condition in current, voltage, or both, that contains values in either positive or negative polarization. The lightning is the most common cause of impulsive transients. The waveform of the impulsive transient due to lightning strike is shown in figure 1.

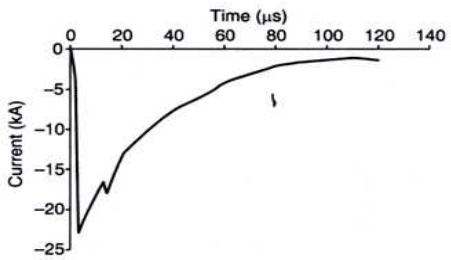

Figure 1 : The waveform of the impulsive transient [6]

Short Duration Voltage Variations: Short duration voltage variations are three sub-categorized according to the event duration as instantaneous, momentary, and temporary. Furthermore, each of these subcategories are divided into sag, swell and interruption. Main reasons of the short duration voltage variation are listed as follow, heavy load energization, loose connection, and fault condition.

Voltage Sag: In modern power systems, one of the most popular power quality problems is voltage sag. Voltage sag can be defined as "the rms value of the voltage decrescent between 0,1pu and 0,9pu and an event that takes place at the fundamental frequency in a period of half a cycle to 1 minute. Natural events, starting of the heavy induction motor, inrush currents of transformers, single line to ground fault are the main reasons of the voltage sags. Voltage sags cause serious financial losses. According to the conducted study, it is reported that 24% of financial losses due to power quality problems occur because of voltage sags [3-6-7].

Voltage Swell: The voltage swell, which does not occur as frequently as voltage sags, is the event that the value of the voltage takes a value between 1.1pu and 1.8 pu. Power system faults are the major causes of the voltage swells such as single line to ground faults. When the single line to ground faults are experienced voltage swells occurs in other healthy phases where there is no fault. Also, capacitor bank deactivation is another reason for the voltage swell. Voltage swell is the synonym with the momentary overvoltage in some cases.

Interruption: It is the situation where the supply voltage takes a value less than 0.1 pu for less than 1 minute. Fuse blown, mis operation of circuit breaker, control malfunctioning, natural events that occurs on the overhead lines are some reasons of the interruption. In figure 2, normal voltage and voltage sag, swell are shown.

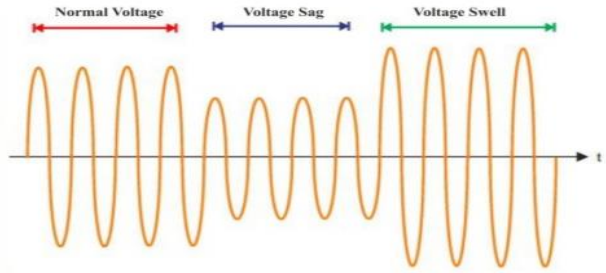

Figure 2 : Voltage distrubances [18]

Long Duration Voltage Variation: Long duration voltage variations are events that occur at the RMS voltage and last longer than 1 minute. Load alternation and switching, natural events are the main causes of long duration voltage variation. It is divided into three subcategories as sustained interruption, undervoltage and overvoltage.

Sustained Interruption: The sustained interruption means outage. It is the case that the supply voltage remains zero for more than 1 minute. It is a power quality event with a high negative impact as the supply voltage is zero and does not reach its nominal value quickly and automatically. Failures occur on the without no redundancy systems, planned maintenance, mis operation of protection devices are the some notable of sustainable interruptions.

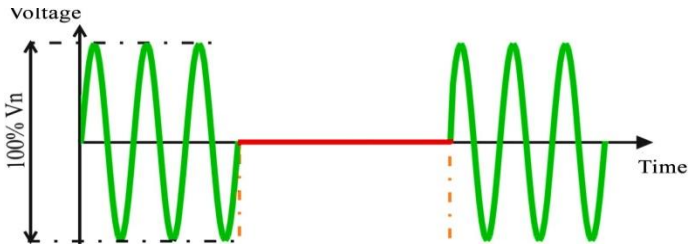

Figure 3 : Interruption [20]

Undervoltage: It is the situation where the voltage value is between 0.8 and 0.9 pu, which takes place in more than one minute.

Overvoltage: It is the situation where the voltage value is between 1.1 pu and 1.2 pu, which takes place in more than one minute. Excess reactive power compensation, lightning, deactivation of large loads, wrong adjustment of tap changer are the main reasons of overvoltage in the power systems. Undervoltage and overvoltage is depicted in figure 4.

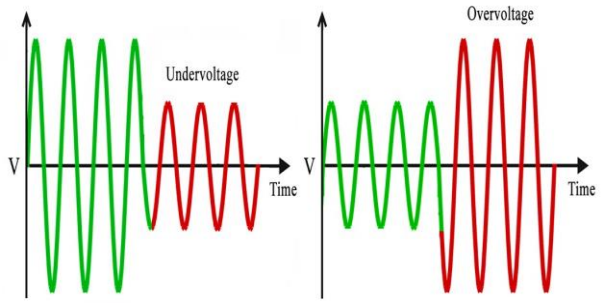

Figure 4 : Undervoltage and Overvoltage [20]

Waveform Distortion: Electric power systems are composed of groups of loads whose characteristics are very different from each other. One of these different load groups in systems is those with nonlinear characteristics. As it is known, under normal conditions, it is expected that the current and voltage waveform has a sinusoidal waveform. Unfortunately, when nonlinear loads are supplied by the sinusoidal waveform voltage, because of the characteristic of the loads, resulting current that is not sinusoidal waveform [8].

To analyze the waveform distortion deeply, Fourier analysis is used. Waveform distortion can be comprised of five categories as explained in the following.

DC Offset: It refers to the presence of DC voltage or current in the AC system.

Harmonics: Harmonics are described as a voltage or current at a multiple of the fundamental frequency of the power system. Power electronic based devices that include rectifiers, inverters such as variable speed drives, uninterruptible power supplies, switch mode power supplies, power, office, and IT equipment's are the main causes of the harmonics in the electrical power systems.

Interharmonics: In [9] interharmonic is defined as; between the harmonics of the power frequency voltage and current, further frequencies can be observed which are not an integer of the fundamental.

Notching: When current passes through the one phase to another phase into the power electronic devices, periodic waveform distortion is occurred and is called notching.

Noise: It is a power quality problem that is undesirable and has a frequency lower than 200khz in electrical power systems. In order to alleviate the effects of noise, some special filters are designed.

III. DEVICES DEVELOPED TO MITIGATE THE EFFECTS OF POWER QUALITY PROBLEMS

The effects of the variations of the power quality to devices used in critical processes in industrial facilities have become even more sensitive with the developments in technology. When this is the case, power quality problems occurring in the electrical power grid can cause serious problems in the facilities it affects. There are some measures that can be taken to reduce these problems and their effects and to ensure that the facilities can operate continuously. In this section, devices that is developed against some power quality events will be reviewed. The devices to be examined are, uninterruptible power supply (UPS), dynamic voltage restorer (DVR), Unified power quality conditioner (UPQC), and distribution static synchronous compensator (D-STATCOM) and filters, respectively. At the end of the chapter, summary table is given including the comparisons of the devices with each other.

A. Uninterruptible Power Supply (UPS)

Uninterruptible Power Supplies are an important solution to preclude vital loads from being affected by situations such as voltage sags or interruptions. Thanks to the battery groups they have, the energy produced is transferred to the load, preventing the load from being affected by this situation. The UPS system includes various energy transformations within itself.

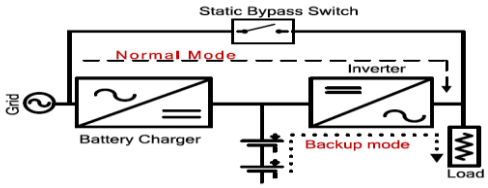

Figure 5: Circuit diagram of UPS [10]

As can be seen from figure 5, AC power is transformed to the DC by means of rectifier unit to charge the battery. And then DC is converted to the AC via inverter unit to provide the power to the loads. When there is no AC mains interruption, loads are fed by the normal mode. Means that battery group is charged and deactivated. During the AC mains interruption, battery group is activated, DC to AC transformation is realized and loads feed by the inverter unit. The operating time of the UPS in long-term interruptions is related to the load group which it feeds. As the load increases, the battery group also changes [10].

B. Dynamic Voltage Restorer (DVR)

One of the most frequently encountered power quality events in the electrical grid and with the greatest economic impact is voltage sag events [11].

Developed technological systems are vulnerable to the power quality events and have less immunity to these events. One of the devices developed to decrease the effects of voltage sag

events on sensitive equipment is the dynamic voltage restorer. As can be seen from the figure 6, DVR is connected to the system in series via injection transformer. The working principle of the DVR is based on detecting this voltage sag and during the voltage sag event injecting the required voltage into the system.

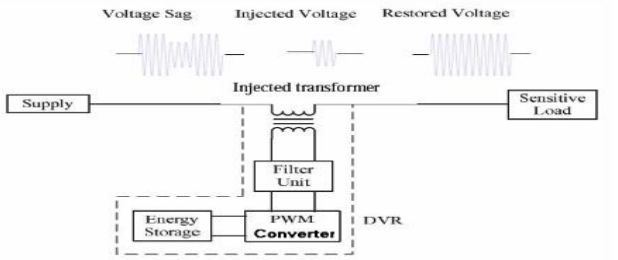

Figure 6: Circuit diagram of DVR [19]

In fact, the DVR is used to regulate the voltage that belongs to the load and keep it within the operating limits. For this reason, it is also used in voltage swell events. Additionally, DVR is also used to recompense of harmonics and reduce the transients [12].

C. UNIFIED POWER QUALITY CONDITIONER (UPQC)

UPQC comprise of the combination of shunt and series active power filters to provide an effective solution to different power quality problems simultaneously. Basic circuit diagram is shown in figure 7.

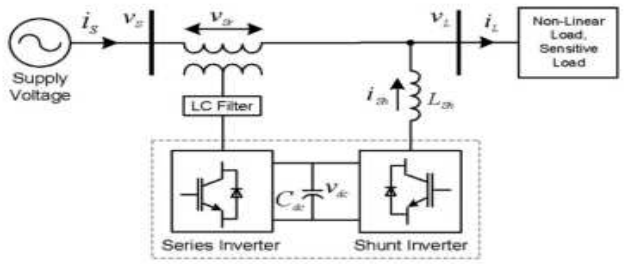

Figure 7: Circuit diagram of UPQC [14]

As can be seen the circuit diagram of UPQC, series active power filter is connected to the system via transformer. By this connection voltage compensation is achieved. On the other hand, reactive power compensation for the loads is realized with shunt active power filter. Shortly, UPQC can be considered as a logical solution as it can simultaneously solve power quality problems such as voltage swell, sag, imbalance, flicker, harmonics, and current-related power quality problems such as current harmonics, imbalances, reactive currents, and excessive neutral currents [13-14].

D.DISTRIBUTION STATIC SYNCHRONOUS COMPENSATOR (D-STATCOM)

DSTATCOM is a power quality improver device that is designed to balance the current and decrease the current harmonics. Additively it is also used to power factor improvement, neutral current compensation, and voltage regulation [15]. D-STATCOM consists of source converter (VSC), dc bus capacitor, transformer and filter as illustrated in the figure 8.

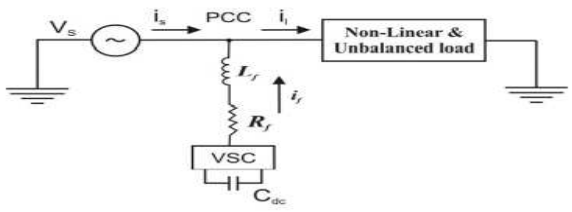

Figure 8: Circuit diagram of D-STATCOM [15]

D. FILTERS

The most important problem caused by nonlinear loads, which is an important component in electrical power systems, is harmonics. Harmonics cause many problems in electrical power systems by affecting compensation panels, conductors, measuring devices, protection devices, transformers, and motors. The main of these problems can be listed as overheating, mismeasurement, and decrease in efficiency and usage life of equipment. Various harmonic filters have been developed to eliminate these negativities, and these filters have become an indispensable part of electric power systems. Filters are split into two groups as active and passive. In this chapter, types of filters are explained.

Passive Filters consists of passive circuit elements. According to the design, passive filters have low or high impedance value. This type of filters can be connected to the circuit either series or parallel. It is a low-cost power quality solution and is often connected close to non-linear load groups. The most important point to consider when using passive filters is the tuning of the passive filter parameters [16].

The difficulties of adjusting the filter parameters due to the change in the values of the circuit elements used in the filter, the resonance problem, and the decrease in the filter performance due to the load variation are the important disadvantages of passive filters. To get over the negativities of passive filters, active filters are developed. Active filters analyze the harmonics drawn by the load and eliminate the harmonics by injecting the same harmonics in a suitable phase into the system in opposite phase. It is also a suitable solution for reactive power and neutral current compensation, voltage regulation, current and voltage imbalances [17].

The following table provides a brief comparison chart of some of the devices that is developed against various power quality events.

	D-STATCOM	UPS	UPQC	DVR
Problem	Sag Swell	Sag Swell Interruption Flicker Harmonics Transients	Sag Swell Interruption Flicker Harmonics Transients	Sag Swell Harmonics
Cost	*	****	***	**
Speed	Low	Supreme	Higher	High
Rating	Low	Highest	Higher	High

Table 1: Comparison of Improvement Device

IV. CONCLUSION

In this study, electrical power quality problems, which are frequently encountered in the electrical power grid and their serious effects are discussed. Since the features and effects of the events that occur different, the devices developed to mitigate the power quality problems differ among themselves. A detailed study is required to minimize the effects of these events on the systems and industry and to choose the right product.

REFERENCES

[1] IEEE A Draft Standard Glassory of Power Quality Terminology,1999

[2] M.H. Bollen, *Understanding Power Quality Problems* John Wiley&Sons Inc., New Jersey,2000.

[3] R. Torgosz and J.Manson,'' Pan Europan LPQI Power Quality Survey'',*19th Int.Conf on Electricity Dist.,May 2007.*

[4] R.C. Dugan, M. F McGranghan, S.Santoso and H.W Beaty,*Electrical Power SystemsQuality*,2nd ed.New York:Mc Graw-Hill,2003

[5] S. Chattopadhyay, M.Mitra, S.Sengupta *Electrical Power Quality* ; New York ;Springer,2011

[6] IEEE Std 1159-2019''Recommended Practice for Monitoring Electric Power Quality''

[7] M.F. Kangarlu,E.Babaei and F.Blaabjerg, '' A comprehensive review of dynamic voltage restorers,'' Electrical Power and Energy Systems,vol.92,pp.136-155

[8] T.S. Sangu and L. Singh,'' Comparative Analysis of Custom Power Devices for Power Quality Improvement in Non-linear Loads'' Proceedings of 2015 RAECS UIET Panjab University Chandigarh 21-22nd December 2015

[9] IEC-61000-2-1Electromagnetic Combability (EMC) Part 2

[10] M.Aamir, K.A. Kalwar and S. Mekhilef,'' Review: Uninterruptible Power Supply (UPS) system,'' Renewable and Sustainable Energy Reviews, vol 58, pp1395-1410

[11] P.A. Raut and M.N.Kalgunde, '' An overview and design of dynamic voltage restorer to improve the power quality in microgrid '' International Conference on Energy Systems and Applications (ICESA 2015)

[12] J. G. Nielsen, M. Newman, H. Nielsen, and F. Blaabjerg, "Control and Testing of a Dynamic Voltage Restorer (DVR) at Medium Voltage Level", Power Electron. IEEE Trans., vol. 19, no. 3, pp. 806–813, 2004.

[13] A. H. Bhat and P. Agarwal, "Three-phase, power quality improvement ac/dc converters", Electr. Power Syst. Res., vol. 78, no. 2, pp. 276–289, Feb. 2008

[14] V. Khadkikar, "Enhancing Electric Power Quality Using UPQC¬: A Comprehensive Overview", Power Electron. IEEE Trans., vol. 27, no. 5, pp. 2284–2297, 2012

[15] O.P. Mahela and A.G.Shaik, '' A review of distribution static compensator, '' Renewable and Sustainable Energy Reviews,vol50,pp531-546

[16] S. Singh and S.S.Letha, '' Various Custom Power Devices for Power Quality Improvement: A Review'' 2018 International Conference on Power Energy, Environment and Intelligent Control (PEEIC)

[17] O. Uzan,'' Alçak Gerilim Dağıtım Sistemlerinde Güç Kalitesi''Msc Thesis, Dept.Elect.Tur.,Gazi Univ,2013

[18] Sridhar.S, K. Uma Rao, Nihaal. M. S and Shetty Aashik'' Real Time Wireless Condition Monitoring of Induction Motor'' IEEE Industrial Electronics and Applications Conference November 2016.

[19] R. Sedaghati, M. Ghasemi and M Hayatdavudi'' Performance Study of Dynamic Voltage Restorer (DVR) in order to Power Quality Improvement'' 2012 Proceedings of 17th Conference on Electrical Power Distribution

[20] Available https://wiki.testguy.net/t/power-quality-analysis-basic-theory-and-applications-explained/70

[21] Electricity Transmission System Supply Reliability and Quality Regulation, Published by Energy Market Regulatory Authority.

Investigation of Effects of Cooling Channels on Flow Properties in Nasa C3X Turbine Blade

M. E. TOLU[1], O. BABAYİĞİT[1] and D. N. OZEN[2]

[1]Karamanoglu Mehmetbey University, Karaman/Türkiye, metolu@kmu.edu.tr, obabayigit@kmu.edu.tr
[2]Necmettin Erbakan University, Konya/Türkiye, dnozen@erbakan.edu.tr

***Abstract* - Cooling of turbine blades play a significant role in the studies carried out to increase efficiency in gas turbines. As the cooling process in turbine blades is enhanced, gas turbines are enabled to operate at higher temperatures. This allows higher efficiency to be obtained from the fuel burned in gas turbines. The NASA C3X turbine blade has been a turbine blade model that has been frequently studied in scientific studies on cooling turbine blades. In this study the effect of cooling channels on the flow of the NASA C3X turbine blade, which was modeled by obtaining geometric coordinate data from the literature, was investigated. Solid modeling of the original turbine blade with 10 cylindrical cooling channels were made by using SolidWorks® program and the flow analyzes were performed by using ANSYS Fluent® simulation program. This study aims to measure the accuracy of the designed solid model, flow volume and the selected turbulence model for using them in further studies. The data obtained as a result of the analyzes on how the cooling channels affect the flow properties are presented in the results section of the study.**

***Keywords* - Gas turbine, turbine blades, turbine blade cooling, cooling channels, flow analyzes.**

I. Introduction

GAS turbines, in their most basic terms, are systems that operate according to the action and reaction principle, which is Newton's third law of motion. In gas turbines operating according to the Brayton cycle, the compressed air in the compressors reaches high pressure and high temperature. Subsequently, the air transferred to the combustion chamber is burned with fuel there. The resulting very high energy is transferred to the turbine blades and the conversion of heat energy into mechanical energy is ensured. Finally, the waste air is discharged from the exhaust (Figure 1).

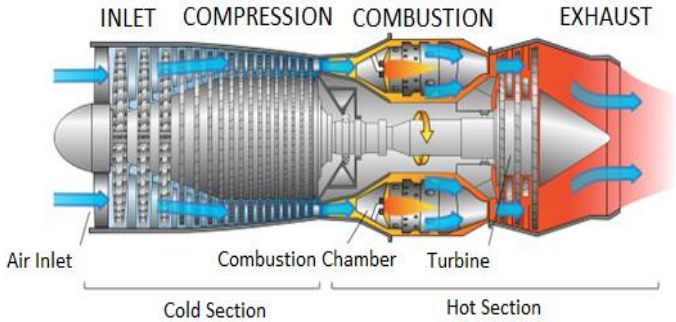

Figure 1: Schematic representation of a gas turbine [1].

The conversion of heat energy into mechanical energy in turbines is provided by the high-energy air hitting the moving turbine blades (rotor) and moving these blades. Thus, the conversion of heat energy into mechanical energy and the transfer of this mechanical energy through the shaft connected to the turbine are realized.

Turbines have fixed blades (stator) as well as moving blades. These blades meet the flow before the moving blades and are responsible for directing the air flow to the moving blades in the most efficient way (Figure 2). Proper cooling of the stator blades will enable the rotor blades to operate at higher temperatures. In this case, the efficiency obtained from gas turbines will increase, and turbines with higher powers will be produced.

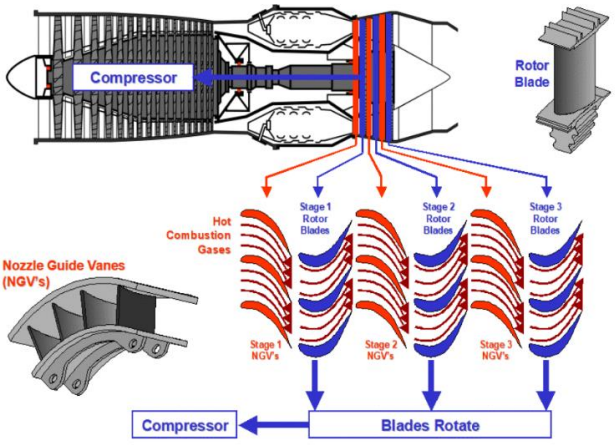

Figure 2: Display of stationary and moving blades used in turbines [2].

II. Literature Survey and Blade Design

NASA C3X type stationary turbine blade, which is one of the blade types used in turbines and frequently used by scientists in their studies, is the turbine blade whose cooling efficiency will be analyzed with its design with ten cylindrical cooling channels.

The solid modeling of NASA C3X turbine blade and the design of the cooling channels were created by using the SolidWorks® modeling program (Figure 3), through the coordinate data (Figure 4,5) obtained as a result of the literature study [3].

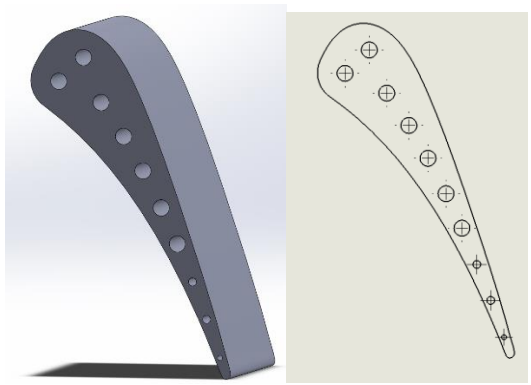

Figure 3: NASA C3X Turbine blade solid model and drawing.

R_{LE} = 1.168 cm (0.460 in.) R_{TE} = 0.173 cm (0.068 in.)

Position number	x--cm (in.)		y--cm (in.)		Position number	x--cm (in.)		y--cm (in.)	
1	0.1097	(0.0432)	11.6546	(4.5885)	40	7.4849	(2.9468)	-0.0617	(-0.0243)
2	0.3894	(0.1533)	12.1890	(4.7988)	41	7.3188	(2.8814)	0.3559	(0.1401)
3	0.7658	(0.3015)	12.6764	(4.9907)	42	7.1483	(2.8143)	0.7737	(0.3046)
4	1.2723	(0.5009)	13.0233	(5.1273)	43	6.9736	(2.7455)	1.1895	(0.4683)
5	1.8743	(0.7379)	13.1376	(5.1723)	44	6.7950	(2.6752)	1.6035	(0.6313)
6	2.4707	(0.9727)	12.9939	(5.1157)	45	6.6116	(2.6030)	2.0155	(0.7935)
7	2.9835	(1.1746)	12.6538	(4.9818)	46	6.4237	(2.5290)	2.4254	(0.9549)
8	3.3985	(1.3380)	12.1976	(4.8022)	47	6.2309	(2.4531)	2.8329	(1.1153)
9	3.7376	(1.4715)	11.6817	(4.5991)	48	6.0328	(2.3751)	3.2380	(1.2748)
10	4.0272	(1.5855)	11.1364	(4.3844)	49	5.8296	(2.2951)	3.6406	(1.4333)
11	4.2885	(1.6884)	10.5766	(4.1640)	50	5.6203	(2.2127)	4.0401	(1.5906)
12	4.5326	(1.7845)	10.0094	(3.9407)	51	5.4051	(2.1280)	4.4364	(1.7466)
13	4.7648	(1.8759)	9.4369	(3.7153)	52	5.1834	(2.0407)	4.8290	(1.9012)
14	4.9870	(1.9634)	8.8605	(3.4884)	53	4.9548	(1.9507)	5.2177	(2.0542)
15	5.2019	(2.0480)	8.2814	(3.2604)	54	4.7191	(1.8579)	5.6020	(2.2055)
16	5.4110	(2.1303)	7.7003	(3.0316)	55	4.4760	(1.7622)	5.9817	(2.3550)
17	5.6157	(2.2109)	7.1176	(2.8022)	56	4.2248	(1.6633)	6.3564	(2.5025)
18	5.8171	(2.2902)	6.5336	(2.5723)	57	3.9654	(1.5612)	6.7249	(2.6476)
19	6.0160	(2.3685)	5.9487	(2.3420)	58	3.6975	(1.4557)	7.0874	(2.7903)
20	6.2126	(2.4459)	5.3632	(2.1115)	59	3.4204	(1.3466)	7.4430	(2.9303)
21	6.4074	(2.5226)	4.7767	(1.8806)	60	3.1339	(1.2338)	7.7909	(3.0673)
22	6.5997	(2.5983)	4.1897	(1.6495)	61	2.8374	(1.1171)	8.1308	(3.2011)
23	6.7894	(2.6730)	3.6015	(1.4179)	62	2.5314	(0.9966)	8.4615	(3.3313)
24	6.9756	(2.7463)	3.0122	(1.1859)	63	2.2149	(0.8720)	8.7826	(3.4577)
25	7.1575	(2.8179)	2.4221	(0.9536)	64	1.8885	(0.7435)	9.0935	(3.5801)
26	7.3335	(2.8872)	1.8301	(0.7205)	65	1.5519	(0.6110)	9.3932	(3.6981)
27	7.5024	(2.9537)	1.2357	(0.4865)	66	1.2052	(0.4745)	9.6815	(3.8116)
28	7.6624	(3.0167)	0.6391	(0.2516)	67	0.8494	(0.3344)	9.9578	(3.9204)
29	7.8115	(3.0754)	0.4115	(0.0162)	68	0.4999	(0.1968)	10.2116	(4.0203)
30	7.8161	(3.0772)	-0.0053	(-0.0021)	69	0.3848	(0.1515)	10.3035	(4.0565)
31	7.8082	(3.0741)	-0.0516	(-0.0203)	70	0.2822	(0.1111)	10.4094	(4.0982)
32	7.7879	(3.0661)	-0.0935	(-0.0368)	71	0.1938	(0.0763)	10.5273	(4.1446)
33	7.7572	(3.0540)	-0.1288	(-0.0507)	72	0.1212	(0.0477)	10.6556	(4.1951)
34	7.7180	(3.0386)	-0.1542	(-0.0607)	73	0.0630	(0.0256)	10.7920	(4.2488)
35	7.6736	(3.0211)	-0.1681	(-0.0662)	74	0.0264	(0.0104)	10.9342	(4.3048)
36	7.6269	(3.0027)	-0.1699	(-0.0669)	75	0.0064	(0.0025)	11.0802	(4.3623)
37	7.5816	(2.9849)	-0.1588	(-0.0625)	76	0.0046	(0.0018)	11.2278	(4.4204)
38	7.5408	(2.9688)	-0.1356	(-0.0534)	77	0.0216	(0.0085)	11.3741	(4.4780)
39	7.5077	(2.9558)	-0.1026	(-0.0404)	78	0.0569	(0.0224)	11.5171	(4.5343)

Figure 4: Coordinate data of NASA C3X turbine blade [3].

Hole No.	U--cm (in.)	V--cm (in.)	Diameter--cm (in.)	Cr
1	2.377 (0.936)	1.311 (0.516)	0.630 (0.248)	1.118
2	1.057 (0.416)	1.534 (0.604)	0.630 (0.248)	1.118
3	1.981 (0.780)	3.119 (1.228)	0.630 (0.248)	1.118
4	1.981 (0.780)	4.674 (1.840)	0.630 (0.248)	1.118
5	1.869 (0.736)	6.182 (2.434)	0.630 (0.248)	1.118
6	1.666 (0.656)	7.747 (3.050)	0.630 (0.248)	1.118
7	1.412 (0.556)	9.235 (3.636)	0.630 (0.248)	1.118
8	1.087 (0.428)	10.759 (4.236)	0.310 (0.122)	1.056
9	0.737 (0.290)	12.253 (4.824)	0.310 (0.122)	1.056
10	0.345 (0.136)	13.757 (5.416)	0.198 (0.078)	1.025

Figure 5: Coordinate data of NASA C3X turbine blade cooling channels [3].

Experimental studies on this subject are limited in the literature due to its very high costs and complex process. One of the most well-known studies is the experimental study of Hylton et al. in 1983. In this experimental study, Hylton et al. selected three C3X turbine blades to simulate the gas turbine first stage [1].

In another study that references this work, Zheng et al. studied five different turbulence models including standard *k-ε*, realizable *k-ε*, SST *k-ω*, transition *k-kl-ω* and *v2f* to simulate the air flow and heat transfer of a turbine guide vane. In the light of the obtained results, it is stated that the SST k-ω turbulence model gives a good result in predicting the heat transfer accurately [4].

In this study, the study of Zheng et al. in 2015 was taken as reference when determining the geometric parameters of the turbine blade, choosing the turbulence model to be used for analysis, and determining the boundary conditions. The *SST k-ω* turbulence model, which they stated as the turbulence model that gave the most efficient results in their studies, was also selected for the flow analyzes in this study. The turbine blade geometric parameters (Table 1) and the inlet and outlet boundary conditions (Table 2,3) are also given in tables below.

Table 1: The geometrical parameters of C3X vane [4].

Blade chord	Setting angle	Air exit angle	Axial chord	Vane spacing	Throat
144.93 mm	59.89°	72.38°	78.16 mm	117.73 mm	32.92 mm

Table 2: The boundary conditions of the external gas path [4].

P_{Tin} (Pa)	T_{Tin} (K)	Tu (%)	Tv	P_{Sout} (Pa)
413286	818	8.3	30	254172

Table 3: The boundary conditions of the internal gas path [4].

No.	1	2	3	4	5	6	7	8	9	10
M (g/s)	22.2	22.1	21.8	22.8	22.5	22.5	21.6	7.44	4.77	2.56
T_{Sc} (K)	342	344	335	336	330	355	336	350	377	387
D_h (mm)	6.3	6.3	6.3	6.3	6.3	6.3	6.3	3.1	3.1	1.98
Tu (%)	10	10	10	10	10	10	10	10	10	10

Especially in recent years, with the increase in computer aided analysis methods, studies on flow and heat transfer in turbine blades have increased considerably. Using three-dimensional simulations, Yousefi et al. investigated the effects on the temperature distribution of the grooved channels, the convective heat transfer coefficient of the blade surface, the performance factor and the friction coefficient of the gas turbine blade. The researchers, who carried out their work on a modified NASA C3X gas turbine blade, in which the longitudinal ribs in the cooling channels are handled in six different configurations (Figure 6), found that the ribs in the cooling channels increased the heat transfer by 25%, while increasing the friction factor by only 3%. In addition, the performance factor has increased by 24%, while the maximum temperature has been reduced by 25 K° [3].

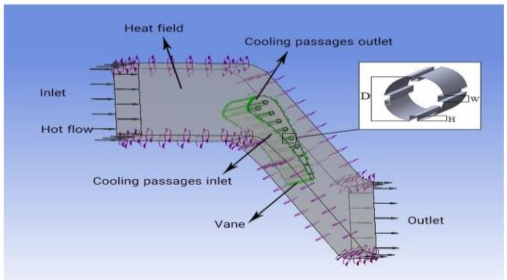

Figure 6: Geometric characteristics of ribs in cooling channels [5].

In another study conducted in 2021, Karimi et al. aimed to optimize an internal-cooled gas turbine blade by increasing the cooling performance and reducing the sensitivity of the performance to operational uncertainties. The researchers, who used the v2f turbulence model as the turbulence model to minimize the simulation errors in their studies, used the polynomial chaos method to digitize the uncertainties. The researchers stated that the main purpose of their study was to increase the service life of the blades by minimizing the maximum temperature of the blades and maximum temperature gradient [6].

Vo et al. simulated the combined heat transfer in the first-stage cooling blade (Figure 7) of a W501F engine in their study examining the effects of thermal barrier coating thickness and the refrigerant on the pressure ratio and temperature ratio of the main fluid, hot gas, in blade film cooling. As a result of the study, it was understood that a decrease of 100 K° in the fluid used as a refrigerant caused a 58 K° decrease in the average blade temperature. On the other hand, it was determined that the heat transfer coefficient decreased by 35% when a 0.8 mm thick thermal barrier coating was formed on the blade surface [5].

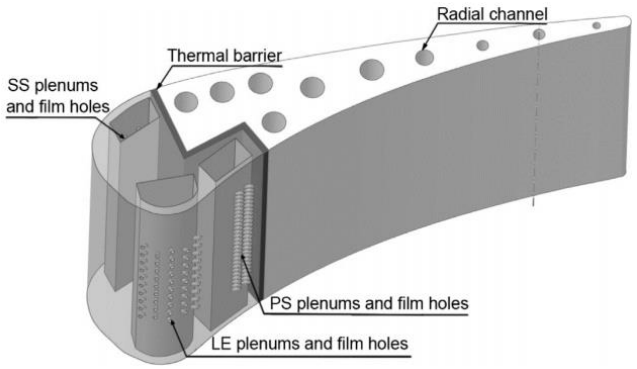

Figure 7: Geometric model of the C3X blade used in the study [7].

In a 2016 study, Mazaheri et al. optimized the shape and position of the cooling channels of a C3X turbine blade (Figure 8). In their study, where they selected the objective functions as the maximum temperature gradient and the maximum temperature along the three-dimensional blade, they modeled the shape of the cooling channels using a new method based on Bezier curves and forty design variables [6].

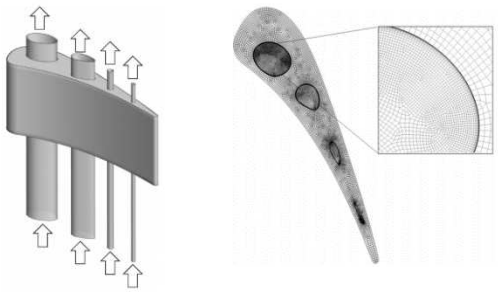

(a) (b)

Figure 8: (a) C3X blade and cooling channels, (b) Mesh structure [8]

III. Flow Analysis and Results

NASA C3X turbine, designed with reference to an experimental study conducted by Hylton et al. in 1983, was modeled in accordance with the original with ten cylindrical cooling channels. After the design process, the flow volume was created and the flow was simulated using the ANSYS® simulation program (Figure 9). A study by Zheng et al. in 2015 was taken as reference in the creation of the flow volume geometry and the determination of the boundary conditions. While creating the flow volume, in the light of the data obtained from the reference study, a flow volume with a length equal to the axial inlet length of the blade for the flow inlet region and twice the axial beam length for the flow outlet region was determined.

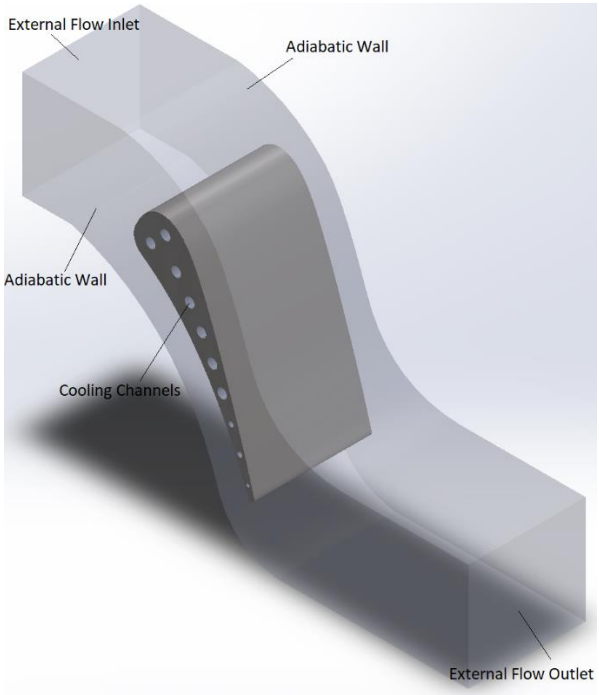

Figure 9: Flow volume modelled around NASA C3X blade

In order to simulate the flow, a suitable turbulence model must be selected. In the study by Zheng et al., which we took as a reference in the selection of the turbulence model, it was stated that compared to other models, the SST k-ω turbulence model predicts the flow in such a way that it can obtain data very close to the data obtained from experimental studies.

The SST k-ω turbulence model, first proposed in a study by Menter et al. in 1994, emerged as a mixture of k-ω and k-ε turbulence models and a turbulence model that does not contain the errors of these two models [9]. Due to all these reasons, the SST k-ω turbulence model was chosen as the turbulence model in this study.

At this stage of the study, flow inlet and outlet regions were determined and reference boundary conditions were defined for both external and internal cooling flow, and the flow was simulated using the ANSYS® program. The results obtained were taken as the output of the program and presented as graphics.

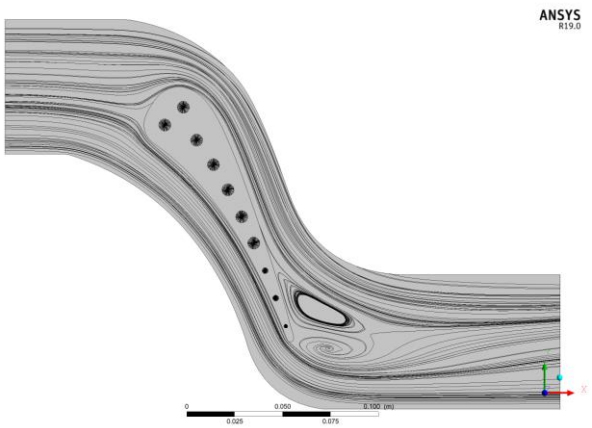

(a)

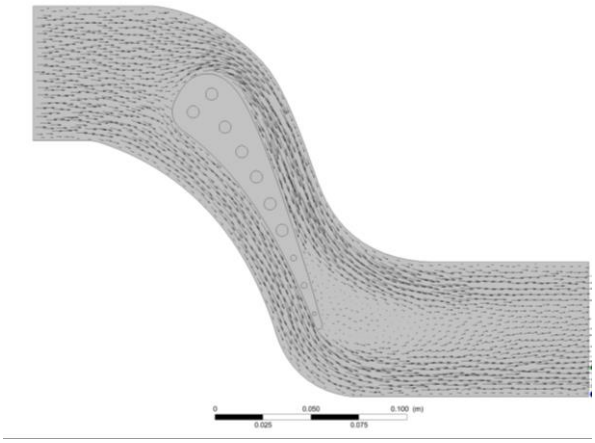

(b)

Figure 10: (a) Streamlines, (b) Velocity vector lines

When Figure 10 (a) is examined, it is clearly seen that flow separation occurs at the beginning of the pressure edge of the blade and the external flow cannot follow the pressure edge of the airfoil. It is also observed that significant reverse and circular flows occur at the ends of the pressure edge of the blade and in the continuation of the blade.

Similarly, in Figure 10 (b), the beginning of flow separation and the resulting flow separation are clearly understood. With the flow separation, it can be determined that there is a significant decrease in velocities in the regions close to the pressure edge of the blade.

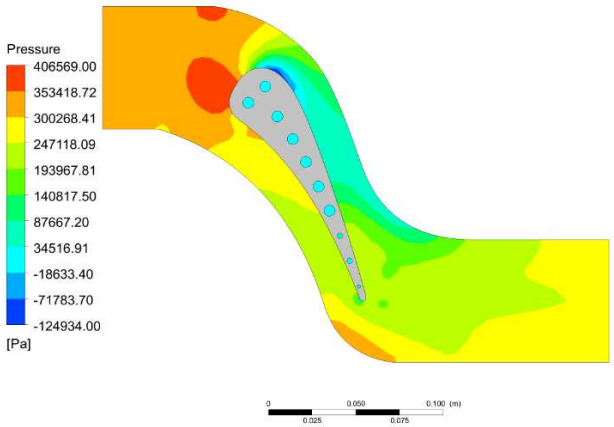

(a)

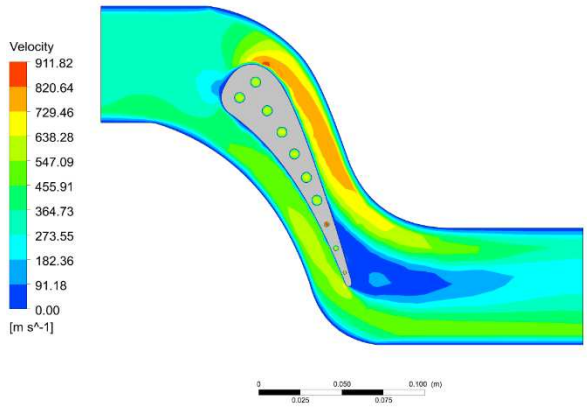

(b)

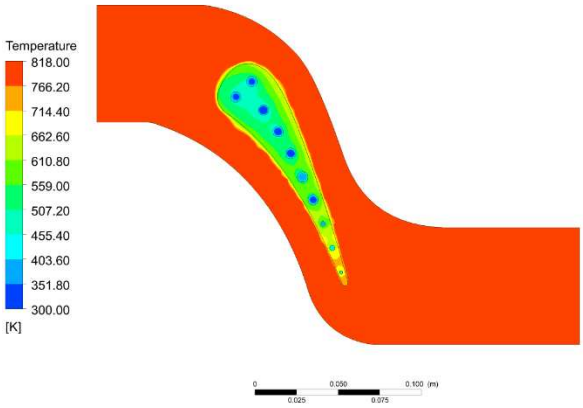

(c)

Figure 10: (a) Pressure distribution, (b) Velocity distribution, (c) Temperature distribution after the analysis

In the pressure diagram in Figure 11 (a), it is understood that the pressure reaches its highest values at the drive end, where the flow first hits the blade. In addition, it is seen that the pressure decreases at the suction side where flow separation occurs.

In Figure 11 (b) we can see the velocity distributions. Flow velocity becomes zero at the walls due to the no-slip condition. In addition, the flow velocity in the leading edge of the blade, where the flow is first encountered, is calculated to be extremely low, while the flow velocity is increased, especially in the region where flow separation is experienced at the suction edge. In addition, it can be seen that the flow rate in the seventh cooling channel is higher than the other channels. This is because although the cooling channel hydraulic diameter is suddenly reduced, the flow rate is almost the same as the flow rate through the previous channels. Since the flow rates passing through the next cooling channels are lower, the speed was not very high in those regions either.

Besides, when the velocity diagram is compared with the pressure diagram, it can be seen that the pressure decreases in the regions where the speed increases, and the speed decreases in the regions where the pressure increases as expected.

Looking at the temperature distribution in Figure 11 (c), it seems that an additional application of cooling at the trailing edge of the blade might be beneficial, although the cooling flow appears to cool the blade properly.

IV. CONCLUSION

NASA C3X turbine blade solid model with ten cylindrical cooling channels was designed using Solidworks® program. After the flow volume was created, the turbulence model and boundary conditions determined using the reference study were transferred to the ANSYS® simulation program and the flow was analyzed using this program. As a result of the flow analysis, the following conclusions were obtained:

- It has been observed that the cooling channels are quite effective in reducing the fin temperature.
- It has been revealed that the airfoil has a significant effect on the flow structure and the data to be obtained at the end of the flow analysis.
- As a result of the analysis, it was concluded that the position of the blade can be optimized in order to prevent the observed flow separation and related reverse flow.
- It was understood that it would be beneficial to repeat the analyzes with different methods in order to obtain more precise results.

V. REFERENCES

[1] Available at the website of the University of Calgary: https://energyeducation.ca/encyclopedia/Gas_turbine

[2] Available at: https://www.summaryplanet.com/engineering/Jet-engine-design.html

[3] L. D. Hylton, M. S. Mihelc, E. R. Turner, and D. A. Nealy, "Analytical and experimental evaluation of the heat transfer distribution over the surfaces of turbine vanes," *NASA Lewis Research Centre,* NASA-CR-168015, 1983.

[4] S. Zheng, Y. Song, G. Xie, and B. Sunden, "An assessment of turbulence models for predicting conjugate heat transfer for a turbine vane with internal cooling channels," *Heat Transfer Research,* 46(11), 1039-1064, 2015.

[5] A. Yousefi, A. Nejat, and M. H. Sabour, "Ribbed channel heat transfer enhancement of an internally cooled türbine vane using cooling conjugate heat transfer simulation," *Thermal Science and Engineering Progress*, 19, 100641, 2020.

[6] M. S. Karimi, M. Raisee, S. Salehi, P. Hendrick, and A. Nourbakhsh, "Robust optimization of the NASA C3X gas turbine vane under uncertain operational conditions," *International Journal of Heat and Mass Transfer,* 164, 120537, 2021.

[7] D. T. Vo, D. T. Mai, B. Kim, J. Ryu, "Numerical study on the influence of coolant temperature, pressure, and thermal barrier coating thickness on heat transfer in high-pressure blades," *International Journal of Heat and Mass Transfer,* 189, 122715, 2022.

[8] K. Mazaheri, M. Zeinalpour, H. R. Bokaei, "Turbine blade cooling passages optimization using reduced conjugate heat transfer methodology," *Applied Thermal Engineering,* 103, 1228-1236, 2016.

[9] F. R. Menter, "Two-equation eddy viscosity turbulence models for engineering applications," *American Institute of Aeronautics and Astronautics Journal,* 32/8, 1598-1605, 1994.

The Role of Thickness and Position of Partial Metal Foam in Jet Impingement Cooling

M. ALBAYRAK[1], K. DAĞIDIR[1] and B. SARPER[1]

[1] Tarsus University, Mersin/Turkey, kayhandagidir@tarsus.edu.tr
[1]Tarsus University, Mersin/Turkey, melisa_albayrak@tarsus.edu.tr
[1]Tarsus University, Mersin/Turkey, bugrasarper@tarsus.edu.tr

Abstract - **In this study, the effects using partial metal foam in electronics cooling are analyzed numerically. The focus is on the role of thickness and location of the partial metal foam on convective heat transfer, while porosity ($\varepsilon = 0.9005$), pore density ($\omega = 20$ PPI), permeability ($K = 0.9 \times 10^{-7}$) and jet Reynolds number ($Re_J = 50$) do not change. The jet flow is considered to be two-dimensional and laminar, and the flow and heat transfer in the porous media are modeled using the Brinkman-Darcy-Forchheimer and local thermal non-equilibrium (LTNE) models, respectively. As a result of the study, it is determined that convective heat transfer improves by up to 36.26% in the use of metal foam compared to the case without metal foam.**

Keywords – **Electronics Cooling, Jet Impingement, Partial Metal Foam, Porous Media.**

I. INTRODUCTION

NOWADAYS, researchers make an effort to develop innovative methods for the improvement of technologies based on energy efficiency. Applications related to porous materials, also called foam, can also be considered as one of these innovative methods. Porous materials are used extensively in heat transfer applications due to properties such as light weight, high thermal conductivity, high permeability, and large heat transfer surface areas. Metal foams are frequently preferred in various industrial applications such as electronics cooling, battery cooling and heat recovery [1, 2].

It is predicted that the use of metal foam may be beneficial in the jet impingement applications, primarily used in the electronics cooling. Wong and Saeid [3] numerically investigated the effects of the porous material completely covering the flow domain in a heated channel in laminar jet impingement. In that study, it was stated that the average Nusselt number augmented with increasing porosity. Dorea and Lemos [4] numerically investigated the heat transfer characteristics of a heated surface covered with porous material in laminar jet impingement. In that study, it was noted that the porous medium affected the temperature distribution in the stagnation zone. Buonomo et al. [5] experimentally investigated the effects of the use of porous material on the heat transfer behavior of a wall heated by constant heat flux and cooled by a laminar jet. The study reported that the use of metal foam improved heat transfer from the heated wall. Buonomo et al. [6] numerically investigated the heat transfer characteristics of the laminar impinging jet in a parallel plate channel partially covered with a porous medium. The study emphasized that the use of metal foam provided an improvement in heat transfer. Hosseinalipour et al. [7] numerically investigated the influence of a porous block placed on a heated surface on the heat transfer characteristics in the laminar impinging jet. In the study, it was observed that the use of porous material could change the Nusselt number distribution on the heated plate.

The position and thickness of the metal foams placed in the flow domain are fixed in the recent studies. It is known that metal foams are used in different positions and thicknesses as applied in different application areas [8]. It is anticipated that the use of metal foams in different positions and thicknesses in impinging jets can improve heat transfer rate. Thus, in this study, the use of a partial aluminum foam at different locations for various thicknesses with the constant values of porosity, pore density, permeability and Reynolds number is investigated numerically.

II. NUMERICAL METHOD

A. Problem Description and Mathematical Model

Schematic representation of the impinging jet geometry investigated in this study is given in Fig. 1a. Since the problem is symmetrical, only the half of the geometry is taken into account and the symmetrical solution is realized. In the schematic representation, W, L, s, H and g represent half of the nozzle width, half of the heated surface length, half of the adiabatic surface length, nozzle-to-heated surface distance and gravitational acceleration, respectively. The target plate is heated locally and has a constant temperature (T_H). Other parts of the target plate and upper surfaces are adiabatic. The air at the inlet of the jet nozzle has uniform velocity (u_0) and temperature (T_0). At the outlet, the outflow boundary condition is applied. The Reynolds number used in the study is 50 and the flow is laminar and steady-state.

The configurations of the aluminum foam are given in Fig. 1b. The aluminum foam used in the study is first placed on the upper surface and then positioned on the heated surface. Except for the Case 0 and Case 1, the aluminum foam length (L_p) is fixed and is 27 mm. W, L, H and s are 3 mm, 30 mm, 30 mm and 180 mm, respectively. In Case 0, no metal foam is used, and in Case 1, the metal foam covers the whole area except the

underneath of the jet nozzle. The thickness of the aluminum foam (t_p) is gradually changed and its effect on convective heat transfer is evaluated for other cases.

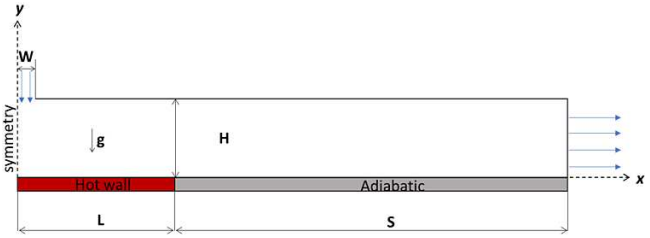

a) Schematic representation of the symmetrical flow domain.

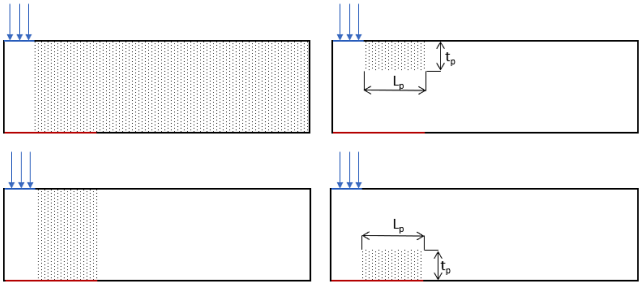

b) Position and thickness of porous region.

Figure 1: Schematic representations of the flow domain considered cases.

All thermophysical properties of air does not change with temperature. It is considered that the metal foam has uniform, homogeneous and isotropic porous medium properties. In numerical analyses, the Brinkman-Darcy-Forchheimer flow and Local Thermal Nonequilibrium (LTNE) energy models are used together [9]. Conservation equations for the clear zone and porous zone are expressed separately [10].

Navier-Stokes and energy equations for the flow region without metal foam are given in Equations from (1) to (4).

Continuity equation:

$$\frac{\partial u}{\partial x}+\frac{\partial v}{\partial y}=0 \tag{1}$$

x-momentum equation:

$$\rho_f\left(u\frac{\partial u}{\partial x}+v\frac{\partial u}{\partial y}\right)=-\frac{\partial P}{\partial x}+\mu_f\left(\frac{\partial^2 u}{\partial x^2}+\frac{\partial^2 u}{\partial y^2}\right) \tag{2}$$

y-momentum equation:

$$\rho_f\left(u\frac{\partial v}{\partial x}+v\frac{\partial v}{\partial y}\right)=-\frac{\partial P}{\partial y}+\mu_f\left(\frac{\partial^2 v}{\partial x^2}+\frac{\partial^2 v}{\partial y^2}\right) \tag{3}$$

Energy equation:

$$\left(\rho c_p\right)_f\left(u\frac{\partial T_f}{\partial x}+v\frac{\partial T_f}{\partial y}\right)=k_f\left(\frac{\partial^2 T_f}{\partial x^2}+\frac{\partial^2 T_f}{\partial y^2}\right) \tag{4}$$

Here, the terms u and v represent the velocities in the x and y directions, respectively. T and P represent the fluid temperature and pressure, respectively. The subscript f represents the fluid. Density, viscosity, specific heat and thermal conductivity are represented by the symbols ρ, μ, c_p and k, respectively.

Terms in the Navier-Stokes and energy equations given for the porous media are obtained by applying the representative elementary volume approach and the volume average technique [11,12]. Thus, these terms are expressed with the subscript of p.

Navier-Stokes and energy equations for the porous media are given in Equations from (5) to (9).

Continuity equation:

$$\frac{\partial u_p}{\partial x}+\frac{\partial v_p}{\partial y}=0 \tag{5}$$

x-momentum equation:

$$\frac{\rho_f}{\varepsilon^2}\left(u_p\frac{\partial u_p}{\partial x}+v_p\frac{\partial u_p}{\partial y}\right)=-\frac{\partial P_p}{\partial x}+\underbrace{\frac{\mu_f}{\varepsilon}\left(\frac{\partial^2 u_p}{\partial x^2}+\frac{\partial^2 u_p}{\partial y^2}\right)}_{Brinkman\ term}-\underbrace{\frac{\mu_f}{K}u_p}_{\substack{Darcy\\ term}}-\underbrace{\frac{C_F}{K^{\frac{1}{2}}}\rho_f\sqrt{{u_p}^2+{v_p}^2}u_p}_{Forchheimer\ term} \tag{6}$$

y-momentum equation:

$$\frac{\rho_f}{\varepsilon^2}\left(u_p\frac{\partial v_p}{\partial x}+v_p\frac{\partial v_p}{\partial y}\right)=-\frac{\partial P_p}{\partial y}+\underbrace{\frac{\mu_f}{\varepsilon}\left(\frac{\partial^2 v_p}{\partial x^2}+\frac{\partial^2 v_p}{\partial y^2}\right)}_{Brinkman\ term}-\underbrace{\frac{\mu_f}{K}v_p}_{\substack{Darcy\\ term}}-\underbrace{\frac{C_F}{K^{\frac{1}{2}}}\rho_f\sqrt{{u_p}^2+{v_p}^2}v_p}_{Forchheimer\ term} \tag{7}$$

In equations given for porous media, ε, K and C_F express the porosity, permeability and Forchheimer coefficient, respectively.

The energy equation is separately considered for both the fluid (air) phase and the solid (aluminum foam) phase.

Fluid phase:

$$\left(\rho c_p\right)_f\left(u_p\frac{\partial T_f}{\partial x}+v_p\frac{\partial T_f}{\partial y}\right)=\varepsilon k_f\left(\frac{\partial^2 T_f}{\partial x^2}+\frac{\partial^2 T_f}{\partial y^2}\right)+h_{sf}\,a_{sf}\left(T_s-T_f\right) \tag{8}$$

Solid phase:

$$(1-\varepsilon)\,k_s\left(\frac{\partial^2 T_s}{\partial x^2}+\frac{\partial^2 T_s}{\partial y^2}\right)-h_{sf}\,a_{sf}\left(T_s-T_f\right)=0 \tag{9}$$

In the LTNE energy model, h_{sf} and a_{sf} are calculated using the Eqs. (10) and (11) [13].

$$h_{sf} = \begin{cases} 0.75\, Re_{d_b}^{0.4}\, Pr_{air}^{0.37} \left(\frac{k_f}{d_b}\right), & 1 \le Re_{d_b} \le 40 \\ 0.51\, Re_{d_f}^{0.5}\, Pr_{air}^{0.37} \left(\frac{k_f}{d_b}\right), & 40 \le Re_{d_b} \le 1000 \\ 0.26\, Re_{d_f}^{0.6}\, Pr_{air}^{0.37} \left(\frac{k_f}{d_b}\right), & 1000 \le Re_{d_b} \le 2 \times 10^5 \end{cases} \quad (10)$$

$$\alpha_{sf} = \frac{3\pi d_b}{(0.59\, d_p)^2}\left(1 - e^{-\frac{1-\varepsilon}{0.04}}\right) \quad (11)$$

Here, subscript s represents the solid phase, α_{sf} and h_{sf} represent the specific surface area density and the heat transfer coefficient of porous media, respectively.

$$\frac{K}{{d_p}^2} = 0.00073(1-\varepsilon)^{-0.224}\left(\frac{d_b}{d_p}\right)^{-1.11} \quad (12)$$

$$c_f = 0.00212(1-\varepsilon)^{-0.132}\left(\frac{d_b}{d_p}\right)^{-1.63} \quad (13)$$

Here, d_b and d_p represent fiber and pore diameters, respectively.

The related dimensionless numbers are calculated by the following equations.

The jet Reynolds number is:

$$Re_j = \frac{\rho_f u_o 2W}{\mu_f} \quad (14)$$

The Prandtl number is:

$$Pr_{air} = \frac{\mu_f c_p}{k_f} \quad (15)$$

The local Nusselt numbers for fluid and solid zones are:

$$Nu_f = \frac{h_f 2W}{k_f} \quad (16)$$

$$Nu_s = \frac{h_s 2W}{k_f} \quad (17)$$

The local and average total Nusselt numbers are:

$$Nu_{tot} = \frac{h_{tot} 2d}{k_f} = \frac{(h_f + h_s)2d}{k_f} \quad (18)$$

$$Nu_{tot,ave} = \frac{h_{tot,ave} 2W}{k_f} = \frac{(h_{f,ave} + h_{s,ave})2W}{k_f} \quad (19)$$

The metal foam properties used in the analyses are given in Table 1. Investigations are performed at a constant jet Reynolds number of 50.

Table 1. Aluminum foam properties [14].

ω [PPI]	ε	Kx10^7 [m^2]	C_F
20	0.9005	0.90	0.088

B. *Numerical Solution Procedure*

Numerical analyses are performed using the ANSYS Fluent 2021 R2, a commercial computational fluid dynamics software. The SIMPLE algorithm is applied for the coupling of velocity and pressure, and the PRESTO scheme is used for interpolation of the pressure. The momentum equations are discretized by the 2nd order upwind scheme. The convergence criteria are met with an approximation of 10^{-5} for the velocity components and 10^{-8} for the temperature components.

C. *Grid structure*

In the simulations, a rectangular grid structure is used, which is concentrated towards the heated plate and the adiabatic upper surface. For the grid independency study, solutions are performed on four different grids, and the total average Nusselt numbers are calculated on the heated surface for each grid. When the results in Table 2 are examined, it is considered that the number of 25200 cells is sufficient for final simulations.

Table 2. Results of the grid independency.

Cell no.	$Nu_{tot,ave}$	Error (%)
6240	4.066	-
11200	4.098	0.799
25200	4.128	0.736
99360	4.154	0.623

D. *Validation of the Solution Algorithm*

The numerical model applied in this study is validated using a similar study in the literature [9]. The average Nusselt numbers obtained as a result of the validation performed for three different Peclet numbers (350, 750, and 1500) as shown in Fig. 2. As seen in Fig. 2, the numerical model agrees with the literature [9], especially at low Peclet numbers, and these results are considered to be sufficient in terms of validation of the solution algorithm.

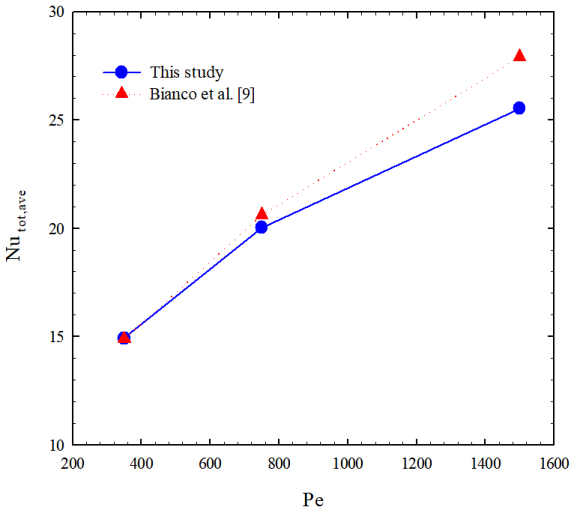

Figure 2: Results of the validation study.

III. Results and Discussion

In this study, the role of partial aluminum foam thickness and location on the jet impingement cooling characteristics of a heated plate is numerically investigated. The focal point of the study is on the influence of the thickness and location of the partial metal foam on the convective heat transfer characteristics, while porosity ($\varepsilon = 0.9005$), pore density ($\omega = 20$ PPI), permeability ($K = 0.9 \times 10^{-7}$) of the aluminum foam and jet Reynolds number ($Re_J = 50$) are held constant.

Velocity and temperature contours are given in Fig. 3 for all studied cases. In Case 0, there is no aluminum foam in the flow domain. In Case 1, the aluminum foam covers the entire flow domain except for the stagnation region, while in Case 2, the top of the heated plate is completely covered with aluminum foam, except for the stagnation region. In Case 0, the air coming out of the nozzle impinges the heated plate and then flows to the outlet where the pressure is lower. In the wall jet region, the boundary layer thickness gradually increases, and at about x=0.04'm, the fluid separates from the surface. In addition, a large secondary flow zone arises next to the jet nozzle. Parallel to the hydrodynamic boundary layer, the thermal boundary layer thickness also increases in this case, as expected. In Case 2, the velocity and temperature fields are almost the same as in Case 1. From Case 3 to Case 7, the thickness of the partial aluminum foam is gradually increased towards the heated plate in 5 mm increments. In Case 3, it is seen that a large secondary cell is formed in the vicinity of aluminum foam, and this cell is divided into two with an increase in the thickness of the foam. In Cases 6 and 7, the cells downstream of the foam appear, while the cells underneath the foam disappear. When examining the temperature contours, it is seen that the cold air leaving the nozzle significantly affects the aluminum foam from the Case 3 to Case 5. In these cases, the temperature of the air inside the foam is almost equal to the jet temperature. Further increase in the foam thickness increases the interaction of the heated plate with the foam, causing the foam to heat up slightly. In Case 8 and beyond, the foam is in contact with the heated plate, while the foam thickness is reduced by 5 mm decrements. When the velocity contours are examined, the air penetrates into the aluminum foam in Case 8, but a secondary cell is formed at about x=0.04 m. The gradual reduction in foam thickness causes the formation of another cell downstream of the jet nozzle, and the width of the secondary cell increases as the foam thickness decreases. This indicates that the aluminum foam exhibits an obstacle behavior. When the temperature contours are examined, it is seen that the aluminum foam is heated by absorbing the heat from the heated plate, and the air temperature in the foam is uniform.

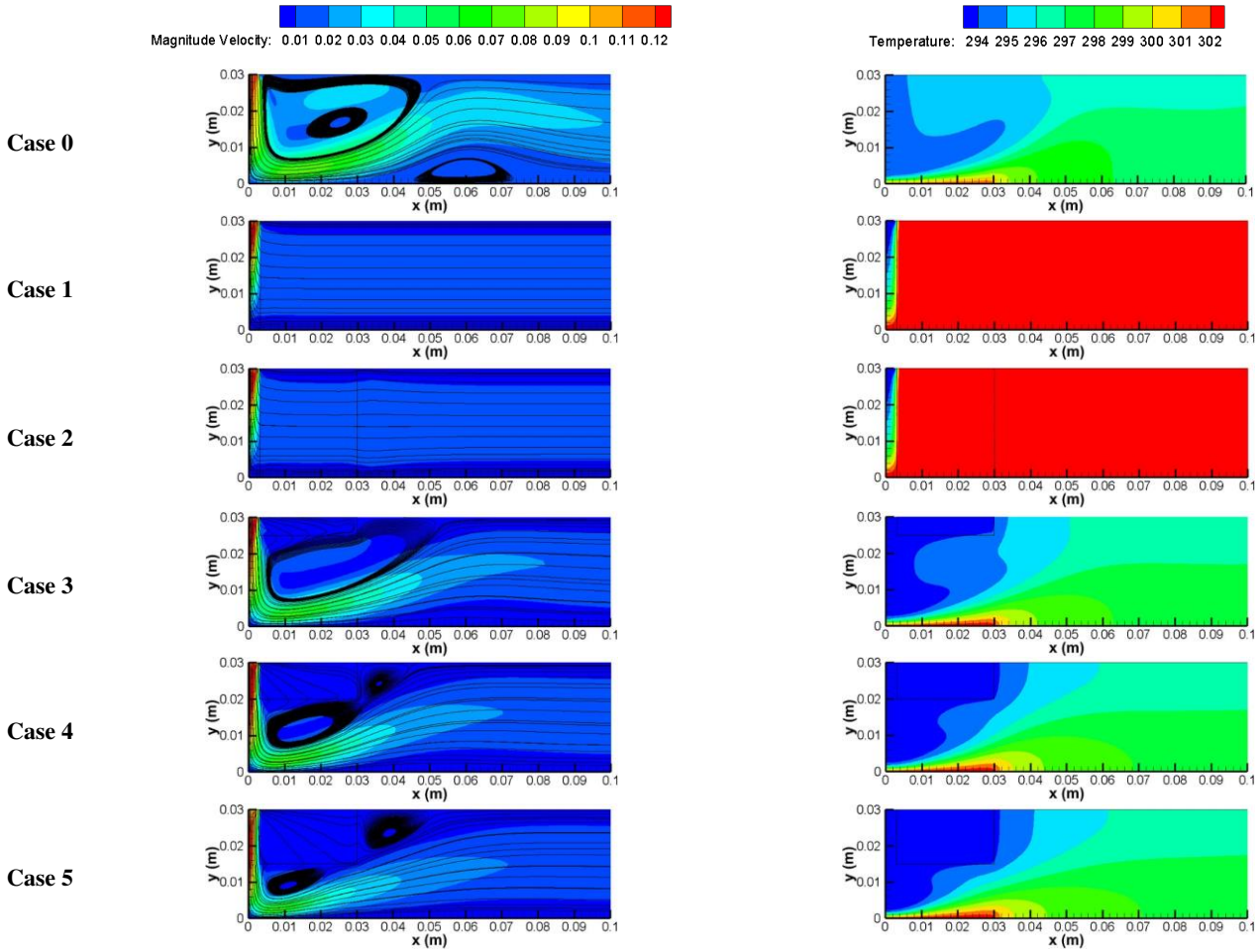

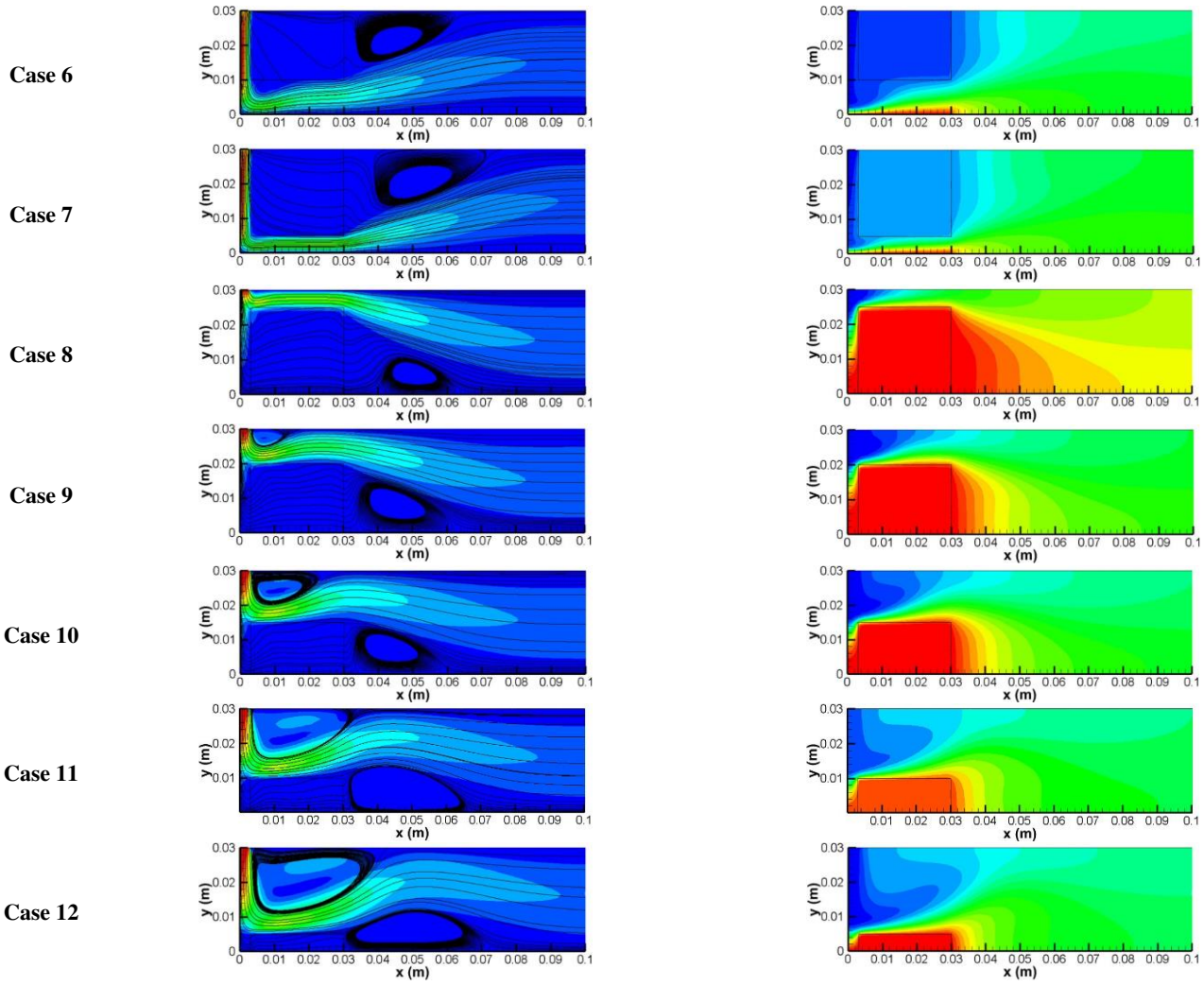

Figure 3: Velocity and temperature contours for different cases.

The total local Nusselt number variation on the heated plate for all cases is shown in Fig. 4. In Cases 1 and 2, the local Nusselt number values are close to each other and higher than in other cases studied. In contrast to Case 2, the local Nusselt number increases towards the outlet in Case 1. This is due to the fact that the aluminum foam fills the flow region up to the outlet in Case 1. In Cases 1 and 2, the local Nusselt number values are very low in the stagnation region, since the aluminum foam fills the flow region. When the aluminum foam is placed on top, the local Nusselt number values are higher in the stagnation region due to the cross-sectional narrowing with the increase of the foam thickness. When the foam is placed on the heated plate, the local Nusselt number values in the stagnation region are very close to zero, similar to the Cases 1 and 2. At this point, the increase in foam thickness increases the local Nusselt number, especially in the wall jet region.

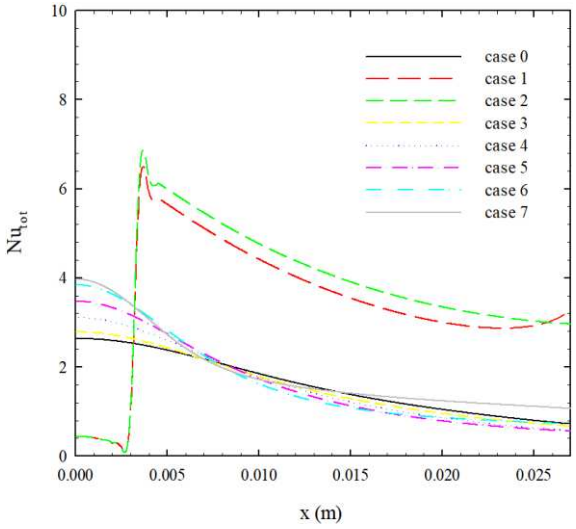

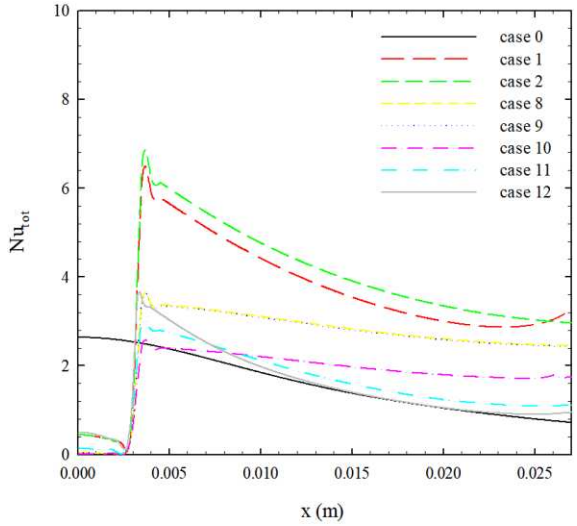

Figure 4: Total local Nusselt number variation at the heated plate for different cases.

The total average Nusselt number variation on the heated plate due to the change in aluminum foam thickness is shown in Fig.5. The use of aluminum foam improves convective heat transfer, while the increase in foam thickness promotes this improvement. In addition, it is seen that aluminum foam affects the Nusselt number more when it is in contact with the heated plate than when it is not, and the Nusselt number is the highest when the top of the heated plate is completely covered with aluminum foam.

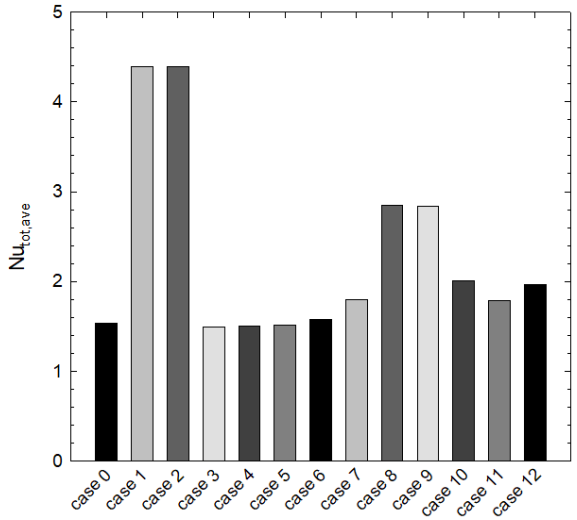

Figure 5: Total average Nusselt numbers for different cases.

IV. Conclusion

In this study, the role of thickness and location of the partial metal foam on jet impingement cooling of a heated plate is numerically investigated. The important findings of the study are as follows:

- The location and thickness of the partial metal foam significantly affect the temperature and velocity fields.
- In all cases except Cases 1 and 2, secondary flows occur within the flow domain.
- Temperature fields are significantly affected by the velocity distribution.
- Secondary flows occurring near the jet nozzle and in the vicinity of aluminum foam are affected by foam location and thickness.
- Increasing the foam thickness while the foam is on top improves convective heat transfer. Similar results are valid for cases where the foam is on the heated plate, but the results obtained for Case 10 and 11 are quite close to each other.
- While convective heat transfer is highest in Cases 1 and 2, the heat transfer rate is also higher when aluminum foam comes into contact with the heated plate.
- When the results are evaluated, it is considered that the aluminum foam is a good alternative to improve convective heat transfer in impinging jet applications.

References

[1] A. T. W. Kuruneru, K. Vafai, E. Sauret, and Y. T. Gu, "Application of porous metal foam heat exchangers and the implications of particulate fouling for energy-intensive industries," *Chemical Engineering Science*, vol. 228 (115968), 2020.

[2] S. Rashidi, M. H. Kashefi, K. C. Kim, and O. Samimi-Abianeh, "Potentials of porous materials for energy management in heat exchangers - A comprehensive review," *Applied Energy*, vol. 243, pp. 206–232, 2019

[3] K. C. Wong and N. H. Saeid, "Numerical study of mixed convection on jet impingement cooling in a horizontal porous layer under local thermal non-equilibrium conditions," *International Journal of Thermal Sciences*, vol. 48:5, pp. 860-870, 2009.

[4] F. T. Dorea and M. J. S. Lemos, "Simulation of laminar impinging jet on a porous medium with a thermal non-equilibrium model," *International Journal of Heat and Mass Transfer*, vol. 53:23–24, pp. 5089-5101, 2010.

[5] B. Buonomo, L. Cirillo, O. Manca, N. Mansi, and S. Nardini, "Confined impinging jets in porous media," *Journal of Physics: Conference Series*, vol. 745(032142), 2016.

[6] B. Buonomo, O. Manca, S. Nappo, and S. Nardini, "Numerical investigation on laminar slot-jet impinging on a surface at uniform heat flux in a channel partially filled with a porous medium," *Energy Procedia*, vol. 148, pp. 790-797, 2018.

[7] S. M. Hosseinalipour, S Rashidzadeh, M. Moghimi, and K Esmailpour, "Numerical study of laminar pulsed impinging jet on the metallic foam blocks using the local thermal non-equilibrium model," *Journal of Thermal Analysis and Calorimetry*, vol. 141, pp. 1859-1874, 2020.

[8] K. Dağıdır, B. Sarper and MT Erdinç , "The numerical investigation of the effects of porous material pore density and thickness on heat transfer and pressure drop in in-line type pipe bundles," *Dokuz Eylul University Faculty of Engineering Journal of Science and Engineering*, vol. 24:71, pp. 447-461. 2022.

[9] V. Bianco, B. Buonomo, A. Pasqua, O. Manca, "Heat transfer enhancement of laminar impinging slot jets by nanofluids and metal foams," *Thermal Science and Engineering Progress*, vol. 22: 100860, 2021.

[10] S. Akar, S. Rashidi, and J.A. Esfahani, "Appropriate position of porous insert in a heat exchanger by thermohydraulic analysis", *Heat Transfer-Asian Res.*, vol. 46, pp. 1363-1379, 2017.

[11] S. Whitaker, "The Method of Volume Averaging," Springer, Netherlands, 1998.

[12] D. A. Nield, A. Bejan, "Convection in Porous Media," Fourth Ed., Springer, New York. 2013.

[13] A. Bhattacharya, V. V. Calmidi, R. L. Mahajan. Thermophysical properties of high porosity metal foams, *International Journal of Heat and Mass Transfer*, vol. 45, pp. 1017-1031, 2002.

[14] V. Calmidi, R. L. Mahajan, "Forced convection in high porosity metal foams," *Asme J. Heat Transfer*, vol. 122, pp. 557-565, 2000.

A Numerical Approach for Modeling the Shunt Damping of Thin Panels with Arrays of Separately Piezoelectric Patches

Peyman Lahe Motlagh[1], Mustafa Kemal Acar[2]
[1] Gebze Technical University, Kocaeli/Turkey, peyman.lahe@gtu.edu.tr
[2] Gebze Technical University, Kocaeli/Turkey, mkemalacar@gtu.edu.tr

***Abstract* - Two-dimensional thin plates are widely used in many aerospace and automotive applications. Among many methods for the attenuation of vibration of these mechanical structures, piezoelectric shunt damping is a promising way. It enables a compact vibration damping method without adding significant mass and volumetric occupancy. Analyzing the dynamics of these electromechanical systems requires precise modeling tools that properly consider the coupling between the piezoelectric elements and the host structure. This paper presents a methodology for separately shunted piezoelectric patches for achieving higher performance on vibration attenuation. The Rayleigh-Ritz method is used for performing the modal analysis and obtaining the frequency response functions of the electro-mechanical system. The effectiveness of the method is investigated for a broader range of frequencies, and it was shown that separately shunted piezoelectric patches are more effective.**

***Keywords* - piezoelectric patches, Rayleigh-Ritz model, shunt damping, electromechanical systems**

I. INTRODUCTION

Mechanical structures are exposed to vibrations caused by operational or environmental sources, which can be undesirable, Over the decades, many passive and semi-passive systems have been proposed for reducing these vibrations [1], [2]. Piezoelectric structures have been widely used in a range of applications including vibration control [3], [4], energy harvesting [5], [6], structural health monitoring [7]. Over the past few decades, among the transducers that convert the mechanical (electrical) energy to electrical (mechanical) energy, piezoelectric transducers are mostly preferred to the electromagnetic [8], [9], and electrostatic [8], [10], ones due to their high power density and ease of manufacturing at different size scales [11]. The most common use of piezoelectric materials in the form of patches/layers is by integrating them to the surfaces of flexible beam/plate-like structures, and then utilize them in bending motion for generating an electrical signal and vice versa (applying a voltage to generate a bending deformation). Piezoelectric patches have been used for shunt damping applications that focus on designing simple electrical circuits that efficiently reduce the structural vibrations [12]. Ideally, performance requirements include stability and low energy consumption. The shunt circuit is said to be passive if it does not require an external power supply (e.g. R-shunt) and semi-passive if the circuit operation needs external power supply but does not deliver any power to the mechanical structure (e.g. SSDI) [13], [14]. A resistor connected to the piezoelectric transducer provides the simplest means of achieving energy dissipation and thus vibration damping [5]. In energy harvesting, vibration control, and actuation/sensing applications, piezoelectric materials are typically in the form of thin square patches that are bonded to specific locations on the surface of the thin plates. For the implementation of these structures, [2], [15] presents an electro-elastic model of a thin-laminated composite plate with surface bonded piezoelectric patches by considering the mass and stiffness contribution of the patches as well as the two-way electromechanical coupling effect. Based on the above studies conducted on the modeling of piezoelectric patches bonded on thin plate structures, a new approach is proposed in this study to obtain broadband frequency shunt damping. To cover the electro-mechanical equations for separately shunted circuits and neutral axis shift was included in the electro-mechanical model to accommodate when a single patch is used on one side of the host plate. In addition, an optimization study is performed to determine the optimized design parameters of the shunt circuit (i.e. Resistor values and number of patches) to minimize the vibration amplitudes at the first three modes of the structure. It was shown that the separated patches improved the shunt damping performance which was a significant observation of the present study.

II. ANALYTICAL MODEL OF A THIN PLATE WITH MULTIPLE PIEZOELECTRIC PATCHES

In this section, a brief description of the model of a thin plate with multiple piezoelectric patches is given based on the Kirchhoff plate theory [15]. Figure1, presents the host plate with all four edges clamped (CCCC) boundary conditions and the structurally integrated piezoelectric patches in separated and connected configurations, respectively.

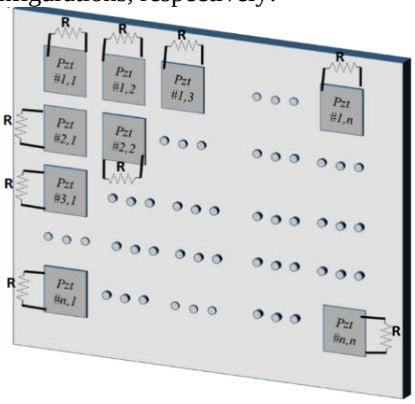

Figure 1: Separated configuration of the piezoelectric patches and the host plate

III. CONSTITUTIVE EQUATIONS OF THE THIN PLATE WITH PIEZOELECTRIC PATCHES

Since the piezoelectric patches are typically manufactured as a thin plate, piezoelectric patch skin can be modeled as a two-dimensional Kirchhoff plate. According to Kirchhoff plate theory, the deflection of the middle surface is small compared to the thickness of the skin. Since the normal stress σ_{zz} in the thickness direction is much smaller compared to the in-plane stresses, it can be ignored under the assumption of the thin plate theory. The material of the structural layer is assumed to be isotropic:

$$\begin{pmatrix}\sigma_{xx}\\ \sigma_{yy}\\ \tau_{xy}\end{pmatrix} = \frac{Y_s}{1-{\upsilon_s}^2}\begin{bmatrix}1 & \upsilon_s & 0\\ \upsilon_s & 1 & 0\\ 0 & 0 & (1-\upsilon_s)/2\end{bmatrix}\begin{pmatrix}\varepsilon_{xx}\\ \varepsilon_{yy}\\ \gamma_{xy}\end{pmatrix} \quad (1)$$

The constitutive equations of a piezoelectric patch are expressed in a reduced form as Eq. (2) [16], [17]:

$$\begin{pmatrix}\sigma_{xx}\\ \sigma_{yy}\\ \tau_{xy}\\ D_3\end{pmatrix} = \begin{bmatrix}\bar{c}_{11} & \bar{c}_{12} & 0 & -\bar{e}_{31}\\ \bar{c}_{12} & \bar{c}_{11} & 0 & -\bar{e}_{31}\\ 0 & 0 & \bar{c}_{66} & 0\\ \bar{e}_{31} & \bar{e}_{31} & 0 & {\varepsilon^s}_{33}\end{bmatrix}\begin{pmatrix}\varepsilon_{xx}\\ \varepsilon_{yy}\\ \gamma_{xy}\\ E_{33}\end{pmatrix} \quad (2)$$

Where $\bar{c}_{ij}$ are reduced elastic moduli of the piezoelectric patches, $\bar{e}_{ij}$ and ε^s_{33} are piezoelectric constant and dielectric permittivity, respectively. Hamilton's principle is used to determine the equation of motion Eq. (3):

$$\delta \oint_{t_1}^{t_1}(KE - PE + W_p)\,dt = 0 \quad (3)$$

Where kinetic energy, potential energy, and applied external work is indicated as KE, PE, and Wp respectively. Kinetic energy of the system can be formulated as:

$$KE = \tfrac{1}{2}\iint_S m(x,y)\dot{w}^2\,dS \quad (4)$$

where S is the area of the system including the top surfaces of the piezo-patches and the thin composite plate. Here, $m(x,y)$ and $\dot{w}$ are the mass per unit area and the velocity terms. The equivalent mass per unit area can be derived as Eq. (5):

$$m(x,y) = \rho_s h_s + \rho_p h_p P(x,y) \quad (5)$$

Here ρ_s, ρ_p are densities and h_s and h_p are the thicknesses of the host plate and the piezoelectric patch, respectively. The indicator function $P(x,y)$ is defined to identify the areas where k piezoelectric patches are attached to the surface of the structural layer by :

$$P(x,y) = \sum_{i=1}^{k}\left[H\left(x-x_{i,1}\right) - H(x-x_{i,2})\right] \times \left[H\left(y-y_{i,1}\right) - H(y-y_{i,2})\right] \quad (6)$$

Where $x_1, x_2, y_1, and\ y_2$ are the vertices of the area along x- and y-axes, respectively, and H denotes the Heaviside unit step function. Potential energy of the system can be written as:

$$PE = PE_s + PE_p = \tfrac{1}{2}\iiint_{V_s}\left\{(\sigma_{xx}\varepsilon_{xx})_s + \left(\sigma_{yy}\varepsilon_{yy}\right)_s + \left(\tau_{xy}\gamma_{xy}\right)_s\right\}dV_s + \tfrac{1}{2}\iiint_{V_p}\left\{(\sigma_{xx}\varepsilon_{xx})_p + \left(\sigma_{yy}\varepsilon_{yy}\right)_p + \left(\tau_{xy}\gamma_{xy}\right)_p\right\}dV_p \quad (7)$$

where, V_s and V_p are the volumes of the thin composite plate and the piezo-ceramic patch, respectively. The potential energy stored in the piezo-patches can be written as:

$$PE_P = \tfrac{1}{2}\sum_{l=1}^{2}\iint_{S_p} P(x,y)\left\{D_{11}^p\left(\frac{\partial^2 w}{\partial x^2}\right)^2 + 2D_{12}^p\left(\frac{\partial^2 w}{\partial y^2}\right)\left(\frac{\partial^2 w}{\partial x^2}\right) + D_{11}^p\left(\frac{\partial^2 w}{\partial y^2}\right)^2 + 4D_{66}^p\left(\frac{\partial^2 w}{\partial xy}\right)^2 - \bar{e}_{31}v(t)\left(\frac{h_s+h_p}{2}\right)\left(\frac{\partial^2 w}{\partial x^2} + \frac{\partial^2 w}{\partial y^2}\right)\right\}dS_p \quad (8)$$

where S_p is the surface area of the piezo-patches, v(t) is the voltage and D_{ij}^p is the bending stiffness matrix of the patches which can be obtained as:

$$D_{11}^p = \int_{\frac{h_s}{2}}^{\frac{h_s}{2}+h_p}\bar{c}_{11}\,z^2dz = \int_{-\frac{h_s}{2}-h_p}^{-\frac{h_s}{2}}\bar{c}_{11}\,z^2dz = \bar{c}_{11}\left(\frac{h_p^3}{3} + \frac{h_s^2 h_p}{4} + \frac{h_s h_p^2}{2}\right)$$

$$D_{12}^p = \int_{\frac{h_s}{2}}^{\frac{h_s}{2}+h_p}\bar{c}_{12}\,z^2dz = \int_{-\frac{h_s}{2}-h_p}^{-\frac{h_s}{2}}\bar{c}_{12}\,z^2dz = \bar{c}_{12}\left(\frac{h_p^3}{3} + \frac{h_s^2 h_p}{4} + \frac{h_s h_p^2}{2}\right)$$

$$D_{66}^p = \int_{\frac{h_s}{2}}^{\frac{h_s}{2}+h_p}\bar{c}_{66}\,z^2dz = \int_{-\frac{h_s}{2}-h_p}^{-\frac{h_s}{2}}\bar{c}_{66}\,z^2dz = \bar{c}_{66}\left(\frac{h_p^3}{3} + \frac{h_s^2 h_p}{4} + \frac{h_s h_p^2}{2}\right) \quad (9)$$

The applied external work of the point force can be written as:

$$W_p = \iint_S f(t)\delta(x-x0)\delta(y-y0)\,dS \quad (10)$$

where $f(t)$ is the force amplitude, and $\delta(x)$ and $\delta(y)$ are the Dirac delta functions along the x and y axes.

Based on the modal expansion, the relative displacement of piezoelectric patch skin is approximated by a linear combination of the assumed modes as Eq. (11), where $\mu_{ij}(t)$ are the generalized modal coordinates, N is the total number of vibration modes in y and R is the total number of vibration modes x coordinates. Assumed modes are indicated by $U_{ij}W_{ij}(x,y)$, where $W_{ij}(x,y)$ are the trial functions satisfying the boundary conditions, and U_{ij} are the corresponding coefficients.

$$w(x,y,t) = \sum_{i=1}^{N}\sum_{j=1}^{N} U_{ij}\,W_{ij}(x,y)\mu_{ij}(t) \quad (11)$$

$$\left[K_{rn,kl} - \omega_{rn}^2 M_{rn,kl}\right][U_{rn}] = \{0\} \quad (12)$$

Here, assumed mode shape coefficients U_{ij}'s are the eigenvectors and natural frequencies ω_{ij}'s are the square root of the eigenvalues of Eq. (12). Then, the equation of motion of the plate and piezoelectric patches can be derived as Eq. (13) in which w is displacement of the system:

$$m(x,y)\ddot{w} + \Bigg[\{D^s + P(x,y)D^{sp}\}\begin{Bmatrix}\left(\frac{\partial^2 w}{\partial x^2}\right)^2 + \left(\frac{\partial^2 w}{\partial y^2}\right)^2 + 2\upsilon_s\left(\frac{\partial^2 w}{\partial x^2}\frac{\partial^2 w}{\partial y^2}\right) \\ +2(1-\upsilon_s)\left(\frac{\partial^2 w}{\partial x \partial y}\right)^2\end{Bmatrix} + P(x,y){D_{11}}^p\left\{\left(\frac{\partial^2 w}{\partial x^2}\right)^2 + \left(\frac{\partial^2 w}{\partial x^2}\right)^2\right\} + 2P(x,y)\left\{{D_{12}}^p\left(\frac{\partial^2 w}{\partial x^2}\frac{\partial^2 w}{\partial y^2}\right) + 2{D_{66}}^p\left(\frac{\partial^2 w}{\partial x \partial y}\right)^2\right\}\Bigg] + P(x,y)\bar{e}_{31}v(t)\left(\frac{h_s+h_p}{2} - z_0\right)\left(\frac{\partial^2 w}{\partial x^2} + \frac{\partial^2 w}{\partial y^2}\right) = f(t)\delta(x-x0)\delta(y-y0) \quad (13)$$

where ${D_{11}}^p$, ${D_{12}}^p$, ${D_{66}}^p$, D^s and D^{sp} are as follows

$${D_{11}}^p = \bar{c}_{11}\left(\frac{{h_p}^3}{3} + \frac{{h_s}^2 h_p}{4} + \frac{h_s {h_p}^2}{2} - z_0\left(h_p h_s + {h_p}^2\right) + {z_0}^2 h_p\right)$$

$${D_{12}}^p = \bar{c}_{12}\left(\frac{{h_p}^3}{3} + \frac{{h_s}^2 h_p}{4} + \frac{h_s {h_p}^2}{2} - z_0\left(h_p h_s + {h_p}^2\right) + {z_0}^2 h_p\right)$$

$${D_{66}}^p = \bar{c}_{66}\left(\frac{{h_p}^3}{3} + \frac{{h_s}^2 h_p}{4} + \frac{h_s {h_p}^2}{2} - z_0\left(h_p h_s + {h_p}^2\right) + {z_0}^2 h_p\right) \quad (14)$$

$$D^s = \frac{Y_s {h_s}^3}{12(1-{\upsilon_s}^2)}$$

$$D^{sp} = \frac{Y_s}{1-{\upsilon_s}^2}\left(\frac{{h_s}^3}{12} + {z_0}^2 h_p\right) \quad (15)$$

In the separated configuration, each patch is connected to an electric circuit independently as in Figure 1-(a), by applying Kirchhoff's current law for each patch, the circuit equation can be written as Eq. (16):

$${C_p}^k\left(\frac{dv_k(t)}{dt}\right) + \frac{v_k(t)}{(Z_l)_k} = i_k(t), (k = 1,2,\dots,Number\ of\ patches) \quad (16)$$

The relationship between W_{ij} and $v_k(t)$ can be written as Eq. (17):

$$\left[\frac{1}{(Z_l)_k} + j\omega {C_p}^k\right]V_k(t) + j\omega\sum_{n=1}^{N}\sum_{r=1}^{N}\frac{F_0 U_{ij} W_{ij}(x_0,y_0){\tilde{\theta}_{ij}}^k}{{\omega_{ij}}^2 - \omega^2 + (2j)\xi_{ij}\omega_{ij}\omega} + j\omega\sum_{i=1}^{N}\sum_{j=1}^{N}{\tilde{\theta}_{ij}}^k\frac{\sum_{k=1}^{k}{\tilde{\theta}_{ij}}^k v_k(t)}{{\omega_{ij}}^2 - \omega^2 + (2j)\xi_{ij}\omega_{ij}\omega} = 0 \quad (17)$$

Then $v_k(t)$ are the only unknowns in this equation, and they can be derived as:

$$\begin{bmatrix}V_1\\ \vdots\\ V_k\\ \vdots\\ V_n\end{bmatrix} = A^{-1}\begin{bmatrix}b_1\\ \vdots\\ b_k\\ \vdots\\ b_n\end{bmatrix} = \begin{bmatrix}\left\{\frac{1}{(Z_l)_1} + j\omega {C_p}^1 + a'_{11}\right\} & \cdots & a'_{1k} & \cdots & a'_{1n}\\ \vdots & \ddots & \ddots & \ddots & \vdots\\ a'_{k1} & \ddots & \left\{\frac{1}{(Z_l)_k} + j\omega {C_p}^k + a'_{kk}\right\} & \ddots & a'_{kn}\\ \vdots & \ddots & \ddots & \ddots & \vdots\\ a'_{n1} & \cdots & a'_{nk} & \cdots & \left\{\frac{1}{(Z_l)_n} + j\omega {C_p}^n + a'_{nn}\right\}\end{bmatrix} \quad (18)$$

where $a\ and\ b$'s are defined as

$$a'_{ls} = j\omega\sum_{j=1}^{N}\sum_{i=1}^{N}\frac{{\tilde{\theta}_{ij}}^l{\tilde{\theta}_{ij}}^s}{{\omega_{ij}}^2 - \omega^2 + 2j\xi_{ij}\omega_{ij}\omega}, (i,j = 1,\dots,N), (l,s = 1,2,\dots,number\ of\ patches) \quad (19)$$

$$b_k = j\omega\sum_{i=1}^{N}\sum_{j=1}^{N}\frac{F_0 U_{ij} W_{ij}(x_0,y_0){\tilde{\theta}_{ij}}^k}{{\omega_{rn}}^2 - \omega^2 + 2j\xi_{rn}\omega_{rn}\omega}, (k = 1,2,\dots,number\ of\ patches) \quad (20)$$

By finding V, the relative displacement of the plate can be defined as:

$$w(x,y,t) = \sum_{i=1}^{N}\sum_{j=1}^{N}U_{ij}\,W_{ij}(x,y)\left\{\frac{F_0 U_{ij} W_{ij}(x_0,y_0) + \sum_{k=1}^{K}\theta_{ij}A^{-1}[b_1 \ \cdots \ b_k \ \cdots \ b_n]^T}{{\omega_{ij}}^2 - \omega^2 + 2j\xi_{ij}\omega_{ij}\omega}\right\}e^{j\omega t} \quad (21)$$

Table 1. Geometric and material properties

Properties	**Plate**	**Piezoelectric (PZT-5A)**
Young's modulus (GPa)	70	69
Mass density (kg/m3)	2700	7800
Piezoelectric constant (C/m2)	-	-190
Permittivity constant (nF/m)	-	9.57
Damping ratio	0.01	0.01

A. Vibration Metric to evaluate the Shunt Damping Performance

In this study, Equivalent Radiated Power (ERP) is used as the vibration metric to evaluate the shunt damping performance of

the system. ERP is mostly used for vibrating panels which includes information about maximum possible acoustic radiation at the excitation frequencies and it is used to demonstrate the amount of reduction on a structure when some sort of vibration control technique is performed [23]. The ERP can be defined as:

$$\mathrm{ERP}(t) = \frac{1}{2}\rho_f c_f \int_S \dot{w}(x,y,t)^2 dS \tag{22}$$

$$\overline{\mathrm{ERP}(t)} = \frac{1}{2}\rho_f c_f \int_S \dot{\omega}_{rel}(x,y,t)^2 dS \Big/ \frac{1}{2}\rho_f c_f \int_S dS \tag{23}$$

Once the normalized ERP is calculated, percent reduction compared to the open circuit (OC) condition is calculated using Eq. (24). The results are summarized in Section 5.

$$(Percentage\ reduction\ via\ shunt\ damping)_i = 100 \times \left| \frac{\max(\overline{\mathrm{ERP}}_{minimom})_i - \max(\overline{\mathrm{ERP}}_{OC})_i}{\max(\overline{\mathrm{ERP}}_{OC})_i} \right| \tag{24}$$

IV. Results and Discussion

In this section, comparison of the analytical and finite-element models and Electromechanical frequency response functions (FRF) results for connected and separated configurations will be presented. Validation of the analytical model via FEM for a wide range of piezoelectric patch size/thickness is presented in Figure 2 for a single patch. The area ratio is changed from A_p/A_s =0.005 up to A_p/A_s =0.75 (whereas A_p and A_s are the piezoelectric patch and the host structure area, respectively). The thickness ratio is also changed from h_p/h_s =0.1 up to h_p/h_s =1.0

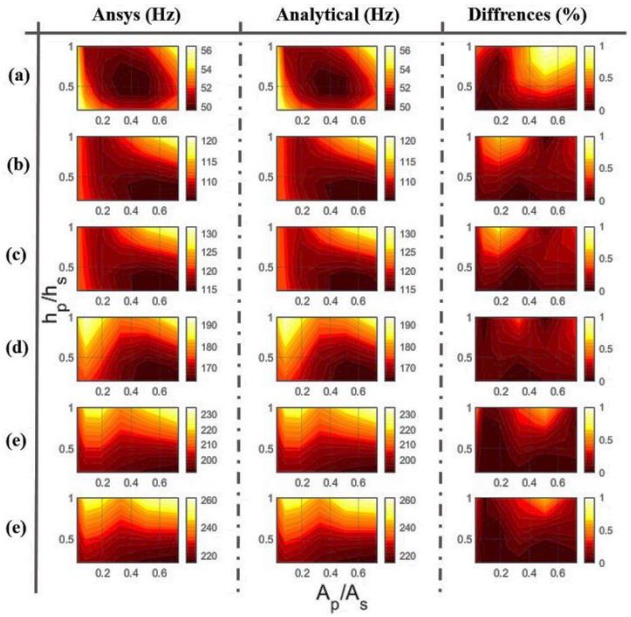

Figure 2: Comparison of the natural frequencies of the first 6 mode shapes (a-e). The first, second and third column shows the Ansys, analytical results, and difference between those results respectively.

Figure 4 shows the comparison of the natural frequencies of the first 6 modes when size and thickness ratios are varied. The first and second column show the Ansys and analytical model results, respectively. The third column shows the percent difference between those results, and it can be observed that for all the first 6 modes of the structure, the difference between the analytical and Ansys model remains within 1%. It shows that the analytical model accurately predicts the natural frequencies of the system when the patch size and thickness are varied.

For a better comparison between cases of separated patches configurations, the $\overline{ERP}$ is investigated for the first 6 modes of the system and 1 patch and 36 patch results are compared in Figure 3. At each step, the is calculated while the R value varied between short circuit (R=100Ω) to open circuit (R=1 MΩ). Then the optimum resistance R_{opt} value is obtained when the $\overline{ERP}$ is minimum over the whole frequency range. The same procedure is repeated for 1 patch and 36 patches. As the numbers of patches are increased, the amplitude of the optimum case is reduced over the full range of frequencies.

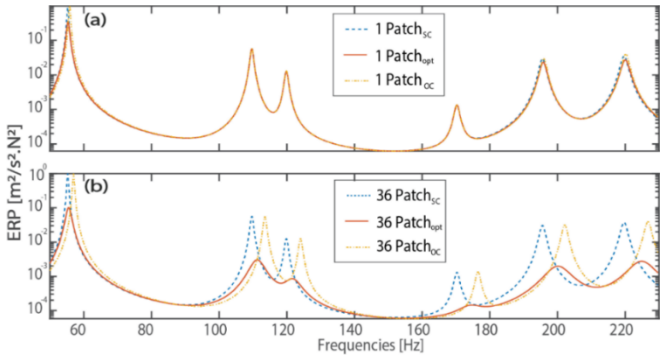

Figure 3: Comparison of $\overline{ERP}$, (a) 1 patch vs (b) 36 patches, dashed blue lines are for the case of SC, solid red lines are for the optimum case and dashed orange ones are for the case of OC.

V. Conclusion

This paper presents a methodology and a formulation for separately shunted piezoelectric patches for achieving higher performance on vibration attenuation. The Rayleigh-Ritz method was used for performing the modal analysis of the electro-mechanical system. The developed model includes mass and stiffness contribution of the piezoelectric patches as well as the electromechanical coupling effect. The vibration performance of the separately shunted piezoelectric patches were compared with the connected configurations. Finally, an optimization study was performed to investigate the effect of the distribution of the resistor values for the first three modes of the structure. The case studies would increase significantly and make the computational cost very high. For that reason, various optimization methods can be explored to reduce the computational cost in future studies.

REFERENCES

[1] A. Erturk and D. J. Inman, Piezoelectric energy harvesting. John Wiley & Sons, 2011.

[2] P. Lahe motlagh, "Novel Techniques for Electromechanical Modeling of Straight/Curved Panels Integrated with Multiple Piezoelectric Patches," 2020. doi: 10.13140/RG.2.2.33665.68964.

[3] P. L. Motlagh, A. Aghakhani, and I. Basdogan, "Passive vibration control of a plate via piezoelectric shunt damping with FEM and ECM," in Smart Materials and Nondestructive Evaluation for Energy Systems IV, 2018, vol. 10601, p. 1060103.

[4] D. Casagrande, P. Gardonio, and M. Zilletti, "Smart panel with time-varying shunted piezoelectric patch absorbers for broadband vibration control," J. Sound Vib., vol. 400, no. Supplement C, pp. 288–304, Jul. 2017, doi: 10.1016/j.jsv.2017.04.012.

[5] P. L. Motlagh, B. Bediz, and I. Basdogan, "A spectral Tchebychev solution for electromechanical analysis of thin curved panels with multiple integrated piezo-patches," J. Sound Vib., vol. 486, p. 115612, 2020.

[6] P. L. Motlagh, M. R. Anamagh, B. Bediz, and I. Basdogan, "Electromechanical analysis of functionally graded panels with surface-integrated piezo-patches for optimal energy harvesting," Compos. Struct., vol. 263, p. 113714, May 2021, doi: 10.1016/j.compstruct.2021.113714.

[7] H. A. Tinoco, L. Robledo-Callejas, D. J. Marulanda, and A. L. Serpa, "Damage detection in plates using the electromechanical impedance technique based on decoupled measurements of piezoelectric transducers," J. Sound Vib., vol. 384, pp. 146–162, Dec. 2016, doi: 10.1016/j.jsv.2016.08.011.

[8] S. P. Beeby et al., "A micro electromagnetic generator for vibration energy harvesting," J. Micromechanics Microengineering, vol. 17, pp. 1257–1265, Jul. 2007.

[9] B. Yang et al., "Electromagnetic energy harvesting from vibrations of multiple frequencies," J. Micromechanics Microengineering, vol. 19, no. 3, p. 035001, Jan. 2009, doi: 10.1088/0960-1317/19/3/035001.

[10] E. O. Torres and G. A. Rincon-Mora, "Electrostatic Energy-Harvesting and Battery-Charging CMOS System Prototype," IEEE Trans. Circuits Syst. Regul. Pap., vol. 56, no. 9, pp. 1938–1948, Sep. 2009, doi: 10.1109/TCSI.2008.2011578.

[11] M. Powering, "portable devices—a review of non-regenerative and regenerative power supply systems with special emphasis on piezoelectric energy harvesting systems KA Cook-Chennault et al 2008," Smart Mater. Struct., vol. 17, p. 043001.

[12] N. W. Hagood and A. von Flotow, "Damping of structural vibrations with piezoelectric materials and passive electrical networks," J. Sound Vib., vol. 146, no. 2, pp. 243–268, Apr. 1991, doi: 10.1016/0022-460X(91)90762-9.

[13] J. Liu, L. Li, X. Huang, and L. Jezequel, "Dynamic characteristics of the blisk with synchronized switch damping based on negative capacitor," Mech. Syst. Signal Process., vol. 95, no. Supplement C, pp. 425–445, Oct. 2017, doi: 10.1016/j.ymssp.2017.03.049.

[14] X. Han, M. Neubauer, and J. Wallaschek, "Improved piezoelectric switch shunt damping technique using negative capacitance," J. Sound Vib., vol. 332, no. 1, pp. 7–16, Jan. 2013, doi: 10.1016/j.jsv.2012.08.001.

[15] M. M. Gozum, A. Aghakhani, G. Serhat, and I. Basdogan, "Electroelastic modeling of thin-laminated composite plates with surface-bonded piezo-patches using Rayleigh–Ritz method," J. Intell. Mater. Syst. Struct., vol. 29, no. 10, pp. 2192–2205, Jun. 2018, doi: 10.1177/1045389X18758189.

[16] H. Yoon, B. D. Youn, and H. S. Kim, "Kirchhoff plate theory-based electromechanically-coupled analytical model considering inertia and stiffness effects of a surface-bonded piezoelectric patch," Smart Mater. Struct., vol. 25, no. 2, p. 025017, 2016, doi: 10.1088/0964-1726/25/2/025017.

[17] A. Erturk and D. J. Inman, "An experimentally validated bimorph cantilever model for piezoelectric energy harvesting from base excitations," Smart Mater. Struct., vol. 18, no. 2, p. 025009, Feb. 2009, doi: 10.1088/0964-1726/18/2/025009.

[18] D. Fritze, S. Marburg, and H.-J. Hardtke, "Estimation of radiated sound power: A case study on common approximation methods," Acta Acust. United Acust., vol. 95, no. 5, pp. 833–842, 2009, doi: 10.3813/AAA.918214.

Biomedical Engineering

Computer Engineering

Electrical and Electronics Engineering

Mechanical Engineering

Mechatronic Engineering

Metallurgical and Materials Engineering

Civil Engineering

ICENTE'22

INTERNATIONAL CONFERENCE ON ENGINEERING TECHNOLOGIES

November 17-19, 2022

Konya/TURKEY

icente.selcuk.edu.tr